NASA/CP—1999-209423

P 788

First NASA/Industry High Speed Research Program Nozzle Symposium

IN-07
ANALYTIC (1+38)
150778

September 1999

The NASA STI Program Office . . . in Profile

Since its founding, NASA has been dedicated to the advancement of aeronautics and space science. The NASA Scientific and Technical Information (STI) Program Office plays a key part in helping NASA maintain this important role.

The NASA STI Program Office is operated by Langley Research Center, the Lead Center for NASA's scientific and technical information. The NASA STI Program Office provides access to the NASA STI Database, the largest collection of aeronautical and space science STI in the world. The Program Office is also NASA's institutional mechanism for disseminating the results of its research and development activities. These results are published by NASA in the NASA STI Report Series, which includes the following report types:

- TECHNICAL PUBLICATION. Reports of completed research or a major significant phase of research that present the results of NASA programs and include extensive data or theoretical analysis. Includes compilations of significant scientific and technical data and information deemed to be of continuing reference value. NASA's counterpart of peer-reviewed formal professional papers but has less stringent limitations on manuscript length and extent of graphic presentations.

- TECHNICAL MEMORANDUM. Scientific and technical findings that are preliminary or of specialized interest, e.g., quick release reports, working papers, and bibliographies that contain minimal annotation. Does not contain extensive analysis.

- CONTRACTOR REPORT. Scientific and technical findings by NASA-sponsored contractors and grantees.

- CONFERENCE PUBLICATION. Collected papers from scientific and technical conferences, symposia, seminars, or other meetings sponsored or cosponsored by NASA.

- SPECIAL PUBLICATION. Scientific, technical, or historical information from NASA programs, projects, and missions, often concerned with subjects having substantial public interest.

- TECHNICAL TRANSLATION. English-language translations of foreign scientific and technical material pertinent to NASA's mission.

Specialized services that complement the STI Program Office's diverse offerings include creating custom thesauri, building customized data bases, organizing and publishing research results . . . even providing videos.

For more information about the NASA STI Program Office, see the following:

- Access the NASA STI Program Home Page at ***http://www.sti.nasa.gov***

- E-mail your question via the Internet to help@sti.nasa.gov

- Fax your question to the NASA Access Help Desk at (301) 621-0134

- Telephone the NASA Access Help Desk at (301) 621-0390

- Write to:
  NASA Access Help Desk
  NASA Center for AeroSpace Information
  7121 Standard Drive
  Hanover, MD 21076

NASA/CP—1999-209423

First NASA/Industry High Speed Research Program Nozzle Symposium

Proceedings of a conference held at and sponsored by
NASA Glenn Research Center
Cleveland, Ohio
November 17–19, 1992

National Aeronautics and
Space Administration

Glenn Research Center

September 1999

This report is a formal draft or working paper, intended to solicit comments and ideas from a technical peer group.

This report contains preliminary findings, subject to revision as analysis proceeds.

Available from

NASA Center for Aerospace Information
7121 Standard Drive
Hanover, MD 21076
Price Code: A99

National Technical Information Service
5285 Port Royal Road
Springfield, VA 22100
Price Code: A99

1999176538

AERO-PERFORMANCE AND AERO-MIXING TESTS OF 2D-CD MIXER/EJECTOR NOZZLES

Part I–Aero-Performance Tests

J.W. Askew and J. Yetter
GE Aircraft Engines
Cincinnati, Ohio

51-07

709509

22P.

Objectives

- **Establish Aerodynamic Performance Characteristics And Design Criteria Of 2D Suppressor Ejector Nozzles For Trade Studies At Take-Off Flight Conditions**
- **Quantify The Effects Of Key Geometric And Aerodynamic Variables On Performance**
- **Test And Evaluate Geometric Parameter Variants Consistent With Those Of Acoustic Test (e.g. Suppressor Area Ratio)**
- **Obtain Detailed Data That Can Be Used Later For Verifying And Validating CFD Codes For Performance Prediction Of 2D Suppressor Ejector Nozzles**

This Chart Shows The Four Objectives Of The Aerodynamic Performance Test Of 2D Mixer/Ejector Nozzles. The Primary Objective Is To Begin Establishing a Design Data Base For 2D Mixer/Ejector Nozzles.

Model Test Facility/Condition NASA Langley 16-Foot Transonic Wind Tunnel

- **$M_\infty = 0 \rightarrow 0.7$; $R_N > 1 \times 10^6$**
- **NPR = 1.5 → 6.0 (Design NPR = 4.0)**
- **$W_{8\ \mathrm{Design}}$ = 15 Lbm/Sec (Cold)**

The Aerodynamic Performance Test Was Conducted In The NASA-Langley 16-Foot Transonic Wind Tunnel at Wind-Off Condition (M = 0) And At Free-Stream Mach Numbers Of 0.32, 0.40, 0.55, and 0.70. The Nozzle Pressure Ratio (NPR) Was Varied From Jet-Off (NPR = 1.0) To A Maximum of 6.0. The Model Was Designed At NPR = 4.0 And A Jet Total Temperature of 75°F. All Tests Were Conducted With A Jet Total Temperature of Approximately 75°.

NASA Langley Air-Powered Nacelle/Mixer-Ejector Nozzle Installation

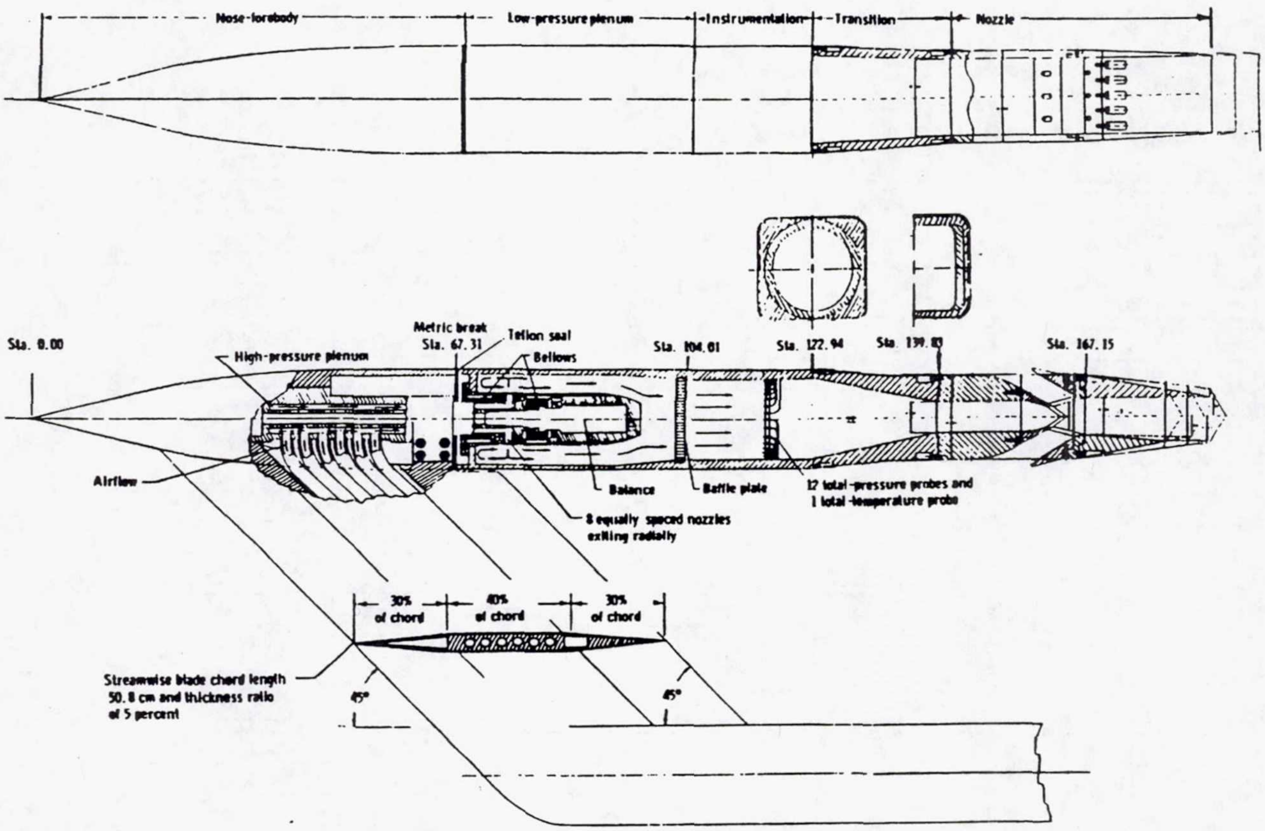

The Single-Engine (Air-Powered) Nacelle/Mixer-Ejector Nozzle Model Was Supported In The 16-Foot Tunnel By A Sting/Strut Support System. This Chart Shows A Sketch Of The Model Installation.

HSCT 2D Mixer/Ejector Nozzle Test Configurations

Config. no.	Configuration Code	Suppressor Area Ratio (SAR)	Chute Expansion Ratio (CER)	Mixing Area Divergence Area Ratio (MAD)	Flap Length, (L) inch	Center-Body (CB)	A8 sqr in	Notes
1	1110	2.80	1.22	1.20	7.40	Off	9.31	AOA = 0, +5 & -5 deg
3	1210			1.40	7.40	Off	9.31	AOA = 0, +5 & -5 deg
4	1220			1.40	11.10	Off	9.31	AOA = 0 deg
2	1120 *			1.20	11.10	Off	9.31	AOA = 0 deg
17	1121	3.17	1.22	1.20	11.10	Short	7.69	AOA = 0 deg
18	1122			1.00	11.10	Long	7.69	AOA = 0 deg
19	1221			1.40	11.10	Short	7.69	AOA = 0 deg
20	1222			1.20	11.10	Long	7.69	AOA = 0 deg
5	2110	2.80	1.38	1.20	7.40	Off	9.31	AOA = 0, +5 & -5 deg
7	2210			1.40	7.40	Off	9.31	AOA = 0, +5 & -5 deg
8	2220			1.40	11.10	Off	9.31	AOA = 0 deg
6	2120			1.20	11.10	Off	9.31	AOA = 0 deg
21	2121	3.17	1.38	1.20	11.10	Short	7.69	AOA = 0 deg
22	2122			1.20	11.10	Long	7.69	AOA = 0 deg
23	2221			1.40	11.10	Short	7.69	AOA = 0 deg
24	2222			1.20	11.10	Long	7.69	AOA = 0 deg
9	3110	3.30	1.22	1.20	7.40	Off	8.04	AOA = 0, +5 & -5 deg
11	3210			1.40	7.40	Off	8.04	AOA = 0, +5 & -5 deg
12	3220			1.40	11.10	Off	8.04	AOA = 0 deg
10	3120			1.20	11.10	Off	8.04	AOA = 0 deg
25	3121	3.88	1.22	1.20	11.10	Short	6.42	AOA = 0 deg
26	3122			1.00	11.10	Long	6.42	AOA = 0 deg
27	3221			1.40	11.10	Short	6.42	AOA = 0 deg
28	3222			1.20	11.10	Long	6.42	AOA = 0 deg
13	4110	3.30	1.38	1.20	7.40	Off	8.04	AOA = 0, +5 & -5 deg
15	4210			1.40	7.40	Off	8.04	AOA = 0, +5 & -5 deg
16	4220			1.40	11.10	Off	8.04	AOA = 0 deg
14	4120			1.20	11.10	Off	8.04	AOA = 0 deg
29	4121	3.88	1.38	1.20	11.10	Short	6.42	AOA = 0 deg
30	4122			1.00	11.10	Long	6.42	AOA = 0 deg
31	4221			1.40	11.10	Short	6.42	AOA = 0 deg
32	4222			1.20	11.10	Long	6.42	AOA = 0 deg

** Additional Configuration: 1320 - MAD=1.0*
1420 - MAD=0.8

The 2D Mixer/Ejector Nozzle Models Were Designed To Represent The Takeoff Flight Condition Of A GEAE HSCT Nozzle Concept. Five Major Nozzle Geometric Variables Were Evaluated During The Performance Test, And Are Defined In The Next Two Charts. Thirty-Four (34) Model Configurations Were Tested. Tests With Angle-Of-Attack Of 0, +5, And -5 Were Conducted.

2D Mixer/Ejector Nozzle Concept

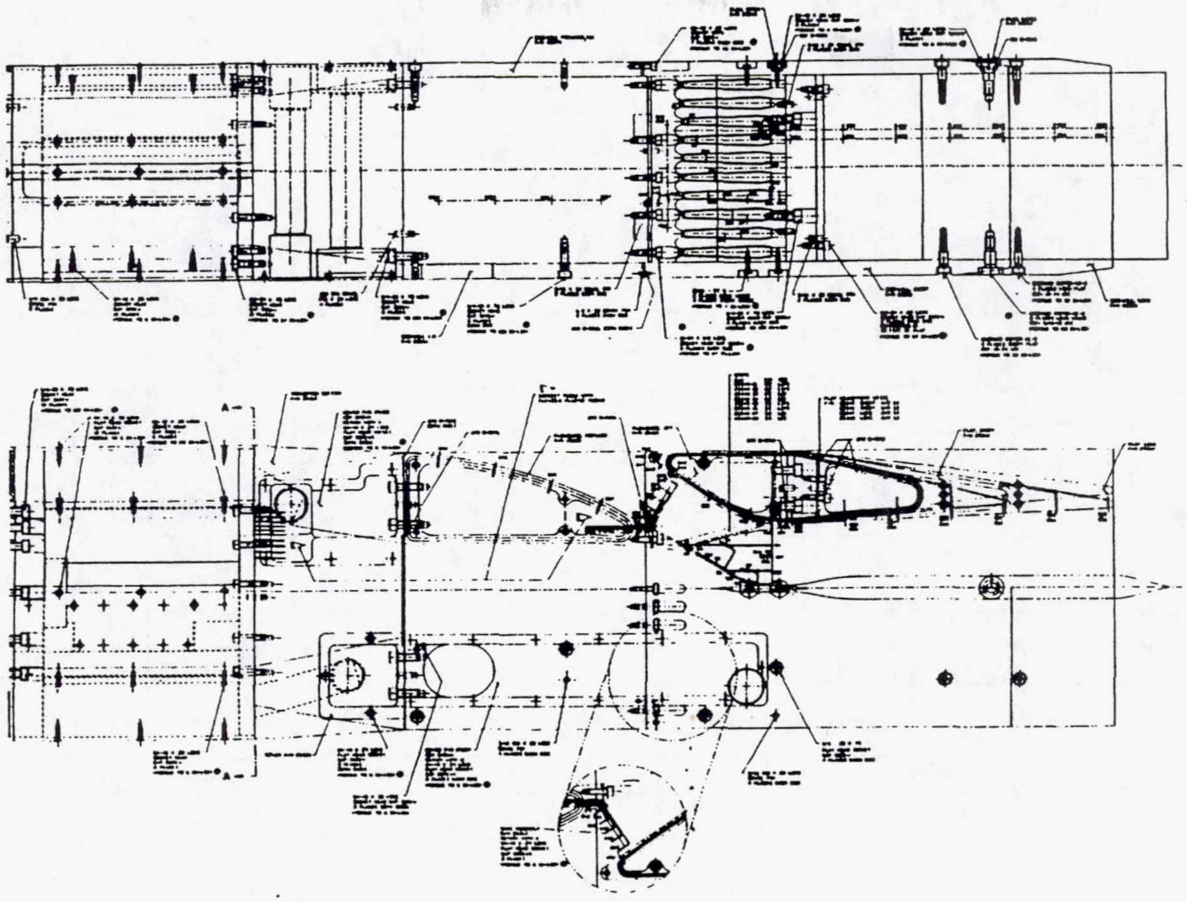

This Chart Shows The 2D Mixer/Ejector Nozzle Model Design And Instrumentation Layout. Sixty-Seven (67) Pressure Measurements Were Taken During Each Test Including 15 Total Pressure Measurements Located In The Ejector Inlet. These Total Pressures, Along With Local Static Pressures, Were Used To Calculate The Secondary Flow Entrainment. This Chart, Also, Shows How Both Center-Bodies Were Installed In The Model During Testing.

Configuration/Mach Number Comparison

MAD=1.2, L_F=11.10", w/o C.B.

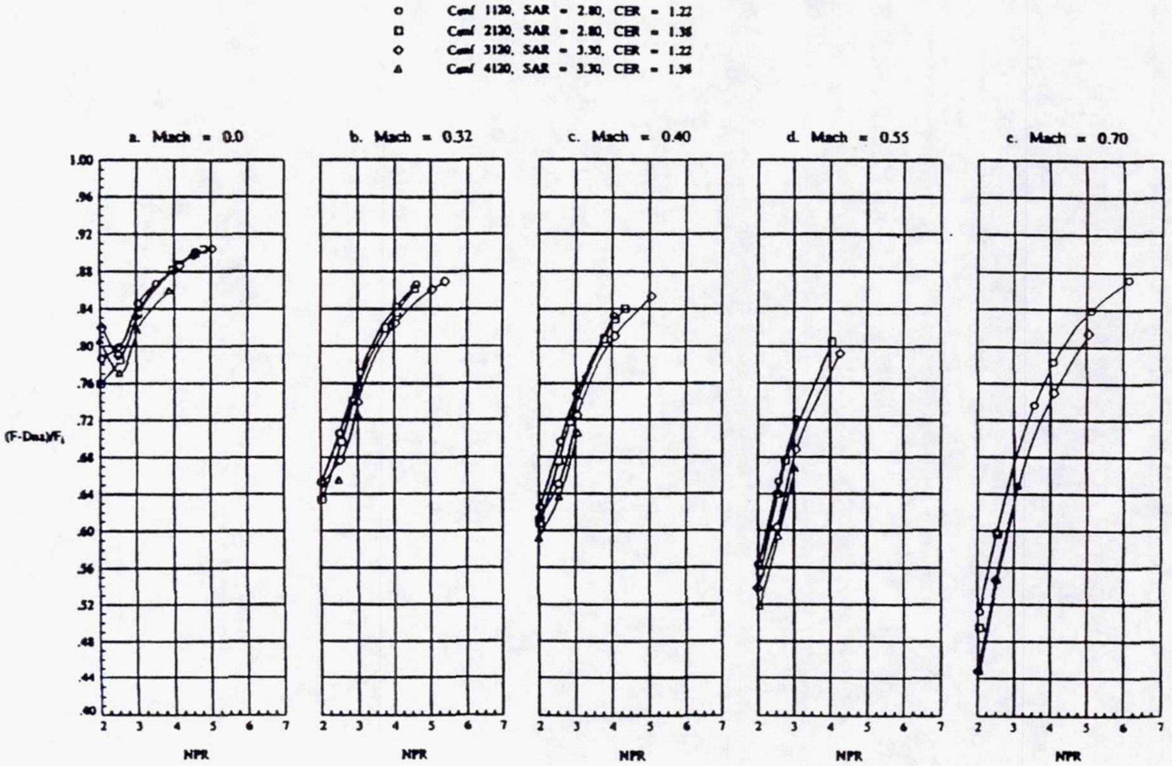

Selected Test Data Are Presented In The Following Charts.

This Chart Shows The Comparison Of The Nozzle Performance (Thrust-Minus-Drag Coefficient) As A Function Of The Freestream Mach Numbers, And NPR For The Configurations That Have Mixing Area Divergence (MAD) Equal to 1.2, Long Nozzle Flap Length (LF), And No Centerbody. At Mach Equal 0.0, The Nozzle Performance Shown Is the Gross Thrust Coefficient (Cfg).

Configuration/Mach Number Comparison

MAD=1.2, L_F=11.10", w/o C.B.

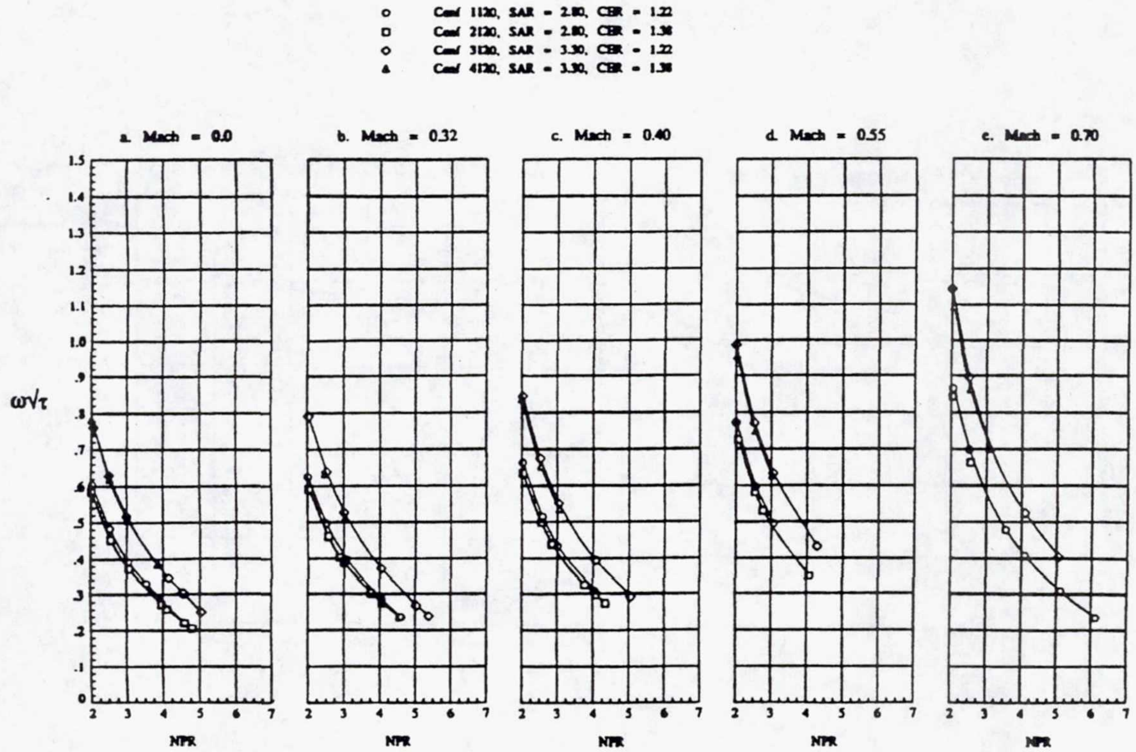

Shown In This Chart Is Comparison Of The Nozzle Entrainment Or Pumping As A Function Of Freestream Mach Number And NPR, For The Configurations That Have MAD Of 1.2, Long Nozzle Flap, And No Centerbody. The Entrainment Is Defined In Corrected Mass Flow Rate Ratio

$$\left(\frac{W_S}{W_P} \sqrt{\frac{T_{TS}}{T_{TP}}} = \omega\sqrt{\tau} \right)$$

Where:

W_S = **Secondary Mass Flow Rate**
W_P = **Primary Mass Flow Rate**
T_{TS} - **Secondary Total Temperature**
T_{TP} = **Primary Total Temperture**

Ejector Static Pressure Distribution
Effect Of Nozzle Pressure Ratio (NPR)

SAR=2.8, MAD=1.2, CER=1.38, L_F=11.10", w/o C.B., M=0.32

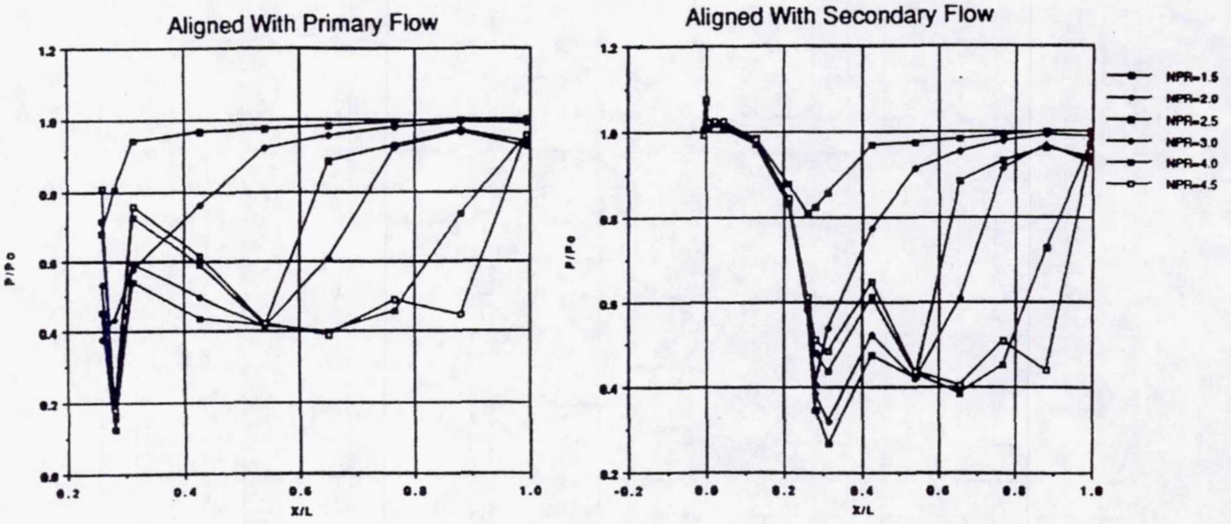

This Chart Shows The Ejector (Nozzle Flap) Pressure Distribution As NPR Varies. The Left-Hand-Side Graph Is A Plot Of The Pressures Aligned With The Primary Flow Element Of the Mixer. The Right-Hand-Side Graph Is A Plot Of The Pressures Aligned With The Secondary Flow Element Of The Mixer. The Mixer Exit Plane Is Located At X/L Equal To .264. The Plots Show How The Flows In The Ejector Expands And Recompresses Inside The Ejector. This Flow Characteristics Was Found To Be A Function Of NPR and MAD.

Ejector Static Pressure Distribution Effect Of Mach Number (M)

SAR=2.8, MAD=1.2, CER=1.38, L_F=11.10", w/o C.B., M=0.32

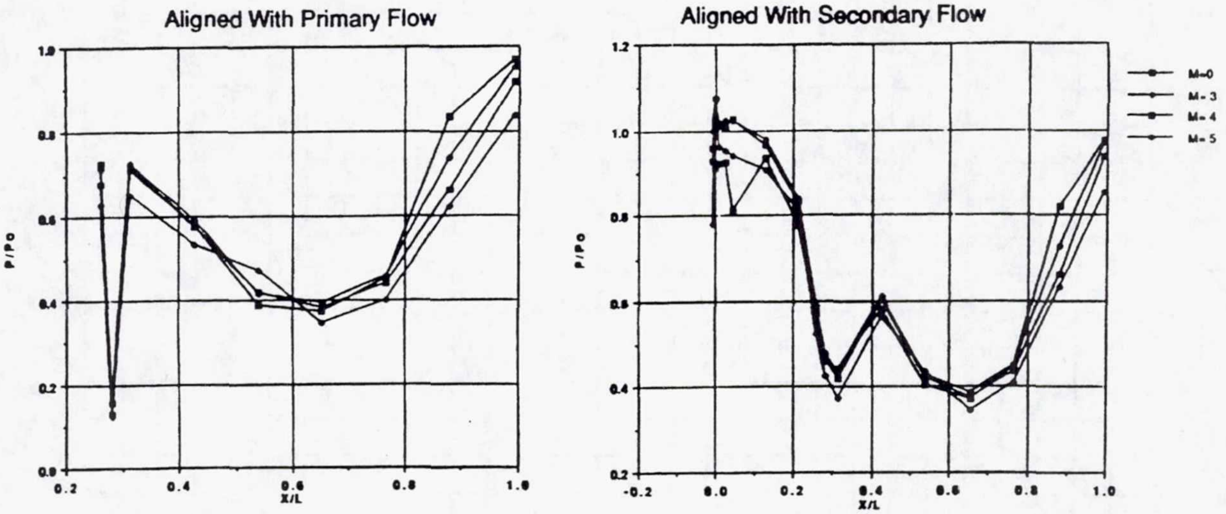
Aligned With Primary Flow

Aligned With Secondary Flow

The Static Pressure Distribution Inside The Ejector As A Function Of Freestream Mach Number Is Shown In This Chart. Again, The Left-Hand-Side Graph Plots The Pressures Aligned With The Primary Flow Element Of The Mixer, And The Right-Hand-Side Graph Plots The Pressures Aligned With The Secondary Flow Element Of The Mixer. The Pressure Distribution Varies Slightly With Mach Number.

Configuration/Mach Number Comparison

MAD=1.2, L_F=11.10", w/ Long C.B.

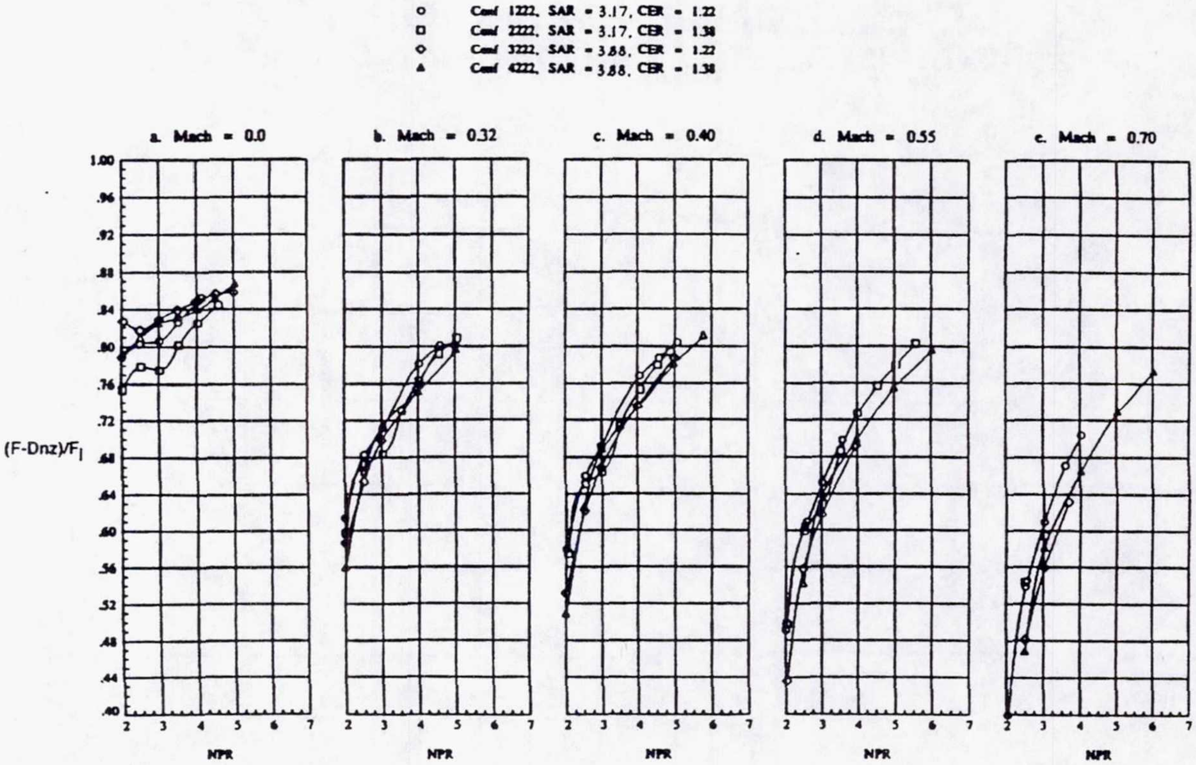

This Chart Shows The Comparison Of The Nozzle Performance As A Function Of Freestream Mach Number And NPR. The Configurations With The Long Centerbody, MAD Of 1.2, And Long Flap Length, Are Presented.

Configuration/Mach Number Comparison

MAD=1.2, L_F=11.10" w/ Long C.B.

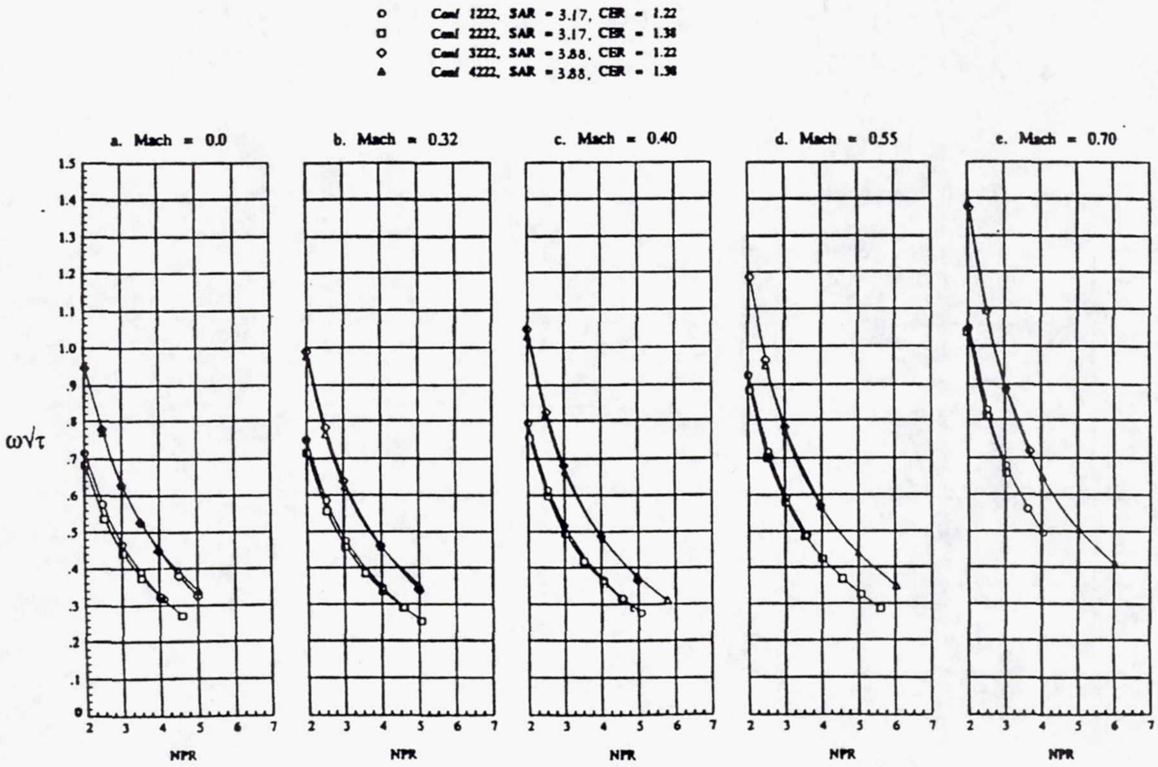

The Corrected Mass Flow Rate Ratio (Describing Ejector Entrainment) For The Configurations With The Long Centerbody, MAD = 1.2, And Long Flap Length, Is Shown In This Chart As A Function Of Freestream Mach Number And NPR.

Ejector Static Pressure Distribution Effect Of Nozzle Pressure Ratio (NPR)

SAR=3.17, MAD=1.2, CER=1.38, L_F=11.10", Long C.B., M=0.32

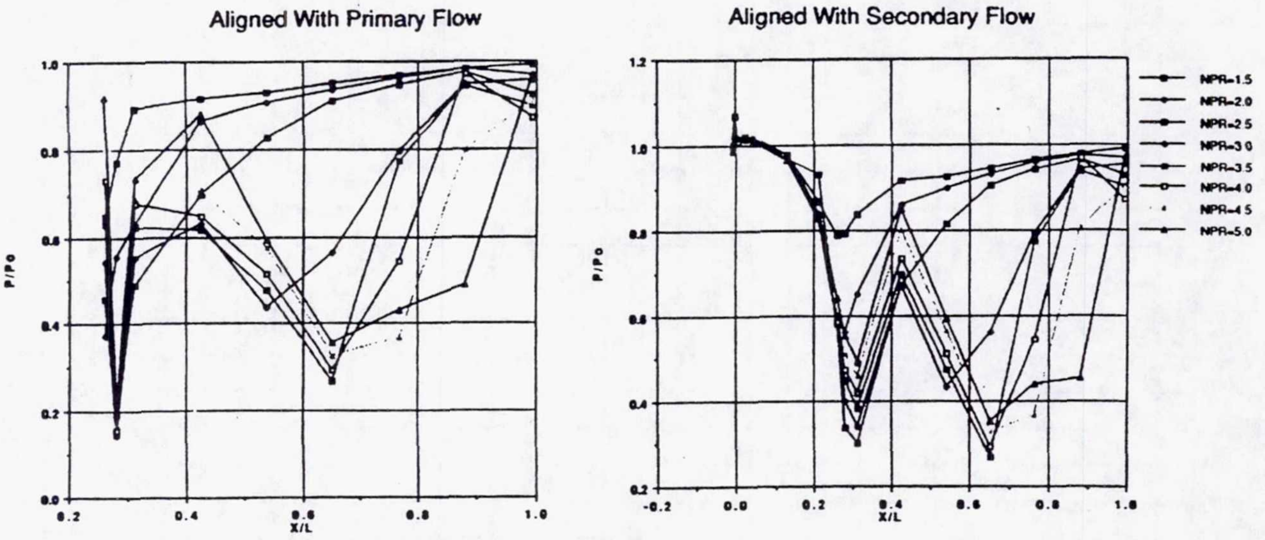

Ejector (Nozzle Flap) Pressure Distribution As A Function Of NPR For A Configuration With The Long Centerbody At Freestream Mach Number of 0.32. Again Note The Expansions And Recompressions.

Ejector Static Pressure Distribution
Effect Of Mach Number (M)
SAR=3.17, MAD=1.2, CER=1.38, L_F=11.10", Long C.B., NPR=4.0

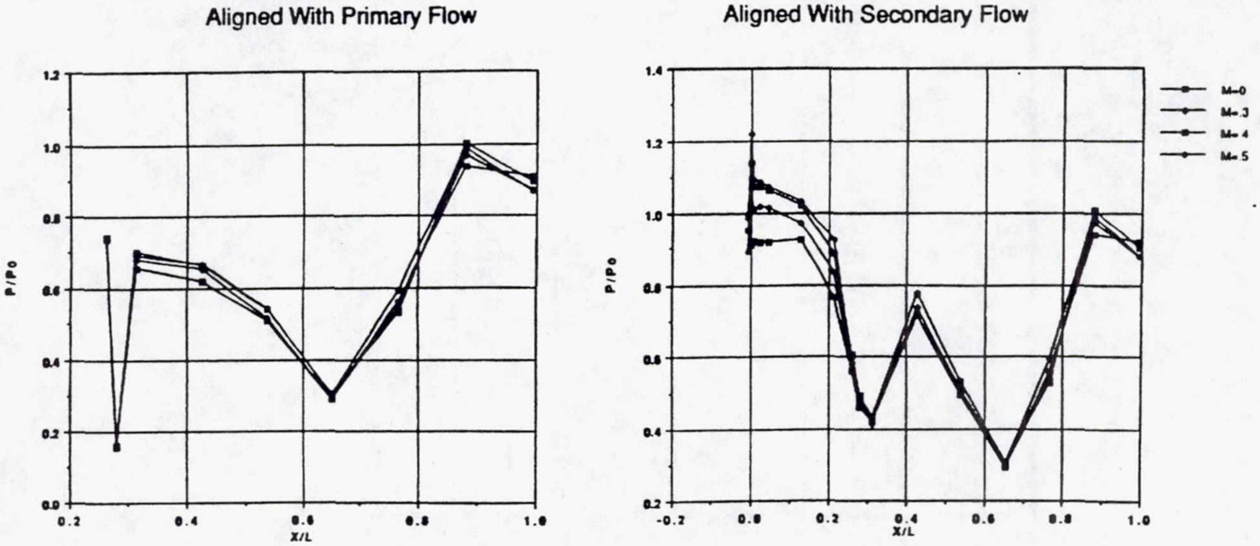
Aligned With Primary Flow

Aligned With Secondary Flow

This Chart Shows The Effect Of Mach Number On The Ejector Pressure Distribution For A Long Centerbody Configuration. Note That Mach Numbers Have Small Effects On The Strengths Of The Flow Expansions And Recompressions.

Thrust Coefficient Losses Stackups (Estimated)

Conf. 2110, NPR=4.0

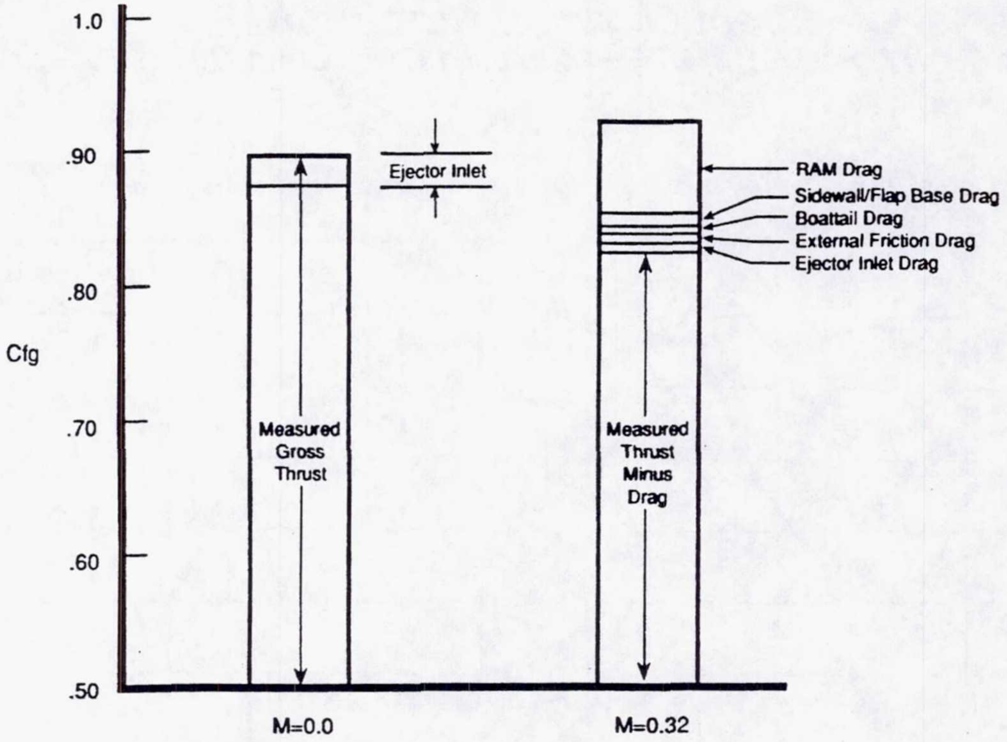

The Impact Of Drag Losses In Nozzle Efficiency (Cfg) As Contributed By Different Nozzle Components Is Shown In This Chart. At Freestream Mach Number Of 0.32, The Different Drag Components Are Stacked On The Measured Thrust-Minus-Drag Force And Compared With The Static Measured Thrust. For These High Flow Ejector Nozzles, Ram Drag Is The Largest Loss Contributor At Flight Conditions. To Improve The Isolated Installed Performance Of The Nozzle Will Require The Reduction In Friction, Boattail, Ejector Inlet, And Base Drags, Which Are Based On Nozzle Design Parameter.

Thrust Coefficient Comparison And Loss Stackups (Estimated)

M=0.0, NPR=4.0

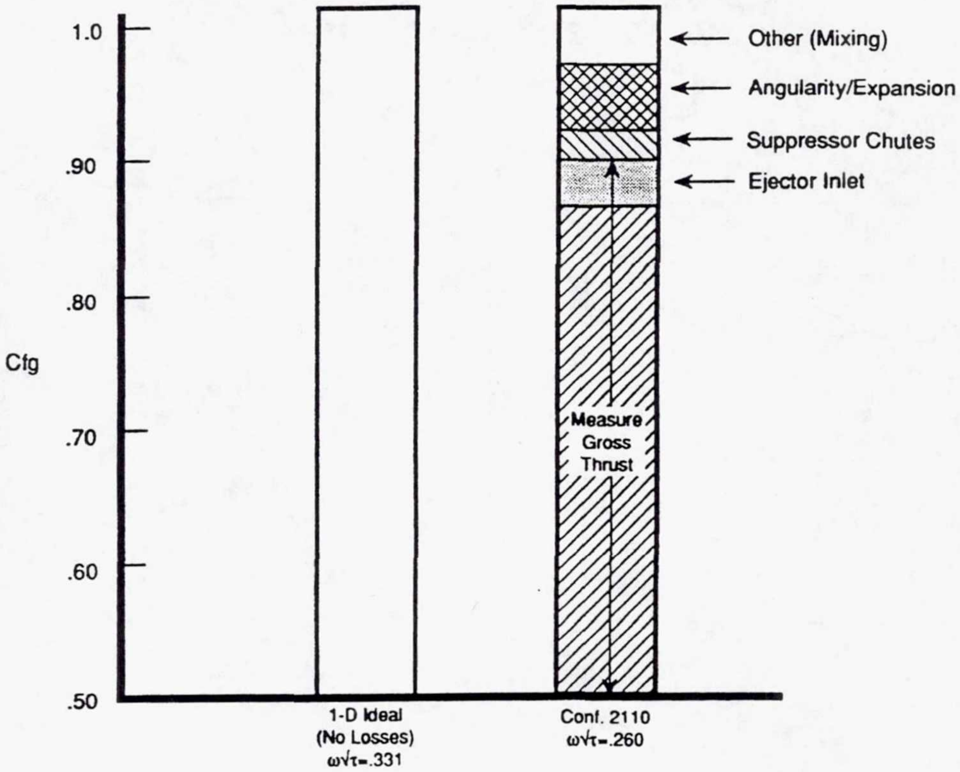

This Chart Compared The Stack Up In Measured performance With A One-Dimensional (1D) No Loss Analysis (Assuming Constant Area Mixing). Nozzle Internal Loss Mechanisms Are Due To Suppressor Chutes, Ejector Inlet, Angularity/Expansion, Mixing and Internal Shocks (Recompressions). To Improve Performance, Losses Associated With These Mechanisms Will Have To Be Minimized. Also, Note That For A Given Ejector Size, Secondary Flow Entrainment Is About 80% Of The Ideal Flow Entrainment.

Effect Of Mixing Area Divergence (MAD)

SAR=2.8, CER=1.22, Long Flap, M=0.0

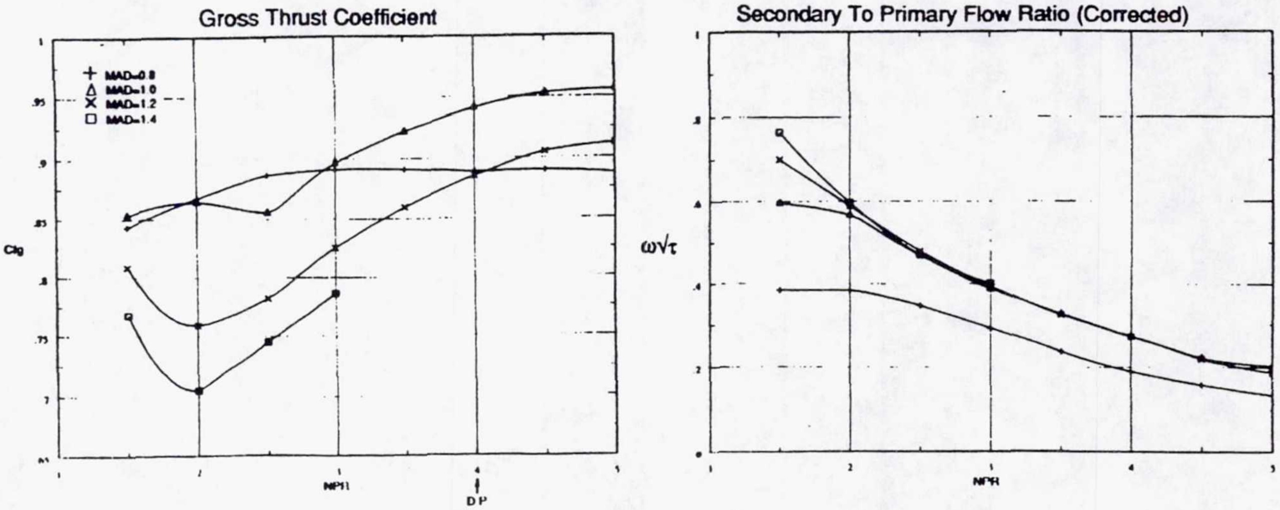

Ejector Area Sizing Is Critical To The Performance And Secondary Flow Entrainment Of Supersonic Ejector Nozzles. Shown In This Chart Is The Effect Of The Ejector MAD On The Nozzle Performance (Cfg) And Flow Entrainment (ω√τ) As NPR Varies. In The Left-Hand-Side Graph, It Can Be Seen That To Obtain Optimum Cfg, The Ejector Area Ratio Has To Be Optimized To Provide The Correct Flow Area Distribution To Match The Combined Flows Inside The Ejector In Order To Properly Diffuse The Combined Flow To The Appropriate Nozzle Back (Ambient) Pressure. From The Cfg Curve, At MAD = 0.8, The Nozzle Is Operating In A Typical Under-Expanded Region At The Design Point (Exit pressure Is Higher Than Back Pressure). However, As The MAD Is Increased To 1.0 The Cfg Increases. This Condition Moves Into The Over-Expanded Region (Small Over-Expansion) Region Which Means The Exit Pressure Is Lower Than The Nozzle Back Pressure. Furthermore, As MAD Continues To Increase, Cfg Decreases. This Is Due To The Exit Pressure Becoming Much Lower Than The Back Pressure And Recompression Occurs Inside The Nozzle. The Right-Hand-Side Graph Shows That Flow Entrainment Increases As MAD Increases Until The Secondary Flow Becomes Compounded Compressible Choked, Then, Entrainment Remains Constant With Increasing MAD. This Is Caused By The Ejector Moving From A Subsonic Operating Regime To A Supersonic Operating Regime.

Effect Of Mixing Area Divergence (MAD)

SAR=2.8, CER=1.22, Long Flap, M=0.0, NPR=4.0

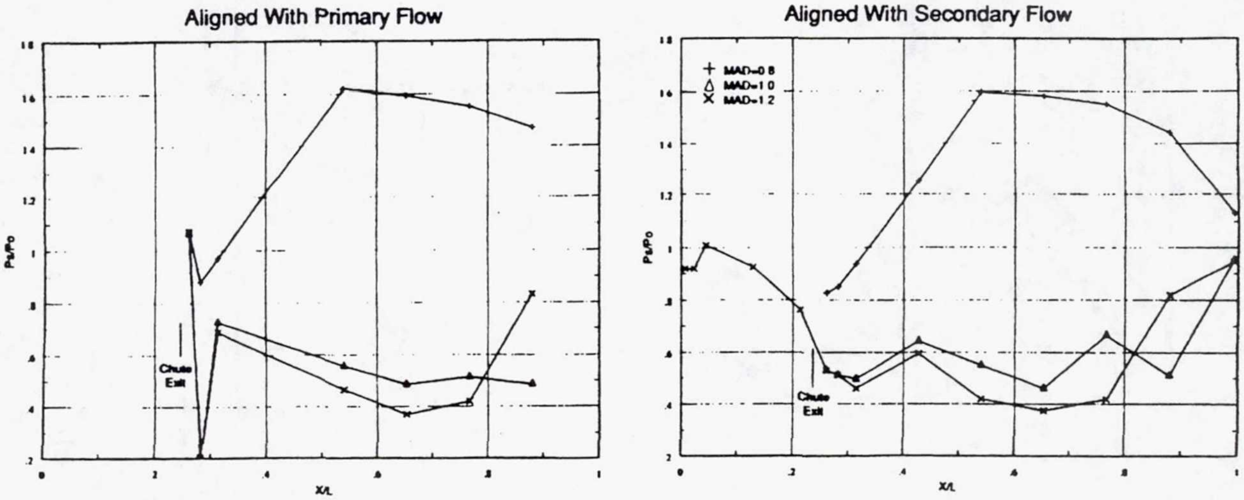

The Effect Of MAD On The Ejector Pressure Distribution Is Shown In This Chart. At MAD Of 0.8, It Can Be Seen That The Ejector Is Operating In A Subsonic Regime, Where The Flow Expands A Little As It Leaves The Mixer Chutes And Then Diffuses Through The Ejector, Then Expands Back To The Nozzle Back Pressure (Under-Expanded). At MAD of 1.0 and 1.2 The Flow Greatly Expands Downstream Of The Mixer Chutes, Then, Is Recompressed, And Is Followed By Another Expansion. For These Two Conditions, The Flow Has To Recompress Inside The Ejector To Obtain A Pressure Equivalent To The Nozzle Back Pressure. For MAD Of 1.2, This Recompression Is Much Stronger And Occurs Further Upstream Of The Ejector Exit.

Effect Of Mixing Area Divergence (MAD)

SAR=2.8, CER=1.22, Long Flap, M=0.0

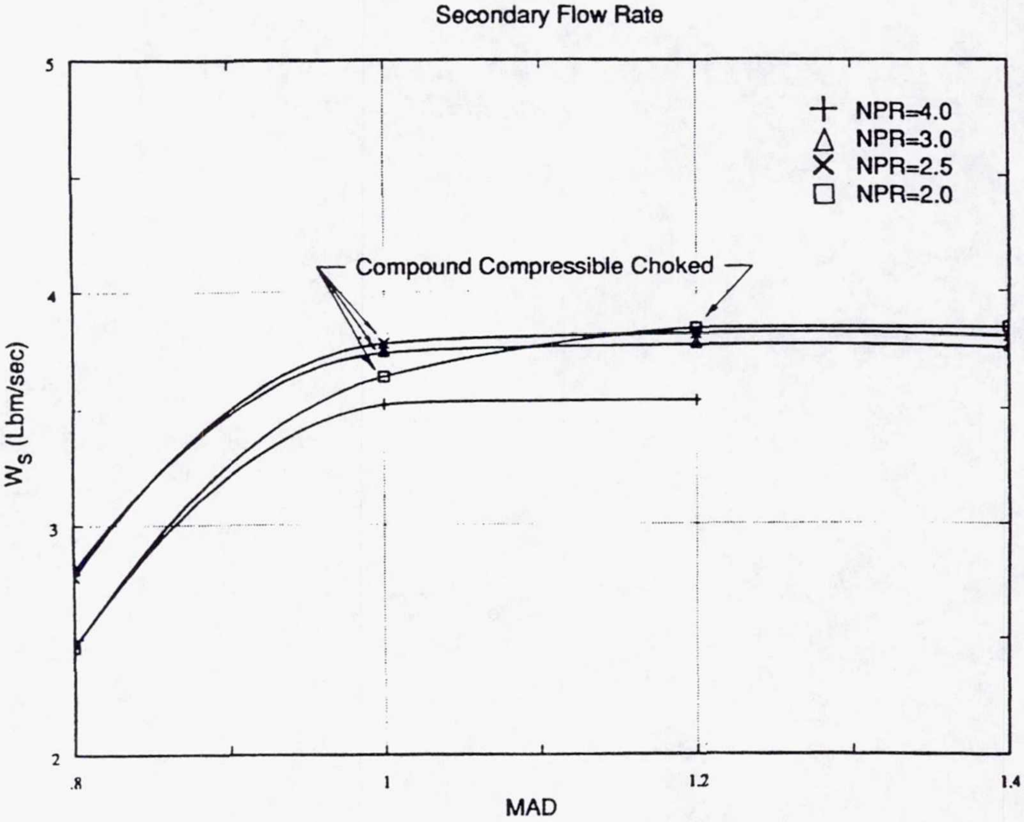

This Chart Demonstrates The Compound Compressible Choking Characteristics Of The 2D Mixer/Ejector Nozzle. Note That At The Design Point (NPR = 4.0), The Nozzle Becomes Choked At A MAD Of A Little Less Than 1.0. The Curve Between MAD Of 0.8 And 1.0 Is Spline Fitted.

Effect Of Chute Expansion Ratio (CER)

SAR=3.3, M=0.0

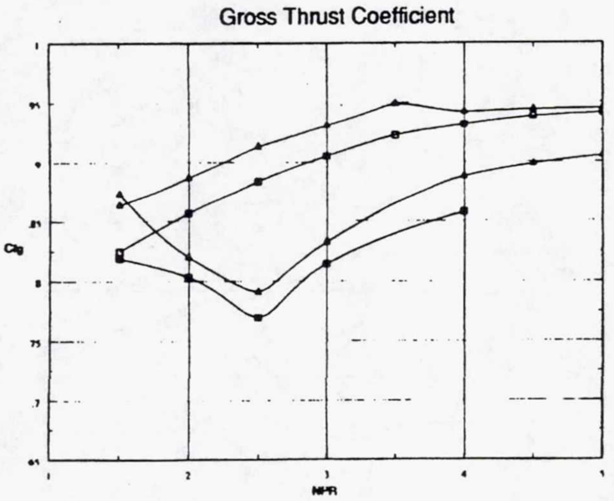
Gross Thrust Coefficient

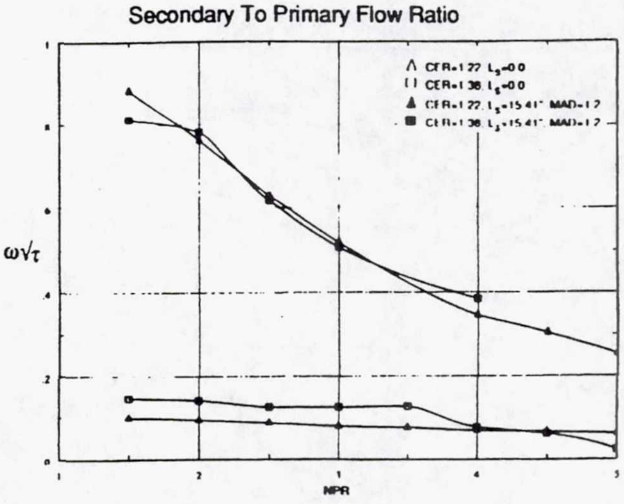
Secondary To Primary Flow Ratio

To Increase The Amount Of Secondary Flow Entrainment, it Was Theorized That A Lower Primary Flow Static Pressure At The Exit Of The Mixer Chutes Would Be Necessary. To Achieve This Lower Pressure, A Larger Primary Flow (Chute Expansion Ratio) (CER) Was Tested. This Chart Shows The Effect Of CER On Performance And Flow Entrainment As NPR Varies. Also, Shown Are The Effects With and Without An Ejector Shroud. The Left-Hand-Side Graph Shows That If CER Is Increased From 1.22 To 1.38, Cfg Will Decrease. This Is Apparent With And Without An Ejector Shroud. Also, Note That The Cfg Without An Ejector Shroud Is Greater Than The Cfg With An Ejector Shroud With A MAD = 1.2. This Means That The Ejector Is Not Providing Thrust Augmentation But Instead It Is A Loss Contributor (For This Configuration). However, From The Right-Hand-Side Graph, As NPR Is Increased The Secondary Flow Entrainment Increases.

Effect Of Ejector Shroud Length (L_S)

SAR=3.3, CER=1.22, M=0.0

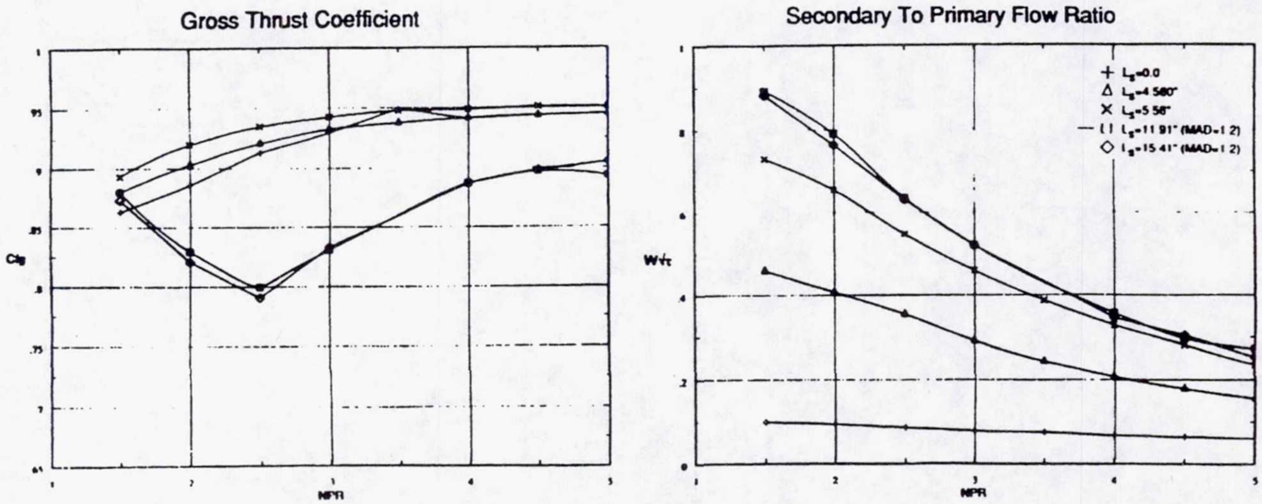

This Chart Shows The Effect Of Ejector Shroud (Ls) Length On Performance And Flow Entrainment. When Ls Is 0.0 (No Ejector Shroud) The Nozzle Cfg Is Relatively Good And Entrainment Is Minimum. When The Inlet Scoop Is Added (Ls-4.58") Performance Is Somewhat Reduced While Flow Entrainment Is Increased. Adding A One Inch Nozzle Flap (Ls=5.58") With A Constant Area Ratio To The Scoop, Increases Cfg and Entrainment. Finally, By Adding Longer Flap Length And Nozzle Divergence, Secondary Flow Entrainment Increases And Then Becomes Constant, And Cfg Decreases With Increasing Flap Length (This Is Due To The Internal Losses In The Ejector Caused By Overexpansion).

The Following Two Charts Describe The Initial Conclusions Made From The Test Results.

Conclusions

- **Ejector Pumping Goal Was Achieved (W_S/W_P 0.6 → 0.8 @ T_{T8}=1950°R)**
- **Ejector Pumping Is A Function Of MAD (or A_9) And NPR Until Compounded Compressible Choked**
- **Over-Expansion Cause Nozzle Instability (Internal Shocks)**
- **Good Ejector Inlet Recovery (90% → 95%)**

• SAR Effect: 2.8 → 3.3	**– 3.1% Decrease In Thrust Coefficient** **– 31.7% Increase In Secondary Flow Entrainment**
• CER Effect: 1.22 → 1.38	**– 1.7% Decrease In Thrust Coefficient** **– 1.8 % Decrease In Secondary Flow Entrainment**
• L_F Effect: 7.40" → 11.10"	**– .72% Decrease In Thrust Coefficient** **– .60% Increase In Secondary Flow Entrainment**
• Flight Effect: M=0.0 → 0.32	**– 5% Decrease In Thrust Coefficient (Measured)** **– 5.8% Increase In Secondary Flow Entrainment**
• MAD Effect: 1.2 → 1.0	**– 6.5% Increase In Thrust Coefficient (Static)** **– Constant Secondary Flow Entrainment (Compounded Compressible Choked)**

Recommendations

- **For Desired Secondary Flow Entrainment, Ejector Will Have To Be Optimized (MAD) To Obtain Optimal Performance**
- **Primary (Core) Flow Over-Expansion Is To Be Avoided To Obtain Optimal Performance**
- **Emphasis Must Be Placed On Improving Nozzle Gross Thrust Coefficient, Since Large Flight Effects Exist (i.e., Ram Drag)**
- **Tests Should Be Re-Conducted With Optimal Ejector Configurations To Determine/Confirm Effects Of SAR, CER, And L_F**

This Chart Presents The Recommendations As A Result Of This Test Program.

1999176539

AERO-PERFORMANCE AND AERO-MIXING TESTS OF 2D-CD MIXER/EJECTOR NOZZLES

Part II–Sample of Aero-Mixing Test Data and Inference

V.G. Mengle, H-W. Shin, J.W. Askew, and C.E. Whitfield
GE Aircraft Engines
Cincinnati, Ohio

52-07

409510

14P

ARL Test Objectives

- **Better Qualitative & Quantitative Understanding of the Flowfield**
  - **mixing process**
  - **shock structures**

Both Inside & Outside of the scaled 2D Mixer/Ejector Nozzle Models

- **Provide Aerodynamic Design Data Base**

- **Provide Database for CFD-code Validation**

Methods/Instruments

- **2-Component Laser Velocimetry Survey - Internal and External**
- **Kiel Probe Survey (Total P & T) - Exit Plane**
- **Static Pressure Taps - Ejector Walls, Chutes, Inlet Ramp**

Test Objectives: The tests on suppressor/ejector nozzle models conducted in G.E.'s Aerodynamic Research Laboratory (ARL) are supposed to complement the aero-performance tests, reported in Part I, and the acoustic tests soon to be conducted in G.E.'s Cell 41. In particular, the tests were done with the above three objectives in mind, namely, to improve the understanding of internal and external fluid-dynamics of such nozzles, its aerodynamic characteristics (chute and ram drag etc.) and, to a lesser extent, CFD-code validation. *In this brief paper, however, we focus only on the first objective, namely, a better understanding of the flow-field in terms of the internal mixing process and internal shock structures.* Moreover, due to brevity of presentation only a limited amount of data is shown to give a flavor of the test results and, hence, only limited conclusions are drawn.

Methods/Instruments: The LV system, which is described later, gives the projection of the mean velocity vector on the vertical plane and a measure of its variability. Laser velocimetry surveys were done inside the ejector as well as in the external plume. In addition, a Kiel probe was used to survey total pressure and total temperature at the ejector exit plane and static pressure taps were used on ejector flaps/walls, chutes and the inlet ramp.

Schematic of a Typical 2D-CD Mixer/Ejector Model

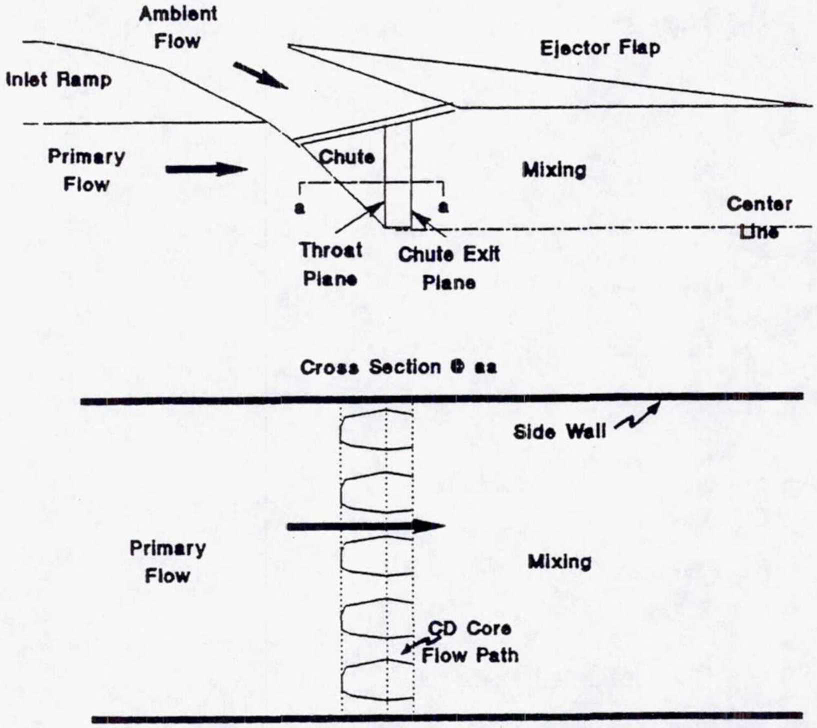

The above figure shows, from a fluid-dynamic perspective, the schematic of a typical suppressor/ejector nozzle model used in ARL tests. It is essentially a "two-dimensional (2D)" or rectangular nozzle with a top and bottom row of ten suppressors or chutes (five per row) and a rectangular box-type ejector. There are four hot jets of primary fluid through the convergent-divergent (CD) passages between the five chutes and two half-width CD primary jets at the two sides touching the side-walls. Notice that the primary flow path diverges away from the nozzle center-line (on its upper side), especially, after the throat plane until it meets the ejector flap where it forms a concave corner. The ambient fluid flows through the passage formed by the inlet ramp and the flush inlet of the ejector flaps from top and bottom to enter the ten chutes. The primary and the secondary flows then interact/mix with each other downstream of the chute exit plane inside the ejector and eventually exit it to form the external plume. In these tests, the following geometrical parameters were varied: * Chutes - Suppressor Area Ratio (SAR), defined as the ratio of the sum of primary and secondary flow areas to the secondary flow area at the chute exit plane; CD or convergent primary flow passage; top and bottom chutes aligned or non-aligned; gap or no gap between top and bottom chute-rows * Ejector - Mixing Area Ratio (MAR), defined as ejector exit area to reference mixing area (essentially variable flap angle); flap length; inlet lip (flush or scoop).

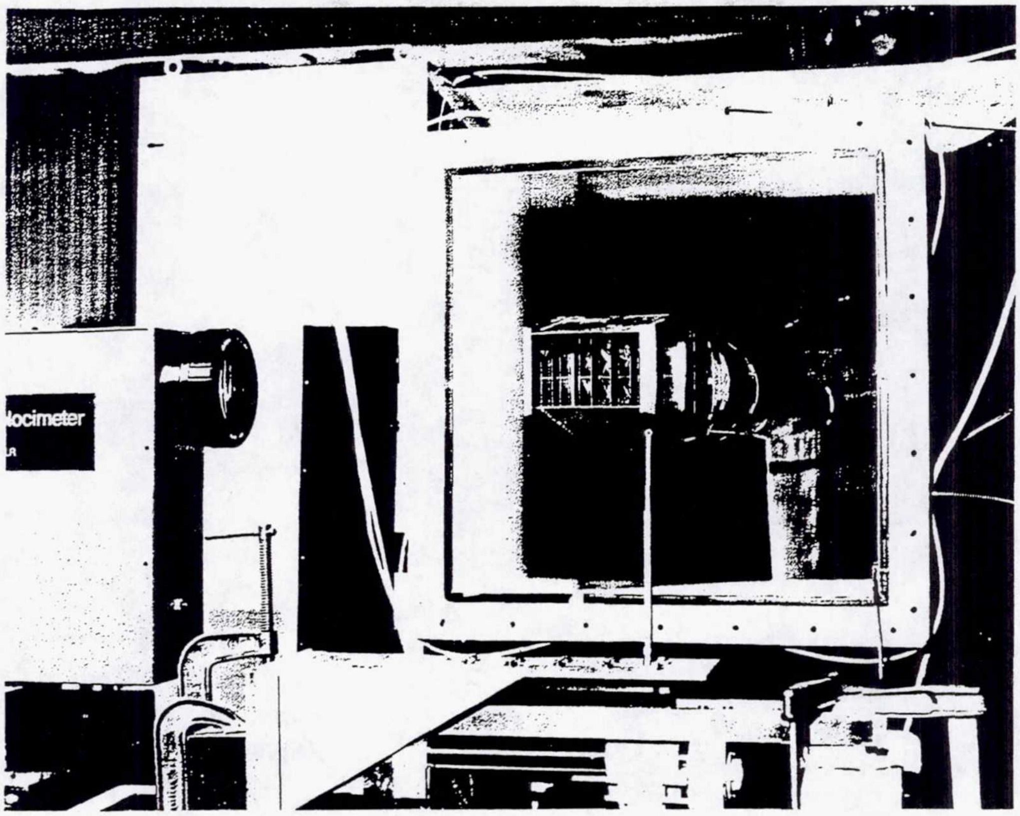

The above photograph shows a suppressor/ejector nozzle model mounted on a sting in the ARL wind-tunnel with the LV-system on. The baseline ARL model configuration has SAR = 2.5, CD area ratio = 1.23, aligned chutes with no gap, MAR = 1.2 with 9.25" ejector flaps (measured from the chute exit plane) and flush ejector inlet. For internal LV measurements the side walls of the ejector were made of glass framed in a metallic window which unfortunately prevented LV measurements to be made very close to the frame-border. The static pressure measurements were done initially in a separate test in which the glass side walls were replaced by appropriately instrumented metal walls. The model is supported in the wind-tunnel by a sting/strut system. The sting is 7.0 " in diameter and 108.5" in length and has a two flow capability with 5.5 lbm/s for each flow. For this test, only the outer annular flow path, heated to 850 deg. R., was used with the inner one closed off. The ARL wind-tunnel is a free-jet, single return, continuous flow, ambient wind-tunnel of 2' X 2' exit section and capable of providing 300 ft/s without blockage and is used to partially simulate the take-off condition. The LV system is a Laser Two-Focus (L2F) velocimeter. The scattered light from small particles (seeding) in the flow is detected as they pass through two focal volumes (with centers in the vertical plane) formed by two highly focused laser beams. The velocity is derived from the time of flight of particles moving from one focus to another with known focal separation (laser transit anemometry). The projection of the mean velocity vector on the vertical plane (both magnitude & direction) and a measure of its variability can be inferred.

An Example of Internal LV Survey

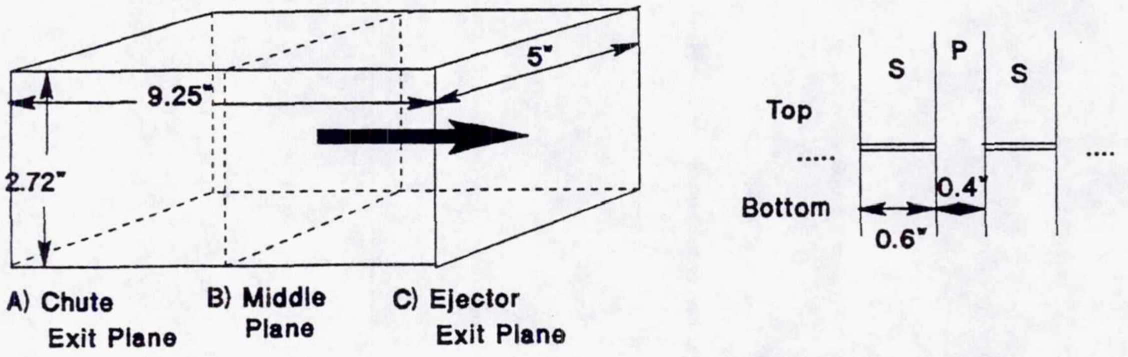

Ejector

Diverging Flaps (MAR = 1.2)
Flush Inlet

Chutes

CD (Core Exp. Ratio=1.23)
Suppresor Area Ratio=2.5
Aligned; No Gap

An example of some internal LV measurements for the baseline chute configuration will be shown. The above figure shows the nominal layout of the ejector box within which these LV measurements were made. With MAR = 1.2, note that the ejector flaps were divergent, not parallel. LV-data was taken at three vertical planes, namely, the chute exit plane A, the ejector exit plane C and the middle plane B (at the mid-point between planes A and C) to assess the progress of the mixing between the two flows. Plane A has 21 X 8 grid points, plane B has 19 X 9 grid-points and plane C has 21 X 11 grid-points, all symmetric about the two symmetry axes (the vertical axis passing through the central chutes and the horizontal one between the two chute rows). These planes cover four central primary jet widths and four chute-widths spanwise, and both chute heights vertically. Internal LV measurements were also taken on certain axial traverses for examining the shock structure. For the test data to be shown the nozzle pressure ratio (NPR), Ptotal/Pambient, was 4.0, total primary temperature was 860 deg. R, wind-tunnel total temperature was 518.5 deg. R and wind-tunnel Mach number was about 0.2.

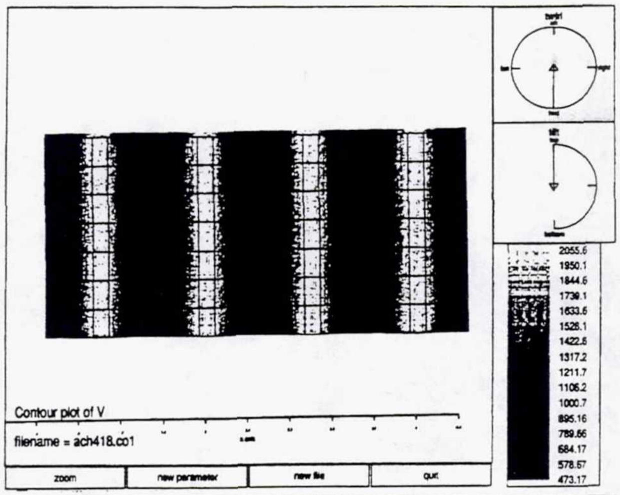

Contour plot of V

filename = ach418.c01

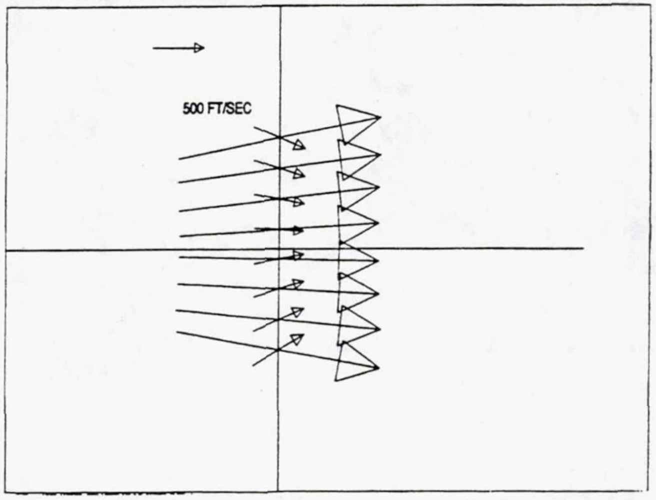

For the test configuration discussed earlier, the top figure shows contour plots of the magnitude of the mean velocity vector at the chute exit plane A. To be sure, it is the projection of the mean velocity vector on the vertical plane whose magnitude alone is plotted, although its direction varies spatially and is shown in the next figure. A smoothing surface contour routine has been used to interpolate between all the discrete data points and 15 colors/shades have been used at even intervals from the measured minimum to the measured maximum values. (This scheme is also followed in the figures to follow.) The maximum measured primary jet velocity is 2056 ft/s (Mach number of approximately Mp = 1.87) and the secondary air velocity is 473 ft/s (Mach no. of approximately Ms = 0.42). The CD primary flow-path turns out to be overexpanded under these conditions.

The bottom figure shows the angular distribution of the mean velocity vectors for vertical traverses on the center-lines of the central chute (small arrows) and the adjacent hot jet (large arrows). The primary flow diverges from the central axis, whereas, the secondary flow converges towards it. This is consistent with the flow paths for the two flows (see the geometry) and implies that there is axial vorticity distribution at this plane due to non-equal vertical components of the two flows. To be sure, spanwise velocity components can also contribute to axial vorticity but the LV-system used is not capable of measuring them. The angular distribution is further discussed in the next figure.

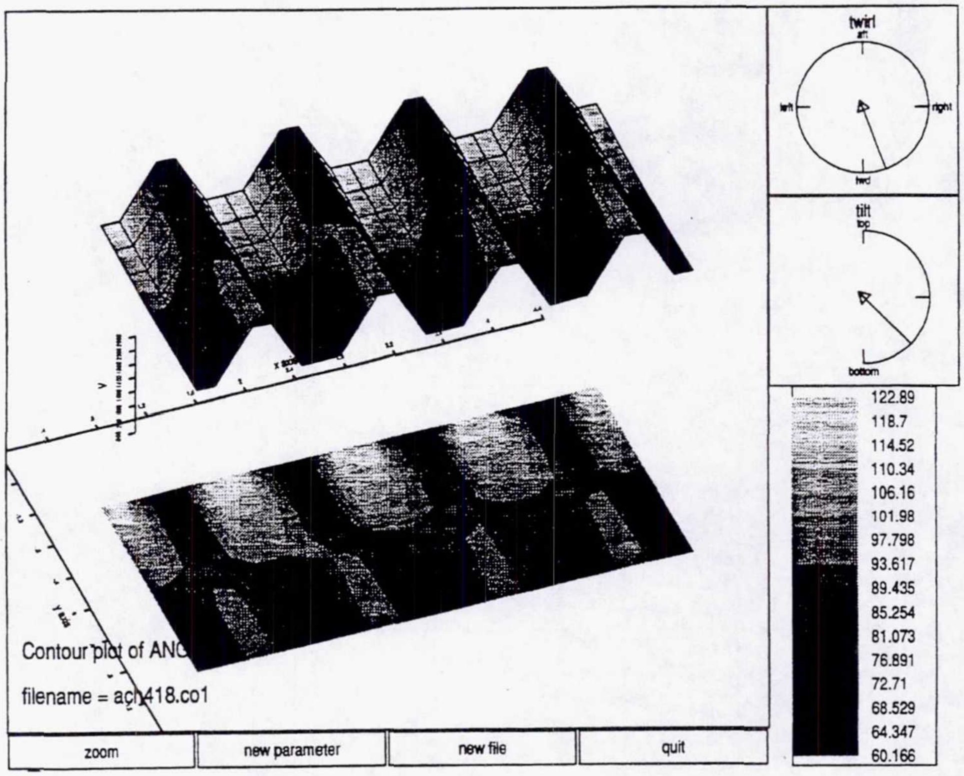

The above figure is a composite surface-contour plot of the mean velocity vector distribution at the chute-exit plane A: the height is proportional to the magnitude and the contours represent the angle (from the vertical pointing downwards). The flow appears to be periodic from jet-to-jet (at least for the central four jets) and fairly uniform along the height of the jets and a large central portion of the chutes. With such a coarse grid it is not possible to distinguish between the abrupt change in velocity due to the jet-border and that due to weak oblique shocks that may exist from the chute side-walls due to overexpansion. The primary flow diverges away from the axial direction with angles varying from 0 degrees to it at the center to almost 12 to 13 degrees at chute height. The secondary flow converges towards it with angles varying from 0 to 30 degrees. (Note the inlet ramp angle is also 30 degrees.) The difference in the vertical components of the two flows contributes to axial vorticity distribution at the chute vertical edges and is known to enhance mixing in such flows (Elliot et al). We discuss this in some detail in the next few figures. Composite plots such as above have been obtained for all planes of observation but are not shown here due to brevity. Only velocity magnitude contours are shown.

Elliott, J.K., Manning, T.A., Qiu, Y.J., Grietzer, E.M., Tan, C.S., Tillman, T.G., AIAA Paper No. 92-3568, July 1992.

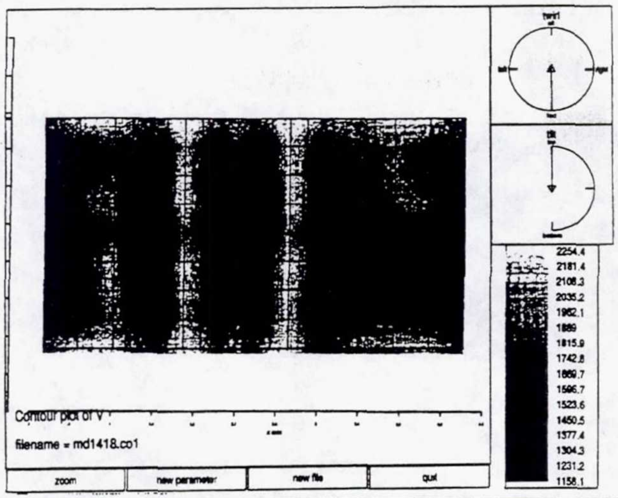

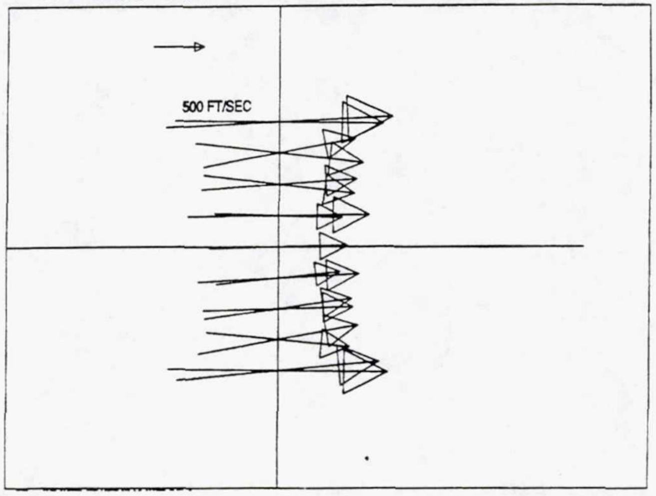

As before, the top figure shows a contour plot of the magnitude of mean velocity (its projection in the vertical plane) at the mid-plane B and the bottom figure shows the velocity directions at the center-lines of the middle chute and the adjacent hot jet. The min-max values are considerably different here than in plane A, whence the colors/shades also have different values. The minimum speed of the secondary flow near the central region is now 1158 ft/s, a large increase from its chute exit value of 473 ft/s; the primary flow is also accelerated to 2254 ft/s from 2056 ft/s at chute exit. Note the following peculiar features: * The horizontal spreading of high velocity region in the top and bottom portions *The protrusion of high velocity "tongues" in the vertical center-planes of chutes from top and bottom * The migration of high velocity primary flow from the central portion to the top and bottom and, hence, its consequent "pinching" in the middle * The loss of spanwise periodicity (although the two central jets appear similar). *The roughly symmetric flows between top and bottom portions. *The decrease in the overall flow angularity. The spreading of the supersonic primary jets does not appear to be significant. However, the vortex-sheets from adjacent chute side-walls appear to curl on the top and bottom. These features, we believe, are present, firstly, because the impact of the diverging primary jets with the top and bottom ejector flaps spreads them horizontally there. Further, the axial vorticity component distorts the vortex-sheets due to self-induction. The original contact surface area between the two flows thus increases tremendously and enhances the mixing process.

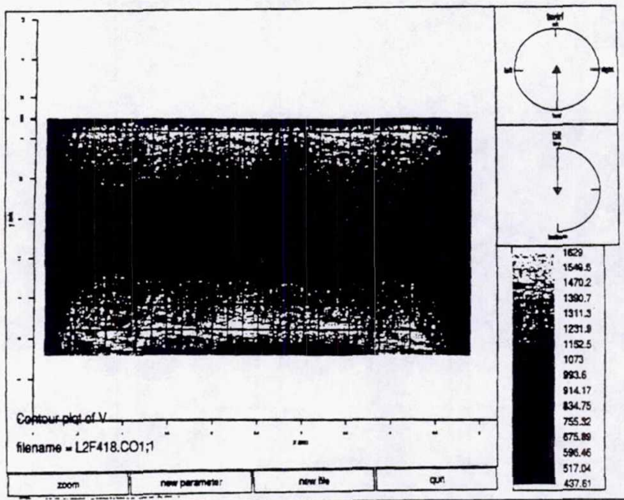

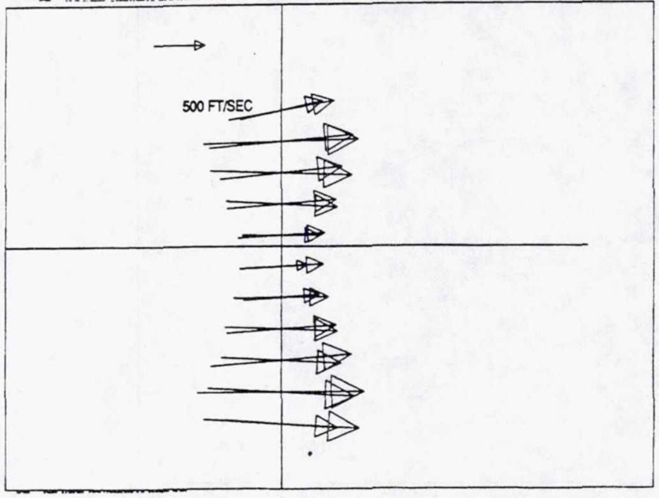

The above figure shows the mean velocity contours at the ejector exit plane C. The flow is still highly non-uniform with high speeds (1629 ft/s) at the top and bottom, and low speeds (517 ft/s) in the central region - so called "inverted" velocity profiles. The average exit speed is much smaller than that at the chute exit plane. Also note from the bottom figure that the flow is fairly horizontal. The three-dimensional velocity profile thus shows not only several minima and maxima but also several saddle points, between the minima, which are known to be responsible for more rapid mixing downstream. There appears also to be a low speed region on the sides and must be related to the progression of the internal side-wall boundary layers. Similarly, the shear-layers on the top and bottom flaps can also be seen. Kiel probe measurements were also done at this exit plane and showed similar topology of the total pressure and total temperature contours with a trough in the central portion and some loss in the peaky horizontal ridges at the top and bottom compared to the upstream primary-flow stagnation values.

Proposed Mixing Mechanism

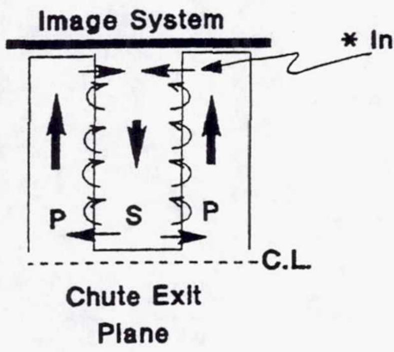

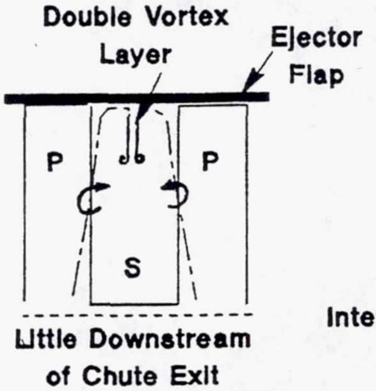

*Also Supported by CFD Simulations
(GEAE; deBonis)

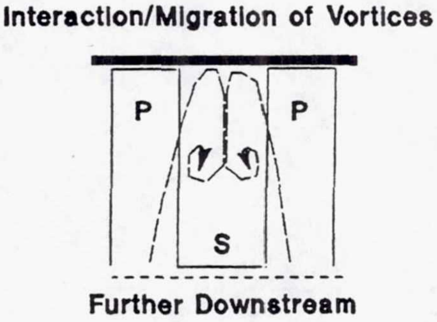

In the above figures, the dominant mixing mechanism is proposed for such suppressor/ejector flows through vortex-dynamics. We have seen that vortex-sheets are shed from the chute side-walls. These have two vorticity components: the vertical component, largely due to the difference in the axial velocity components of the two streams, and the axial component, largely due to the difference in the vertical velocity components. The initial axial convective Mach number is calculated to be supersonic and, hence, will produce only small spreading. Thus the destabilizing effect of the vertical vorticity component and, hence, mixing due to it will not be dominant for upstream stations. The axial vorticity, on the other hand, can significantly change the shape of this vortex sheet, even far upstream, through self-induction and drastically alter the "engulfing" process (see Elliott et al (op cit)). The top left figure shows schematically the axial vorticity distribution generated at the chute vertical edges. The ejector flap can be replaced by an image vortex system for examining the flow in just the transverse plane where the flow is effectively incompressible. Self-induction will pull the vortex-sheets from one chute together at the top and push them outwards in the middle. This will eventually lead to double vortex layers in the middle vertical planes of chutes with opposite vorticity on their two surfaces, as shown in the middle figure. The edges of these double vortex-layers will curl due to induction as shown in the last figure and the concentrated "mushroom" vortex cores will further interact leading to more engulfment. Such vortex dynamics can also be inferred from CFD simulations done in G.E. and deBonis (AIAA Paper # 92-3570).

Sample of Axial LV Survey

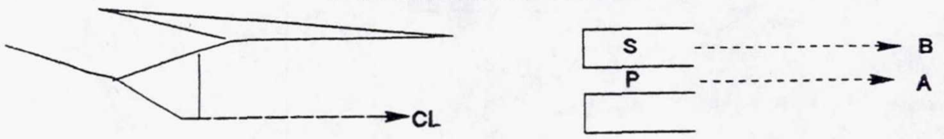

NPR = 4, Total Primary T = 860 deg R, Mach No.(wt) = 0.2

Can Infer Internal Shock Location/Strength

Potential Core Lengths, Merging Lengths

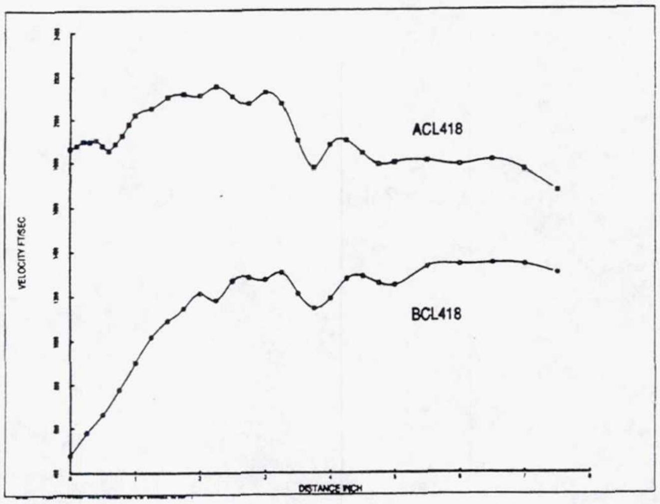

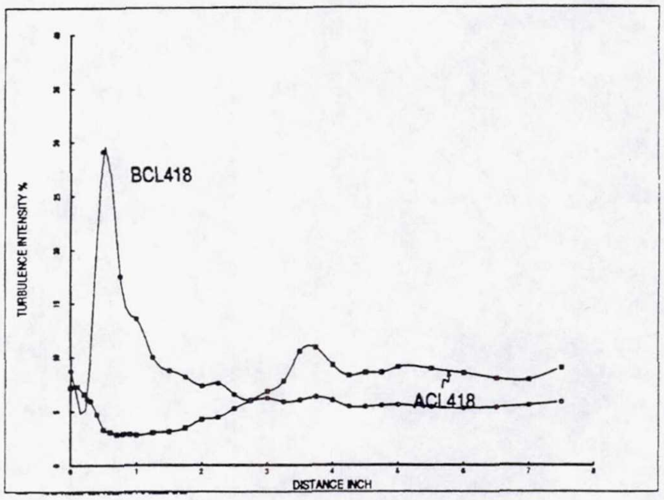

The above figures show samples of axial LV traverses between the two rows of chutes in the center-lines of the middle chute (BCL) and the adjacent hot jet (ACL). The left figure shows the mean velocity magnitudes and the right figure shows the variability in these mean values in terms of an rms value as percentage of the local mean value. Note that the traverses were made only up to 7.5 inches from the chute exit plane and LV measurements were not done in the very last 1.75 inches up to the ejector exit plane because of the metallic frame on the side walls. The directions of the mean velocities on these traverses, which are in a symmetry plane were, indeed, found to be horizontal. Hence, the increases and decreases in the mean velocities can be considered as actual accelerations and decelerations of the flows. The most prominent feature in the mean velocities is the sharp dip in the primary flow (traverse ACL) at around 3.5 inches, which is upstream of the middle-plane B surveyed earlier. The dip appears to correspond to a shock-surface (recall that the primary flow is supersonic) and is also accompanied by a peak value in the corresponding rms % intensity. Another small dip in the primary flow at around 0.5 inches perhaps corresponds to the weak shocks due to overexpansion. Also note the initial high acceleration in the secondary flow (traverse BCL) and the subsequent almost constant speed after a small dip and rise at 3.5 inches. Such axial LV surveys between two growing shear layers can thus be used to estimate the potential core lengths of individual jets and the merging length for two adjacent jets by examining the location of turbulence intensity peaks and the start of decay of mean velocity.

Another Example of Internal Axial LV-Survey

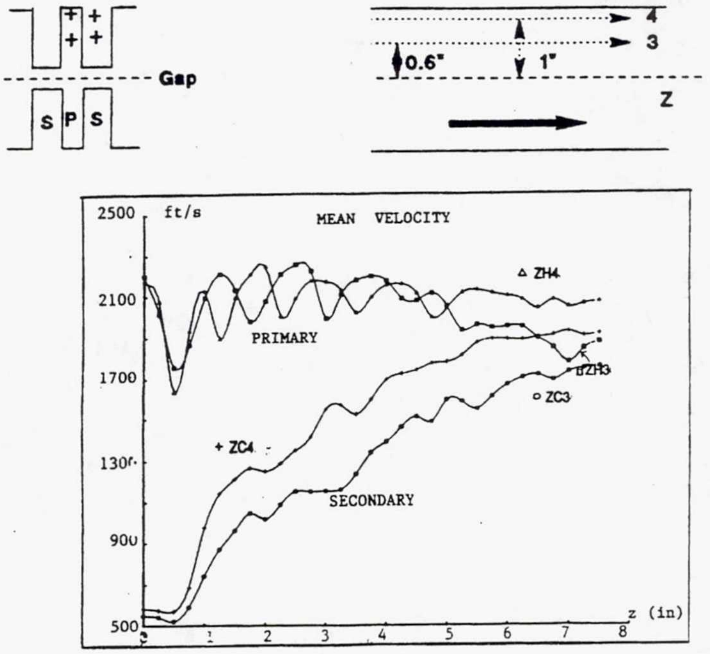

Internal Shock Cell Structure from CD Chutes Can Be Inferred

Here are some other examples of internal axial LV surveys to illustrate the internal shocks that may exist in such suppressor/ejector flows. However, these LV surveys are for a different chute configuration because such surveys were unfortunately not made for the previously discussed configuration. The above chute configuration has primary CD area ratio = 1.38, SAR (based on throat plane areas, not exit plane areas as before) = 2.8, top and bottom chutes aligned but with a gap between them. The ejector configuration was the same as before and so were the operating conditions. Note that this chute configuration leads to a series of cruciform shaped primary flow cross-sections at chute exit plane rather than a series of rectangular jets as before. The LV traverses were taken in both the primary and the secondary flow center-lines at two different heights and their notations are self-explanatory (H = Hot(Primary), C = Cold Secondary)). A series of large mean velocity dips in the primary flow (ZH4, ZH3) show the crossing through shock-waves which most probably are due to the intersection of oblique shock-waves starting at the chute side-walls due to possible overexpansion or the Mach-disks between them. With sufficient number of such axial surveys it is, hence, possible to construct the shock-cell structure and their strengths. Although the secondary flow traverses (ZC4, ZC3) show a steady increase in speed it does not necessarily mean that the secondary flow itself is accelerating on these lines; rather, it is the speed of the hot primary flow (which, as we saw earlier, is actually going up and spreading horizontally to these locations) that is being captured.

Ejector Wall Pressure Distribution

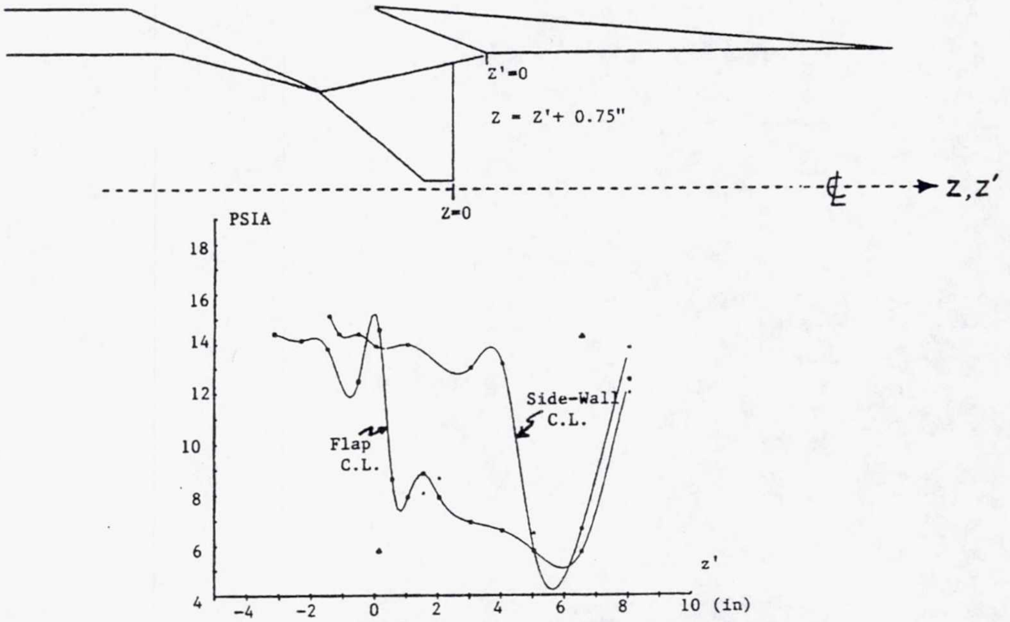

* **Flow Is Shocked Internally with Divergent Flaps**
* **With Parallel Flaps the Dominant Rear Shock was Pushed Out**

Recall that LV-data could not be taken throughout the whole length of the ejector, especially, the very aft end because of optical obstructions from the metallic frame on the side walls of the ejector. In order to get a hint of what is going on near this aft portion, just upstream of the ejector exit plane, we present in the above figure the static pressure distribution on the upper flap and the sidewall centerline for the baseline configuration. Although there were two rows of pressure taps on the upper flap, one on the secondary flow centerline and the other on the primary centerline, only the former taps functioned properly and are shown above. The most prominent features are: (1) the abrupt increase in both pressure distributions beginning at the same location (about 7.25 inches from the chute exit plane), and (2) the very low pressures (about 4 to 5 psia) attained inside the ejector. The sharp increase obviously implies a shock-surface there, perhaps, the front foot of a lambda shock, as is usual when a boundary layer is present. The previous LV-traverse appears to have just missed this shock because no LV data was taken there. The flap centerline distribution is reminiscent of an internal normal shock for CD nozzles in quasi one-dimensional analysis. Here, although the ejector is, indeed, like a CD nozzle the internal flow has highly three-dimensional characteristics, as was seen earlier. Thus not only is the side-wall centerline wetted by the hot primary fluid from the half-width end-jet but the flap secondary centerline is also wetted by the primary jets, due to their vertical and horizontal migration as mentioned before. We note here that this shock did not exist internally when the flaps were kept parallel.

SUMMARY

1. Extensive internal LV-data was acquired for the first time in scaled 2D suppressor/ejector nozzles. Only a sample of it was shown and interpreted.

2. Mixing Process:

   - Spanwise mixing between jets in the same horizontal row appears fairly good

   - Top-to-bottom (row-to-row) mixing is poor with low velocity, low total temperature/pressure fluid in the middle and high corresponding values near the two flaps

   - Mixing mechanism proposed using vortex dynamics in which axial vorticity plays a major role.

3. Internal Shocks:

   - Diverging flaps showed strong rear shock; whereas parallel flaps did not.

   - Detailed shock-cells from overexpanded CD chutes were also captured.

4. Axial evolution of mixing effectiveness can thus be found and effect of various parameters studied.

RECOMMENDATIONS

1. One way to enhance mixing between the primary and the ambient flow for such class of suppressor/ejector nozzles is to design the strengths of and distances between the "mushroom" vortices, say, through appropriate distribution of axial vorticity at the chute trailing edges, in order to hasten the random interaction between them.

2. Need better fundamental understanding of confined, supersonic/subsonic skewed shear layers to further improve the mixing characteristics.

omit this
page

Session II

Nozzle Systems and Test Results

1999176540

ACOUSTIC AND AERO-MIXING TESTS OF FLUID SHIELD NOZZLES

Part I–Acoustics

S3-07

M. Salikuddin, J. Brausch, and V. Mengle
GE Aircraft Engines
Cincinnati, Ohio

409514
30P.

CONCEPTUAL FLADED VARIABLE CYCLE ENGINE

(WITH MULTI-CHUTE SUPPRESSOR EXHAUST NOZZLE PARTIALLY SURROUNDED BY A FLUID SHIELD)

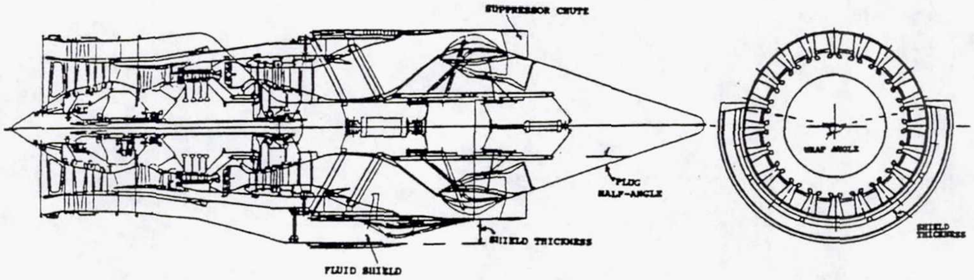

BENEFITS:

- HIGH FREQUENCY NOISE SUPPRESSION
- LOW TEMPERATURE FLADE FLOW
- OVERSIZING OF FLADE TO MEET TAKEOFF NOISE REQUIREMENT

Introduction: Environmental acceptability and economic viability are crucial issues in the development of the next generation HSCT (High Speed Civil Transport). Low noise exhaust nozzle technology has significant impact on both these issues. The exhaust system design that meets FAR 36 Stage 3 takeoff acoustic requirements and provides high levels of cruise and transonic performance and adequate takeoff performance at an acceptable weight is essential to the success of any HSCT program.

High Flow Approach to HSCT Noise Problem: One concept that appears to be promising in reducing takeoff noise is the use of high flow approach to reduce the jet exhaust velocity. Further noise reduction to meet Far 36 Stage 3 takeoff requirement can be met by using an efficient multi-chute suppressor to reduce low-frequency noise and a fluid shield to attenuate high-frequency noise emanating from the exhaust-nozzle jet.

Conceptual Faded Variable Cycle Engine: Major components of a fluid shield nozzle, as illustrated in the conceptual fladed variable cycle engine, are a multi-chute single stream suppressor, a plug, and a fluid shield partially surrounding the core flow. While the suppressor reduces low-frequency noise, the fluid shield attenuates high-frequency noise due to mean shear reduction similar to conventional bypass nozzles.

VARIATION OF AEROTHERMODYNAMIC AND GEOMETRICAL PARAMETERS FOR FLADE CYCLE

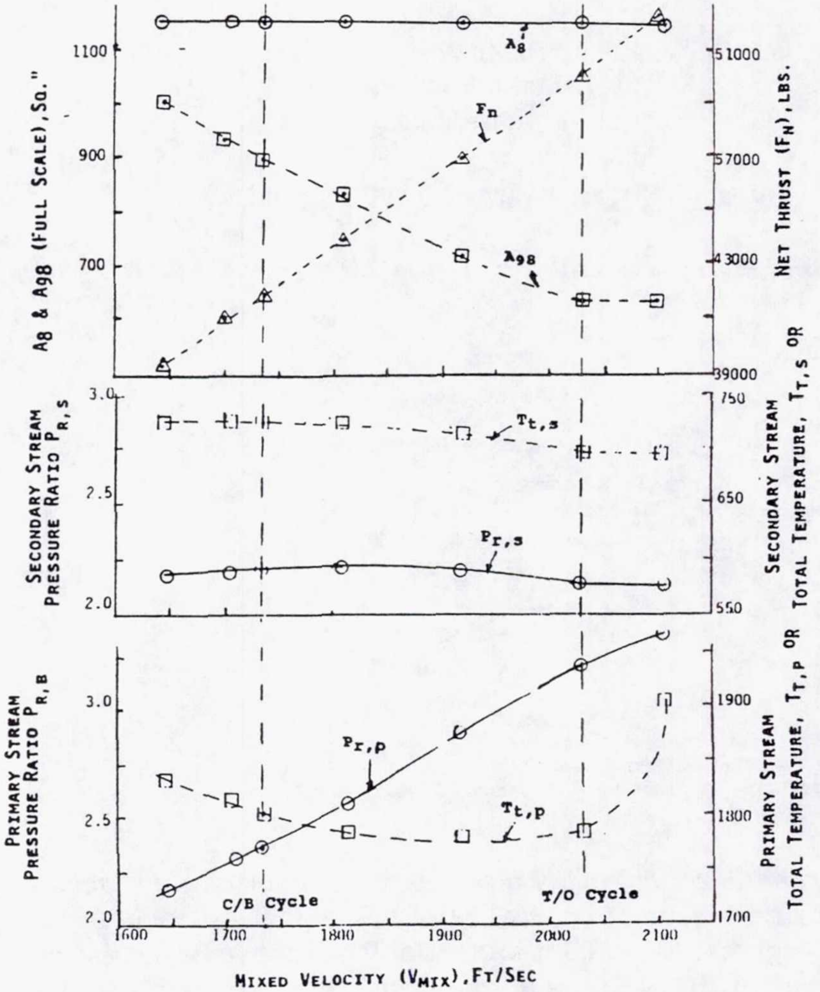

Variation of Flade Cycle Parameters: The fluid shield scale model design and the selection of test conditions are based on the GEAE's $M = 2.4$ Flade Cycle and the preliminary design concept of the fluid shield nozzles. This cycle employs a nominal split of 650/400 pps in the core and flade stream at takeoff. The aerothermodynamic cycle conditions and some full scale Flade cycle parameters at the takeoff flight Mach number of $MF = 0.32$ are shown here. While the secondary stream (fluid shield) total temperature and nozzle pressure ratio remain more or less constant throughout the throttle variation, they vary considerably for the core stream. The core area at the exit plane (A8) is maintained constant throughout the throttle variation. Whereas, the fluid shield exit plane area (A98) is changed throughout the throttle variation. This is an important difference between the scale model nozzle and the full scale preliminary design, in that the fluid shield area at the exit plane remains constant for the models.

36-CHUTE SUPPRESSOR ASSEMBLY WITH POROUS PLUG AND 1"-THICK FLUID SHIELD NOZZLE

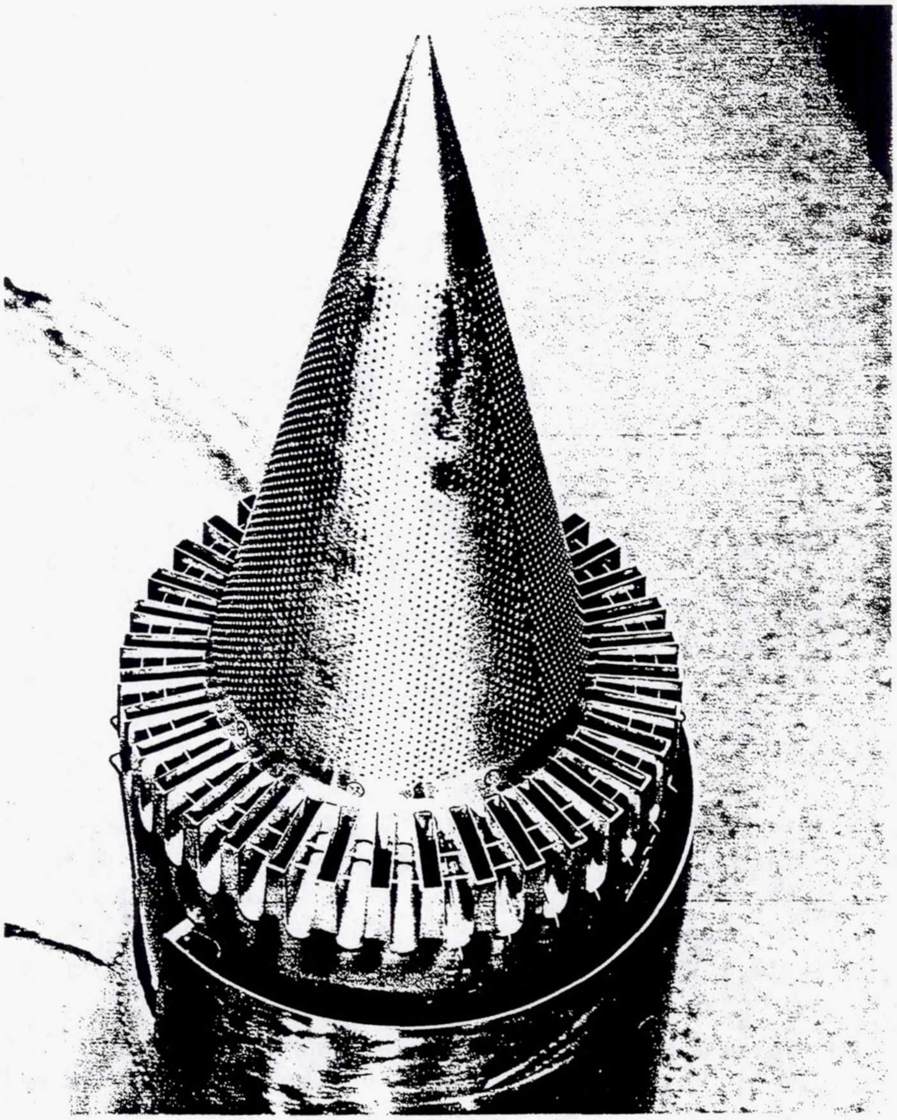

Scale Model Fluid Shield Nozzles: To assess the effect of A98 variation three fluid shield nozzles are built with different A98, such that, the baseline shield (A98 = 11.734 sq") matches with full scale Flade cycle at higher power codes close to takeoff condition, whereas, a second shield with higher A98 (i.e., A98 = 18.2 sq") matches with the full scale Flade cycle at lower power codes close to cutback conditions. The third shield with much higher A98 (i.e., A98 = 24.8 sq") is built to explore the effect of shield for a much larger weight flow ratio and its assembly is shown here.

FIXED SUPPRESSOR GEOMETRY

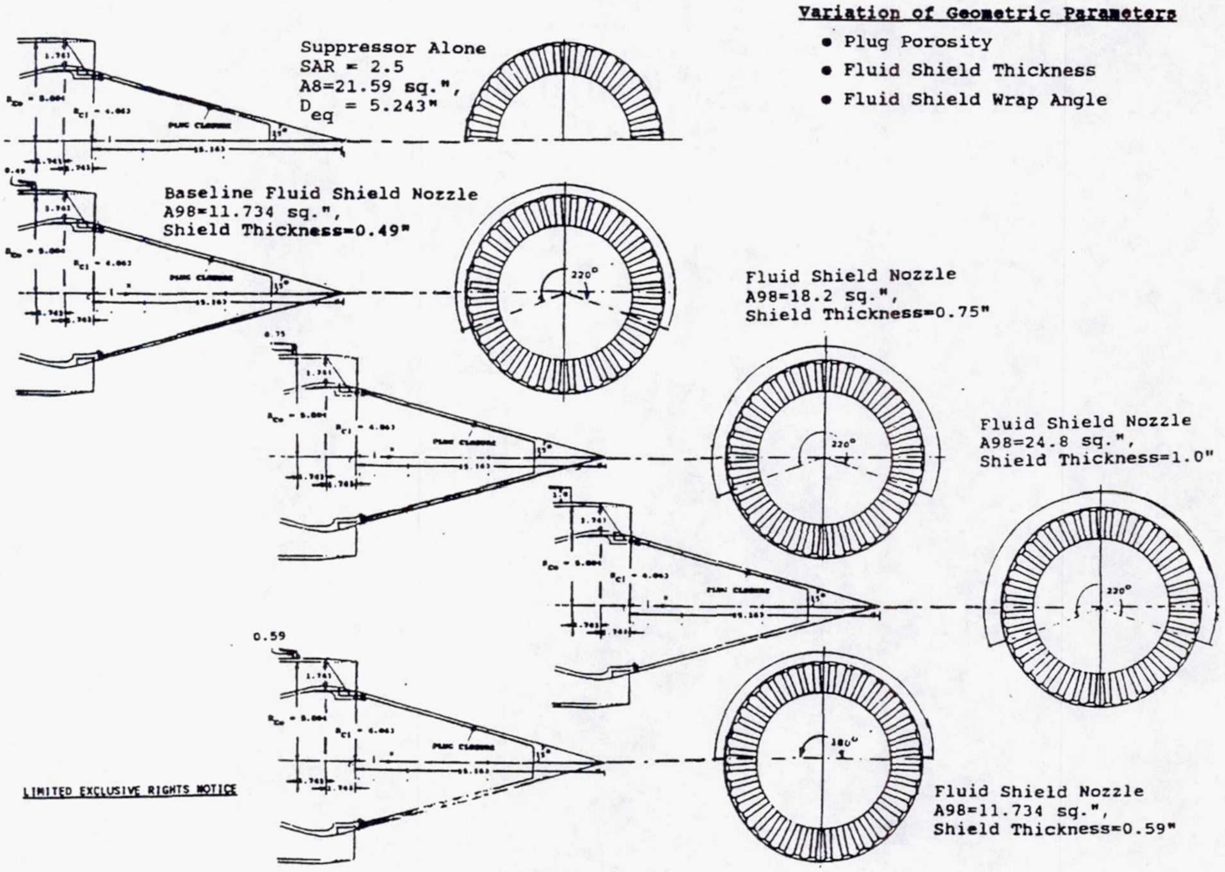

LIMITED EXCLUSIVE RIGHTS NOTICE

Fluid Shield Nozzle Configurations for Acoustic Tests: A single reference suppressor nozzle design with suppressor area ratio of 2.5 is used for all the fluid shield configurations. The reference suppressor nozzle is designed for lower specific thrust core engine cycles with jet velocities in the range of 1500 to 2400 ft/sec at takeoff. The design of these scale models allows variations of fluid shield parameters, like, shield thickness and wrap angle and plug porosity. Variation of fluid shield parameters include three different thicknesses of 0.5", 0.75", and 1.0", with a fixed wrap of 220° and with corresponding A98 of 11.74 sq", 18.2 sq", and 24.8 sq", respectively, and two wrap angles of 180° and 220° with a fixed A98 of 11.74 sq". Plug parameters include a rigid wall and a 10% porous surface.

SIDE VIEW AT 45° AZIMUTHAL PLANE

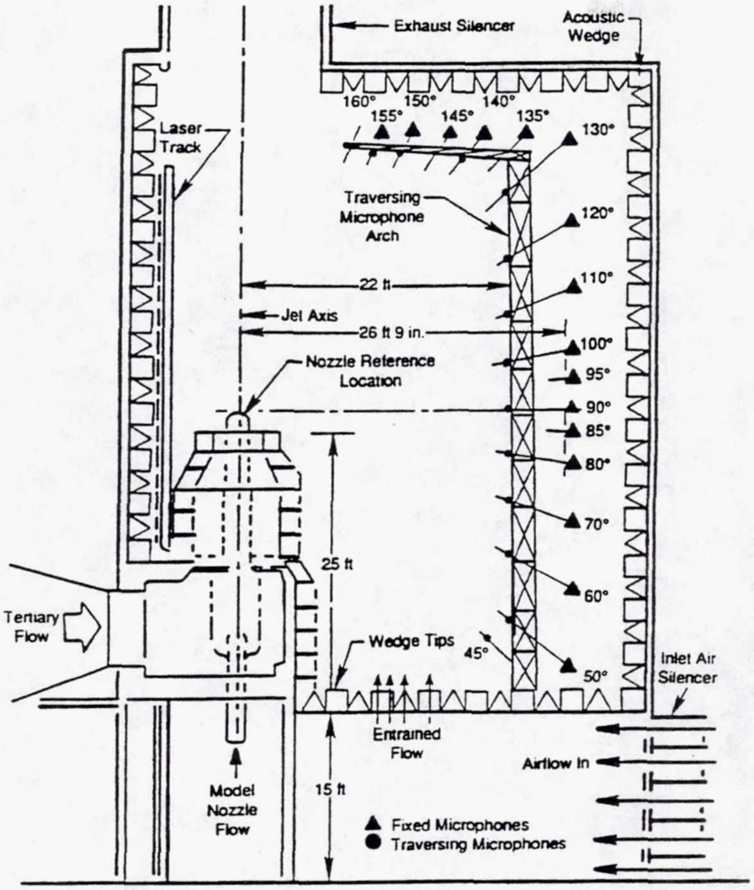

GEAE Anechoic Freejet Facility (Cell 41): The GEAE anechoic free-jet noise facility is a cylindrical chamber 43′ in diameter and 72′ tall. The streams of heated air for the dual flow arrangement are produced by two separate natural gas burners. Each stream can be heated to a maximum of 1960°R with nozzle pressure ratios as high as 5.5, resulting in a maximum jet velocity of 3000 feet/second. The tertiary flow at its maximum permits simulation up to a Mach number of about 0.4 through the 48" diameter free-jet exhaust.

The facility is equipped with two systems of microphone arrays to measure the acoustic characteristics of the test models in the farfield, a fixed array of microphones and an array on a traversing tower. The traversing tower can be positioned at any azimuthal angle (ϕ) between +55° to -55° with respect to the fixed microphone array. The facility is also equipped with laser velocimeter (LV) system and shadowgraph system for jet flowfield measurement and flow visualization, respectively.

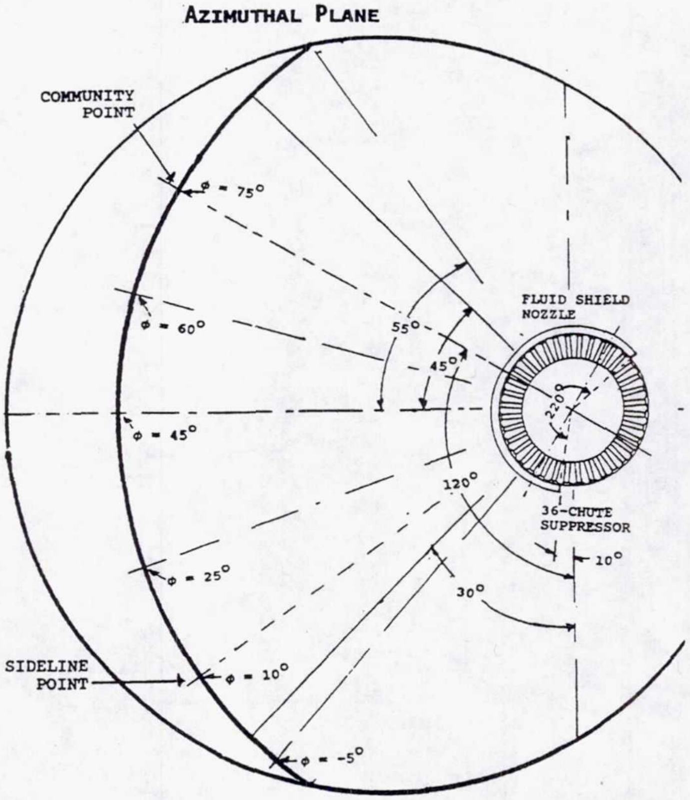

Fluid Shield Nozzle Orientation in Cell 41: Fluid shield nozzles in Cell 41 are oriented such that the side line and community points lie at azimuthal locations of $\phi = 10°$ and $\phi = 75°$, respectively, as shown in this plan view. Farfield acoustic measurements are made at these two azimuthal locations by using the traversing microphone array for all fluid shield test conditions. For selected cases additional azimuthal measurements are made to study the azimuthal directivity of farfield noise.

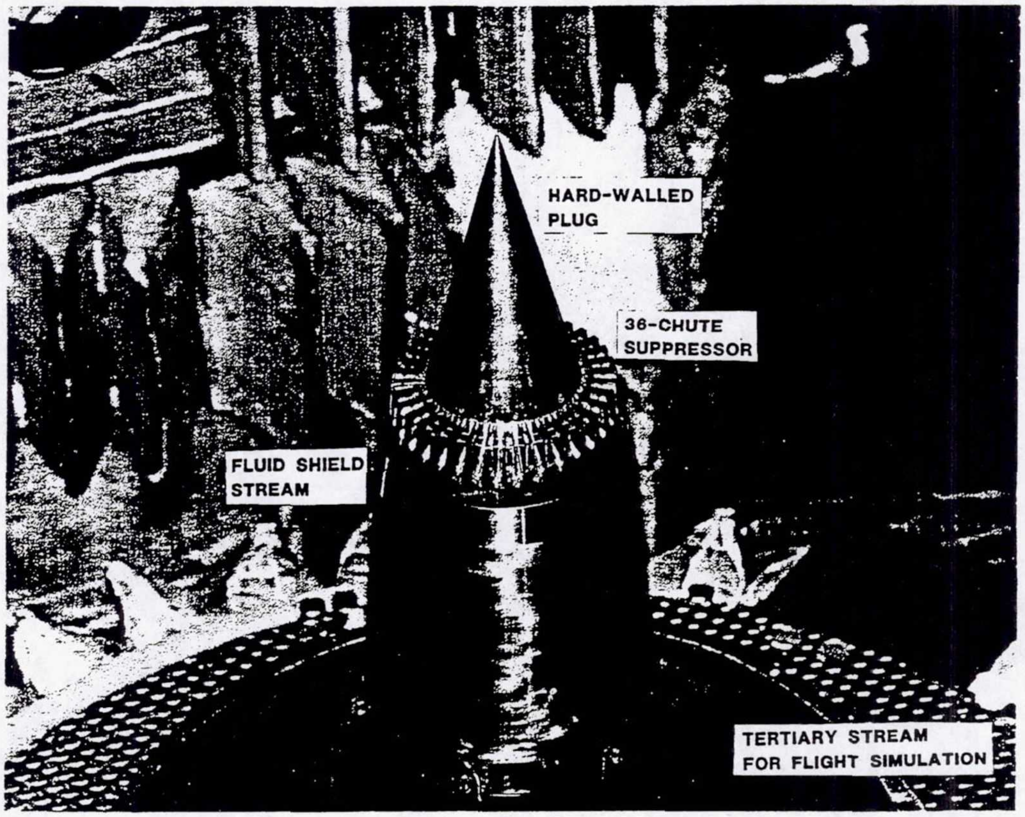

Fluid Shield Nozzle Mounted in Cell 41: A photographic view of the fluid shield nozzle installation is shown in this figure.

NOISE SUPPRESSION DUE TO POROUS PLUG

SUPPRESSOR ALONE CONFIGURATION,

V_F=360 FT/S, A8=1175 SQ", AT 1629 FT. SIDELINE

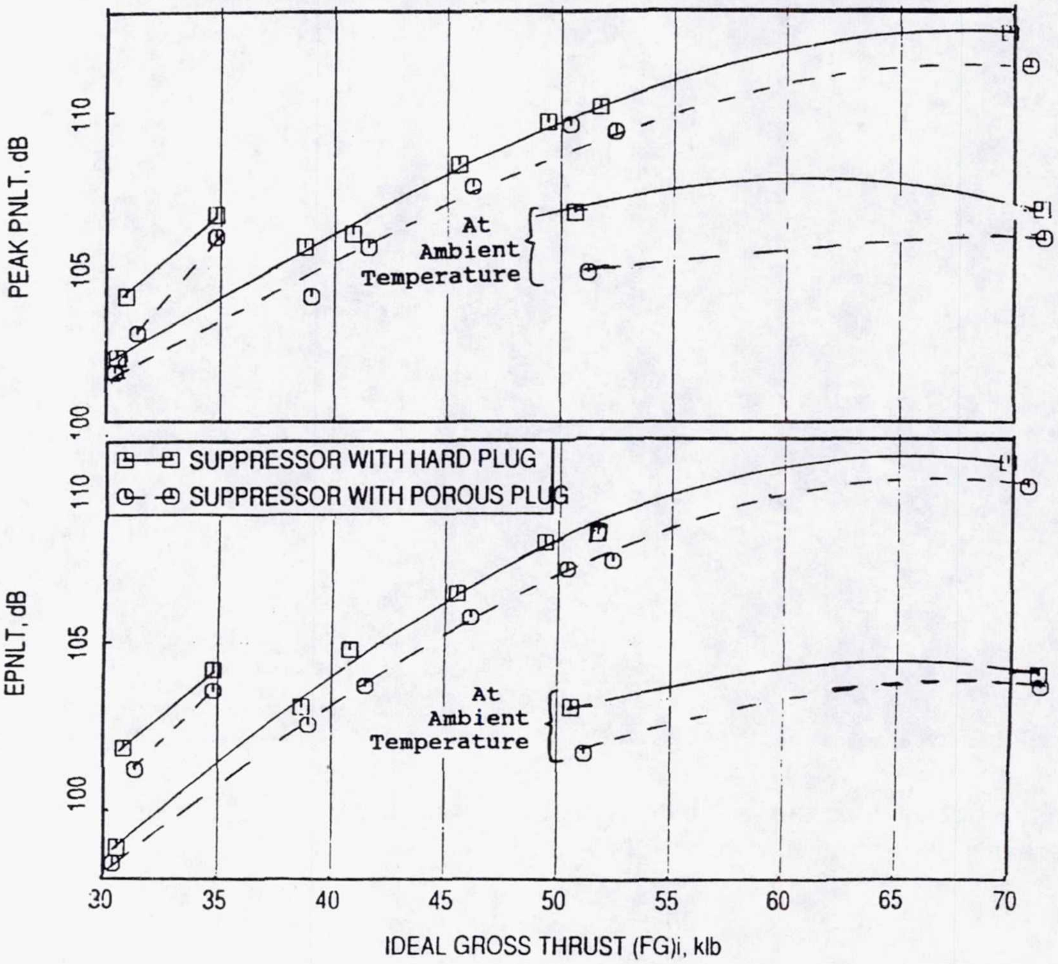

Noise Suppression due to Porous Plug as Functions of Ideal Gross Thrust: The objective of using a porous plug is to reduce the shock-associated broadband noise for super critical nozzle pressure ratios. The porous surface of the plug reduces shock strength and thereby, reduces the shock-associated broadband noise. As a typical example, the peak PNLTs and EPNLTs are plotted with respect to ideal gross thrust for different test conditions for the suppressor alone configurations showing the effect of the 10% porous plug with respect to hard-walled plug. Use of the porous plug introduces suppression of about 1-2 EPNdB for entire operating range compared to hardwall plug configuration. Similar results are obtained for fluid shield nozzle configurations.

SUPPRESSOR ALONE CONFIGURATION
NPR=2.7, T_T=1381°R, V_J=2030 FT/S, V_F=360 FT/S, A8=1175 SQ", SL=1629 FT

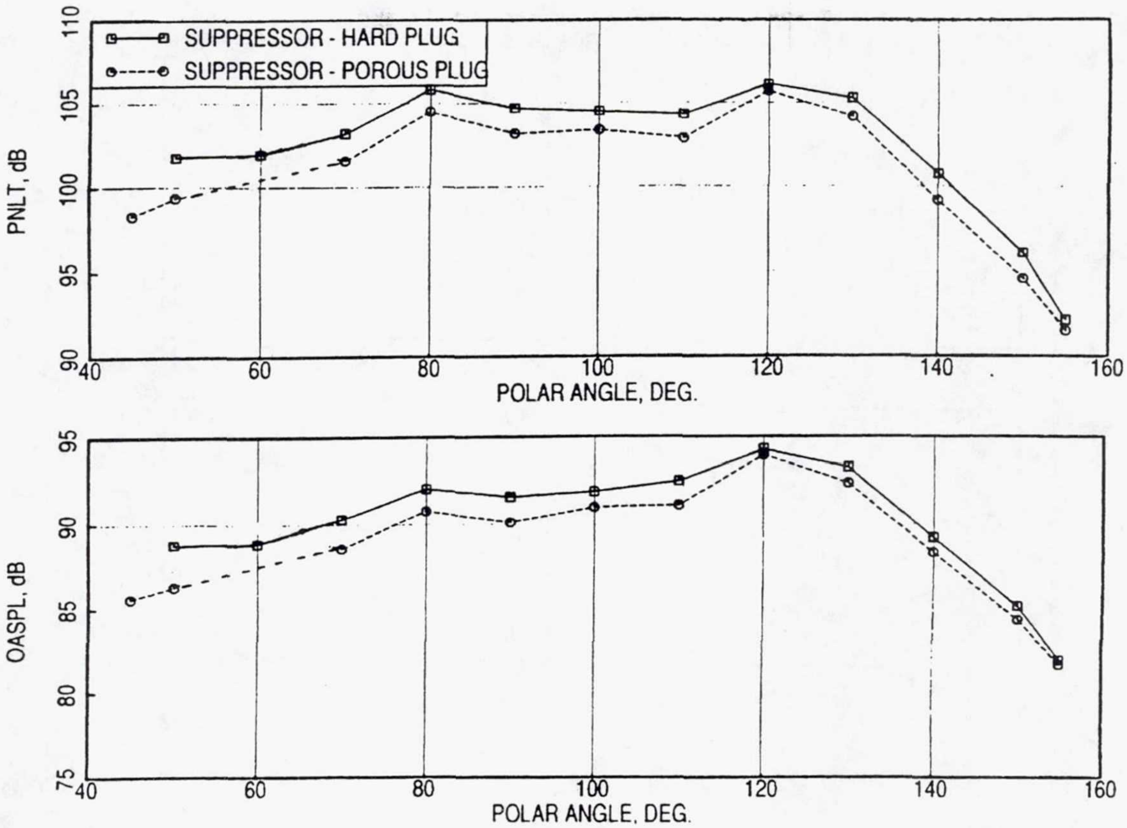

Noise Suppression due to Porous Plug in Terms of PNLT and OASPL Directivities: PNLT and OASPL directivities are examined for a typical test condition with nozzle pressure ratio of 2.7 and total temperature of 1381° R. Noise suppression due to porous plug is observed at all polar angles, except, the magnitude of suppression seems to be slightly higher at the forward quadrant, where shock associated noise is prominent.

(SUPPRESSOR ALONE CONFIGURATION)
NPR=2.7, T_T=1381°R, V_J=2030 FT/S, V_F=360 FT/S, A8=1175 SQ", SL=1629 FT

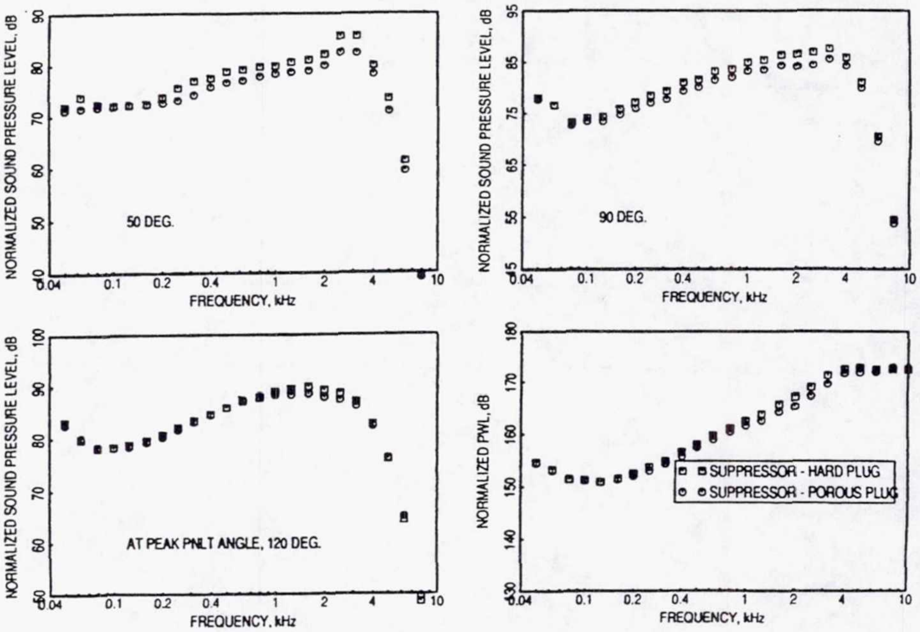

Noise Suppression due to Porous Plug in Terms of SPL and PWL Spectra: SPL and PWL spectral comparisons indicate noise suppression due to porous plug is more effective at higher frequencies.

The amount of porous plug benefit seems to be much less than what was noted by other research works of porous plugs. An interpretation of the possible phenomena, which might have prevented the strong shock to interact with the plug surface and, thereby, might have prevented the shock strength reduction process. This will be elaborated later on the basis of shadowgraph photographs. On the basis of acoustic results it may be still beneficial to use porous plug compared to a hard-walled plug if the aerodynamic performance is not severely degraded compared to hard-walled plug.

NOISE SUPPRESSION DUE TO FLUID SHIELD NOZZLE WITH POROUS PLUG

(V_F=360 FT/S, SL=1629 FT.)

(ASSUMES SAME TAKEOFF THRUST REQUIREMENT FOR ALL SHIELD THICKNESSES)

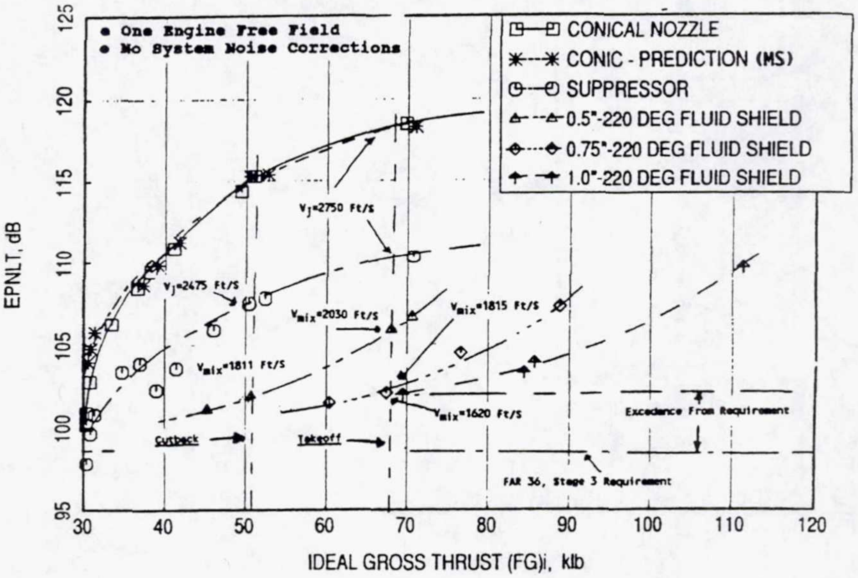

Noise Suppression Due to Fluid Shield Nozzles as Functions of Ideal Gross Thrust: EPNLTs for conical nozzle, suppressor nozzle alone configuration, and the three fluid shield nozzles with the same 220° wrap angle are plotted with respect to ideal gross thrust for the tests conducted at Flade cycle aerothermodynamic conditions. In this the conical nozzle and the suppressor are scaled to 1175 square inches, which is the core nozzle exit area size (A8) for the full scale Flade cycle. Keeping the same scaling for the suppressor with fluid shield configurations, the combined exit area due to core and flade (i.e., A8 + A98) becomes 1813.6, 2165.5, and 2524.7 square inches for the three fluid shield configurations. The 0.5"-thick shield corresponds to the Flade cycle at takeoff condition.

As observed, a benefit of about 8-9 EPNdB is realized due to the suppressor alone compared to conical noise at takeoff and approach conditions. Additional noise attenuation of about 4 EPNdB is achieved by the 0.5"-thick shield and as high as 8-9 EPNdB is achieved by 0.75"-thick and 1.0"-thick shields at takeoff condition. However, compared to the FAR-36 Stage 3 requirement the fluid shield configurations fall short by about 2-3 EPNdB.

(NOMINAL $(FG)_i$ = 70 KLBS, V_F=360 FT/S, SL=1629 FT)

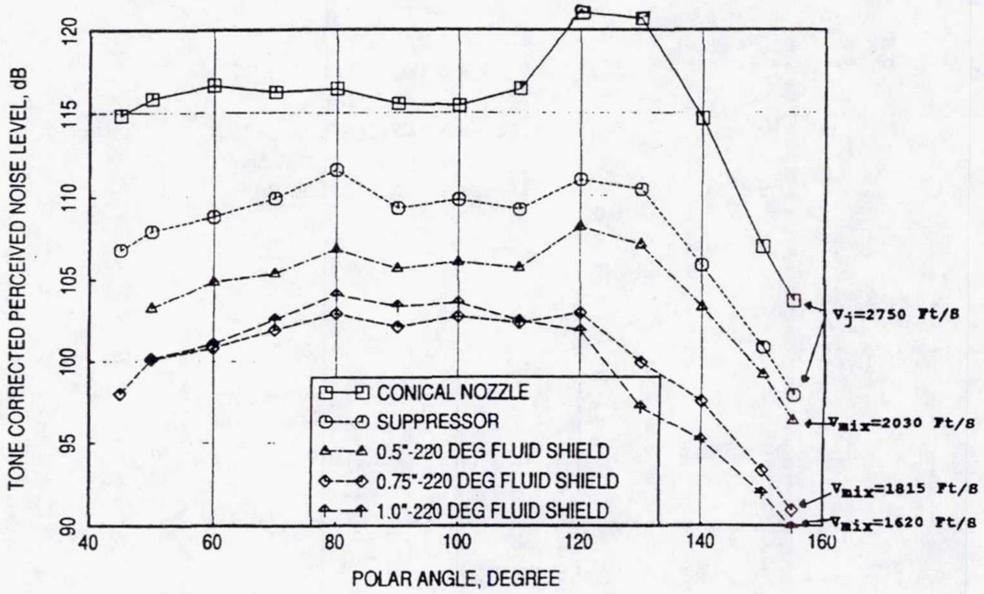

Noise Suppression Due to Fluid Shield Nozzles in Terms of PNLT Directivities at an Ideal Thrust Level of 70 klbs: Noise benefits in terms of PNdB are observed in this figure due to the mechanical suppressor alone and its combination with fluid shields with respect to a conical nozzle. At this thrust level both 0.75"- and 1.0"-thick shields seem to yield comparable amount of attenuations.

(NOMINAL (FG)$_i$ = 70 KLBS, V_F=360 FT/S, SL=1629 FT)

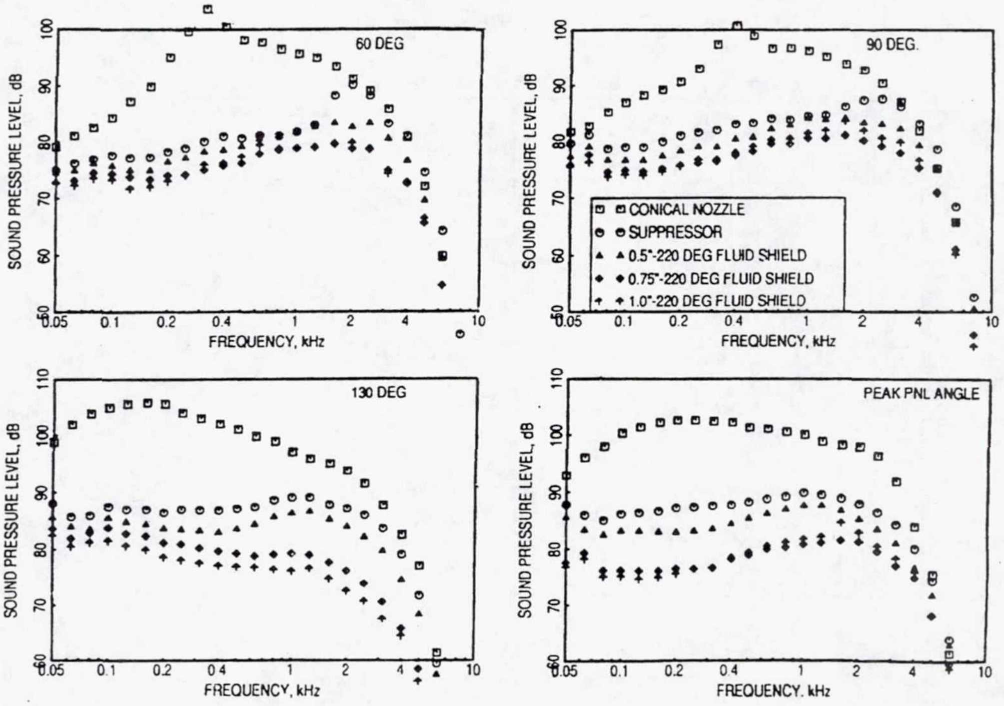

Noise Suppression Due to Fluid Shield Nozzles in Terms of SPL Spectra at an Ideal Thrust Level of 70 klbs: Noise benefits in terms of SPLs are shown in this figure due to the mechanical suppressor alone and its combination with fluid shields with respect to a conical nozzle. High frequency noise attenuation due to fluid shields increases with shield thickness. The SPL levels are comparable at some polar angles between 0.75"-thick and 1.0"-thick shields.

NOISE SUPPRESSION DUE TO 0.75"-THICK FLUID SHIELD NOZZLE WITH POROUS PLUG

(ALL CONFIGURATIONS SCALED TO 2165.5 SQ")

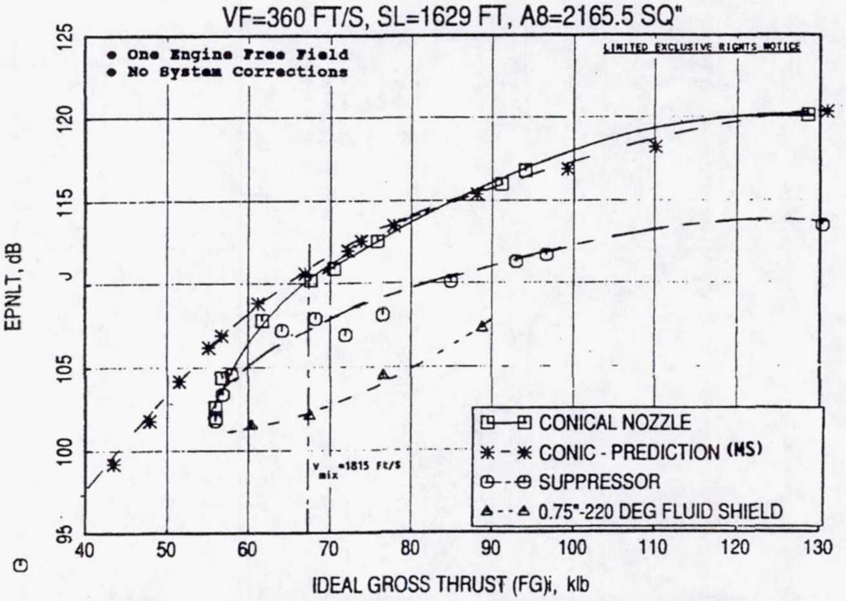

SPLITTING FLOW INTO 2 STREAMS GIVES ADDITIONAL 5 EPNDB BENEFIT AT TAKEOFF SIDELINE POINT FOR 0.75"-THICK SHIELD AT SAME TOTAL THRUST AND AIRFLOW LEVELS.

Noise Suppression Due to 0.75"-Thick Fluid Shield Nozzle in Equal Area Basis of 2165.5 Square Inch: Substantial advantage in terms of noise attenuation due to fluid shields is observed compared to the suppressor alone configuration at fixed thrust levels. However, the exit area of the suppressor alone configuration being smaller compared to the combined areas of the suppressor/shield configurations the jet velocity of the suppressor is much higher compared to the mixed velocities of the fluid shield configurations. The noise level for the suppressor alone configuration will be lower if its exit area would be higher, like those for the fluid shield configurations. To identify the effectiveness of the shields the EPNdBs for the conic nozzle and the suppressor alone configurations are scaled to the areas corresponding to the combined exit areas of each of the fluid shield configurations.

This figure illustrates the noise benefit realized by the 0.75"-thick fluid shield nozzle, that the fluid shield gives substantial additional EPNdB attenuation compared to the suppressor alone configuration in the range of 60-90 klbs ideal gross thrust.

NOISE SUPPRESSION DUE TO 0.5"-THICK & 1.0"-THICK FLUID SHIELD NOZZLES WITH POROUS PLUG

(V_F=360 FT/SEC, SL=1629 FT)

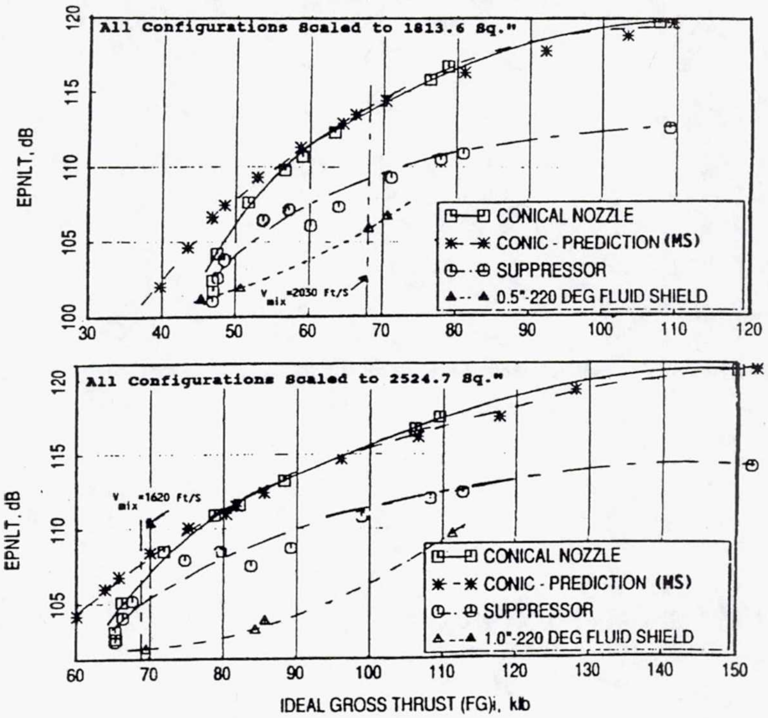

Noise Suppression Due to 0.5"-Thick and 1.0"-Thick Fluid Shield Nozzles in Equal Area Basis: For the 0.5"-thick fluid shield nozzle, the fluid shield yields substantial additional EPNdB attenuation compared to the suppressor alone configuration in the range of 50-75 klbs ideal gross thrust. for the 1.0"-thick fluid shield nozzle, the fluid shield gives substantial additional EPNdB attenuation compared to the suppressor alone configuration in the range of 70-110 klbs ideal gross thrust.

ANNULAR FLOW OVER A CYLINDRICAL PLUG

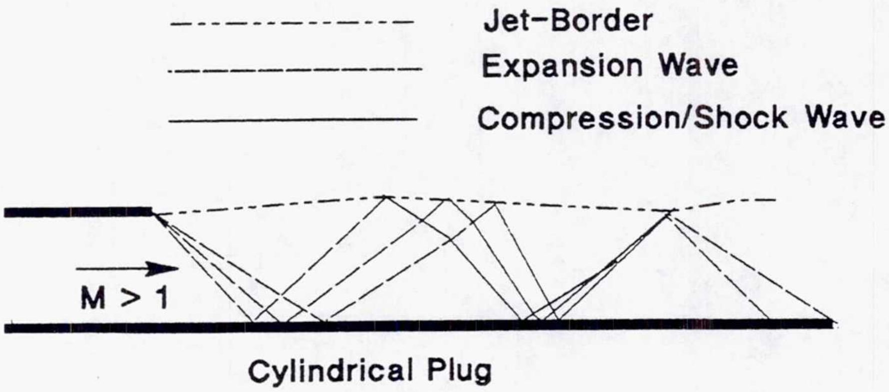

POROSITY WEAKENS OBLIQUE REFLECTED WAVES

∗ How do Chute Side Walls Affect this ?

- Shadowgraph !

Effect of Porosity on Shock-Structures: We examine here the difference in shock-structures between annular flow in nozzles without chutes and those with chutes to explain the relatively poor noise suppression effect of plug porosity obtained in the latter case. The above figure shows the initial development of expansion and shock waves for an underexpanded, annular nozzle with uniform, supersonic exit flow (Mach no. > = 1) over a cylindrical plug, as in Maestrello or Kibens & Wlezien (KW). Expansion waves start from the top nozzle lip. Waves incident on hard wall are reflected as waves of the same type and those incident on the jet border are reflected as waves of the opposite type. The compression waves coalesce into envelope shock waves. It is well known that the strength of the reflected wave is reduced when the plug surface is made porous. One plausible reason (Ribner; KW) is that the incident expansion wave "sees" alternately hard and "soft" walls (the pores) which creates a smeared reflected expansion wave of effectively reduced strength. This results in reduction of the strength of the shocks to follow, consequently suppressing the shock-associated noise which is predominantly produced in the region of interaction of the shock-waves with the shear-layer turbulence. Whether such a reduction in shock-strengths occurs in nozzles with chutes - where the chute side-walls can drastically alter the shock-structure - needs to be examined. We explore it next via a shadowgraph.

Maestrello, L. (1979), AIAA Paper No. 79-0673; Kibens, V. & Wlezien, R.W. (1985), AIAA J., Vol. 23, No. 5, 78-684; Ribner, H.S. (1981), AIAA J., Vol. 19, No. 12, 1513-1526.

SHADOWGRAPH: FLOWFIELDS ON SHIELDED AND UNSHIELDED SIDES OF A FLUID SHIELD NOZZLE OF 1"-THICK SHIELD WITH POROUS PLUG.

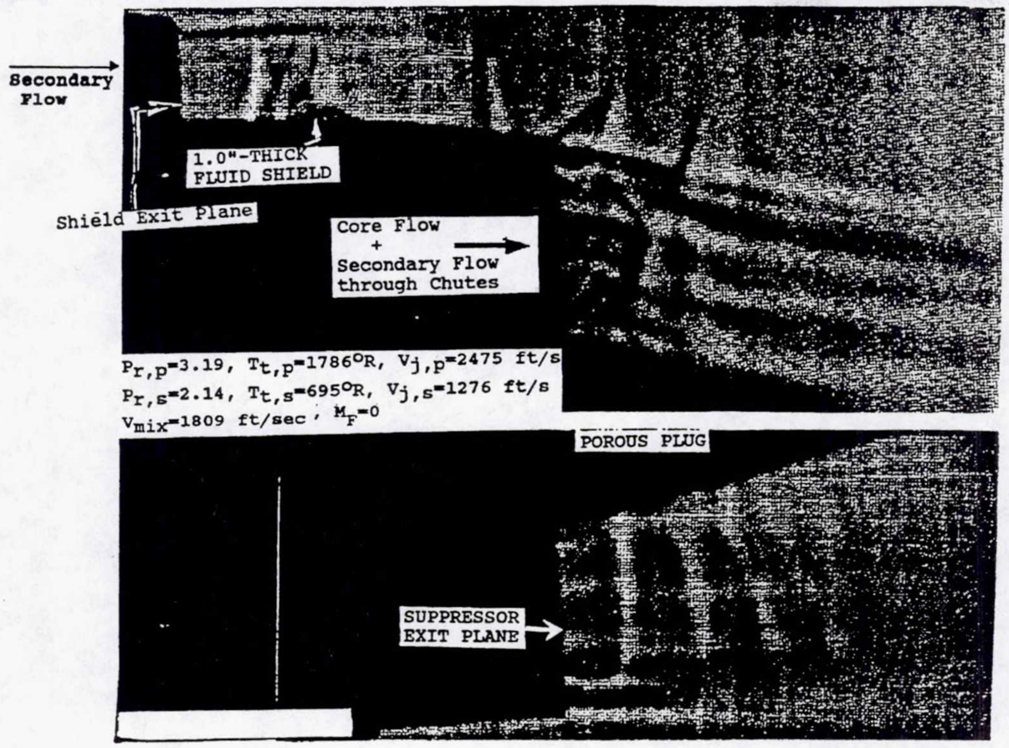

Typical Composite Shadowgraph for Fluid-Shield Nozzle in Cell 41 with Supersonic Shield and Core Flows: It shows the unshielded side on the bottom and the shielded side on the top. Shock surfaces orthogonal to the plane of the paper appear as black lines followed by white lines downstream; whereas, rarefaction waves appear as white lines followed by black stripes. However, vortex-sheets, shear-layers or jet-borders also appear as black/white stripes. Furthermore, in such a side-view of the round nozzle the flow structures from many adjacent chutes are projected at different heights, thus making it difficult to discern the core-flow shock- structure. For example, the five horizontal stripes on either side are simply the projected views of the azimuthal shear layers between the two flows from ten adjacent chutes. Similarly, the expansion/shock pairs in the shield-flow formed near the top chamfered-lips of adjacent chutes (seen clearly here on the top-most chute lip) are projected close to the chute exit plane. (The upstream inverted-V shock structures in the shield-flow are merely due to some protuberances, such as, a bent static pressure tube, etc.) Thus, the remaining features are associated with the core-flow shock-structure. Particularly, note the following: (a) on both sides there are almost vertical stripes; on the unshielded side they seem to become orthogonal to the plug-surface as we go downstream, (b) the vertical shock surface on the shielded side also has a V-shaped shock on its top and a faintly discernible inverted-V shock on the bottom. These shock-structures are, thus, distinctly different from those for unchuted annular plug nozzles discussed in the previous figure. In particular, note the presence of vertical shock-surfaces which bridge the top "lip-wave" and the plug-surface.

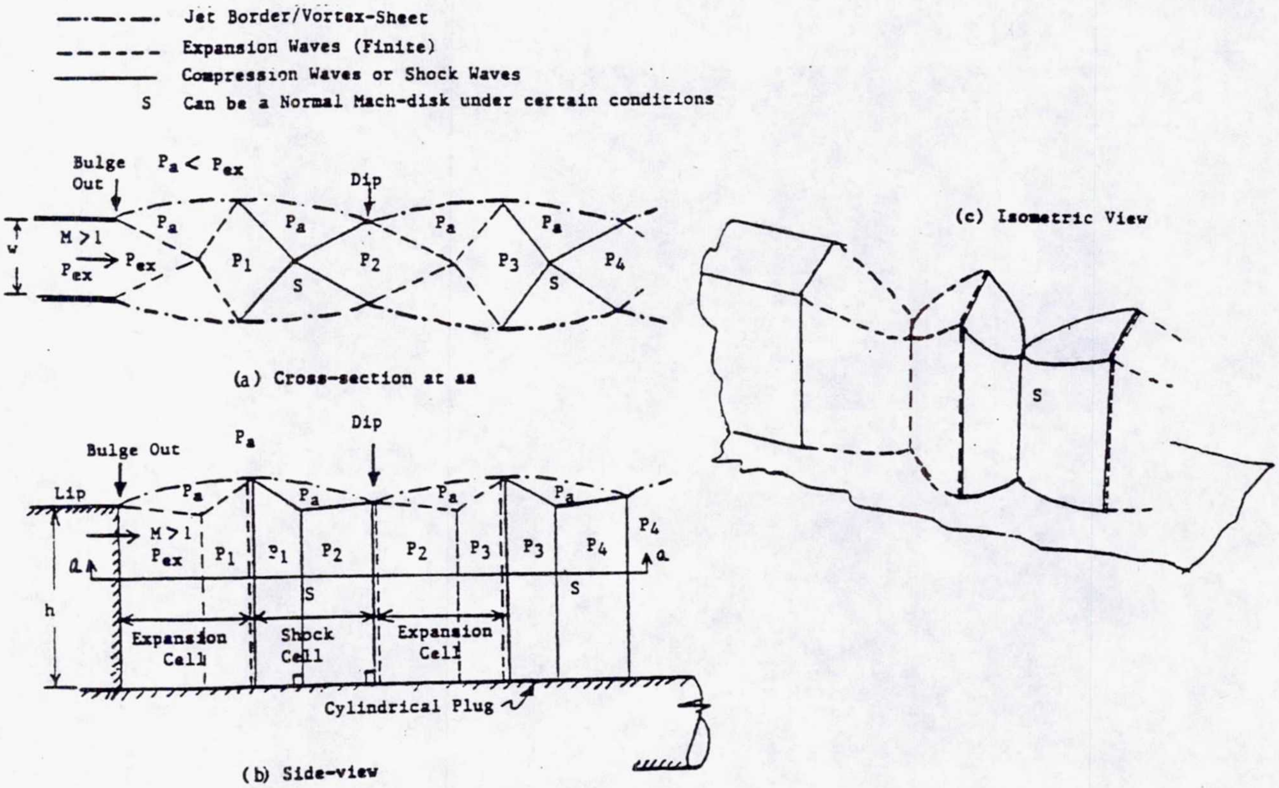

(a) Cross-section at aa

(b) Side-view

Possible 3D Shock-Cell Structure from an Under-Expanded Chuted Nozzle with Non-Porous Cylindrical Plug: In the above figures we attempt to build a three-dimensional model of the core shock-structure to understand the role of plug porosity in such chuted nozzles. As a first step, however, only uniform, supersonic, underexpanded exit flow through one radial chute over a large cylindrical plug is assumed. For a tall chute of high aspect ratio, the wave development, say, below mid-chute height is expected to be two-dimensional and is shown in the top figure. The spatial evolution of the top lip-wave, which must be an expansion wave , and in general, of the overall plume shock-structure needs to be such that its bottom cross-section looks like the top figure. One possible evolution with non-diverging jet-border which also (a) does not violate any pressure inequalities across either type of wave (expansion or shock), e.g., $p1 < pa < pex$, $p2 > pa > p1$ etc. and (b) satisfies the usual wave reflection laws is shown in the bottom figures. The strengths of the shock-surfaces (either those orthogonal to the plug or the top V-shocks) are governed largely by the expansion waves originating at the chute edges and, hence, by the nozzle pressure ratio and not so much by the plug porosity. The top lip-wave simply reflects periodically from the orthogonal shock-structures never to "see" the plug-surface. Thus, the shock-associated noise for this nozzle will not be affected much by plug-porosity. Some similarities can be noticed between this model and the shadowgraph, such as, the shock-surface, S, the inverted-V shocks, the shape of the jet-border, etc. A conical plug will, indeed, modify the foot of these shocks locally and a supersonic shield flow can alter the "ambient" lip pressure; however, the key features of the above argument remain unchanged.

POTENTIAL IMPROVEMENTS FOR FLADE

- SHOCK FREE CHUTE DESIGN (C-D CHUTES).
- IMPROVED CHUTE SUPPRESSOR DESIGN FOR ACOUSTICS AND TAKEOFF CFG (SAR, CHUTE LEADING EDGE ANGLE AND CHUTE FLOW PATH).
- OPTIMIZED SHIELD GEOMETRY (SHIELD THICKNESS AND SHIELD STAGGER).
- CYCLE OPTIMIZATION (BYPASS RATIO AND SHIELD PRESSURE RATIO).

SAR = SUPPRESSOR AREA RATIO

CONCLUSIONS

- ACOUSTICALLY BEST SUPPRESSOR-SHIELD CONFIGURATION (0.75"-THICK OR 1.0"-THICK) EXCEEDS FAR 36, STAGE 3 SIDELINE LEVELS BY 3.5 EPNDB.
- 10% POROUS PLUG YIELDS SUPPRESSION OF ABOUT 1 EPNDB FOR ALL JET VELOCITIES COMPARED TO HARDWALL PLUG CONFIGURATIONS.
- A 3D SHOCK MODEL HAS BEEN PROPOSED FOR CHUTED NOZZLES WHICH MAY EXPLAIN THE HIGHLY REDUCED BENEFIT OF PLUG-POROSITY ON SHOCK-ASSOCIATED NOISE.

Potential Improvements for Fluid Shield Nozzles: The fluid shield nozzle configuration falls short of about 3 to 35 EPNdB in meeting the FAR 36, Stage 3 requirement at takeoff. The fluid shield configuration can be improved to achieve the goal of FAR 36, Stage 3 EPNdB level. The possible improvements to the suppressor and the shields are listed in this table.

Page intentionally left blank

1999176541

ACOUSTIC AND AERO-MIXING TESTS OF FLUID SHIELD NOZZLES

Part II–2D Fluid-Shield Nozzle Aero-Mixing Tests

V.G. Mengle, H-W. Shin, C. Whitfield, S. Wisler, and J. Askew
GE Aircraft Engines
Cincinnati, Ohio

54-07

409515

8p

Sketch of Typical ARL 2D Fluid-Shield Model

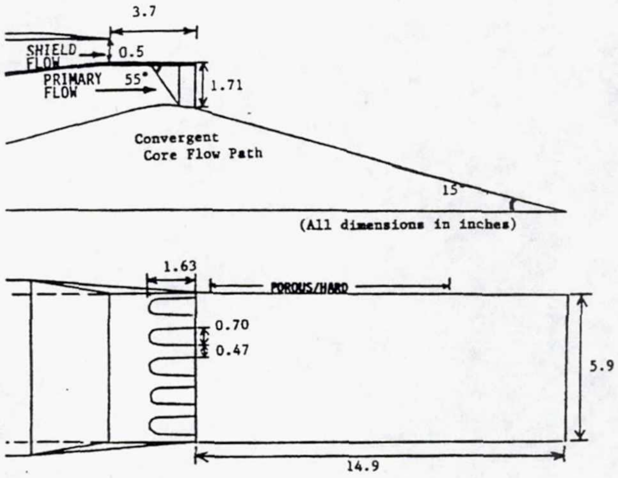

OBJECTIVE: Understand Shock-Structures, Mixing Process & Pressure Distributions

METHOD: Shadowgraph; Static Pressure Taps
Laser Velocimetry; (Planar Laser Sheet)

The objective of the fluid-shield nozzle aero-mixing tests being conducted in GE's Aerodynamic Research Laboratory (AR) is to complement the acoustic tests done on such nozzles in GE's Cell 41 as reported in Part I. The focus is to help understand the fluid-dynamics and the aero-dynamics of such nozzles to improve their performance. In particular, we need a better understanding of: (a) the three-dimensional shock-structures that produce shock-associated noise, (b) the mixing process between the shield-flow, the core-flow, and the ambient flow which affects the fluid-shield evolution and acoustic efficiency, and (c) the pressure distributions on the chutes and the plug which affect the drag. The models in the ARL tests were, however, "two-dimensional" or rectangular in nature and the above figure shows the baseline model layout. It is similar to an "unwrapped" sector of the original round fluid-shield model used in Cell 41 and may also help in the design of future generation 2D fluid-shield nozzles. Shadowgraphs, laser velocimetry, and static pressure tap measurements were the primary tools used and planar laser sheet is planned to be used in the near future for flow visualization. The LV-system used, namely two-focus laser (L2F), is briefly described in the previous paper. This paper gives a flavor of typical tests results and insights obtained about flows in such nozzles.

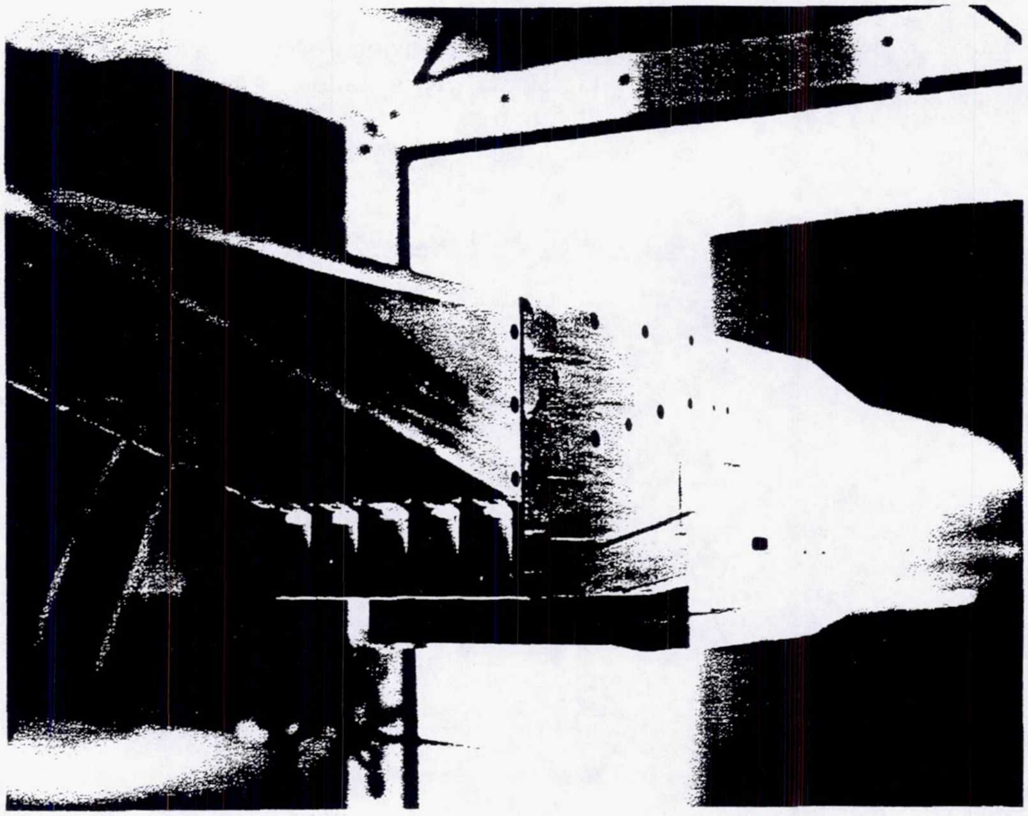

The above photograph shows a close-up of the typical fluid-shield nozzle model mounted on a sting inside a wind-tunnel in ARL. This facility is a single return, continuous flow, ambient wind-tunnel and is operated as a free-jet of 2'x2' exit-section capable of providing a maximum of approximately 300 ft/s flow without any blockage effect. With the blockage due to the sting and the model the maximum speed is estimated to be 225 ft/s which at ambient temperature is a Mach number of about 0.2. The sting is 7.0" in diameter and 108.5" in length. It has two-flow capability with 5.5 lbm/s for each flow and in this test the inner flow passage, which becomes the primary flow, was heated to 850 deg. R. This nozzle model has five side-by-side suppressor chutes, a rectangular fluid-shield nozzle on the top and a half-wedge below. This gives four primary hot jets between the chutes and two half-width primary jets on the two side-ends. This baseline model has convergent core flow passages, a suppressor area ratio (SAR) of 2.5 is defined as the ratio of the sum of primary and secondary flow areas to the primary flow area at the chute exit plane) and chute-depth equal to its height. The fluid-shield thickness can be set at three nominal values: 0.5", 0.75", and 1.0". The inclined surface of the wedge can be made hard or 10% porous with all perforations open to the wedge cavity whose communication, in turn, with the ambient flow below the bottom surface of the wedge could be switched on or off through two vent holes there. Four other chute models with different SAR's, chute depth-to-height ratios or convergent-divergent core flow paths were also made to examine the effect of these parameters.

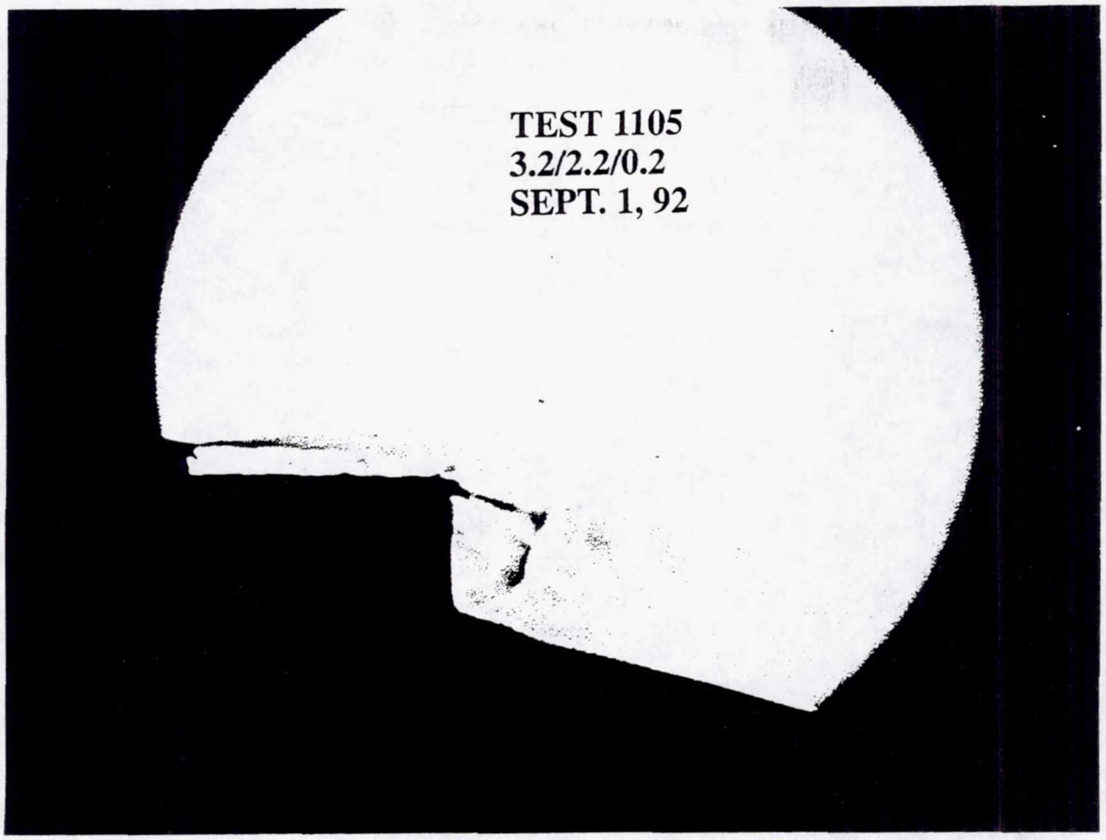

This is an overall shadowgraph for the baseline mode (# 1105F) whose geometric characteristics were described earlier. The primary nozzle pressure ratio (NPR)p)), that is, ratio of primary total pressure to ambient pressure is 3.2, the secondary nozzle pressure ratio (NPR(s)) for the shield-flow is 2.2 and the wind-tunnel Mach number (Mach(wt)) is approximately 0.2. These pressure ratios imply supersonic velocities in both the primary flow and the shield flow. Interpretation of such shadowgraphs was mentioned in Part I. Thus shock and expansion waves are seen to occur in both the flows. More shocks were also observed further downstream on the wedge but were not captured in this photograph due to their high jitter. Some notable features in the top shield flow are: (a) evolution of the expansion-wave from the shield nozzle top lip, (b) bulges and dips in the top shield jet border, (c) evolution of expansion-wave starting from the chute entrance, (d) expansion-wave at the chamfered-edge of the shield-floor (which has an angle of 10 degrees), and (e) oblique shock at the bottom shield-floor lip which intersects the upstream expansion-wave from the chamfered-edge near the jet-border and appears to nullify because this wave-pair does not reflect back from the top shield-jet border. These waves seem to follow the usual laws for planar wave reflections. However, the shield flow will also spill over (spanwise) into the chutes creating complicated three-dimensional wave-surfaces there. These shield-flow wave structures also seem to imply that shocks may exist inside the chutes and which may further reflect from the inclined edges of the chutes.

Sample of LV-Survey

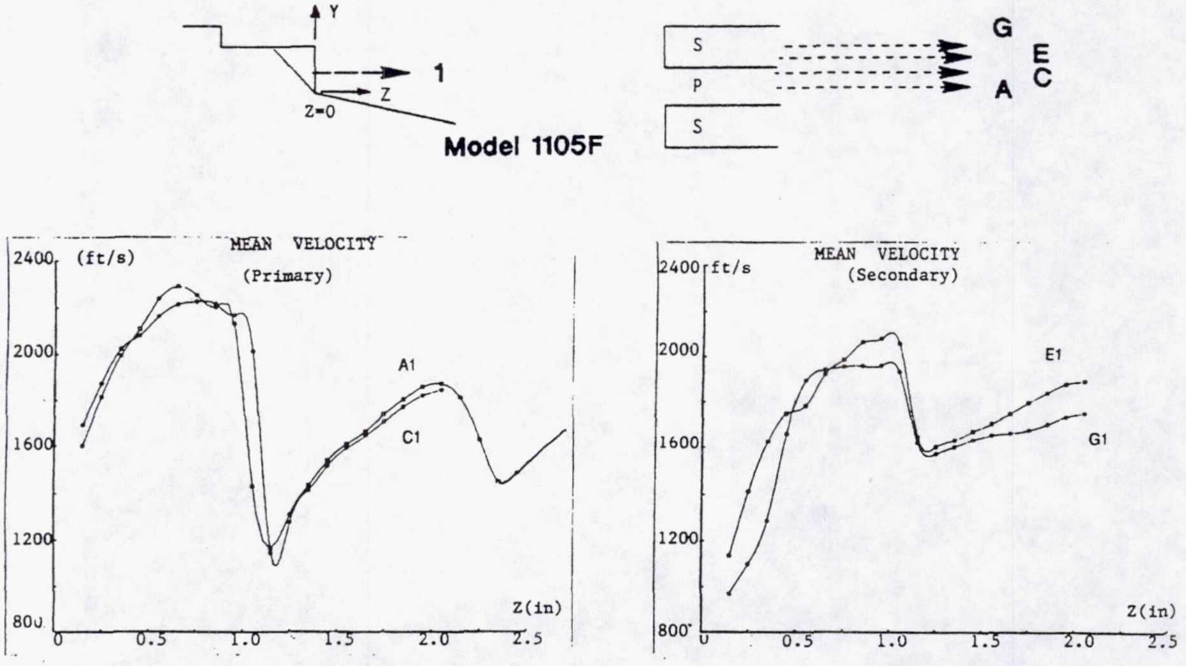

Vertical Shock-Surface A in Both Primary & Secondary Flows !

This is a close-up of the previous shadowgraph to clarify some of the details in the shock-structures on the wedge surface. Some of the flow-structures are labeled for convenience. Note the following features: (a) The shock-cell-like structures develop axially rather than parallel to the wedge surface and do not appear to hug the wedge (boundary layer separation ?). (b) Some hairline-like lines sprouting from the porous wedge surface (most likely Mach lines). These lines were absent for the non-porous wedge. (c) Oblique shocks B and D from top and bottom of the chutes. (d) Shock-surface A joining shocks B and D (Mach-disk?). (e) Shock-surface C connecting B and A (as at a triple shock-point). (f) Vertical shock-surfaces like E. Note that since this is a side-view the appropriate shock-surfaces from flow regions in various vertical planes are superimposed. Hence, it is not possible to conclude with certainty the spanwise locations of these surfaces from this shadowgraph alone. For example, it is not clear whether the shock-surface A is in the primary flow path or the secondary flow path or both. To clarify this and to obtain quantitative data, we not only followed up these shadowgraph experiments with laser velocimetry but, indeed, tailored the LV-traverses individually for each configuration after first scrutinizing these shadowgraphs. Thus a better perspective of these shock-structures can be obtained only after examining the LV-traverse data. We restrict in this paper to only a small sample of the LV-data obtained and, hence, our conclusions here will be very limited.

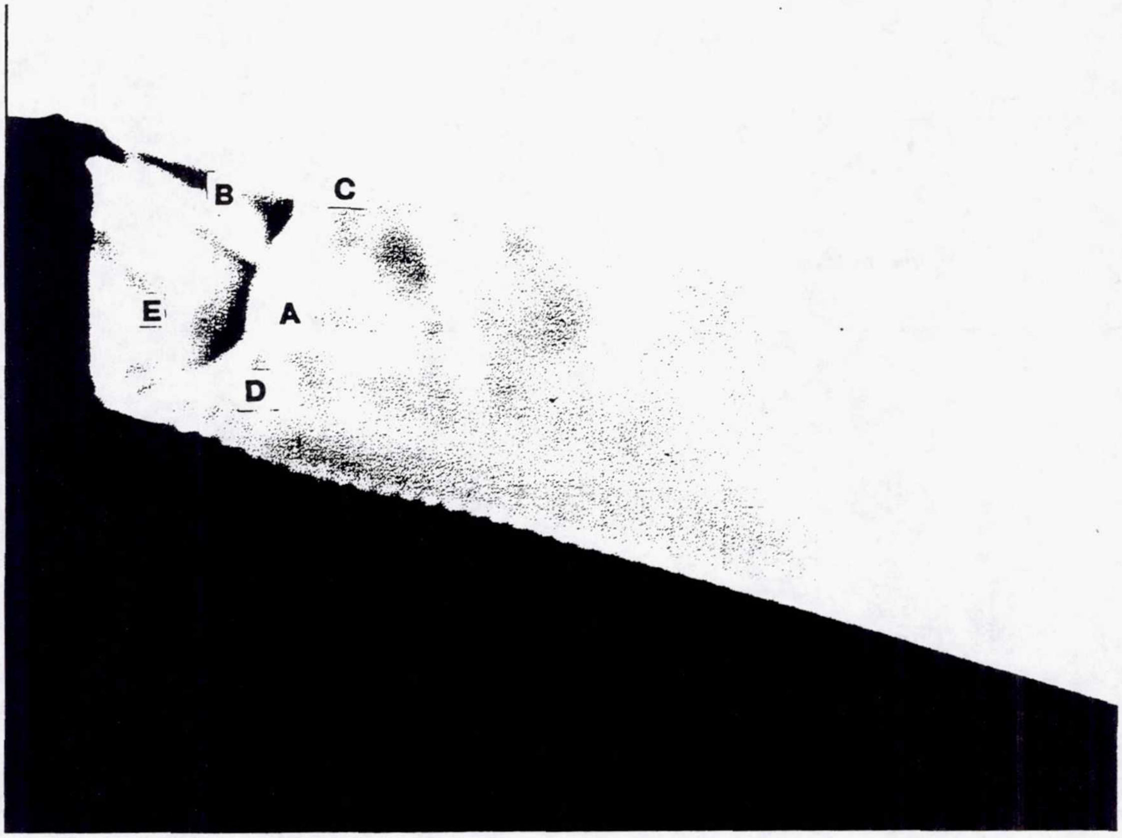

The above figures show a sample of the LV-traverse data. The top two figures show the locations of the LV-traverses: Axial traverse #1 at mid-chute height taken in various vertical planes in the middle chute (center-plane G and side-lip plane E) and the adjacent primary flow (center-lane A and side-lip plane C). The LV-system measures the magnitude and direction of the projection of the mean velocity vector on the vertical plane yz and only the magnitude is shown in the bottom two figures (the directions of A1 and G1 are shown later). Note that the primary flow first accelerates and expands before shocking at Z = 1" and then repeats it after shocking. The most striking feature is the sudden drop in magnitude around Z = 1" in all the traverses. This corresponds to the location of shock-surface A exists along the whole span of the flowfield. Similar traverses in other regions have allowed us to conclude that, e.g., shock E is only in the two end jets, shock B is only in the primary flow and, shocks C and D are in both the flows like shock A. Thus it is possible to build a three-dimensional model of the shock-surface and see where the shear-layers from the chute walls interact with these shock surfaces to locate the dominant source of shock-associated noise.

Velocity Vector Plots

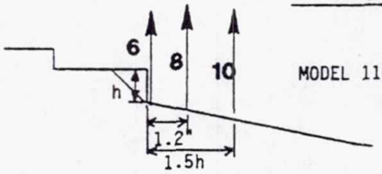

MODEL 1105F

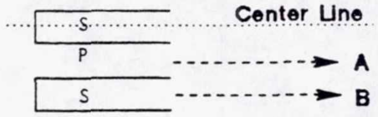

Primary Flow

Secondary Flow

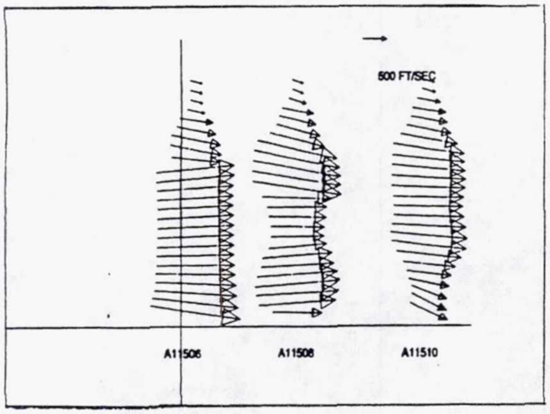

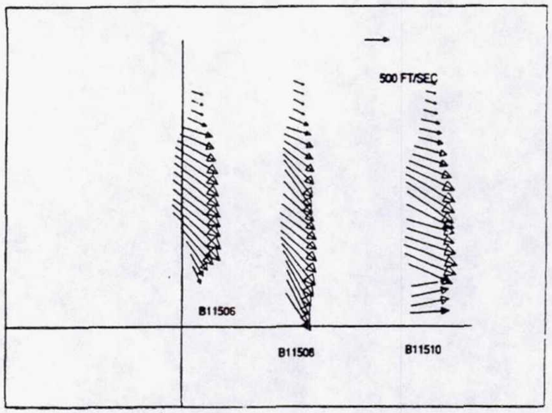

*** Diverging Vertically**
*** Intercepting Lip-Shocks**

*** Axial Vorticity → P & S Mixing**
*** ● chute t.e.: Induces S into P**
● bottom & lifts up b.l.

The above figures show the mean velocity vector-plots (actually, only their projections on the vertical plane) along three vertical traverses in planes A and B. The center of the vector is at the observation point. The diverging velocity vectors in the primary flow just downstream of the exit plan (traverse A6) offer a possible clue in resolving an apparent paradox: With NPR = 3.2, the primary convergent nozzle is expected to be underexpanded with the pressure in the top lip = cavity (between the shield-flow and the primary flow just downstream of the chute exit plane) expected to be close to ambient. However, an oblique lip-shock B is observed in the shadowgraph. Note that although the primary flow passage is convergent in the spanwise direction it is divergent in the vertical direction due to the wedge. For non-parallel exit flows in underexpanded divergent nozzles, the possibility of so-called "intercepting" lip-shocks sticking right behind the usual lip-expansion waves exists, as explained in Courant & Friedrichs book ("Supersonic Flow and Shock Waves," 1976, pp. 389-391) and, perhaps, that explanation applies. here. These figures also show quantitatively the velocity profiles in the horizontal shear-layers between (a) the primary and the shield flow in plane A, and (b) the ambient and the shield flow in planes A and B. The striking difference in the vertical components of the primary and secondary flow at the chute exit plane creates axial vorticity which enhances the mixing between them and induces an uplifting tendency in the primary flow which can separate it from the wedge surface. This is discussed further in the next figure.

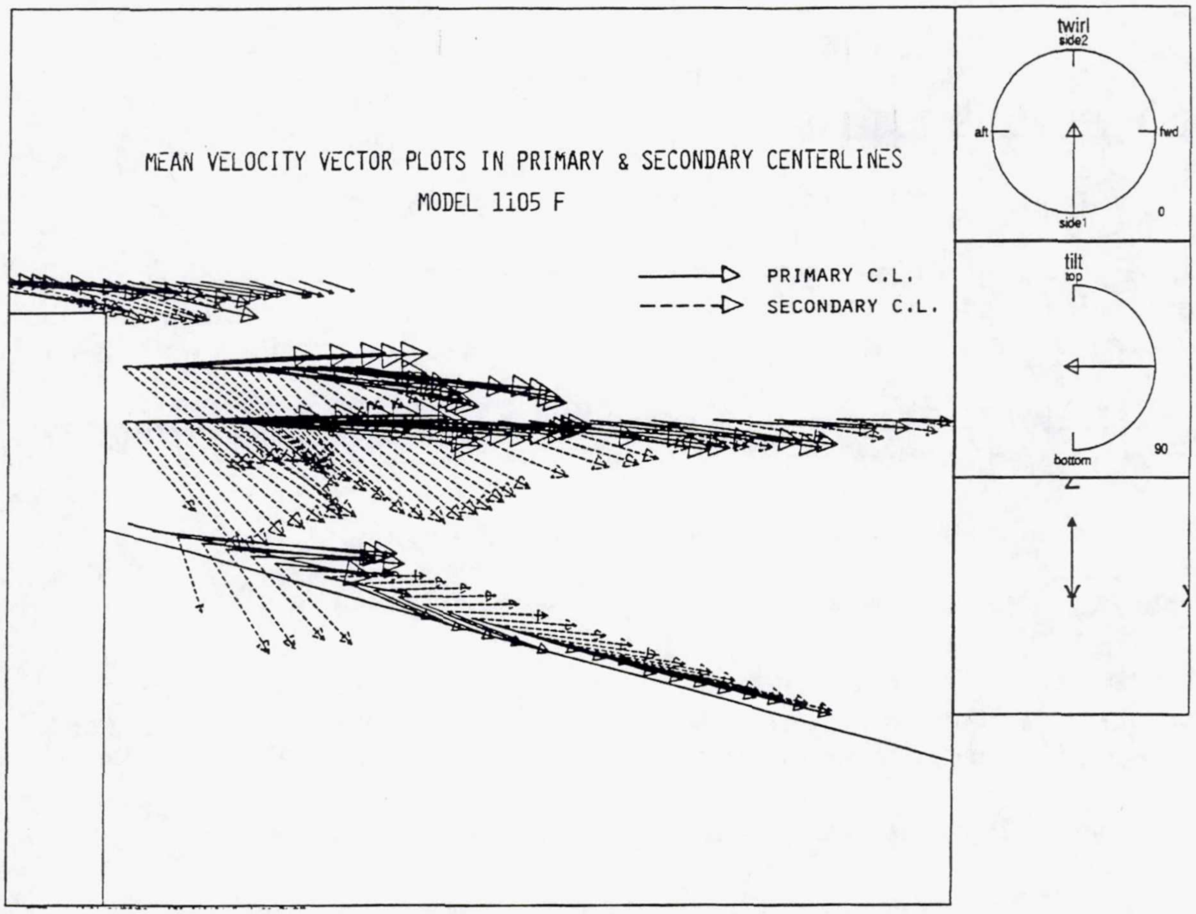

The above figure shows some of the mean velocity vector plots (their projections on the vertical plane) for several LV-traverses on center-lines of each flow. The origin of the vector is at the location of the observation point. It brings out the axial evolution of the angular differences in the two flow regions. The primary flow downstream of the chute exit plane in the upper-half region appears fairly horizontal; whereas, the secondary flow there is inclined downwards - even steeper than the wedge or the chute angle initially and then gradually becoming axial. This has two immediate implications: (1) Shock A, examined earlier, is nearly normal for the primary flow but it is oblique for the secondary flow. (2) The vertical components of these two flows must be generating strong axial vorticity in the shear-layer emitted from the side walls of the chutes. Thus the mixing between the two supersonic flows will be influenced, as in suppressor/ejector nozzles, by not only the vertical vorticity component (arising due to the difference in horizontal velocity components) but also by this axial vorticity component. The axial vorticity will further induce an uplifting of the primary flow and with spanwise spilling of the shield-flow into the chutes strong inverted wing-tip like axial vortices are expected to be shed from the sharp neighboring horizontal edges of adjacent chutes. Also note the sudden change in angles for both flows near the wedge surface which, perhaps, signifies the rear foot of a lambda shock somehow not captured in the shadowgraph.

SUMMARY OF FLOW-FIELD INSIGHTS:

Shield-flow shock-expansion waves are fairly well understood:

- expansion waves evolve from the top shield-lip, the chute entrance and the chamfered-edge of the shield-floor lip-reflecting compression waves coalesce into shock-waves, some of which can focus inside the chutes and re-reflect from them.

- an oblique shock at the shield-floor lip appears to nullify the expansion wave from the chamfered-edge upstream.

Gaining better understanding of shock-structures on the wedge:

- shock cells can separate from the wedge-surface rather than hut it.

- the topology of these shock-surfaces is quite complicated, e.g., a strong Mach-dislike surface spans the whole width of the nozzle and oblique shocks start form the lips of the primary nozzle although it may be underexpanded.

Some understanding of the mixing process was attained:

- the axial vorticity produced at the vertical chute edges due to the vertical components of the shield-flow and the primary flow provides addit8ional mixing; but it also can uplift the primary flow from the wedge-surface.

1999176542

GE/BOEING ACOUSTIC TEST AXISYMMETRIC MIXER/EJECTOR NOZZLE

S5-07

409516

14p.

W.H. Brown and J.F. Brausch
GE Aircraft Engines
Cincinnati, Ohio

BACKGROUND AND OBJECTIVES

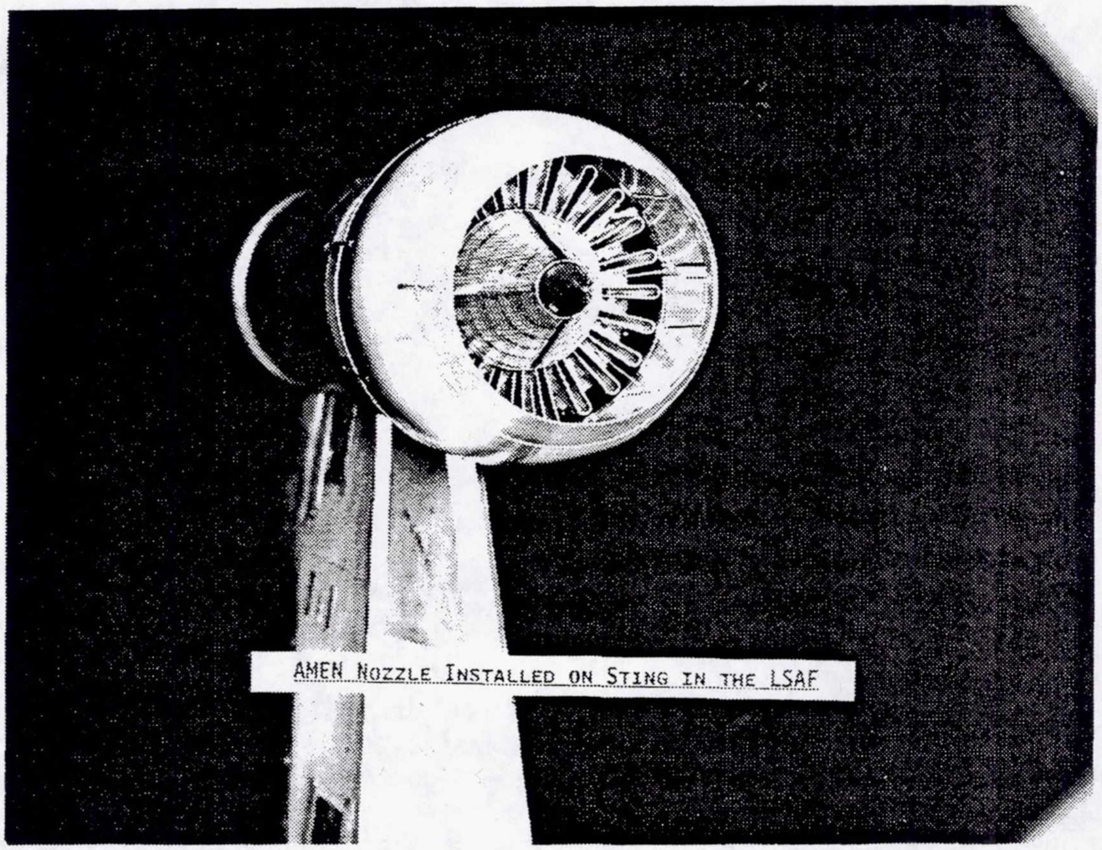

AMEN Nozzle Installed on Sting in the LSAF

Previous studies suggest that the keys to reducing the noise of heated jets are (1) reducing the shear velocity between the jet and the ambient and (2) absorbing as much of the mixing noise as possible before it can propagate to the farfield. Reducing the shear velocity is accomplished in the AMEN concept by the use of suppressor nozzles and ejectors.

In the AMEN concept, the ejector entrains ambient air which is mixed with the engine air to reduce the overall velocity. The AMEN nozzle employs a suppressor area ratio greater than previous studies in an attempt to reduce the mixed jet velocity and obtain high levels of noise suppression at high jet velocities. Treatment of the ejector surface further enhances the acoustic performance by absorbing mixing noise before it can propagate to the ground.

The suppressor nozzle itself serves two functions: (1) it enhances mixing by providing more shear area between the engine flow and entrained air, and (2) it reduces the characteristic dimension of the nozzle so that the wavelengths of the mixing noise are reduced. The use of a plug provides more surface for acoustic treatment as well as the possibility of using porosity to reduce shock noise within the ejector by wave cancellation off the plug surface.

The efficacy of bulk absorbers at two different densities and of two plug surface porosities was evaluated both statically and in simulated flight with both flush and scoop inlets.

IR&D 1.43 SUPPRESSOR SYSTEM PARAMETERS

SUPPRESSOR

SAR 3.7 BASED ON A8; $\approx$ 3.1 BASED ON A89

A8 = 13.2IN^2, D_{8EQ} = 4.1" LSF $\approx$ 1/9 BASED ON L1M CYCLE A8 = 1040 IN^2

RADIUS RATIO = .61

24 C-D CHUTES; $A_{EXIT}/A8 \approx 1.25$ FOR NPR = 4.0, M_J = 1.58 (P_{AMB} = 14.7)

EJECTOR

TIGHT FIT TO SUPPRESSOR O.D.

L_{EJ} = 10.63" (2.59 D_{8EQ}'s)

$A9/A_{MIX} \approx 1.2$

FLUSH AND SCOOP INLETS

TREATED AND HARDWALL

PLUG

15° HALF ANGLE-SHARP TIP CLOSURE

TREATED, HARDWALL AND POROUS (2)

5% AND 10% POROUS SURFACES, .0625" Ø HOLES, .09" WALL THICKNESS

When the suppressor system parameters had been established, a 1D ejector analysis was performed to estimate the entrainment ratio that could be expected. At takeoff, the ratio was estimated to be 1.08 which is consistent with other high SAR nozzles.

The CFL3D flow solver as packaged in the recently released IDA3D system was used for 3D inviscid calculations to establish the flow lines of the model. The primary aero design objectives for the axisymmetric 3D core-side chute geometry were as follows.

* A smooth, shock-free transition from subsonic to supersonic flow through the convergent-divergent core flow passages within the 24 chute elements.

* A well defined sonic line at or near the physical throat.

* A reasonably uniform distribution of core side chute exit static pressure, at least over the majority of the exit flow area.

* Control of possible internal separation due to subsonic flow turning within the passage.

* No recompression of the supersonic flow in the expansion section of the chute, i.e. shock-free operation at the design NPR.

ACOUSTIC TREATMENT

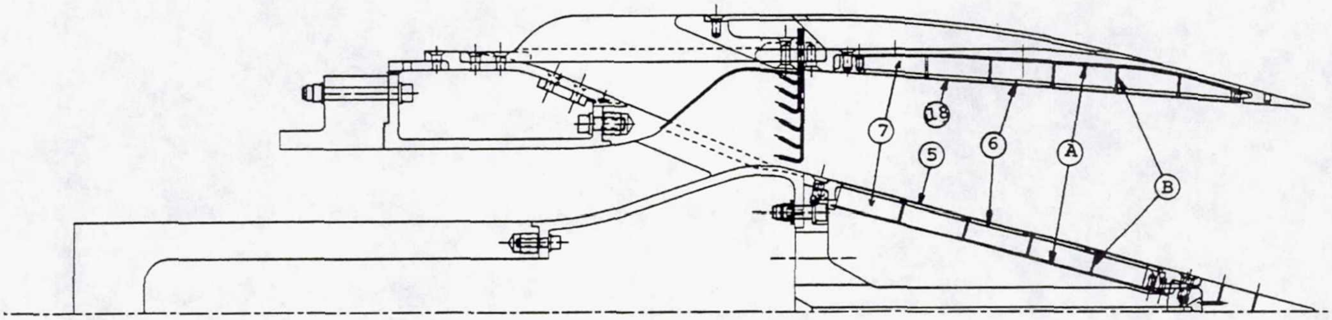

24 C-D Chute/Treated Ejector Acoustic Model System

Flush Inlet - Side View

The acoustic treatment of the plug and ejector trays consists of a perforated sheet metal surface on the flow side 5 and 18 and hard surfaces on the back A , the sides, and the separators B within the trays. Treatment within the trays consists of a layer of 95% porous foam metal 6 about 1/8 inch thick adjacent to the perforate followed by a bulk absorber mat 7 compressed to a density of about 1 lb/ft^3 for T1 and about 2 lb/ft^3 for T2. The foam metal is applied to dampen the effect of flow turbulence on the bulk absorber.

The ejector trays are made hardwall by inserting a contoured solid sheet metal shim between the foam metal and the perforate. The plug uses machined segments with smooth surfaces for the hardwall configuration and similar segments with drilled holes for the 5% and 10% porous plug configurations.

MODEL INSTRUMENTATION

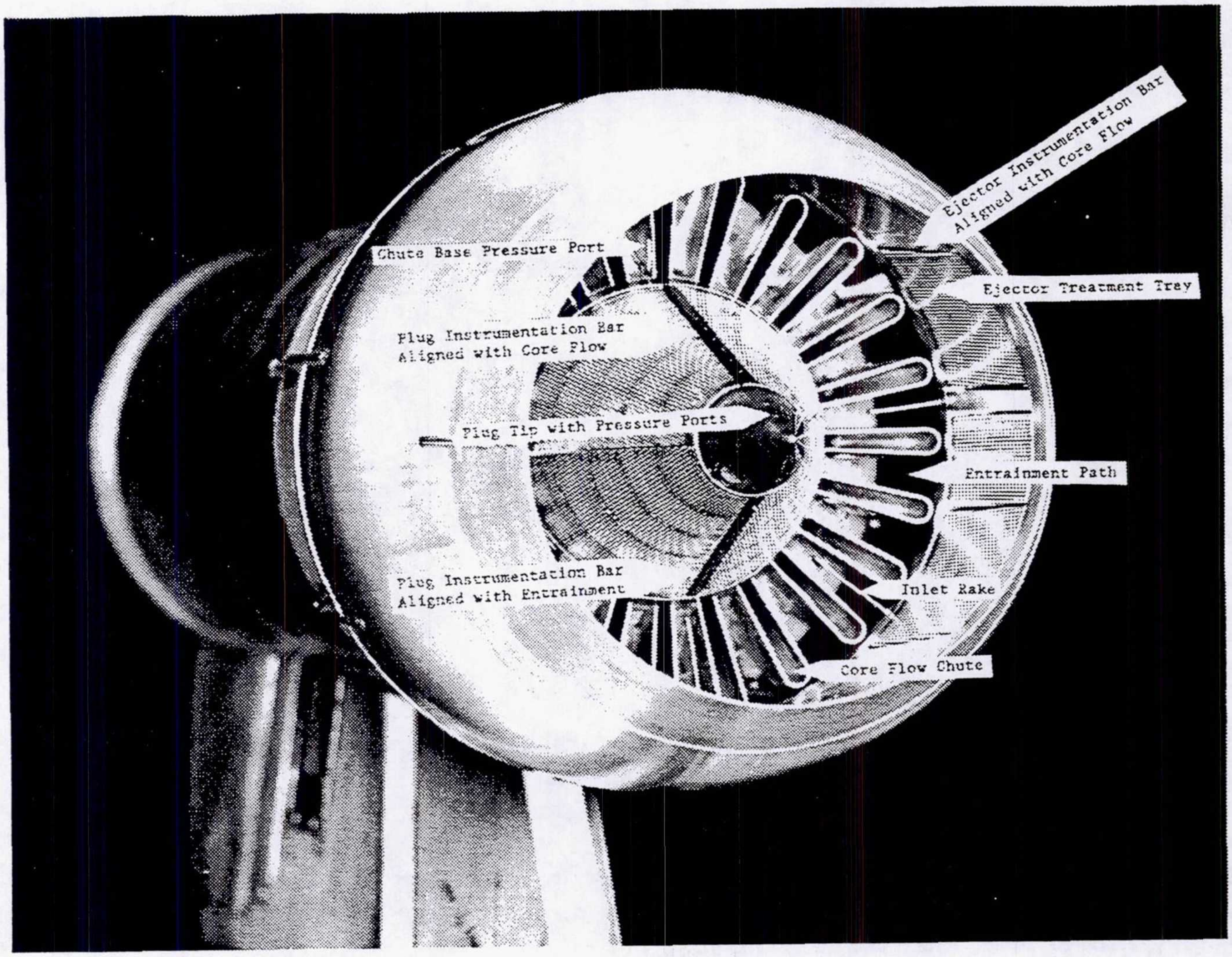

Eighty-three instrumentation measurands were provided on the model for drag assessment, shock detection, flow separation detection, entrainment correlation, structural temperature monitoring, and acoustic treatment environment definition.

Three inlet rake elements can be seen extending from the forward portion of the ejector shroud into the entrainment path. Instrumentation bars on the plug and the inner surface of the shroud are aligned with both hot and cold flow paths to provide axial pressure profiles. Lines for sensing static pressure on the hot flow chutes can be seen particularly where they are positioned to measure base pressures at the chute exit.

MODEL CONFIGURATIONS AND TEST POINTS

MODEL CONFIGURATIONS

CODE	INLET	EJECTOR SHROUD	PLUG
FHH	FLUSH	HARDWALL	HARDWALL
FTT	FLUSH	TREATED	TREATED
FT10	FLUSH	TREATED	10% POROUS
FT5	FLUSH	TREATED	5% POROUS
F22	FLUSH	DOUBLE-DENSITY TREATMENT	DOUBLE-DENSITY TREATMENT
SHH	SCOOP	HARDWALL	HARDWALL
STT	SCOOP	TREATED	TREATED
T10	SCOOP	TREATED	10% POROUS
RC	ROUND CONVERGENT NOZZLE, NO EJECTOR		

These are the configurations for which acoustic data were acquired. The acoustic test points were taken along the VCE GE21/F14 Study L1M cycle line from V_j = 1100 fps to V_j = 2700 fps. Two extra points at V_j = 2400 fps were included to provide data on density effects, one extra point was acquired at $M_t = 0.12$ in addition to the points at $M_t = 0.24$, and one extra point was acquired well off the cycle line at V_j = 2900 fps as a high velocity reference point.

The test program produced 90 entrainment calibration runs (static and wind-on, flush and scoop inlets), 108 aerodynamic performance tests (cold, flush and scoop inlets, static and wind-on), and 206 acoustic and hot aero performance tests (97 static, 109 wind-on, 8 suppressor configurations, and one conic nozzle).

CYCLE LINE SIMULATION

COMPARISON OF INTENDED AND ACHIEVED JET VELOCITY POINTS

L1M CYCLE, STD DAY, 1000 FT ALT, M=0.3

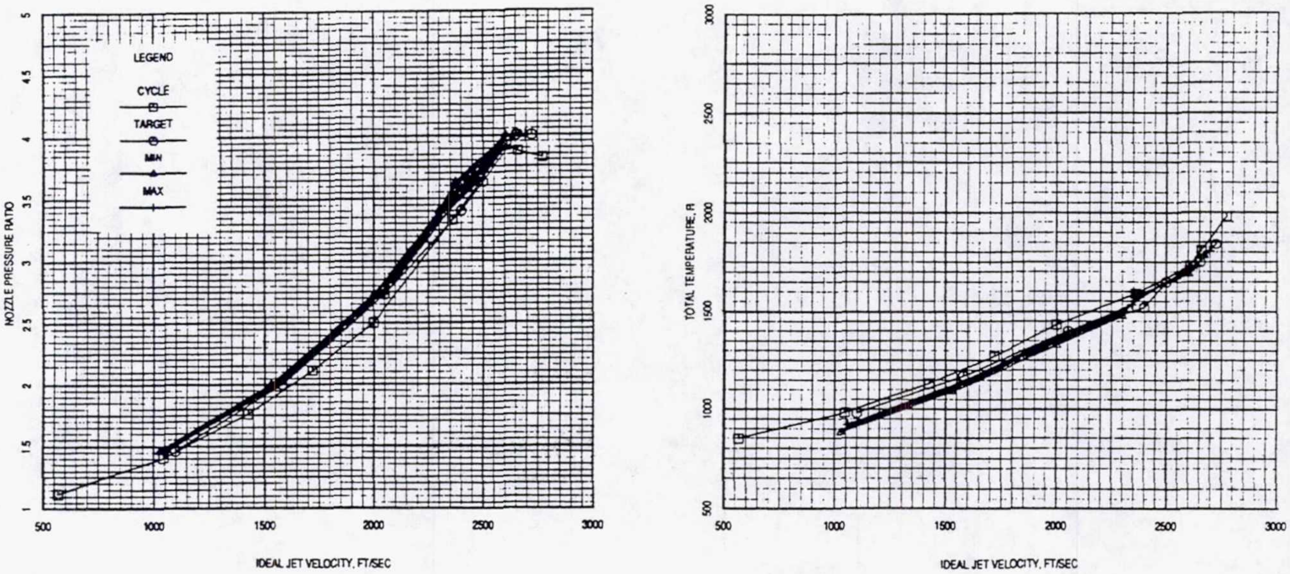

The GE/F14 Study L1M cycle points, the facility set points, and the normal actual range of test points for all suppressor acoustic tests are shown here. Thel model is designed for a maximum temperature of 1500°F. In order to avoid high levels of thermal stress in the model locally due to non-uniform temperatures of the close-coupled burner system, the maximum set point temperature was reduced from 1500°F to 1400°F. In practice, the nozzle pressure ratio fell slightly above the target value and the jet total temperature fell slightly below the target valus for given values of jet velocity. The minimum-to-maximum ranges show that the set point repeatability from configuration to configuration was quite good. The actual deviations from the cycle line are small enough to be unimportant from the acoustic standpoint.

ASPIRATION RATIO

NORMALIZED ASPIRATION RATIO - 10% POROUS PLUG CONFIG

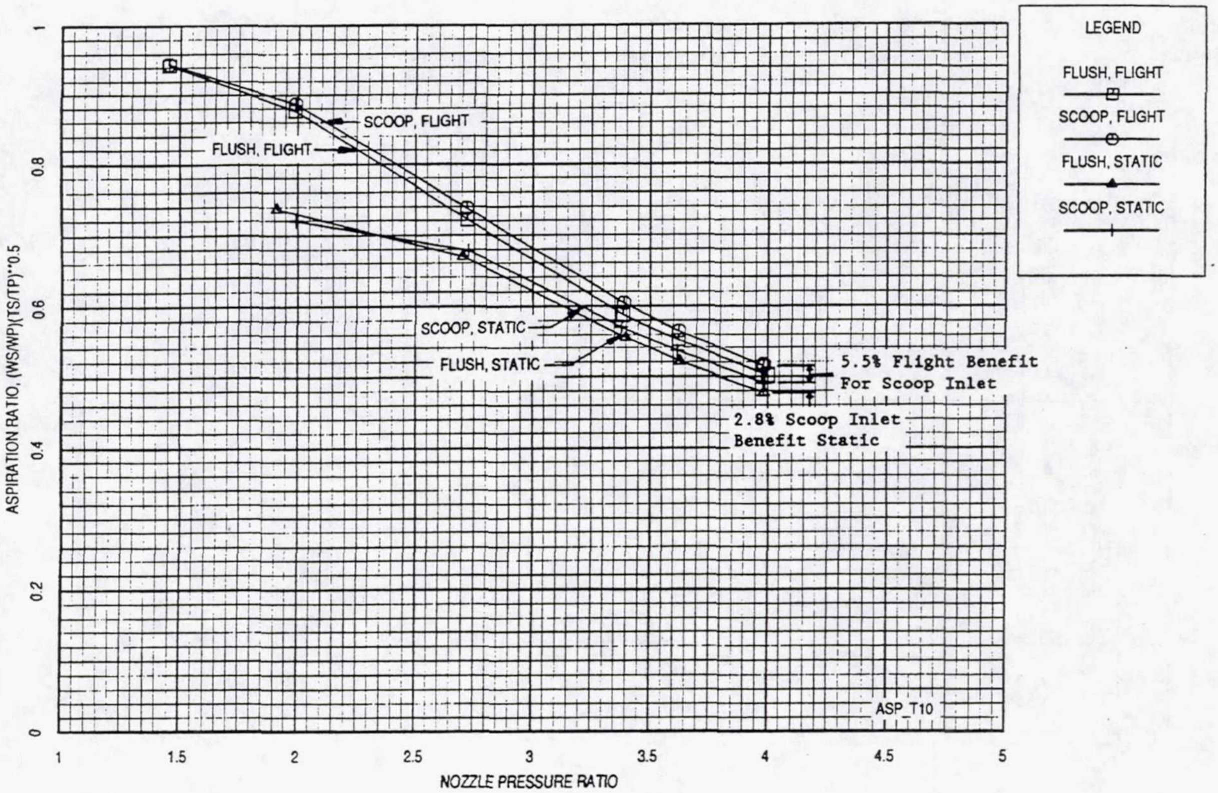

The aspiration ratio here is normalized by the square root of the ratio of the total temperatures of the secondary flow and the primary flow. At almost all conditions, the scoop inlet entrains more air than the flush inlet. The one exception is the static case at very low NPR, and it is not evident why that should be so.

Both inlet configurations apparently benefit from the axial momentum imparted to the entrainment flow by flight. The benefit is greatest at low NPR and diminishes as the velocity of the aspirated flow in the ejector inlet path increases. Even so, flight increases the aspiration ratio about 5.5% at takeoff conditions with either inlet.

The scoop inlet is 2.7% - 2.8% better than the flush inlet both statically and in flight at takeoff conditions. Statically, the scoop inlet is better at high NPR because it has a larger total inlet area than does the flush inlet. Therefore, the entrainment flow velocity around the lip would be lower than that of the flush inlet thereby reducing the likelihood of separation at the lip. Even if separation occurred, the percentage reduction on inlet flow area probably would be less with the scoop inlet than with the flush inlet.

FLOW COEFFICIENTS

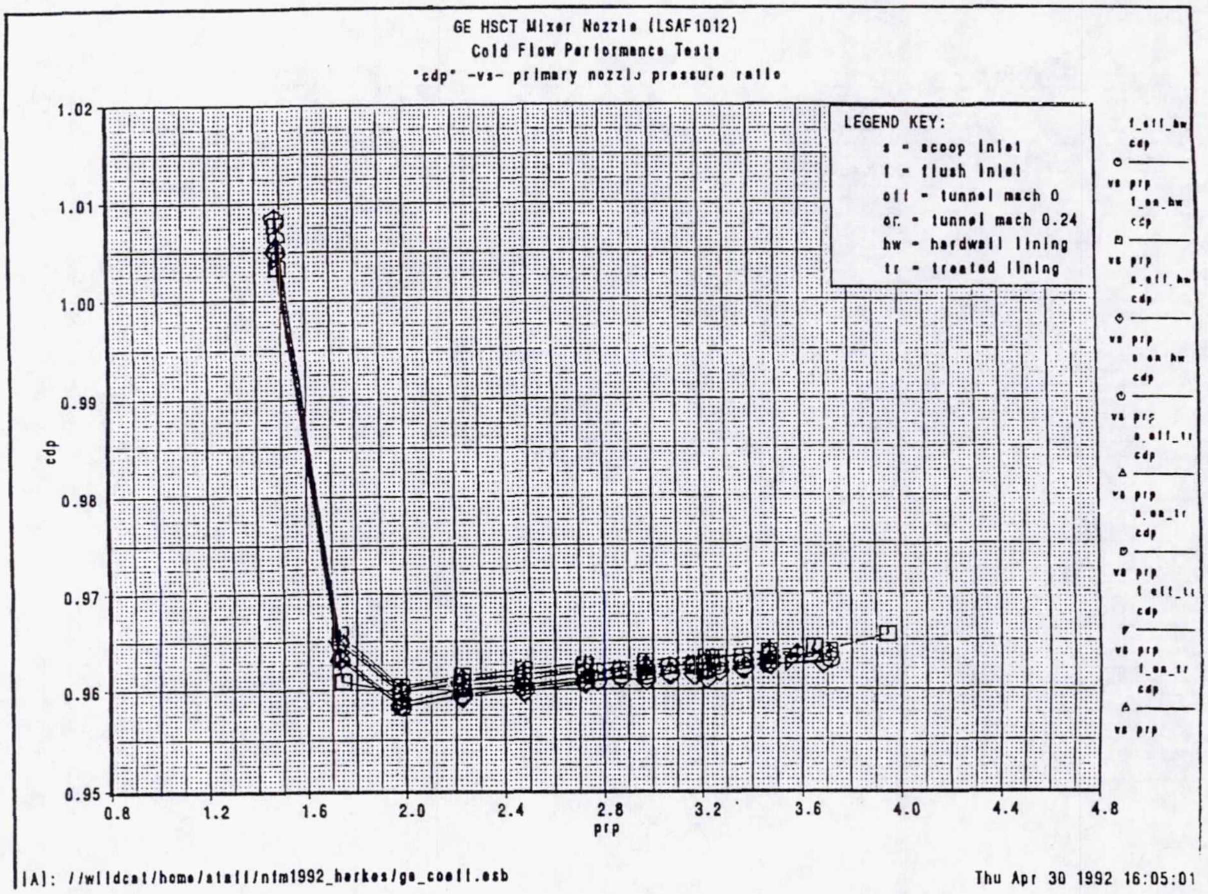

Cold primary flow coefficient data were very insensitive to inlet design, treatment or tunnel speed and are shown here. The data were consistent within about +/- 0.1% of the .962 value. The slight positive slope of discharge coefficient with increasing nozzle pressure ratio implies that there was a slight Reynolds number effect on the model.

THRUST COEFFICIENTS

GE HSCT Mixer Nozzle (LSAF 1012)

Cold Flow Performance Tests

Comparison Of Wind-On And Wind-Off Thrust

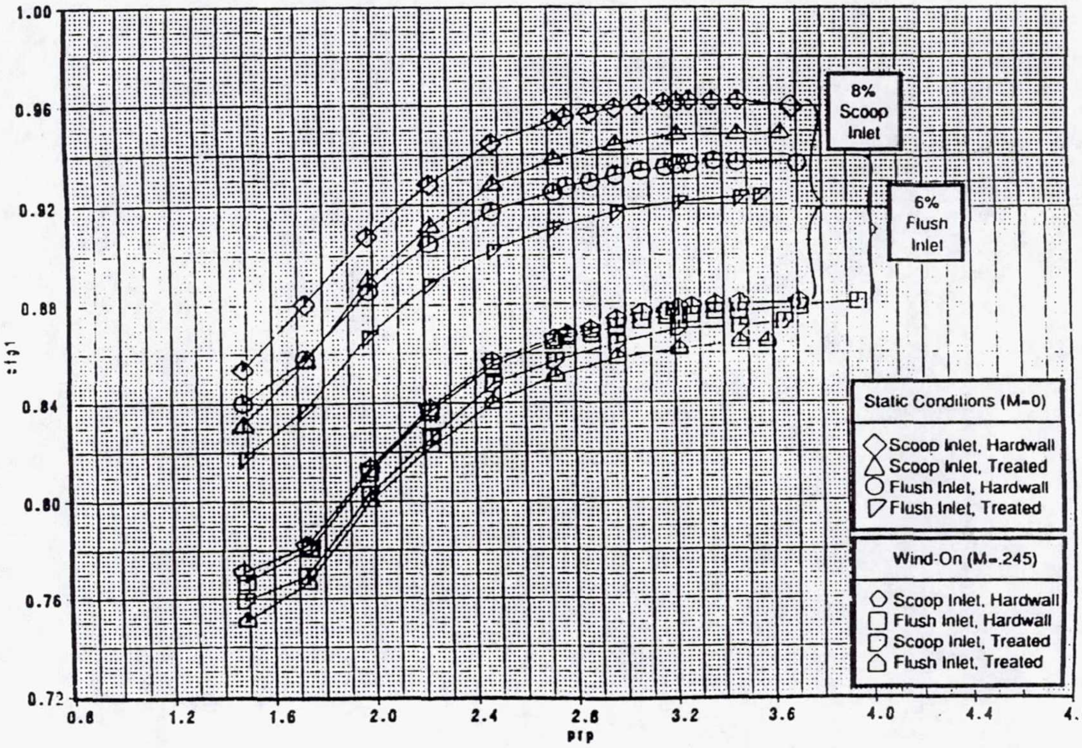

With hardwalls, the flush inlet had a thrust penalty of 0.1 to 0.3% Cfg relative to the scoop inlet. The thrust losses due to treatment installation on the scoop inlet were approximately 0.8 to 1.0% Cfg and about 1.4% Cfg with the flush inlet.

A comparison of the wind-on and static data shows that the scoop inlet suffers a larger drag penalty than the flush inlet. Analysis of the inlet static pressure data indicates that the scoop inlet lost 50% more inlet thrust force due to the external flow than did the flush inlet. In other words, the scoop inlet had a drag increase, which according to the measured data, was about 8% Cfg for the scoop inlet compared to 6% Cfg for the flush inlet as shown here. Integration of the inlet pressure area forces explains 40% to 50% of the loss. It is suspected that the pressure-area forces calculated were somewhat low because the coarse spacing of pressure taps missed the peak suction areas.

HOT VS COLD AERODYNAMIC PERFORMANCE

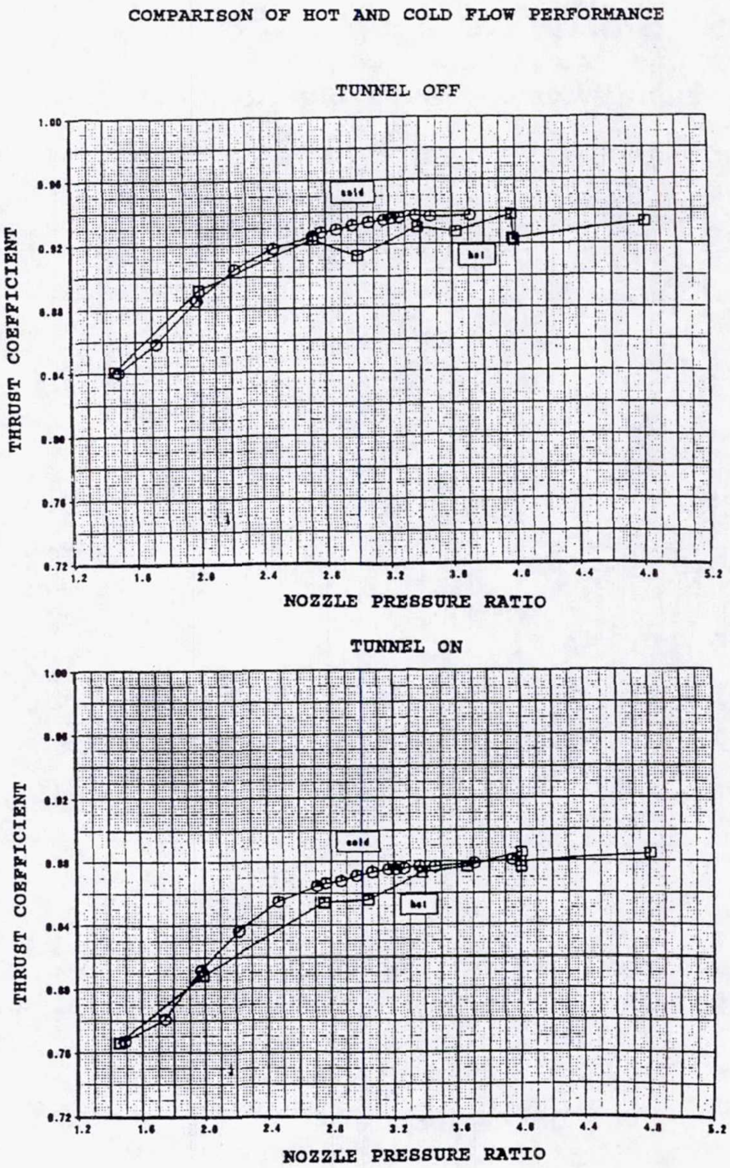

Thrust coefficients measured with hot flow and with cold flow were obtained for both static and flight conditions. For both static and flight conditions, the cold flow data is well behaved. In the static case, the hot flow results agree within about 1/2% Cfg at NPRs up to 2.7 and differ by no more than 2% above that. In the flight case, only two hot points differ from the corresponding cold points by more than about 1/2%, and they fall within 2% of the cold values. This is considered to be reasonable agreement and permits the use of cold flow Cfg results to help interpret hot flow data.

OVERALL RESULTS

SYSTEM EFFECTIVE PERCEIVED NOISE LEVEL BY CONFIGURATION
FLUSH INLET, M=0.245
A8=1040 SQ IN, DIST=1629 FT, STD DAY

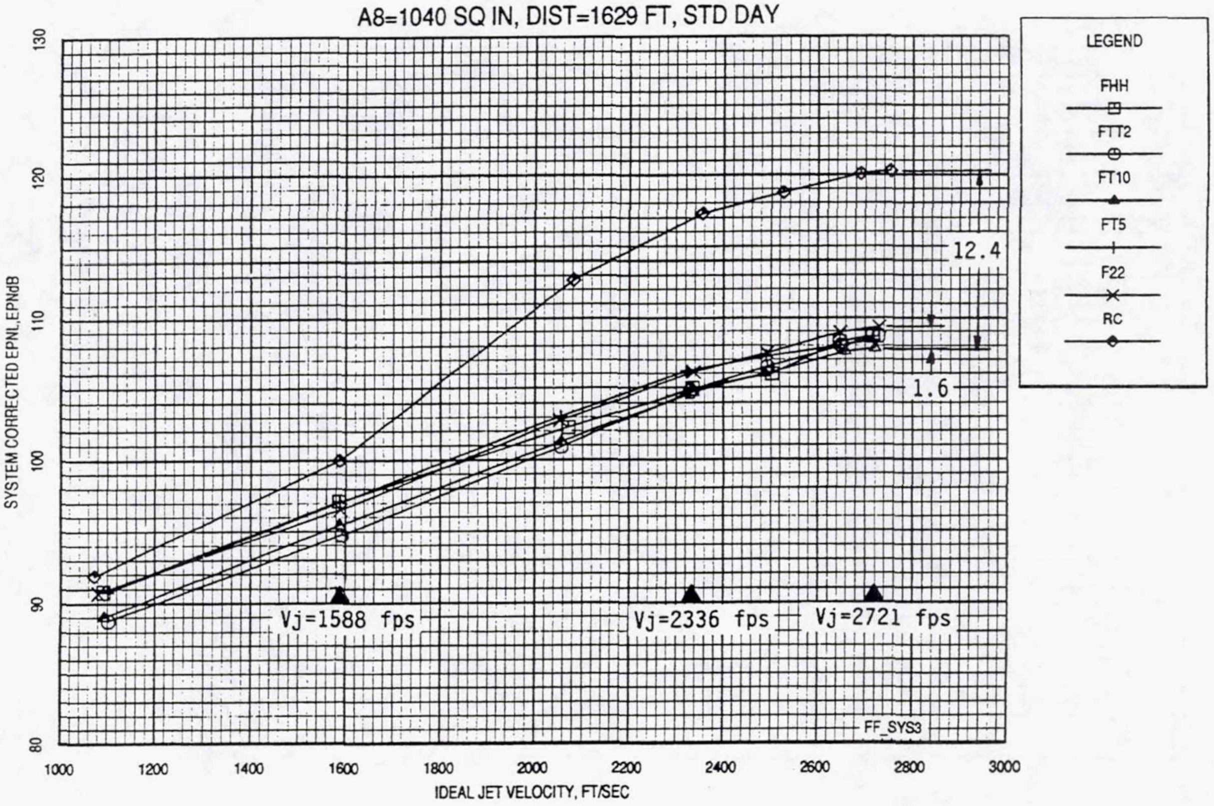

An overview of the acoustic performance of all configurations can be obtained from plots of system EPNL. These plots contain only those test points that simulate the L1M cycle line. Excluded are the test points taken to provide insight into the effects of density variation at a constant VIP and the alternate flight speed of MT = 0.12.

This acoustic performance evaluation is based upon data processed at Boeing. This procedure ensures that the configuration-to-configuration comparisons will be internally consistent.

FLUSH INLET, FLIGHT, EPNL

This figure shows that the maximum suppression relative to a conic nozzle is 12.4 EPNdB at takeoff and 12.3 at cutback. In both cases, the 10% porous plug configuration (FT10) provides the best noise suppression performance. The maximum spread among the suppressor nozzles is 1.6 dB at takeoff with the hardwall configuration falling near the center of the band. At lower velocities the spread is greater and the hardwall configuration is the noisiest as expected.

OTHER EPNLS

The flush inlet configuration statically produced 13.0 EPNdB of suppression at takeoff and 14.3 EPNdB at cutback. The scoop inlet configuration produced 12.5 EPNdB suppression at takeoff and 13.3 EPNdB at cutback in static operation. In simulated flight, it produed 12.0 EPNdB at takeoff and 11.7 EPNdB at cutback.

FLUSH INLET, FLIGHT, PNL

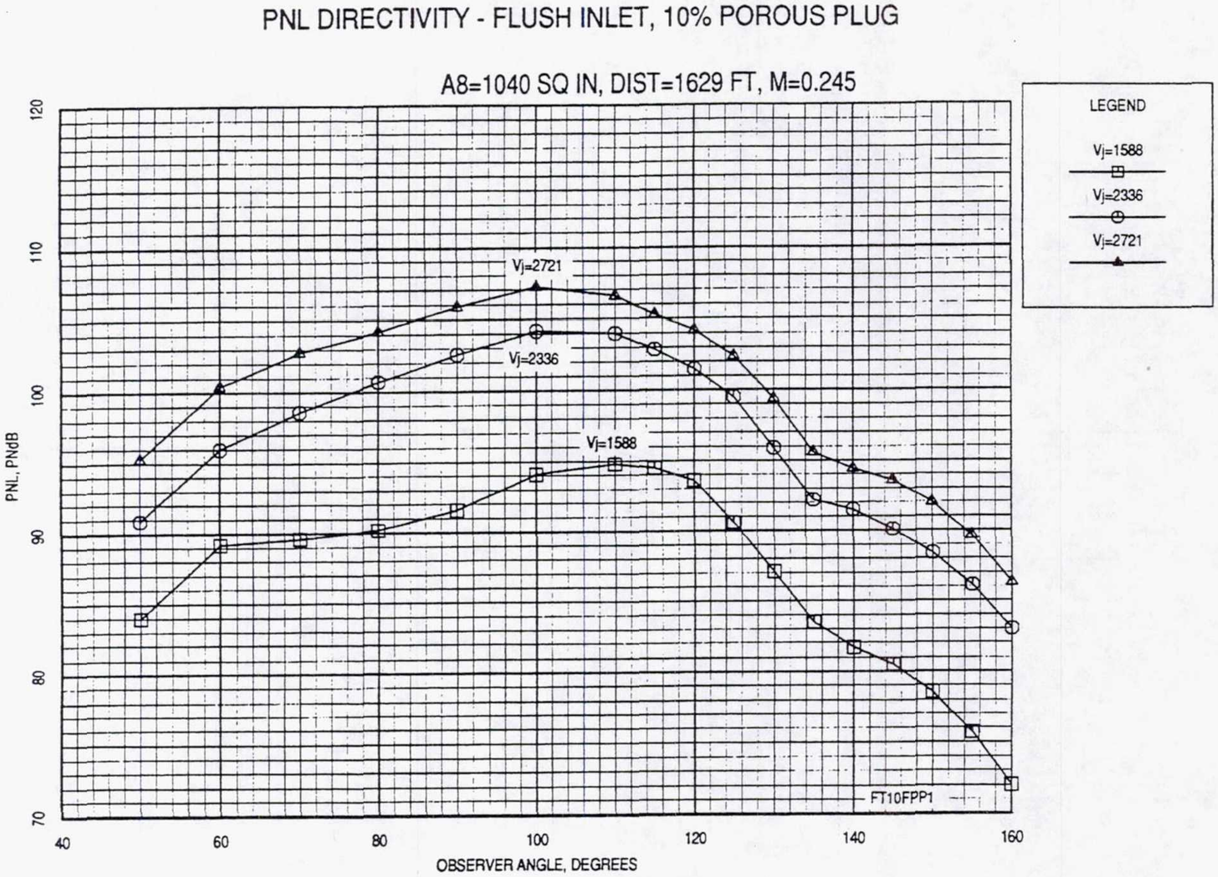

PNL directivities are provided for the takeoff and cutback conditions and for a low velocity (1588 fps) condition for the 10% porous plug configuration. The two higher velocity directivities are generally parallel over the entire theta range. The directivity at the lowest velocity also tends to parallel the other two except in the range between 60 and 120 degrees in which it droops. Spectra can be examined to see if a clue to the observed behavior can be found.

FLUSH INLET, FLIGHT, SPL

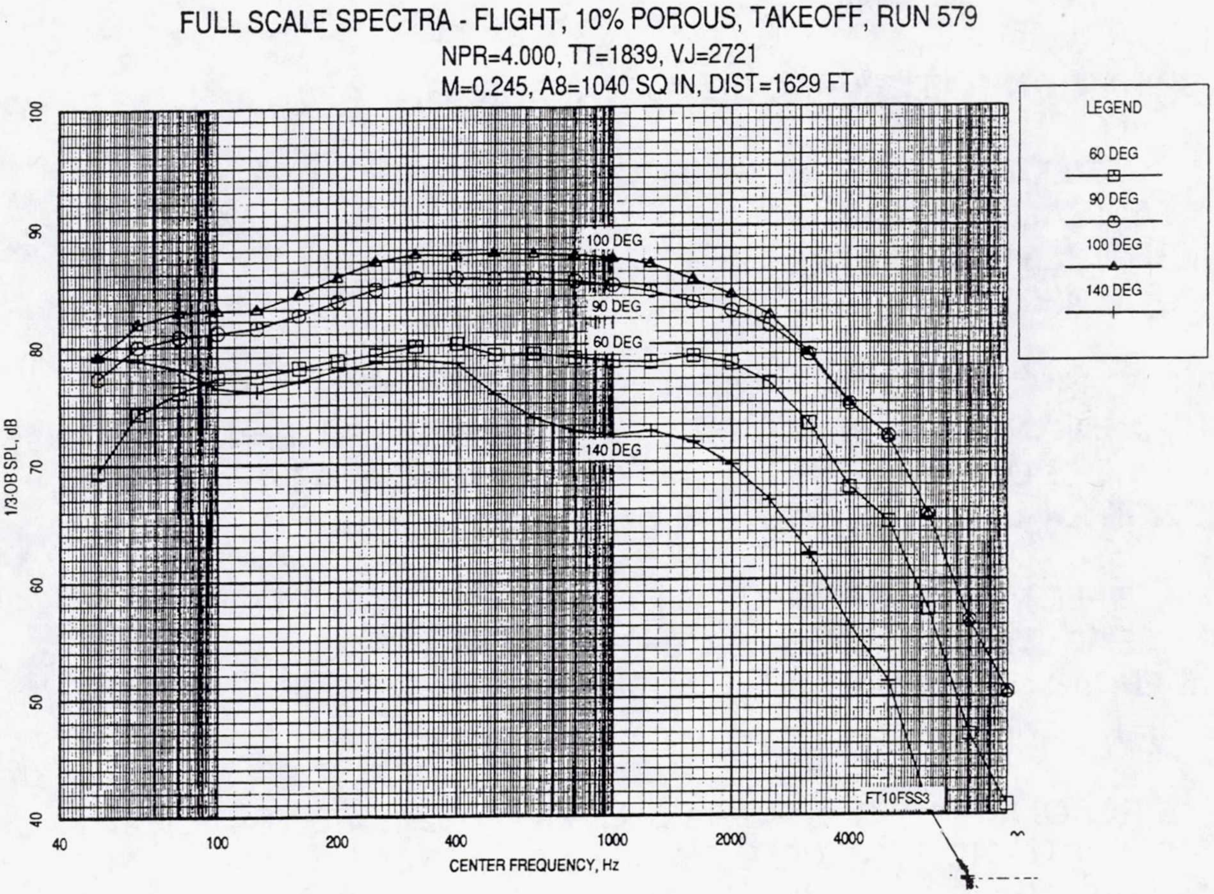

Spectra at the peak PNL angle show similar behavior at the higher two jet velocities and disimilar behavior at the lowest velocity. At the lowest velocity, the jet is overexpanded, and a clear double hump appears in the peak angle spectrum indicating a strong shock noise component. At the higher jet velocities, the peak angle spectra have broad flat peaks even though the jet probably is underexpanded at least at the highest velocity. This behavior has not been explained.

A retest of the same model in GE's acoustic test cell will provide data for comparison that is free from strong flow distortion at the model entrance.

CONCLUSIONS AND RECOMMENDATIONS

* ASPIRATION RATIO IS GOOD AT TAKEOFF:

UNCORRECTED PUMPING = 93% IN FLIGHT AND 89% STATICALLY
FLIGHT BENEFIT = 5%
SCOOP BENEFIT = 3%

* THE FLUSH INLET CONFIGURATION WITH TREATED EJECTOR SHROUD AND 10% POROUS PLUG PROVIDES 12.4 EPNdB SUPPRESSION RELATIVE TO THE CONIC NOZZLE AT TAKEOFF CONDITIONS AND Mt = 0.245

* THE EFFECT OF TREATMENT AT HIGH JET VELOCITIES IS UNCLEAR. THE HARDWALL CONFIGURATION FALLS WITHIN THE 1.6 EPNdB SPREAD OF ALL FLUSH INLET CONFIGURATIONS IN FLIGHT

* IT IS RECOMMENDED THAT THE AMEN NOZZLE BE TESTED IN GE'S ACOUSTIC TEST CELL TO OBTAIN A FACILITY-TO-FACILITY COMPARISON OF ACOUSTIC RESULTS

* HOT FLOW THRUST COEFFICIENTS ARE IN REASONABLE AGREEMENT WITH THE COLD FLOW MEASUREMENTS AND ARE OFF BY NO MORE THAN 2% Cfg

1999176543

PRATT & WHITNEY TWO DIMENSIONAL HSR NOZZLE TEST IN THE NASA LEWIS 9- BY 15-FOOT LOW SPEED WIND TUNNEL: AERODYNAMIC RESULTS

John D. Wolter
NASA Lewis Research Center
Cleveland, Ohio

and

Christopher W. Jones
Pratt & Whitney Aircraft Engines
East Hartford, Connecticut

56-07

409520

20P.

This paper discusses a test that was conducted jointly by Pratt & Whitney Aircraft Engines and NASA Lewis Research Center. The test was conducted in NASA's 9- by 15-Foot Low Speed Wind Tunnel (9x15 LSWT). The test setup, methods, and aerodynamic results of this test are discussed. Acoustical results are discussed in a separate paper by J. Bridges and J. Marino.

Overview

- Background & Previous Work
- Goals & Objectives
- Description of the Test
- Results
- Summary

TBE Noise Suppression Requirement

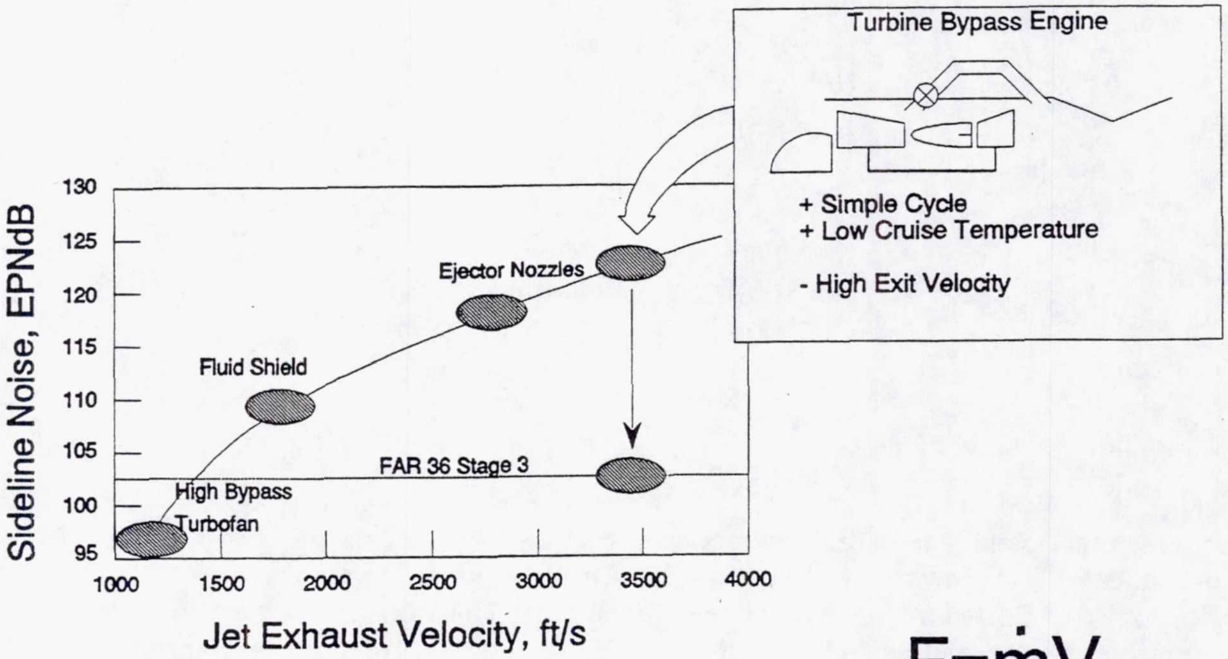

$$F=\dot{m}V$$

One of the proposed engine concepts for the HSCT is the turbine bypass (TBE) engine. This turbojet engine cycle is appealing in its simplicity and low temperature at cruise conditions. However, this engine has a high exit velocity, making it very noisy during take-off and approach. This figure shows the relationship between jet velocity and sideline noise. The TBE engine is at the high end of this spectrum. Consequently, to reduce the noise generated by this type of engine to FAR 36 Stage 3 levels, approximately 20 dB of noise suppression are needed.

To address this requirement, ejector nozzles are being studied. A large amount of ambient air is mixed with the jet exhaust to lower the exhaust velocity. Because the thrust generated is proportional to both the massflow and the velocity, the ejector provides a means of reducing exit velocity while maintaining thrust levels. To adequately lower the exit velocity, the secondary mass flow should be 120% (or more) of the primary mass flow.

The Mixer Ejector Concept

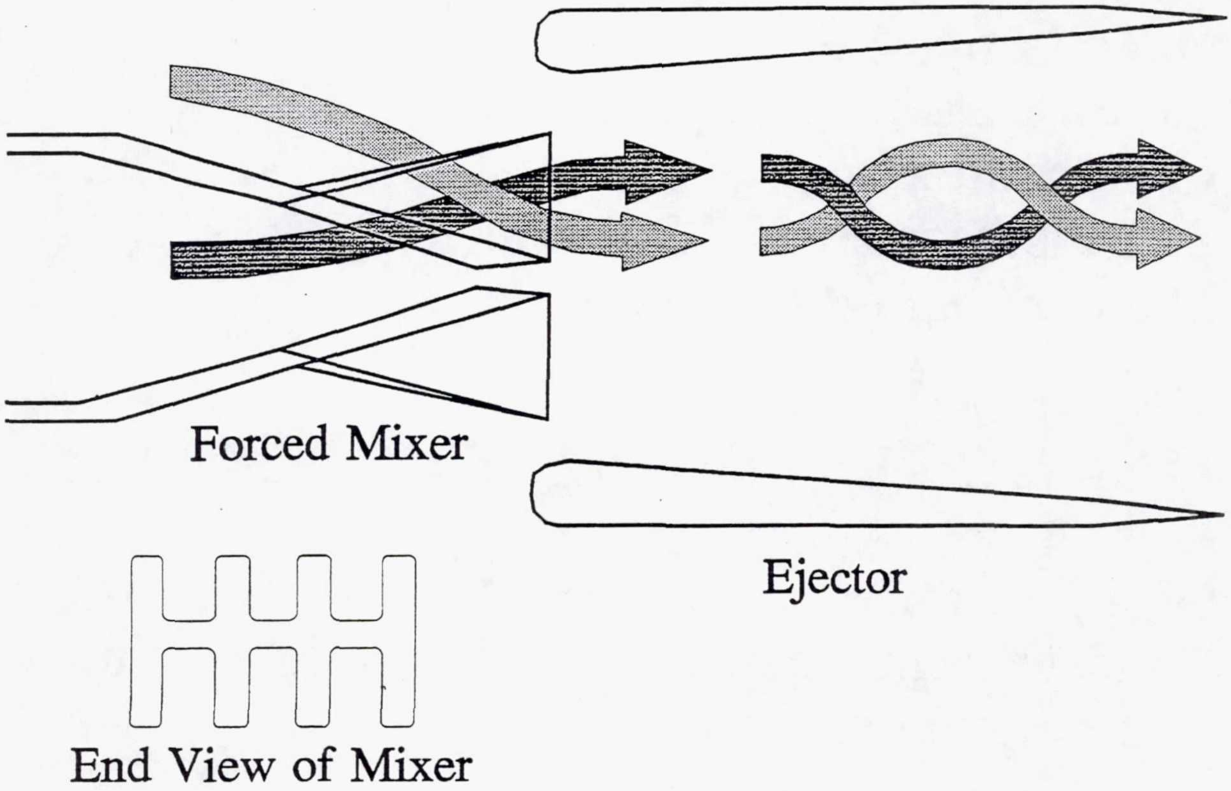

The high velocity jet must mix thoroughly with the entrained air to achieve the noise benefits of an ejector. Using conventional ejector technology, the mixing section of the nozzle would have to be impractically large to achieve this mixing. Instead, a mixer ejector is employed. The primary flow is supplied through a multi-lobed mixer nozzle. The secondary flow is drawn in between the lobes. This provides a large interface area between the flows.

In 1989, Pratt & Whitney and NASA Lewis tested a mixer ejector model in Lewis' 9- by 15-Foot Low Speed Wind Tunnel. This model achieved 120% massflow augmentation with measurable reduction in noise levels. However, at the design condition, the nozzle exhibited hot streaks exiting the ejector and shock noise, due to a mismatch in the primary exit pressure. While this nozzle demonstrated the mixer ejector concept was capable of reducing noise levels, the noise suppression for this nozzle was well below that needed to reach Stage 3. Furthermore, only limited acoustic data could be derived from the test data because the nozzle was operated at modest temperatures, much lower than those of an HSCT engine.

NASA/P&W 2-D HSR Nozzle Noise Test

Design Objectives:

- Increase ejector pumping
- Increase mixing
- Decrease noise to FAR 36 Stage 3 levels
- Maintain high thrust levels

Test Objectives:

- Measure levels of pumping, mixing, noise, and thrust
- Obtain data for comparison to CFD
- Validate techniques/facilities for design/testing of these nozzles

The subject of this study was a new two dimensional mixer ejector nozzle based on the nozzle tested in 1989. The principle difference between the current nozzle and its predecessor is the design of the primary nozzle. These changes were guided by computational studies, which predicted ejector pumping of 145% of the primary flow. The intent of the changes to the design were to increase pumping and mixing and thereby reduce the noise generated by the jet, while maintaining high levels of thrust.

The objectives of the test were to evaluate ejector pumping, mixing, acoustics, and thrust performance relative to the previous test; to obtain detailed data for comparison with computational fluid dynamics; and to validate methods and facilities for the design (P&W) and test (NASA) of this type of hardware.

Anatomy of the HSR P&W 2-D Mixer Ejector Nozzle

Inventory:

- 2 Mixer Designs
- 3 Shroud Lengths
- 3 Shroud/Sidewall Acoustic Treatments
- Sidewalls with Windows for Flow Visualization

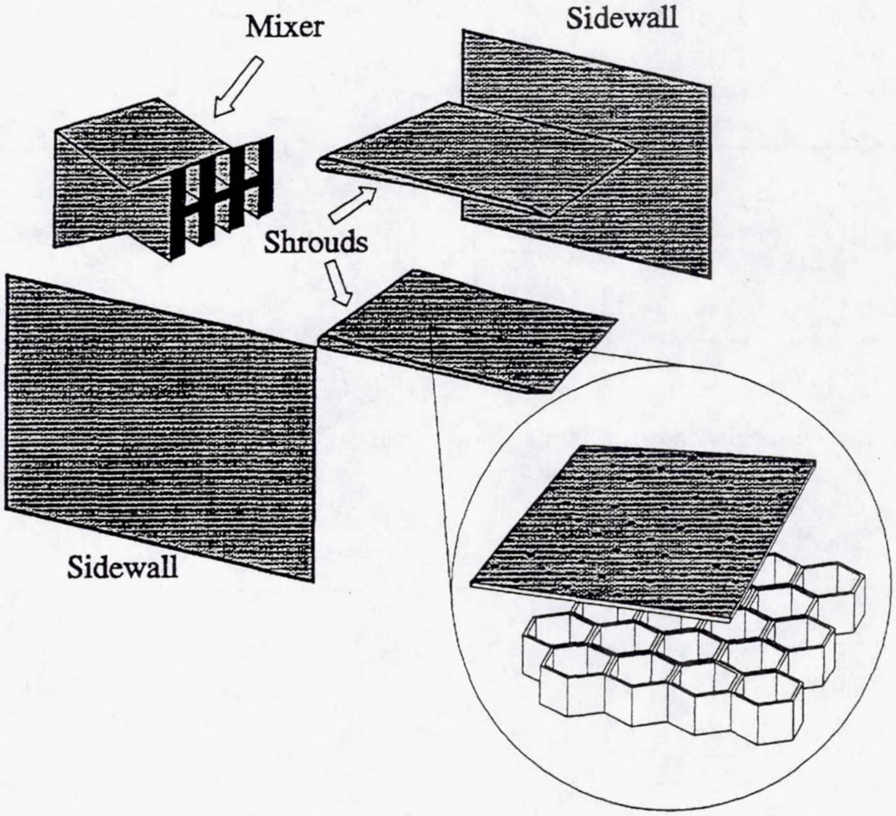

The model consisted of an 8 lobe forced mixer enclosed in an ejector box. The top and bottom of the box were formed by contoured shrouds, whereas the sidewalls were flat plates. This construction was chosen for economy and configuration flexibility. The shrouds could be attached to the sidewalls in one of three spacings to allow variations in primary/secondary area ratio. Shroud boxes in three lengths and three acoustic treatments were constructed. Two mixers were available. In addition, sidewalls with glass windows were built for flow visualization.

The three forms of acoustic treatment were: hardwall (no treatment), bulk, and tuned. Both the bulk and tuned treatments consisted of a honeycomb structure covered by a perforated plate. In the bulk treatment, the honeycomb cells were filled with a broadband acoustic absorber material. In the tuned treatment, the cells were empty, and the height of the cells was tuned to quiet the estimated predominant frequency of the jet noise.

2D Mixer-Ejector Mixer Nozzles

Vortical Mixer

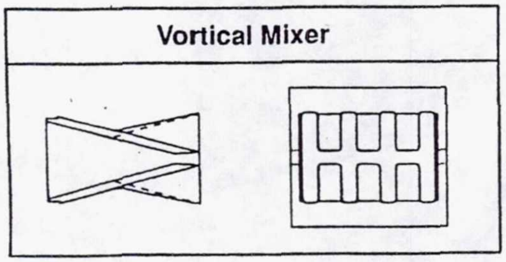

Axial Mixer

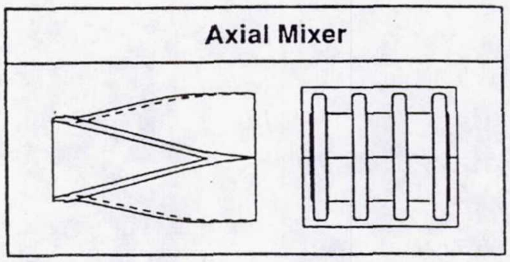

Relative Merits

o Non-axial discharge generates large-scale vorticity, promoting rapid mixing o Less wetted surface area o Shorter, more compact design	o Higher thrust performance o More predictable nozzle design
o Non-axial discharge generates higher thrust losses	o Less rapid mixing o Larger wetted area (increased friction) o Longer, less compact

The two mixers tested in this study represented different approaches to achieve substantial mixing. The vortical mixer discharges the hot exhaust at an angle to promote mixing via strong vortices in the axial direction. This approach would be expected to suffer large thrust loss due to the non-axial discharge of the flow. The axial mixer, on the other hand, discharges flow axially, potentially reducing thrust loss at the expense of mixing. The axial mixer is longer, making it heavier, and more difficult to store while in non-suppressor mode.

8-BY 6-FOOT AND 9-BY 15-FOOT WIND TUNNELS

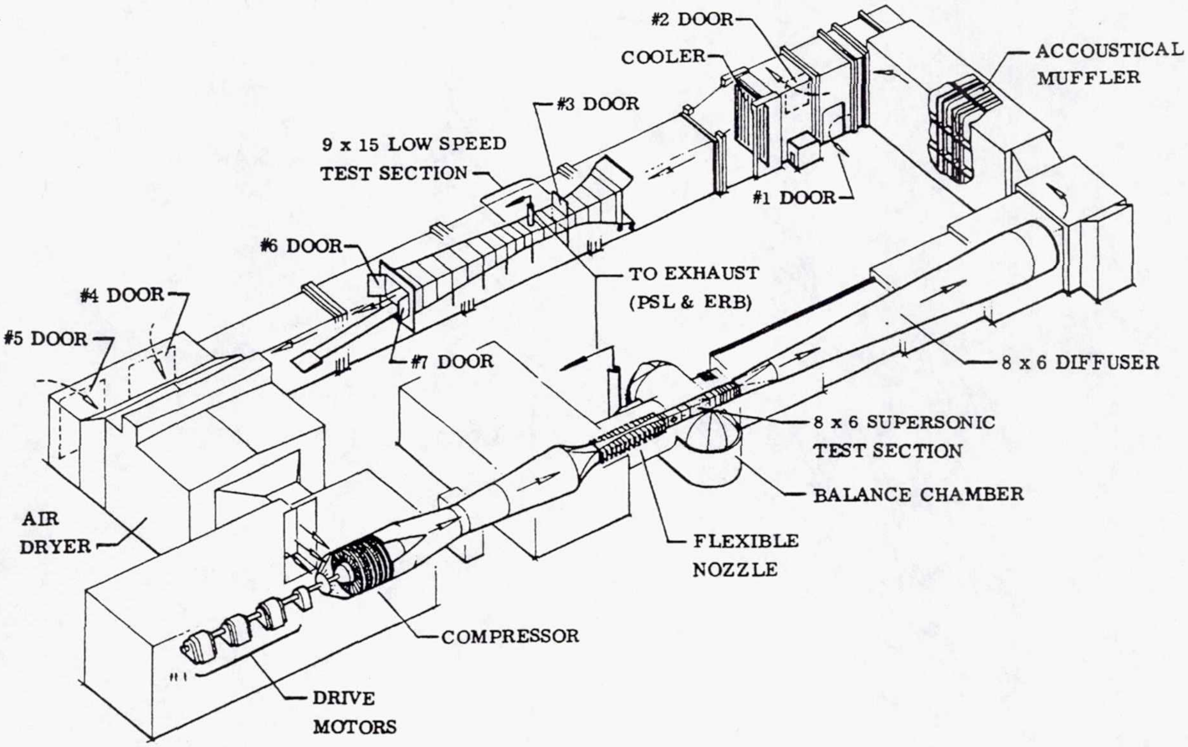

The test was conducted in the NASA Lewis 9- by 15-Foot Low Speed Wind Tunnel (9x15). This facility is a test section in the return leg of Lewis' 8- by 6-Foot Supersonic Wind Tunnel. The 9x15 is capable of wind speeds of 30 to 175 mph (up to Mach 0.2). The test section is lined with acoustic boxes to provide an anechoic environment for acoustic testing. Microphones were placed in the test section to measure noise angles at variouse angles to the model.

JET EXIT RIG WITH TRANSITION FOR AXISYMMETRIC NOZZLES

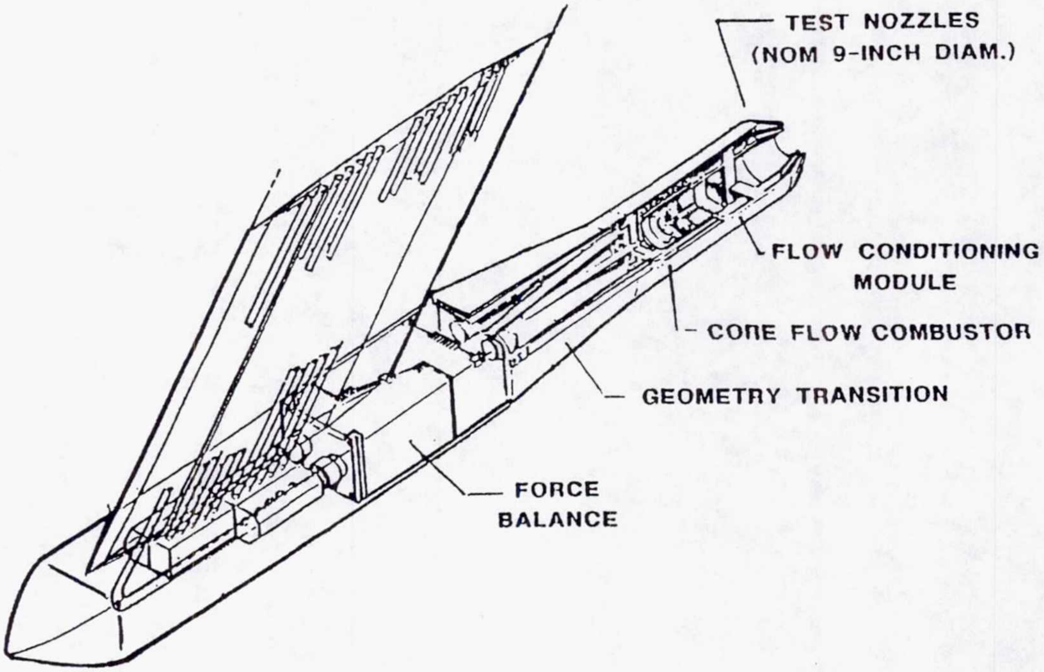

The nozzle was mounted to NASA Lewis' Jet Exit Rig, a small-scale jet engine simulator. The Jet Exit Rig provides two independent streams of air at up to 450 psia. In the axisymmetric configuration shown here, the inner stream can be heated in a hydrogen combustor to up to 2000 degrees Rankine. A flow through balance measures forces on the model. Flow into the jet exit rig is measured by a set of choked flow venturis mounted upstream of the rig. For this test, the outer air passage was blanked off and all air was supplied to the model through the inner stream.

The Jet Exit Rig is a new test rig at NASA Lewis. To date, force balance output from the rig have been unrepeatable. Therefore no forces and moments were acquired. Further testing of the model to obtain this information is currently planned.

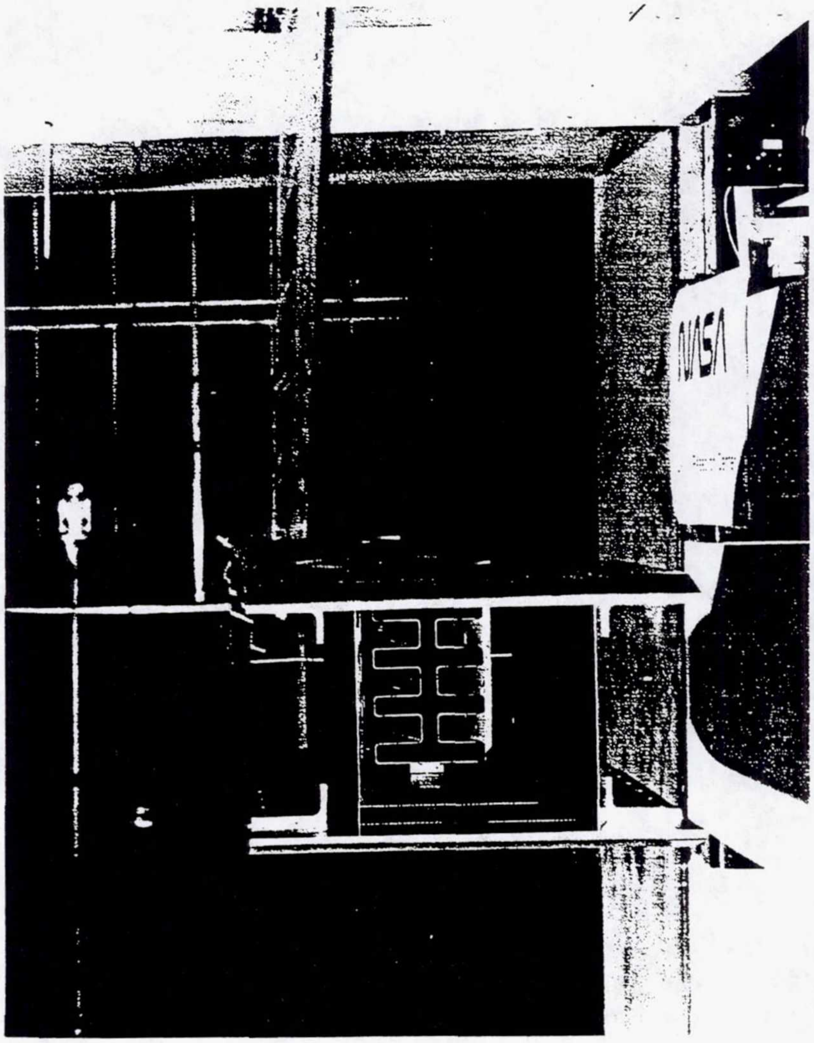

This figure shows the model mounted in the wind tunnel. The model is mounted sideways, with the "sidewalls" on the top and bottom. From this view, the lobes of the vortical mixer can be seen. On the walls of the shroud, the bulk acoustic liners can be seen. The microphone arrays (not in picture) are to the left. Note that the model is mounted off the tunnel centerline to allow greater separation between the model and microphone arrays.

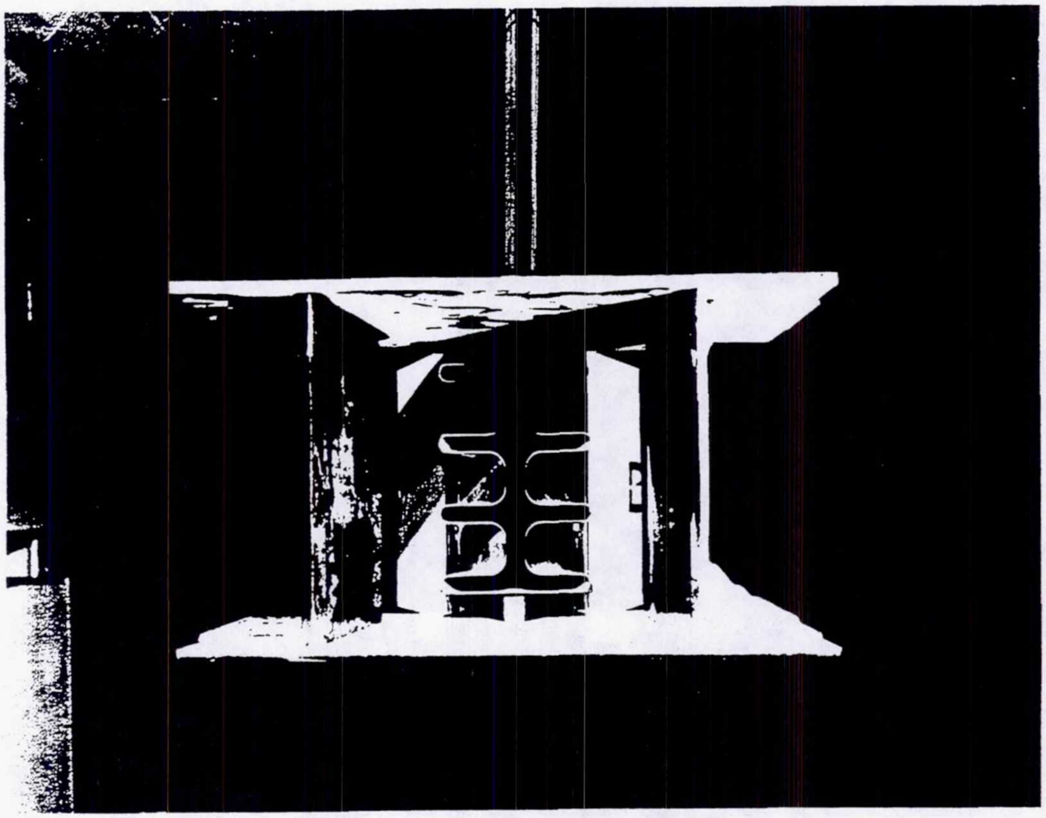

This figure shows the 1989 model for comparison with the current nozzle. Most of the visible differences between the two are in the mixer nozzle. The current design incorporates a convergent-divergent primary flow path, as compared to the convergent primary nozzle previously used. The shape and aspect ratio of the mixer lobes were changed based on computational studies of the mixing performance. The current nozzle also included the treated shrouds discussed earlier; the 1989 entry included only hardwall shrouds.

Measurements

- Primary Weight Flow
- Primary Total Conditions (fixed rake)
- Forces & Moments
- Acoustics
- Mixer & Shroud Pressures
- Ejector Exit Total Conditions (traverse rake)
- Ejector Internal Flowfield (schlieren, light sheet)
- Ejector Exit Flowfield (LDV)

A variety of measurements were made to gain an understanding of the characteristics of this model. Temperatures and pressures were measured immediately uptstream of the primary nozzle, in both streams near the mixer exit, and on the shrouds. Forces and moments were measured using the six component flow-through balance in the Jet Exit Rig. Arrays of microphones measured the acoustic output from various directions. A limited number of configurations were studied in further detail using a 15 element total pressure and total temperature traverse rake at the ejector exit plane, and with schlieren, laser light sheet, and laser doppler velocimetry (LDV). The schlieren and laser light sheet testing was performed by K. Mitchell et. al. of NASA Langley and is presented in this symposium.

Test Matrix Variables for 2D Nozzle

- Power Setting (NPR and $T_{T,jet}$)
- Tunnel Mach Number
- Primary Nozzle
- Shroud Length
- Ejector Area
- Ejector Treatment

A large number of test variables were studied. Three variables defined the nozzle flow conditions: the nozzle pressure ratio, the primary jet total temperature, and the tunnel Mach number. There were several configuration variables: the choice of nozzle, shroud length, ejector area, and ejector treatment. Typical ranges of these variables were as follows:

NPR	0 - 4.5
$T_{T,jet}$	520 °R - 1960 °R
M_{tunnel}	0 - 0.2
Primary Nozzle	Axial or Vortical
Shroud Length	Short, Long, or Intermediate
Ejector Area	Design, Larger, or Smaller
Ejector Treatment	Hardwall, Bulk, or Tuned

Typical Operating Line (based on PW-STF945)

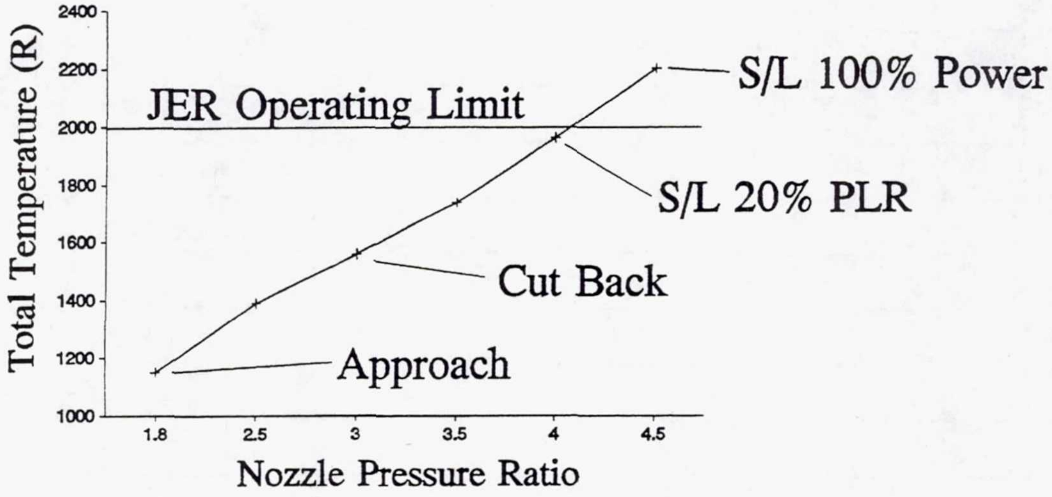

The choice of jet temperature/nozzle pressure ratio pairs for the test matrix was made based on the operating line of the PW-STF945, a Pratt & Whitney turbine bypass engine concept. The jet temperature in the jet exit rig was limited to 2000 °R, so the highest power setting was tested at a lower temperature. The design point for the nozzle was at a NPR of 4.0 and jet temperature of 1960 °R, which corresponds to 80% power at sea level. This setting represents the conditions the nozzle would experience shortly after take-off.

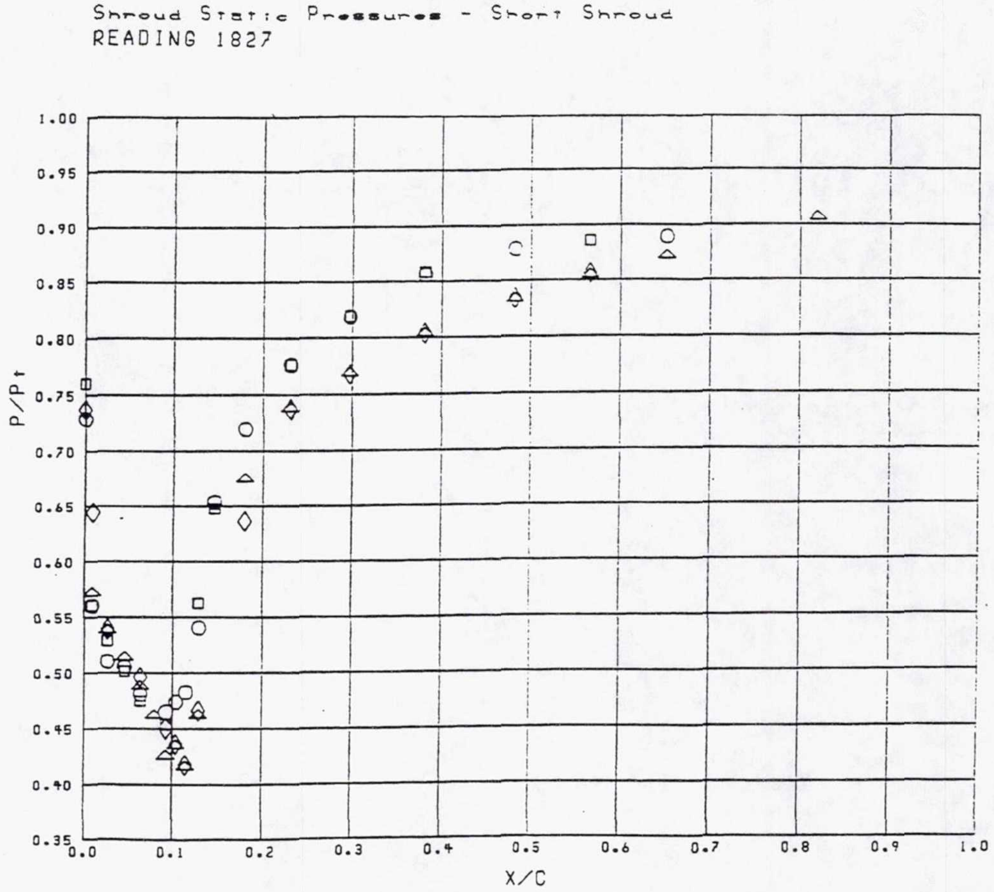

This figure shows the ratios of static to total pressure measured along the shroud wall. The pressure decreases rapidly as the secondary flow is accelerated through the choked secondary throat, and then rises smoothly to ambient pressure. This behavior characterizes the relatively shock-free flow in the ejector and is representative of most configurations.

Ejector Secondary Airflow CFD Calibration Method

- Define a "flow coefficient", $C_{d\text{–}CFD}$, based upon a choked reference area and a representative duct pressure

Definition of Reference Secondary Area

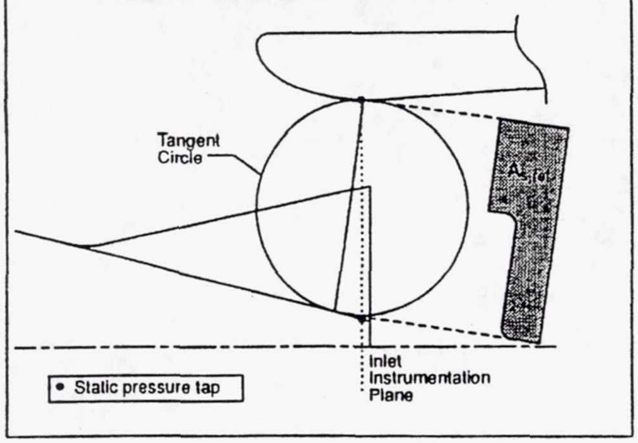

- Define a representative duct pressure:

$$\bar{p}_{sec} = {}^1/_2\,(p_{shroud} + p_{valley})$$

- Define $w_{s,ref}$ as choked flow at $A_{s,ref}$

The test setup did not allow for direct measurement of the secondary passage mass flow. Therefore, an alternate method was used for determining this flow. Selected pressures, measured on the shrouds and outside surfaces of the mixer nozzle, were used to determine a representative pressure in this passage. Two CFD studies were made of this secondary passage geometry, one using the VSAero potential flow code, and one using the PARC Navier-Stokes code. From the results of these studies, a discharge coefficient of .95 was calculated for this passage. Mass flow through the secondary duct was calculated as choked flow through a reference area near the exit of the mixer.

Goal Pumping Level Achieved by Both Mixer Nozzles

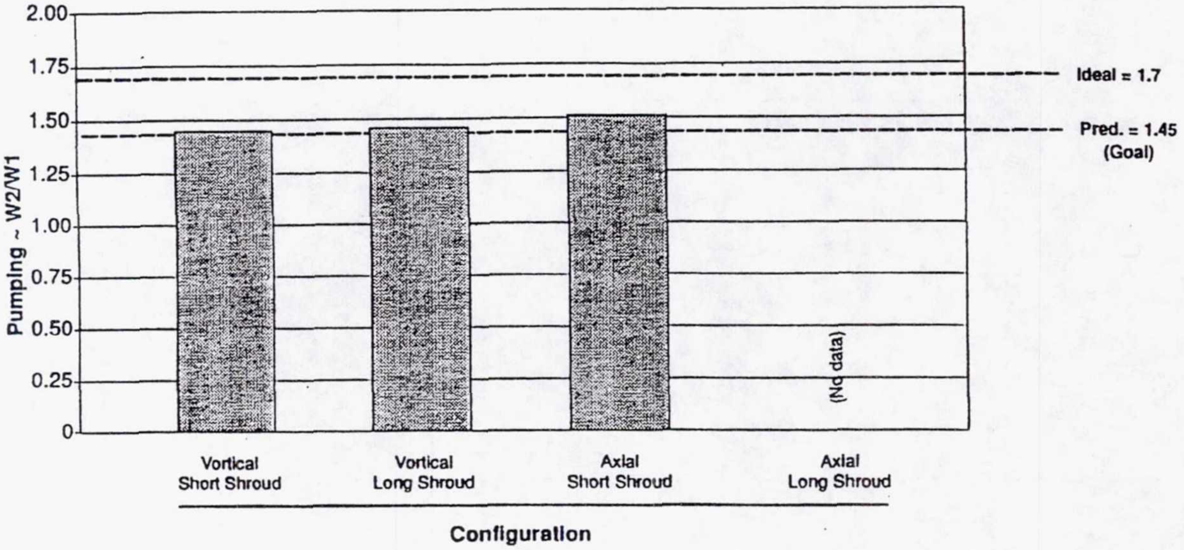

All of the configurations tested showed high levels of pumping. As opposed to the approximately 120% pumping in the 1989 test, these nozzles showed pumping in the 145% to 150% range. This pumping level was found to be independent of the liners used.

Experimental Traverse Results

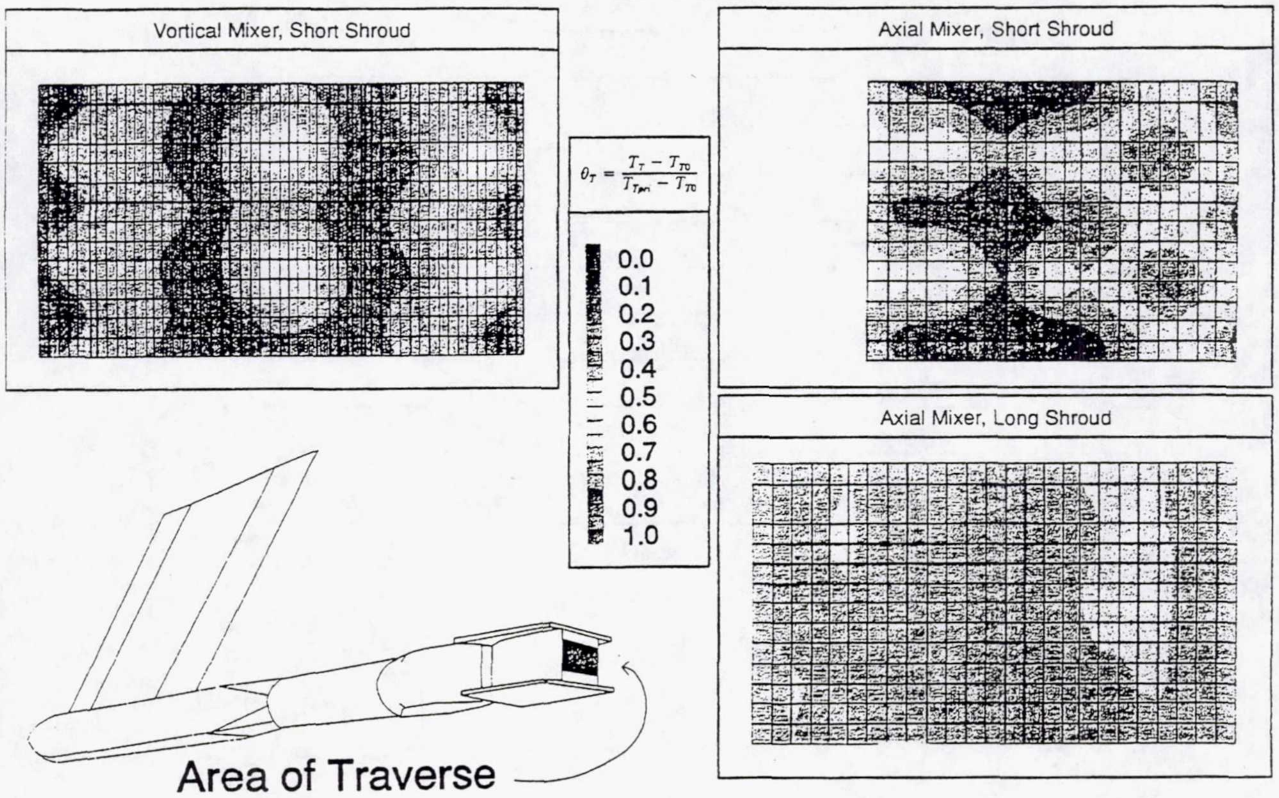

Rake surveys of the total temperature and total pressure of the flow at the exit of the ejector were performed on several configurations. A non-dimensional temperature parameter was calculated ranging from zero (representing secondary stream inflow temperature) to one (representing primary stream total temperature). Contour plots of this parameter show increased mixing of the streams by the vortical mixer compared to the axial mixer and increased mixing for the long shrouds compared to the short shrouds. These results compare favorably to those of the 1989 test, which showed severe hot streaks near the shroud walls.

Results of Exit Traverse Show Improved Mixing

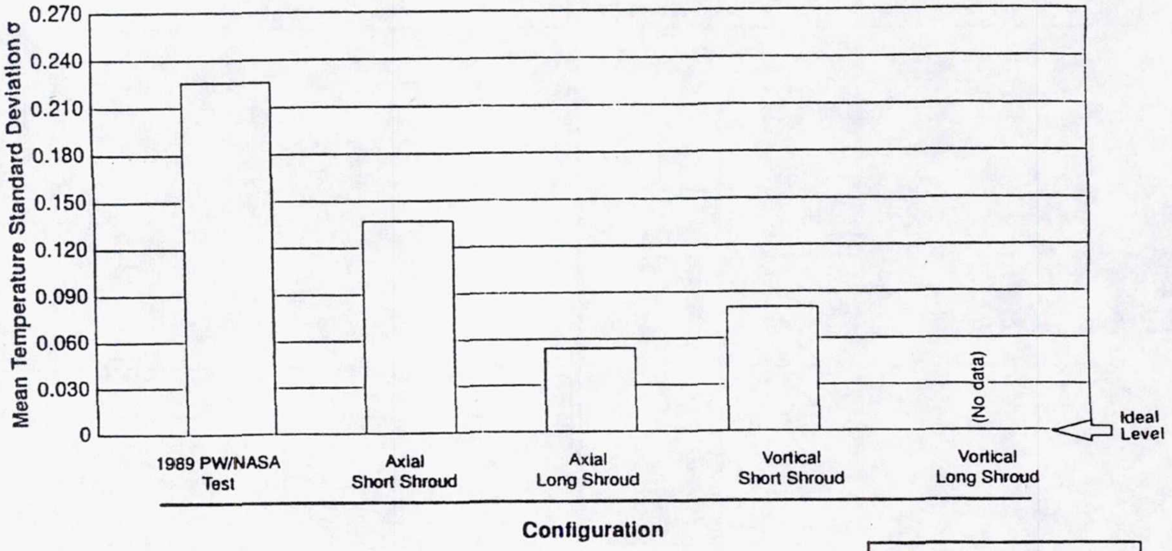

$$\theta_T = \frac{T_T - T_{T\infty}}{T_{T\,prim} - T_{T\infty}}$$

$$\sigma = \sqrt{\frac{1}{N}\sum_{i=1}^{N}(\theta_T - \bar{\theta}_T)^2}$$

The standard deviation of the temperature parameter over the survey region yields a relative measure of the mixing in the nozzle; lower standard deviation indicates greater uniformity which implies better mixing of the streams. Applying this metric to the 1989 test and the current test, the newer mixers exhibited improved mixing.

Summary

Two nozzles in multiple configurations were tested. Aero results were:

- Significant increases in pumping and mixing were obtained relative to the previous test.
- The vortical mixer showed greater mixing than the axial mixer.
- Liners did not have significant effects on pumping.
- Force balance data were unrepeatable. Further testing is planned to get these data.

1999176544

PRATT & WHITNEY 2D MODEL IN LeRC 9'×15' ACOUSTICS

James Bridges
NASA Lewis Research Center
Cleveland, Ohio

and

Jodilyn Marino
Pratt & Whitney
East Hartford, Connecticut

S7-07

409522

22P.

Mixer-Ejector Sound Suppression Concept

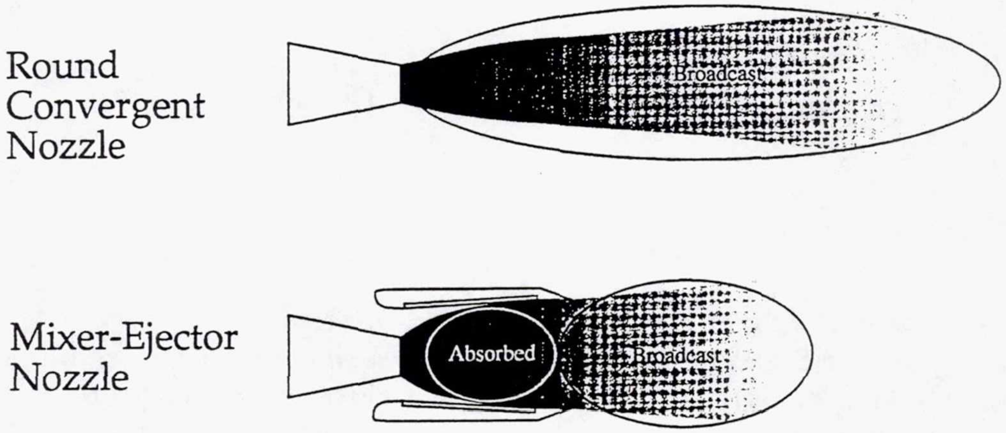

Note: SPL ~ U^8D^2

The theory of mixer-ejectors for noise suppression is illustrated in this cartoon. Since jet noise SPL scales as velocity to the eighth power and diameter squared, increasing the jet diameter while lowering its velocity and keeping thrust constant decreases the noise. However, in supersonic craft, the drag penalty for increasing diameter at supersonic cruise makes this option very expensive. One would like to have a large engine during takeoff which could be shrunk during cruise. The retractable ejector is such an expandable engine. If the mixer flow can be expanded to the size of the ejector exit, the noise generated downstream of the ejector will be much less than the small diameter mixer nozzle alone. Of course, this also requires that the noise created in expanding the flow to fill the ejector be absorbed by a liner in the ejector walls so that none of this noise is heard. Since this mixing of internal hot gas and external cold air must take place in as short a distance as possible, the mixer must be very effective and therefore probably much noisier than a simple nozzle.

HSR 9x15 Test Highlights-Acoustics

- Showed 12-16 dB EPNL sound reduction over baseline round jet.
- Showed dependence of jet noise on
  - -nozzle geometry
  - -ejector length
  - -ejector area ratio
  - -ejector liner material
  - -ejector liner location
- Obtained agreement between new NASA all-digital acoustic data system and P&W analysis system.

Highlights to be covered in this presentation. The 4dB uncertainty in sound reduction is the difference between the sound of the baseline conic nozzle and its predicted value, which is thought to be caused by the close proximity of the microphones to the nozzle in the 9x15 tunnel. The measurements were thus not in a geometric far-field and attempts to extrapolate them to far field have not been successful.

The agreement between NASA and Pratt & Whitney acquisition and analysis systems is important because there are many elements to these systems and now the new NASA system can be relied on to produce results with much quicker turn-around in tests run at Lewis.

Effect of Mixer/Ejector Geometry

2Dvortical vs. 2Daxial vs. RCref
Short Ejector, Bulk Liner

- **Geometry def'n:**

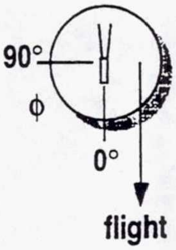

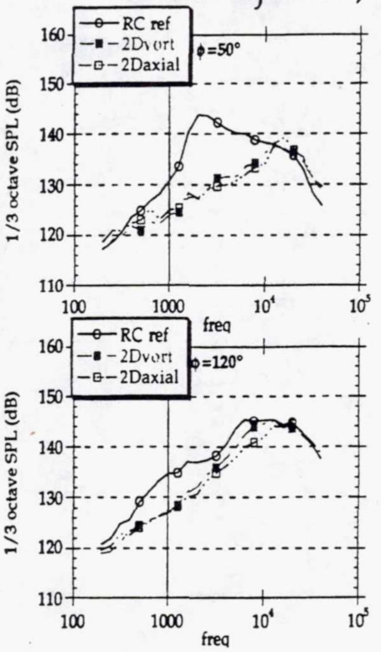

- **Power condition:** Sideline PLR
- **Model scale: 10.2**
- **Data scaled to 1 foot, lossless condition**

This is the first of many viewgraphs of data which will have the same form. Each viewgraph contains 1/3 octave SPL spectra taken from four different angles to the jet. Note that the polar angle f is measured from the direction of flight. Also, the data presented here was taken at the Sideline PLR power setting (NPR=4.0, Tj=1960°R) unless otherwise specified. The data is presented in model scale and has been translated to a 1 foot radial distance, removing the atmospheric attenuation.

This slide compares the sound spectra of the two mixer geometries with the bulk-lined, short ejector in place. The baseline round convergent (RC ref) nozzle sound spectra is shown for reference. Both geometries show suppression at all angles, although the suppression at f = 120° is small. The difference between the two mixer geometries is small, even in spectral detail.

Effect of Mixer/Ejector Geometry

2Dvortical vs. 2Daxial vs. RCref
Long Ejector, Bulk Liner

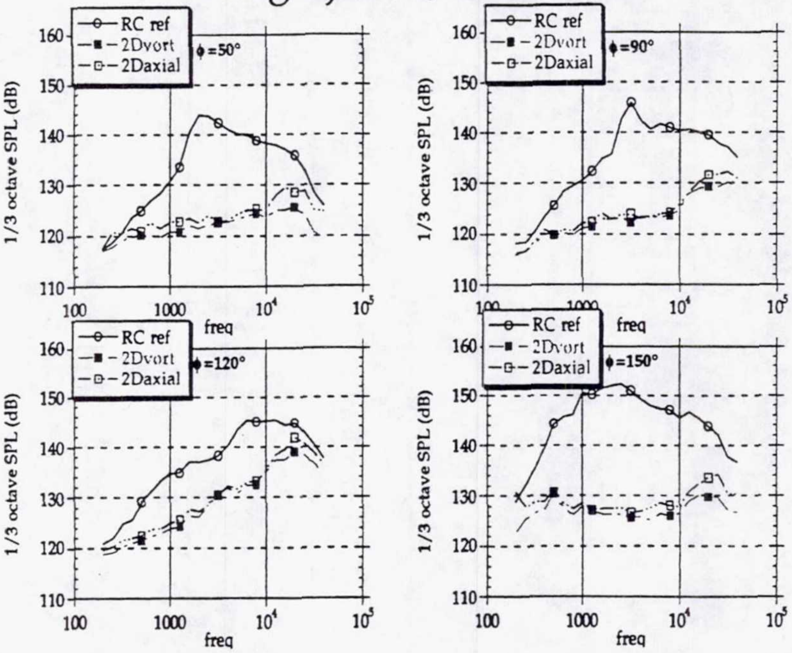

This slide compares the sound spectra of the two mixer geometries with the bulk-lined, long ejector in place. Again, both geometries show suppression at all angles, and again, the difference between the two mixer geometries is small. However, the vortical nozzle is slightly quieter than the axial, especially around the peak frequency of 20kHz, which weighs most heavily in computing EPNL. By comparing this slide with the previous one the difference between long and short ejectors can be seen.

Effect of Ejector Length

Short vs. Medium vs. Long Ejector
2Dvortical Mixer, Bulk Liner

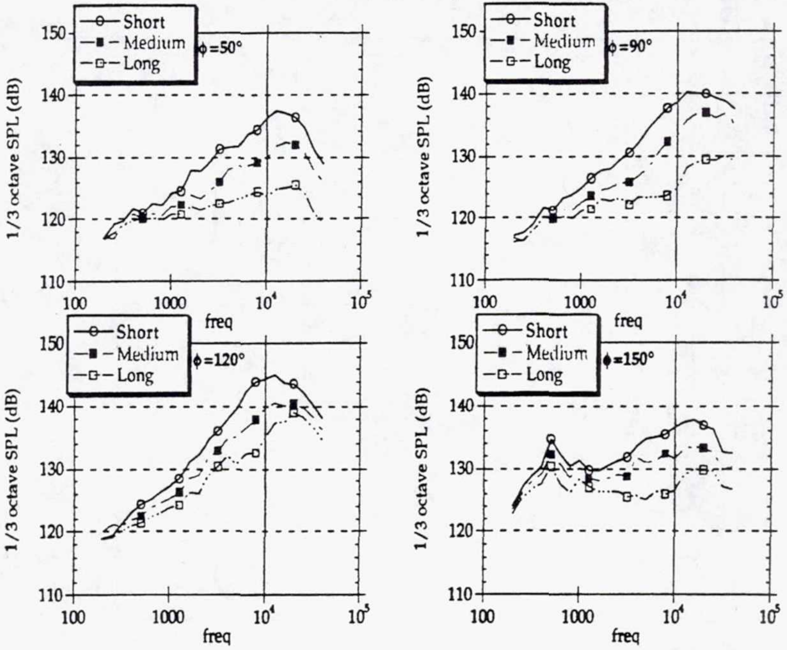

The effect of ejector length is isolated in this comparison of sound spectra of the 2D vortical mixer with the short, medium and long bulk-lined, ejectors. As the lengths of these ejectors were 10.44, 14.64, and 18.84 inches respectively, the amount of suppression (in dB) is approximately proportional to the the ejector length.

Effect of Ejector Pumping

2Dvortical, Long Ejector, No Liner

Ratio of Secondary to Primary Weight Flow:
EjAR=3.3: 1.62 EjAR = 3.8: 1.86

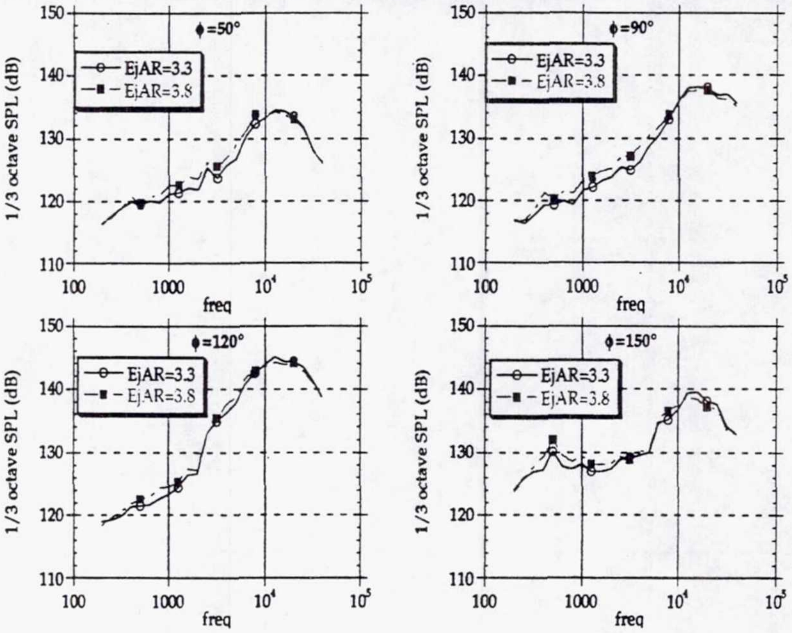

One parameter of the mixer-ejector design which is thought to be important is the pumping ratio, the mass pulled into the ejector relative to the mass through the primary nozzle. In the 9x15 test, the ejector area ratio (EjAR = ratio of ejector secondary area to nozzle primary area) was adjusted from the design point of 3.3 to 3.8. This resulted in a 15% increase in the pumping*, but made no discernable difference in the jet noise. It would seem that the pumping ratio would need to be minimized to reduce thrust losses resulting from the engagement of low momentum ambient fluid. Tests will be conducted in the near future to determine how low the ejector area ratio can be made before an acoustic impact is observed.

*Measurement of pumping ratio is covered in companion presentation by Wolter and Jones.

Effect of Treatment Type

Bulk vs. Tuned vs. No Lining
2Dvortical Mixer, Long Ejector

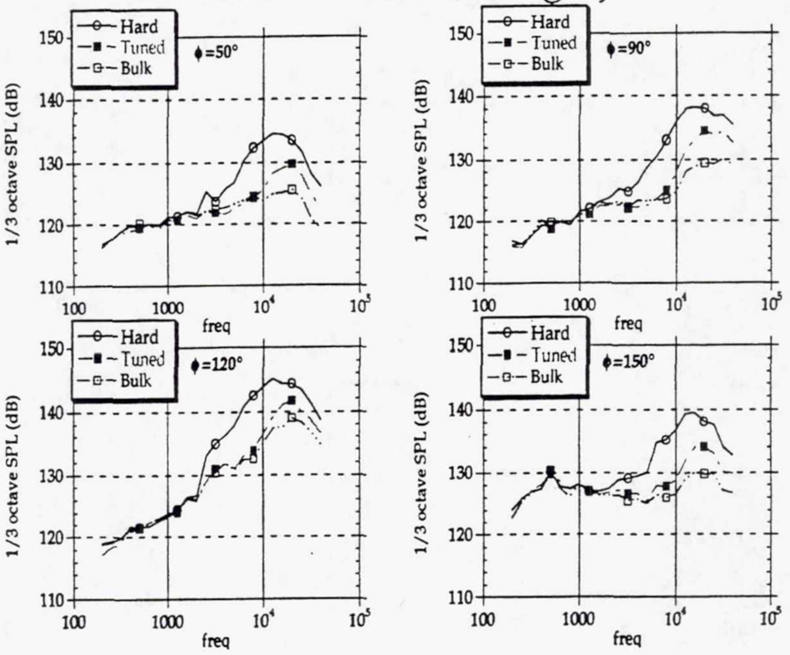

Two types of liner material were used during the test. The tuned liner consistedof a honeycomb panel faced with sheet metal perforated plate*. The bulk liner was similar only the honeycomb was filled with an absorbtive fiber. Both liners held up well during tests (except when the leading edge of the liners were subjected to direct flow from the mixer, which lifted the entire panel from the ejector) and were effective as can be seen in these plots. The bulk liner had a bit better attenuation and was used in the majority of the tests.

*Wolter and Jones give details of liner construction.

Insertion Loss for Acoustic Liners

2Dvortical Mixer, Long Ejector

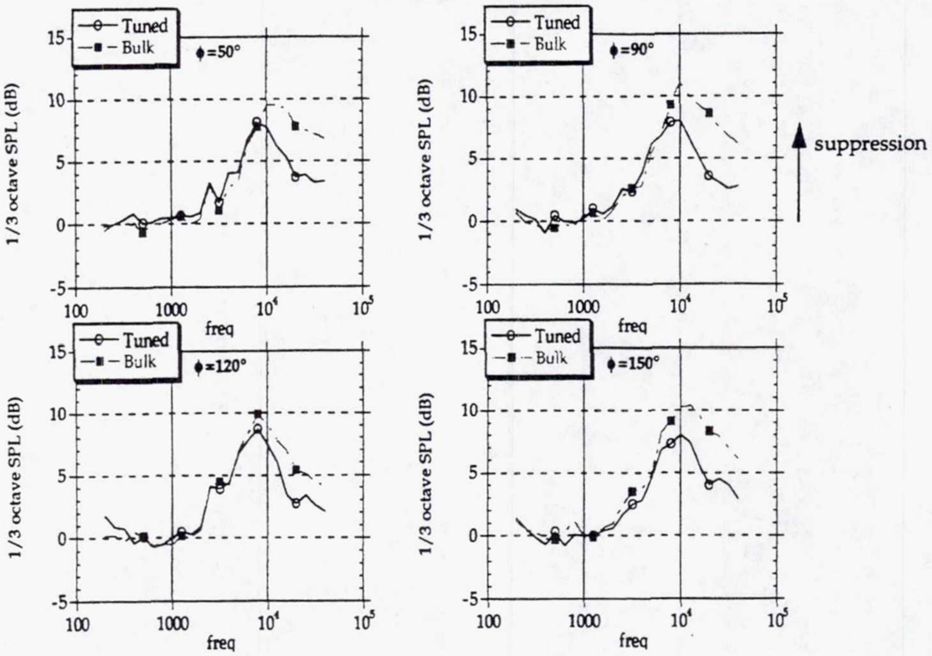

This slide gives a direct measure of the sound absorbed by the two types of liners when they were used with the vortical mixer and long ejector. Each curve is the difference between the no liner (hardwall) data and with liner data. The difference between the tuned and bulk material seems to be in their ability to suppress the highest frequencies, including the peak frequency of 20kHz.

Effect of Treatment Location-Azimuthal

2Dvortical Mixer, Long Ejector

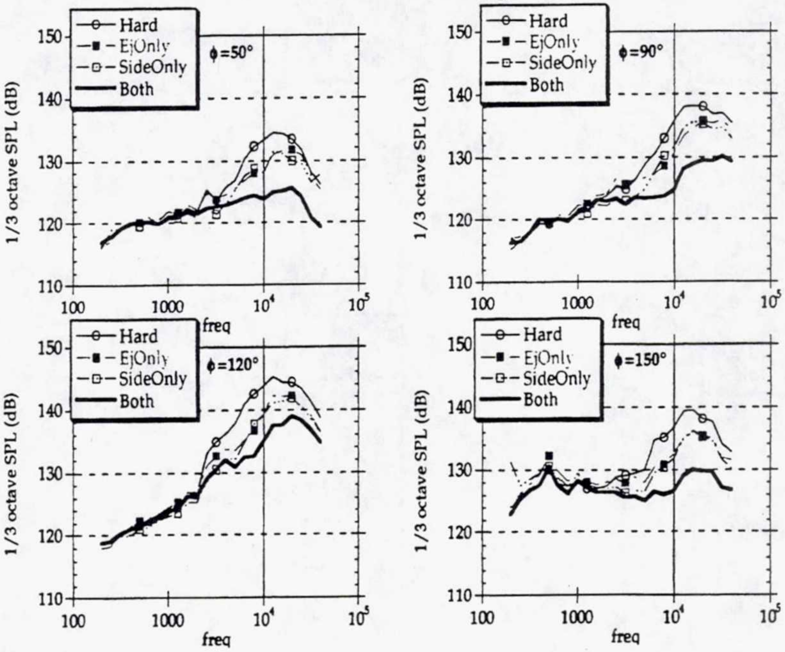

Because of nonaxisymmetry of the mixer-ejector, some azimuthal directionality was expected in the sound produced and in the efficacy of liners on the different walls. Not shown are near-field results taken by the azimuthal microphone array which show that the sound field of the 2D mixer-ejectors were essentially axisymmetric. What is shown in this slide is the sound when the liners were placed on different walls of the ejector. In the plots, sound measured with bulk liner on the walls which constitute the sideplates of the ejector box (parallel to the lobes of the mixer) are noted by SideOnly, while the sound measured when the bulk liner was placed on the ejector walls is called EjOnly. The similarity of the these two curves and the fact that they are about halfway between the no liner and fully lined sound spectra indicates that the mixing noise within the ejector had no azimuthal preference.

Effect of Treatment Location-Axial

2Dvortical Mixer, Long Ejector

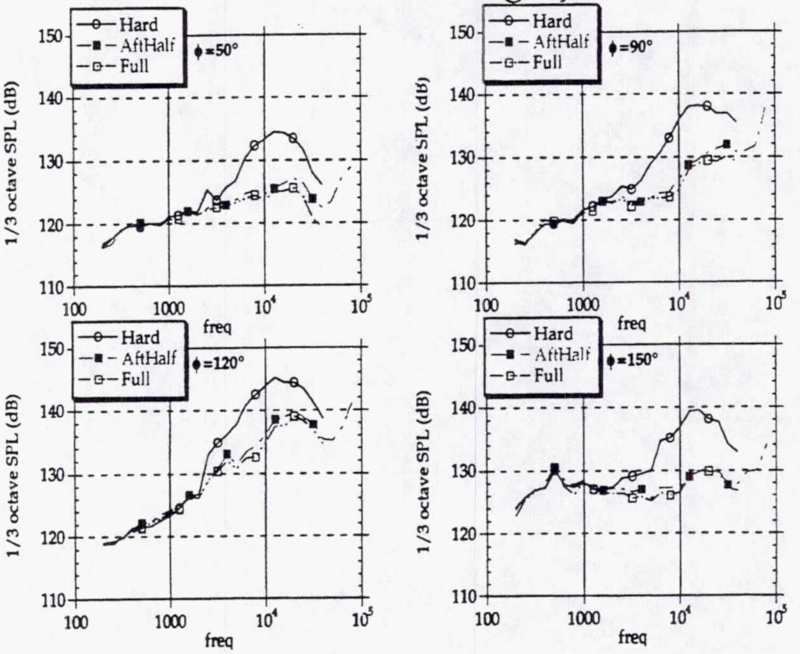

The axial dependence on liner placement was tested by putting the liner in only the aft half of the ejector and comparing the sound of this configuration with that of the unlined and fully lined ejector. As seen in the plots, when the liner was in the aft half of the ejector it absorbed almost the same amount of sound as when the entire length of the ejector was lined, leading to the conclusions that (1) the liner in the front half of the ejector was ineffectual and (2) most of the internally generated mixing noise is either produced near the end of the ejector or is highly directed downstream.

Parasitic Upstream Noise in Rig

Round Convergent Nozzle
Cold Flow, NPR = 1.4 vs. Stone's Prediction

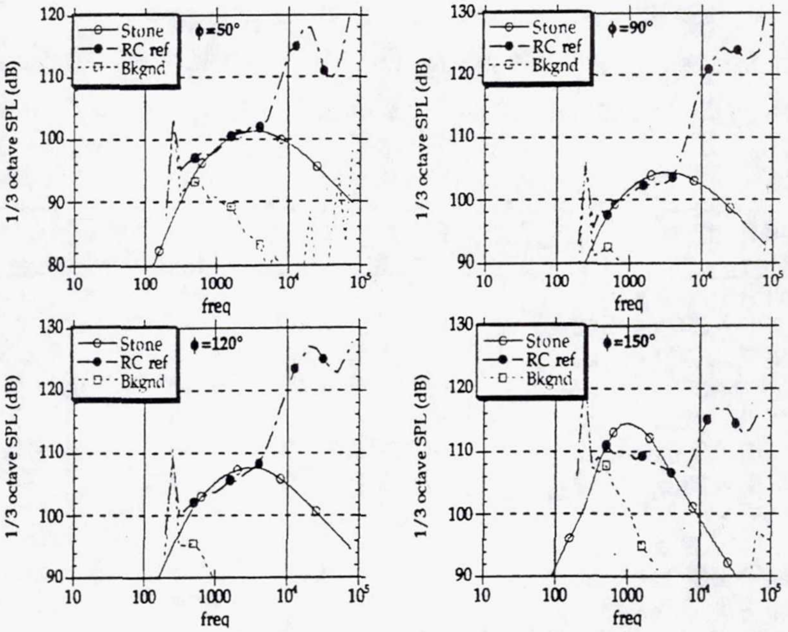

One problem encountered during the test was upstream "valve" noise in the rig. This can be seen clearly in these plots which show the sound spectra measured in a cold low speed jet flow and the predicted spectra. Also shown is the tunnel background spectra, which is well-below the jet noise and is not a factor. At around 20kHz, the same frequency range as the lobed mixer produces sound, the upstream noise can be seen protruding above the prediction.

Procedure for Estimating Upstream Noise

1) Extrapolate cold, subsonic ASME nozzle data to high NPR.

- The scaling with NPR is assumed to be independent of angle in accordance with experience with internal combustor noise.
- Spectral shape is best fit to internal noise in 10k-60kHz band.

2) Effect of temperature is extrapolated from 530°R and 1150°R data in RCref nozzle.

3) Sound absorption by liner calculated from cold, subsonic data in RCref and 2Dvortical jets.

geometric angle	Extrapolated from cold, low NPR data (x = log10(f))	Effect of jet temperature	Short bulk liner	Long bulk liner
50	-710.0 + 4*NPR + 385x - 45x2	-0.003*(T-530)	+3	+2
60	-740.0 + 4*NPR + 393x - 45x2	-0.003*(T-530)	+1	-1
70	-736.0 + 4*NPR + 393x - 45x2	-0.003*(T-530)	-4	-6
80	-735.0 + 4*NPR + 393x - 45x2	-0.003*(T-530)	-8	-11
90	-745.0 + 4*NPR + 395x - 45x2	-0.003*(T-530)	-8	-13
100	-742.0 + 4*NPR + 395x - 45x2	-0.003*(T-530)	-6	-10
110	-743.0 + 4*NPR + 395x - 45x2	-0.003*(T-530)	-7	-14
120	-738.5 + 4*NPR + 393x - 45x2	-0.003*(T-530)	-7	-13
130	-738.0 + 4*NPR + 393x - 45x2	-0.003*(T-530)	-3	-9
140	-747.5 + 4*NPR + 393x - 45x2	-0.003*(T-530)	-1	-5
150	-710.5 + 4*NPR + 385x - 45x2	-0.003*(T-530)	+2	-4

Several attempts were made to isolate the source of this noise, such as changing elements in the rig, etc., but the noise seemed independent of these changes. Unable to remove the source of the upstream noise, a method was developed to predict the contribution of the parasitic noise at the test conditions. This involved extrapolating the noise spectrum from low NPR, cold data where the noise was clearly dominating the jet noise, extrapolating the slight modification caused by the difference in temperature (both effects measured in the RC nozzle) and adding the suppression of the parasitic noise by the ejector liners, again measured at low NPR. This table quantifies and documents the fits which were used for estimating the upstream noise at high NPR, hot test conditions.

Estimate of Upstream Noise Contamination

Data: 2Dvortical, Long Ejector, Bulk Liner
Analytical: Estimate of Upstream Noise:
Cold + Heat Effect + Ejector Shielding

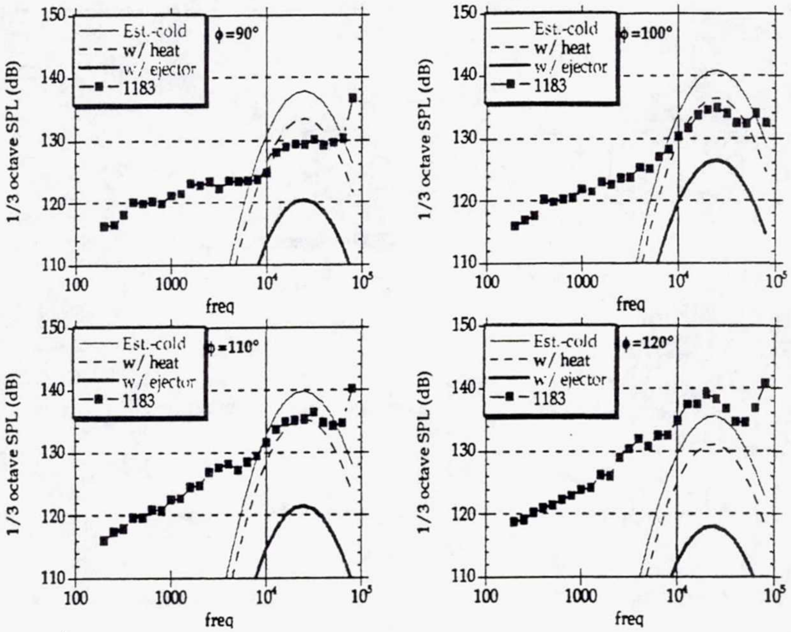

These plots show the data for the 2Dvortical mixer with long, bulk-lined ejector and the estimated upstream noise. The curve "Est-cold" is the sound of the upstream noise at the test NPR, but without the burner. The curve "w/heat" shows the slight reduction found when the burner was operating and "w/ejector" the final estimated contribution of the upstream noise to the measured sound. In all but the first two (upstream) polar angles, the estimated sound was well below the measured sound, indicating that the upstream noise did not contaminate the data. However, given the unfortunate spectral overlap between the upstream noise and the jet noise and the uncanny similarity between the upstream noise spectrum and the jet noise data, some uncertainty remains. This will be cleared by aeroacoustic tests of these nozzles in GE's Cell 41 facility this spring.

Correlation of Mixing and Noise

Relative EPNL with Bulk Liner in Ejector and
Total Temperature Profiles at Ejector Exit

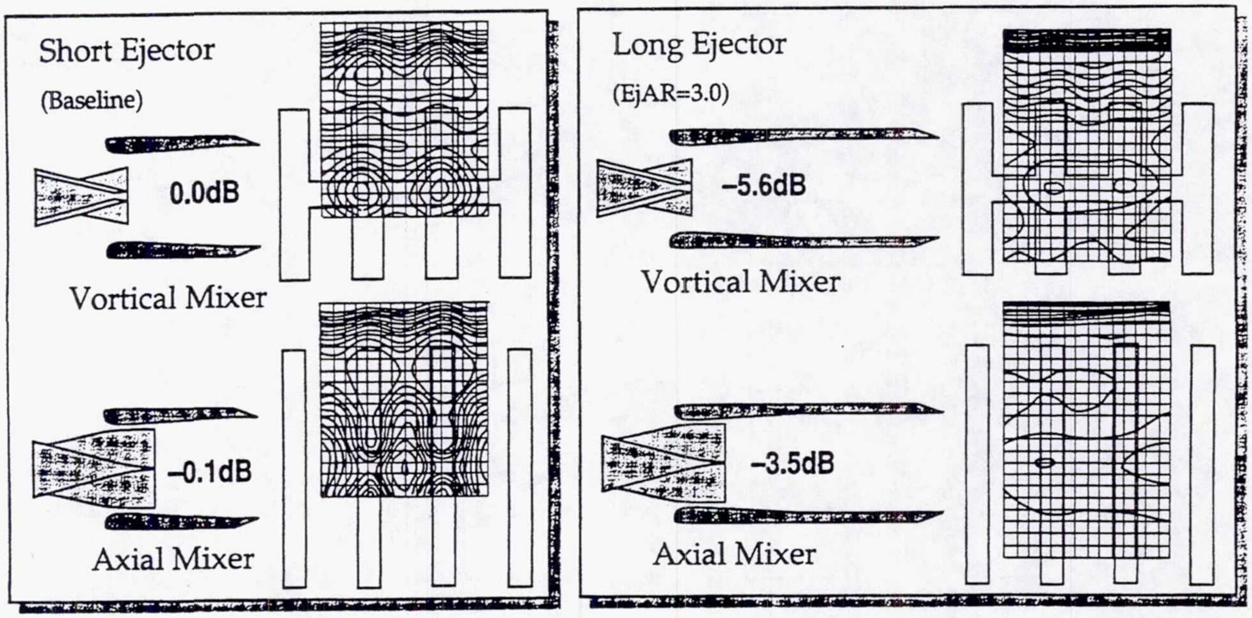

During the design phase of this test, a parametric CFD study was made to determine optimal size and shape of the lobed mixer. At this time the figure of merit for aeroacoustics was the temperature profile at the ejector exit plane. It was thought that the mixer which minimized "hot streaks" and provided the most complete mixing in the ejector would have the quietest flow out of the ejector. How well was this borne out in the tests? The plots above show the total temperature as measured at the exit of the ejector and a relative EPNL (2Dvortical with short ejector taken as arbitrary baseline).

Comparing temperature profiles for the short ejector, the axial mixer has stronger gradients and therefore would have been expected to be noisier. However, it is indistinguishable from the vortical mixer. Comparing temperature profiles from the long ejector (which are not completely comparable due to an unfortunate configuration error which gave the vortical mixer an EjAR = 3.0 instead of 3.3--but this difference should have no acoustic effect--see earlier slide!), the axial mixer clearly has a smoother profile and yet produced more sound.

Source Location–Case I

If External >> Internal, smoother exit profiles indicate
increased internal mixing,
decreased External sound, and
reduced Total Sound.

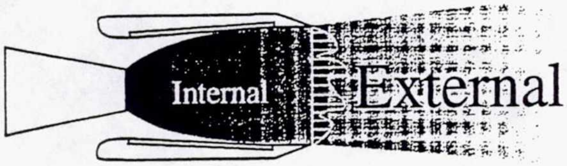

Total Sound

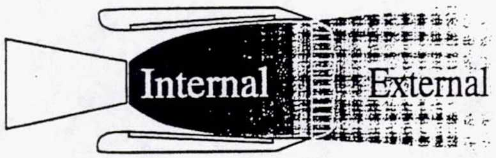

Total Sound

Obviously, there is a flaw with the figure of merit which was used in the design phase. Or more precisely, a flaw in the assumptions which went into it choice.

Consider the situation where the noise generated external to the ejector was much greater than that produced (and radiated out of) the ejector. In this case, improving the external flow by smoothing the temperature and velocity profiles at the ejector exit would reduce the noise generated by external mixing and result in a quieter total sound, even if the improvement in flow profile came at the expense of increased internal mixing and sound generation. This was the picture used in deciding on the figure of merit.

Source Location–Case II

If Internal >> External, smoother exit profiles indicate
increased internal mixing,
increased Internal sound, and
increased Total Sound.

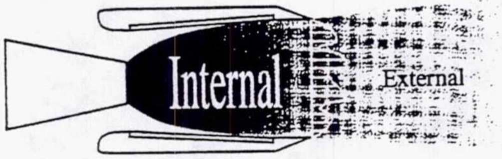

Total Sound

Total Sound

This is the correlation observed in 9x15 data...

Consider instead the situation where the noise generated inside the ejector dominates that produced outside. Now, increasing the mixing within the ejector increases the internal sound, and hence the total sound, rather than reducing it. In other words, having a smoother exit profile means that more sound is being generated internal to the ejector, and since this sound is greater than the external sound, the result is a louder, not quieter, jet. This seems to be the correlation which is observed in the 9x15 tests.

Source Location–Liner Effect

If External >> Internal, inserting liner would have negligible effect on Total Sound.

An even better indicator that the total sound is coming predominantly from the mixing within the ejector is the fact that the liners can be seen to have an effect. If the external noise was dominant, changing the internal noise by adding absorptive material would not be noticable.

Effectiveness of Liner

Short Ejector

Small insertion loss indicates that Externally-generated sound dominates in short ejector configurations.

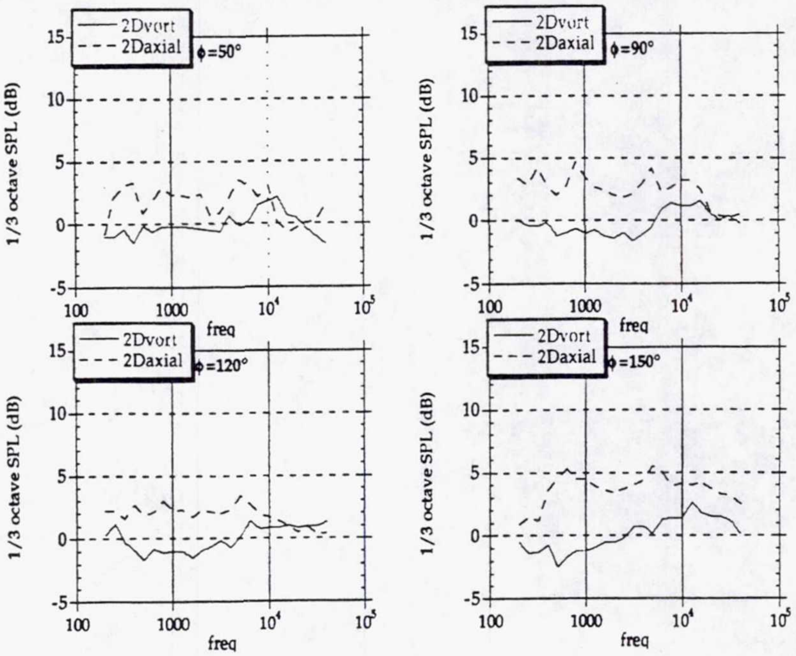

In the short ejector configuration, the absorption by the liner is very small, roughly none with the vortical mixer and less than 3dB with the axial mixer. Here, the mixing noise produced within the ejector is only comparable to or smaller than the noise produced downstream of the ejector. Apparently, the axial mixer produces more sound near the mixer (especially considering that it protruded roughly 3/4" further into the ejector than the vortical anyway) than the vortical mixer. Either that, or the internal mixing of the axial mixer produced sound which was directed more to the liners and less downstream.

Effectiveness of Liner

Long Ejector

Significant insertion loss indicates that Internally-generated sound dominates in long ejector configurations.

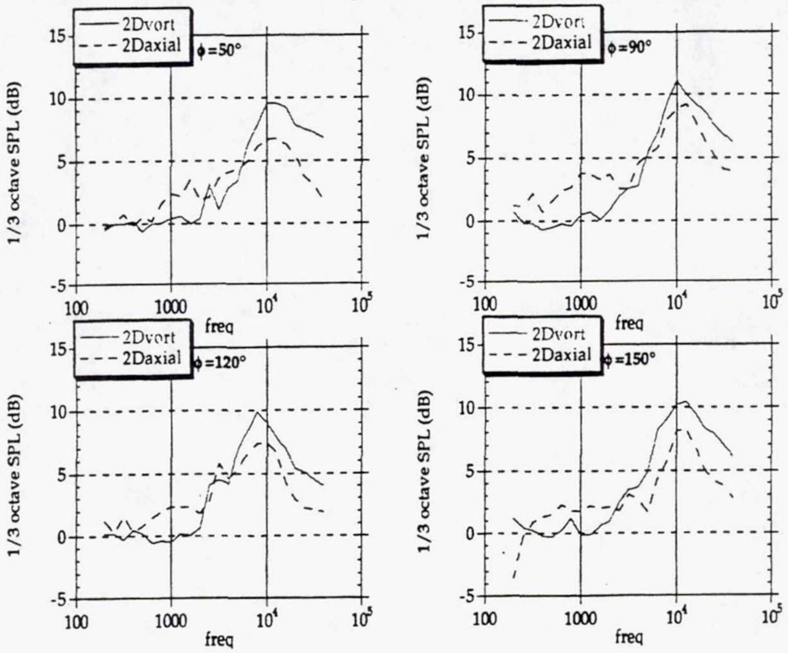

When the ejector is extended to cover more of the mixing (and perhaps change the mixing by the change in static pressure with increasing length), the noise from the mixing which occurs within the ejector is clearly stronger than that which occurs downstream of the ejector. In this case, inserting a liner in either mixer configuration produces significant absorption. Actually, one cannot say whether the sound coming from within the fully lined ejector is greater than that generated downstream, as the liner may have brought the internal noise down to the level of the external. However, the insertion loss at the Sideline PLR condition is roughly the same as that of the upstream parasitic noise, indicating that if more attenuation was possible with a better liner, the total noise could still be reduced with the long ejector.

2Daxial With and Without Center Gap

Schlieren showed that 2Dsplit had significant shock cell structure

Short Ejector, No Liner

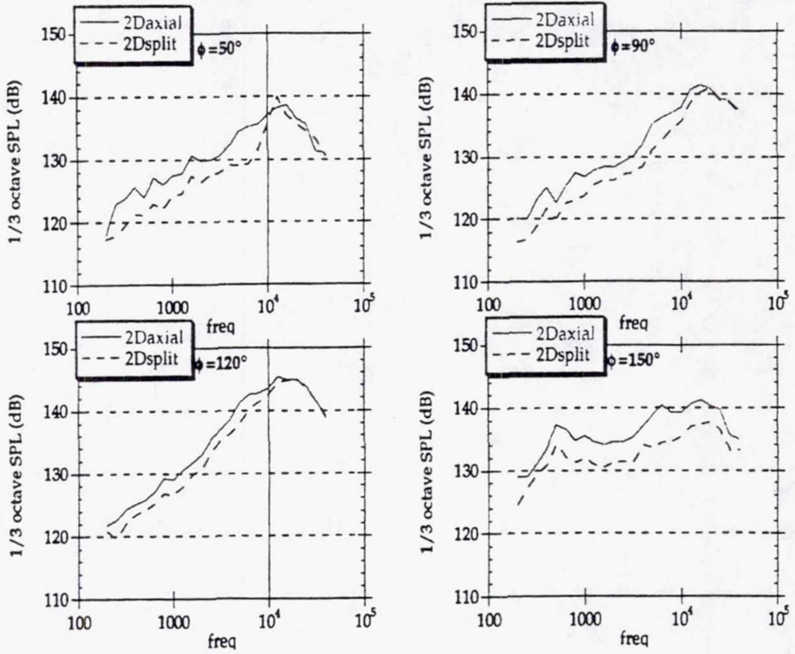

Another interesting observation concerning the noise-mixing relationship within the ejector was made during runs using focussed-Schlieren, results of which are presented elsewhere at this Symposium. Due to a flaw in the design of the axial mixer, the two halves of the nozzle split apart making the axial nozzle similar topologically to the vortical. However, the nozzle was no longer convergent-divergent and shock-free. The gap opened up produced a long shock train which was clearly visible in the Schlieren. One would think that this would produce additional sound (probably above 40kHz judging by the shock spacing), but in fact, the sound was reduced, especially at low frequencies such as are produced far downstream in the jet.

The point of this observation may be that different mixing mechanisms, such as screech or edgetone, may prove better in the mixer design even though they are, by themselves, thought to be more noisy. The mixing which occurs within the ejector must not only be effective, but also have beneficial directivity and spectra to allow effective liner strategies and have minimal impact in the human-factor weighting of jet noise evaluation.

Conclusions

9'x15' test results suggest the following course for improvement:

- Find ways to increase internal mixing while beneficially changing either the amplitude, directivity, or spectrum of its sound generation.
- Optimize ejector length to balance internal sound (after absorption) with external sound.
- Improve ejector liners and see how near-field (nonlinear) acoustics changes their performance.

Post-test analysis of the 9x15 test data show several important parametrics for the continued development of mixer-ejectors for jet noise suppression. The analysis finds several misconceptions or incorrect assumptions which must be corrected and understood before the next iteration of mixer-ejectors is designed. Most importantly, the data shows that in the present application, 'mixing' cannot be treated as a scalar quantity to be reduced or increased; the mixing processes produced by different mixer geometries within the ejector must be understood in more detail and their noise generation differentiated to drive the optimization of mixer design. Simple-minded increase of the mixing within the ejector when the internal noise already dominates the total sound will only increase the jet noise, not reduce it. It appears from here that the optimal ejector length will be that which encloses enough of the flow so that bnternal noise is balanced by external noise. It appears that a reasonable-length ejector can still benefit from an increase in absorption by the liner, indicating that the upcoming liner technology program will be directly applicable to the current mixer-ejector program.

1999176545

TEST RESULTS BOEING NFM NOZZLE IN LSAF

G.L. Nihart
The Boeing Company
Seattle, Washington

S8-07

409523

14 p.

Near-fully Mixed (NFM) Nozzle

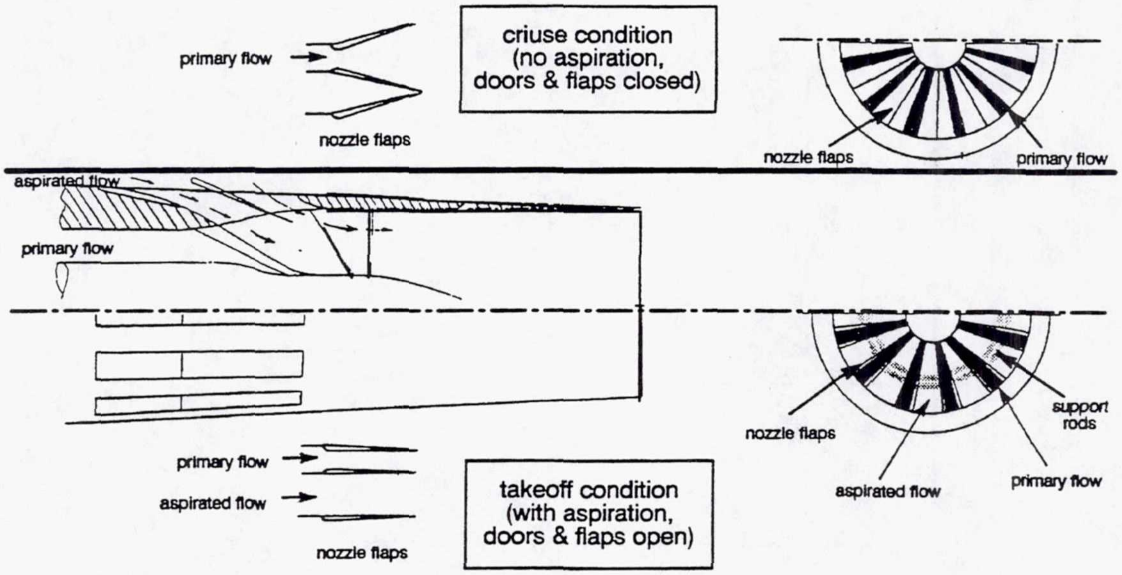

The 1990 test nozzle was based on a design designated the Near-Fully Mixed (NFM) nozzle.

The key features of this nozzle are:

- 12 aspiration chutes that stay in the flow at all operating conditions
- Hinged flaps that change the primary nozzle throat area and expansion ratio
- The flaps close off the aspiration flow at the cruise condition

Sideline EPNLs as Functions of Thrust
for Three Treated Shrouds

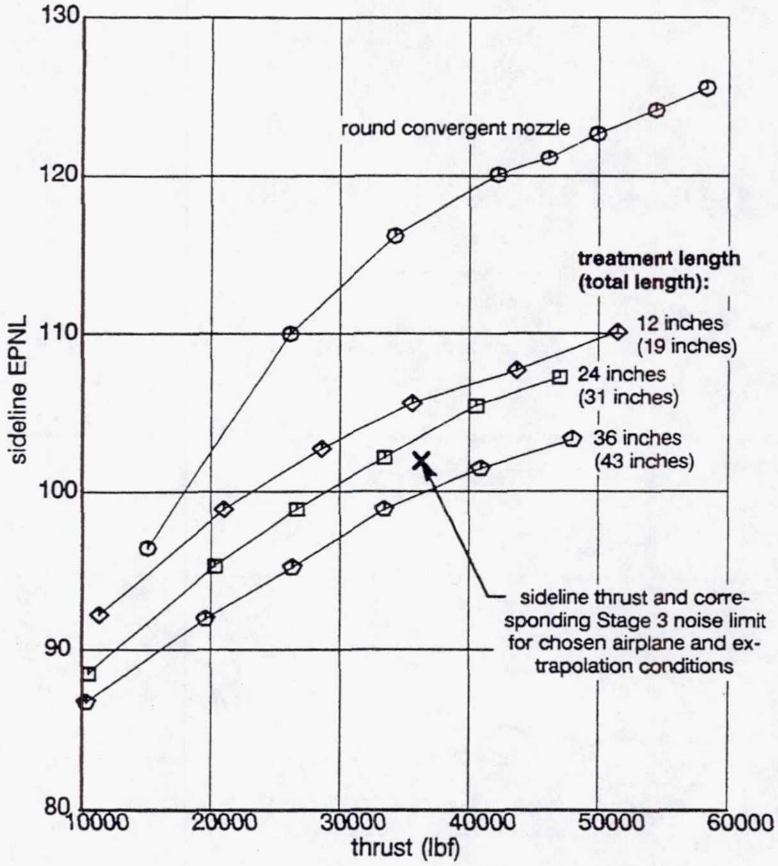

Test results of this nozzle show up to 20 EPNdB of noise suppression. This would provide compliance with Stage 3 noise requirements for a Turbine Bypass Engine (TBE). This noise suppression requires a very long (treated L/D of 4.0) treated ejector.

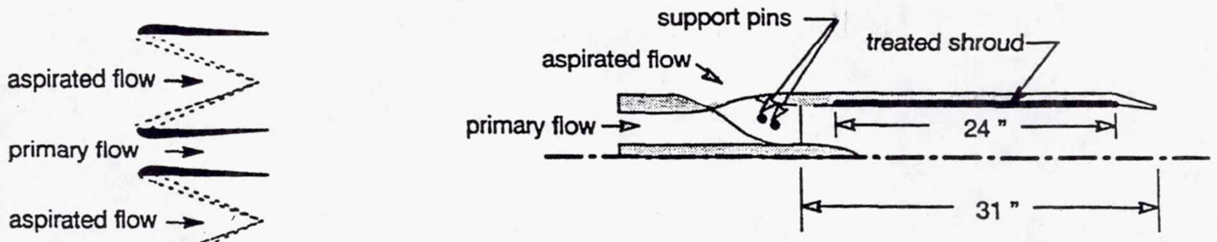

1990 VERSION OF NFM NOZZLE

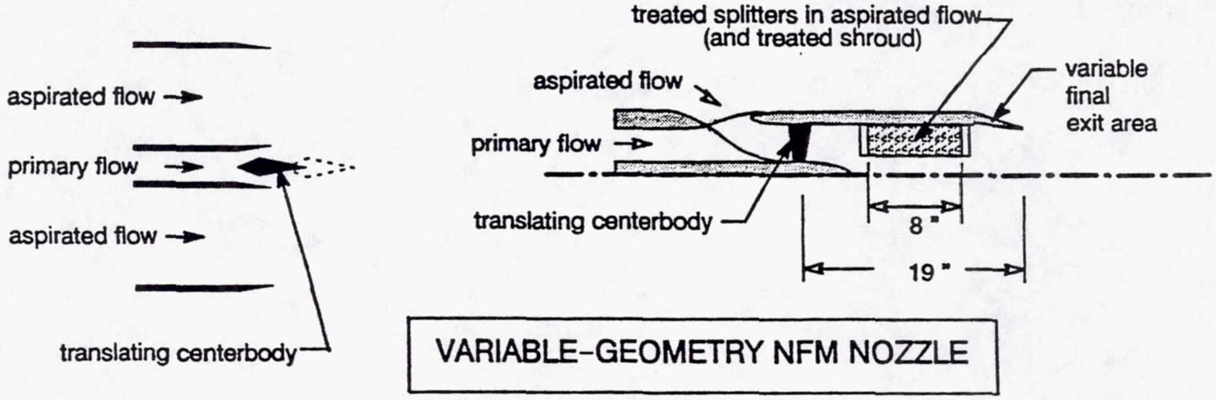

VARIABLE-GEOMETRY NFM NOZZLE

The 1992 version of the NFM Nozzle used translating plugs to vary the primary expansion ratio. The ejector lining was up to an equivalent of 3.3 L/D (2.7 L/D shown) using radial splitters. This nozzle was called the Variable Geometry NFM Nozzle and also featured a variable exit area.

1990 NFM NOZZLE TEST RIG

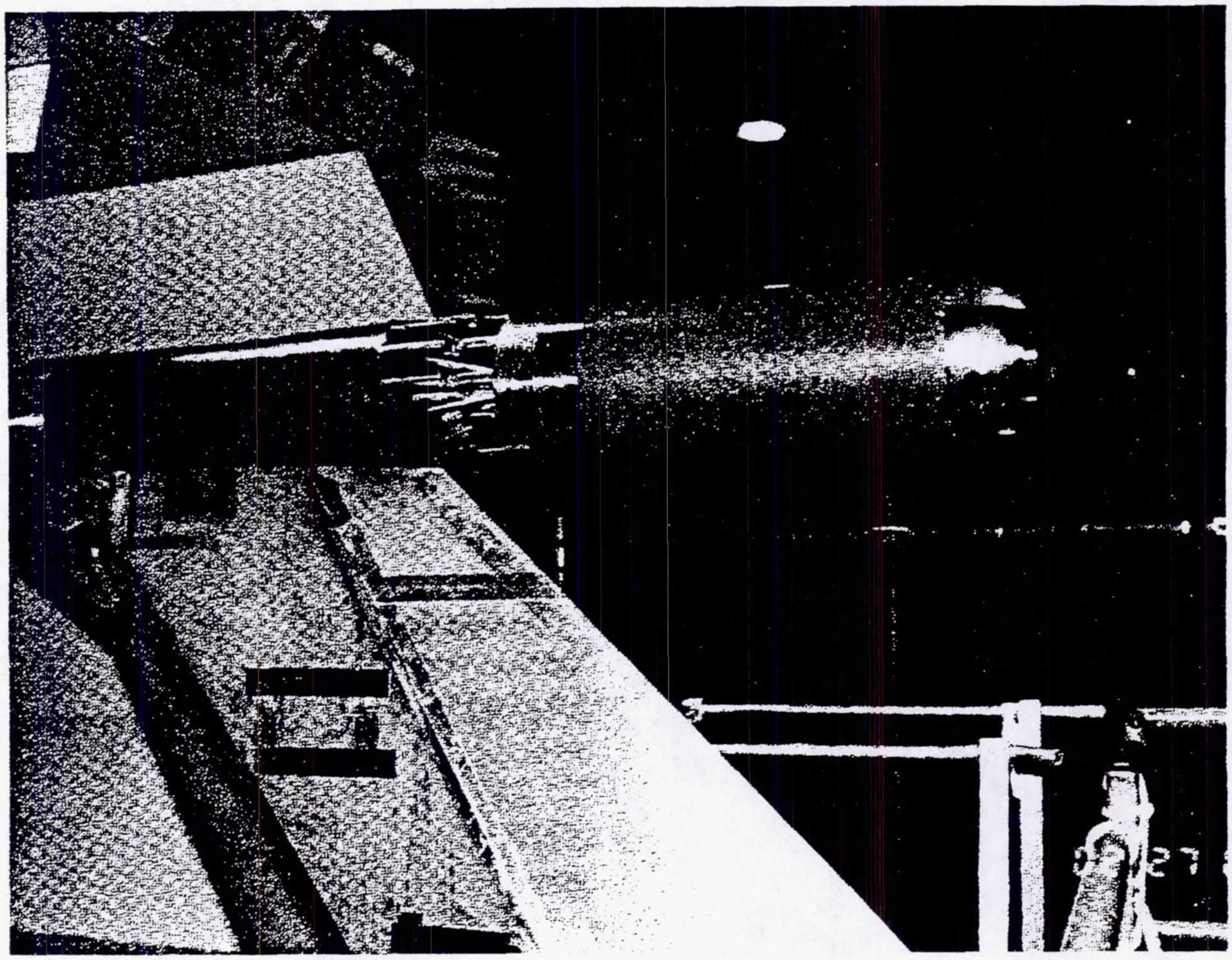

This is a picture of the 1990 NFM Nozzle test in the Low Speed Aeroacoustic Facility (LSAF) Wind Tunnel. The ejector shown is the 2.7 L/D lining length. The 20 EPNdB suppression was achieved with an ejector with a 1/3 longer treated section.

1992 VARIABLE GEOMETRY NFM NOZZLE TEST

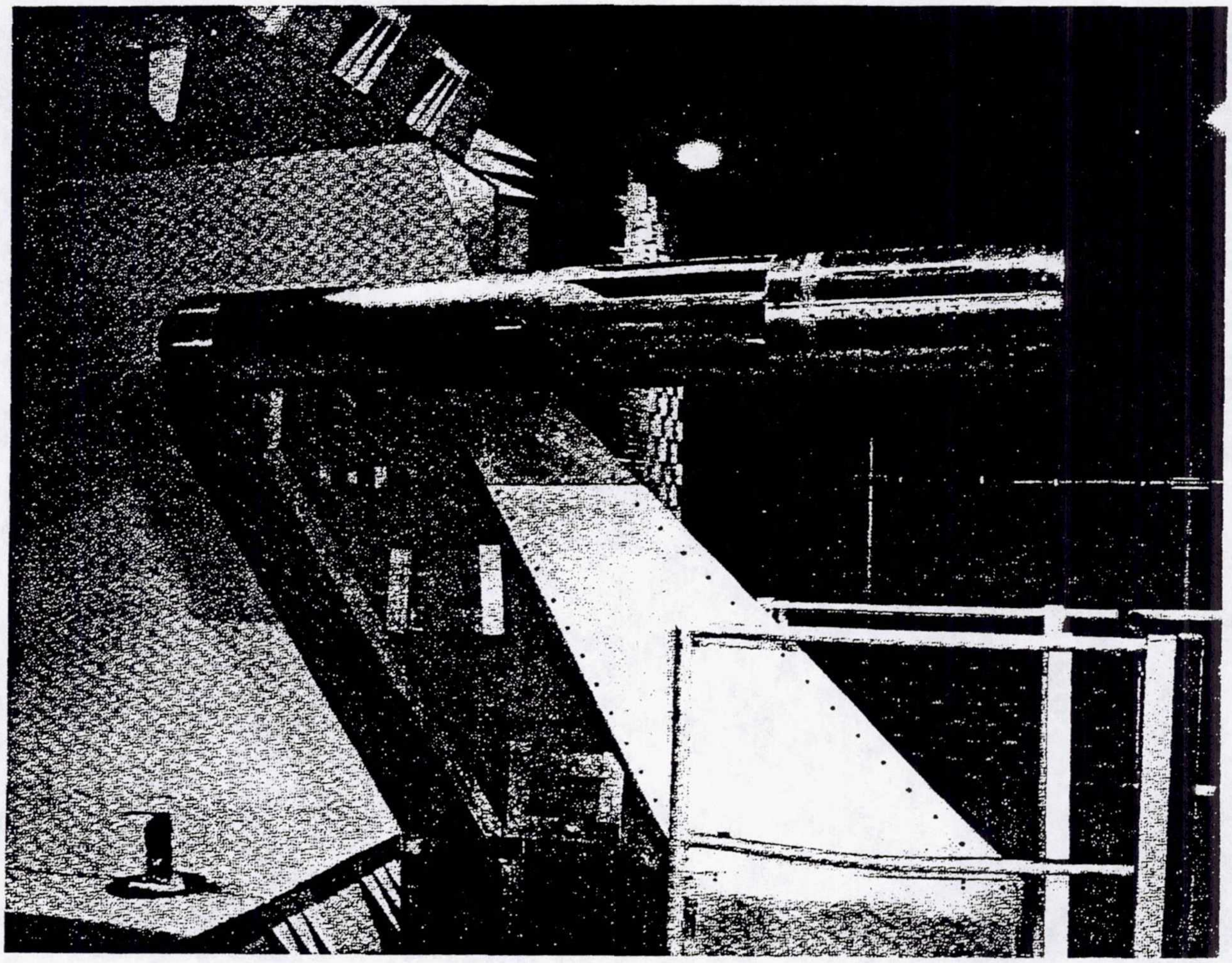

This is a picture of the 1992 Variable Geometry NFM Nozzle test in LSAF. The ejector inlet featured a 15° ramp angle, probably could use 45°, so the inlet is considerable longer than it needs to be. The ejector is the longest tested, equivalent treatment area is 3.3 L/D.

1992 VARIABLE GEOMETRY NFM NOZZLE

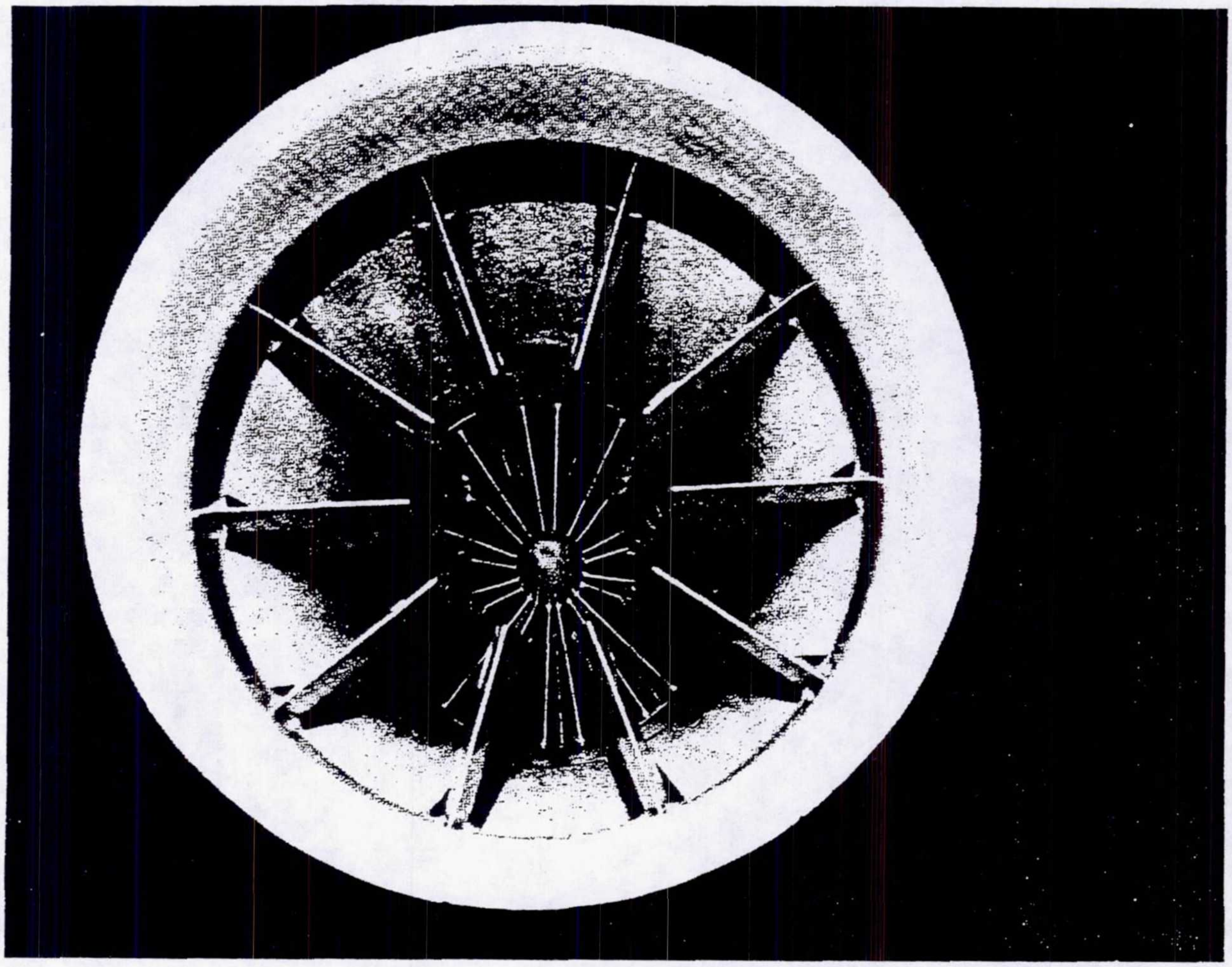

The 1992 Variable Geometry NFM Nozzle is shown. The radial acoustic splitters are shown in the foreground and the primary nozzles and plugs are in the background.

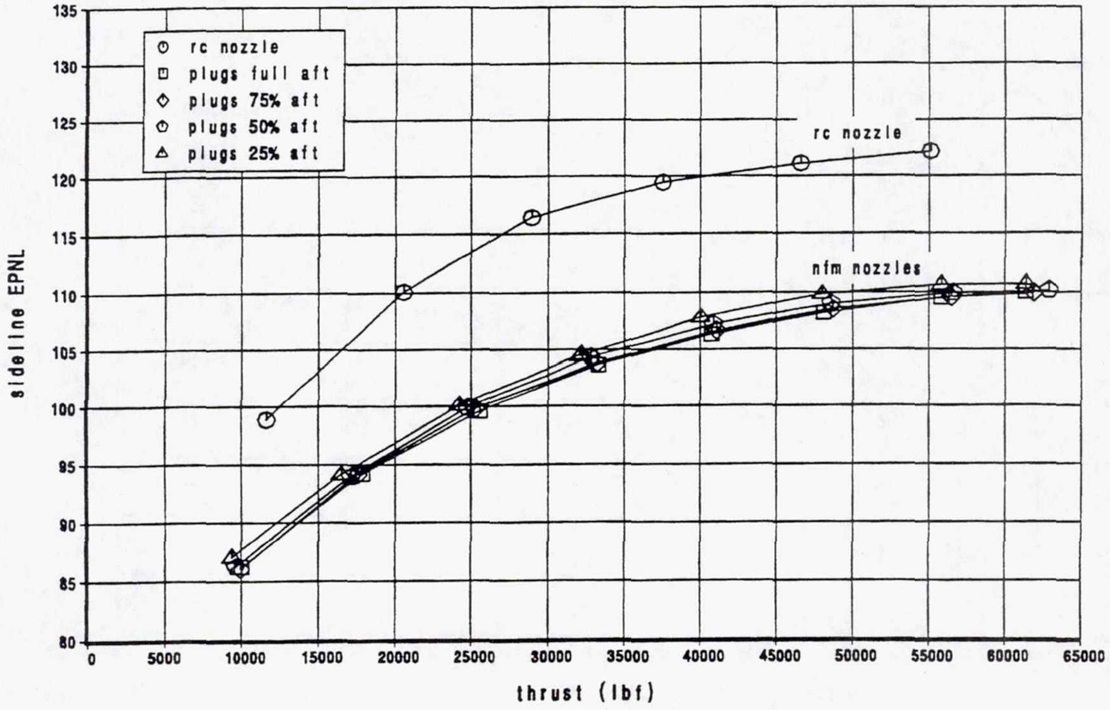

PLUG POSITION EFFECT ON NOISE

Noise test results showed little noise benefit for plug position. The plug position selected was at 50% aft based on thrust performance.

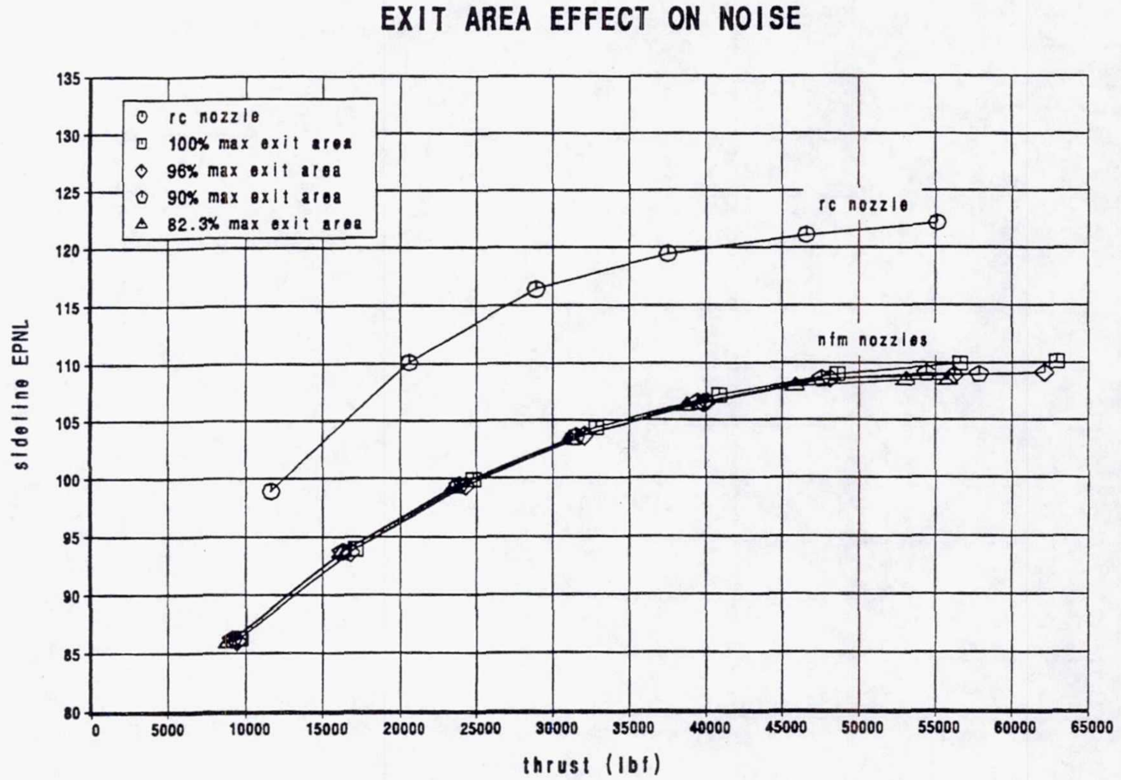

Noise test results showed little noise effect with different ejector exit areas. The largest area (100%) was selected based on static thrust measurements.

EJECTOR TREATMENT BENEFIT - STATIC

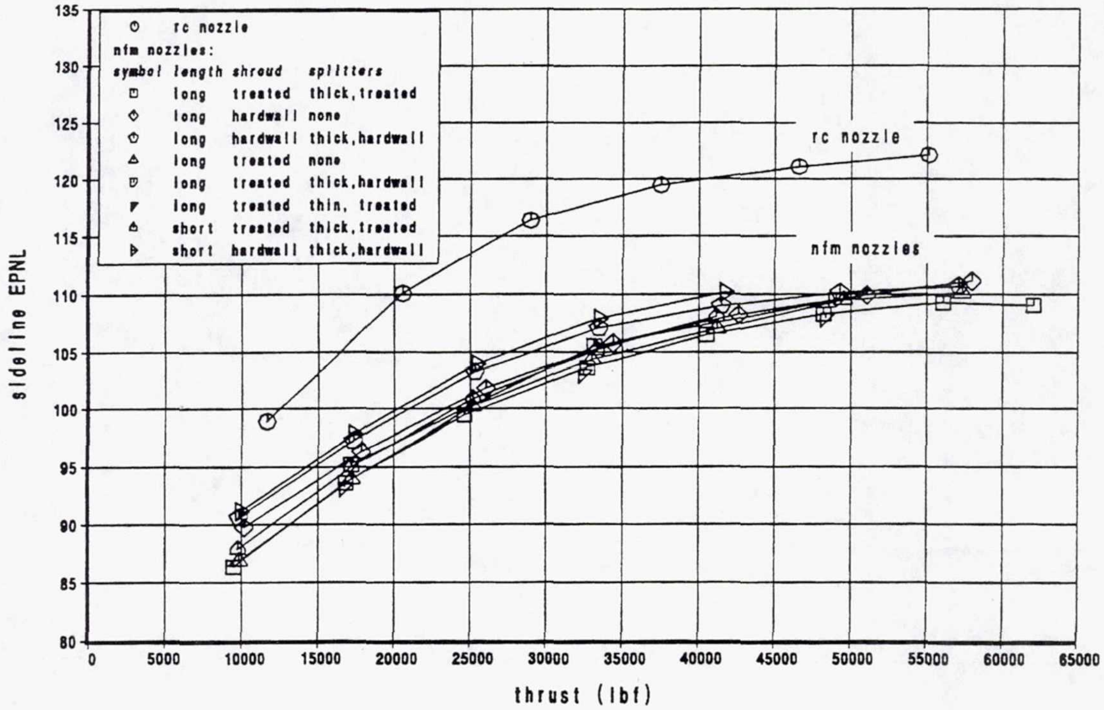

Several treatment configurations were tested from hardwall shroud, hardwall shroud and hardwall splitters and different treated configurations. The maximum static suppression achieved was 15 EPNdB.

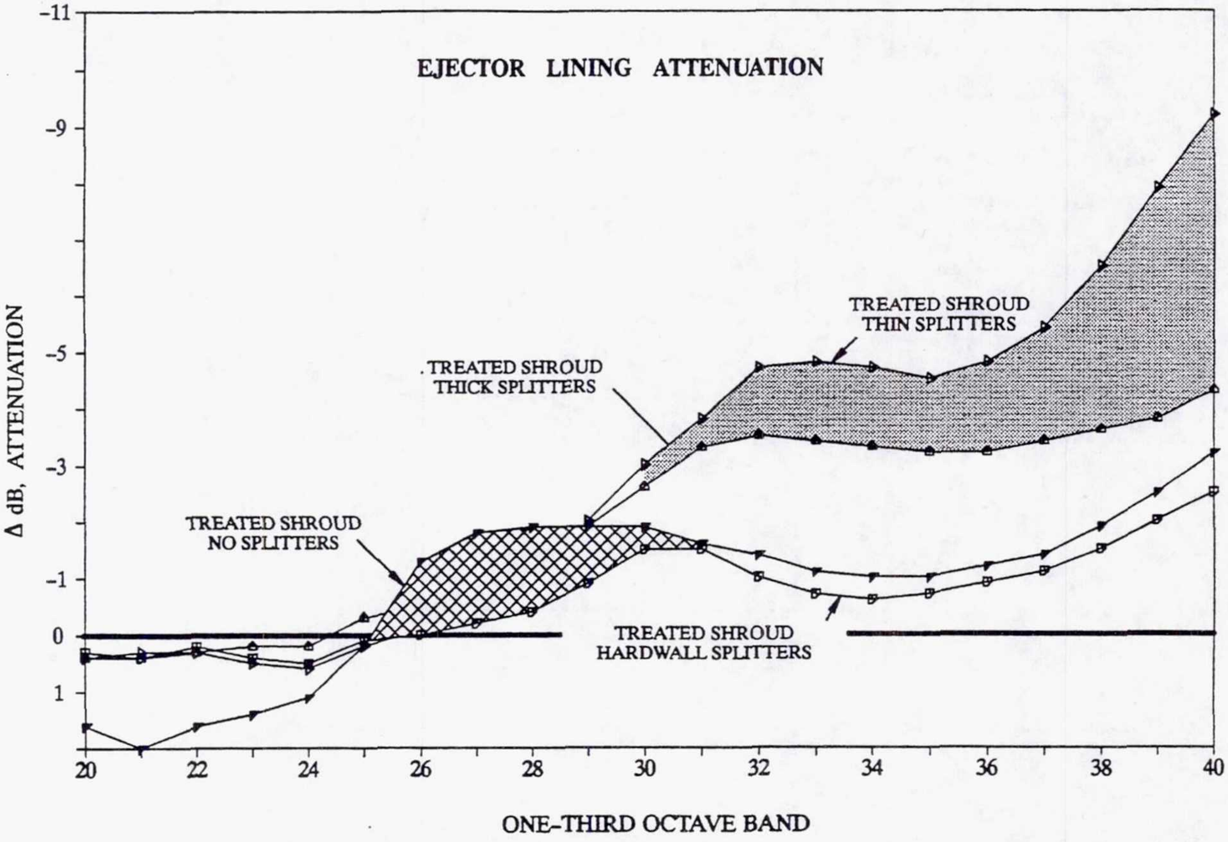

Ejector lining attenuation spectra for the longest ejector relative to the hardwall shroud (no splitters) configuration. The treated shroud was tuned to 700 Hz (Band 28) and the splitters to 2000 Hz (Band 33).

This data reveals several points:

-- Hardwall splitters increased noise in the 400-700 Hz range (Bands 26-28)

-- Lining attenuation is spread out over several one-third octave bands due to the temperature variation in the ejector

-- The thin splitter configuration was more effective than the thick splitter configuration.

THICK AND THIN SPLITTER LINING DESIGN

CONVENTIONAL LINING DESIGN

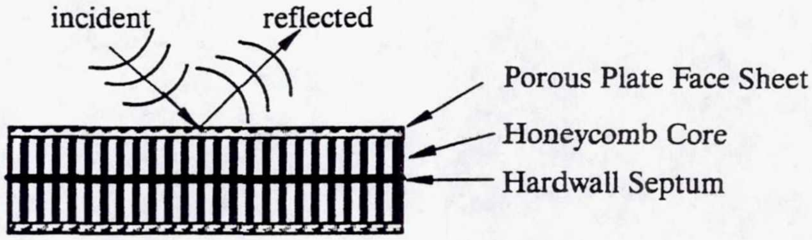

THIN SPLITTER LINING DESIGN

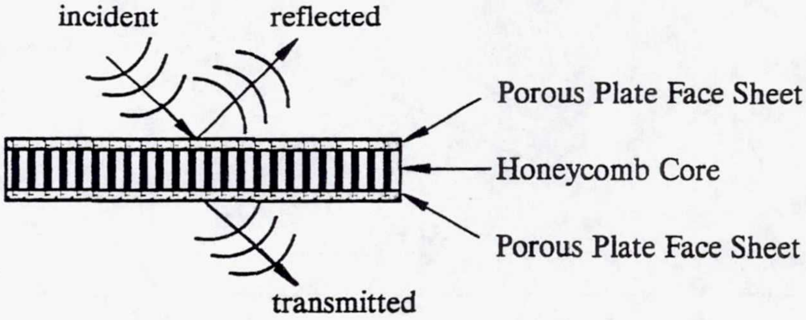

The thick splitter design (conventional) was a double-honeycomb core with a hardwall septum in between. The thin splitter configuration was with a single core thickness and a porous face sheet on both sides.

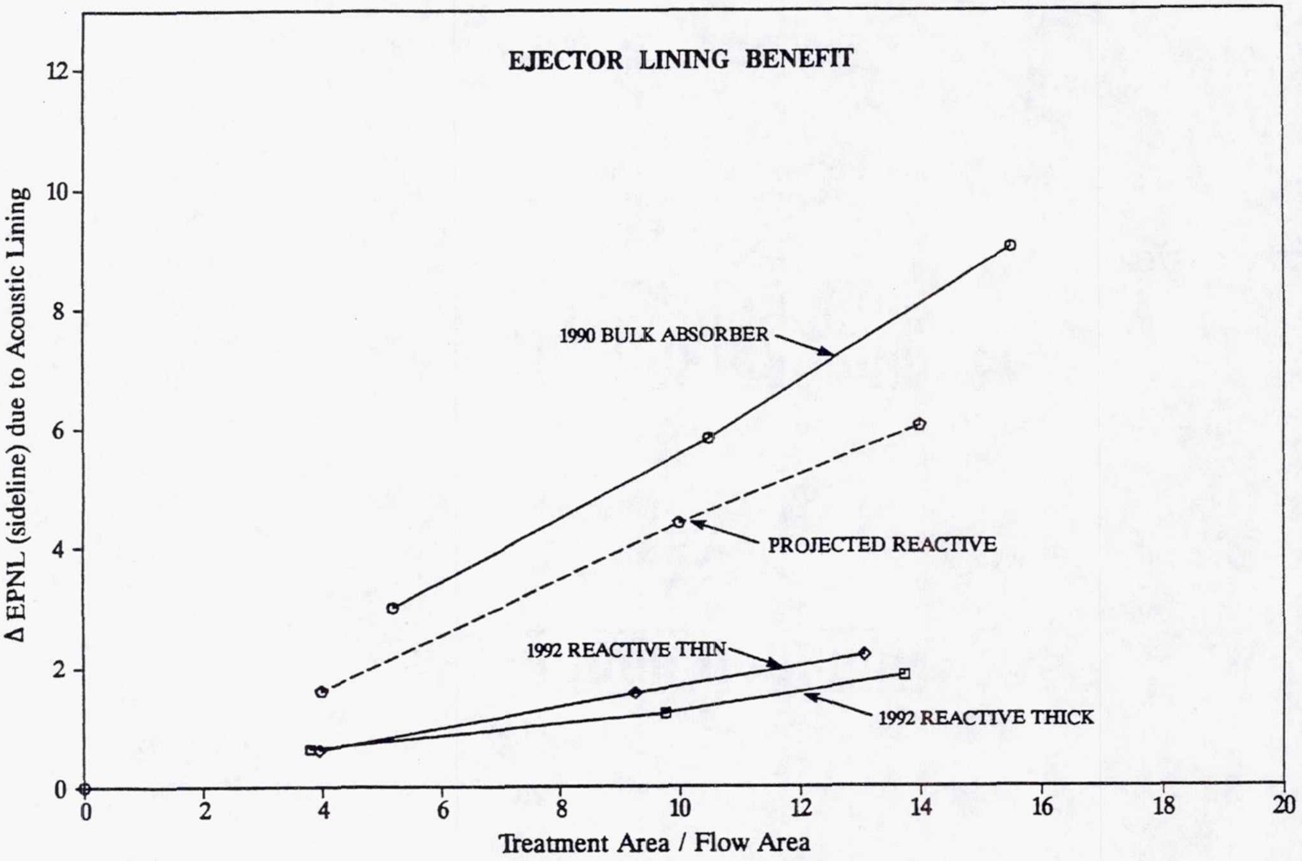

Ejector treatment noise suppression results are linear with treatment area. The 1990 bulk absorber was much more effective than the 1992 reactive lining tested. The design of the reactive lining shroud treatment was tuned to low in frequency and all of lining should have been more porous. A projection of what could be achieved with reactive lining is also shown. Lining axial location, downstream of the mixer, was important but radial location did not seem to be important.

FORWARD FLIGHT EFFECT RC AND NFM NOZZLES

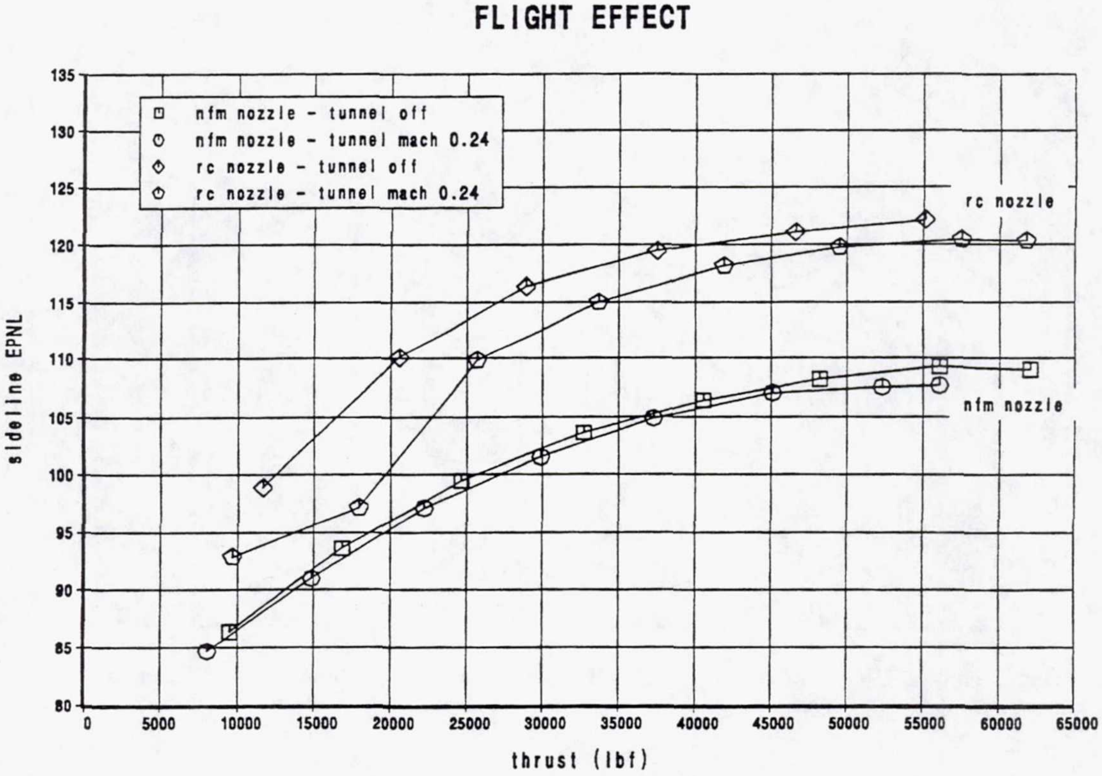

There was very little flight effect benefit for the suppressed nozzle, an indication that the noise is predominantly internally-generated. The maximum "in-flight" suppression level is reduced to 13.6 EPNdB.

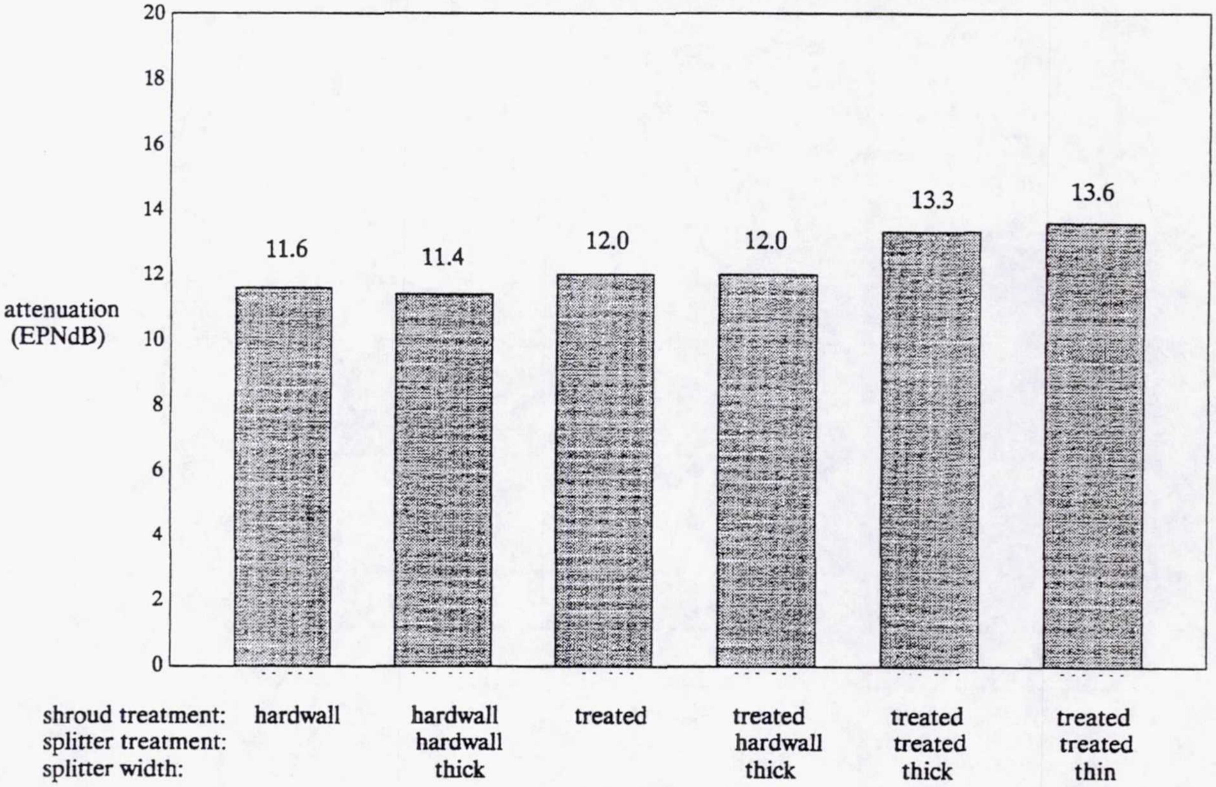

Noise Attenuation (re: RC Nozzle) at Sideline Condition for Variable–Geometry Near–Fully Mixed Nozzle at a Nozzle Pressure Ratio of 4.0

The NFM nozzle noise suppression ranged from a low of 11.4 EPNdB for the hardwall shroud and hardwall splitter configuration to 13.6 EPNdB for the treated shroud and treated thin splitter. To be noted the hardwall splitters increased noise by 0.2 EPNdB and the treated thin splitter was 0.3 EPNdB more effective than the thick splitter.

OMIT THIS
PAGE

Session III

Fundamental Experiments

1999176546

SUPERSONIC JET MIXING ENHANCEMENT DUE TO NATURAL AND INDUCED SCREECH

E.J. Rice
NASA Lewis Research Center
Cleveland, Ohio

and

G. Raman
Sverdrup Technologies, Inc.
Brookpark, Ohio

59-07

409525

16P

OUTLINE OF PRESENTATION

- REVIEW OF EXPERIMENTAL APPARATUS
- EFFECT OF NATURAL SCREECH ON JET MIXING
  - CONVERGING NOZZLE, UNDEREXPANDED JET
  - CONVERGING-DIVERGING NOZZLE, DESIGN PRESSURE
- EFFECT OF INDUCED SCREECH ON JET MIXING
  - PRODUCED BY PADDLES IN SHEAR LAYERS
  - SIMILAR TO EDGE TONES
  - CONVERGING-DIVERGING NOZZLE, DESIGN PRESSURE
- EFFECT OF PADDLES ON NEAR-FIELD JET NOISE
- CONCLUDING REMARKS

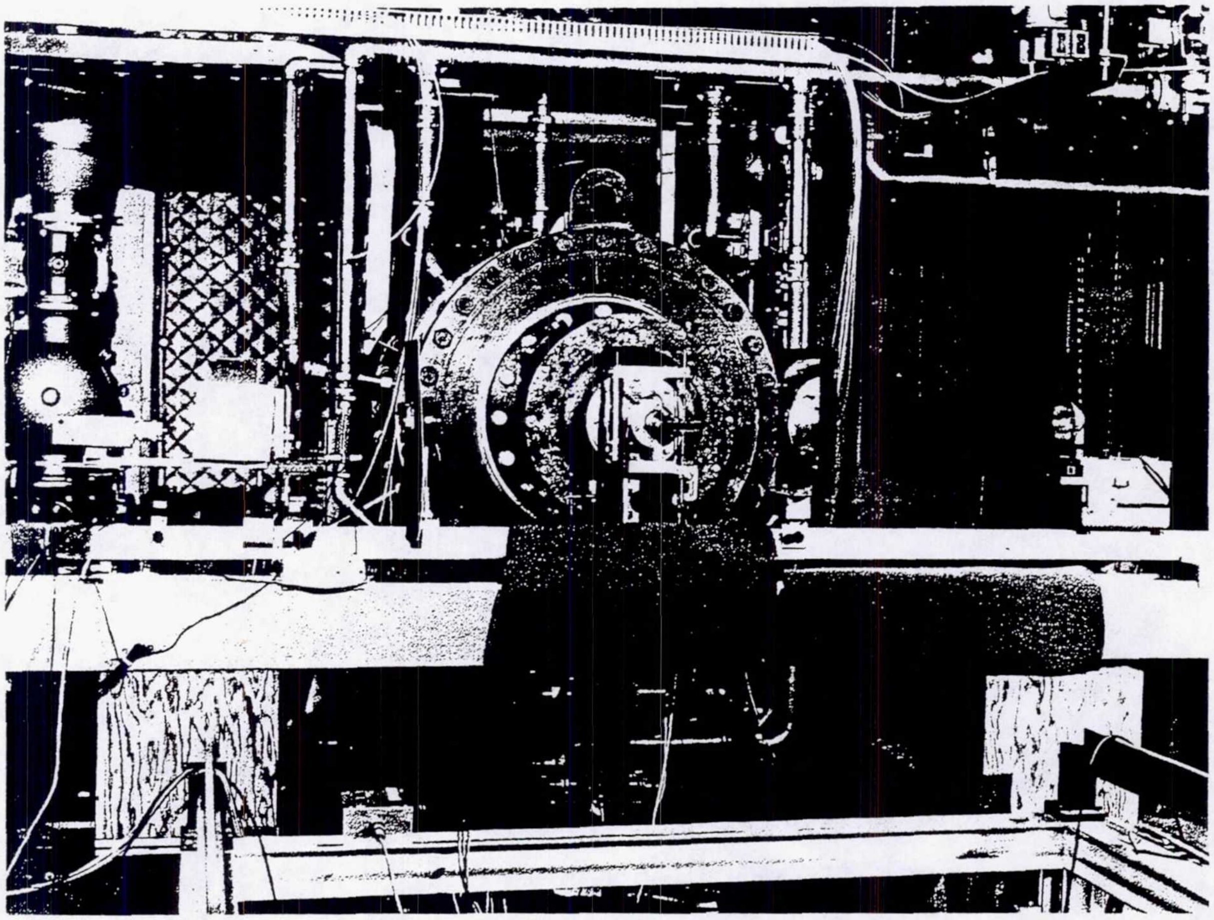

The 30 inch diameter plenum chamber that delivers high pressure air to the rectangular nozzle is seen in the center of the figure. The details of the structure around the nozzle will be shown shortly. At the lower part of the figure is the optical beam that supports the strobed Schlieren system. The strobe on the far right provides the synchronized short duration flash. The next object is the Fresnel lens with a two dimensional grid. A lens focuses the grid onto an image grid which is a reduced print of the two dimensional grid. Refraction of the light by density gradients in the vicinity of the nozzle cause misalignment of the two grids producing lightened and darkened areas on a frosted glass which is viewed by the video camera.

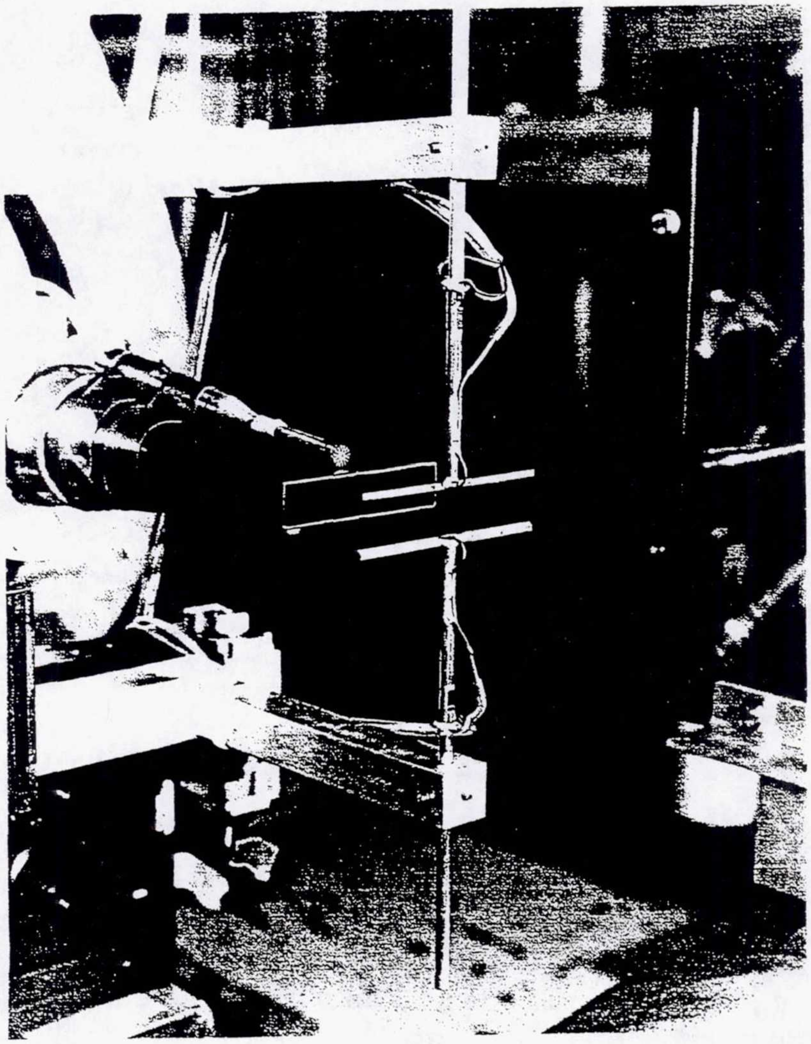

The rectangular CD nozzle is seen with a 0.25 inch microphone attached to measure the screech amplitude at the nozzle lip. Mounted downstream from the nozzle are the paddles which induce the screech. The jet is dominated by the flapping mode of instability and as the jet impinges upon a paddle the pressure increases. The paddle acts as an acoustic source sending sound back to the nozzle lip. The flow emerging from the nozzle is excited by this pressure wave causing the flapping instability which closes the feedback loop. The paddles are mounted on a three-dimensional movement so that paddle position can be adjusted for maximum screech feedback and mixing enhancement. The first experimental results which will be shown use a set of baffles mounted similarly to the paddles of this figure. However, the baffles are extensive surfaces which block the acoustic feedback from the shock cells to the nozzle lip while allowing the supersonic jet to pass through. Using baffles reduce screech and mixing while paddles induce screech and increase jet mixing.

EFFECT OF SCREECH LEVEL ON MIXING OF UNDEREXPANDED JET

CONVERGENT RECTANGULAR NOZZLE, ASPECT RATIO = 4.97, M_{exp} = 1.55

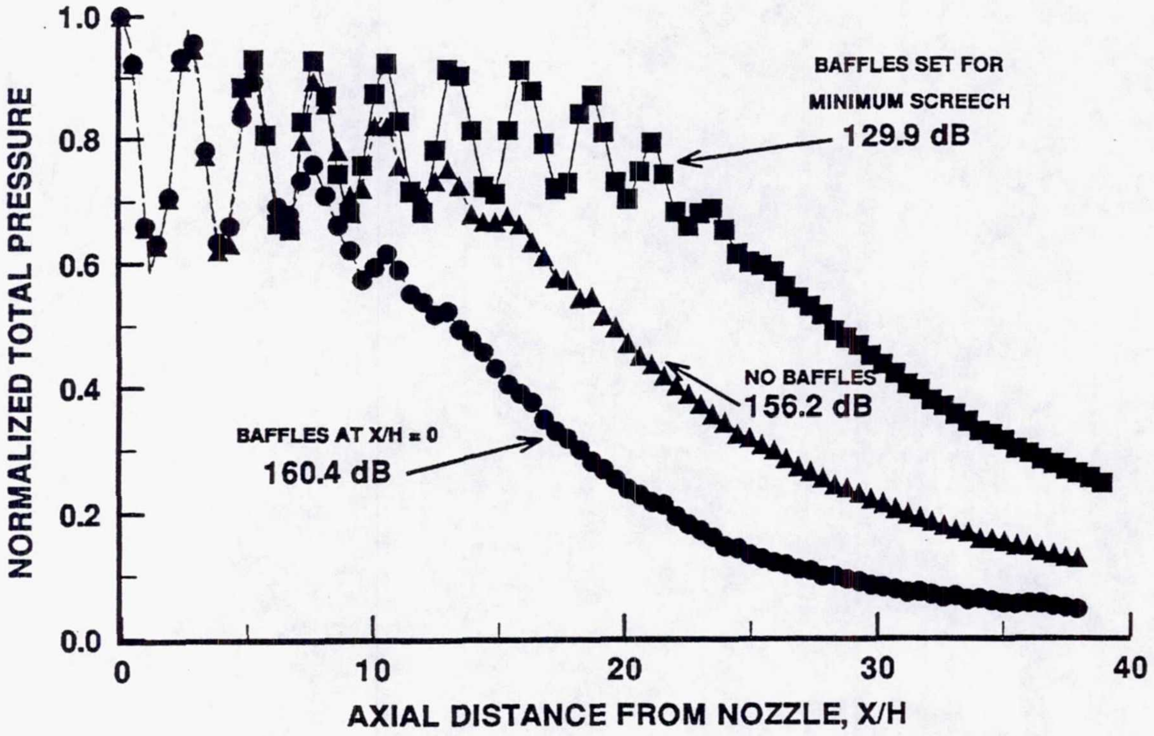

Three sets of normalized total pressure data are shown here as a function of the axial distance from the nozzle exit normalized by the small nozzle exit dimension. This total pressure data is the raw pressure as measured by a total pressure tube without correction for local static pressure or drop over the tube bow shock. This is a converging nozzle run underexpanded and the total pressure oscillations with axial distance show the presence of strong shocks in the jet flow. The middle curve shows the data for the bare jet. The screech level at the nozzle lip is seen to be 156.2 dB, and the potential core length is about 10 as expected. When the baffles are used to eliminate the screech feedback path, the screech is reduced to 129.9 dB. The potential core is increased to 20 showing a dramatic reduction in jet mixing. The lower curve is the result of parking the baffles at X/H = 0. The screech is seen to increase to 160.4 dB and the potential core reduce to about 5 indicating an increase in mixing over the bare jet.

EFFECT OF SCREECH ON MIXING OF PROPERLY EXPANDED JET

CONVERGING-DIVERGING NOZZLE, ASPECT RATIO = 4.82, M_{exp} = 1.39

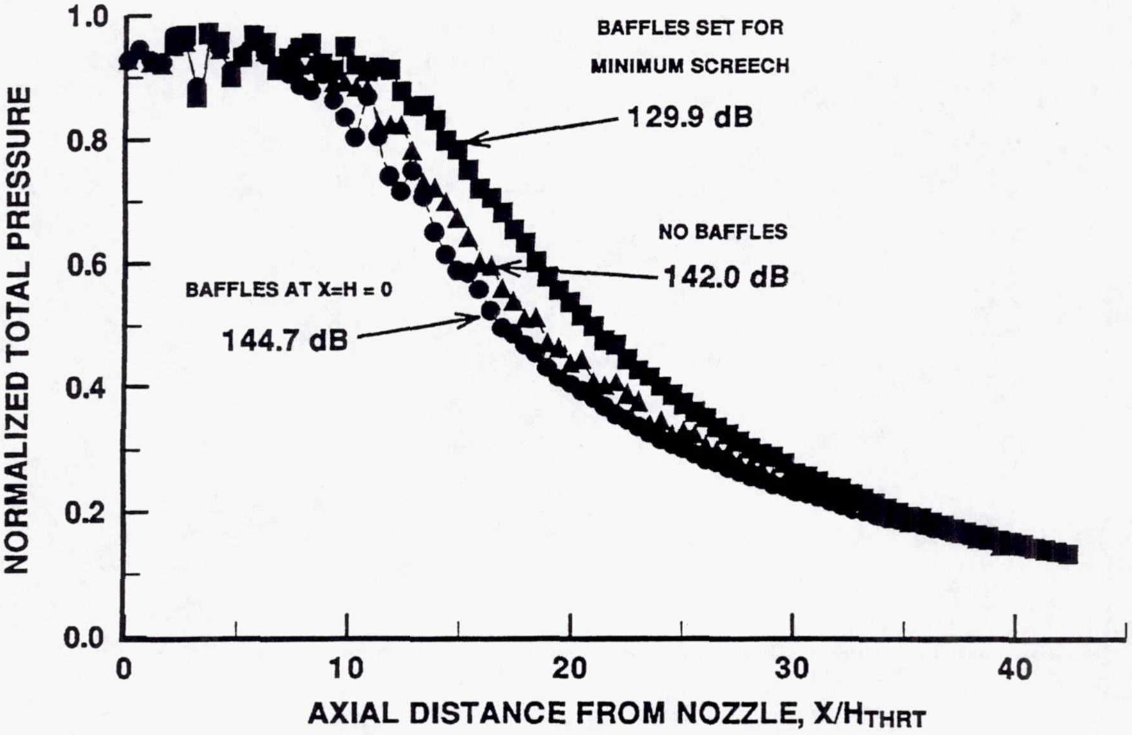

This figure shows the results of repeating the previous experiment with a properly expanded flow from a converging-diverging rectangular nozzle. The results are qualitatively the same but with much reduced screech levels and effect on jet mixing. There is about a 15 dB level difference between the extreme curves with only a modest change in mixing.

EFFECT OF SCREECH ON MIXING - COMPARE TWO NOZZLES

CONVERGING AND CONVERGING-DIVERGING, $M_{exp} = 1.4$

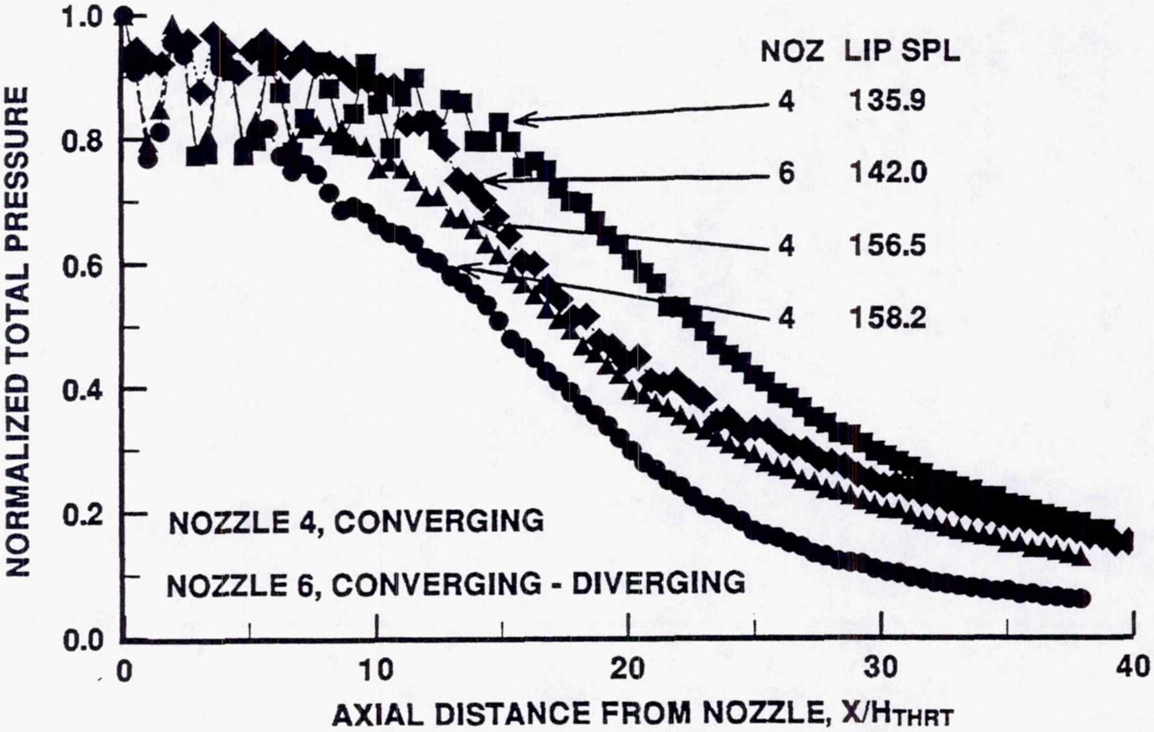

The centerline total pressure is shown for the converging-diverging nozzle (#6) operated at design pressure and also for the converging nozzle (#4) operated underexpanded both at a Mach number of 1.4. Nozzle #4 is seen to be somewhat less sensitive to screech level than at a 1.55 Mach number from a previous figure, but also the screech level variation is less (22 dB) than that of the previous figure (30 dB). The most interesting point to be made here is that the bare jet from the CD nozzle mixes almost as well as that of the converging nozzle although the screech level is much lower (142 and 156.5 dB).

INDUCED INSTABILITY OF SUPERSONIC JET

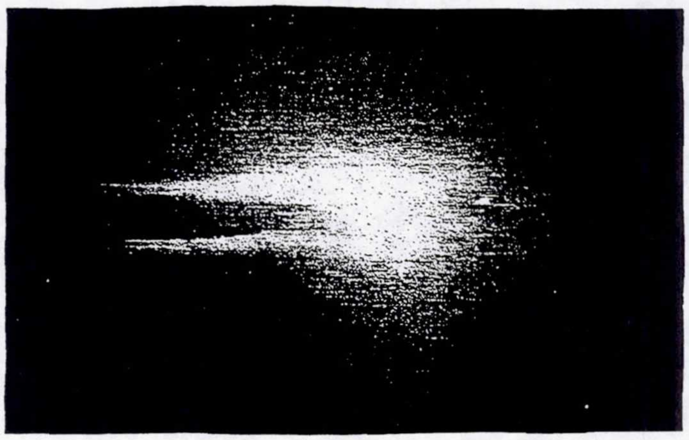

a. Natural jet

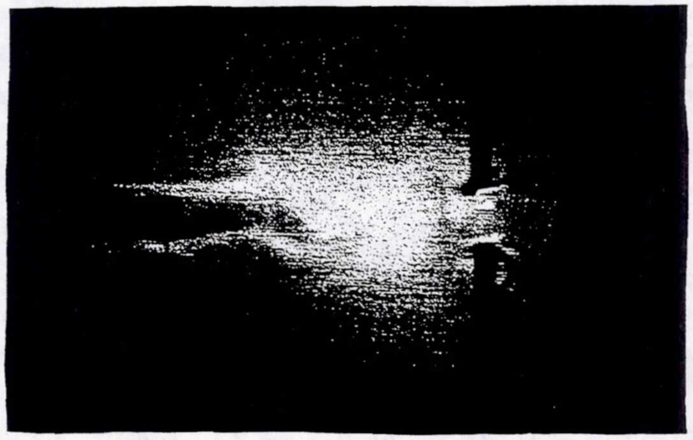

b. Induced flapping instability
paddles at $X/H_{exit}=7.18$

Induced instability of supersonic jet (M=1.4), Schlieren photographs, converging-diverging nozzle, design pressure

The discussion returns to the use of paddles to induce screech. This figure shows Schlieren photographs of the natural jet and the jet with paddles in place to produce maximum induced screech. Both are for the properly expanded flow at 1.4 Mach number for a converging-diverging rectangular nozzle. With the paddles in place the jet is seen to have a large amplitude flapping instability produced by the acoustic feedback from the paddles to the nozzle lip. The instability wavelength is seen to be comparable to the jet dimension so a large increase in mixing can occur.

MIXING INCREASE - INDUCED SCREECH

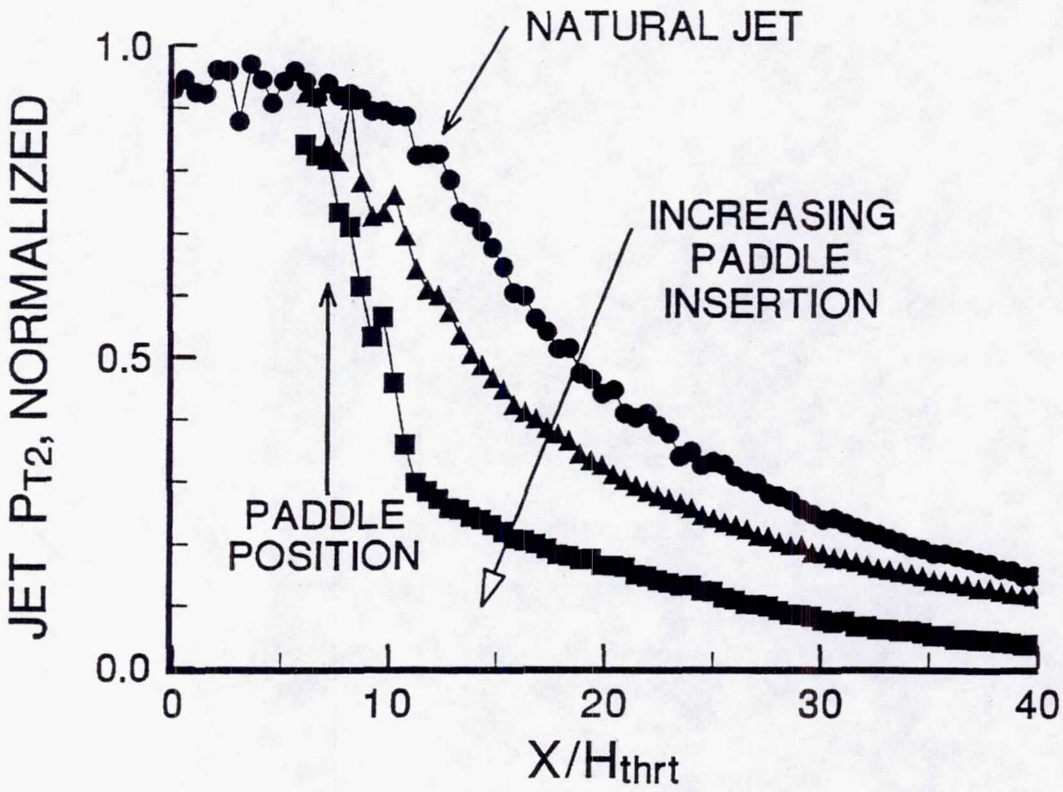

The increased mixing due to the induced screech caused by the paddles is shown as measured by the jet centerline total pressure. The jet is again the properly expanded flow from the rectangular converging-diverging nozzle operating at 1.4 Mach number. Note that the total pressure oscillations, due to shock structure in the jet, are very small compared to previous figures for underexpanded jets. As the paddles are inserted further into the flow, the centerline total pressure drops dramatically. The drop in total pressure starts upstream of the paddles since the flapping oscillations are large there.

COMPARISON OF TOTAL PRESSURE DISTRIBUTIONS

EFFECT OF PADDLES, PRESSURE PROBE AT X=7 INCHES

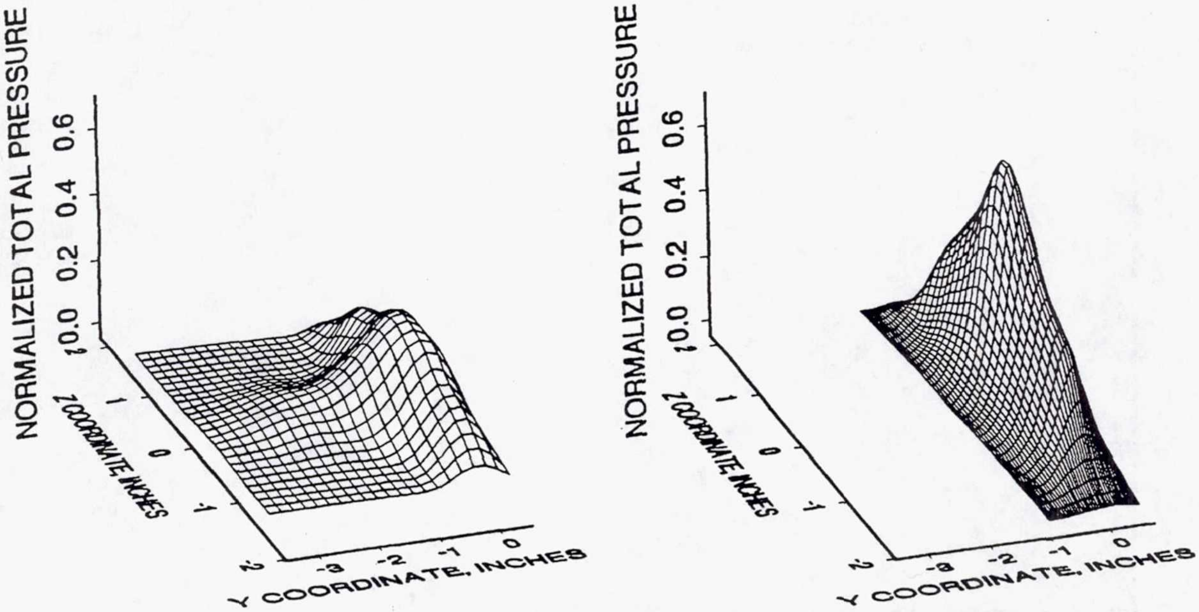

PADDLES AT X=4 INCHES

NO PADDLES

The total pressure distribution in a cross-sectional plane seven inches downstream from the nozzle exit are shown here. Without paddles the pressure distribution is seen to have a high peak on the axis and to have mixed very little in the direction of the nozzle small dimension (Y coordinate). With paddles located four inches from the nozzle, the mixing is seen to be dramatically increased with the centerline pressure reduced and a large amount of flow being pushed out in the Y direction due to the flapping instability.

HALF VELOCITY COORDINATES FOR THE NATURAL AND INDUCED SCREECH JETS

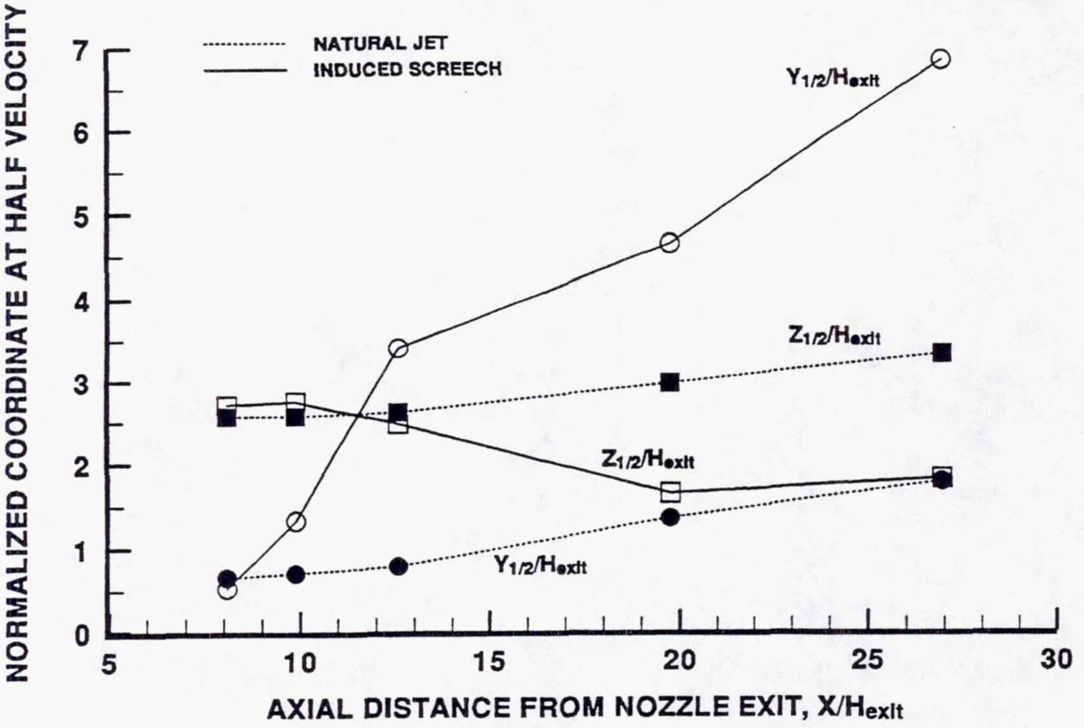

Estimates of the half-velocity coordinates as they develop downstream of the nozzle are shown. These are estimates since the transverse coordinate at 1/4 the centerline total pressure rather than 1/2 the centerline velocity were used. For the natural jet both the Y and Z coordinates are seen to slowly grow as mixing increases with no cross-over occurring. However with induced screech caused by the paddles, the jet Y coordinate is seen to increase drastically due to the flapping and mixing of the jet. An apparent coordinate cross-over occurs, but this is just due to the violent jet flapping in the Y direction and is not coordinate switching as often discussed in connection with low aspect ratio elliptic jets.

COMPARISON OF MEASURED MASS FLOW AT SEVERAL AXIAL STATIONS
NATURAL JET AND JET WITH PADDLES

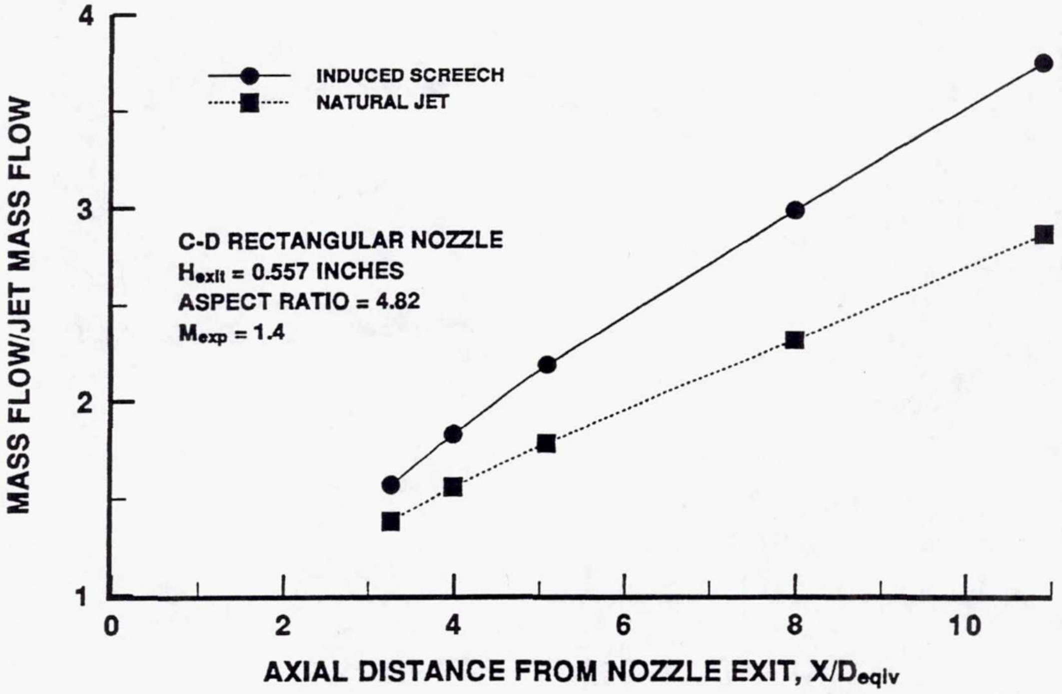

The increase in entrained mass flow due to induced screech is shown in this figure. The mass flow was derived from the total pressure measurements assuming constant static pressure. The entire cross-sectional plane (out to zero total pressure) was included at five axial locations. The equivalent circular nozzle diameter (same area) was used for normalization. At the larger axial distances, the entrained flow is seen to increase by about 48% (total flow by 31%).

MEASURED INTEGRATED AXIAL MOMENTUM OF JETS
NATURAL JET AND JET WITH PADDLES TO INDUCE SCREECH

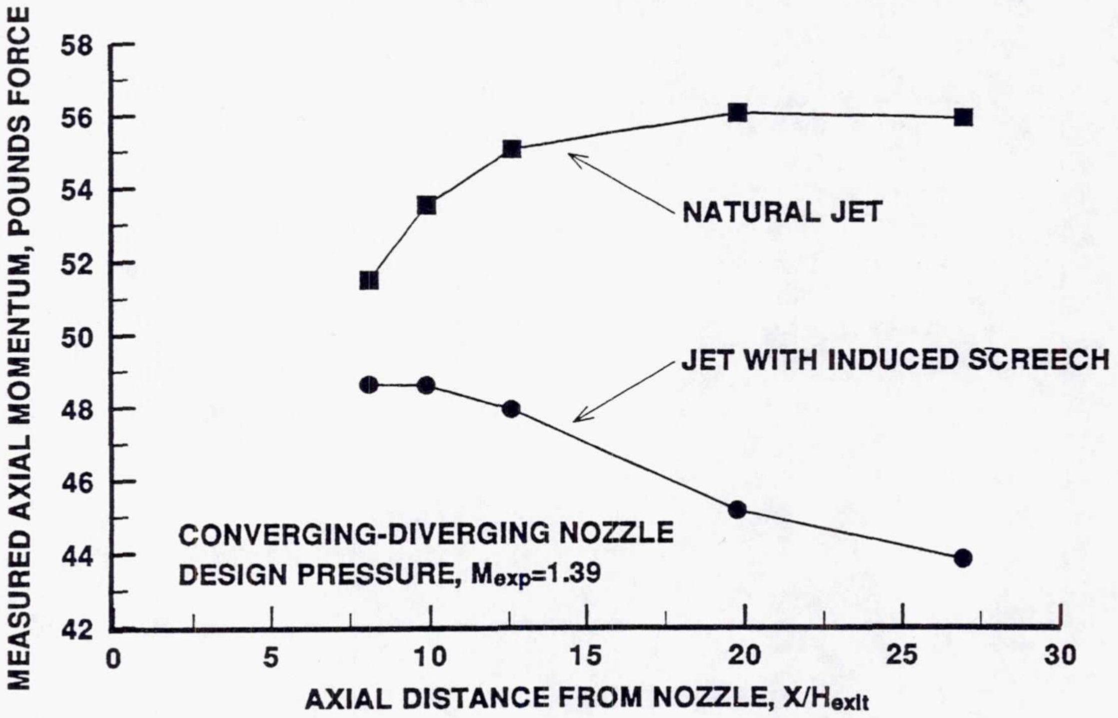

The measured axial momentum, as calculated from the total pressure traverses, for the jet with and without paddles is shown here. Again the nozzle is the converging-diverging rectangular nozzle properly expanded at 1.4 Mach number. For the natural jet the momentum trend is as expected. Due to the reduced local static pressure near the nozzle caused by air entrainment, the total pressure and thus the integrated momentum of the jet appears low. As the local static pressure increases to room pressure, the momentum asymptotically approaches a value of 56 pounds force. The ideal thrust of this jet is about 57 pounds force. With induced screech caused by the paddles, there is some momentum loss due to the forces on the paddles, but then there seems to be a continuous drop in momentum well downstream from the paddles perhaps due to the violent mixing in this region. Force data using strain gages on the paddle supports has been taken to clarify the above momentum phenomenon and to measure the paddle drag for trade-off studies.

NEAR-FIELD NOISE MEASUREMENTS, CD NOZZLE, M_{exp}=1.395

NATURAL JET, 1/3 OCTAVE, F = 2500 HZ

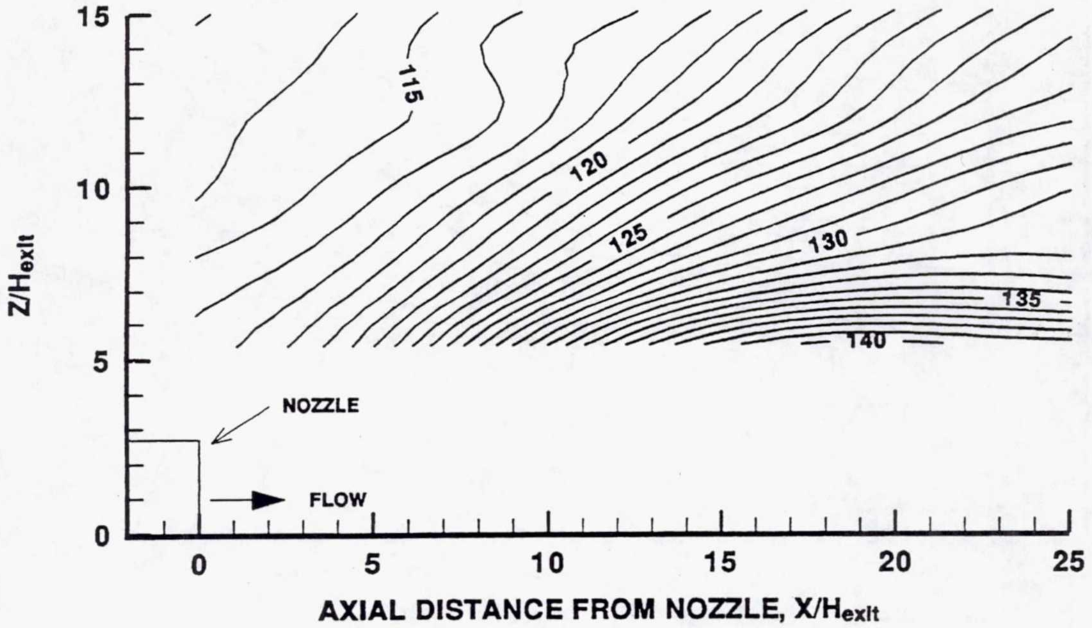

Near-field noise measurements in the Z-X plane are shown in this figure. The Z coordinate is that of the large dimension of the rectangular nozzle. The nozzle is shown in broad-side view in the lower left. This frequency, 2500 Hz, is the 1/3 octave peak in the mixing noise. Near the jet when the constant noise contours run roughly parallel to the jet, the potential of the hydrodynamic field (coherent structures) is being measured. This potential field grows and then decays with axial distance. In this case, for the natural jet, the coherent structures are seen to peak out at a normalized axial distance of about nineteen. The noise field produced by these structures occurs as a lobed pattern of constant noise contours, in this case occurring downstream beyond the range of this graph. This noise field is presented for comparison with the next figure with induced screech due to paddles.

NEAR-FIELD NOISE MEASUREMENTS, CD NOZZLE, M_{exp}=1.395

LONG PADDLES, X_{pad}/H_{exit}=7.18, 1/3 OCTAVE, F=2500 HZ

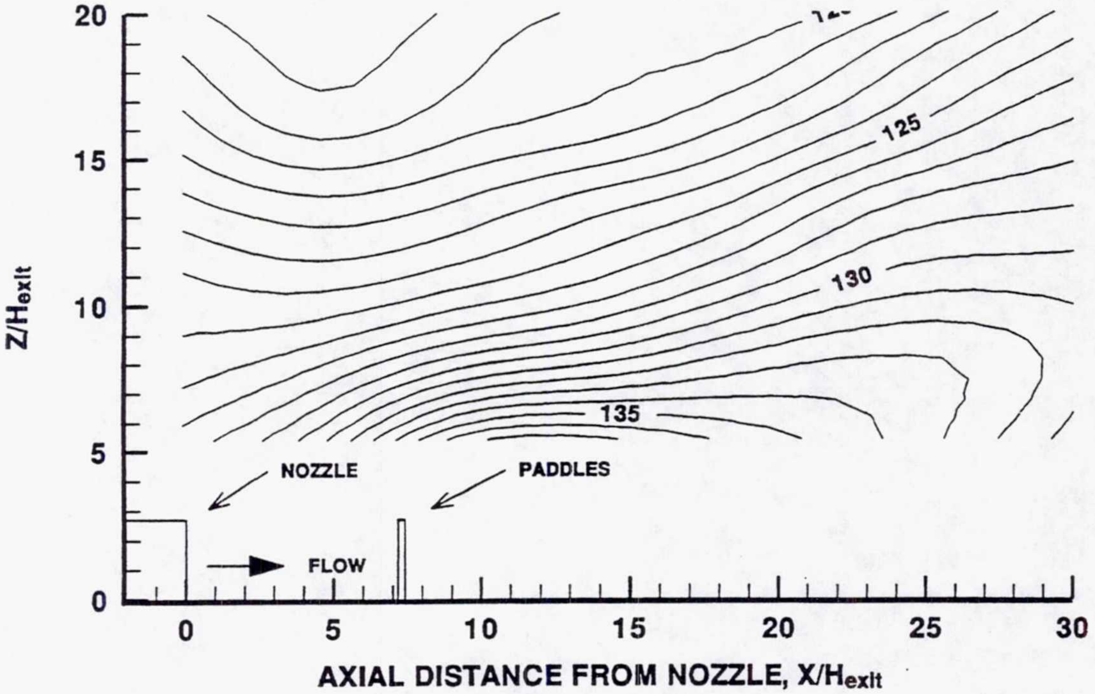

This is similar to the previous figure except that paddles are included to induce screech. The screech frequency is about double the broadband mixing noise frequency shown by the constant noise contours in this figure. Notice that the hydrodynamic field peaks out at a normalized axial distance of about twelve (nineteen without paddles). The noise radiation field, as seen by the lobe shaped contours, can be seen evolving from the region just downstream from the hydrodynamic field peak. The paddles are thus seen to move the mixing process and the noise radiation evolution up closer to the nozzle exit.

CONCLUDING REMARKS

- THE MIXING OF AN UNDEREXPANDED JET FROM A RECTANGULAR NOZZLE WAS EXTREMELY SENSITIVE TO THE SCREECH TONE AMPLITUDE
- FOR A CONVERGING-DIVERGING NOZZLE OPERATED AT DESIGN PRESSURE
  - THE MIXING WAS FAIRLY INSENSITIVE TO SCREECH TONE AMPLITUDE
  - THE MIXING WAS COMPARABLE TO THAT OF AN UNDEREXPANDED JET AT MUCH HIGHER SCREECH TONE EXCITATION AMPLITUDE
- PADDLES CAN BE USED IN THE JET SHEAR LAYERS
  - A HIGH AMPLITUDE SCREECH TONE CAN BE INDUCED
  - THE JET MIXING CAN BE DRAMATICALLY INCREASED
  - DRAG LOSSES MUST BE DOCUMENTED TO ALLOW TRADE-OFF STUDIES
- THE PADDLES MAY HAVE A BENEFICIAL EFFECT ON THE MIXING NOISE-ACOUSTIC TREATMENT INTERACTION (PRELIMINARY)

1999176 547

MIXING ENHANCEMENT IN SUPERSONIC JETS BY DELTA-TABS

K.B.M.Q. Zaman
NASA Lewis Research Center
Cleveland, Ohio

510-07

409528
20P.

BACKGROUND

Collaborators: Prof. Mo Samimy and Mark Reeder
Ohio State University, Columbus, OH

Previous Work: K. K. Ahuja (NASA CR)
H. K. Tanna (JSV '77)
Bradbury & Khadem (JFM '75)

The investigation was initiated during the summer of 1990 when Prof. Mo Samimy from OSU came to visit as a Summer faculty fellow. He was accompanied by graduate student Mark Reeder. Mark came back as summer student during the following two summers to work with Zaman on the project.

Notable previous works on the subject are:

1. K. K. Ahuja and W. H. Brown, "Shear Flow Control by Mechanical Tabs," AIAA Paper 89-0994, 1989.

2. H.K. Tanna, "An Experimental Study of Jet Noise, Part II: Shock Associated Noise", J. Sound & Vibration, Vol. 50, 429-444, 1977.

3. L.J.S. Bradbury and A. H. Khadem, "The Distortion of a Jet by Tabs", J. Fluid Mechanics, Vol. 70, 801-813, 1975.

OBJECTIVES

Objectives: Study Mechanism of Effect on *Free Jets*

- Compressibility Effect
- Tab geometry Effect

(⇨ Delta-tab)

- Quantify Mixing Enhancement
- Streamwise Vorticity generation Mechanism

Publications:

- AIAA Paper No. 91-2263
- Proc. 8th Turb. Shear Flow Symp., '91
- AIAA Paper No. 92-3548

Carry out fundamental experiments studying mechanisms of effect: (1) experiments on subsonic and supersonic jets to assess influence of compressibility, (2) parametric study on tab geometry to optimize effect for given flow blockage (this effort led to 'delta-tab'), (3) quantify mixing enhancement in the jet, (4) analyze mechanisms of streamwise vorticity generation.

Prior publications on the investigation:

1. Samimy, M., Zaman, K.B.M.Q., and Reeder, M.F., "Supersonic Jet Mixing Enhancement by Vortex Generators", AIAA Paper No. 91-2263, 1991.

2. Zaman, K.B.M.Q., Samimy, M., and Reeder, M.F., "Effect of Tabs on the Evolution of an Axisymmetric Jet", Proc. 8th Turbine. Shear Flow Conference., Univ. of Munich, F. R. Germany, 1991.

3. Zaman, K.B.M.Q., Reeder, M.F., and Samimy, M., "Supersonic Jet Mixing Enhancement by 'Delta-Tabs'", AIAA Paper No. 92-3548, 1992.

FACILITY

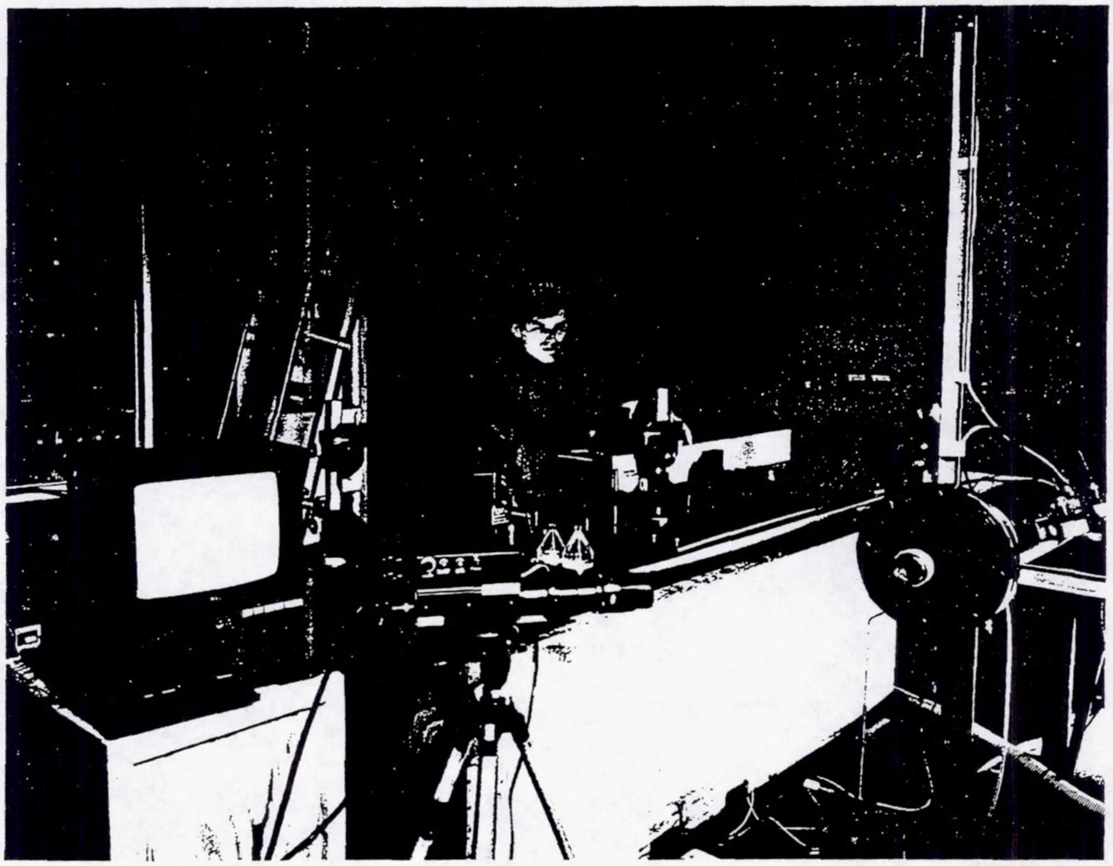

Shows overall experimental set up. Plenum chamber supplied with compressed air with maximum pressure of 70 psig. Jet discharges into the ambient. Flow visualization pictures recorded on Super-VHS recorder via image intensified CCD camera. 4-Watt Argon ion laser was light source. One-quarter inch microphone used to record far field noise spectra.

Schematic of Jet Nozzle

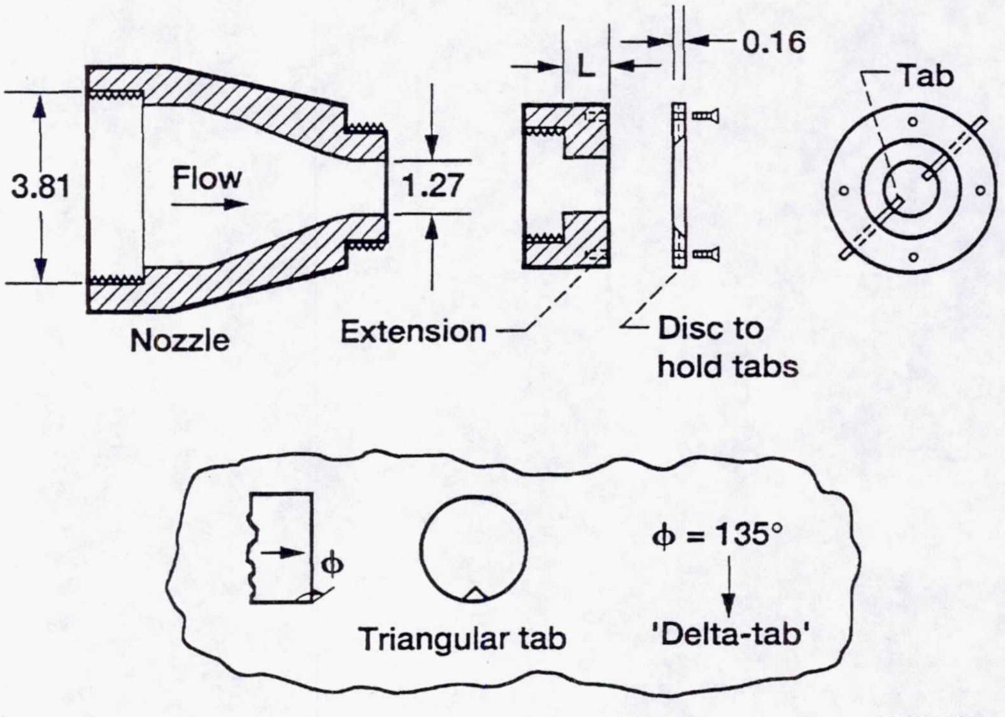

CD-92-59689

Schematic of 0.5 inch diameter, axisymmetric, convergent nozzle. Geometry of delta-tab shown in inset. Flow blockage due to each delta-tabs was between 1.5% to 2% of nozzle exit area.

FLOW VISUALIZATION

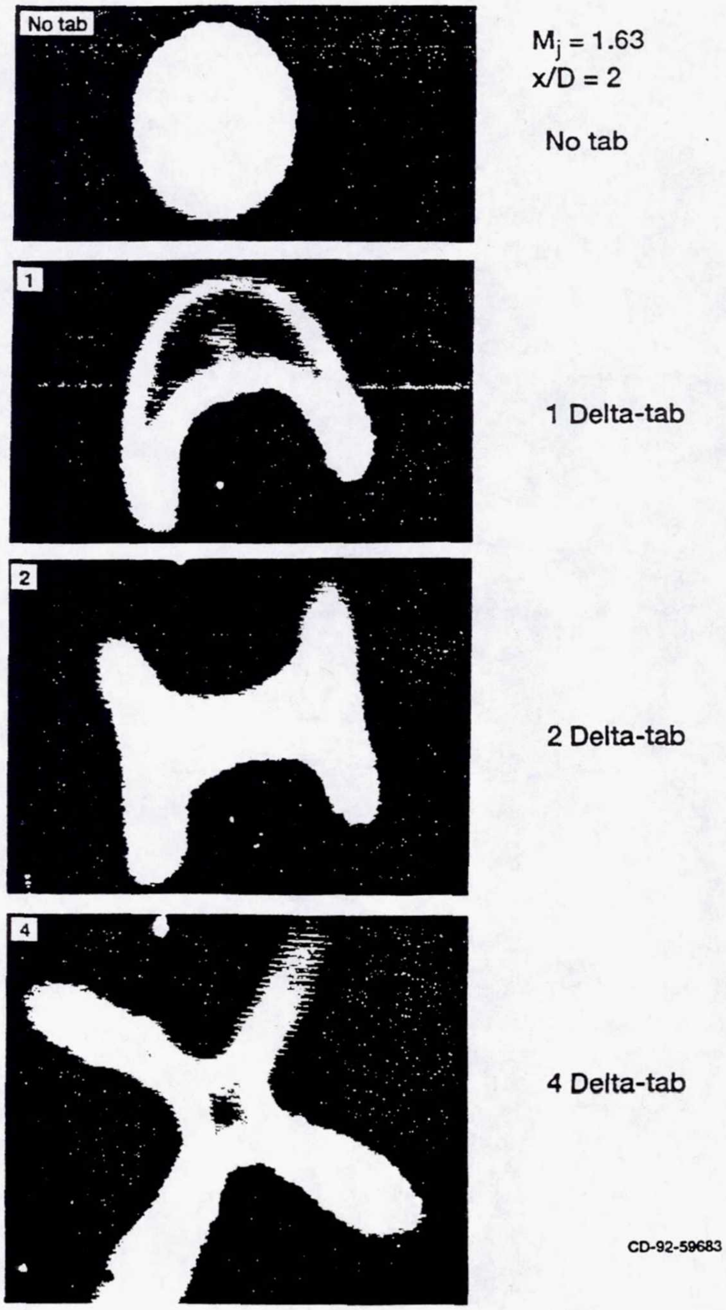

Effects of 1,2 and 4 delta-tabs on jet cross section at $x/D = 2$ compared to the no-tab case. Cold supersonic core of the jet caused moisture condensation from entrained air in the mixing layer. Thus, Laser sheet illuminated the mixing layer.

FLOW VISUALIZATION

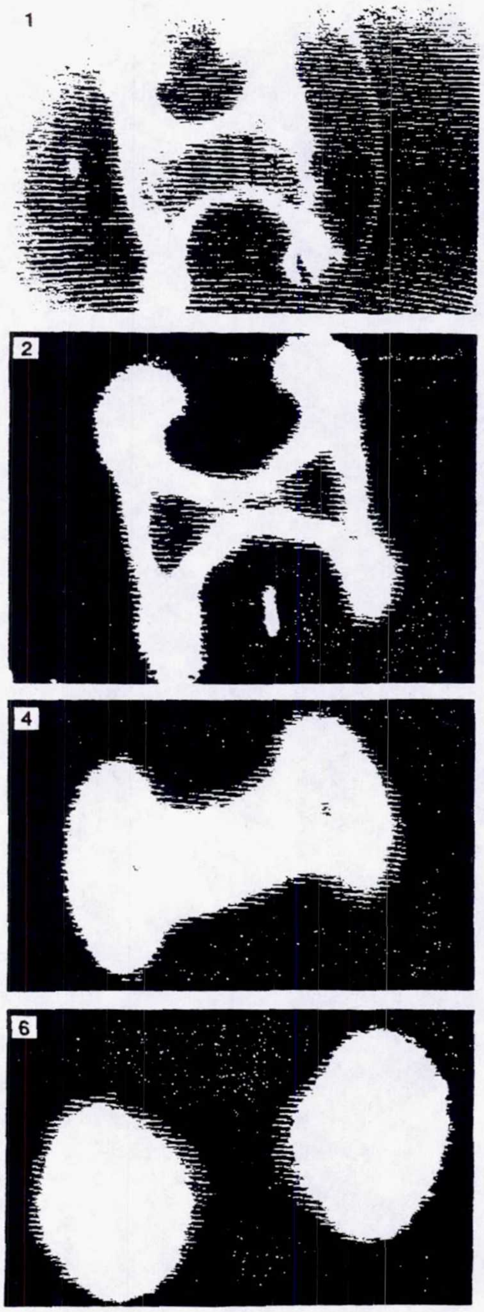

Effect of 2 delta-tabs at indicated streamwise locations. Jet is completely bifurcated by x/D = 6.

FLOW VISUALIZATION

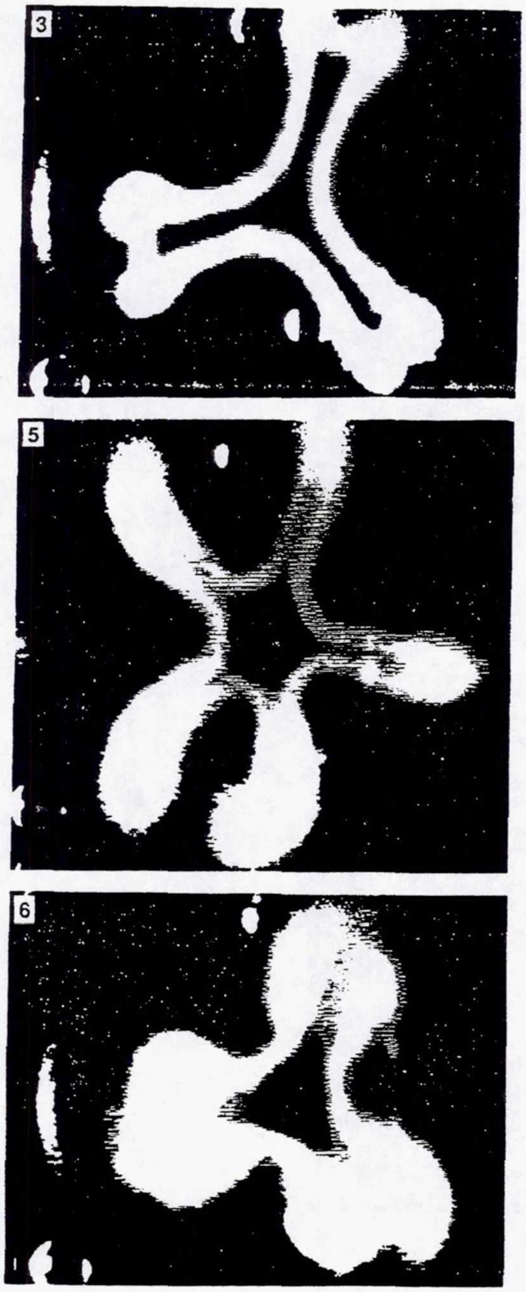

$M_j = 1.63$
$x/D = 2$

3 Delta-tab

5 Delta-tab

6 Delta-tab

CD-92-59682

Effects of 3, 5 and 6 delta-tabs on jet cross section at x/D = 2. Jet cross section settles back to 'three-finger configuration', in the 6 delta-tab case, through interaction of streamwise vortices.

FLOW VISUALIZATION

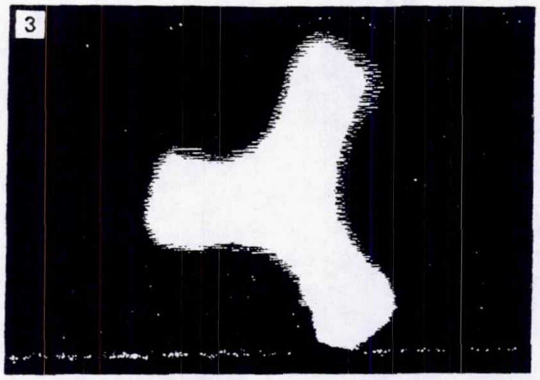

$M_j = 0.3$
$x/D = 2$

3 Delta-tab

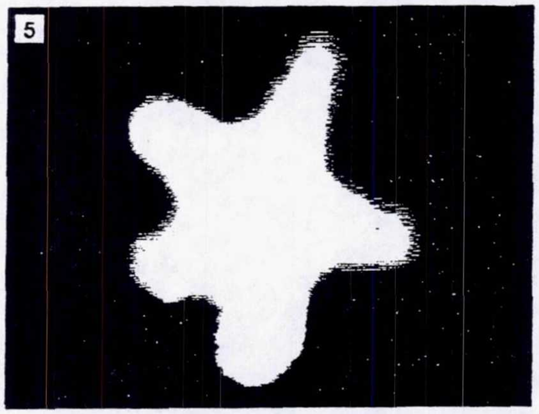

5 Delta-tab

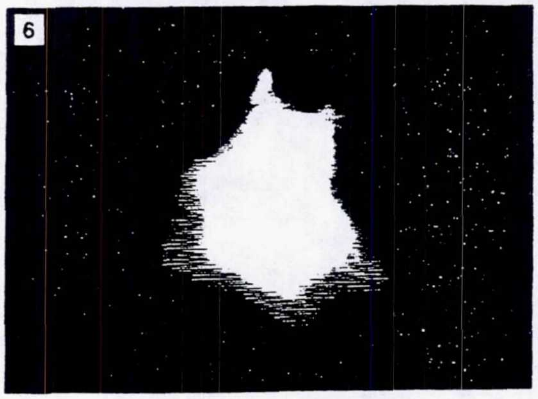

6 Delta-tab

CD-92-59688

Exactly same tab geometries as in viewgraph #8. Effect on a subsonic jet. Pictures here are obtained by seeding the core of the jet with smoke. Effect is similar at subsonic and supersonic conditions.

SCHEMATIC OF VORTICES

LIKELY VORTICITY DYNAMICS

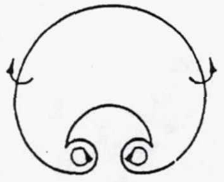

Vorticity distribution for 1-tab

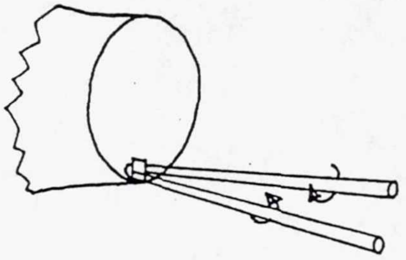

Streamwise vortex pair from a tab

Pair of streamwise vortices from a tab as conjectured early on in the investigation.

FLOW VISUALIZATION

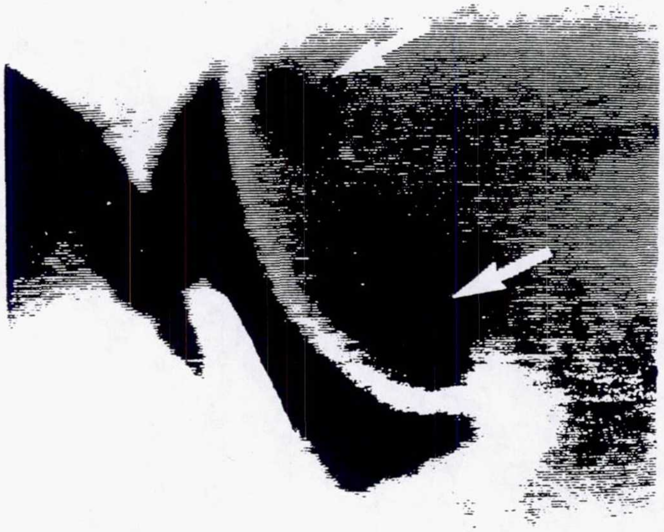

$M_j = 1.63$
$x/D = 2$
Delta-tab

CD-92-59684

Locations of the cores of streamwise vortex pair originating from a delta-tab. View is from upstream, and ambient was seeded with smoke.

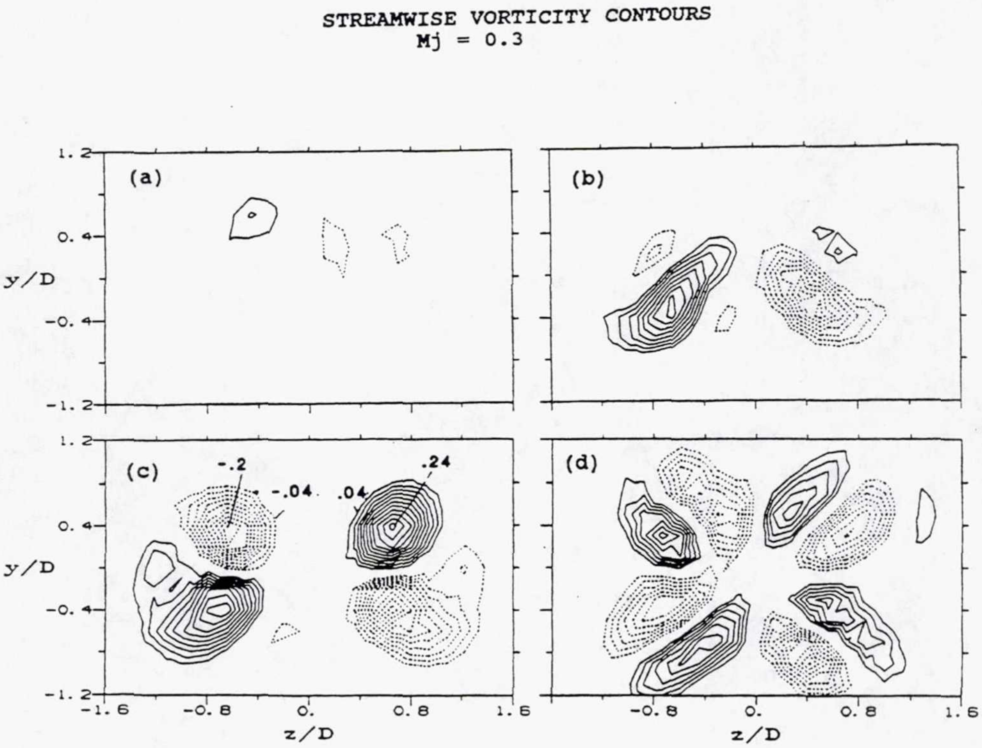

Contours of $\omega_x c/U_\infty$ measured at x/D = 3, for Mj = 0.3. (a) no-tab, (b) 1 delta-tab, (c) 2 delta-tabs, (d) 4 delta-tabs.

FAR-FIELD SOUND SPECTRA

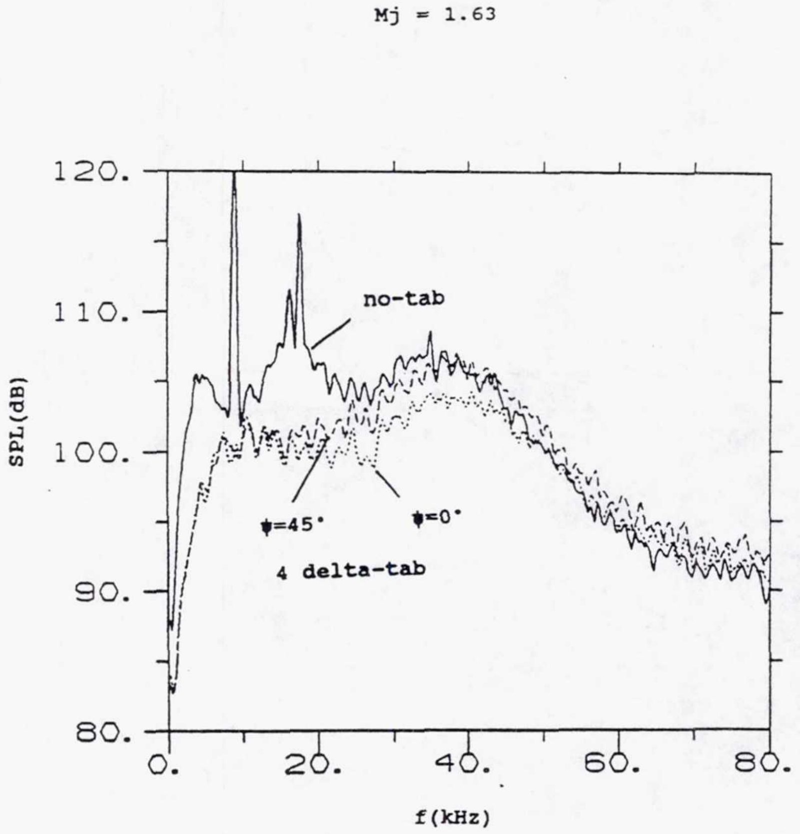

Effect of 4 delta-tabs, at two azimuthal angles relative to a delta-tab, compared with the no-tab case. Measurements are for r/D = 70 at the nozzle exit plane.

THRUST MEASUREMENT

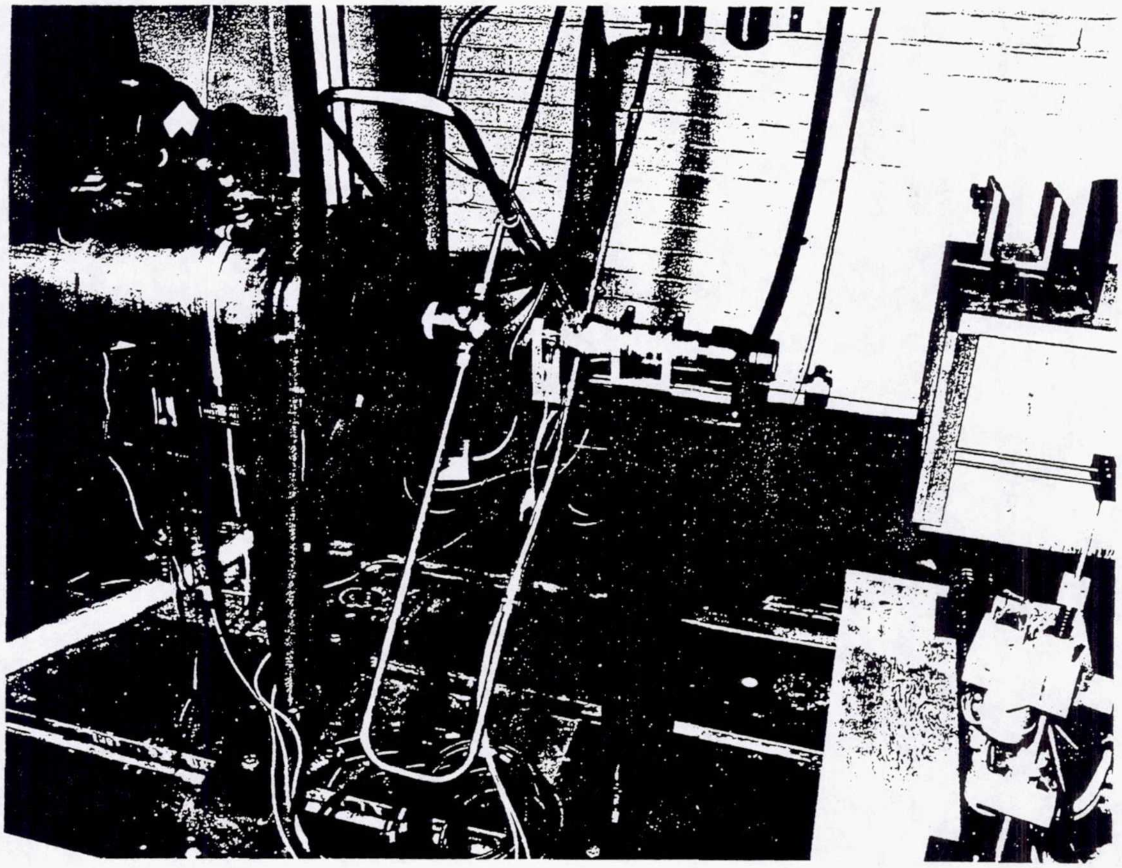

Experimental set up for thrust measurement.

THRUST DATA

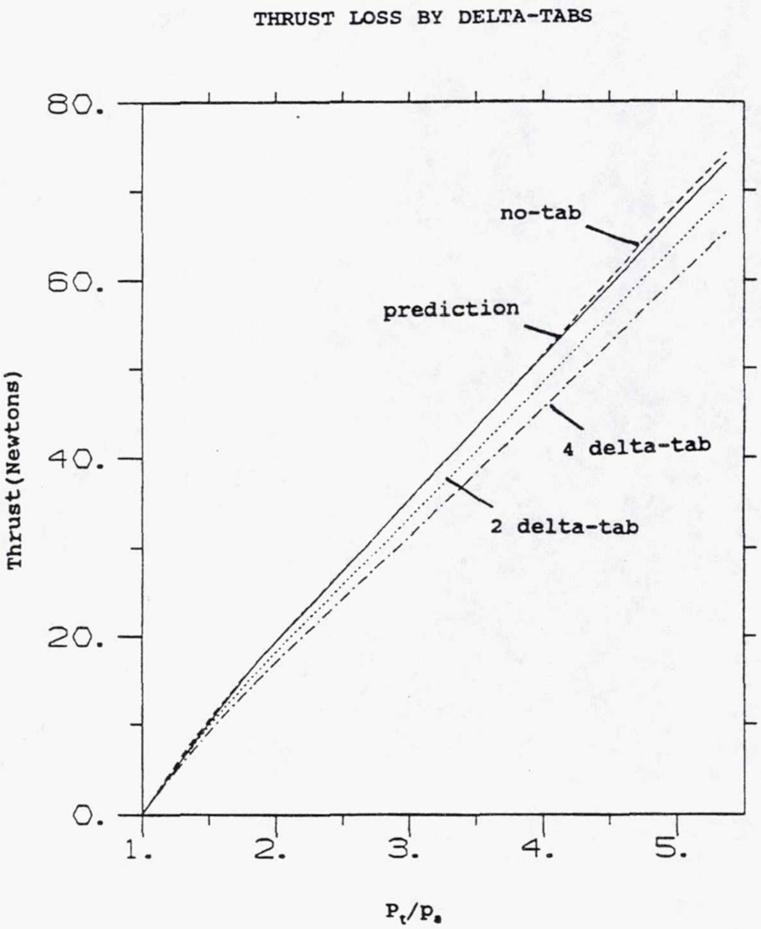

Thrust vs. nozzle pressure ratio for the effect of different numbers of delta-tabs. Prediction is with assumption of isentropic, plug flow. Gross thrust loss is approximately 3 percent per delta-tab (not taking into account the thrust loss due to the mere blockage.)

Jet Mixing Efficiency

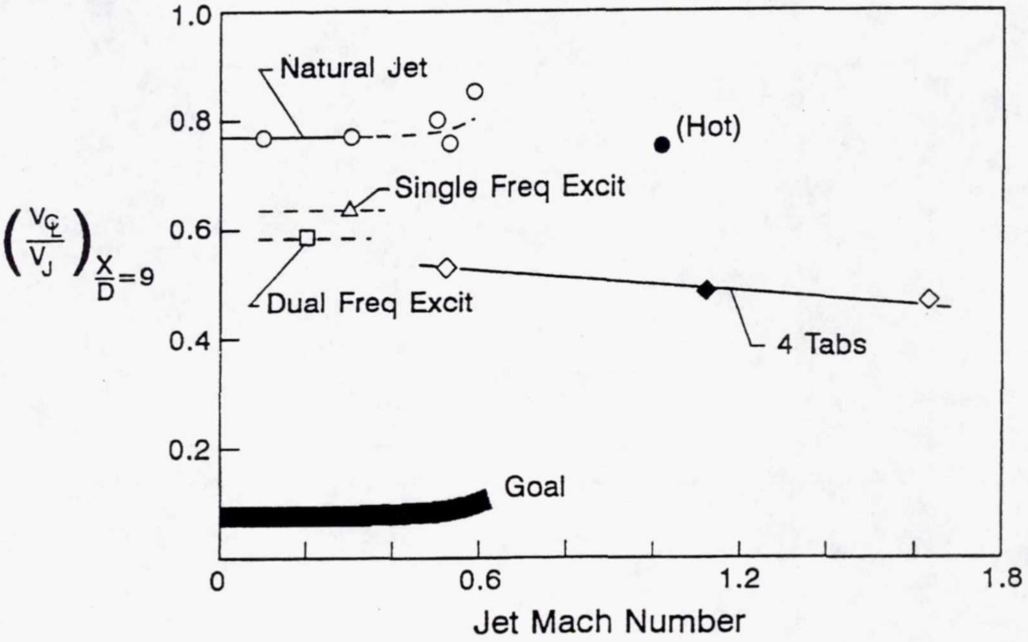

As indicated qualitatively by centerline velocity measured at 9D from nozzle exit (Lower value accompanied by faster spread.) Data for 'best case' single frequency acoustic excitation result, and dual frequency excitation result (inducing subharmonic resonance) are shown. 4 delta-tabs do better, and also work in supersonic regime (solid data point from Dr. Ahuja's experiment with hot jets and using simple tabs).

JET SPREADING

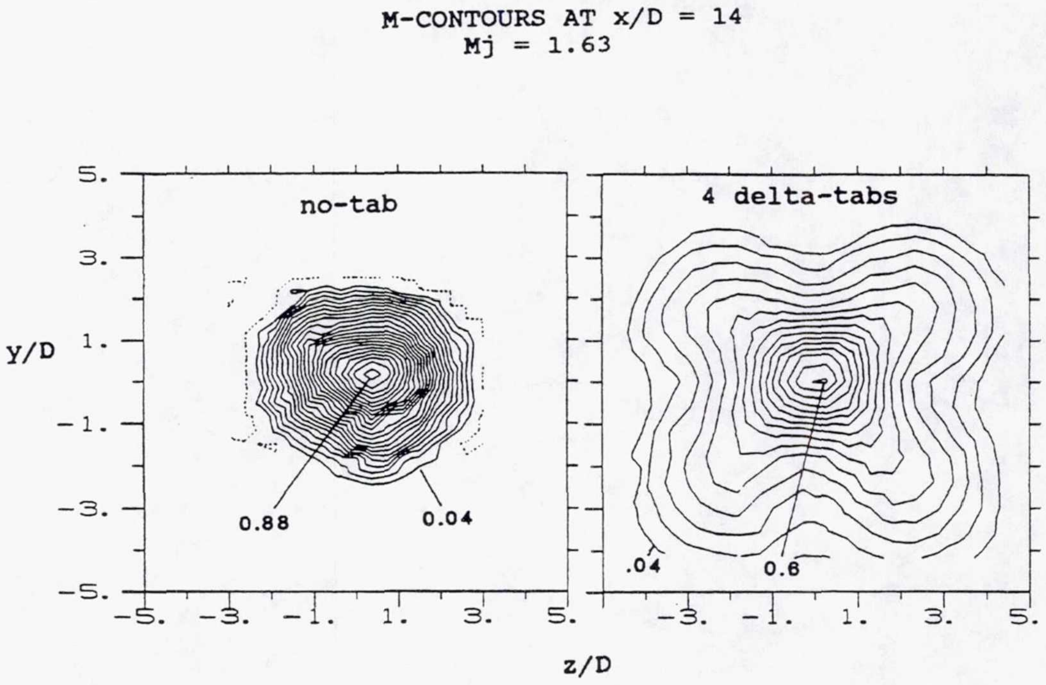

As indicated by Mach number contours, on a cross sectional plane at 14D from nozzle exit, measured with a Pitot tube. Four delta-tabs substantially increases jet spreading.

JET SPREADING

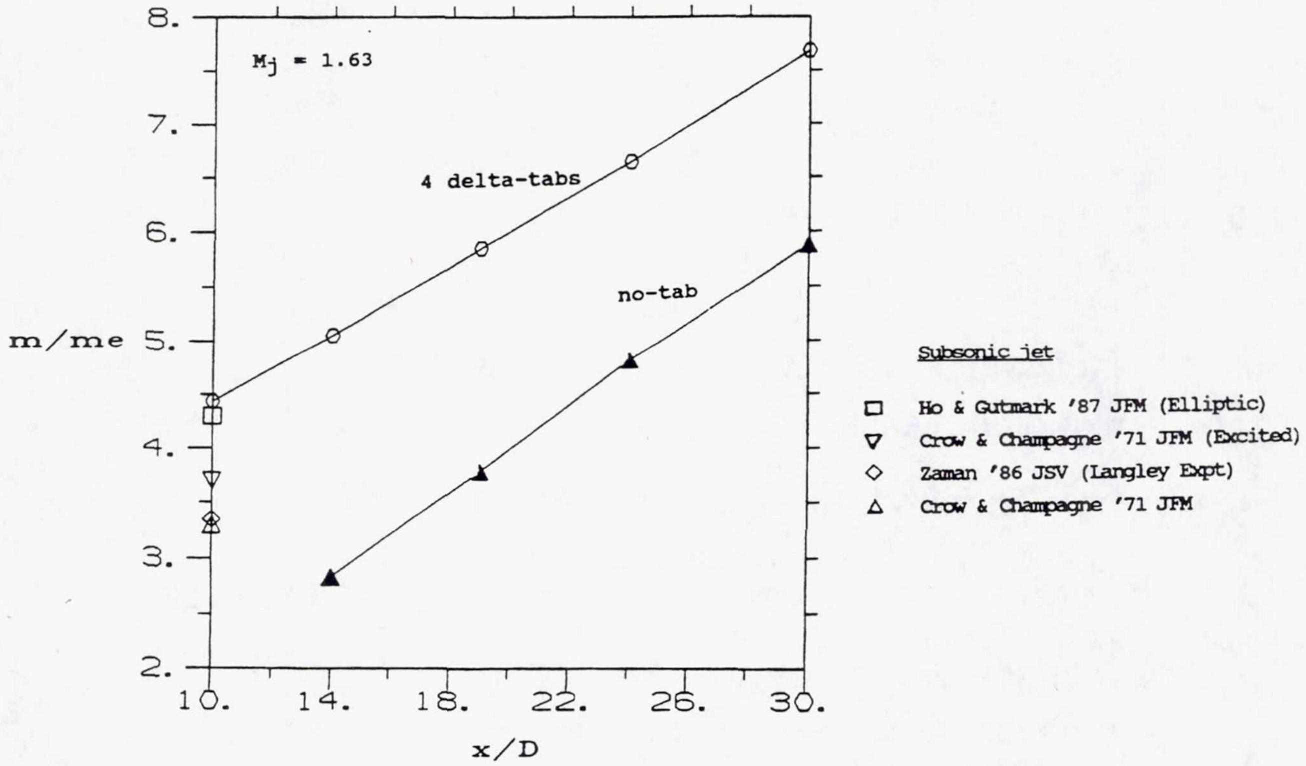

As indicated by mass flux, normalized by mass flux at nozzle exit, obtained by integrating data as in viewgraph #17. Effect of 4 delta-tabs compared with natural jet case. Four data points on left margin are from indicated References for subsonic jets. For the noncircular jet case, 'D' represents equivalent diameter (hydraulic diameter was used in the reference)

In calculating m_e (mass flux at the nozzle exit), the area change due the blockage by the tabs has been taken into account. This was not done for similar data shown in the references cited in connection with viewgraph #3. Furthermore, the data shown in those references were only estimates which were obtained by measuring four diametral profiles. The data in viewgraph #18 should be more accurate.

SUMMARY

- JET CROSS SECTION ALTERED ALMOST ARBITRARILY
  - MIXING INCREASED SIGNIFICANTLY
- EACH TAB PRODUCES PAIR OF STREAMWISE VORTICES
  - EFFECT WITH DELTA-TAB ACCENTUATED
  - VORTEX PAIR OF OPPOSITE SIGN COULD BE PRODUCED
- EFFECT INDEPENDENT OF COMPRESSIBILITY
  - TABS DO NOT WORK IN OVEREXPANDED CONDITION
- EFFECT INDEPENDENT OF INITIAL BOUNDARY LAYER STATE
  - WORKS IN JET WITH HIGH CORE TURBULENCE
- APPROXIMATELY 3% THRUST LOSS PER DELTA-TAB

CURRENT AND FUTURE ACTIVITY

- MIXING WITH DIFFERENT NOZZLE GEOMETRIES WITH/WITHOUT DELTA TABS
    - -RECTANGULAR, 3:1 ELLIPTIC, 6-LOBED MIXER
- FUNDAMENTAL EXPERIMENTS
    - -VORTICITY EVOLUTION 2, 6 DELTA-TAB CASES
- ANALYSIS
    - -STREAMWISE VORTICITY GENERATION MECHANISMS
        - --WHY DELTA TAB WORKS BETTER
        - --AXISYMMETRIC VS. PLANE GEOMETRY
    - -ISSUE OF AREA CHANGE VS. VORTEX BREAKDOWN CAUSING MIXING ENHANCEMENT
- MARK REEDER & MO SAMIMY AT OSU
    - -WATER TUNNEL MEASUREMENT
        - --ADDRESS UNSTEADY ASPECTS
    - -RALEIGH-SCATTERING BASED MEASUREMENT FOR SUPERSONIC JETS

1999176548

VIBRATING SPLITTER INSERT TO ENHANCE MIXING AND REDUCE SUPERSONIC JET NOISE

Krish K. Ahuja
Georgia Institute of Technology
Atlanta, Georgia

511-07

409529

26P.

INTRODUCTION

Coaxial Jet Rig

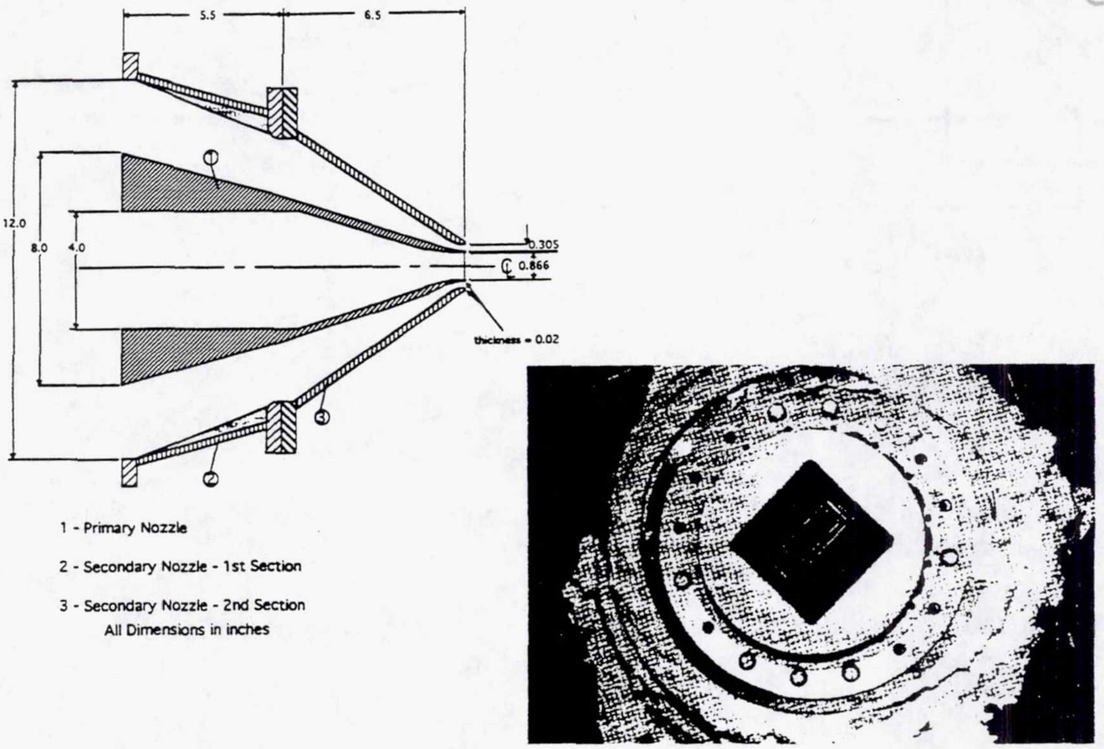

1 - Primary Nozzle
2 - Secondary Nozzle - 1st Section
3 - Secondary Nozzle - 2nd Section
All Dimensions in inches

A number of concepts of reducing supersonic jet noise have recently been tested using small-scale nozzles at Georgia Tech Research Institute by the author. One of them included a coaxial rectangular nozzle. Both nozzles had an equivalent diameter of 2 inches.

This configuration provides considerable reduction in noise and also some control on the noise directivity. (See DGLR/AIAA 92-02-127: "Supersonic Jet Noise Reduction by Coaxial Rectangular Nozzles," by K. K. Ahuja, J. Manes, and K. Massey.)

It is shown in this presentation, that the inner nozzle can be replaced by splitter plates (inserts) that provide even further noise reduction at supersonic conditions through enhanced mixing.

Terminology for the Measurement Angles

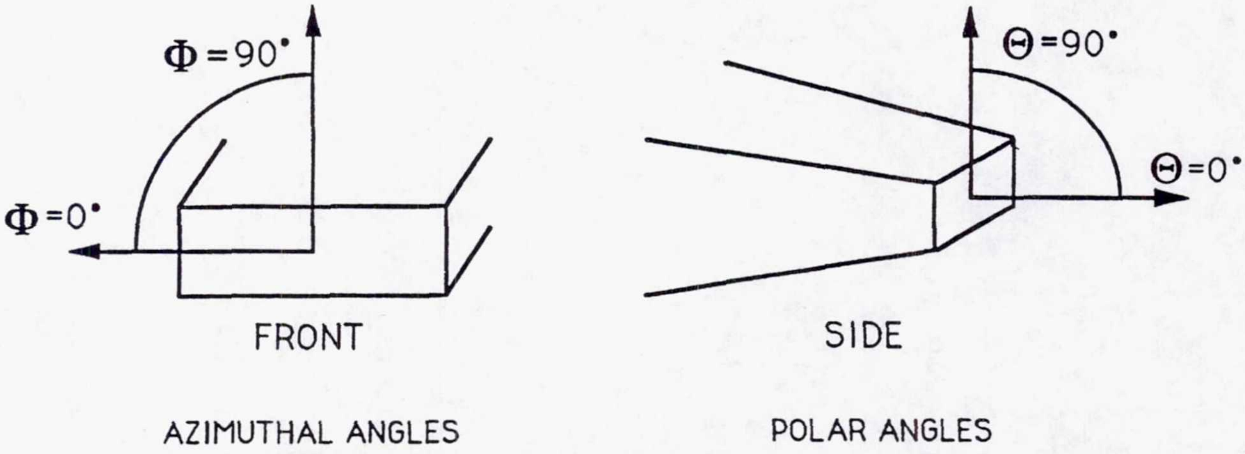

Data for two azimuthal angles (f) were obtained, namely, Φ 0° and 90°. The terminology is shown in this Figure.

For each azimuthal angle, far-field acoustic data were acquired at various polar angles, Θ, of 30° to 120° with respect to the jet axis.

Four Equivalent Operating Conditions with Different Noise Spectra

1. *Coaxial*
2. *Equivalent Round*
3. *Equivalent Rectangular*
4. *Coaxial*

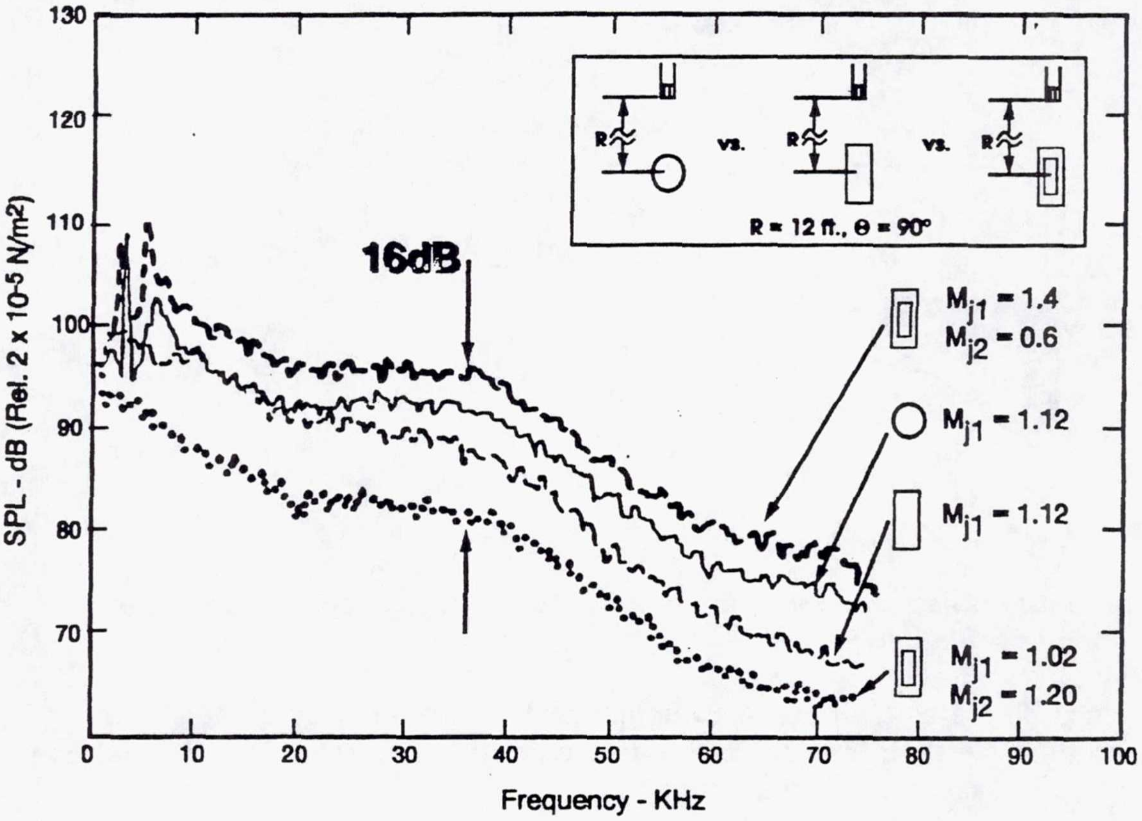

It was found that for the same thrust, mass flow rate and total exit area, different configurations can produce different noise levels as shown in this plot of narrowband SPL versus frequency at Φ 0°and $\Theta = 90°$.

Single Nozzle Coaxial Insert Configuration

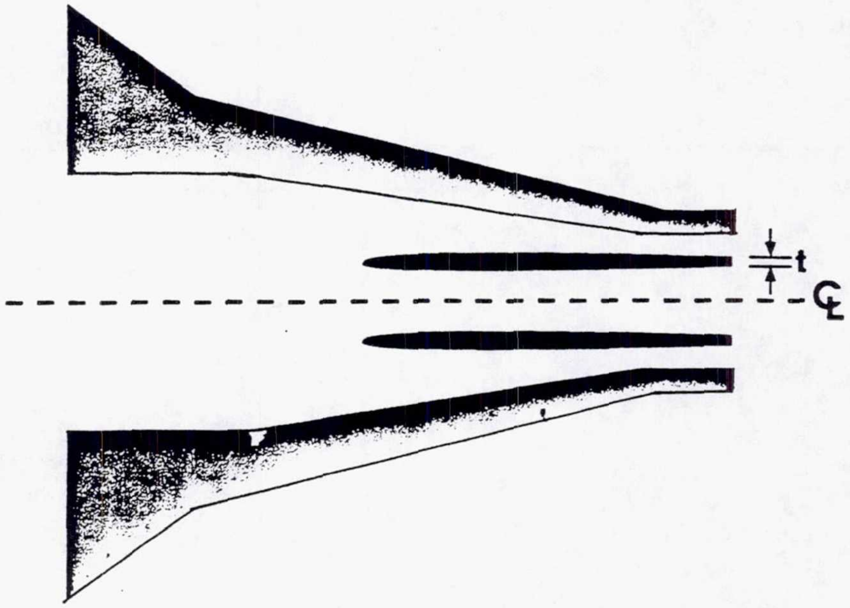

To obtain optimum noise reduction, the coaxial nozzles have to be operated at inverted velocity profile conditions.

Our goal was to find a single nozzle configuration that will provide comparable noise reductions. We therefore devised a nozzle configuration that has inner and outer lips but is in essence a single nozzle.

Our approach was to use a single rectangular nozzle and add an insert of different lip thicknesses to enhance mixing. This is shown schematically in this figure.

EFFECT OF INNER NOZZLE LIP THICKNESS

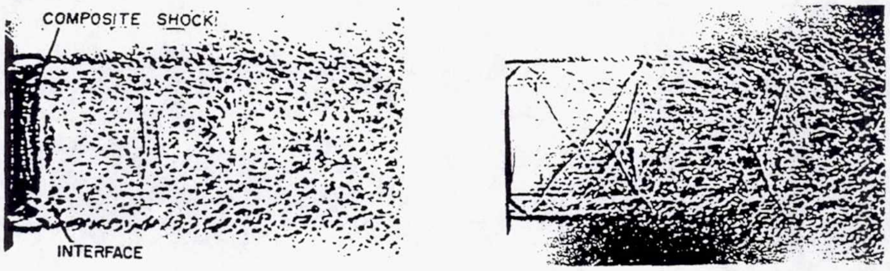

(a) P3 ARRANGEMENT ($t/r = 0.18$)

(b) P4 ARRANGEMENT ($t/r \doteq 0$)

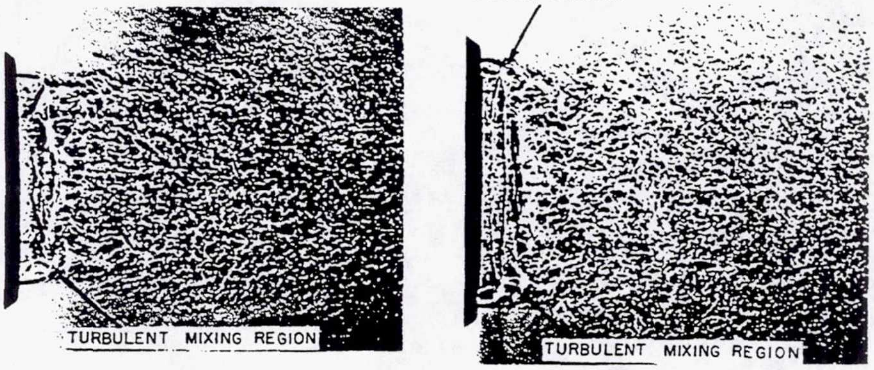

(c) P2 ARRANGEMENT ($t/r = 0.5$)

(d) P1 ARRANGEMENT ($t/r = 0.9$)

$\xi_1 = 2.22$, $\xi_2 = 3.04$ $P_{amb} = 14.5$ PSIA

TYPICAL SPARK SHADOWGRAPHS SHOWING SHOCK STRUCTURE AND FLOW FIELD OF INTERACTING COAXIAL SUPERSONIC JET FLOWS FROM COAXIAL TWO-NOZZLE CONFIGURATIONS WITH DIFFERENT LIP THICKNESSES.

We exploited the fact that the base of the inner nozzle plays significant role in the flow development of a coaxial nozzle. A typical example on the effect of lip thickness from Dosanjh, Ahuja, Bassiouni and Bhuticini (AIAA Paper #75-002, 1975) for round coaxial nozzles is presented in this figure. Here "t" is the thickness of the inner lip and "r" is the radius of the inner nozzle. Drastic changes in jet mixing are noticed as a function of lip thickness.

Large Scale Structure Behind a Blunt Trailing Edge

Nash, Quincey, and Callinan; Aeronautical Research Council; R&M No. 3427; 1966

$M_\infty = 0.925$

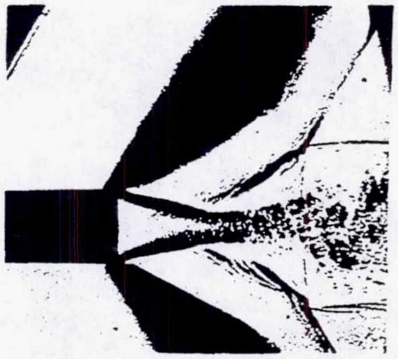

$M_\infty = 1.0$

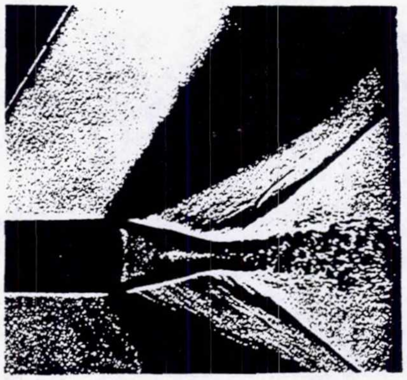

$M_\infty = 1.05$

We purposely used a blunt trailing edge. Well-defined large-scale flow oscillations are found in the wake of the base of splitter plates with blunt trailing edges. An example is given in this figure. (These large-scale structures could be used as the source of excitation of a jet.)

Jet Mixing Enhancement by Hydrodynamic Excitation

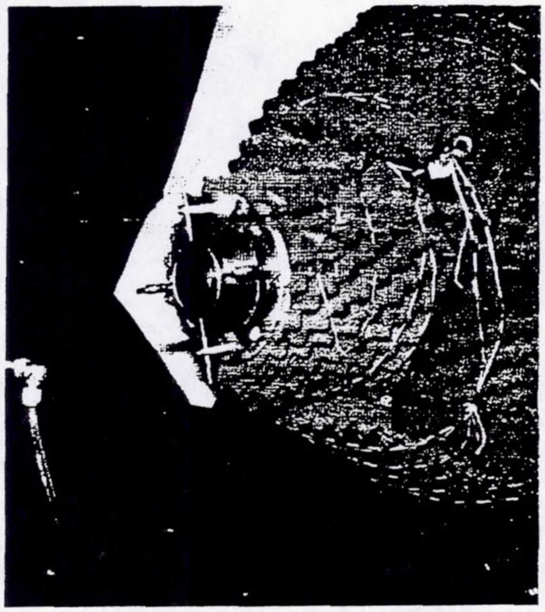

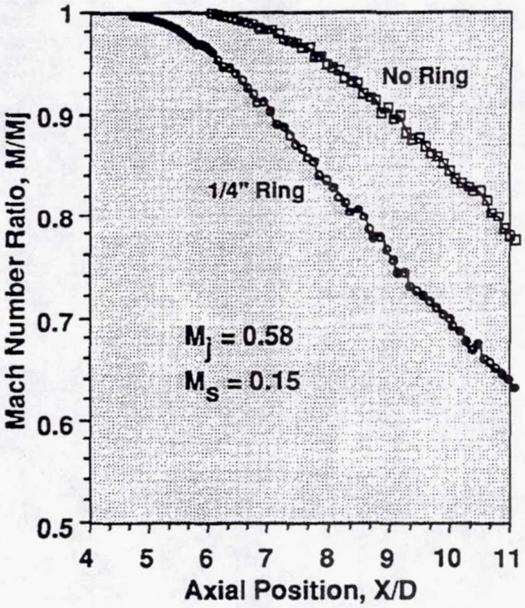

Brown and Ahuja (AIAA Paper 90-4005, 1990) have shown that hydrodynamic excitation with the right frequency and wavelength can excite a jet and enhance its mixing. In this example, the vortex-shedding frequency downstream of a ring was matched with the most preferred frequency of the inner round jet, which resulted in enhanced mixing as shown on the centerline, mean Mach number distribution.

Vortex Generated by Quick Change in the Inclination Angle of an Airfoil

Swirydczuk, J.:Experiments in Fluids; Vol. 9; No. 4; 1990)

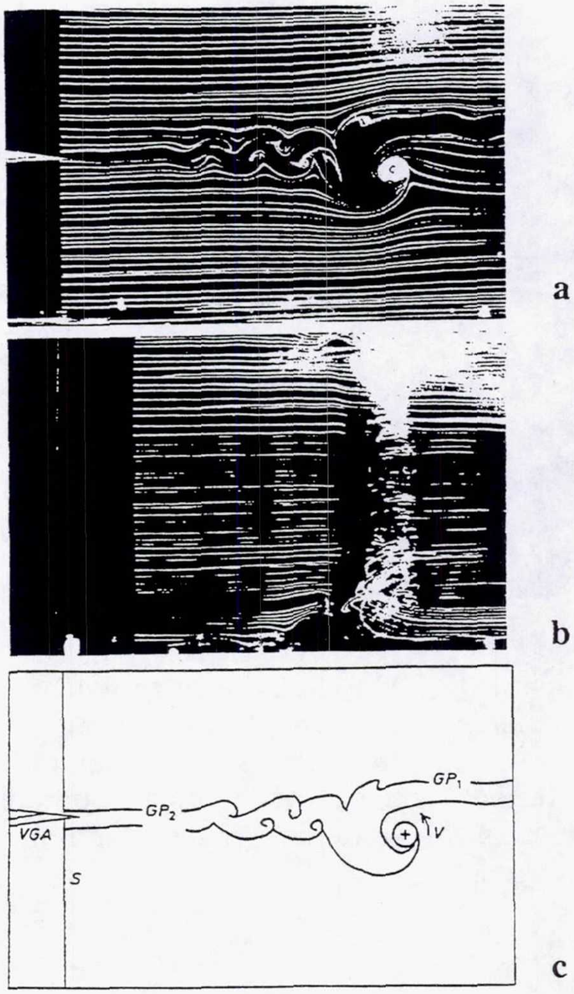

This figure from Swirydczuk shows that a vortex can be generated by a quick change in the inclination angle of an airfoil. In our case, the splitter plate would simulate a succession of quick changes in inclination if it were to vibrate. If the vibration frequency, the vortex shedding frequency, and the most preferred frequency of jet match, we should expect enhanced mixing.

Cross-section of Primary Nozzle Extension and Insert

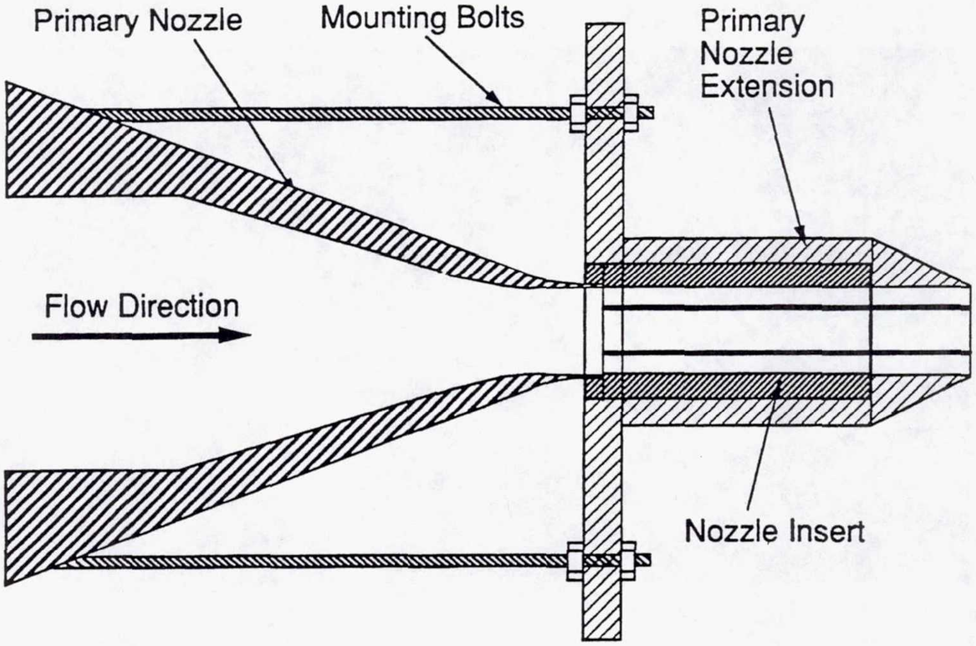

Thus our goal can now be better defined. It was to obtain noise reductions that are larger than those obtained by the coaxial rectangular nozzles by using a single nozzle through exploitation of the vortex shedding of the insert. In this process, make the most of any beneficial effects of the splitter vibration. Also the presence of base pressure, different from that of the ambient, which is a strong function of the base geometry would produce shocks/expansions downstream of the insert lips different from those from the outer lip of the nozzle. This may provide partial weakening of the shocks from the outer lip and thus further reduce noise.

The primary nozzle of the coaxial jet facility described earlier was extended for the present study in the manner shown in this figure.

Primary Nozzle Insert Arrangement

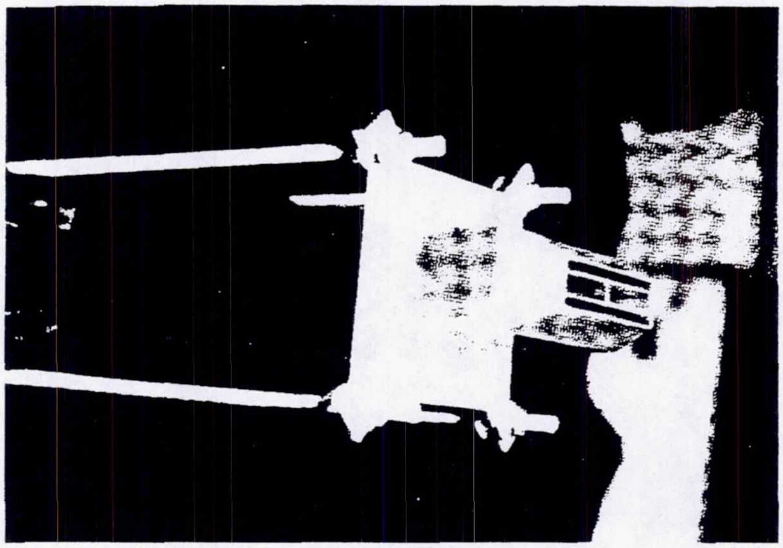

This figure shows the nozzle fitted with two parallel splitter plates.

Effect of Insert on Jet Mixing Enhancement and Shock Cell Modification

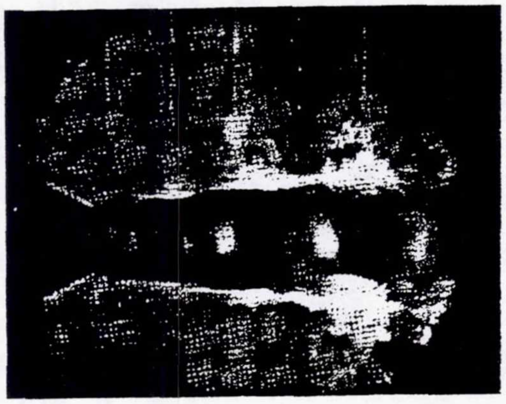

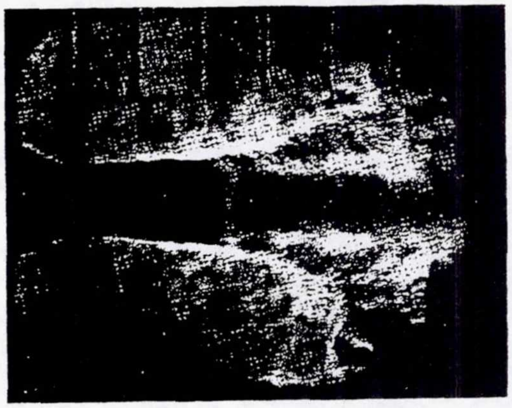

Extensive schlieren and smoke flow visualization studies were conducted. This figure shows typical results at M = 1.4. Whenever, there was a vibration of the splitter insert, drastic changes in the flow were obtained.

Here the photo on the left shows the jet shock structure with no insert. The figure on the right shows the flow with an insert that was vibrating. The plume is clearly much wider and the radial extent of the shocks has clearly reduced significantly indicating that the volume of the supersonic region has decreased significantly also.

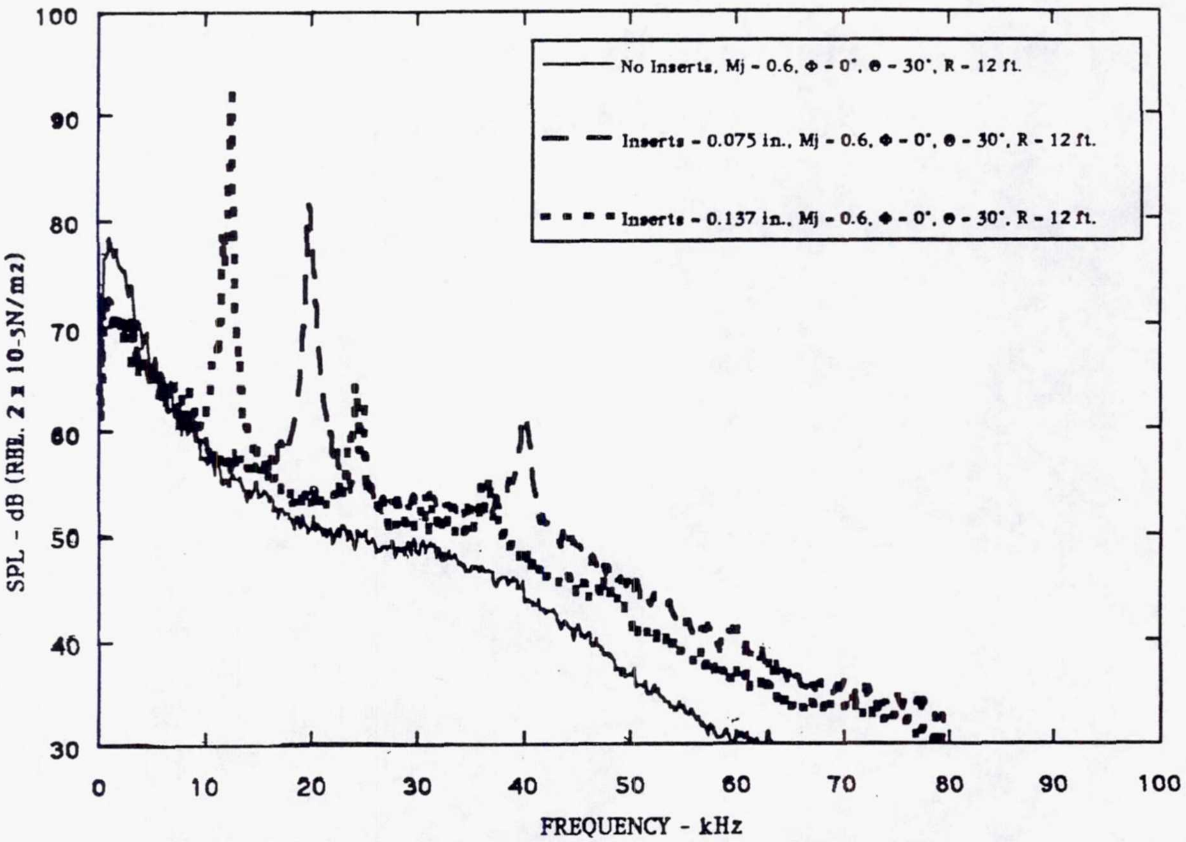

Narrow Band (Δf = 128Hz) Noise Spectra Comparison of Rectangular Nozzle, No Inserts vs. Inserts

Acoustic data were acquired for two insert thicknesses: 0.075 inches and 0.137 inches. It was found that the vortex shedding from the insert produced a high amplitude tone. At low mach numbers these tones were as much 30 dB higher than the background jet noise. This figure shows these tones for a jet mach number, Mj, of 0.6 for Φ 0° and Θ = 30°. The tone frequencies change as the thickness of the insert is changed. The low frequency jet noise is reduced and the high frequency noise increases.

NO INSERTS VS. INSERTS (SUPERSONIC MACH NUMBERS)
Mj = 1.3, Φ 0°, Θ = 30° to 120°

The next ten figures compare the far field noise spectra for the "no-insert" and the "with-insert" configuration. Unlike the subsonic operating conditions, the discrete tones from the insert vortex shedding are not that dominant for the supersonic conditions. Yet significant reductions in noise are obtained, more so at the lower frequencies. At Θ = 90° and in the forward arc, an increase in the high frequency noise is obtained. This is due to the enhanced mixing and thus increased turbulence. If the insert configuration is used in conjunction with a lined ejector, further enhancement in mixing can be realized while at the same time the high frequency noise can be absorbed by the ejector lining.

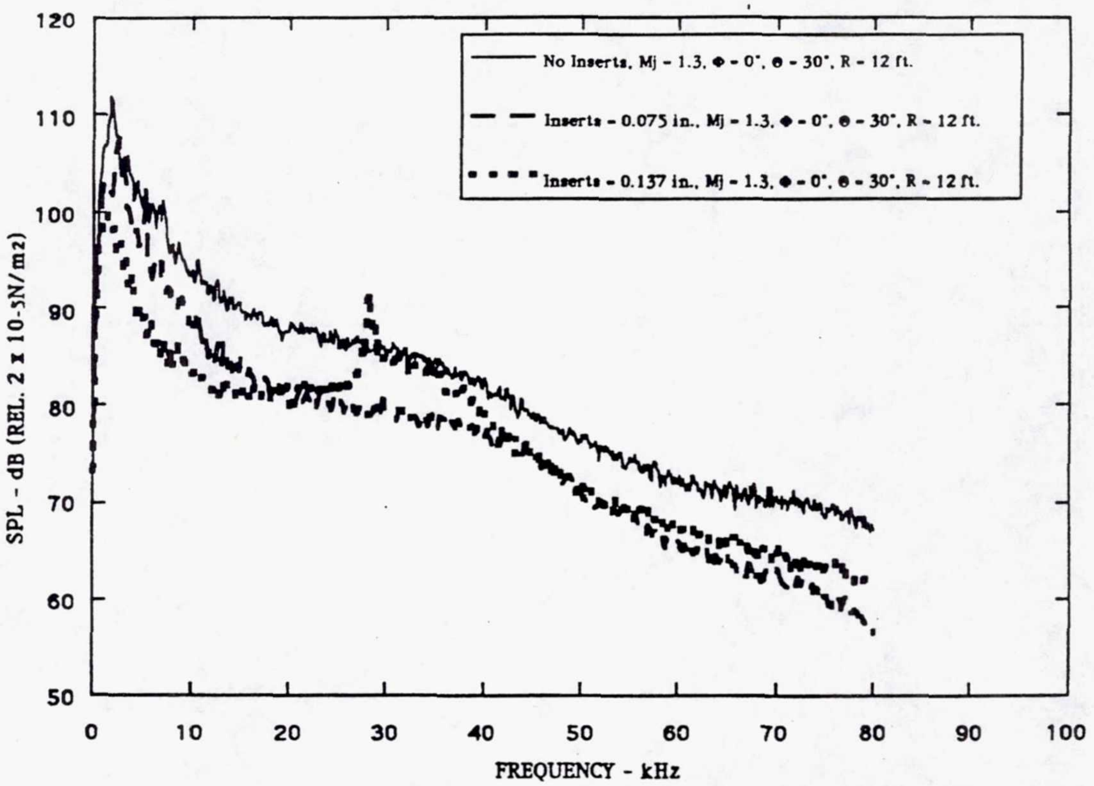

Narrow Band (Δf = 128Hz) Noise Spectra Comparison of Rectangular Nozzle, No Inserts vs. Inserts

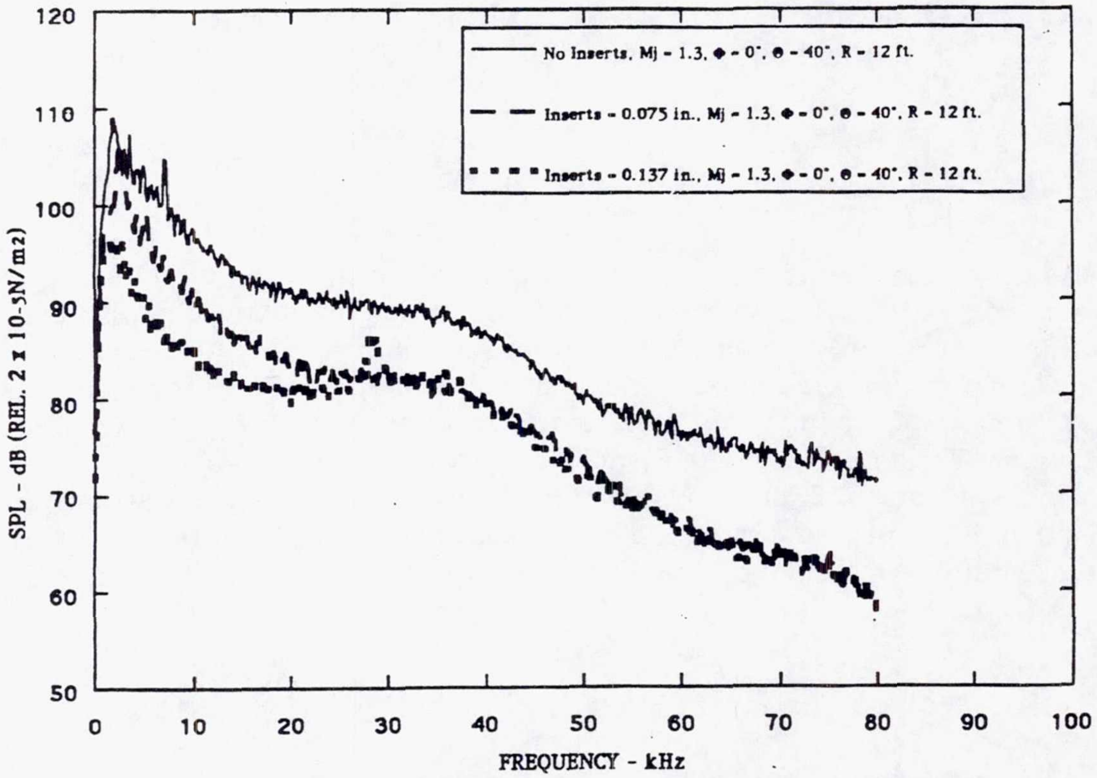

Narrow Band (Δf = 128Hz) Noise Spectra Comparison of Rectangular Nozzle, No Inserts vs. Inserts

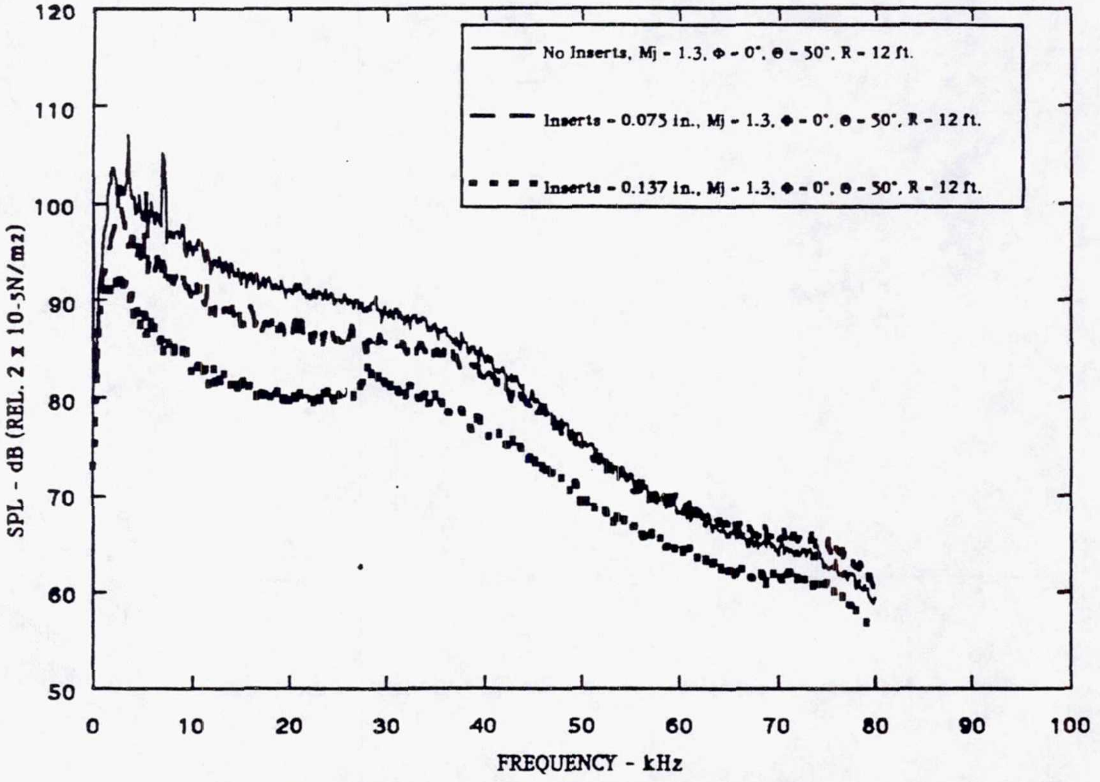

Narrow Band (Δf = 128Hz) Noise Spectra Comparison of Rectangular Nozzle, No Inserts vs. Inserts

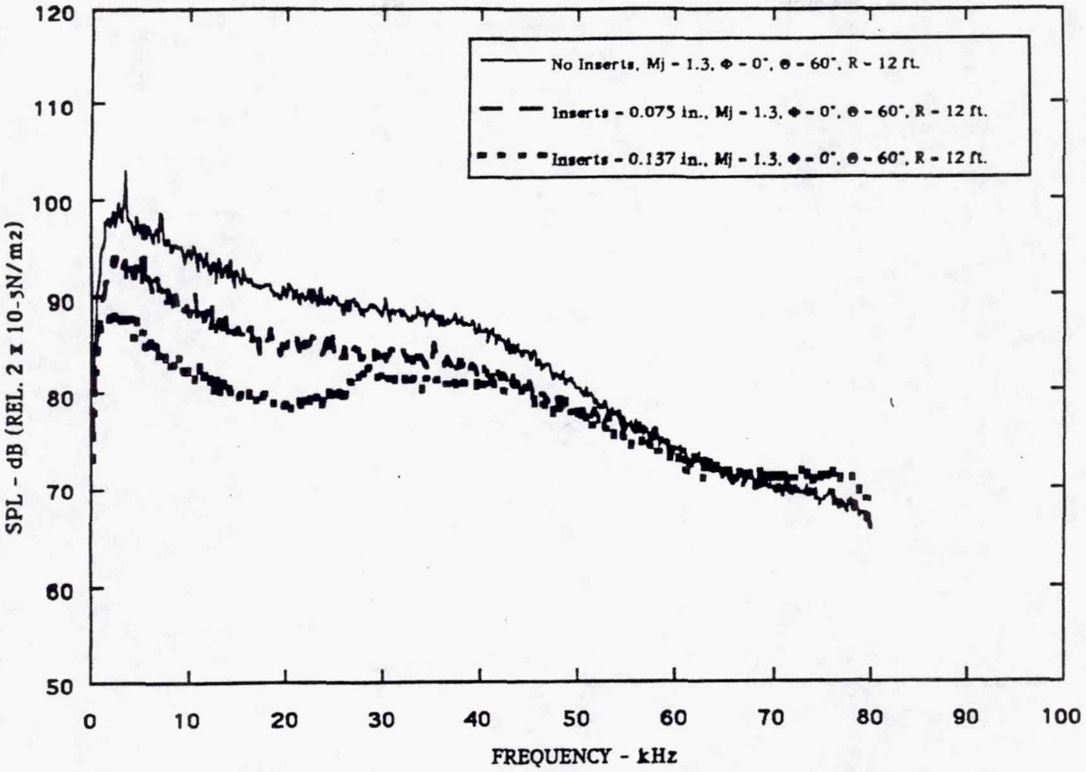

Narrow Band (Δf = 128Hz) Noise Spectra Comparison of Rectangular Nozzle, No Inserts vs. Inserts

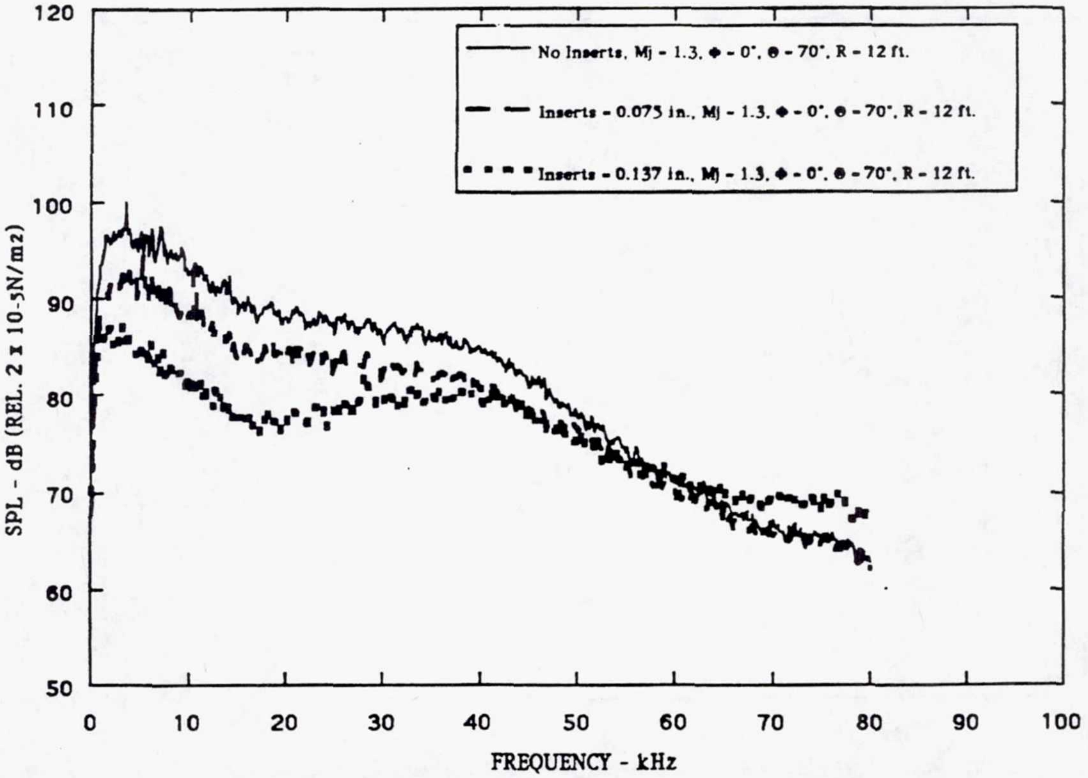

Narrow Band (Δf = 128Hz) Noise Spectra Comparison of Rectangular Nozzle, No Inserts vs. Inserts

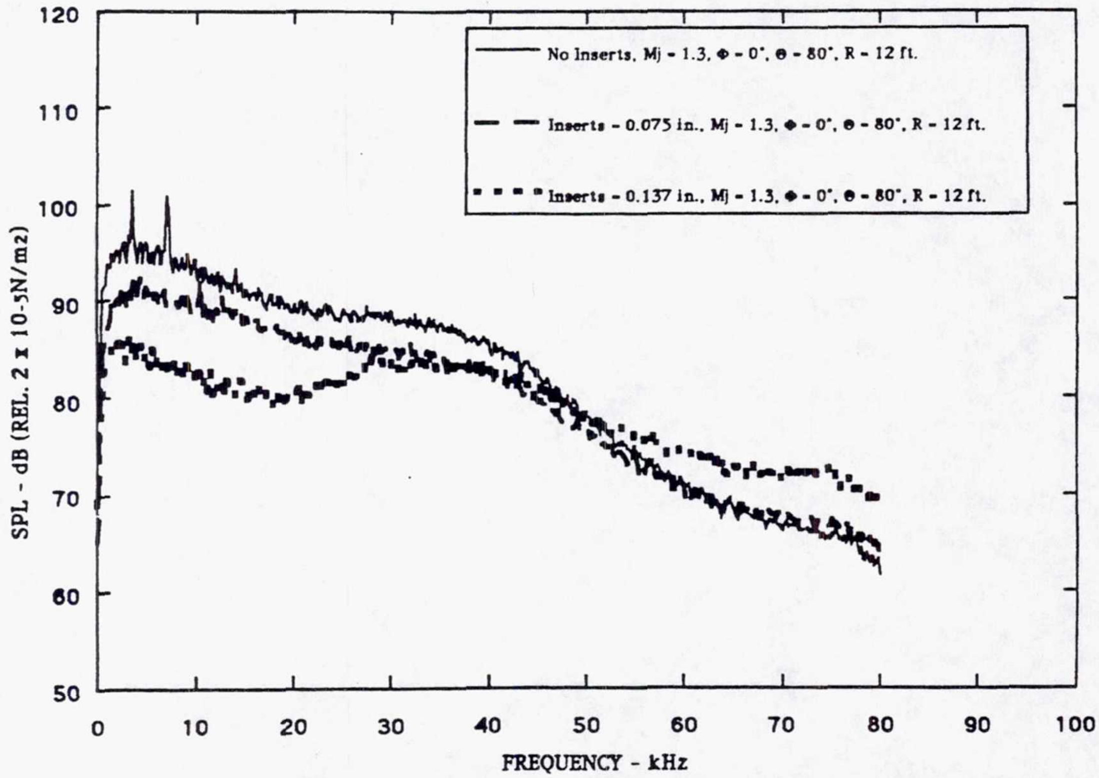

Narrow Band (Δf = 128Hz) Noise Spectra Comparison of Rectangular Nozzle, No Inserts vs. Inserts

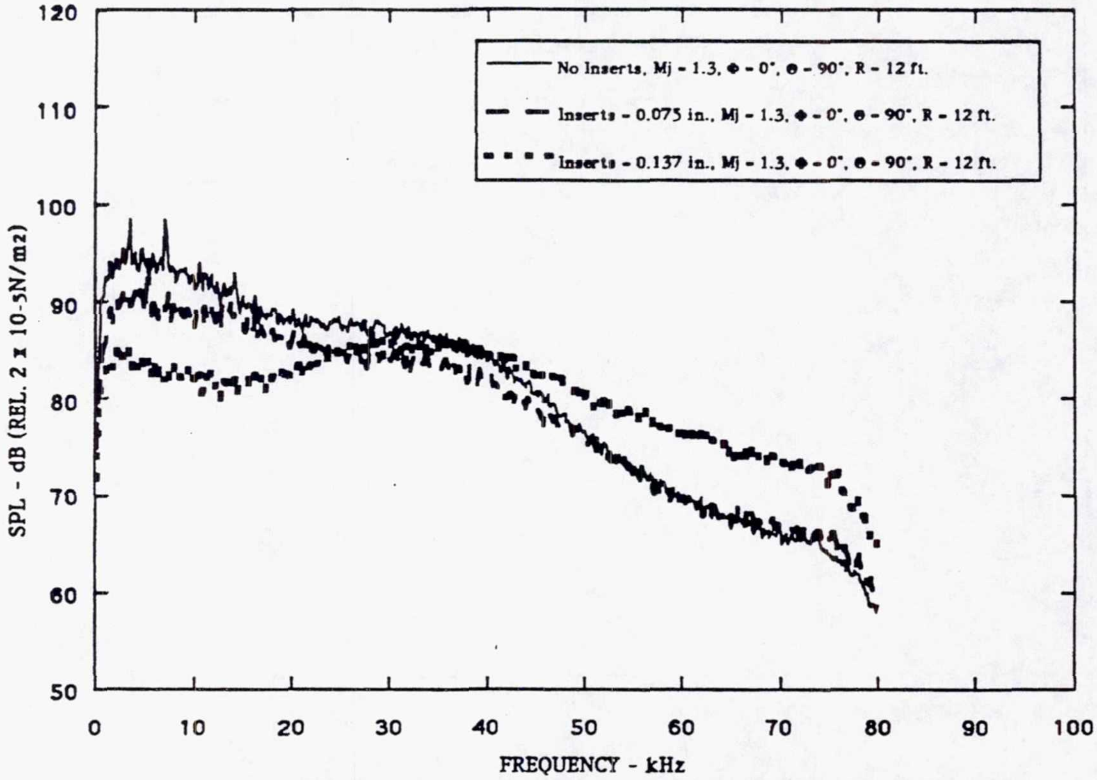

Narrow Band (Δf = 128Hz) Noise Spectra Comparison of Rectangular Nozzle, No Inserts vs. Inserts

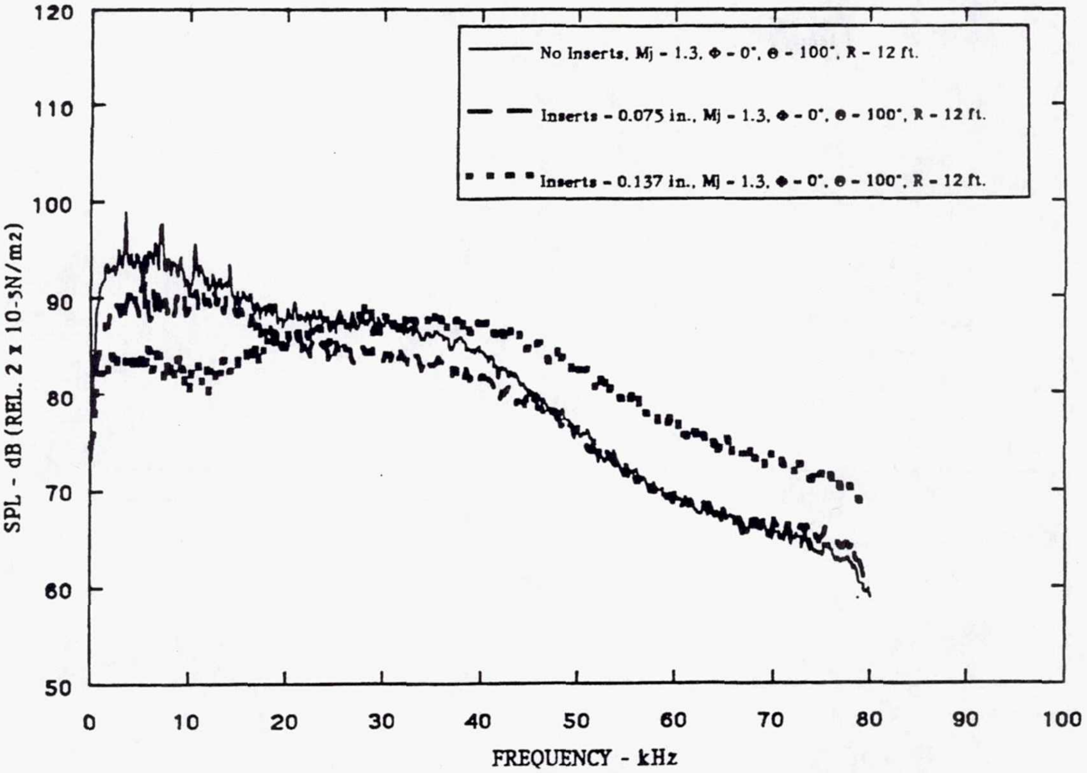

Narrow Band (Δf = 128Hz) Noise Spectra Comparison of Rectangular Nozzle, No Inserts vs. Inserts

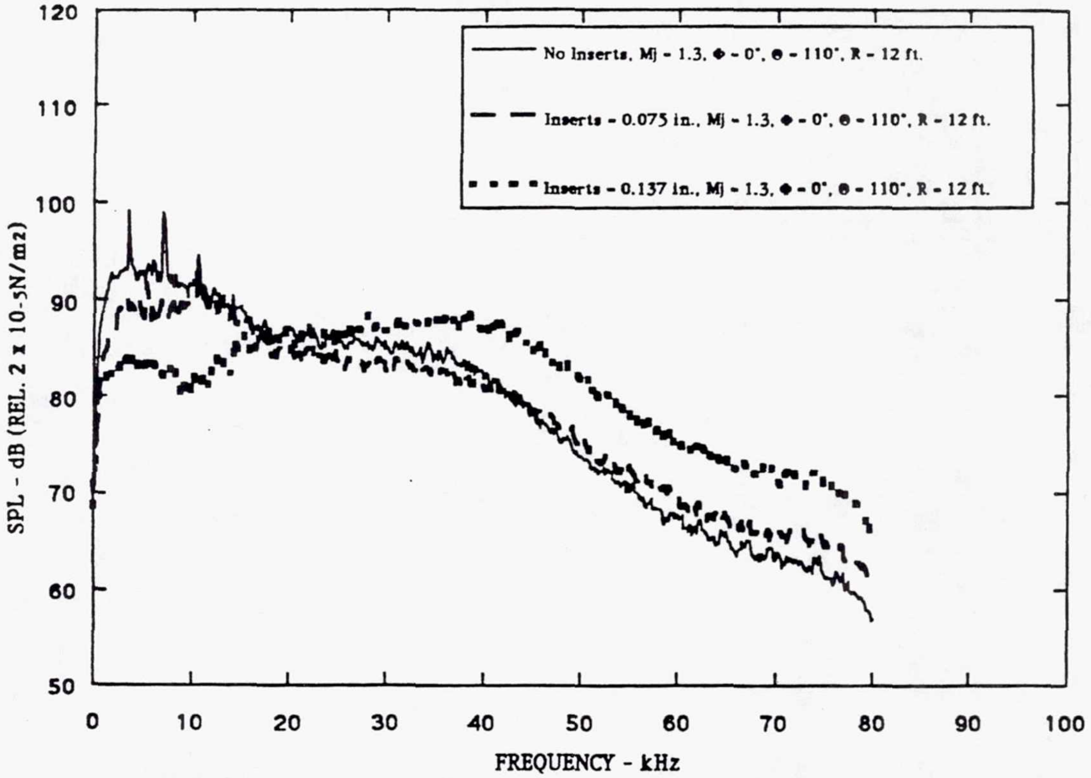

Narrow Band (Δf = 128Hz) Noise Spectra Comparison of Rectangular Nozzle, No Inserts vs. Inserts

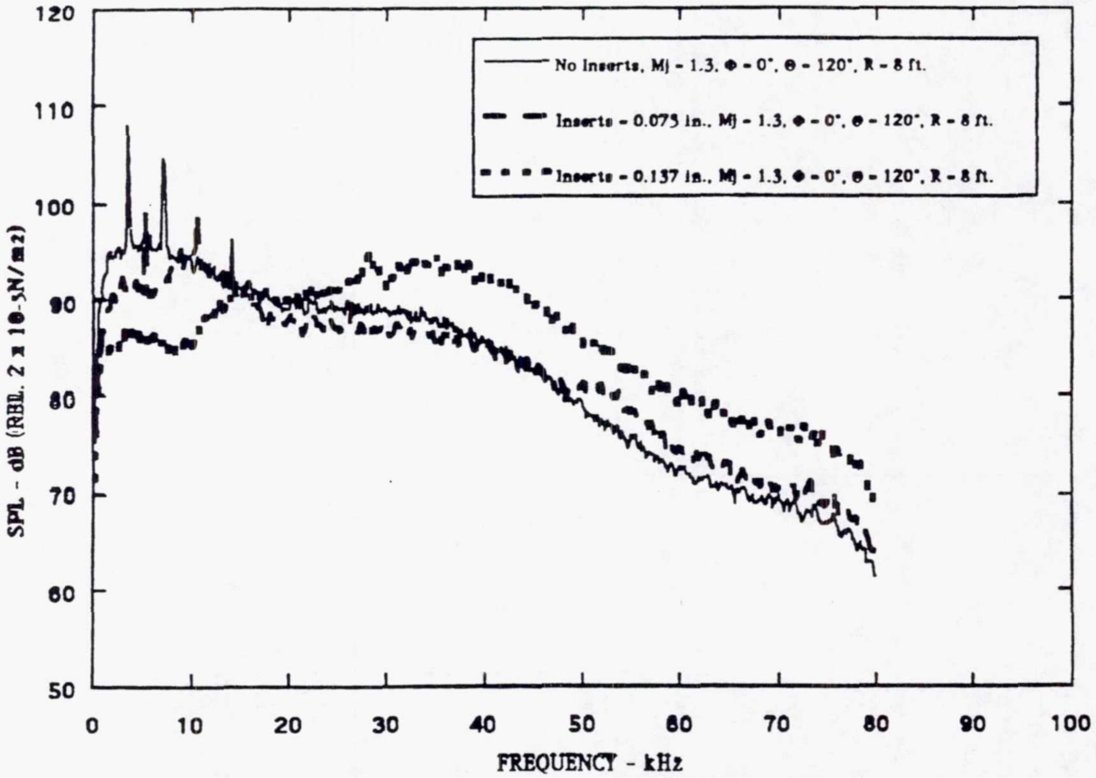

Narrow Band (Δf = 128Hz) Noise Spectra Comparison of Rectangular Nozzle, No Inserts vs. Inserts

Φ 90° PLANE

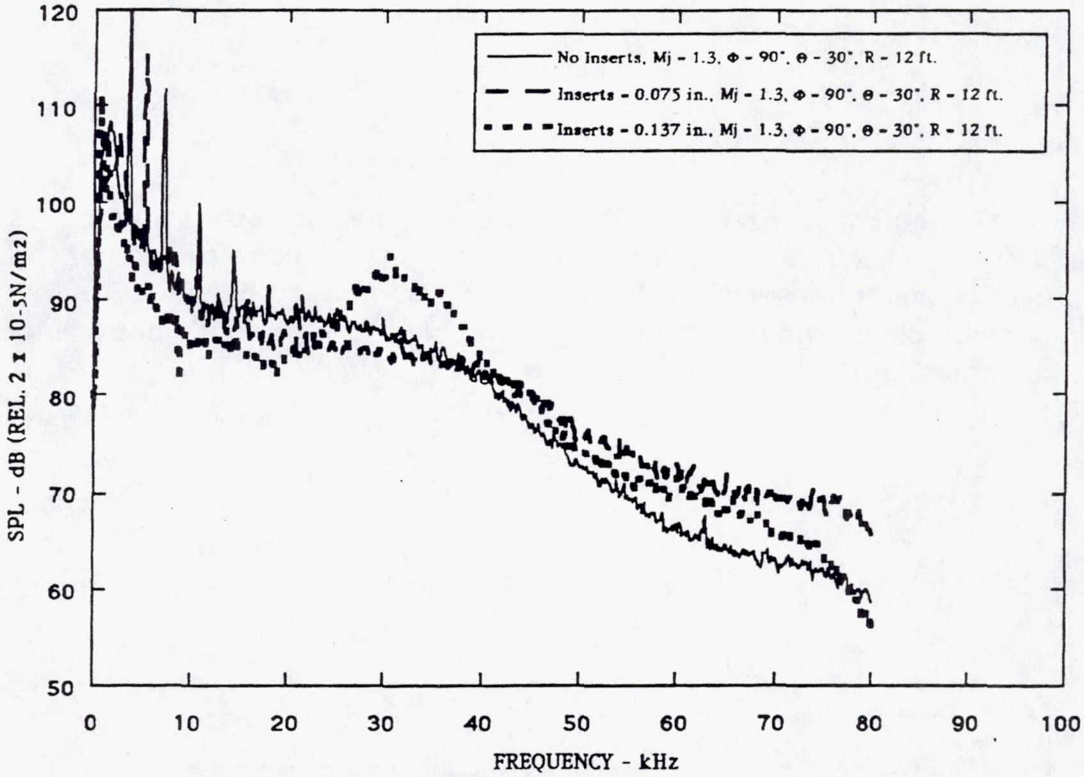

Narrow Band (Δf - 128Hz) Noise Spectra Comparison of Rectangular Nozzle, No Inserts vs. Inserts

The inserts are not as effective in the Φ 90° plane as they are in Φ 0° plane. In the Φ = 90° plane, all screech tones are eliminated by the inserts. Reduction in low frequency noise is still obtained.

EFFECT OF INSERTS ON FAR-FIELD DIRECTIVITY

The next seven figures show the far-field OASPL directivity for Φ 0° for Mj = 0.8, 0.9, 1.0, 1.1, 1.2, 1.3 and 1.4. The data for Φ 0° is used as data at this azimuthal angle for the "no-insert" condition are least dominated by screech. These data clearly indicate the important role of the inserts in reducing supersonic jet noise at all angles.

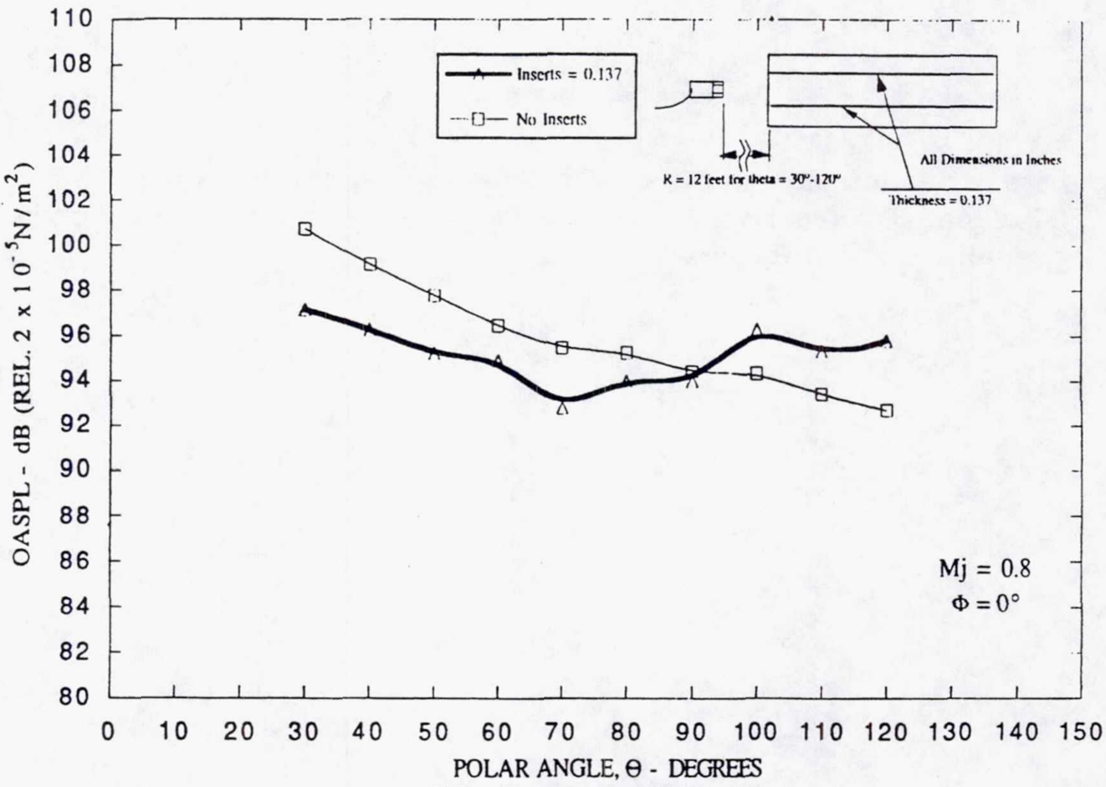

Effect of Inserts on Farfield Directivity.

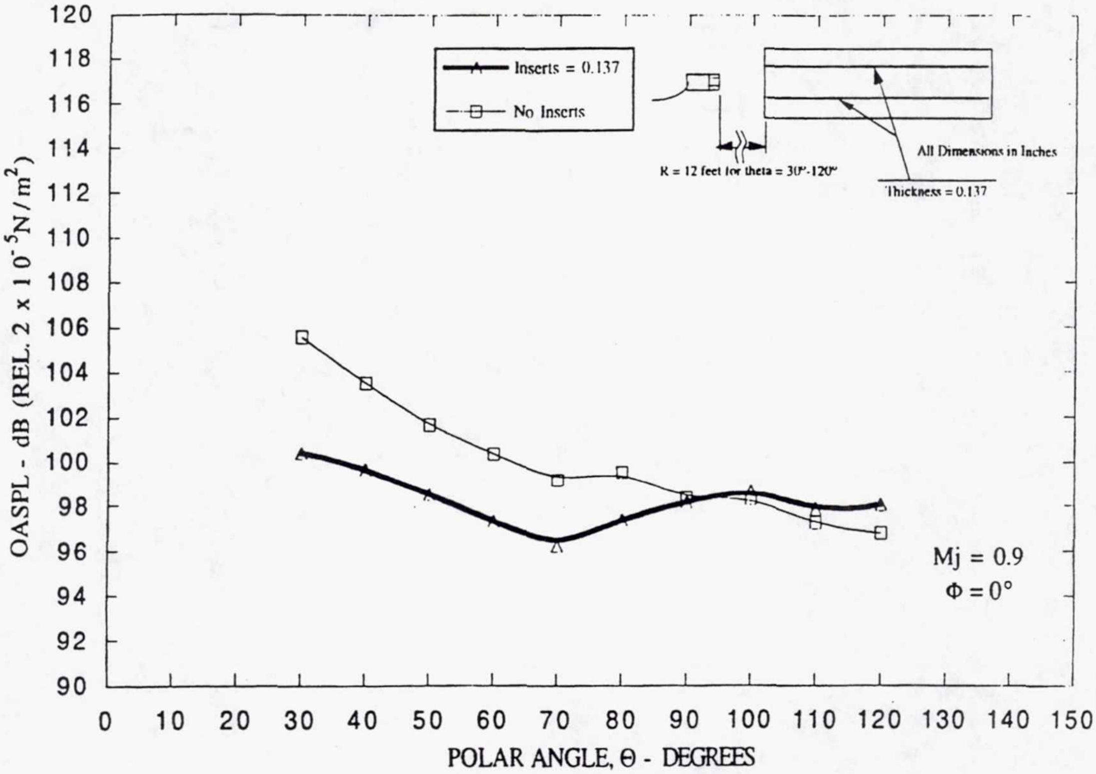

Effect of Inserts on Farfield Directivity.

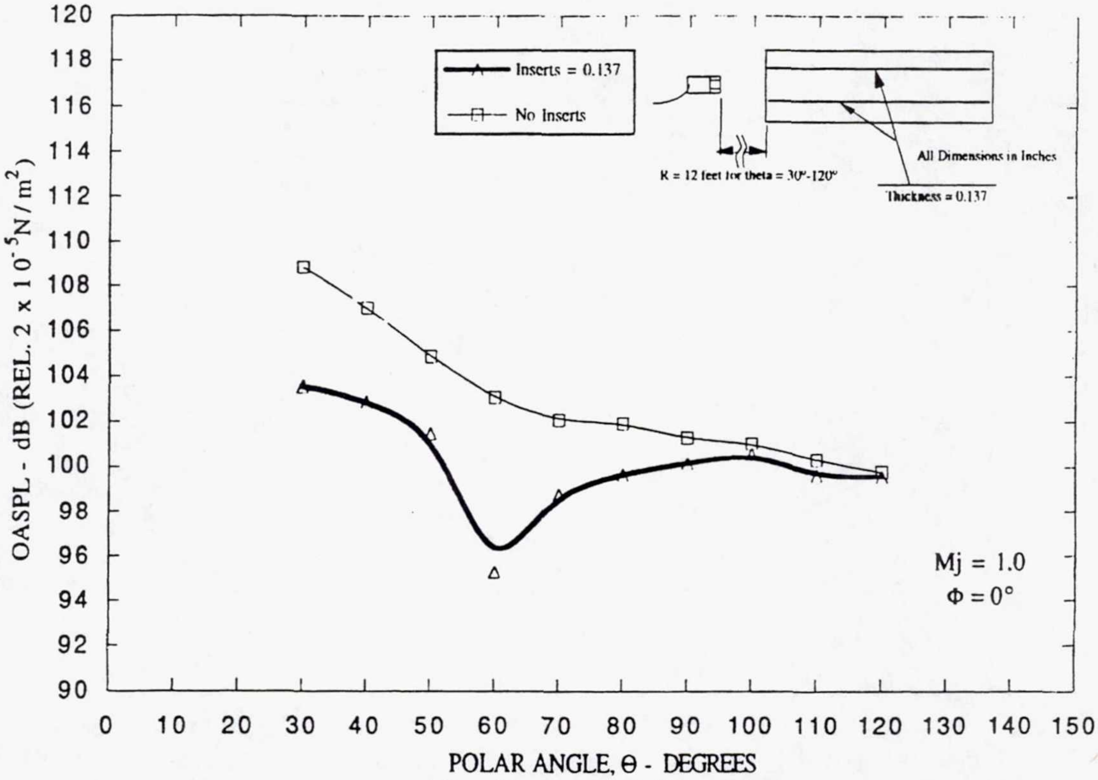

Effect of Inserts on Farfield Directivity.

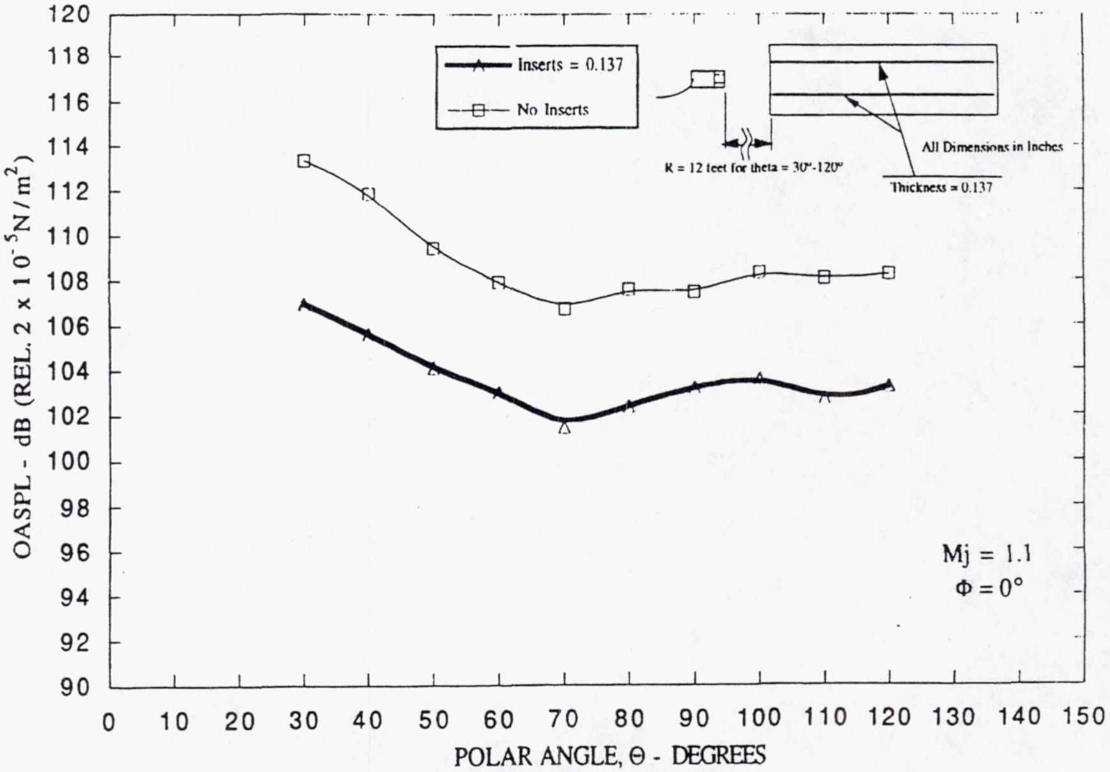

Effect of Inserts on Farfield Directivity.

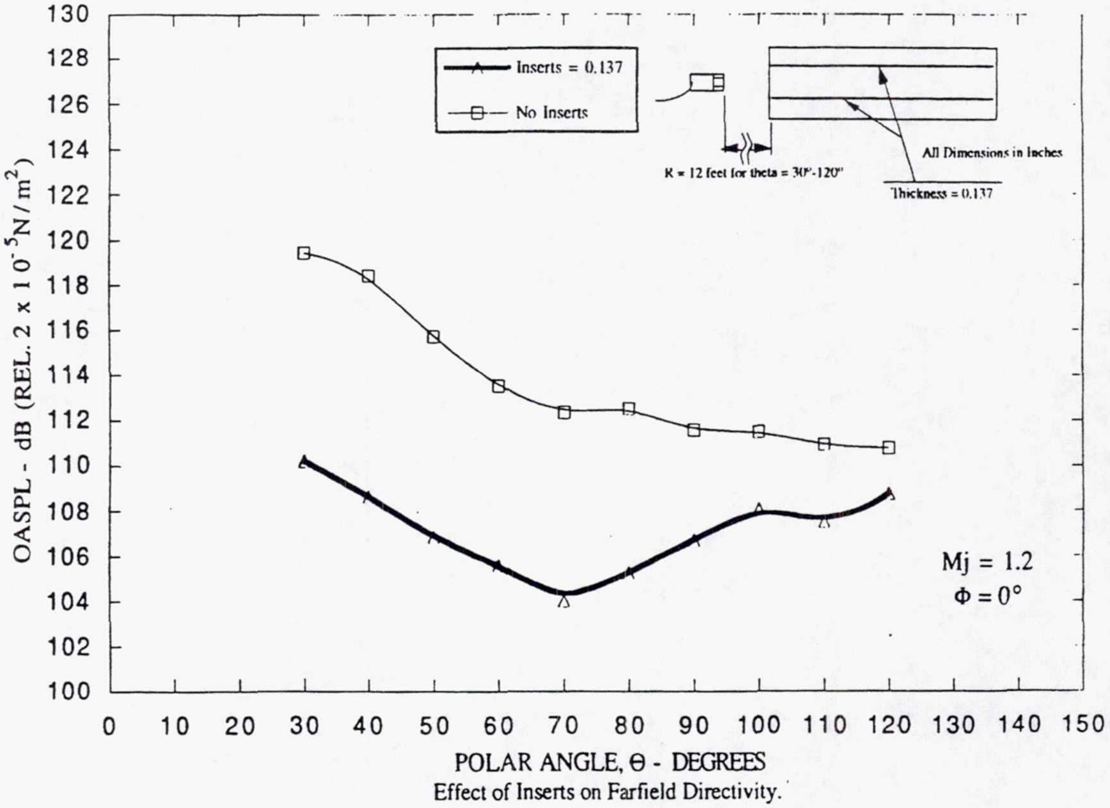

Effect of Inserts on Farfield Directivity.

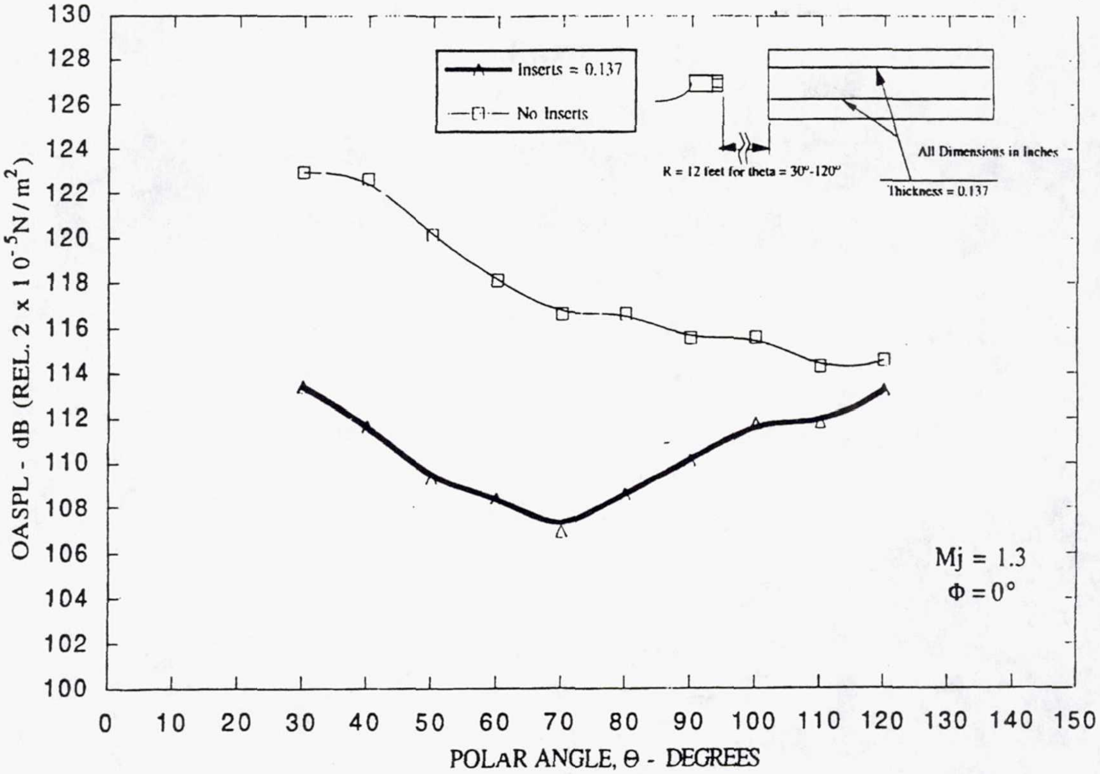

Effect of Inserts on Farfield Directivity.

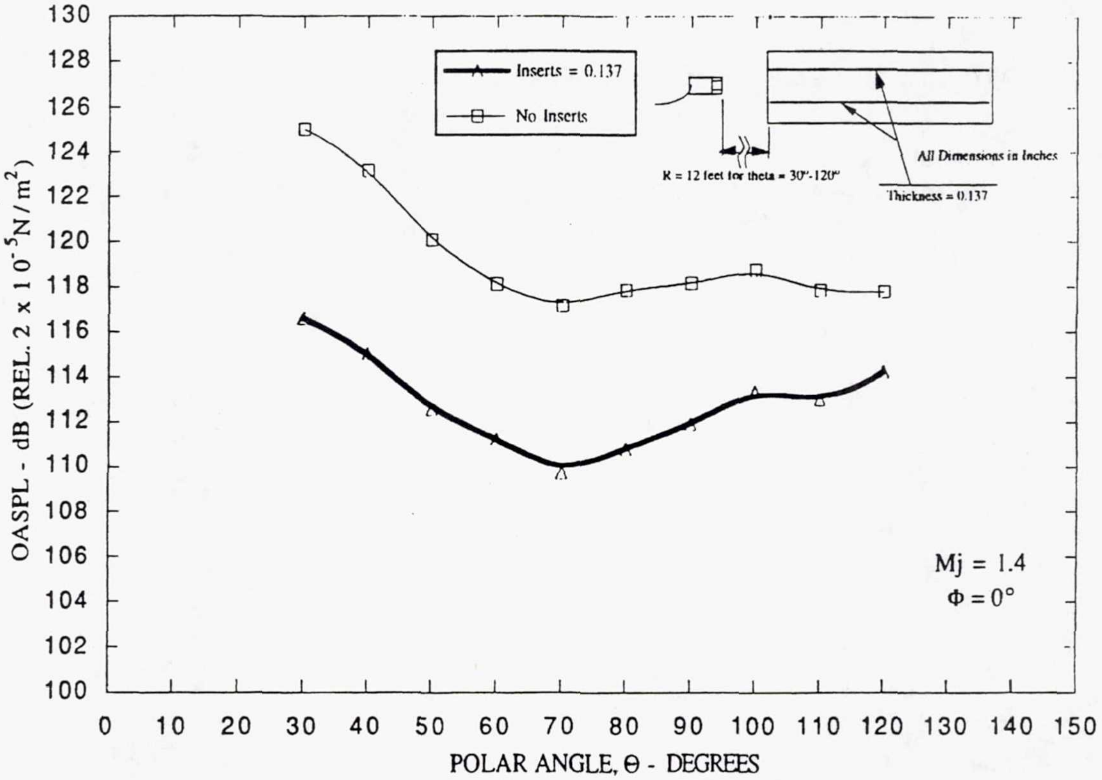

Effect of Inserts on Farfield Directivity.

Vibration Induced by a PZT

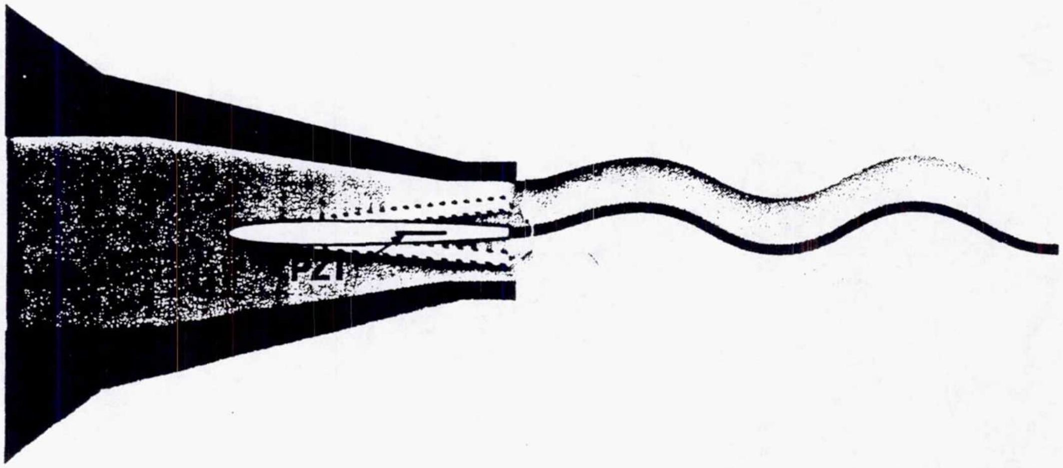

Additional experiments of inserts in conjunction with ejectors are planned.

Also, as shown in this figure, we plan to impart vibration of known frequency and amplitude to the insert by a PZT transducer in an "active control" sense with a goal of further enhancing the mixing and reducing the noise.

Insert Plates (0.02 in) Removed from Insert Holder

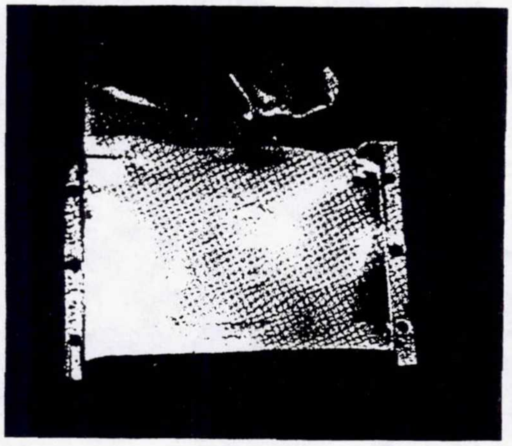

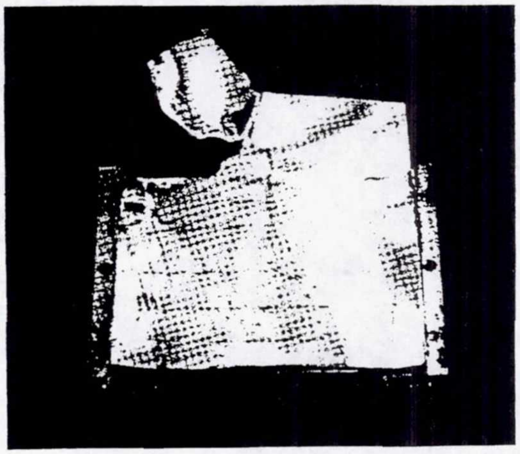

In this "proof-of-concept" study, serious structural failures of the insert plate were experienced. In particular, the inserts experienced significant vibration and a number of inserts broke. A typical example of the damage is shown in this figure. Either a new material or a different method of mounting is needed.

CONCLUDING REMARKS

1. A "Proof of Concept" Study Conducted.
2. Inserts Appear to Provide Significant Noise Reduction at all Angles for Supersonic Conditions.
3. High Amplitude Tones Generated at Subsonic Mach Numbers.
4. Amenable to Active Control
    - Vibration
    - Insert Lip Thickness?
5. Experiments Planned for Ejector Configuration.
6. More Detailed Flow Measurement Also Planned.

1999176549

TECHNIQUES FOR MIXING ENHANCEMENT IN SUPERSONIC SHEAR LAYERS

V. Kibens, M.C. Joshi*, and D.E. Parekh
McDonnell Douglas Aerospace
St. Louis, Missouri and *Long Beach, California

A. Glezer
Georgia Institute of Technology
Atlanta, Georgia

A. Krothapalli
Florida State University
Tallahassee, Florida

and

C.B. Rogers
Tufts University
Medford, Maine

512-34

409530

12P.

OUTLINE

- CURVED SHEAR LAYERS
- PIEZOELECTRIC EXCITATION
- STREAMWISE VORTICITY INJECTION
- EJECTOR EFFECTS

EXPERIMENTAL APPARATUS

Depiction of Curved Channel Geometry and Definition of Coordinate System

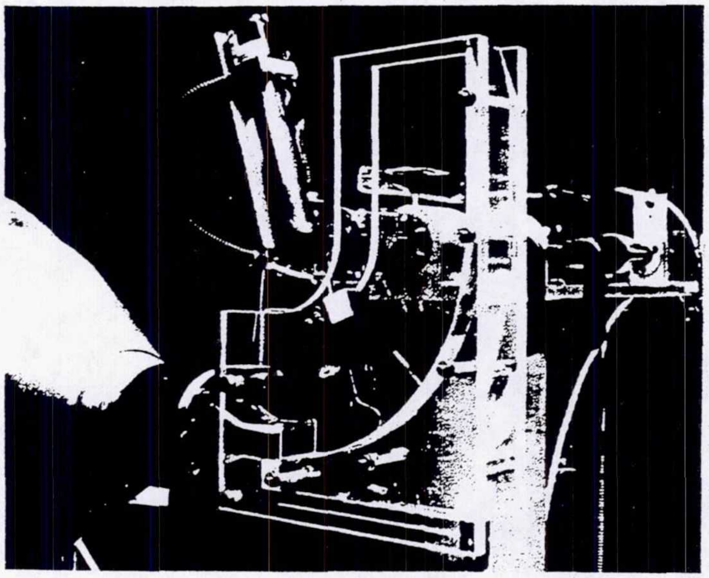

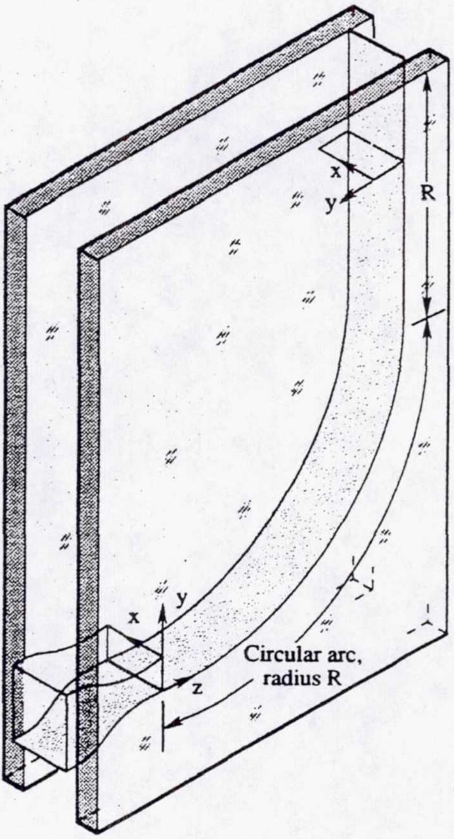

The flow exited from a rectangular, converging-diverging nozzle, with a design Mach number M = 1.47, an exit aspect ratio of 2:1, and the longer dimension equal to 33.8 mm. As shown in Fig. 1, the nozzle flow exited onto a curved surface bounded by transparent side walls made of Plexiglas. The channel turned the flow by 90 degrees. The wall curvature started at the nozzle exit, and consisted of a section of circular arc, followed by a straight section of length equal to one radius of turning curvature. The straight section was added to avoid major channel termination effects. Four curved channels were tested, with radii R = 10.2, 15.2, 20.32, and 30.5cm. The test apparatus also included a straight channel with no curvature, and unconstrained wall jets on a flat and curved plate.

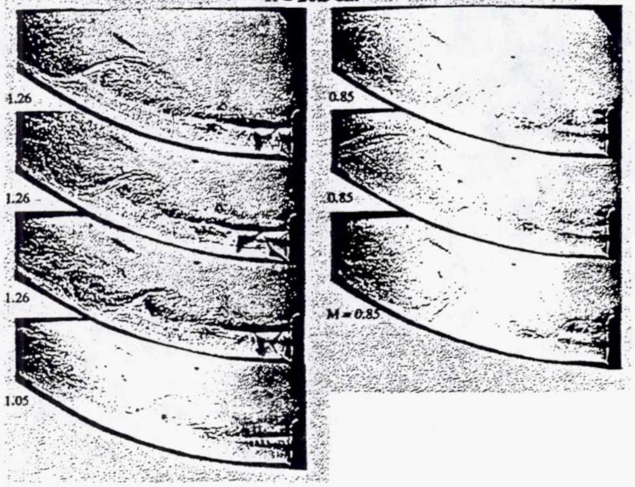
Schlieren Visualization of Flow in Curved Channel
R = 20.3 cm

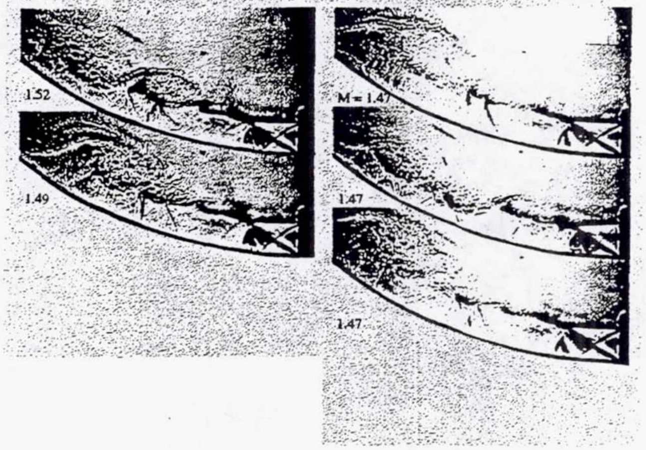
Schlieren Visualization of Flow in Curved Channel (Cont)
R = 20.3 cm

Fig. 2 shows the flow for channel curvature ratio R/h = 11.9. At M = 1.05, large scale structures (LSS's) begin to appear close to the end of the first shock cluster at the nozzle exit. These structures propagate and grow during their passage through the visible channel extent. The distance of the shear layer from the channel floor at z = 10h fluctuates extensively with minimum and maximum values of h/4 and h respectively. This oscillation appears correlated with a whipping motion of the shear layer at the nozzle exit. The flow is highly unsteady at the origin of the shock system. The shock lines extend and retract as much as ± h/2. Beginning with M = 1.19, the flow exhibits continuous LSS formation at the end of the first shock cluster at the nozzle exit. LSS formation and shock system unsteadiness persist to Mach numbers close to the design value of 1.47. Even at the design value the flow still generates large structures, though at a reduced rate and amplitude. Observation of the frame-by-frame sequences of the flow visualization videos suggests that the formation of the LSS's involves interaction between the shock structure, the shear layer motion, and the resonance properties of the cavity consisting of the Plexiglas walls and floor that constitute the channel boundaries. This conclusion is reinforced by the presence of a strong audible tone whose secondary spectral characteristics change with changes in the modes exhibited by the shear layer dynamics but whose primary pitch remains constant.

CURVED CHANNEL SUMMARY

Sketch of Parameter Map Showing Zones of Increased Mixing

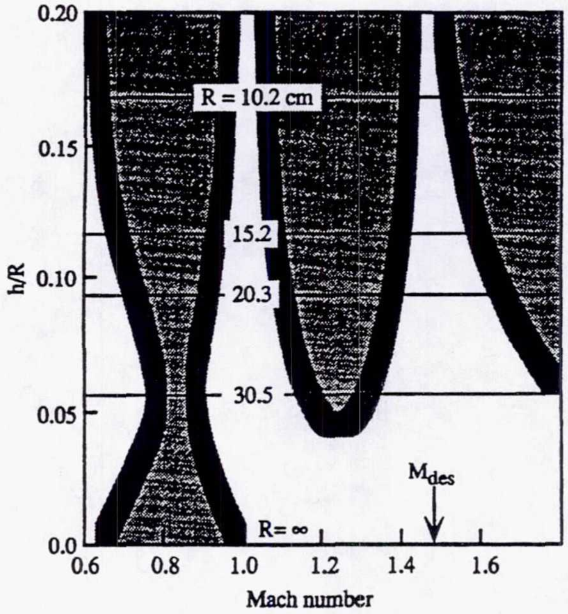

The observations regarding LS mixing in the various geometries can be summarized as shown in Fig. 3. Zones of mixing activity are displayed on a map whose ordinate is the ratio of the nozzle height to the curvature radius, h/R, and the abscissa is the Mach number. The straight channel case is at $h/R = 0$, and the curved channels are designated by the values of their radii of curvature. This map is intended only as a qualitative portrayal of the variation of LS activity in the various channels and is based on subjective evaluation of mixing activity upon viewing the flow visualization data. Nevertheless, it summarizes the general trends of activity observed as a function of geometry and Mach number. Strong subsonic mixing is present for all except the lowest curvature case, $R = 30.5$cm. Subsonic mixing is most intense for the smaller radii of curvature. The value $M = 1$ separates regions governed by different LS formation mechanisms. For a straight channel and for curved channels with $h/R < 0.05$, no mechanism exists to promote LS supersonic mixing. For $h/R > 0.05$, vigorous LSS formation occurs in the Mach number range $1 < M < M_{des}$; greatest mixing is observed for M@ 1.25. The intensity of mixing in this Mach number range increases with h/R. A diminution of LS activity is seen at the design Mach number for all geometries; mixing resumes again for $M > M_{des}$.

CONCLUSIONS

The primary conclusion from this work is that curved shear layers generated at supersonic pressure ratios exhibit vigorous LSS development, which denotes increased mixing of the supersonic and subsonic streams. This effect contrasts with supersonic flow in a straight channel, for which no LSS development occurs. The LSS development appears to be coupled to shock cell motion and feedback associated with channel cavity resonances. The nozzle lip and the intersection of the shear layer with the first shock cell apex appear to be regions of highest feedback sensitivity. LSS's exiting from the channel generate acoustic waves; however, sound spectra are independent of Mach number.

A standard wall jet (without sidewalls), using the same nozzle as the curved channel flows, exhibits no LS activity if the plate is flat; considerable LS activity occurs for M>1 if the plate is curved.

EXCITATION OF SUPERSONIC SHEAR LAYERS BY PIEZOELECTRIC ACTUATORS

Use of Piezoelectric Actuators in Supersonic Shear Layer

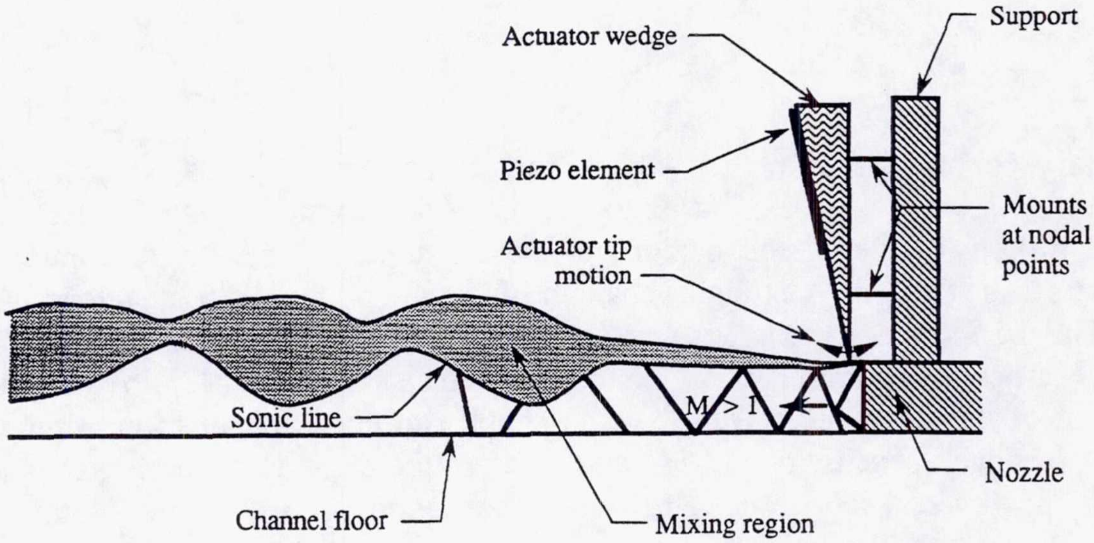

Wedge-shaped actuator elements made of a high strength aluminum alloy were driven at a 5kHz resonance frequency by attached piezoelectric wafers. The actuator wedge tips were placed at a nozzle exit adjacent to the supersonic flow boundary. They moved in an arc tangent to a line in the streamwise direction. A lower variable perturbation frequency was used to modulate the primary resonance waveform. Excitation effectiveness was evaluated in a supersonic channel flow as well as in a free jet flow. Both flows issued from a 2:1 aspect ratio nozzle with a design Mach number of 1.47. Perturbation levels achieved at 5kHz were adequate to effect substantial modifications of flow and noise characteristics for both flows. Amplitude modulation of the excitation waveform was effective only for modulation frequencies below 700 Hz.

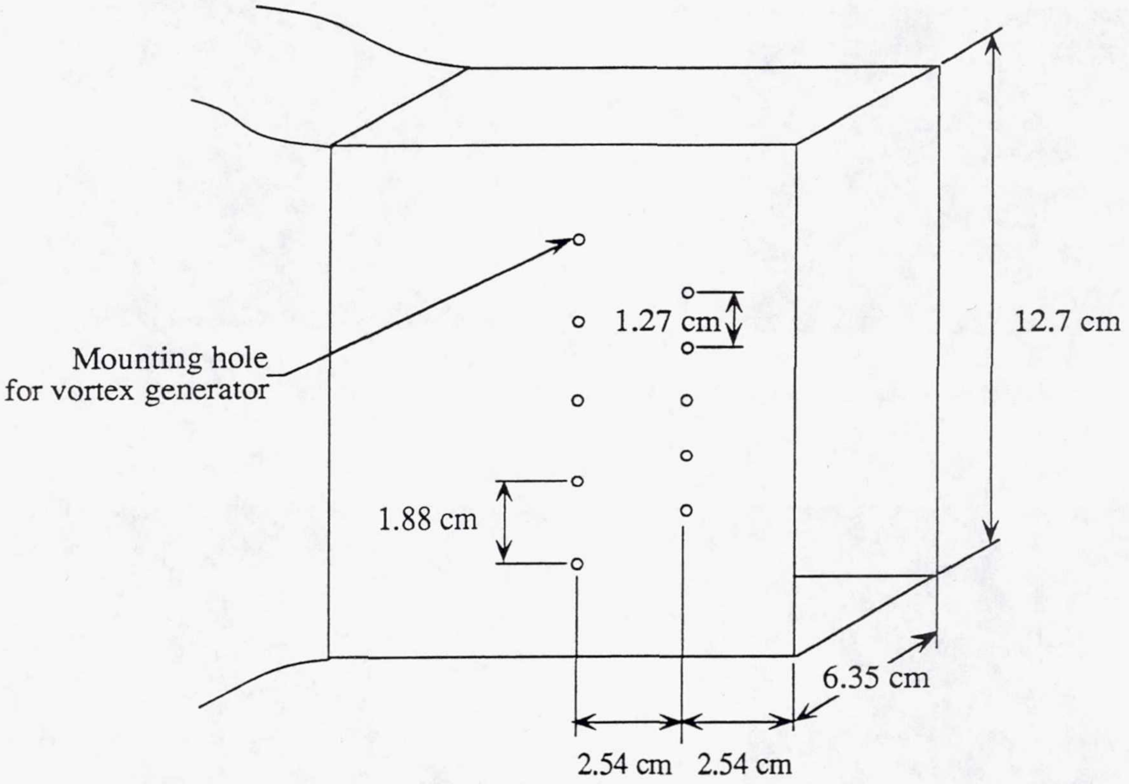

Schematic of retangular nozzle extension.

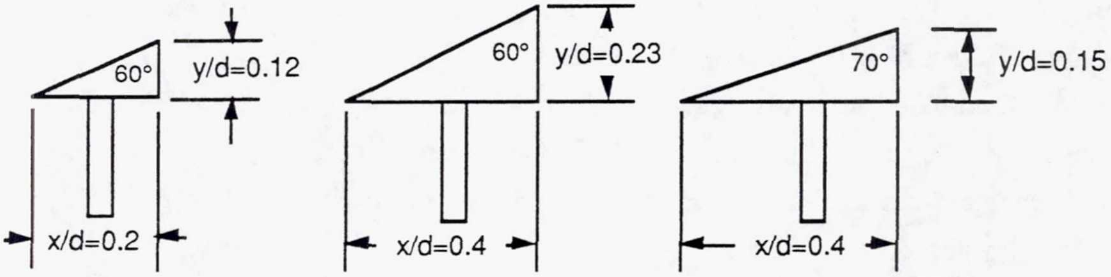

Half-delta wing vortex generators

The apparatus consists of a 2:1 rectangular nozzle extension in which are mounted half-delta wing vortex generators. In this study, the 40 different configurations considered include variations of generator size, generator leading-edge sweep angle, generator angle of attack, number and relative placement of generators, and Mach number.

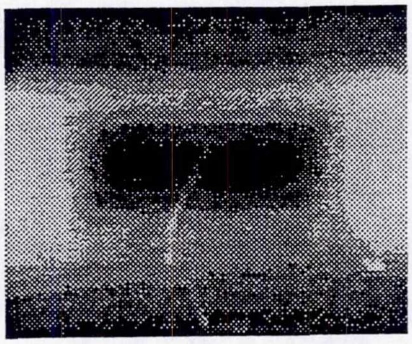

(a) Reference

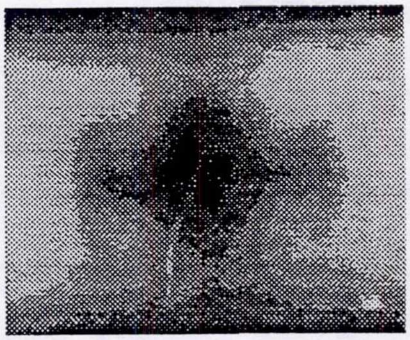

(b) "O" Case

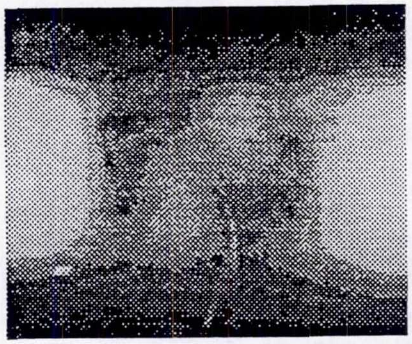

(c) "N" Case

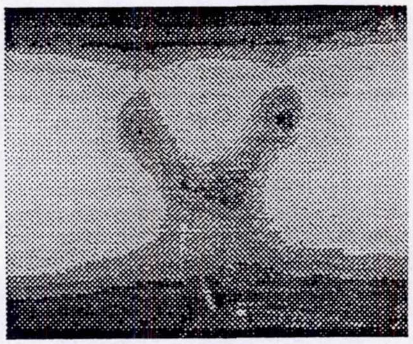

(d) "U" Case

These jet cross-sectional images were taken at 3.7 hydraulic diameters downstream of the jet exit at a speed of 200 m/s (M=0.6). The test cell was seeded with a ROSCO fog machine and illuminated with a laser light sheet from a copper vapor laser. Thus, dark regions in the middle of the images represent the unseeded jet core flow which has not mixed with the ambient seeded air. Each image shown represents an average of 330 instantaneous images.

The first picture is the reference case of the jet without vortex generators. It shows how the shape of the exit geometry is retained downstream. All three other pictures have one set of vortex pairs on top and bottom. In the "O" case, the vortex pairs are formed by two generators, with the common flow away from the jet centerline. The "N" case shows the effect of asymmetry by having the common flow of the top pair being offset laterally from the common flow of the bottom pair. Both pairs have a common flow into the center of the jet in this case. Finally, the "U" case is generated by a vortex pair on the top with common flow toward the jet center and a vortex pair on the bottom having a common flow away from the jet centerline.

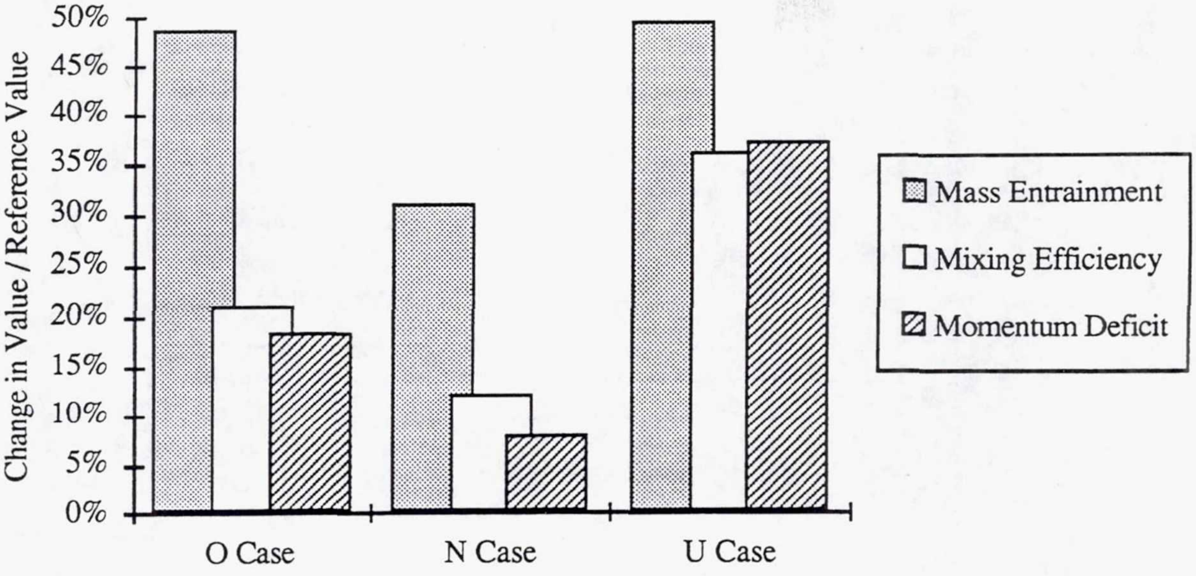

The mixing data indicates that the streamwise vortices improve both large-scale and small-scale mixing. Mass entrainment into the jet increases by up to 50%. Increases in mixing efficiency and shear layer growth are close to 40% for some configurations. The generator configurations dictate the shape of the jet potential core, and almost any arbitrary shape can be obtained by proper placement of the generators. Flow visualization and mean velocity measurements present consistent images of the jet mixing patterns. Along with changes in shape, the core length also decreases by as much as a factor of two. The core length, however, is not a good measure of mixing in these highly three-dimensional flows. Integral measures, such as mass entrainment or mixing efficiency, are much more appropriate.

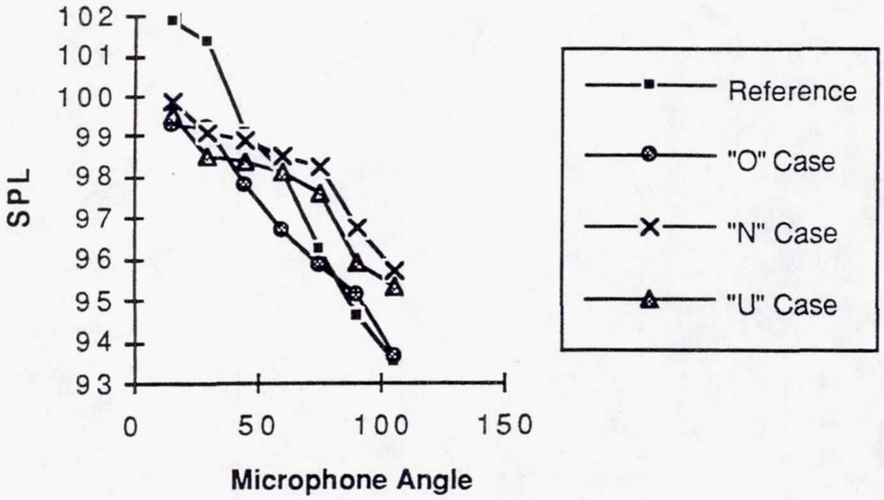

The acoustic results show that streamwise vortices are effective at reducing the overall sound pressure level for polar angles less than 60° but increase noise slightly at angles around 90°. At all polar angles considered, the streamwise vortices reduce low frequency noise but increase high frequency noise. The vortices apparently reduce low frequency noise by modification of the jet mixing noise sources through a global reduction of the high shear regions of the flow. The increased turbulence associated with the vortices, however, produces the increase in high frequency noise. The fact that most of the acoustic energy is at lower frequencies for polar angles close to the jet axis accounts for the net reduction in overall jet noise downstream of the jet. To the side of the jet, the increase in high frequency noise dominates the decrease in low frequency noise resulting in an increase in overall jet noise. From a practical standpoint, the shift of acoustic energy from low to high frequencies is acceptable since higher frequencies are easier to attenuate and contribute proportionately less to "perceived noise levels." Finally, the noise reduction increases with both Mach number and generator angle of attack (up to 30°).

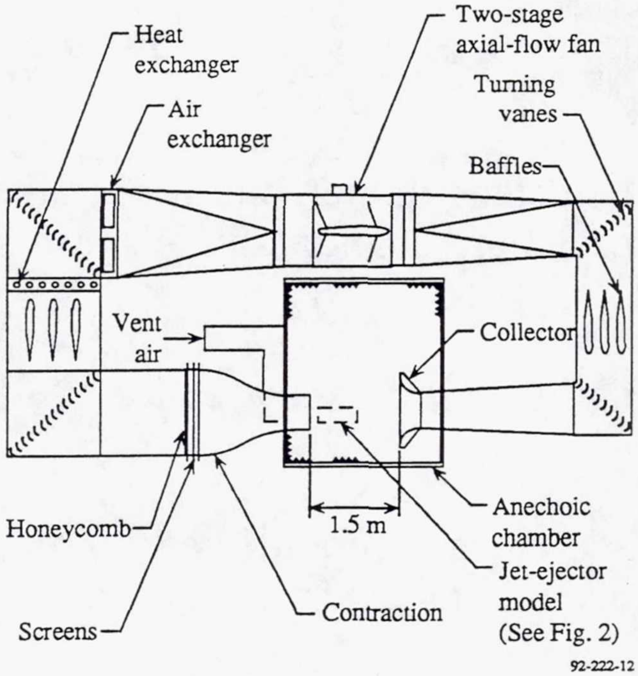

Schematic of FSU Wind Tunnel

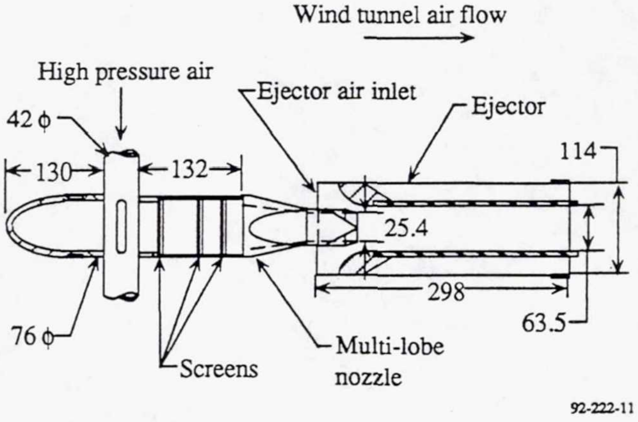

* All dimensions in mm.

Jet-Ejector Configuration

The upper figure shows the open-jet, closed-return, anechoic wind tunnel at Florida State University. The lower figure show a typical jet-ejector model tested in this facility. Experiments on sound generation from rectangular jet ejectors have included both single and multi-lobe nozzles. This facility also provides heated primary flows at temperatures up to 900° K and simulated forward flight at velocities over 50 m/s.

Summary of Jet-Ejector Studies

- Relative to single rectangular jet, multi-lobe nozzle reduces overall noise in aft quadrant but increases noise radiated to the side.

- Elevated temperatures significantly reduce or eliminate screech peaks.

- Low area ratio (<4) ejectors provide best noise suppression of screech-dominated underexpanded jets.

- For underexpanded jets, the noise modification by an ejector or by elevated temperature decreases as Mach number increases.

1999176550

APPLICATION OF A FLIP-FLOP NOZZLE ON PLUME MIXING ENHANCEMENT

Stefan Schreck and Mark Michaelian
Department of Aerospace Engineering
University of Southern California
Los Angeles, California

and

Chih-Ming Ho
Department of Mechanical, Aerospace, and Nuclear Engineering
University of California at Los Angeles
Los Angeles, California

513-07

409531
16P

OUTLINE

Motivation

Problem Statement

Approach
- **Rectangular Jet**
- **Jet De-stabilization**
- **Acoustic Self-Excitation**

Integration of the Design: Flip-Flop Nozzle

Evaluation
- **Jet Spreading**
- **Far-Field Noise**

Summary

MOTIVATION

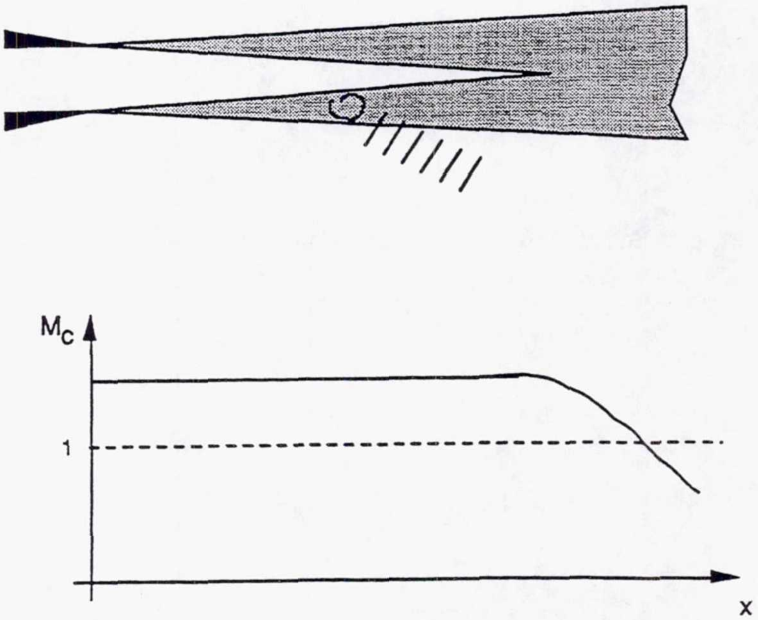

Figure 1: Eddy Mach Wave Radiation

Mach wave radiation is a major source of noise in high speed jets. It is created by turbulent eddies which travel at supersonic speed within the shear layer of the jet (Figure 1). Downstream of the potential core, the convection speed of the eddies decays and noise production is reduced. Once the convection speeds drops below the speed of sound, eddy Mach wave radiation ceases. Mach wave radiation may be reduced by shortening the core length of the jet. This requires a faster growth of the shear layer, i. e. enhanced mixing in the jet. We investigated the possiblity of mixing enhancement by the excitation of the instability waves in a supersonic rectangular jet.

PROBLEM STATEMENT

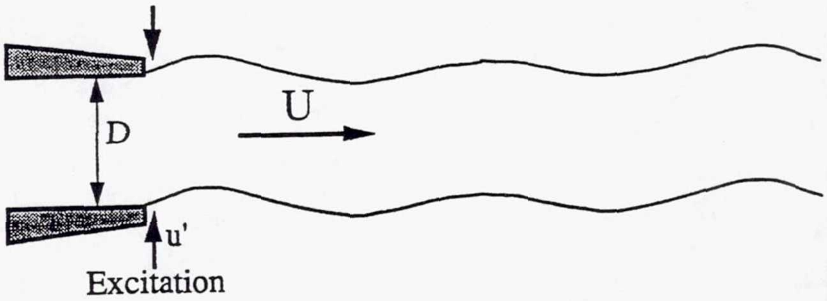

Forcing Frequency: $f = 0\,(U/D)$

Forcing Amplitude: $u' = 0\,(0.01\text{-}0.1\ U)$

Power Requirement: $P \sim u'^2 f \sim U^3$

Figure 2: Excitation of the Instability Waves in Jets

Acoustic or mechanical excitation of the instabiliy waves has been shown to increase the growth rate of the shear layers in low speed jets. The application of this technique to supersonic jets, however, has been hampered by the demanding requirements on the excitation system. If the preferred mode of the jet is to be excited (Figure 2), the forcing frequency scales with the jet velocity U and is typically of the order of 0.2-0.4 U/D, where D denotes the jet diameter. The forcing amplitude u' is of the order of 0.01-0.1U. Thus, the power requirement increases with the third power of the jet velocity. Loud speakers and piezo cristal actuators, which have been used to force the shear layer instabilties in low speed jets, cannot meet the power requirement for large amplitude excitation of the instability waves in supersonic jets.

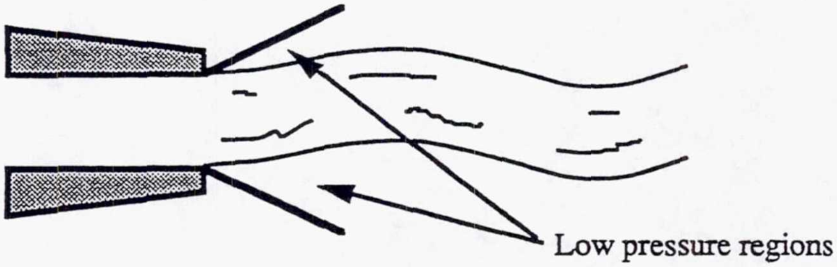

Figure 3A: Flapping Mode of Rectangular Jets

Asymmetric nozzle designs have been considered for the control of jet noise in supersonic jets. Ho and Gutmark (1984) reported an increase in the growth rate of the shear layer in elliptical jets by vortex self induction. Seiner et al. (1992) found that the increased mixing in a small aspect ratio elliptical jet reduces noise radiated at supersonic speeds.

Part I: Flapping Mode of Rectangular Jets -- Besides vortex self induction, small aspect ratio rectangular jets also feature an asymmetric flapping mode similar to that in two-dimensional jets (Figure 3A). This flapping mode may be excited to enhance mixing in supersonic jets. To reduce the force necessary to deflect a rectangular jet, we applied the Coanda effect to de-stabilize the jet. Acoustic self-excitation was then used to flip-flop the jet at a high frequency.

Part II : Destabilizing a Rectangular Jet -- The Coanda effect was used to increase the deflection of the jet from the centerline when excitation is applied. Coanda discovered that a jet attaches to a wall that is placed adjacent to the jet column. The attachment is caused by a low pressure region created between the jet and the wall, which pulls the jet towards the wall. If walls are placed symmetrically on both sides of a two-dimensional jet, the jet might become bi-stable, i. e. it may attach to either

APPROACH (con't)

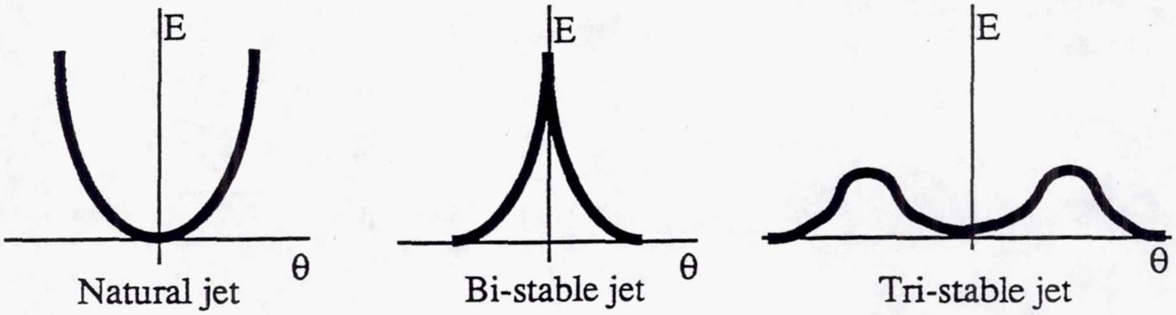

Figure 3B: Stability of the Jet Column

side (Figure 3A). Depending on the configuration, a naturally stable, a bi-stable, or a tri-stable jet may be achieved (Figure 3B). Proper choice of the size and location of the walls creates a destabilzed jet that does not attach to either wall but is less stable in the central position. Such a jet can be deflected from the centerline with less force than the natural jet.

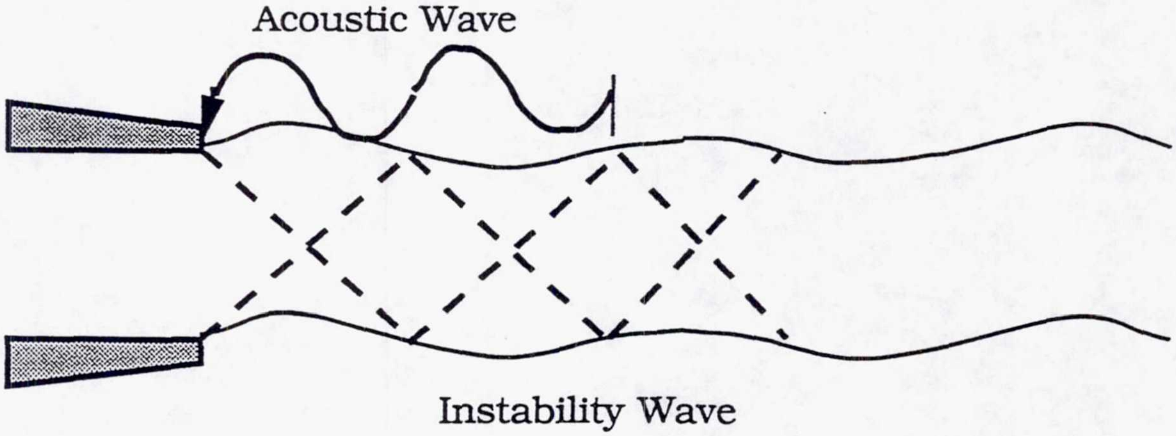

Figure 4: Acoustic Self-Excitation

Part III: Acoustic Self Excitation -- Shock cell structures exist in non-ideally expanded jets. They are confined within the potential core of the jet and interact with the shear layer as shown in Figure 4. This process emits acoustic sound waves that travel outside of the jet upstream to the nozzle lip. When the acoustic waves and the downstream traveling instability waves form a closed loop, the instability waves are excited by their own acoustic radiation and a discrete screech tone is audible. We used the acoustic power of the upstream travelling waves to excite the flapping mode of the jet.

INTEGRATION OF THE DESIGN - A Flip-Flop Nozzle

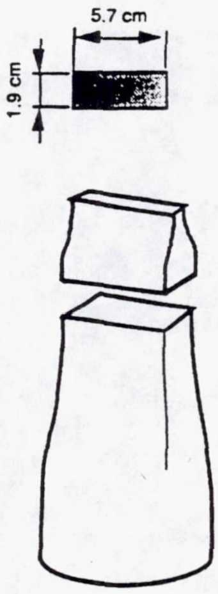

Figure 5A: The Rectangular Nozzle

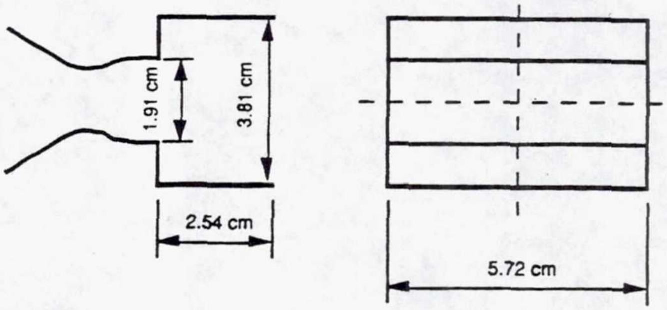

Figure 5B: Collar of the Flip-Flop Nozzle

The ideas of using the flapping mode of a rectangular jet, destabilizing the jet column, and the self-excitation of the flapping mode by screech were integrated into a flip-flop nozzle. Figure 5A shows the orginal rectangular nozzle. An initially axisymmetric contraction reduces the cross-sectional area of the settling chamber from d = 15.3cm to a square opening of 5.7cm x 5.7cm. The rectangular nozzles feature a two-dimensional contraction from 5.7cm x 5.7cm to 1.9cm x 5.7cm. Two nozzles designed for ideal expansion at M = 1.45 and M = 1.90 respectively were manufactored. The aspect ratios of both nozzles are 3:1. Figure 5B shows the flip-flop nozzle. A collar is mounted onto the nozzle creating a sudden expansion in the minor axis plane of the jet. This design fulfills two functions: similar to the side walls in Figure 3A, it destabilizies the jet by low pressure regions located in the two pockets inside the collar; it also acts as a resonator amplifying selctive acoustic waves created by the shock cell structures in the jet.

EVALUATION OF THE FLIP-FLOP NOZZLE

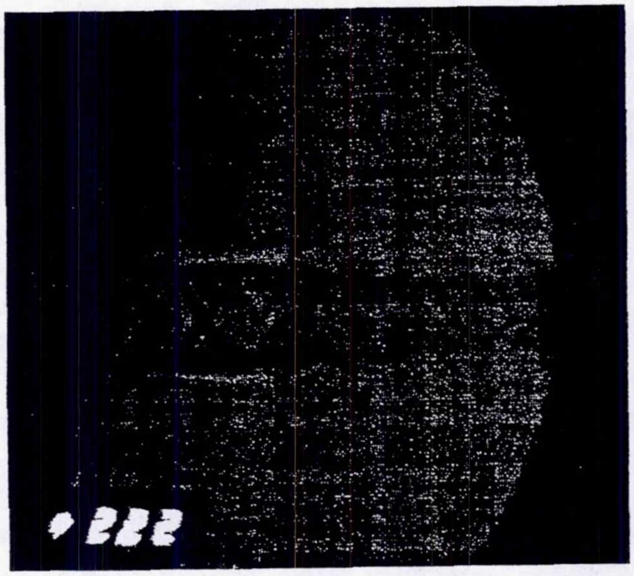

Figure 6: Shadowgraph Image of the Ideally Expanded Rectangular Jet at M=1.45

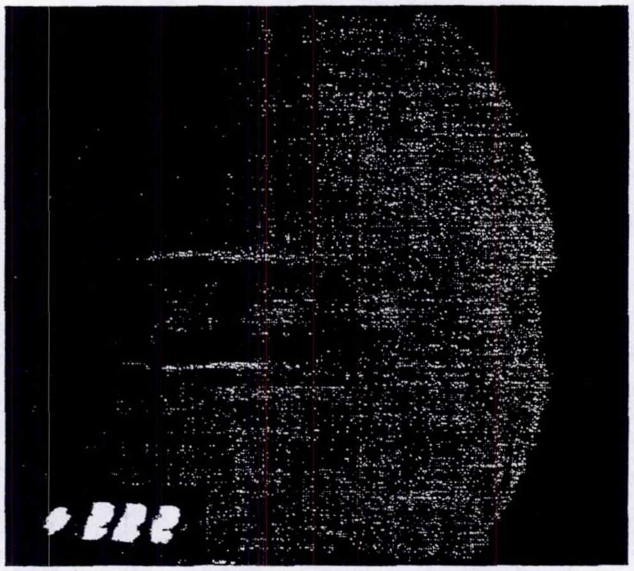

Figure 7: Shadowgraph Image of the Rectangular Jet Designed for Ideal Expansion at M=1.9 run at M=1.45

To evaluate the performance of the flip-flop nozzle, the flip-flop jet was compared with an ideally expanded jet at $M = 1.45$. Since the flip-flop jet has to be run overexpanded to make use of acoustic self-excitation, a rectangular nozzle designed for ideal expansion at $M = 1.9$ was used. Shadowgraph images of the jets were recorded with a video camera. Digitized images from the recordings are presented here.

The Rectangular Jet

Figure 6 shows minor axis planes of the ideally expanded rectangular jet at $M = 1.45$. The jet spreads slowly and the potential core extends beyond the viewing area of the shadowgraph system. Figure 7 shows the rectangular jet designed for ideal expansion at $M = 1.9$ run at $M = 1.45$. Although this jet is overexpanded and screech is present, the spread rate is similar to that of the ideally expanded jet at $M = 1.45$.

THE TRI-STABLE JET

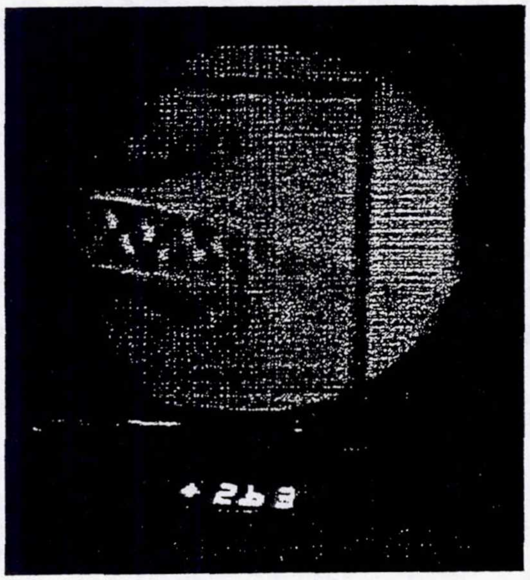

Figure 8A: Shadowgraph Image of the Tri-Stable Jet Attached to the Left Wall.

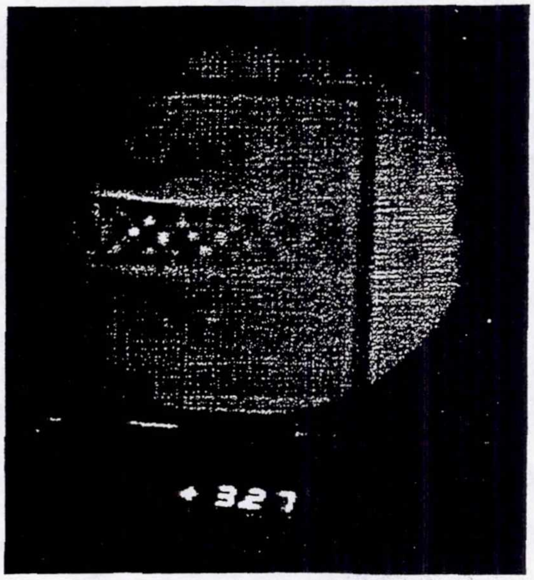

Figure 8B: Shadowgraph Image of the Tri-Stable Jet in the Center Position.

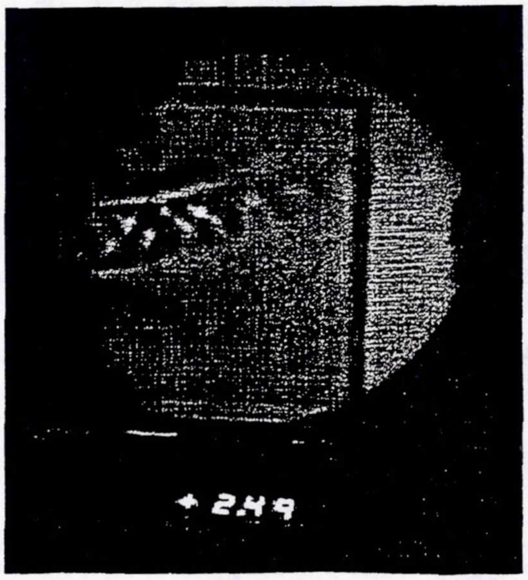

Figure 8C: Shadowgraph Image of the Tri-Stable Jet Attached to the Right Wall.

Figures 8A, 8B, and 8C illustrate the effect of walls on the stablity of a rectangular jet. 5cm long walls were mounted on both sides of the rectangular jet at an angle of 20 degrees. For visual access, plexiglass plates were placed along the narrower sides of the expansion section. In the configuration shown, the jet column is stable in three positions: attached to either wall and in the center. The jet was moved from one position to the other by injecting air normal to the jet at the lip of the nozzle.

THE FLIP-FLOP NOZZLE

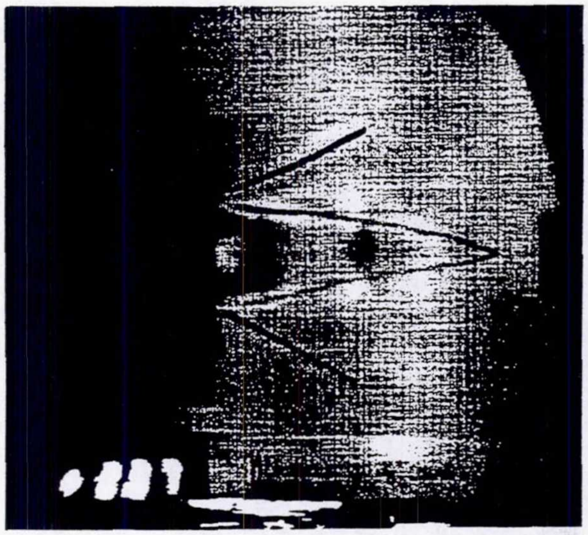

Figure 9A: Shadowgraph Image of the Flip-Flop Nozzle Showing the Large Spreading of the Jet

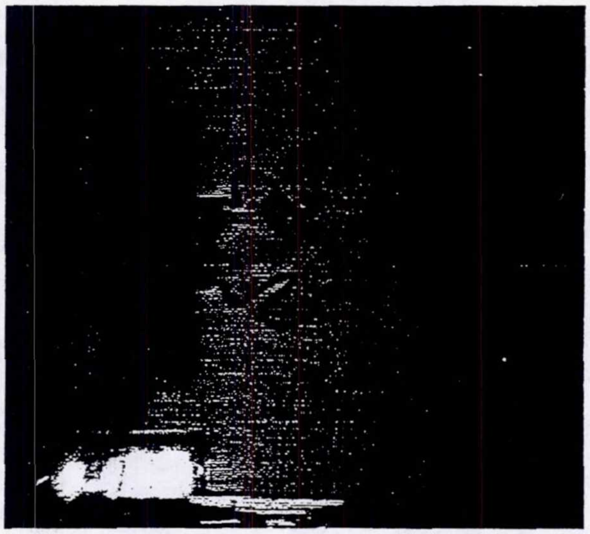

Figure 9B: Phase-Averaged Image of the Flip-Flop Nozzle Showing the Large Coherent Structures in the Jet

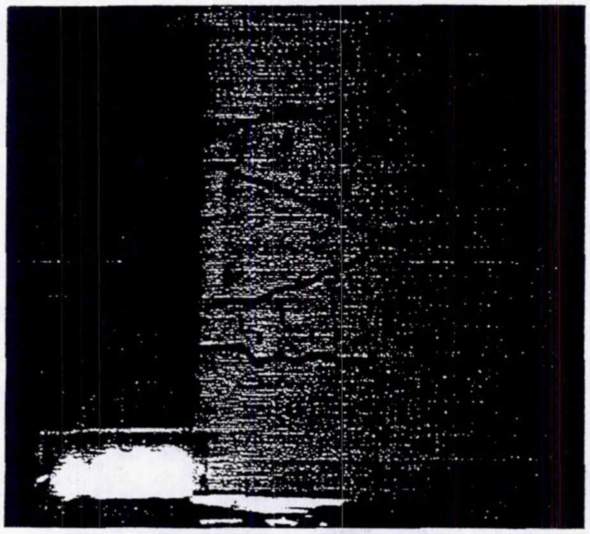

Figure 9C: Shadowgraph Image of the Major Axis Plane of the Flip-Flop Nozzle

Figures 9A, 9B, and 9C show images of the flip-flop jet at M = 1.45. In Figure 9A, a time averaged shadowgraph image of the minor axis plane is shown. The outline of the shear layer is highlighted with a marker to demonsrate the spreading of the jet. For Figure 9B, a strobe light was used. The light was triggered with the acoustic signals from the self-excitation of the jet. In the phase-averagd image, large coherent structures are visible in the minor axis plane of the jet. Again, a marker was used to outline the structures. These structures are created by the asymmetric distortion of the jet column. In the major axis plane (Figure 9C), coherent structures are less visible. Note the fast growth of the shear layer towards the centerline of the jet.

CHARACTERISITICS OF THE ACOUSTIC EXCITATION

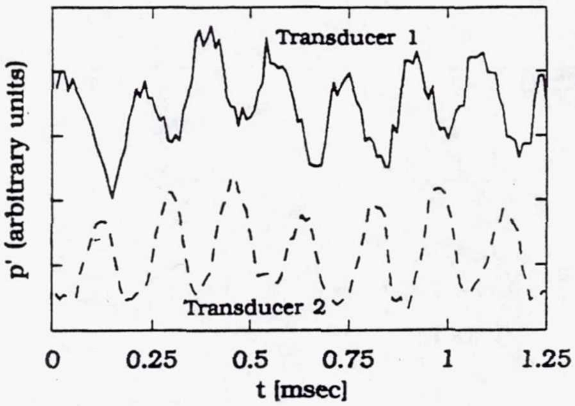

Figure 10A: Time Traces of the Excitation Signals

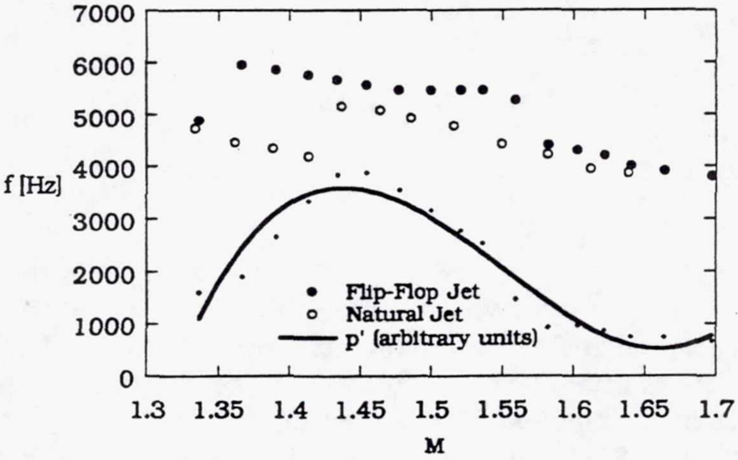

Figure 10B: Frequency and Amplitude of the Excitation Signal

PCB piezo crystal pressure transducers were placed next to the nozzle lip to investigate the characteristics of the acoustic self excitation. In Figure 10A times trace of the pressure signals recorded on both sides of the flip-flop nozzle are plotted. Note the phase shift of 180 degrees between the two signals. The peak frequency of the pressure signals are presented in Figure 10B for the natural jet and the flip-flop nozzle. Outside the range of M=1.35 to M=1.55, the peak frequencies of the two jets are identical. They represent the natural screech components in the rectangular jets. In the range from M=1.35 to M=1.55, the frequency of the flip-flop nozzle locks into the resonance frequency of the collar. The amplitude of the pressure signals is also shown in Figure 10B. The amplitude increases significantly at resonance.

CENTERLINE VELOCITIES

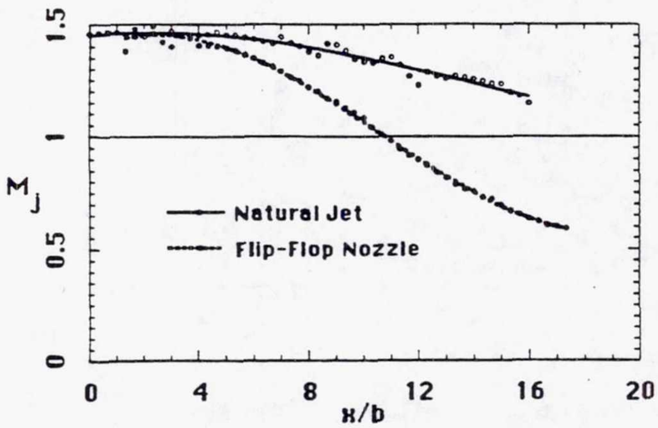

Convective Mach Number of K.-H. Instability Waves in Cold Jets:

$M_c = (M_j+1)/2$

Figure 11: Centerline Velcocities

Measured centerline velocities of the two jets are presented in Figure 11. The downstream distance is normalized by the minor axis diameter b = 1.9cm. The length of the potential core is considerably reduced by the flip-flop nozzle. The velocity at the centerline of jet reaches Mj = 1 at about x/b = 10 for the flip-flop nozzle and an estimated x/b = 20 for the natural jet. Using the equation for the convection speed of Kelvin-Helmholtz instability waves in cold jets, Mc < 1 for Mj < 1. Consequently, Mach wave radiation ceases in the flip-flop jet at x/b = 10 versus x/b = 20 in the natural jet.

FAR-FIELD NOISE

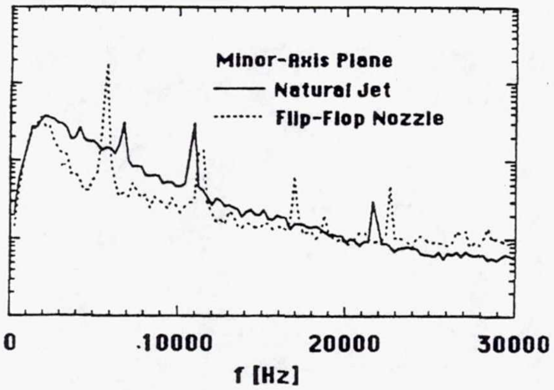

Figure 12A: Noise Spectra in the Minor Axis Planes

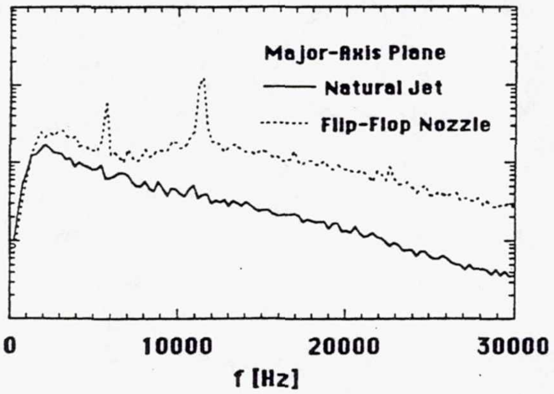

Figure 12B: Noise Spectra in the Major Axis Planes

The goal of enhanced mixing in supersonic jets is the reduction of eddy Mach wave radiation. The far-field noise of the flip-flop nozzle was measured with 1/2" B&K microphones placed in the minor and major axis planes 50 equivalent jet diameters away from the nozzle and 30 degrees off the jet axis. The locations of the microphones coincide with the main direction of the Mach wave radiation. In Figure 12A, the noise spectrum taken in the minor axis plane of the flip-flop nozzle is presented together with that of the ideally expanded natural jet at $M=1.45$. The spectrum for the flip-flop nozzle is dominated by discrete tones associated with the excited instability waves in the jet. Broadband noise is considerably reduced. The overall SPL is about the same as that for the natural jet. Figure 12B shows the respective spectra in the major axis planes. Conversely to the minor axis plane, broad band noise is increased at the high frequency end of the spectrum. The overall SPL is increased by about 4dB.

DISCUSSION AND CONCLUSIONS

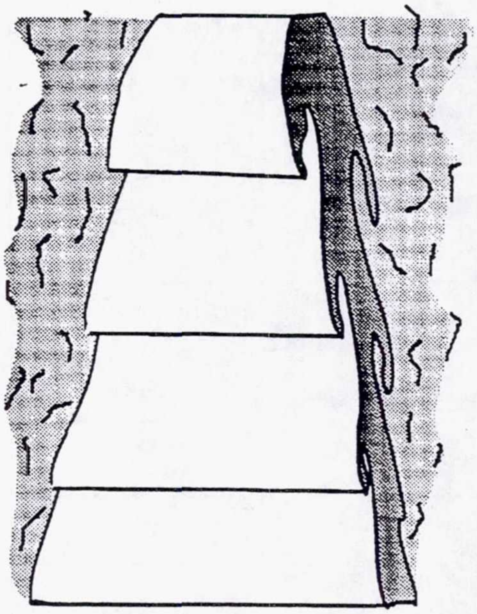

Figure 13: Breakdown of the Jet Column

We have demonstrated that mixing in supersonic jets can be enhanced by utilizing the flapping mode of small aspect ratio rectangular jets. High amplitude excitation of the flapping mode was accomplished by destabilizing the jet column and by amplification of the natural screech tones. The result is a considerable reduction in the length of the potential core of the jet and a rapid decay of the convection speed of the Kelvin Helmholtz instability waves. Acoustic measurements in the far-field of the jet indicate that noise radiation is not reduced in the current design of a flip-flop jet at $M = 1.45$. This is due to an increase in the mixing noise. Unlike in two-dimensional jets, the large scale coherent structures in the flip-flop jet do not extend infinitely along the major axis of the jet. On both ends of the rectangular jets, the coherent structures cannot maintain their two-dimensional shape and rapidly break down into small scall turbulence. This is illustrated by the sketch in Figure 13. The disintegration of the coherent structures is responsibe for the fast mixing of the jet. The increase in the high-frequency content of the noise spectra taken in the major axis plane is associated with the breakdown of the coherent structures.

The contribution of Mach wave radiation to the total acoustic power of the jet increases with the Mach number. We hope that at $M = 2.0$, the increase in mixing noise of the flip-flop nozzle will be more than offset by the reduction in Mach wave radiation. We also consider using the flip-flop nozzle in conjunction with an ejector. The rapid mixing in the flip-flop jet would increase the efficiency of ejectors in entraining ambient air. Lining on the inner walls could be used to absorb the high-frequnecy mixing noise in the major axis plane. Supported by NASA Grant NAG-1-1096 and Zumberge Research Innovation Fund, USC.

CONCLUSIONS

MIXING ENHANCEMENT

- FLAPPING MODE OF RECTANGULAR JET
- DESTABILIZATION OF THE JET COLUMN
- SELF-EXCITATION BY SCREECH
- SIMPLE, PASSIVE DEVICE

1999176557

EFFECT OF SWIRL ON NOISE FROM A HIGH ASPECT RATIO RECTANGULAR NOZZLE

M.K. Ponton, J.M. Seiner, and L.K. Mitchell
NASA Langley Research Center
Hampton, Virginia

S24-07

409532
16P.

INTRODUCTION

Based on extensive work performed by Dr. Thomas H. Sobota (Advanced Projects Research Incorporated (APRI)) *on swirling flows in circular-to-rectangular* transition sections, a model assembly was designed and fabricated in support of a Phase I Small Business Innovation Research Contract between the NASA-Langley Research Center and APRI. This assembly was acoustically tested as part of this Phase I effort, the goal being to determine whether the controlled introduction of axial vorticity could affect the various noise generation mechanisms present in an underexpanded supersonic rectangular jet.

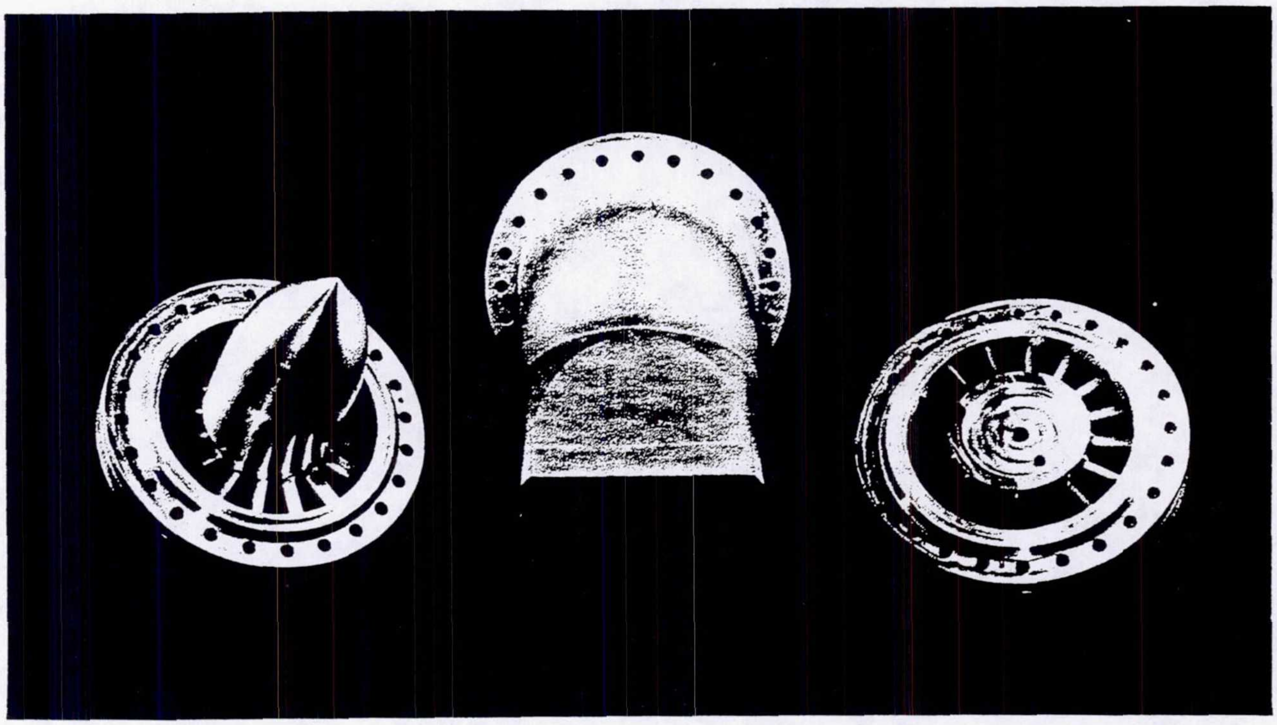

Figure 1: **TEST ARTICLE DEFINITION**

Figure 1 presents the nozzle hardware tested in this investigation. In the center of the figure is the convergent rectangular nozzle of aspect ratio 5 (exit dimensions: 1.020 in. by 5.100 in.). Three turning vane assemblies were fabricated, each containing sixteen symmetric airfoils at a fixed angle to the nozzle axis. The three turning vane angles used were 0, 15, and 30 degrees. Pictured in the left of the figure is the 30 degree swirl stage connected to the centerbody assembly. The upstream side of the centerbody is hemispherical and the downstream side is conical. The design philosophy of the centerbody and the internal contour of the nozzle assembly (i.e., the assembly which transitions from the round inlet to the rectangular exit) was such that when the centerbody is inserted into the nozzle, the internal area decreases smoothly from inlet to exit. Pictured to the right of the nozzle is the 15 degree turning vane subassembly. All hardware was fabricated from 6061-T6 aluminum alloy.

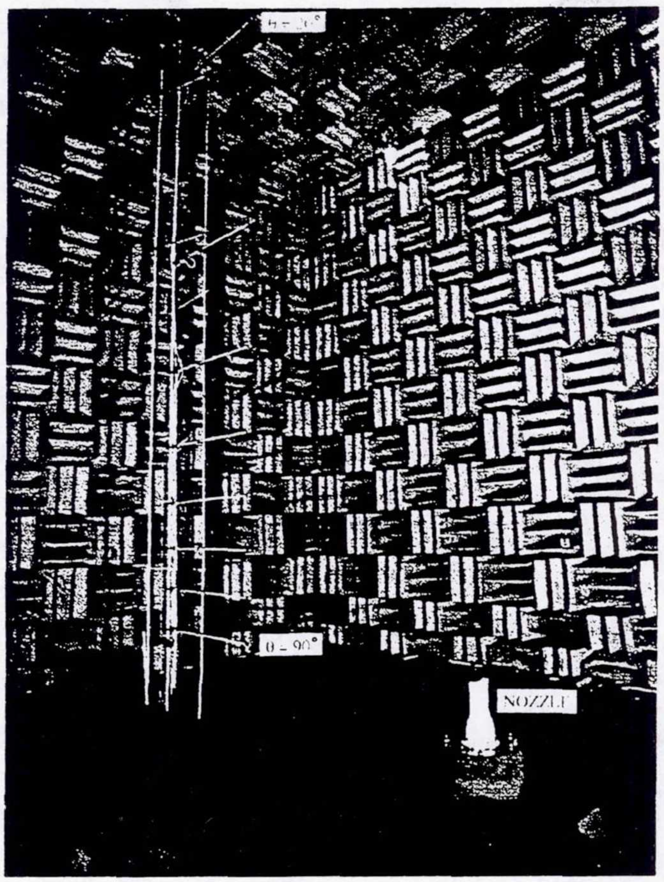

Figure 2: **EXPERIMENTAL SETUP**

The acoustic experiment was performed in the Langley Anechoic Noise Facility (LANF). This facility's interior dimensions within the wedge tips are 27.5 by 27 by 24 ft high. The LANF is capable of supplying continuous dry unheated air. Electronically controlled valves maintained the nozzle pressure ratio to within 0.5 percent of the desired set point. All pressure transducers used in the flow control system received daily calibration.

Spectra were acquired via a linear microphone (Fig. 2) array located parallel to the jet axis at a radial distance of 85.7 inches. Eight microphones were located at polar angles (θ) from 20 to 90 degrees at equal intervals of 10 degrees (the polar angle is referenced to the downstream jet axis from the nozzle exit; in Fig. 2, only the 20 and 90 degree microphones are labeled). The sensors used were 1/4-inch free-field microphones. No protective grid cap was used during data acquisition. The acoustic signals were filtered (63 Hz to 100 Khz), amplified and then multiplexed whereby spectra were then computed using a spectrum analyzer. The spectra were recorded from 50 Hz to 40 Khz using 128 spectral averages (filter bandwidth = 50 Hz). The overall voltage levels (bandlimited 63 Hz to 100 kHz) were measured with a digital RMS voltmeter which performed 256 samples per reading.

Narrowband spectra were gathered for 8 azimuthal angles (ϕ = 0, 15, 30, 45, 60, 75, 90, 135 degrees) where the azimuthal angle is referenced from the minor axis of the rectangular nozzle. Four nozzle pressure ratios were measured (1.69, 3.0, 3.5, 4.0) for the three swirl angles tested (0, 15, and 30 degrees).

Due to the magnitude of the acoustic measurements, select conditions are presented. All data presented are corrected to a circular arc of radius 85.7 inches by assuming spherical spreading. This correction is performed so that peak acoustic amplitude radiation angles can be determined.

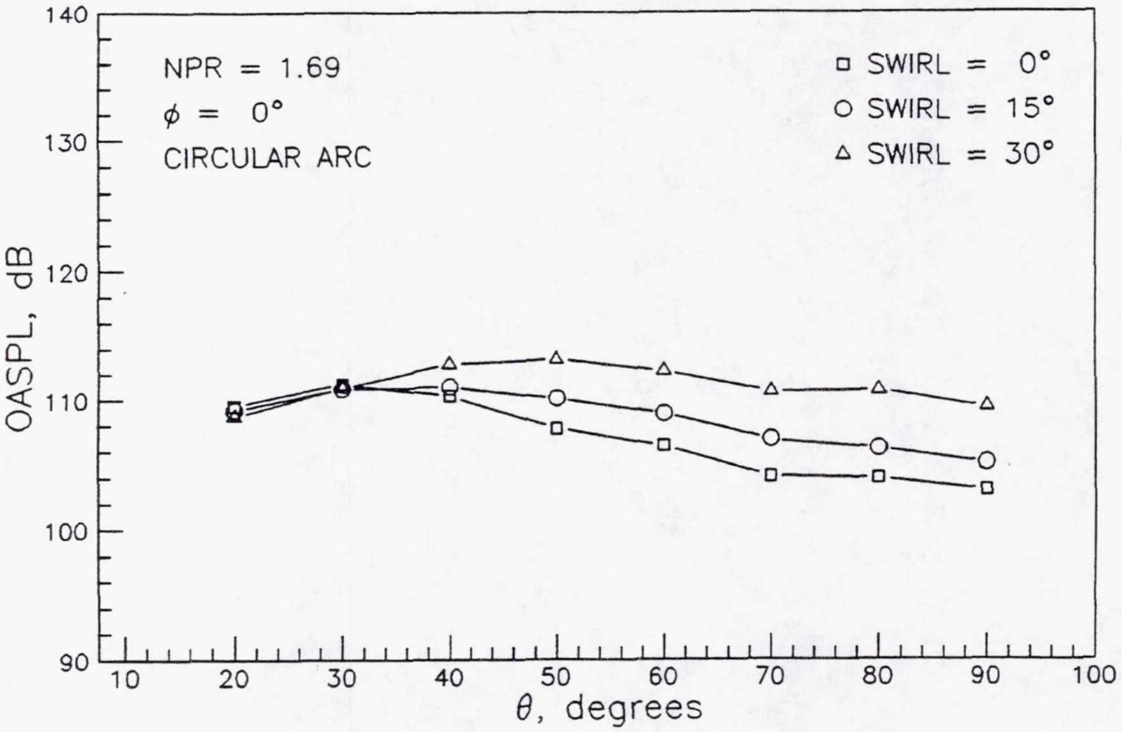

Figure 3: **OVERALL SOUND PRESSURE LEVEL (NPR = 1.69, Φ = 0 DEGREES)**

For the subsonic condition tested, Figure 3 shows that an increase in jet swirl increases the overall sound pressure level, the exceptions being at low polar angles. The low polar angles represent the peak jet noise direction which is determined by examining the direction of the maximum acoustic amplitude associated with the peak jet noise Strouhal number.

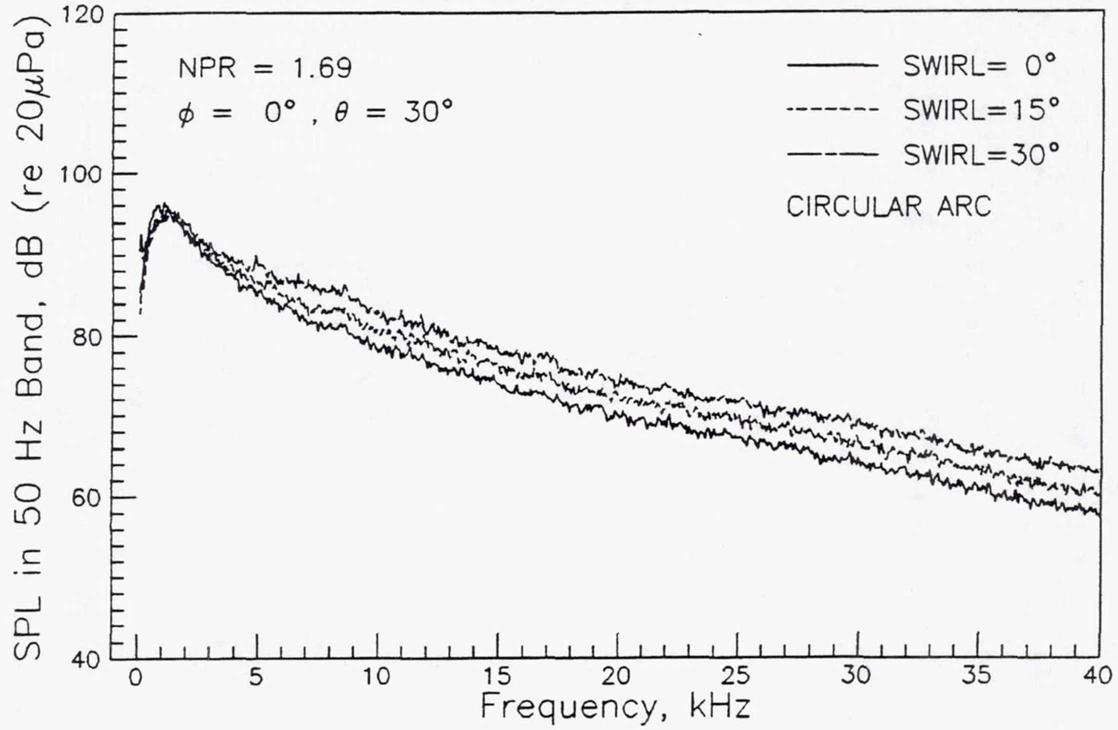

Figure 4: **NARROWBAND SPECTRA (NPR = 1.69, Φ = 0 DEG., Θ = 30 DEG.)**

The peak jet noise components can be seen in Figure 5 centered at approximately 1 kHz (the maximum jet noise amplitude for the no swirl case occurred at the measured polar angle of 20 degrees). Although the OASPL at polar angles of 20 and 30 degrees for 0 degree azimuthal angle is invariant with swirl angle (Fig. 3), Figure 4 indicates a slight decrease in the amplitude of the low frequency peak jet noise component while a broadband increase occurs for the higher frequencies when swirl is introduced.

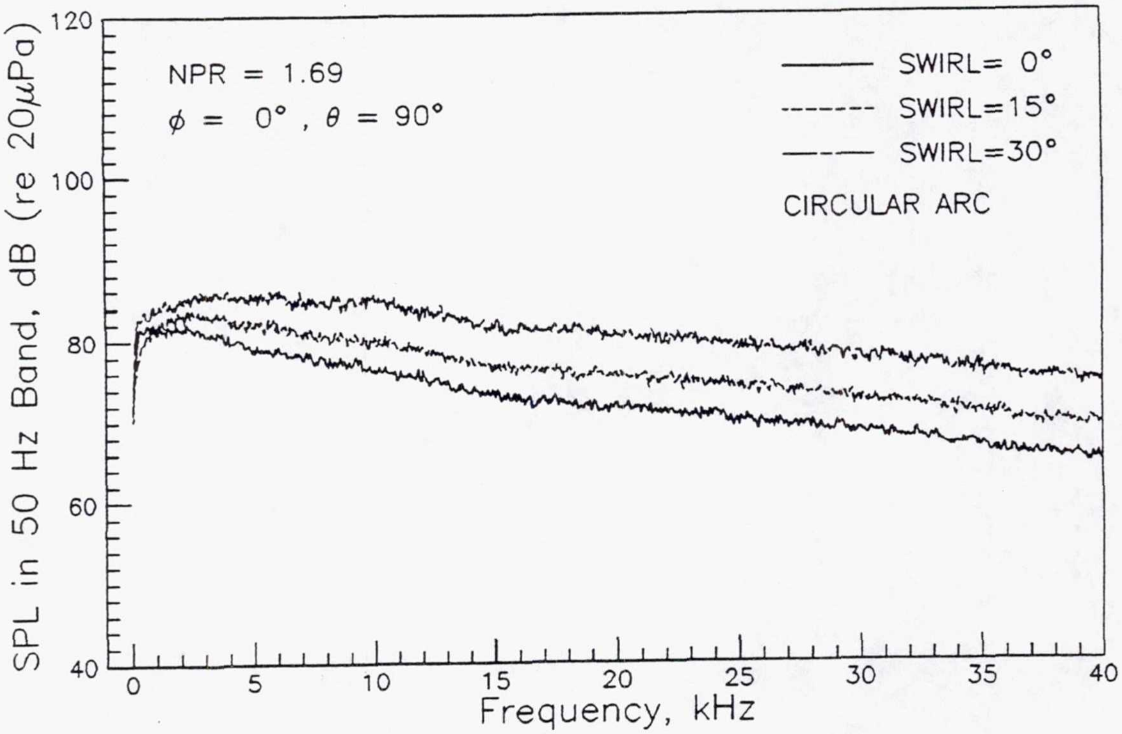

Figure 5: **NARROWBAND SPECTRA (NPR=1.69, Φ=0 DEG., Θ=90 DEG.)**

The broadband increase seen in Figure 4 is also evident at other polar angles of which Figure 5 is representative. Similar peak jet noise reductions and high frequency increases are seen for the other azimuthal angles tested. These high frequency increases may be an indicator that the addition of axial vorticity has increased the amplitude of the high frequency sources located near the nozzle exit. It is at this location that the dominant portion of high frequency noise is generated.

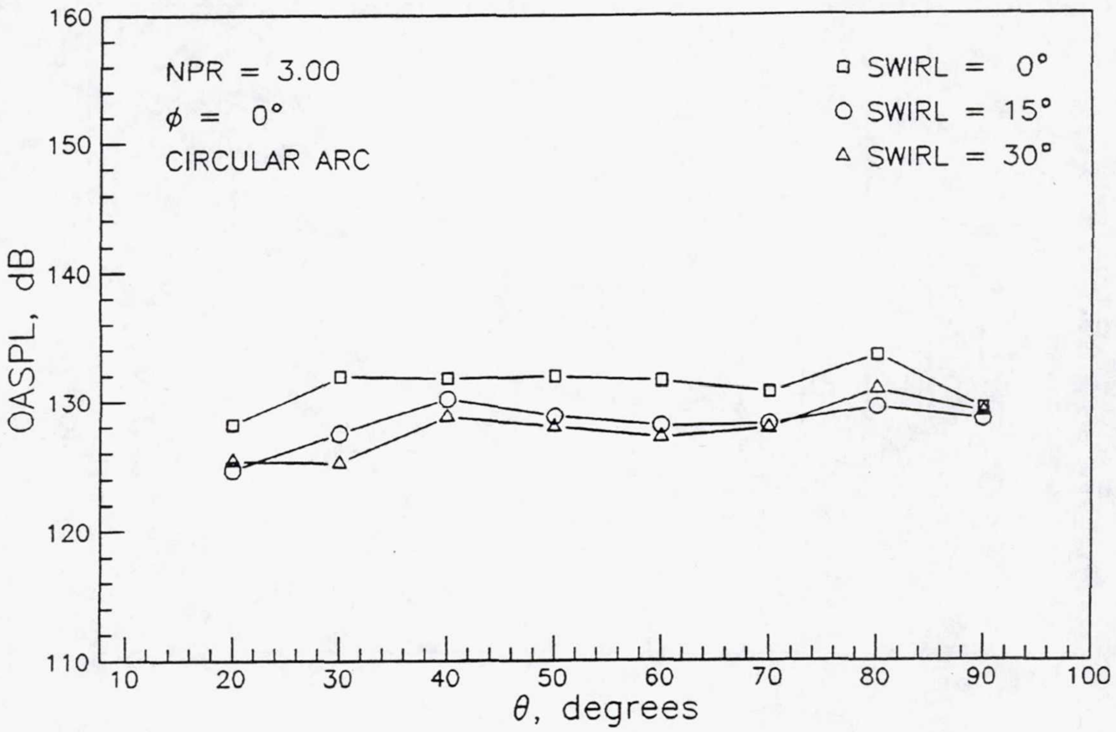

Figure 6: **OVERALL SOUND PRESSURE LEVELS (NPR = 3.00, Φ = 0 DEG.)**

The overall sound pressure level data (Fig. 6) indicate that an increase in jet swirl can provide noise reduction for supersonic operating conditions. Although not shown, for higher azimuthal angles the OASPL benefit occurs only at low polar angles.

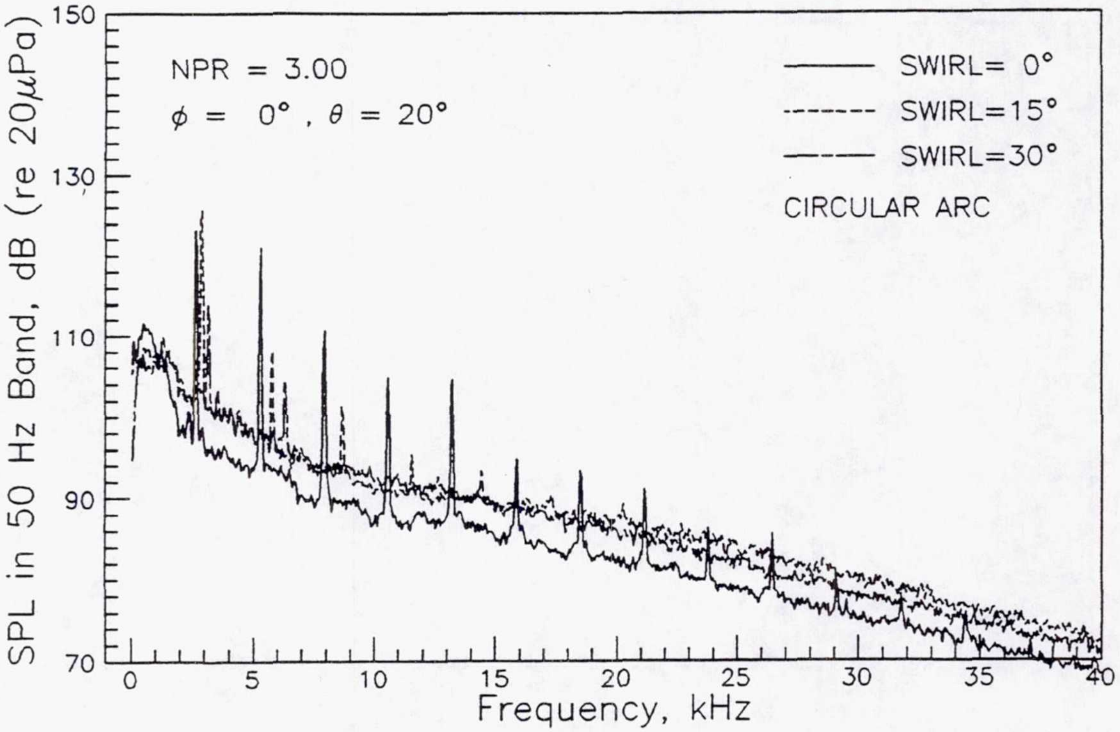

Figure 7: **NARROWBAND SPECTRA (NPR = 3.00, Φ = 0 DEG., Θ = 20 DEG.)**

Figure 7 indicates that swirl reduces the low frequency jet noise amplitude seen at approximately 1 kHz (this is more evident in the peak jet noise direction of $\theta = 30$ degrees presented in Fig. 8). Note that swirl has increased the frequency of the screech fundamental (located between 2 and 3 kHz). The amplitude of the screech harmonics have significantly decreased with increasing swirl (true for most polar angles). Except for the low frequency jet noise peak, increasing swirl increases the broadband spectrum level. The difference in the spectrum levels of the 15 and 30 degree swirl angles is small below 20 kHz.

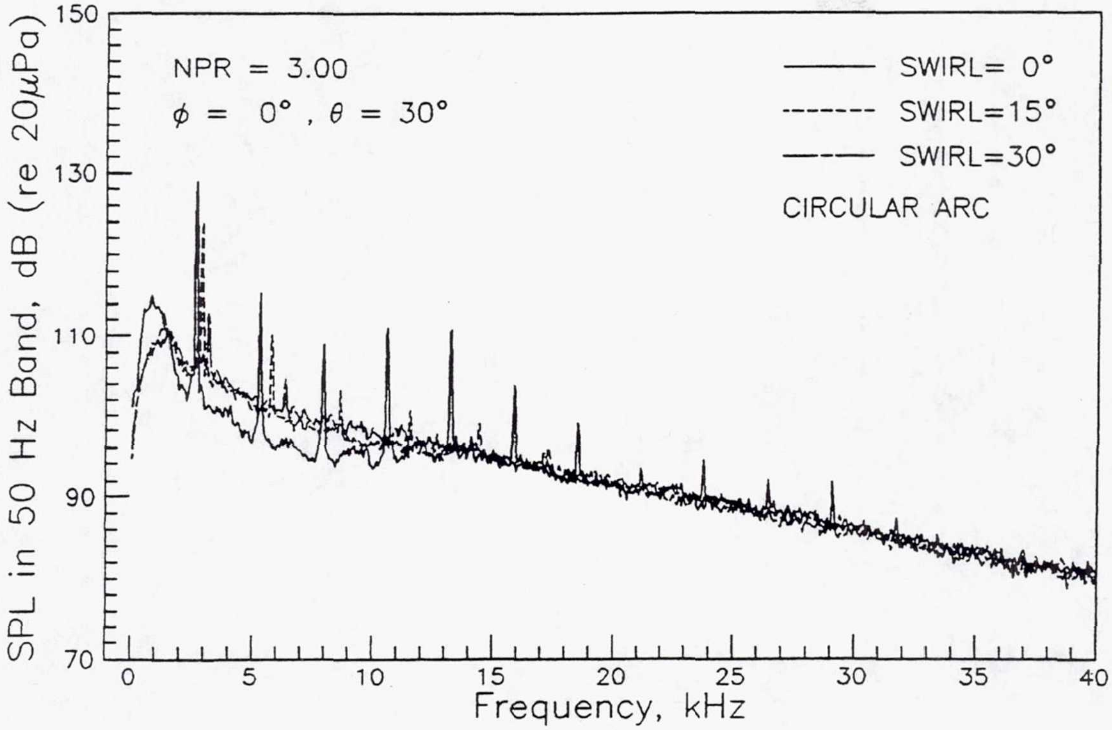

Figure 8: **NARROWBAND SPECTRA (NPR=3.00, Φ=0 DEG., Θ=30 DEG.)**

At a polar angle of 30 degrees (Fig. 8), the spectral shape for the baseline configuration (0 degree swirl) has changed where the amplitude above about 9 kHz has increased to closely match the swirling configurations. As the polar angle increases, the spectral shape of the no swirl case begins to match that of the swirling flows. The high frequency amplitude also begins to increase with swirl as the polar angle approaches 90 degrees.

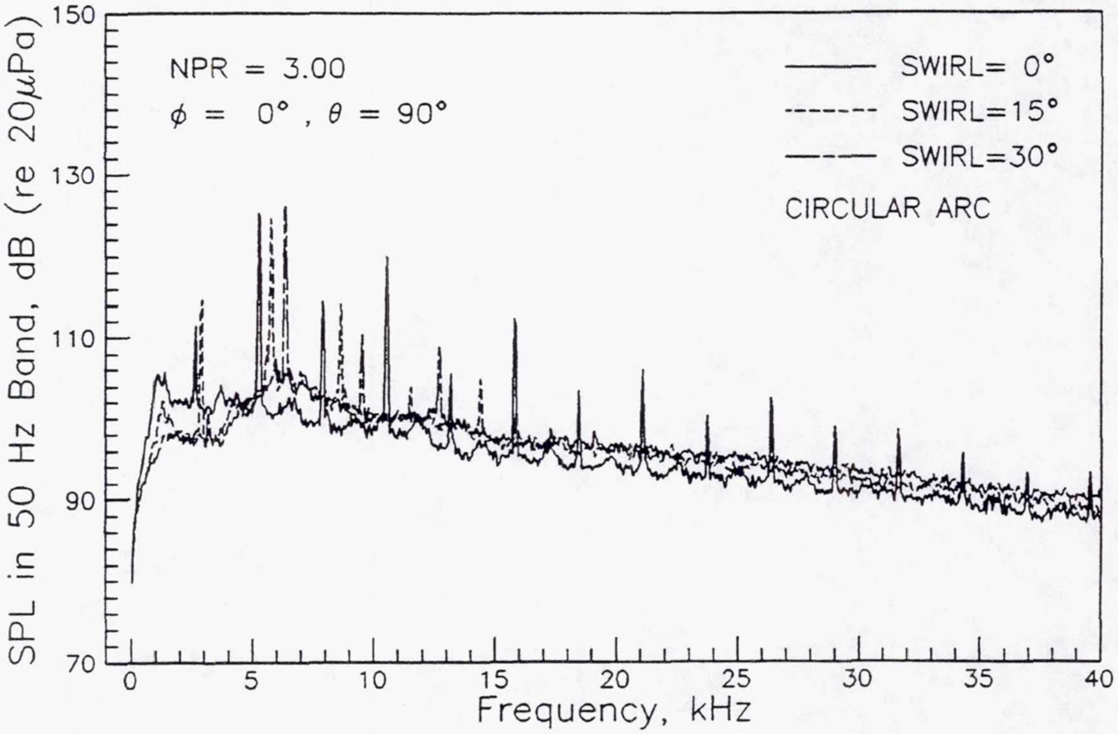

Figure 9: **NARROWBAND SPECTRA (NPR=3.00, Φ=0 DEG., Θ=90 DEG.)**

Figure 9 shows that while the low frequency reductions seen at the low polar angles are still present (approximately 1 kHz), the addition of swirl has increased not only the spectrum level at high frequencies but also the broadband shock associated noise at approximately 6.5 kHz. The affect of swirl on the amplitude of the second and third screech harmonics is minimal while the amplitude of higher harmonics is still reduced.

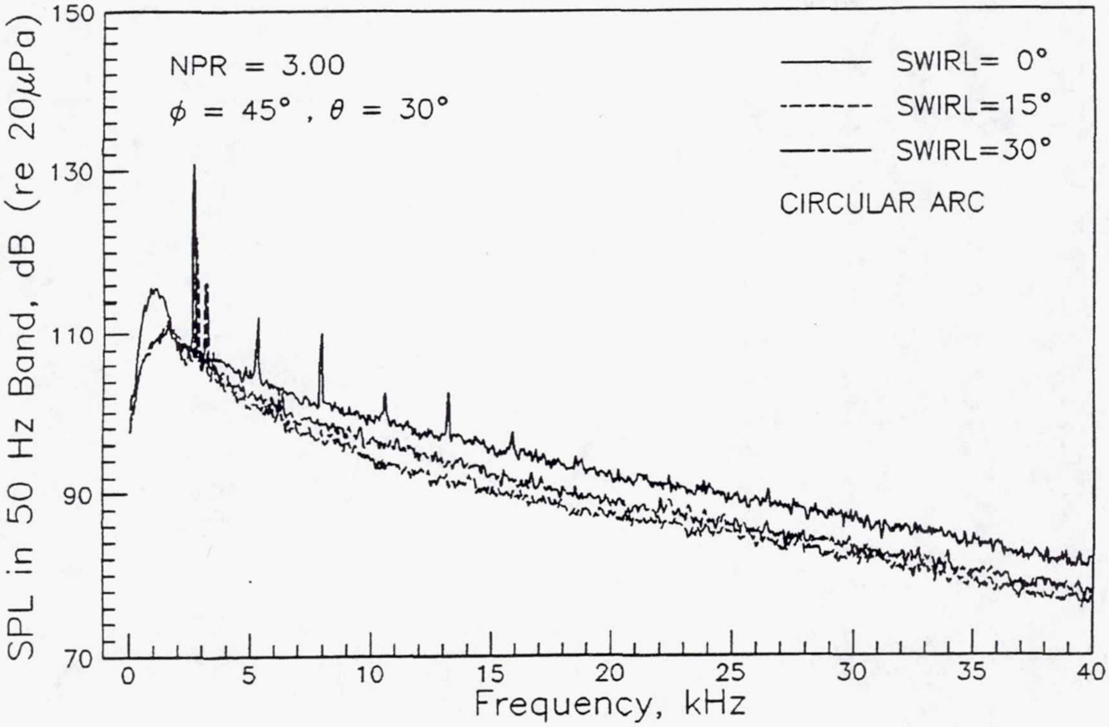

Figure 10: **NARROWBAND SPECTRA (NPR=3.00, Φ= 45 DEG., Θ=30 DEG.)**

At an azimuthal angle of 45 degrees, Fig. 10 indicates that the high frequency amplitude decreases for increasing swirl. This effect is true only for low polar angles. Similar to the $\phi = 0$ degree condition, the amplitude of the screech fundamental and its harmonics is reduced by swirl addition. Also for the azimuthal angle of 45 degrees, the low frequency jet noise amplitude is reduced by introducing axial vorticity as can be seen in the broadband component located at 1 kHz.

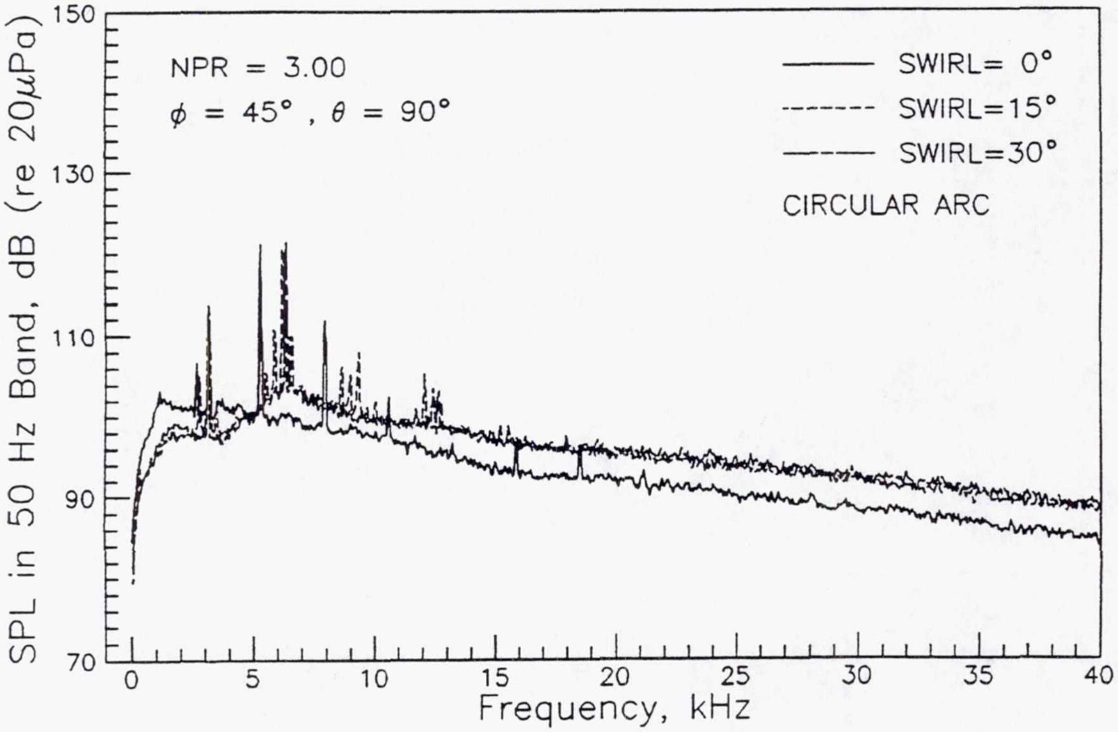

Figure 11: **NARROWBAND SPECTRA (NPR=3.00, Φ=45 DEG., Θ=90 DEG.)**

The acoustic effects of swirl addition at Phi=45 degrees (Fig. 11) is similar to those at $\phi=0$ degrees (fig. 9) for the normal polar angle. These effects are: low frequency jet noise reduction, increase in broadband hock noise, increase in the high frequency spectrum level, minimal affect on the second (and for the 15 degree swirl case third) screech harmonic amplitude. Also note that at the emission angle of Fig. 11, the addition of swirl has created additional narrowband peaks to occur in the spectrum which can be seen near the screech harmonics.

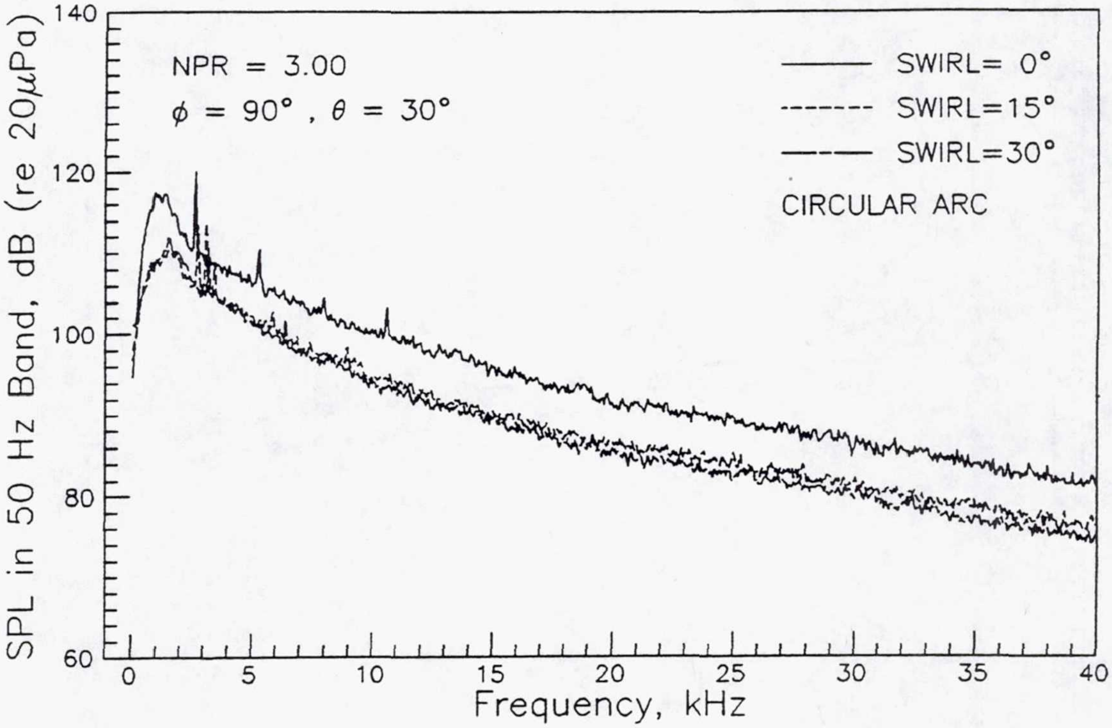

Fig. 12: **NARROWBAND SPECTRA (NPR=3.00, Φ=90 DEG., Θ=30 DEG.)**

Figure 12 represents data measured along the major axis of the nozzle (i.e., in a direction normal to the plane containing the minor axis and the nozzle centerline). Broadband amplitude decreases are evident when swirl is introduced into the flowfield. Note that for the baseline condition (0 degree swirl) screech emission is not large in this radiation direction. The spectral differences between the 15 and 30 degree swirl configurations are minimal in this figure.

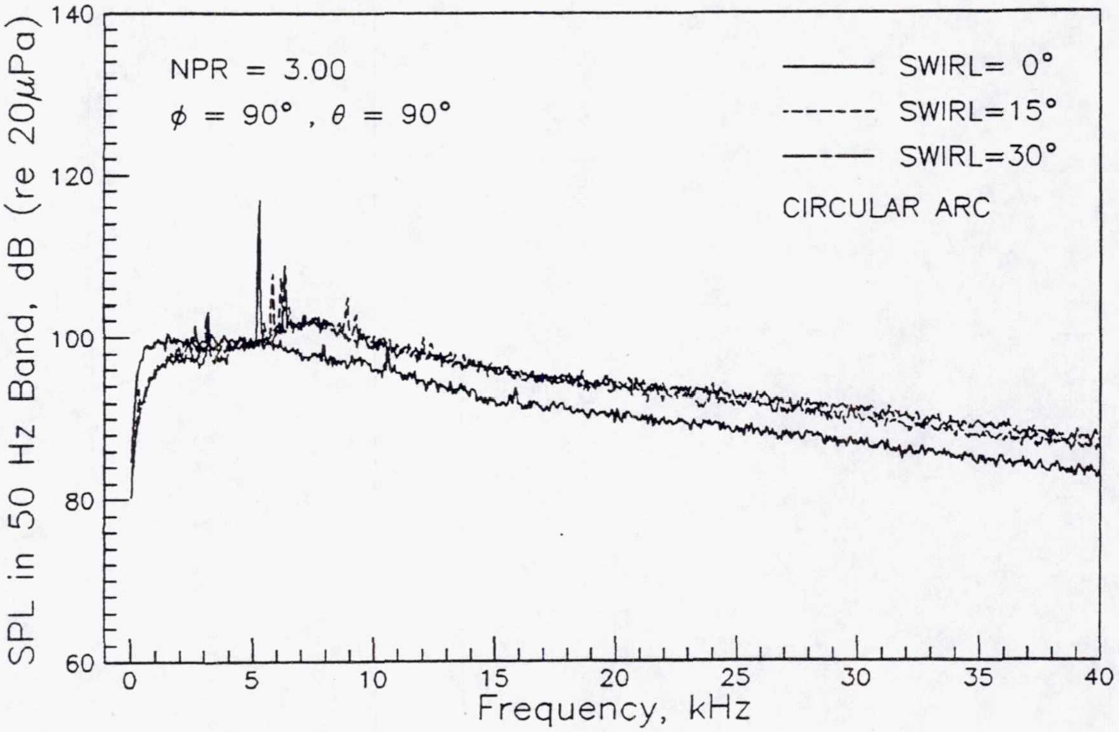

Figure 13: **NARROWBAND SPECTRA (NPR=3.00, Φ=90 DEG., Θ=90 DEG.)**

Figure 13 indicates that the effects seen by swirl addition in Figures 9 and 11 (ϕ=0 and 45 degrees, respectively) are still present at ϕ=90 degrees except that the second harmonic amplitude is no longer similar between the no swirl and swirl conditions.

CONCLUSIONS

Introducing axial vorticity in the manner of this research program has been observed to cause:

- Broadband high frequency increase (NPR = 1.69)
- Peak low frequency jet noise reduction
- Broadband shock noise increase (supercritical NPR's)
- Screech harmonic reduction (NPR = 3.0, 3.5)

19991765 52

APPLICATION FOCUSED SCHLIEREN TO NOZZLE EJECTOR FLOWFIELDS

L. Kerry Mitchell, Michael K. Ponton, John M. Seiner, James C. Manning
NASA Langley Research Center
Hampton, Virginia

and

Bernard J. Jansen and Nicholas T. Lagen
Lockheed Engineering and Sciences Company
Hampton, Virginia

515-07

409533

16P.

RESEARCH OBJECTIVE

Motivation: Eddy Mach wave emmission reduction via enhanced mixing
- Ejector shroud
- Contour of mixer exit

Experiment Objective: Visualize mixing performance on inside of ejector

The motivation of the testing was to reduce noise generated by eddy Mach wave emmission via enhanced mixing in the jet plume. This was to be accomplished through the use of an ejector shroud, which would bring in cooler ambient fluid to mix with the hotter jet flow. In addition, the contour of the mixer, with its chutes and lobes, would accentuate the merging of the outer and inner flows. The objective of the focused schlieren work was to characterize the mixing performance inside of the ejector. Using flow visualization allowed this to be accomplished in a non-intrusive manner.

INTRODUCTION TO FOCUSING SCHLIEREN

Figures of Merit:

DU = depth of unsharp focus, to be minimized
ε = angular resolution (~ 1 / sensitivity), to be minimized

Design considerations:

DU requires large D, ε requires small D
Tunnel walls impose constraints on size, mounting

Compromise:

DU = 1.3"
ε = 16 arc-sec

Focusing schlieren was utilized in this work because of its advantages over conventional schlieren. Conventional schlieren requires the use of high quality optical windows. These windows, when subject to aerodynamic stresses on a wind tunnel model, may adversely affect image quality. In addition, with conventional schlieren, the image is integrated over the optical path. With focusing schlieren, it is possible to focus on specific planes in the flowfield. The figures of merit for focusing schlieren are the depth of unsharp focus, that is, the distance over which features become fuzzy; and the angular resolution, which is inversely proportional to the sensitivity of the system. Both of these are to be minimized, which leads to a tradeoff. In this installation, the wind tunnel walls provided additional constraints, as the source and collecting optics were placed outside of the tunnel. As a result, the depth of unsharp focus was 1.3 inches and the angular resolution was 16 arc-seconds.

LARGE-FIELD FOCUSING SCHLIEREN APPARATUS

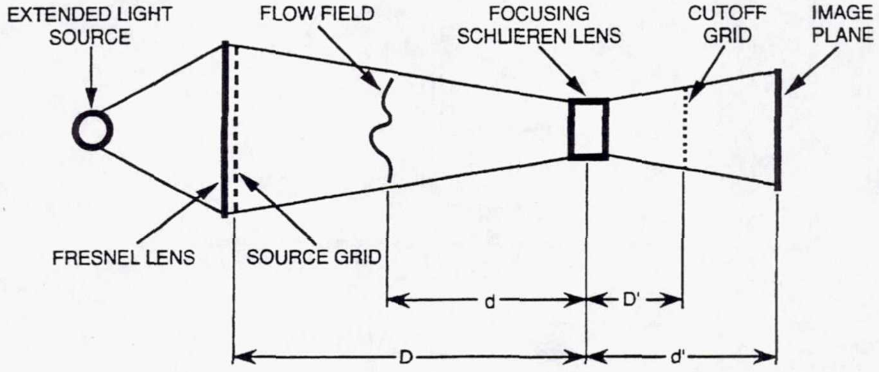

NASA Facility	Lewis	Langley
D (in)	115	88.5
d (in)	50	34.3
D' (in)	27.2	29.3
d' (in)	39.3	61.5
DU (in)	1.31	0.90
ε_{min} (arc-sec)	15.8	19.1

Schematically, a large-field focusing schlieren apparatus consists of source, collecting, and imaging optics. The source optics were comprised of an extended light source (e.g., laser), which was diffused into a fresnel lens. After the lens, the light passed through a source grid, which served to break the light into several slit sources. These sources passed through the flowfield, where they were diffracted by the density gradients in the flow, and were collected by the cutoff grid, the photographic negative of the source grid. This had an analogous function to the knife edge in a conventional schlieren system. Finally, the image was produced on the image plane which was in turn either photographed or videotaped. It was the movement of the image plane which allowed the system to focus on different planes in the flowfield.

SHARP FOCUS SCHLIEREN APPARATUS
NASA LEWIS 9 X 15 WIND TUNNEL

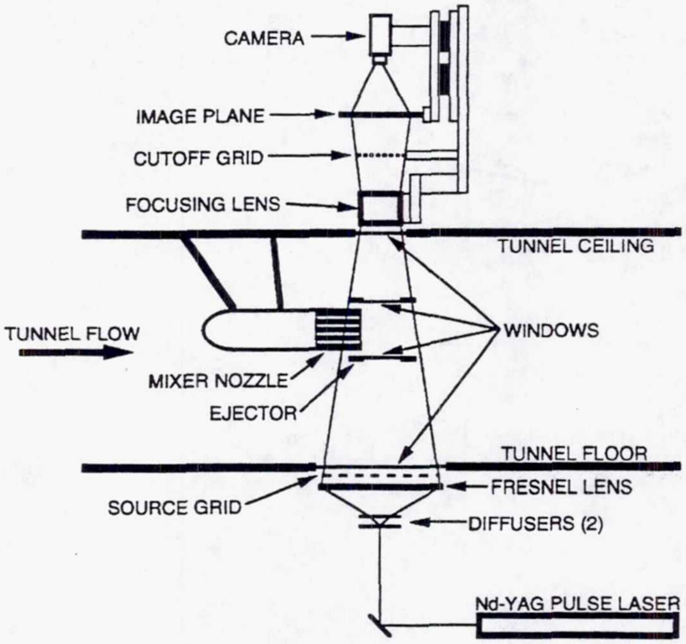

For the present work, the system was installed with the optical axis vertical in the Lewis 9x15 Low Speed Acoustic Wind Tunnel. The light source was a Nd-YAG pulsed laser, frequency doubled to a 532 nm (green) line. The beam left the laser nominally horizontal and was folded to vertical for passage through the tunnel. Two diffusers were used to spread the beam so that it would fill the fresnel lens and source grid. The diffusers, source grid and fresnel lens were mounted underneath, and isolated from, the tunnel floor. The light intersected the ejector flowfield and was collected by optics mounted above the tunnel ceiling. The collecting lens, cutoff grid, and imaging optics were all mounted on a vertical support, isolated from the tunnel A 35 mm still camera and a video camera were used to record images from the image plane. The image plane and cameras were mounted on a vertical traverse, allowing remote selection of focusing planes. The installation of the source and receiving optics was such that the system was not subject to tunnel vibrations. Because of the focusing nature of the schlieren, imperfections and slight motions of the windows in the tunnel walls did not affect the image quality.

HSR NOZZLE STUDIED WITH SHARP FOCUS SCHLIEREN


Mixer ejector nozzle

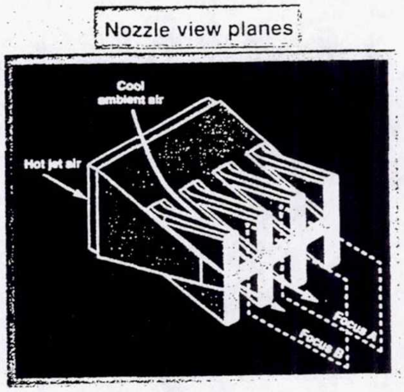
Nozzle view planes

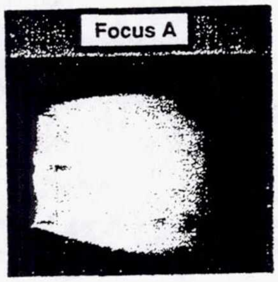
Focus A

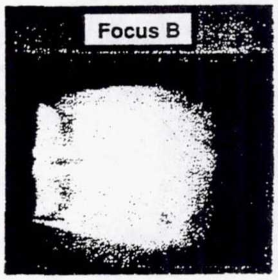
Focus B

This figure illustrates the nozzle and representative images obtained with the focus schlieren. The mixer nozzle is shown installed in the Lewis 9 x 15 Foot Low Speed Aeroacoustic Wind Tunnel. Also shown is a schematic of the mixer, indicating two planes of focus. Plane A is through a chute at the center of the mixer and plane B is toward one end. Representative views at each of the focus planes are shown. Differences in the detailed structure of the plume can be seen between the central and outer views.

Right End View at Mixer Exit

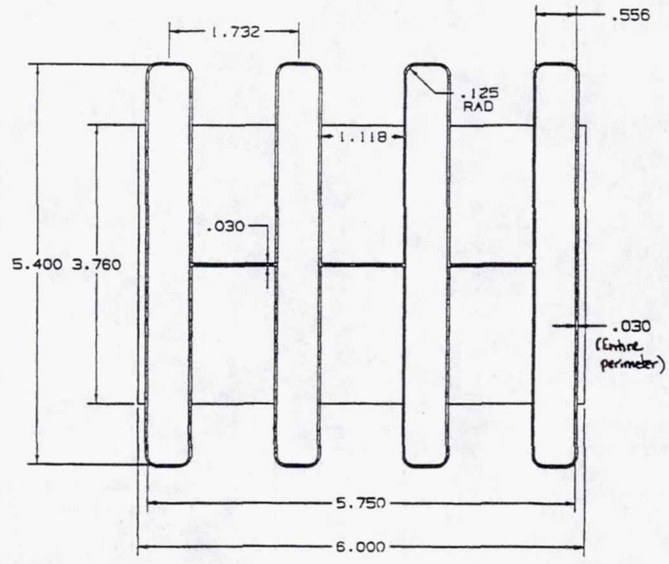

Right End View at Mixer Exit

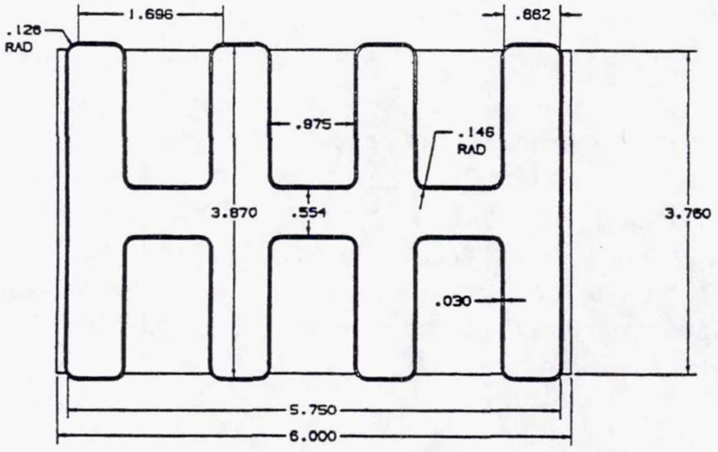

This figure shows the two mixers tested. The upper was identified as the "axial" mixer, and is essentially 4 high aspect ratio rectangular jets. The central portion between lobes was to be sealed, but video analysis revealed that this seam leaked. The lower mixed was the "vortical" mixer, in which the four lobes were joined by a central channel almost as wide as a lobe. The height of the lobes was adjusted so that both mixers had the same exit area.

AVERAGED DIGITIZED VIDEO RECORD

POSITION = 3.41"

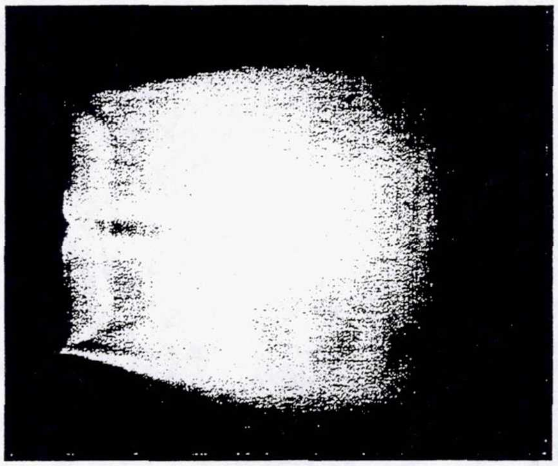

An averaged video record is shown, for the vortical mixer operating without the ejector shroud. Ten video frames were averaged over 1/3 second. The nozzle was operating in an underexpanded condition, at a nozzle pressure ratio of 4.0 and a total temperature of 1500F. The focal plane was at the center of the nozzle, and diamond shocks from the central channel of the mixer are clearly visible.

AVERAGED DIGITIZED VIDEO RECORD

POSITION = 3.41"

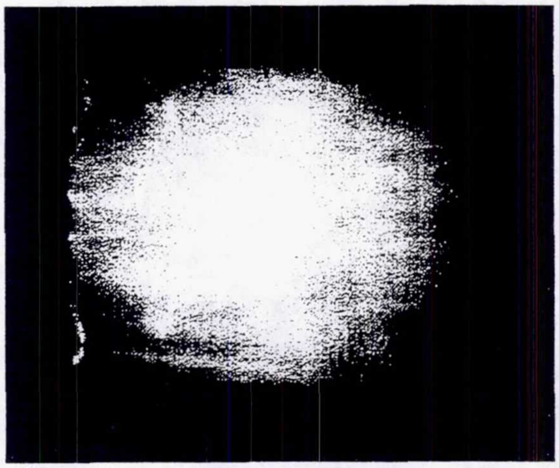

In this record, the mixer was operating with the ejector, at a nozzle pressure ratio of 3.5 and a temperature of 1275F, the nozzle's design point. The focal plane was again at the center, and weak diamond shocks are visible. The weak shock structures were validation of the shock-free design of the mixer. Also present were shocks at the inlet of the ejector, indicators of performance degradations.

AVERAGED DIGITIZED VIDEO RECORD
POSITION = 5.95"

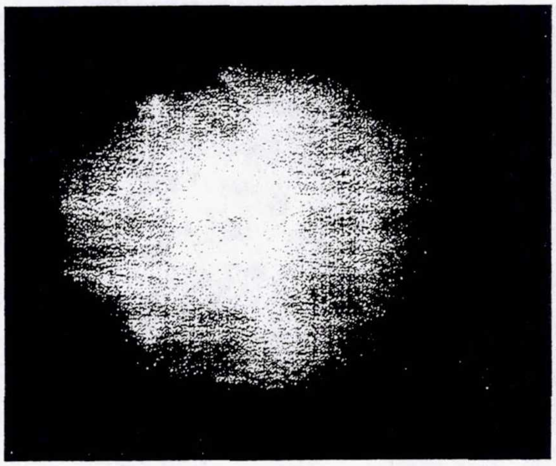

This record was taken at a focal position through an outer lobe, a distance of 1.5 "*depth of unsharp focus*" *from the center.* The operating conditions were the same as the previous figure. The difference are seen in the shock structures; the central diamond shock is no longer visible due to not being in the region of unsharp focus.

DIGITIZED VIDEO RECORD SHOWING STREAKS CAUSED BY INTERNAL NOZZLE LEAK

(FOCUSED AT THE EJECTOR WINDOW)

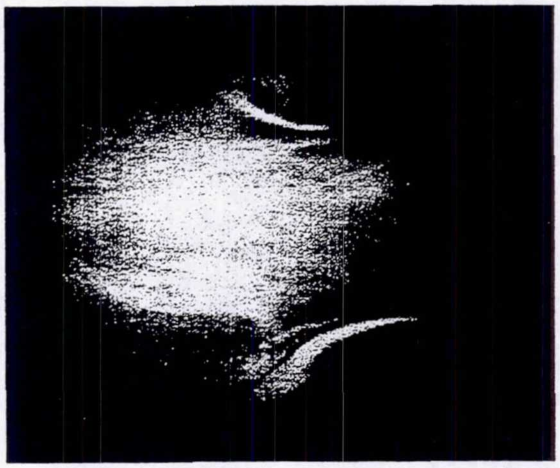

In the previous record, background streaks were apparent. These were due to sealant from the mixer leaking onto the ejector windows. By focusing on the window, these streaks became very clear. As the focus moved to the center, the streaks were essentially unnoticed.

35mm PHOTOGRAPH SHOWING MACH WAVE EMISSION

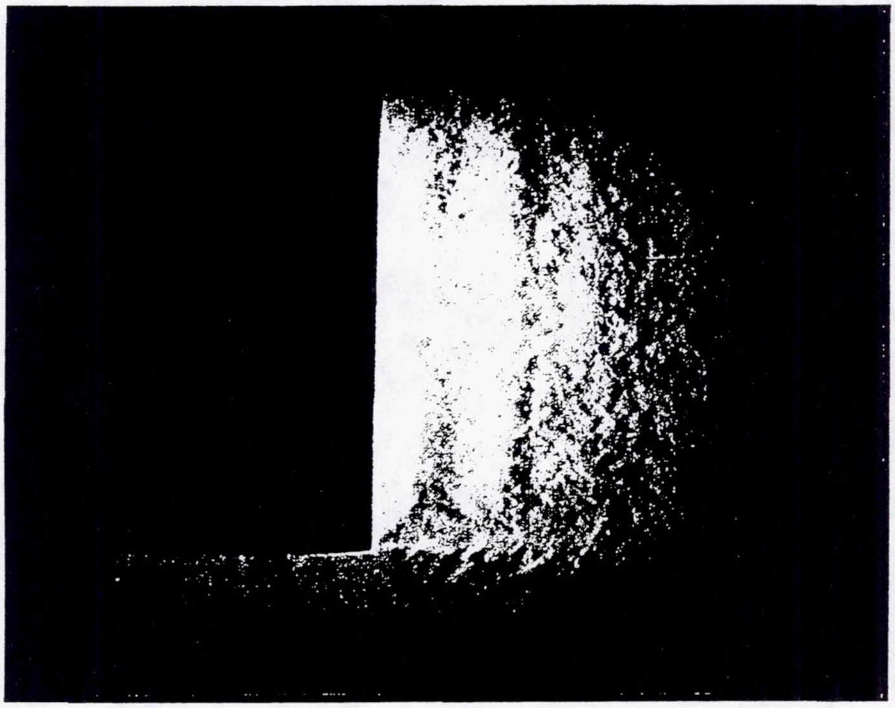

This record shows the axial mixer, operating underexpanded at a nozzle pressure ratio of 4.0 and a temperature of 1500F. Instead of averaging video frames, this still was taken with a 6 ns exposure on a 35 mm camera. This nearly instantaneous snapshot of the free jet shows clearly the eddy Mach wave emission from the shear layer, and the shock cell structures in the plume.

IMAGE PROCESSED SHARP-FOCUS SCHLIEREN
Pratt & Whitney Axial Mixer, no ejector

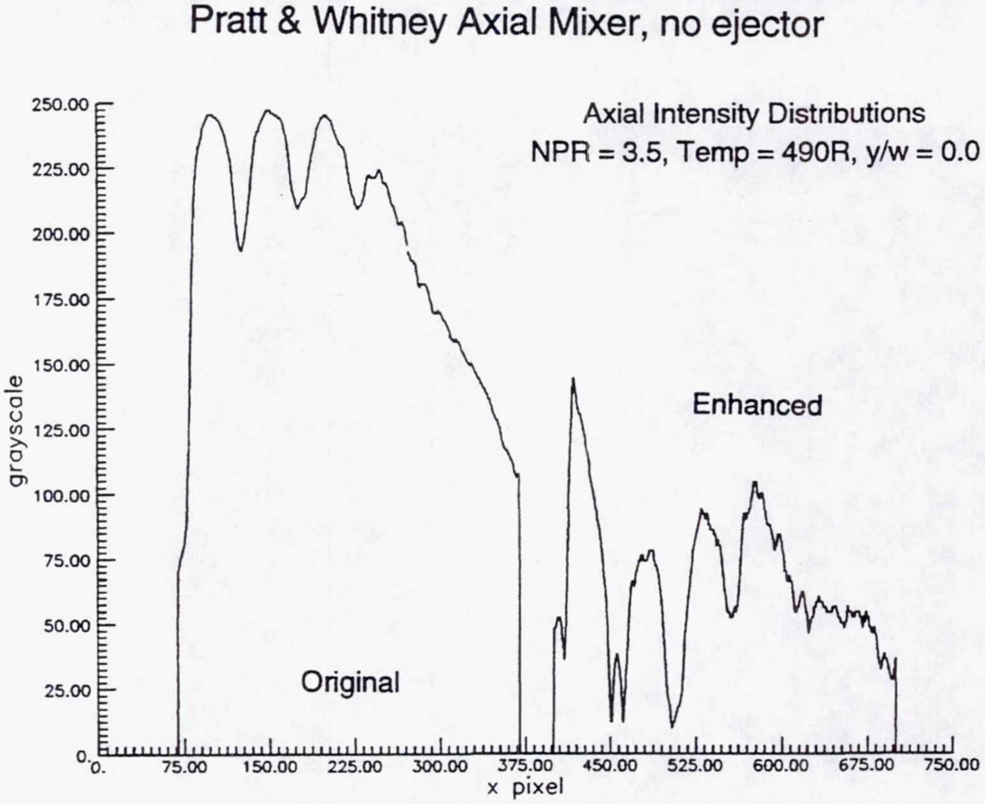

By utilizing a frame grabber and a computer in conjunction with the video taping of the schlieren, the images can be digitized and quantitative information can be obtained. For an averaged record of the axial mixer, horizontal slices of brightness were plotted. This was for a nozzle pressure ratio of 3.5 and ambient temperature. When the brightness through the center of the plume was plotted, peaks and valleys were observed that corresponded to the shock system immediately downstream of the exit. This distribution was enhanced by removing the effect of background illumination and increasing the contrast. The peaks were then correlated to shock strength and the distance between peaks to the shock cell length.

IMAGE PROCESSED SHARP-FOCUS SCHLIEREN
Pratt & Whitney Axial Mixer, no ejector

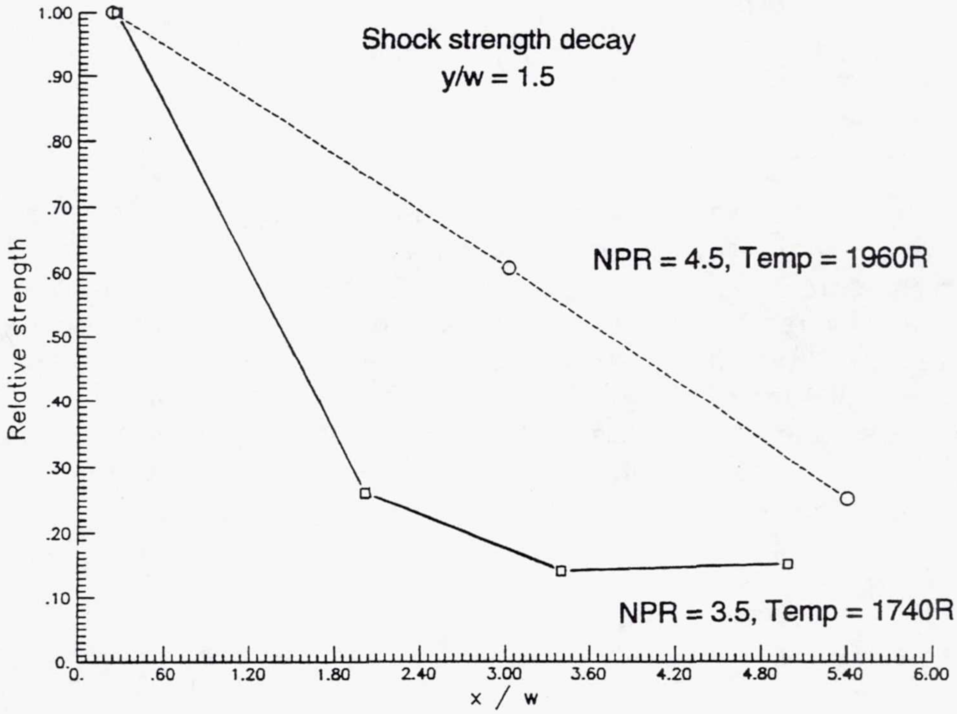

Upon digitizing a video record and plotting the brightness against downstream location, relative information about the shock systems were obtained. In this figure, the decay in relative strength is plotted for the axial mixer operating close to design and off design. (For reference, the first shock had strength 1.0.) In the present work, this was used more as an indicator of trends and proof of concept then as a scientific study of shock decay.

Focusing schlieren systems are viable for wind tunnel applications, as long as the constraints imposed by the tunnel are accommodated, and care is taken with the setup. Focusing schlieren systems have advantages over conventional schlieren in that: they can focus on planes in the flowfield, high-quality optical windows are not required, and images can be enhanced with appropriate usage of image processing tools. For mixer/ejector studies, focusing schlieren systems allow non-intrusive investigation of ejector flowfields, global visualization of shock cells and other structures, and quasi-quantitative characterizing of mixing performance.

CONCLUSIONS

Focusing schlieren systems are viable for wind tunnel applications:
- Design constraints imposed by tunnel
- Setup difficult, not impossible

Merits of focusing schlieren systems:
- Planes of the flowfield can be visualized
- Schlieren-quality model windows and optics can be avoided
- Acquisition of no-flow data can assist in image enhancement

Focusing schlieren systems can be useful in mixer/ejector studies:
- Non-intrusive nature allows investigation of ejector flowfields
- Global visualization of structures
- Quasi-quantitative mixing metrics

Session IV

Analytical Aeroacoustics I

1999176553

PARC ANALYSIS OF THE NASA/GE 2D NRA MIXER/EJECTOR NOZZLE

J.R. DeBonis
NASA Lewis Research Center
Cleveland, Ohio

516-07

409534

32P.

Interest in developing a new generation supersonic transport has increased in the past several years. Current projections indicate this aircraft would cruise at approximately Mach 2.4, have a range of 5000 nautical miles and carry at least 250 passengers. A large market for such an aircraft will exist in the next century due to a predicted doubling of the demand for long range air transportation by the end of the century and the growing influence of the Pacific Rim nations. Such a proposed aircraft could more than halve the flying time from Los Angeles to Tokyo. However, before a new economically feasible supersonic transport can be built, many key technologies must be developed.

Among these technologies is noise suppression. Propulsion systems for a supersonic transport using current technology would exceed acceptable noise levels. All new aircraft must satisfy FAR 36 Stage III noise regulations. The largest area of concern is the noise generated during takeoff. A concerted effort under NASA's High Speed Research (HSR) program has begun to address the problem of noise suppression. One of the most promising concepts being studied in the area of noise suppression is the mixer/ejector nozzle.

This study analyzes a typical noise suppressing mixer ejector nozzle at take off conditions, using a Full Navier-Stokes (FNS) computational fluid dynamics (CFD) code.

Objectives

- **Analyze the NASA/GE 2DCD mixer/ejector nozzle**
- **Gain a better understanding of mixer/ejector nozzle flow fields**
- **Provide data for improved designs**
- **Evaluate the ability of the PARC code to predict mixer/ejector nozzle flow fields**

The use of CFD can provide valuable information for aerodynamic analysis and design. The objectives of the study are to gain better insight into the nozzle flowfield and provide useful data for improvement of this design and future nozzle designs. Also, by comparing the analytical predictions to experimental data we can evaluate the ability of the CFD code to accurately predict mixer/ejector nozzle flowfields.

NASA/GE 2DCD
Mixer/Ejector Nozzle

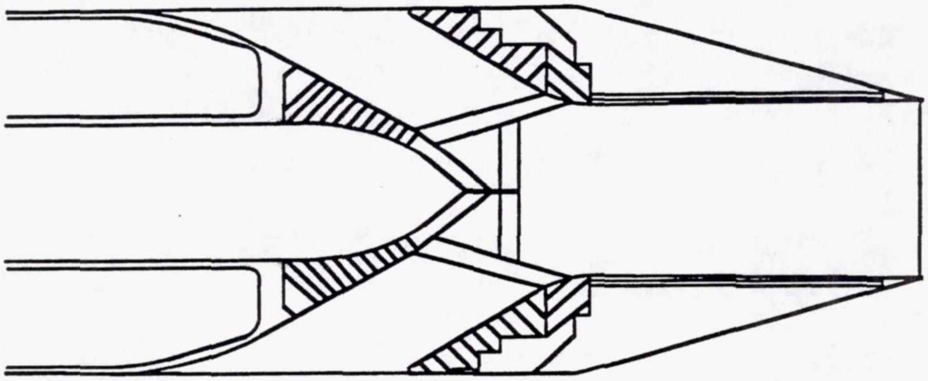

The General Electric Aircraft Engine Company, under a NASA NRA contract, has designed a two-dimensional (i.e. rectangular) mixer/ejector nozzle for noise suppression. This nozzle is intended to be used in conjunction with a mixed flow turbofan engine.

Mixer/Ejector Nozzles

- **Entrain large amounts of secondary flow**
- **Rapidly mix two flows together to lower jet velocity**
- **Lower jet velocity results in lower noise**
- **Maintain high thrust due to large mass augmentation**

$$F = \dot{m}v$$

Mixer/ejector nozzles entrain large amounts of secondary flow through an array of lobed chutes that are deployed into the primary stream. The low velocity secondary flow is rapidly mixed with the high energy primary flow from the engine to lower the total jet velocity. This lower jet velocity results in lower noise; however high thrust is maintained because of the large amount of flow augmentation.

NASA/GE 2DCD Nozzle

- **Rectangular (2D) mixer/ejector**
- **Short shroud**
- **SAR = 2.5 (suppressor area ratio)**
- **Convergent-divergent chutes**
- **Design secondary flow entrainment of 60 percent**
- **Test conditions**

  $M_{\infty} = 0.27$ $\quad$ $NPR = 4.0$

  $T_{op} = 850$ R $\quad$ $T_{os} = 530$ R

The NASA/GE 2DCD Nozzle is a rectangular mixer/ejector designed for noise suppression. It is designed to entrain approximately 60 percent secondary flow. The nozzle's mixer chutes are a convergent-divergent design. This is intended to eliminate the shock structure in the primary stream. The nozzle studied here is one of several configurations tested in GE's Aerodynamics Research Lab to study its aerodynamic and mixing characteristics. The configuration chosen as the baseline case has a short mixing section and a suppressor area ratio (SAR) of 2.5. The nozzle was studied at the following conditions, NPR = 4.0, $M_{\infty} = 0.27$, $T_{0p} = 850$ R and $T_{0s} = 530$ R.

Nozzle Schematic

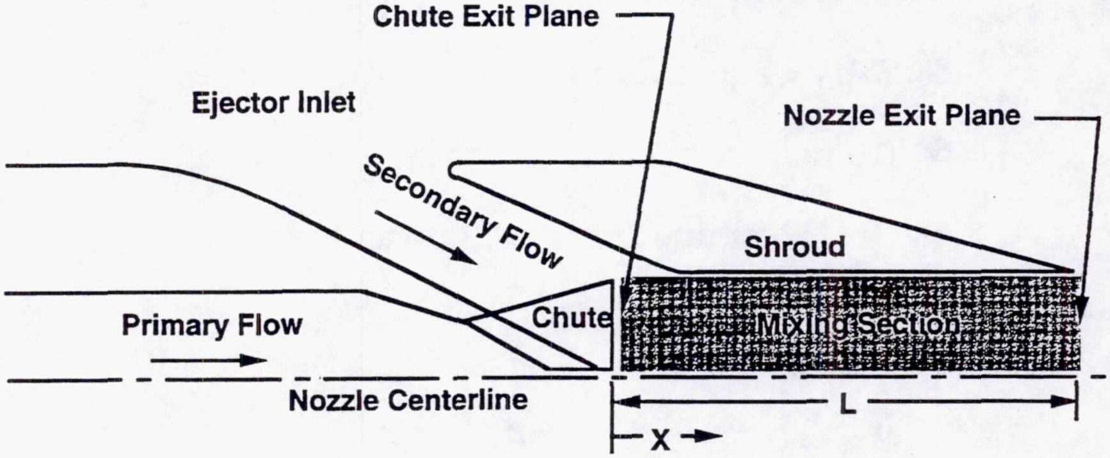

This figure shows the basic flow paths and key elements of the nozzle. The primary flow from the engine passes between the mixer chutes. The secondary flow entrained from the freestream, is drawn into the ejector inlet and through the mixer chutes. At the chute exit plane the two flows meet. A series of streamwise vortices created by the chutes mix the two flows as it passes through the mixing section and exits the nozzle.

Typical Mixer/Ejector Nozzle Chute Geometry

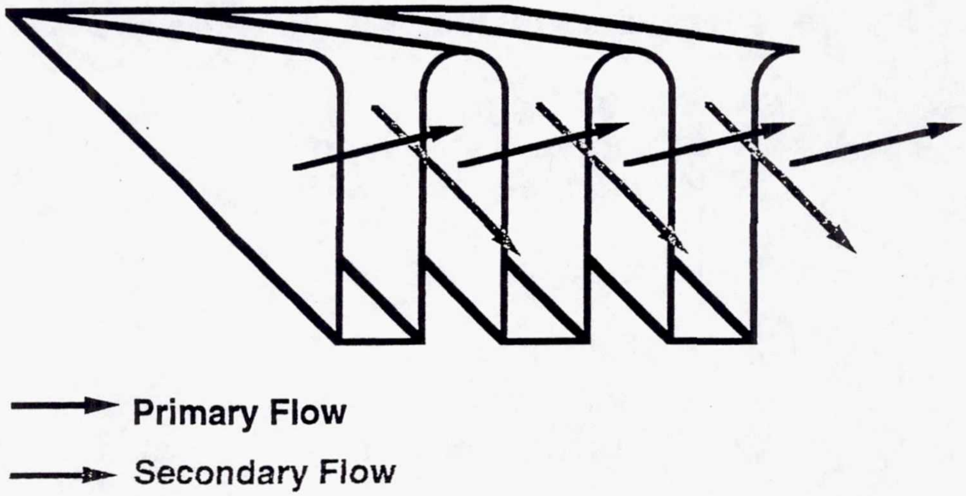

The mixer ejector chutes create the vorticity which mixes the two streams together. These chutes are deployed into the primary stream at takeoff and then retracted when noise suppression is no longer necessary at cruise. The primary flow is directed slightly upward as it moves between the chutes. The secondary flow is drawn down through the chutes and exits them with a downward velocity component. This vertical misalignment of the two flows creates streamwise vorticity at the chute exit plane. This vorticity rolls up into a discrete vortex and stretches as is moves through the mixing section.

Experiment

- Conducted in GE's Aerodynamic Research Lab (ARL)
- Parameters tested
  - ▲ Shroud length
  - ▲ Suppressor area ratio (SAR)
  - ▲ Mixing area ratio (MAR)
- Data includes
  - ▲ Wall static pressures
  - ▲ Kiel probe traverses (P_o, T_o)
  - ▲ LDV measurements

The experimental data was taken at GE's ARL freejet facility. Many nozzle configurations were tested to study the effects of various parameters. These parameters included shroud length, suppressor area ratio, mixing area ratio, and ejector inlet geometry. Mixing area ratio is a measure of the mixing section convergence or divergence and is defined as the ratio of mixing section exit area to mixing section entrance area. Data was taken for a range of nozzle pressure ratio's and freestream mach numbers. The data taken included wall static pressures, Kiel probe traverses of total pressure and temperature and LDV measurements of velocity, flow angle and turbulence intensities.

Grid

- **920,671 grid points**
- **8 Grid blocks**
- **Models 1/2 of a chute wavelength**
- **No sidewall effects**
- **Generated on Iris workstation**
  - ▲ **I3G for grid surfaces**
  - ▲ **INGRID3D for grid volumes**

Because of the complexity of the geometry the computational grid is also very complex. The grid consists of 920,671 grid points. This large number of points was necessary to resolve all the internal walls and shear layers present in the flow field. The domain was divided into 8 grid blocks. These blocks divide the geometry such that each individual block is easy to grid. For example, the primary flow path, the chute and the mixing section are all separate grid blocks. Each block is relatively easier to grid than the combined sections. Also, modifications to the grid are made easier, because only the affected grid blocks must be changed. The six surfaces which define a grid block were generated using the I3G interactive grid code. These surfaces were then input into GRIDGEN3D which was used to create the grid volume. The blocks were combined into the completed grid in a post processing step.

Computational Domain

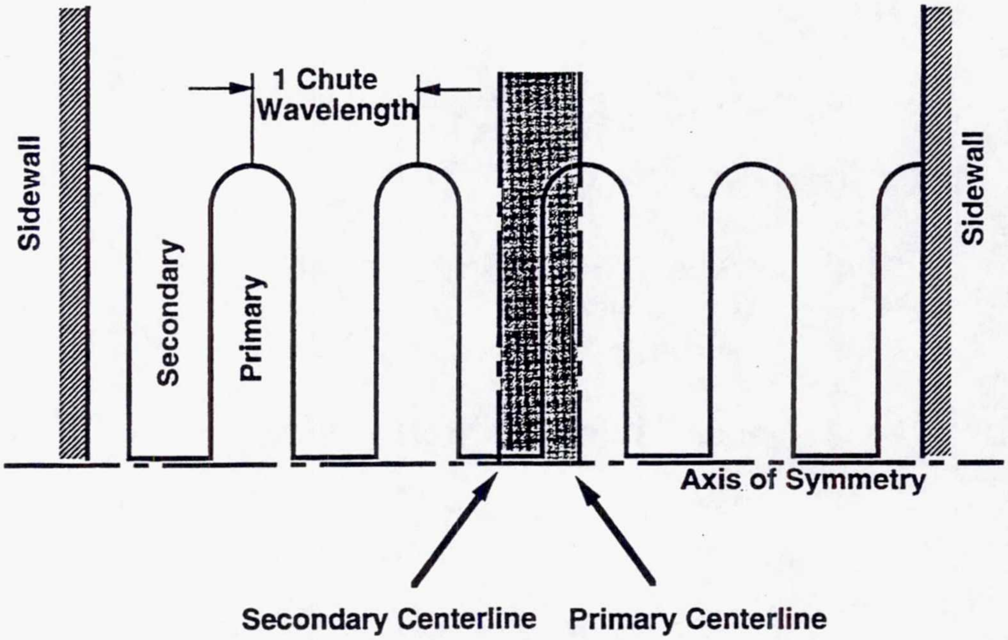

To reduce grid size and computational time, the grid modeled one half of a chute wavelength (defined as the distance from the peak of one mixer lobe to another). Symmetry planes are specified along both the primary and secondary flow centerlines. This is a reasonable approximation for the flow in the center of the nozzle. With this approximation, the effects of the sidewalls are neglected. Also, only the top half of the nozzle is modeled due to the symmetry of the geometry.

Computational Grid

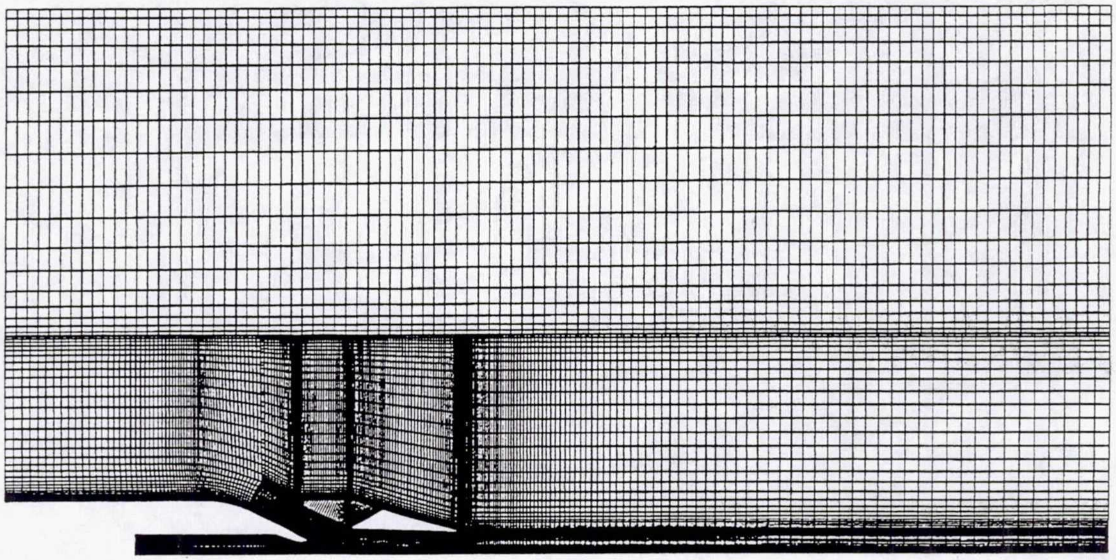

The external flow field as well as the nozzle flow field was modeled. This was done to insure proper calculation of secondary flow entrainment and to study the development of the plume. The external flow was modeled using separate grid blocks. Once the freestream flow has converged, these grid blocks are no longer solved, and the more cpu time can be used on the internal flow field.

Computational Grid
Nozzle Detail

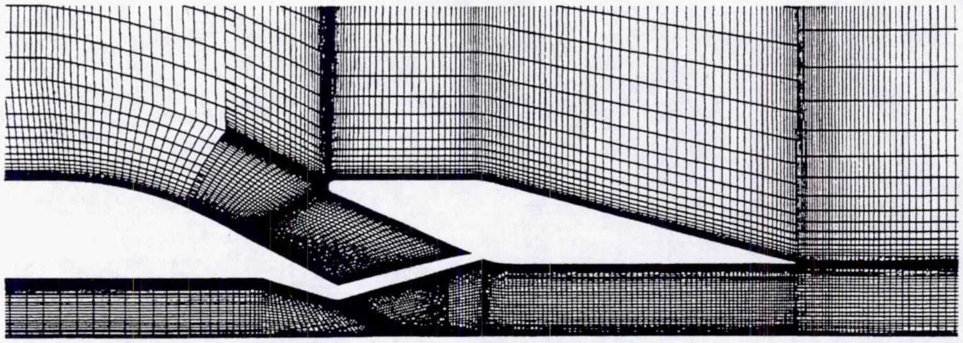

a. Primary Centerline
Ae/Amix = 1.0

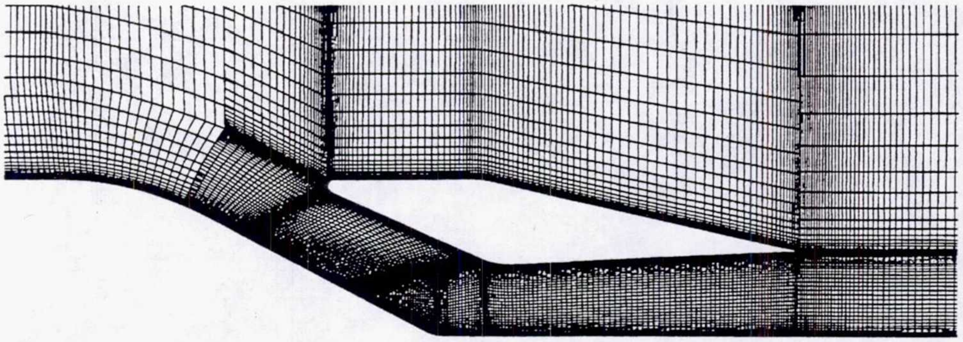

b. Secondary Centerline
Ae/Amix = 1.2

A close-up of the nozzle portion of the grid is shown. Both the primary and secondary flow paths can be seen. Different mixing section area ratios are shown for the primary and secondary flow paths.

The PARC Code

- **Central Differencing**
- **Beam and Warming algorithm**
- **Multiple grid blocks (noncontiguous interfacing)**
- **Generalized boundary conditions**
- **Turbulence models**
  - ▲ **Thomas model (algebraic)**
  - ▲ **K-ε model**

The PARC code is a multipurpose flow solver that was developed at the U.S. Air Force's Arnold Engineering Development Center (AEDC). PARC is central differencing code which solves the Reynolds averaged Navier-Stokes equations using a Beam and Warming algorithm. It has the capability to solve grids made up of multiple grid blocks. The interfaces between blocks do not have to be contiguous. This greatly simplifies grid generation of the multiple blocks. Data is passed between blocks using a trilinear interpolation scheme. Also, the code allows the user to specify any portion of any grid surface as a boundary condition. There are several options available to model turbulence. Both an algebraic model based on the method of P. D. Thomas and a 2 equation K - e model based on a Speziale formulation were used in this analysis.

Mach Number Contours
Ae/Amix = 1.2

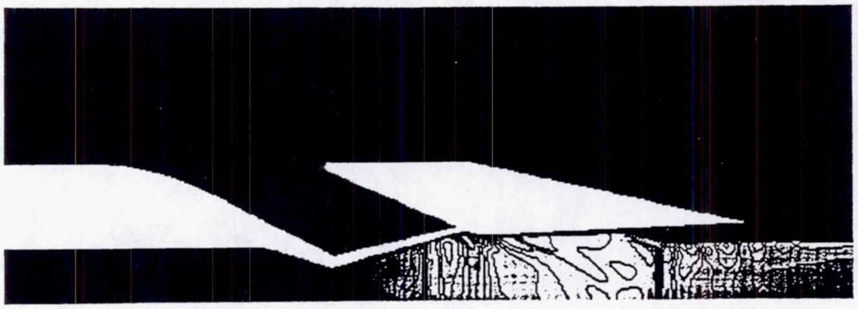

a. Primary Centerline

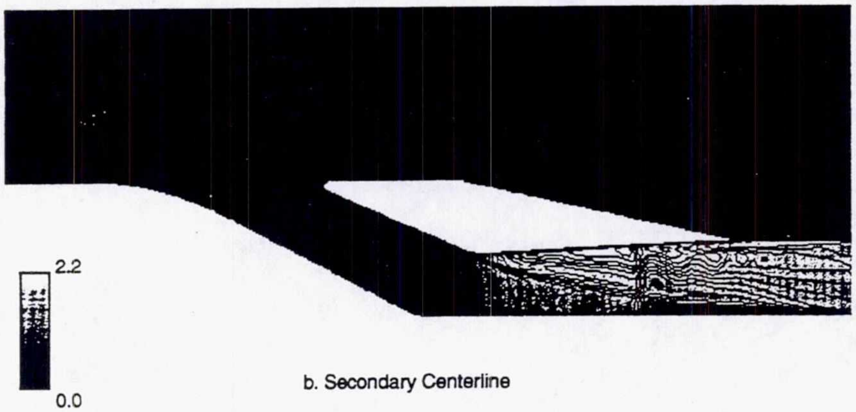

b. Secondary Centerline

The flow field for the baseline diverging mixing section configuration is presented as a typical flowfield for this nozzle. The primary flow accelerates as it flows between the mixer chutes. The flow chokes just upstream of the chute exit plane and then expands. It undergoes a compression as the flow is turned slightly entering the mixing section. The flow then over expands through the mixing section. The flow shocks near the nozzle exit to reach the ambient pressure. A separation occurs on the shroud wall approximately 60 percent of the way through the mixing section.

On the secondary flow centerline, the flow accelerates through the mixing section and shocks similar to the primary flow centerline. An area of high mach number flow is apparent near the shroud wall and grows in size through the mixing section. No separation is evident on the secondary centerline.

Total Temperature Contours
Ae/Amix = 1.2

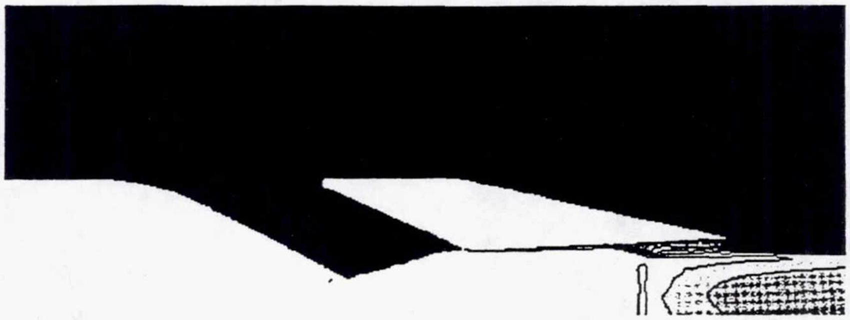

a. Primary Centerline

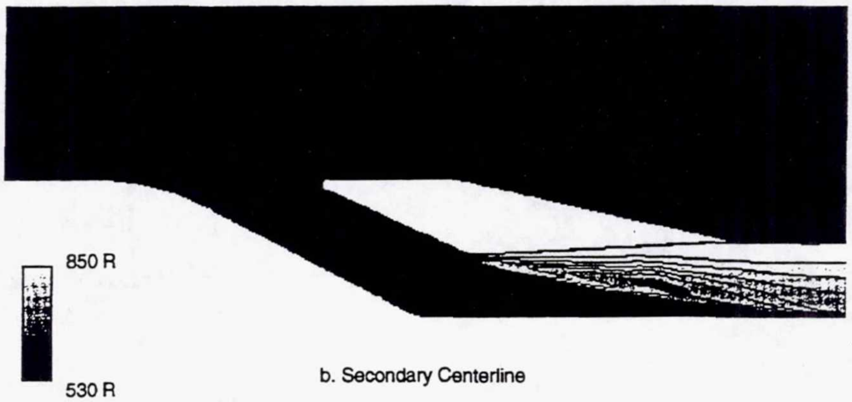

b. Secondary Centerline

Because the total temperatures of the two streams differ, we can use the total temperature to distinguish the two streams and evaluate the mixing. On the primary centerline the temperature shows very little decay and hence little mixing before the nozzle exit. The separation is evident because the lower temperature ambient air is pulled inside the nozzle by the recirculation. The high temperature flow found on the upper region of the secondary centerline indicates that some primary flow has rolled over into the secondary centerline plane due to the vortical mixing. This explains the existence of the high mach number region show in the previous figure.

Area Plotted

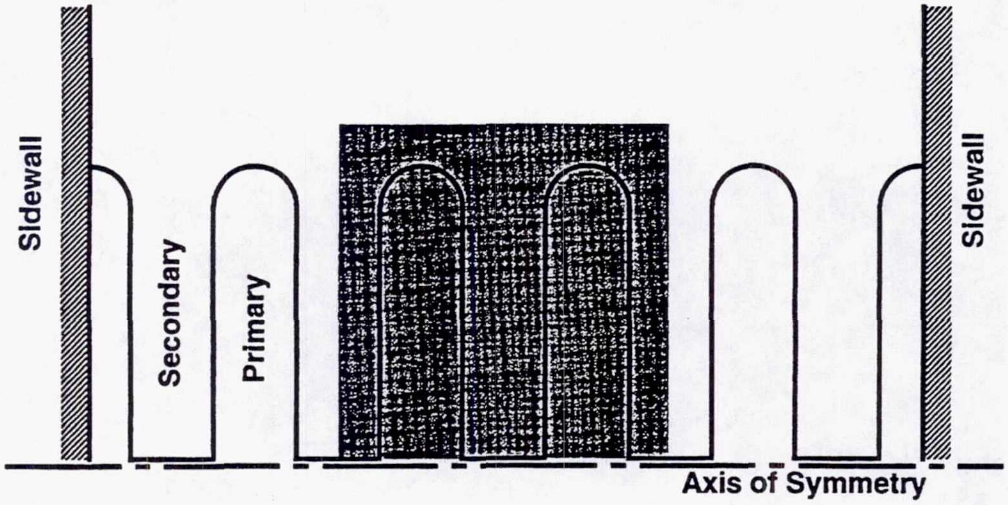

The figure illustrates the area shown for the data plots in the mixing section. The solution has been reflected for clarity to show two complete primary flow passages and one complete secondary passage.

Velocity Vectors
Ae/Amix = 1.2

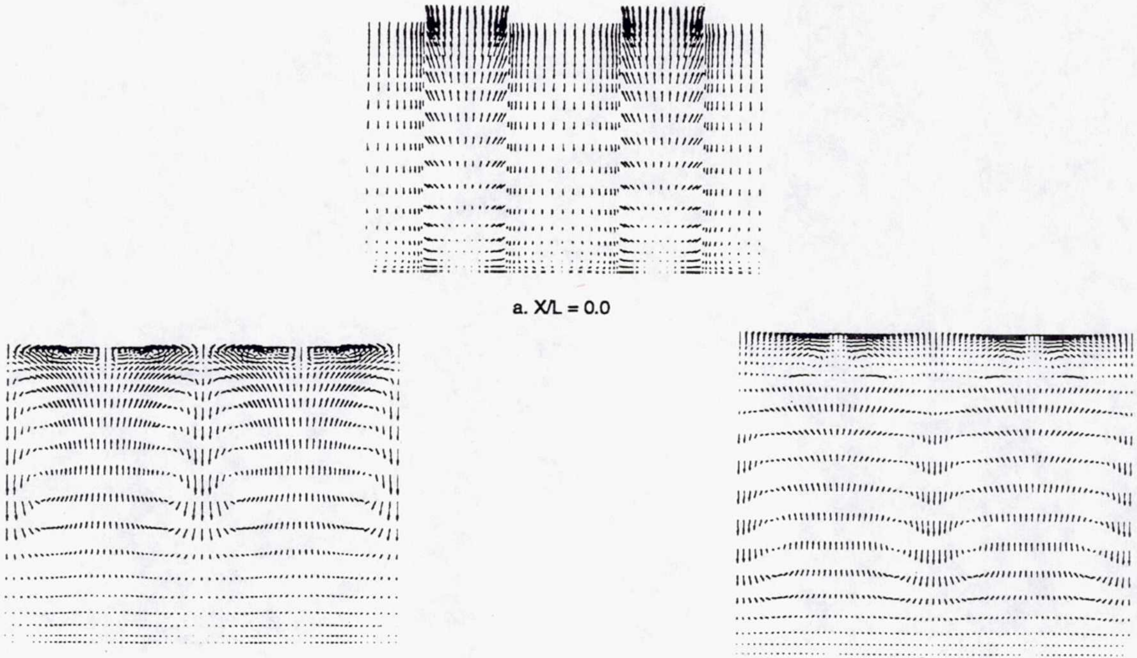

a. X/L = 0.0

b. X/L = 0.5

c. X/L = 1.0

Velocity vectors at three locations in the mixing section show the development of the vortices generated by the mixer chutes. At the chute exit plane (X/L = 0.00), the vertical velocities of the two streams are in opposite directions. This generates a sheet of vorticity along the trailing edge of the chutes. This vorticity rolls up into a discrete vortex in the upper portion of the mixing section. As the flow moves downstream the vortex center moves toward the nozzle centerline and the vortex stretches. At the nozzle exit plane the vortex has stretched to occupy almost the entire exit area.

Total Temperature Contours
Ae/Amix = 1.2

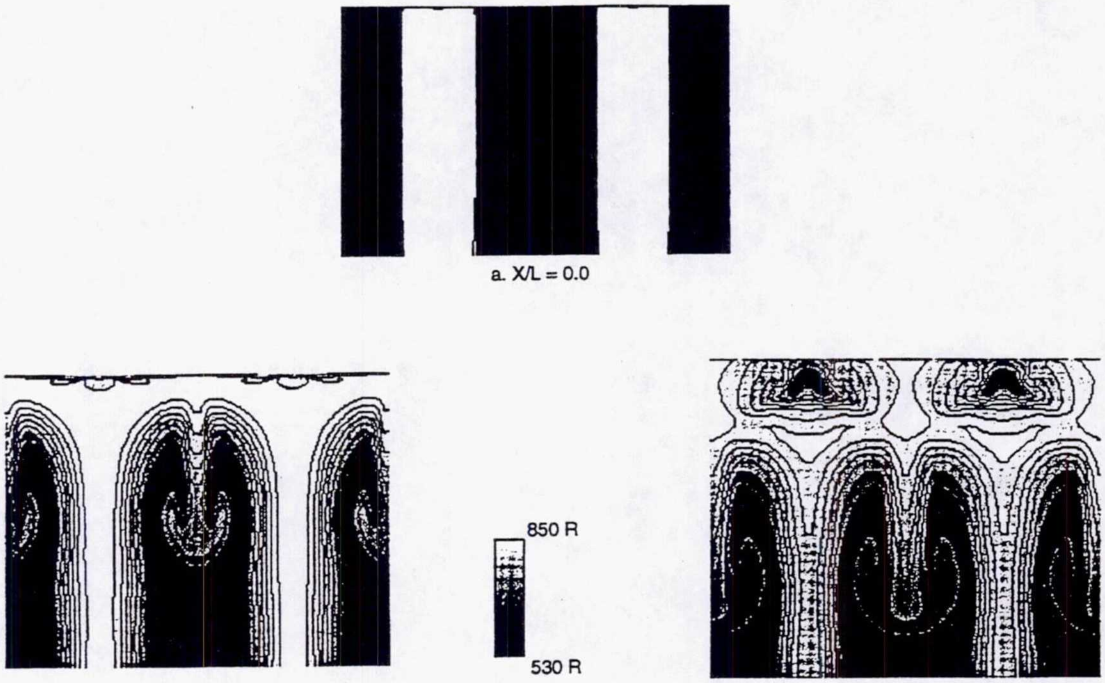

a. X/L = 0.0

b. X/L = 0.5

c. X/L = 1.0

The total temperature contours help visualize the mixing of the streams in the mixing section. The vortex pulls the primary flow over and into the secondary flow plane. As the flow moves through the mixing section, the primary flow continues to migrate into the secondary flow plane and mix with the secondary flow. At the nozzle exit, there are still significant portions of primary and secondary flow that remain unmixed. The separation can be seen near the shroud wall at the nozzle exit. The recirculating flow brings in ambient air which is evident by the lower temperature region near the shroud. This recirculating region occurs only on the primary flow centerline and does not extend across the entire width of the nozzle.

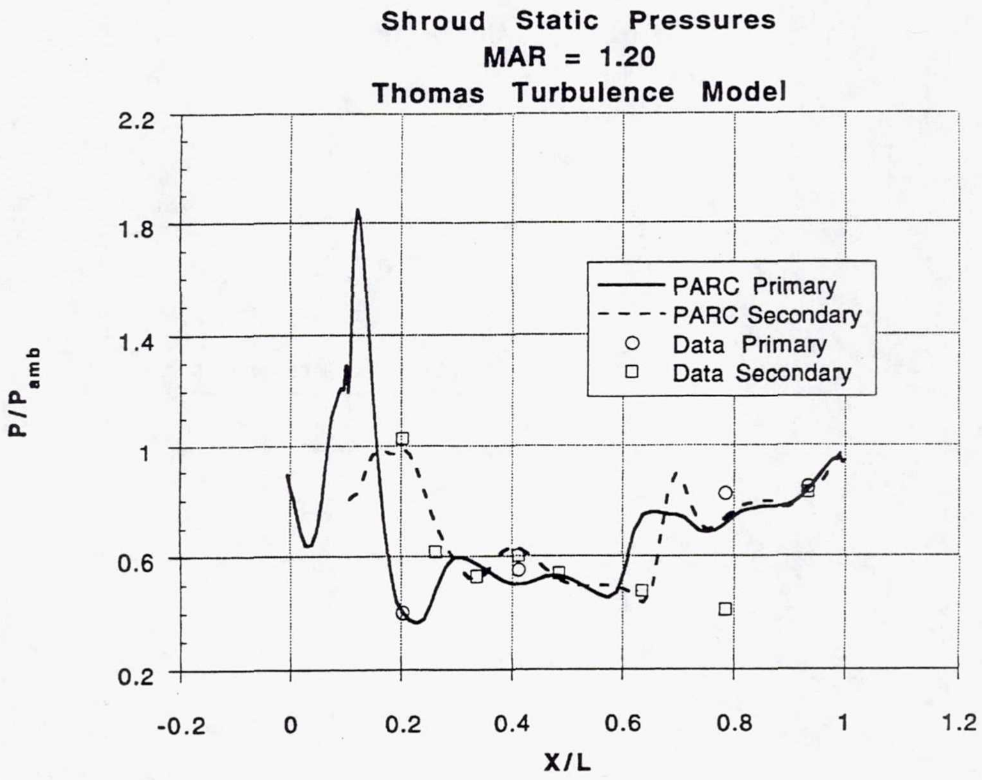

Static pressures on the mixing section shroud walls are presented on both the primary and secondary flow centerlines. The primary flow shocks as it is turned parallel to the shroud wall. Both flows then greatly over expand well below ambient pressure through the mixing section. The flow then shocks and diffuses back to ambient pressure at the exit. Near the region of the separation, the pressures at each location have not yet equalized. This could help explain the localized separation bubble. The predictions agree well with the experimental data. It appears that the PARC code predicts the shock location upstream of the experimental location. This shock has been observed to be unsteady in the experiment and therefore can not be properly resolved using the steady state method of PARC.

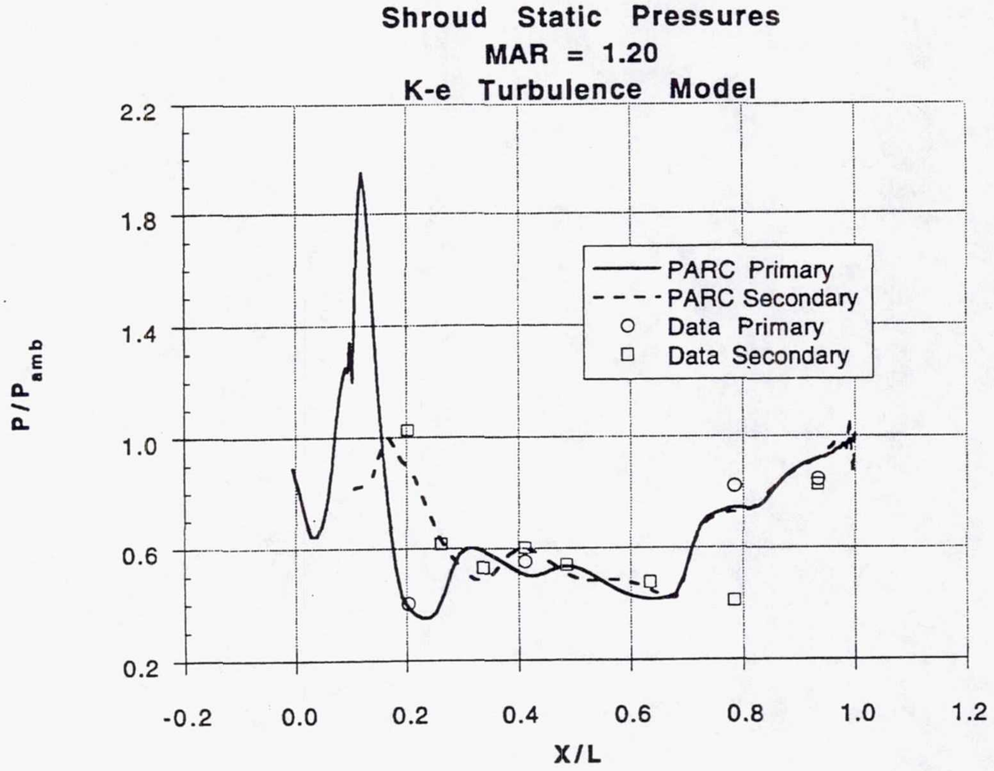

The K-e turbulence model predicts a very similar pressure distribution for the first half of the mixing section. The shock is predicted slightly further downstream from the Thomas model data. Also, the static pressures have equalized across the width of the nozzle before the shock. The separation also occurs across the entire nozzle width.

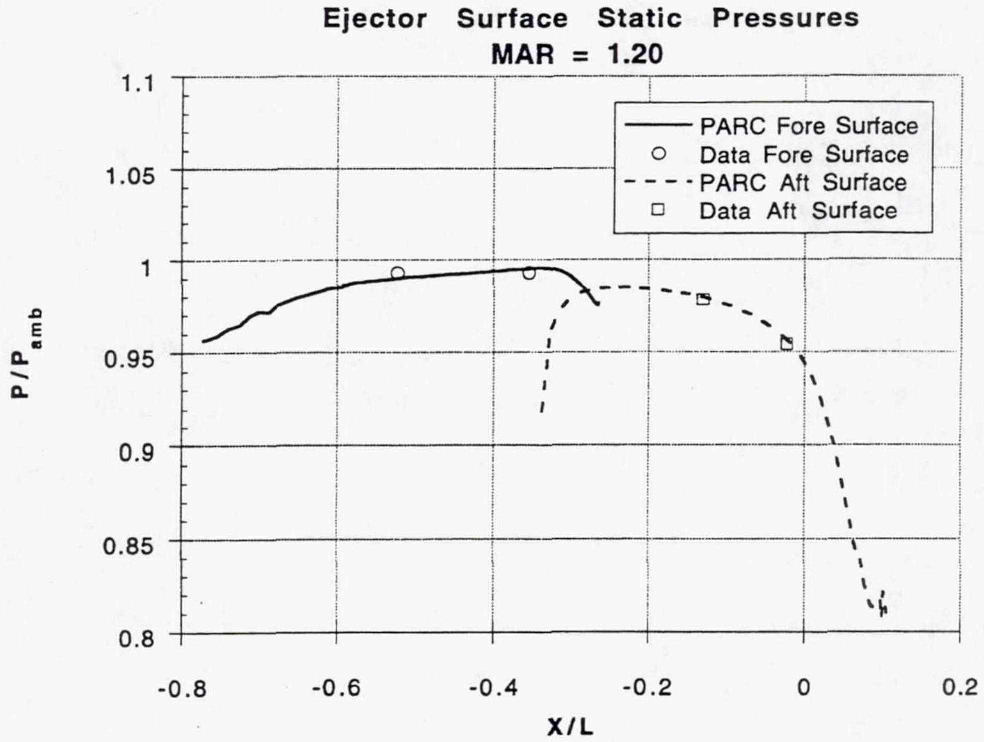

Static pressures on the both the fore and aft ejector surfaces compare very well with experimental data.

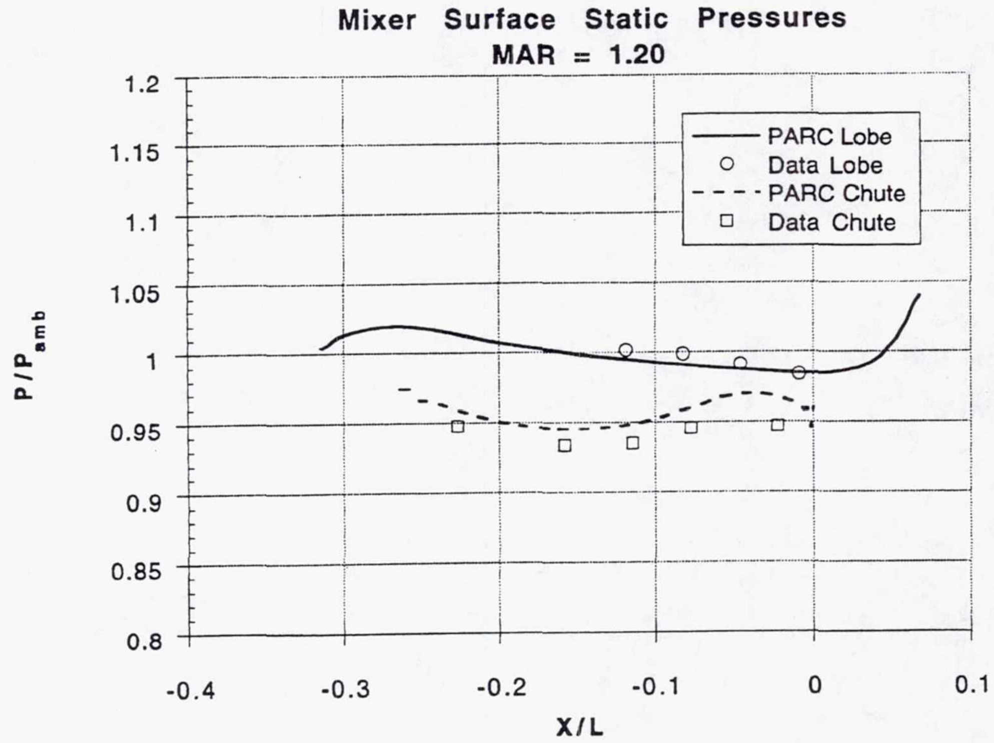

Static pressures are shown on both the centerline of the mixer lobe peak, and the centerline of the mixer chute. Agreement is very good on the mixer lobe peak. The prediction is not as good on the chute centerline. However the maximum error is less than 2 percent.

Velocity Contours
Nozzle Exit Plane
$A_e/A_{mix} = 1.2$

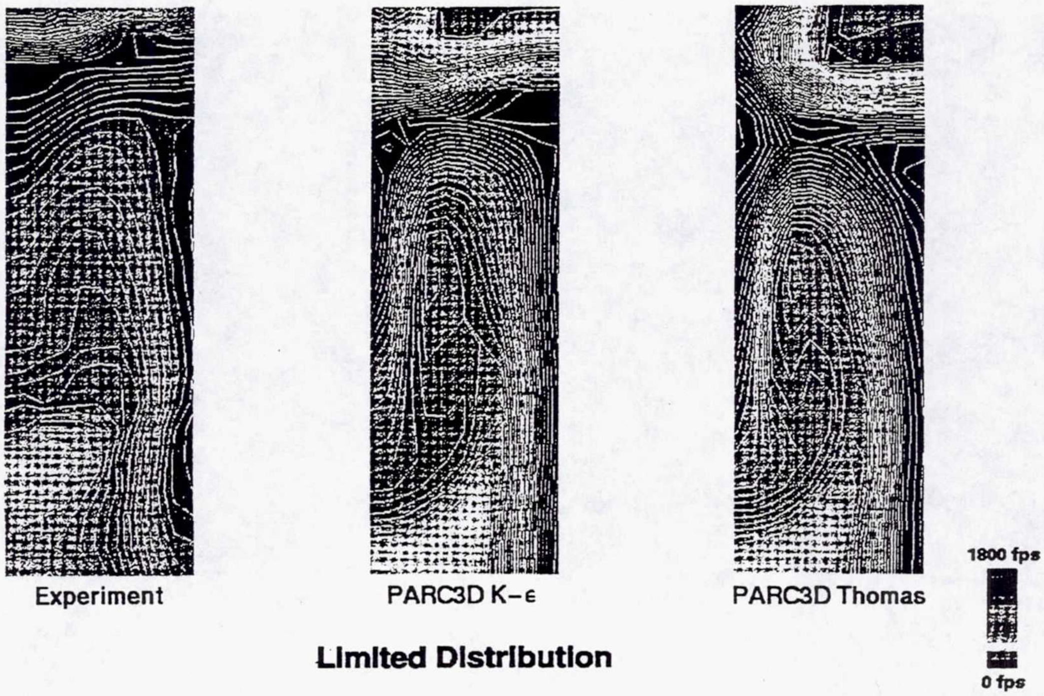

Limited Distribution

A 2 component LDV system measured axial and vertical velocities at the nozzle exit plane. The computational results were modified to eliminate the third velocity component. This result was then interpolated onto the experimental grid in order to make a direct comparison. The PARC code has predicted the general trends of the flow field. However, two major differences are observed between computation and experiment. First, the experiment shows a great deal more mixing than predicted by PARC. The K-e solution predicts slightly more mixing than the algebraic model. But, both analytical results greatly under predict mixing. This is most likely a results of the turbulence models used. Also, in the experiment upstream flow disturbances not modeled in the analysis may have been present which could have aided in mixing. The second major difference between analysis and measurement is in the separated region on the shroud wall indicated by a very low velocity region in the upper portion of the contours. Both turbulence models show that the separated region still exists at the exit plane. The experiment seems to infer that the flow has reattached by the exit plane. The prediction of reattachment downstream of the actual location is typical of the PARC code. The K-e model predicts a thinner separated region than the Thomas model. The Thomas model solution shows that the separation does not span the entire width of the nozzle and is somewhat unrealistic.

Flow Angle Contours
Nozzle Exit Plane

$A_e/A_{mix} = 1.2$

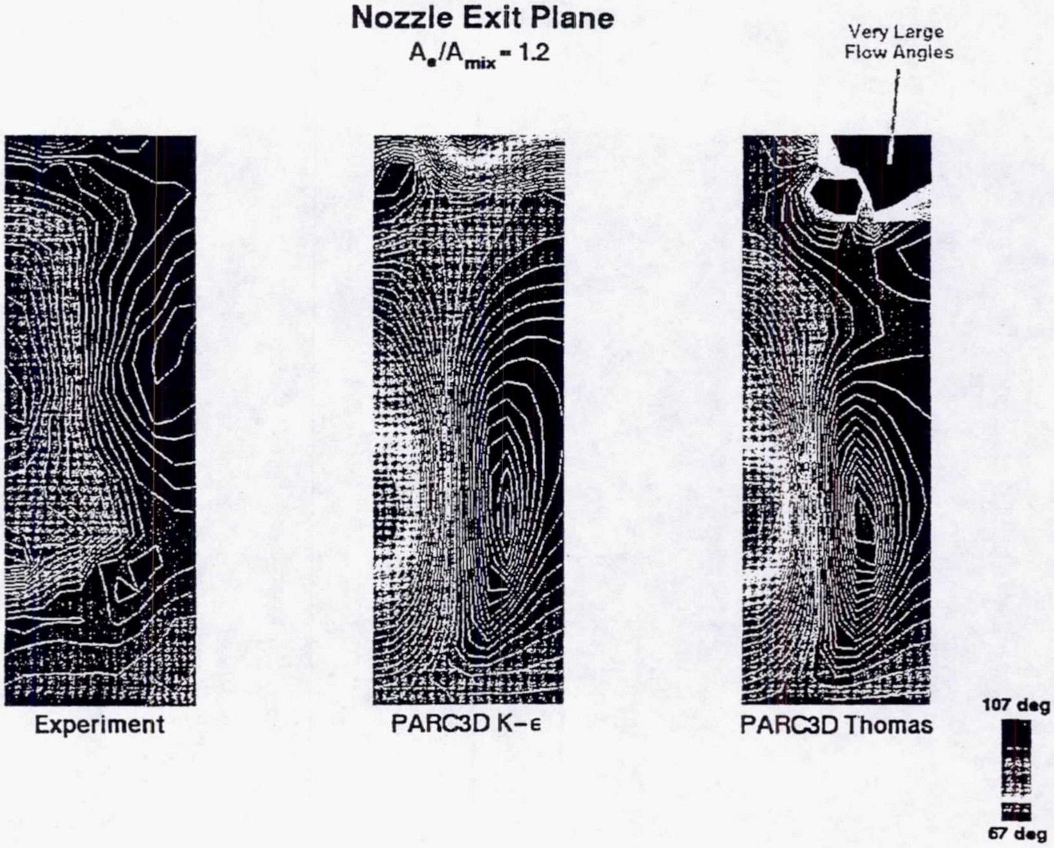

Experiment

PARC3D K-ε

PARC3D Thomas

Very Large Flow Angles

The flow angles presented here are defined as the angle the 2D velocity vector makes with the vertical plane; 0 degrees down, 90 degrees axial. The flow angles also indicate that the PARC code has predicted less mixing and late separation reattachment. The vortex appears as two parallel elliptical areas with opposite flow direction. The predicted size of these regions agrees well with the data. The experimental position of the vortex is closer to the shroud wall than predicted by PARC. This is probably due to the separation region still remaining in the analysis forcing the vortex away from the wall. The Thomas model predicted very large flow angles in the recirculating region. These large angles were neglected in order to make a clear comparison.

MAR Study

- Current Designs operate over expanded
- Determine the optimum Mixing Area Ratio (MAR) for nozzle performance
- Modified existing grid
- Used previous solution as initial solution
- Four configurations studied
  - ▲ MAR = 0.90 } convergent
  - ▲ MAR = 0.95 } convergent
  - ▲ MAR = 1.00 - constant
  - ▲ MAR = 1.20 - divergent

The flow in the mixing sections of the nozzle configurations tested in ARL was over expanded and thus had poor thrust performance. In order obtain maximum thrust performance for this nozzle, a study was done to determine the optimum mixing area ratio (MAR). Because the grid was generated in multiple blocks, only the affected blocks had to be modified. This greatly simplified the grid generation process. A completed solution was used as the initial conditions for the new case. This decreased the number of iterations necessary for convergence. Four cases were run to find the optimal MAR value. They were; 1.20, 1.00, 0.90, and finally 0.95.

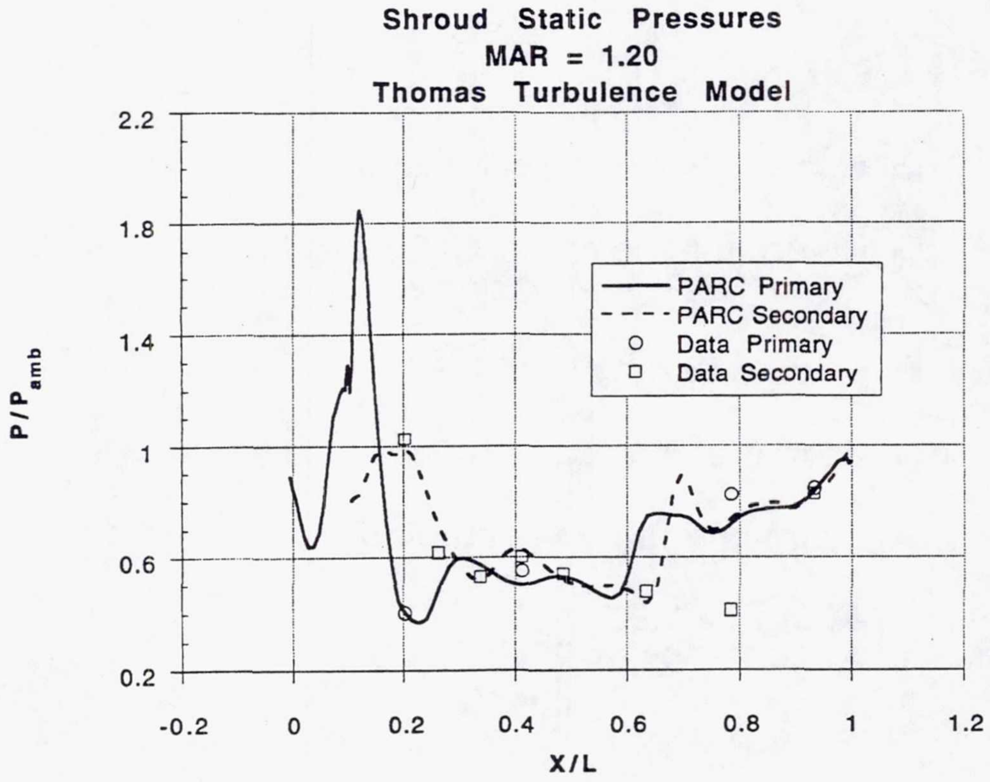

Static pressures on the shroud surface are presented to show the effect of the mixing area ratio on the flow expansion. For the baseline case, MAR = 1.20 the flow greatly over expands to under 50 percent of ambient pressure. To match ambient pressure at the nozzle exit the flow shocks. The large divergence of the shroud also causes the flow to separate from the shroud wall. The shock wave is not clearly defined by the wall pressures due to the large separation.

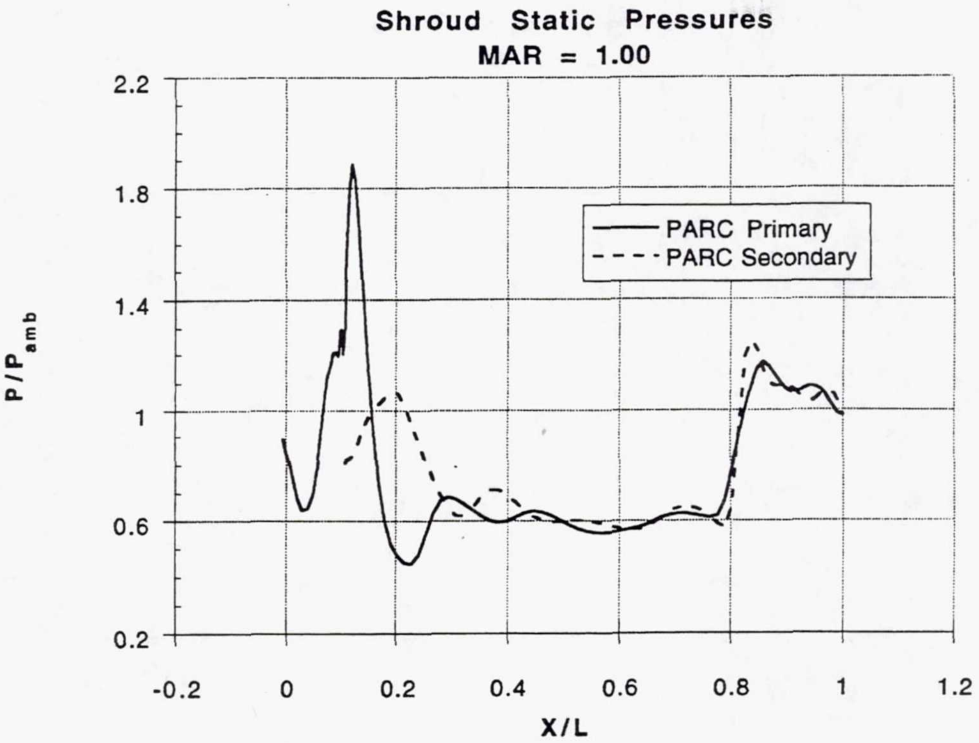

The constant area mixing section also shows an over expansion. The resulting shock can be clearly seen because no separation was evident.

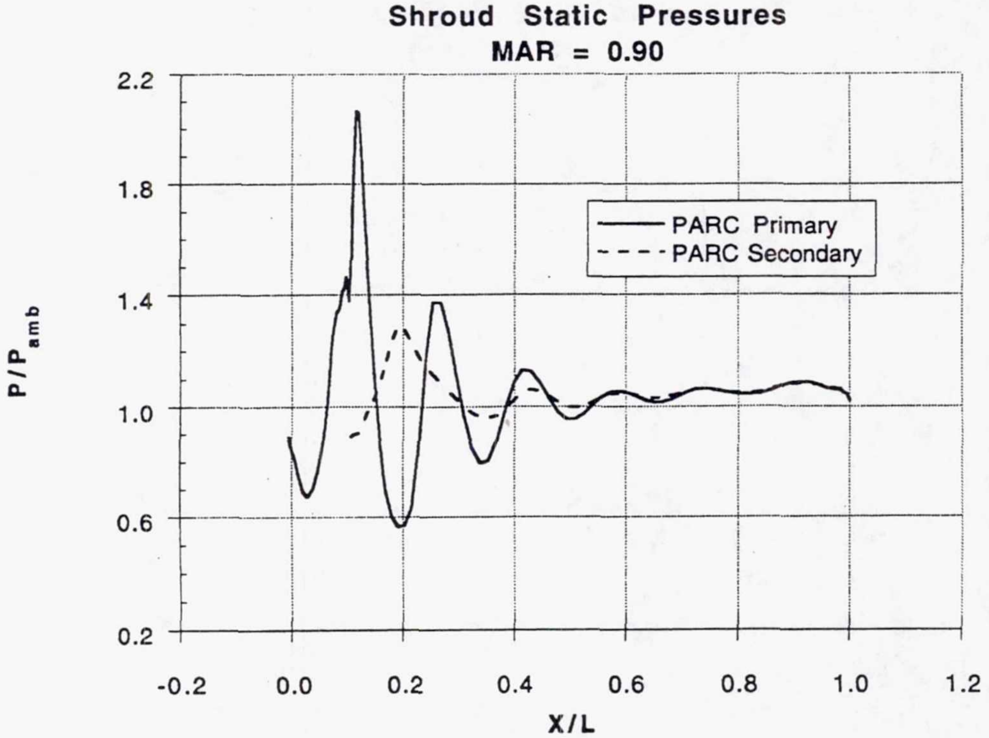

For the first converging case analyzed the flow appears to be slightly over expanded. Mass flow augmentation was reduced significantly.

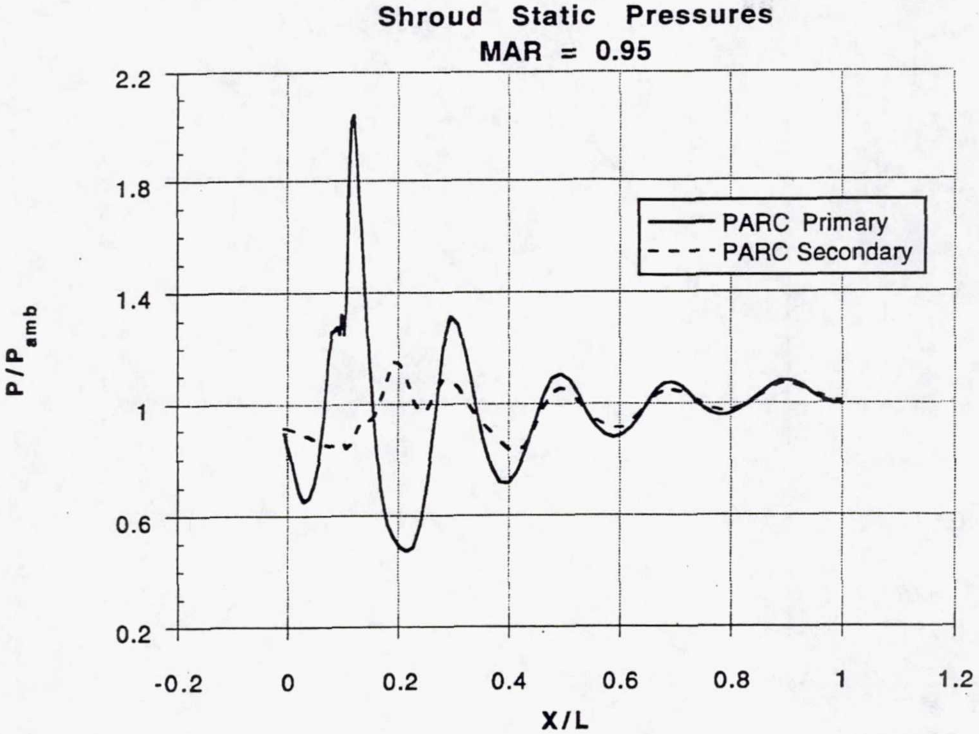

The final case run was MAR = 0.95. The pressure distribution shows that the flow contains a series of oblique shocks in the mixing section. At the nozzle exit the flow is near ambient pressure.

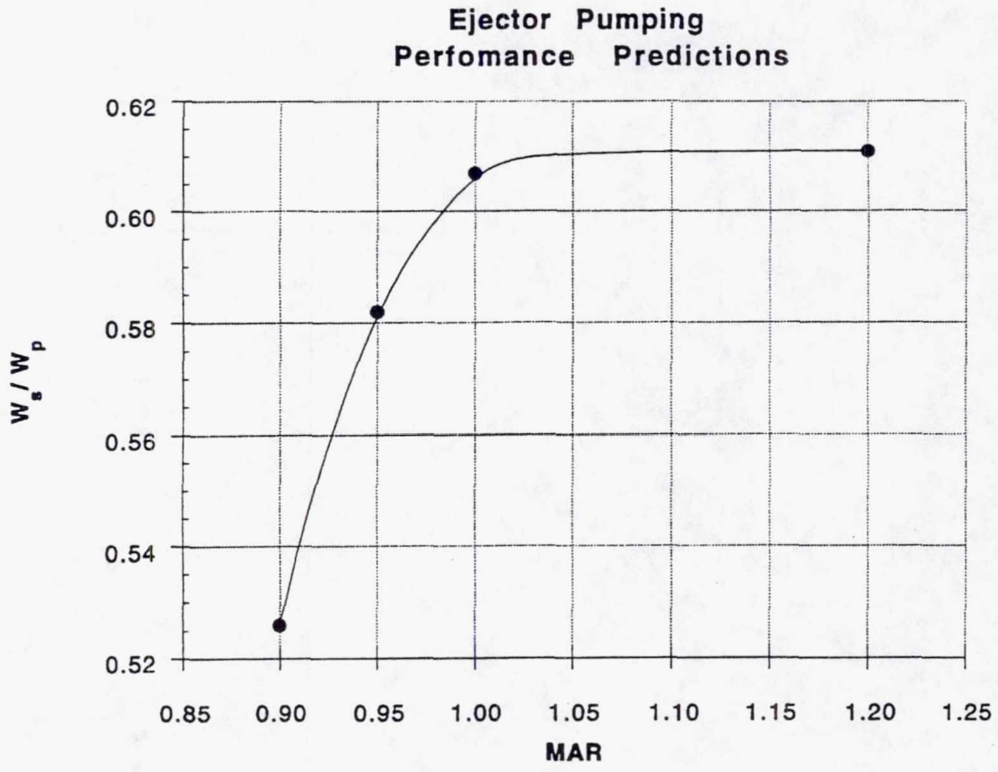

The effect of the mixing area ratio on ejector pumping can be seen in this figure. For a MAR greater than 1, the secondary flow is choked and the exit area of the nozzle has no influence on amount of flow entrained. The amount of flow entrainment meets the goal value of 0.60 for mixing area ratios greater than 0.98. For the converging cases, the secondary flow is not choked and the reduction in nozzle exit area reduces the amount of secondary flow which is entrained.

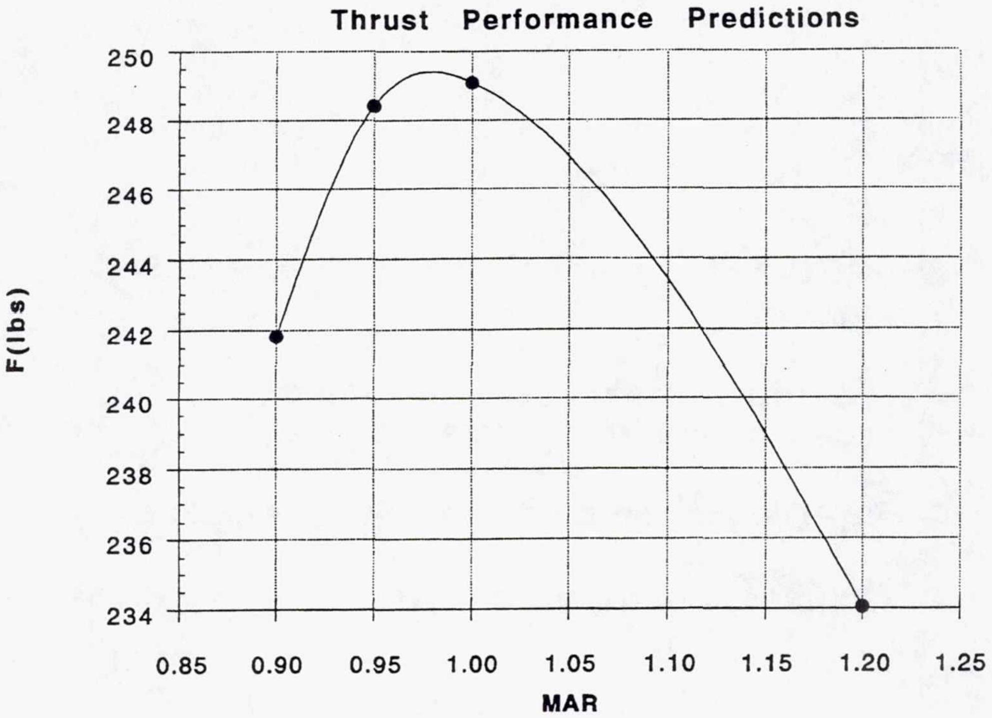

The thrust vs. mixing area ratio curve show a definite peak near MAR = 0.97. As MAR is increased beyond this point thrust is lost due to over expansion and eventually separation. For a MAR less than 0.97 thrust is lost due to a reduced amount of secondary flow and under expansion. The thrust values presented are pure thrust and do not take into account any drag penalties.

Conclusions

- **PARC code accurately predicts major flow features**
- **K-e turbulence model gives some improvement in separated regions**
- **PARC under predicts the extent of mixing**
- **Optimum nozzle performance at MAR = 0.97**

Mixer/ejector nozzles have the potential to lower jet noise without significant thrust loss. A full Navier-Stokes analysis of the NASA/GE 2DCD mixer/ejector nozzle was performed. The PARC code predicts with good accuracy the basic flow field of the nozzle. Pressure distributions compare very well with experimental data. However, the PARC code under predicts the extent of the primary and secondary flow mixing. The two equation K-e turbulence model and the algebraic Thomas model produce very similar results. But the K-e model does produce more realistic results in the separated region. A study to determine the mixing area ratio for best thrust performance concluded that this MAR should equal 0.97.

1999176554

ANALYSIS OF A SECOND GENERATION MIXER-EJECTOR EXHAUST SYSTEM

T.J. Barber, R.E. LaBarre, and L.M. Chiappetta
United Technologies Research Center
East Hartford, Connecticut

51-07

409535

36P

OUTLINE

- Analysis Background
- Grid Generation Approach
- Navier-Stokes Analysis Approach
- Discussion of Results

This presentation will describe previous approaches for analyzing mixer-type nozzle geometries. A key reason preventing a complete numerical solution has been short- comings in grid generation. A new grid generation procedure will be described and Navier-Stokes solutions obtained using such a grid will be presented. Finally, comparisons with experimental data measured in the NASA Lewis RC 9 by 12 tunnel will be presented.

ANALYSIS BACKGROUND

Mixer and Mixer-Ejectors Exhaust Systems

- **Empirical Models Based on Data Correlations**
- **Linearized and Potential Analyses: Barber, McGirk**
- **Navier-Stokes Calculations: Lord, Mityas**
- **Design Based Methods: Barber, PW(internal)**

Analytical design of mixer-type geometries has been limited by a designers inability to generate adequate computational grids for steep or vertical side-wall lobe surfaces. Most current design systems have been empirically based. Linearized potential analyses have been developed by Barber and Murman, but these are valid only for low penetration devices. Similarly, a full potential technique developed by McGirk is restricted to non-powered configurations. Complete numerical solutions (Navier-Stokes) through lobe region and in the mixing nozzle of a conventional subsonic E3-type forced mixer have been obtained by Lord, and for a mixer-ejector device by Mityas (both from PW). Both used a stacked conformal grid technique developed by Ives. Alternative design type approaches have also been developed by Barber. By using a Cartesian grid in conjunction with empirically based inital profiles, PNS methods for the mixing duct (downstream of the mixer nozzle).

GRID GENERATION APPROACH

- **Background: Conformal Mapping + Stacking (Ives)**
  - **Initial case took over 6 weeks but now about 1 week**
- **Ideal: MultiBlock Using C and H Axially + ??? in Crossplane**
- **NASA LeRC Approach: Transfinite Interpolation + Axial Stacking**
- **UTRC Approach: Block-Structured in Crossplane + Axial Stacking**
  - **New grid generated in less than a day**

Navier-Stokes solutions have also been calculated on grids developed by axially stacking a series of conformally mapped grids. A major difficulty in this approach was that such a grid genration technique took from 2 to 5 weeks. An alternative approach has been developed at NASA Lewis RC based on axially stacking grids generated by transfinite interpolation methods. This approach was also time-consuming and required plenty of hands on-development. Ideally one would like the analysis code to be able to accept multiblock type grids. Also desirable is that the local grid about the shroud be a C-type body fitted grid (this will become evident later). The next few charts will describe UTRC block-structured grid generation technique developed by Dannenhoffer (UTRC).

BLOCK-STRUCTURED GRID GENERATION PROCESS

- Design Blocking Plan in Topology Plane Based on ...
  - Flow requirements
  - Topology restrictions
- Generate Block-Structured Grid by Automatic Means
  - Use expert system for design heuristics
  - Use optimization to "fine-tune" grid
- Assess Grid Quality

In a block-structured grid generation technique, the field is broken up into several simpler, no-overlapping blocks or sub-domains. In general grid generation techniques using multi-block methods are labor intensive. In this new approach, the grid generation process is divided into the following major steps: 1) the design of blocking plan by deciding upon suitable grid topology for a given configuration, 2) the implementation of the blocking plan so that the computer knows how to generate the grid, and 3) the generation of the grid using either an algebraically and/or a PDE-based grid generator.

The design of a suitable blocking plan, or flowfield decomposition, has been simplified through the use of a rule-based expert system. A decomposition knowledge base is used to analyze a given configuration, set up an appropriate blocking plan, and perform a nonlinear optimization to fine-tune the blocking and the resultant grid.

TOPOLOGY PLANE

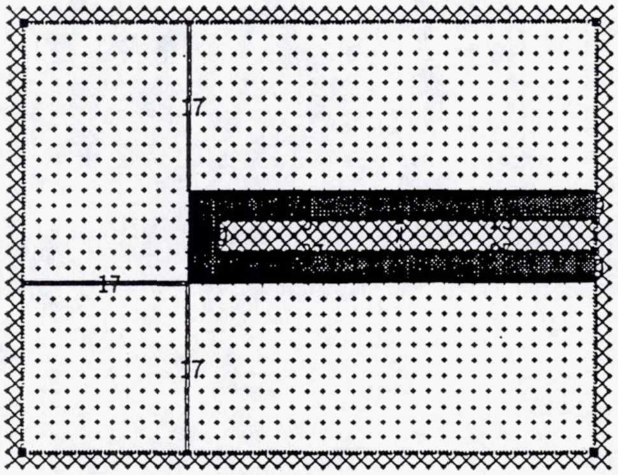

- **Integer Cartesian grid**
- **Abstraction of boundaries**
- **Connection to "real" geometry**
- **Specification of grid line directions**
- **Definition of "size" of each region**

The topology plane is an abstraction of the blocking plan, whereby a user is allowed to sketch directly into the computer which then automatically transforms the plan into a computational grid in the physical plane. The entire topology plane is covered by an integer Cartesian grid called the background grid. The topology plane shown is a sketch of a NACA0012 airfoil and its wake. Note the airfoil surface is conceptualized as a rectangle.

BLOCKING PROCESS (NACA0012 AIRFOIL — CY MESH)

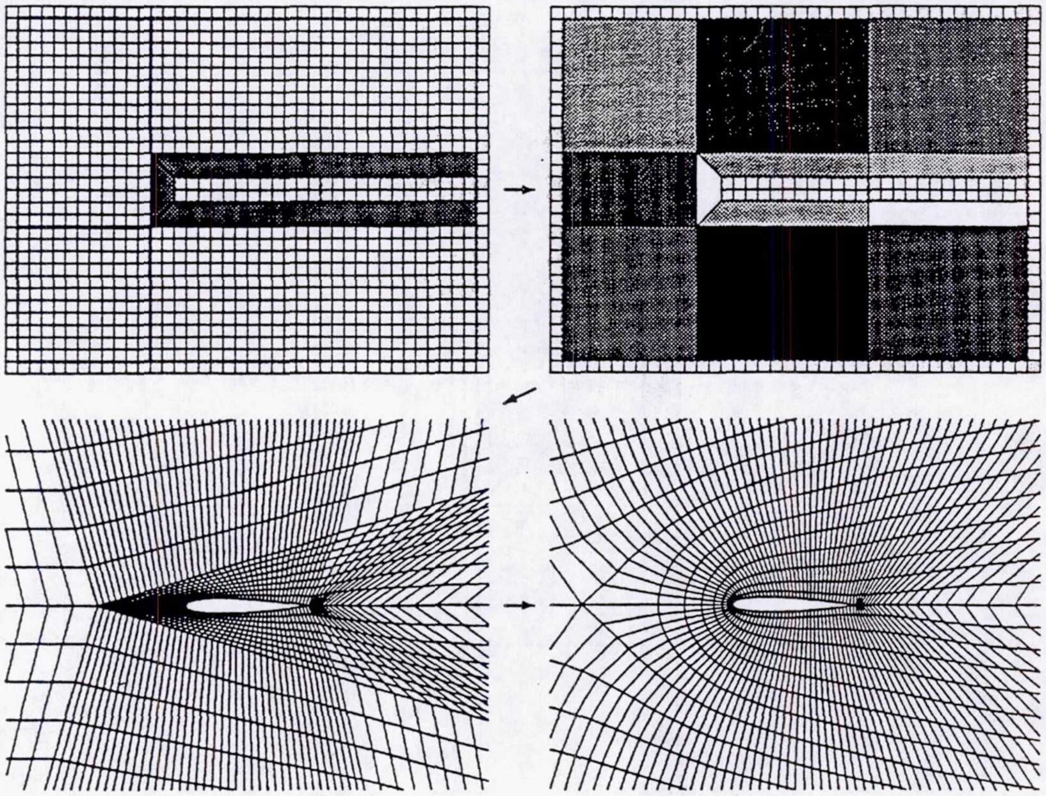

The multi-step grid generation process for an isolated NACA0012 airfoil is illustrated for a CY-type grid. The first step involves abstraction of the boundaries, specification of the geometry, and generation of the surface adjacent blocking. Next, the remaining region is filled initially with the largest possible rectangular blocks, but then these are subdivided to ensure 1-to-1 block face matching. These blocks are then sized (N by M) and an initial algebraic CY grid generated. Finally, a smoothed mesh is generated using 100 iterations of a Poisson PDE mesh generator.

NACA0012 AIRFOIL — SIMPLE TOPOLOGIES

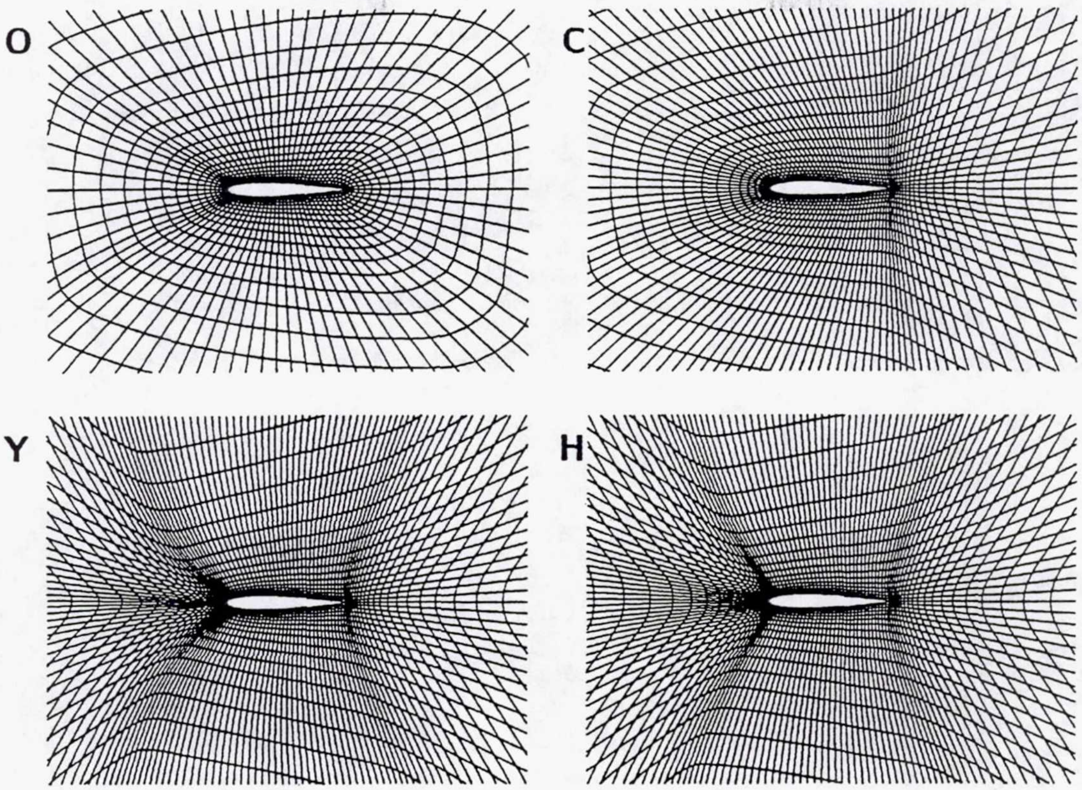

The flexibility of the method is clearly demonstrated in four different computational grids generated for the NACA0012 airfoil. The only differences in each generation process was the selection of different surface blockings in the topology plane.

BLOCKING PROCESS

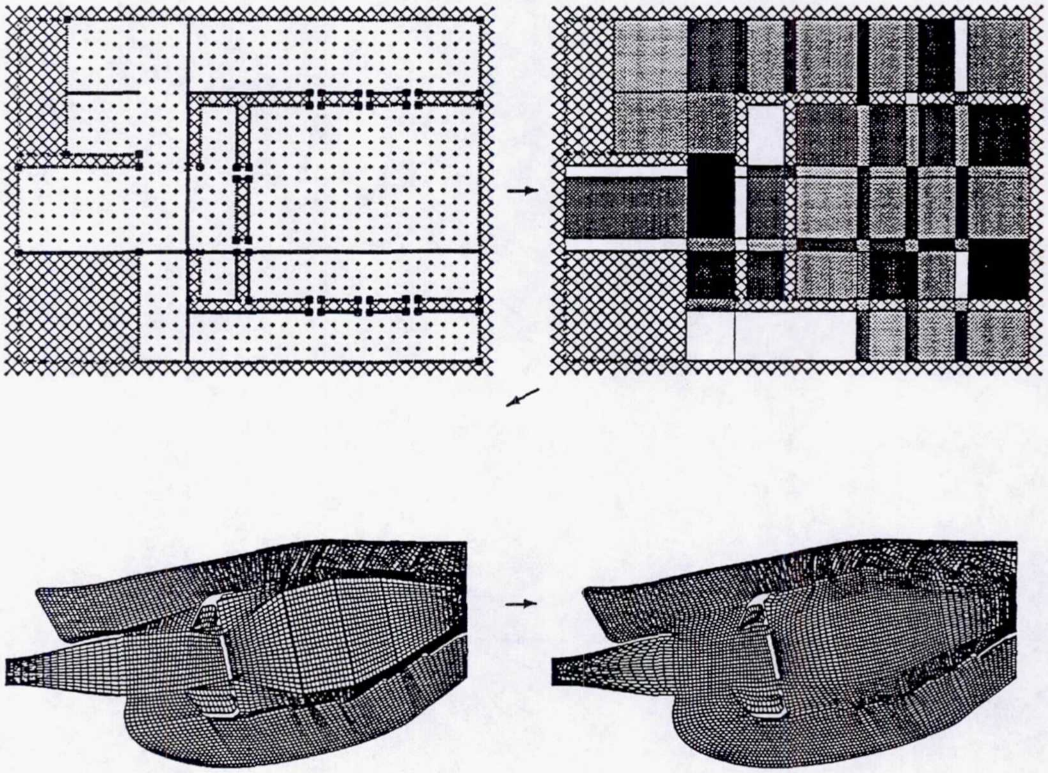

An application of the block-structured grid generation process to a 2-dimensional complex gas turbine geometry is shown in this slide. The topology plane, blocking pattern, initial grid and final multiblock grid are shown for a typical modern gas turbine combustor/pre-diffuser combination. The 2D grid of 6600 nodal points over 17 blocks, was generated on an IBM6000 workstation.

BLOCK STRUCTURED GRID GENERATION - 1

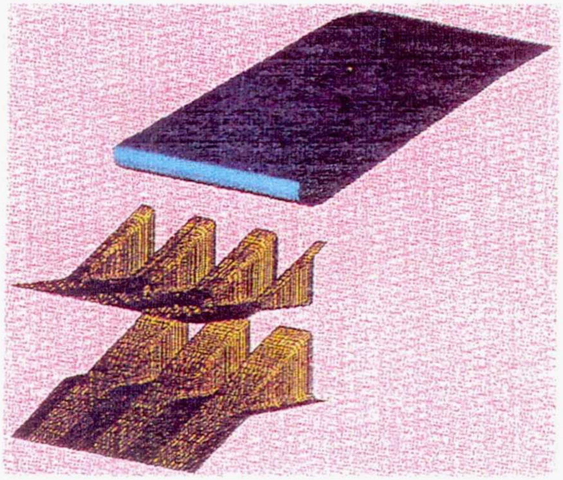

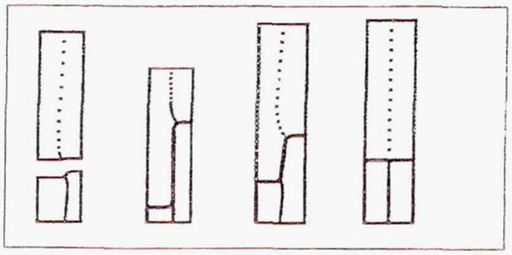

Multi-Block Scheme

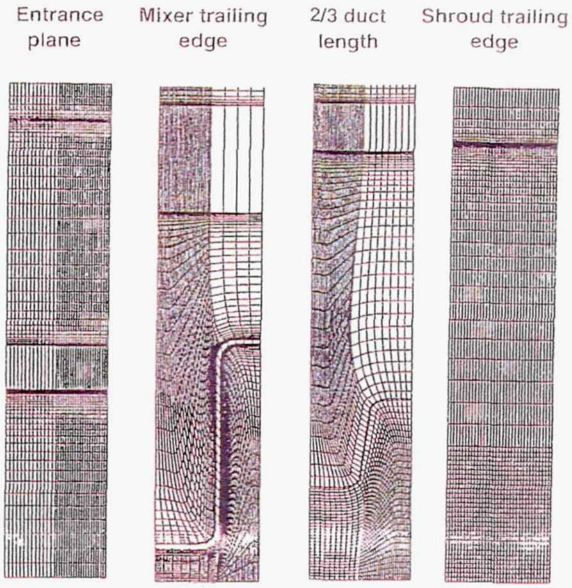

2D Cross-Section Cuts

This chart shows the PW GEN 1 mixer-ejector geometry, the blocking pattern for several axial slices (in the physical plane), and four axial block-structured grid planes. Note that the grid continues through the mixer nozzle and shroud walls using a single grid element. The maximum grid distortion occurs at the mixer nozzle trailing edge. The grid then relaxes to a nonuniformly distributed Cartesian grid at the shroud trailing edge. The grid is composed of 90 axial planes, 35 spanwise planes and 90 vertical planes.

Page intentionally left blank

BLOCK STRUCTURED GRID GENERATION - 2

Axial View, 90 by 90 Mesh

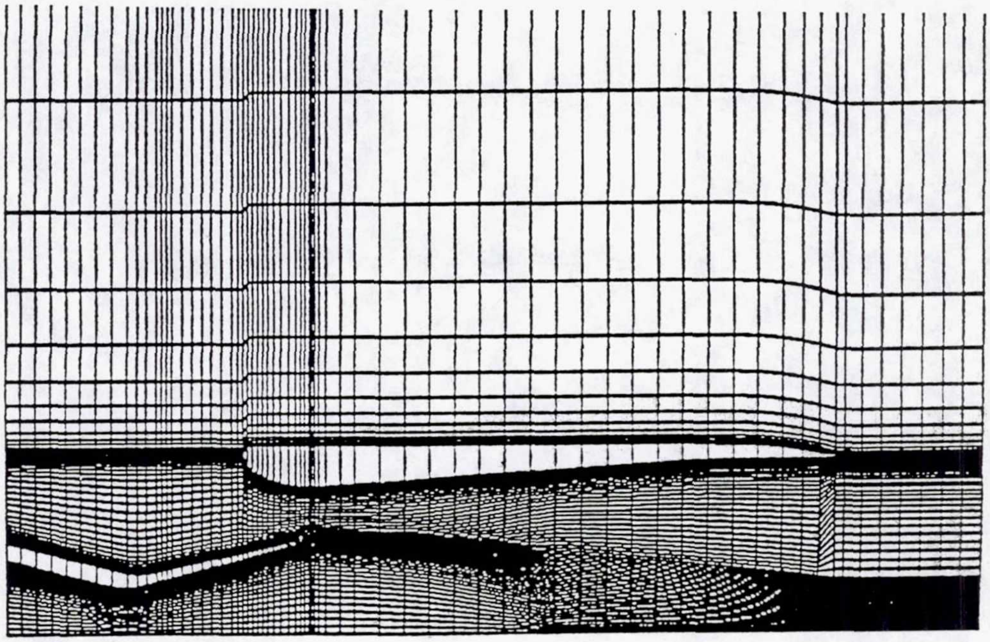

This chart shows an axial slice through the mixer nozzle crest plane. One can clearly see the grid concentrated near all surfaces. The grid relaxation downstream of the mixer nozzle trailing edge is also evident. One can also see the inappropriateness of the Cartesian type grid near the shroud leading edge. The effect of the large grid skew in this region will be explored later.

GRID METRIC MEASURES

- Cell Skewness $=\frac{\min(d_1,d_2)}{\max(d_1,d_2)}$ Where d is the Diagonal of a Cell
  - **Bounded between 0 and 1**
- Cell Aspect Ratio $= \frac{\min(s_1,s_2,s_3,s_4)}{\max(s_1,s_2,s_3,s_4)}$ Where s is the Side of a Cell
  - **Bounded between 0 and 1**
- Cell Area

An important issue to be addressed in any complex grid generation process should be the quality of the grid, both locally and on average. This chart shows three possible grid measures that were explored: skewness, aspect ratio, and cell area.

NAVIER-STOKES ANALYSIS APPROACH: NASTAR

- Finite-Volume Method
- Second-Order Centered Difference Formulation
- Pressure Correction Method (Rhie)
- Generalized Curvilinear Formulation
- Single Block Method in Production Use
  - β-site Multi-Block Version in Limited Use
- Jones-Launder (k, ϵ) Turbulence Model
- Explicit Numerical Dissipation Introduced

The Navier-Stokes analysis used in the mixer-ejector analysis is called NASTAR, a code developed at PW by Chae Rhie. The analysis is a second order accurate centered difference finite-volume method. The technique is based on the pressure correction approach originally developed in the TEACH series of codes. The current code only handles single block grids. The turbulence model used is the standard two-equation Jones-Launder (k,epsilon) model. Explicit dissipation is imposed through a user specified "cell Reynolds number parameter."

NAVIER-STOKES ANALYSIS APPROACH: NASTAR

Discretization Model

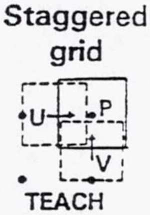

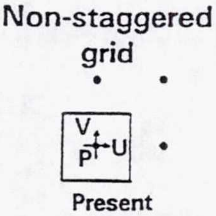

Grid	Dependent variable	Comments
Staggered (TEACH)	Contra-variant velocity	Non-conservative, no pressure dissipation
Non-staggered (Present)	Cartesian velocity	Conservative, pressure dissipation

The NASTAR code is a cell centered non-staggered grid scheme, differenced in terms of Cartesian velocity components. This is in contrast to the standard TEACH philosophy which uses a staggered grid for defining the dependent variables. Furthermore, the TEACH code velocity vectors are expressed in the more complicated contravariant form.

DISCUSSION OF RESULTS

- **Comparisons With Exp. Data and PARC Results**
  - **Shroud Loading, Exit Plane (T_T, k, U) Profiles, Pumping Ratio**
- **Comparison With PARC Results**
  - **T_T and Ω_s Internal Development**
- **Additional Comments on NASTAR Results**
  - **Dependence on Damping Parameter**
  - **Compressibility Effect on Turbulent Mixing**
  - **Non-Physical Total Pressure Losses**

A presentation of our calculated results will be presented in three sections. First, a comparison with both the measured experimental data, obtained from the NASA Lewis RC 9 by 12 facility, and the NASA Lewis PARC Navier-Stokes calculations. Secondly, NASTAR and PARC calculations will be compared to examine the internal flow development in the mixing duct. Finally, results will be presented to qualify the NASTAR numerical predictions.

RESULTS COMPARISONS: NASTAR, PARC

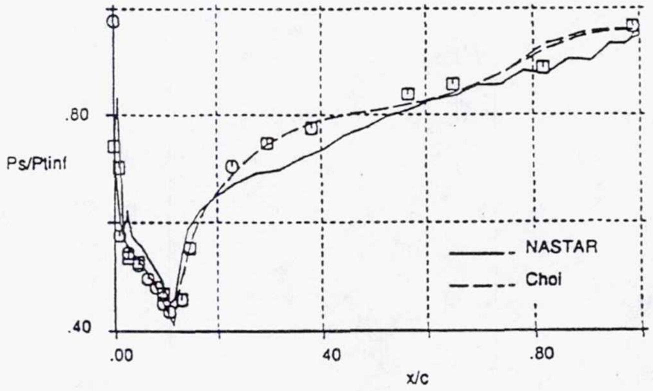

Shroud Loading

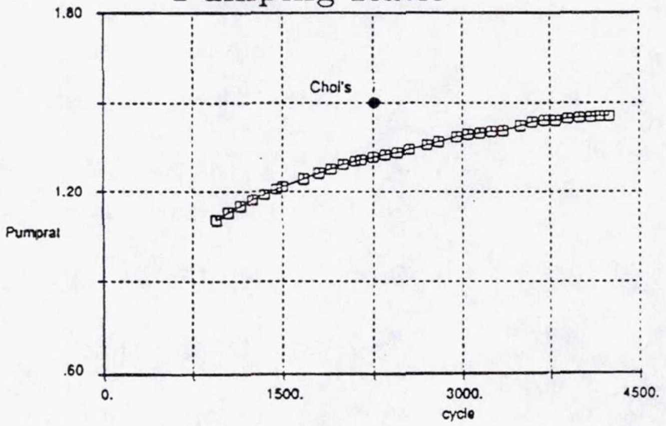

Pumping Ratio

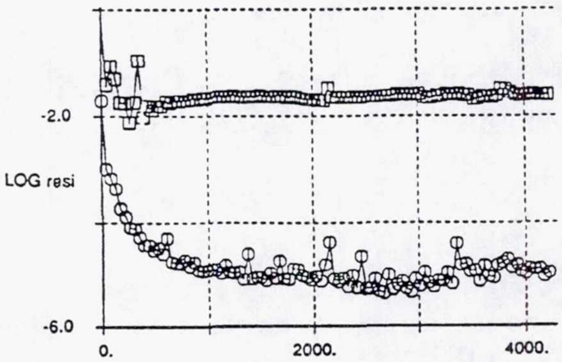

Static pressure loadings on the interior surface of the ejector shroud are presented for the NASTAR and PARC codes. Surface static pressure tap data is also presented. Both codes do a reasonable job of predicting the lip suction effect and the mixing to ambient static effect. Some of the NASTAR convergence characteristics are also presented. The L2 norm residual indicates that convergence is achieved by 1000 iterations, however a calculation of the ejector pumping indicated that more that 4000 iterations are required to reach a steady pumping level. This confirms our previous experience, that mixing dominated flows require substantially more iterations to converge than do pressure dominated problems.

2nd GENERATION MIXER EJECTOR ANALYSIS

Exit Plane Total Temperature

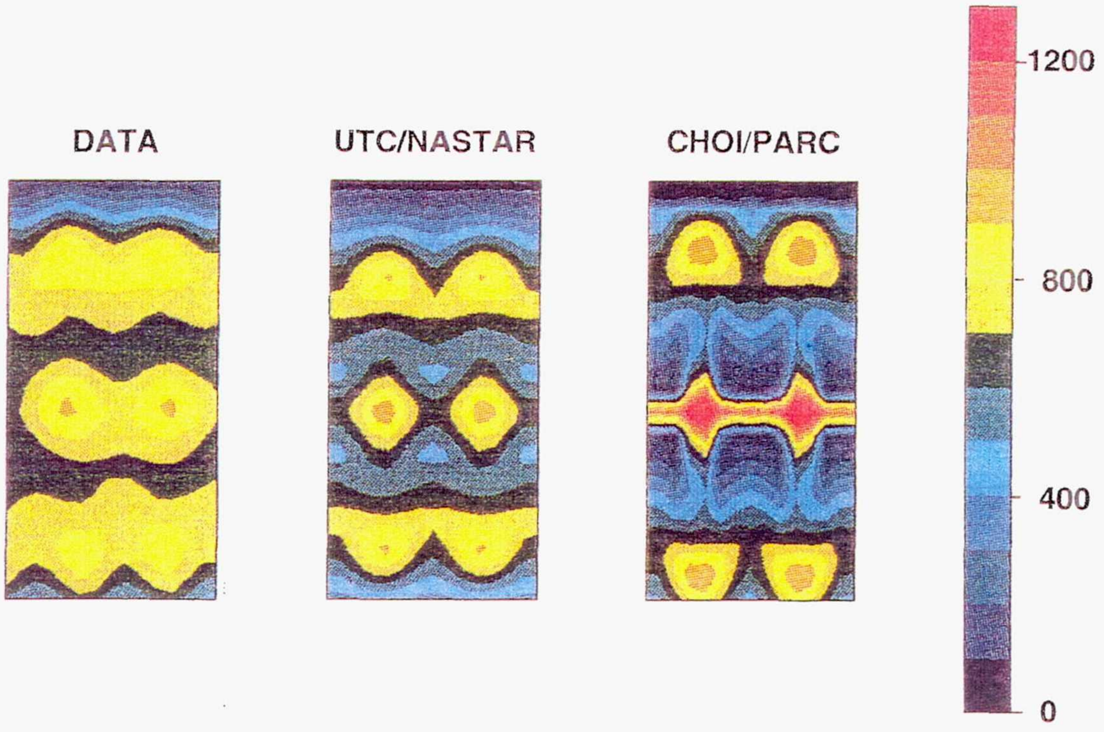

A comparison of the calculated and measured total temperature (degs. F) across the shroud exit plane is presented. The computational results have both been interpolated and plotted in terms of the measured grid locations. While the calculations have been performed assuming two (2) planes of symmetry, the results have been reflected to effectively show a four (4) lobe pattern. The central hot spot features are produced by cross-flow stagnation points located along the nozzle central axis, i.e. the induced streamwise vorticity, by symmetry, does not penetrate down to the axis at several distinct locations. The upper and lower horizontal features are the residual thermal effect of the lobe along the shroud walls. Note that the PARC results show an appreciably hotter centerline flowfield that will be seen in other data comparisons.

Page intentionally left blank

2nd GENERATION MIXER-EJECTOR ANALYSIS

Shroud Exit Plane Profiles

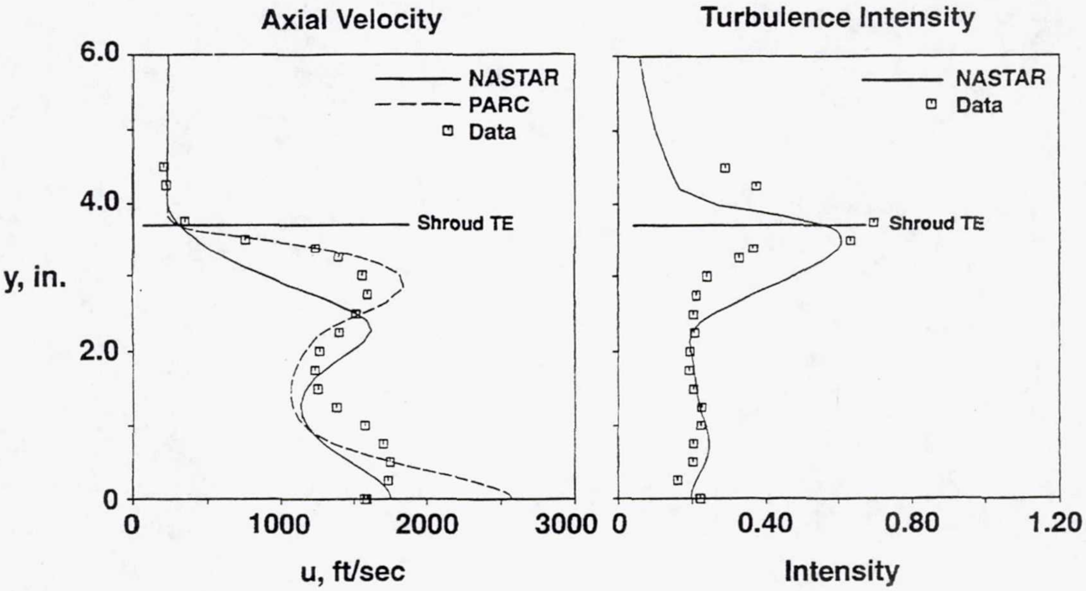

Velocity and turbulence intensity measurements were also obtained at the exit plane of the shroud for a single lateral slice only. In performing the experiments however, the shroud location was not reset to the baseline location at which the calculations were performed. The axial velocity comparisons with data however illustrate peaks along the centerline and near the shroud. The higher centerline thermal field predicted by the PARC code is confirmed by the higher centerline velocity predictions (less mixing means higher jet speeds and less thermal attenuation, and more predicted noise).

The turbulence intensity is compared with only the NASTAR predictions. The PARC code version used in this study had only a Baldwin-Lomax algebraic turbulence model and did not predict a turbulence intensity level. The comparisons indicate that the highest turbulence intensities occur near the shroud and not along the centerline. The question therefore is where are the largest noise sources, near the largest velocity and thermal gradients or near the largest turbulence levels?

Page intentionally left blank

2nd GENERATION MIXER-EJECTOR ANALYSIS

Navier-Stokes Total Temperature Comparisons

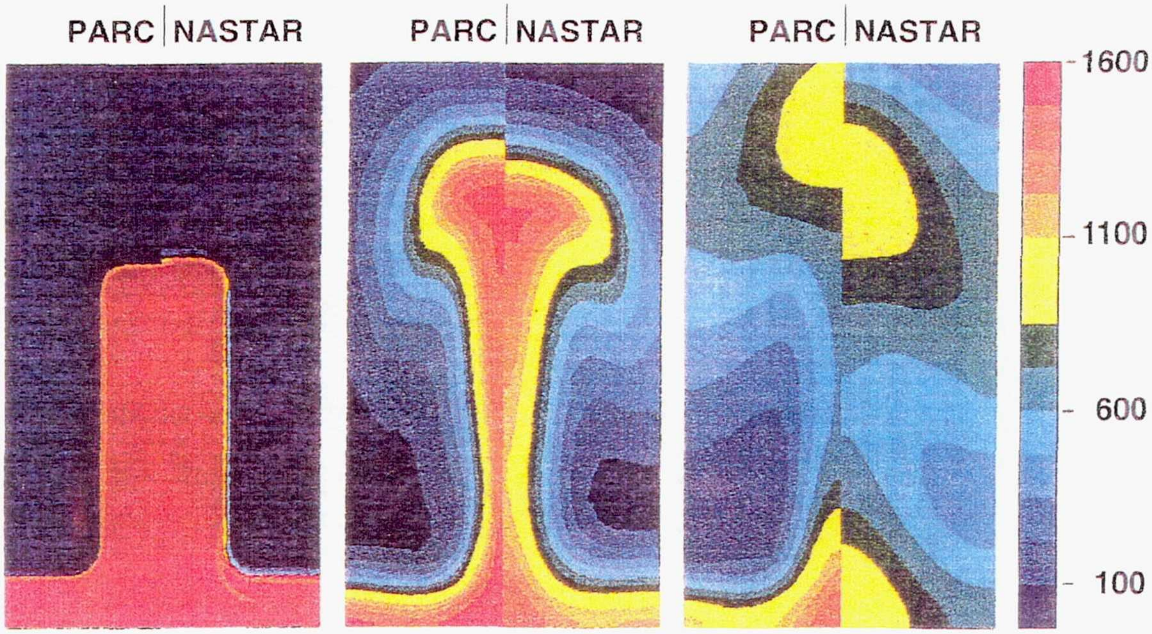

Mixer exit

Halfway

Shroud exit

In this slide, a side-by-side total temperature comparison is presented for the NASTAR and PARC Navier-Stokes calculations within the mixing duct. The apparent mismatch at the nozzle exit plane is simply a plotting artifact introduced by each code using a different number of grid points interior to the nozzle wall. Both codes predict the expected kidney shaped patterns, with the PARC code producing the expected hotter centerline line pattern.

Page intentionally left blank

2nd GENERATION MIXER-EJECTOR ANALYSIS

Navier-Stokes Streamwise Vorticity Comparisons

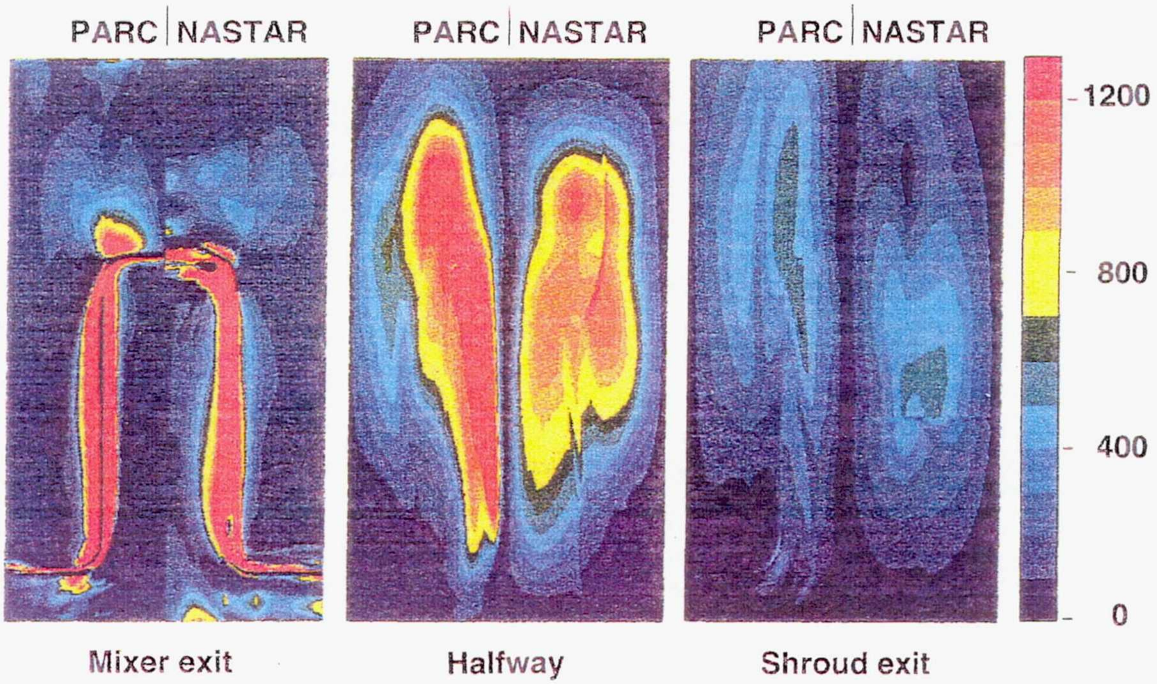

In this slide, a side-by-side streamwise vorticity comparison is presented for the NASTAR and PARC Navier-Stokes calculations within the mixing duct. Both codes predict similar vortical patterns, distribution and intensity.

Page intentionally left blank

DESIGN - ANALYSIS COMPARISON

Mixer Nozzle Exit Vertical Velocity Profiles

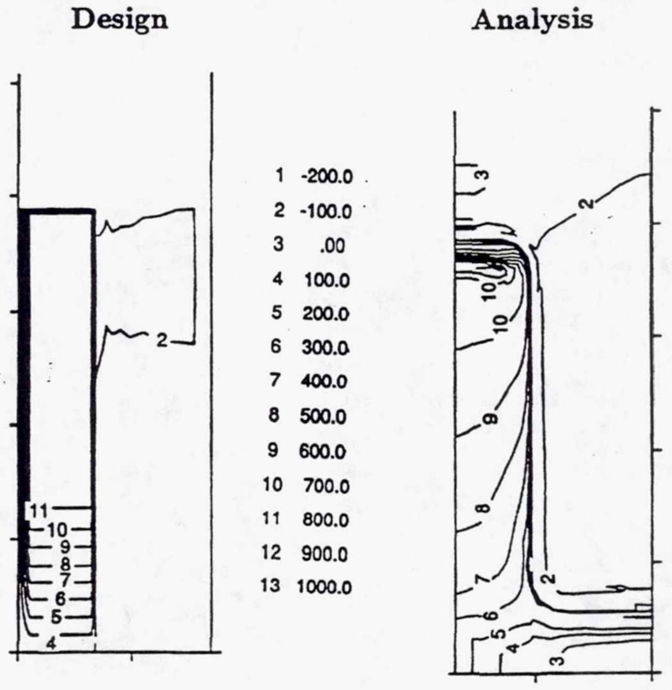

An important issue in performing the CFD calculations is the choice of boundary conditions to be specified at the inlet plane. In the design calculations performed at PW, profiles at the mixer nozzle exit plane were specified. The axial velocity was assumed uniform but the vertical component was developed using a uniform vertical velocity in the lobe (as in the model developed by Paterson, Skebe and Barber) and a linear variation to zero vertical velocity at the central axis. A comparison of the full nozzle calculation, from the upstream plenum, and this modeled boundary condition illustrates a linearly varying profile occurs all through the lobe.

DESIGN - ANALYSIS COMPARISON

Mixer Nozzle Exit Turbulence Energy (k) Profiles

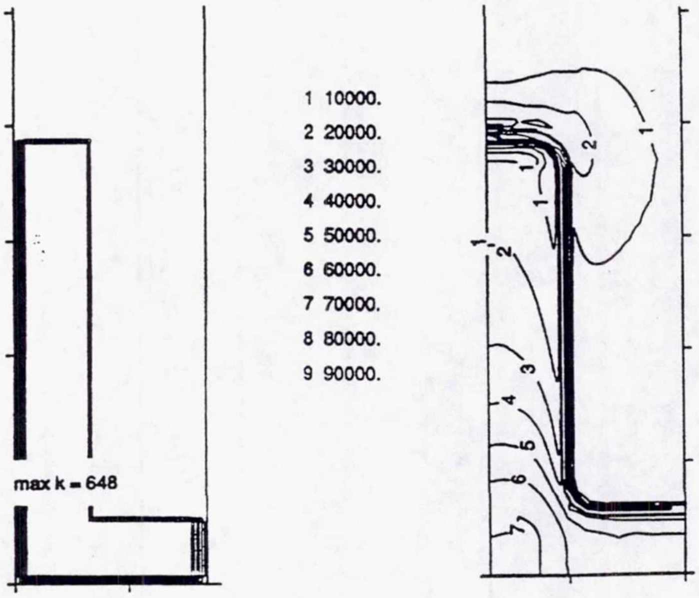

Design **Analysis**

In the design calculations performed at PW, profiles at the mixer nozzle exit plane were specified. Turbulence variable initialization however is more difficult than for the velocity profile. One typically assumes that the boundary layer is in equilibrium and that the rate of turbulence production equals its rate of dissipation. This slide compares such an assumption versus a calculation intialized in the plenum region for the turbulence intensity (k). Clearly the equilibrium assumption is about three orders of magnitude in error.

DESIGN - ANALYSIS COMPARISON

Mixer Nozzle Exit Turbulence Dissipation (ϵ) Profiles

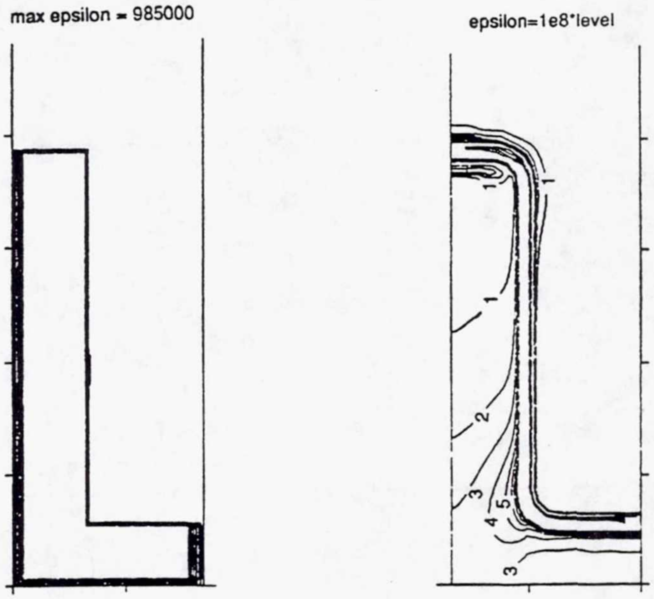

Design **Analysis**

In the design calculations performed at PW, profiles at the mixer nozzle exit plane were specified. Turbulence variable initialization however is more difficult than for the velocity profile. One typically assumes that the boundary layer is in equilibrium and that the rate of turbulence production equals its rate of dissipation. This slide compares this assumption versus a calculation intialized in the plenum region for the turbulence dissipation. Clearly the equilibrium assumption is about three orders of magnitude in error.

NASTAR DEPENDENCE ON DAMPING PARAMETER

$Re_{cell} = 20$

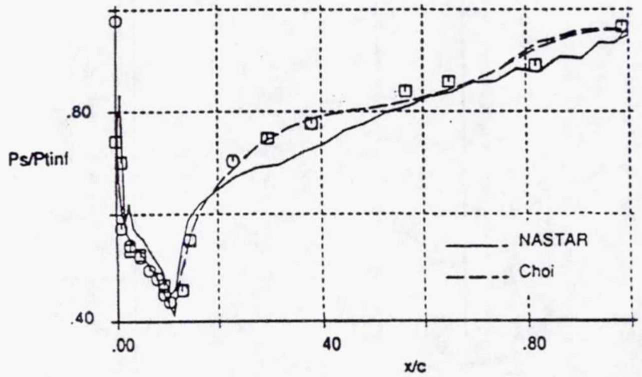

$Re_{cell} = 10$

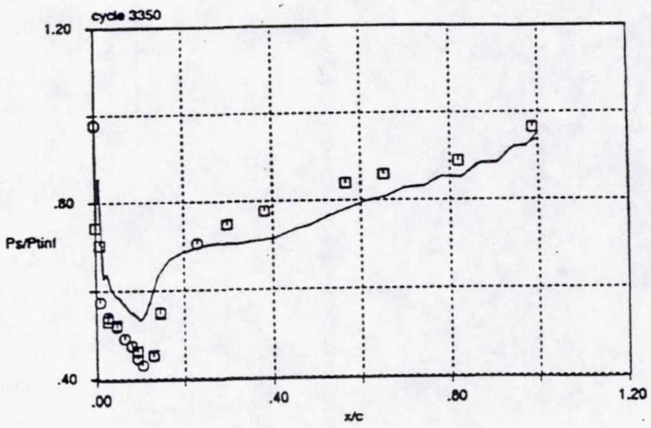

As mentioned earlier, the NASTAR code applies a user specified level of external damping through a coefficient proportional to the "cell Reynolds number". The effect of damping on this mixing dominated flow is clearly evident in the shroud loading levels. Lower cell Reynolds number levels imply higher levels of damping and correspondingly more mixing, resulting in lower shroud suction levels. One also observes, as expected, lower levels of ejector pumping.

EFFECT OF COMPRESS. ON TURBULENT MIXING

- **Conventional (k, ϵ) model developed for incompressible flows**
- **NASA, Cal Tech data indicates strong dependence on convective Mach number:** $M_c = \frac{U_1 - U_2}{a_1 + a_2}$
- **Dash introduced factor for round jets based on** $M_T = k/a$
- **Sarkar model introduces simple correction based on** M_T

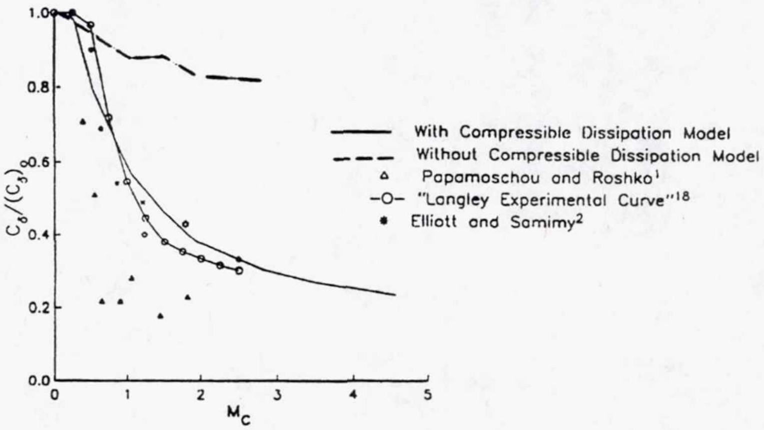

Conventional two-equation turbulence models like the Jones and Launder model have been developed and calibrated for largely incompressible flows. Extensive experimental data taken for free shear layer flows (CalTech, NASA Langley, U. Illinois, etc.) have shwon that the spreading rate, i.e. the rate of mixing, is proportional to the convective Mach number of the two streams. Recognizing this, Dash of SAIC proposed a compressibility correction factor to the turbulent eddy viscosity in terms of the turbulence Mach number. Recently Sarkar at ICASE and Zeeman at NASA Ames developed modifications to the Jones/ Launder model to account for compressibility. The enclosed figure illustrates the effect of this modification.

Page intentionally left blank

EFFECT OF COMPRESS. ON TURBULENT MIXING

Dash f_μ Parameter Where $\mu_{comp} = f_\mu \mu_{incomp}$

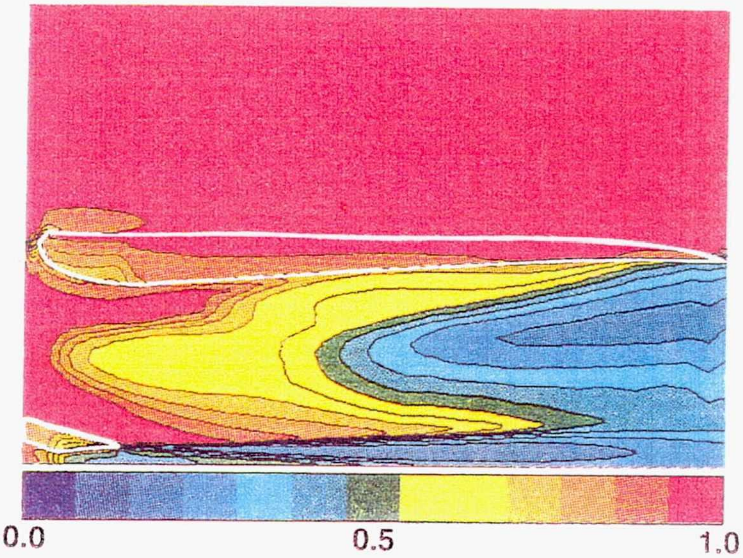

The effect of compressibility on the turbulent eddy viscosity in the NASTAR calculation was assessed through post-processing. The "f" parameter introduced by Dash was evaluated using the calculated dependent variables. Clearly the rate of mixing will be influenced by this effect.

Page intentionally left blank

NASTAR RESULTS ANALYSIS

Non-Physical Total Pressure Losses

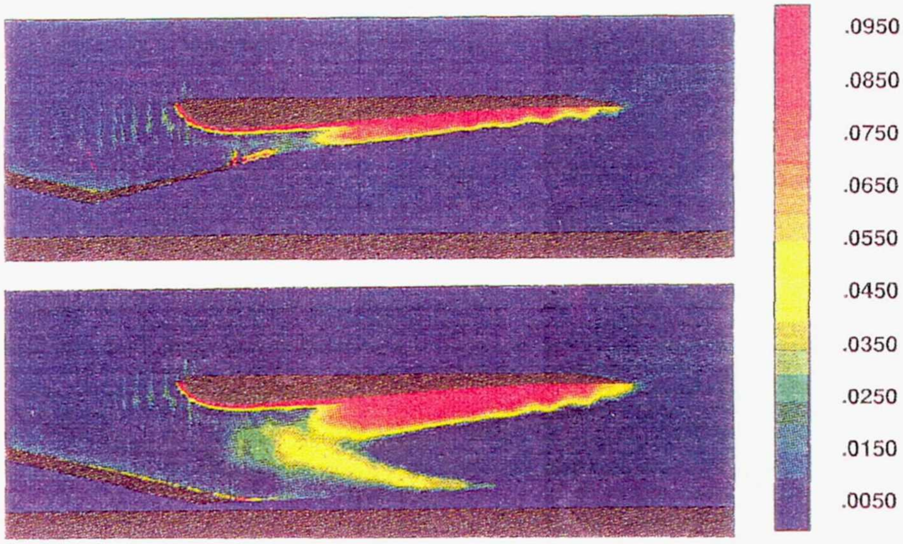

The quality of the NASTAR predictions can be assessed by evaluating the local (at each grid point) total pressure loss. Many Euler codes track this variable, recognizing that it is conserved everywhere in the flowfield, except across shocks. Therefore, any changes from freestream level have been commonly associated with "numerical" losses. In the current application, pressure losses also arise in regions where viscous losses occur. This chart presents the calculated total pressure loss on an axial slice through the lobe crest plane. One can observe a series of pressure loss regions upstream of the cowl leading edge, in regions where no losses should occur (wall boundary layers, shocks). These numerical losses can be largely attributed to the large skewness of the H-type mesh in the neighborhood of the shroud leading edge.

Page intentionally left blank

CFD ANALYSIS SUMMARY

- NASTAR Navier-Stokes Analysis Completed
- Predictions Closely Matches Experimental Data
- Procedure Developed for Rapid Generation of Grids Over Complex Geometries
  - Metric Measure Introduced for Quantitative Assessment of Grids
- NS Design Approach Underpredicts Level of Mixing

1999176555

PARC ANALYSIS OF HSR NOZZLES

Nicholas J. Georgiadis
NASA Lewis Research Center
Cleveland, Ohio

518-07

409536

22P.

PARC FNS ANALYSES:

1. **3D ANALYSIS OF PRATT & WHITNEY 2D MIXER-EJECTOR NOZZLE (Y. CHOI)**
2. **AXISYMMETRIC ANALYSIS OF NASA LANGLEY SINGLE FLOW PLUG NOZZLE (N. GEORGIADIS)**

Only recently has computational fluid dynamics (CFD) been relied upon to predict the flow details of advanced nozzle concepts. Computer hardware technology and flow solving techniques are advancing rapidly and CFD is now being used to analyze such complex flows. Validation studies are needed to assess the accuracy, reliability, and cost of such CFD analyses. At NASA Lewis, the PARC2D/3D full Navier-Stokes (FNS) codes are being applied to HSR-type nozzles. This report presents the results of two such PARC FNS analyses. The first is an analysis of the Pratt and Whitney 2D mixer-ejector nozzle, conducted by Dr. Yunho Choi (formerly of Sverdrup Technology-NASA Lewis Group). The second is an analysis of NASA-Langley's axisymmetric single flow plug nozzle, conducted by the author.

OVERVIEW OF PARC:

- **3D AND 2D/AXISYMMETRIC VERSIONS**
- **NAVIER-STOKES AND EULER MODES**
- **CENTRAL DIFFERENCING-BEAM AND WARMING ALGORITHM**
- **TURBULENCE MODELS:**
    1. **THOMAS (STANDARD ALGEBRAIC MODEL)**
    2. **BALDWIN-LOMAX**
    3. **K-EPSILON**

The PARC2D/3D internal flow Navier-Stokes codes[1] are used to analyze a variety of propulsion flows. PARC solves the Reynolds-averaged Navier-Stokes equations in conservation law form with the Beam and Warming approximate factorization algorithm[2]. Both algebraic and two-equation turbulence models are available in PARC to analyze turbulent flows. The algebraic turbulence models are the P.D. Thomas model[3] and the Baldwin-Lomax model[4]. The two-equation models are the Chien low Reynolds number k-ϵ model[5] (modified for compressibility by Nichols[6] and added to the 2D/axisymmetric PARC code in 1990) and the Speziale low Reynolds number k-ϵ model[7] (added to the 3D PARC code in 1991).

PRATT & WHITNEY 2D MIXER-EJECTOR NOZZLE GEOMETRY

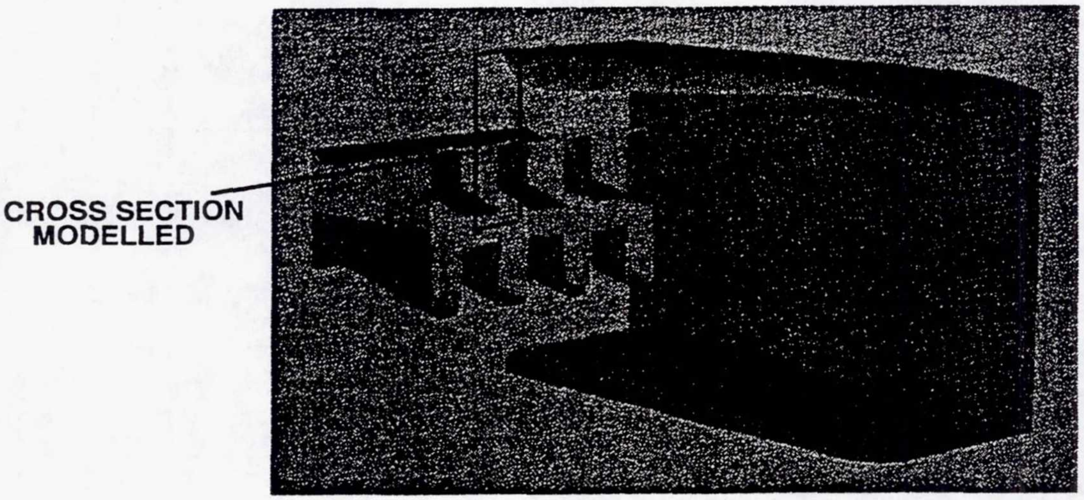

The first of the two PARC analyses discussed in this report was the 3D calculation of the flowfield of the Pratt and Whitney 2D mixer-ejector nozzle that was tested in the NASA Lewis (LeRC) 9′ x 15′ wind tunnel. A cut-away view of the nozzle geometry is shown in the figure. The configuration shown, with the short shroud enclosing the mixing region (as opposed to the intermediate length and long shrouds) is the one considered in the analysis described here. A parallel analysis of this nozzle was conducted by United Technologies Research Center (UTRC) using a Pratt and Whitney finite volume Navier-Stokes code, NASTAR. The two codes were used to calculate the nozzle flowfield for the case having the following operating conditions: Free stream pressure = 14.5 psia, free stream total temperature = 530° R, primary total temperature = 1960° R, and nozzle pressure ratio (NPR) = 4. The two codes' predictions of this flow case were compared to experimental data collected in the LeRC 9′ x 15′ wind tunnel tests.

3D COMPUTATIONAL GRID FOR NOZZLE FLOWFIELD

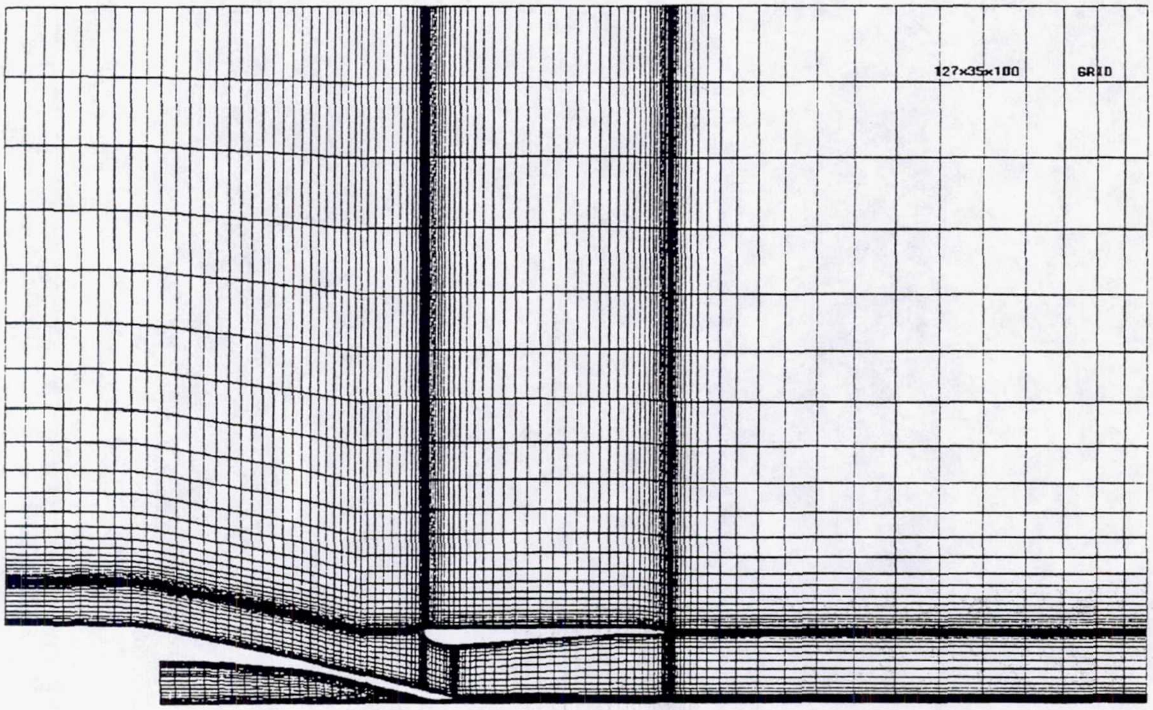

Generation of the 3D computational grid required significant effort. Two grids were constructed for the Pratt and Whitney 2D mixer-ejector nozzle. The first was composed of three blocks (one each for the following regions: upstream of the nozzle, in the mixer, and downstream of the mixer) and had a total of 493,500 points. The second was a single block grid with 444,500 points. The grid shown in the figure is the single block grid; however, the multiblock grid looks nearly the same as that shown in this figure.

The two grids were initially constructed to compare the accuracy and efficiency of the PARC code in using single block and multiblock grids for the same flow case. After a series of iterations had been conducted for both cases, it was determined that the multiblock solution was having much difficulty converging at one of the block interfaces. The multiblock grid case was then stopped and the rest of this report will only discuss the single block case.

AXIAL CUTS THROUGH 3-D GRID

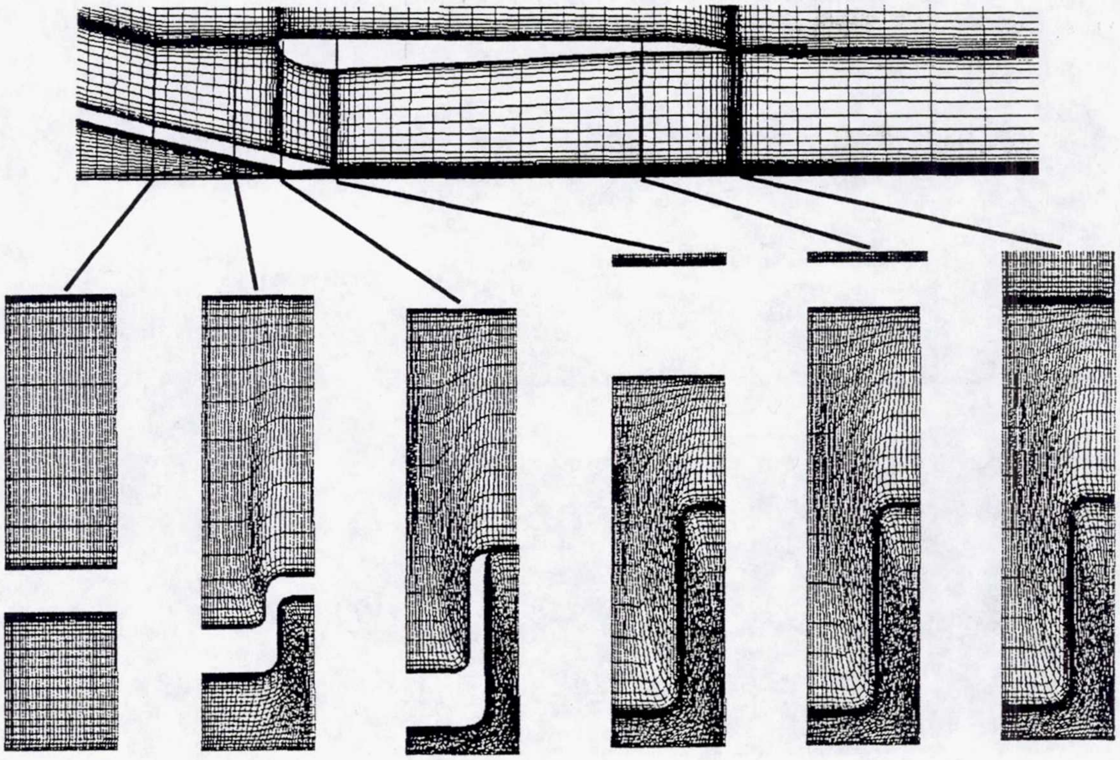

The figure shows six axial cuts through the single block grid in order to demonstrate the complexity of the grid. The first two sections (X = 2.13 and X = 4.06) are cut through the primary nozzle and ejector inlet. The third section (X = 5.67) is at the leading edge of the shroud. The fourth section (X = 6.62) is cut through the shroud at its maximum thickness position. The fifth section (X = 15.35) cuts through the shroud at approximately 85 percent chord. The sixth cut (X = 17.08) is just downstream of the shroud's trailing edge.

MACH NUMBER CONTOURS FOR P&W MIXER-EJECTOR NOZZLE

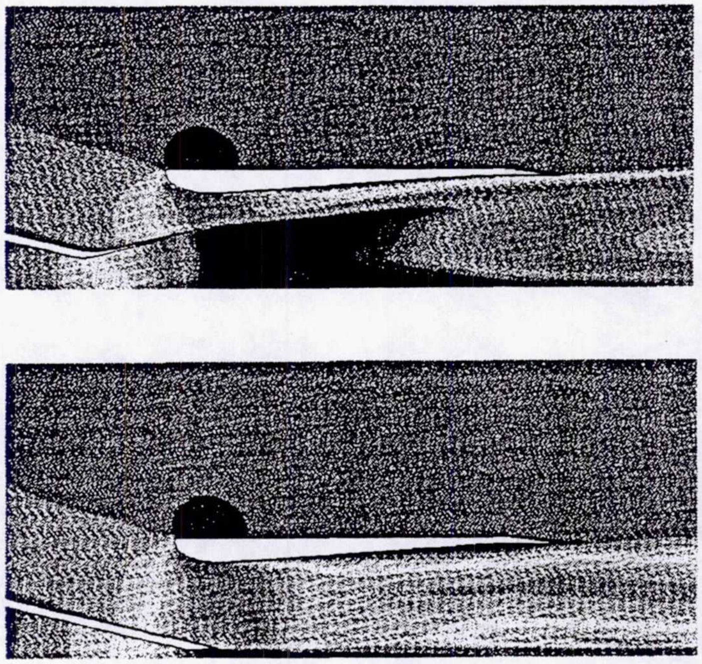

PEAK SIDE

VALLEY SIDE

Mach number contours in the planes of the peak side and valley side of the primary nozzle are shown in the figure. The primary flow chokes within the primary nozzle and expands to over Mach 2.0 downstream of the primary nozzle exit. The secondary flow entering the mixing region chokes near the maximum thickness location of the shroud. The peak side Mach number contour plot shows that two high energy flow streaks (one down the centerline and the second extending through the mixing region near the shroud) continue past the exit of the mixing region.

TOTAL TEMPERATURE CONTOURS FOR P&W MIXER-EJECTOR NOZZLE

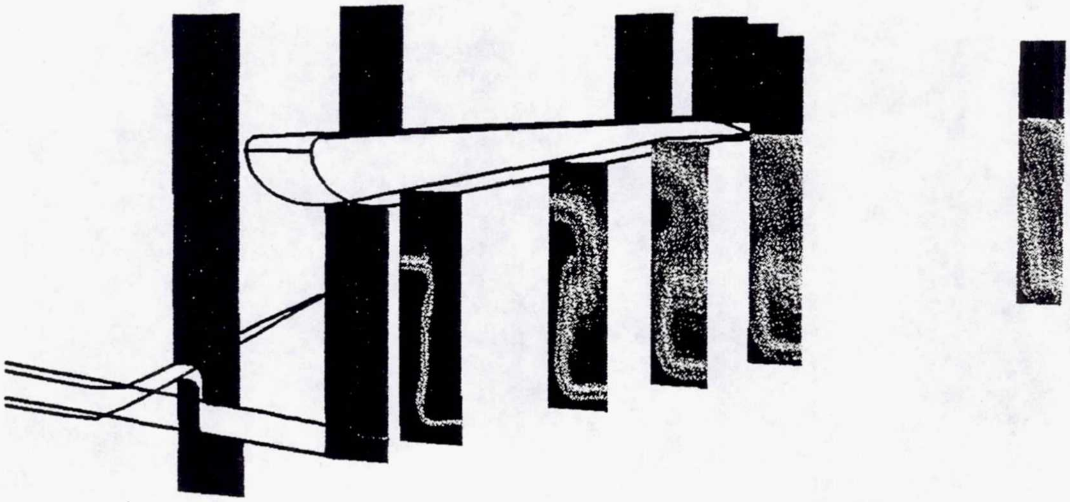

The total temperature contours (shown at several cross sections beginning in the primary nozzle and extending past the shroud exit) also show the two hot streaks. At the mixing region exit plane, the total temperature at the centerline remains at the primary total temperature while the total temperature in the other hot streak decreases to about 65 percent of the primary total temperature.

2nd GENERATION MIXER EJECTOR ANALYSIS

Exit Plane Total Temperature

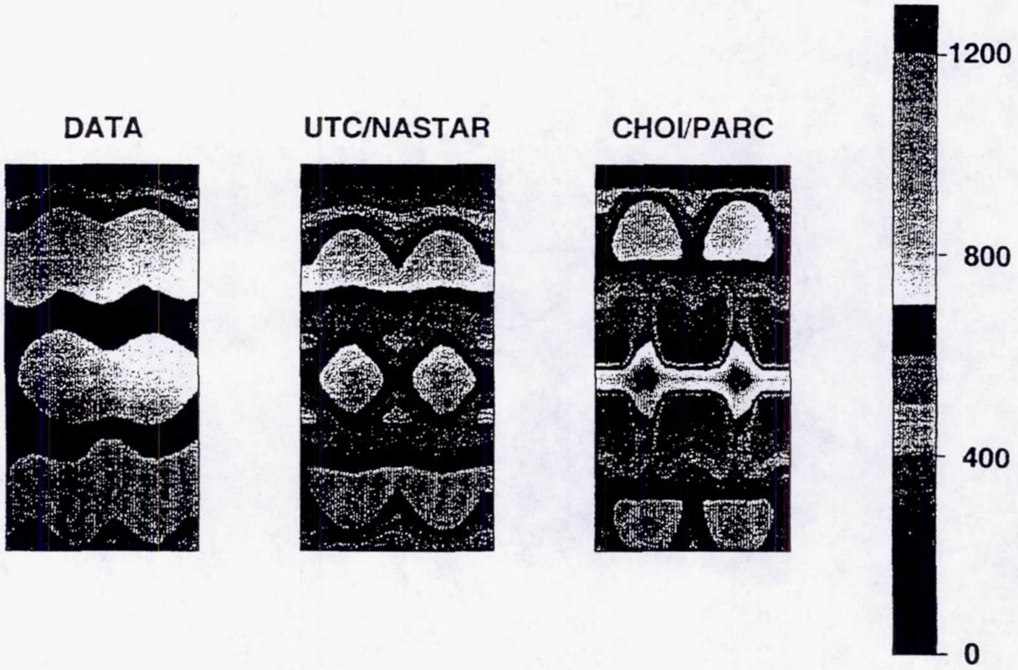

A comparison of experimental data obtained in the LeRC 9′ x 15′ tests to the PARC calculation and UTRC's NASTAR calculation of the total temperature field slightly downstream of the shroud exit plane is shown in the figure (taken from a Pratt and Whitney presentation). The two CFD solutions are each reflected about the planes of symmetry for comparison to the data. Both CFD solutions demonstrate less mixing than does the experimental data, with the PARC solution demonstrating less mixing than the NASTAR solution. The major differences between the codes used to obtain the two solutions are that PARC is a finite difference code and used the Thomas algebraic turbulence model while NASTAR is a finite volume code and used the k-ϵ turbulence model.

COMPARISON OF CFD RESULTS TO EXPERIMENTAL DATA

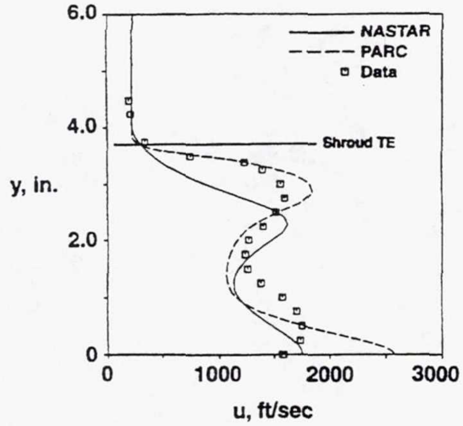

VELOCITIES AT EXIT PLANE

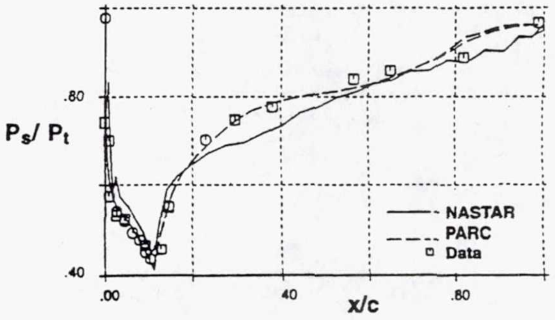

PRESSURES ALONG SHROUD

The comparison between experimental data and CFD calculations of velocity profiles at the shroud exit plane in the left side of the figure also shows that the PARC solution underpredicts the extent of mixing. The position of the two velocity peaks (one at the centerline and the other close to the shroud) correspond to the positions of the total temperature peaks shown in a previous figure. The comparison of static pressures along the shroud (shown in the right side of the figure) show that the PARC solution matches the experimental data well. The PARC solution predicted the pumping ratio (secondary flow rate divided by primary flow rate) to be 1.51. This also matches the experimental data (pumping ratio = 1.46) well.

LONG SHROUD CALCULATION

- **SAME FLOW CONDITIONS AS FOR SHORT SHROUD**
- **NEW SHROUD LENGTH: (1.7 x SHORT SHROUD LENGTH)**

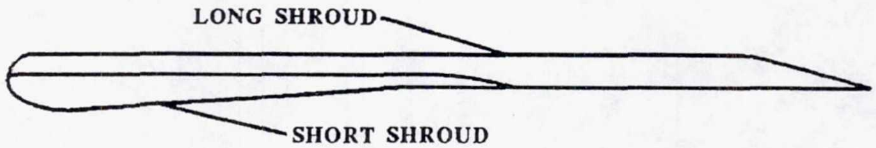

- **MIXING ENHANCED (COMPARED TO SHORT SHROUD):**
  - **(1) ~20% LOWER MAXIMUM EXIT VELOCITY**
  - **(2) ~25% LOWER STAGNATION PRESSURE AND TEMPERATURE**
- **PUMPING UNCHANGED**

After completion of the short shroud case, calculations were also made for a long shroud case. The figure shows a comparison between the cross sections of the short shroud and the long shroud (length = 1.7 x short shroud). The operating conditions of the nozzle and free stream were the same as for the short shroud case. The same size grid (444,500 points) was also used for the calculations.

The long shroud results indicated that mixing was enhanced relative to the short shroud solution. At the exit plane, the maximum velocity at the centerline decreased by 20 percent relative to the short shroud case and the maximum total pressures and temperatures decreased by about 25 percent. The secondary flow pumping was unchanged from the short shroud case.

LANGLEY SINGLE FLOW PLUG NOZZLE

- VENTED AND NON-VENTED PLUGS
- *15° PLUG HALF ANGLE*
- HEAVILY INSTRUMENTED TO MEASURE:
  1. PLUG SURFACE TEMPERATURES, PRESSURES, SHEAR STRESS
  2. *JET PLUME QUANTITIES (INCLUDING LDV & FLOW VISUALIZATION)*
  3. FLOWFIELD ACOUSTICS

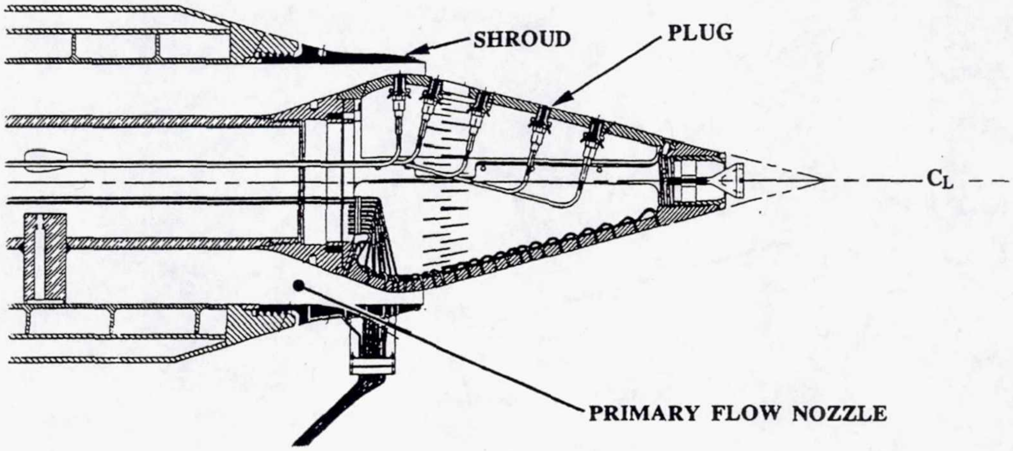

The second analysis is that of the NASA Langley single flow plug nozzle (conducted with the PARC2D/axisymmetric code). This nozzle will be tested in NASA Langley's Jet Noise Laboratory (JNL) and will provide an extensive set of data for CFD code validation. During these tests, Dr. Jack Seiner of NASA Langley[8] intends to measure several quantities including temperatures, pressures, shear stress, and heat transfer along the plug; pressures, temperatures, velocity profiles, and Reynolds stresses (with LDV) in the plume; and acoustics in the flowfield. The plug will be removable to allow for installation of a ventilated plug (to control flow separation and shocks occurring between the plug surface and the free shear layer that forms between the primary flow and the surrounding air).

GEOMETRY FOR GRID GENERATION AND PARC2D CALCULATIONS

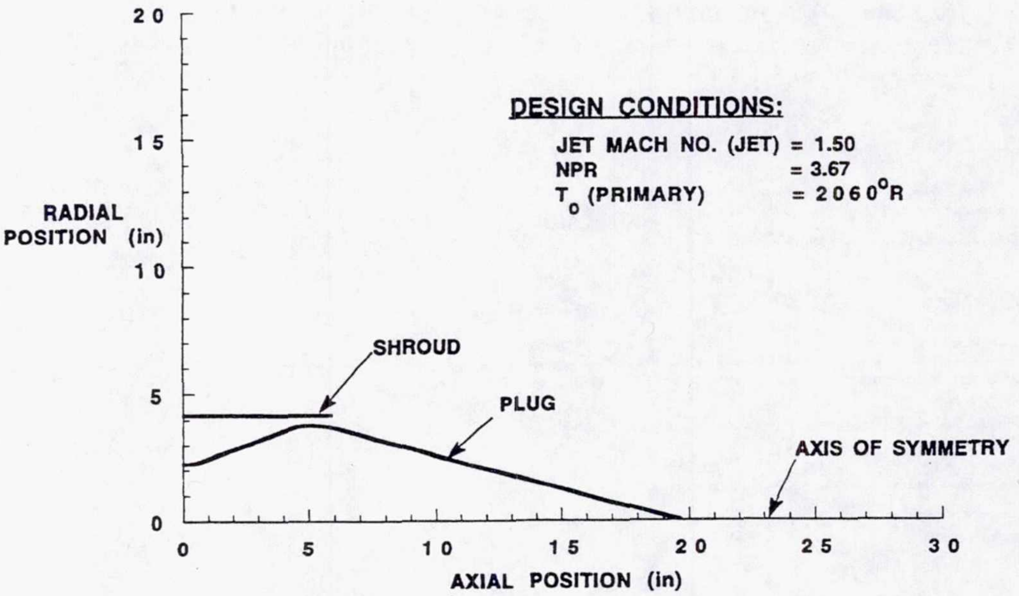

The geometry of the nozzle flow field modelled in the PARC calculations is shown in this figure. The axial and radial coordinate axes shown in this figure are the same for the rest of the plots in this report. A splitter plate (.020 inches thick) separates the primary flow from the ambient air and extends to X = 5.8 inches. The plug has a 15 degree half angle that extends to X = 19.6 inches. The nozzle area ratio and NPR are set to provide a Mach number of 1.50 at the nozzle exit plane. The total temperature of the primary flow is 2060° R. In the JNL tests, the primary nozzle flow will exit into quiescent air. For the PARC calculations, the freestream Mach number was set to Mach 0.3 because PARC (like many FNS codes) has difficulty in converging very low Mach number (incompressible) flows.

GRID FOR PARC2D CALCULATIONS OF LANGLEY SINGLE FLOW PLUG NOZZLE

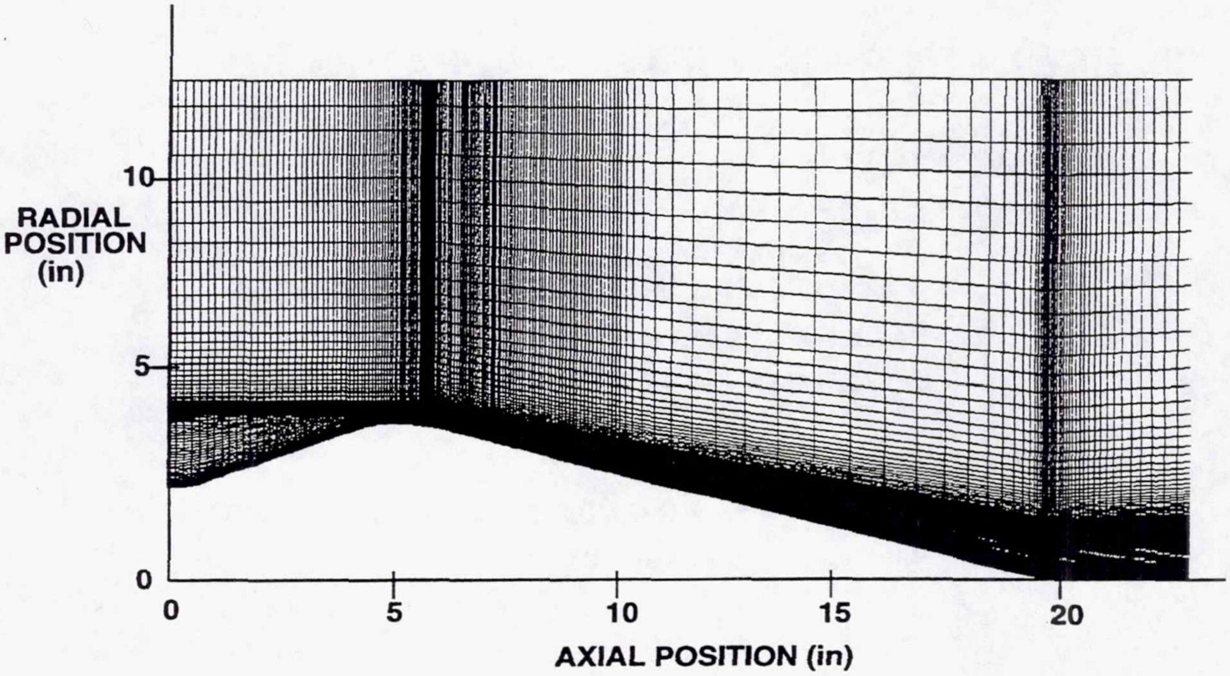

Several grids (having different numbers of grid points but representing the same physical space) were constructed with the INGRID code. The figure shows one of the computational grids in the vicinity of the nozzle. The physical size of all the grids was 120 inches in the axial direction (in order to model the jet mixing with the ambient air far downstream of the plug tip) by 12 inches in the radial direction. In the following comparisons of flowfield solutions, three grids are referred to as coarse, medium, and fine. The sizes of these grids were 237 x 145, 315 x 145, and 415 x 129, respectively.

TURBULENCE MODELS IN PARC:

A. **ALGEBRAIC MODELS:**

1. **P.D. THOMAS**
   - **STANDARD ALGEBRAIC MODEL IN PARC**
   - **OPTIMIZED FOR FREE SHEAR LAYERS**
2. **BALDWIN-LOMAX**
   - **OPTIMIZED FOR ATTACHED WALL BOUNDED FLOWS**

B. **2-EQUATION MODELS (k-ε):**

1. **CHIEN (Low Re) - PARC2D/AXISYMMETRIC**
2. **SPEZIALE (Low Re) - PARC3D**

The figure shows the turbulence models that are currently available in the PARC code. The standard algebraic turbulence model in PARC is based upon the work of P.D. Thomas. This model calculates turbulent viscosity near surfaces (wall-bounded part of model) and in regions where flows are mixing (free shear layer part of model) but was optimized for the latter. The Baldwin-Lomax model only calculates turbulent viscosity in wall-bounded regions. These two algebraic models may also be run in conjunction (Baldwin-Lomax for wall-bounded regions and Thomas model only in free shear layer regions) to provide a third algebraic model.

These algebraic models are all simple mixing length models that use an empirically determined turbulent mixing length distribution to calculate turbulent viscosity. These models often model complex flows inadequately because their mixing length distributions are not applicable to all flows. Two-equation models (such as k-ϵ) avoid this single mixing length limitation by solving additional transport equations to calculate turbulent viscosity but are substantially more computationally expensive than the algebraic models. As mentioned previously, k-ϵ models have been added recently to the PARC code (Chien low Reynolds number model in the 2D/axisymmetric code and the Speziale low Reynolds number model in the 3D code). The three algebraic turbulence models (Thomas, Baldwin-Lomax/Thomas combination, and Baldwin-Lomax) and the Chien k-ϵ turbulence model were used for the initial PARC calculations.

MACH NUMBER CONTOURS ALONG PLUG AND IN JET PLUME

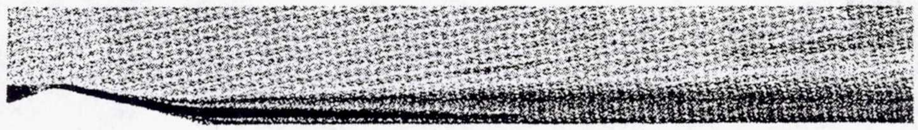

Thomas

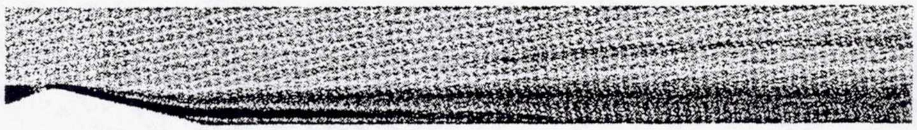

Baldwin-Lomax /Thomas

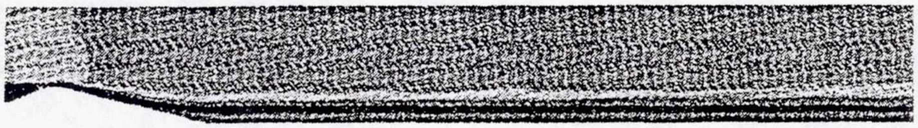

Baldwin-Lomax

K-Epsilon

The figure shows Mach number contours for the flow region extending from the entrance of the nozzle and freestream out to the plume at approximately X = 80 inches for the four turbulence models that were initially considered using the coarse grid. The plume of the k-ϵ solution (bottom contour plot) decays most rapidly. The Baldwin-Lomax plot (second from the bottom) shows that there is essentially no dissipation of the flow after the plug tip. This occurs because the Baldwin-Lomax model calculates turbulent viscosity only in wall bounded regions. After the plug tip (X= 19.6 inches), there is no solid surface, so no turbulent viscosity is being calculated there. The combination Baldwin-Lomax/Thomas solution (contour plot just above Baldwin-Lomax) was obtained by calculating turbulent viscosity in the wall bounded regions of the nozzle with Baldwin-Lomax and in the jet plume with the free shear layer model part of the Thomas model. Because Baldwin-Lomax (alone, with no free shear layer model) has the limitation of not being able to calculate turbulent viscosity in the plume, it was only used to obtain the one solution shown in the figure above and will not be discussed in the following comparisons of solutions obtained with the three other models: Thomas, Baldwin-Lomax/Thomas, and k-ϵ.

VELOCITY PROFILES FOR FINE GRID SOLUTIONS

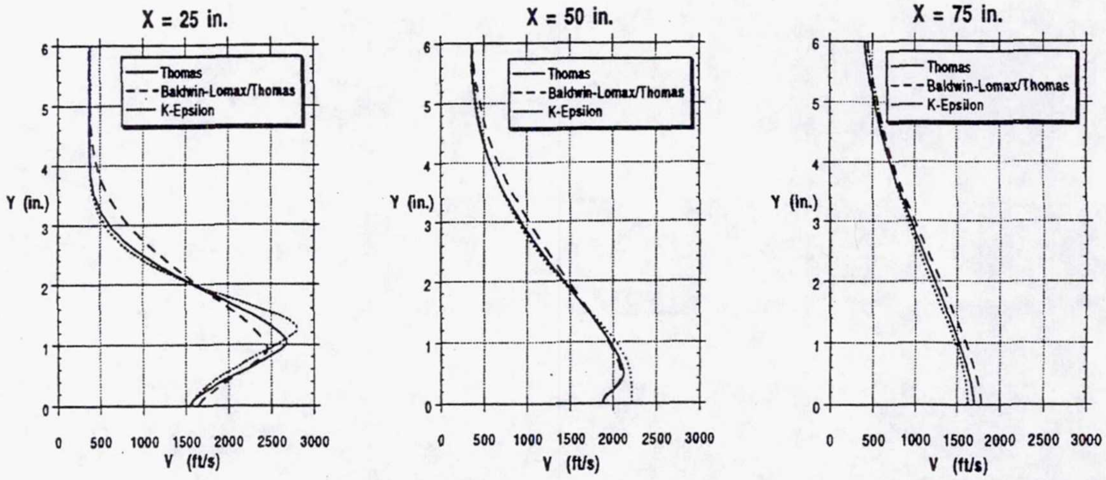

Velocity profiles in the plume at three axial locations downstream of the end of the plug are shown in the figure for the fine grid (415 points in the axial direction) solutions. The three locations are all measured relative to the nozzle inflow, as shown in the previous figure of the nozzle geometry. The plot for X = 25 in. shows that the k-ϵ solution has the highest maximum velocity of the three solutions. This is still the case at X = 50 in. where the plumes have mixed with the ambient air to lower the maximum velocity of each plume. At X = 75 in., the k-ϵ solution shows the lowest maximum velocity, indicating that the k-ϵ model calculates more turbulent viscosity in the plume to mix the high energy flow of the jet with the ambient air.

TOTAL TEMPERATURE PROFILES FOR FINE GRID SOLUTIONS

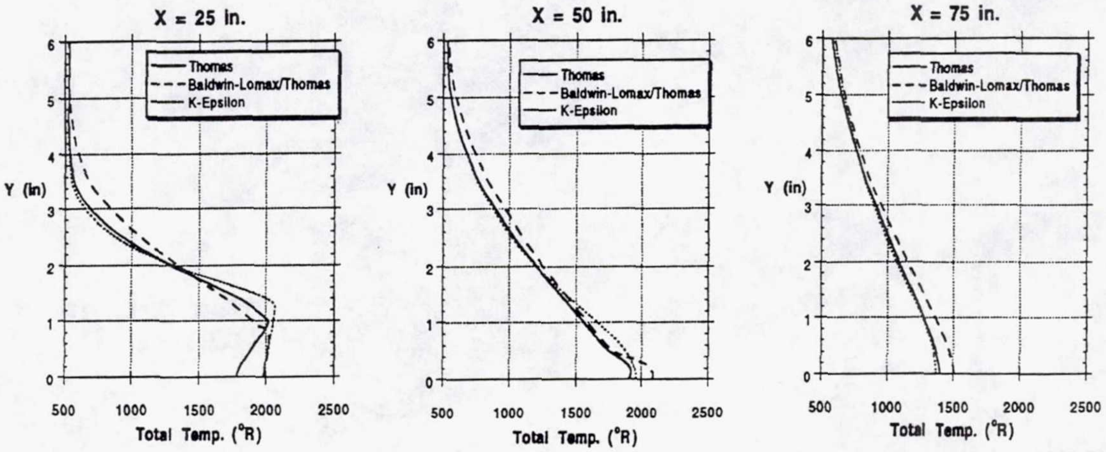

A comparison of total temperature profiles at the same locations as in the previous figure demonstrates the same trend among the turbulence models. At the location nearest the plug tip (X = 25 in.), the k-ϵ solution shows the highest maximum total temperature while downstream at X = 75 in., the k-ϵ solution shows the lowest maximum total temperature. Although the two algebraic turbulence model solutions used different turbulence models in the wall bounded regions near the nozzle, they both used the Thomas model in the region of the flowfield where the jet plume mixes with the ambient air and both demonstrated less mixing in this region than the k-ϵ solution does. The comparison of Pratt & Whitney nozzle flow calculations that was previously discussed also showed that the NASTAR k-ϵ solution produced more mixing than the PARC Thomas model solution (although those solutions were obtained not only with different turbulence models but with different codes).

SHOCK FUNCTION
(BASED ON PRESSURE GRADIENT)

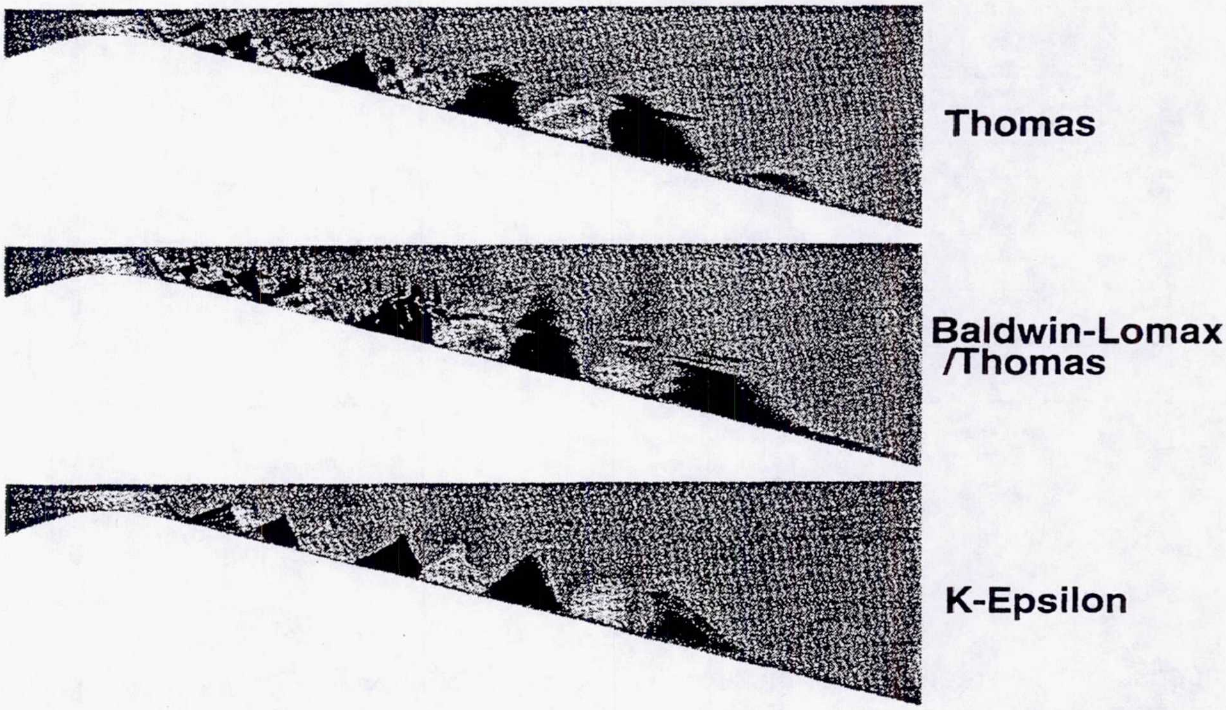

The shock function contours in the figure show shock cell patterns that form between the plug and the shear layer (of the jet and ambient air) downstream of the nozzle exit. PLOT3D (used to generate the contour plots) defines this shock function as follows

$$\text{Shock function} = \frac{V}{c} \bullet \frac{\text{grad}(P)}{|\text{grad}(P)|}$$

The two solutions obtained with the Thomas and Baldwin-Lomax/Thomas models show that these algebraic models have considerable difficulty in producing realistic looking shock cell patterns. The k-ϵ solution shows a more well defined shock cell pattern. A comparison of these solutions indicates that simple algebraic turbulence models may not be adequate for predicting flow details such as shock cell structure.

EFFECT OF PLUG SURFACE BOUNDARY CONDITION ON SHOCK CELL PATTERN

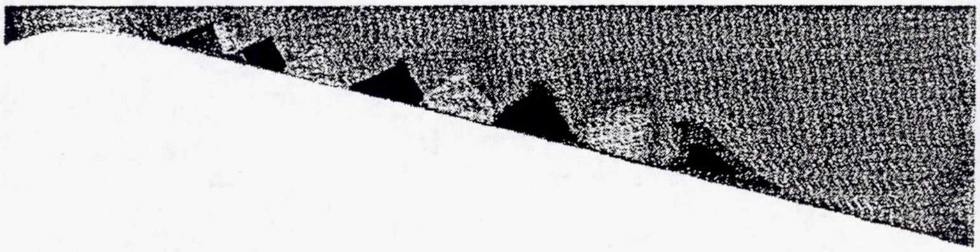

K-Epsilon (no-slip wall)

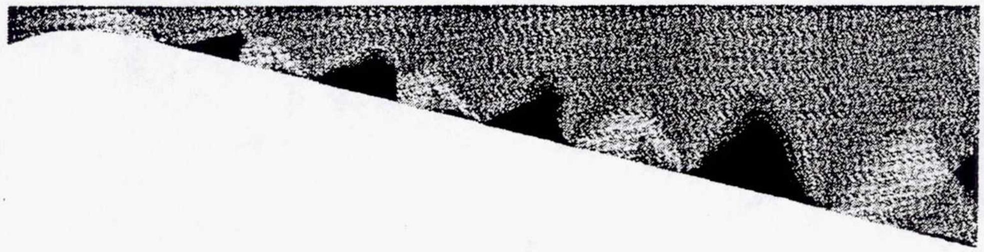

K-Epsilon (slip wall)

The figure shows a comparison of shock cell patterns obtained with k-ϵ using two different boundary conditions for the plug surface. The first was the standard no-slip surface which allows a boundary layer to develop while the second was a slip wall boundary which does not produce a boundary layer. With the standard no-slip boundary, the turbulent viscosity generated in the boundary layer tends to smear the shock structure just outside of the nozzle exit plane. The slip surface boundary case was examined to determine the shock structure without this boundary layer influence. The comparison of the two shock cell patterns demonstrates that the plug surface boundary condition does have a substantial influence on the flow's shock structure, particularly just downstream of the nozzle exit.

STATIC PRESSURE DISTRIBUTION ALONG PLUG

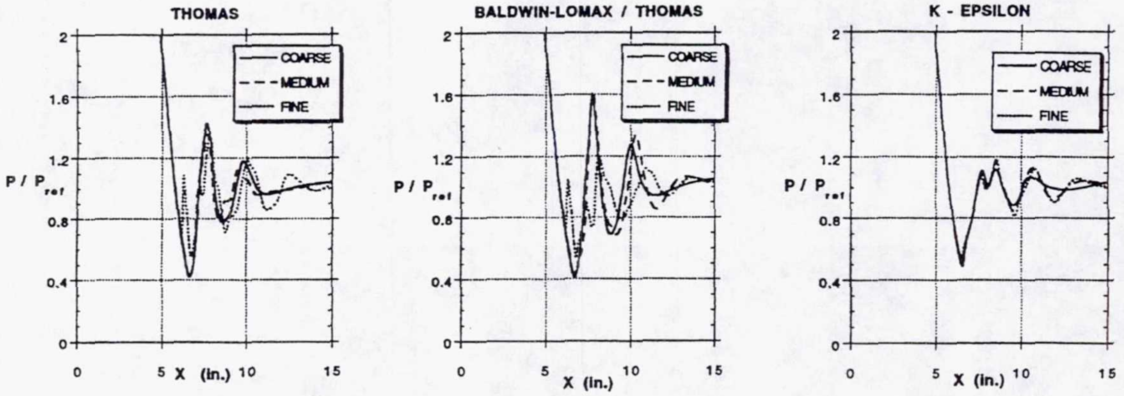

The three plots in the figure show static pressure distributions along the plug for the three turbulence models that were used to obtain solutions with the coarse, medium, and fine grids. The k-ϵ solutions show much less grid resolution effects on pressure predictions relative to the Thomas and Baldwin-Lomax/Thomas solutions. Both sets of algebraic turbulence model solutions show significant differences in pressure distributions from one grid size to another.

CONCLUDING REMARKS

- PARC 2D/3D CODES ARE BEING USED TO ANALYZE COMPLEX HSR NOZZLE FLOWS
- COMPARISONS TO EXPERIMENTAL DATA SHOW CAPABILITIES/LIMITATIONS OF PARC
- FUTURE COMPARISONS WILL DEMONSTRATE EFFECT OF CODE IMPROVEMENTS (TURBULENCE MODELS, ETC.)

The PARC analyses that have been discussed are only two of the current and planned PARC FNS analyses of HSR nozzles. The comparison of the PARC calculations to experimental data for the Pratt and Whitney 2D mixer-ejector nozzle indicate that PARC is able to predict quantities such as pumping ratio and pressure distributions along the shroud well, while failing to predict the extent of mixing between the primary and secondary flows. The large discrepancy between the PARC solution and the experimental data may be the result of the algebraic turbulence model that was used. If this same flow case is reinvestigated with PARC using the new Speziale k-ϵ turbulence model, the mixing behavior might change substantially. The Langley single flow plug nozzle tests will provide an excellent set of flow data to compare to the PARC calculations that have already been obtained and those to be obtained in the future.

Several improvements to the PARC code, including addition of new turbulence models and better artificial dissipation schemes, have been implemented or are planned for the future. These improvements will hopefully allow PARC to provide more accurate quantitative flow predictions for HSR-type nozzle flows.

1999176556

STATUS ON NUMERICAL COMPUTATION OF SUPERSONIC JET PLUMES

Sanford M. Dash
Science Applications International Corporation
Fort Washington, Pennsylvania

519-07

409537

46P.

TOPICS

- **OPENING REMARKS AND OBSERVATIONS**
- **CFD CODES / STATUS AND UTILITY**
  - **PARCH/GTP and CRAFT/JR**
- **TURBULENCE MODELING FOR SUPERSONIC JETS**
  - **Building-Block Approach**
  - **Compressible-Dissipation and Vortex-Stretching Upgrades**
- **COMPLEX FLOWS / STATUS**
  - **Jets with Shocks**
  - **Jets with Plug Nozzles**
  - **Rectangular Jets**
  - **Jets in Vortical External Flow**
- **UNSTEADY FLOWS / STATUS**
  - **Related Interior Ballistic/Propulsive Activities**
  - **Exploratory Work for HSCT**

This paper will provide an overview of our status to predict the structure of supersonic jet plumes as relevant to noise suppression research for the High-Speed Civil Transport (HSCT) program. Topics to be discussed will include: the CFD codes utilized; advances made in turbulence modeling; an ability to analyze complex flows; and, the present utility of unsteady flow simulations.

PRESENT UTILITY OF CFD FOR THE PREDICTION OF SUPERSONIC JET NOISE

(A) PREDICTION OF STARTLINE PROFILES (MEAN AND TURBULENT) AT NOZZLE/EJECTOR EXIT PLANE TO INITIATE JET CALCULATIONS

(B) PREDICTION OF MEAN FLOW STRUCTURE AND TURBULENT STRESSES FOR INPUT INTO JET NOISE MODELS

- **Instability models require jet mixing characteristics for balanced-pressure jets and additionally require shock cell structure for imperfectly expanded jets**
- **Acoustic analogy models additionally require turbulent stresses**

(C) PREDICTION OF UNSTEADY FLOW STRUCTURE

- **To enhance our understanding of noise producing mechanisms and turbulent/wave interactions**
- **To predict jet instabilities for frequencies resolvable**

At present, the utility of CFD for predicting supersonic jet noise is indirect and uncoupled from the source noise model. CFD is needed to predict the detailed internal flow structure in nozzle/ejectors as required to properly initialize jet/plume calculations. It also provides inputs to jet source noise models. Instability models require the jet mixing characteristics and jet shock cell structure. Acoustic analogy models additionally require turbulent stress inputs. Unsteady CFD simulations can serve to enhance our understanding of noise producing mechanisms and turbulent/wave interactions (for large turbulent scales). They can also predict nonlinear jet instabilities for frequencies resolvable by the CFD grid size/time step.

CURRENT PROGRAMS OF RELEVANCE TO AIRCRAFT JET SIMULATION

- **NASA LaRC SUPERSONIC JET RESEARCH → HSCT NOISE SUPPRESSION**
  - CFD Methodology, Turbulence Model Upgrades/Assessment, Simulation of Noise Suppression Concepts, Unsteady Jet Simulation

- **SPIRITS UPGRADE PROGRAM → JET IR SIGNATURES**
  - Gas Turbine Tailpipe/Plume Simulation, End-to-End CFD (Air Force - AFEWC/AFGL/WL)
  - Helicopter Plume Simulation/Vortical Wake Interactions (Army - MICOM)

- **TURBULENCE INTERACTION PROGRAM → LASER PROPAGATION**
  - Aircraft Jet/Aerodynamic Interactions (Air Force - WL); Emphasis on Turbulent Structure

- **UNSTEADY JET/PLUME SIMULATIONS → COMBUSTION/ AERODYNAMICS**
  - Hypervelocity Guns (ETC/LPG/RAM)—LES Simulation (ARL/AFOSR)
  - Short-Duration Lateral Control Jets—Army (MICOM/SDC)
  - Transient Start-up in Vertical Launcher—Navy (NSWC)

We are presently engaged in several programs which have relevance to aircraft jet simulation and noise suppression. Our program with NASA Langley has emphasized the specialization of Navier-Stokes codes to supersonic jet flowfield simulation, turbulence model upgrades/assessment for jets, simulation of noise suppression concepts such as plug nozzles, and most recently, unsteady jet simulation. Our work to date in this program is summarized in a series of AIAA and JANNAF publications (Refs. 1-8), and, is described in detail in NASA CR's now under preparation (Refs. 9 and 10). Related work on jets emphasizing IR signature prediction has been performed under SPIRITS upgrade programs supported by the Air Force and Army. The Air Force work has led to the development of a specialized version of the PARCH code (PARCH/GTP) for the complete simulation of gas turbine tailpipe (augmentor/nozzle) and jet/plume flowfields included hot part temperature predictions (via coupling of a thermal solver). The helicopter jet/plume work has emphasized plume interactions with the vortical downwash flow. SPIRITS activities are described in Refs. 11-19. A new Air Force program has just been initiated for laser propagation through the aircraft plume/wake which will involve analyzing the detailed 3D aerodynamic interactions with the plume structure. The emphasis is on predicting the turbulent fluctuations and length scales which effect laser transmission. Unsteady jet/plume activities have been focussed on the simulation of combusting/multi-phase interior ballistic flow problems and on transient solid propellant rocket propulsive flows using the CRAFT NS code (Refs. 20-28).

COMPUTER CODES DEVELOPED FOR AIRCRAFT PLUME FLOWFIELD SIMULATION

PARABOLIC		
BOAT	-	Component of SPF/1 (contained in SPIRITS 4.2)
SPLITP	-	Component of SPF/2&3 (contained in SPIRITS ACM)
TTPSI	-	New implicit version of BOAT; Calculates internal (core/fan) mixing and external plume
TTSL	-	New simplified version of SPLITP with advanced turbulence models for jet/shear layer research

PARABOLIZED NAVIER-STOKES		
SCIPVIS	-	Extended version of SCIPPY for detailed mixing/shock structure
SCIP3D	-	3D version of SCIPVIS
SCRINT	-	Implicit Beam-Warming code with finite-rate chemistry
SCRINT3D	-	3D version of SCRINT
SCHAFT	-	2D/3D implicit/upwind (Roe/ TVD) code with finite-rate chemistry

OVERLAID VISCOUS/INVISCID		
SPF/1,2,3	-	Unified versions of BOAT/SCIPPY and SPLITP/SCIPPY for tactical missile applications (JANNAF)
RAXJET	-	Unified version of BOAT/SCIPPY plus integral BL and external potential flow solver for aircraft plumes (NASA)
TTJET	-	Unified version of TTPSI and FLOVAR for internal core/fan mixing; Module in Aerodyne TURBINE-EXIT code

FULL NAVIER-STOKES		
PARCH/GTP	-	Specialized gas turbine version of PARCH utilized for internal (core/fan) and external analysis; Component of SPIRITS/GT developed under Phase I AFEWC supported effort
PARCH/3D	-	3D version of PARCH utilized for jet research activities
CRAFT	-	2D/3D implicit/upwind (Roe/ TVD) code with finite-rate chemistry used for unsteady plumes with LES

Over the years, we have developed a large number of computer codes catering to the simulation of aircraft jet/plume flowfields. Parabolic codes suffice for studying balanced-pressure laboratory jets. The TTSL code is presently being utilized to study turbulence model behavior for laboratory jets and shear layers. Overlaid viscous/inviscid models have had utility in predicting aircraft afterbody drag (Refs. 29-31) and IR signatures (Refs. 32 and 33) but are not applicable to jet noise problems since interactive phenomena (e.g., the attenuation of shock strengths by turbulent dissipation) are not adequately simulated. In our earlier jet-noise oriented studies for NASA LaRC, it was found that parabolized Navier-Stokes codes performed quite well in predicting shock cell structure for imperfectly expanded jets (see Refs. 34-38). Our most recent Navier-Stokes work (Refs. 1, 3, 4) indicates that these earlier comparisons were somewhat misleading and may have involved canceling errors. Full NS methodology is required to analyze jets with shocks since: (1) full stress terms are required in the vicinity of shock/shear layer interactions; and (2) localized upstream influence effects (the upstream propagation of the pressure disturbances through the subsonic region of the jet shear layer) must be accounted for. Our NS work has involved the specialization and application of two families of codes, PARCH and CRAFT.

FEATURE	PARCH	CRAFT
EQUATIONS	• 2D/AXI - 2D CODE • 3D - 3D CODE	• 1D/2D/AXI/3D - SINGLE CODE
	• EULER/THIN LAYER OPTIONS	• EULER/THIN LAYER OPTIONS
NUMERICS	• FINITE-DIFFERENCE DISCRETIZATION WITH FINITE-VOLUME CORRECTIONS TO CELL JACOBIANS	• FINITE-VOLUME DISCRETIZATION
	• BEAM-WARMING CENTRAL DIFFERENCE ALGORITHM/ DIAGONALIZED OR BLOCK MATRIX INVERSION - JAMESON 2ND/4TH ORDER DISSIPATION • ROE/TVD RUN OPTION - FOR PERFECT/ SINGLE-COMPONENT GAS	• ROE/TVD UPWIND ALGORITHM - CONSISTENT FOR REAL, MULTI-COMPONENT GAS MIXTURES - STANDARD BLOCK OR LU MATRIX INVERSION - FULLY IMPLICIT INCLUDING SOURCE TERMS
	• TIME ASYMPTOTIC NUMERICS - INDEPENDENT TIME-STEPS - 2ND ORDER SPATIAL ACCURACY	• TIME-ACCURATE AND TIME-ASYMPTOTIC NUMERICS - 2ND ORDER TEMPORAL AND SPATIAL ACCURACY - PSEUDO-TIME ITERATION TO ELIMINATE APPROXIMATION AND FACTORIZATION ERRORS
GRID AND BOUNDARY CONDITIONS	• FIXED GRID/GRID BLANKING - PATCHING FOR COMPLEX GEOMETRIES • MULTI-ZONE BLOCKING • GENERALIZED EXPLICIT BC	• DYNAMIC GRID FOR NON-STEADY FLOWS WITH MOVING BOUNDARIES • MULTI-ZONE BLOCKING • IMPLICIT BC/LIMITED GENERALITY
THERMO-CHEMISTRY	• GENERALIZED FINITE-RATE, MATRIX SPLIT/LOOSELY COUPLED • EQUILIBRIUM AIR (TANNEHILL FITS)	• GENERALIZED FINITE-RATE, LARGE MATRIX/STRONGLY COUPLED • EQUILIBRIUM AIR (TANNEHILL FITS)
TURBULENCE	• kε TURBULENCE MODEL - LOOSELY OR STRONGLY COUPLED TO FLUID DYNAMICS - CHIEN LOW RE TERMS - COMPRESSIBILITY CORRECTIONS - 2D/AXI JET CORRECTIONS	• kε TURBULENCE MODEL - STRONGLY COUPLED TO FLUID DYNAMICS - COMPRESSIBILITY CORRECTIONS - 2D/AXI JET CORRECTIONS • LES SUBSCALE MODELS
MULTI-PHASE FLOW	• EQUILIBRATED G/P MIXTURE • G/P NONEQUILIBRIUM CAPABILITY FOR STEADY 2D/AXI FLOWS WITH NO RECIRCULATION	• GENERALIZED STEADY/NON-STEADY G/P NONEQUILIBRIUM AND GAS/LIQUID UPGRADES - NEW CONSERVATIVE/IMPLICIT PARTICLE-CLOUD SOLVER USING HIGHER-ORDER UPWIND NUMERICS

Features of PARCH and CRAFT are compared in the table above. PARCH is an extension of the AEDC PARC code which has been widely utilized for gas turbine exhaust simulation largely because it includes unique grid patching capabilities (Refs. 39 and 40) which facilitate analyzing complex geometries. CRAFT, an extension of the TUFF code of Molvik and Merkle (Ref. 41), employs improved finite-volume implicit/upwind (Roe/TVD) numerics and is more robust and accurate than PARCH. Its utility for gas turbine exhaust flows had been limited since it lacked patched grid methodology and generalized boundary conditions. These limitations have recently been removed.

RESEARCH VERSIONS OF CRAFT NS CODE

CODE NAME	CRAFT/JR	CRAFT/ETC-LPG	CRAFT/RAM	CRAFT/TMP	CRAFT/LU
APPLICATION	High-Speed Jet Research	ETC and LPG Gun Flowfields	Ram Accelerator Flowfields	Tactical Missile/ Plumes, VLS	Numerical Research
SPONSORS	NASA LaRC, ONR	BRL	AFOSR & WL/MNSH	MICOM, NSWC	Internal Research
EQUATIONS	1D/2D/AXI/3D	1D/2D/AXI/3D	1D/2D/AXI/3D	1D/2D/AXI/3D	1D/2D/AXI/3D
THERMO-CHEMISTRY	Perfect Gas, Two-Component Gas Mixture, H/N/O Finite-Rate Chemistry, Equilibrium Air Chemistry	Imperfect Gas, Combustion Chemistry, Vaporization, Liquid EOS	Imperfect Gas, Finite-Rate Extended C/H/N/O Kinetics	Generalized Finite-Rate Chemistry	Perfect Gas
TURBULENCE	kε, Compressibility Extensions, LES (preliminary)	kε, LES (preliminary)	kε/Chien, Compressibility Extensions	kε/Chien, Compressibility Extensions	kε
MULTI-PHASE CAPABILITIES	None	Gas/Liquid Equilibrated Mixture	None	Fully-Coupled Particulate Solution, New Solver	None
GRID	Fixed	Dynamic	Dynamic	Fixed	Fixed
SOLUTION	Implicit/Upwind (Roe/TVD) Strongly-Coupled Fluid/Species/ Turbulence, Variable Matrix Size	Implicit/Upwind (Roe/TVD) Strongly-Coupled Fluid/Species/Turbulence, Variable Matrix Size	Implicit/Upwind (Roe/TVD) Strongly-Coupled Fluid/Species/Turbulence, Variable Matrix Size	Implicit/Upwind (Roe/TVD) Strongly-Coupled Fluid/Species/Turbulence, Variable Matrix Size	LU Upgrade for Robustness, Faster Convergence (CFL ~ 25-50)
NEW WORK	BC Upgrades, Grid Patching akin to PARCH	Nonequilibrium, Droplet Formation/Combustion/Dispersion Model	Adaptive Dynamic Gridding for Unsteady Flows, LES	Adaptive Gridding for Unsteady Multi-Phase Flows, Patching for Gas and Particles	Rewrite of Code Structure to Optimize LU Storage for 3D

A number of research versions of the CRAFT code have been developed whose primary emphasis has been the simulation of unsteady combusting/multi-phase flows as occur in hypervelocity guns and missile propulsion. Limitations for simulating gas turbine exhaust flowfields have been removed by the development of a new version of CRAFT (Ref. 42) with grid patching methodology paralleling that of PARC and generalized, fully-implicit boundary conditions (Ref. 43) which permit much faster convergence than PARC. Detailed validation/assessment studies of this new patched version of CRAFT are in progress for steady flow problems (Ref. 44) and will include comparative studies with PARCH predictions.

OBSERVATIONS ON THE PREDICTION OF SUPERSONIC JET MEAN FLOW STRUCTURE

- **DETAILED PORTRAYAL OF EXIT PLANE PROPERTIES REQUIRED**
  - **Boundary layers strongly influence growth of developing shear layer/can override decrease in mixing associated with high Mach number compressibility**
  - **For rectangular nozzles, corner vortical behavior required**
  - **For real engines, internal mixing required including vortical enhancements**
- **FOR JETS WITH SHOCKS, PARABOLIZED APPROXIMATIONS NOT VALID**
  - **Shock/shear layer interactions at end of each shock cell require full turbulent stress terms**
- **FOR ROUND/BALANCED-PRESSURE LABORATORY JETS, ADEQUATE TURBULENCE MODELING IS BECOMING AVAILABLE**
  - **Compressible-dissipation for shear layer unified with vortex-stretching for round jet**
- **FOR NON-CIRCULAR LABORATORY JETS, FOR JETS WITH SHOCKS AND/OR FOR JETS WITH PLUG NOZZLES, ADEQUATE TURBULENCE MODELING IS NOT AVAILABLE**
- **FOR REAL JETS INTERACTING WITH VEHICLE AERODYNAMICS, SIMULATION CAPABILITIES ARE RUDIMENTARY**

The prediction of supersonic jets using Navier-Stokes methodology has many uncertainties. Unless the nozzle exit plane conditions are very well defined, it may be meaningless to perform a calculation since downstream "history" effects are quite significant. Modest boundary layers influence jet core size and vortical effects from internal corner regions strongly influence the downstream flow. For real engines with internal mixing, the turbulence in the exhaust strongly influences the downstream development of the jet. Jets with shocks require full NS methodology and improvements to current turbulence model (pressure-dilatation terms). Even for the simplest round, balanced-pressure jet, adequate turbulence models are just now becoming available. For more complex jets, turbulence modeling is presently inadequate.

BALANCED-PRESSURE SUPERSONIC JETS

- THE STRUCTURE OF BALANCED-PRESSURE SUPERSONIC JETS (JET GROWTH RATE/VELOCITY DECAY RATE) IS DEPENDENT ON THE FOLLOWING PARAMETERS:
  (1) VELOCITY RATIO — U_E/U_J
  (2) JET MACH NUMBER — M_J
  (3) JET TEMPERATURE — T_J
  (4) EXIT PLANE CHARACTERISTICS
- THE ONLY ISSUE IN SUPERSONIC AXISYMMETRIC JET FLOWFIELD SIMULATION IS THE TURBULENCE MODELING—A TOPIC UNTO ITSELF (DGLR/AIAA PAPER NO. 92-02-106)
- ISSUES RELEVANT TO MACH EMISSION BY SEINER et al. (DGLR/AIAA PAPER NO. 92-02-046)

For simple, balanced-pressure supersonic round jets, the structure is dependent on the 4 parameters listed above. The ability to predict this structure resides in the adequacy of the turbulence model implemented (to be discussed below) and on knowing the mean flow and turbulent characteristics at the nozzle exit plane.

AXISYMMETRIC JET PROBLEM

ENCOMPASSES:

- 2D SHEAR LAYER COMPRESSIBILITY
- PLANAR/AXI TRANSITION
- WAVE/SHEAR LAYER INTERACTIONS

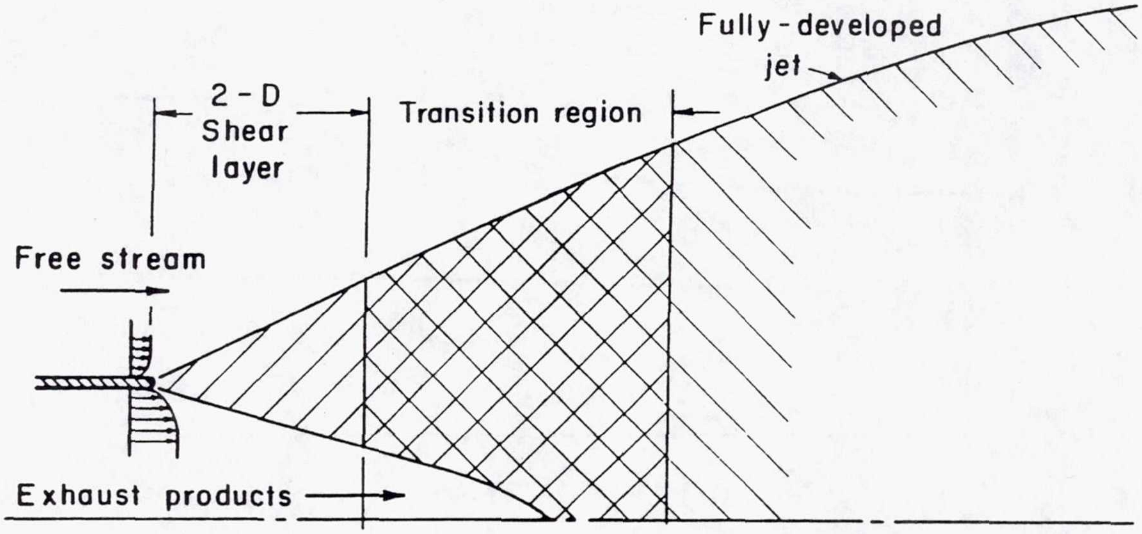

The structural features of the balanced-pressure round, axisymmetric jet are shown above. For supersonic jets, high Mach number compressibility effects diminish the growth rate of the developing shear layer but do not influence the mixing beyond the transition region. Length scale characteristics for the shear layer and fully developed round jet are different. Corrections to the length scale equation are required for a turbulence model to analyze both regions of the jet.

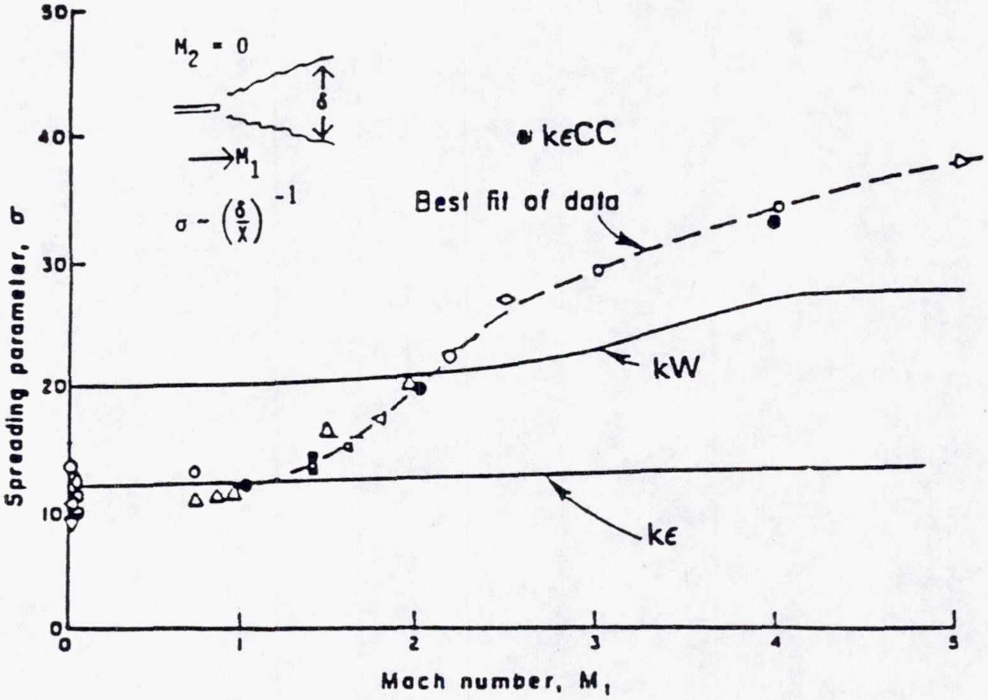

The high Mach number compressibility effect on shear layer growth rate is illustrated in this figure. Data for asymptotic shear layer behavior for the single-stream (one stream moving/one stream stationary), isoenergetic problem indicates that as the Mach number of the moving stream increases above sonic, the growth rate decreases (the spread rate parameter, σ, is inversely proportional to growth rate – $\sigma \sim x/\Delta y$). The kε model does not predict this effect; the kW turbulence model of Spalding (Ref. 45) which has been widely used for round jet flows predicts the correct spread rate only at Mach 2; the kεCC compressibility-corrected model of Dash et al. (Ref. 46) matches this data as per its calibration.

TURBULENCE MODEL STATUS

- **AFTER MANY YEARS OF TURBULENCE MODEL ASSESSMENT AND UPGRADE (1975-1985), A HYBRID kϵCC/kW MODEL FOR AXISYMMETRIC JETS EVOLVED WHICH REPRODUCED ALL AVAILABLE DATA SETS**
  - **MODEL NOT EXTENDIBLE TO MORE COMPLEX JETS**
  - **RECENT DATA WHICH PROVIDES INFORMATION ON TURBULENCE STRUCTURE INDICATES THAT kϵCC DOES NOT PREDICT OBSERVED REDUCTION IN TURBULENCE INTENSITIES**
- **SYSTEMATIC APPROACH TO DEVELOP NEW kϵ-BASED JET TURBULENCE MODEL OF GREATER GENERALITY INITIATED**
  - **POPE VORTEX STRETCHING CORRECTION FOR AXISYMMETRIC EFFECTS**
  - **COMPRESSIBLE-DISSIPATION MODELS FOR COMPRESSIBILITY**
  - **TUNED USING "BUILDING-BLOCK" APPROACH**

Earlier high-speed jet and shear layer data was used in the formulation of a hybrid kϵCC/kW model which reproduced the available data base of high-speed jet flows (see Ref. 47). This data did not include measurements of turbulent stresses. An effort was recently initiated to revisit this turbulence modeling problem based on the availability of new concepts for dealing with compressibility (e.g., the compressible-dissipation models of Sarkar and Zeman, Refs. 48 and 49) and on new data which contained measurements of turbulent stresses (e.g., the shear layer data of Dutton et al. and Samimy et al., see Refs. 50 and 51).

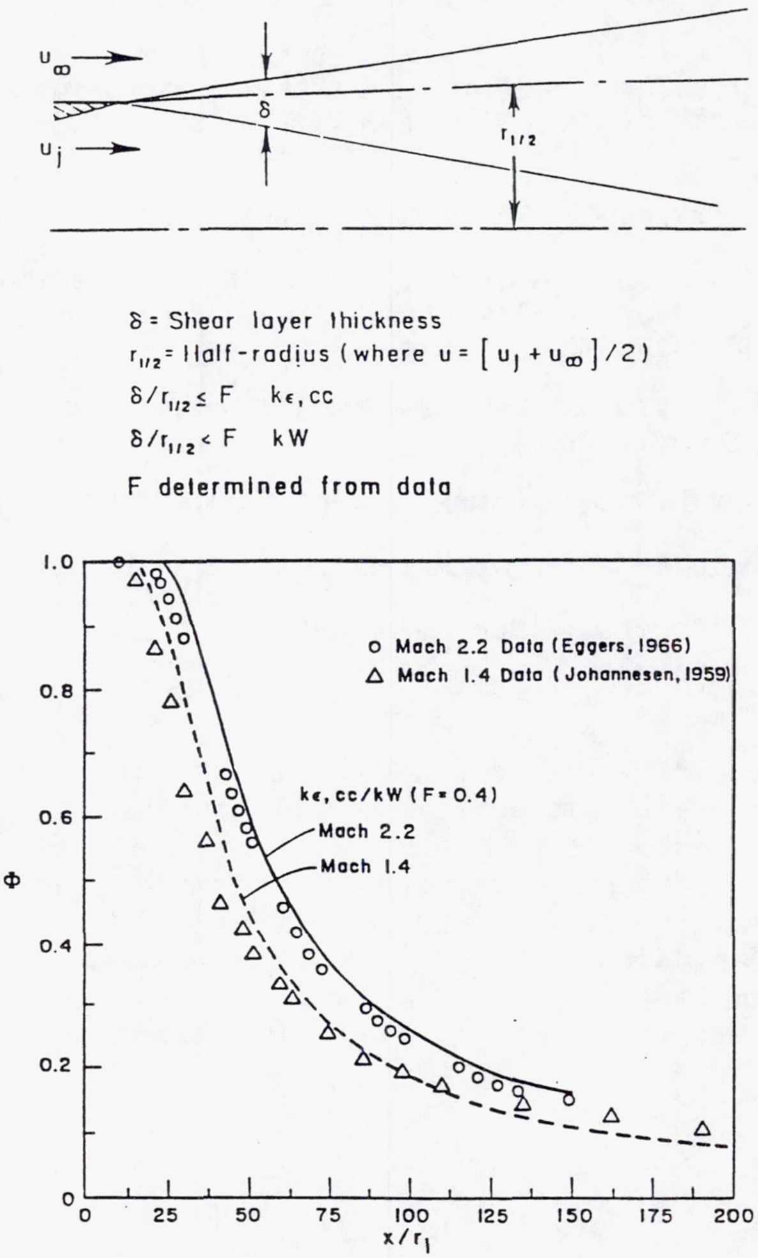

This figure illustrates the features of the hybrid kεCC/kW turbulence model (Ref. 47) and its ability to reproduce the velocity decay of Mach 1.4 and 2.2 isoenergetic laboratory jets exhausting into still air.

BUILDING-BLOCK PHILOSOPHY

- **THE PHILOSOPHY OF THE TURBULENCE MODEL BUILDING-BLOCK APPROACH IS AS FOLLOWS:**

  (1) A TURBULENCE MODEL SHOULD BE CAPABLE OF ANALYZING ALL THE UNIT PROBLEMS EMBODIED IN THE COMPLETE FLOW PROBLEM OF INTEREST

  (2) TO ACHIEVE THIS CAPABILITY, IT SHOULD BE SYSTEMATICALLY APPLIED TO VARIED UNIT PROBLEMS, WORKING FROM THE SIMPLEST PROBLEM TO THE MOST COMPLEX PROBLEM

  (3) FAILURE TO MATCH DATA AT ANY LEVEL MUST BE REMEDIED BY FIXES TO THE TURBULENCE MODEL – AD HOC OR FUNDAMENTAL

  (4) THE DATA SETS PREVIOUSLY ANALYZED MUST BE RE-ANALYZED WITH THE FIXED MODEL TO ASSESS IF EARLIER CASES THAT "WORKED" NO LONGER DO SO DUE TO THE FIX MADE

A building-block approach was followed in the construction of this new turbulence model. Recognizing that simple $k\epsilon$ based turbulence models are not applicable to generalized classes of flows without problem-specific corrections, the goal of developing a unified version of $k\epsilon$ for round jets was pursued initially. The philosophy followed is listed above.

BUILDING-BLOCK DATA FOR JET FLOWFIELDS

– BUILDING-BLOCK 1 –
LOW-SPEED PLANAR FREE SHEAR FLOWS

- ASYMPTOTIC
  - Velocity Ratio Effects (Rodi Correlation)
  - Density Ratio Effects (Brown/Roshko, etc.)
- NON-ASYMPTOTIC
  - Initial Profile Effects
  - Free Stream Turbulence Effects
  - Pressure Gradient Effects

•
•
•

– BUILDING-BLOCK 2 –
LOW-SPEED AXISYMMETRIC FREE JETS (WAKES)

- SELF SIMILAR BEHAVIOR/FARFIELD
  - Velocity Ratio Effects
  - Density Ratio Effects
- TRANSITIONAL REGION + FARFIELD
  - Initial Profile Effects
  - Free Stream Turbulence Effects
  - Pressure Gradient Effects

•
•
•

- COMPLETE JET (BB/1 NEEDED)

– BUILDING-BLOCK 3 –
HIGH-SPEED PLANAR FREE SHEAR FLOWS

- ASYMPTOTIC
  - Isoenergetic/One & Two Streams
  - Non-isoenergetic/One & Two Streams
- NON-ASYMPTOTIC
  - Initial Profile Effects
  - Free Stream Turbulence Effects
  - Wave/Shear Layer Interactions

•
•
•

– BUILDING-BLOCK 4 –
HIGH-SPEED AXISYMMETRIC FREE JETS (WAKES)

- SELF SIMILAR BEHAVIOR/FARFIELD
  - Velocity Ratio/Density Ratio Effects
  - Compressibility (Mach Number) Effects
- TRANSITIONAL REGION + FARFIELD
  - Balanced Pressure – Initial Profile, Freestream Turbulence Effects
  - Imbalanced Pressure – Above Plus Wave/Shear Layer Interactions

•
•
•

- COMPLETE JET (BB/3 NEEDED)

The supersonic jet problem contains a number of unit problems nested within it. Building-block data has been gathered for each of these nested unit problems. Model development/upgrade has proceeded from Block 1 to Block 4. For Block 1, the basic, unmodified kϵ turbulence model is adequate and correctly simulates the data of relevance to straight-back jets. Block 2 requires the addition of round jet corrections to the length scale equation, while Block 3 requires high Mach number compressibility-corrections. The unification of these two effects is dealt with by the data of Block 4. References 5 and 8 described the building-block methodology and data utilized in greater detail. Unless the turbulence model reliably predicts this complete set of building-block data, it cannot be used with any confidence for simple round jets nor can it be extended to the analysis of more complex jet problems.

AXISYMMETRIC CORRECTIONS TO THE kϵ TURBULENCE MODEL

JET CENTERLINE DECAY CORRECTIONS

Launder, et al. (kϵ1/kϵ2 models)

$$C_2 = 1.92 - aF$$

$$C_\mu = .09 - bF$$

where

$$F = \left\{\frac{r^{1/2}}{2 \cdot U_{CL}}\left(\left|\frac{dU_{CL}}{dx}\right| - \frac{dU_{CL}}{dx}\right)\right\}^{.2}$$

$a = .067$ ($= .053$ for kϵ2) and $b \sim .1$

McGuirk and Rodi

$$C_1 = 1.14 - 5.31 \frac{r^{1/2}}{U_{CL}} \frac{dU_{CL}}{dx}$$

Morse

$$C_1 = 1.4 - 3.4 \left(\frac{k}{\epsilon} \frac{dU}{dx}\right)^3_{CL}$$

POPE — VORTEX STRETCHING CORRECTION

$$\rho \frac{D\epsilon}{Dt} = \frac{\partial}{\partial X_i}\left(\frac{\mu_t}{\sigma_\epsilon}\right)\frac{\partial \epsilon}{\partial X_i} + \frac{\epsilon}{k}\left(C_1 P + \rho\epsilon\{-C_2 + C_3 \chi\}\right)$$

where

$$\chi = \omega_{ij}\, \omega_{jk}\, S_{ki}$$

with

$$S_{ij} = \frac{1}{2}\frac{k}{\epsilon}\left(\frac{\partial u_i}{\partial x_j} + \frac{\partial u_j}{\partial x_i}\right)$$

and

$$\omega_{ij} = \frac{1}{2}\frac{k}{\epsilon}\left(\frac{\partial u_i}{\partial x_j} - \frac{\partial u_j}{\partial x_i}\right)$$

For an axisymmetric jet (with no swirl), χ becomes:

$$\chi = \frac{1}{4}\left(\frac{k}{\epsilon}\right)^3 \left(\frac{\partial u}{\partial r} - \frac{\partial v}{\partial x}\right)^2 \frac{v}{r}$$

The kϵ turbulence model requires modifications for the round jet. Earlier work involved making the coefficients dependent on parameters related to the jet centerline velocity decay. Pope introduced a more generalized vortex-stretching correction (Ref. 52) as an additional source term to the ϵ equation. Note that going to a full second-order closure model does not alleviate the need for such corrections (see, e.g., the recent second-order closure work of Shih et al. which also requires the addition of a vortex-stretching correction term, Ref. 53).

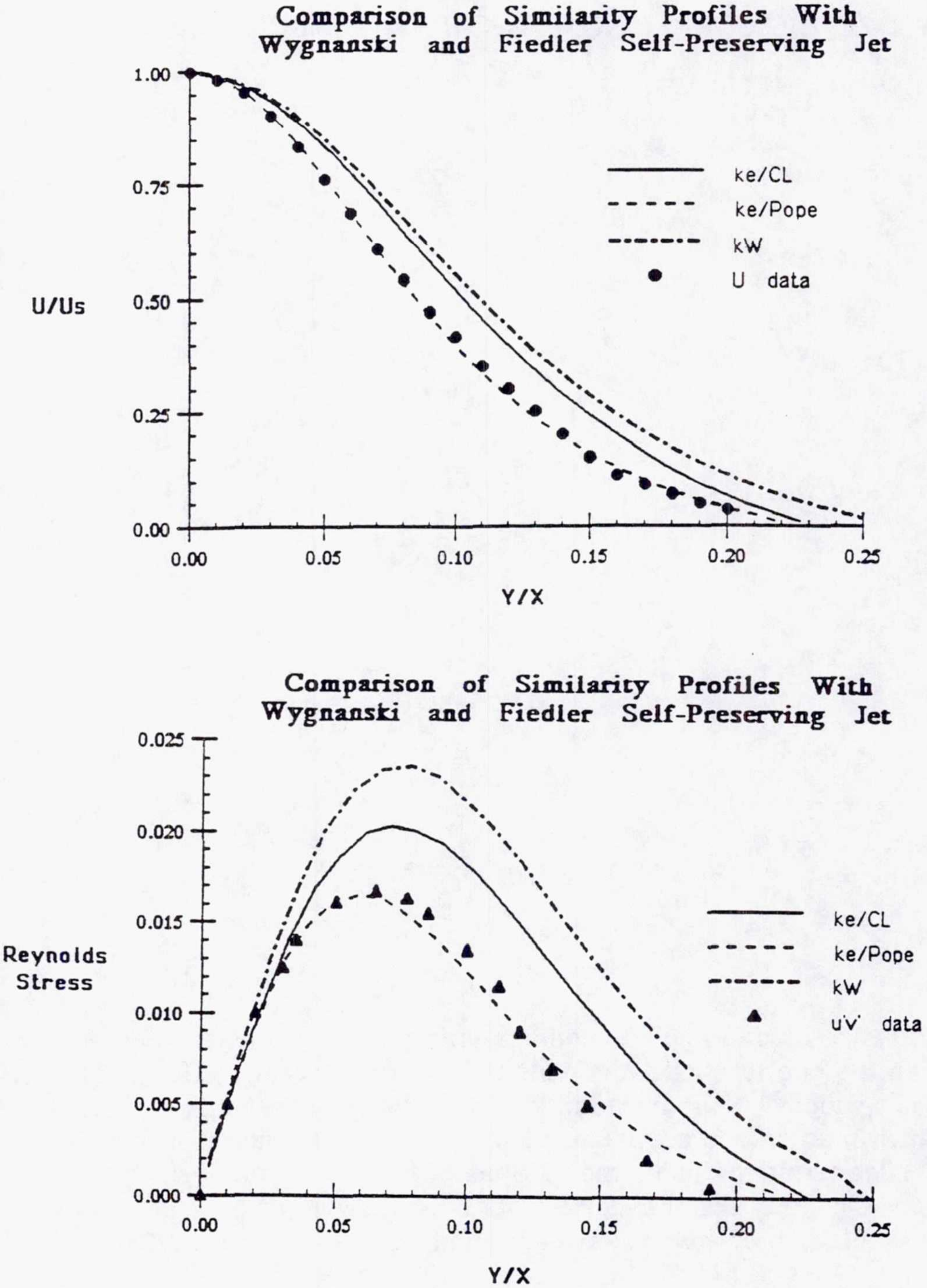

Comparisons of self-similarity profile predictions of axial velocity and Reynolds-stress in the asymptotic round jet farfield with the data of Wygnanski and Fiedler (Ref. 54) indicates that the Pope vortex-stretching correction to kϵ performs better than the simpler CL corrections (Launder correction used) and than the kW model using published coefficients for all models/corrections.

COMPRESSIBLE-DISSIPATION MODELS

ϵ, is taken to be comprised of a solenoidal, incompressible component, ϵ_s, and a dilatational, compressible component, ϵ_c, and thus:

$$\overline{\rho}\epsilon = \overline{\rho}(\epsilon_s + \epsilon_c)$$

Both Sarkar and Zeman integrate the incompressible form of the dissipation equation to obtain ϵ_s and model ϵ_c as follows:

Sarkar:

$$\epsilon_c = \alpha_1 \, \epsilon_s \, M_\tau^2$$

Where M_τ is the turbulent fluctuation Mach number

$$M_\tau = (2k)^{1/2} / a$$

Zeman:

$$\epsilon_c = C_d \, F(M_\tau)\epsilon_s$$

where

$$\begin{aligned} F(M_\tau) &= 1. - \exp\left[-(M_\tau - .1)^2/.36\right] && \text{for } M_\tau > .1 \\ F(M_\tau) &= 0 && \text{for } M_\tau \le .1 \end{aligned}$$

In their calibrations of these compressible-dissipation models, Sarkar found $\alpha_1 = 1.0$ to provide best agreement and Zeman found $C_d = .75$ to work best.

Sarkar (Ref. 48) and Zeman (Ref. 49) formulated compressible-dissipation modifications to extend their Reynolds-stress models to analyze high-speed shear layer. Both of their models make the dilatational component of dissipation, ϵ_c, a function of the fluctuation Mach number, M_τ ($\sim \overline{q'}/a$). In the earlier kϵ-based heuristic model of Dash et al. (Ref. 46), the coefficient of turbulent viscosity was made dependent on M_τ ($\mu_t = C_\mu (M_\tau) \rho k^2 / \epsilon$). Sarkar and Zeman calibrated their models with fundamental isotropic decay data obtained from direct numerical simulations. Dash calibrated his model (kϵCC) with the isoenergetic/single-stream shear layer data shown earlier.

HIGH-SPEED, SINGLE-STREAM ISOENERGETIC SHEAR LAYER DATA ANALYSIS

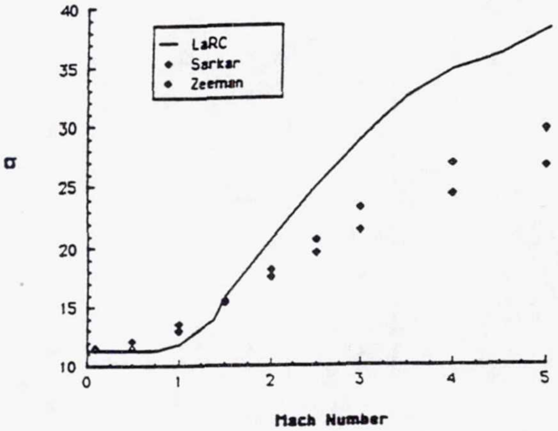

$k\epsilon$ with Sarkar and Zeman CD Models

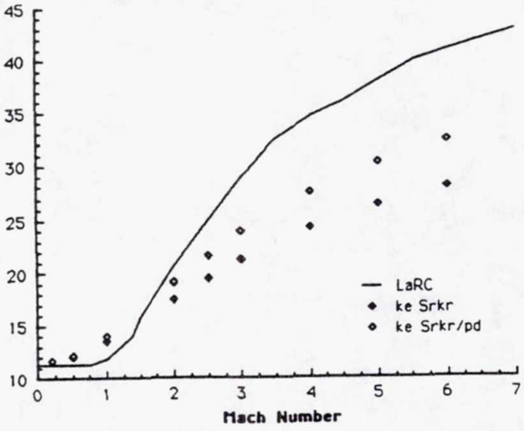

$k\epsilon$ with Sarkar CD and PD Models

Dash et al. incorporated the Sarkar and Zeman compressible-dissipation models into the $k\epsilon$ framework (Refs. 2 and 5). The performance of both these models vs the isoenergetic/single-stream high-speed shear layer data (LaRC correlation: solid line) is shown above and concurs with the performance reported by Sarkar and Zeman in their Reynolds-stress formulations. Both models predict too much of a decrease in spread rate for $M < 1.5$ and too little a decrease in spread rate for $M > 1.5$. Sarkar also formulated a pressure-dilatation extension (Ref. 55) which improved the performance at higher Mach numbers.

kϵCD TURBULENCE MODEL

The kϵCD turbulence model utilizes a "compressible" turbulent viscosity, μ_t, given by:

$$\mu_t = C_\mu \rho k^2 / (\epsilon_s + \epsilon_c)$$

The incompressible value of turbulent dissipation, ϵ_s, is obtained from the equation:

$$\rho \frac{D\epsilon_s}{Dt} = \frac{\partial}{\partial X_i}\left[\frac{(\epsilon_s + \epsilon_c)}{\epsilon_s}\frac{\mu_t}{\sigma_\epsilon}\frac{\partial \epsilon_s}{\partial X_i}\right] + \frac{\epsilon_s}{k}\left(C_1 \underline{P} - C_2 \rho \epsilon_s\right)$$

The compressible-dissipation, ϵ_c, is given by:

$$\epsilon_c = \epsilon_s\left[\alpha_1 \tilde{M}_\tau^2 + \beta \tilde{M}_\tau^4\right]$$

where $\tilde{M}_\tau$ includes a Zeman lag

$$\tilde{M}_\tau = M_\tau - \lambda$$

and the coefficients utilized are as follows:

α_1 = 1 (same as Sarkar)
λ = .1 (same as Zeman)
β = 60 (fits LaRC data the best)

The equation for turbulent kinetic energy, k, is given by:

$$\rho \frac{Dk}{Dt} = \frac{\partial}{\partial X_i}\left[\frac{\mu_t}{\sigma_k}\frac{\partial k}{\partial X_i}\right] + \underline{P} - \rho\left(\epsilon_s + \epsilon_c\right) + \overline{p'd'}$$

where the turbulent production, $\underline{P}$, in both the k and ϵ_s equations utilizes the compressible μ_t

Following the building-block philosophy discussed earlier, the Sarkar/Zeman corrections need to be modified since they do not match the LaRC isoenergetic/single-stream data. The modified version of kϵ has been entitled "kϵCD." The modifications entail using the Sarkar formulation with Zeman lag, and, adding an extra M_τ^4 term with coefficient β calibrated to match the LaRC data.

HIGH-SPEED, SINGLE-STREAM ISOENERGETIC SHEAR LAYER DATA ANALYSIS WITH kϵCD TURBULENCE MODEL WITH AND WITHOUT PRESSURE-DILATATION

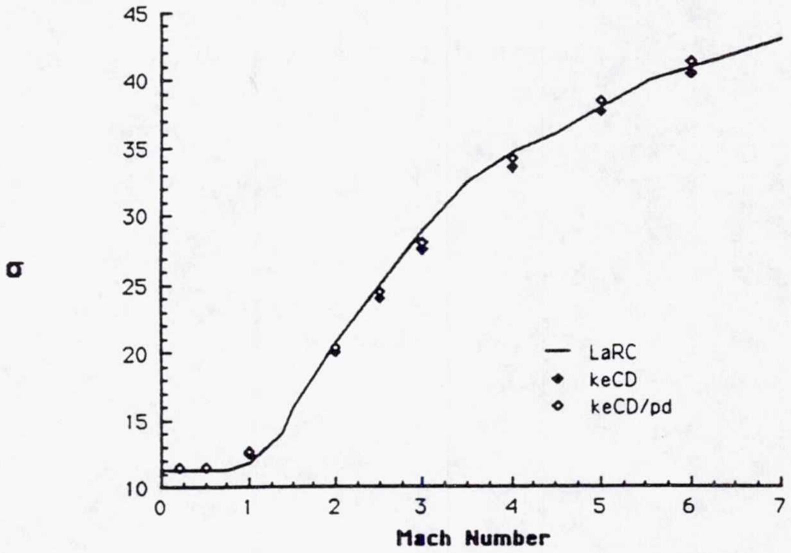

The kϵCD model matches the LaRC spread data. Inclusion or deletion of the Sarkar pressure-dilatation (pd) term does not alter the performance of this model against this data set. In subsequent shear layer comparisons, the pd term is not implemented. A new strain-based pressure dilatation model of Lele (Ref. 56) appears promising and will be assess in the near future. In subsequent viewgraphs we will show that the kϵCD model also reproduces the non-isoenergetic/two-stream shear layer data of Dutton and Samimy, including the turbulent stress measurements. The earlier kϵCC model of Dash also reproduces the spread and mean flow profile data but does <u>not</u> reproduce normal stress data which has significant acoustic implications if acoustic analogy models are utilized for noise prediction.

Quantity	Case 1	Case 1d	Case 2	Case 3	Case 3r	Case 4	Case 5
$r = U_2/U_1$	0.78	0.79	0.57	0.18	0.25	0.16	0.16
$\lambda = (1-r)/(1+r)$	0.12	0.12	0.27	0.69	0.60	0.72	0.72
$s = \rho_2/\rho_1$	0.76	0.76	1.55	0.57	0.58	0.60	1.14
$\lambda_s = \dfrac{(1-r)(1+s^{1/2})}{2(1+rs^{1/2})}$	0.12	0.12	0.28	0.62	0.55	0.65	0.73
$M_r = \Delta U/\bar{a}$	0.40	0.40	0.91	1.37	1.44	1.73	1.97
M_c	0.20	0.20	0.46	0.69	0.72	0.86	0.99
M_1, M_2	2.01, 1.38	2.02, 1.39	1.91, 1.36	1.96, 0.27	2.22, 0.43	2.35, 0.30	2.27, 0.38
T_{t1}, T_{t2}, K	295, 295	275, 275	578, 295	285, 285	315, 285	360, 290	675, 300
U_1, U_2, m/s	515, 404	498, 392	700, 399	499, 92	561, 142	616, 100	830, 131
P, kPa	46	55	49	53	53	36	32
$Re = \bar{\rho}\Delta U/\bar{\mu}$ (10^6/m)	7.7	7.7	12	26	27	21	13
δ_1, δ_2, mm	2.5, 2.6	2.4, 2.4	2.9, 2.5	3.1, 3.0	1.6, 4.3	2.2, 1.7	1.7, 1.3
θ_1, θ_2, mm	0.20, 0.20	0.19, 0.20	0.29, 0.21	0.22, 0.36	0.12, 0.37	0.20, 0.17	0.10, 0.14
l_U, mm	300	125	100	25	50	10	10
$l_{\sigma u}$, mm	300	225	200	75	125	100	75
$l_{\sigma v}$, mm	300	475[a]	250	150	175[a]	125	100
$l_{\langle u'v'\rangle}$, mm	350	475[a]	250	150	175[a]	125	100
$Re_b = \bar{\rho}\Delta Ub/\bar{\mu}(10^5)$, devel.	0.7	1.0[a]	1.3	2.5	3.4[a]	0.6	0.8
Growth region, mm	300–450	125–475	100–450	25–200	50–150	10–175	10–150
db/dx	0.020	0.026	0.038	0.059	0.058	0.050	0.049
Sim. locations, mm	350–450	325–375	300–400	150–200	125–175	100–150	75–125
$\sigma_u/\Delta U$, peak	0.22	0.21	0.17	0.18	0.16	0.18	0.18
$\sigma_v/\Delta U$, peak	0.15	0.15	0.099	0.078	0.086	0.065	0.053
σ_u/σ_v, peak	1.53	1.41	1.71	2.33	1.84	2.74	3.53
$-\langle u'v'\rangle/(\Delta U)^2$, peak	0.017	0.016	0.0086	0.0069	0.0073	0.0066	0.0058
$-\langle u'v'\rangle/(\sigma_u\sigma_v)$, mean	0.48	0.49	0.54	0.52	0.51	0.52	0.54
l_m/b, mean	0.15	0.15	0.11	0.090	0.092	0.088	0.086

[a] The mixing layer may not have been developed in terms of this quantity.

Shown above is the matrix of high-speed shear layer data obtained by Dutton and coworkers at the University of Illinois.

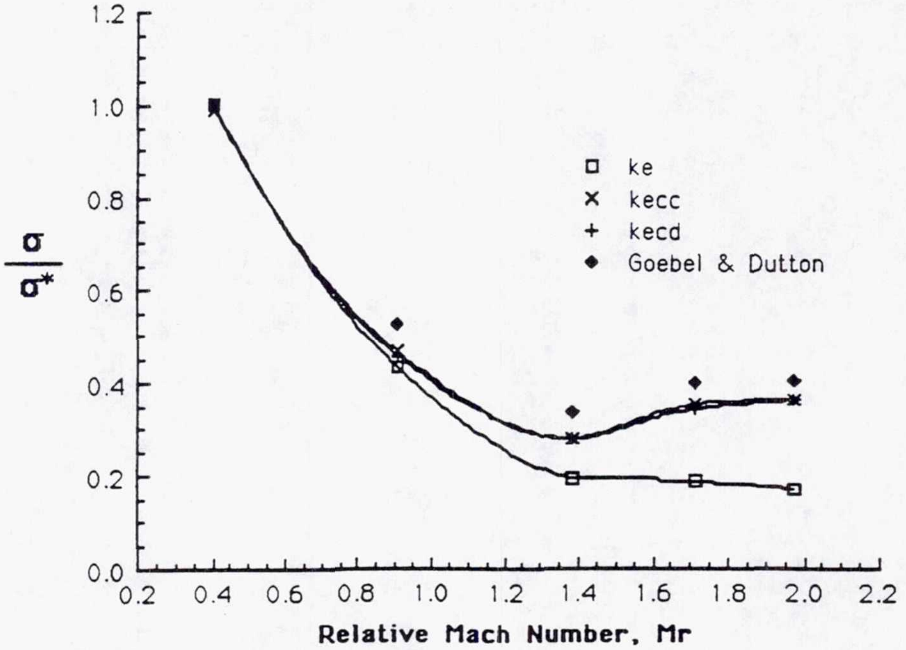

Comparison of the Shear Layer Spread Rates Predicted by The Various Turbulence Models With Dutton Experimental Data

The spread rate comparisons are shown above. Both the kϵCC and kϵCD compressibility-corrected turbulence models reproduce the spread data. The kϵ model mixes too quickly. At $M_r = 2$, the kϵ model is mixing too quickly by a factor of 2½ while the kϵCC and kϵCD models agree with the data to within 10%.

Comparison of Maximum Experimental Qprime Values of Dutton et al With 2D Compressible Shear Layer Models

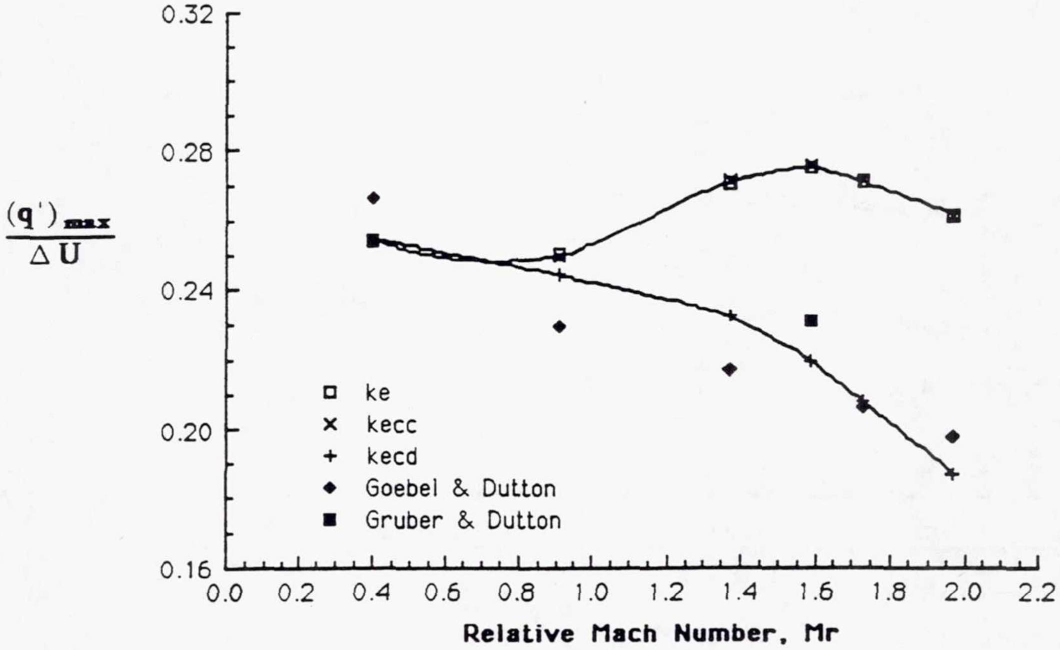

Data for the peak value of rms velocity fluctuation, $\overline{q'}$, is shown above and compared with $k\epsilon$, $k\epsilon$CC and $k\epsilon$CD predictions. Here, the $k\epsilon$ and $k\epsilon$CC model both fail to reproduce the observed decrease in velocity fluctuations while the $k\epsilon$CD model reproduces the data trends quite nicely.

Comparison of the Asymptotic Turbulence Intensity Profiles
For The Gruber and Dutton High Speed Shear Layer Case

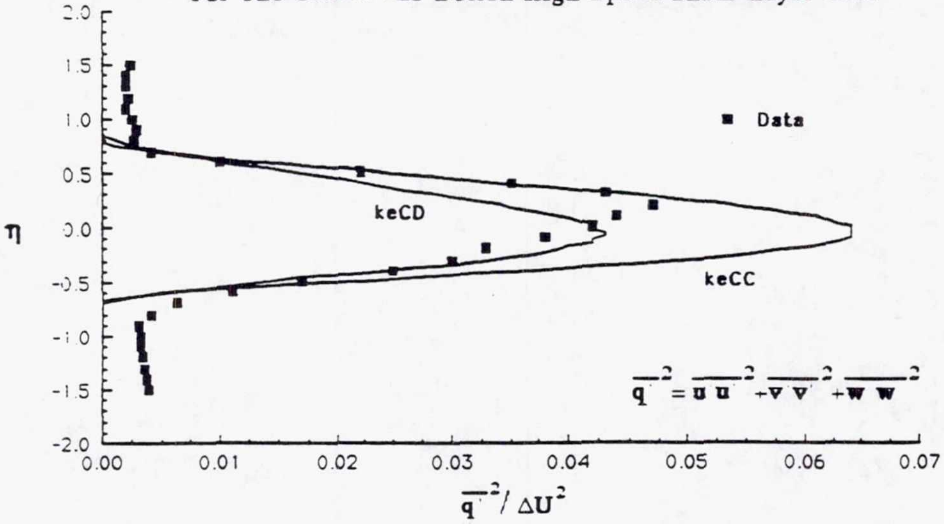

Quantity	Primary Stream	Secondary Stream
Stagnation Pressures:	$P_{t1} = 552$ kPa	$P_{t2} = 43.4$ kPa
Stagnation Temperatures:	$T_{t1} = 279$ K	$T_{t2} = 289$ K
Static Pressures:	$P_1 = 40.3$ kPa	$P_2 = 40.3$ kPa
Freestream Velocities:	$U_1 = 543$ m/s	$U_2 = 91.2$ m/s
Static Temperatures:	$T_1 = 132$ K	$T_2 = 285$ K
Sonic Velocities:	$a_1 = 230$ m/s	$a_2 = 338$ m/s
Mach Numbers:	$M_1 = 2.36$	$M_2 = 0.27$
Freestream Densities:	$\rho_1 = P/RT_1 = 1.06$ kg/m^3	$\rho_2 = P/RT_2 = 0.49$ kg/m^3
Freestream Viscosities:	$\mu_1 = 9.10 \times 10^{-6}$ Pa-s	$\mu_2 = 1.77 \times 10^{-5}$ Pa-s

A comparison of predicted and measured profiles of rms velocity fluctuation is shown above for recent data of Dutton et al. The shear layer widths of the kϵCC and kϵCD predictions are identical but the kϵCC model over-predicts fluctuation levels by more than 33%. The kϵCD predictions agree with the data quite well.

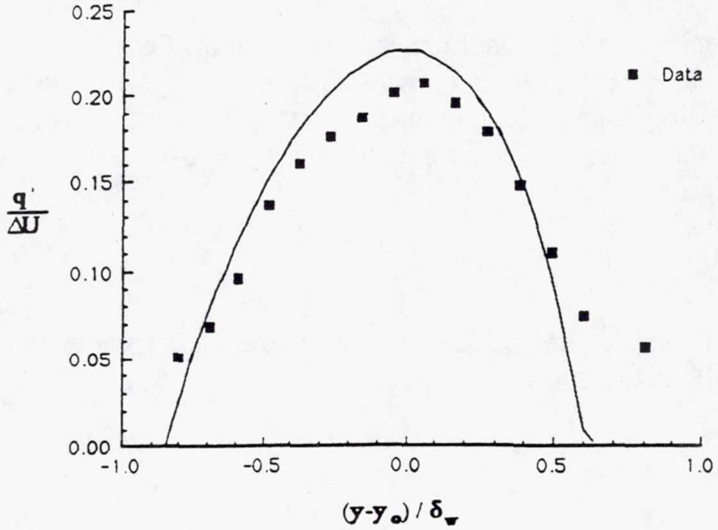

Asymptotic fluctuating velocity comparison for Samimy case with convective Mach number of 0.64 using kεCD

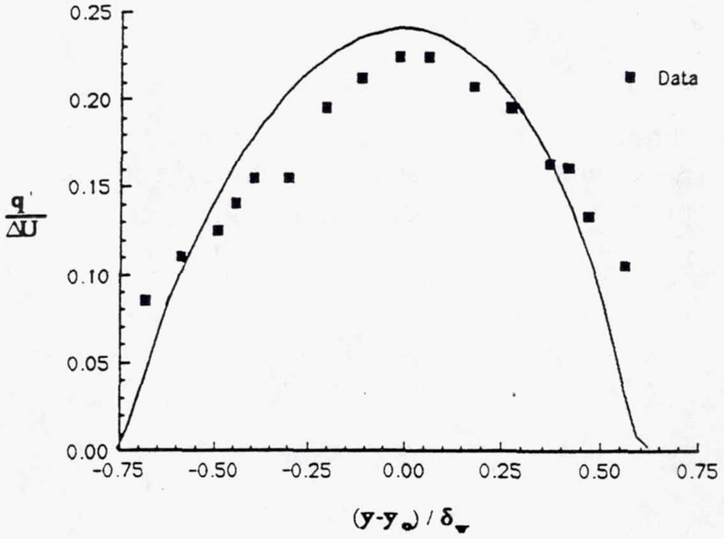

Asymptotic fluctuating velocity comparison for Samimy case with convective Mach number of 0.51 using kεCD

Good agreement between kεCD predictions and the data of Samimy et al. obtained at Ohio State, was obtained for all operating conditions. Shown above are comparisons with rms velocity fluctuation data for two sets of conditions. These detailed comparative studies have indicated that the kεCD model works quite well for high-speed shear layers.

JET MODIFICATION TO kϵCD

The compressible-dissipation formulation needs to be modified since it slows down the jet mixing more than required beyond the core region. An ad hoc modification to ϵ_c has been implemented which suppresses its action as the shear layer transitions to a jet. The modification proposed takes the form:

$$\epsilon_c = C_J(f)\left[\alpha_1 \tilde{M}_\tau^2 + \beta \tilde{M}_\tau^4\right]$$

where f is the ratio of shear layer thickness to jet half-radius implemented in the hybrid model and $C_J(f)$ is the cubic

$$C_J(f) = 3\left(\frac{(f_{max} - f)}{f_{max}}\right)^2 - 2\left(\frac{(f_{max} - f)}{f_{max}}\right)^3$$

which varies from 1 to 0 as f varies from 0 to f_{max}. A value of $f_{max} \sim .5$ appears to yield the best agreement with the data thus far analyzed. For $f > f_{max}$, $C_J = 0$ and compressible-dissipation is fully suppressed

For high-speed jets, modifications are required to suppress compressible-dissipation effects beyond the transitional region. The modifications are summarized above. The modified model is entitled "kϵCDj."

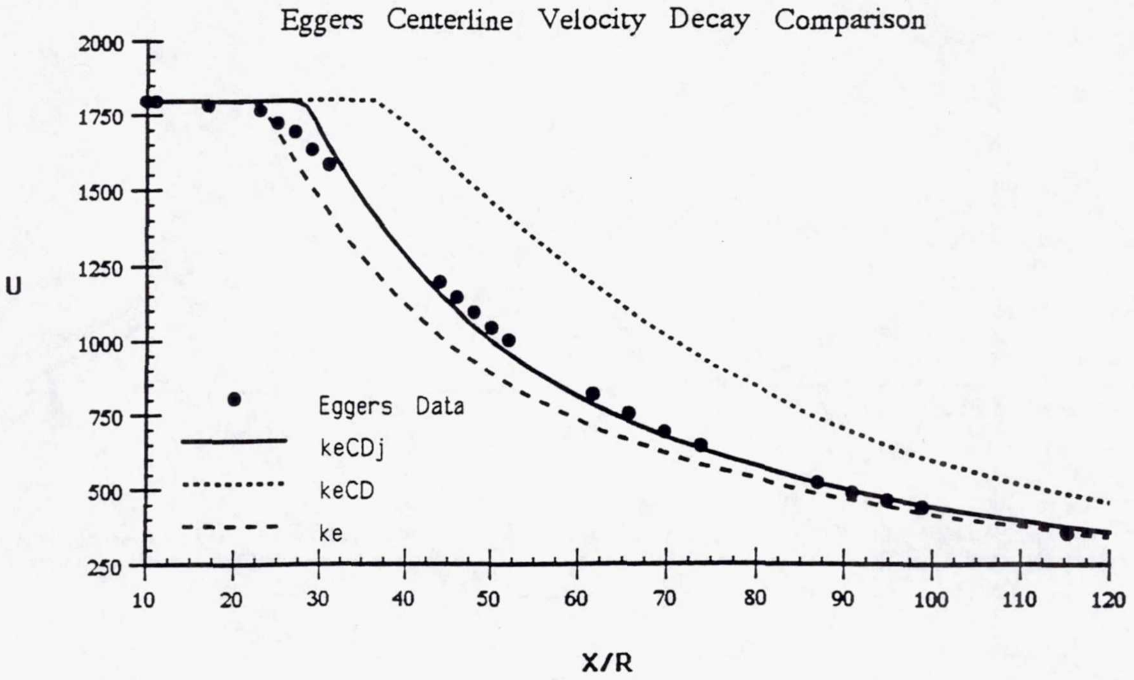

The performance of kϵCDj in predicting the Mach 2.2 isoenergetic jet into still air data of Eggers' (Ref. 57) is shown above. The kϵ model is shown to mix too quickly while the kϵCD model mixes too slowly. All variants of kϵ for round jets employ the Pope vortex-stretching correction.

Seiner 900 F jet velocity profile comparison at X = 1 inch using the ke and keCD/j turbulence models

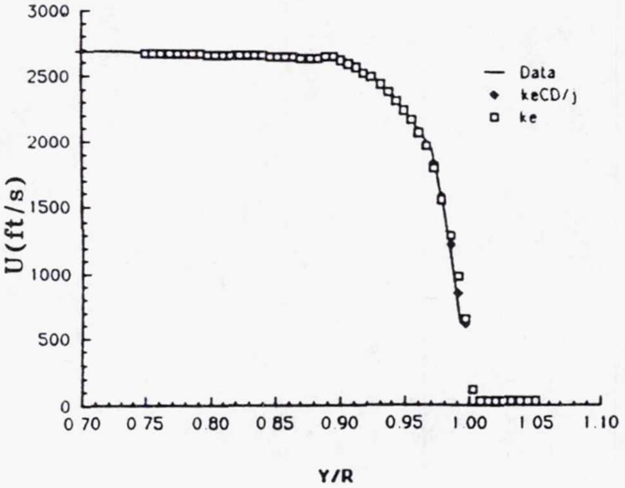

Seiner 900 F jet velocity profile comparison at X/D = 2.5 using the ke and keCD/j turbulence models

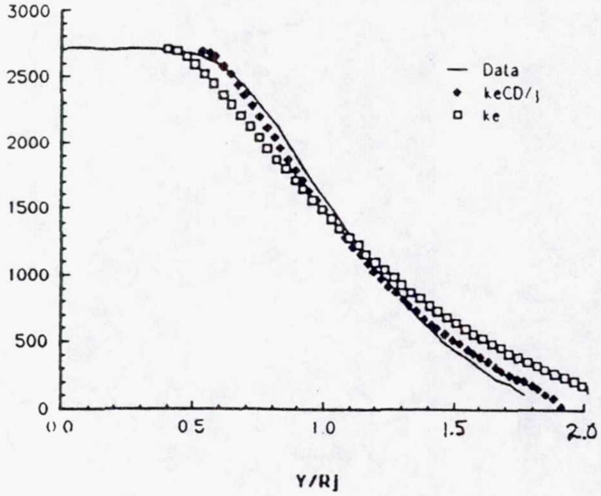

Seiner 900 F jet velocity profile comparison at X/D = 5 using the ke and keCD/j turbulence models

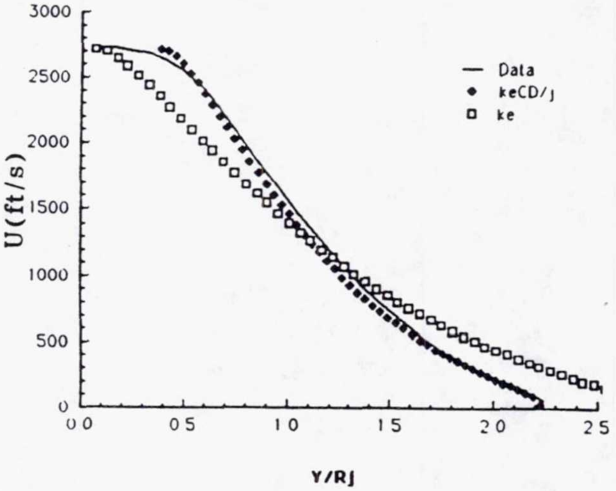

Seiner 900 F jet velocity profile comparison at X/D = 15 using the ke and keCD/j turbulence models

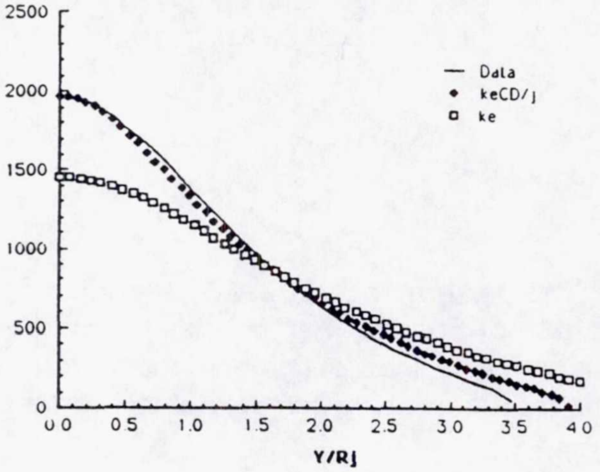

The kϵCDj model does an adequate job of predicting the recent Mach 2 jet into still air data of Seiner et al. (Ref. 58) with jet total temperatures ranging from 300 to 1400°K. Comparisons of predictions with velocity profiles at selected axial stations for the 755°K (900°F) are shown above utilizing kϵCDj and kϵ. The kϵ model performance is quite poor while kϵCDj is seen to accurately reproduce the measurements.

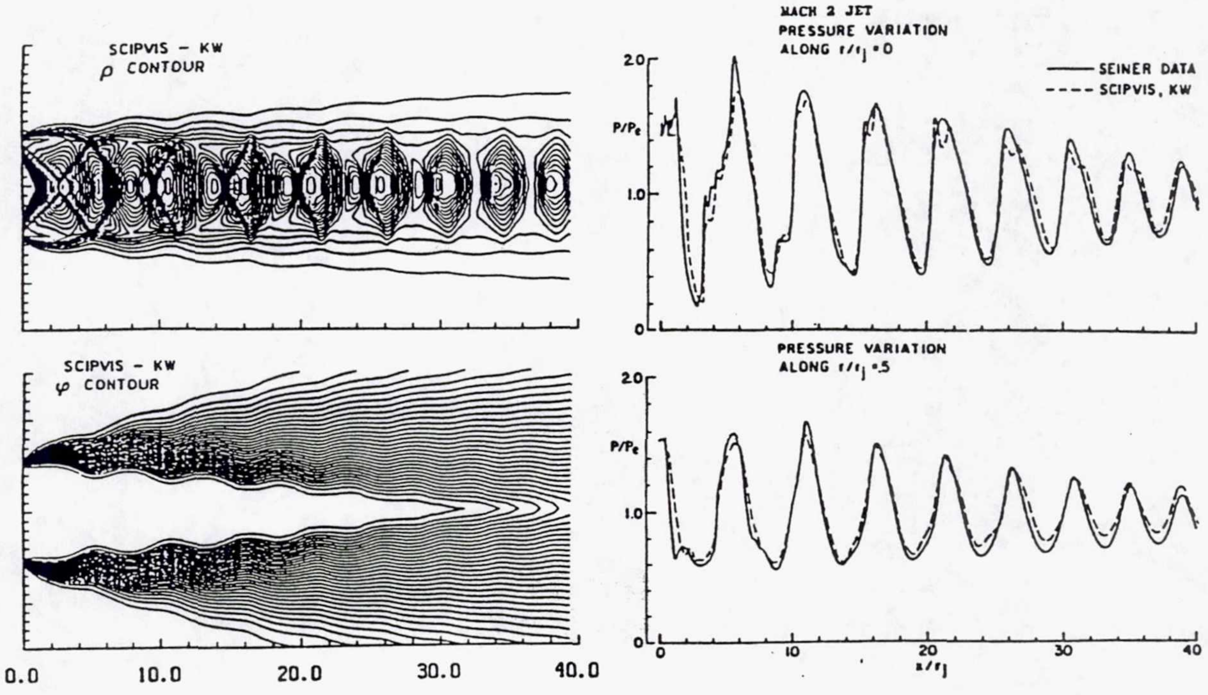

The predicted (SCIPVIS PNS code) flowfield structure of a Mach 2 imperfectly expanded jet exhausting into still air is exhibited above along with comparisons of axial centerline and off-axis pressure variations (from Refs. 34 and 37). The density contours exhibit the shock cell pattern while the tracer species contours ($\phi = 1$ in unmixed jet; $= 0$ in external stream) exhibit the extent of the turbulent mixing layer. As the mixing layer thickens, the wave intensities are attenuated by turbulent dissipation. Broad band shock noise, generated by the interaction of the shock waves with the turbulent mixing layer, is most intense in the "transitional region" of the jet where the shear layer is thick and the wave intensities are still substantial. The noise generated is propagated along the oblique recompression shocks to the region where the shocks terminate at the sonic line and is emitted to the freestream from this region at the end of each shock cell.

OBSERVATION 1 – PNS AND RNS SOLUTIONS EXHIBIT SAME RATE OF MIXING, BUT RNS SOLUTIONS SHOW GREATER WAVE-ATTENUATION BEYOND SECOND SHOCK CELL

- CRAFT RNS HAS LESS ATTENUATION THAN PARCH RNS

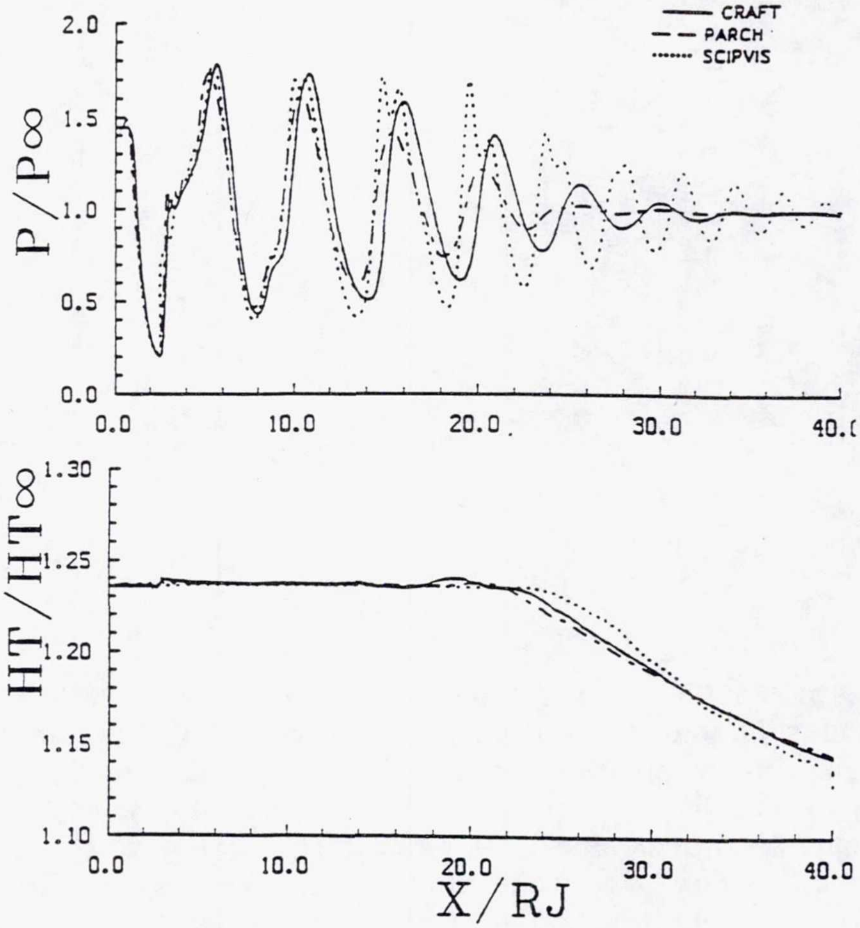

In applying time-asymptotic Navier-Stokes methods to this jet problem, it was found (Ref. 1) that the predicted shock pattern differed from the PNS solution. The above figure shows comparisons of the predicted shock structure and centerline tracer species decay for this jet using the same turbulence model ($k\epsilon$ in this case) and two different NS codes, PARCH and CRAFT. The PNS and RNS solutions produce the same rate of mixing but differ significantly with regard to shock attenuation by the turbulence.

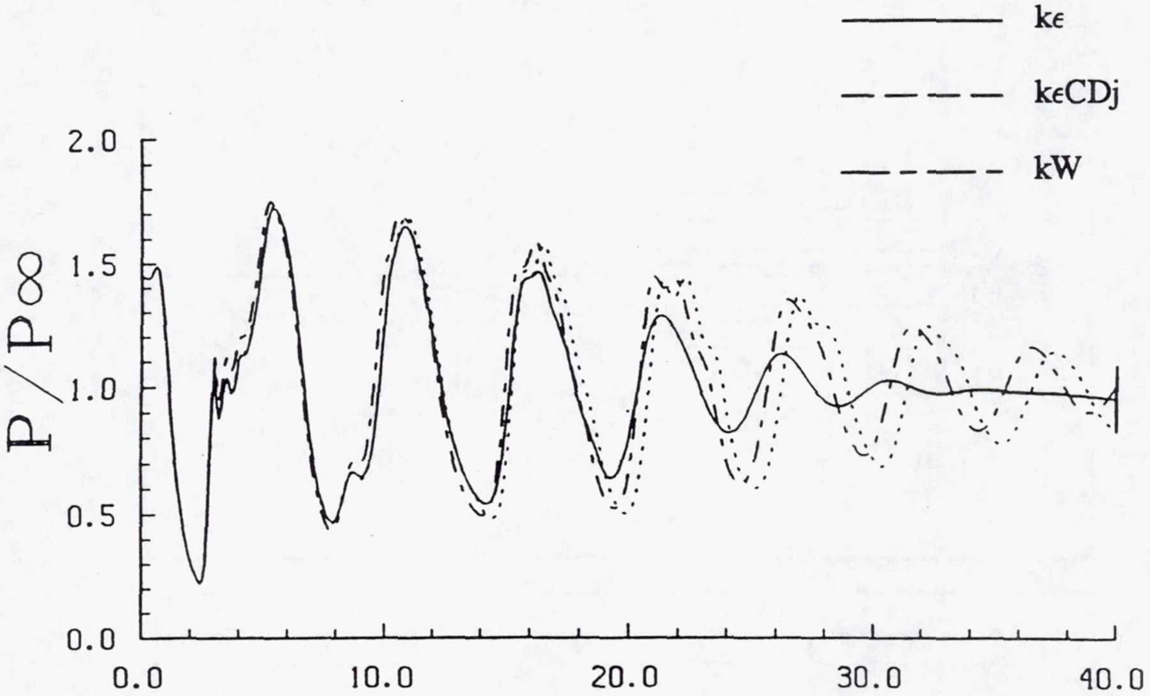

Our ability to analyze jets with shocks using time-asymptotic NS methodology is not yet firmly in place. Shown above are comparisons of kϵ and kϵCDj predictions (both with Pope vortex-stretching) and kW predictions, all performed using the PARCH/GTP code. While the kW model (which works for Mach 2 shear layers and balanced-pressure Mach 2 jets) agreed quite well with data for this case using the SCIPVIS PNS code (see earlier viewgraph), it doesn't work as well using NS methodology. The performance of kϵCDj is comparable to that of kW. These comparisons indicate that models which work in simple balanced-pressure situations, may not work in situations with strong/localized pressure-gradients. The kϵCDj model needs to be extended to include an adequate pressure-dilatation model for the analysis of the complex interchange of turbulence/mechanical energy in the shock/shear layer interaction region at the end of each shock cell. Data for such localized interactions, including details of the turbulence would be extremely helpful in support of this modeling upgrade.

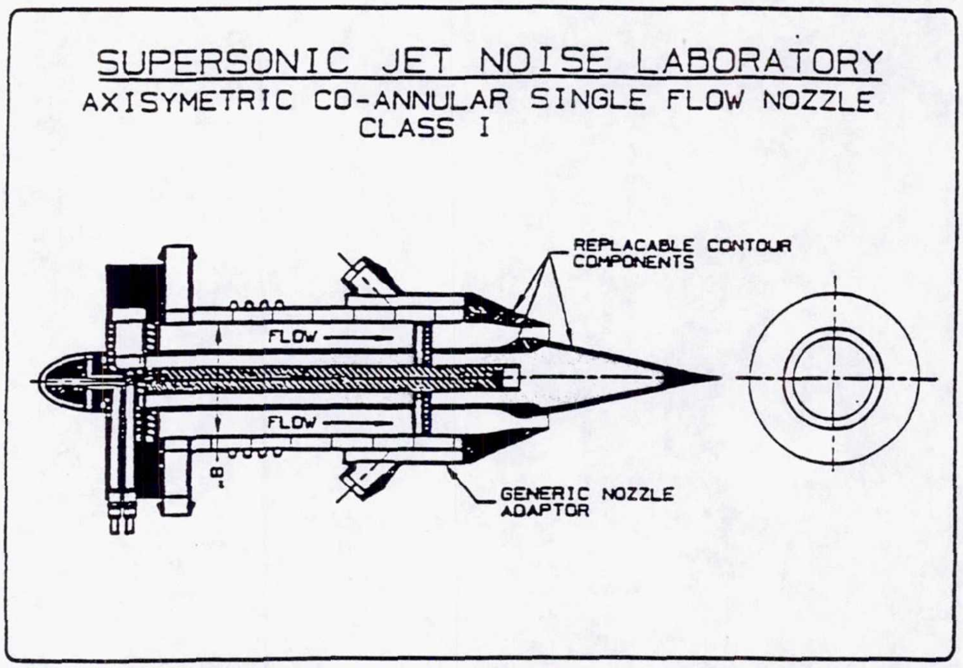

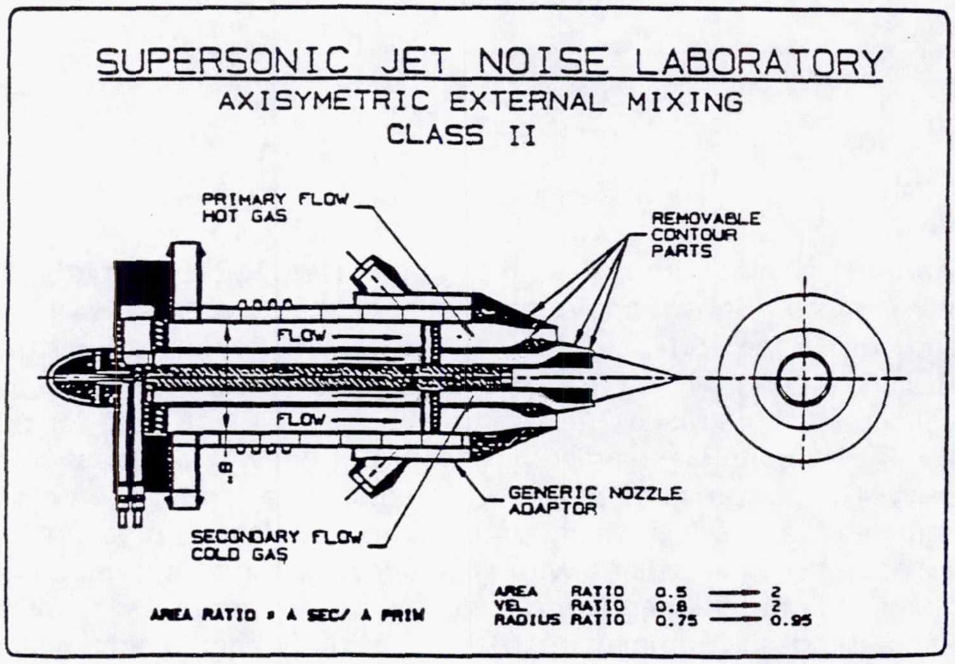

Fundamental data is now being obtained for Class I and Class II co-annular nozzles to support fluid dynamic model development and validation. Pre-test predictions for these nozzles have been performed as described in Refs. 3 and 4. In addition to turbulence issues associated with shear layer compressibility, 2D/axi vortex-stretching and shock/shear layer interactions (all of which are present in these flows), the additional complexities of near wall turbulence and shock/boundary layer interactions must be dealt with.

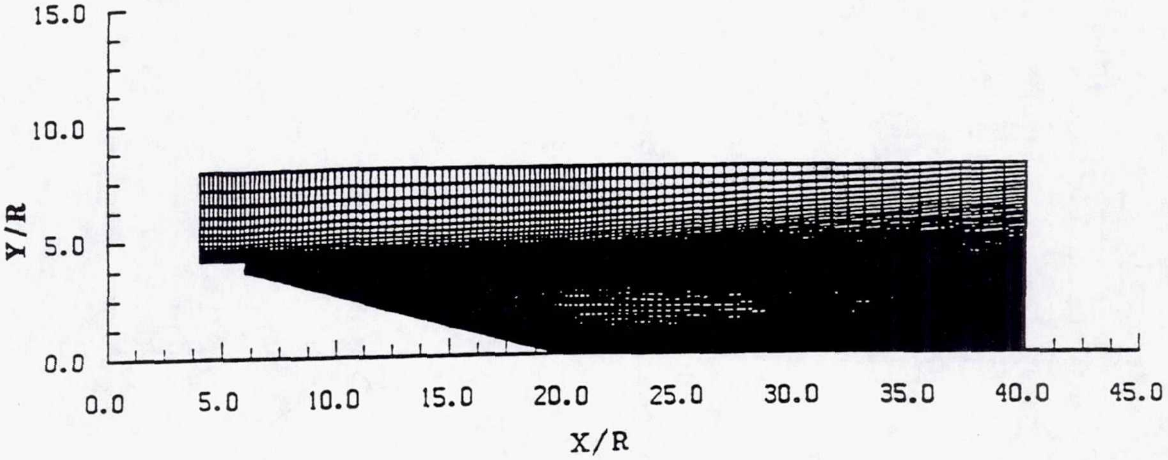

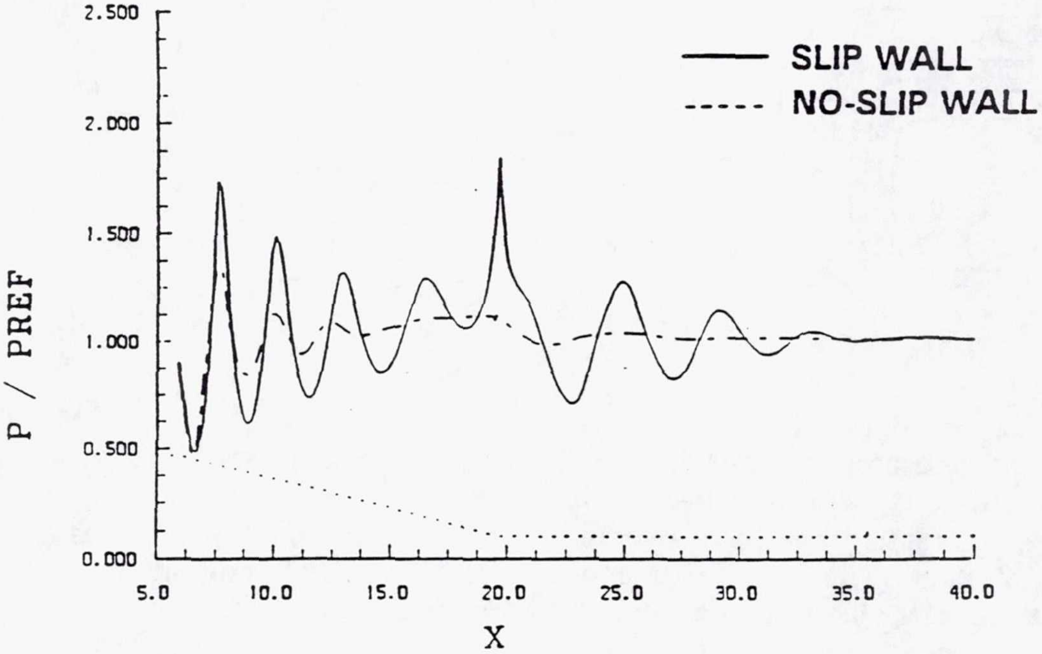

The influence of the plug boundary layer on wave attenuation was found to be quite pronounced. The figure above exhibits the predicted pressure variation along the plug surface/jet centerline with slip wall boundary conditions and with a turbulent boundary layer (no-slip). The boundary layer effects are quite marked which led to our investigation of varied classes of near wall turbulence modeling (Van Driest algebraic, Chien low Re, Rodi one-equation — see Refs. 3 and 4).

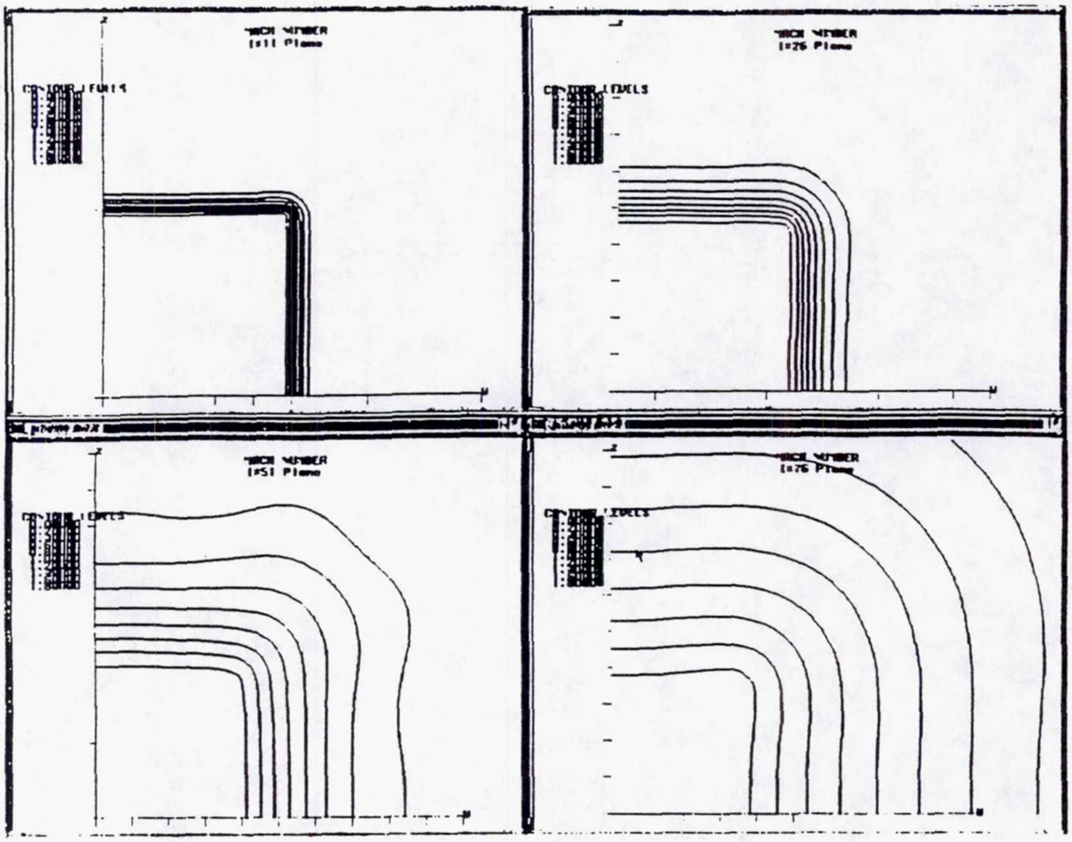

Work has recently been initiated on the analysis of exhausts from nonaxisymmetric laboratory nozzles (square, rectangular, elliptic) for which detailed flowfield survey data is being obtained by Seiner and co-workers at NASA LaRC. For our initial investigation, we have selected a square nozzle case with a design Mach number of 1.88. The nozzle was operated at off-design conditions to produce a nominal exit Mach number of 1.6, with a static pressure ratio of 1.5. At the exit plane, the nozzle has a divergence of 20° in the vertical direction with no divergence in the horizontal direction. The jet is isoenergetic and the flow field survey consisted of static and pitot pressures.

As a prelude to the analysis of the actual laboratory jet, we have computed the equivalent, perfectly expanded jet (i.e., on-design operation with no flow divergence). The PARCH3D code was used with the basic $k\epsilon$ turbulence model. The code was upgraded to include appropriate entrainment boundary conditions at the outer free boundaries and quarter plane symmetry was assumed. Predicted contours of Mach number are shown above at several axial stations. The jet calculation utilized uniform inflow conditions at the nozzle exit plane. The contours do <u>not</u> go smoothly from square to circular cross sections. A pronounced bulge in the corner region is predicted.

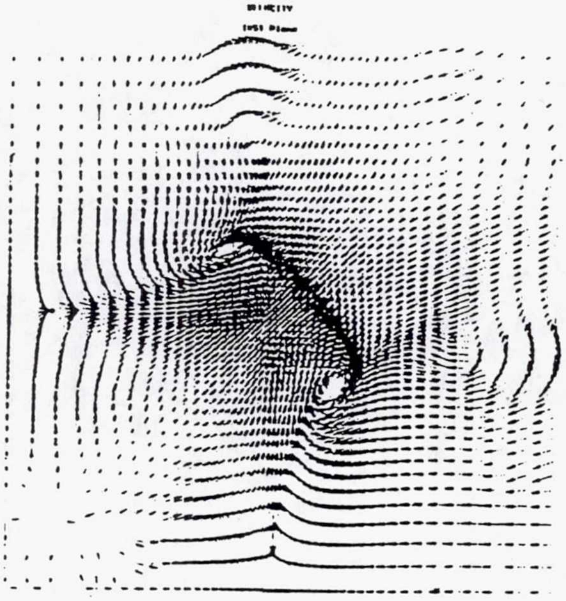

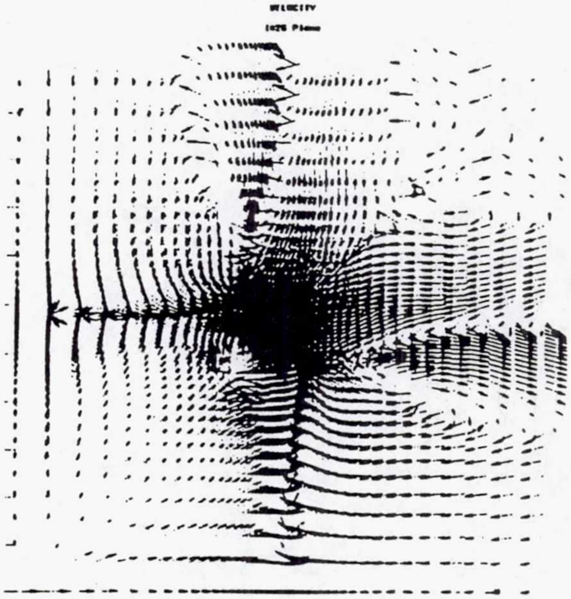

The bulge is associated with the streamwise vortex patterns produced by the corner region mixing as exhibited by cross-flow patterns at planes I = 26 ($\bar{x}$-5) and I = 51 ($\bar{x}$-10). At the symmetry planes, the shear layer mixing initially behaves in a 2D manner, but in the vicinity of the corner the mixing is highly three-dimensional. This produces counter-rotating vortices with the cross-flow having a spiral type behavior.

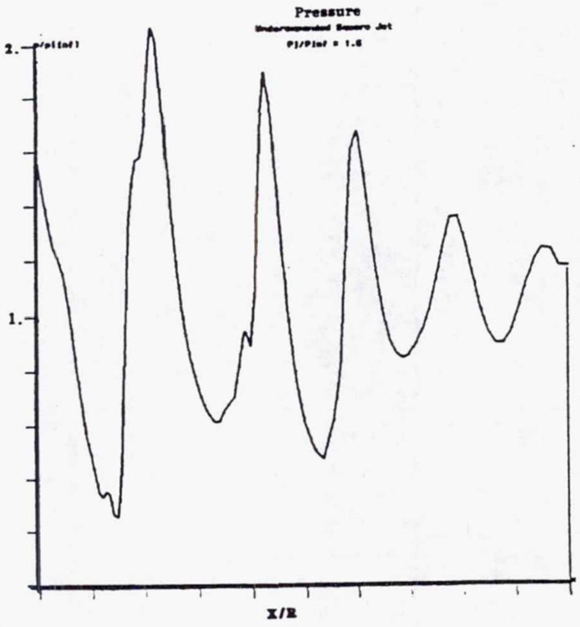

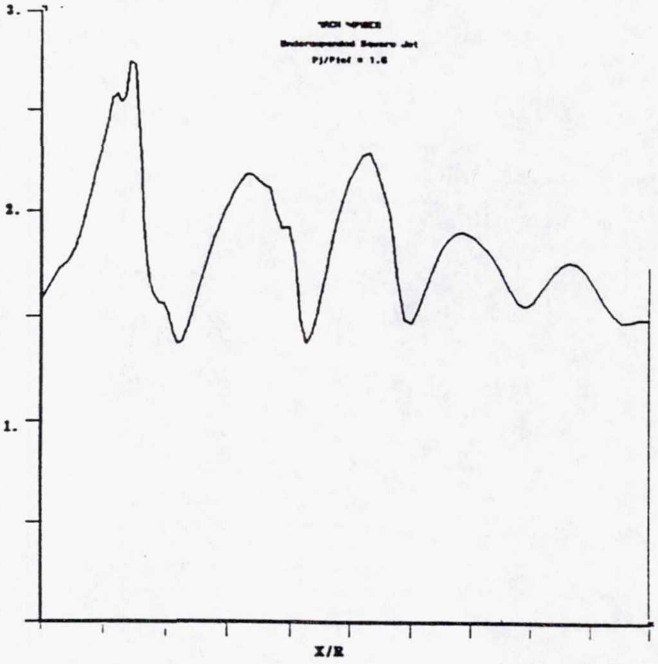

Calculations of the square jet at off-design conditions are significantly more complex than the balanced-pressure case. Pressure and Mach number variations along the jet axis are comparable to those obtained for the axisymmetric jet but the wave attenuation is more rapid since the mixing is faster. Note from the Mach number variations that no Mach disc forms in this flow (the Mach number behind the first shock at the pressure peak is about 1.3).

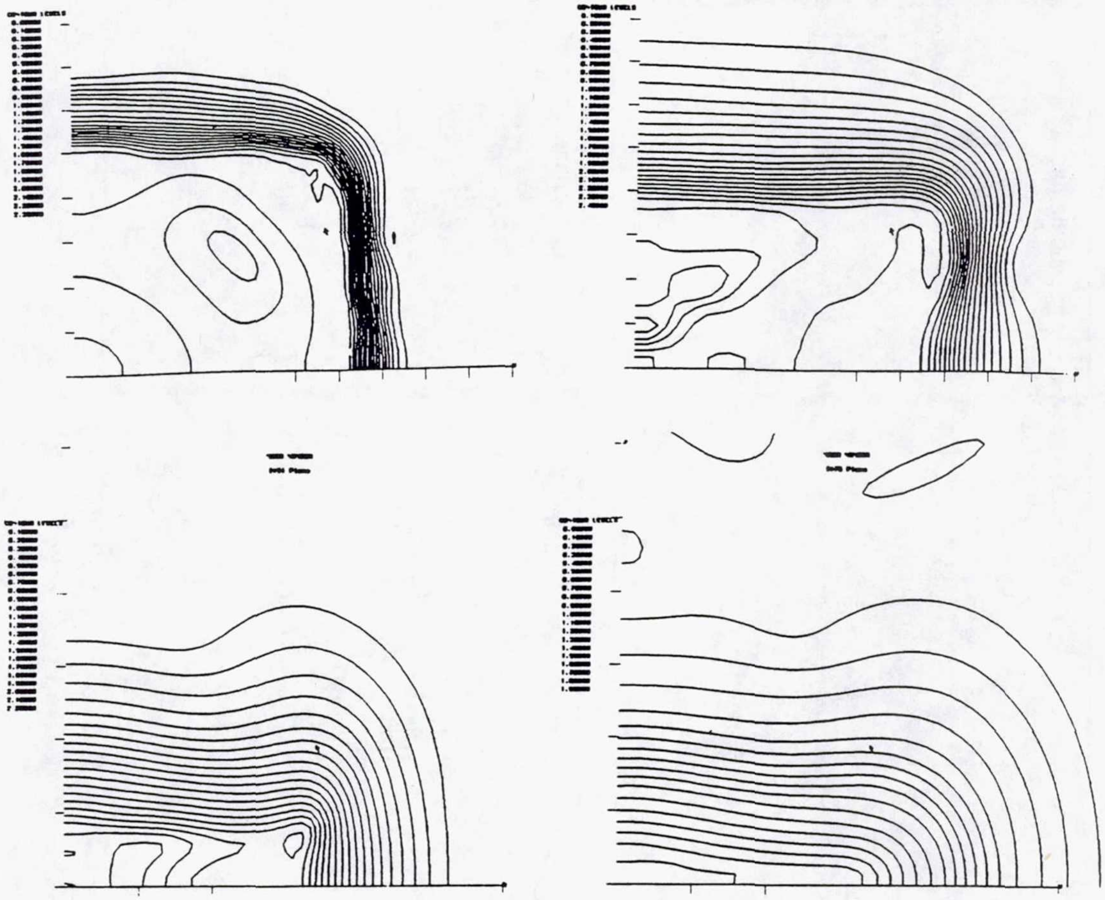

Mach number contours at selected axial stations show the jet to take on a rectangular shape since the degree of underexpansion associated with the exit plane angularity is more severe in the spanwise direction than the vertical direction (which has a 20° variation from axis to nozzle lip at the exit plane).

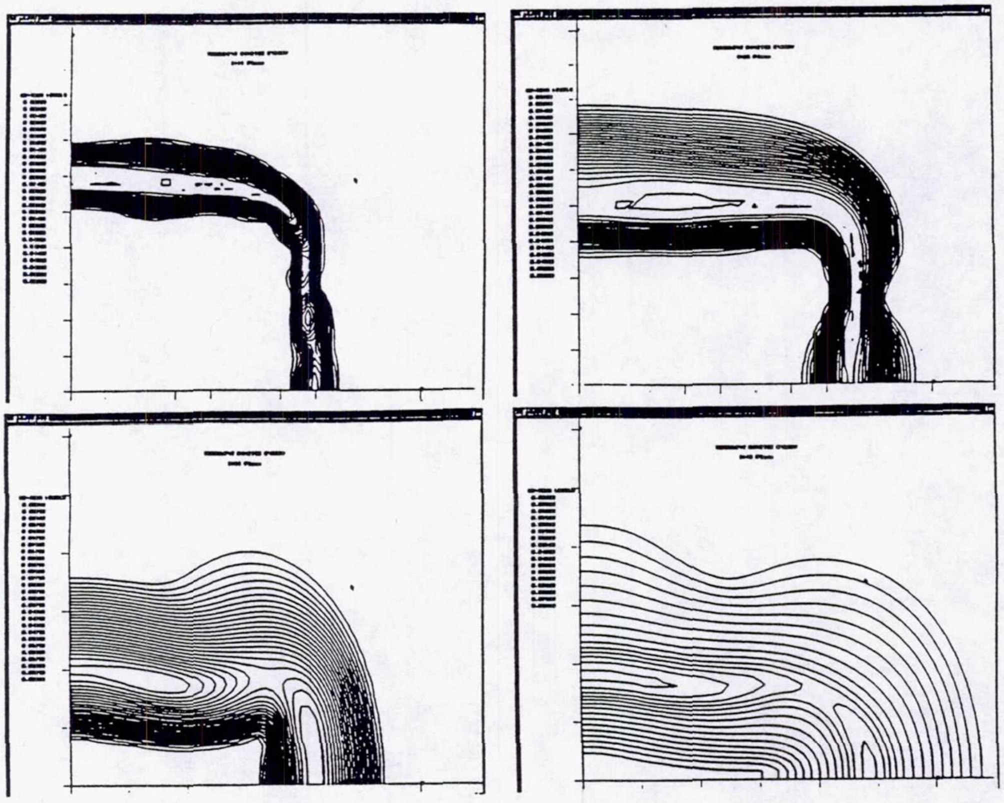

The turbulent kinetic energy contours show the jet cross-sectional shape quite well with additional bulges associated with the complex internal wave pattern.

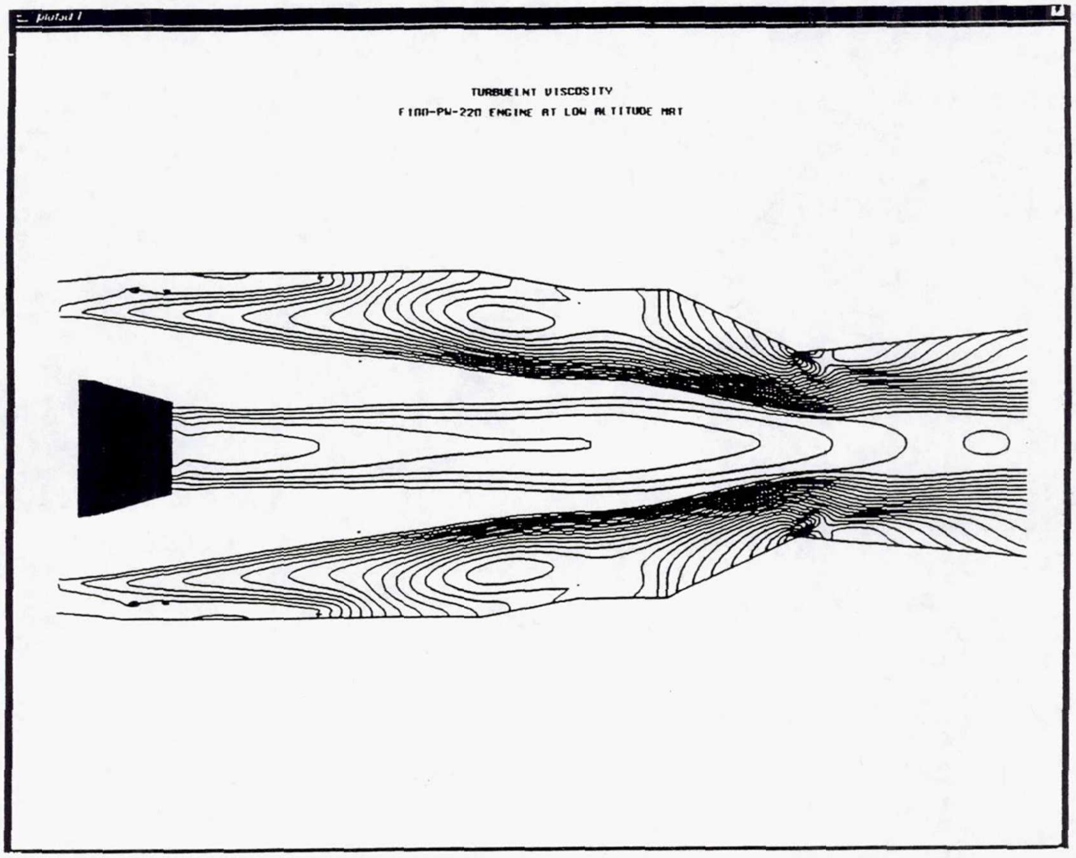

Our gas turbine tailpipe/exhaust plume work related to IR signature prediction has entailed the development of a user friendly version of PARCH entitled PARCH/GTP which calculates the tailpipe (augmentor/nozzle) and jet/plume flowfield. PARCH/GTP is coupled to engine cycle decks and has a pre-processor which initializes the internal flow solution based on cycle inputs. Initial work has focused on internal core/fan mixing including the prediction of "hot-part" surface temperatures (presently via an uncoupled thermal balance analysis). Shown above is the internal turbulent structure for an F100-PW-220 engine at low altitude for an MRT throttle setting with surface boundary layers not resolved. Details of this work are reported in Refs. 11-14, 16 and 18.

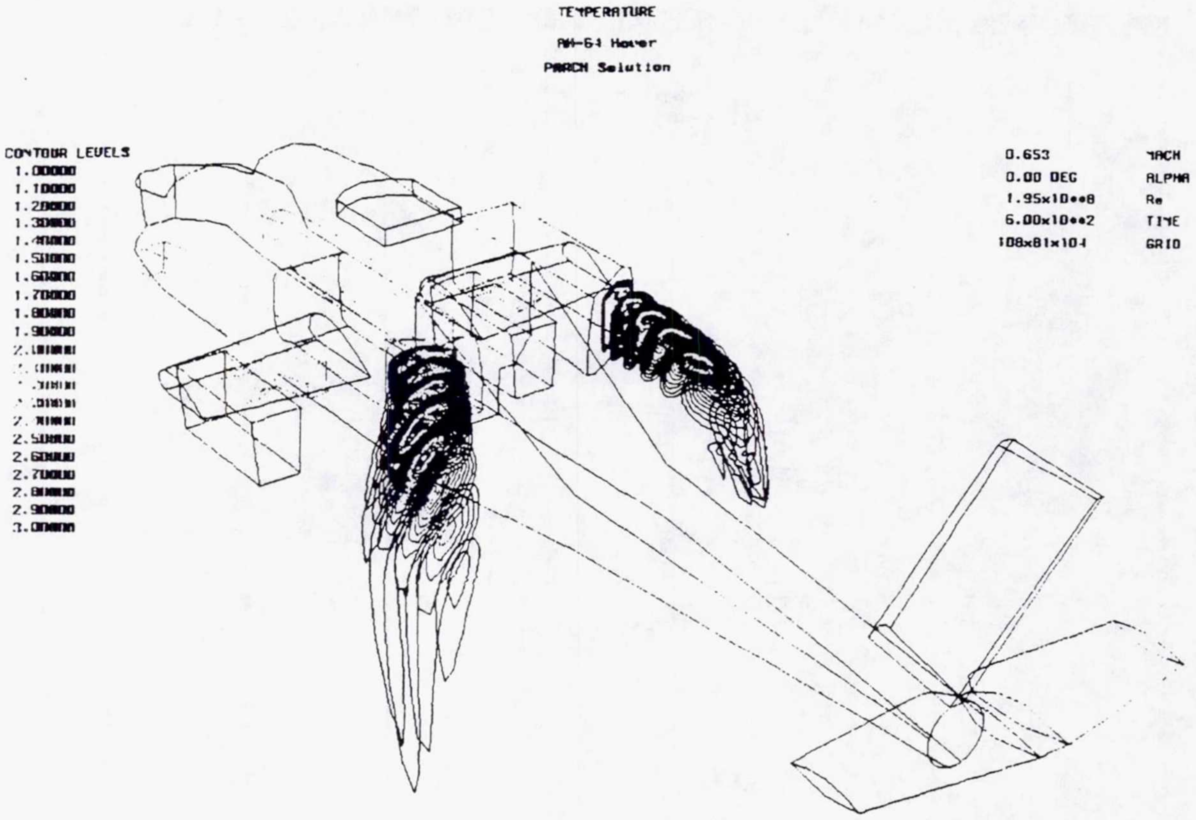

Our helicopter exhaust plume work has involved developing methodology for plume interactions with the vortical wake downwash flow. A multi-step procedure is employed utilizing:

(1) a Lagrangian vortex-tracking model which analyzes the vortex shed from the blades and its interaction with the helicopter body—this provides inflow boundary conditions under the blades for subsequent Euler/NS calculations;

(2) a coarse grid Euler solution of the complete flowfield to determine plume trajectories; and,

(3) an embedded fine grid NS solution of the plume structure (Euler and NS solutions utilize the PARCH code where grid patching has proven invaluable in gridding such a complex 3D flow).

Shown above are predicted plume temperature contours for an Apache helicopter in hover. Note the distortion of the plume cross-sectional shape by the vortical downwash. Further details of this work are reported in Refs. 13, 15, 17 and 19.

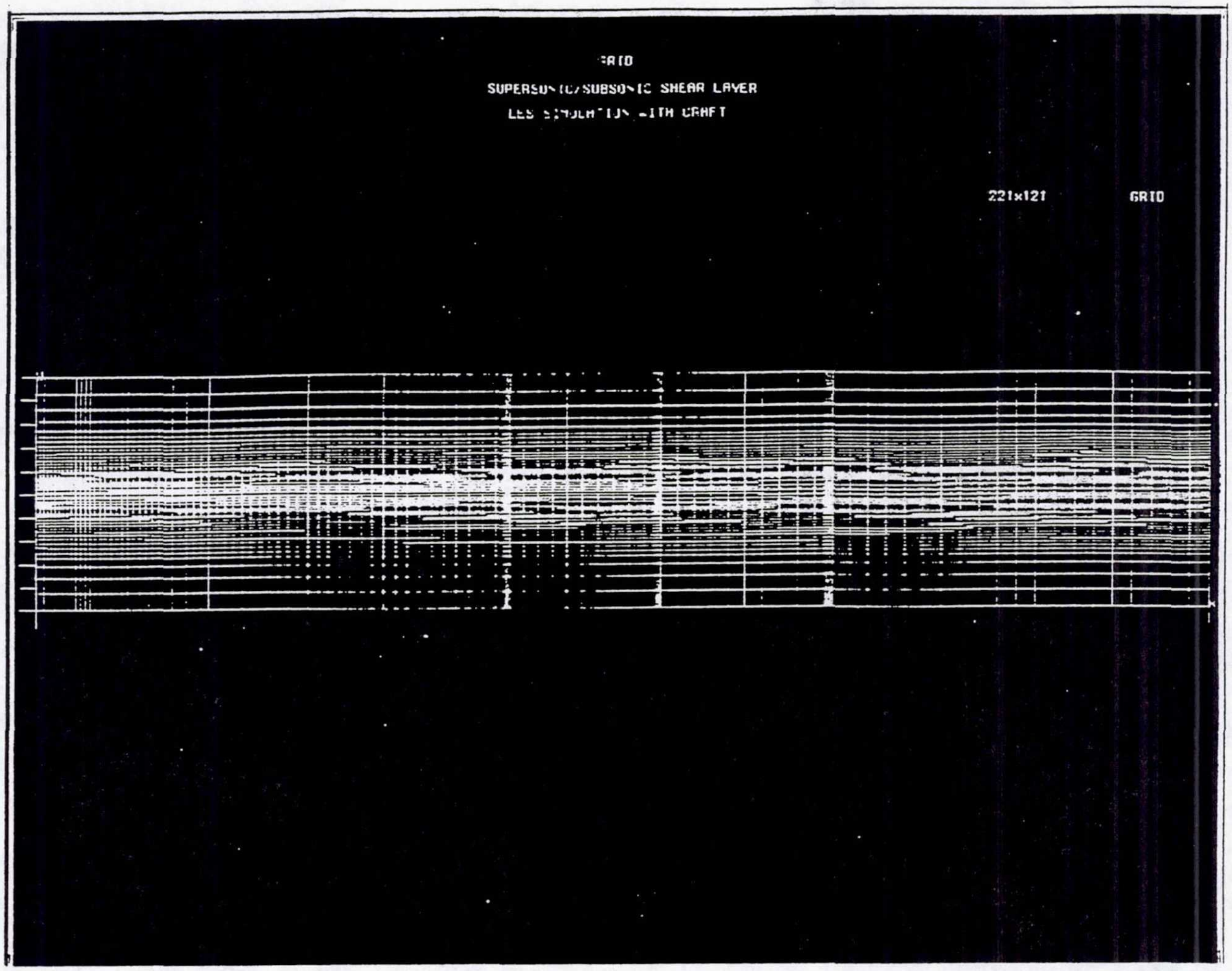

Our unsteady jet/plume work has been focused on transient, short-duration ($\sim 5\mu s$) simulations of combusting/multi-phase interior ballistic and missile propulsive problems using the CRAFT code (see Refs. 20-28). Many of the problems require dealing with non-linear instabilities and the treatment of wave/combustion interactions with turbulent large scale structure, dealt with using LES methodology. Movies have been generated for several of the flow problems calculated which best exhibit transient structural features. We have initiated jet/acoustic-oriented activities by analyzing a simple ducted shear layer problem (Mach 1.2 lower stream/Mach .2 upper stream, isoenergetic, balanced-pressure) with a small amplitude, periodic excitation of the subsonic stream (1% velocity fluctuation, sinusoidal frequency of 250Hz). The above figure shows the grid utilized and the three axial stations where averaging was performed.

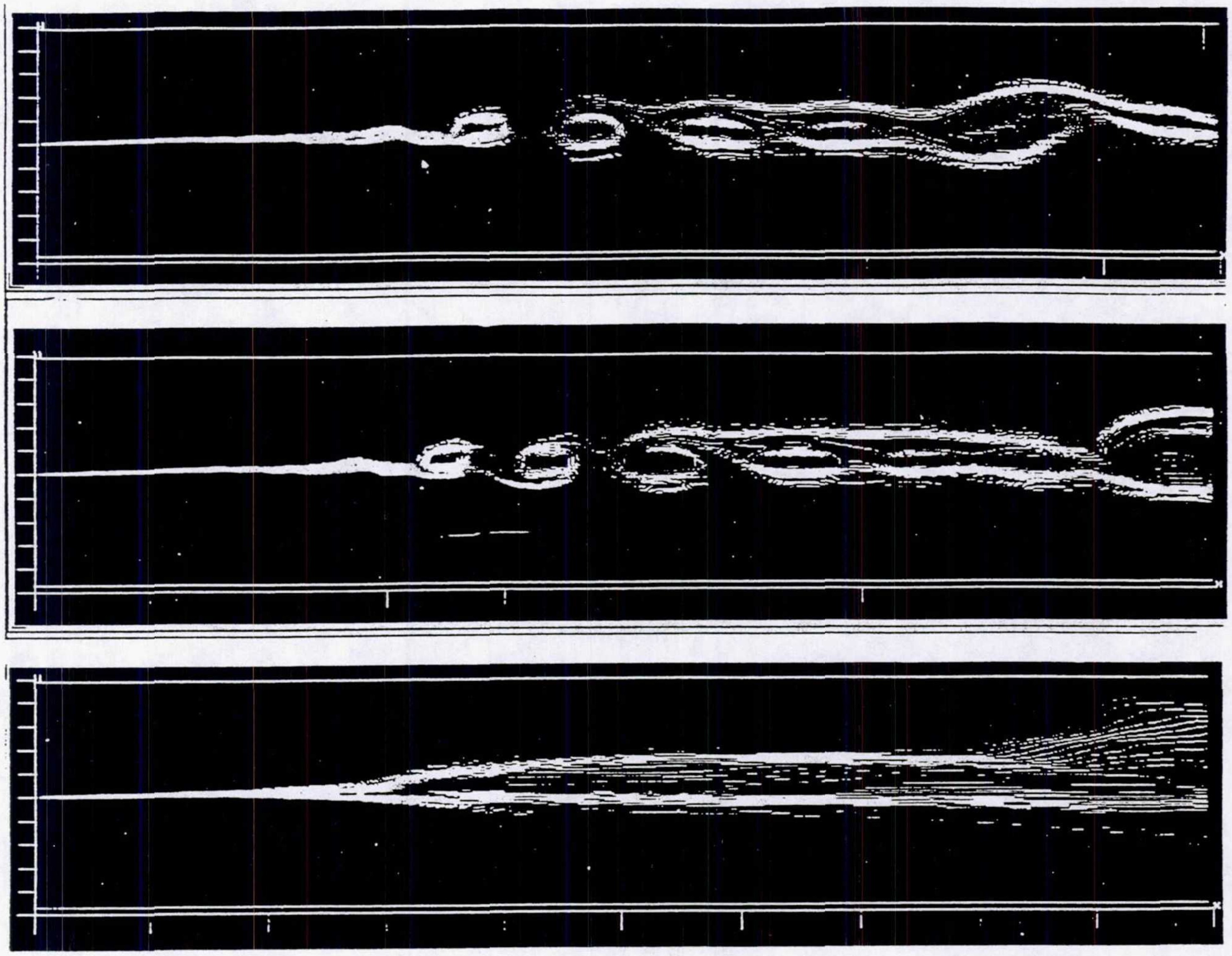

The above figure shows the large-eddy structure (instantaneous velocity contours) at two time frames of the calculation (upper two figures) and time-averaged velocity contours (lower figure). The shear layer destabilizes when the weak compression from the splitter plate reflects off the lower wall back to the shear layer.

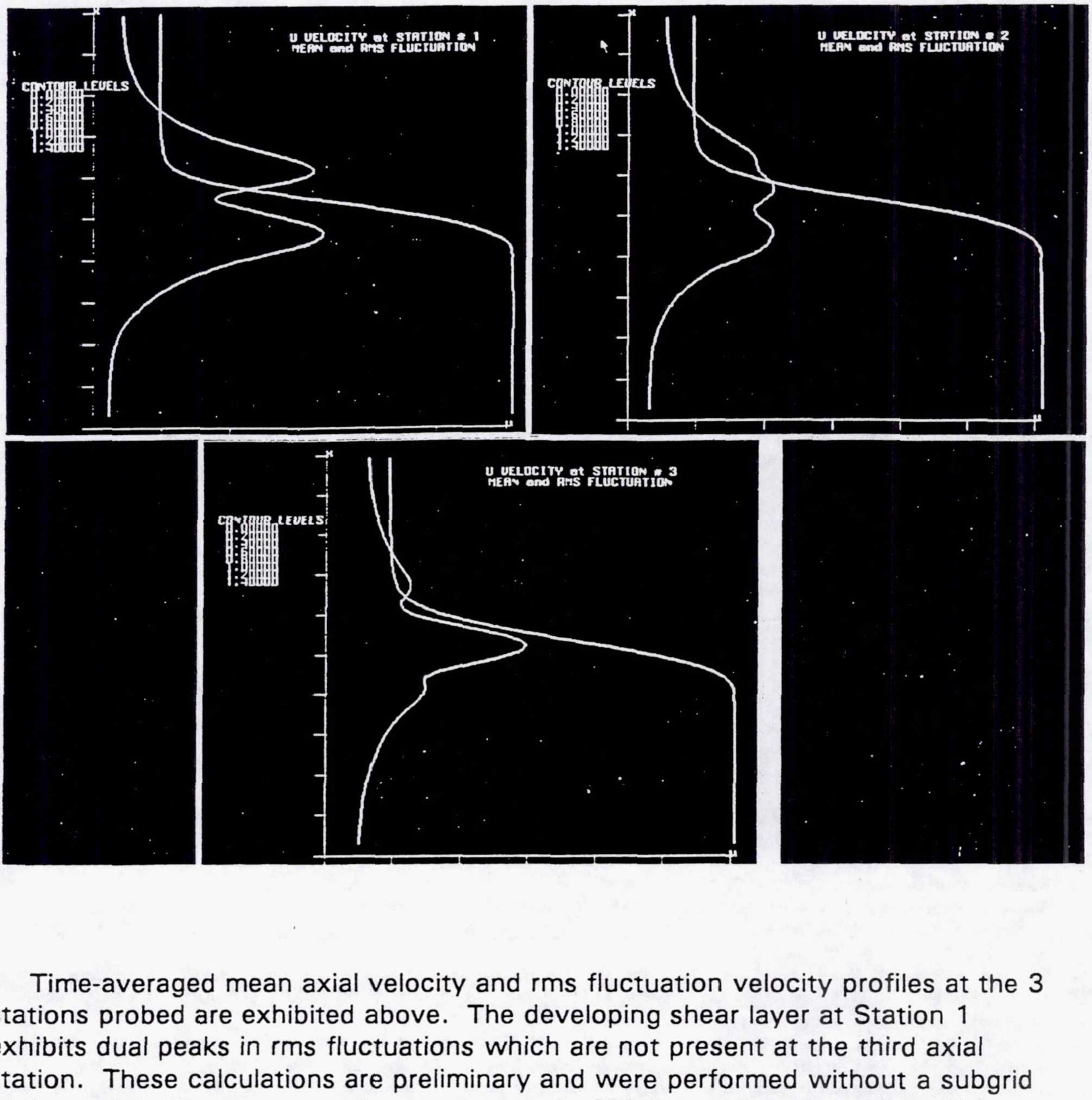

Time-averaged mean axial velocity and rms fluctuation velocity profiles at the 3 stations probed are exhibited above. The developing shear layer at Station 1 exhibits dual peaks in rms fluctuations which are not present at the third axial station. These calculations are preliminary and were performed without a subgrid scale model. We are presently exploring basic CFD issues in utilizing CRAFT implicit Roe/TVD numerics (e.g., the influence of higher-order temporal and spatial accuracy, the temporal step-size, grid resolution, magnitude/frequency of excitation, etc.). We are working with Prof. Menon/Georgia Tech on the LES subscale modeling and seek to include a model which properly deals with compressibility effects and two-way transfer of turbulence energy.

REFERENCES

1. Dash, S.M., Sinha, N., York, B.J. and Lee, R.A., "Progress in the Development of Advanced Computational Models for the Analysis of Generalized Supersonic Jet Flowfields," AIAA 13th AeroAcoustics Conference, AIAA-90-3915, Tallahassee, FL, October 1990.
2. Dash, S.M., "Observations on Practical Turbulence Modeling for High-Speed Jet/Plume Flowfields," AIAA 22nd Fluid and Plasmadynamics Conference, AIAA-91-1789, June 24-26, 1991.
3. Sinha, N., Dash, S.M. and York, B.J., "Predictions of Jet Mean-Flow Structure in Support of HSCT Noise-Suppression Concepts," AIAA/SAE/ASME/ASEE 27th Joint Propulsion Conference, AIAA-91-2253, Sacramento, CA, June 24-26, 1991.
4. Dash, S.M., Sinha, N., York, B.J., Kenzakowski, D.C., and Lee, R.A., "Computer Codes for HSCT Exhaust Flowfield Simulation and Observations on Turbulence Modeling," AIAA-91-3297, 9th AIAA Applied Aerodynamics Conference, September 23-26, 1991.
5. Dash, S.M., Walker, B.J., and Seiner, J.M., "A Building-Block Approach for Turbulence Model Validation/Upgrade Focussed on High-Speed Jet Flows," 19th JANNAF Propulsion Mtg., Feb. 24-27, 1992.
6. Dash, S.M., Sinha, N., and York, B.J., "The Critical Role of Turbulence Modeling in the Prediction of Supersonic Jet Shock Structure for Acoustic Applications," DGLR/AIAA 92-02-102, DGLR/AIAA 14th AeroAcoustic Conf., Aachen, Germany, May 11-14, 1992.
7. Dash, S.M., "Flow Predictions in Supersonic Jets - Invited Survey," DGLR/AIAA 92-02-063, DGLR/AIAA 14th AeroAcoustic Conference, Aachen, Germany, May 11-14, 1992.
8. Dash, S.M. and Kenzakowski, D.C., "A Compressible-Dissipation Extension to the $k\epsilon$ Turbulence Model and Building-Block Data for its Validation," AIAA-92-2766, 1992 AIAA SDIO Technology Conference, May 19-21, 1992.
9. Dash, S.M., Kenzakowski, D.C. and York, B.J., "Extensions to the $k\epsilon$ Turbulence Model for the Analysis of Supersonic Jets," NASA CR in preparation.
10. Sinha, N. and Dash, S.M., "Navier-Stokes Simulation of Supersonic Jets," NASA CR in preparation.
11. Dash, S.M., "PARCH Propulsive/Plume Flowfield Codes," EO Aerial Targeting Models User's Meeting, Wright-Patterson AFB, Oct. 24-25, 1989, pp. 421-446.
12. Dash, S.M., Kenzakowski, D. and York, B.J., "Propulsive/Plume Flowfield Upgrades to SPIRITS," Electro-Optics Aerial Targeting Model User's Meeting, WRDC, WPAFB, Ohio, November 1990, pp. 491-551.
13. Dash, S.M., Kenzakowski, D.C., Lee, R.A., Sinha, N., and York, B.J., "SPIRITS IR Model: Part II - Fluid Dynamic Upgrades for Aircraft and Helicopter Exhausts," 19th JANNAF Exhaust Plume Technology Meeting, May 1991.
14. S.M. Dash, D.C. Kenzakowski, B.J. York, N. Sinha and R.A. Lee, "SPIRITS Aircraft Exhaust Upgrades, Validation Studies and Exploratory Work with Advanced Turbulence Models," SAIC/FW TP-228, EO Aerial Targeting Models Users' Meeting, Wright-Patterson Air Force Base, OH, October 1991.
15. Lee, R.A. and Dash, S.M., "Helicopter Plume Flowfield Simulation for SPIRITS," 1st JANNAF SPIRITS Users Group Mtg., U.S. Army Missile Command, 17-18 June 1992.
16. Dash, S.M., Sinha, N., and Kenzakowski, D.C., "New Methodology for the Analysis of Aircraft Exhaust Plume Flowfields," 1st JANNAF SPIRITS Users Group Meeting, U.S. Army Missile Command, 17-18 June 1992.
17. Lee, R.A., Dash, S. M., and Sinha, N., "Analysis of Helicopter Wake/Body/Plume Interactions," SAIC/FW TR-100, prepared for ARI, Sept. 1992.
18. Kenzakowski, D.C., York, B.J., Dash, S.M., "Recent Gas Turbine Tailpipe/Exhaust Plume Upgrades for SPIRITS and Future Plans," presentation at EOATMUM92, Naval Air Warfare Center, Point Mugu, CA, Oct. 20-22, 1992.
19. Lee, R.A. and Dash, S.M., "Helicopter Exhaust Plume Flowfield Simulation for SPIRITS-HC," presentation at EOATMUM92, Naval Air Warfare Center, Oct. 20-22, 1992.
20. Sinha, N., Hosangadi, A. and Dash, S.M., "The CRAFT NS Code and Preliminary Applications to Steady/Unsteady Reacting, Multi-Phase Jet/Plume Flowfield Problems," 19th JANNAF Exhaust Plume Technology Mtg., CPIA Pub. 568, May 1991, pp. 203-226.
21. Sinha, N., Hosangadi, A. and Dash, S.M., "Development of an Upwind/Implicit Computational Model for the Advancement of Army ETC Guns," ETC Modeling and Diagnostics Workshop Proceedings, Vol. 2, BRL SP-92, U.S. Army Ballistic Research Laboratory, Aberdeen Proving Ground, MD, October 1991.
22. Sinha, N., A. Hosangadi, and Dash, S.M., "Simulation of ETC Gun Phenomena Using CRAFT Implicit/Upwind Computer Code," 28th JANNAF Combustion Meeting, Brooks AFB, San Antonio, TX, Oct. 28 - Nov. 1, 1991.
23. Sinha, N., Dash, S.M., and Hosangadi, A., "Applications of an Implicit, Upwind NS Code, CRAFT, to Steady/Unsteady Reacting, Multi-Phase Jet/Plume Flowfields," AIAA-92-0837, AIAA 30th Aerospace Sciences Meeting, Reno, NV, January 6-9,1992.
24. Wren, G.P., Oberle, W.F., Sinha, N., Hosangadi, A., and Dash, S.M., "U.S. Army Activities in Multidimensional Modeling of Electrothermal-Chemical Guns," *IEEE Conference, Electromagnetic Launcher Symposium*, Austin, TX, April 28-30, 1992.
25. Sinha, N., York, B.J., Dash, S.M., Drabczuk, and R., Rolader, G.E., "Progress Towards the Development of Transient Ram Accelerator Simulation As Part of U.S. Air Force Armament Directorate Research Program," AIAA-92-3248, *AIAA/SAE/ASME/ASEE 28th Joint Propulsion Conf.*, Nashville, TN, July 6-8, 1992.
26. B.J. York, N. Sinha, S.M. Dash, A. Hosangadi, D.C. Kenzakowski, and R.A. Lee, "Complete Analysis of Steady and Transient Missile Aerodynamic/Propulsive/Plume Flowfield Interactions," AIAA-92-3603, *AIAA/SAE/ASME/ASEE 28th Joint Propulsion Conf.*, Nashville, TN, July 6-8, 1992.
27. Sinha, N., York, B.J., Dash, S.M., Drabczuk, R., and Rolader, G.E., "Transient Simulation of Ram Accelerator Flowfields," 29th JANNAF Combustion Meeting, 19-23 Oct. 1992.

REFERENCES (cont.)

28. Hosangadi, A., Sinha, N., and Dash, S.M., "CRAFT Code Multi-Dimensional Simulation of ETC Interior Ballistics," 29th JANNAF Combustion Meeting, 19-23 Oct. 1992.
29. Dash, S.M., Wilmoth, R.G. and Pergament, H.S., "An Overlaid Viscous/Inviscid Model for the Prediction of Nearfield Jet Entrainment," AIAA Journal, Vol. 17, September 1979, pp. 950-958.
30. Dash, S.M., Pergament, H.S. and Thorpe, R.D., "Computational Models for the Viscous/Inviscid Analysis of Jet Aircraft Exhaust Plumes," NASA CR-3289, May 1980.
31. Wilmoth, R.G. and Dash, S.M., "A Viscous-Inviscid Interaction Model of Jet Entrainment," Computation of Viscous-Inviscid Interactions, AGARD CP-291, September 1980, pp. 13.1 - 13.15.
32. Dash, S.M., Pearce, B.E., Pergament, H.S. and Fishburne, E.S., "The Prediction of Rocket and Aircraft Exhaust Plume Structure: Requirements in IR Radiation Signature Studies," AIAA-79-0095, New Orleans, LA, January 1979.
33. Pearce, B.E., Fishburne, E.S., Pergament, H.S. and Dash, S.M., "Near Nose-On Aircraft Plume Emission Predictions by a New Computational System," JANNAF 11th Plume Technology Meeting, CPIA Pub. 306, Vol. I, May 1979, pp. 345-442.
34. Dash, S.M. and Wolf, D.E., "Fully-Coupled Analysis of Jet Mixing Problems, Part I: Shock-Capturing Model, SCIPVIS," NASA CR-3761, January 1984.
35. Dash, S.M. and Wolf, D.E., "Interactive Phenomena in Supersonic Jet Mixing Problems, Part I: Phenomenology and Numerical Modeling Techniques," AIAA Journal, Vol. 22, July 1984, pp. 905-913.
36. Dash, S.M. and Wolf, D.E., "Interactive Phenomena in Supersonic Jet Mixing Problems, Part II: Numerical Studies," AIAA Journal, Vol. 22, October 1984, pp. 1395-1404.
37. Dash, S.M., Wolf, D.E. and Seiner, J.M., "Analysis of Turbulent Under-Expanded Jets - Part I: Parabolized Navier-Stokes Model, SCIPVIS," AIAA Journal, Vol. 23, April, 1985, pp. 505-514.
38. Seiner, J.M., Dash, S.M. and Wolf, D.E., "Analysis of Turbulent Under-Expanded Jets - Part II: Shock Noise Features Using SCIPVIS," AIAA Journal, Vol. 23, May 1985, pp. 669-677.
39. Cooper, G.K. and Sirbaugh, J.R., "PARC Code: Theory and Usage," AEDC-TR-89-15, Dec. 1989.
40. Cooper, G.K. and Sirbaugh, J.R., "The PARC Distinction: A Practical Flow Simulator," AIAA-90-2002, July 1990.
41. Molvik, G.A. and Merkle, C.L., "A Set of Strongly-Coupled Upwind Algorithms for Computing Flows in Chemical Nonequilibrium," AIAA-89-0199, January 1989.
42. Lee, R.A., "Grid Patching Upgrades to the CRAFT Navier-Stokes Code," SAIC/FW TR- in preparation.
43. York, B.J. and Hosangadi, A., "Implicit, Riemann-Based Boundary Condition Upgrades to the CRAFT Navier-Stokes Code," SAIC/FW TR- in preparation.
44. Kenzakowski, D.C. and York, B.J., "Validation/Assessment Studies of Grid Patched Version of CRAFT for Steady Flowfields," SAIC/FW TR- in preparation.
45. Spalding, D.B., "The Vorticity-Fluctuations (kW) Model of Turbulence; Early Papers," CFD/82/17, Imperial College, London, UK, November 1982.
46. Dash, S.M., Weilerstein, G., and Vaglio-Laurin, R., "Compressibility Effects in Free Turbulent Shear Flows," Air Force Office of Scientific Research, TR-75-1436, August 1975.
47. Pergament, H.S., Sinha, N. and Dash, S.M., "A Hybrid Two-Equation Turbulence Model for High Speed Propulsive Jets," AIAA-86-1723, Huntsville, AL, June 1986.
48. Sarkar, S. and Lakshmanan, B., "Application of a Reynolds Stress Turbulence Model to the Compressible Shear Layer," AIAA J., May 1991, pp. 743-749.
49. Zeman, O. "Dilatational Dissipation: The Concept and Application in Modeling Compressible Mixing Layers," Physics of Fluids, February 1990.
50. Goebel, S.G. and Dutton, J.C., "Experimental Study of Compressible Turbulent Mixing Layers," AIAA J., Vol. 29, April 1991, pp. 538-546.
51. Samimy, M. and Elliot, G.S., "Effects of Compressibility on the Characteristics of Shear Layers," AIAA J., Vol. 28, March 1990, pp. 439-445.
52. Pope, S.B., "An Explanation of the Turbulent Round-Jet/Plane-Jet Anomaly," AIAA J., March 1978, pp. 279-281.
53. Shih, T.-H., Chen, J.-Y., Lumley, J.L., "Second-Order Modeling of Boundary-Free Turbulent Shear Flows," AIAA J., June 1992, pp. 1553-1560.
54. Wygnanski, I. and Fiedler, H.E., "Some Measurements in the Self-Preserving Jet,: J. of Fluid Mech., Vol. 38, 1969, pp. 577-612.
55. Sarkar, S., "Modeling the Pressure-Dilatation Correlation," NASA CR 187566, ICASE Report No. 91-42, NASA LaRC, Hampton, VA, May 1991.
56. Lele, S.K. [Stanford Univ.], "Strain-Based Pressure Dilatation Model," Workshop on Enhanced Turbulence Mixing for Take-off Noise Reduction, Williamsburg, VA, Oct. 28-30, 1992.
57. Eggers, J.M., "Velocity Profiles and Eddy Viscosity Distributions for Mach 2.22 Jet Exhausting Into Still Air," NASA TN d-3601, 1966.
58. Seiner, J.M., Ponton, M.K., Jansen, B.J., Lagen, N.T., "The Effects of Temperature on Supersonic Jet Noise Emission," DGLR/AIAA Paper No. 92-02-046, DGLR/AIAA AeroAcoustics Conference, Aachen, Germany, May 1992.

19991765 57

ANALYSIS OF NUMERICAL METHODS FOR APPLICATION TO JET NOISE PROBLEMS

J.N. Scott
Ohio State University
Columbus, Ohio

520-07

409539

24p.

OUTLINE

- Review results of Navier-Stokes solutions of unsteady jet flow
- Analysis of numerical methods using solutions of model problems

Stability and accuracy analysis

-Viscous Burgers equation

Propagation of acoustic disturbances

-Linearized Euler equations

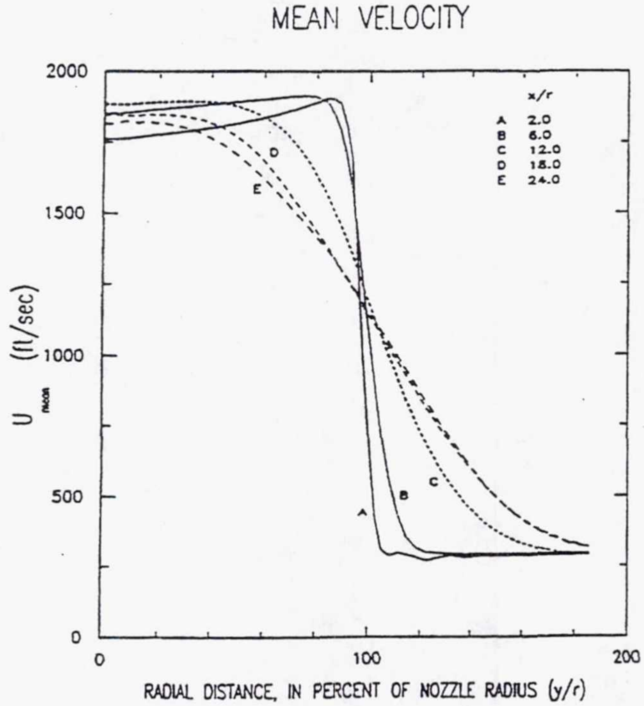
MEAN VELOCITY

MACH 1.3
Re = 675,800

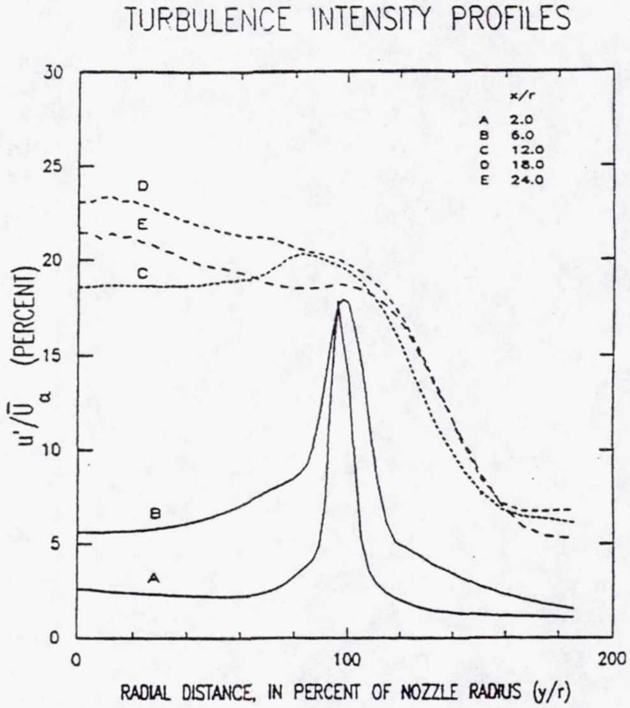
TURBULENCE INTENSITY PROFILES

MACH 1.3
Re = 675,800

Velocity Profile and Turbulence Intensity: The computed results for the axial variation of velocity profile are shown here for a jet having an exit Mach number of 1.3. From this figure it can be seen that the shear layer spreads in the axial direction so that the flow is fully mixed before it reaches 6 diameters downstream of the exit.

The turbulence intensity shows that near the exit plane the intensity spikes at the jet lip as expected. This figure also gives an indication of the spreading of the jet since the turbulence intensity does not drop off toward the jet axis beyond 6 diameters downstream form the jet exit.

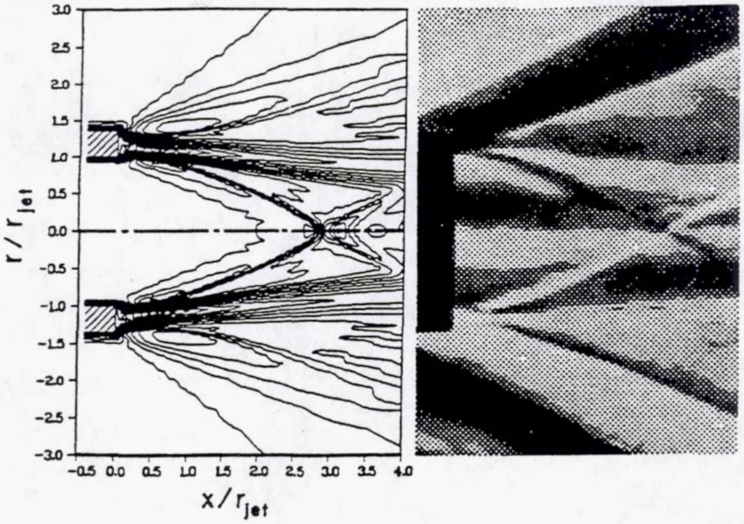

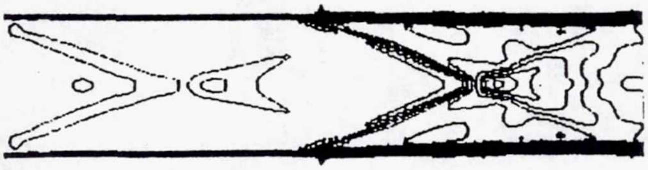

Shock Structure: The presence of shocks in the jet have been identified as a major contributor to the production of jet noise. Of particular interest is the interaction of the shocks with the shear layer, intersecting shocks and the interaction of shocks with the large scale vortices.

It is shown here that Mach contours obtained from the results of the numerical method give a representation of the shocks at the exit of a jet having an exit Mach number of 2, that are in good agreement with the shocks observed in Schlieren photographs. In this figure the Mach contours are also compared with the results from a previous computation by Hasen.

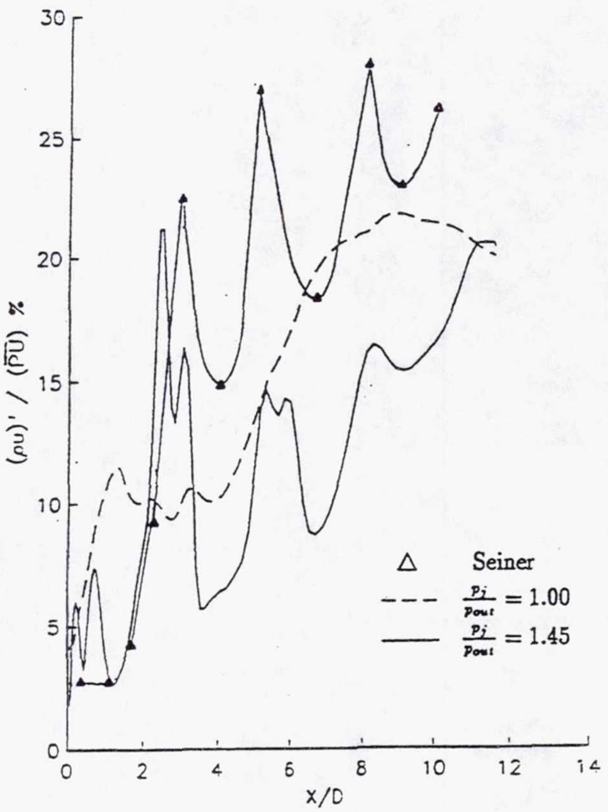

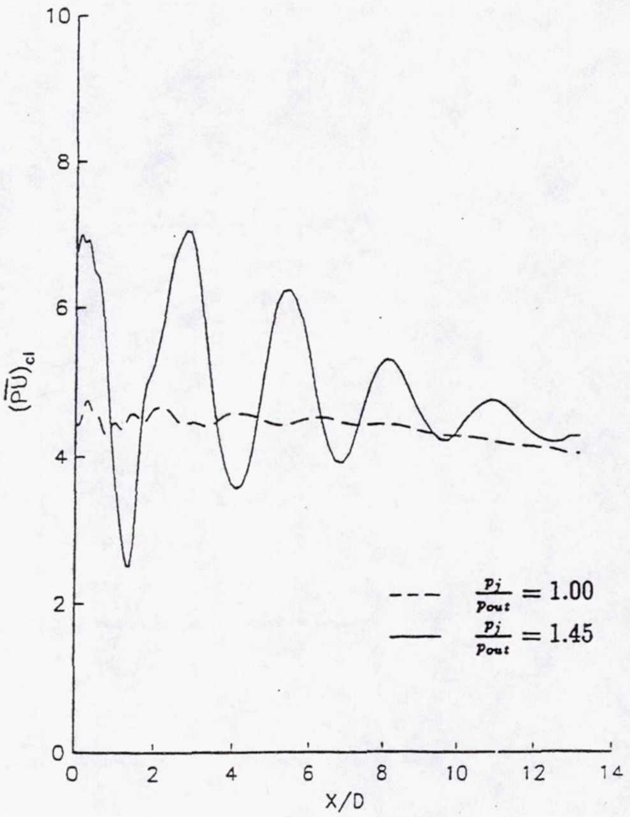

Downstream Shock Pattern: As the shocks interact with the shear layer they are reflected as expansions toward the centerline. This alternating shock-expansion cycle has been measured experimentally through the fluctuating mass flux along the jet lip line for a Mach 2 jet by Seiner and Norum.

Here the computed results show that the numerical method accurately predicts the locations of shock cycle along the jet lip line. It is noted that the numerical result is in good agreement with the experimental data in predicting the amplitude of the fluctuation through the first shock cell. However the numerical result under predicts the experimental data downstream of the first shock.

The numerical results for the mass flux variation are also used to monitor the location and decay of the shock cells along the jet centerline as shown in this figure.

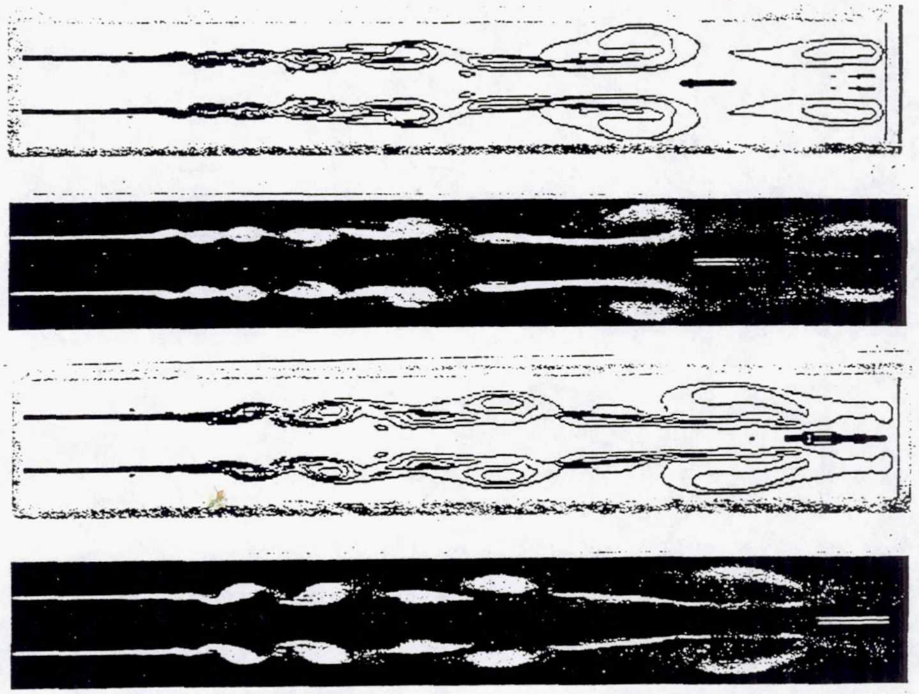

VORTICITY FIELD

Vorticity Field: The vorticity field is important in the analysis of unsteady jet flow because it not only shows the shedding and interaction of the large scale vortex structures but it also provides information about the jet mixing and the spreading rate of the jet. Furthermore the unsteady behavior associated with the vortex shedding and interaction is directly linked with the production of jet noise. Specifically, the vorticity is essentially the strength and distribution of the quadrupole sources within the jet. This is related to the Lighthill stress tensor. This figure shows the vorticity field for a Mach 2 jet in which the merging or pairing of vortex rings is observed as well as the growth and stretching of the vortices as they are convected downstream.

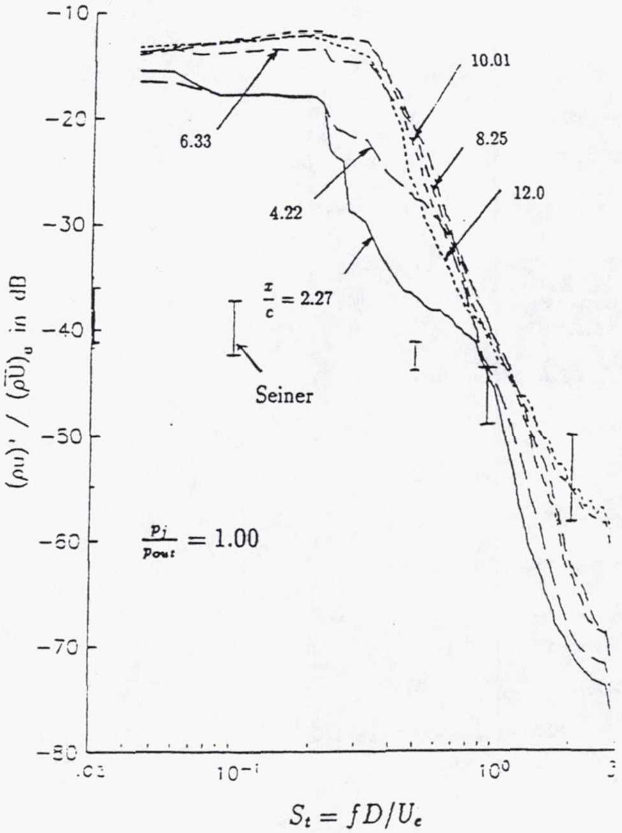

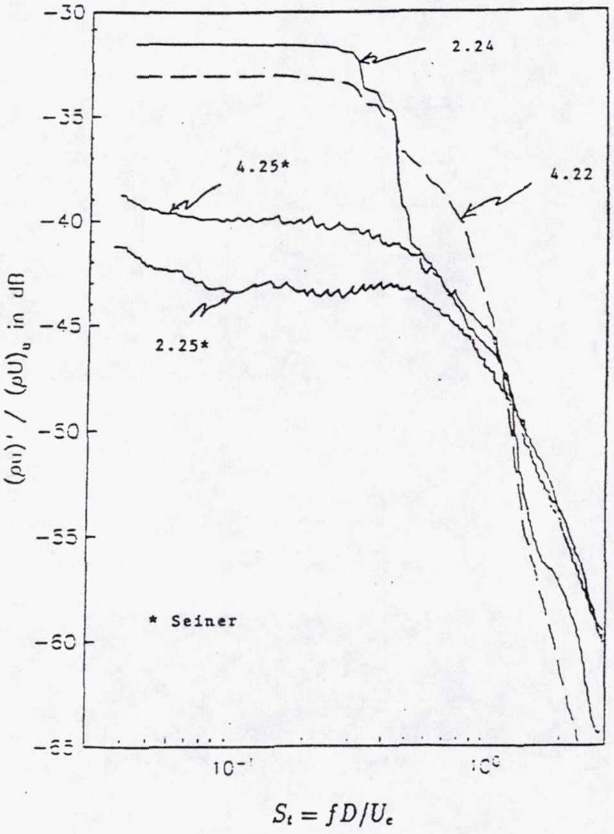

Mass Flux Spectrum: An indication of the suitability of a numerical scheme for the analysis of jet noise is its ability to predict the spectrum of the fluctuating mass flux of the jet. This gives a significant amount of information about the numerical results and how they can be improved. The computed mass flux spectra for different axial locations are shown here for the Mach 2 jet and are compared with the experimental data of Seiner and Norum for two different computations. One computation is run using a computational grid consisting of 90 points in the radial direction and 125 points in the axial direction. This computation is run for 30,000 time steps.

As seen in (b) the computational results over predict the experimental data by a substantial margin and under predict the high frequencies. Significant improvement in the agreement has been accomplished by doubling the number of grid points in each direction to achieve better resolution of the high frequency behavior. In addition increasing the run time to 100,000 time steps has improved the prediction of the low frequency range. Further grid refinement and run time studies are continuing.

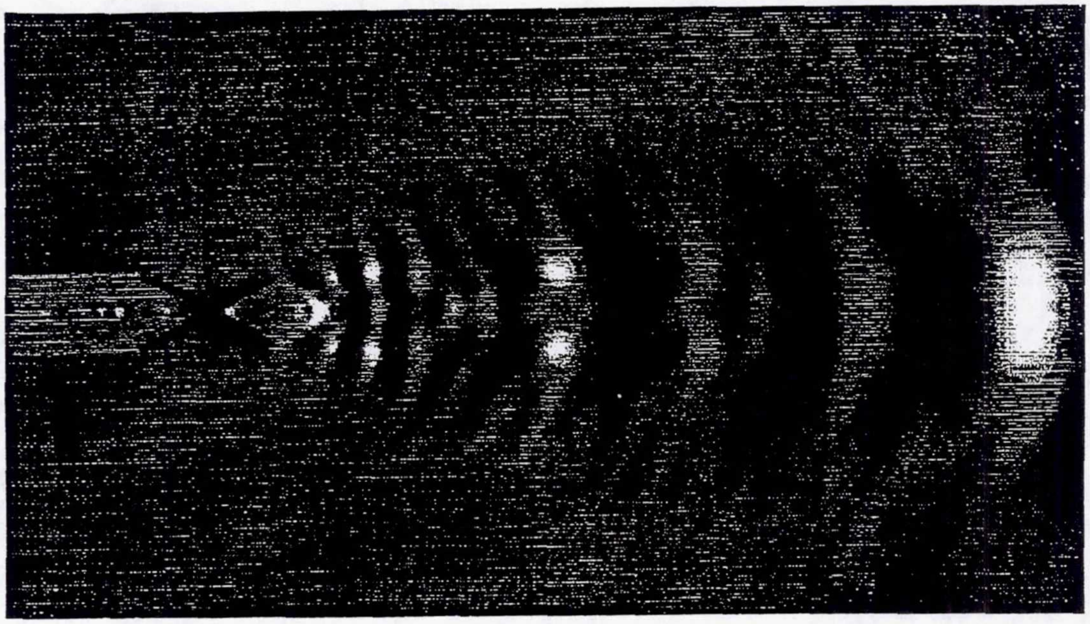

Pressure Field: One of the most significant features in the analysis of unsteady jet flow is the pressure field. This reveals significant information about the shock structure, the interaction of the shocks with the shear layer as well as the vortices. In this figure the shocks are quite clear at the jet exit and the alternating light and dark regions along the lip line are the vortex rings which are growing in the streamwise direction The pressure field also gives a good indication of pressure waves propagating away from the jet shear layer. This data also provides an excellent diagnostic tool in the evaluation boundary conditions; particularly if they are producing non-physical reflections. Many of these features can be seen in this figure which shows the pressure field of the Mach 2 jet.

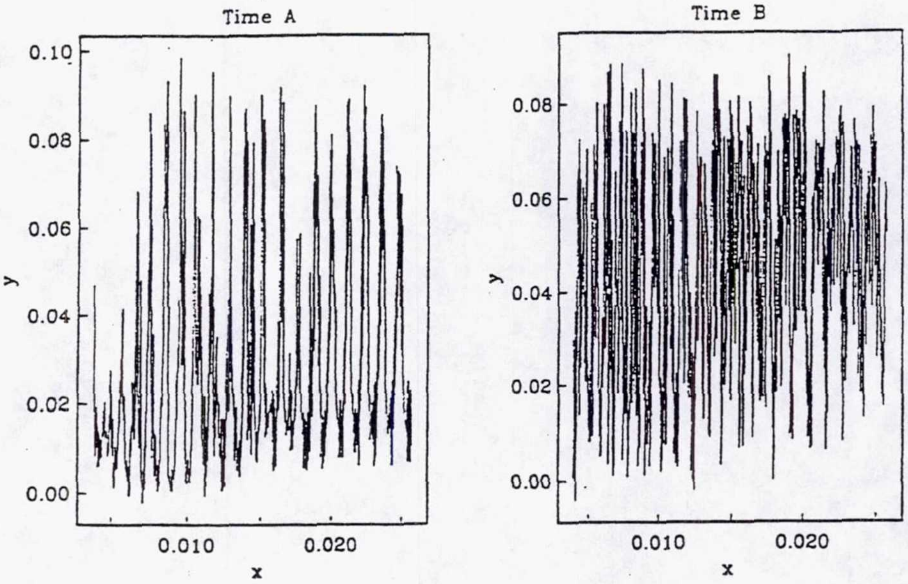

Two Point Correlation Data

In evaluating the computed jet flow results it is desirable to compare two point correlation data with experimental data if possible. While there is little data of this type available for supersonic jets there has been a substantial accumulation of this type of data for subsonic jets. The computational data shown here are time histories of fluctuating mass flux for two point correlations in the Mach 2 jet shear layer for data taken at 1 and 3 diameters. These data have been used to obtain auto correlation, coherence, cross correlation, cross spectrum, transfer function, spectrum and time history. Comparison of this type of data with experimental data will be of significant value in evaluating the capability of the numerical approach for predicting spectral quantities.

Burgers Equation

The 1-D linear viscous Burgers equation:

$$\frac{\partial u}{\partial t} + c\frac{\partial u}{\partial x} = \nu\frac{\partial^2 u}{\partial x^2} \tag{1}$$

Difference Schemes

The Lerat-Peyret schemes:

Predictor:

$$\begin{aligned} \overline{u}_j &= (1-\beta)u_j^n + \beta u_{j+1}^n - \alpha q(u_{j+1}^n - u_j^n) \\ &\quad + \alpha r[\gamma(u_{j+2}^n - 2u_{j+1}^n + u_j^n) \\ &\quad + (1-\gamma)(u_{j+1}^n - 2u_j^n + u_{j-1}^n)] \end{aligned} \tag{2}$$

Corrector:

$$\begin{aligned} u_j^{n+1} &= u_j^n - \frac{q}{2\alpha}[(\alpha-\beta)u_{j+1}^n + (2\beta-1)u_j^n \\ &\quad + (1-\alpha-\beta)u_{j-1}^n + \overline{u}_j - \overline{u}_{j-1}] \\ &\quad + \frac{r}{2\alpha}[(2\alpha-1)(u_{j+1}^n - 2u_j^n + u_{j-1}^n) \\ &\quad + (1-\beta)(\overline{u}_{j+1} - 2\overline{u}_j + \overline{u}_{j-1}) \\ &\quad + \beta(\overline{u}_j - 2\overline{u}_{j-1} + \overline{u}_{j-2})] \end{aligned} \tag{3}$$

where, $q = c\Delta t/\Delta x$ is the Courant number, and $r = \nu\Delta t/\Delta x^2$ is the diffusion parameter or cell Reynolds number.

Table for Parametric Study

Table 1: Data for Calculation of Amplification Factor and Phase Error.

$q = c\frac{\Delta t}{\Delta x}$	—	0.25	0.5	0.75	1.0
$r = \nu\frac{\Delta t}{\Delta x^2}$	0.0	0.25	0.5	0.75	1.0

Scheme	α	β	γ
MacCormack (FB)	1.0	0.0	0.0
MacCormack (BF)	1.0	1.0	1.0
Lax-Wendroff	0.5	0.5	0.5
Rubin-Burstein	1.0	0.5	0.5
Peyret-Taylor	$1+\frac{\sqrt{5}}{2}$	0.5	0.5

Analysis of Stability and Accuracy Characteristics of a Class of Finite Difference Schemes

The stability and accuracy of a class of finite difference schemes are analyzed by solving the viscous form of the Burgers equation. The class of equations under consideration is defined by the generalized Lerat-Peyret predictor-corrector scheme given here. The parameters q and r represent the Courant number and the cell Reynolds number respectively. Different combinations of the remaining parameters give different forms of well known finite difference schemes. The five schemes investigated are shown in the accompanying table with the various combinations of parameters which produce these schemes. It should be noted that the choice of parameters is not restricted to those shown. Thus it becomes possible to investigate any combination of parameters and thereby conceivably optimize the numerical procedure for any spatial and/or temporal step size.

Von Neumann Stability Analysis

The amplification factor is:

$$\rho(\xi) = (Real\ part) + i * (Imaginary\ part) \tag{4}$$

- Exact expression for the modulus of the amplification factor:

$$\begin{aligned} |\rho(\xi)|^2 &= \{Rl[\rho(\xi)]\}^2 + \{Im[\rho(\xi)]\}^2 \\ &= a^2\left[q - 2bqr + 2b^2(\beta-\gamma)r^2\right]^2 + \Big\{1 - bq^2 \\ &\quad + 2b^2(\beta-\gamma)qr + 2b\Big[\frac{\beta(1-\beta)}{\alpha}b - 1\Big]r \\ &\quad + 2b^2\left[1 - b(\beta+\gamma-2\beta\gamma)\right]r^2\Big\}^2 \end{aligned} \tag{5}$$

where, $a = \sin(\xi), b = 1 - \cos(\xi)$.

- Exact expression for the relative phase error:

$$\phi = \begin{cases} \frac{c}{(-q\xi)}\tan^{-1}\left\{\frac{Im[\rho(\xi)]}{Rl[\rho(\xi)]}\right\}, & Rl[\rho(\xi)] \geq 0 \\ \\ \frac{c}{(-q\xi)}\pi - \frac{c}{(-q\xi)}\left|\tan^{-1}\left\{\frac{Im[\rho(\xi)]}{Rl[\rho(\xi)]}\right\}\right|, & Rl[\rho(\xi)] < 0 \end{cases} \tag{6}$$

- Approximate expressions for ξ near zero:

$$|\rho(\xi)| = 1 - r\xi^2 + \Psi_0\,\xi^4 \tag{7}$$

where,

$$\begin{aligned} \Psi_0 &= \frac{1}{2}\Big\{\frac{1}{4}q^2(q^2-1) + rq(\beta-\gamma) - rq^2 \\ &\quad + r\Big[\frac{1}{6} + \frac{\beta(1-\beta)}{\alpha}\Big] + r^2\Big\}. \end{aligned}$$

For the relative phase error,

$$\phi = -c\left[1 - \frac{1}{6}(1-q^2)\xi^2 + \Gamma_0\,\xi^4\right] \tag{8}$$

where,

$$\begin{aligned} \Gamma_0 &= \frac{1}{120} + \frac{1}{24}q^2 - \frac{1}{20}q^4 + \frac{1}{2}\Big[\frac{\beta(\beta-1)}{\alpha}r - r^2 \\ &\quad + (\gamma-\beta)\left(rq - \frac{r^2}{q}\right) + rq^2\Big]. \end{aligned}$$

Von Neumann Stability Analysis

Performing a Von Neumann stability analysis for the generalized class of two-level space centered difference equations gives expressions for the amplification factor and relative phase error as functions of the parameters which determine the specific algorithms under consideration. Exact stability criteria are derived for each of the five schemes as applied to the solution of the Burgers equation. Exact results have been plotted for several values of Courant number and cell Reynolds number for each scheme. These results are of significant value in assessing the dissipation and dispersion characteristics of each scheme.

Approximate expressions for the amplification factor and relative phase error are given for values of wave number near pi.

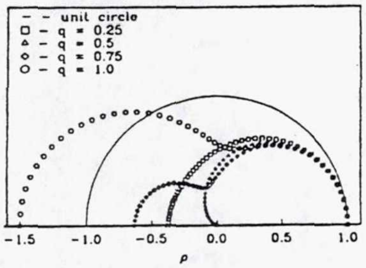
a. Amplification Factor

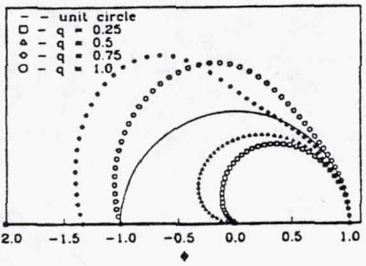
b. Phase Error

Figure 2: Amplification Factor and Phase Error for MacCormack (FB and BF) Scheme ($r = 0.25$)

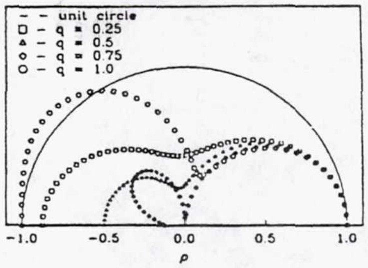
a. Amplification Factor

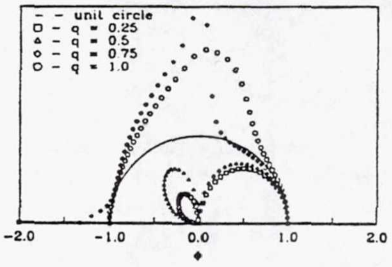
b. Phase Error

Figure 3: Amplification Factor and Phase Error for MacCormack (FB and BF) Scheme ($r = 0.5$)

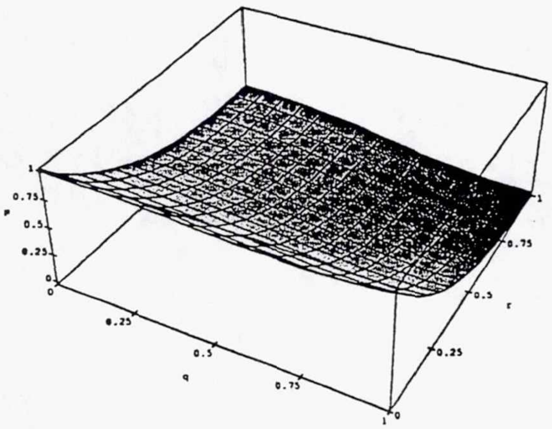

Figure 4: Surface of Amplification Factor for MacCormack Scheme ($\xi = 0.35\pi$)

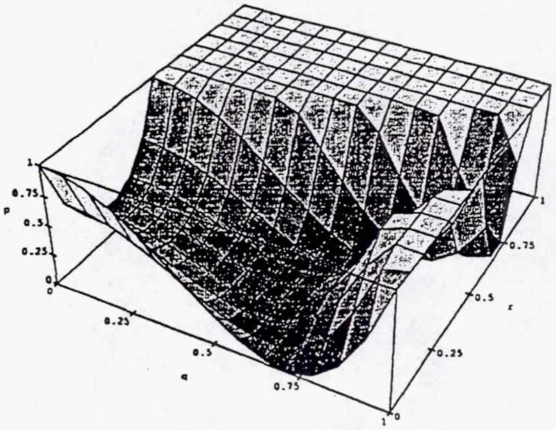

Figure 5: Surface of Amplification Factor for MacCormack Scheme ($\xi = \pi$)

Plots of Amplification Factor and Relative Phase

The amplification factor and relative phase error have been plotted for each scheme in the usual manner as indicated here. This figure shows such plots for the MacCormack scheme for two different values of cell Reynolds number, r = 0.25 and r = 0.5. Note that each plot shows the variation of amplification factor and phase error for several different values of Courant number. Similar plots for each scheme give show ranges of stability for different combinations of these two parameters.

The data form these analyses are also used to produce surface plots of the amplification factor for different values of wave number as shown. Here amplification factor surfaces are shown for the MacCormack scheme for wave numbers of 0.35 pi and pi. These plots show the variation of the amplification factor for a given wave number as a function of Courant number, q, and cell Reynolds number, r.

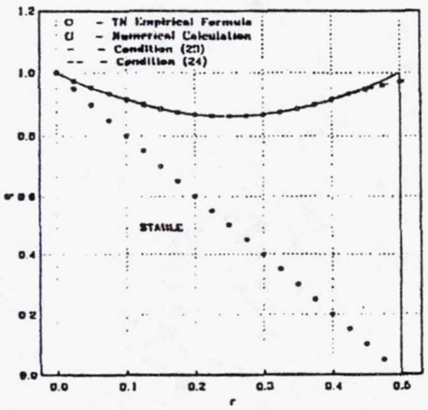

Figure 6: Comparison of Exact Stability Criterion and Empirical Formula for MacCormack Scheme

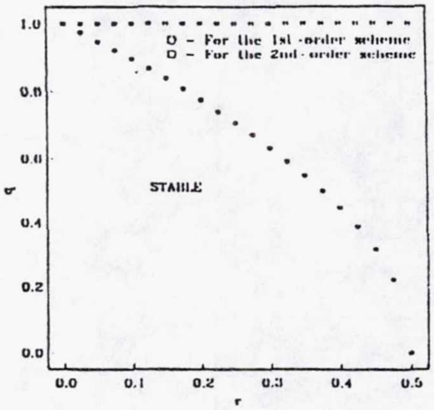

Figure 7: Comparison of Exact Stability Criteria for Lax Wendroff Scheme

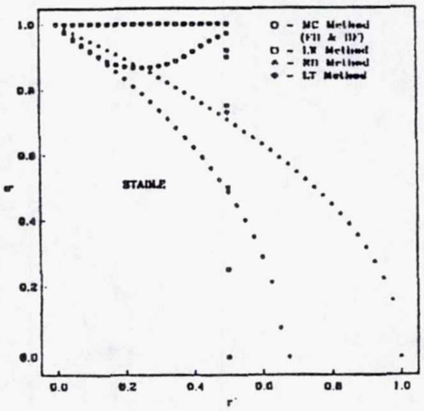

Figure 8: Stable Region for Each Scheme

Stability Criteria

Plots of Courant number vs. cell Reynolds number establish the exact stability criteria. One of the most interesting findings in this analysis is the stability criteria for the MacCormack scheme. In the past stability criteria for this method was established using an empirical formulation developed by Tannehill. This results in a stability limit defined by the diagonal line running from q = 1.0 to r = 0.5. The limit obtained from the exact result is defined by the line which runs along from r = 0. to 0.5 between q values of 0.85 and 1.0. This nearly doubles the stability region thereby resulting in a much greater range of choices of Courant number and cell Reynolds number. Ultimately this means that restrictions on spatial and temporal step size are not as stringent as previously thought. Comparisons of stability criteria for all of the schemes investigated are also shown in this figure.

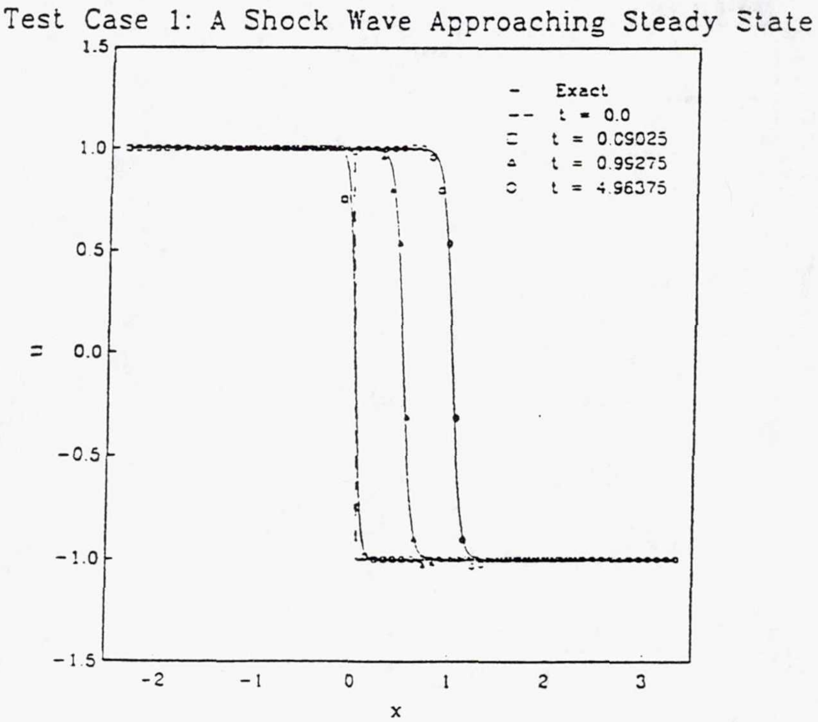

α = 1.0, β = 0.0, γ = 0.0
q = 0.95, r = 0.5, ν = 0.05, Δx = 0.095, Δt = 0.09025

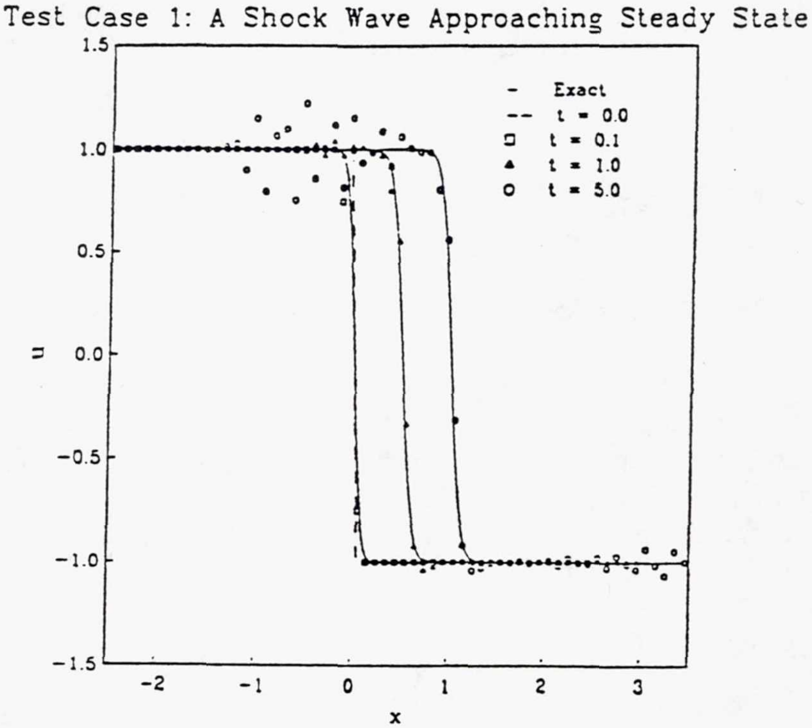

α = 1.0, β = 0.0, γ = 0.0
q = 1.0, r = 0.5, ν = 0.05, Δx = 0.1, Δt = 0.1

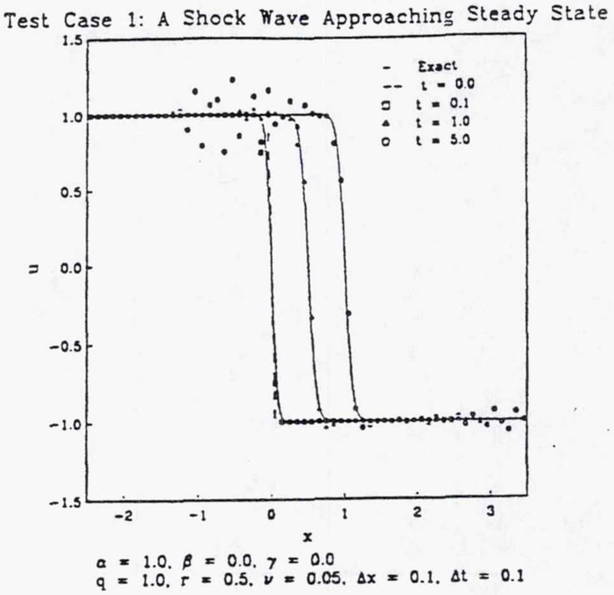

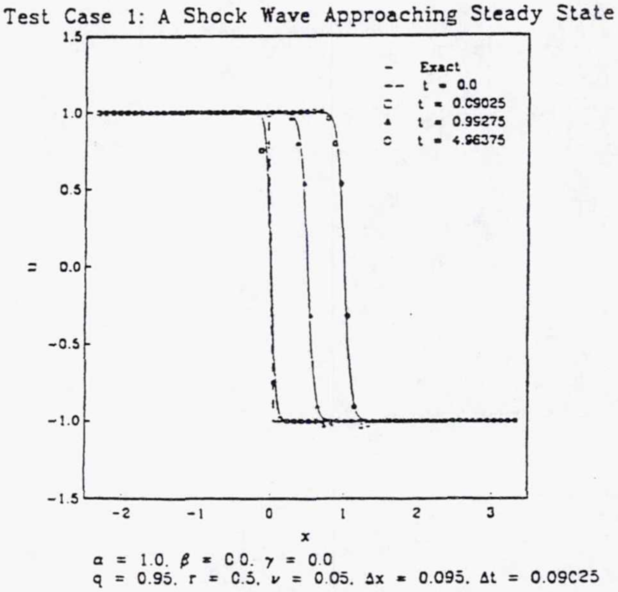

Test of Stability Criteria for the MacCormack Scheme

To test the new stability criteria for the MacCormack scheme, the Viscous Burgers equation was solved for the propagation of a shock wave to a steady state solution. This was done using values of Courant number of 1.0 and 0.95 and a cell Reynolds number of 0.5 which is the upper limit. Here it can be seen that for the Courant number of 1.0 the shock solution is unstable resulting in oscillations in the final solution. However in reducing the Courant number to 0.95 which is just barely under the stability limit, the shock converges to a steady state result which contains no oscillations as shown. This verifies the exact stability limit produced from this analysis.

The truncation error was also calculated, which shows dispersion and dissipation. The definition of the truncation is the following:

$$\begin{aligned}
&\frac{\partial u}{\partial t} + c\frac{\partial u}{\partial x} - \nu\frac{\partial^2 u}{\partial x^2} \\
&= \frac{1}{\Delta t}[u_j^{n+1} - (Au_{j-3}^n + Bu_{j-2}^n + Cu_{j-1}^n + Du_j^n + Eu_{j+1}^n + \\
&\quad Fu_{j+2}^n + Gu_{j+3}^n) + \text{T.E.}]
\end{aligned} \tag{2}$$

where, T.E. is the truncation error,

$$\text{T.E.} = \Phi_1\cdot(\Delta x)^3\frac{\partial^3 u}{\partial x^3} + \Phi_2\cdot(\Delta x)^4\frac{\partial^4 u}{\partial x^4} + \Phi_3\cdot(\Delta x)^5\frac{\partial^5 u}{\partial x^5} + \Phi_4\cdot(\Delta x)^6\frac{\partial^6 u}{\partial x^6} \tag{3}$$

and,

$$\begin{aligned}
\Phi_1 &= \frac{1}{6}q(q^2-1) \\
\Phi_2 &= \frac{1}{24}q^2(1-q^2) + \frac{1}{12}r + \frac{1}{2}\frac{\beta(1-\beta)}{\alpha}r + \frac{1}{2}(\beta-\gamma)qr - \frac{1}{2}q^2 r \\
\Phi_3 &= \frac{1}{120}q(q^4-1) - \frac{1}{4}qr + \frac{1}{6}q^3 r + \frac{1}{2}(\gamma-\beta)r^2 + \frac{1}{2}qr^2 \\
\Phi_4 &= \frac{1}{720}q^2(1-q^4) + \frac{1}{360}r + \frac{1}{12}\frac{\beta(1-\beta)}{\alpha}r + \frac{1}{12}(\beta-\gamma)qr - \\
&\quad \frac{1}{24}q^4 r + \frac{1}{12}[1+3(\gamma+\beta)-6\gamma\beta]r^2 - \frac{1}{4}q^2 r^2 - \frac{1}{6}r^3
\end{aligned}$$

The derivation of truncation error is shown in the Appendix. The coefficients $\Phi_1, \cdots, \Phi_4$ were calculated.

Truncation Error Calculation

A generalized expression for the truncation error for the spatial differences has been obtained in terms of the *α*, *β* and *γ* parameters along with the cell Reynolds number and Courant number. The odd derivative terms give the dispersion and the even derivative terms give the dissipation. Since the derivatives themselves are small, their coefficients determine the magnitude of the respective terms. The coefficients are given here for the two leading dispersion terms and the two leading dissipation terms. The expressions given here are somewhat simplified. Although not included here, a more rigorous analysis including the time difference has also been performed.

Table 1: A Shock Wave Approaching Steady State

(S: Stable, U: Unstable)

Case	q	r	u_0	Re	Schemes			
					MC	L-W	R-B	L-T
a	0.1	0.5	1.0	20.0	S	S	S	S
b	0.2	0.5	1.0	20.0	S	S	S	S
c	0.5	0.1	1.0	1000.0	S	S	S	S
d	0.5	0.2	1.0	1000.0	S	S	S	S
e	0.4	0.8	1.0	200.0	U	U	S	U
f	0.6	0.8	1.0	200.0	U	S	U	U
g	1.0	0.5	1.0	200.0	U	S	U	U
h	0.95	0.5	1.0	200.0	S	S	U	U

Parametric Study of Shock Wave

A parametric study of a shock wave approaching steady state was conducted for eight different sets of conditions for each of the numerical schemes being investigated. The eight different combinations of parameters are given in this table along with the designation of whether each scheme produced a stable (S) or unstable (U) solution.

Table 2: Truncation Error for Shock Wave Case

		$\frac{(\Delta x)^3}{\Delta t}$	Φ_1 ($\times 10^{-2}$)	$\frac{(\Delta x)^4}{\Delta t}$	Φ_2 ($\times 10^{-2}$)			
Case	ν	($\times 10^{-2}$)	All Schemes	($\times 10^{-4}$)	MC	L-W	R-B	L-T
a	0.5	10.0	1.650	100.0	3.958	16.46	10.21	6.909
b	0.5	20.0	3.20	400.0	3.327	15.83	9.577	6.278
c	0.01	0.50	6.250	2.50	0.3646	2.865	1.615	0.9548
d	0.01	0.1250	6.250	0.3125	0.0521	4.948	2.448	1.128
e	0.05	0.1563	5.60	0.3906	0.8267	20.83	10.83	5.548
f	0.05	0.2344	6.40	0.8789	6.773	13.23	3.227	2.052
g	0.05	1.0	0.0	10.0	20.83	8.333	14.58	17.88
h	0.05	0.950	1.544	9.025	18.03	5.529	11.78	15.08

		$\frac{(\Delta x)^5}{\Delta t}$	Φ_3 ($\times 10^{-3}$)	$\frac{(\Delta x)^6}{\Delta t}$	Φ_4 ($\times 10^{-3}$)			
Case	ν	($\times 10^{-6}$)	All Schemes	($\times 10^{-7}$)	MC	L-W	R-B	L-T
a	0.5	1000.0	0.7499	1000.0	0.7757	52.86	42.44	36.94
b	0.5	8000.0	0.9973	16000.0	1.089	50.99	40.58	35.08
c	0.01	0.1250	11.82	6.250	0.3845	5.801	3.718	2.618
d	0.01	0.7813	14.74	0.1953	0.1398	13.19	9.027	6.827
e	0.05	0.9766	53.29	0.2441	56.01	57.32	40.65	31.85
f	0.05	3.296	96.45	1.236	91.26	22.07	5.404	3.394
g	0.05	100.0	83.33	100.0	81.94	29.86	40.28	45.78
h	0.05	85.74	69.98	81.45	71.75	19.67	30.09	35.59

Truncation Error Results

For each of the eight cases investigated the coefficients of the two leading dispersion and dissipation terms in the truncation error are tabulated for each numerical scheme. This table shows the relative magnitudes of the dispersion and dissipation terms truncation error. The magnitude of the physical dissipation coefficient is also shown. It is noted that the magnitude of the dissipation terms in the truncation error are much smaller than the physical dissipation - generally at least 2 to 3 orders of magnitude smaller.

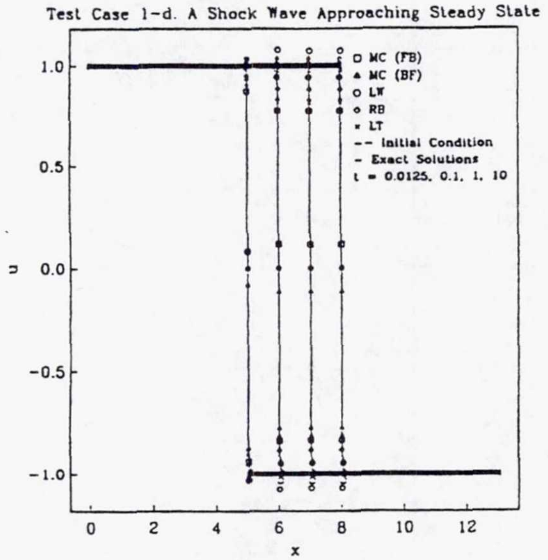

Re = 1000, ν = 0.01
q = 0.5, r = 0.2, Δt = 0.0125, Δx = 0.025
(Shock wave initially located at a grid point.)

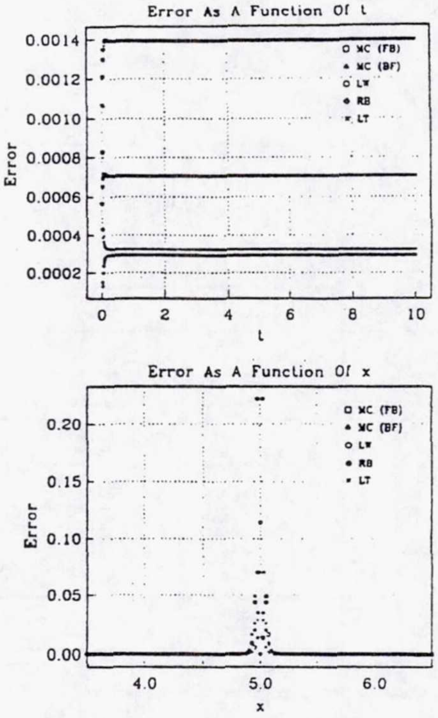

Re = 1000, ν = 0.01
q = 0.5, r = 0.2, Δt = 0.0125, Δx = 0.025
(Shock wave initially located at a grid point.)

Typical Shock Wave Result

This figure shows the evolution of a shock wave approaching steady state using the different numerical schemes. This result shows the relative dispersion characteristics of each of the numerical methods investigated here. Also included in this figure are the comparisons of numerical error as functions of time and space for each of the schemes. The error as a function of time achieves constant values for each scheme almost immediately indicating that each solution is stable. The error as a function of x indicates that the spatial error is concentrated in the immediate vicinity of the shock as one would expect. This representation of the spatial error also shows that the smearing due to dissipation is relatively small. It also reveals that the dispersive behavior of the Lax-Wendroff scheme is the greatest, while that of the Lerat-Peyret method gives the most favorable result.

Comparison of Numerical Schemes Applied to Acoustics Computation

1 Governing Equations

Let

$$\begin{aligned} \rho &= \rho_0 + \rho' \\ u &= u_0 + u' \\ v &= v_0 + v' \\ p &= p_0 + p' \end{aligned}$$

The linearized two-dimensional Euler equation is,

$$\frac{\partial \mathrm{U}}{\partial t} + \frac{\partial \mathrm{F}}{\partial x} + \frac{\partial \mathrm{G}}{\partial y} = 0 \tag{1}$$

where,

$$\mathrm{U} = \begin{bmatrix} \rho' \\ u' \\ v' \\ p' \end{bmatrix}$$

$$\mathrm{F} = \begin{bmatrix} \rho_0 u' + \rho' u_0 \\ u_0 u' + p'/\rho_0 \\ u_0 v' \\ u_0 p' + \gamma p_0 u' \end{bmatrix}$$

$$\mathrm{G} = \begin{bmatrix} \rho_0 v' \\ 0 \\ p'/\rho_0 \\ \gamma p_0 v' \end{bmatrix}$$

Define

$$S(x,y) = \sin\left(\frac{k\pi\sqrt{x^2+y^2}}{\sqrt{L_x^2+L_y^2}}\right)$$

The initial conditions are

$$\begin{aligned} \rho' &= \rho_0 S(x,y) \\ u' &= u_0 S(x,y) \\ v' &= v_0 S(x,y) \\ p' &= p_0 S(x,y) \end{aligned}$$

Here, set

$$\rho_0 = u_0 = v_0 = p_0 = 1$$

Comparison of Numerical Schemes for Computation of Acoustic Waves

The linearized Euler equations govern the propagation of acoustic waves. Thus it is appropriate to investigate the application of different numerical methods to the solution of these equations in order to evaluate their suitability for analyzing acoustic phenomena. Such investigations will provide insight as to whether selected numerical methods are appropriate for solving the time-dependent Navier-Stokes equations in acoustic problems. Among the critical problems such as jet noise it is essential that the numerical methods used for analysis not only be able to accurately predict the unsteady flow features but they must also be able to resolve the acoustic phenomena. The linearized Euler equations are shown here in the form used to investigate characteristic features of selected numerical methods in computing the propagation of acoustic type disturbances being convected in a mean flow. The governing equations are given here along with the initial conditions.

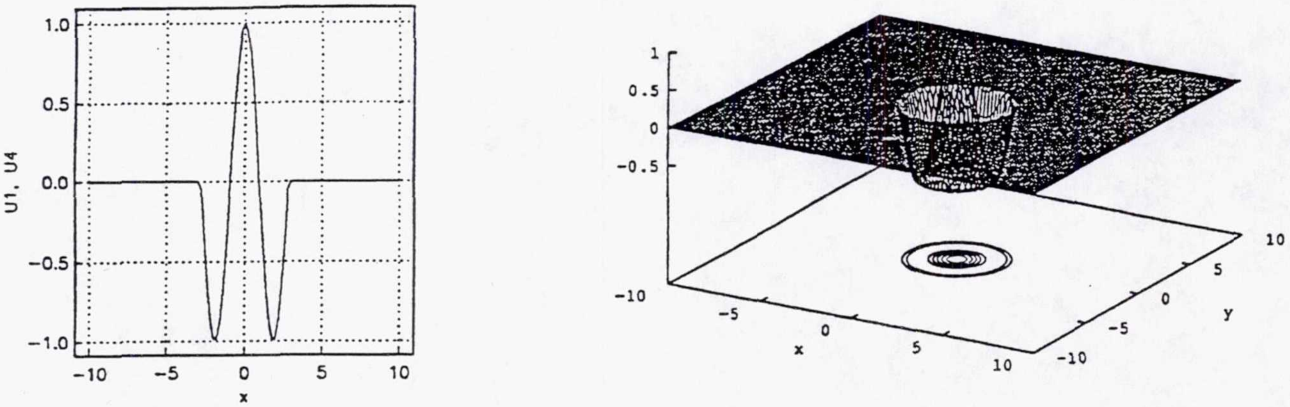

Initial Condition

The initial condition is sinusoidal disturbance initiated at time t=0.0. This initial disturbance is actually a cosine with its peak initially at the origin. This figure shows the pressure surface plot and the two dimensional wave form at t=0. The convection velocity is then imposed in the positive x direction.

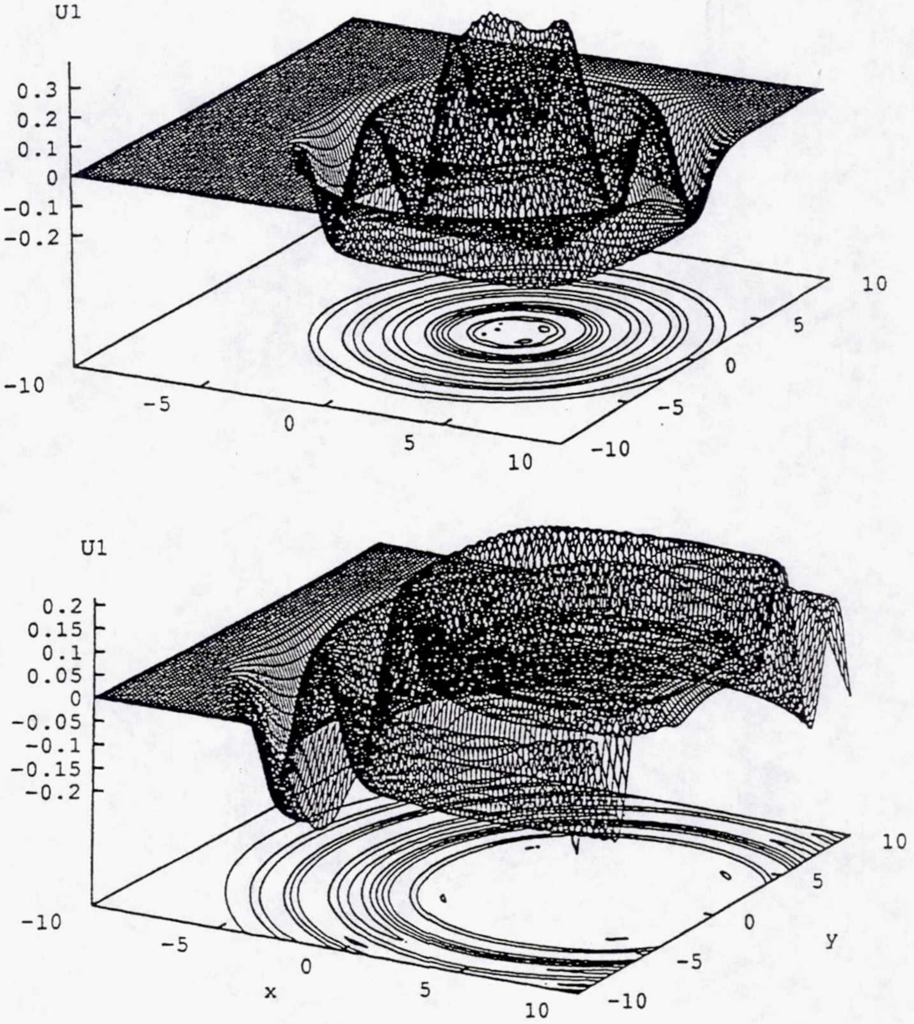

Lerat-Peyret Scheme, M = 0.5. a. 100 time steps. b. 200 time steps.

Computed Results

Each scheme is used to compute the propagation of waves from a point source being convected in a mean flow. The disturbances computed include density, the u and v velocity components and the pressure. Computations have been performed with both subsonic (M = 0.5) and supersonic (M = 2.0) convection velocities. The pressure and density waves exhibit identical behavior for all schemes at both the subsonic and supersonic convection speeds. While the velocity disturbances exhibited different behavior it did not seem to be as informative. Thus the wave forms shown here are for the pressure disturbances only. This figure shows the results from the Lerat-Peyret scheme for the subsonic case at 100 and 200 time steps. It can be seen that the center of the disturbance has propagated downstream to where the waves are passing out of the out flow boundary with no distortion or non-physical reflections. For the subsonic case the MacCormack scheme exhibits the same behavior as the Lerat-Peyret scheme. The computations were carried out until the disturbance passed through the outflow boundary.

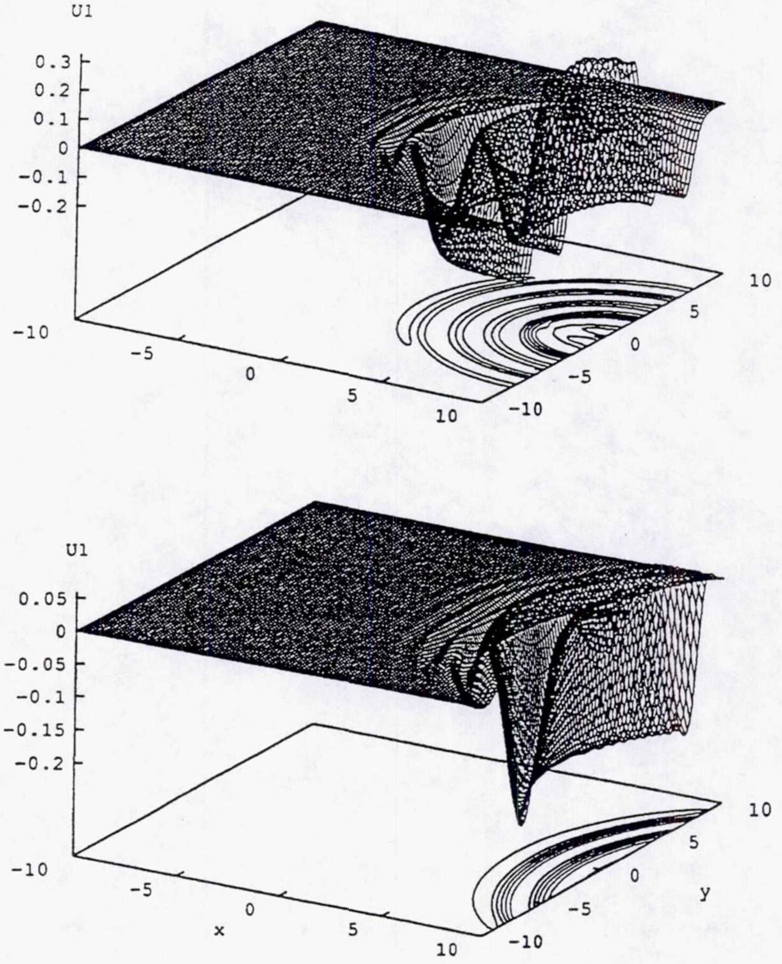

Lerat-Peyret Scheme, M = 2. a. 100 time steps. b. 200 time steps

Computed Results (con't)

The computed results for the supersonic convection velocity using the Lerat-Peyret scheme are shown at 100 and 200 time steps. Here it can be seen that the waves also pass out through the boundaries without any distortion or reflections. It can also be seen here that there is no appreciable growth of the dispersion characteristics. The MacCormack results are very similar to the Lerat-Peyret through 200 time steps however some difficulties develop in the vicinity if the boundary on the negative y side of the computational domain beyond that time. The influence of the boundary conditions is currently being investigated.

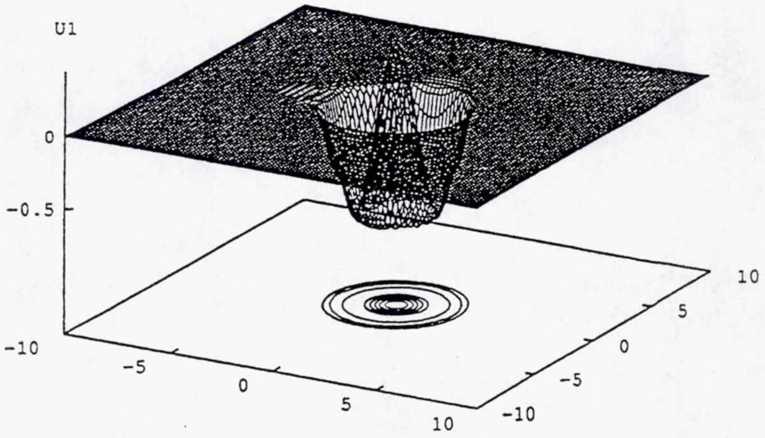

Tam-Webb Scheme, M = 0.5.   200 time steps.

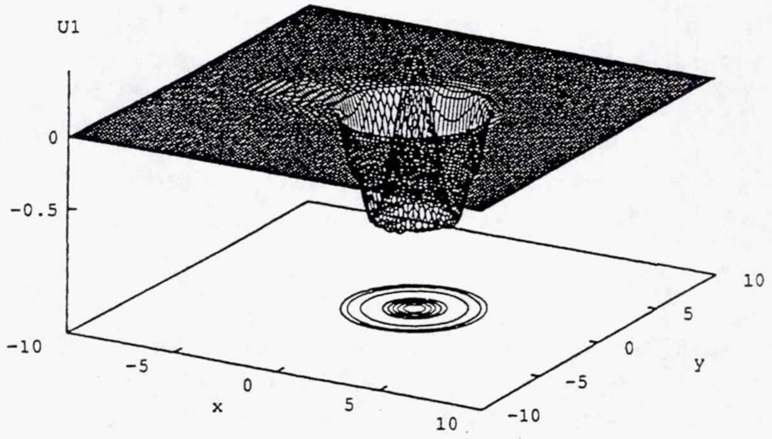

Tam-Webb Scheme, M = 2.   200 time steps.

Computed Results for the DRP Scheme

The results for the DRP scheme are shown at 200 time steps for both the subsonic and supersonic cases. Note that the disturbance center has not propagated nearly as far in the streamwise direction in 200 time steps as that for the Lerat-Peyret and MacCormack schemes. Also note that the waves have not spread as far from the center as for the other two schemes. This is due to the rigid constraint on the time step size associated with the DRP scheme. This small time step requirement is associated with the fact that the finite difference scheme has the same dispersion preserving properties as the original partial differential equation governing the flow. For this investigation the DRP scheme required 50 time steps to one for each of the other schemes.

CONCLUSIONS

Numerical methods do a very good job of simulating flow features of unsteady jets, including:

Shock structure
Jet spreading rate
Vortex shedding and interaction
Velocity profiles
Fluctuating quantities

Limitations: grid size, time step size, run time

Results provide encouragement for adaptation to jet noise problems

New insight into the suitability of numerical methods for jet noise analysis has been obtained through their application to model problems. Specifically:

- Stability criteria

- Truncation error
  - Dissipation characteristics
  - Dispersion characteristics

- Propagation of acoustic disturbances

1999176558

NUMERICAL SIMULATION OF FREE SHEAR FLOWS TOWARDS A PREDICTIVE COMPUTATIONAL AEROACOUSTICS

W.Y. Soh
Sverdrup Technology, Inc.
Lewis Research Center Group
Brook Park, Ohio

S21-71

201.

409543

Implicit spatial differencing technique with fourth order accuracy has been developed based on the Pade compact scheme. A Dispersion Relation Preserving concept has been incorporated into the numerical scheme. Two dimensional Euler computation of a spatially-developing free shear flow, with and without external excitation, has been performed to demonstrate the capability of numerical scheme developed. Results are in good agreement with theory and experimental observation regarding the growth rate of fluctuating velocity, the convective velocity, and the vortex-pairing process. Far-field sound pressure generated by the unsteady shear flow solution using Lighthill's acoustic analogy shows a strong directivity with a zone of silence at the flow angle.

Sound Wave Propagation Phenomena
- Subset of Fluid Flow Phenomena

Flow Equations (Compressible)

$$\frac{\partial \rho}{\partial t} + \nabla \cdot (\rho \mathbf{u}) = 0$$

$$\frac{\partial}{\partial t}(\rho \mathbf{u}) + \nabla \cdot (\rho \mathbf{u}\mathbf{u}) = -\nabla p + Vis.$$

$$\frac{\partial}{\partial t}(\rho e) + \nabla \cdot (\rho e + p)\mathbf{u} = Vis. + Cond.$$

(Incompressible)

$$a_0^2 \frac{\partial p}{\partial t} + \nabla \cdot (\rho_0 \mathbf{u}) = 0$$

$$\rho \Longrightarrow \rho_0$$

Three Basic Modes		
	$\frac{\partial S}{\partial t} + (\mathbf{u} \cdot \nabla)\, S = \cdots$	Entropy Mode
	$\frac{\partial \omega}{\partial t} + (\mathbf{u} \cdot \nabla)\, \omega = \cdots$	Vorticity Mode
	$\frac{\partial^2 p}{\partial t^2} - a^2\, \nabla^2 p = \cdots$	Sound Mode

	S and ω wave	Sound Wave
Frequency	u'_0/l'	u'_0/l'
Speed	u'_0	a_0
Length	l', $(l_{dis},\ l_{int})$	$l_s = l'\,(a_0/u'_0)$

Dissipation Scale - Kolmogorov Length Scale : $(\nu^3/\epsilon)^{\frac{1}{4}}$

Integral Scale - Geometry

Far-Field Sound Pressure Prediction

Length Scale Difference Between Sound and Flow Fields is Very Large $\Longrightarrow$
Separation (Decoupling) of the Sound Wave Motion
from the Flow Dynamics is Needed.

- Solution to Wave Equation
- Acoustic Analogy - Lighthill

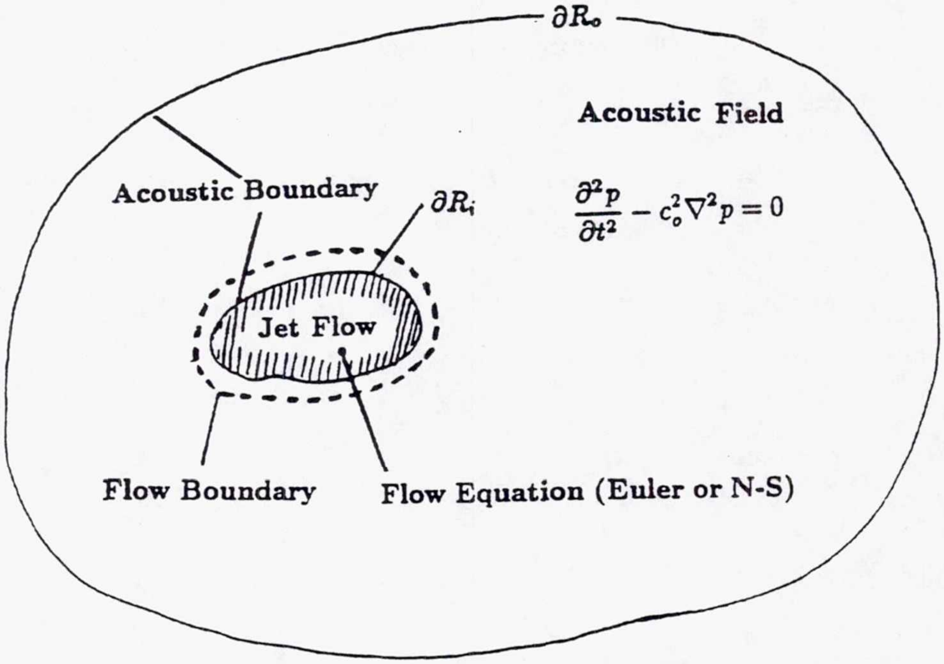

Figure 1. Separation of the flow and acoustic fields for solution to the wave equation

Lighthill's Acoustic Analogy

$$\frac{\partial^2 p}{\partial t^2} - a_0^2 \frac{\partial^2 p}{\partial x_i^2} = a_0^2 \, [\underbrace{\frac{\partial^2}{\partial x_i \partial x_j}(\rho u_i u_j - \tau_{ij})}_{\text{(I)}} - \underbrace{\frac{\partial F_i}{\partial x_i}}_{\text{(II)}} + \frac{\partial m}{\partial t}] + \underbrace{\frac{\partial^2}{\partial t^2}(p - a_0^2 \rho)}_{\text{(III)}}$$

(I) Quadrupole Source (II) Dipole Source (III) Monopole Source

Powell's Dipole Formulation at Low Mach Number : (I) $\Longrightarrow \rho_0 \nabla \cdot (\omega \times \mathbf{u})$

$$p(x_i, t) - p_0 = \frac{1}{4\pi a_0^2} \frac{x_i x_j}{|x_i|^3} \int_V \frac{\partial^2}{\partial t^2} T_{ij}(\mathbf{y}, t - \frac{|x_i - y_i|}{a_0}) \, d\mathbf{y} \qquad \text{Far Field}$$

$$\text{Intensity} \quad I = \frac{1}{16\pi^2 p_0 a_0^5} \frac{x_i x_j x_k x_l}{|x_i|^6} \int \int_V \overline{[\frac{\partial^2 T_{ij}}{\partial t^2}] [\frac{\partial^2 T_{kl}}{\partial t^2}]} \, d\mathbf{y} d\mathbf{y}'$$

Low Mach Number : Emission Time $t - \frac{|x_i - y_i|}{a_0} \Longrightarrow \frac{t - |x_i|}{a_0}$

High Mach Number : Emission Time is Crucial.

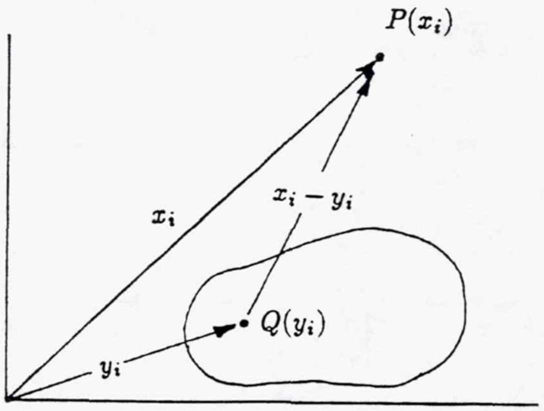

Figure 2. $P(x_i)$ is the field point and $Q(y_i)$ the source point

Need for Unsteady Flow Computation - Sound Source

Large Vortical Structure in Free Shear Flows :

- Freymuth (1966)
- Crow and Champagne (1971)
- Brown and Roshko (1974)
- Winant and Browand (1974)

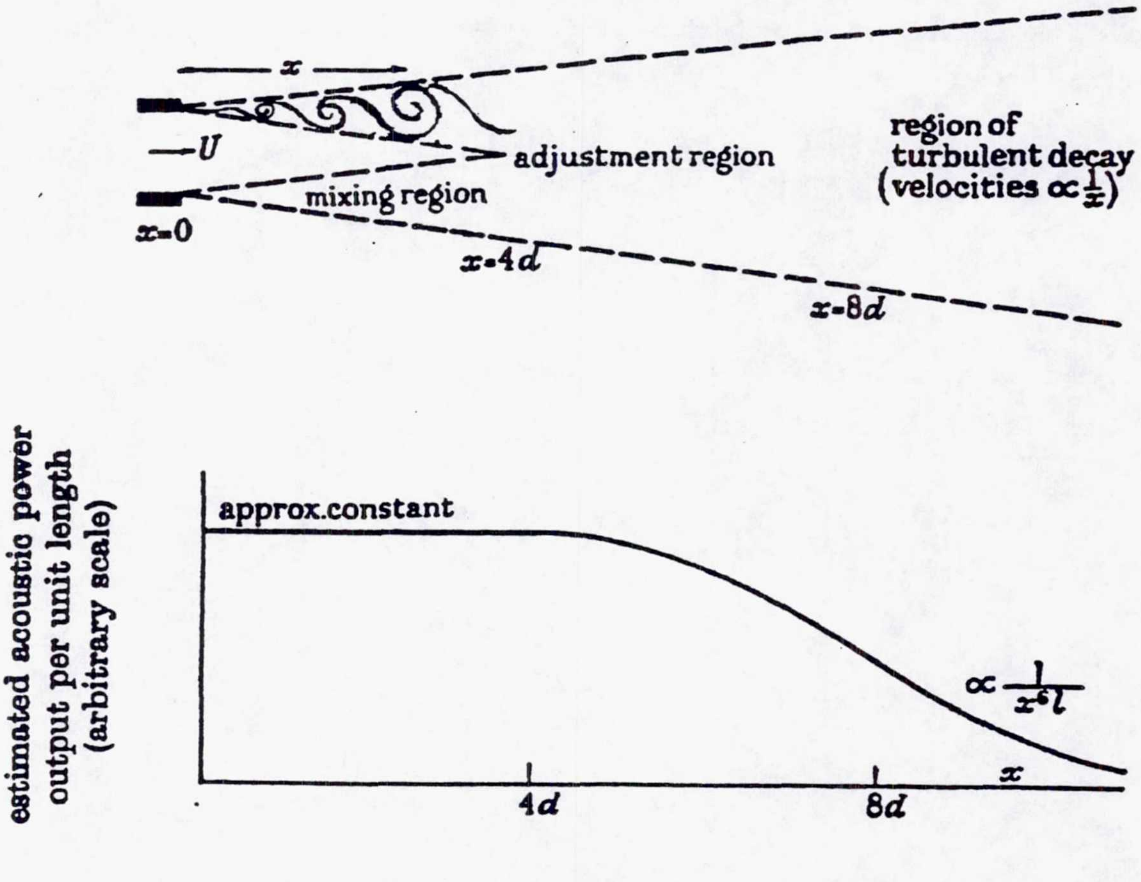

Figure 3. Top: Flow development with large vortical structure, Bottom: Acoustic power emitted by a typical subsonic jet.

Numerical Method Solving Flow Equations

Governing Equation

Euler Equations in Cartesian Coordinates :

$$\frac{\partial \mathbf{q}}{\partial t} + \frac{\partial \mathbf{f}}{\partial x} + \frac{\partial \mathbf{g}}{\partial y} = \mathbf{0}$$

$$\mathbf{q} = \begin{pmatrix} \rho \\ \rho u \\ \rho v \\ \rho e \end{pmatrix}, \quad \mathbf{f} = \begin{pmatrix} \rho u \\ \rho u^2 + p \\ \rho u v \\ (\rho e + p) u \end{pmatrix} \quad \text{and} \quad \mathbf{g} = \begin{pmatrix} \rho v \\ \rho u v \\ \rho v^2 + p \\ (\rho e + p) v \end{pmatrix}$$

Euler Equations in Generalized Coordinates :

$$\frac{\partial \mathbf{Q}}{\partial t} + \frac{\partial \mathbf{F}}{\partial \xi} + \frac{\partial \mathbf{G}}{\partial \eta} = \mathbf{0}$$

$$\mathbf{Q} = J\mathbf{q}, \quad J = x_\xi y_\eta - y_\xi x_\eta \quad \mathbf{F} = J(\xi_x \mathbf{f} + \xi_y \mathbf{g}), \quad \mathbf{G} = J(\eta_x \mathbf{f} + \eta_y \mathbf{g})$$

Finite Difference Formulations

Fourth Order Finite Difference Formulation :

$$f'(x) = \frac{4}{3}\left(\frac{f_{i+1} - f_{i-1}}{2h}\right) - \frac{1}{3}\left(\frac{f_{i+2} - f_{i-2}}{4h}\right)$$

Fourth Order Dispersion Relation Preserving Scheme (Tam and Webb) :

$$f'(x) = a\,\frac{f_{i+1} - f_{i-1}}{2h} + b\,\frac{f_{i+2} - f_{i-2}}{4h} + c\,\frac{f_{i+3} - f_{i-3}}{6h} \quad \text{where} = \frac{9 - 8a}{5} \quad c = \frac{3a - 4}{5}$$

Fourier Transform of $f(x)$ and Its Inverse :

$$\tilde{f}(\kappa) = \frac{1}{\sqrt{2\pi}} \int_{-\infty}^{+\infty} f(x) e^{-i\kappa x}\, dx \quad \text{and} \quad f(x) = \frac{1}{\sqrt{2\pi}} \int_{-\infty}^{+\infty} \tilde{f}(\kappa) e^{i\kappa x}\, d\kappa$$

Fourier Transform of Six-Point Equation :

$$i\tilde{\kappa}\tilde{f}(\kappa) = i(a \sin \tilde{\kappa} + \frac{b}{2} \sin 2\tilde{\kappa} + \frac{c}{3} \sin 3\tilde{\kappa})\tilde{f}(\kappa) \quad \text{where} \quad \tilde{\kappa} = \kappa h$$

Wave Relationship : $\tilde{\kappa}_n = \tilde{\kappa} + \frac{b}{2} \sin 2\tilde{\kappa} + \frac{c}{3} \sin 3\tilde{\kappa}$

Optimization By Minimizing I :

$$I = \int_{-\pi/2}^{\pi/2} (\tilde{\kappa} - \tilde{\kappa}_n)^2 \, d\tilde{\kappa}$$

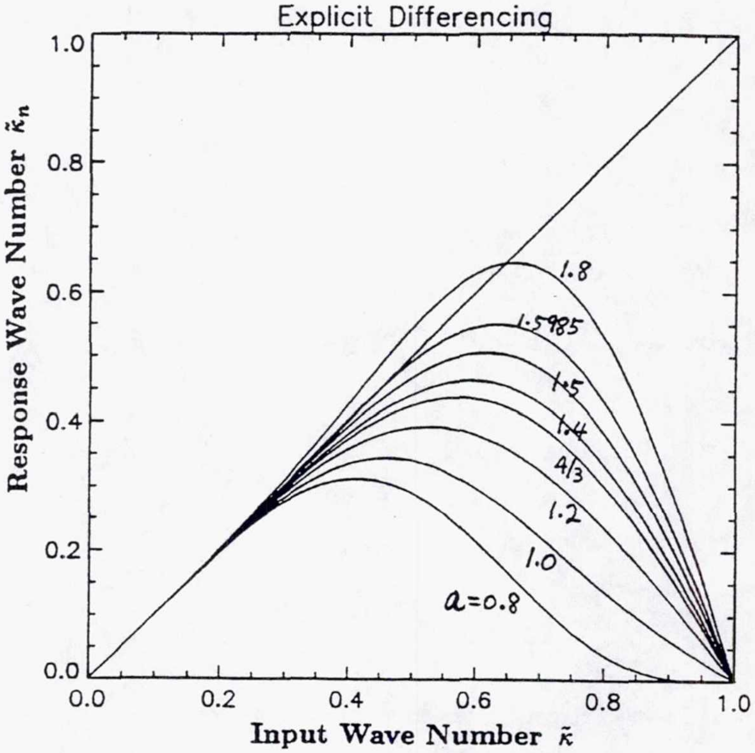

Figure 4. Wave relation for explicit differencing scheme

Pade Compact Differencing Scheme

General Pade Differencing Formulation For $f'(x)$:

$$\ldots \alpha_2 f'_{i-2} + \alpha_1 f'_{i-1} + f'_i + \alpha_1 f'_{i+1} + \alpha_2 f'_{i+2} \ldots = \ldots a_2 \frac{f_{i+2} - f_{i-2}}{4h} + a_1 \frac{f_{i+1} - f_{i-1}}{2h}$$

General Fourth Order Pade Formulation :

$$\alpha f'_{i-1} + f'_i + \alpha f'_{i+1} = b \frac{f_{i+2} - f_{i-2}}{4h} + a \frac{f_{i+1} - f_{i-1}}{2h}$$

where $a = \frac{2\alpha+4}{3}$ and $b = \frac{4\alpha-1}{3}$. Above formulation becomes sixth order for $\alpha = \frac{1}{3}$.

Wave Relationship :

$$\tilde{\kappa}_n = \frac{a \sin \tilde{\kappa} + \frac{b}{2} \sin 2\tilde{\kappa}}{1 + 2\alpha \cos \tilde{\kappa}}$$

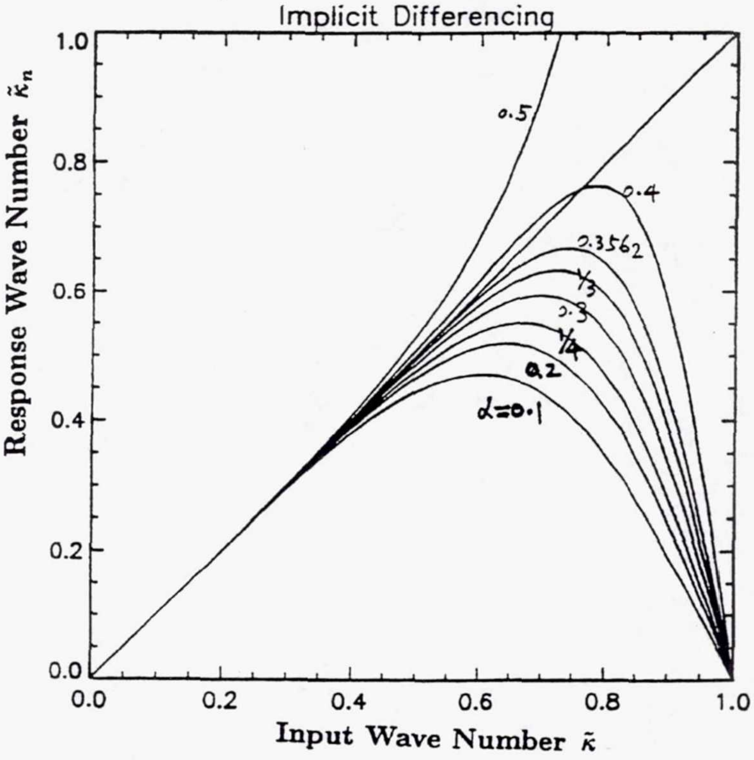

Figure 5. Wave relation for Pade implicit differencing scheme

Time Advancing Scheme - Second Order Accurate

Four-Stage Runge-Kutta Technique (Jameson et al.) :

$$\mathbf{Q}^{(1)} - \mathbf{Q}^n = \frac{1}{4}\Delta t\mathbf{W}^{(0)}$$
$$\mathbf{Q}^{(2)} - \mathbf{Q}^n = \frac{1}{3}\Delta t\mathbf{W}^{(1)}$$
$$\mathbf{Q}^{(3)} - \mathbf{Q}^n = \frac{1}{2}\Delta t\mathbf{W}^{(2)}$$
$$\mathbf{Q}^{(4)} - \mathbf{Q}^n = \Delta t\mathbf{W}^{(3)} + \omega_e(\frac{\partial^6 \mathbf{q}}{\partial \xi^6} + \frac{\partial^6 \mathbf{q}}{\partial \eta^6})$$

Boundary Condition

Non-Conservative Form of Euler Equations :

$$\frac{\partial \mathbf{q}}{\partial t} + \mathbf{A}\frac{\partial \mathbf{q}}{\partial \xi} + \mathbf{B}\frac{\partial \mathbf{q}}{\partial \eta} = 0 \quad \text{where} \quad \mathbf{A} = \frac{\partial \mathbf{F}}{\partial \mathbf{q}} \quad \text{and} \quad \mathbf{B} = \frac{\partial \mathbf{G}}{\partial \mathbf{q}}$$

With Tranformation $d\mathbf{q} = \mathbf{R}_\xi d\tilde{\mathbf{q}}$ For ξ Direction :

$$\frac{\partial \tilde{\mathbf{q}}}{\partial t} + \mathbf{R}_\xi^{-1}\mathbf{A}\mathbf{R}_\xi\frac{\partial \tilde{\mathbf{q}}}{\partial \xi} + \mathbf{R}_\xi^{-1}\mathbf{B}\mathbf{R}_\xi\frac{\partial \tilde{\mathbf{q}}}{\partial \eta} = 0$$

$$\mathbf{R}_\xi^{-1}\mathbf{A}\mathbf{R}_\xi = \mathbf{\Lambda}_\xi = \text{diag}(U, U, U + a_\xi, U - a_\xi)$$

where $a_\xi = c\sqrt{\xi_x^2 + \xi_y^2}$. Here, c is the speed of sound and $U = \xi_x u + \xi_y v$.
Diagonal Matrix For η : $\mathbf{R}_\eta^{-1}\mathbf{B}\mathbf{R}_\eta = \mathbf{\Lambda}_\eta = \text{diag}(V, V, V + a_\eta, V - a_\eta)$
where $a_\eta = c\sqrt{\eta_x^2 + \eta_y^2}$ and $V = \eta_x u + \eta_y v$.par Characteristic Equations :

$$\mathbf{R}_\xi^{-1}\frac{\partial \mathbf{q}}{\partial t} + \mathbf{\Lambda}_\xi\mathbf{R}_\xi^{-1}\frac{\partial \mathbf{q}}{\partial \xi} + \frac{\mathbf{R}_\xi^{-1}}{J}\frac{\partial \mathbf{G}}{\partial \eta} = 0$$

$$\mathbf{R}_\eta^{-1}\frac{\partial \mathbf{q}}{\partial t} + \mathbf{\Lambda}_\eta\mathbf{R}_\eta^{-1}\frac{\partial \mathbf{q}}{\partial \eta} + \frac{\mathbf{R}_\xi^{-1}}{J}\frac{\partial \mathbf{F}}{\partial \xi} = 0$$

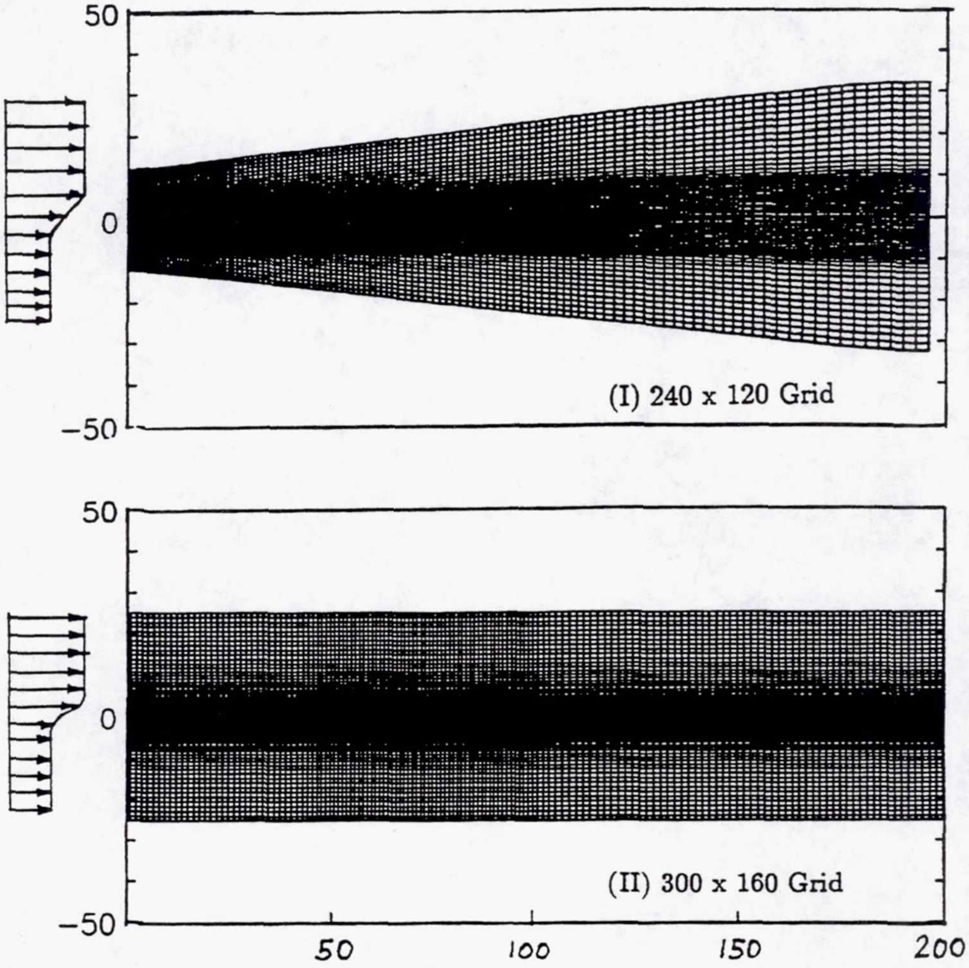

Figure 6. Grids used in the free shear flow simulation. (I) 240 × 120 , (II) 300 × 160.

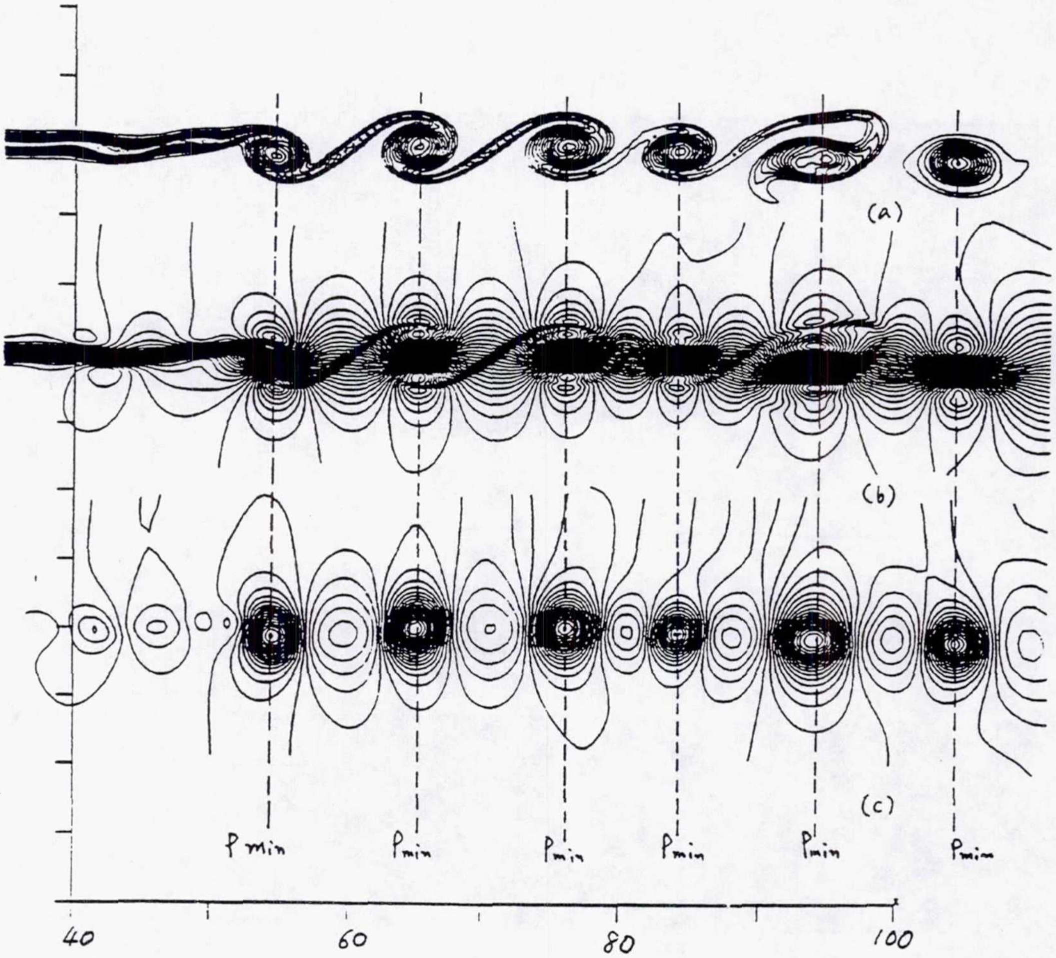

Figure 7. Contour plots of (a) vorticity, (b) Mach number, (c) static pressure for subsonic free shear flow of $M_1 = 0.6$ and $M_2 = 0.3$.

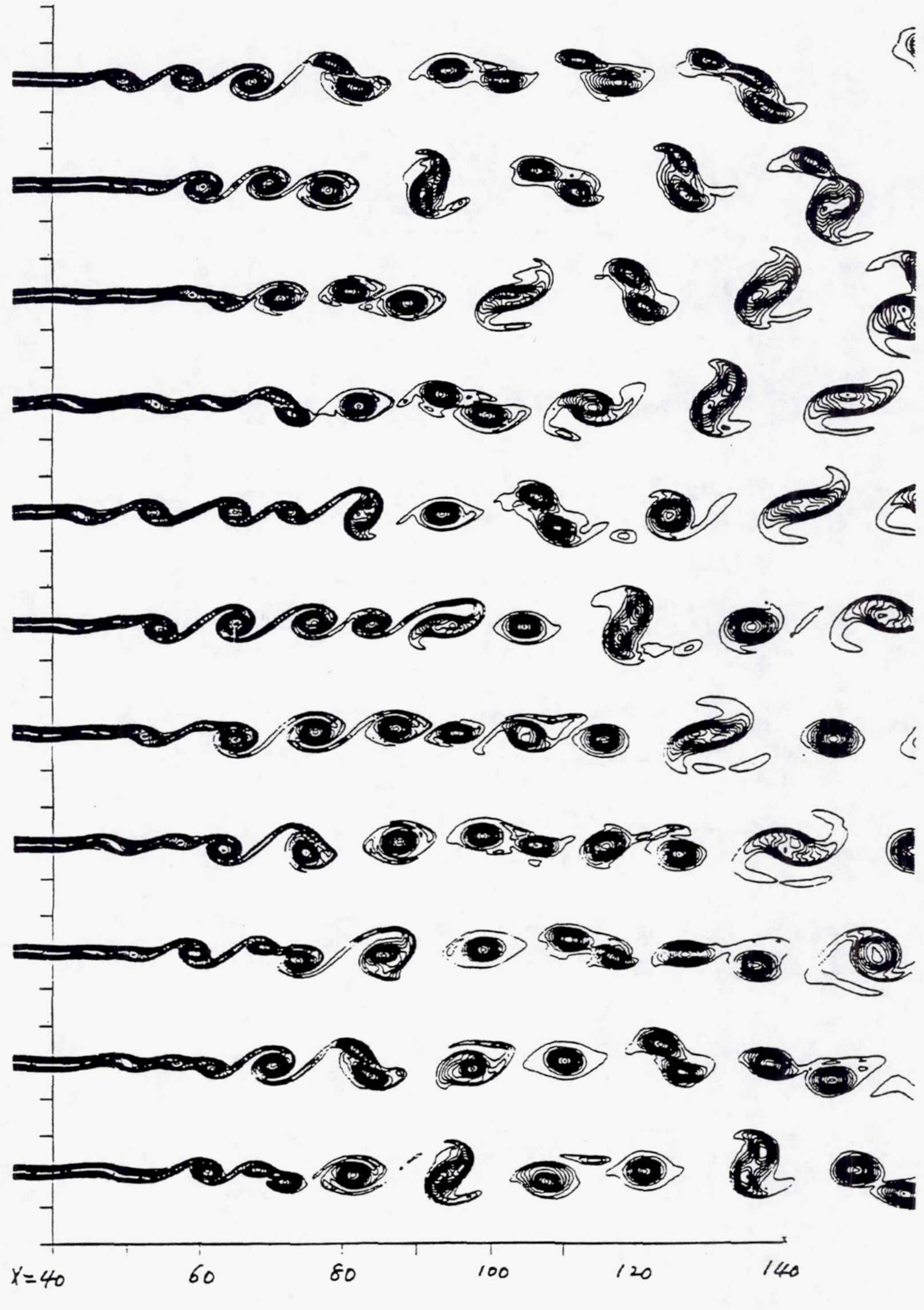

Figure 8. Vorticity contour plots at every $200\Delta t$ for subsonic shear of $M_1 = 0.6$ and $M_2 = 0.3$.

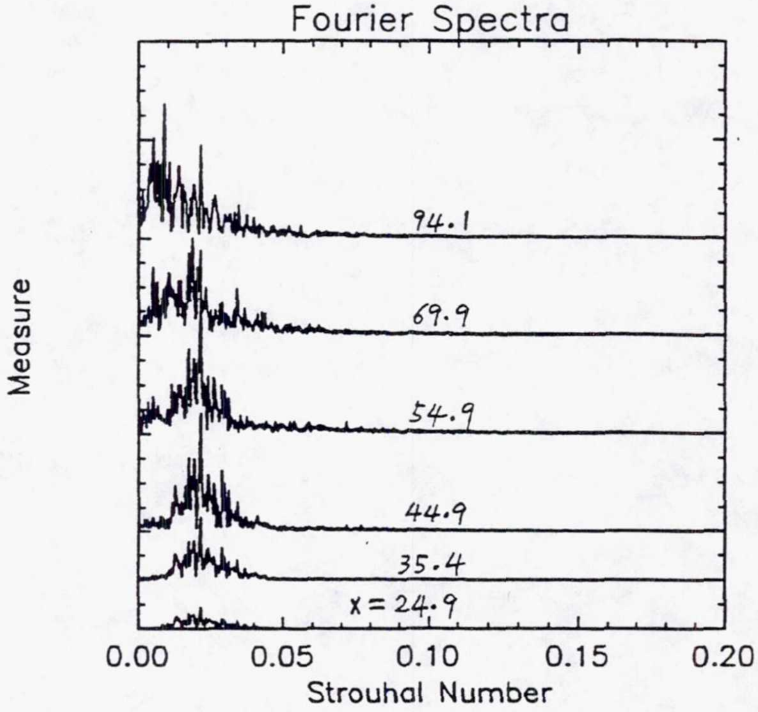

Figure 9. Fourier spectra of $u'_{\rm rms}$. $St = f\theta/U$, f=frequency, θ=momentum thickness, U= mean velocity of the shear.

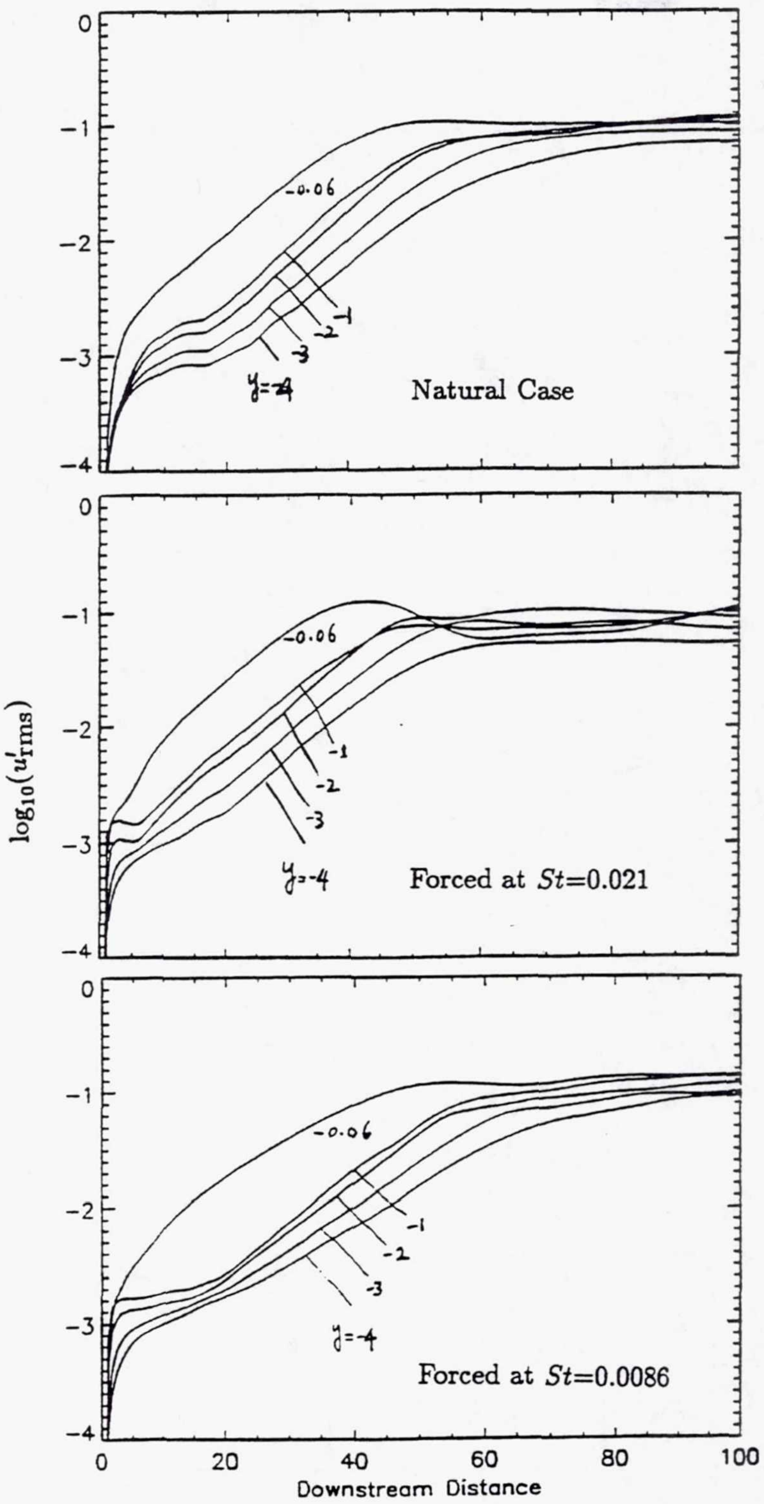

Figure 10. Development of $u'_{\rm rms}$ for $M_1 = 0.6$ and $M_2 = 0.3$ subsonic shear flow.

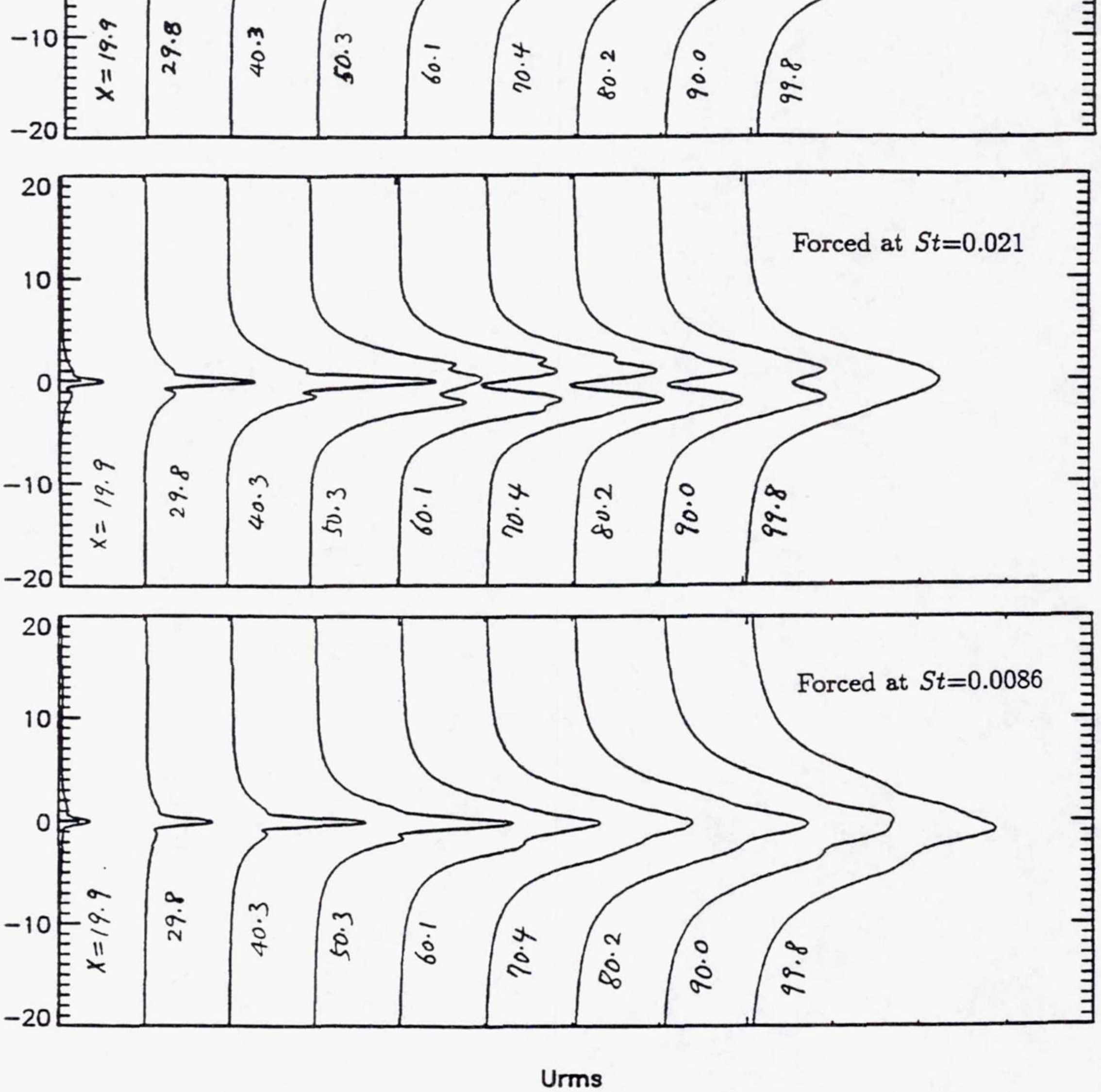

Figure 11. u'_{rms} profile for $M_1 = 0.6$ and $M_2 = 0.3$ subsonic shear flow.

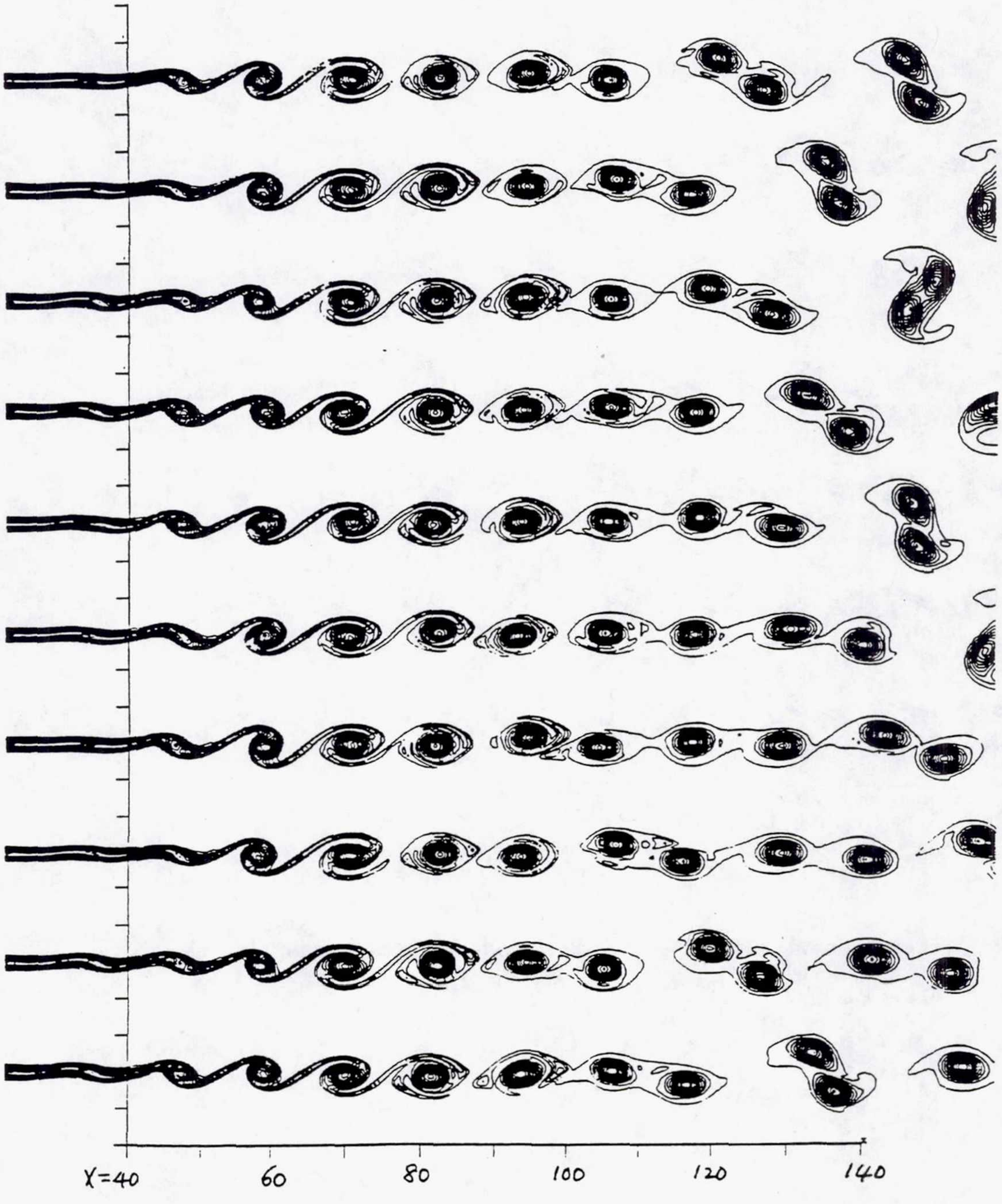

Figure 12. Vorticity contour plots of subsonic shear flow excited at the most preferred frequency of $St = 0.021$. Plots are made at every excitation period.

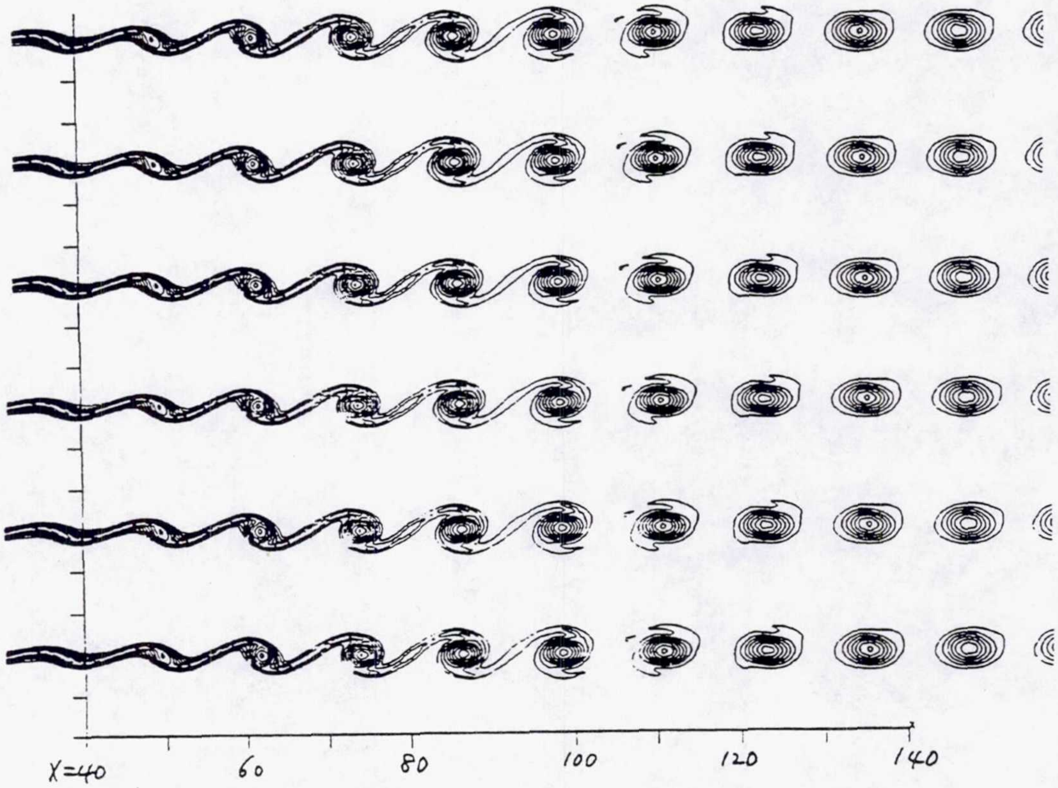

Figure 13. Vorticity contour plots at every two periods for excited supersonic shear of $M_1 = 1.6$ and $M_2 = 1.2$.

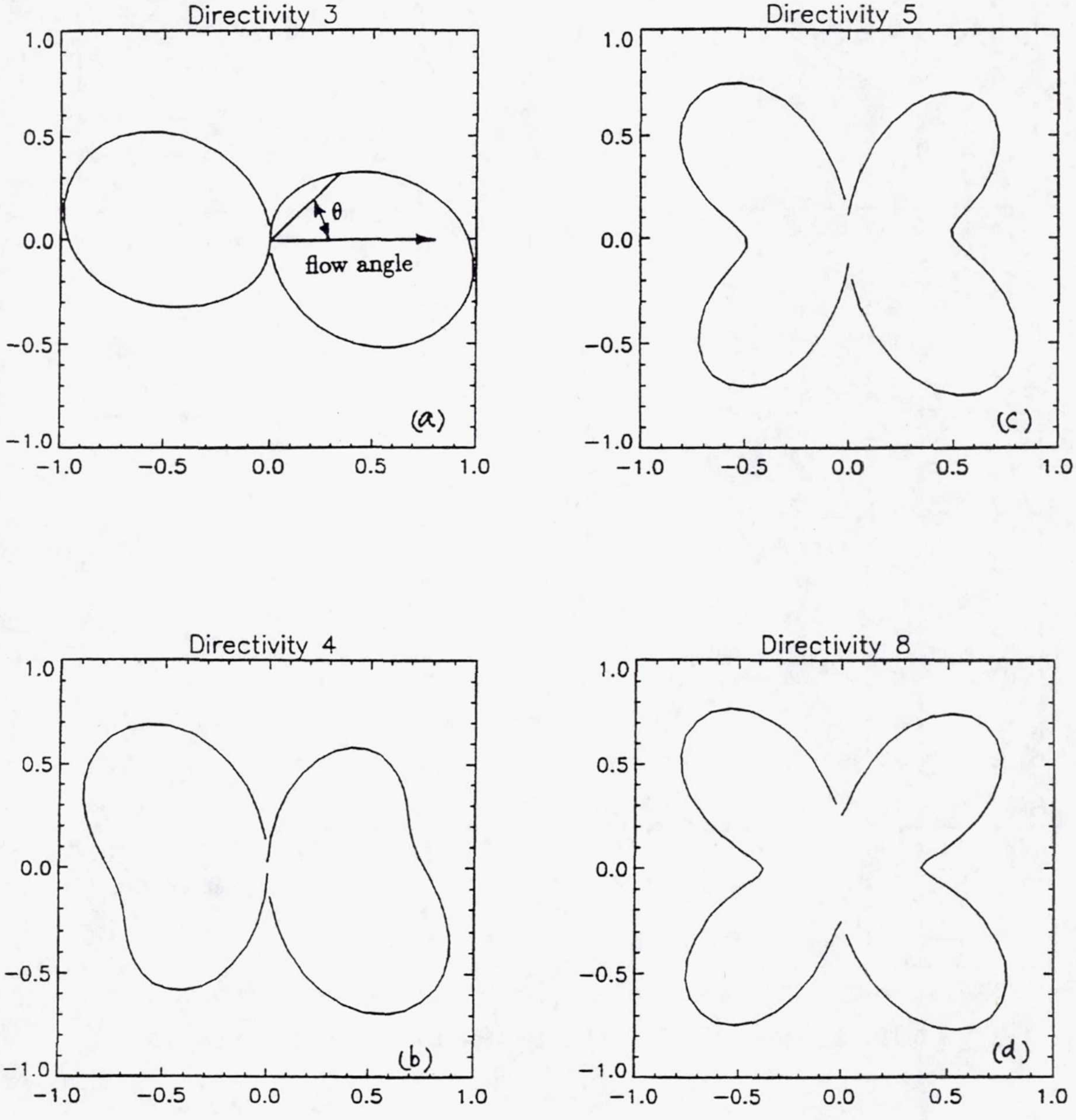

Figure 14. Directivity of far-field sound pressure generated by each flow element of unforced shear. Elements : (a) x=20-30, (b) x=30-40, (c) x=40-50, (d) x=70-80.

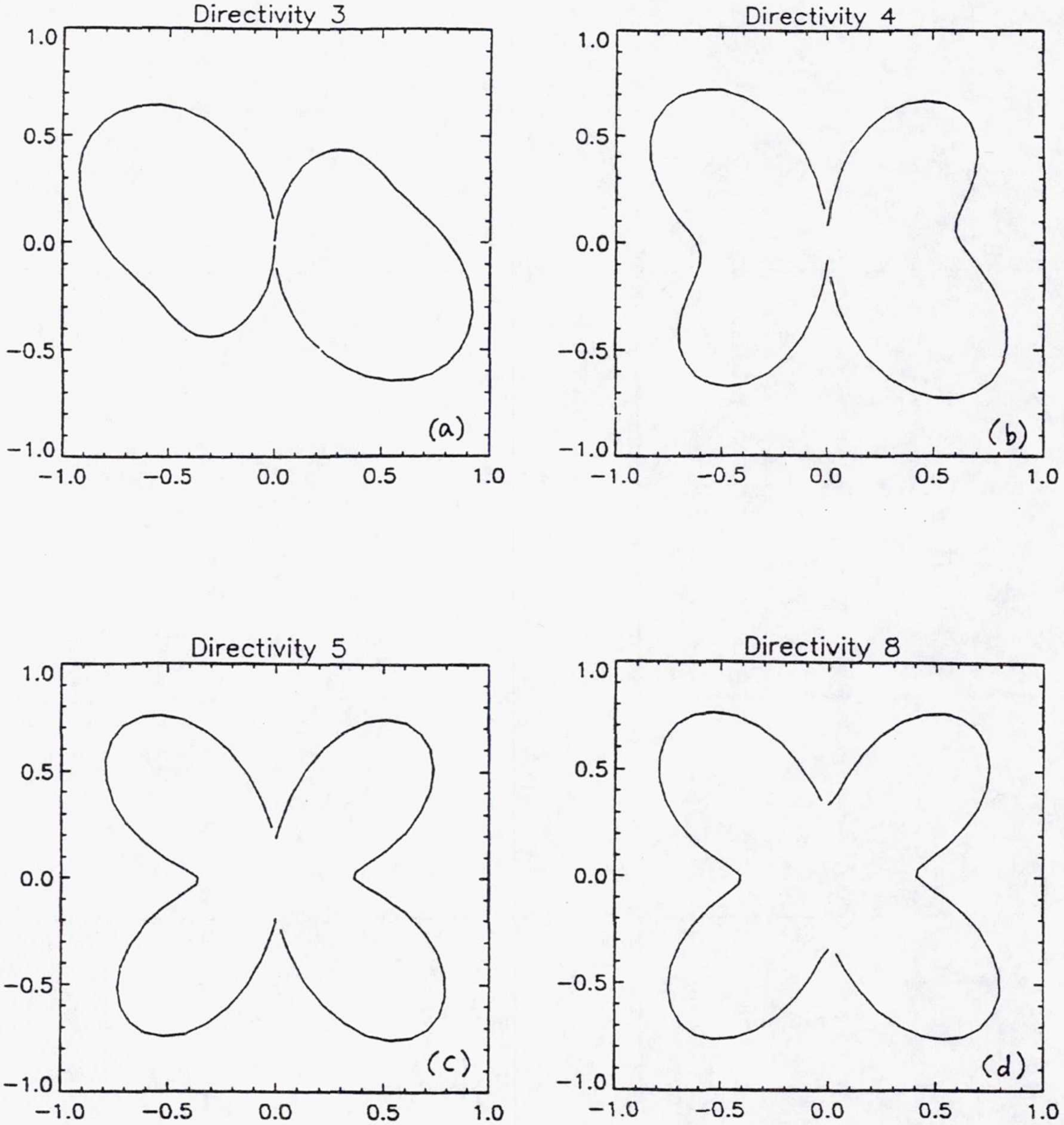

Figure 15. Directivity of far-field sound pressure generated by each flow element of excited shear at $St = 0.021$. Elements : (a) x=20-30, (b) x=30-40, (c) x=40-50, (d) x=70-80.

Conclusion and Future Plan

- Higher Order DRP scheme is suitable for free shear flow computation.
- Numerical results agree with linear theory and experiments.
- Far field sound pressure exhibits strong directivity when computed by Lighthill's acoustic analogy.
- DRP base scheme to solve wave equation is under development. This method will be tested solving far-field pressure generated by monopoles, dipoles, quadrupoles.
- Wave equation solver will be incorporated into flow solver to predict far field pressure.

19991765 59

RECENT PROGRESS IN 3D NOISE COMPUTATIONS

C. Berman and G. Gordon
AeroChem Research Laboratories, Inc.
Princeton, New Jersey

and

G. Karniadakis, E. Jackson, and S. Orszag
Cambridge Hydrodynamics, Inc.
Princeton, New Jersey

S22-71

409545

28p.

OUTLINE

- **Flow/Acoustics Overview**
- **LES Computations**
- **Sound Wave Propagation**
- **Noise Source Theory**
- **Quadrupole Source Tests**
- **VLES $(K - \epsilon)$**
- **Frequency Domain Analysis**

The paper briefly covers many aspects of flow and acoustics computations needed to develop methods for computing the sound of three-dimensional noise suppressors. Special emphasis is given to recent developments that can lead to more accurate and reliable results requiring less computer resources.

OBJECTIVES

Develop computational methods for flow/acoustic predictions.

Validate methods through data–prediction comparisons.

- **Round Jet**
- **Rectangular Jet**
- **Thermal Acoustic Shield**

The objective of this program is to develop methods of performing flow and acoustics computations that can be used for estimating the effect of various jet nozzle geometries on far field noise. While the basic formulation is currently being tested for simple round nozzles, the program aims to also make comparisons between prediction and experimental data for a rectangular nozzle and a thermal acoustic shield. In this way we hope to provide validation for the overall approach.

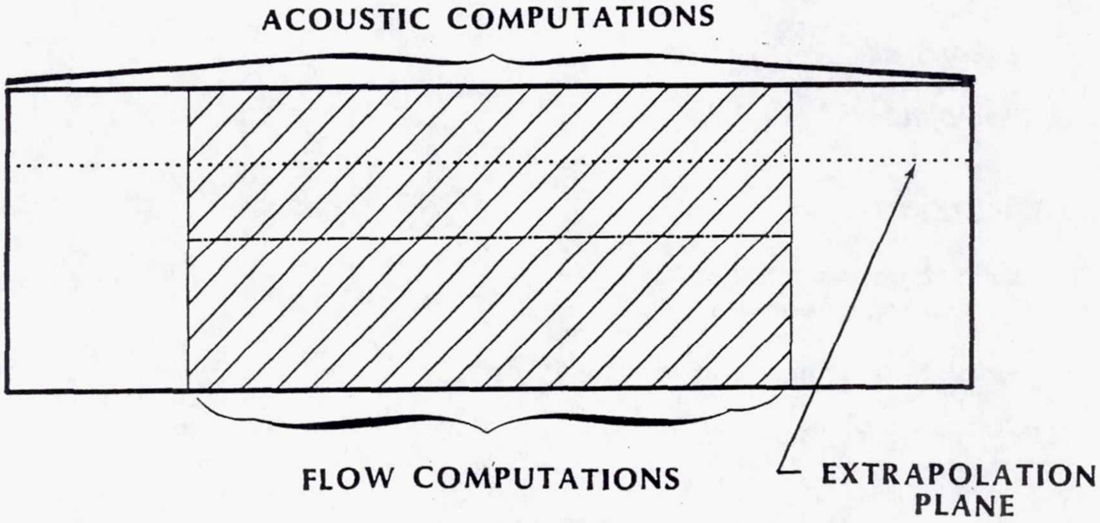

The approach chosen is to first compute the time-dependent, three-dimensional flow field and then compute the acoustics field using an appropriate form of an acoustic wave equation. The flow is computed on a nonuniformly spaced grid with points clustered more closely near the nozzle exit and the main jet flow region. The sound is computed on a uniformly spaced grid. Turbulent flow information is interpolated onto the uniform acoustic grid. The sizes of the flow and computational domains are chosen to be large enough to minimize boundary effects; they need not be the same. In the above figure the flow and acoustic domains have the same transverse dimensions, but the acoustic domain is longer to provide for better angular resolution and range in sound directivity. Acoustic results are collected as a function of time on a sideline plane and Fourier transformed in time. Standard Green's function techniques are used to extrapolate the sideline spectrum to the far field. Our experience is that good extrapolation results are obtained if the sideline is at least one-quarter wavelength from the noise source.

NEKTON

SOLUTIONS FOR

- *Navier Stokes Equation*
- *Heat Transfer*
- *Mass Diffusion*

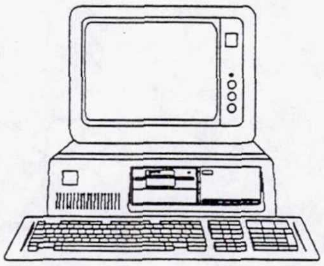

NAVIER STOKES

- *Explicit time treatment of convective terms.*
- *Implicit time treatment of viscous terms.*
- *Pressure solved via Poisson equation.*

GRAPHICAL, MENU DRIVEN USER INTERFACE

An incompressible, time-dependent, three-dimensional flow code called NEKTON is being used to compute the turbulent flow field. A nonuniform density version is available but has not been used on this program. A major attribute of NEKTON is its ability to handle complex geometries as might be found for noise suppressor nozzles.

SPECTRAL ELEMENT TECHNIQUE

FINITE ELEMENTS

Element size and shape chosen to:

- *Match Geometry*
- *Select Resolution*

SPECTRAL TECHNIQUE

Basis functions are Legendre polynomials.

Number of terms determines accuracy.

SOLUTION VIA WEIGHTED RESIDUAL COLLOCATION METHOD

NEKTON is solved using a spectral element technique. The solution within each element is represented as a series of Legendre polynomials. Grid spacing is smallest near element boundaries to improve accuracy in matching conditions across them.

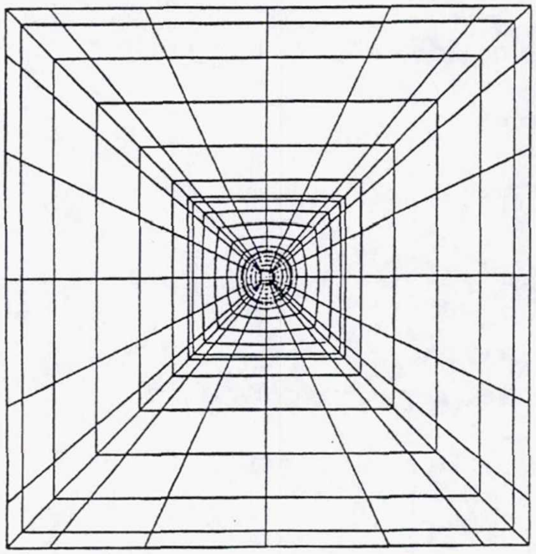

The grid points in a plane normal to the jet axis are shown for a round jet. The element boundary is a circle at the nozzle radius.

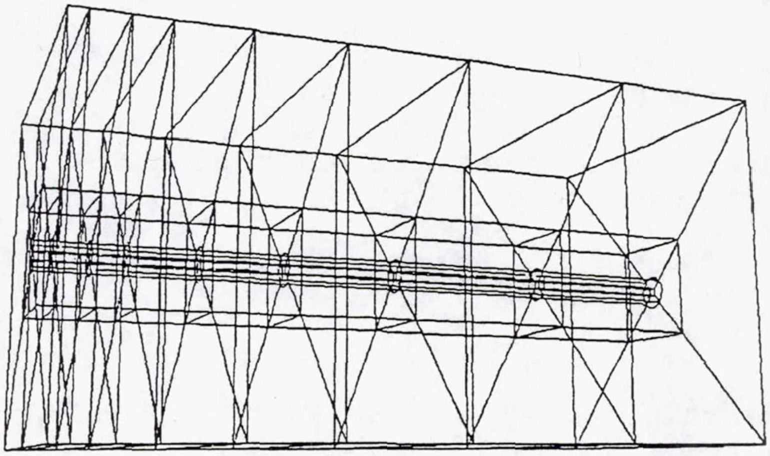

A three-dimensional perspective of the nonuniform grid is shown. Note that points are closer together near the nozzle exit.

RENORMALIZATION GROUP THEORY OF TURBULENCE

(A. Yakhot, S. Orszag, V. Yakhot, M. Israeli, J. Sci. Comp.)

- Self-Consistent Analysis of Navier-Stokes Equations in Wavenumber Space, k
- Analytically Determine Effect of Small Fluctuations, k > K, on Large Scale Fluctuations
- Determine Relation for Instantaneous Eddy Viscosity, ν, in Terms of Dissipation, ϵ

$$\frac{d\nu}{dK} = \epsilon F(\nu, K)$$

- Obtain Algebraic Expression for ν Valid for Both High and Low Reynolds Number Regions of Flow

Large eddy simulation methods require subgrid scale modeling. Renormalization group theory, RNG, provides this modeling based on self consistent solutions for the small scale solutions to the Navier-Stokes equation driven by larger scale fluctuations. The subgrid scale length is the grid spacing, and eddy viscosity is calculated in terms of this length. The larger the subgrid scale is the larger the eddy viscosity.

WAVE EQUATION

$$c^{-2}p_{tt} - p_{xx} - p_{yy} - p_{zz} = s(x, y, t)$$

$$t = n\Delta t$$

$$x = i\,\Delta x$$

$$y = j\,\Delta y$$

$$z = k\Delta z$$

$$p_{tt}(x, y, z, t) = \left(p^{n+1}_{i,j,k} - 2p^{n}_{i,j,k} - p^{n-1}_{i,j,k}\right) / (\Delta t)^2$$

$$p_{xx}(x, y, z, t) = \left(p^{n}_{i+1,j,k} - 2p^{n}_{i,j,k} + p^{n}_{i-1,j,k}\right) / (\Delta x)^2$$

The acoustic solution is found using a convected wave equation in a Lagrangian frame. We start with the standard finite difference form for the wave equation in a frame fixed to the local fluid.

FINITE DIFFERENCE REPRESENTATION

$$p_{i,j,k}^{n+1} = 2p_{i,j,k}^{n} - p_{i,j,k}^{n-1} + h_x\left(p_{i+1,j,k}^{n} - 2p_{i,j,k}^{n} + p_{i-1,j,k}^{n}\right)$$

$$+ h_y(\ldots) + h_z(\ldots)$$

$$h_x = c^2(\Delta t)^2/(\Delta x)^2$$

$$h_y = c^2(\Delta t)^2/(\Delta y)^2$$

$$h_z = c^2(\Delta t)^2/(\Delta z)^2$$

The finite difference wave equation formulation is continued here with the introduction of the Courant number as a standard parameter that must not be large for explicit solution methods. It is found that this method gives sufficiently accurate results over the spatial range of propagation of interest in this formulation. A second order Adams-Bashforth differencing scheme has also been used to synchronize with variable time step flow results, but this exhibits the effects of dissipation over long propagation distances. We also note that there must be a sufficient number of grid points per wavelength. Results are excellent with 20 points per wavelength, fairly good with 10 points, and marginal with 5 to 6 points per wavelength.

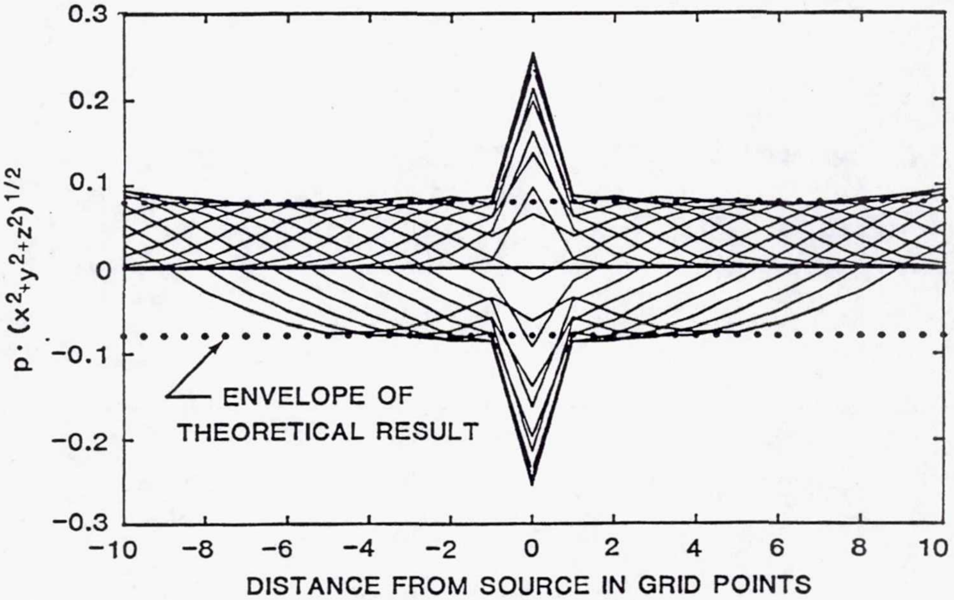

Acoustic results are shown for the finite difference solution due a point source located at the center of a cube 21 grid points on a side. The frequency is chosen so that one wavelength equals the length of one side of the cube. The pressure is multiplied by distance from the center of the domain. Thus, the product of pressure and distance should be constant according to theory. The boundary condition corresponds to radiation for a wave propagating at normal incidence to the boundary.

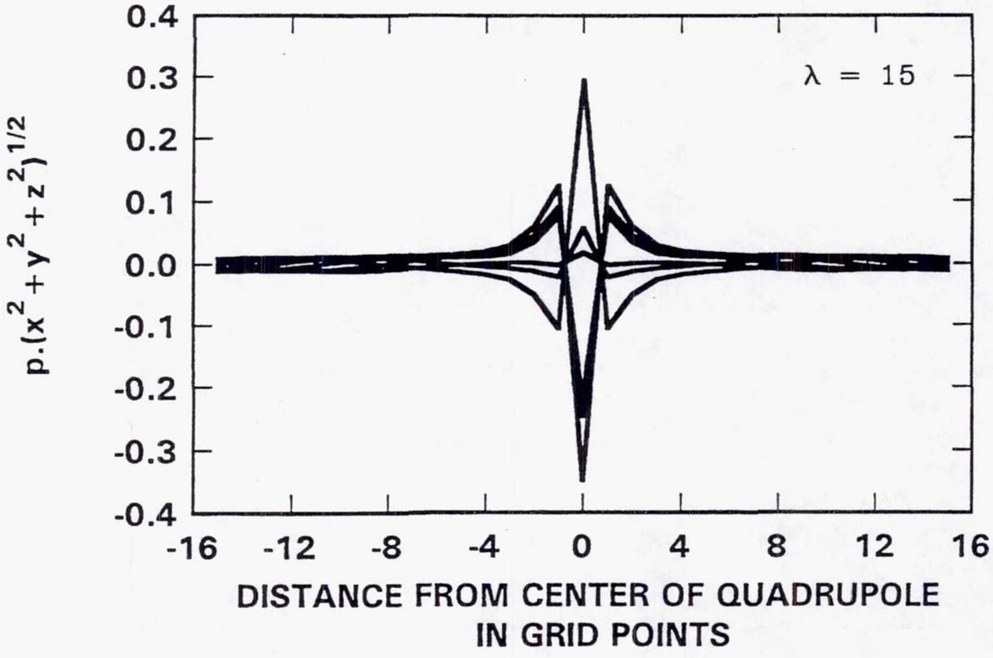

Longitudinal quadrupole sources

The acoustics field is shown for a quadrupole composed of a source whose strength is two units and two sinks of unit strength located one grid point away. The length of the computational domain is 31 grid points and the wavelength is 15. A closer look at the results shows that the far field variation is attained in about 0.25 wavelengths.

CONVECTED (PHILLIPS) WAVE EQUATION

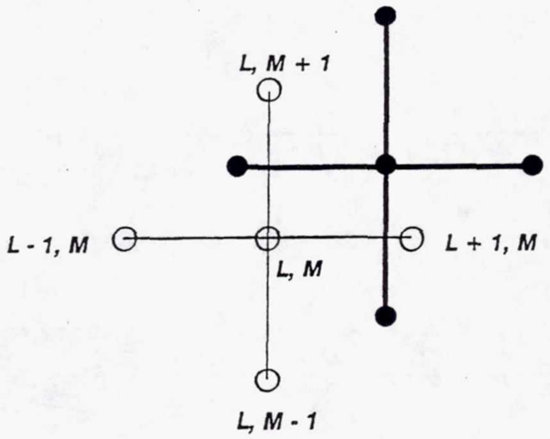

- Solve Wave Equation in Lagrangian System
- Eulerian and Lagrangian Systems Coincide Before Each Incremental Time Step
- Interpolate Back and Forth Between Systems

The convected wave equation is solved by employing the standard second order algorithm in a frame of reference moving with the local fluid velocity. The method is semi-Lagrangian in nature in that one moves with the flow for only one time step and then immediately interpolates the newly computed pressure field back into the fixed frame. For the next time step the fixed and moving frames coincide at the beginning of the computation and the source strength is specified at the fixed points. For the wave equation the pressure field must be known at the time step prior to the beginning of the computation. This is obtained from a separate interpolation of results from the fixed frame to the Lagrangian frame where the computation is to take place.

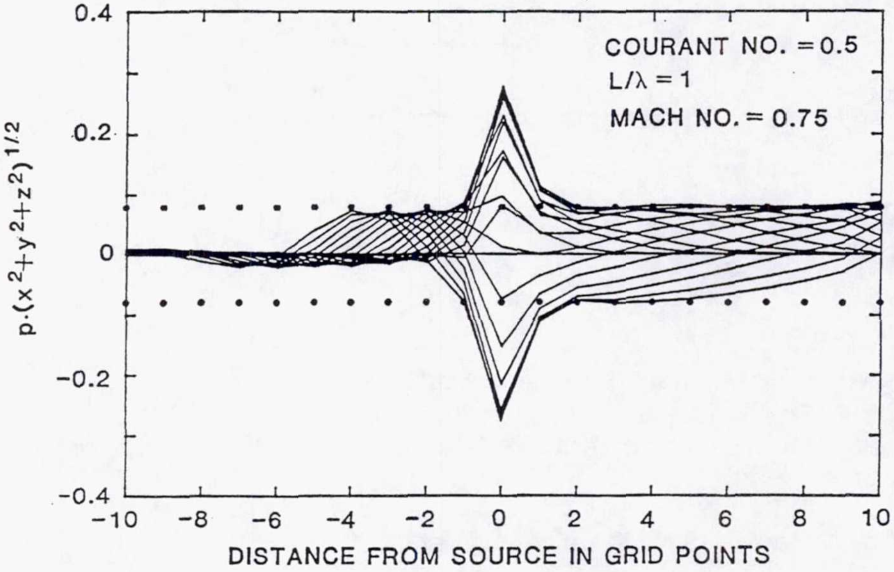

The product of pressure and distance from a monopole source is plotted for the case of a uniform flow at M = 0.75. Note that the wavelength is shortened upstream of the source (the left hand side) as the waves propagate against the flow. Here the waves have not travelled as far in the fixed frame against the flow as in the downstream direction. According to theory the amplitude of sound in a uniform wind does not depend on whether the observer is upstream or downstream of the monopole. In practice the amplitudes differ because the wind is not uniform if a boundary layer is present which refracts the waves.

LIGHTHILL'S EQUATION

$$\frac{\partial^2 \rho}{\partial t^2} - c_0^2 \frac{\partial^2 \rho}{\partial x_i^2} = \frac{\partial^2 T_{ij}}{\partial x_i \partial x_j}$$

$$T_{ij} = \rho U_i U_j + p_{ij} - c_o^2 \rho \delta_{ij}$$

Incompressible Limit

$$\frac{\partial^2 T_{ij}}{\partial x_i \partial x_j} = \rho_o \frac{\partial U_i}{\partial x_j} \frac{\partial U_j}{\partial x_i}$$

Lighthill's equation is presented. The feature of interest to us is the double divergence form of the quadrupole source term. We will find it useful to write the source term for the Phillips equation in this form. Lighthill's equation is not of interest to us here because we are only able to obtain the incompressible flow solution.

PHILLIPS' EQUATION

$$\frac{D^2\sigma}{Dt^2} - \frac{\partial}{\partial x_i}\left(c^2\frac{\partial\sigma}{\partial x_i}\right) = \gamma\frac{\partial U_i}{\partial x_j}\frac{\partial U_j}{\partial x_i} + \frac{D}{Dt}\left(\frac{1}{c_p}\frac{DS}{Dt}\right)$$

+ viscous terms

$$\sigma = \ln\frac{p}{p_0}$$

$$\frac{D}{Dt} = \frac{\partial}{\partial t} + U_k\frac{\partial}{\partial x_k}$$

The Phillips equation is a convected wave equation for the log of pressure and is the form which we have chosen to use for jet noise computations. For small pressure fluctuations this can be linearized to give the equation for small pressure fluctuations. If one keeps the original variable without linearization, it becomes an equation for a quantity that is proportional to decibels. The numerical solution follows the convected wave equation approach discussed previously. The effect of a variable speed of sound is included in the equation. As written the source term contains a product of derivatives of velocity only. This is the total velocity including the effects of compressibility. The Lilley equation is a higher order wave equation in the same independent variable. While it is also a valid equation, we see no advantage in using it. Its more complex source term involving a product of three velocity derivatives creates numerical complications.

$$\frac{\partial U_i}{\partial x_j}\frac{\partial U_j}{\partial x_i} = \frac{\partial^2 U_i U_j}{\partial x_i \partial x_j} + \textit{density dependent terms}$$

In order to obtain accurate acoustic results at low Mach numbers and at angles far from the peak noise angle, the Phillips noise source term is written as a sum of a double divergence of velocity dependent terms and other terms dependent on compressibility. These terms specifically depend on fluctuations in density. We will consider that the density fluctuations can be neglected as long as the fluctuations in Mach number are sufficiently small (note that the Mach number itself does not need to be small). The remaining source term is in a quadrupole form similar to that in Lighthill's equation. Thus, the source term bears some similarity Lighthill's, but the Phillips equation operator accounts for propagation effects due to variable flow properties within the jet.

DOUBLE DIVERGENCE FORM

$$\partial^2 T_{11}/\partial x_1^2 = \frac{T_{11}(n+1) - 2T_{11}(n) + T_{11}(n-1)}{(\Delta x_1)^2}$$

$\partial^2 T_{12}/\partial x_1 \partial x_2$: *CENTRAL DIFFERENCES*

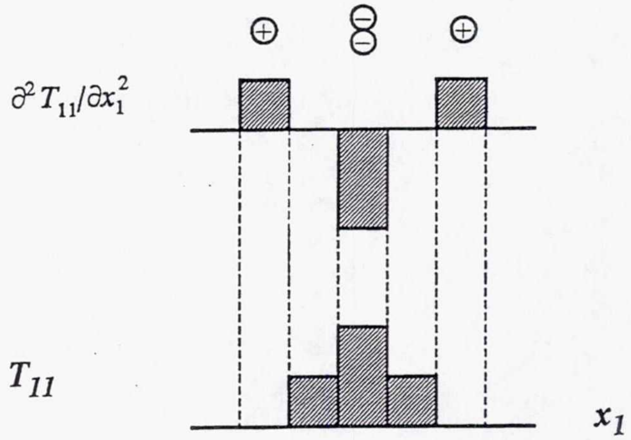

An illustration is presented of the application of the double divergence form representing a quadrupole to numerical analysis. The finite difference formulas are given for longitudinal quadrupoles (same direction for both derivatives) and lateral quadrupoles (different direction for the derivatives). The sketch at the very bottom is the distribution of T_{11}. This is arbitrary and is a crude finite difference representation of a Gaussian distribution. If the finite difference formula at the top of the page is applied to this distribution, then the shaded figure in the center is obtained. The meaning is that there is a large negative second derivative that contributes at the center of the distribution. Smaller positive contributions appear on either side. If the magnitudes of these derivatives are represented as a distribution of monopoles (the circles in the figure), then the quadrupole is composed of a negative monopole of two units in strength (or two single negative monopoles each of unit strength placed very close to each other) and individual positive monopoles of unit strength on either side of the center. The summation of all of these sources adds up to zero indicating that the monopole strength of the distribution is zero. Sound is emitted due to the retarded time effect, i.e., the sources at different locations are to be evaluated at different times, in phase with the time of travel of a sound wave between the points. For an infinite speed of sound the retarded time is zero. In practice the finite difference volume integral of the source strength at zero retarded time yields values extremely close to zero, which is the theoretical result. This degree of accuracy at zero retarded time is an indication that accurate results will be obtained for small values of retarded time, corresponding to very low frequencies and large wavelengths. This is the most difficult case to compute numerically, and our success here is the reason for expressing the Phillips source term in the form of a quadrupole.

FINITE DIFFERENCE SOURCE TEST: ONE-DIMENSIONAL CASE

Space Derivative Form

$$J = \int \frac{\partial^2 T}{\partial y^2} (y, \tau) \, dy = \sum_n [T(y_{n+1}) - 2T(y_n) + T(y_{n-1})]$$

$$T(y_n) = \exp[-(y_n/b)^2] \cos[\omega (\tau - y_n/u_c)]$$

$$\tau = t - y_n/c_0$$

Time Derivative Form

$$J = \frac{1}{c_0^2} \int \frac{\partial^2}{\partial t^2} T \, (y, \tau,) \, dy = -\left(\frac{\omega}{c_0}\right)^2 \sum_n T(y_n)$$

Analytical Result

$$J = -(\omega/c_0)^2 \sqrt{\pi} \, b \exp[-(\omega/c_0)^2 \, (1 - c_0/u_c)^2]$$

A one-dimensional test of the double divergence quadrupole form is developed. An analytical form of the source is presented as the product of a travelling wave and a Gaussian amplitude in space. The time-dependent sound field is determined using Lighthill's theory. This will be compared on the next slide to the finite difference acoustic solution obtained by substituting the above quadrupole distribution into the right hand side of the wave equation and integrating in time and space. Note that the analytical solution contains a convective amplification effect corresponding to a convective Mach number of 1 in this one-dimensional case.

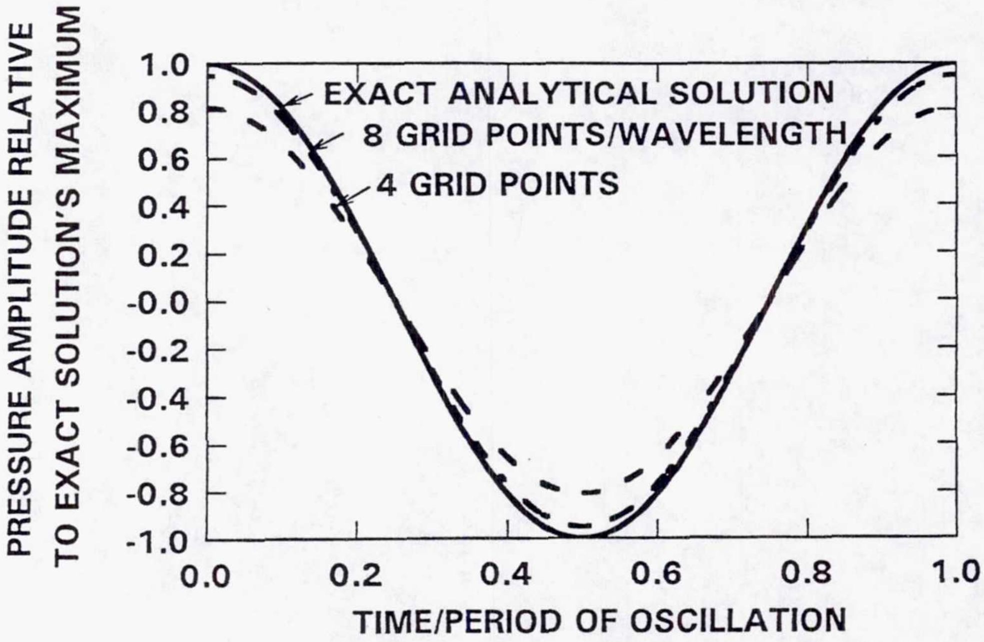

One-dimensional Gaussian space dependence
Wavelength = Gaussian half width

A comparison is presented between an exact numerical solution for the one-dimensional sound field produced by a quadrupole source derived from a Gaussian distribution in space which varies sinusoidally in time and the finite difference implementation of the problem. The accuracy of the solution increases with the number of points per wavelength. The agreement for only 8 points per wavelength is excellent considering the coarseness of the mesh. Other comparisons at finite values of source convection speed and other frequencies, both high and low, also show excellent agreement.

SIMULATED QUADRUPOLE SOURCE

$$T_{ij} = \delta_{ij} \exp(-r/b) \exp(i\omega t)$$

$$\partial^2 T_{ij}/\partial x_i \partial x_j \rightarrow c_0^{-2} (x_i x_j/R^2) \partial^2 T_{ij}/\partial t^2$$

Far Field Density Perturbation:

$$\rho = \frac{2(\omega b/c_0)^2 b}{R[1 + (\omega b/c_0)^2]^2}$$

An analytical solution for the three-dimensional sound field produced by a three-dimensional source distribution is derived and will be used as a basis for comparison with the finite difference wave equation solution using the finite difference quadrupole form of the same source. The source is in the form of a radial exponential amplitude falloff in space and a sinusoidal variation in time. The analytical solution is obtained using Lighthill's time derivative form of a quadrupole. We note, but do not show in this presentation, that two-dimensional comparisons have been made for the noise generated by vortical flow fields. In this case all solutions were numerical and were based on values of the velocity field and its derivatives. Comparisons were made between: (1) the Lighthill result based on expressing the quadrupoles in terms of time-derivatives (which we feel is the most accurate method); (2) the Phillips source term composed of products of derivatives; and (3) the double space derivative form which we propose for the Phillips equation. In all cases there was good agreement between the Lighthill time-derivative form and the double space derivative form. The original Phillips form did not result in nearly as good agreement.

PRESSURE DUE TO SPHERICAL VOLUME
QUADRUPOLE SOURCE

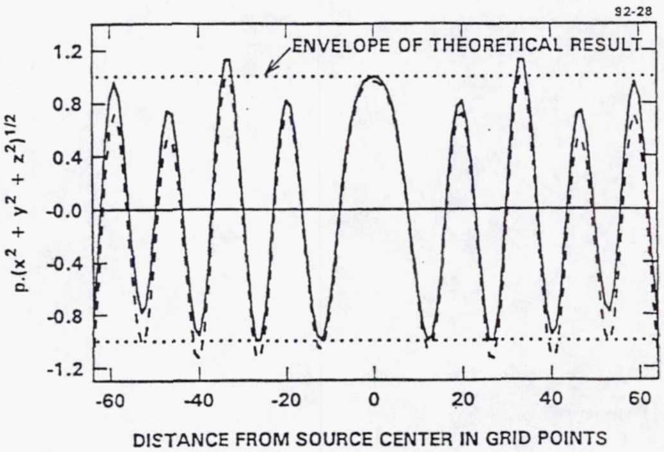

Pressure Along Line Midway
between Centerline and Domain Boundary
Wavelength = 12.8 Grid Points
———————— *Double Space Derivative Form of Source*
– – – – – – – *Double Time Derivative Form of Source*

A finite difference computation of the wave equation was performed with a source term which was the double divergence of a quantity that fell off exponentially in space from the center of the computational domain and varied sinusoidally in time. The computational domain was the same one in full jet acoustics simulations and the computations were carried out on an IRIS 4D35G workstation. Results are compared to the analytical Lighthill result and the Lighthill result obtained by performing a finite difference solution of the wave equation with the source given by Lighthill's time derivative form. Data are displayed along the centerline of the jet axis and along a parallel line located midway between the centerline and a sidewall. Differences between the finite difference Lighthill computation and the envelope obtained from the analytical Lighthill result are due in part to numerical errors in the finite difference approach, but primarily to errors in the wall boundary condition. In comparing the two finite difference techniques note that the difference in height between peaks and valleys is nearly the same even when they seem to be displaced from each other. Thus, a frequency analysis at the dominant frequency would yield similar results independent of the method of expressing the source term. This is then a validation of the accuracy of the double divergence form. In the case of solving Lighthill's equation, the time derivative form might be preferred, but for the Phillips equation we are required to use a space derivative form for the source.

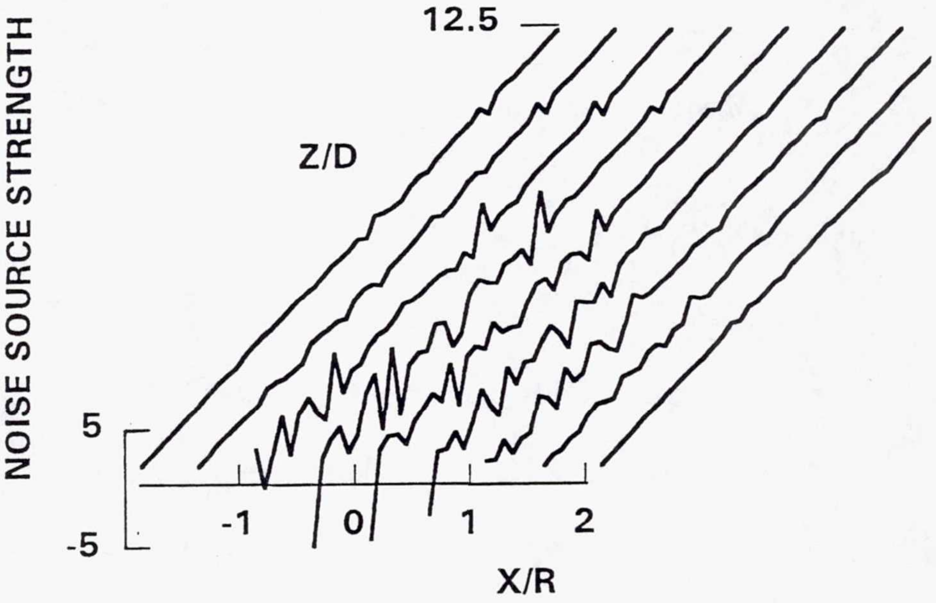

Displayed here is a plot of the distribution of the noise source strength computed using the double divergence method on actual instantaneous turbulent jet velocity data generated by NEKTON. The results are given in a plane passing through the jet axis. Note the wave type behavior in the axial direction.

K - ϵ Model

STANDARD APPROACH

- **Obtain K and L (K, ϵ)**
- **Model or Assume $U_{convection}$**

RNG BASED K - ϵ

- **Modified Equations and Constants**
- **Decreased Eddy Viscosity**
- **Very Large Scale Time Dependent Flow**
  - **Large Scale Turbulent Eddy Size**
  - **Convection Velocity**

We are now considering a very large eddy simulation, VLES, based on a K-ϵ model of turbulence. However, there have been some important developments in this approach. By using basic principles of renormalization group theory some of the constants in the K-ϵ formulation are changed. The net effect is that the eddy viscosity is reduced. Thus, in the new formulation the Reynolds number based on eddy viscosity is larger, and it is easier to develop turbulent fluctuations in the large scale flow. If the standard high viscosity K-ϵ model is used as the basis for noise calculations, there is not enough information available to independently model the turbulence noise source terms. Important quantities for noise are a characteristic eddy size and the eddy convection velocity. A characteristic eddy scale can be obtained from the computations, but then this needs to be related to the scale relevant to noise. Convection velocity must be modeled based on other principles. However, if the new lower viscosity K-ϵ model is used, then a VLES solution is obtained. Sound can be computed using the time-dependent approach, or if a time-averaged frequency domain method is used, information can be obtained about the eddy scales and convection velocity.

TIME REQUIREMENTS

COMPRESSIBLE FLOW > $\overbrace{\text{NONUNIFORM } \rho > \text{UNIFORM } \rho}^{\text{INCOMPRESSIBLE FLOW}}$ >

DATA CONVERSION ? > ACOUSTIC PROPAGATION >

FAR FIELD EXTRAPOLATION

In our current formulation the amount of time needed to perform the turbulent flow computations is large compared to the time needed to compute the acoustics. However, the memory requirements of both the flow and acoustics codes are large. One way of reducing both time and memory requirements is to use a frequency domain acoustic analysis. For the time-dependent problem long flow run times are needed to build up enough statistical reliability in the turbulence fluctuations to adequately predict noise spectra. For the frequency domain problem only mean flow, rms fluctuations, length scale, and convection speed are needed. The turbulence spectra can be modeled in terms of these quantities so shorter flow computation times would be adequate. Memory for the acoustic computations would be reduced for the frequency domain problem since the computations, using a source approach could be limited to the jet region itself and not include the near propagation field as needed for the time-dependent case.

FREQUENCY DOMAIN PHILLIPS EQUATION

- **Locally Parallel Flow**
- **Solve in Two-Dimensional X−Y Cross Plane Using Ray Acoustics**
- **Obtain Δ dB Transmission Through Ray Tubes**
- **Find Transmission to Single Far Field Observer from All Points in Jet**
- **Equation is Invariant on Change of Sign of X or Y**
- **3d Convected Helmholtz Equation**

A frequency domain analysis is being formulated in terms of the Phillips equation. The assumptions are those of locally parallel flow and the applicability of ray acoustics in the cross plane normal to the main jet axis. Ray acoustics is usually viewed as a high frequency approximation. We see it as a solution applicable to cases where reflections are small. Because we solve for the sound due to all sources that produce sound at a single angle, we believe that the reflected sound is less important than the directly transmitted component. Variations in pressure in this case are given in terms of a power flow argument with varying ray tube area and acoustic impedance. Differences in the standard approach and that resulting from the Phillips equation are due to the convective time derivative and the explicit appearance of gradients of sound speed in the Phillips equation. These effects can be transformed out so that the equation to be solved appears in the form of the standard Helmholtz equation. The most important feature is calculating the transmission loss through cutoff regions where exponential decay, rather than wave propagation, is found. The computation is started with a plane wave just at the edge of the jet propagating in towards the jet at an angle corresponding to the far field direction of interest. This approach is valid because the equation is unchanged with respect to changes in sign to the coordinates normal to the jet axis. We note that a three-dimensional convected Helmholtz is currently under development. This would serve as a standard against which to test our ray approximation in lower frequency situations.

RAY TRACING IN PLANE NORMAL TO JET AXIS

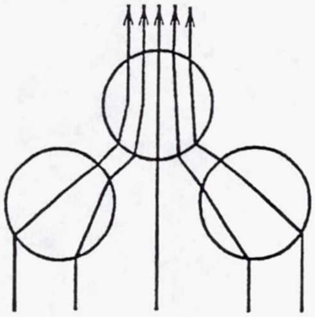

SINGLE ANGLE, MANY SOURCES

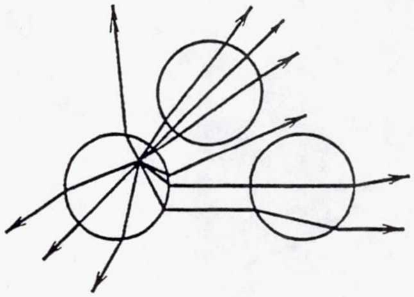

SINGLE SOURCE, MANY ANGLES

Most ray tracing is illustrated by the directions of rays emanating from a single source. This approach is costly for jet noise computations since a separate two-dimensional computation is needed for each source point in the jet, i.e., no information obtained from one source point computation is applicable to the computation of sound from any other point in the jet. We favor performing a backwards ray tracing approach starting with a plane wave propagating in towards the jet from the far field observer. By tracing out the rays due to this wave, we can place all sources in one ray tube or another. In this way the results of one two-dimensional computation are applicable to all sources within the jet that radiate at the given angle. WKB techniques are useful in determining variations in pressure amplitude other than those due to ray tube area variations.

1999176560

COMPUTATION OF SUPERSONIC JET MIXING NOISE USING PARC CODE WITH A κ–ε TURBULENCE MODEL

A. Khavaran
Sverdrup Technology, Inc.
Lewis Research Center Group
Brook Park, Ohio

and

C.M. Kim
NASA Lewis Research Center
Cleveland, Ohio

523-71

409547

20P.

BACKGROUND

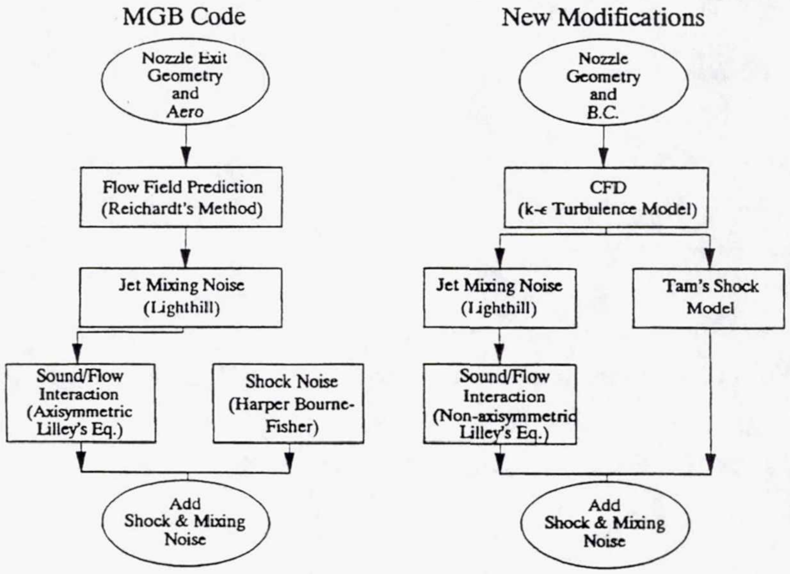

A number of modifications have been proposed in order to improve the jet noise prediction capabilities of the MGB code. This code which was developed at General Electric, employees the concept of acoustic analogy for the prediction of turbulent mixing noise. The source convection and also refraction of sound due to the shrouding effect of the mean flow are accounted for by incorporating the high frequency solution to Lilley's equation for cylindrical jets (Balsa and Mani). The broadband shock-associated noise is estimated using Harper-Bourne and Fisher's shock noise theory. The proposed modifications are aimed at improving the aerodynamic predictions (source/spectrum computations) and allowing for the non-axisymmetric effects in the jet plume and nozzle geometry (sound/flow interaction). In addition, recent advances in shock noise prediction as proposed by Tam can be employed to predict the shock-associated noise as an addition to the jet mixing noise when the flow is not perfectly expanded. Here we concentrate on the aerodynamic predictions using the PARC code with a k-ϵ turbulence model and the ensuing turbulent mixing noise. The geometry under consideration is an axisymmetric convergent-divergent nozzle at its design operating conditions. Aerodynamic and acoustic computations are compared with data as well as predictions due to the original MGB model using Reichardt's aerodynamic theory.

MODELING APPROACH

- Source Spectrum Calculations
  - Lighthill's Acoustic Analogy
  - Ribner and Batchelor Assumptions
  - Calculation of Source Strength and its Spectrum Using CFD
- Sound/Flow Interaction
  - High Frequency Asymptotic Solution to Lilley's Equation for a Multipole Source Convecting in an Axisymmetric Parallel Flow (Balsa and Mani)
  - Calculation of Directivity Factors Based on CFD Results

GOVERNING EQUATIONS

Lighthill's Equation

$$\frac{\partial^2 \rho}{\partial t^2} - c^2 \nabla^2 \rho = \frac{\partial^2 T_{ij}}{\partial x_i \partial x_j}$$

$$T_{ij} = \rho V_i V_j + \delta_{ij}(p - c^2 \rho) - e_{ij}$$

$$e_{ij} = \mu(\frac{\partial V_i}{\partial x_j} + \frac{\partial V_j}{\partial x_i} - \frac{2}{3}\delta_{ij}\frac{\partial V_k}{\partial x_k})$$

$$\frac{e_{ij}}{\rho V i V_j} \sim O(\frac{1}{Re}), \qquad Re = \frac{\rho U L}{\mu}$$

$$\frac{1}{c^2} dp - d\rho = (\frac{\partial \rho}{\partial s})_p ds$$

- The effects of source convection and refraction are included in the source term.

Lilley's Equation

$$\frac{D}{Dt}\left(\frac{D^2\sigma}{Dt^2} - \frac{\partial}{\partial x_i}c^2\frac{\partial\sigma}{\partial x_i}\right) + 2\frac{\partial V_j}{\partial x_i}\frac{\partial}{\partial x_j}c^2\frac{\partial\sigma}{\partial x_i} = -2\frac{\partial V_j}{\partial x_i}\frac{\partial V_k}{\partial x_j}\frac{\partial V_i}{\partial x_k} + \frac{D}{Dt}\left[\frac{D}{Dt}\left(\frac{1}{c_p}\frac{Ds}{Dt}\right)\right] + \text{viscous terms}$$

$$\sigma = \frac{1}{\gamma} ln \frac{p}{p_o}$$

$$\frac{D}{Dt} = \frac{\partial}{\partial t} + V_k\frac{\partial}{\partial x_k}$$

- The effects of source convection and refraction are included in the operator term of Lilley's eq.

Source Spectrum Calculations

- Mean-square sound pressure autocorrelation in the far field due to a finite volume of turbulence (in absence of convection and fluid shielding)

$$\overline{p^2}(R,\theta,\phi) = \frac{R_i R_j R_k R_\ell}{16\pi^2 C_a^4 R^6} \int_{\vec{y}} \int_{\vec{\xi}} \frac{\partial^4}{\partial \tau^4} \overline{(\rho V_i V_j)(\rho' V_k' V_\ell')} d\vec{\xi} d\vec{y},$$

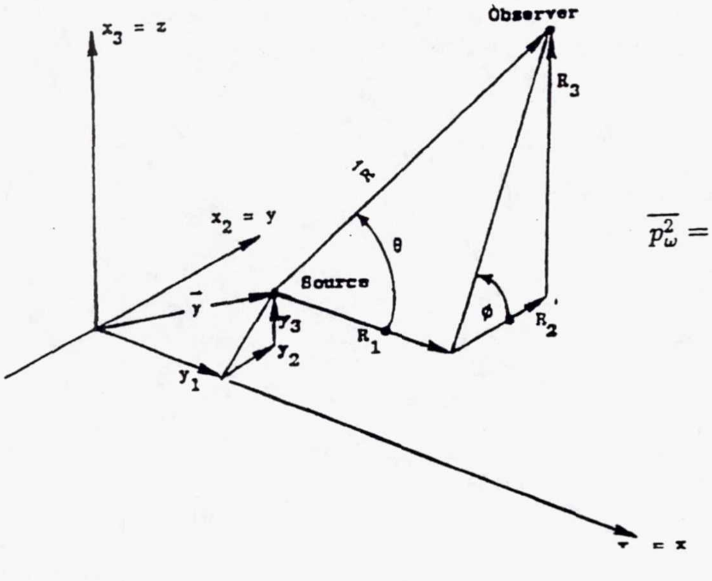

$$\overline{p_\omega^2} = \frac{1}{2\pi} \int_{-\infty}^{+\infty} \overline{p^2} e^{i\omega\tau} d\tau$$

SOURCE SPECTRUM CALCULATIONS

- Fourth-order velocity correlation tensor

$$S_{ijk\ell} = \overline{V_i V_j V_k' V_\ell} = \int_{-\infty}^{+\infty} (V_i V_j)(V_k' V_\ell')dt$$

- Source strength (Quasi-incompressible turbulence)

$$I_{ijk\ell} = \rho^2 \int_{\vec{\xi}} \frac{\partial^4}{\partial \tau^4} S_{ijk\ell} d\vec{\xi}$$

- Reduction in order of correlation tensor (Ribner)

$$S_{ijk\ell} = S_{ik}S_{j\ell} + S_{i\ell}S_{jk} + S_{ij}S_{k\ell}$$

$$S_{ij}(\tau, \vec{\xi}) = \int_{-\infty}^{+\infty} V_i V_j' dt$$

- Separable second-order tensors

$$S_{ij}(\tau, \vec{\xi}) = R_{ij}(\vec{\xi})G(\tau)$$

- Isotropic turbulence model of Batchelor

$$R_{ij}(\vec{\xi}) = Te^{-\pi(\xi/L_x)^2} \times \left\{[1 - \pi(\xi/L_x)^2]\delta_{ij} + \pi\xi_i\xi_j/L_x^2\right\}$$

$$T = \frac{1}{3}\overline{V_i V_i}, \qquad \xi^2 = \xi_1^2 + \xi_2^2 + \xi_3^2$$

- Gaussian correlation time delay

$$G(\tau) = e^{-(\tau/\tau_o)^2}$$

- Source spectrum component

$$I_{1111}(\Omega) \sim \rho^2 k^{\frac{7}{2}} (\Omega\tau_o)^4 e^{\frac{-(\Omega\tau_o)^2}{8}}$$

$$L_x \sim \frac{k^{3/2}}{\epsilon}, \qquad \tau_o \sim \frac{L_x}{\sqrt{k}}, \qquad k = \frac{1}{2}\overline{V_i V_i}$$

SOURCE SPECTRUM CALCULATIONS

- Characteristic time delay of correlation

$$\tau_o \sim \frac{1}{(\partial U/\partial r)} \quad or \quad \tau_o \sim \frac{k}{\epsilon}$$

- Doppler shifted frequency

$$\Omega = 2\pi f\overline{C}, \qquad M_c = .5M + \beta_c M_j$$

$$\overline{C} = \sqrt{(1 - M_c cos\theta)^2 + (\alpha_c k^{.5}/C_\infty)^2}$$

The proportionality constant in finding τ_o and the convection constants α_c and β_c are determined empirically.

SOUND/FLOW INTERACTION

- Mean square pressure in the far-field

$$\overline{p^2}(R,\theta,\Omega) = \int_{\vec{y}} \Lambda(a_{xx} + 4a_{xy} + 2a_{yy} + 2a_{yz})d\vec{y}$$

- Source term

$$\Lambda \sim \frac{(\frac{\rho_\infty}{\rho})^2 I(\Omega)}{(4\pi R C_\infty C)^2(1 - M cos\theta)^2(1 - M_c cos\theta)^2}$$

- Shielding function

$$g^2(r) = \frac{(1 - M cos\theta)^2(\frac{C_\infty}{C})^2 - cos^2\theta}{(1 - M_c cos\theta)^2}$$

$$M(r) = U(r)/C_\infty, \qquad M_c = U_c/C_\infty$$

Directivity factors $a_{xx} \ldots$ are functions of the Shielding factor $g^2(r)$.

Geometry and Computational Grid

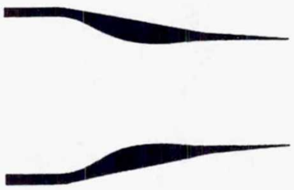

Design Parmaters for C-D Nozzle

Throat diameter	5.1 in.
Exit diameter	5.395 in.
Distance from throat to exit	5.525 in.
Exit velocity	2409 fps
Ambient velocity	400 fps
Pressure ratio	3.121
Stagnation temperature	1716 °R

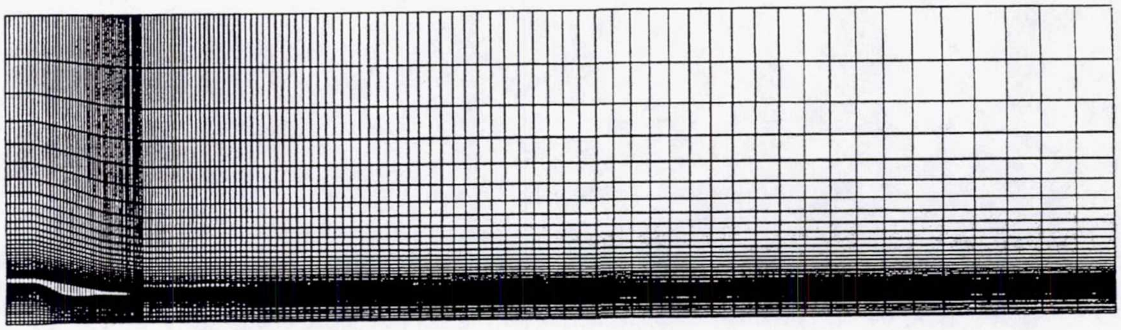

MACH NUMBER

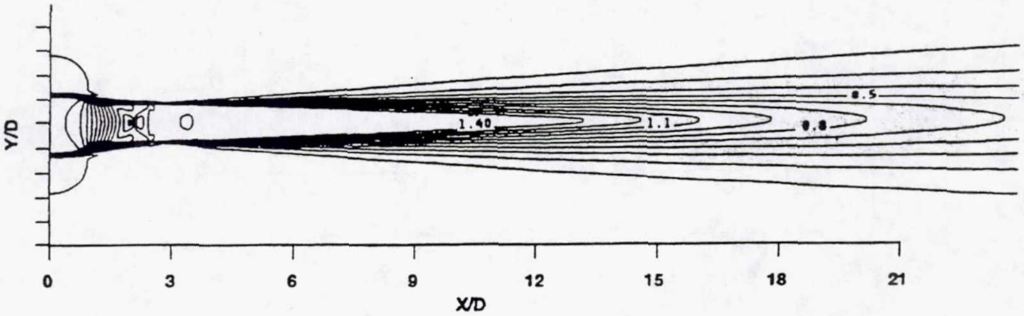

Mach number contour plot for the convergent-divergent nozzle at the design condition (NPR = 3.12), using PARC code with a k-ϵ turbulence model. The upstream conditions are specified at three diameters within the nozzle. The flowpath for this nozzle has been designed to obtain an isentropic, uniform and parallel flow at the exit for the design Mach number of 1.4.

COMPARISON OF VELOCITY PROFILE WITH DATA

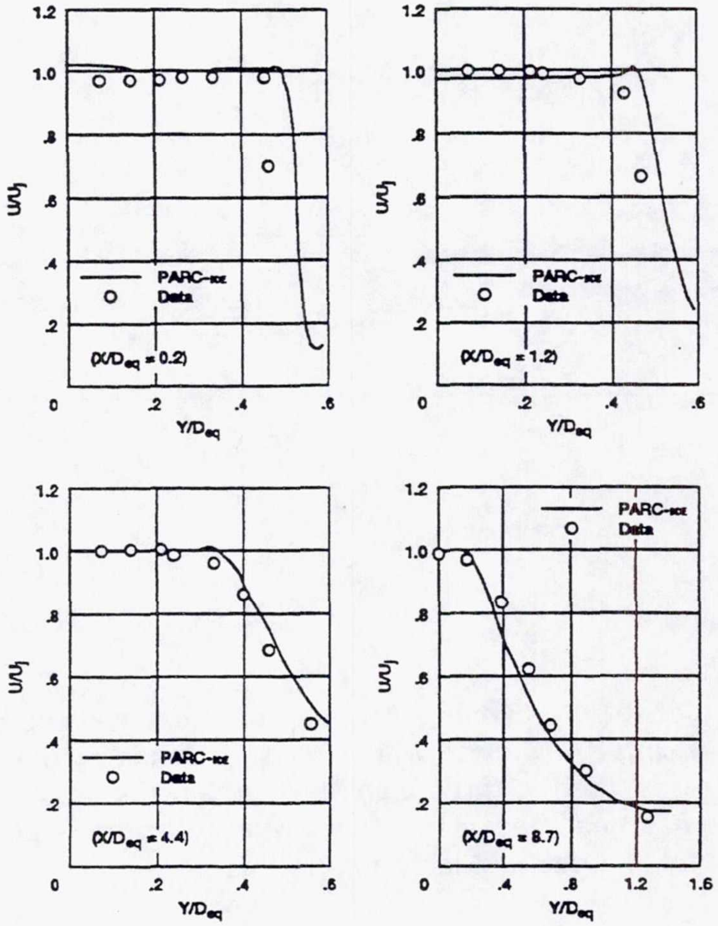

Comparison of velocity profiles with data at four different axial locations. The axial and radial dimensions are normalized with respect to the jet throat diameter D_{eq}.

VELOCITY PROFILE

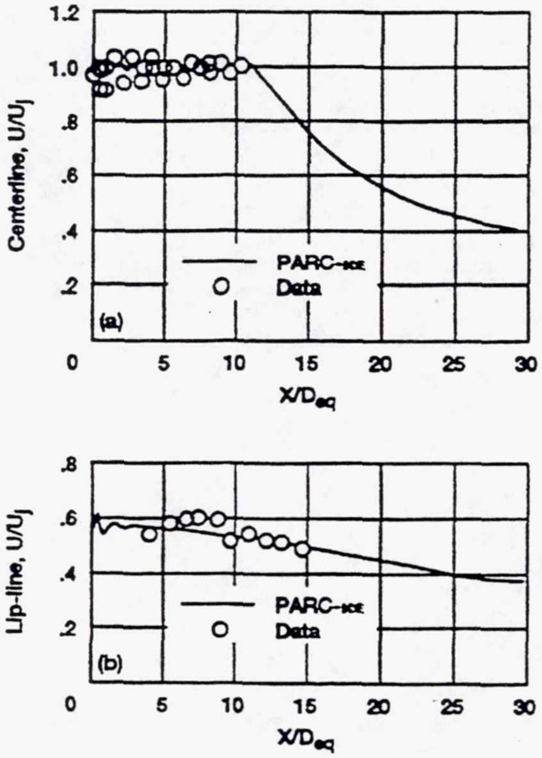

Comparison of velocity profiles with data on the (a) centerline (b) lip-line.

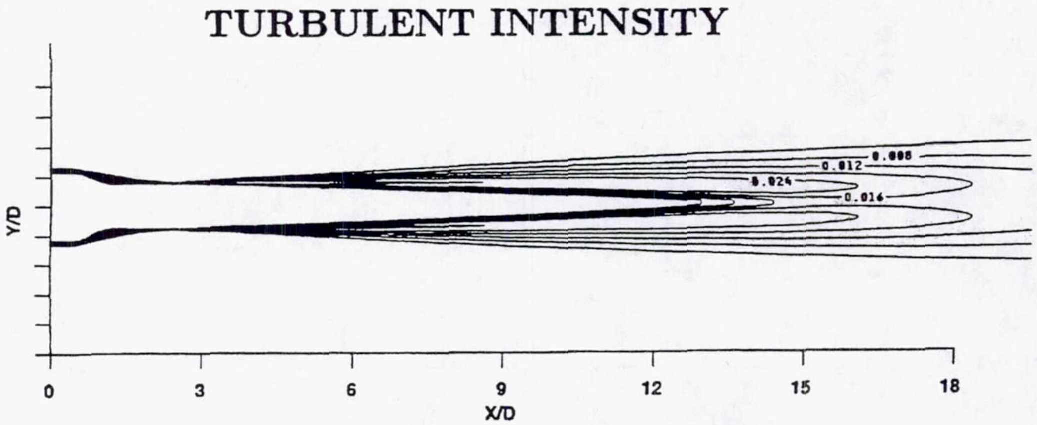
TURBULENT INTENSITY

Turbulent intensity contour plot. The contour levels are normalized with respect to square of ambient sound speed.

COMPARISON OF PARC TURBULENT INTENSITY WITH DATA

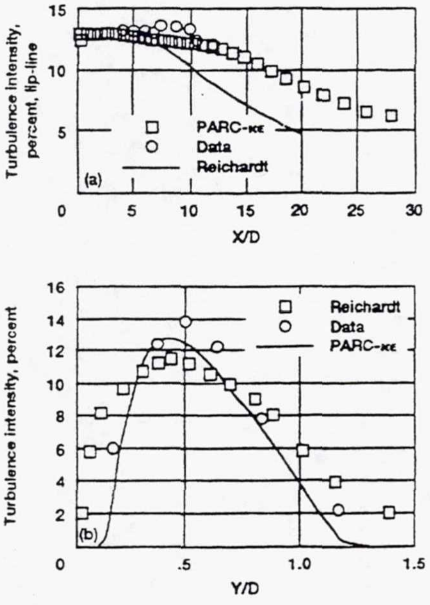

Comparison of PARC turbulent intensity profiles with data and predictions due to Reichardt's theory on the (a) lip-line (b) X/D=8.21. Radial distance Y is measured from the centerline and all percentages are based on the jet exit velocity U_j. Figure (a) shows that a maximum level of 13% is predicted by both prediction methods although the Reichardt's theory shows a much faster decay along the lip-line. The agreement between PARC and data is reasonably acceptable.

COMPARISON OF PARC TURBULENT INTENSITY WITH REICHARDT'S SOLUTION

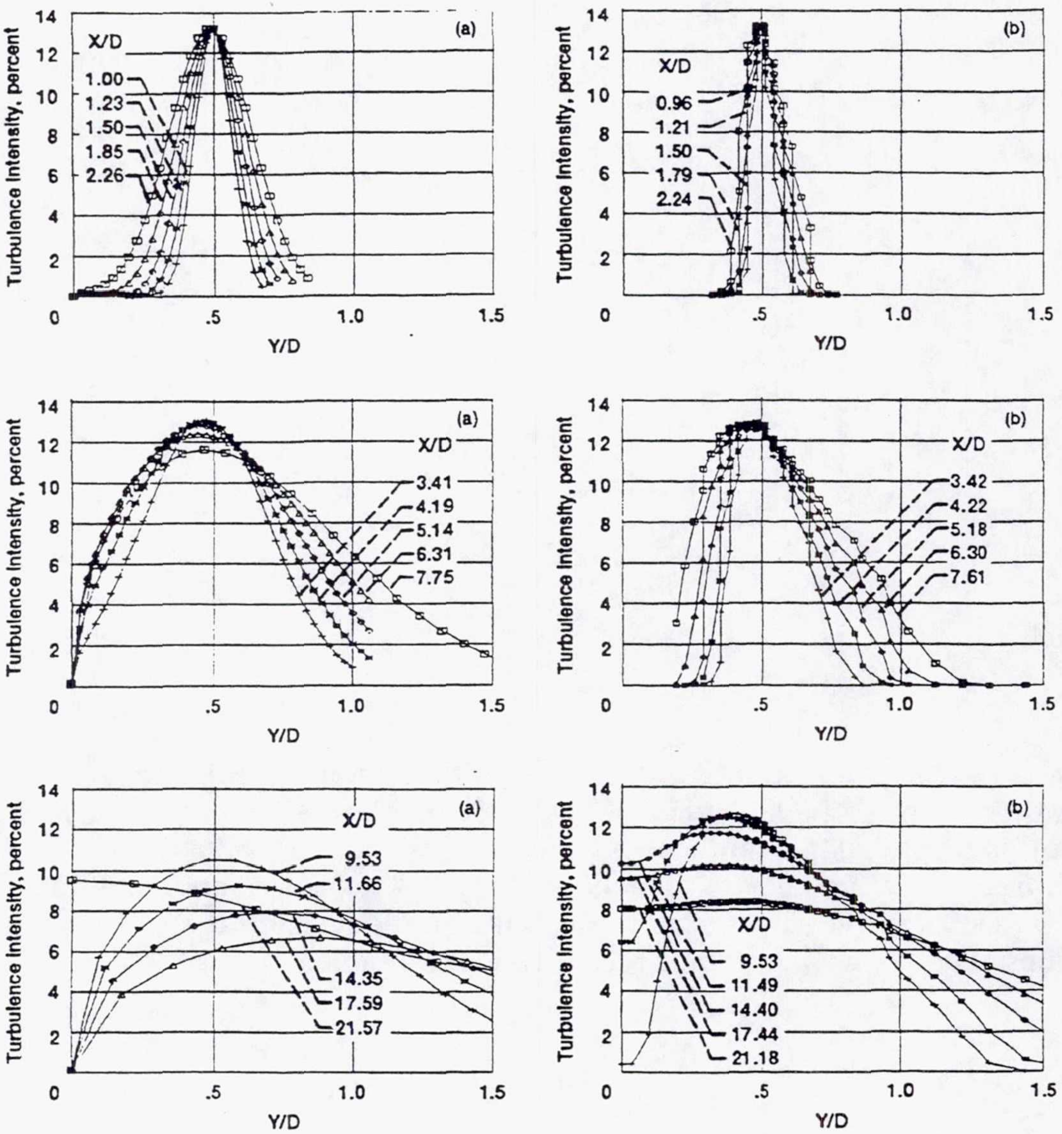

Comparison of turbulent intensity between (a) Reichardt's theory (b) PARC-kϵ. The radial profiles of turbulence can be compared at various axial locations. Figures (b) show that the centerline value of turbulent intensity peaks at X/D = 14.4 which is nearly twice the length of the potential core for this jet and decays farther along the jet. This is in agreement with experimental observations. Reichardt's model, on the other hand, fails to properly predict radial profiles of turbulence farther downstream of the potential core.

STROUHAL NUMBER

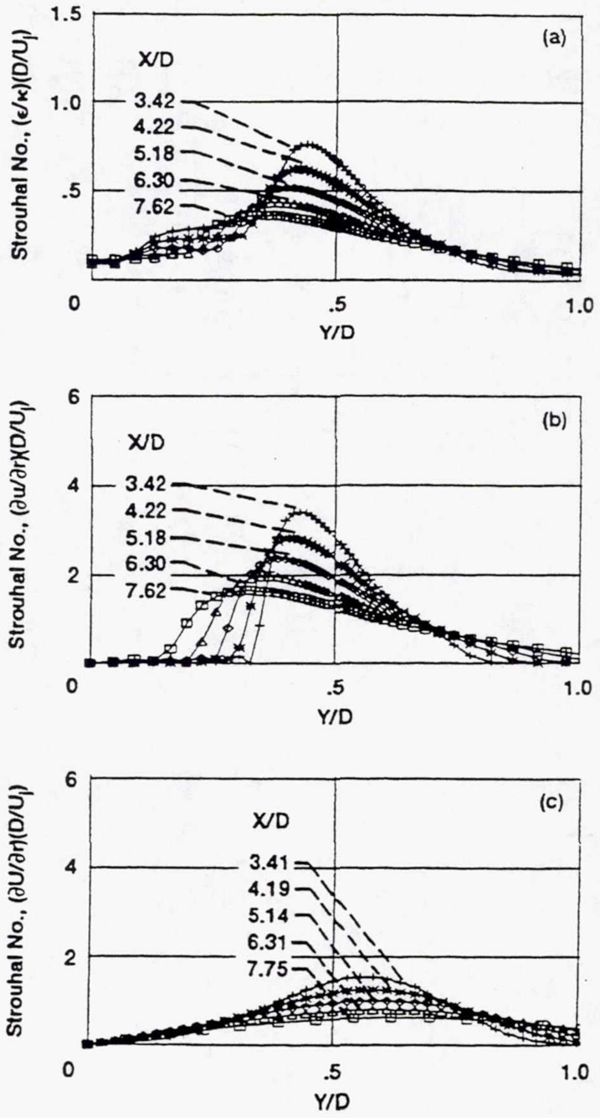

The Strouhal number based on the inverse of the characteristic time delay of correlation nondimensionalized with respect to jet exit velocity and diameter. Figures (a) and (b) are concluded from PARC results using the two definitions ϵ/k and $\partial U/\partial r$ respectively. They show that, outside a proportionality constant, similar results can be obtained for the correlation time factor as a function of source location. Figure (c) is based on Reichardt's aerodynamic predictions and should be compared with Figure (b).

COMPARISON OF OVERALL SOUND PRESSURE LEVEL DIRECTIVITY WITH DATA

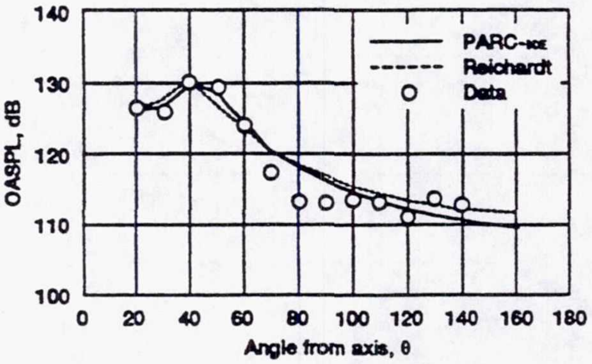

The overall sound pressure level directivity (OASPL) as estimated from PARC-kϵ is compared with data and predictions of Reichardt aerodynamic theory (on a 40 foot radius). The characteristic time delay τ_o is obtained from $1/\tau_o = 2(\epsilon/k)$. The convection constants α_c and β_c are determined empirically.

COMPARISON OF SPECTRAL COMPONENTS OF NOISE WITH DATA

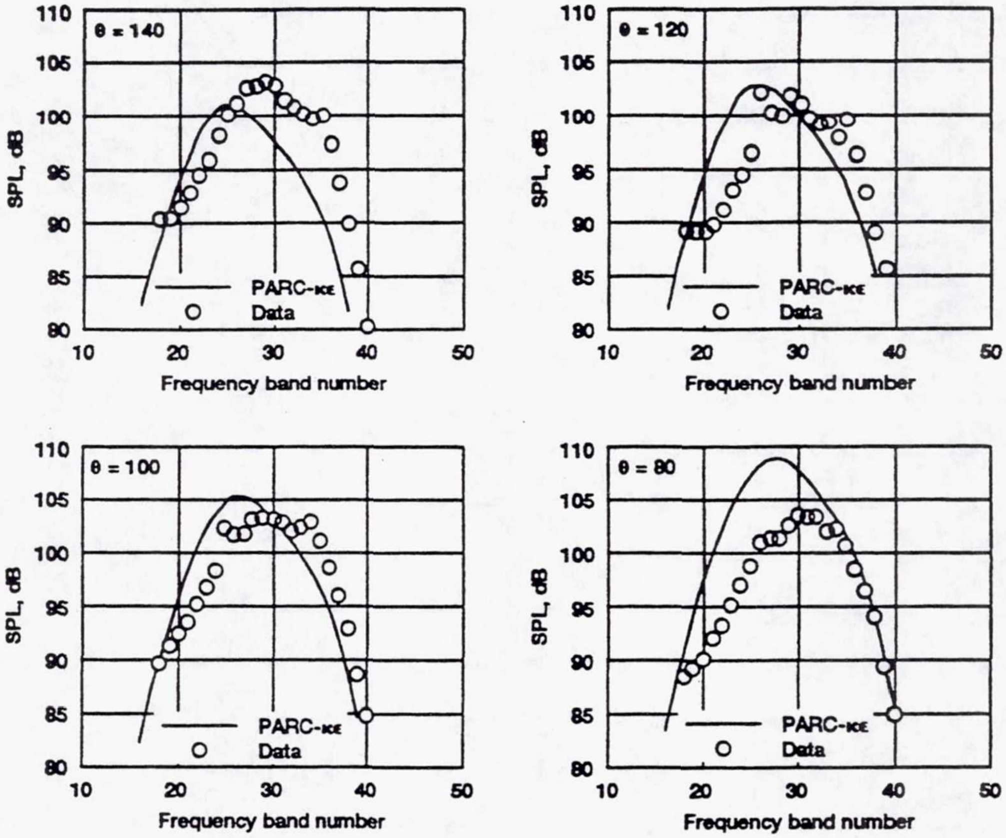

Comparison of noise spectra with data (based on 1/3 octave center frequency) at various observation angles. Band number 24 corresponds to 1 kHz.

COMPARISON OF SPECTRAL COMPONENTS OF NOISE WITH DATA

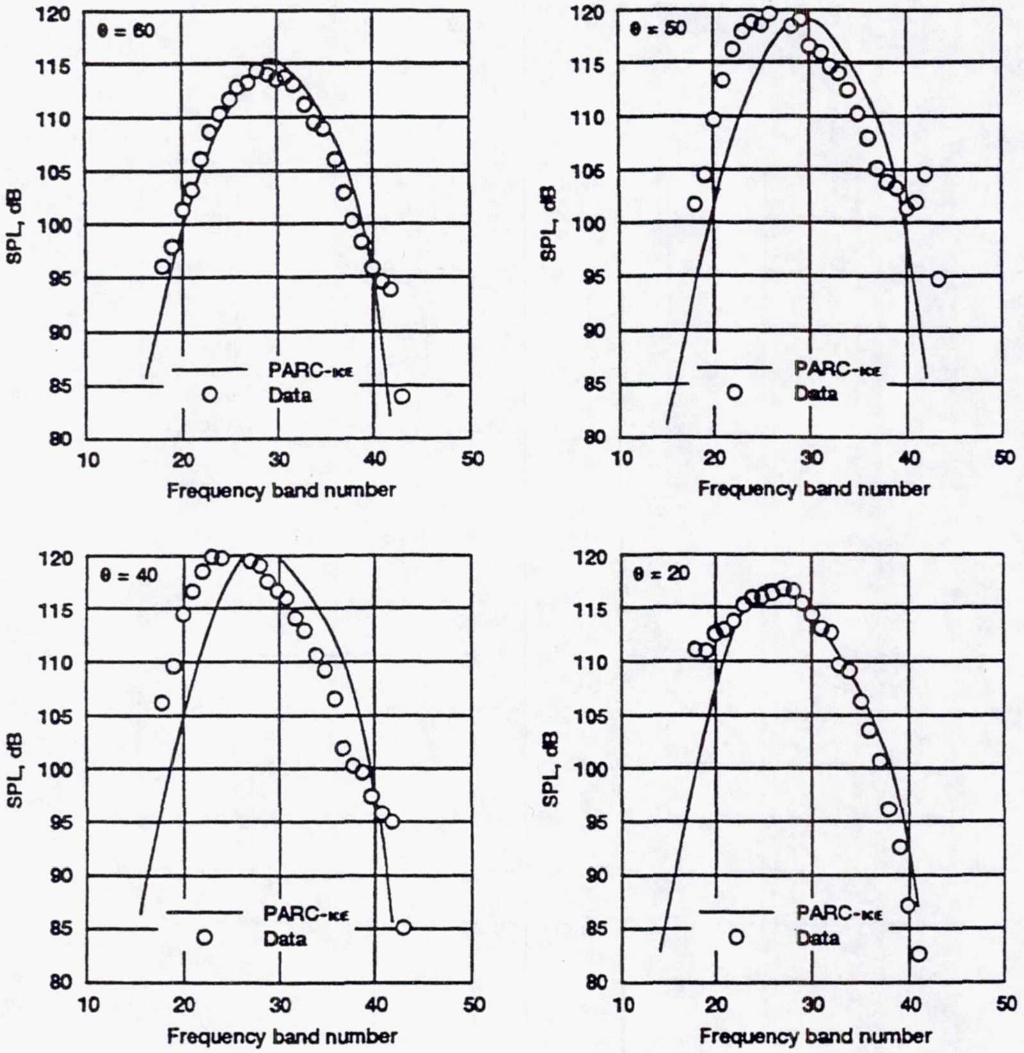

Comparison of noise spectra with data (based on 1/3 octave center frequency) at various observation angles. Band number 24 corresponds to 1 kHz.

SUMMARY

- Source Strength has been successfully predicted using PARC code with a k–ϵ turbulence model
- The limitation on aerodynamic grid selection has been removed by adopting a two-stage aerodynamic and acoustic algorithm
- The time-delay of correlation was calculated directly from kinetic energy of turbulence and its dissipation rate
- Constants used in supersonic convection factor need to be determined empirically
- The SPL directivity and spectra demonstrate good agreement with data especially at angles where mixing noise is dominant

OMIT THIS
PAGE

Session V

Analytical Aeroacoustics II

1999176561

NOISE FROM SUPERSONIC NON-CIRCULAR JETS

S24-71

Philip J. Morris and Dennis K. McLaughlin
Pennsylvania State University
University Park, Pennsylvania

409549
24P.

Sources of Supersonic Jet Noise

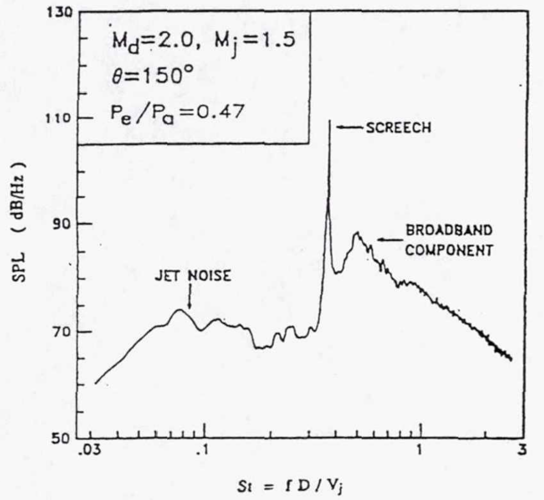

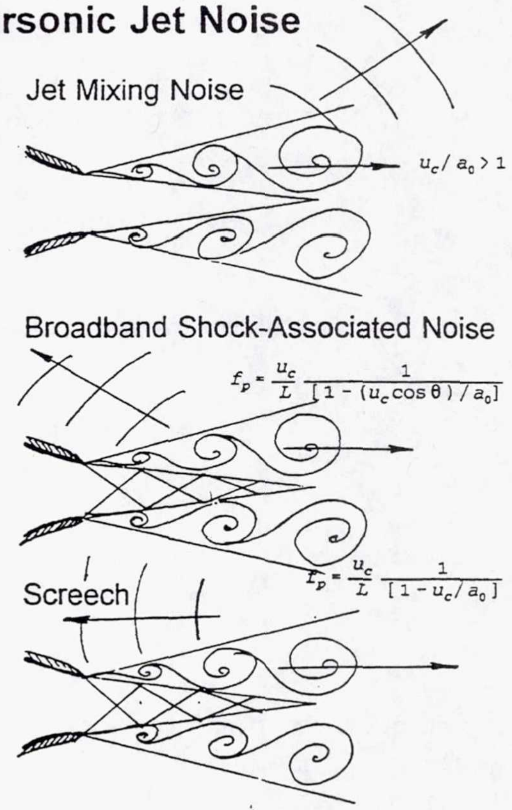

The three main sources of noise in supersonic jets are jet mixing noise, broadband shock-associated noise, and screech. Each of these noise sources may be associated with the large-scale structures in the jet mixing layer. These large-scale structures are also responsible for the gross mixing of the jet. As is discussed below, these structures have a high axial coherence and are both temporally and spatially nearly periodic. In circular jets they may be axisymmetric or helical in nature with the latter form dominating at high jet exit Mach numbers. When the structures convect downstream supersonically *with respect to the ambient speed of sound* they radiate intense noise, predominantly in the downstream arc. This noise mechanism is called *jet mixing* or *eddy Mach wave* noise. If the jet is operating off-design a quasi-periodic shock-cell structure is formed in the jet plume. The interaction between the downstream-travelling large-scale turbulent structures in the jet shear layer and the shock-cell structure results in *broadband shock-associated noise*. This noise source radiates predominantly in the upstream arc with a peak frequency that depends on the shock cell spacing, the convection velocity of the large-scale turbulent structures, and the angle to the jet downstream axis. When this interaction noise radiates directly upstream it can trigger the phase-locked shedding of large-scale vortex structures from the jet lip. This results in *jet screech*. This is an intense, tonal noise radiation with a frequency that also depends on the shock cell spacing and the convection velocity of the large structures.

Jet Noise Theories

Acoustic Analogy (Lighthill, FFowcs-Williams)

Extended Analogies (Phillips, Lilley)

Instability Wave Models (Tam, Morris)

Direct Simulation (CAA)

The earliest theories of jet noise were based on the *acoustic analogy* approach. This includes the original work of Lighthill and extensions to high speed jets by Ffowcs-Williams In these models, the entire jet noise source field is replaced by an equivalent distribution of sources radiating into an otherwise uniform fluid. Exact solutions may be obtained for such a model; however the details of the noise sources are contained in the unsteady turbulent flow of the of the jet and must be modeled empirically. It should be noted that, though this formulation is an exact manipulation of the equations of motion, predictions depend on an empirical description of the jet turbulence. Later work by Phillips and Lilley introduced a convected wave equation formulation of the acoustic analogy that accounted explicitly for the effects of the jet mean flow: refraction effects. For supersonic jets, instability wave models developed by Tam and Morris linked the jet mixing noise radiation to the large-scale instability waves in the jet. In this case, both the large-scale unsteady flow properties and their acoustic radiation were modeled and calculated directly. Finally, recent advances in computer capabilities make the direct numerical simulation of both the turbulent flow field and the radiated sound field a viable proposition.

Calculations for Circular Jets

Jet Mixing Noise

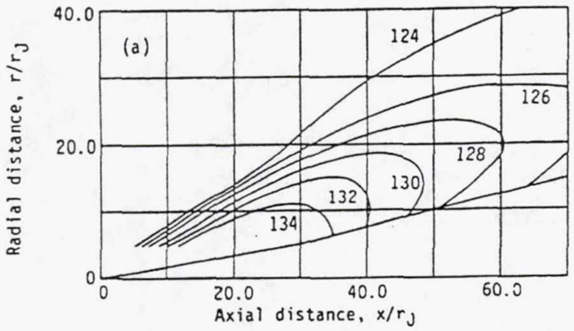

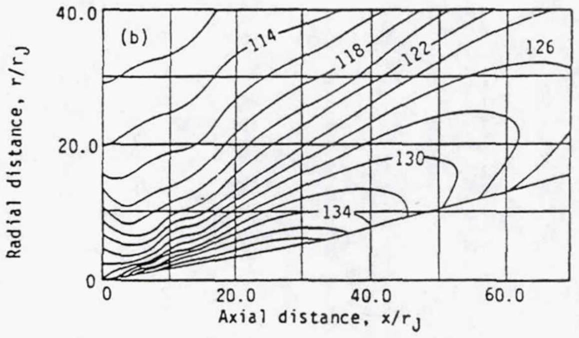

Calculations
Morris and Tam (1979)

Experiment
Yu & Dosanjh (1971)

Morris and Tam (1979) and Tam and Burton (1984) made predictions of the noise radiated by supersonic circular jets on the basis of an *instability wave model.* In this model the large-scale structures were described as instability waves supported by the jet's mean flow. The effects of the slow divergence of the mean flow in the axial direction were included through the use of a multiple-scales analysis. The instability waves in the flow were matched to their outer acoustic field with the method of matched asymptotic expansions. Comparisons between the predictions and measurements of both the near and far pressure fields in high and low Reynolds number experiments were very good.

Calculations for Circular Jets

Broadband Shock-Associated Noise

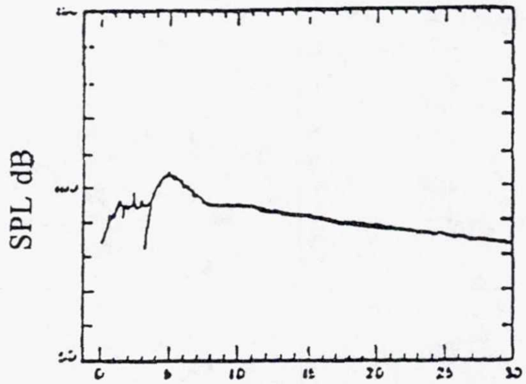

Tam (1987): M_j=1.67, M_d=1.5, θ =90

Tam (1987) also made predictions of broadband shock-associated noise in circular jets. The model was based on a description of the large-scale turbulent fluctuations in the jet shear layer as a random superposition of instability waves. The shock-cell structure was calculated using a linearized model. The broadband shock-associated noise sources were modelled as the weakly nonlinear interaction between the downstream travelling large-scale structures and the quasi-periodic shock-cell structure. A semi-empirical prediction scheme was developed on the basis of this model that captured, reasonably well, the amplitude, directivity, and frequency spectrum of the broadband shock-associated noise.

Calculations for Circular Jets

Screech

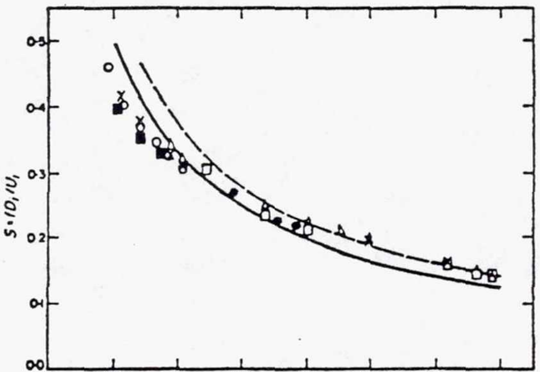

Tam, Seiner & Yu (1986): $1.0<M_d<2.0$

A model for the screech tones in circular supersonic jets operating off-design has been developed by Tam, Seiner and Yu (1986). This model once again is based on the interaction between the large-scale structures in the jet shear layer and the quasi-periodic shock-cell structure as the noise source. However, in this case, the interaction noise that radiates directly upstream triggers the shedding of vortices at the jet exit. These, in turn, interact with the shock-cell structure to produce noise. This can occur in a phase-locked loop producing intense tonal noise radiation. The theory is able to predict the frequency of the screech but not its amplitude.

Calculations for Non-Circular Jets

Screech

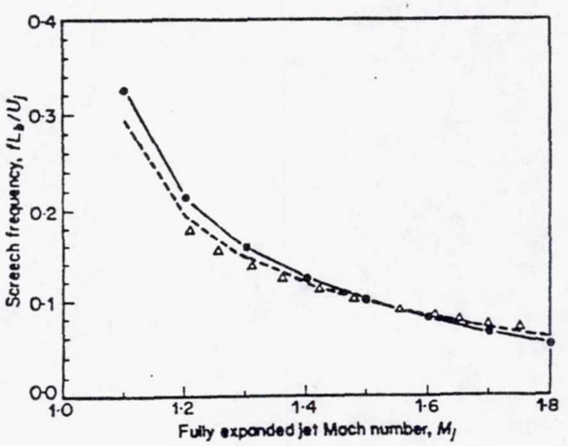

Morris, Bhat & Chen (1989)

The screech frequency depends on the shock-cell spacing in the jet. The shock-cell structure may be modeled as a pressure perturbation at the jet exit that drives "wave-guide" modes in the jet column. In the simplest case the jet, acting as a wave-guide, may be described as a cylindrical vortex sheet. The shock-cell spacing depends on the jet operating conditions and the jet exit geometry. The effects of jet geometry were included by Morris, Bhat and Chen (1989). They used a boundary-element method to account for the effects of arbitrary jet exit geometry on the shock-cell spacing. Predictions of the shock-cell spacing and screech frequency for circular, elliptic and rectangular jets agreed very well with measurements. The figure shows a prediction of screech frequency (Strouhal number) as a function of fully-expanded jet Mach number for an elliptic jet with aspect ratio 2:1.

Calculations for Non-Circular Jets

Shock Cell Structure

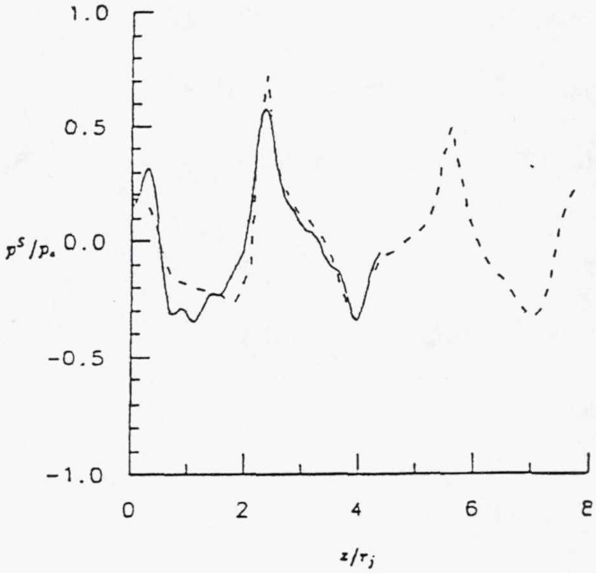

Bhat & Morris (1990)

The shock-cell structure in a jet operating off-design may be described reasonably well with a vortex sheet model for the jet. However, the details of the shock-cell pressure perturbations depends on the damping effects of the turbulence in the jet shear layer and the slow variation of the jet radius in the axial direction. These effects were included in a model for the elliptic jet by Bhat, Morris and Baty (1990). The mean flow divergence effects were described with a multiple scales analysis and an eddy viscosity was used to describe the damping effects of the jet turbulence. Predictions and measurements for an elliptic jet are shown below.

Noise Radiation from Elliptic Jets

General Formulation

Problem formulated in Elliptic Cylindrical Coordinates

Inner Solution:

- Large Scale Structures/Instability Waves
- Method of Multiple Scales

Outer Solution:

- Wave Equation

Matching of Inner and Outer Solutions:

The procedure for the calculation of noise radiation by non-circular jets follows that developed for circular jets. However, the analysis and numerical calculations are more complicated. The problem is first formulated in elliptic cylindrical coordinates. The large-scale structures are described as instability waves driven by the jet mean flow. The effects of flow divergence are accounted for with the method of multiple scales. The pressure fluctuations outside the jet are described by the wave equation in elliptic cylindrical coordinates. Solutions may be found in terms of Mathieu and modified Mathieu functions. This outer solution for the sound field and the inner solution for the instability waves may be matched using the method of matched asymptotic expansions. The far field noise is obtained from the method of stationary phase. Further details of the analysis are contained in Morris and Bhat (1991).

Mode Classification in Elliptic Jets

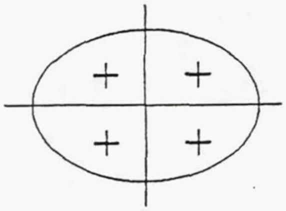

ce$_{2n}$: Varicose Mode

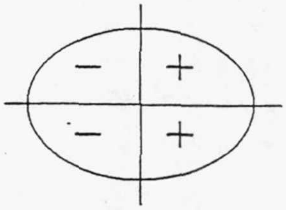

ce$_{2n+1}$: Flapping Mode: Minor

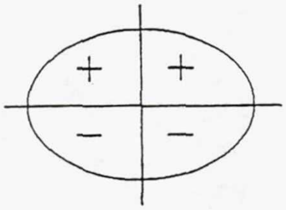

se$_{2n+1}$: Flapping Mode - Major

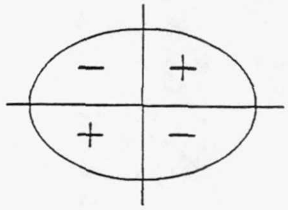

se$_{2n}$

In a circular jet the large-scale structures or instability waves are classified by their azimuthal mode number. Mode number zero corresponds to an axisymmetric structure and higher mode numbers give helical disturbances. These motions have been observed in low and high speed circular jets. In the elliptic (and rectangular) jet the type of structures that are possible depend on their symmetry properties about the major and minor axes. A mode that is even about both axes is called the *varicose* mode. This corresponds to the axisymmetric mode in the limit of a circular jet. A mode that is even about the minor axis but odd about the major axis is a *flapping* mode about the major axis. For high aspect ratio jets or two-dimensional jets this is expected to be the dominant instability. There is also a flapping mode about the minor axis and a mode that is odd about both major and minor axes. The various modes may be classified in the elliptic jet case by their Mathieu function type. $\boldsymbol{ce}_{2n}$ is the varicose mode; $\boldsymbol{se}_{2n+1}$ is the flapping mode about the major axis.

INNER SOLUTION FOR THE INSTABILITY WAVES/LARGE-SCALE STRUCTURES

Variation of Axial Growth Rate

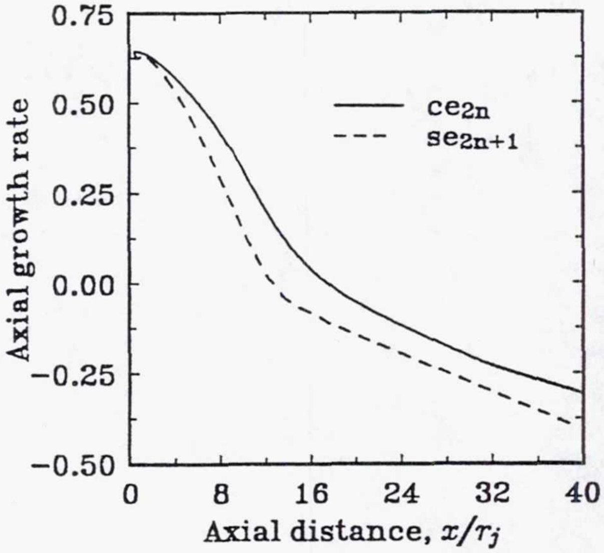

The solution of the equations for the instability waves or large scale structures determines the axial growth rate and wavenumber of a given frequency disturbance. Calculations have been performed a limited number of frequencies and jet operating conditions. The figure shows the axial variation of the growth rate for a Strouhal number 0.2 instability wave in an aspect ratio 3:1 elliptic jet. The jet is operating on-design with an exit Mach number of 2.0 and a jet static temperature ratio of 1.0. Calculations are shown for both the varicose and flapping modes. The varicose, $\boldsymbol{ce}_{2n}$, mode is more unstable than the flapping, $\boldsymbol{se}_{2n+1}$, mode for this operating condition and reaches its maximum amplitude, where the growth rate is zero, further downstream.

Variation of Axial Phase Velocity

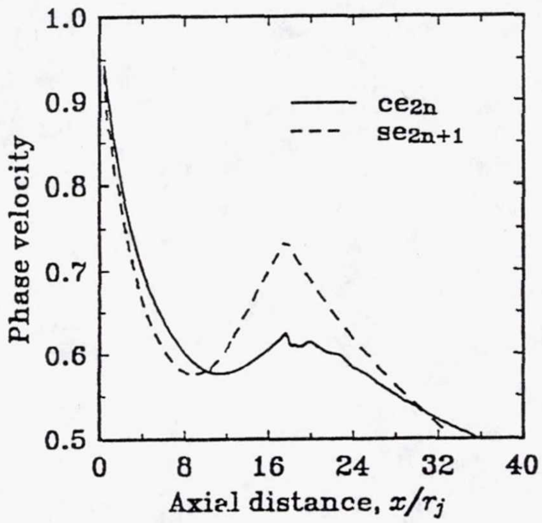

The phase velocity of the instability wave or large-scale structure is given by the ratio of its frequency to its wavelength. The figure below shows the axial variation of the phase velocity for the varicose and flapping modes for the operating conditions of the previous figure. The phase velocities of the two modes are very similar in the potential core region varying from the jet exit velocity to 60% of the jet velocity. Downstream of the end of the potential core the phase velocity decreases, being approximately proportional to the jet centerline velocity. For these jet operating conditions any wave of constant amplitude with a phase velocity greater than 50% of the jet exit velocity radiates energy to the far field. This is described qualitatively in the next figure.

LARGE-SCALE STRUCTURE WAVENUMBER SPECTRUM AND RADIATED NOISE

Amplitude and Phase Variation of Large Scale Structure/Instability Wave

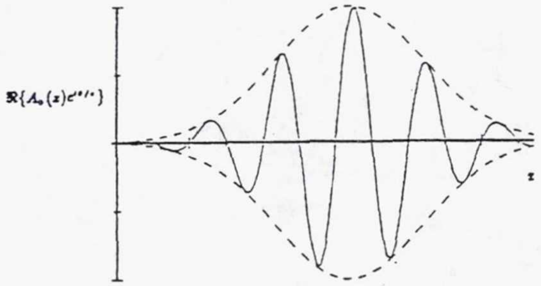

Wavenumber Spectrum

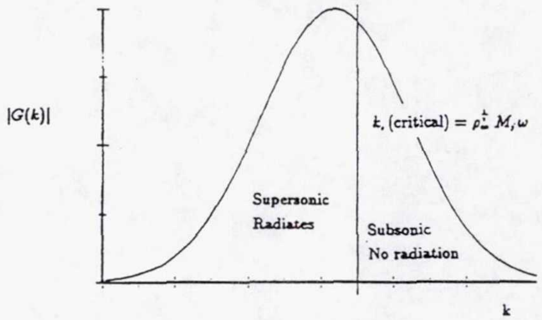

In the inner region the instability wave has an amplitude that grows initially and then eventually decays at larger axial distances. The wave fronts also travel downstream at a certain phase velocity. When this inner solution is matched with the outer acoustic solution it is found that only those components of the wave's wavenumber spectrum that are supersonic with respect to the ambient speed of sound can radiate to the far field. This is directly related to the problem of the wavy-wall. If the wall moves subsonically the pressure perturbations decay exponentially with distance normal to the wall. If the wall is moved supersonically the pressure perturbations remain constant along the characteristic directions and propagate to the far field. In the jet case the critical wavenumber is given by

$$M_j \omega \rho_a^{1/2}$$

where M_j is the jet Mach number, ω is the wave frequency, and ρ_a is the ratio of the ambient and jet densities. The directivity in the far field is related directly to the variation of the amplitude of the wavenumber spectrum with wavenumber.

LARGE-SCALE STRUCTURE WAVENUMBER SPECTRUM

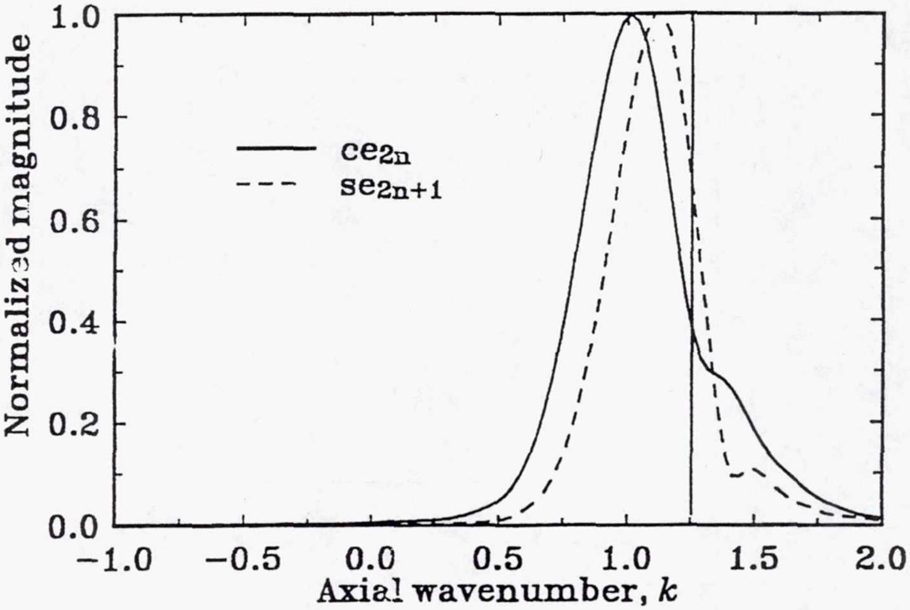

This figure shows the calculated wavenumber spectra for the varicose and flapping modes at the same frequency and operating conditions given before. The varicose mode spectrum peaks at a lower wavenumber than the flapping mode. This corresponds to a larger radiation angle to the jet downstream axis. Since the relative initial levels of the two modes are unknown, the wavenumber spectra have been normalized by their peak amplitudes. The corresponding far field directivities are shown in the next two figures.

Far Field Directivity: Flapping Mode

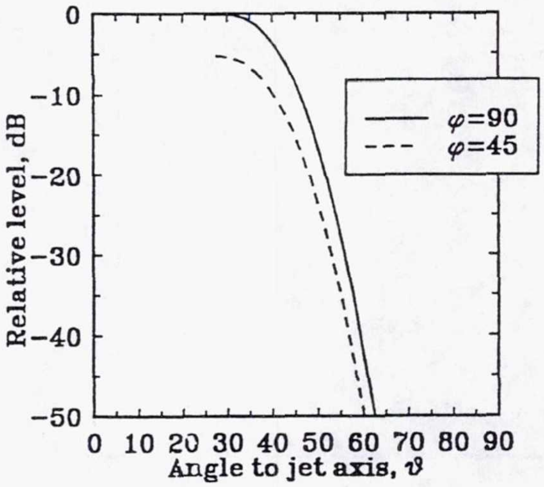

This figure shows the predicted far field directivities for the flapping mode. The angle ϕ, gives the azimuthal angle relative to the major axis plane. That is $\phi = 0$ corresponds to the major axis plane and $\phi = 90$ corresponds to the minor axis plane. The flapping mode radiates most strongly in the minor axis direction and does not radiate at all in the major axis plane.

Far Field Directivity: Varicose Mode

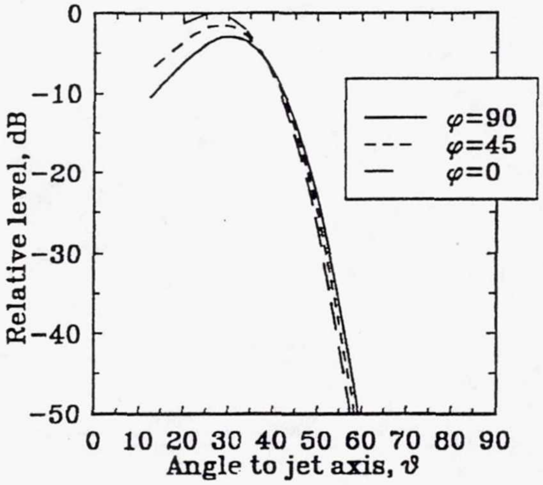

This figure shows the directivities for the varicose mode. At these operating conditions the varicose mode radiates most strongly in the major axis plane and has peak levels that are 4 to 5 dB lower in the minor axis plane.

Experimental Results

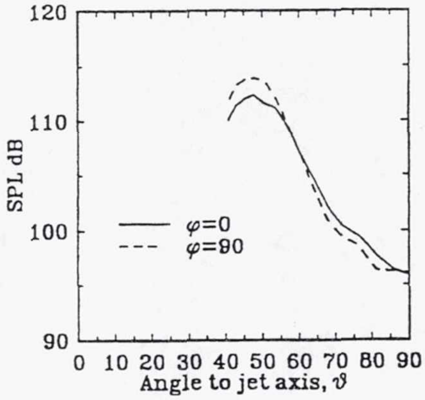

St=0.2, AR=3:1, M_j=2.0

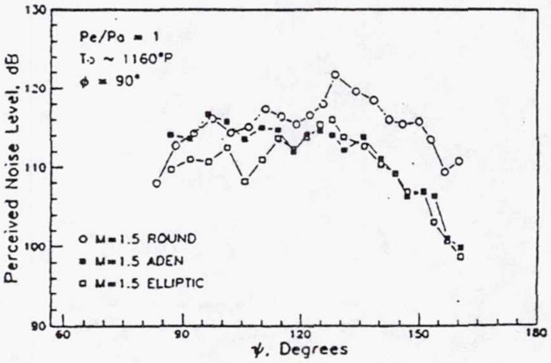

Perceived Noise Levels

Measurements of the noise radiation from supersonic elliptic jets operating both on- and off-design have been made at NASA Langley Research Center. The measured power spectral density levels at a Strouhal number of 0.2 on the major and minor axes are shown in the figure on the left above. The peak radiation angle is found at approximately 45° to the downstream axis. This is a higher angle than the predicted value of approximately 35°. The relative levels between the minor and major axes is approximately 4 dB; however, if the full spectral content is included, as in a perceived noise level calculation shown on the right below, the differences between the minor axis levels and those of a circular jet are seen to be much greater at all angles to the jet downstream axis.

Summary and Conclusions

Future Work:

Calculations for a wide range of operating conditions:

Build database for prediction purposes

Comparison with moderate and high Reynolds number experiments

Prediction of absolute levels

More robust numerical methods

It is planned to extend the present calculations to a wider range of jet operating conditions and instability wave frequencies. In addition, on the basis of these calculations, it is planned to assemble a database that will be used in a semi-empirical prediction scheme for design purposes. It is also planned to compare the predictions with both high and moderate Reynolds number experiments that are described below. This will also provide information on the relative levels of the various modes and give guidance as to how this modal content may be modeled. Predictions are also underway for a circular jet with the goal of calculating the absolute levels of the radiated noise. Finally, more robust numerical schemes than those presently in use are being developed.

THE LOW TO MODERATE REYNOLDS NUMBER APPROACH

Schematic of the jet noise facility test chamber

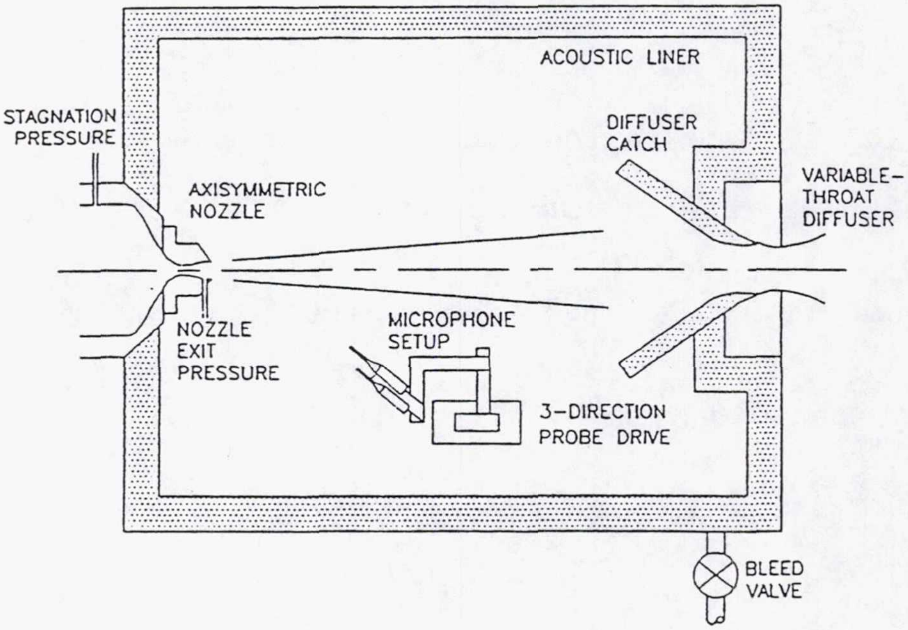

Low to moderate Reynolds number jets have been used successfully in the past to identify large scale structures in axisymmetric jets as major noise producers. At moderate Reynolds numbers, the radiated noise is very similar in directivity and spectral distribution to conventional high Reynolds number jets. The lower Reynolds numbers, however, allow the relationship between the flow instability waves and radiated noise to be more easily quantified. At the typical lower flow densities of these jets, hot-wire anemometry and artificial flow excitation by glow discharge devices are much easier to implement. Therefore, noise reduction techniques which require control over flow instabilities can be investigated in the low to moderate Reynolds number regime and then later applied to the high Reynolds number. Investigations into these types of noise reduction schemes are very difficult in more conventional high Reynolds number jets due the high levels of small scale turbulence present.

PRESENT EXPERIMENTAL FOCUS

The present experimental focus is on axisymmetric and elliptical (aspect ratios 2:1 and 3:1) jets operating at Mach numbers 1.5 to 2.0. The low densities of hot jets are simulated using helium and air mixture jets. Various excitation schemes using different glow discharge geometries will be used in an attempt to determine the modal content of the instabilities in the initial flow developmental regions of the jets. Identifying the modal content of the elliptic jet is particularly important in validating current analytical prediction methods that require the modal content as input for jet initial conditions. The effect of exciting or suppressing different modes on the noise radiation will also be investigated.

SIMULATION OF HOT-AIR JETS WITH HELIUM/AIR MIXTURE JETS

M = 1.5 AXISYMMETRIC JETS; r/D = 40

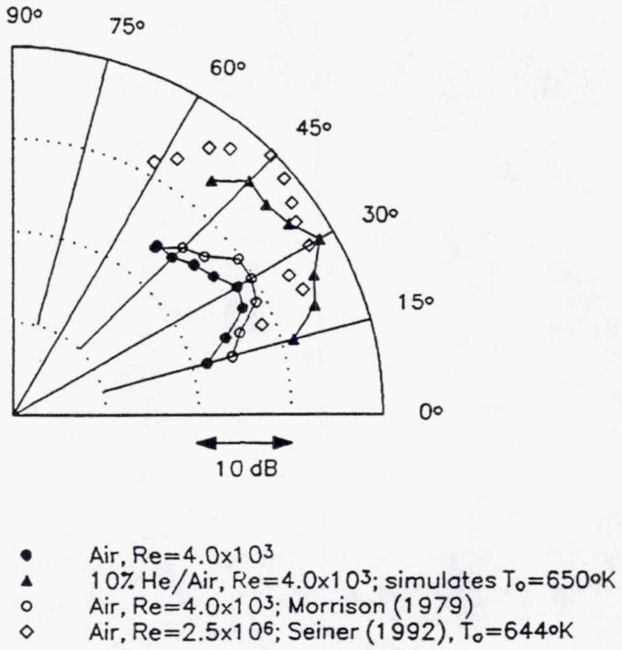

Successful simulation of the hot air jets using helium/air mixture jets is demonstrated in this figure where the OASPLs are compared for both the jets operating at M = 1.5. The OASPLs for helium/air mixture jets are measured along a circular arc of 40 diameters centered at the nozzle exit. The data for the hot jets are extrapolated from the far field to r/D = 40. The noise levels measured from the hot jets are significantly higher than from comparable cold jets.

SOUND PRESSURE LEVEL DISTRIBUTION
M = 1.5

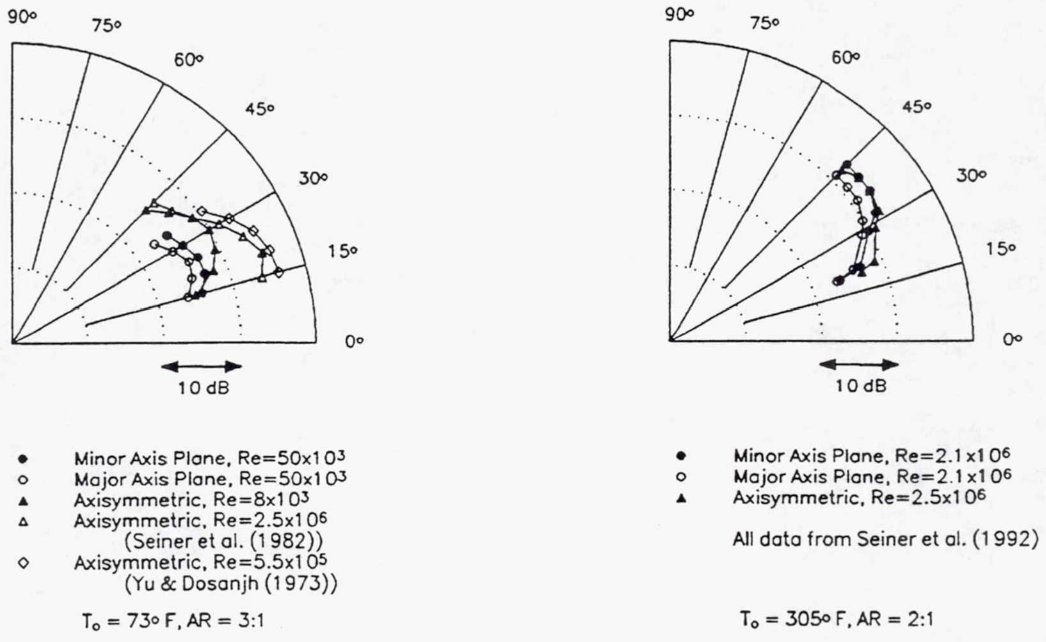

Measurements of both high and moderate Reynolds number jets show noise reduction in elliptical supersonic jets compared to their axisymmetric counterparts due to the increased mixing in the non-round geometry. The reduction in the major axis plane is higher than in the minor axis plane. Higher noise reduction from the elliptic jets compared to round jets, is expected from the helium/air mixtures simulating hotter jets.

Most dominant jet instability Strouhal number vs.
simulated-jet to ambient temperature ratio
M = 2.1, Re = 8400

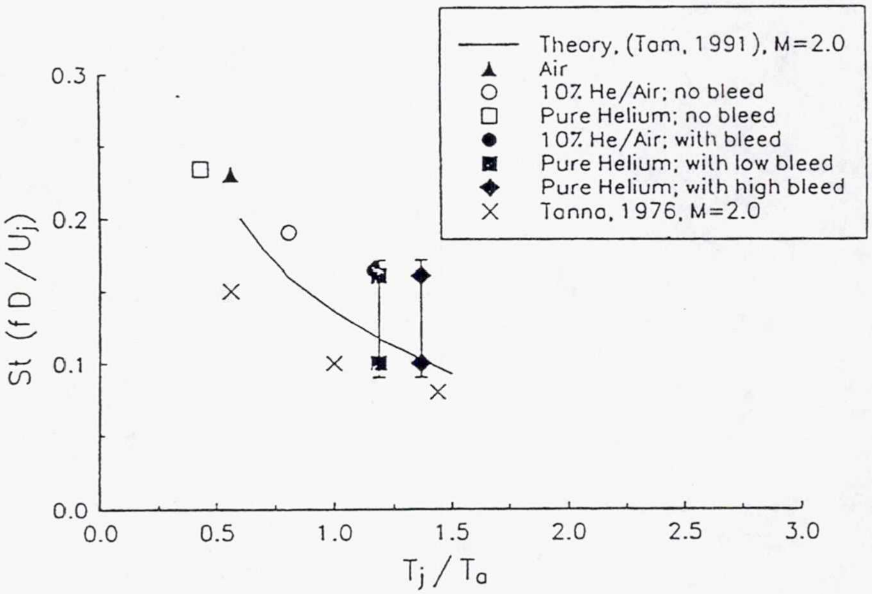

The Strouhal number of the most dominant jet instability as a function of the ratio of simulated-jet to ambient temperature is shown for the present study and for the work of other experiments and theorists. The bars indicate a range of frequencies with significant amounts of energy. The effective temperature ratio is inversely related to the jet to ambient density ratio. Due to the enclosed nature of the test chamber, as an experiment progresses, helium builds up in the test chamber and raises the jet to ambient density ratio, thus lowering the effective temperature ratio of the jet. To counter the helium accumulation in the test chamber, atmospheric air is bled into the test chamber through a bleed valve. The remarks to bleed in the legend indicate how much outside air is bled into the test chamber during the experiment. Higher bleed conditions result in higher effective temperature ratios. Although the frequency of the dominant jet instability is seen to increase as the effective jet temperature ratio is increased, the corresponding Strouhal number decreases due to a higher increase in the jet velocity. As is evident from the graph, the present experimental work agrees with existing measurements and theoretical predictions. Work now will proceed with determining the modal content of the hot jets.

The conclusions discussed in the previous slides are summarized.

CONCLUSIONS

- **Noise reductions of elliptic jets are significant, particularly in the major axis plane.**
- **Hot jets are successfully simulated using helium/air mixture jets.**
- **Measurements are performed for jets of pure air, pure helium and 10% helium by mass fraction.**
- **Helium/air jets radiate more noise than comparable jets of pure air due to the increased jet exit velocity.**
- **Frequency of the dominant jet instability increases with increasing helium concentration.**
- **The dominant Strouhal numbers measured for M=1.5 and M=2.1 jets exhibited good agreement with the predictions of Tam et. al.**

REFERENCES

Bhat, T. R. S., Morris, P. J. and Baty, R. S. (1990) "A linear shock cell model of non-circular jets using conformal mapping with a pseudo-spectral hybrid scheme," *AIAA Paper No*. 90-3960.

Morris, P. J. and Bhat, T. R. S. (1991) "The Prediction of Noise Radiation from Supersonic Elliptic Jets," *AGARD CP* 512, AGARD 78th B Specialists' Meeting, Bonn, Germany, pp. 20-1-20-12.

Morris, P. J. and Tam, C. K. W. (1979) "On the Radiation of Sound by Jets" in *Mechanics of Sound Generation in Flows*, Springer-Verlag.

Morris, P. J., Bhat, T. R. S. and Chen, G. (1987) "A linear shock cell model for jets of arbitrary exit geometry," *Journal of Sound and Vibration*, **132**(2), pp. 199-211.

Tam, C. K. W. and Burton, D. E. (1984) "Sound generated by instability waves of supersonic flows, Part 2. Axisymmetric jets," *Journal of Fluid Mechanics*, **138**, pp. 273-295.

Tam, C. K. W. (1987) "Stochastic model theory of broadband shock associated noise from supersonic jets," *Journal of Sound and Vibration*, **116**, pp. 265-302.

Tam, C. K. W., Seiner, J. M. and Yu, J. C. (1986) "Proposed relationship between broadband shock-associated noise and screech tones," *Journal of Sound and Vibration*, **110**(2), pp. 309-321.

1999176562

LARGE EDDY SIMULATION IN THE COMPUTATION OF JET NOISE

R.R. Mankbadi, M.E. Goldstein, L.A. Povinelli, M.E. Hayder, and E. Turkel
NASA Lewis Research Center
Cleveland, Ohio

S25-71

409551

8P.

Navier-Stokes Equations in Aeroacoustics

- **Noise can be predicted by solving Full (time-dependent) Compressible Navier-Stokes Equation (FCNSE) with computational domain extended to far field -- but this is not feasible.**

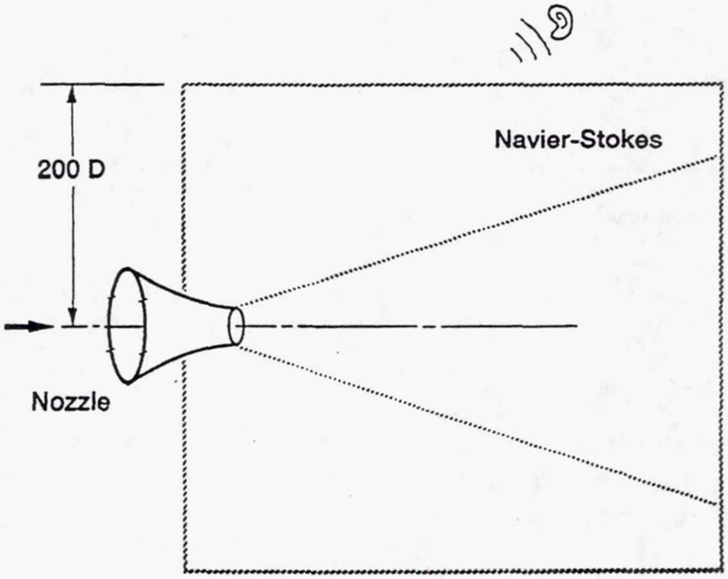

The fluctuating near field of the jet produces propagating pressure waves that produce far-field sound. The fluctuating flow field as a function of time is needed in order to calculate sound from first principles. Noise can be predicted by solving the full, time-dependent, compressible Navier-Stokes equations with the computational domain extended to far field --- but this is not feasible as indicated above. At high Reynolds number of technological interest turbulence has large range of scales. Direct numerical simulations (DNS) can not capture the small scales of turbulence. The large scales are more efficient than the small scales in radiating sound. The emphasize is thus on calculating sound radiated by large scales.

SUBSONIC JETS

- **Development of the coherent structure is largely controlled by the Strouhal number**

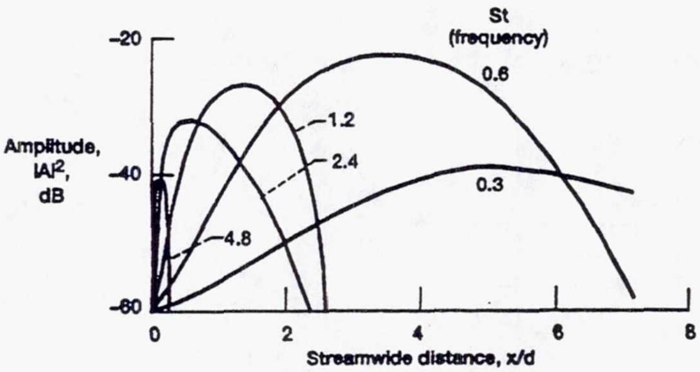

- **The structure is both axisymmetric and three-dimensional**

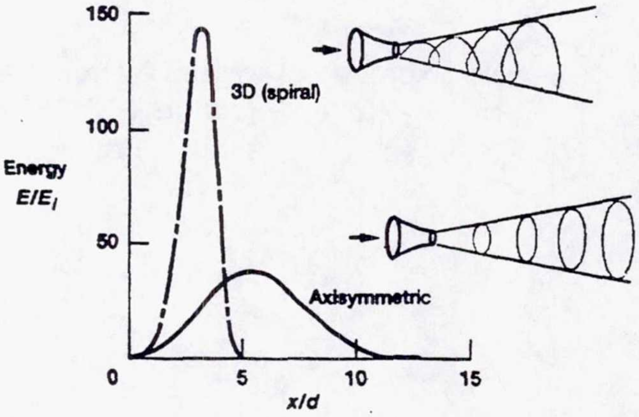

The large-scale structure in the initial region of the jet, where most of the noise is produced is modelled by extending ideas from the nonlinear stability theory. The large-scale component is modelled as

$$\tilde{u}_i = \Sigma_{m,n} |A_{mn}(x)| \; \hat{u}_{i,mn}(r,x) \quad \exp[i\psi_{mn}(x) \; - u\omega_m t \; + iN\phi] \; + CC \qquad (1)$$

The transversal profile is taken as the eigen function given by the locally-parallel linear stability theory. For a review on this approach see Mankbadi (1992, Applied Mechanics Reviews). The amplitude and phase are determined from nonlinear theory. Results of this theory as seen above indicates that the development of the large structure is largely controlled by the Strouhal number. At large-enough amplitudes the process is nonlinear in the sense that one mode can generate/cancel other modes, which represents a possible technique for noise control. The results also indicates that the three-dimensional mode of the structure could dominate the axisymmetric one, depending on the Strouhal number, initial conditions, and axial location.

● PREDICTION OF SUBSONIC JET NOISE USING LIGHTHILL'S THEORY

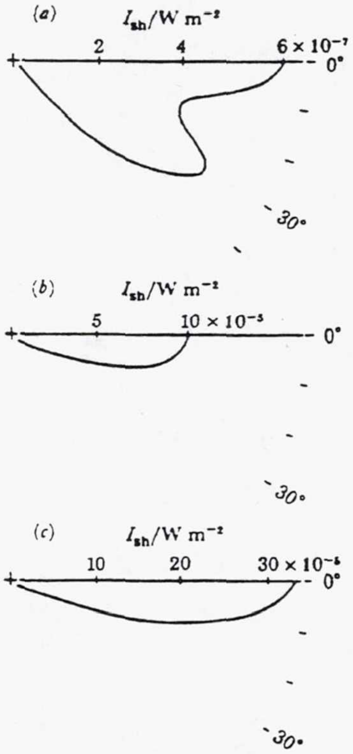

Polar distribution of the shear noise intensity I_{sh} for $n = 0$. (a) $St = 0.18$; (b) $St = 0.30$; (c) $St = 0.80$.

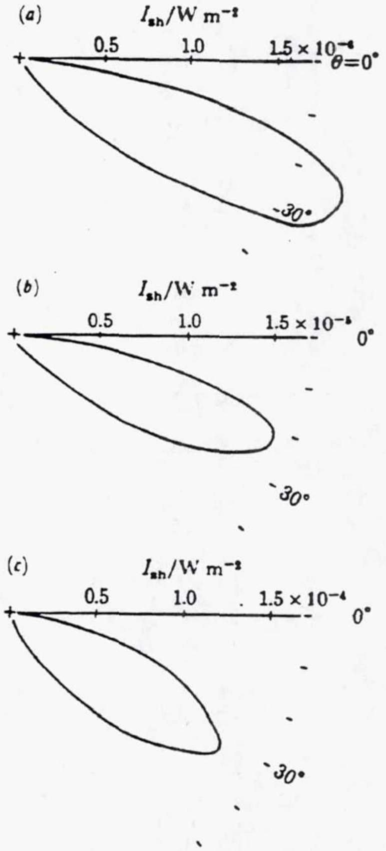

Polar distribution of the shear noise intensity I_{sh}(W m^{-2}) for $n = 1$. (a) $St = 0.18$; (b) $St = 0.30$; (c) $St = 0.80$.

The above shows the directivity of the axisymmetric modes and that of the first helical modes. These results are from Mankbaldi and Liu (1984) in which Lighthill's (1952) theory is used to calculate the shear noise produced by the large-scale structure in the initial region of the jet.

SUPERSONIC JET NOISE

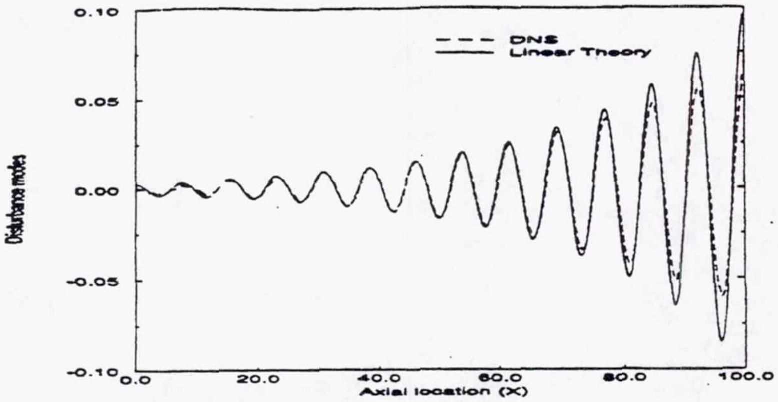

GROWTH OF DISTRUBANCE IN UNSTEADY AXISYMMETRIC JET

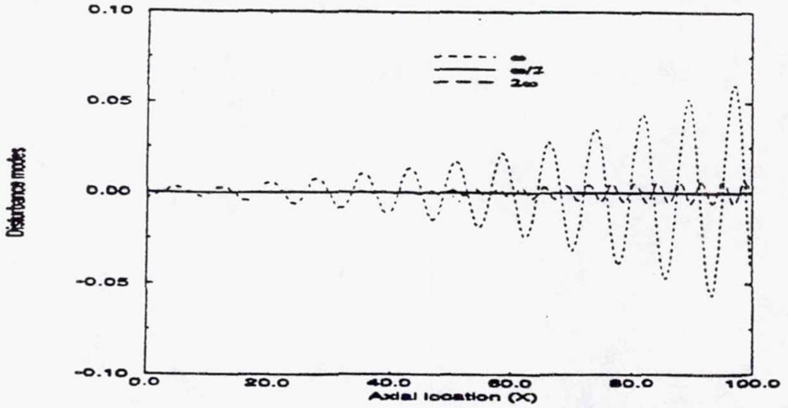

EXCITATION OF DISTURBANCE MODES IN AXISYMMETRIC JET AT $r = 1$

The large scale structure is calculated using the full Navier-Stokes equations. Gottlieb & Turkel scheme is applied to shear flows. The numerical scheme is fourth-order accurate in space and second-order accurate in time. The results are validated by comparing the predicted growth of input disturbance against the results of the linear stability theory. As the amplitude of disturbance becomes large nonlinearity come into effect and the linear stability theory is no longer valid.

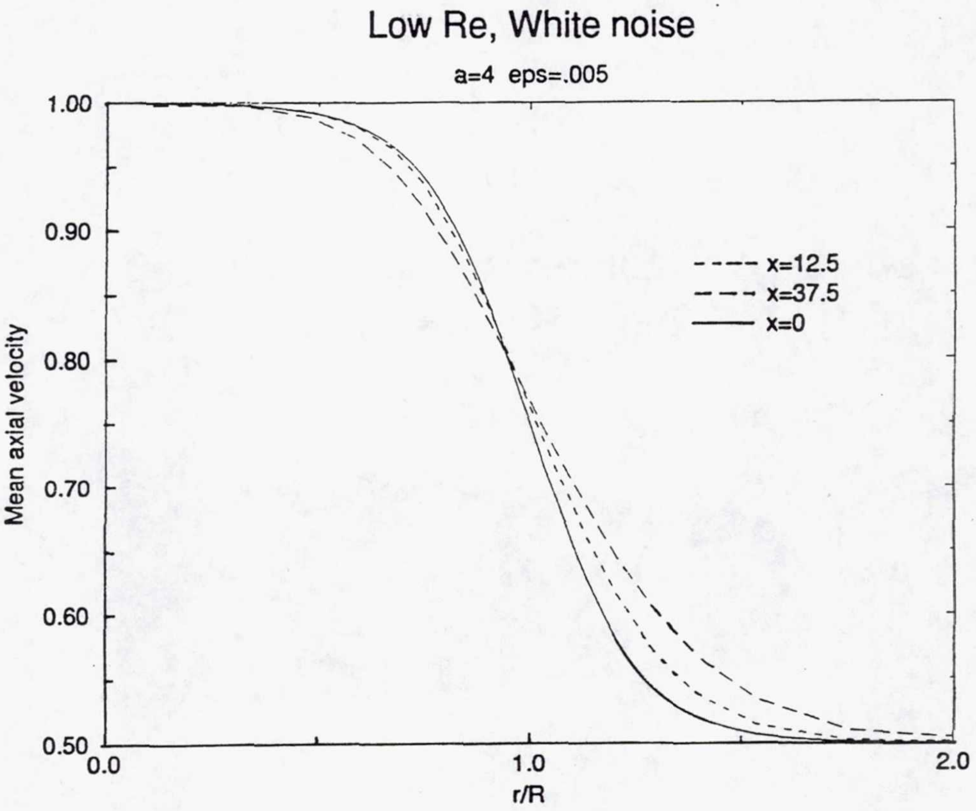

The small scale turbulence is modelled following Smagorinski's (1963):

$$\tau_{ij} = q_R^2 \delta_{ij} / 3 - 2\nu_R S_{ij} \tag{2}$$

where q_R^2 is the energy of the residual turbulence,

$$S_{ij} = \frac{1}{2}\left(\frac{\partial \langle u_i \rangle}{\partial x_j} + \frac{\partial \langle u_j \rangle}{\partial x_i}\right) \tag{3}$$

is the strain rate of the resolved scale, and ν_R is the effective viscosity of the residual field. Here we take

$$\begin{gathered} \nu_R = (C_S \Delta_f)^2 \sqrt{2 S_{mn} S_{nm}}\, , \\ C_S = 0.23 \end{gathered} \tag{4}$$

and Δ is the filter width.

The above figure shows the radial distribution of the mean flow axial velocity at several streamwise locations.

FOURIER COMPONENT OF NEAR-FIELD SOUND SOURCE

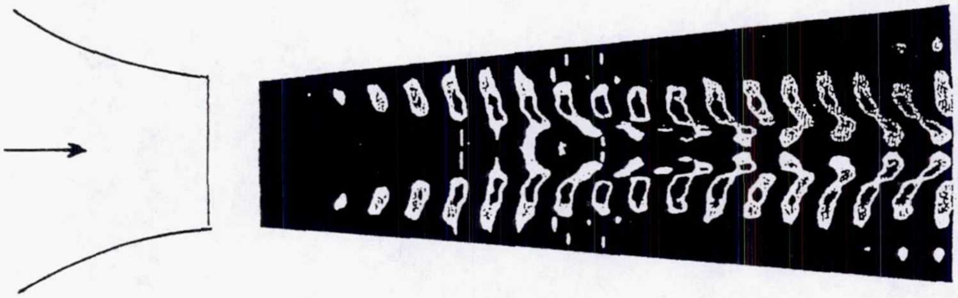

This figure shows the Fourier component of the near-field sound source (Strouhals number = 0.5) of a supersonic jet at Mach number 1.5 as seen by an observer in the far-field at 30° to the jet axis.

FUTURE PLANS

- Subgrid-Scale Models:

  Compressibility Effects -- Erelbacher (1990)
  Dynamical -- Moin et al. (1992)
  One-Equation Model -- Hortituti (1985)

- Validation of the near field against experimental results

- Far-Field Sound:

  Lilley (1974)
  Linearized Euler Equation

- Validation of the far-field sound against experimental data

1999176563

DIRECT NUMERICAL SIMULATION OF SUPERSONIC JET FLOW AND NOISE RADIATION

Christopher K.W. Tam and Jay C. Webb
Florida State University
Tallahassee, Florida

526-71

409552

14P.

OBJECTIVE

TO SIMULATE TURBULENT MIXING NOISE GENERATED DIRECTLY BY THE LARGE SCALE INSTABILITY WAVES OF THE SUPERSONIC JET

$M_j = 1.7 \qquad T_j / T_a = 1.0$

SOME ASPECTS OF DIRECT NUMERICAL SIMULATION

1. PHYSICAL DOMAIN

   Mapping -- Computation Domain

2. GOVERNING EQUATIONS

   Turbulence Modeling for Fine Scale Turbulence

3. COMPUTATION SCHEME

   Dispersion-Relation-Preserving Scheme and Artificial Selective Damping

4. RADIATION, OUTFLOW AND INFLOW BOUNDARY CONDITIONS

5. INITIAL CONDITIONS

   (Mean flow calculation is now possible)

6. INFLOW EXCITATION

   Excitation of Large Scale Instability Waves

7. COMPUTATIONAL DIAGNOSTICS

   Spectra and Directivities

May aspects are involved in performing direct numerical simulation. Here I have listed seven items. We have completed the first five. This will allow us to compute the time independent mean flow.

1. PHYSICAL DOMAIN

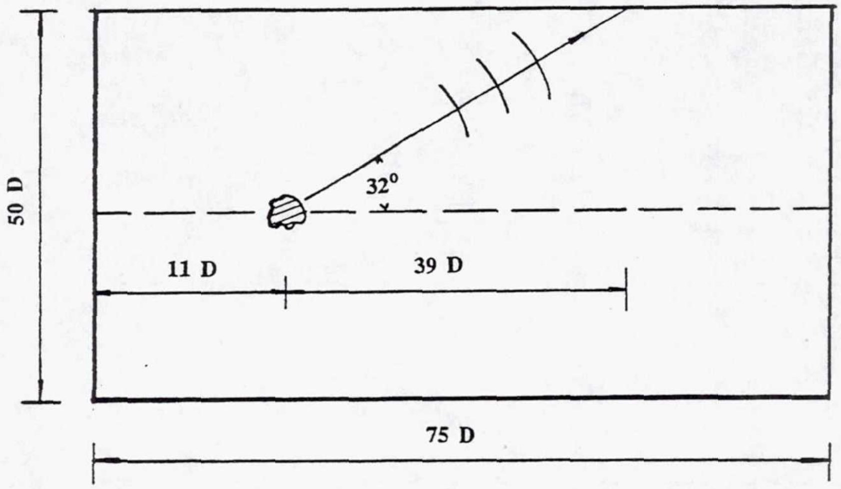

$M_j = 1.7$ $\quad$ $T_j / T_a = 1.0$

Speed of instability wave = $0.7 \times 1.7\ a_0 = 1.19\ a_0$

$\theta = \arccos(a_0 / 1.19\ a_0) = 33^\circ$

We choose a physical domain of 75 jet diameter by 50 jet diameter. This size is needed to capture the directivity of the radiated sound from the supersonic jet. We estimate that the peak noise occurs at 50 jet diameter downstream along the upper and lower edge of the computation domain. At 75 diameter downstream the outflow Mach number is about 0.5

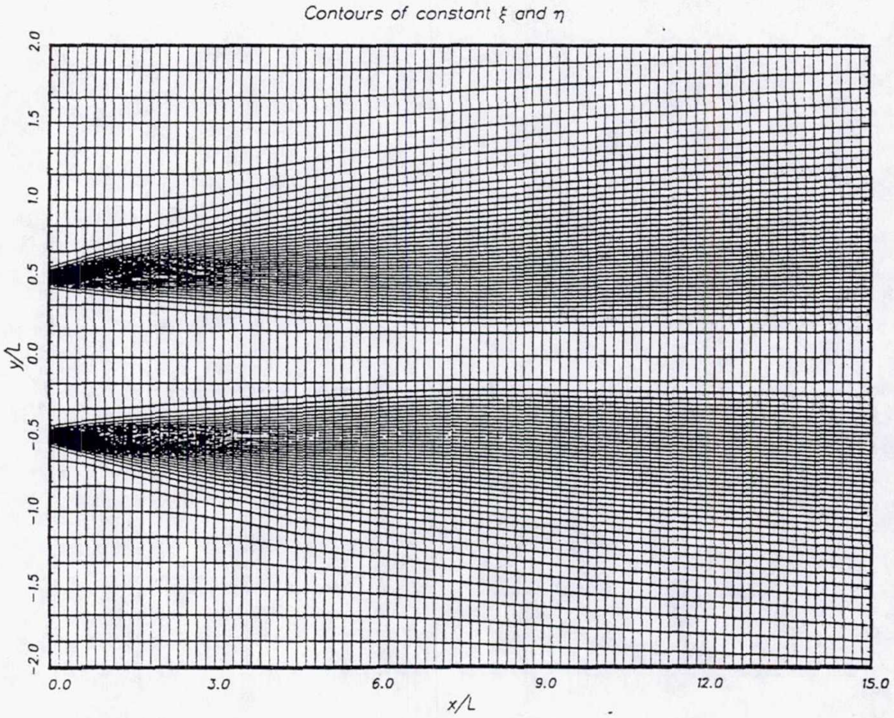

Mapping near the nozzle exit region

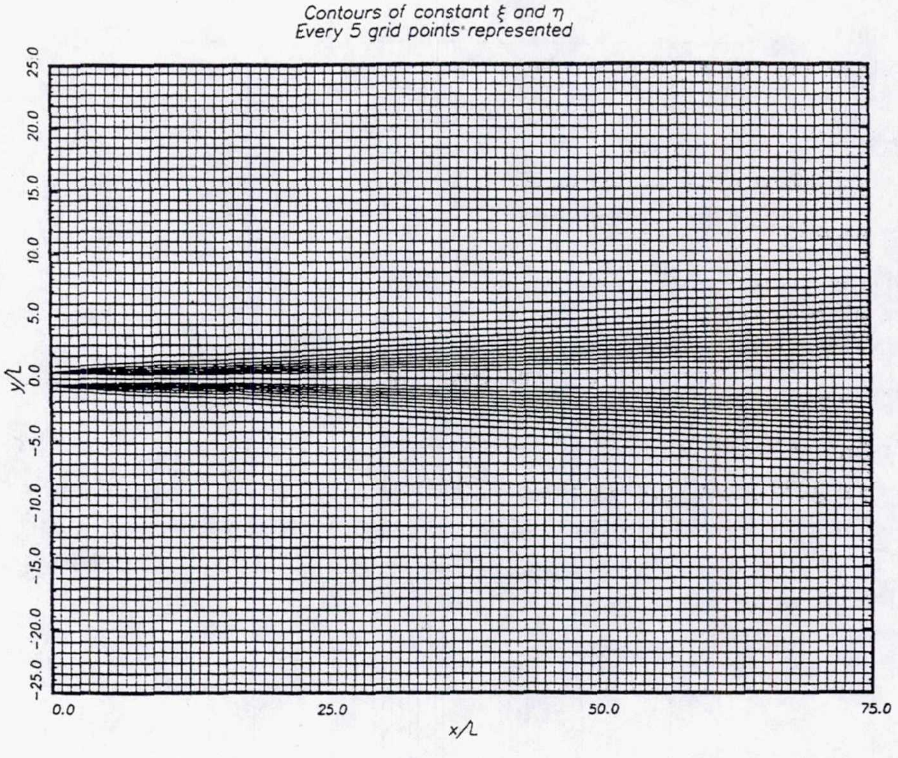

Mapping for the entire computational domain

This is the mapping of the entire computation domain. Each mesh spacing contains 5 grid points. It is clear from the density of the grid lines that a lot of the computation points are concentrated in the mixing layers of the jet.

2. GOVERNING EQUATIONS (WITH PRANDTL'S KINETIC ENERGY-EDDY VISCOSITY MODEL)

Continuity

$$\frac{\partial \rho}{\partial t} + \frac{\partial \rho u}{\partial x} + \frac{\partial \rho v}{\partial y} = 0$$

Momentum

$$\frac{\partial \rho u}{\partial t} + \frac{\partial \rho u^2}{\partial x} + \frac{\partial \rho u v}{\partial y} = -\frac{\partial p}{\partial x} - \frac{\partial}{\partial x}\left(\frac{3}{2}\rho k\right) + \frac{\partial}{\partial y}(\tau_{xy})$$

$$\frac{\partial \rho v}{\partial t} + \frac{\partial \rho u v}{\partial x} + \frac{\partial \rho v^2}{\partial y} = -\frac{\partial p}{\partial y} - \frac{\partial}{\partial y}\left(\frac{3}{2}\rho k\right) + \frac{\partial}{\partial x}(\tau_{xy}) + \frac{\partial}{\partial y}(\tau_{yy})$$

Energy

$$\frac{\partial p}{\partial t} + \frac{\partial p u}{\partial x} + \frac{\partial p v}{\partial y} + (\gamma - 1)p\left(\frac{\partial u}{\partial x} + \frac{\partial v}{\partial y}\right) = 0$$

Turbulent kinetic energy

$$\frac{\partial \rho k}{\partial t} + \frac{\partial \rho k u}{\partial x} + \frac{\partial \rho k v}{\partial y} = \rho \nu_t \left(\frac{\partial u}{\partial y}\right)^2 - c_2 \frac{\rho k^{3/2}}{\delta} + \frac{\partial J}{\partial y}$$

$$\nu_t = c_1 \delta k^{1/2} \quad , \quad \delta = c_3 x + \delta_0$$

$$\tau_{xy} = \rho \nu_t \frac{\partial u}{\partial y} \quad , \quad \tau_{yy} = \rho \nu_t \frac{\partial v}{\partial y} \quad , \quad J = \rho \frac{\nu_t}{\sigma_t} \frac{\partial k}{\partial y}$$

This shows the governing equations used in the direct numerical simulation. The fine scale turbulence will not be resolved. Instead only its effect on the mean flow is simulated through the use of an eddy viscosity. We have the continuity, momentum, and energy equations. In addition, the Prandtl's kinetic energy eddy viscosity model is adopted. This model characterizes the fine scale turbulence be a scalar, namely, the turbulence kinetic energy. This is a bit less sophisticated than the two equation k-ϵ model. For our purpose we believe the Prandtl's model is sufficient and certainly can switch to the more elaborated model later on if the need arises.

3. COMPUTATION SCHEME

Use **DISPERSION-RELATION-PRESERVING** Scheme

(AIAA Paper 92-02-033)

SPATIAL DERIVATVE

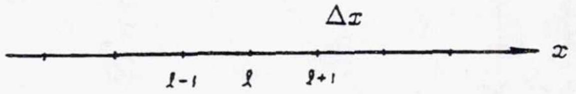

$$\left(\frac{\partial f}{\partial x}\right)_{\ell} \simeq \frac{1}{\Delta x}\left[\sum_{n=-N}^{N} a_n f_{\ell+n}\right]$$

TRADITIONAL FINITE DIFFERENCE SCHEMES

DETERMINE a_n BY TAYLOR SERIES EXPANSION

FOR DRP SCHEMES THE a_n 's ARE CHOSEN TO

BEST APPROXIMATE THE DERIVATIVE IN THE

WAVE NUMBER SPACE

For computation purpose we use the Dispersion-Relation-Preserving Scheme we developed recently. This scheme matches the wave number of the finite difference equation to that of the partial differential equation. By construction the dispersion relations are preserved.

TEMPORAL DERIVATIVE

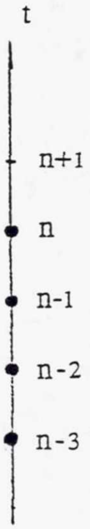

$$\left(\frac{df}{dt}\right)_n = K_n$$

FOUR LEVELS SCHEME

$$f_{n+1} = f_n + \Delta t \sum_{m=0}^{3} b_m K_{n-m}$$

SCHEME IS CONSISTENT TO ORDER $(\Delta t)^2$

AND OPTIMIZED IN FREQUENCY SPACE

SUCH THAT $\overline{\omega}$ IS THE BEST APPROXIMATION

OF ω

To march in time a four level explicit time marching scheme is used. The coefficients of the scheme are optimized so that the Laplace transform is preserved.

ARTIFICIAL SELECTIVE DAMPING TERMS ARE ADDED

(J. Computational Acoustics, to appear 1993)

$$\frac{du_\ell}{dt} = \mu \sum_{j=-3}^{3} b_j u_{\ell+j} + \dots$$

The Fourier Transform is

$$\frac{d\tilde{u}}{dt} = \mu \left[\sum_{j=-3}^{3} b_j e^{ij\alpha\Delta x} \right] \tilde{u} = \mu f \tilde{u}$$

f is a truncated Fourier Cosine Series

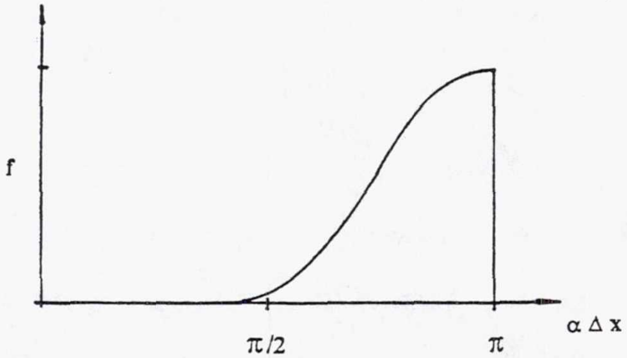

In most numerical simulations parasite waves characterized by grid-to-grid oscillations are inevitably generated. These are numerical noise and must be eliminated. We have developed a way to electively damp out the parasite waves without affecting the long waves or the acoustic waves of the computation. This selective damping terms have been incorporated into our direct numerical simulation.

4. RADIATION, INFLOW AND OUTFLOW BOUNDARY CONDITIONS (AIAA Paper 92-02-033)

Use Asymptotic Solutions to Construct Radiation Inflow and Outflow Boundary Conditions

RADIATION BOUNDARY CONDITION

$$\left(\frac{1}{V(\theta)}\frac{\partial}{\partial t}+\frac{\partial}{\partial r}\right)\begin{bmatrix}\rho\\ u\\ v\\ p\end{bmatrix}+\frac{1}{2r}\begin{bmatrix}\rho-\bar{\rho}\\ u-\bar{u}\\ v-\bar{v}\\ p-\bar{p}\end{bmatrix}=0+O(r^{-5/2})$$

$$V(\theta)=a_0[M\cos\theta+(1-M^2\sin^2\theta)^{1/2}]$$

$\overline{p}$, $\overline{u}$ etc. are time averages over the last 50 time steps

OUT FLOW BOUNDARY CONDITIONS ALLOW ACOUSTIC ENTROPY AND VORTICITY WAVES TO EXIT

Radiation, inflow, and outflow boundary conditions are needed in the simulation. A discussion of this has been given in AIAA paper 92-02-033. We use asymptotic solutions to construct radiation boundary conditions. The radiation boundary conditions allow the acoustic waves to propagate out of the computation domain and at the same time allows steady entrainment flow to come in. The radiation boundary conditions are nearly the same as those of Bayliss and Turkel except for the mean flow part.

5. INITIAL CONDITIONS

USE KNOWN (EMPIRICAL) JET MEAN FLOW

AS STARTING CONDITIONS

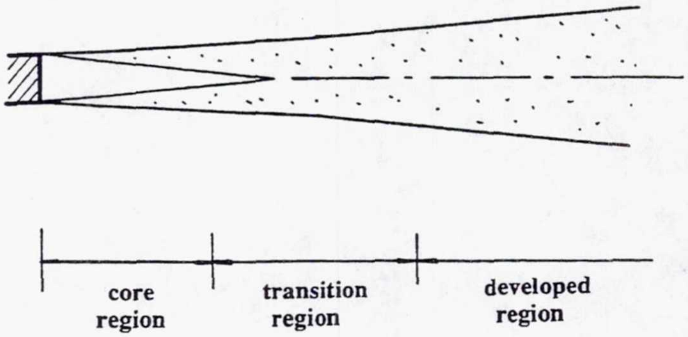

To start the solution initial conditions must be prescribed. Since a large amount of empirical data about the jet mean flow are available we use them as initial conditions. The mean pressure is taken to be constant by the boundary layer approximation.

SELECTED RESULTS OF DIRECT NUMERICAL SIMULATION

$M_j = 1.7 \qquad T_j / T_a = 1.0$

$\Delta X = D / 6.0$

$\Delta Y = \Delta X$ (outside the jet)

$\Delta t = 0.0768 \, \Delta X / a_0$

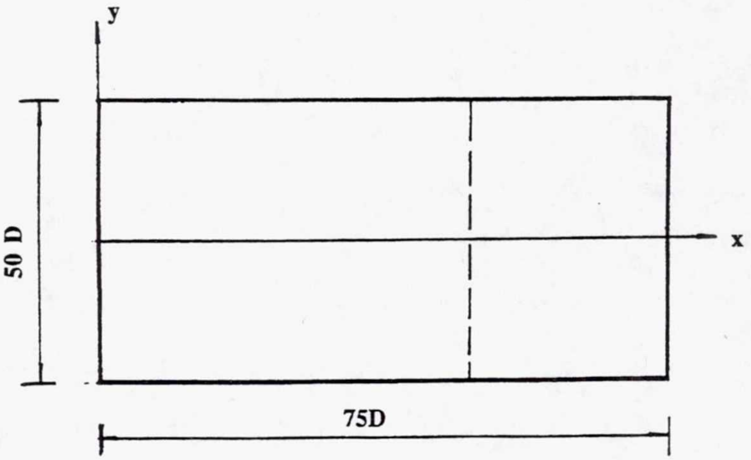

Time Evolution of pressure ($P/\rho_j U_j^2$)

at $x = 50$ D

Initial Condition

at $t = 0$ $\quad p = 1/(\gamma M_j^2)$

(boundary layer approximation)

The next several viewgraphs show how the pressure disturbances generated by the initial conditions propagate out the computation domain at x = 50 D downstream. There is very little reflection from the radiation boundary conditions. One of the viewgraphs shows the reflection of small amplitude parasite waves. These waves are immediately damped and never could reach the jet flow. The last but one viewgraph shows the vector field of the jet and entrainment flow. Only the flow direction at a point is presented. Velocity magnitude is not involved. This figure shows the present simulation can capture the entrained flow which most CFD codes cannot.

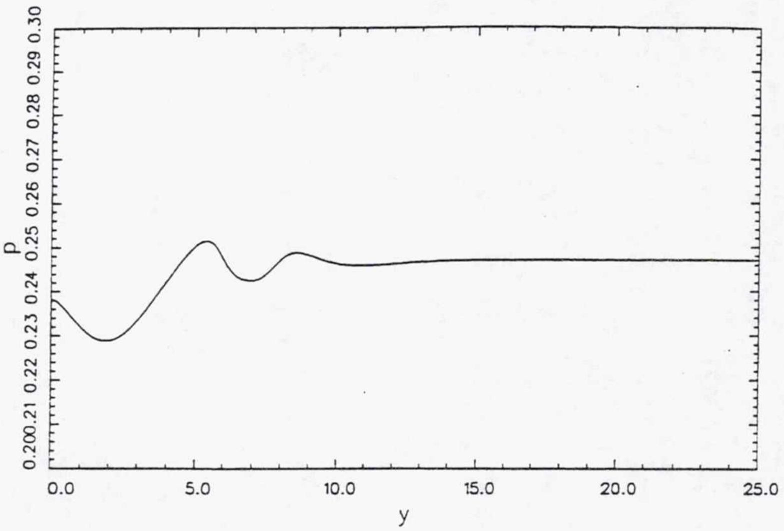

time steps:500

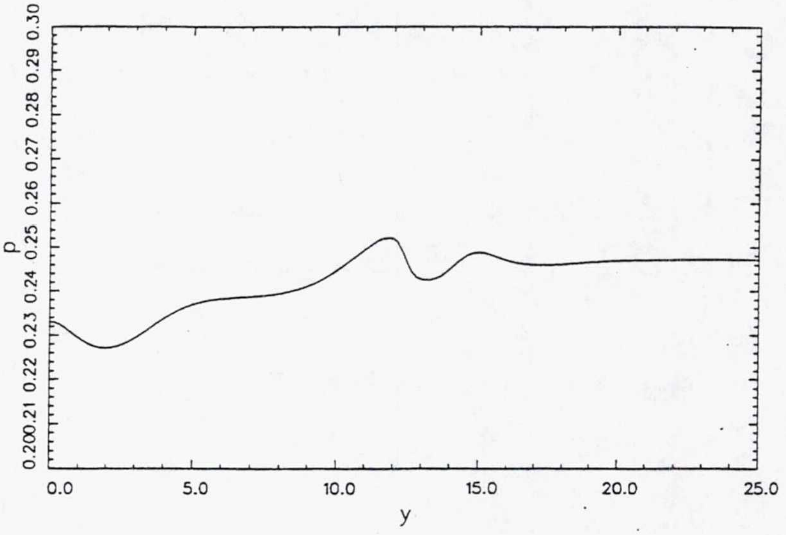

time steps:1000

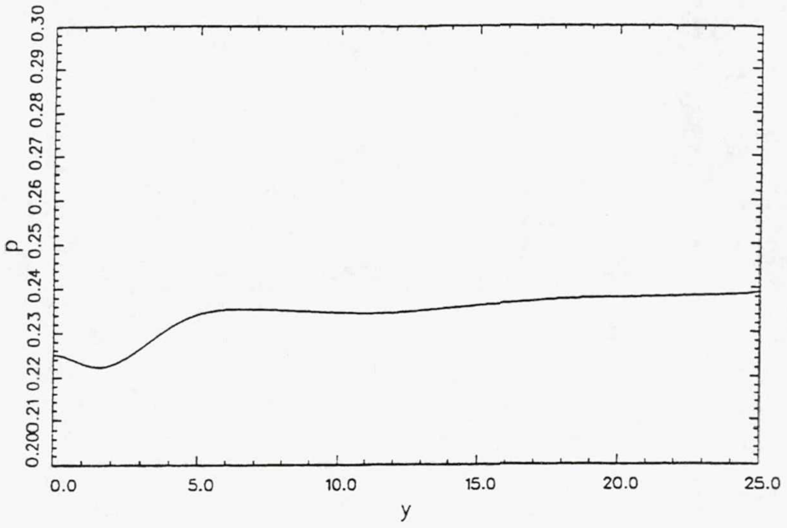

time steps:2400

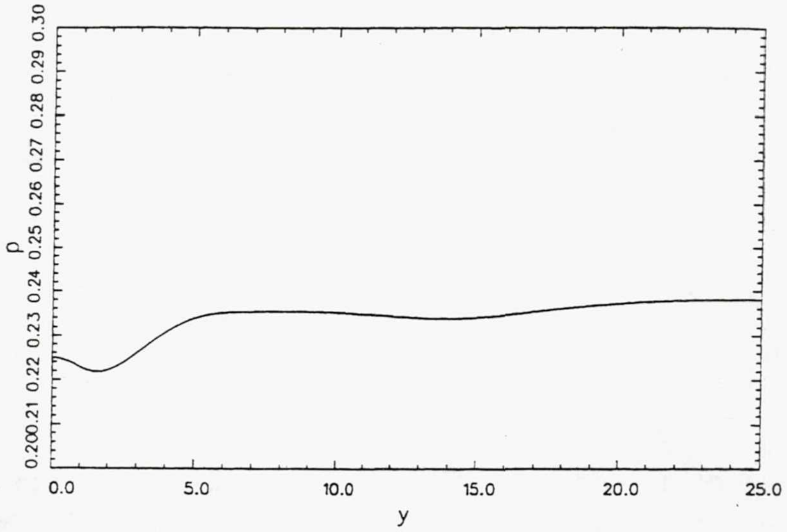

time steps:2600

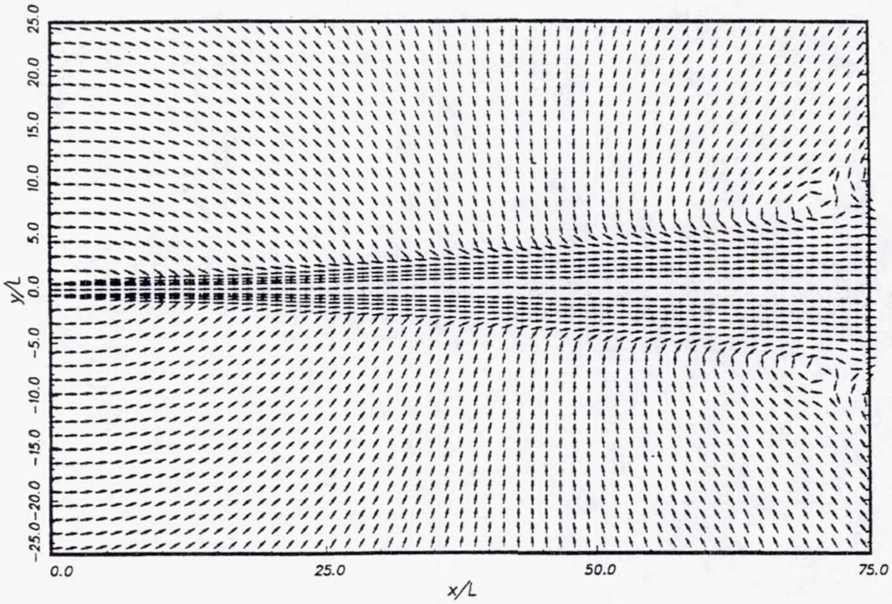

Vector Field Map, 5000 time steps

SUMMARY

IT SEEMS THAT IT IS FEASIBLE TO PERFORM DIRECT NUMERICAL SIMULATIONS OF NOISE GENERATION AND RADIATION FROM SUPERSONIC JETS

We use an algebraic mapping to put a large number of mesh points in the mixing layer of the jet were there is a large velocity gradient. As can be seen the mapping does concentrate points in the shear layers. This map covers the initial region of the jet downstream of the nozzle exit.

1999176564

PREDICTION, MEASUREMENT, AND SUPPRESSION OF HIGH TEMPERATURE SUPERSONIC JET NOISE

John M. Seiner and T.R.S. Bhat
Jet Noise Laboratory
NASA Langley Research Center
Hampton, Virginia

and

Bernard J. Jansen
Lockheed Engineering and Sciences Company
Hampton, Virginia

527-71

409553

34P.

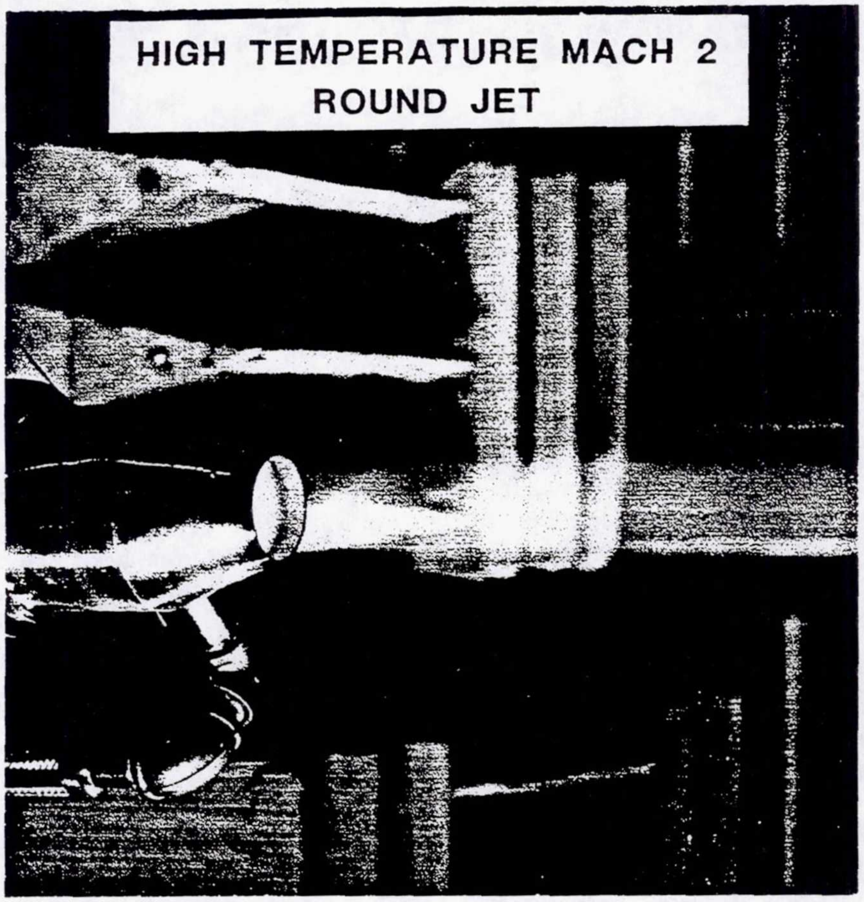

Figure 1

The photograph in figure 1 displays a water cooled round convergent-divergent supersonic nozzle operating slightly overexpanded near 2460°F. The nozzle is designed to produce shock free flow near this temperature at Mach 2. The exit diameter of this nozzle is 3.5 inches. This nozzle is used in the present study to establish properties of the sound field associated with high temperature supersonic jets operating fully pressure balanced (i.e. shock free) and to evaluate capability of the compressible Rayleigh model to account for principle physical features of the observed sound emission. The experiment is conducted statically (i.e. $M_f = 0.$) in the NASA/LaRC Jet Noise Laboratory. Both aerodynamic and acoustic measurements are obtained in this study along with numerical plume simulation and theoretical prediction of jet noise. Detailed results from this study are reported previously by Seiner, Ponton, Jansen, and Lagen (1992).

TAM AND OERTEL'S CONVECTIVE MACH NUMBER RELATIONS

I. Supersonic instability waves

$$M_c = V_c / C_A = (V_j - V_c) / C_j = V_j / (C_j + C_A)$$

II. Kelvin-Helmholtz instability waves (eddy Mach wave emission)

$$M_c' = V_c' / C_A = (V_j - V_c') / C_j + 1 = (V_j + C_j) / (C_j + C_A)$$

III. Subsonic instability waves

$$M_c'' = V_c'' / C_A = (V_j - V_c'') / C_j - 1 = (V_j - C_j) / (C_j + C_A)$$

Figure 2

In the early 1980's, Oertel (1982) observed the existence of three distinct families of waves in the shear layer of an unheated high Mach number supersonic jet generated by a shock tube. Using time resolved photographic renditions, Oertel distinguished one family of waves from another by observation of their different convection velocities. He noted that the first family of waves were convected supersonically relative the sum of the local jet and ambient sound speed. The second family was convected supersonically relative to the ambient sound speed. The third family was convected subsonically; its speed governed by the difference between the local jet and sound speeds. For hot jets, however, even this wave could eventually convect supersonically at extreme Mach and jet total temperatures. Oertel developed simple convective Mach number relations for these families of waves, as shown in figure 2. Here, $V_{c,}$ V_j, c_j, c_a, represent the convection, local jet velocity, local jet sound speed, and ambient sound speed.

More recently in a benchmark paper, Tam (1989) demonstrated that Oertel's convective Mach number relations actually satisfied those obtained from solution of the compressible Rayleigh equation. The second family of waves were found to be associated with the familiar Kelvin-Helmholtz instability waves. The first family of waves were obtained by extension of the Rayleigh model to include radial modes. Both the first and second families of waves are expected to be important sources of noise emission because of their supersonic phase speed. The third family of waves are technically unimportant because of their subsonic phase speed in the range of both Mach and jet total temperatures typically encountered in aircraft jet engines being considered for the NASA HSR program.

DEFINITION OF MACH WAVE ANGLE

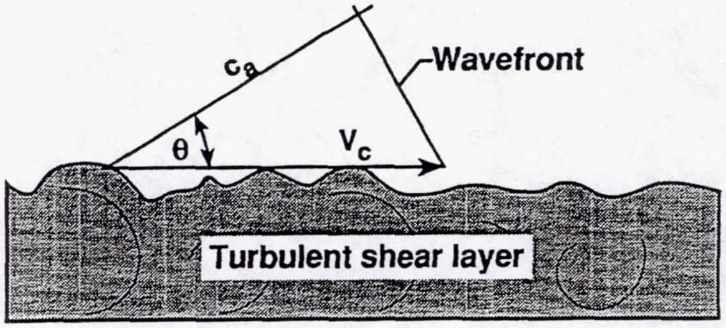

Figure 3

Figure 3 illustrates the convention used to define the Mach wave angle is shown in the figure. Here, V_c, is the convection velocity of turbulence in the jet shear layer and, c_a, is the ambient sound speed. The acoustic wavefront is propagated, as shown, at an angle, θ, to the turbulent shear layer.

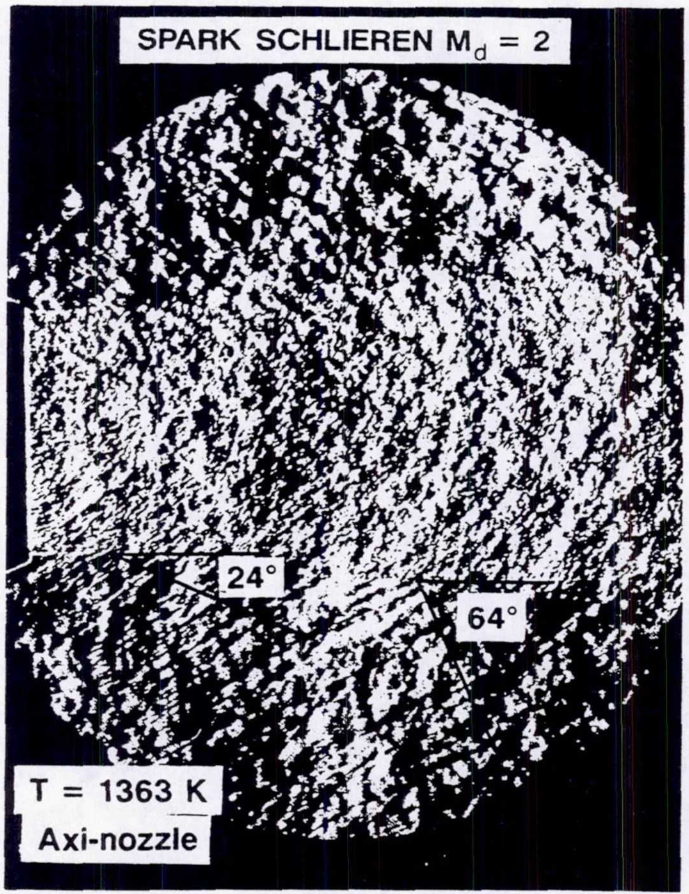

Figure 4

By way of illustration, consider the spark schlieren photograph of figure 4. This photographic record was obtained using $M_d = 2$ water cooled nozzle. The nozzle was operated overexpanded (i.e. $M_j = 1.8$) at 1370°K. This record, taken with a vertical knife edge and spark duration < 0.1 μ-sec., captures a nearly instantaneous view of both the flow and near acoustic field. The acoustic waves that emanate from along the edge of the jet shear layer are produced by turbulence convecting supersonically. For this Mach number and jet total temperature, one expects that both the first and second families of waves will have supersonic phase speeds based on the convective Mach number relations in figure 3.

The schlieren record shows the presence of at least three types of acoustic waves. The first set are waves with very short wavelength , located near the nozzle exit. A second set of low amplitude waves, with a wavelength of at least an order of magnitude greater than those centered at the nozzle exit, appear to be propagating at low angles to the jet shear layer. The 24° vector indicates a best guess estimate of their direction. The third set of waves have even longer wavelengths and are of significantly greater amplitude. These waves appear to be inclined at 64° to the jet axis as indicated on the figure. The axial wavelength appears to increase with increasing downstream distance.

MACH WAVE EMISSION ANGLE

MACH ANGLE : $\theta = \cos^{-1}(1 / M_C) = \cos^{-1}(C_A / \alpha V_J)$

$\theta_C = 28^{\circ}$ - **SUPERSONIC INSTABILITY WAVE**

$\theta_C \approx 24^{\circ}$ - **SCHLIEREN RECORD**

$\theta_C' = 56^{\circ}$ - **KELVIN-HELMHOLTZ INSTABILITY**

$\theta_C' \approx 64^{\circ}$ - **SCHLIEREN RECORD**

Figure 5

Mach waves are emitted from the supersonic shear layer at an angle, θ, that depends on the convection speed of turbulence in the jet shear layer. This is illustrated graphically in figure 3 and can be computed as shown in figure 5 as the inverse cosine of , $1/M_c$, the convection Mach number. As we have seen from figure 2, the convection Mach number for each wave family can be determined from Oertel's relationships or computed from the phase speed based on solution of the compressible Rayleigh equation. In figure 5, α, represents a compilation of those terms necessary to compute the convection velocity, V_c, using these relationships for each family of wave. It is important to note, however, that turbulence is a dispersive medium. Thus the convection velocity is dependent on the turbulence frequency and axial location away from the jet axis, and consequently $\alpha = \alpha(x,\omega)$. For purposes of illustration with the spark schlieren of figure 4, the jet exhaust velocity and temperature are used to calculate a value for α. This can only be expected to provide a nominal value for the convection Mach number and Mach emission angle.

As shown in figure 5, the nominal value for the Mach emission angles for the first two families of instability waves is reasonably close to that displayed in the figure 4 schlieren. Later it will be shown that instability wave analysis also predicts that supersonic instability waves dominate high frequency Mach wave emission and originate closer to the jet axis than do the Kelvin-Helmholtz instability waves.

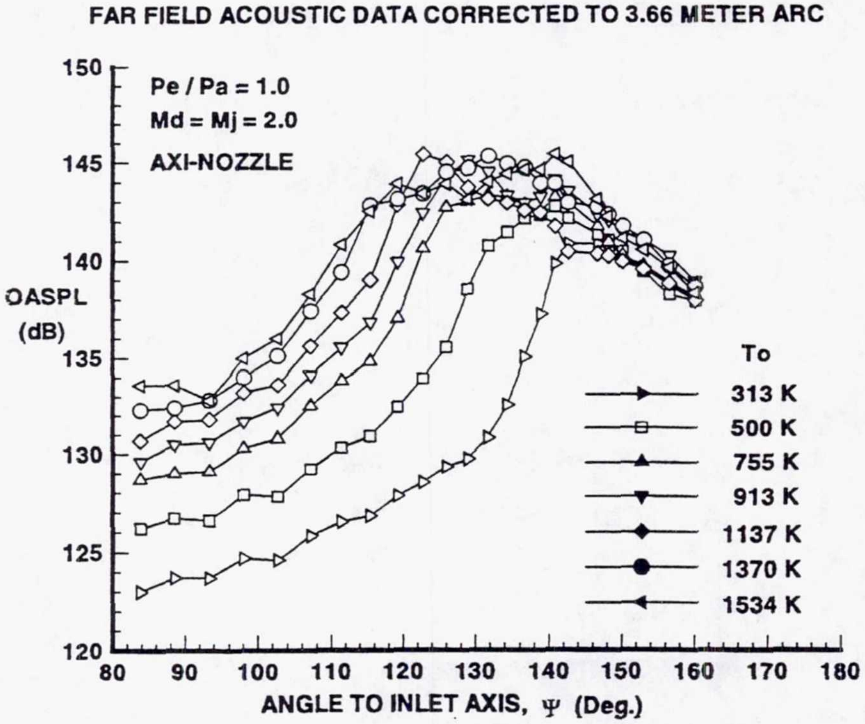

Figure 6

In figure 6, the overall sound pressure level (OASPL) in dB is shown for several jet total temperatures investigated using the $M_d = 2$ round nozzle. All results shown are for operation of the nozzle fully pressure balanced. The data is presented in terms of the angle to the nozzle inlet axis. The OASPL is computed from each microphone's digitized time record. The nozzle thrust is nearly constant for all temperature conditions. The relatively rapid rise in the OASPL from low temperatures to smaller increases at high temperature is expected, since the convective Mach number depends on the absolute jet temperature ratio T_j/T_a, where T_j, and T_a are respectively the jet total and ambient temperatures.

For each temperature there is a well defined peak amplitude region. The Mach wave emission process is confined to angles greater than $\psi = 90^\circ$. At 313°K the peak OASPL lies near $\psi_p = 145^\circ$. The angle, ψ_p, that defines other peak angles of emission, decreases with increasing jet temperature as expected form the convective Mach number relations of figure 2. At 1370°K, these convective Mach number relations predict that the supersonic instability waves would have the peak amplitude of emission occur at an angle of $\psi = 143^\circ$ and the K-H instability waves an angle of $\psi = 122^\circ$. The 1370°K data of figure 6 show a major peak in OASPL near $\psi_p = 129^\circ$ and a minor peak near $\psi_p = 137^\circ$. Thus reasonable agreement exist between the observed peak amplitude emission angles and those calculated nominal values.

NARROW BAND FAR FIELD ACOUSTIC SPECTRA
($M_j = 2.002$, $T_o = 1370°K$)

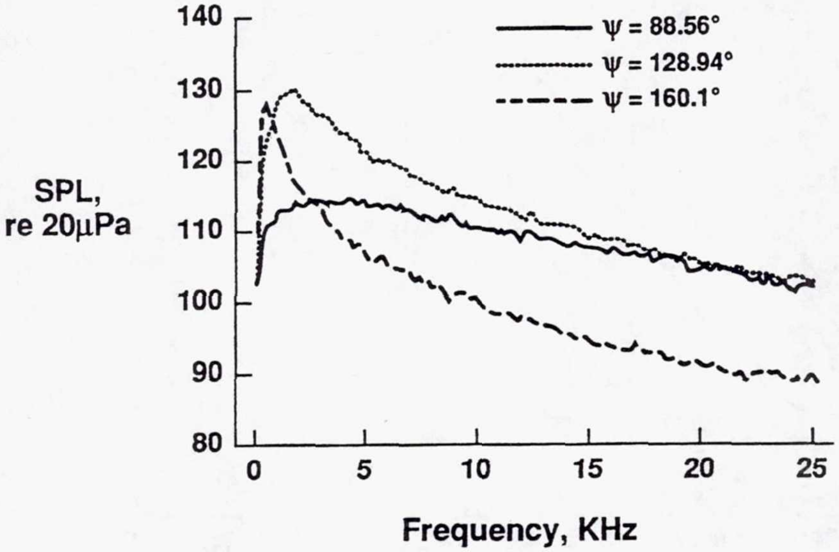

Figure 7

Several narrow band spectra at inlet angles of ψ = 88.9°, 128.9°, and 160.1° are shown in figure 7 for the T_j = 1370°K jet temperature condition. These spectra have been corrected to spectrum levels and only the first 25 kHz. of the 100 kHz. processed spectrum is shown to enhance details at low frequency.

The 88.6° spectrum lies outside the Mach wave emission field and is very flat without a well defined frequency of peak amplitude. The spectrum at the 128.9° shows a large increase in low frequency content with a well defined peak spectral value near 1.5 kHz. The spectrum at 160.1°, which lies well beyond the peak OASPL emission direction, indicates an even greater increase in low frequency emission with a very narrow band spectral peak. Very little high frequency noise is emitted in this direction, relative to the other two angles in figure 7.

DISTRIBUTION OF SPECTRUM PEAK AMPLITUDE LEVELS

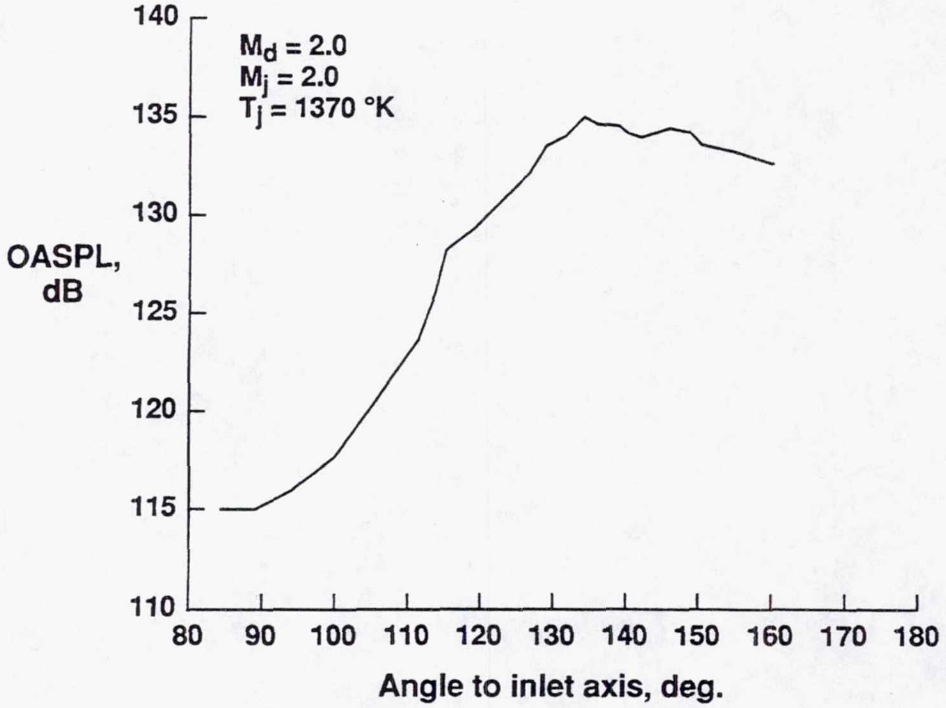

Figure 8

The angular distribution of spectral peak amplitude levels are shown in figure 8 for the jet total temperature of $T_j = 1370°K$. This data is generated from narrow band spectra like those of figure 7. The data of figure 8 indicates that the angular location, where the Mach wave emission process becomes important, lies between $\psi = 100°$ and $110°$. After reaching a peak value at $\psi = 134°$, the peak amplitude spectral values remain relatively constant with increasing angular position.

STROUHAL FREQUENCY TREND WITH ANGLE TO INLET AXIS

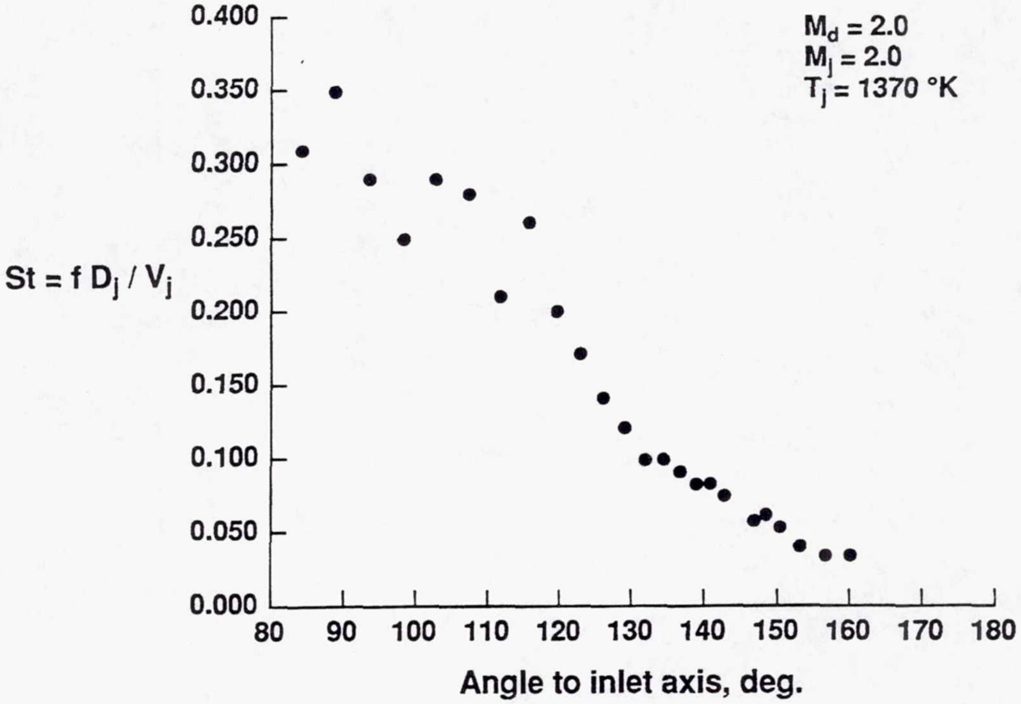

Figure 9

For the same jet operating, figure 9 shows the angular dependence of the frequency identifying the peak spectral amplitude. The data is presented in terms of the Strouhal frequency, S_t, where $S_t = fD/V_j$. The Strouhal frequency is seen to decrease from values near 0.35 at $\psi = 90°$ to values near 0.03 at $\psi = 160°$. The scatter in Strouhal frequencies at lower angles of ψ is due to limitation in identification of a spectrum peak amplitude from a flat spectrum, like that shown in the figure 7 spectrum for $\psi_p = 88.56^0$. The angular dependence of the Strouhal frequency and spectral peak amplitude are important characteristics of the Mach wave emission process.

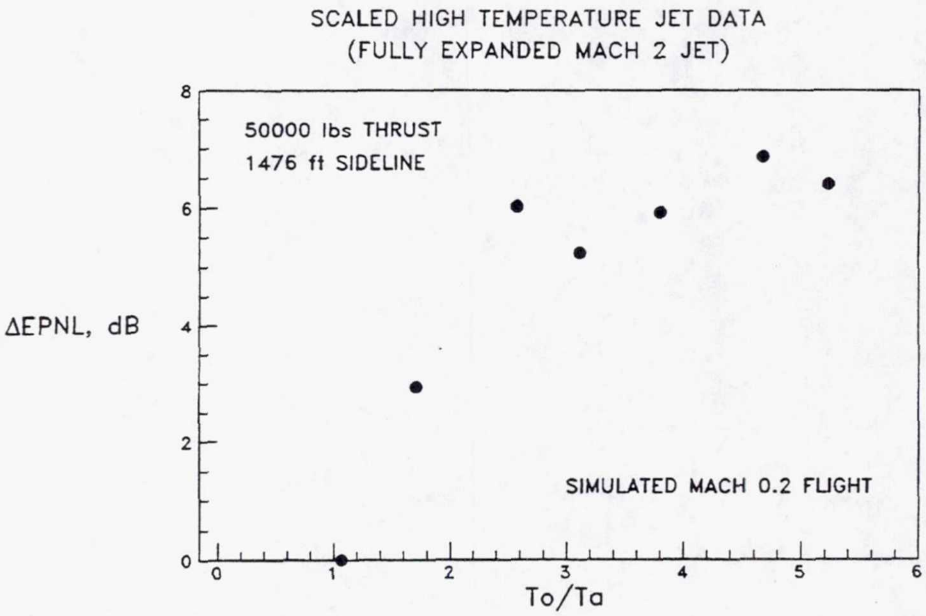

Figure 10

The results of the high temperature study of jet noise associated with the round fully pressure balanced Mach 2 nozzle, provides valuable insight of the scaled noise field for HSR applications. Figure 10 shows computed values of EPNL for several jet total temperatures, ranging from ambient to 1534°K. The EPNL values are shown relative to the near ambient jet total temperature of 313°K. The data is corrected to 50000 lbs. of thrust at a sideline distance of 1476 feet. Forward flight is simulated for $M_f = 0.2$ to enable the EPNL calculation. Jet noise is corrected for forward flight using standard modules found in the NASA ANOPP code (Zorumski 1982).

The EPNL metric is found to remain relatively constant, near 6 PNdB greater than the reference temperature of 313°K, for temperature ratio's greater than 2.5 (i.e. $T_j = 755$°K). The principle reason why the EPNL metric asymptotes with temperature is related to the generation of significant high frequency jet noise that is not weighted into the metric. Typical HSR jet total temperatures are expected to be near 1140°K for a 700 lbm./sec. engine at take-off power. In the HSR program, a mixer/ejector achieving fully mixed flow at the ejector exit with 100% pumping would have an exhaust temperature near 755°K.

From the data in figure 10, it is clear that at this temperature the same amount of noise would have to be removed as at the higher temperatures. The current reason, however, why the industry seeks lower temperatures solely rests in the observation that jet noise suppressors have thus far worked much more effectively at lower velocities (i.e. lower jet total temperatures). The pay-off is big, however, if a satisfactory scheme could be devised to achieve suppression at higher jet total temperatures. At high jet temperatures, the engine weight flow is significantly lowered to achieve the same thrust thus reducing engine size and weight. Higher jet engine temperatures also lead to more efficient engine cycles.

AXIAL DEVELOPMENT OF A SUPERSONIC JET

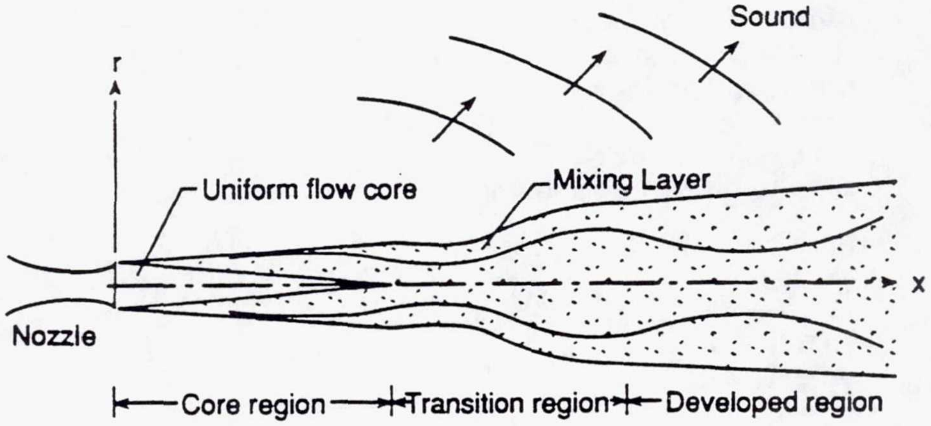

Figure 11

All free jets are divided into three main regions of flow development, as shown in figure 11. The near field region of jet development is known as the core region. In this region the initial shear grows nearly linearly with the slowest growth rate of all regions. For well designed nozzles, a nearly turbulent free region exists bounded by the inner side of the shear layer. The core region extends several jet exit diameters downstream, the axial extent being primarily a function of jet exit and free stream Mach number. For a static Mach 2 nozzle, this distance is approximately 10 diameters. In the fully developed region of jet, the flow develops in a self preserving state where mean flow variables vary like r/x. In this region the jet spreads at a greater rate than in the core region. The transition region is one where the flow adjusts between the core and fully developed region. In this region large changes occur in the turbulent structure; the Reynolds stress tensor peaks in this region. It is the rapid change in turbulent structure in this region that is the cause for the generation of the most intense noise.

JET MEAN FLOW FIELD PARAMETERS

Half-Gaussian profile parameters

h - radius of potential core
R - radial coordinate
$R_{.5}$ - radius to half jet velocity
V - axial velocity
V_{CL} - axial centerline velocity
V_j - fully expanded jet exit velocity

$$V / V_{CL} = 1 \qquad R \leq h$$
$$V / V_{CL} = \mathrm{EXP}(-(\ln 2)\,\eta^2) \qquad R \geq h$$
$$\eta = (R - h) / b$$
$$b = R_{.5} - h$$

Crocco's relation

$$\rho_j / \rho = (1 + .5(\gamma - 1)M_j^2)(T_A / T_o + (1 - T_A / T_o)(V / V_j)) - .5(\gamma - 1)M_j^2 (V / V_j)^2$$

Figure 12

Analysis of the noise radiated by a supersonic jet requires information concerning development of the flow in all three regions of jet flow development, although the core and transition are of most importance. Application of the compressible Rayleigh model to predict noise only requires information concerning the mean flow, whereas application of Lighthill's or Lilley's equation requires considerable information concerning the second derivative of a two point space-time turbulent Reynolds stress tensor. This paper is concerned with evaluation of the former model because of its relative simplicity and prior accuracy in prediction of important aerodynamic and acoustic physical features with low temperature supersonic jets.

The usual approach is to use a half-Gaussian profile to represent the axial mean velocity profile. This means that the Rayleigh analysis assumes that jets spread relatively slowly since the radial mean velocity is neglected relative to the axial component. This appears a satisfactory assumption for simple laboratory jets. Figure 12 shows that to establish the half-Gaussian profile in all regions of jet flow development would only require knowledge of the potential core radius, h, the radius to half jet velocity, $R_{.5}$, and the axial mean centerline velocity, V_{cl}. The jet density is then determined from jet exit operating conditions and Crocco's relation, which holds identically for isothermal jets. For the present Mach 2 jet, the flow is isothermal near a jet total temperature of 500°K.

CENTERLINE VELOCITY DECAY WITH JET TEMPERATURE

Fully Pressure Balanced Mach 2 Jet Into Still Air

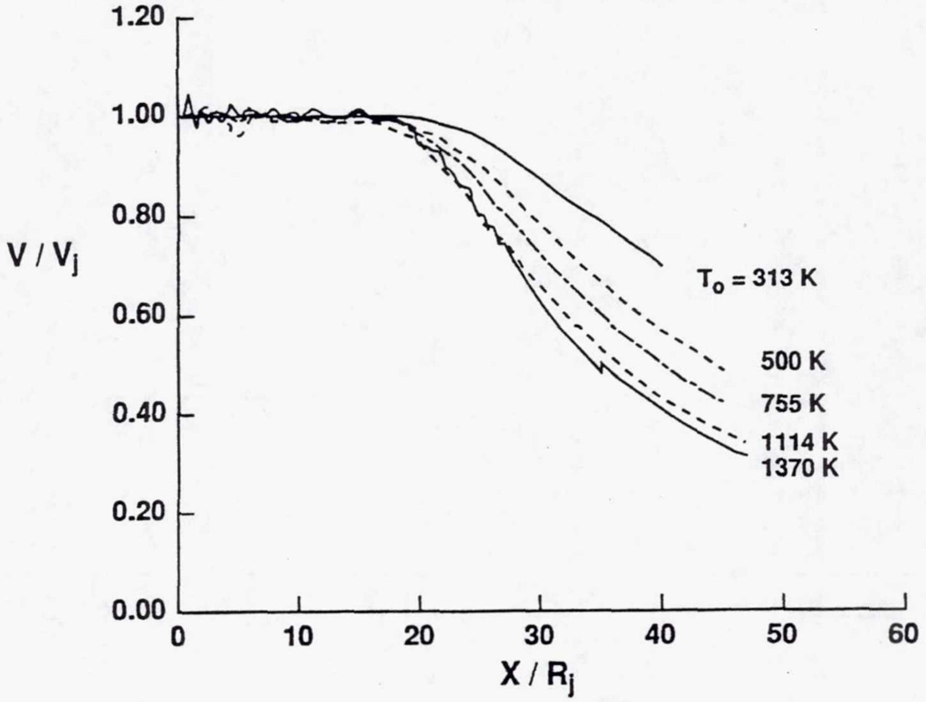

Figure 13

The experimentally determined jet centerline velocity, V_{cl}, is shown in figure 13 for several jet total temperatures ranging from 313 to 1370°K. The centerline velocity data is normalized by the jet exit velocity, which is computed from the operating pressure and temperature stagnation conditions in the nozzle plenum. The axial distance is normalized by the jet exit radius. For this data, the jet nozzle is operated fully pressure balanced and into still air.

Except for the influence of weak shocks in the jet plume, the centerline velocity for all jet total temperatures remains uniform over the first 16 jet radii from the nozzle exit. Beyond this region, the difference in velocity for the various jet temperatures increases substantially with axial distance. Examination of this data shows that the jet potential core length, L_c , generally decreases with increasing jet temperature.

Instability Wave Model - Mean Flow Profiles

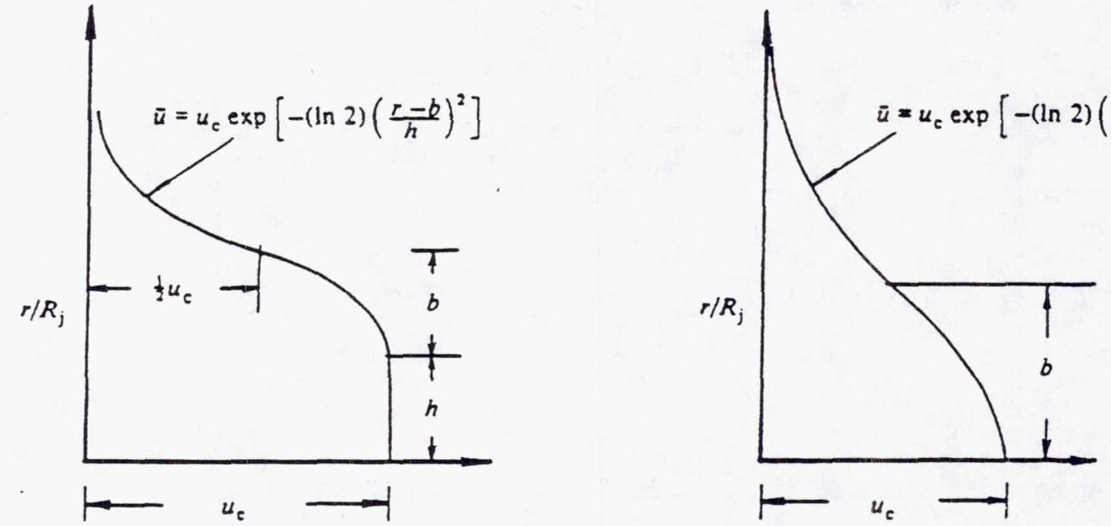

Figure 14

Figure 14 displays typical appearance of the mean velocity profiles obtained using the half-Gaussian profile for flow in the core (left side figure) and transition and fully developed regions (right side figure). Note the radius of the potential core, h = 0, beyond the core region.

TEMPERATURE DEPENDENCE ON MEASURED JET SPREAD RATE PARAMETERS

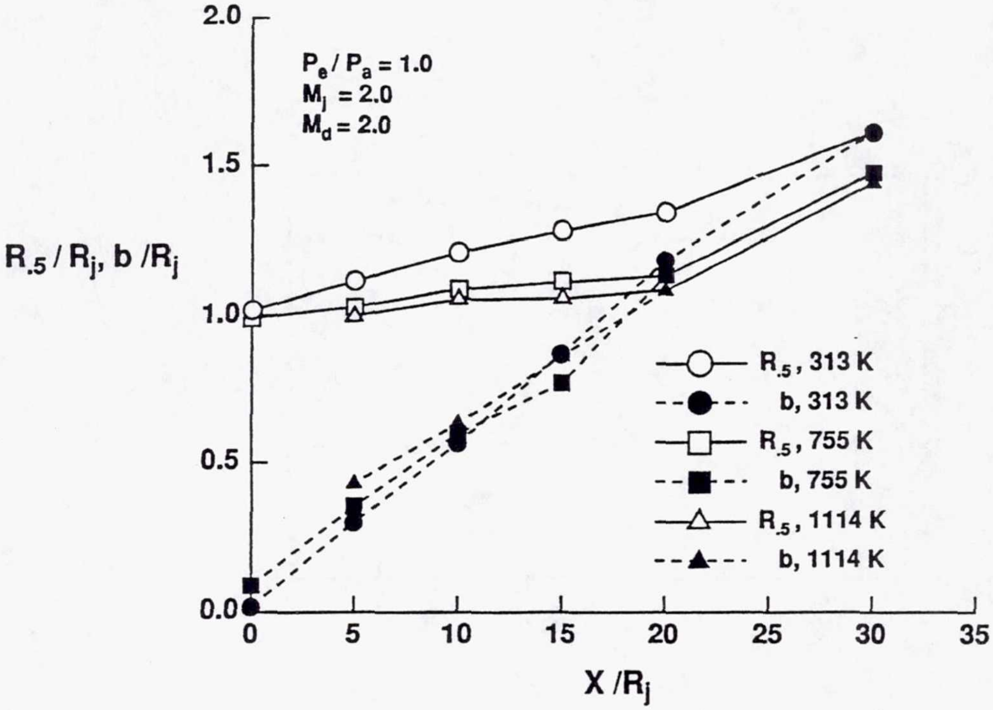

Figure 15

Figure 15 shows the measured axial variation of the radius to half velocity, $R_{.5}$, and velocity half width of the mixing layer, b, as defined in figures 12 and 14, for the three jet total temperatures of 313, 755, and 1114°K. These parameters are *normalized by the nozzle exit radius.* The *axial* development of these spread rate parameters indicates that the shear layer growth of the inner boundary toward the jet centerline is much greater for hot jets than cold jets. The outer radial boundary of the shear layer is observed to grow at a slower rate for hot jets than cold jets. The overall net result is that the potential core of hot jets is slightly reduced compared to cold jets. Figure 15 also indicates that the most significant difference in spread rate occurs between jets operating below and above isothermal jet temperatures.

RADIAL MEAN VELOCITY PROFILES

$(0.1 \le {}^{X}/_{D} \le 15.0)$

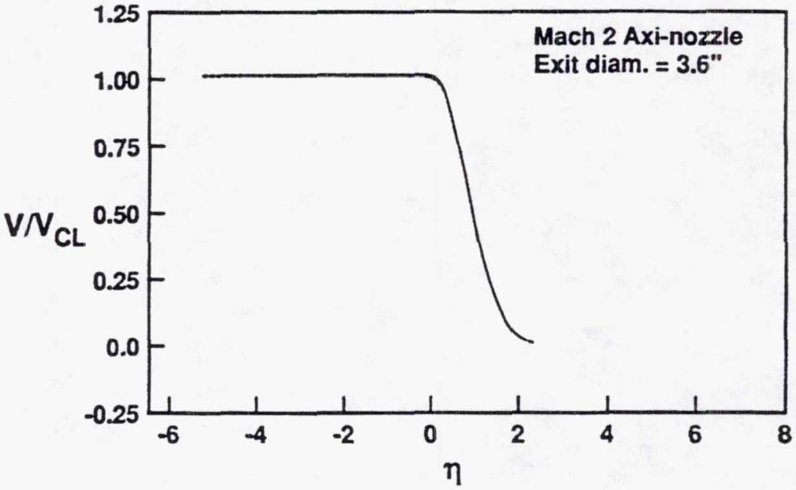

Figure 16

The universal half-Gaussian shape of the measured mean velocity profiles are shown in figure 16 for the three jet temperatures considered above. The data represents a compilation of all measured velocity profiles from the nozzle exit to 30 R_j. The data in the figure is plotted, for clarity, using lines connecting the data points. The collapse of the data points is quite good, providing a satisfactory data base for application of the Rayleigh model.

MEASURED CONVECTION MACH NUMBERS

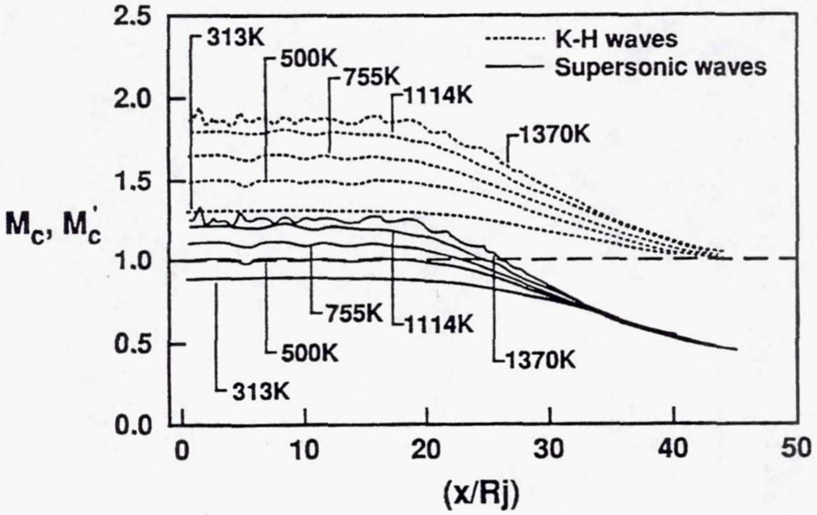

Figure 17

The Mach wave mechanism can produce noise only in those regions where a turbulent structure's phase velocity is supersonic. The phase velocities for the supersonic and Kelvin-Helmholtz instabilities are given in figure 2 in terms of their convection Mach numbers. These equations are used along with the measured properties to compute the convection Mach number for both families of instability waves. Figure 17 presents results of this analysis for all 5 jet total temperatures investigated. When either M_c or M_c' fall below unity, noise emission by the Mach wave process is terminated.

The data in figure 17 show that supersonic phase velocities for supersonic instability waves do not extend far beyond the end of the potential core. On the other hand, the phase velocity for the Kelvin-Helmholtz (K-H) instabilities are supersonic well beyond the end of the potential core. The axial extent of the noise producing region for this second family of waves is thus quite extensive. The K-H waves have supersonic phase speed to near $X/R_j = 46$, independent of the jet total temperature. Thus the axial region for noise emission by the Mach wave emission mechanism does not appear to increase with jet total temperature.

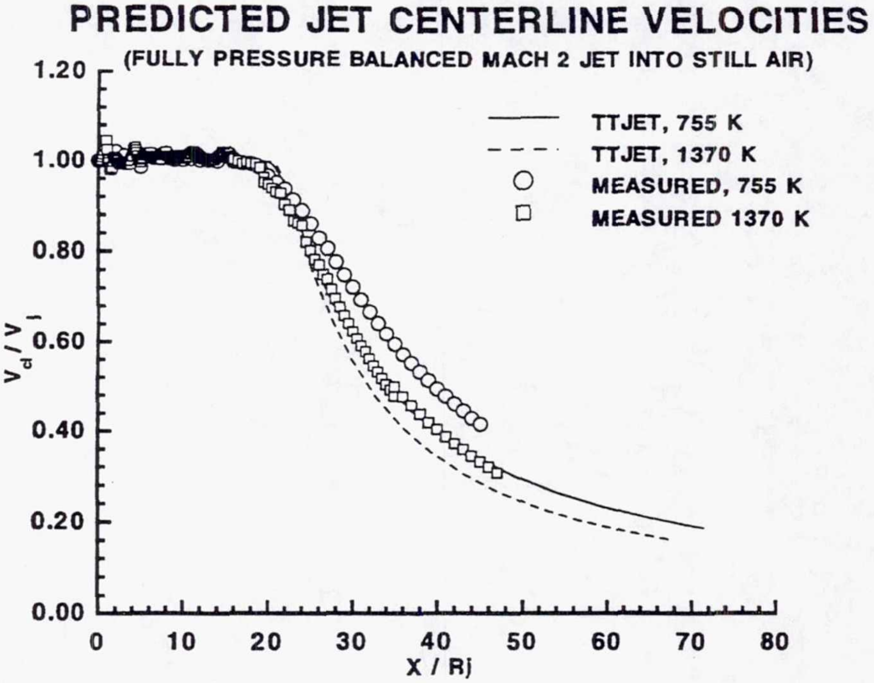

Figure 18

In figure 18, comparison is made between the SAIC TTJET code prediction of Dash and Kenzakowski (1992) for centerline velocity and the measured data for jet total temperatures of 755°K and 1370°K. The TTJET code is a parabolized Navier-Stokes solver with up-wind differencing. and Pope (1978) centerline corrections for vortex stretching. It utilizes a two equation turbulence model with compressibility corrections based on the work of Sarkar, Erlebacher, Hussani, and Kreiss (1989). The predicted potential core length is slightly greater than measured values. When T_o = 755°K the measured and predicted values for L_c are respectively 18.25 R_j and 20.51 R_j. When T_o = 1370°K the respective measured and predicted values are 18.83 R_j and 20.85 R_j.

Beyond the potential core, deviations between the predicted and measured values become more apparent. The predicted jet centerline velocities decay much faster than do measured data. The measured data indicates that differences in centerline velocity decay with temperature are greater than those predicted. The observed differences between measured and predicted centerline data suggest that the TTJET code predicts much greater mixing in this downstream region. This behavior could be attributed to performance of the compressible turbulence dissipation model installed in the code.

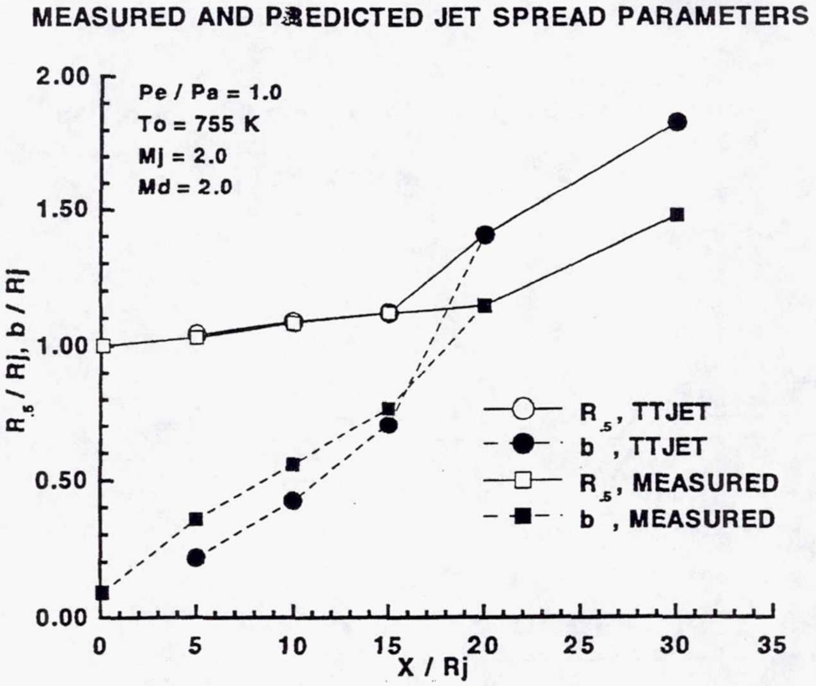

Figure 19

In figure 19, a comparison is made between the measured and TTJET code predictions for $R_{.5}$. These appear to be in outstanding agreement with measured values. However, the specification of a 10% initial boundary layer thickness in the code calculations overestimates the real nozzle exit boundary layer thickness. Thus the numerical jet appears to have a thicker shear layer thickness to X/R_j = 15. Beyond this point, the TTJET code predicts substantially greater mixing than observed experimentally.

It is well known from previous experimental studies that beyond the potential core region the turbulence structure must respond to a rapid transition of the mean flow from annular to axisymmetric shape. The large scale turbulence structure generally transitions from helical to axisymmetric spatial structure. The kε-CD turbulence model does not contain the methodology to accommodate these flow field characteristics. The quantitative difference between the predicted and measured jet spread rate parameters is expected to play an important role in application of the compressible Rayleigh equation. The major noise producing region occurs near the end of the potential core, where the most highly amplified instability wave reaches its maximum growth. This growth is strongly dependent upon representation of the mean flow field. The accelerated rapid mixing of the numerical predictions near the end of the potential core would produce, based on application of the Rayleigh model, slightly lower values for noise if based on mean flow data predicted by the TTJET code.

PREDICTED CONVECTION MACH NUMBERS

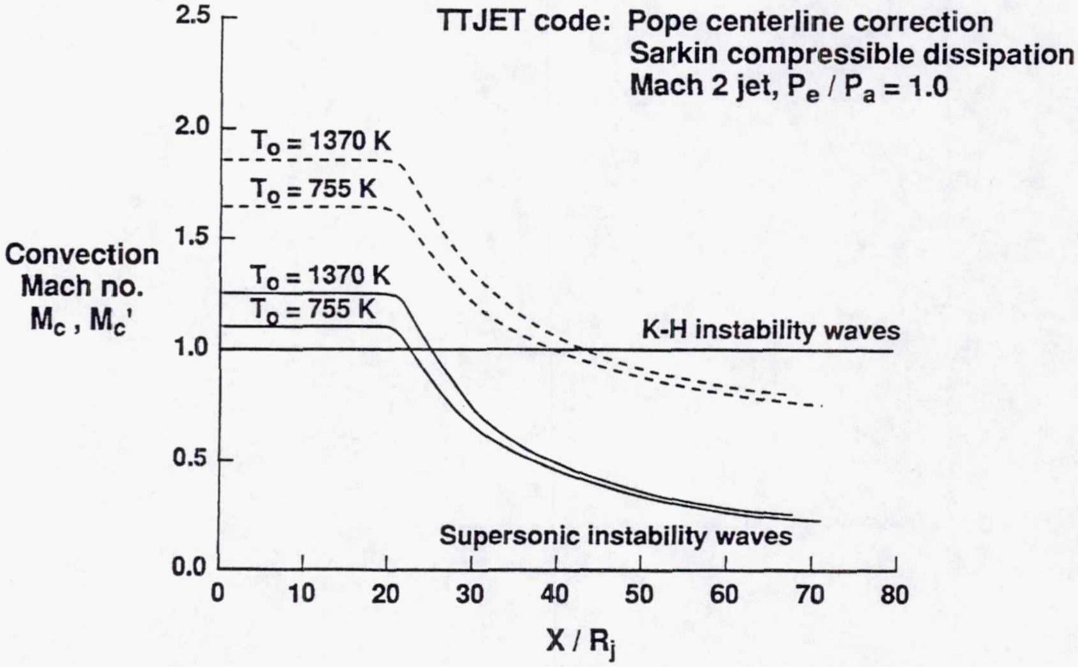

Figure 20

The TTJET code predictions for the convection Mach numbers of the supersonic and Kelvin-Helmholtz (K-H) instability waves are shown in figure 20 for the jet total temperatures of 755°K and 1370°K. The predicted values for M_c and M_c' provide essentially the same information as the experimentally determined values. The TTJET code predicts supersonic phase speeds for the K-H wave to $X/R_j = 42$. This decreased distance, relative to the experimentally determined values in figure 17, is consistent with the more rapid mixing of the numerically simulated jet.

Instability Wave Model

- Compressible Rayleigh's Equation

$$\frac{\partial^2 \hat{p}}{\partial r^2} + \frac{\partial \hat{p}}{\partial r}\left[\frac{2\alpha}{\Omega}\frac{\partial U}{\partial r} + \frac{1}{r} - \frac{1}{\bar{\rho}}\frac{\partial \bar{\rho}}{\partial r}\right] + \left[\bar{\rho} M_j^2 \Omega^2 - \frac{n^2}{r^2} - \alpha^2\right]\hat{p} = 0$$

$$p(r,\theta,x,t) = A(x)\hat{p}(r)\exp\left[i(\alpha x + n\theta - \omega t)\right]$$

$$\alpha = \alpha_r + i\alpha_i \qquad c = \frac{\omega}{\alpha_r}$$

Figure 21

Linear instability wave theory for supersonic jets is now well-known. It can be shown that development of an instability wave of fixed real frequency, ω, is governed by the compressible Rayleigh equation shown in figure 21 in the top equation, where $\Omega = \omega - \alpha U$. Here U and ρ are the mean velocity and density, respectively, and M_j is the fully expanded jet Mach number. The parameter, n, is the azimuthal mode number and α is the axial wavenumber or eigenvalue of the problem. The equation is written in a cylindrical polar coordinate system (r,ϕ,x) with the jet axis aligned with the x-direction. Here, it is assumed that the flow is locally parallel and that fluctuating pressure can be written as in the second expression, where A(x) is the amplitude function. The axial wavenumber, α, is complex as shown, where α_i controls the growth rate and α_r determines the phase speed as shown.

Instability Wave Model - Numerical Scheme

- Set up the Inner & Outer Solutions
- Integrate Numerically in the Shear Layer
  - variable step-size Runge-Kutta algorithm
- Match Solutions at the Intermediate Point

$$\hat{p}_I \hat{p}'_o - \hat{p}'_I \hat{p}_o = \Delta(\omega, \alpha) = 0$$

- Newton-Raphson Iterative Scheme

Figure 22

The procedure used to solve the Rayleigh equation is shown in figure 22. The usual procedure, as indicated, is to formulate the solution as an eigenvalue problem. Here, α, is the unknown eigenvalue, which for a fixed real frequency ω is determined iteratively using a Newton-Raphson scheme. The inner and outer shear layer pressure amplitude functions are determined by intregrating numerically through the shear layer using a variable step-size Runge-Kutta algorithm from both the outer and inner directions and matching an intermediate point.

Instability Wave Model - Inner & Outer Solution

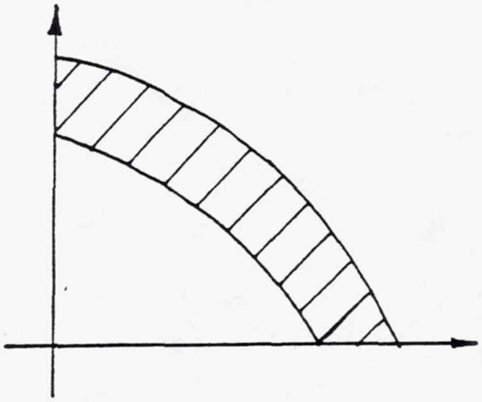

$$\hat{p}(r) = J_n(i\lambda_i r), \lambda_i(\alpha) = \left[\alpha^2 - M_j^2(\omega - \alpha U)^2\right]^{\frac{1}{2}}$$

$$\hat{p}(r) = H_n^{(1)}(i\lambda_o r), \lambda_o(\alpha) = \left[\alpha^2 - \bar{\rho}_\infty M_j^2 \omega^2\right]^{\frac{1}{2}}$$

Figure 23

Figure 23 shows the forms assumed for the instability wave's pressure. These eigenfunctions are consistent with the cylindrical polar coordinate system used in the Rayleigh equation. The upper equation is associated with the inner shear layer, which satisfies boundary conditions associated with the boundedness condition at r = 0. The lower equation is associated with the outer boundary, which satisfies boundary conditions associated with outgoing waves.

Instability Wave Model - Far Field Directivity

$$p(r,\theta,x,t) = \int_{-\infty}^{\infty} g(k) H_n^{(1)}(i\lambda_k r)\exp\left[i(kx + n\theta - \omega t)\right] dk$$

$$\lambda_k = \left[k^2 - \bar{\rho}_\infty M_j^2 \omega^2\right]^{\frac{1}{2}}$$

$$A(x) = A_o(x_o)\exp\left[\int_{x_o}^{x} (i\alpha_r - \alpha_i) dx\right]$$

$$g(k) = \frac{1}{2\pi}\int_{-\infty}^{\infty} A(x)\exp(-ikx)dx$$

$$D(\chi) = \lim_{R\to\infty} \frac{1}{2} R^2 \mid p \mid^2 = 2 \mid g(\bar{\rho}_\infty^{\frac{1}{2}} M_j \omega \cos\chi) \mid$$

Figure 24

Following the procedure of Tam and Burton (1984) of matching the inner and outer solutions, the acoustic pressure, p(r,θ,x,t), in the region outside the jet flow is given by the first equation in figure 24, where the second equation defines the eigenvalue λ_k. The streamwise variation in amplitude and phase of the instability wave, A(x), is given by the third equation. The wavenumber spectrum, g(k), is obtained from the Fourier transform A(x) as indicated in the fourth equation. The farfeild directivity function, D(x), defined as the sound power radiated in a direction per unit solid angle by an instability wave of frequency ω, is given in the bottom equation.

Modes of Instability

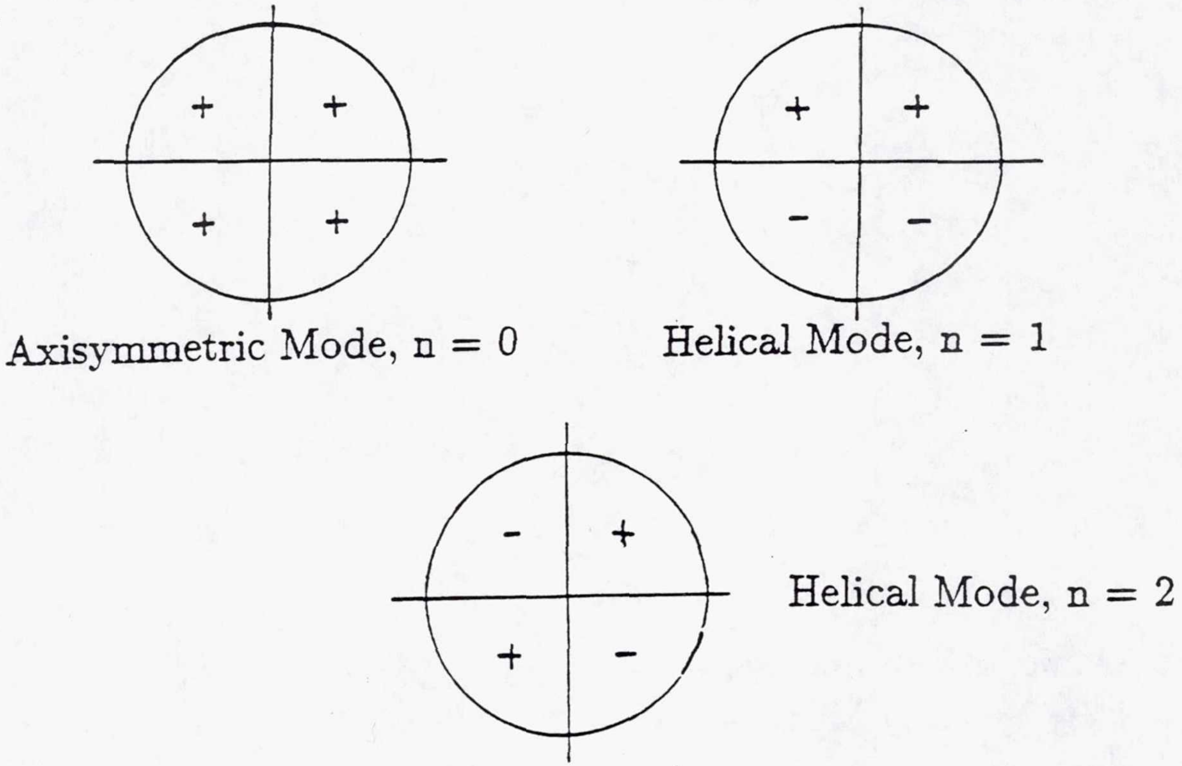

Axisymmetric Mode, n = 0

Helical Mode, n = 1

Helical Mode, n = 2

Figure 25

Figure 25 provides several examples of the instantaneous instability wave pressure in a cross plane associated with the first few fundamental modes n = 0, 1, and 2. These modes are generally considered the most dominant modes of instability, in that they are generally the most highly amplified instability waves in a cylindrical shear layer with a half-Gaussian mean velocity profile.

Modes of Instability

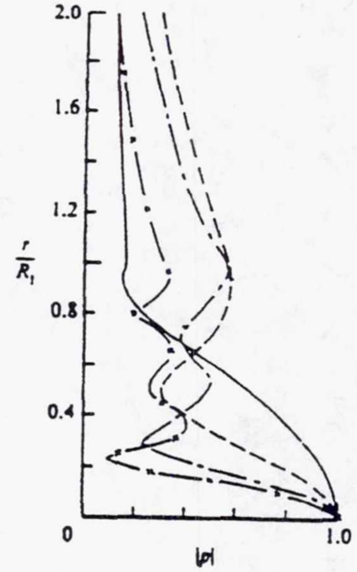

Supersonic Instability Wave. —, (0,1) Mode; – – –, (0,2) Mode; – – –, (0,3) Mode; –x–x–, (0,4) Mode

Figure 26

In figure 26 example radial distributions are shown for the first few elementary supersonic instability wave pressure fields. Even though calculations were performed for jet total temperatures to 1370°K, only the (0,1) mode achieved supersonic phase speed. Thus only this mode would radiate sound to the far field. Higher jet temperatures, however, would be expected to produce higher order supersonic instability waves with supersonic phase speed.

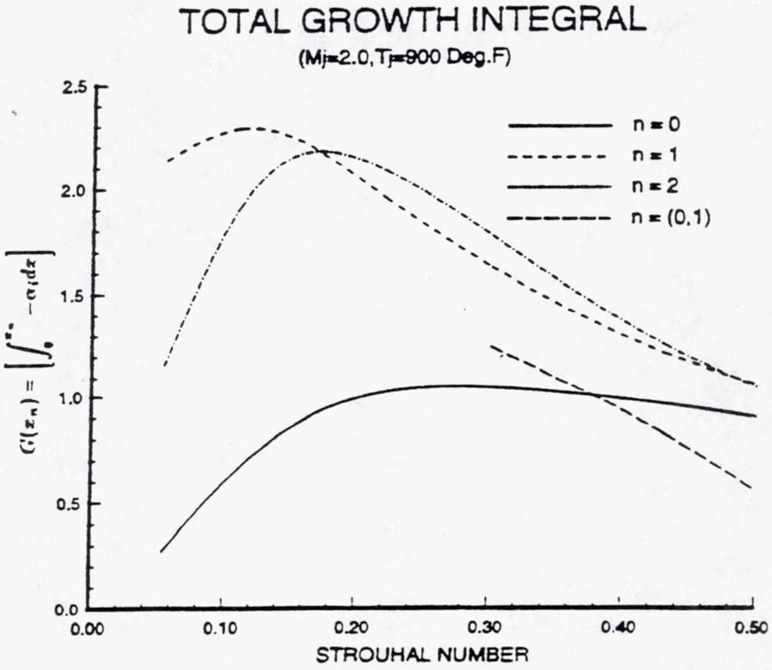

Figure 27

Instability wave theory suggests that noise characteristics of hot supersonic jets in the peak radiation direction are related to those of the most highly amplified instability wave. The total amplification of an instability wave of frequency, ω, and mode number, n, is related to the growth rate of the wave, which is functionally related to the sign and magnitude of α_i, the imaginary part of the axial wavenumber α. The total growth integral, evaluated to a wave's neutral point x_n (i.e. $\alpha_i = 0$), is used as a gauge for the relative importance of a given mode at a specified frequency to produce noise. The total growth integral is plotted as a function of Strouhal number in figure 27 for several K-H modes and the one supersonic instability wave with supersonic phase speed. From figure 27 it can be noted that the axisymmetric K-H wave is relatively unimportant over the entire Strouhal range shown. The same applies to the supersonic instability wave, where supersonic phase speeds were obtained only for Strouhal numbers above 0.3. Both the first and second order helical modes achieve the highest growth rates. In the Strouhal number range for maximum noise emission, $0.05 \leq S_t \leq 0.1$, the first order helical dominates. In the Strouhal number range above 0.1, both first and second order helical modes are equally important. This suggests that one should, in the future, consider even higher order modes for hot jets.

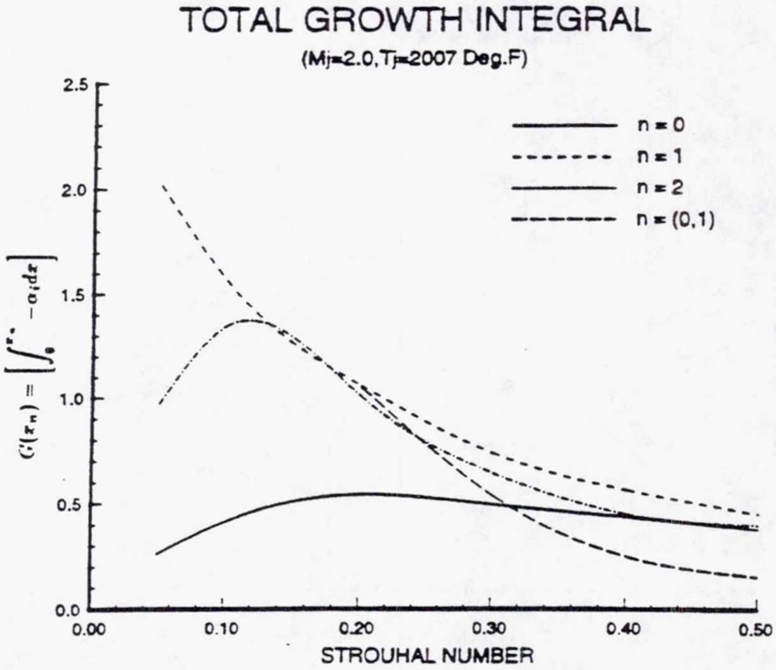

Figure 28

In a similar fashion, the total growth integral results for the jet total temperature of 1370°K is shown in figure 28. Immediately apparent is the increased significance of the supersonic instability wave, which is now competitive with the K-H waves in the Strouhal number range above 0.2. Again the first order helical mode dominates the Strouhal number range associated with peak noise emission, although all amplitudes for K-H waves have diminished from those computed for the previous 755°K jet temperature. The axisymmetric mode only achieves importance in the higher Strouhal number range above 0.3. The fact that all modes calculated have nearly identical importance at higher Strouhal number represents a major difficulty in application of the Rayleigh model. The utility of the Rayleigh model diminishes when many modes become significant, since the present theory cannot assign initial amplitudes to any of the modes. In the present calculations, it is assumed that all modes have equal initial amplitudes. This is a restrictive assumption, since in reality one expects the initial shear layer receptivity to disturbances to be dependent on wave frequency and mode number.

STROUHAL DEPENDENCE WITH JET ANGLE
Spectrum Level Data, 12 ft. Circular Arc

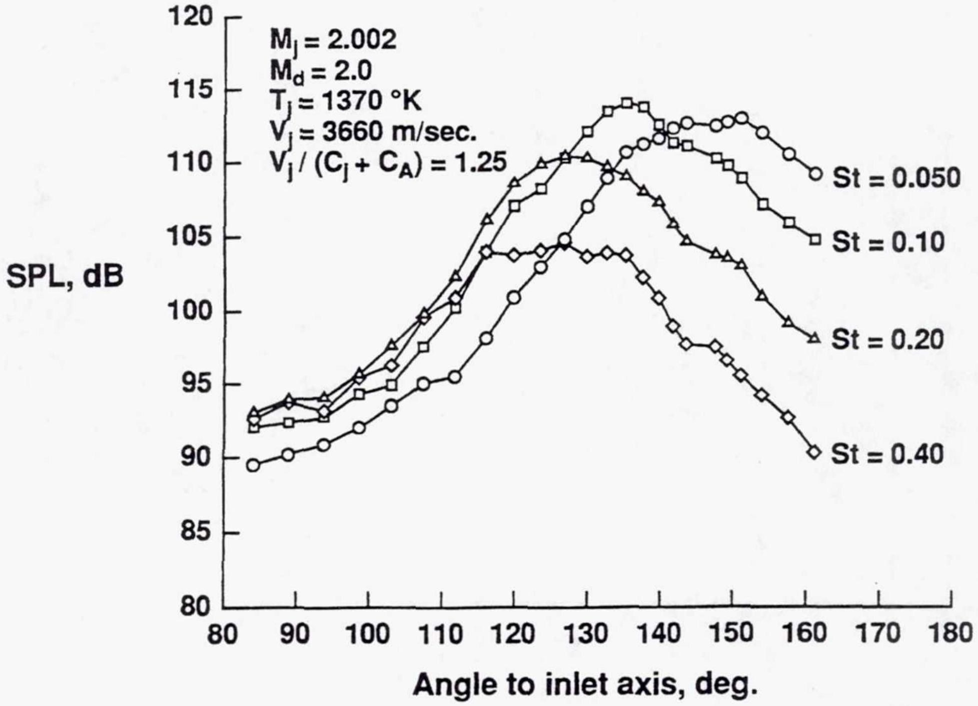

Figure 29

The angular dependence of the Strouhal frequency is important in verification of the application of spatial stability theory to solve the compressible Rayleigh equation for prediction of noise emission. Figure 29 shows this dependence for the major Strouhal frequencies of interest at 1370°K. The data is normalized by the spectral amplitude corresponding to the maximum value, P_o, among all four Strouhal frequency components. This normalization procedure is chosen since instability wave theory cannot predict absolute values for noise radiation. As can be observed, the $S_t = 0.05$ and 0.01 components are dominant frequencies, but peak at different angles to the inlet axis. The 0.4 component is least significant and has a peak amplitude 10 dB less than the 0.1 component. Recalling figure 7, the Mach wave emission process peak is only 15 dB above what may be considered noise generated by small scale turbulence. Thus the 0.4 component directional amplitude characteristics shown in figure 29 may be influenced by noise generated by small scale turbulence.

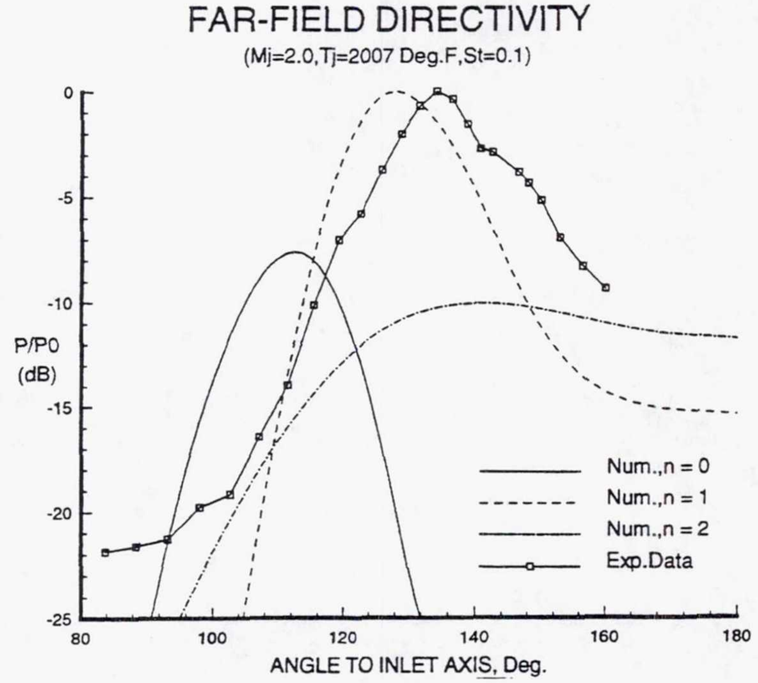

Figure 30

Figure 30 shows a comparison between the measured directivity of the 0.1 Strouhal frequency component and the Rayleigh prediction of noise for the three K-H waves n = 0, 1,2. The jet total temperature is 1370°K, but for this Strouhal frequency there is no solution for a supersonic instability wave. The predicted far field pressure for each of the instability modes is normalized using the same procedure provided in figure 29. All K-H waves are initialized with equal amplitudes at the nozzle exit. From this comparison, it is apparent that the first order helical mode is the most dominant component. Both the axisymmetric mode, n=0, and the second order helical mode, n=2, contribute equal amounts to the sound field. Note that the data shows inflections near those angular positions where each respective mode achieves their peak amplitude. The angular shift between data and computation is related to the finite distance the data was collected from the nozzle (R = 12 ft.). Adjustment for true source location in the jet would shift all measured data several degrees toward the numerically predicted data.

PREDICTION OF FAR FIELD DIRECTIVITY FOR $S_t = 0.4$

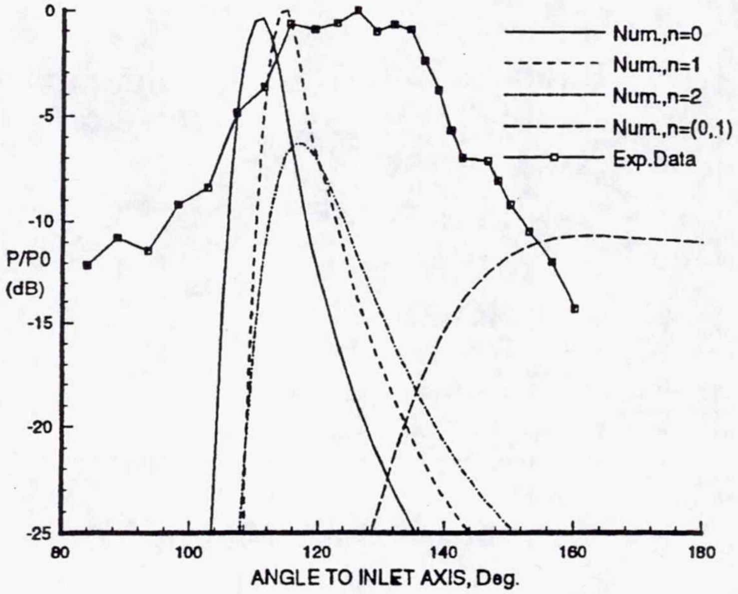

Figure 31

Figure 31 shows a similar comparison between predicted and measured acoustic data for the 0.4 Strouhal frequency component. Here we see that both the axisymmetric and first helical K-H wave is equally important. One also sees that the (0,1) mode supersonic instability wave has a direct influence on the predicted noise radiation at narrow angles to the jet axis. The measured data also shows signs of its existence. In general we see that the comparison to data is not as good as that obtained at lower Strouhal number. This may be due to the influence of noise generated by fine scale turbulence.

NOISE REDUCTION ASSOCIATED WITH HOT NON-ROUND JET EXIT GEOMETRY

1160°R jet temp; constant thrust/ mass flow comparison

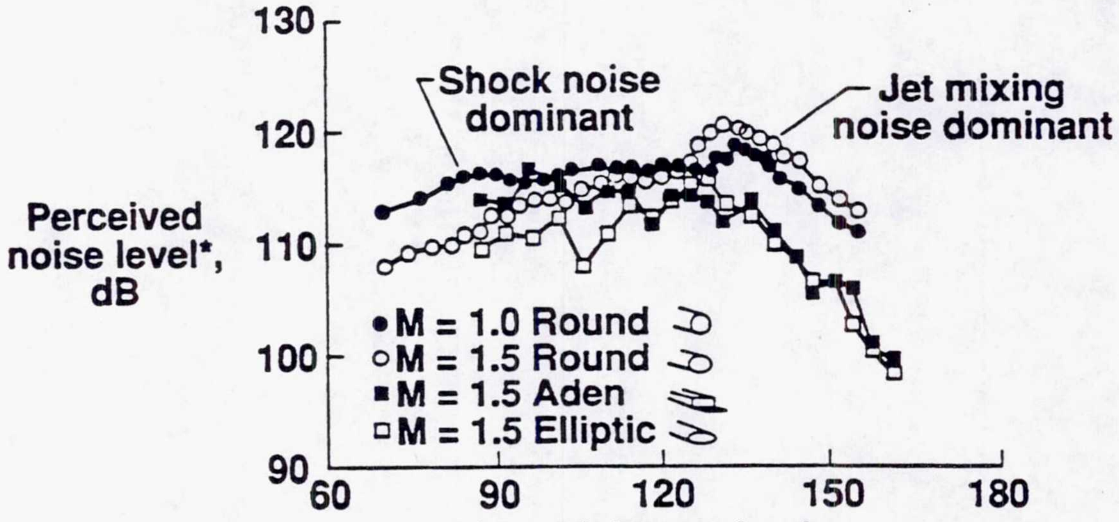

* Scaled to full scale, 50,000 lb thrust at FAR 36 take-off sideline point

Figure 32

A study was recently conducted to determine the noise reduction potential associated with simple single nozzle ducts of various geometries. Figure 32 shows a comparison of noise emitted by a round convergent nozzle, a round convergent-divergent nozzle with exit design Mach number of 1.5, an elliptic convergent-divergent nozzle with an aspect ratio of 2 and design Mach number of 1.5, and an Aden nozzle (i.e. rectangular geometry) with an aspect ratio of 2 and design Mach number of 1.5. The data is presented in terms of perceived noise level in dB as a function of angle to the nozzle inlet axis. The jet temperature for all nozzles was 1160°R and the data has been normalized to 50,000 pounds of thrust at the FAR 36 sideline distance of 1476 feet. As is evident both the elliptic and Aden nozzles produce significant noise reduction in the peak noise direction, $\psi \geq 120^{\circ}$. However, unlike the Aden nozzle, the elliptic nozzle has very low levels of shock noise, so that significant reductions are obtained at all angles to the jet axis. The single elliptic nozzle produces a noise reduction between 7 and 8 PNdB relative to the baseline convergent nozzle.

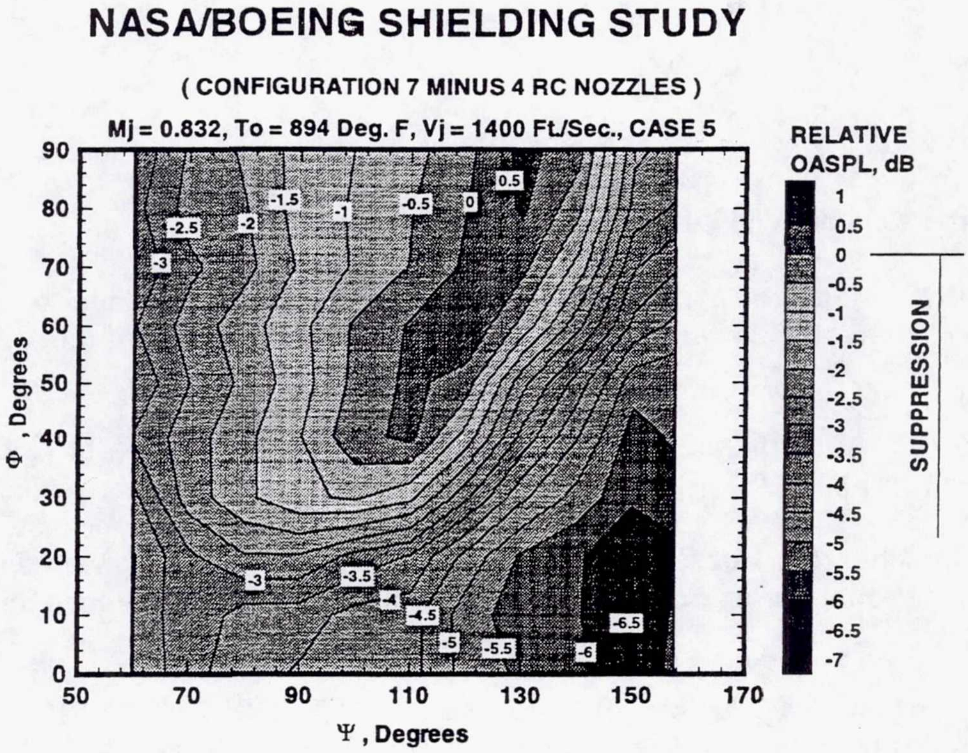

NASA/BOEING SHIELDING STUDY

(CONFIGURATION 7 MINUS 4 RC NOZZLES)

Mj = 0.832, To = 894 Deg. F, Vj = 1400 Ft/Sec., CASE 5

Figure 33

Figure 33 shows a comparison between noise emitted by 4 interacting in line nozzles and 4 non-interacting equivalent baseline round convergent nozzles. The 4 interacting nozzles are separated by 2.5 jet exit diameters. The noise produced by the 4 non-interacting jets is computed from ANOPP with each synthetic nozzle located at the equivalent location of the 4 interacting nozzle locations. The contour map of figure 33 shows the result of substracting the non-interacting jets from the measured noise of the interacting jets. At Φ = 0°, the azimuthal view is sideline along the axis joining all nozzles. At Φ = 90°, the azimuthal view is normal to the plane containing the four nozzles. It can be observed that significant noise reductions occur in the sideline direction. At Φ = 0° and Ψ = 150°, the 6 dB relative noise reduction indicates complete shielding of noise by the near jet of all other noise generated by the remaining nozzles. At Φ = 90° and Ψ = 90°, the -1.5 dB relative noise reduction indicated that aerodynamic interaction of the jet plumes may have led to faster decay of jet centerline velocity and thus lower noise. Only a small region exhibits a slight noise increase at Φ = 90° and Ψ = 130°.

REFERENCES

Dash, S.M., and Kenzakowski, D.C., 1992, Private Communication.

Oertel, H., 1982, "Measured Velocity Fluctuations Inside the Mixing layer of a Supersonic Jet", Recent Contributions to Fluid Mechanics, Berlin, Springer Verlag, pp. 170-179.

Pope, S.B., 1978, "An Explanation of the Turbulent Round-Jet/Plume-Jet Anomaly, AIAA J., March, pp. 279-281.

Sarkar, S., Erlebacher, G., Hussaini, M.Y., and Kreiss, H.O., "The Analysis and Modeling of Dilitational Terms in Compressible Turbulence", ICASE Report No. 89-79.

Seiner, J.M., Ponton, M.K., Jansen, B.J., and Lagen, N.T., 1992, "The Effects of Temperature on Supersonic Jet noise Emission", DGLR/AIAA 92-02-046.

Tam, C.K.W. and Burton, D.E., 1984, "Sound Generated by Instability Waves of Supersonic Jets, Part 2, Axisymmetric Jets", J. Fluid Mech.., Vol. 138, pp. 273-295.

Tam, C.K.W. and Hu, F.Q., 1989, "On Three Famlies of Instability Waves of High Speed Jets", J. Fluid Mech., Vol. 201, pp. 447-483.

Zorumski, W.E., 1982, "Aircraft Noise Prediction Program Theoretical Manual", NASA TM 83199.

1999176565

PREDICTION OF BROADBAND SHOCK NOISE FROM RECTANGULAR NOZZLES

N.N. Reddy
Lockheed Aeronautical Systems Company
Marietta, Georgia

and

C.K.W. Tam
Florida State University
Tallahassee, Florida

S28-71

409555

19P.

OBJECTIVE

TO DEVELOP A SEMI-EMPIRICAL BROADBAND SHOCK ASSOCIATED NOISE PREDICTION PROGRAM FOR SUPERSONIC RECTANGULAR JETS

BROADBAND SHOCK ASSOCIATED NOISE GENERATION MECHANISM

METHODOLOGY

USE THE BROADBAND SHOCK ASSOCIATED NOISE PREDICTION FORMULA FOR CIRCULAR JETS AS A STARTING POINT. MAKE NECESSARY CHANGES TO INCORPORATE NEW PHYSICS OF THE SHOCK CELLS AND FLOW TURBULENCE PERTINENT TO SUPERSONIC RECTANGULAR JETS.

BROADBAND SHOCK ASSOCIATED NOISE GENERATION MECHANISM

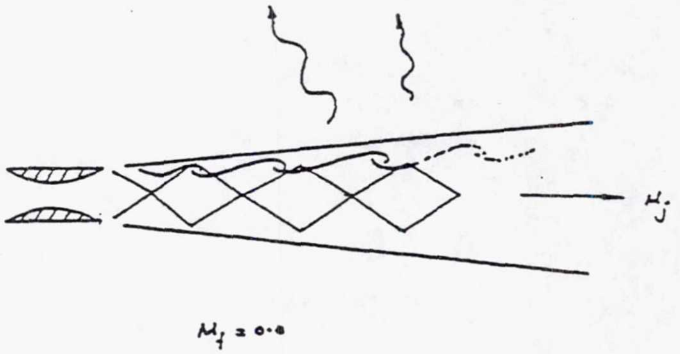

LARGE TURBULENCE STRUCTURES
/ INSTABILITY WAVES

⇕ ⟹ BROAD BAND
SHOCK NOISE

SHOCK CELL STRUCTURE

Large scale turbulence instability waves are generated in the shear layers of supersonic jets. These instability waves interacting with the shock cells generate the sound waves that will radiate. These noise source is known as "Broadband Shock Noise".

RECTANGULAR NOZZLES

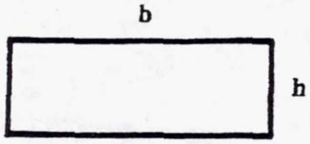

THREE TYPES OF COMMONLY USED NOZZLES

1. C-D IN BOTH PLANES
2. C-D IN THE FLY-OVER PLANE, STRAIGHT SIDE WALLS
3. NOZZLE WITH CUT-OUTS

WILL CONSIDER ONLY TYPE 2 NOZZLES WITH ASPECT RATIO *b/h* LESS THAN *6*

There are three types of rectangular supersonic jet nozzles: (1) Convergent - divergent in both planes, (2) Convergent - divergent in one plane (generally in the fly-over plane) and straight walls in other plane, and (3) Convergent - divergent nozzle with cut-outs. In this study, only convergent-divergent nozzles with straight walls and aspect ratios less than 6 are considered.

RECTANGULAR NOZZLE WITH STRAIGHT SIDE WALLS

TWO SETS OF SHOCK-CELLS

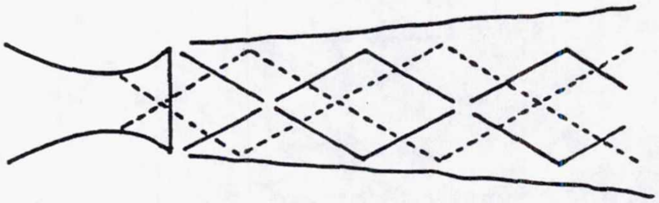

FIRST SET OF SHOCK CELLS STARTS AT THE NOZZLE LIP

$\Delta P \sim (M_j^2 - M_d^2)$

SECOND SET OF SHOCK CELLS STARTS AT THE THROAT

$\Delta P \sim (M_j^2 - 1.0)$

THERE WILL BE BROADBAND SHOCK NOISE EVEN WHEN THE NOZZLE IS OPERATING AT NOMINAL DESIGN MACH NUMBER

In the case of rectangular nozzles with two straight side walls and two convergent-divergent walls, two sets of shock calls will be developed. One set of shock cells generate at the nozzle lip (exit plane). The strength of those shocks are a function of jet Mach number and nozzle design Mach number. The second set of shock cells generate at the nozzle throat and the strength of these shocks is a function of jet Mach number only. From this assumption, it is clear that the shocks will be present even when the nozzle is operating at design Mach number.

VORTEX-SHEET SHOCK CELL SOLUTION

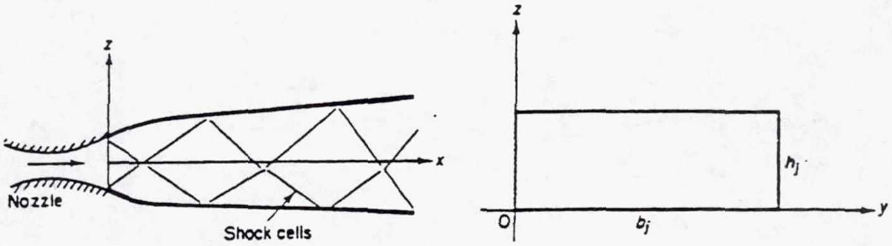

$$p(x,y,z)=\sum_{n=1}^{\infty}\sum_{m=1}^{\infty}\frac{4\Delta p}{nm\pi^2}(1-\cos n\pi)(1-\cos m\pi)\sin\frac{n\pi y}{b_j}\sin\frac{m\pi z}{h_j}\cos k_{nm}x.$$

$$k_{nm}=\left(\frac{n^2}{b_j^2}+\frac{m^2}{h_j^2}\right)^{1/2}\frac{\pi}{(M_j^2-1)^{1/2}},\qquad n,m=1,2,3,\ldots.$$

SHOCK CELL SPACING $L_{mn} = 2\pi/k_{mn}$

SHOCK CELL STRENGTH ~ $\Delta P/nm$

The formulation is based on the assumption that the shear layer is a thin vortex sheet. This theory has been developed and validated for round jets. Recognizing the differences in the flow characteristics between round and rectangular nozzles, this theory has been extended to rectangular nozzles.

CONVECTION VELOCITY

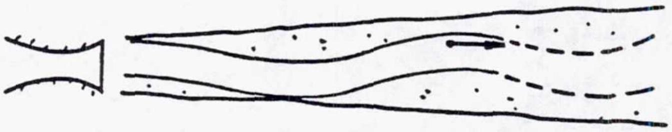

FOR ROUND JETS $U_c/U_j = 0.7$

FOR RECTANGULAR JETS OF LARGE ASPECT RATIO U_c/U_j IS LESS THAN 0.7

TO FIND PROPER CONVECTION VELOCITY WE USE SCREECH DATA

Convection velocity is one of the parameters used in the theoretical development. It is known for circular nozzles, the convection velocity is about 70% of jet exit velocity. For rectangular jets, however, this convection velocity is less than that of the circular nozzles. Some of the experimental data (primarily related to screech tones) were utilized to determine the convection velocity for rectangular nozzles.

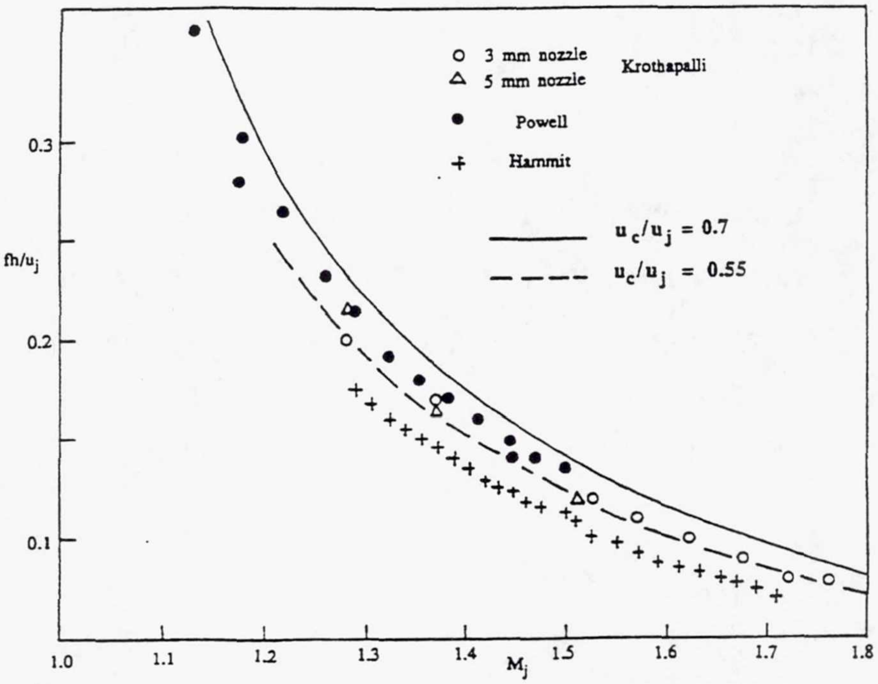

Comparsion between measured and calculated screech tone frequencies of rectangular supersonic jets

This figure illustrates the variation of screech frequency (struhal number) as a function of jet Mach number. These results are compared with the calculations, assuming convection velocities equal to 70% and 55% of jet velocities. It is clear that the experimental data correlates better with convection velocity equal to 55% of jet velocity.

SEMI-EMPIRICAL FORMULA FOR THE CONVECTION VELOCITY OF THE LARGE TURBULENCE STRUCTURES/INSTABILITY WAVES

$$U_c/U_j = 0.5 + 0.2\, e^{-0.5(b/h-1.0)}$$

Using the screech tone experimental data, a semi-empirical formula for convection velocity of rectangular nozzles was derived. This formula is given here.

SPECTRUM FORMULA FOR THE FLY-OVER PLANE

$$S(R,\psi,f) = \frac{\bar{c}\,A_j \rho_\infty^2 a_\infty^4 M_j^2 \overline{A}^2}{R^2 f[1+\frac{\gamma-1}{2}M_j^2]}$$

$$\cdot \left[\sum_{m=1}^{30}\sum_{n=1}^{30} \frac{1}{(2m-1)^2(2n-1)(1+2(n-1)e^{-(n-1)})} \right.$$

$$\cdot\, e^{-(\frac{f_m}{f}-1)^2(1+M_c\cos\psi)^2 L^2(\frac{u_j}{u_c})^2 \frac{1}{2\ell n^2}}$$

$$\left. + \sum_{m=1}^{3} \frac{1}{4m^2} e^{-(\frac{\widehat{f_m}}{f}-1)^2(1+M_c\cos\psi)^2 L^2(\frac{u_j}{u_c})^2 \frac{1}{2\ell n^2}} \right]$$

$$\cdot \begin{cases} A_j/A_{\text{nozzle}}, & \text{for overexpanded jet} \\ 1, & \text{for underexpanded jet} \end{cases}$$

$$\overline{A}^2 = \frac{\left(\frac{M_j^2-M_d^2}{1+\frac{\gamma-1}{2}M_d^2}\right)^2 \frac{\Lambda^2}{1+\Lambda^2}}{1+\left[\left(\frac{M_j^2-M_d^2}{1+\frac{\gamma-1}{2}M_d^2}\right)^2 \frac{\Lambda^2}{1+\Lambda^2}\right]^{3/2}}$$

$$+ \frac{\left(\frac{M_j^2-1}{1+\frac{\gamma-1}{2}}\right)^2 \frac{1}{1+\Lambda^2}}{1+\left[\left(\frac{M_j^2-1}{1+\frac{\gamma-1}{2}}\right)^2 \frac{1}{1+\Lambda^2}\right]^{3/2}}$$

$$\Lambda = b/h$$

Using the shock noise theory for circular nozzles and the experimental data, prediction formula has been derived in the fly-over plane (i.e., in the plan perpendicular to convergent-divergent nozzle walls. Here the formulas are given for overexpanded and underexpanded jet conditions.

COMPARISON WITH MEASURED DATA OF PONTON, MANNING AND SEINER (NASA TM 89002, 1986)

ASPECT RATIO	M_d
1.538	1.66
3.398	1.35
5.325	1.35

(COLD JETS)

FLY-OVER PLANE

θ = exhaust angle

The predictions are compared with the experimental data in the fly-over plane for 3 nozzles with different aspect ratios. These tests were for cold jets under static conditions (without forward speed).

These figures compare the predicted spectra with the measured data for a nozzle with AR = 1.538, Md = 1.66 and $M_J = 1.904$. The comparisons are shown for 135°, 90°, and 75° from jet exhaust.

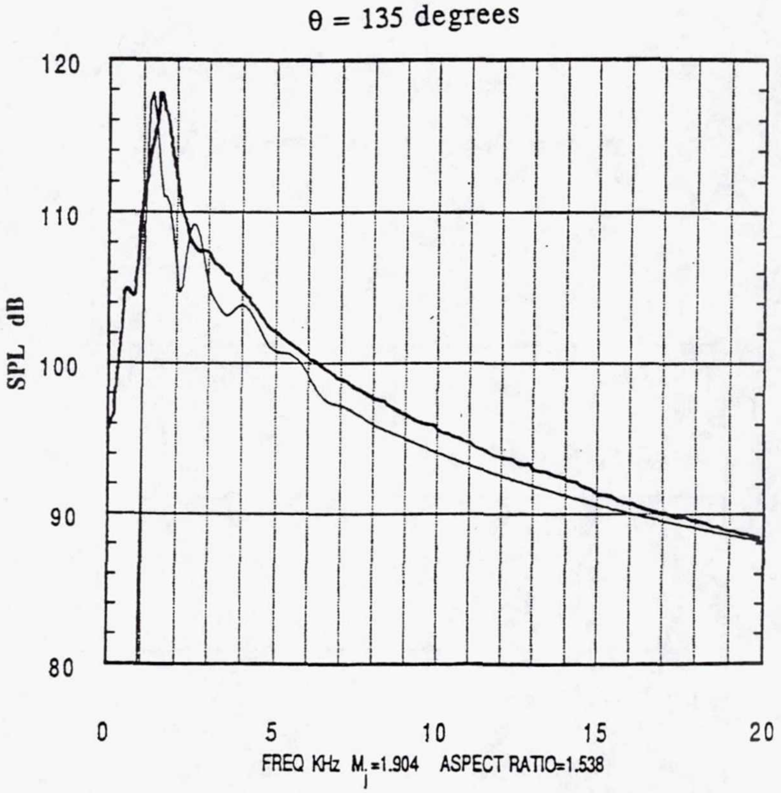

SOUND-PRESSURE-LEVEL SPECTRUM

θ = 90 degrees

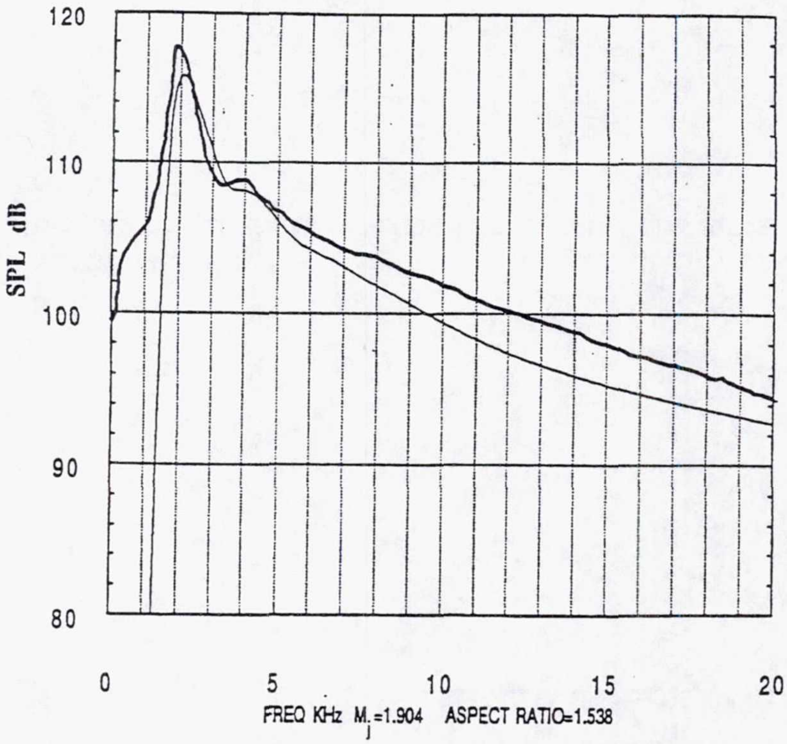

SOUND-PRESSURE-LEVEL SPECTRUM

θ = 75 degrees

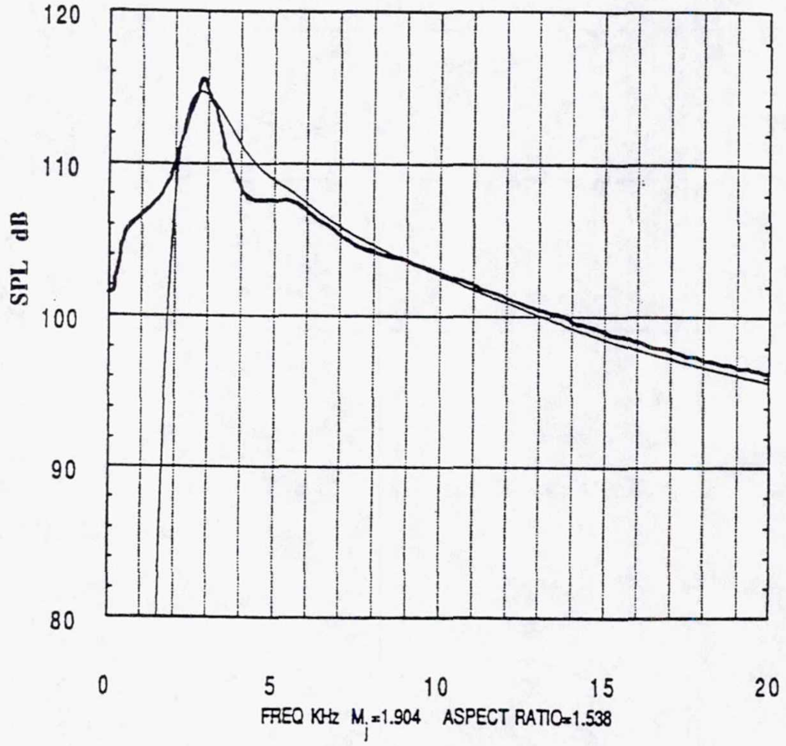

SOUND-PRESSURE-LEVEL SPECTRUM

These figures compare the predicted spectra with the measured data for a nozzle with AR=3.398, Md= M_J=1.35 (perfectly expanded jet). The comparisons are shown for 135°, 90°, and 75° from jet exhaust.

Even though, the jet Mach number is the same as the design Mach number, the evidence of the shock noise is clear from these figures.

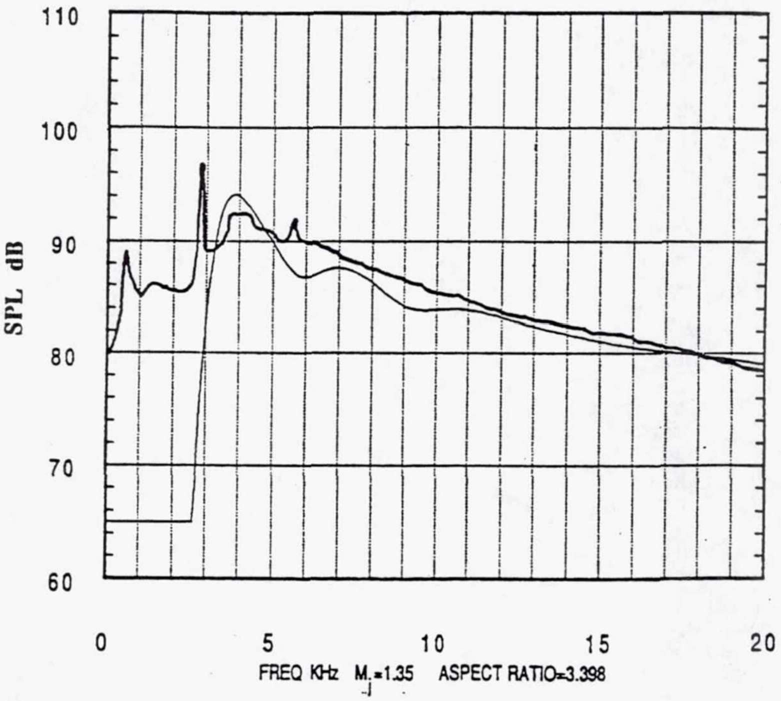
θ = 135 degrees

SOUND-PRESSURE-LEVEL SPECTRUM

θ = 90 degrees

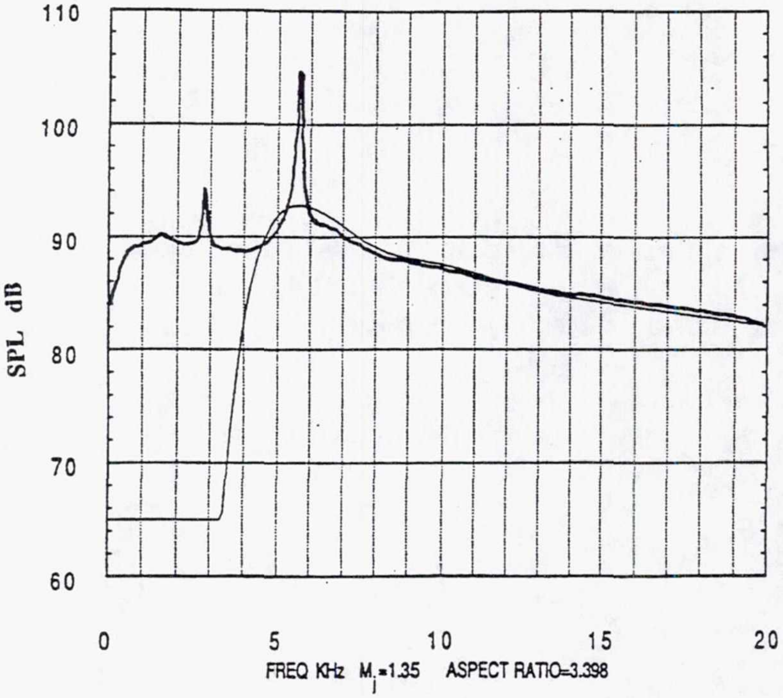

SOUND-PRESSURE-LEVEL SPECTRUM

θ = 75 degrees

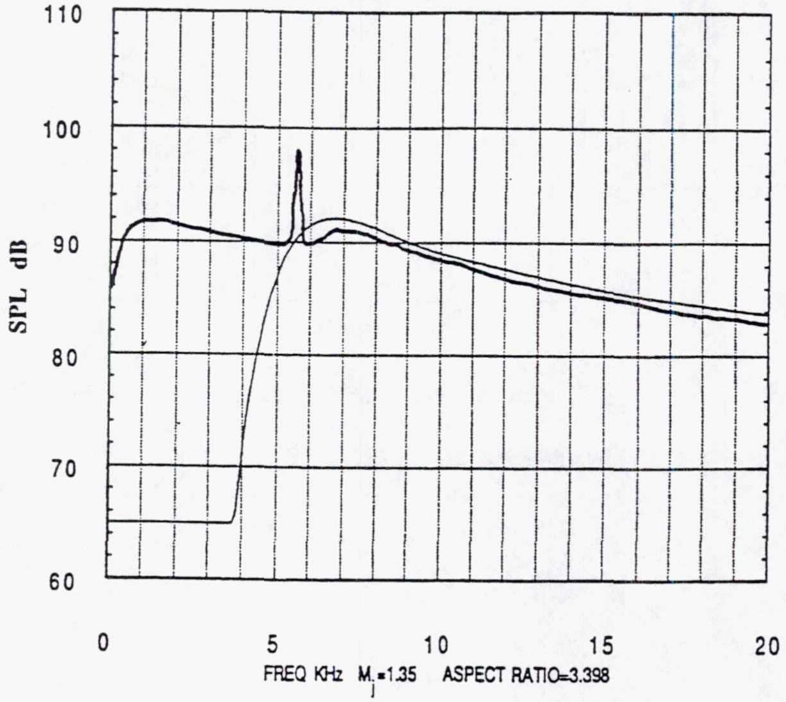

SOUND-PRESSURE-LEVEL SPECTRUM

These figures compare the predicted spectra with the measured data for nozzle with AR = 5.325, Md = 1.35, $M_J = 1.608$. The comparisons are shown for 135°, 90°, and 75° from jet exhaust.

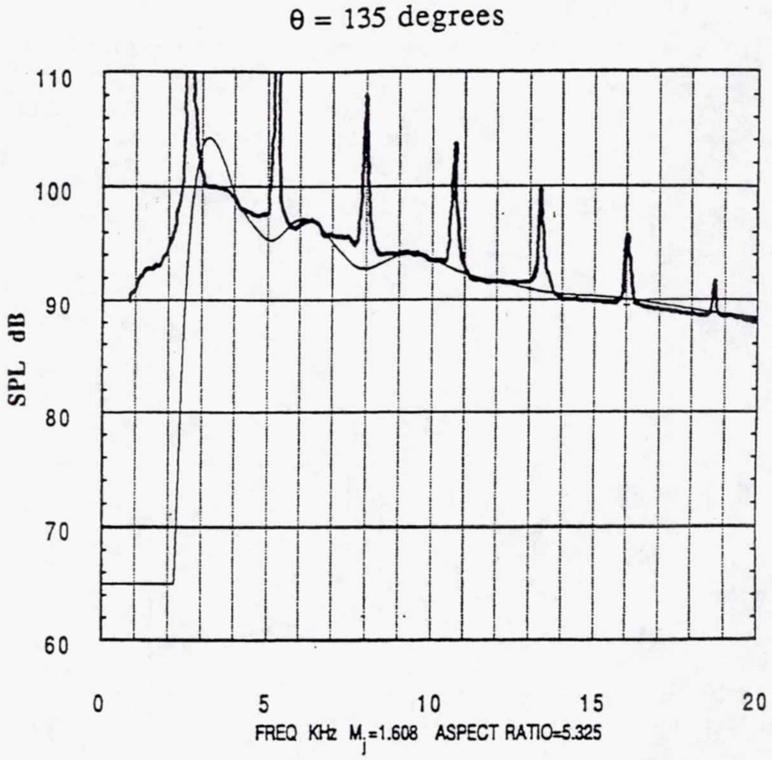

SOUND-PRESSURE-LEVEL SPECTRUM

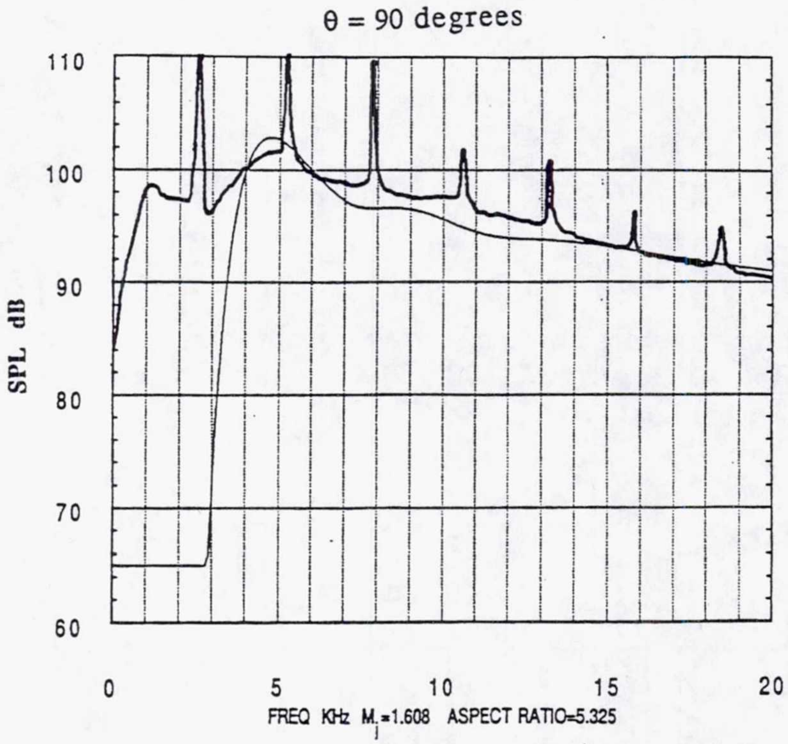
θ = 90 degrees

SOUND-PRESSURE-LEVEL SPECTRUM

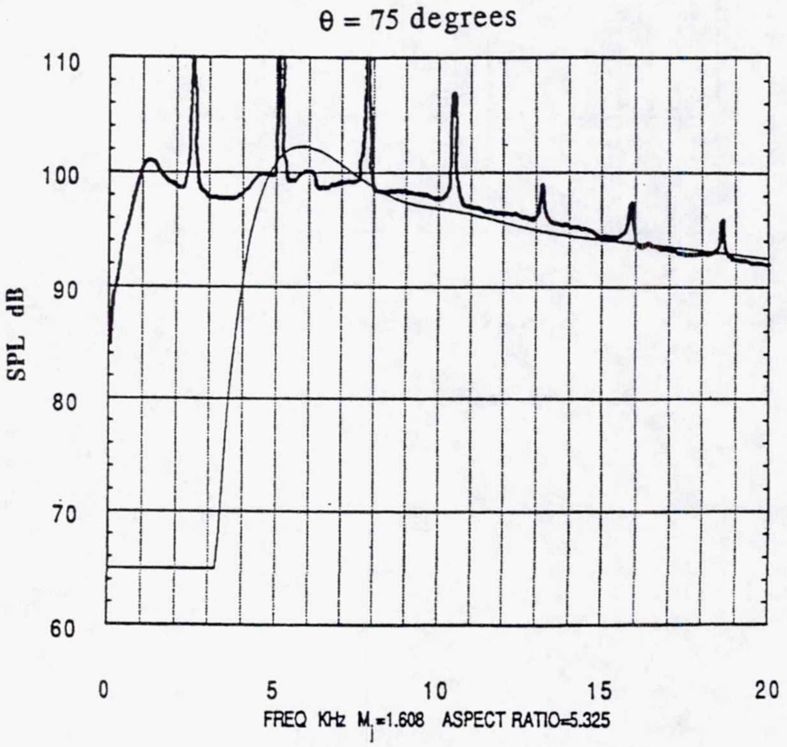
θ = 75 degrees

SOUND-PRESSURE-LEVEL SPECTRUM

SUMMARY

A SEMI-EMPIRICAL FORMULA FOR THE PREDICTION OF THE BROADBAND SHOCK ASSOCIATED NOISE FROM RECTANGULAR SUPERSONIC JETS IN THE FLY-OVER PLANE HAS BEEN DEVELOPED. THE PREDICTED NOISE SPECTRA COMPARED VERY FAVORABLY WITH THE MEASUREMENTS OF PONTON, MANNING AND SEINER (1986). EXTENSION TO SIDE-LINE DIRECTIONS WILL BE CARRIED OUT.

Broadband Shock Noise prediction method for rectangular nozzles with two parallel side walls has been developed. This method applies for the nozzles with aspect ratio less than 6 and in the fly-over plane. The predicted results compare very favorably with the measured data. The prediction method will be extended to side-line plane.

1999176566

CLIMB TO CRUISE NOISE TEST RESULTS

M.C. Joshi, K.J. Yamamoto, and M.J. Donelson
McDonnell Douglas Aerospace-West
Long Beach, California

and

R.A. Golub and J.W. Rawls
NASA Langley Research Center
Hampton, Virginia

S29-71

409557
20P.

OUTLINE

OBJECTIVES

TEST PROCEDURES

DATA-PREDICTION COMPARISONS

HSCT CLIMB NOISE

SUMMARY

CLIMB-TO-CRUISE NOISE

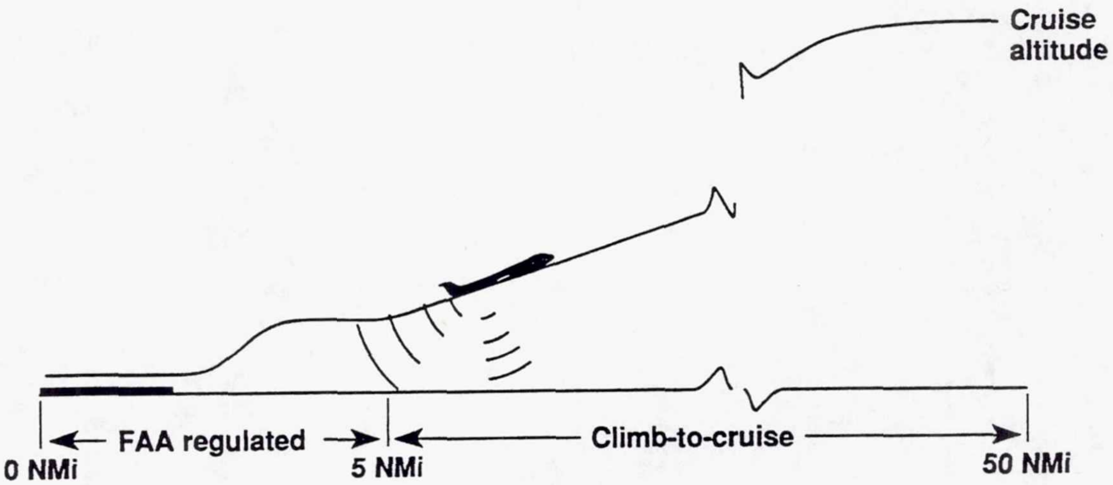

The initial focus of the HSCT suppressor nozzle design was to achieve a 20 dB noise reduction relative to the unsuppressed noise level of a TBE type engine. This would allow the HSCT to meet FAR 36 Stage 3 noise certification requirements at sideline. The design approach also assumed that the suppressor will be retracted soon after takeoff in order to minimize performance losses. Preliminary analyses performed at McDonnell Douglas, however, revealed that some noise suppression may be necessary even beyond 5 miles (and up to 50 plus miles) from the airport in order for the HSCT to be no more noisier than the current Stage 3 subsonic fleet at the farther out communities.

ANOPP PREDICTIONS OF HSCT CLIMB-TO-CRUISE NOISE

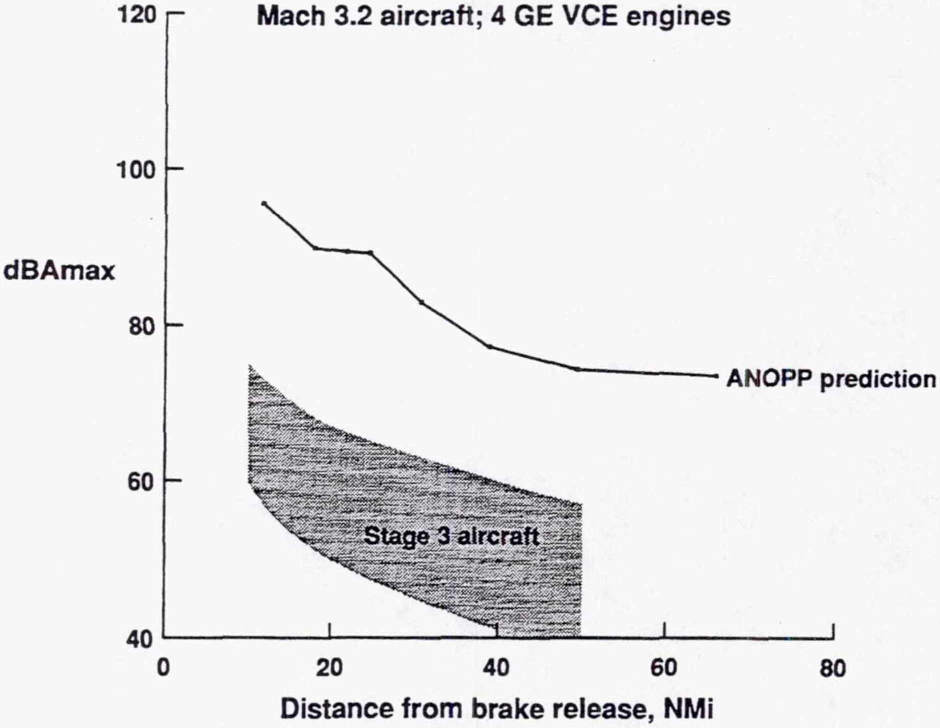

The climb-to-cruise noise predictions (using ANOPP) for a Mach 3.2 HSCT with four VCE engines are shown along with a band covering the corresponding noise levels of modern Stage 3 subsonic airplanes. Notice that the predicted HSCT noise (in maximum A-weighted level) is at least 20 dB higher than the subsonic airplane noise. The confidence or the accuracy of the HSCT noise predictions are unknown due to the facts that the noise methodology is based on a lower flight Mach number, nozzle pressure ratio and temperature data base and is not validated for high flight Mach numbers, nozzles pressure ratios and temperatures. High climb noise may force a suppressor nozzle design redirection or the need to leave the suppressor deployed for a longer time after takeoff (assuming it is still effective acoustically). It is, therefore, necessary that an experimental data base of noise generated by supersonic jets at high flight Mach numbers be developed that will permit a better assessment of HSCT climb noise.

CLIMB-TO-CRUISE NOISE TEST

TEST OBJECTIVES

(1) Perform flight test(s) to assess HSCT subsonic climb noise using aircraft/engine with high NPR, *temperature, and flight speed capabilities.*

(2) Obtain a quality noise database to validate ANOPP and other system noise prediction codes at high NPR, temperature and flight speed.

Upon the recommendation of the HSR Source Noise Working Group an acoustic flight test was planned and performed by NASA Langley with two test objectives: 1) to obtain test data at conditions typical of HSCT during climb in order to assess HSCT climb noise and 2) to obtain a noise database at high NPR, NTR and flight Mach numbers in order to validate ANOPP methodology.

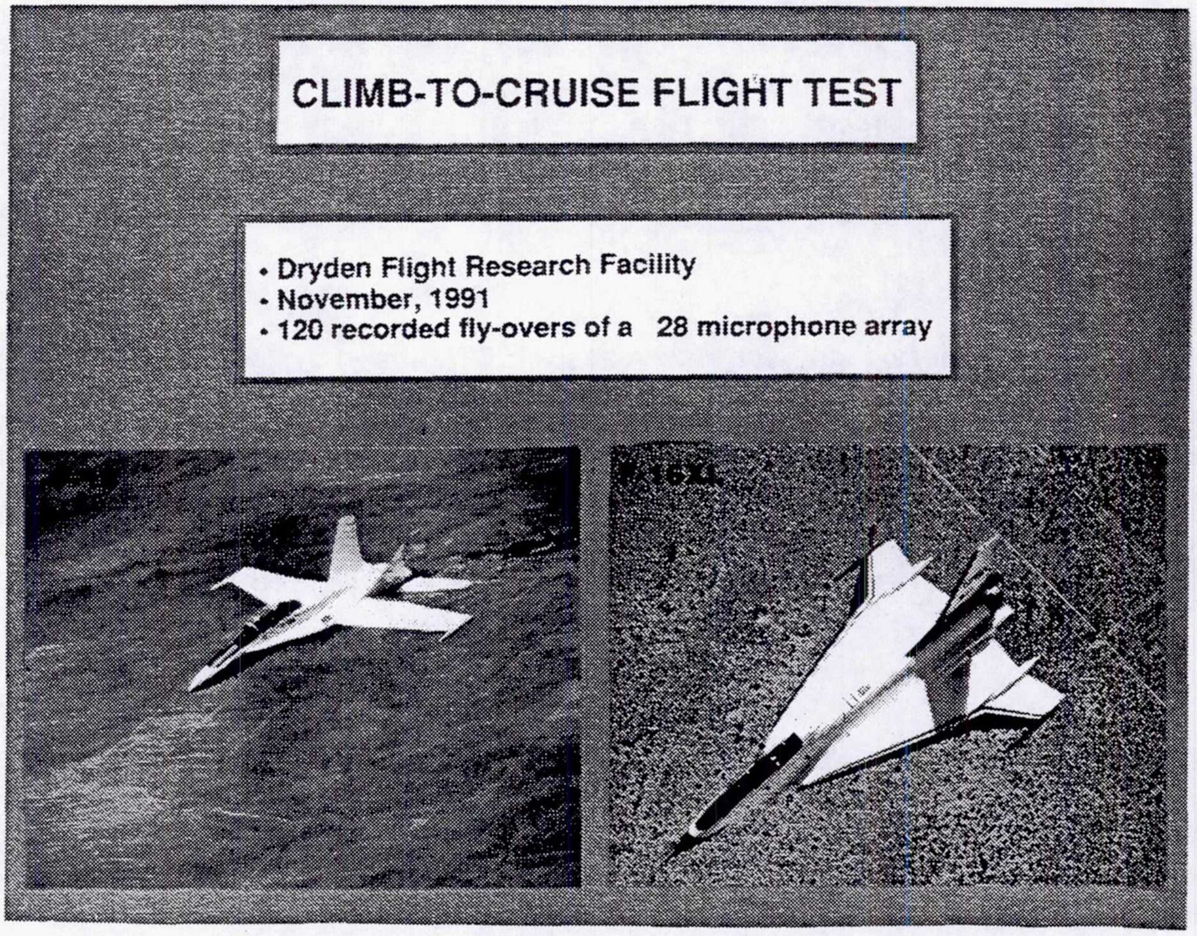

CLIMB-TO-CRUISE FLIGHT TEST

- Dryden Flight Research Facility
- November, 1991
- 120 recorded fly-overs of a 28 microphone array

The test was performed using the F-18 and F-16XL aircraft at Dryden Flight Research Center in November 91. The F-18 is powered by two F404-400 engines which have approximately 10 percent lower Vj than VCE engines. The F-16XL is powered by a single F110-IPE engine and has a Vj approximately 10 percent higher than the Flade engine.

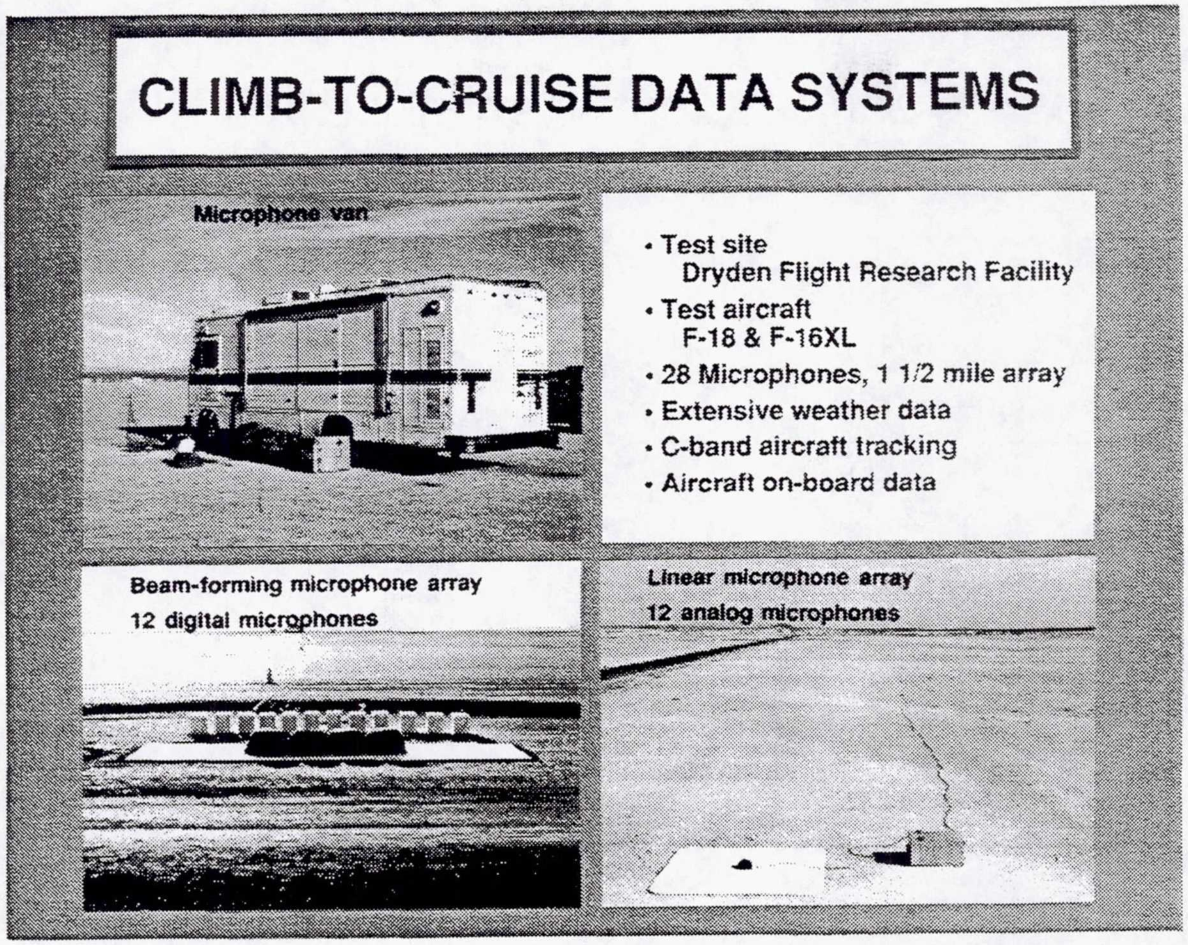

CLIMB-TO-CRUISE DATA SYSTEMS

Microphone van

- Test site
  Dryden Flight Research Facility
- Test aircraft
  F-18 & F-16XL
- 28 Microphones, 1 1/2 mile array
- Extensive weather data
- C-band aircraft tracking
- Aircraft on-board data

Beam-forming microphone array
12 digital microphones

Linear microphone array
12 analog microphones

The data system included two microphone arrays for noise measurement under the flight path. One was a digital array for quick look analysis and another was a linear microphone array consisting of 12 microphones spaced 350 feet apart. The primary purpose of using an array is to be able to ensemble average the signals in order to improve the accuracy and statistical confidence of the measurements. The data from these microphones were recorded on analog tape for later analysis using the NASA Langley ADRAS system. At the test site extensive weather data was obtained using tethered weather balloon, rawindsonde balloon, and two 30 ft weather towers. The aircraft position during the flight was recorded using C-band beacon tracking system. The on-board data system recorded the engine and airplane operating parameters. The F-16XL had a true data system but the F-18 system was only a maintenance system and recorded data only when an event occurred.

CLIMB-TO-CRUISE FLIGHT TEST PROCEDURE

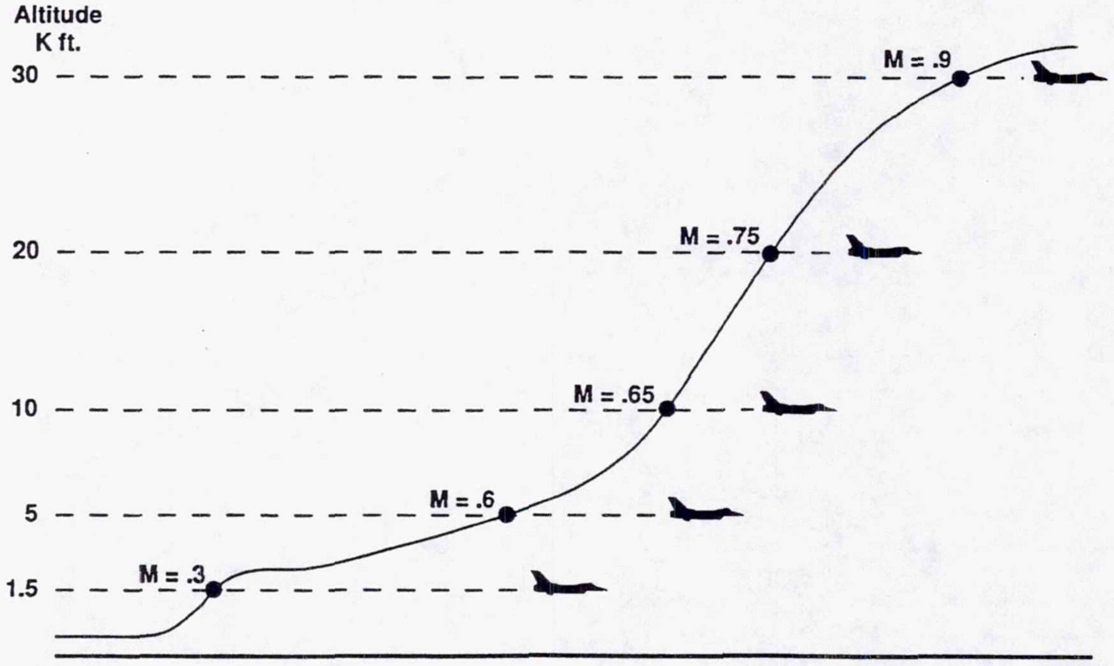

The test procedure included constant speed level flyovers at several altitudes, flight Mach numbers and engine conditions representative of an HSCT during climb-to-cruise. For evaluation of the noise prediction methodology in ANOPP, flyovers at a constant 1500 ft altitude but different flight Mach numbers were planned.

CLIMB-TO-CRUISE TEST MATRIX

- **FULL-SCALE HSCT PARAMETERS MATCHED: ALTITUDE, AIRCRAFT MACH NO., JET VELOCITY (±10%), NOZZLE PRESURE RATIO (3.1 TO 3.5)**

ALT, FT AGL	MACH	# F-18	# F-16 XL
1500	.3	8	9
5000	.6	13	2
10000	.65	15	1
20000	.75	13	
30000	.9	7	
	TOTAL RUNS	56	12

ANOPP TEST MATRIX

- **REQUIRED POWER FOR LEVEL FLIGHT (SECOND ENGINE AT FLIGHT IDLE).**

ALT, FT AGL	MACH	# F-18	# F-16 XL
1500	.3	5	2
1500	.6	6	2
1500	.8	6	2
1500	.95	2	2
	TOTAL RUNS	19	8

The test matrix with target conditions for the climb-to-cruise and ANOPP validation phases of the test program are shown here. Majority of the data were obtained using F-18. One engine was set at the required power for level flight while the second engine was at flight idle. The F-16XL powered by a single high thrust engine experienced significant acceleration during the low altitude climb to cruise flights. To minimize angular smearing and improve data accuracy these flights were conducted in two passes. In one pass, the aircraft got on target conditions approximately 2 to 4 miles upstream of the microphone array. In the second pass the aircraft got on target conditions just above the microphone array.

ENSEMBLE AVERAGING OF MICROPHONE DATA

CLIMB TO CRUISE FLIGHT TEST F-18 SPECTRA
Mach 0.3 at 1500 Feet

Single microphone spectra

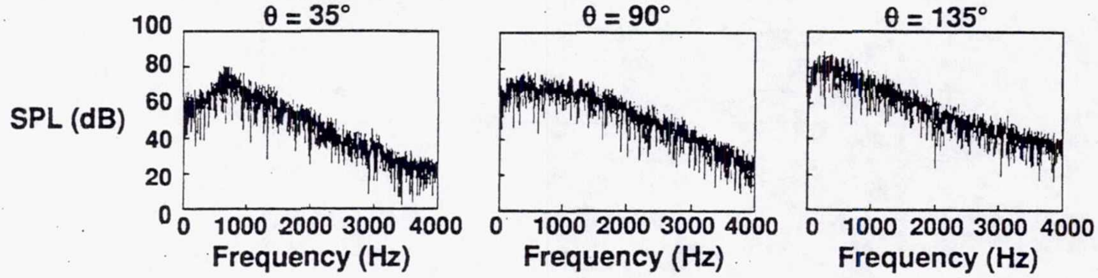

Ensemble averaged spectra

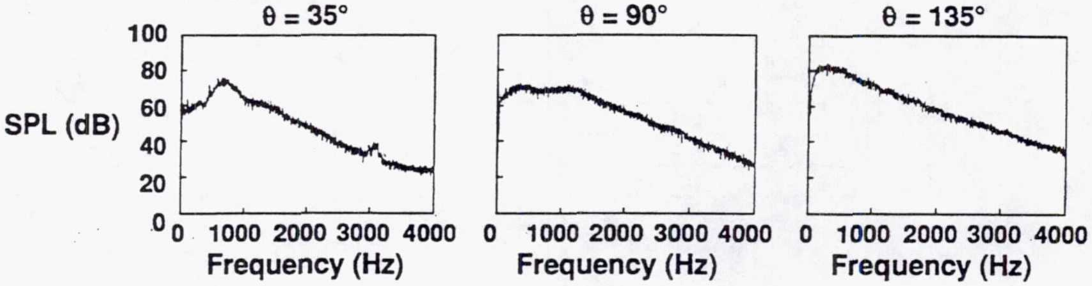

These data show the advantage of using the linear microphone array. The single microphone data have lot of variation in SPLs in adjacent frequencies indicating low statistical confidence. Ensemble averaging significantly improves the accuracy of the measurements.

MEASURED OASPL DIRECTIVITIES

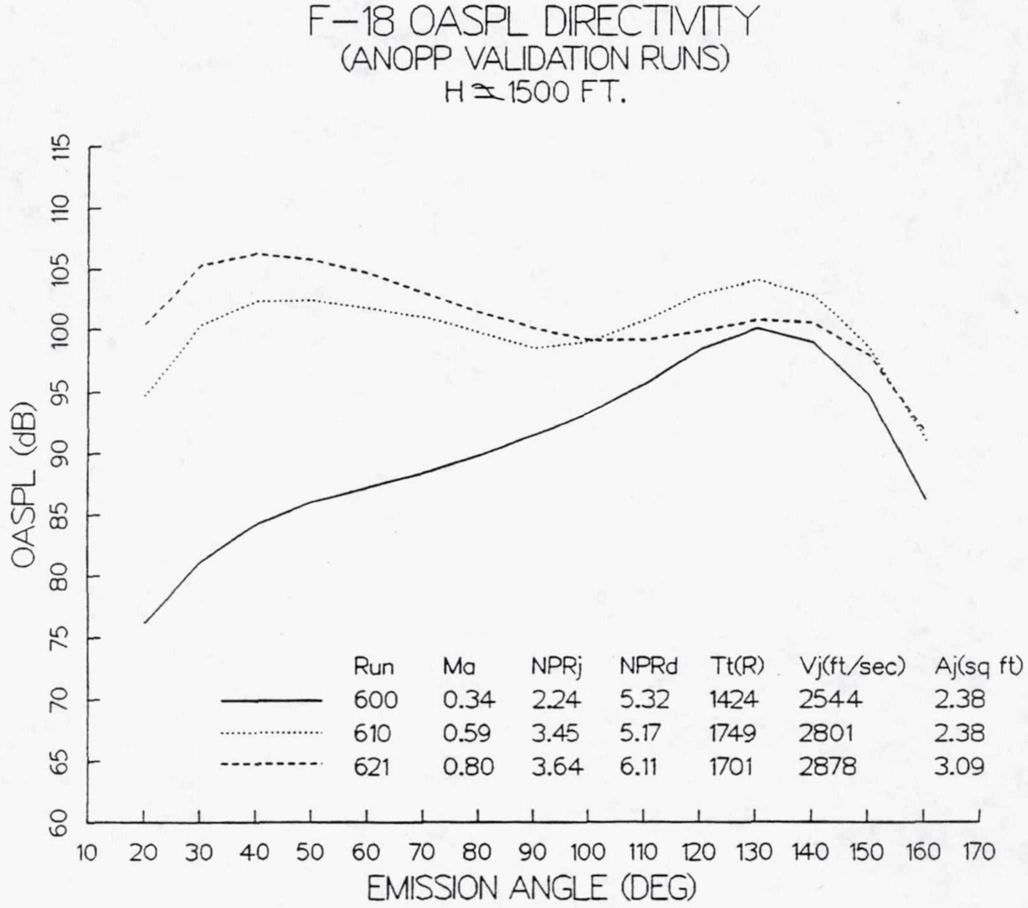

Only selected F-18 data have been analyzed to date. Results of the ANOPP validation runs (600 series) are presented first. At the lowest flight Mach number (M = 0.34) and slightly supercritical nozzle pressure ratio NPR = 2.24 the OASPL directivity is observed (Run 600) to be dominated by the jet mixing noise with the rear arc noise level exceeding the forward arc noise levels by 15 dB. (Unfortunately, noise data at the same NPR but higher flight Mach numbers could not be obtained.) As the flight Mach no. is increased to 0.59 and the nozzle operation is made significantly more supercritical (NPR = 3.45; Run 610), shock noise increases significantly. In the corresponding OASPL directivity, the sound levels in the forward arc (shock noise) and in the rear arc (jet mixing noise) are nearly equal. As the flight Mach no. is further increased to M = 0.8 (Run 621) the shock noise in the forward arc increases. The noise level in the forward arc is now higher than the level in the rear arc.

MEASURED OASPL DIRECTIVITIES COMPARED WITH ANOPP-PREDICTIONS

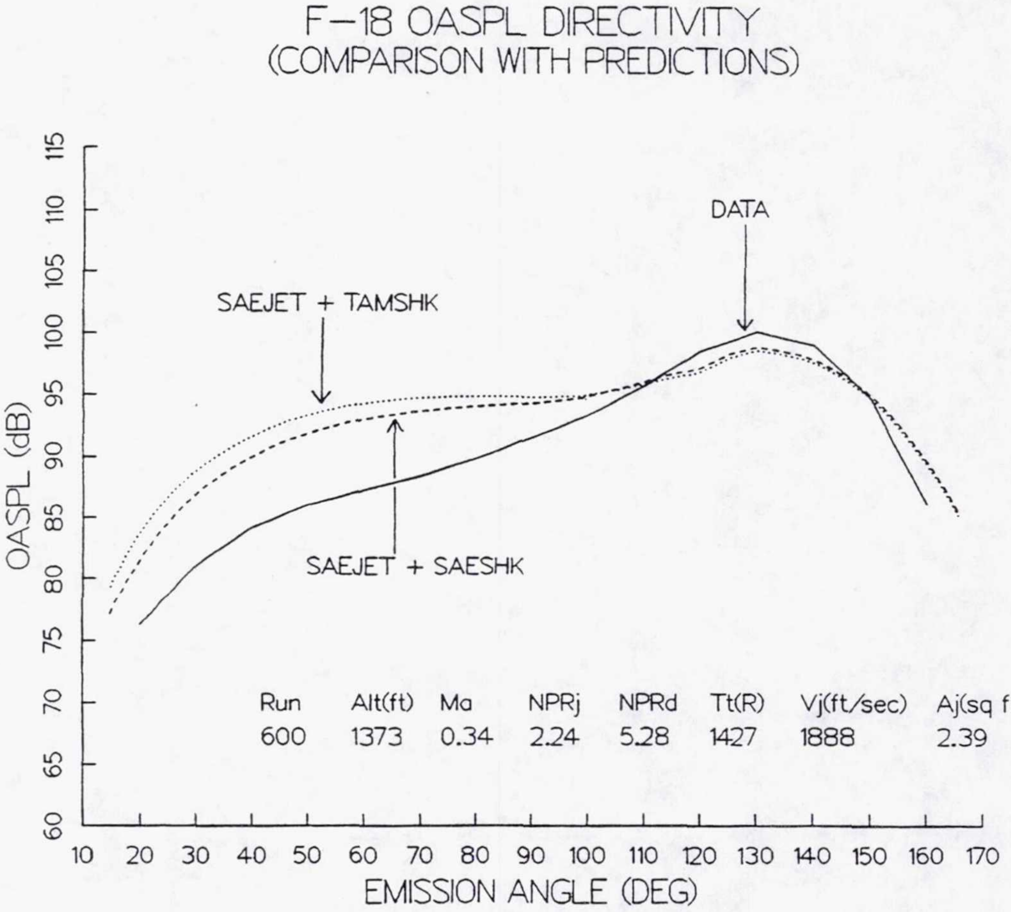

The next several charts show a comparison of the measured flyover noise data (both directivity and one-third octave band spectra) with predictions based on ANOPP. The jet mixing noise was predicted using the SGLJET module based on the SAE ARP 876 methodology. The shock noise was predicted using two different modules - SAESHK based on SAE method and TAMSHK based on Tam's recent theory for a supersonic jet in forward flight. The spectral comparisons are shown at 130 degrees and 50 degrees from inlet to evaluate both mixing and shock noise comparisons. For the low flight Mach no. and slightly supercritical nozzle pressure ratio case (Run 600) the mixing noise prediction (rear arc) is in good agreement with data. But the shock noise is over predicted by 5 dB using SAESHK and by 7 dB by using TAMSHK. The C-D nozzle was operating overexpanded for most flyovers in this test; the predictions therefore used the nozzle throat area and NPR. The significant over prediction of shock noise for this slightly overexpanded nozzle condition is surprising.

MEASURED AND PREDICTED SPL SPECTRA

F–18 SPL SPECTRUM
(COMPARISON WITH PREDICTIONS)

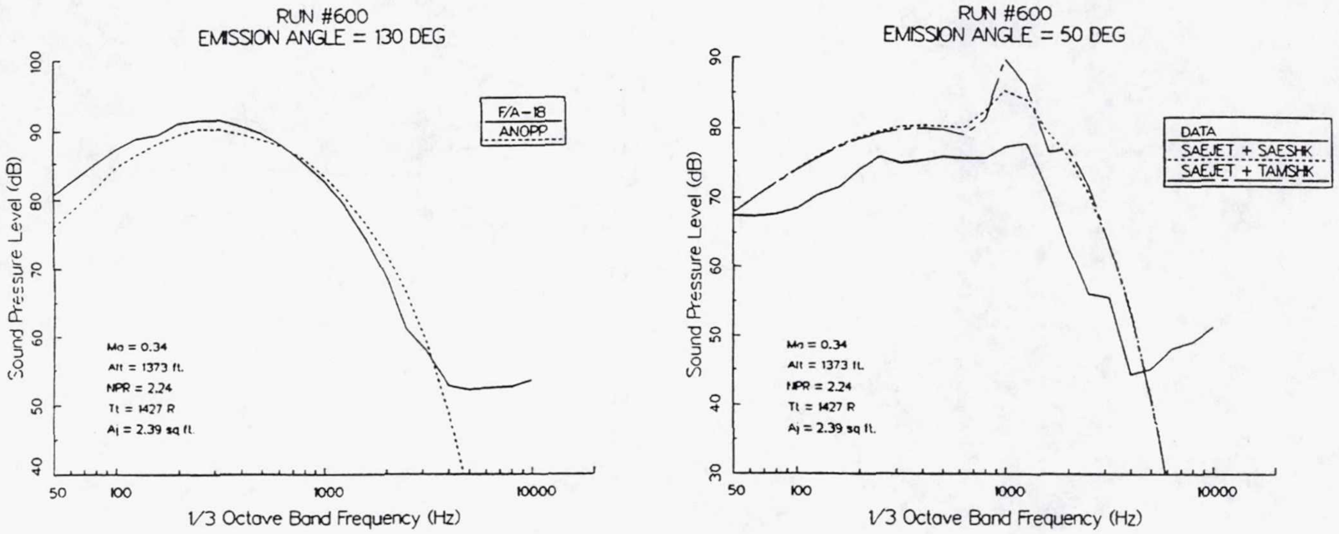

As would be expected from the OASPL comparison the predicted spectrum in the rear arc (0 = 130 degrees) compares well with measurements. This validates the mixing noise prediction methodology at this low flight Mach number.

The predicted spectra in the forward arc (0 = 50 degrees) have the general shape of the measured data but the peak SPL is overpredicted by 7 dB (SAESHK) and by 10 dB (TAMSHK). The peak frequency in the predicted spectra seems to be one one-third octave band lower. Near the spectrum peak TAMSHK predictions also include additional peaks and valleys.

MEASURED OASPL DIRECTIVITIES COMPARED WITH PREDICTIONS

F–18 OASPL DIRECTIVITY
(COMPARISON WITH PREDICTIONS)

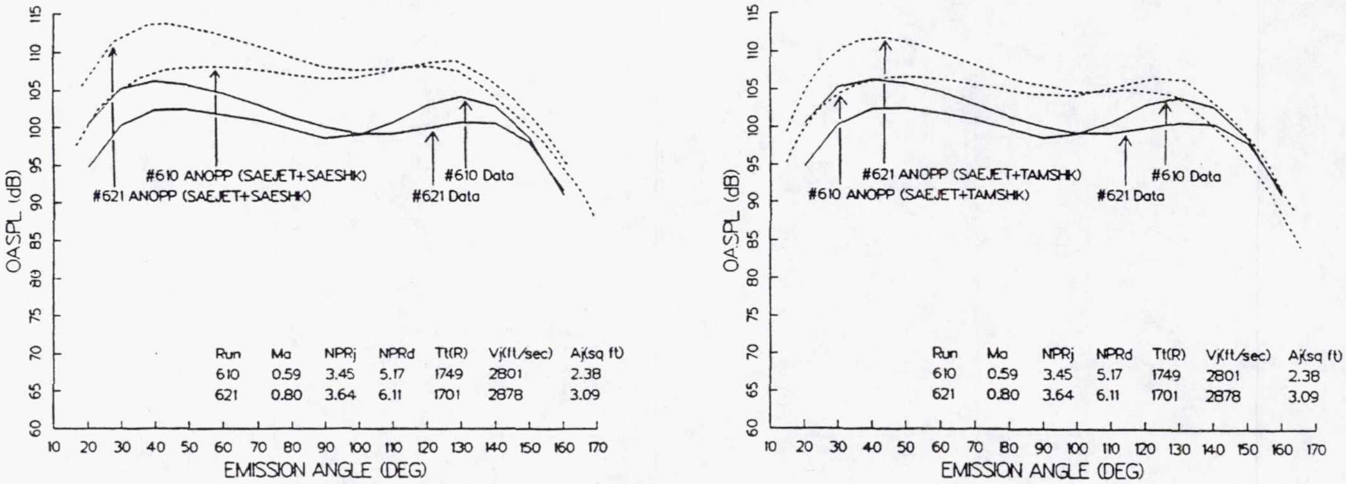

Runs 610 and 621 have very similar engine conditions but the flight Mach numbers are different (0.59 and 0.80). Data show that when the flight Mach no. is increased, the peak OASPL in forward are increases by 4 dB (more shock noise amplification) and the peak OASPL in the rear arc decreases by 3 dB. The changes predicted by the SAE procedures are 6 dB increase in forward arc and 1 dB decrease in rear arc. The absolute levels from predictions are up to 7 dB higher than data.

Similar trends are also seen in the predictions using TAMSHK. The maximum OASPL level is overpredicted by 5 dB.

MEASURED AND PREDICTED SPL SPECTRA AT 130 DEG

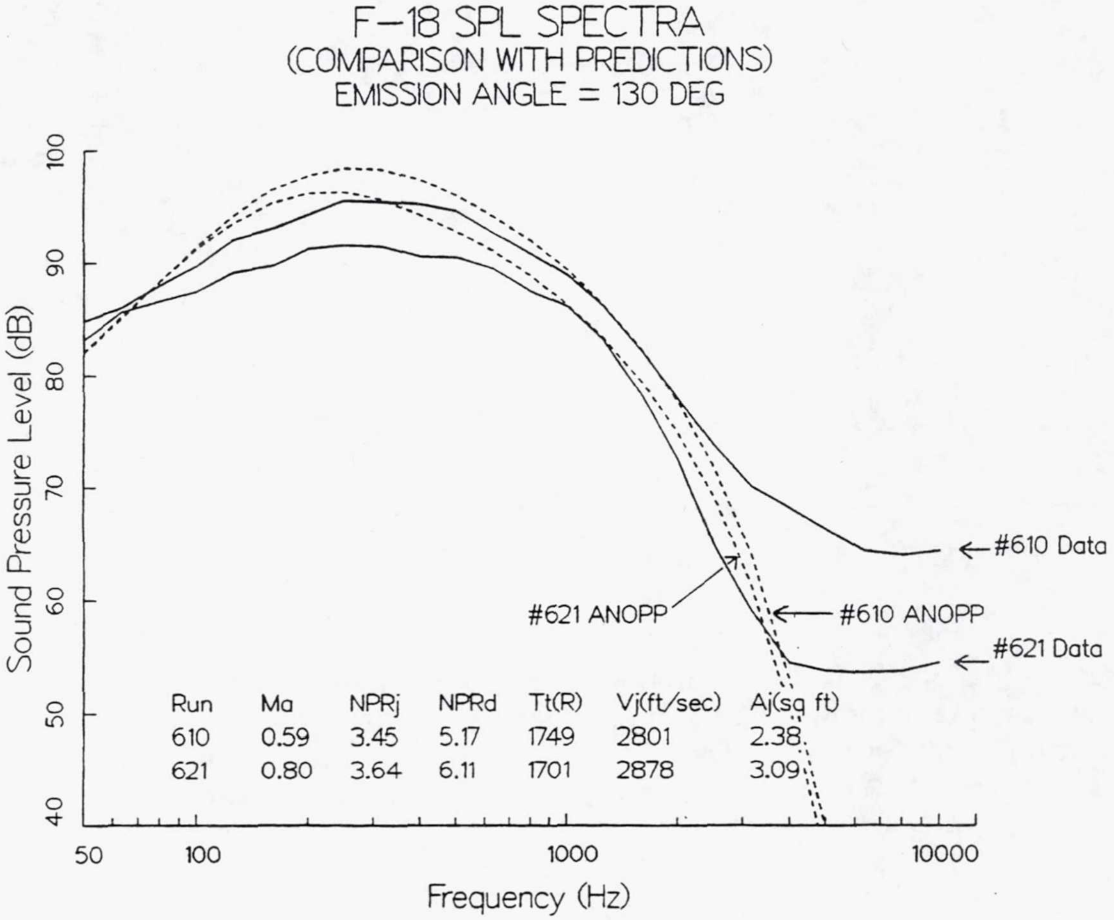

Run	Ma	NPRj	NPRd	Tt(R)	Vj(ft/sec)	Aj(sq ft)
610	0.59	3.45	5.17	1749	2801	2.38
621	0.80	3.64	6.11	1701	2878	3.09

The spectral comparisons also show the SPLs at 130 degrees decreasing with increasing flight Mach number. The predicted absolute levels are again higher than data, and the predicted changes due to changes in flight Mach no. are lower. The general shapes of the predicted and measured spectra are in fair agreement.

MEASURED AND PREDICTED SPL SPECTRA AT 50 DEG

F–18 SPL SPECTRA
(COMPARISON WITH PREDICTIONS)

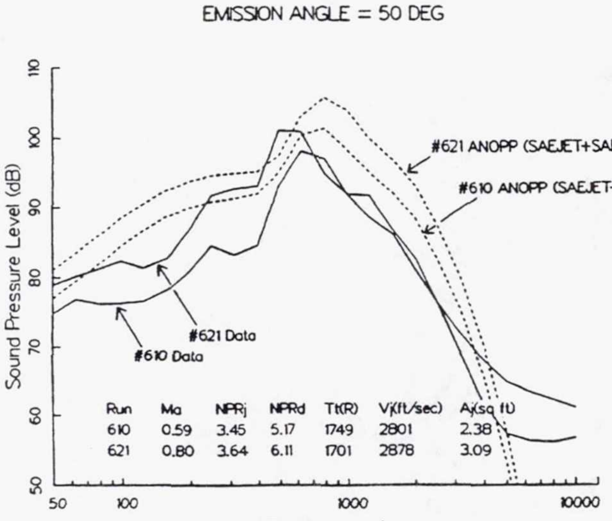

Run	Ma	NPRj	NPRd	Tt(R)	Vj(ft/sec)	Aj(sq ft)
610	0.59	3.45	5.17	1749	2801	2.38
621	0.80	3.64	6.11	1701	2878	3.09

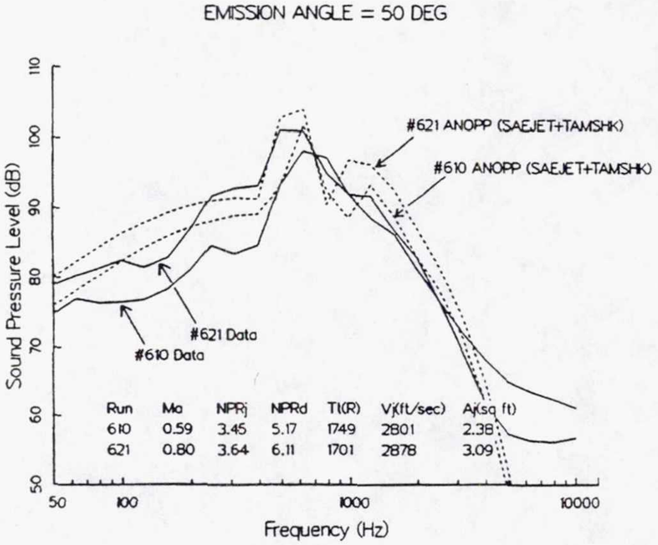

Run	Ma	NPRj	NPRd	Tt(R)	Vj(ft/sec)	Aj(sq ft)
610	0.59	3.45	5.17	1749	2801	2.38
621	0.80	3.64	6.11	1701	2878	3.09

In the forward arc (O = 50 deg) the comparison between the SAESHK based predictions and data reveal both the overprediction as well a higher predicted peak frequency. Using TAMSHK the predictions are in better agreement with data both in amplitude (less than 5dB overprediction in peak SPL) and peak frequency.

CLIMB TO CRUISE NOISE DIRECTIVITIES
DATA VS. ANOPP PREDICTIONS

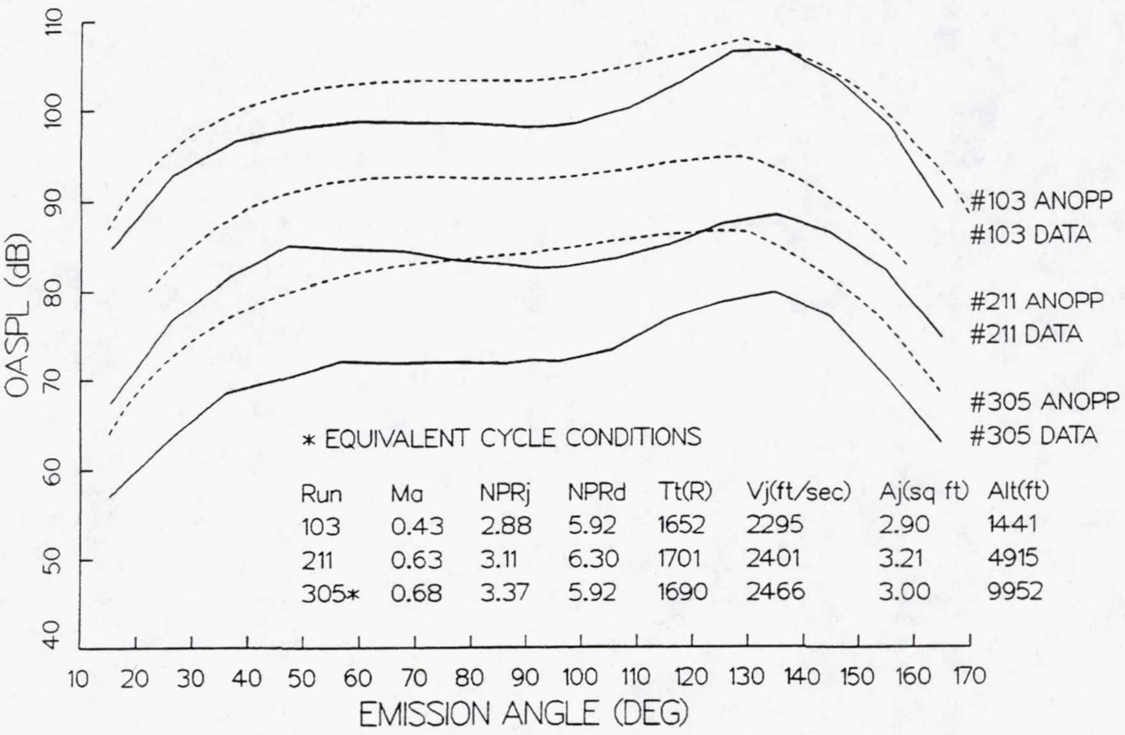

* EQUIVALENT CYCLE CONDITIONS

Run	Ma	NPRj	NPRd	Tt(R)	Vj(ft/sec)	Aj(sq ft)	Alt(ft)
103	0.43	2.88	5.92	1652	2295	2.90	1441
211	0.63	3.11	6.30	1701	2401	3.21	4915
305*	0.68	3.37	5.92	1690	2466	3.00	9952

The climb to cruise runs analyses is now presented. The measured OASPL directivity for three flyovers at approximately 1500, 5000 and 10000 ft (and at conditions representative of HSCT climb) show the large effect of spherical divergence with increasing altitude. But the peak level measured for the high flight Mach number (M = 0.68) run is still in the rear arc indicating dominance of jet mixing noise and either lower than expected shock noise or greater than expected absorption of high frequency broadband shock noise during propagation thru the atmosphere.

The ANOPP predictions for these runs show fair agreement with data for the low NPR, low altitude and low flight Mach no. run but increasingly greater overprediction of shock noise for the higher NPR, higher flight Mach no, higher altitude runs. Additional data need to be analyzed to determine if the differences are primarily due to the flight Mach number, NPR or atmospheric absorption.

MEASURED AND PREDICTED SPL SPECTRA

F–18 CLIMB NOISE SPECTRUM
(COMPARISON WITH PREDICTIONS)

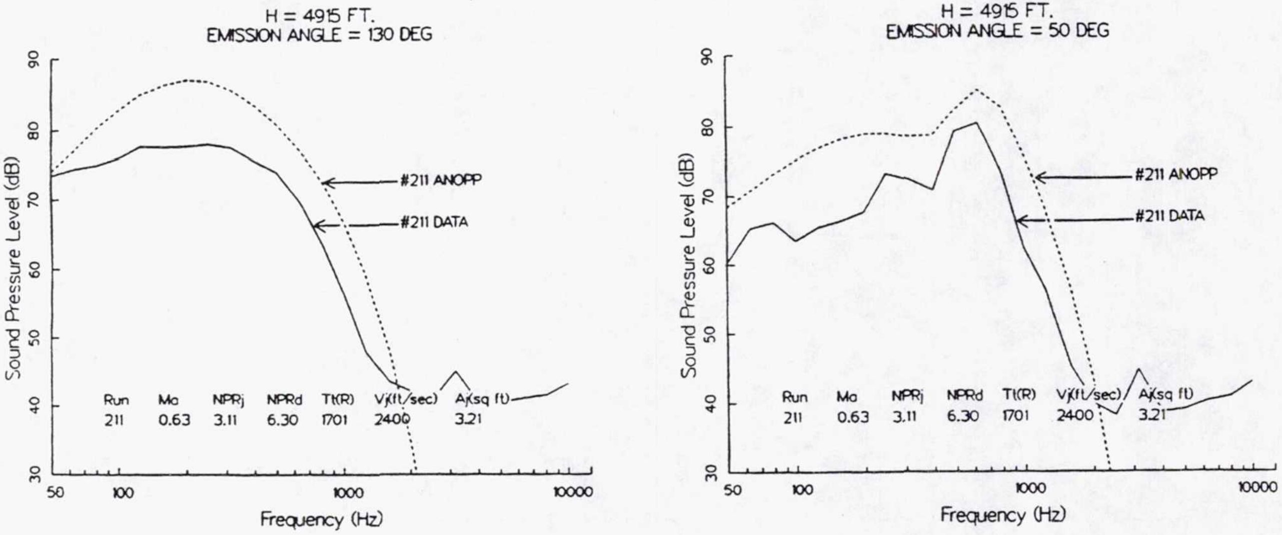

SPL spectral comparisons for the 5000 ft run show an overprediction in levels but generally agreeable spectrum shape. If atmospheric absorption was not accounted for properly, we would expect increasingly larger differences (between data prediction) with increasing frequencies and increasing altitude.

F-18 TO HSCT SCALING PROCEDURE

1. **F-18 SPL NARROW BAND SPECTRA**
2. **SHIFT SPECTRA TO HSCT FREQUENCIES**

$$F_{HSCT} = F_{F\text{-}18} \frac{D_{F\text{-}18}}{D_{HSCT}} \frac{V_{jHSCT}}{V_{jF\text{-}18}}$$

3. **CONVERT TO ONE-THIRD OCTAVE SPECTRA**
4. **CORRECT SPL FOR ABSORPTION DIFFERENCE DUE TO FREQUENCY SHIFT AND DIFFERENT ALTITUDE**
5. **CORRECT SPL FOR DIFFERENCES IN**
    - **NO. OF ENGINES**
    - **JET EXIT VELOCITY AND DENSITY**
    - **NOZZLE AREA**
    - **AIRCRAFT ALTITUDE**
    - **AMBIENT RHO * C**
6. **APPLY A-WEIGHTING**
7. **FIND MAXIMUM dBA**

One of the main objective of this test program was to obtain a data base that includes noise measurements at high flight Mach no., NPR and altitude and to scale these measurements to HSCT conditions in order to obtain a better assessment of the HSCT climb noise. The scaling procedure is outlined here. It includes scaling to HSCT frequencies and adjusting the amplitude for absorption differences as well as differences in F-18 operating conditions and HSCT operating conditions.

Two slightly different scaling approaches were used. In method 1 (intended for a quick assessment based on initial data), the F-18 data at a given altitude was used as the starting point and corrections were made for Vj and altitude differences but not for flight Mach no,. differences. In method 2, F-18 data at a specified flight Mach no. was used as the starting point (in order to properly capture the flight effects in the baseline) and corrected for altitude and Vj differences.

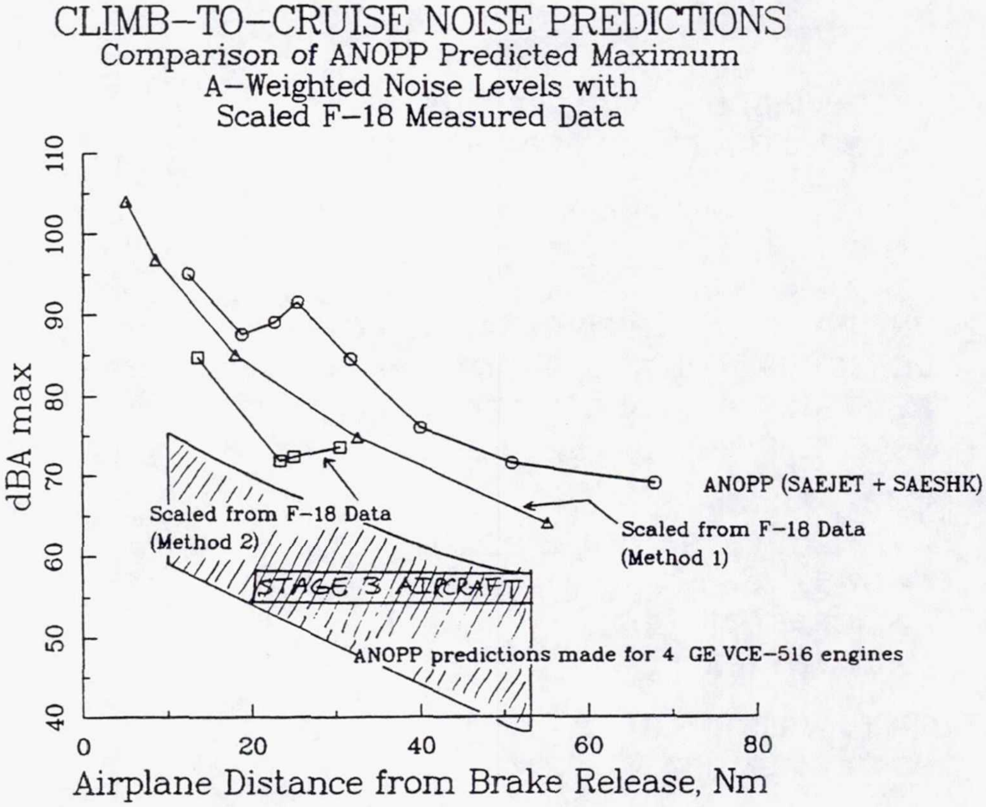

The HSCT climb noise levels as scaled from the F-18 database are shown here. The levels are lower than originally predicted but still higher than the corresponding levels for the current Stage 3 fleet. Furthermore the scaling is based on a very limited database with the F-18 C-D nozzle operating at overexpanded conditions and if the corresponding HSCT is operating underexpanded, the validity of the scaling needs to be examined. Clearly further analysis is required using the other F-18 data to establish the validity. Another concern is the F-16XL database (because of a high thrust single engine configuration) has several flyovers in which the airplane accelerates significantly during the run.

SUMMARY

- **ANALYZED LIMITED DATA FROM F-18 CLIMB-TO-CRUISE AND ANOPP VALIDATION FLIGHT TEST**
- **MAX OASPL PREDICTIONS IN THE FORWARD ARC HIGHER THAN DATA BY UP TO 8dB**
- **FLIGHT AMPLIFICATION OF SHOCK NOISE IN MEASURED DATA IS LESS THAN PREDICTED BY ANOPP METHODS**
- **F-18 CLIMB NOISE DATA SHOW MAX LEVELS TO BE DUE TO MIXING NOISE**
- **HSCT CLIMB NOISE (SCALED FROM F-18 DATA) STILL HIGHER THAN STAGE 3 FLEET NOISE BUT LOWER THAN PREDICTED BEFORE**
- **ADDITIONAL ANALYSIS REQUIRED USING OTHER F-18 RUNS AND F-16XL RUNS**

Flight tests were conducted using F-18 and F-16XL aircraft to acquire supersonic jet noise data at (i) conditions representative of an HSCT in climb to subsonic cruise in order to improve assessment of HSCT climb noise and (ii) 1500 ft altitude but different flight Mach numbers in order to validate ANOPP jet and shock noise prediction methodology. Analyses of limited data and comparison with ANOPP predictions (using SAE mixing noise, SAE shock noise and TAM shock noise methodologies) indicate that the ANOPP methods overpredict the maximum shock noise as well as the amplification of shock noise by increased flight speeds. F-18 climb noise data when scaled up to full scale HSCT indicated the HSCT in subsonic climb to be nosier than current Stage 3 aircraft but lower than ANOPP predictions. In most flights the F-18 was found to be operating with an overexpanded C-D nozzle. Analyses using data from other F-18 and F-16XL flights is required to properly quantify the flight effects, the accuracy of the predictions, and HSCT climb noise.

1999176567

COMPARISONS OF SHOCK NOISE PREDICTIONS WITH FLIGHT DATA

T.D. Norum, R.A. Golub, and W.L. Willshire
NASA Langley Research Center
Hampton, Virginia

S30-71

13p.

409562

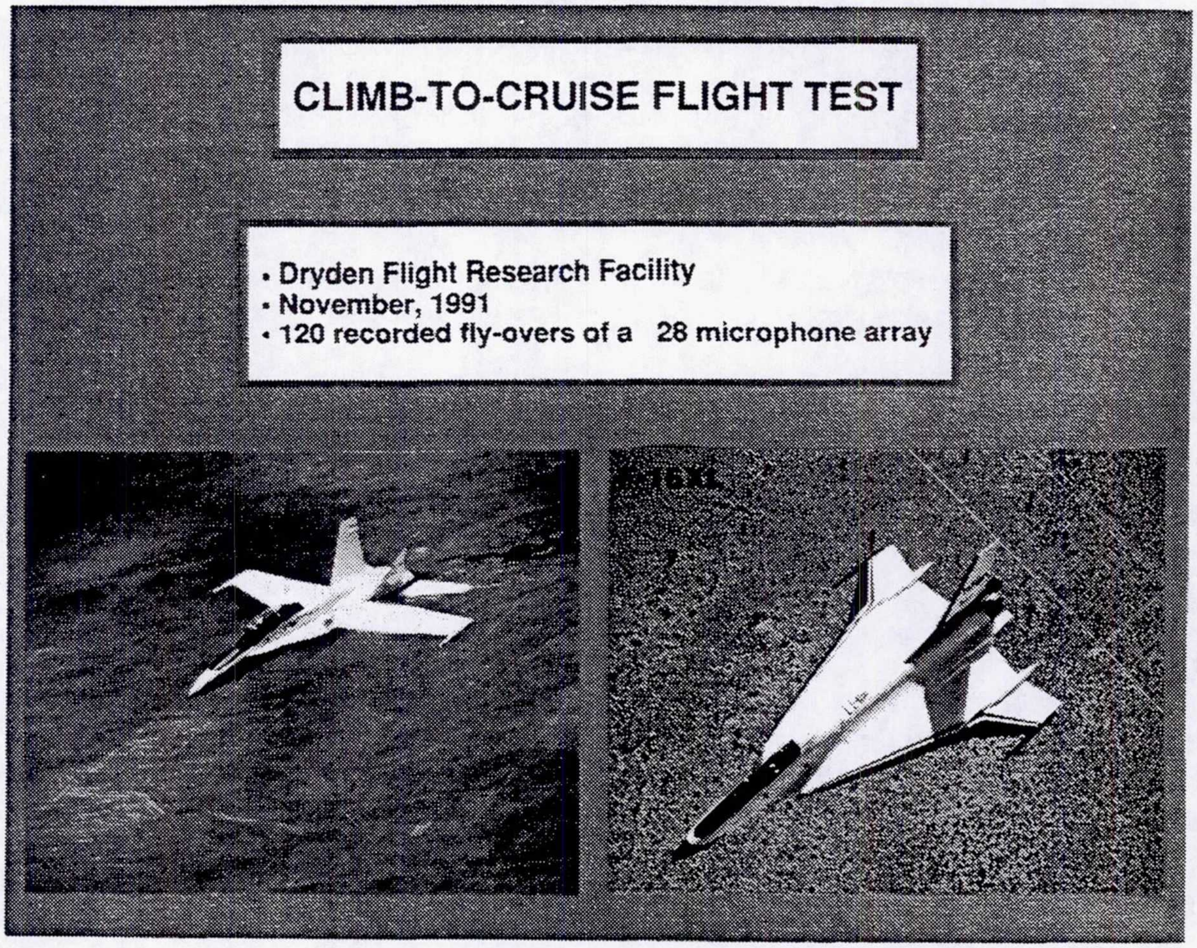

CLIMB-TO-CRUISE FLIGHT TEST

- Dryden Flight Research Facility
- November, 1991
- 120 recorded fly-overs of a 28 microphone array

A flight test was performed at NASA Dryden Research Center in November 1991 utilizing both F18 and F16 aircraft. These flights were designed to provide (1) acoustic data that could be extrapolated to that of an HSCT at various points of its climb-to-cruise operation and (2) a data base for noise from a supersonic jet exhausting from an aircraft moving at high subsonic speeds. This presentation utilizes data obtained from these flyovers to evaluate predictions of broadband shock noise from supersonic jets in flight.

The F18 is particularly suitable for flyovers of shock noise since it can be flown with one engine at flight idle. The second engine can then be operated at a pressure high enough to produce a supersonic nozzle exhaust and still maintain an unaccelerated, level flyover.

F- 18 FLYOVER TEST SETUP

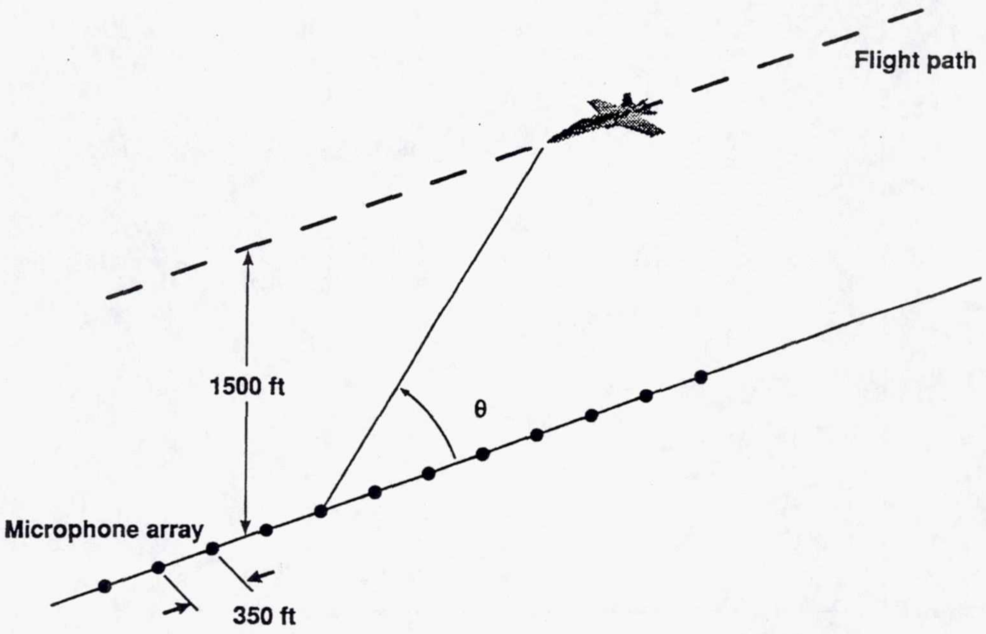

The flight data that will be shown come from constant speed flyovers of an array of 12 microphones by an F18 operating with one engine at flight idle, at an altitude of approximately 1500 feet. Aircraft tracking allowed for ensemble averaging of the 12 microphones and a weather balloon provided the parameters required for atmospheric effects.

NOZZLE CONDITIONS FOR F-18 FLYOVERS

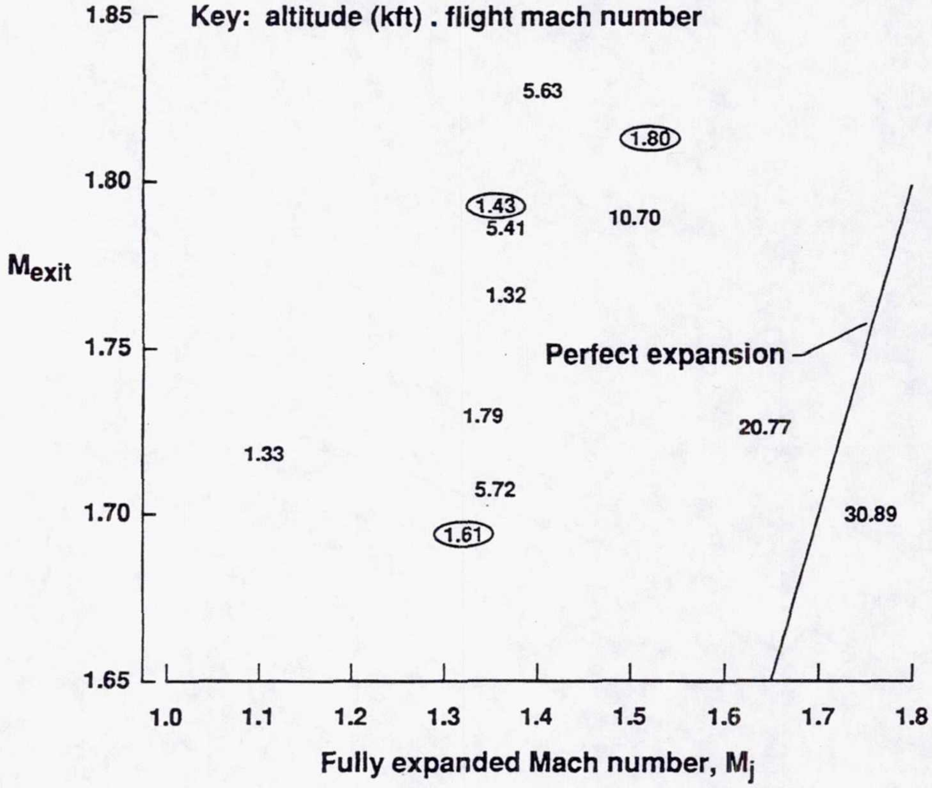

The nozzle operating conditions of the powered engine that were obtained during flight testing of the F18 are shown in this chart. For a given flyover, a data point i given in terms of the altitude in kft followed by jet fully expanded Mach number vs the nozzle exit (design) Mach number. The sloped line on the right represents the fully expanded condition, and shows that the powered nozzle is operating overexpanded in all but a single flight condition (30 kft altitude). The three conditions for which data will be shown are encircled, they being 1 kft (actually about 1500 ft) flyovers at flight Mach numbers of 0.42, 0.61, and 0.80.

SUPERSONIC JET BROADBAND SHOCK NOISE FLIGHT DATA VS PREDICTION

Flight Data

- F-18 Flyover, 12 Microphone Ensemble Average
- Single Supersonic Overexpanded Jet
- Altitude ~ 1500 Feet
- Flight Mach Numbers 0.43, 0.61, 0.80

Tam Theory

- AIAA Journal, 10/92

Model Data With Point Source Flight Corrections

- Frequency - Doppler Shift
- Amplitude - Convective Amplification

This chart summarizes the flight data to be presented and the predictions to which the data will be compared. The majority of the comparisons will be to Tam's theory of broadband shock noise. The latest formulation of this theory, which is directly applicable to an aircraft flyover, is given in last months AIAA journal. Older formulations for predicting broadband shock noise are based on correlations of model scale data from convergent nozzles (i.e., underexpanded jets) and hence cannot be compared directly to the data. However, an attempt is made in this presentation to evaluate the flight corrections of the older formulations that include a Doppler shift of the frequency and a convective amplification of the amplitude of the broadband shock noise.

ELEMENTS OF TAM THEORY OF BROADBAND SHOCK NOISE

- **Large Scale Structures/Instability Waves Interacting with Shocks in Jet Plume**
- **Multiple Scales Model of Shock Cell Structure**
- **Multiple Modes Give Wide Frequency Distribution**
- **Applicable to Convergent-Divergent Nozzles**
- **Analytical Results**

The Tam theory of broadband shock noise involves the interaction of the jet large scale turbulent structures or instability waves with the shock structure in the jet plume. A multiple scales model of the shock cells yields a solution consisting of multiple modes that gives a wide frequency distribution for the broadband noise. Unlike the older methods that are valid only for convergent nozzles, this formulation also applies to convergent-divergent nozzles. The result is analytical and hence does not require correlations from a data base inherent to the older methods.

COMPARISON OF FLIGHT SPECTRA WITH TAM THEORY

Flight Mach number, 0.43 **$M_j = 1.35$**
Altitude, 1440 ft **$M_{exit} = 1.79$**

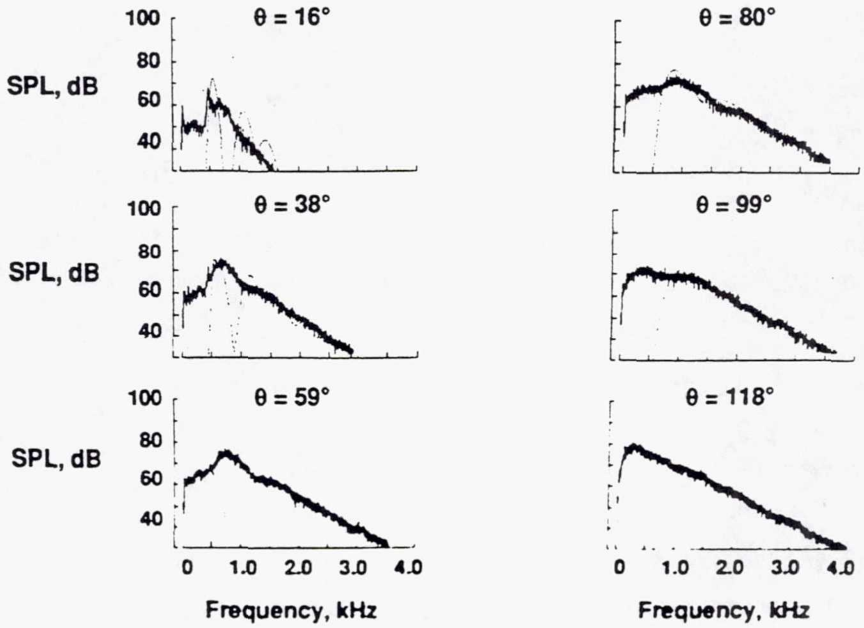

The next three charts show direct comparisons of the narrow band spectra (2 Hz bandwidth) between the flyover data and the Tam predictions. The solid lines are the data as measured, whereas the dotted curves are Tam's predictions modified by the propagation losses appropriate for the weather conditions that were measured at the time of the flyover. The typical spectrum shows a low frequency broadband component due to jet mixing noise followed by a peaked broadband shock noise spectrum at higher frequency. In this chart of the data from the Mach .43 flyover, the curves on the right sown an excellent agreement in the broadband shock noise portion of the spectra at angles close to 90 degrees. At the further upstream shown on the left, the spectral width of the different modes contributing to the Tam spectra become narrower, resulting in a highly peaked disjoint curve, a behavior which incidentally is also present in Tam's predictions for a static jet.

COMPARISON OF FLIGHT SPECTRA WITH TAM THEORY

Flight Mach number, 0.61 $M_j = 1.32$
Altitude, 1430 ft $M_{exit} = 1.69$

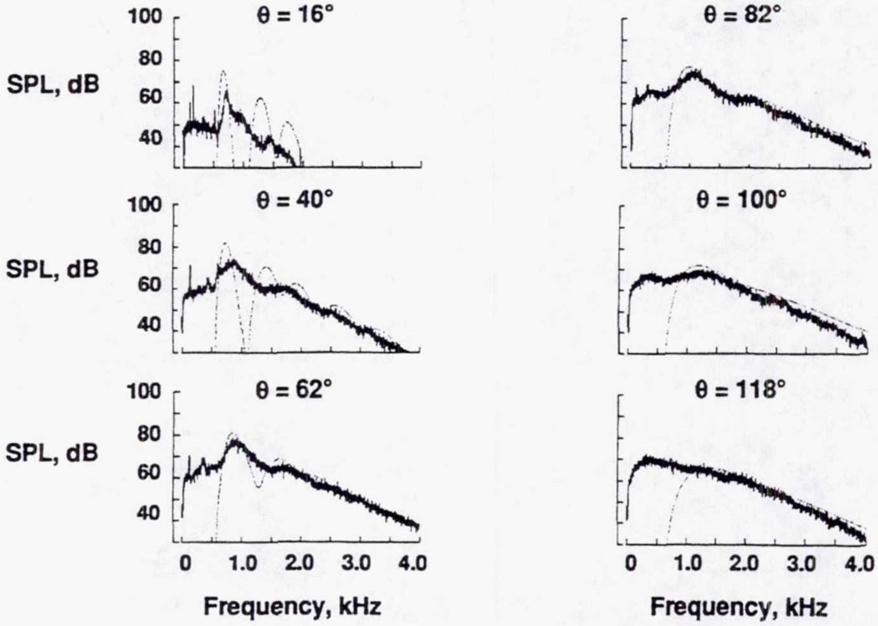

Similar results are seen for the spectral comparisons at the flight Mach number of 0.61. The good agreement between flight data and Tam theory near the overhead position is evident, as is the mode separation of the theory at small angles.

COMPARISON OF FLIGHT SPECTRA WITH TAM THEORY

Flight Mach number, 0.80 $M_j = 1.51$
Altitude, 1420 ft $M_{exit} = 1.81$

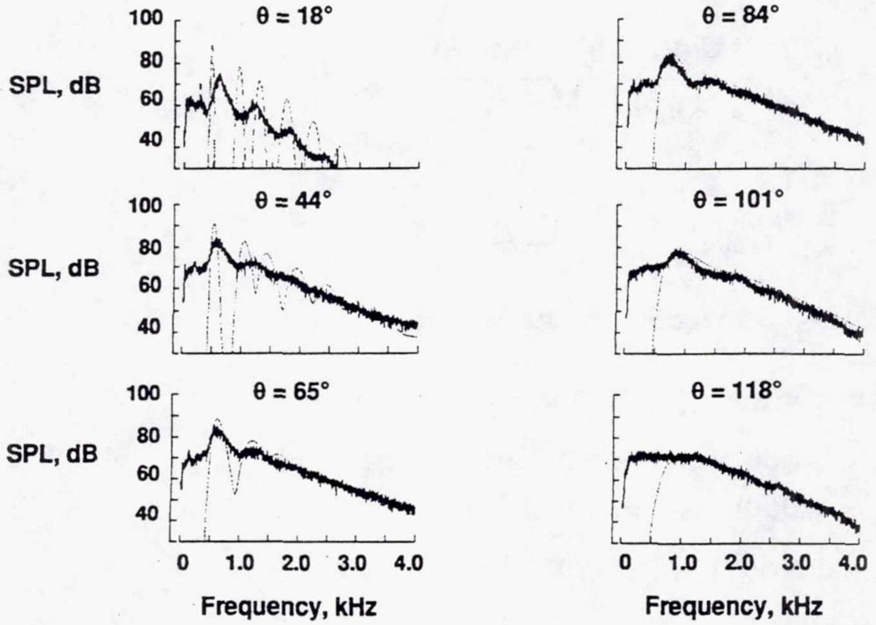

More of the same is seen in this chart for a flight Mach number 0.80. There is excellent agreement of both the peak frequency and the amplitude of the broadband shock noise near 90 degrees. The spectral widths of the contributions of individual modes at the lower angles are even narrower than those at the lower flight speeds.

BROADBAND SHOCK NOISE "POINT SOURCE" FLIGHT PREDICTIONS

Peak Frequency: Doppler Shift of Model Scale Directivity

$$f_p(\theta) = \frac{f_p(\text{flight data at 90 degrees})}{\underset{\substack{\uparrow\\ \text{Model Scale}\\ \text{Static Directivity}\\ \text{Factor}}}{(1+M_c\cos\theta)}\underset{\substack{\uparrow\\ \text{Doppler}\\ \text{Frequency}\\ \text{Shift}}}{(1-M_f\cos\theta)}}$$

Peak Amplitude: Convective Amplification

$$\text{SPL}(\theta) = \text{SPL (flight data at 90 degrees)}$$

- **Additional Atmospheric Absorption**
- **Additional Spherical Spreading**

$$+\ 10\log(1-M_f\cos\theta)^{-4}$$

Comparisons will now be made of the variations with emission angle of both the peak frequency and the peak amplitude of broadband shock noise. In addition to the flight data and Tam' theory, computations that utilize the flight corrections that are used in the older shock noise predictions (e.g., SAE method, Stone's method) will be shown. These flight corrections are derived from analysis of an acoustic point source in motion and include a Doppler shift of the frequency and a convective amplification of the amplitude. The frequency variation to be shown uses the measured peak frequency from the flight spectra at 90 degrees, the known static directivity that has been determined from model data and is a function of the eddy convection Mach number in the jet, and the Doppler frequency shift. The peak amplitude variation also uses the value obtained from the flight data at 90 degrees, additional propagation losses due to the observer at theta being at a distance further than that at 90 degrees, and the convective amplification, which includes a fourth power of the Doppler factor.

PEAK FREQUENCY OF BROADBAND SHOCK NOISE

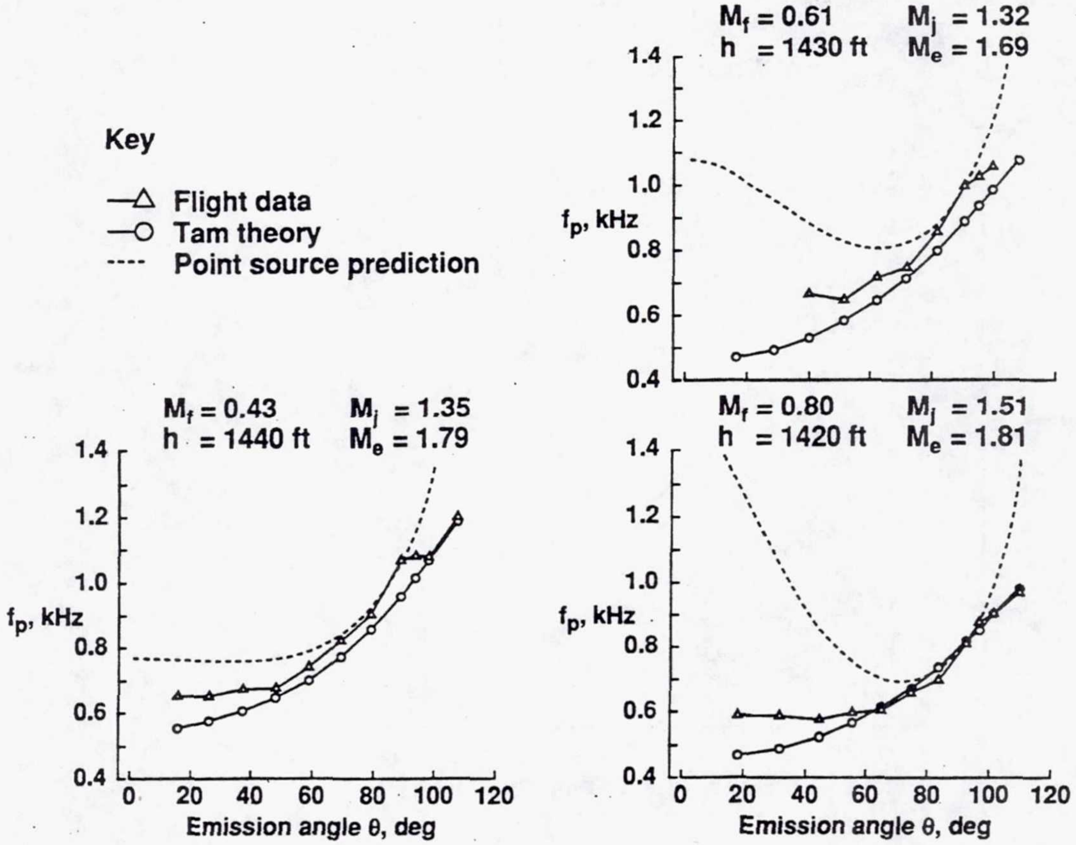

The variation of the peak frequency of the broadband shock noise with emission angle is shown for each of the three flight Mach numbers. A comparison between the flight data and Tam's theory shows the trends to be identical, with the frequency increasing with emission angle in a manner similar to that which occurs for static data. As was seen in the spectra of the previous charts, the measured and predicted frequencies are close, with the Tam theory giving the measured and predicted frequencies, particularly at small emission angles. The frequency variation from the point source prediction has a behavior similar to the other two at the low flight Mach number. However, as the Mach number is increased, the Doppler shift becomes more pronounced, resulting in a frequency variation at small emission angles that is similar to that for an acoustic point source but contrary to the measured flight results for broadband shock noise.

PEAK FREQUENCY OF BROADBAND SHOCK NOISE

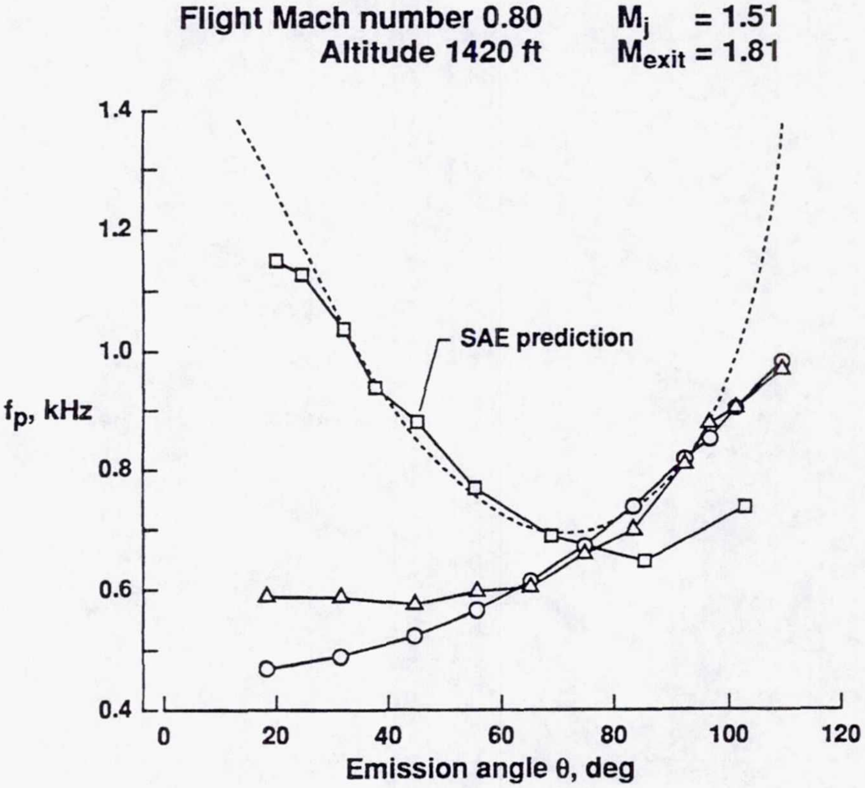

A confirmation of the frequency variation of the older shock noise predictions is shown in this chart. The older methods are designed for underexpanded jets from convergent nozzles and hence do not apply to the overexpanded jets from the convergent-divergent nozzle of the F18. However, a convergent nozzle of the same throat area and flight conditions as the 0.80 Mach number flight is about as underexpanded as the flight nozzle was overexpanded (i.e. they have similar shock cell strengths). Inputting this into the ANOPP implementation of the SAE shock noise method yields spectra whose peak frequency variation has been superimposed on the results of the last plot of the previous chart. As expected, the peak frequency trend of the SAE method closely follows that of the point source prediction, indicating that the method does not predict the correct variation of the frequency of broadband shock noise at high flight speeds.

PEAK AMPLITUDE OF BROADBAND SHOCK NOISE

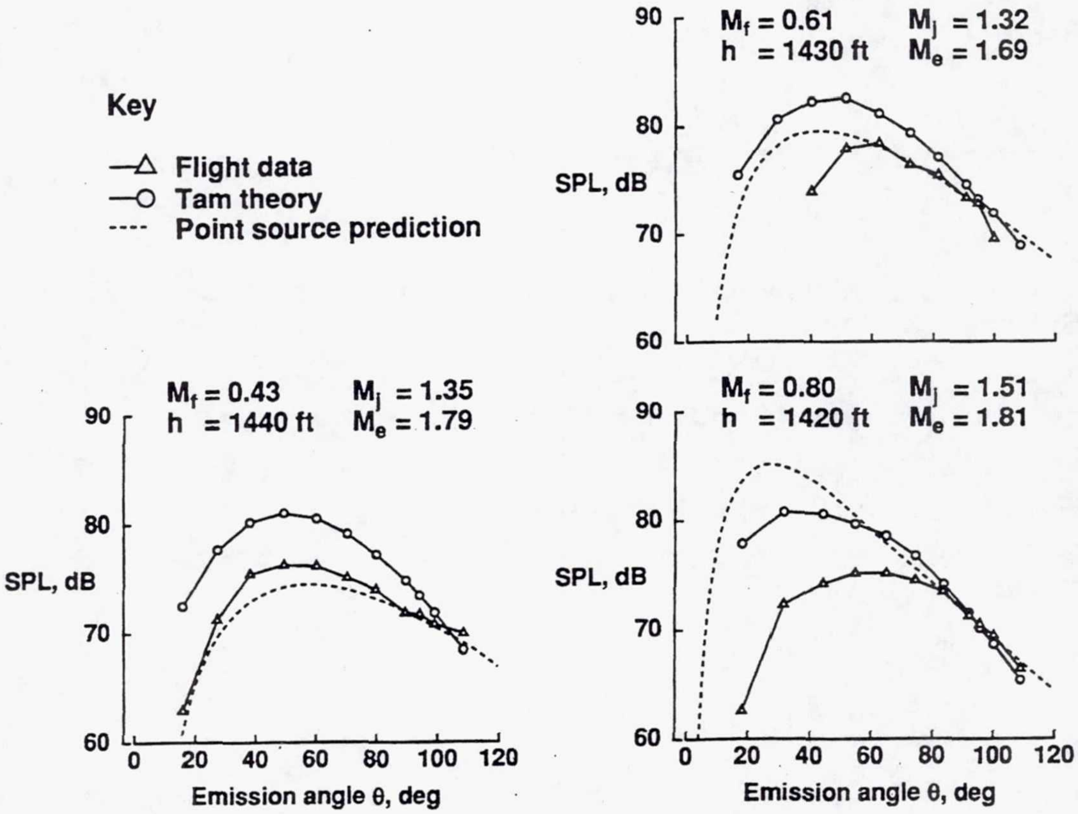

The peak amplitude variations for the three flight Mach numbers are given here. As was seen in the spectra of previous charts, Tam' predicted amplitudes show excellent agreement with the flight data at emission angles near 90 degrees and overpredict the amplitudes at smaller angles. The results from the point source predictions are not as consistent. Recall that, unlike the Tam theory, these predictions are forced to agree with measurements at 90 degrees. In contrast to the flight data which show a similar amplitude variation with emission angle for the three flight speeds, much larger peak amplitudes at small angles are obtained from the point by the convection amplification factor at high speeds. The fact that the measurements do not show this type of increase indicates that a dominating convective amplification factor is invalid as a flight correction to broadband shock noise.

CONCLUSIONS

- **Point Source Flight Predictions Invalid for Broadband Shock Noise at High Flight Speeds**
- **Tam Theory for Broadband Shock Noise in Flight**
  - **Excellent Agreement in Both Frequency and Amplitude at 90 degrees**
  - **Proper Frequency Trend with Emission Angle**
  - **Modification Required for Improved Prediction at Small Emission Angles**

It has been shown that the Doppler frequency shift and the convective amplification factors that result from analyses of acoustic point sources in motion do not apply to broadband shock noise from an overexpanded jet of an aircraft at high subsonic flight speeds. The Tam theory appears to be a much better predictor of broadband shock noise in flight. In addition to predicting both the correct amplitude and frequency distribution at the overhead position of flyovers at flight speeds to Mach 0.8, the correct frequency trend with emission angle was also obtained. Although the theory is not as good in predicting the spectra at small emission angles, the fact that it is analytical in nature should make it relatively easy to modify for improved comparison at the smaller angles.

OMIT THIS PAGE

Session VI

System Studies and Other Issues

1999176568

HSR PROPULSION SYSTEM STUDIES: A STATUS REPORT ON THE DOWN-SELECT PROCESS

W.C. Strack
NASA Lewis Research Center
Cleveland, Ohio

S31-71

HSR Airport Noise Challenge

First Wish:

- *Simple turbojet engines (V_{jet} ~ 3200 ft/s)*
- *Acceptable 20^+dB mixer-ejector nozzles*

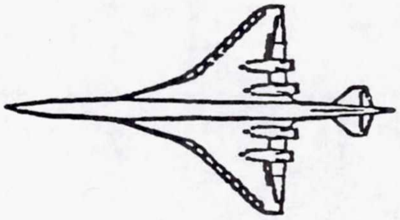

409565

19 P.

1992 Status:

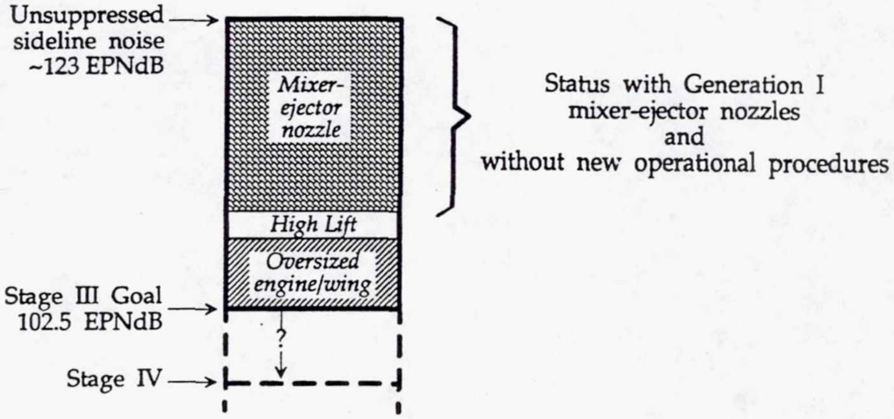

When the HSR program began there was widespread belief that a simple and familiar turbojet-like engine coupled to an advanced technology mixer-ejector nozzle was the propulsion system of choice for achieving FAR 36-Stage 3 noise requirements. Our ability to quickly demonstrate a practical 20^+dB suppression nozzle was confidently presumed by many. Our rate of progress towards that objective, however, has been somewhat humbling. At the moment we are reasonably confident of achieving about 15dB suppression with a mixer-ejector nozzle designed for a high specific thrust turbojet-like cycle. Therefore, if we make no further suppression progress and conservatively assume no new operational procedures such as programmed lapse rate (PLR), then meeting the Stage III goal requires a large amount of engine and/or wing oversizing which is economically prohibitive. The scenario is further aggravated by the possibility of eventually needing to comply with even more stringent regulations (Stage IV).

While this status may be somewhat disappointing to some, it must be remembered that the HSR program plan involves two generations of mixer-ejector nozzles beyond the current generation I nozzle designs. It is premature to conclude that we cannot design a practical 20^+dB mixer-ejector nozzle. On the other hand, it is prudent to consider alternative solutions to the noise problem. Thus, we are investigating four other propulsion system concepts.

HSCT Noise Suppression Concepts

Rear End ***Hybrid*** ***Front End***

Turbine Bypass Engine

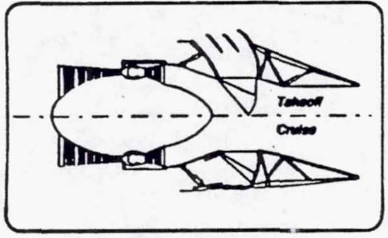

Mixed Flow Turbofan

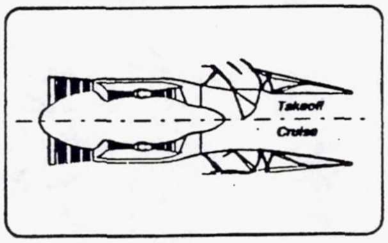

TBE / IFV

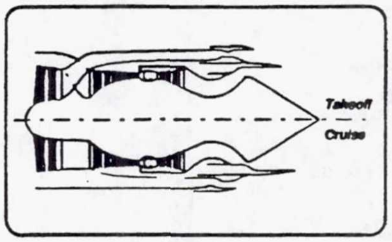

Variable Cycle Engine

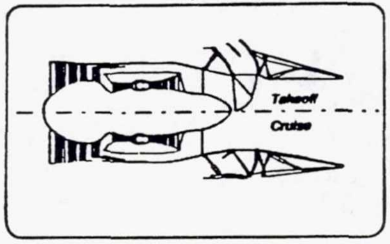

Flade

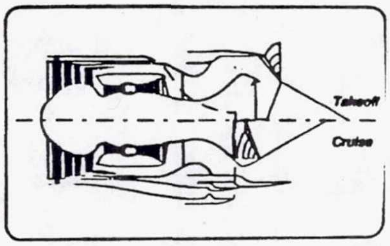

The highest specific thrust concept is the 1-spool turbine bypass engine (a slightly modified turbojet) combined with a very large mixer-ejector nozzle requiring approximately 120 percent airflow augmentation during takeoff. The mixed flow turbofan (MFTF) and variable cycle engine (VCE) concepts have intermediate jet velocities because a low-spool driven fan absorbs much of the core energy. Consequently, much less secondary air is required in the mixer-ejector nozzle to achieve low noise than the turbine bypass engine (TBE). The Flade engine is either a VCE or a MFTF with a third flowpath surrounding the fan and scrolled to the lower half of the engine. The fan driving this flowpath is modulated to absorb power during the takeoff and this provides a fluid acoustic shield underneath the mixer nozzle (no ejector). The TBE with an inlet flow valve (IFV) represents one member of the tandem fan class of concepts wherein a compression system reconfiguration can occur. During takeoff, auxiliary air is brought onboard and routed to the rear compressor while the normal inlet airflow is processed only by the front compressor before exhausting. In the cruise configuration, the auxiliary inlets are closed and the engine becomes a turbojet with an extra pressure loss due to the IFV.

All of these candidate concepts achieve about 1500 ft/s exhaust velocity during takeoff by raising the total airflow to about 1100 lb/sec. They differ in where the airflow is introduced into the cycle and which technologies need to be developed to achieve success.

Effect of Exhaust Velocity on Sideline Noise

Mach 0.322, 689 ft., 650 lb/s

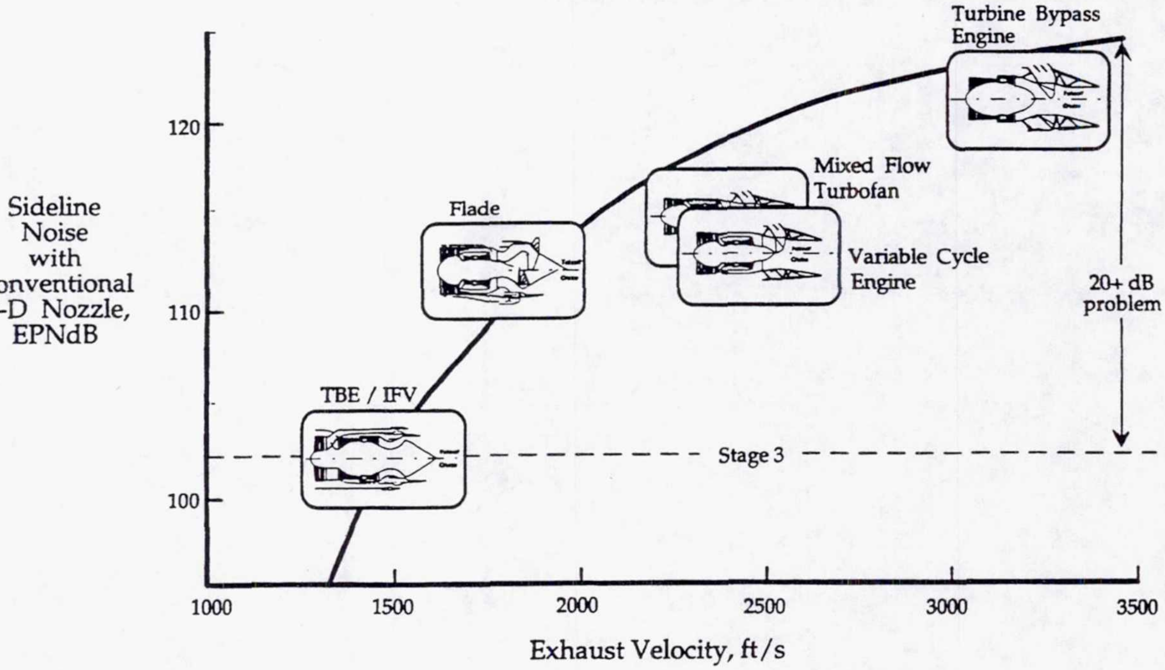

Each of these five concepts can be characterized by its exhaust velocity and, therefore, its suppression requirements compared to a conventional unsuppressed nozzle. While a TBE presents a 20^{+}dB suppression problem to attain Stage III, the TBE/IFV can be designed to achieve Stage III without an elaborate suppression system, and the hybrid concepts fall somewhere in-between these extremes. There are, of course, other discriminating attributes to be considered such as weight, reliability, life, efficiency, thrust lapse, technology risk, tolerance to more severe noise constraints, installation drag, and climb noise. What is needed is an unbiased procedure to evaluate each of these concepts on a system basis that accounts for all of these criteria simultaneously.

Overall HSCT Noise Issues

1. *Which propulsion concept best achieves a balanced compromise of performance, weight, size, noise, complexity, and life ?*
2. *What price do we pay to achieve noise levels below Stage III ?*

Issue 1 is important to resolve because the HSR program is resource-constrained to pursue technologies specific to only two concepts at most. This is also a difficult challenge to resolve with a high degree of confidence due to the large number of independent variables, the complex interactions between propulsion and airframe, multiplicity of merit criteria, and key technology and external uncertainties.

Since it is likely that noise regulations will be tightened sometime in the future it is important to determine the economic penalty associated with such an eventuality. Also, some propulsion concepts are able to accommodate severe noise constraints better than other concepts. Thus, this information could be a key discriminator during the concept selection process. It would be best if we generate a curve of penalty (e.g., ΔDOC) versus ΔdB below Stage III rather than presume a definition of Stage IV. Then, there could be more rational future rule-making.

A Propulsion System Down-Select is Needed to Focus the Phase II Technology Program

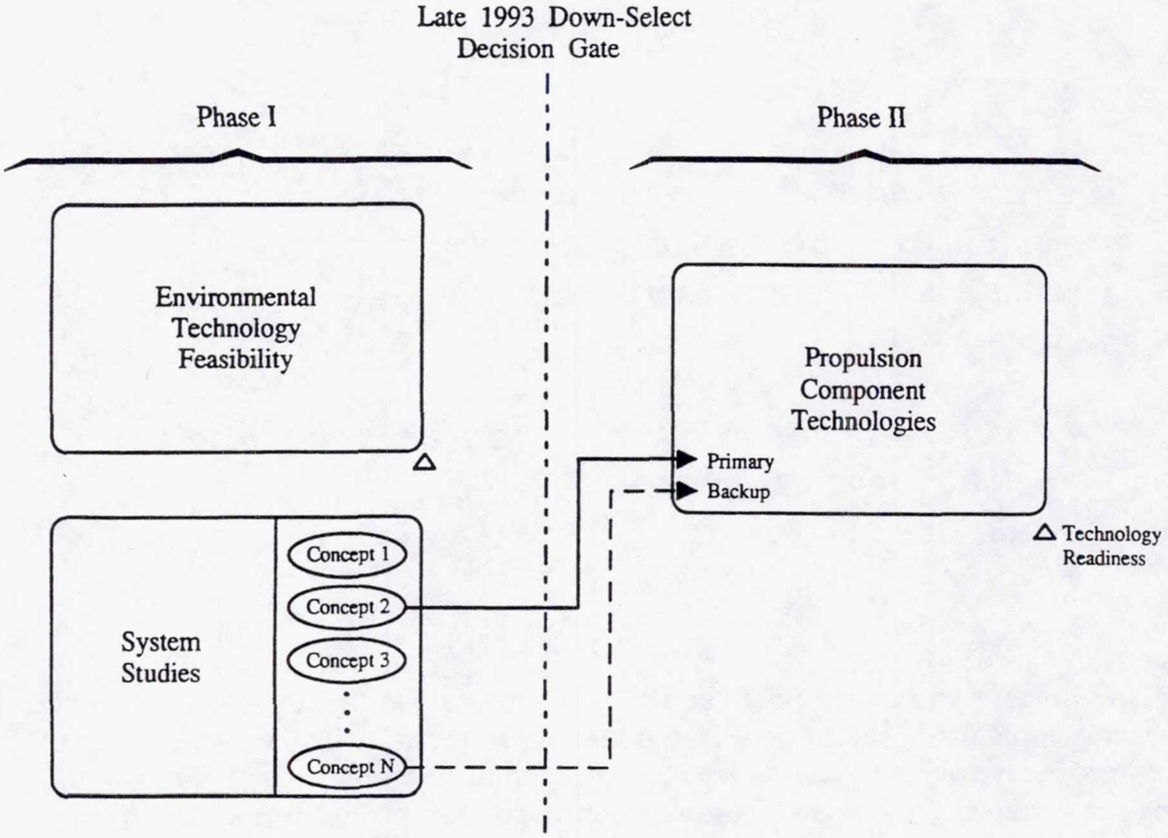

In addition to the mainline environmental technology feasibility effort in HSR Phase I, a systems studies effort is also underway to address the issues listed on the previous chart. The schedule calls for a down-select to both a primary and backup concept by late 1993. This will focus the technology effort in HSR Phase II. Note that this down-select pertains to the NASA sponsored technology thrust only--i.e., it is not a production engine down-select. The intent of the '93 down-select is to insure that the correct concept-specific technology is pursued in the earlier portion of Phase II to enable a low-risk final down-select in late '95.

HSR Propulsion System Selection Process

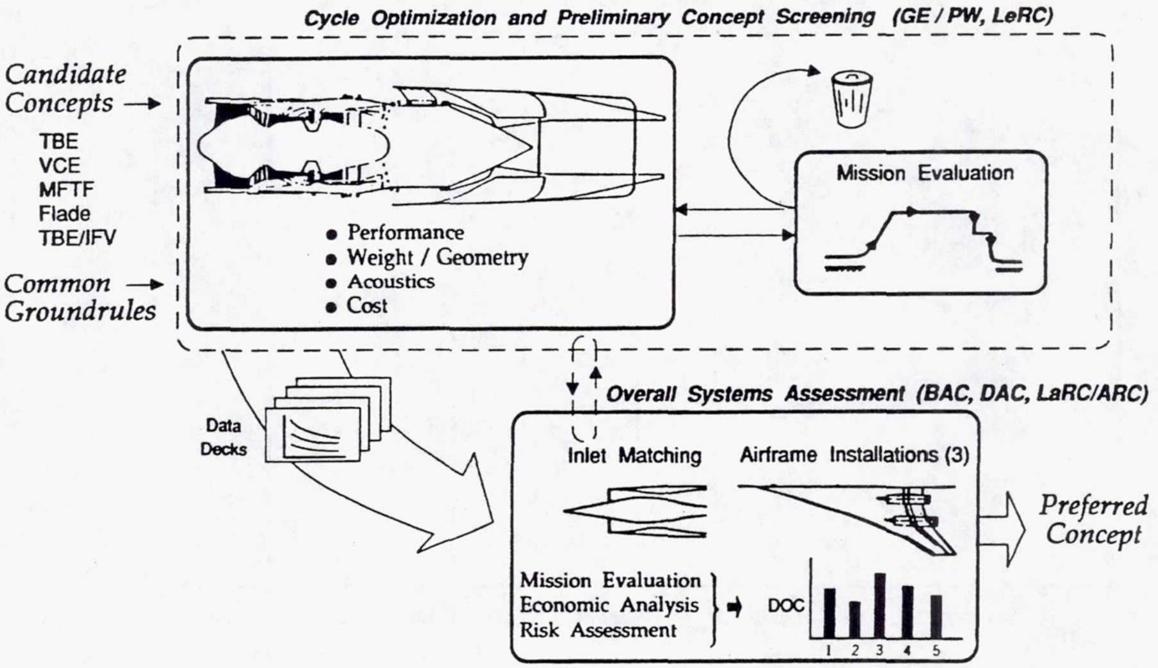

The process by which the down-select information is acquired begins with the establishment of a common set of groundrules for all participants to minimize the risk of disparate results. GE/PW are to perform a preliminary concept screening using takeoff gross weight as the prime evaluation criterion. This means that for each candidate concept the cycle will be optimized and representative airplane and mission models adopted. Propulsion-airframe installation (PAI) differences such as interference drag will not be captured, however. The output of this first level screening is passed to Boeing and Douglas for detailed comparative evaluations that include PAI effects. Boeing and Douglas have adopted somewhat different airframes and mission definitions (e.g., programmed lapse rate assumption) which means that somewhat different results may ensue. The merit criteria will be direct operating cost (DOC) and technical risk.

HSR Propulsion System Concept Selection Criterion

- *Prime discriminators:* *Direct operating cost (DOC)*
  Technical risk (uncertainty band)
- *Risk to be incorporated into DOC when feasible*

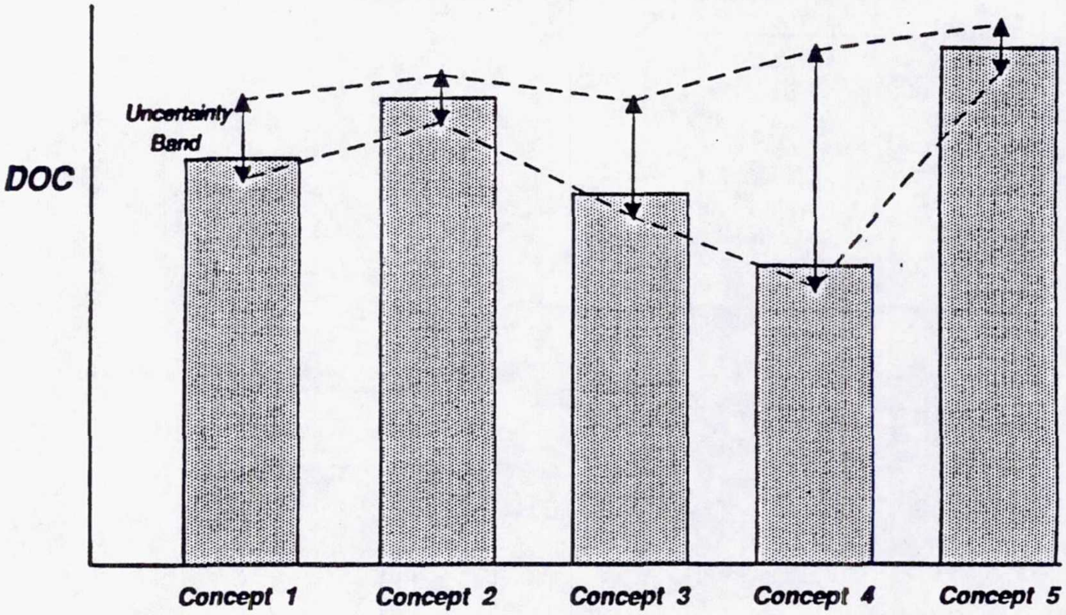

To avoid an unwieldy number of risks associated with the various technologies, risks will be incorporated into DOC wherever possible. For example, if an unconventional component such as a mixer-ejector nozzle requires an expensive R&D program to reach acceptable risk, then the cost of this element is incorporated into the DOC. The end result is an uncertainty band on DOC that reflects the agglomerated risks associated with each concept. Conceivably, the down-select process will produce results as depicted wherein the nominally lowest DOC concept (arbitrarily drawn as concept 4) also has the highest risk. In this case, the decision-maker will need to make a judgement concerning the balance between DOC benefit and increased risk. In the example shown, concept 3 might be preferred over concept 4 due to its lower technical risk.

Monte Carlo Simulation Risk Analysis

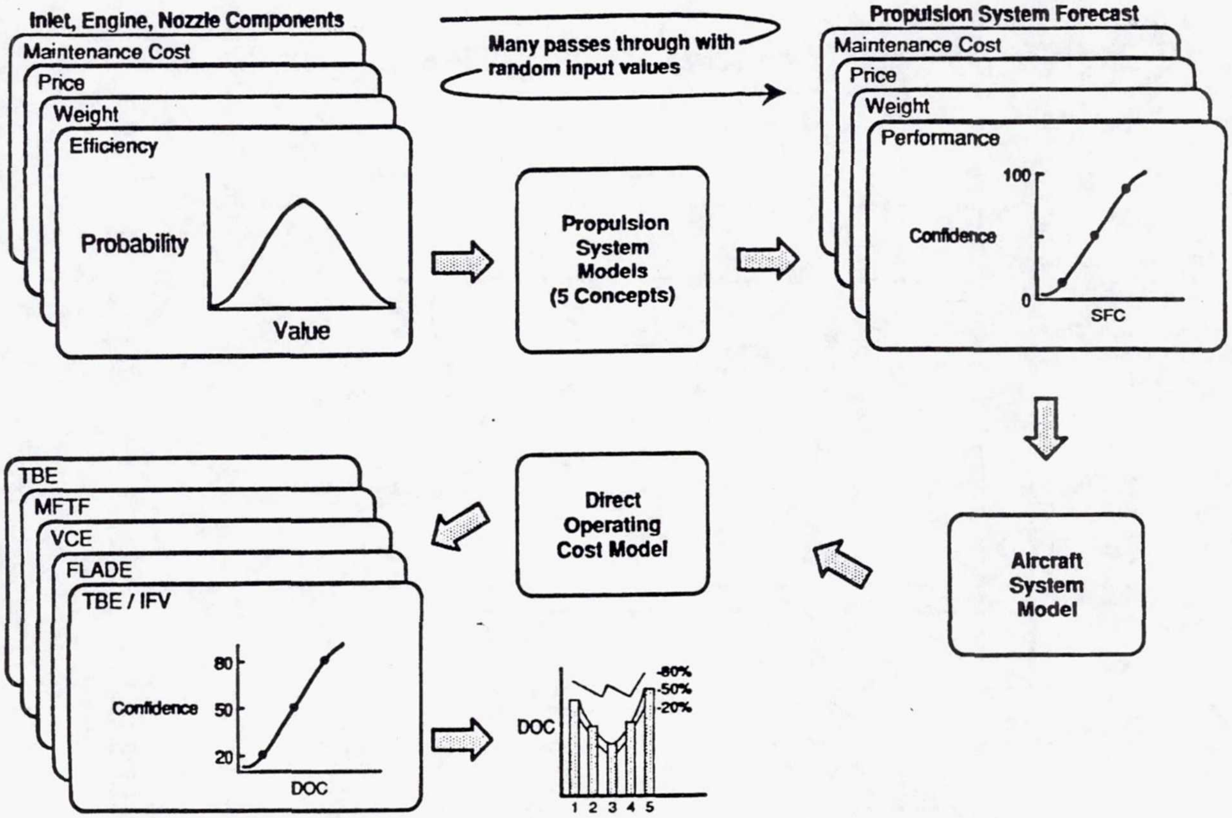

In order to determine the DOC uncertainties for each concept, GE/PW and Douglas are invoking a Monte Carlo simulation risk analysis. Component experts will estimate the probability of attaining several values of the key component criteria such as efficiency weight, acquisition cost, and maintenance cost. This will define sets of probability curves for each propulsion component such as the mixer-ejector nozzle, IFV, Flade fan, and mixed compression inlets. Random sampling of these component probabilities done many times, together with a propulsion systems model, will yield another (smaller) set of curves for each concept. These are confidence curves for the complete propulsion system. Combining this information with aircraft, mission, and economic models will lead to DOC confidence curves for each of the five propulsion concepts. Finally, these DOC confidence curves can be interrogated at three levels to yield the desired DOC uncertainty bands (e.g., 20 percent, 50 percent, and 80 percent).

Boeing prefers to do a more traditional risk analysis instead of a Monte Carlo analysis. They will interrogate a group of experienced technology experts to estimate risks associated with each candidate concept. This traditional approach will provide a check on the Monte Carlo simulation.

Level 2 HSR Program Schedule - Propulsion System Studies

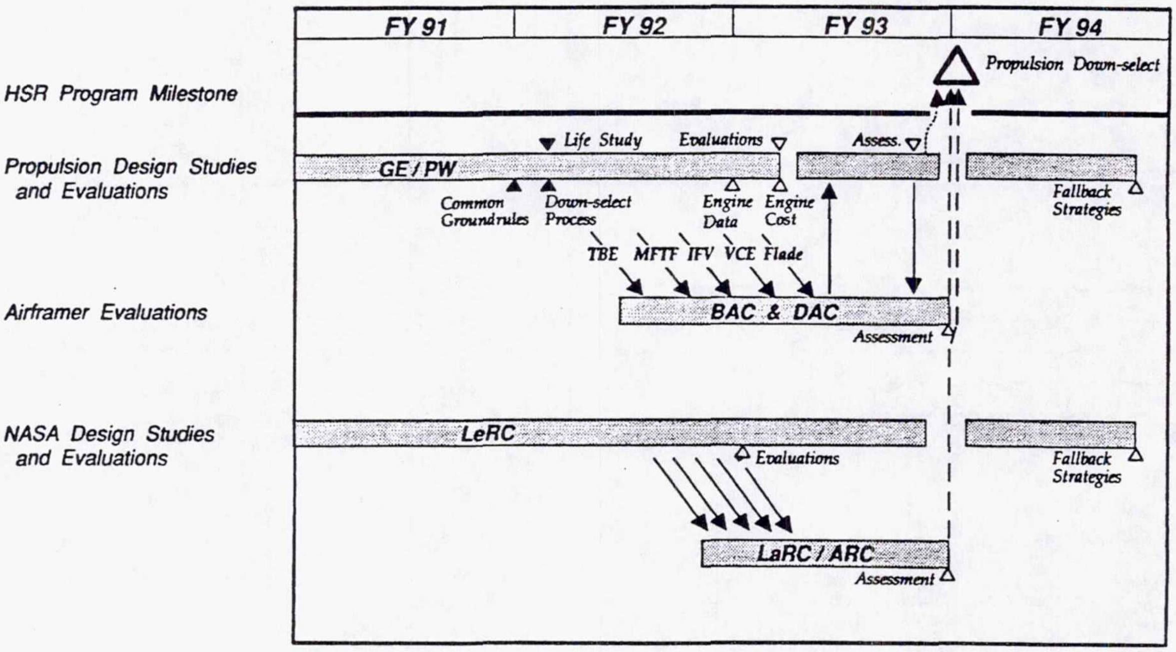

Having established common groundrules amongst GE/PW, Boeing, Douglas, and NASA, the propulsion system design studies are well underway within the propulsion community. Mach 2.4 data have been generated and delivered to the airframers for the TBE, MFTF (bypass ratios of 0.4, .63, 1.13), and the TBE/IFV. The VCE and Flade data are nearly complete. These data include performance, weights, cost, and acoustic information. In the spring of 1993, Boeing and Douglas will have completed a first pass comparison of all of the engine candidates. At this point, all first-order technical issues and concept-specific concerns will be identified. From then on, detailed analyses will be conducted to insure that each concept is fairly judged. This entails exploring ways to mitigate the weaknesses associated with each propulsion concept. The plan calls for sufficient information to be acquired by the beginning of FY94 to enable a credible down-select decision. NASA is also performing design studies and comparative evaluations to strengthen the overall effort. Because the technical challenges are complex and five organizations are involved in designing and evaluating numerous engine and nozzle concepts, there is also an enormous information management challenge to ensure effective use of available resources.

Status of NASA In-House Comparative Propulsion Studies

Mach 2.4, 100% supersonic 5000 n.mi. range, 292 passengers

Stage III sideline constraint
Assumes material goals and mixer-ejector nozzle goals are achieved
LeRC results as of September, 1992

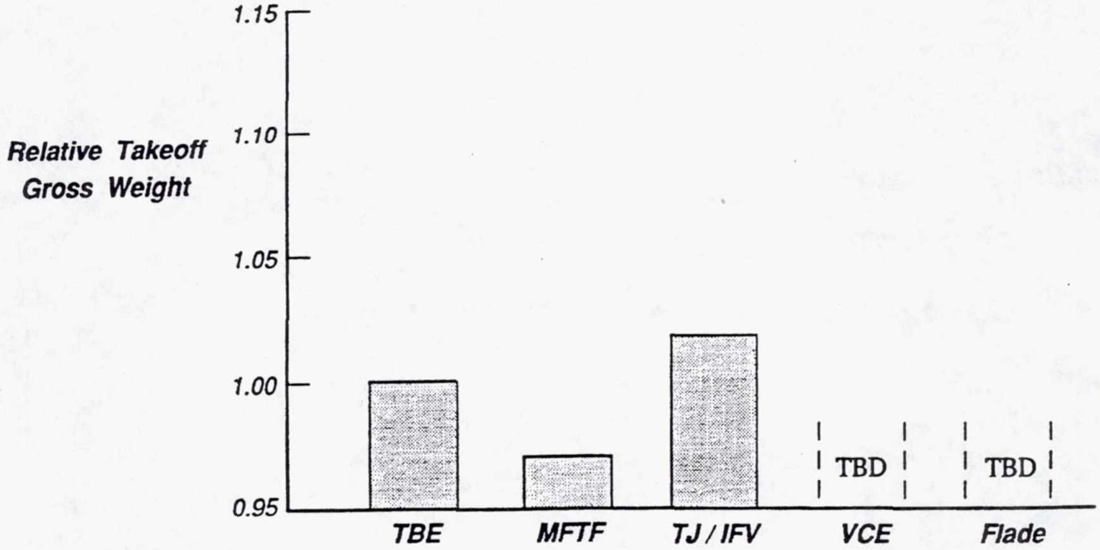

Currently, there is not much comparative data to examine and what data does exist is quite tentative and laced with caveats. Nevertheless, this chart displays NASA's current state of understanding of three of the five concepts. Relative takeoff gross weight is shown assuming the EPM materials goals and the HSR mixer-ejector nozzle goals are achieved (e.g., the TBE nozzle delivers 18^{+}dB suppression in an acceptable size), and that no significant PAI penalties exist. Even with these assumptions the MFTF is superior to the TBE because its cruise efficiency is significantly better. If the PAI differences do not hurt the MFTF, this candidate appears to be very competitive. Because the VCE is essentially a MFTF derivative, it too is expected to compete well--especially on missions with large subsonic legs. The Flade is also anticipated to be quite competitive for similar reasons.

Key Propulsion System Uncertainties

Technical

1. *Adequate mixer - ejector nozzle aero / acoustic performance*
2. *Materials progress*

External

3. *More severe airport noise regulations*
4. *Operational procedure regulations (e.g., programmed lapse rate)*
5. *Climb noise*
6. *Mach number selection*

By itself, the previous chart depicts an oversimplified situation. In reality, there are a number of first-order uncertainties that need to be considered in the selection process. The sensitivity of the comparison with respect to these uncertainties needs to be determined to select wisely.

Impact of Noise Suppression Technology and Noise Constraint

Mach 2.4, all supersonic 5000 n.mi. range, 292 passengers

Cycle, nozzle, wing loading, thrust loading vary along each curve

Ignores aircraft installation differences and possible climb noise constraint

NASA Lewis results as of November 1992

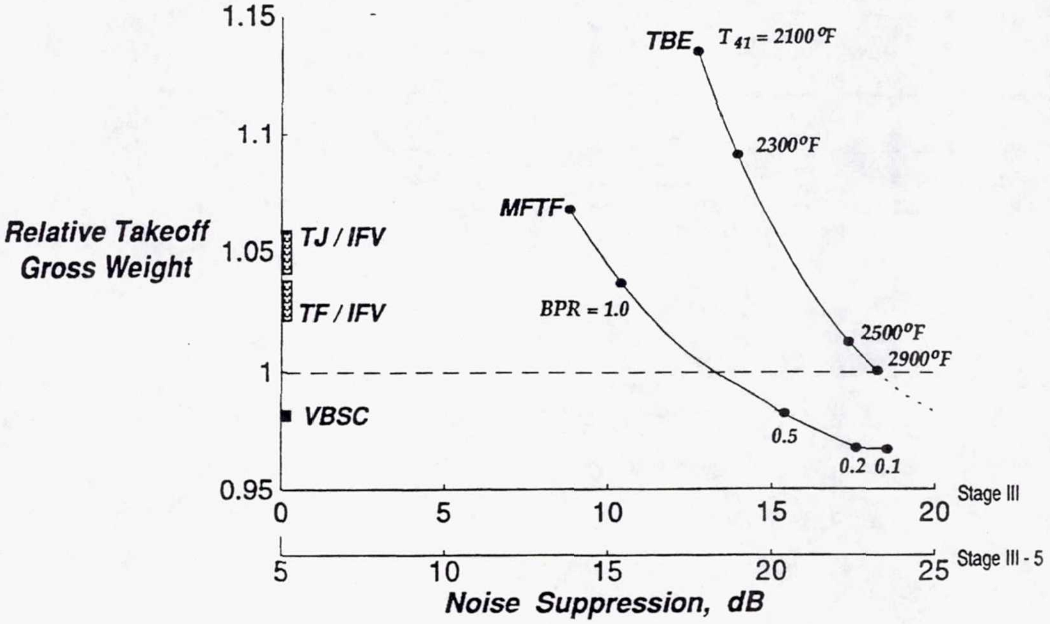

An example of the impact of the first three key uncertainties is displayed here in terms of takeoff gross weight relative to a TBE powered airplane with a 2900°F T_{41}. (The TBE would yield lower TOGW if it were not constrained by turbine blade material limits and unavailability of a suitable high-suppression nozzle.) Note that the TBE is quite sensitive to the degree of success in achieving a quiet nozzle. If only 13dB of suppression is achieved, then the TBE's TOGW penalty is about 14 percent. The TBE curve represents various amounts of wing and engine oversizing to meet Stage III sideline noise. The MFTF (and the other concepts as well) offer more degrees of freedom in the form of cycle changes (BPR) to mitigate the adverse impact of a mixer-ejector nozzle technology shortfall. Hence the MFTF curve is less steeply sloped, and it could accommodate even a 10dB suppressor nozzle without a show-stopping penalty.

The NASA results shown here also indicate that a 400°F material temperature shortfall would not be disastrous although 600°F would be. On the other hand, industry generated data show at least twice the sensitivity displayed here. These differences will be resolved soon.

The impact of a Stage III-5dB noise constraint may be determined by comparing results using the lower abscissa scale with results using the upper scale. For example, the ΔTOGW for a MFTF is about 7 percent for a 15dB suppressor nozzle.

Finally, it should be understood that this figure is just the beginning. Undoubtedly it will change as more realism is added. Firm conclusions based on this alone are premature.

Variable Bypass Supercharged Core (VBSC)

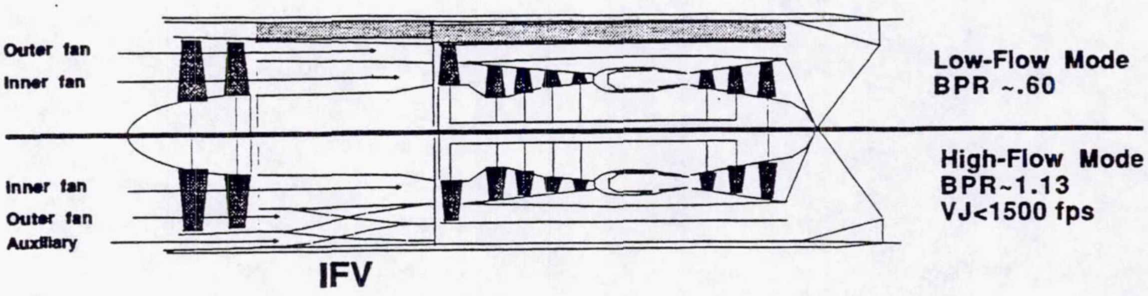

Advantages

- *Core remains supercharged in high-flow mode*
- *Less pressure drop, better cruise TSFC*
- *Less auxiliary inlet air required*
- *Lower engine weight*

The previous chart contained several points for TBE/IFV and TJ/IFV engines. At the moment there is some controversy concerning whether the plotted points are too optimistic or not. Regardless of how that controversy is resolved, it is clear that, while such high flow concepts are appealing because they obviate the need for a high-risk mixer-ejector nozzle, they also suffer serious deficiencies. Namely, a non-supercharged core and consequently low thrust in the takeoff mode, large and heavy engines, and pressure drop through the IFV during cruise. These deficiencies may be partially alleviated by the new concept illustrated here. It is a turbofan/IFV with a flow splitter that keeps the core supercharged by the inner fan flow at all times. It also features a core-driven aft fan stage that prevents bypass ratio from rising at higher flight speeds (opposite of mission requirement).

VBSC

Takeoff and Climb to Cruise

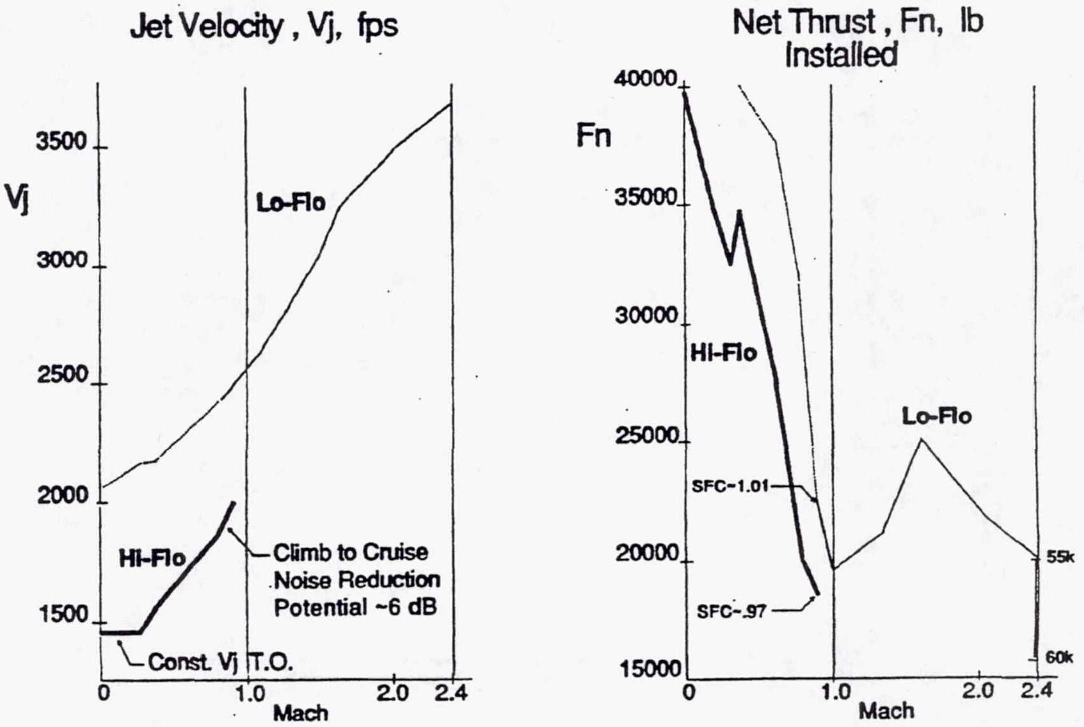

Another advantage of the variable bypass supercharged core (VBSC) concept is its ability to efficiently stay in the high-flow mode throughout climb. This may prove to be important to reduce climb noise. Shown here is the exhaust velocity V_j and net thrust F_n during a typical climb path. Note the modest V_j throughout--rising from 1450 ft/s at Mach 0.3 to 2000 ft/s at Mach 0.9 at which point the mode switch occurs. NASA has conceptualized this engine very recently and has solicited industry feedback (pending) before adopting its inclusion into the down-select process.

TOGW Sensitivity to Nozzle Performance and Weight

Mach 2.4 HSCT

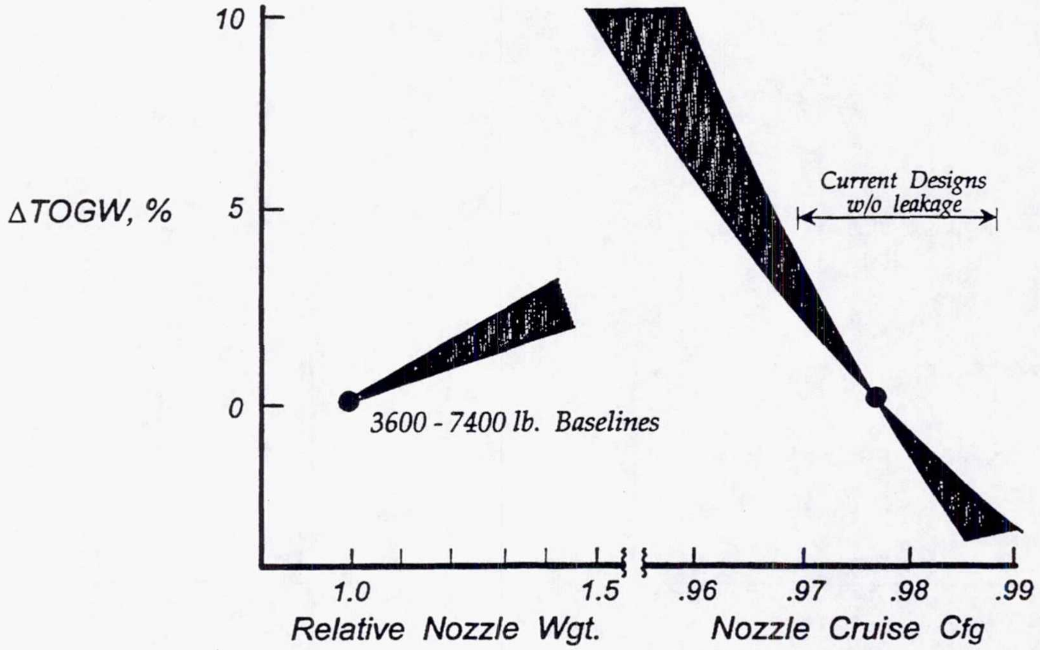

Achieving high nozzle cruise efficiency is absolutely essential. A 1 percent C_{fg} shortfall can increase TOGW by over 4 percent. Clearly, we need confidence in our predictive codes to substitute for lack of experimental data for many of the unconventional nozzle concepts.

Nozzle weight is also a sensitive parameter. As the studies progress, the initially large spread in weight estimates has significantly diminished.

Avoided on this figure is any mention of the takeoff nozzle performance which is often cited as important also. (E.g., it is one of the two merit criteria in the oft-used mixer-ejector nozzle technology goal charts.) This omission was deliberate because some of the high-specific thrust engines are top-of-climb sized and therefore do not suffer large penalties for takeoff C_{fg}'s as low as 0.85 or so. There is also some evidence that even takeoff sized engines could tolerate relatively poor takeoff C_{fg}'s if wing size is free to vary to compensate.

Thrust Augmentation Issue

Some cycles benefit from a mini-augmentor during climb

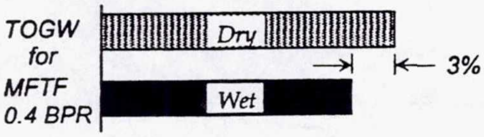

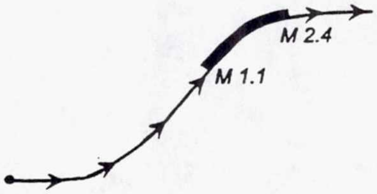

But

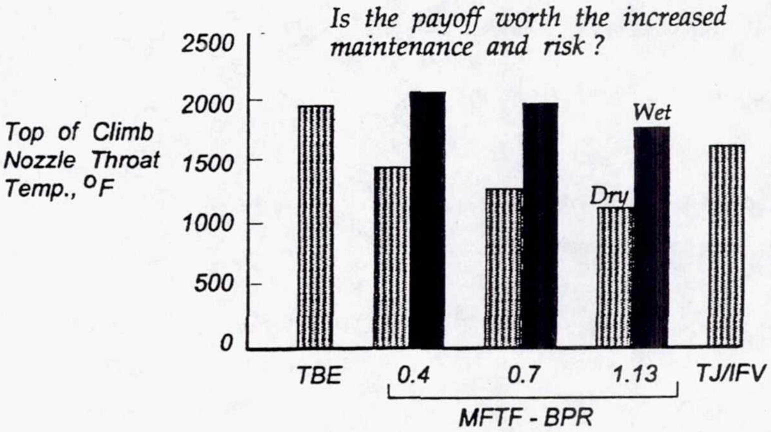

One of the more recently discovered issues is whether to use a mini-thrust augmentor or not in the high specific flow engines. For example, Boeing prefers to use a mini-augmentor during the upper climb path to offset marginal thrust levels that cause inefficient transonic system performance. A 3 percent TOGW reduction is possible using a mini-augmentor rather than a dry engine for a MFTF with 0.4 bypass ratio. However, the use of augmentation also boosts the nozzle temperature levels about 600°F from the 1200-1400°F level to the 1700-2000°F level. The question is whether the TOGW payoff is worth the increased risk and maintenance associated with the higher temperature experienced during the upper climb. This issue is being investigated further.

Nacelle Placement Restraints

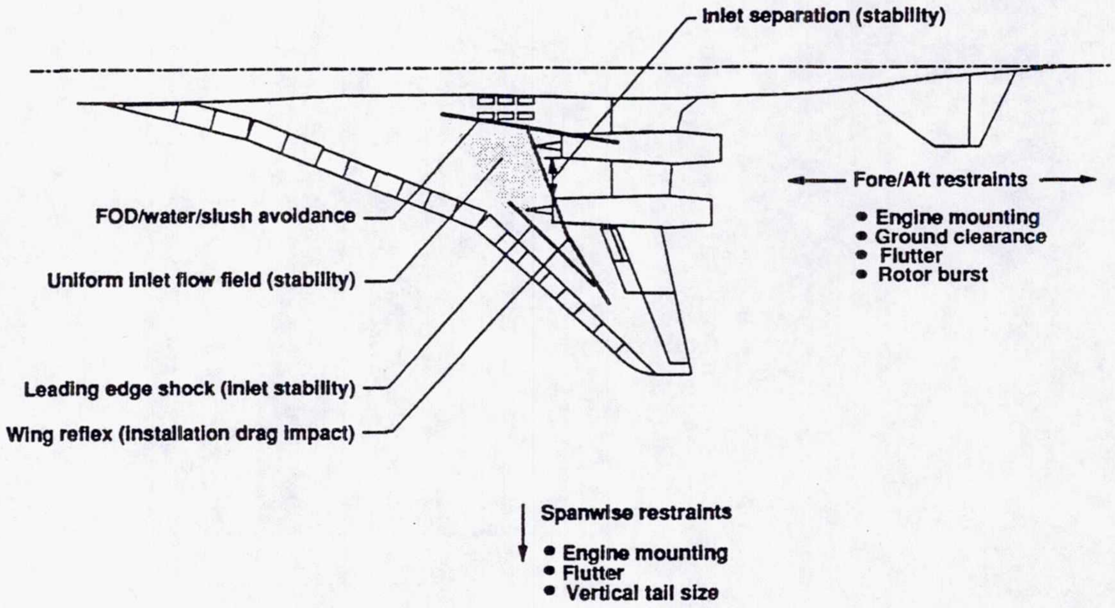

Another powerful influence on the down-select decision is propulsion-airframe integration (PAI). For example, the nacelle shape, which is driven by the propulsion geometry and changes significantly from one concept to another, and placement can dramatically alter the interference wave drag. Hence, to compare the alternative propulsion concepts we need to assure ourselves that PAI effects are properly determined even if this requires more than the usual analysis depth to understand. From early calculations it appears that some of the concepts do not integrate easily with the airframe and some re-design effort is warranted to avoid premature judgements.

Summary

1. *Late 1993 propulsion system down-select requires reliable M-E nozzle database*
   - *-- Adequate progress but not established yet*

2. *Considerable concern exists about M-E nozzle risk*
   - *-- Aero / acoustic performance -- Weight / size -- Life*

3. *Interest shifting toward low specific thrust cycle solutions to noise challenge*

4. *Stage III-5 dB incurs approximately a 7% airplane takeoff weight penalty for mixed-flow turbofans with M-E nozzles*

At the moment, the propulsion system down-select process is hindered by our lack of an adequate experimental mixer-ejector nozzle database to enable high-confidence aero/acoustic/weight modeling. Progress in establishing the needed data base is progressing adequately but fitfully. Certainly there exists considerable concern about M-E nozzles--enough to spawn a new wave of interest in the high-specific flow alternatives. In the end, it is likely to come down to a matter of which technology challenges do we prefer to pursue. The decision may depend upon risks as much as on potential benefits.

1999176569

SUPPRESSOR NOZZLE IMPACT ON AIRCRAFT PERFORMANCE AND DESIGN

Alan K. Mortlock
McDonnell Douglas Company
Long Beach, California

S32-05

409568
8p.

EXHAUST NOZZLE PERFORMANCE PARAMETERS THAT IMPACT AIRCRAFT SIZING

LOW SPEED (e.g. M = 0.3 TO 0.9)

- **ACOUSTIC PERFORMANCE TO MEET NOISE CERTIFICATION LIMITS**
- **SUPPRESSED TAKEOFF/CLIMB THRUST LOSS PERFORMANCE MINIMIZATION**
- **UNSUPPRESSED NOZZLE PERFORMANCE AT SUBSONIC CRUISE (INCLUDING SUPPRESSOR STOWABILITY RE. LEAKAGE/BLOCKAGE)**

HIGH SPEED (e.g. M = 2.4)

- **UNSUPPRESSED NOZZLE PERFORMANCE AT SUPERSONIC CRUISE (INCLUDING SUPPRESSOR STOWABILITY RE. LEAKAGE/BLOCKAGE)**

The exhaust nozzle performance of the HSCT engine is an extremely sensitive design parameter for determining the aircraft size to perform to a mission requirement. The acoustic and thrust performance required during takeoff and climb can determine engine size and consequently effect overall aircraft mission performance. During supersonic cruise the noise suppression devices must be stowed in a manner to prevent leakage or blockage in order to achieve the best efficient nozzle conditions.

Douglas HSCT Baseline Design and Mission Requirements

NUMBER OF PASSENGERS = 300 (3-CLASS)
RANGE = 5,000 N MI, TOFL = 11,000 FT (STD + 27F)
FAR PART 36 STAGE 3 NOISE CERTIFICATION LIMITS

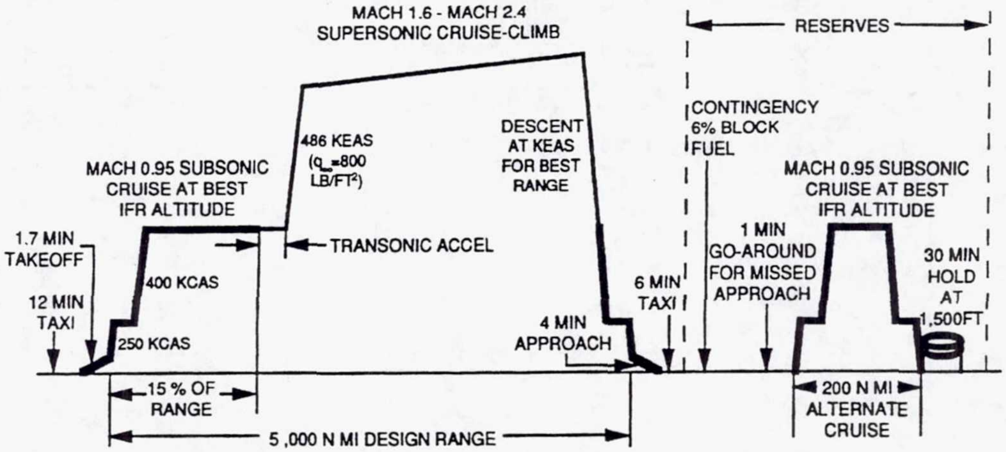

The Douglas baseline design at Mach 2.4 has four basic design constraints which can dominate aircraft size viz: 300 passengers, 5,000 n.m. range, 11,000 ft. takeoff field length and meeting Stage 3 noise limits during takeoff and approach. Aerodynamic features are considered for a 15% subsonic cruise/85% supersonic cruise profile. The necessary fuel reserves to comply with diversions caused by weather, airport and aircraft operatibility reasons are considered. In some cases, the engine size may be controlled meeting noise requirements during takeoff or by size requirements at the top of the supersonic climb portion.

NOZZLE THRUST LOSS SENSITIVITIES

CURRENT BASELINE TAKEOFF PROCEDURE

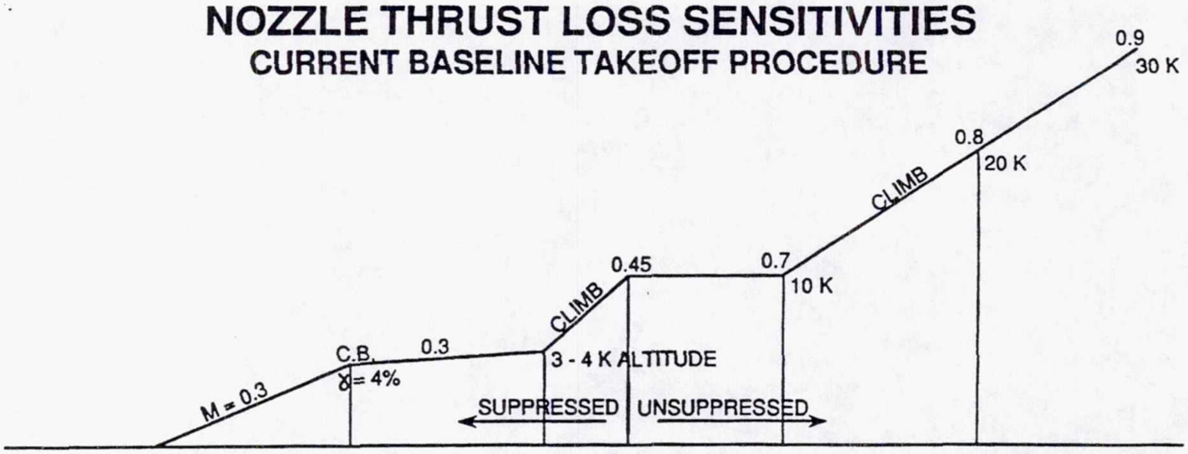

SENSITIVITY STUDIES : (EXAMPLE THRUST COEFFICIENTS ONLY)

STAGE 3 SIZING	(a) Cg 0.95	0.95	0.93	0.98	0.98	0.98
——— " ———	(b) Cg 0.90	0.90	0.88	0.98	0.98	0.98
——— " ———	(c) Cg 0.85	0.85	0.83	0.98	0.98	0.98
		← SUPPRESSED	SUPPRESSED →			
CLIMB TO CRUISE SIZING	(d) Cg 0.95	0.95	0.93	0.90	0.88	0.85
——— " ———	(e) Cg 0.90	0.90	0.88	0.85	0.83	0.80
——— " ———	(f) Cg 0.85	0.85	0.83	0.80	0.78	0.75

Acoustic nozzle thrust losses during takeoff can have an impact on aircraft sizing if the aircraft/engine is sized at the takeoff condition. The effects of takeoff thrust loss impact is reduced if the aircraft/engine is sized at he top of supersonic climb. Additionally, if the climb to cruise portion of the emission needs to be in a suppressed mode for community noise considerations, increased thrust losses at higher subsonic forward speeds will also impact aircraft size due to additional fuel burn.

AIRCRAFT SIZING TO MEET STAGE 3 NOISE LIMITS

- **MEET SIDELINE STAGE 3 LIMITS**
  - **SIZED MTOW DETERMINES STAGE 3 LIMITS**
  - **ENGINE CYCLE/ACOUSTIC NOZZLE ATTENUATION DETERMINED TO MEET STAGE 3 LIMIT**
  - **THIS MAY REQUIRE ENGINE OVERSIZING TO ACHIEVE STAGE 3 SIDELINE NOISE LIMITS OR INCREASED NOZZLE ATTENUATION**
- **DETERMINE TAKEOFF AND APPROACH NOISE LEVELS FOR FINAL SIZED ENGINE/NOZZLE**
  - **PREDICT TAKEOFF AND APPROACH NOISE LEVELS**
  - **COMPARE WITH STAGE 3 LIMITS**

The takeoff power thrust requirements for the HSCT e.g. (approx. 50,000 lbs.) will have associated exhaust jet velocities and noise suppression needs to achieve the Stage 3 sideline noise limits. In general, if the sideline noise limit is attained, the takeoff noise limit under the aircraft flight path will be met by about 2 or three dB. At the approach condition turbo machinery and airframe source noise levels are important to determine meeting approach noise limits. Sideline, takeoff and approach noise predictions will be necessary to determine full Stage 3 noise compliance.

TAKEOFF PROCEDURES FOR NOISE SIZING

CONDITIONS: ISA + 10°C, 70% RH, ZERO WIND, RUNWAY SEA LEVEL PRESSURE (14.7 PSI)
TAKEOFF FIELD LENGTH (TOFL) 11,000 FT FOR SIZING (UPTO 12,000 FT FOR NOISE CERT.)

PROCEDURE:	UP TO 35 FT ALT MIN SPEED	UP TO 35 FT ALT AERO CONFIG	UP TO 35 FT ALT ENG POWER	35 FT ALT. TO CUTBACK MIN SPEED	35 FT ALT. TO CUTBACK AERO CONFIG	35 FT ALT. TO CUTBACK ENG. POWER	CUTBACK DISTANCE PRIOR TO MONITOR (FT)	AFTER CUTBACK MIN SPEED	AFTER CUTBACK AERO CONFIG.	AFTER CUTBACK ENG. POWER
A	$V_2 + 10$	TOFL FIXED	MEET STG 3 SIDELINE	$V_2 + 10$	BEST L/D	NO CHANGE	1500 TO 3000	$V_2 + 10$	BEST L/D	4% GRAD OR 1 ENG.-OUT
B	$V_2 + 10$	TOFL FIXED	MEET STG 3 SIDELINE	$V_2 + 10$	BEST L/D	ATR	1500 TO 3000	$V_2 + 10$	BEST L/D	4% GRAD OR 1 ENG.-OUT
C	$V_2 + 10$	TOFL FIXED	MEET STG 3 - 3db SIDELINE	← SAME AS PROCEDURE A →						
(ADDITIONAL DAC) D	$V_2 + 10$	TOFL FIXED	MEET STG 3 SIDELINE	$V_2 + 10$	NO CHANGE	NO CHANGE	1500 TO 3000	$V_2 + 10$	FIXED	4% GRAD OR 1 ENG.-OUT

There are a number of takeoff procedure options that can be studied to determine the optimum procedure to achieve the lowest MTOW while meeting the sideline Stage 3 limit. There ar no HSCT noise certification rules in existence at this time. Therefore, the following options are being studied:

(i) Assume the current subsonic Stage 3 takeoff procedure

(ii) Assume automated aerodynamic changes can be employed during takeoff

(III) Assume (ii) above including thrust reduction changes during takeoff to minimize sideline noise.

DESIGN SIZING POINT VS. NOISE

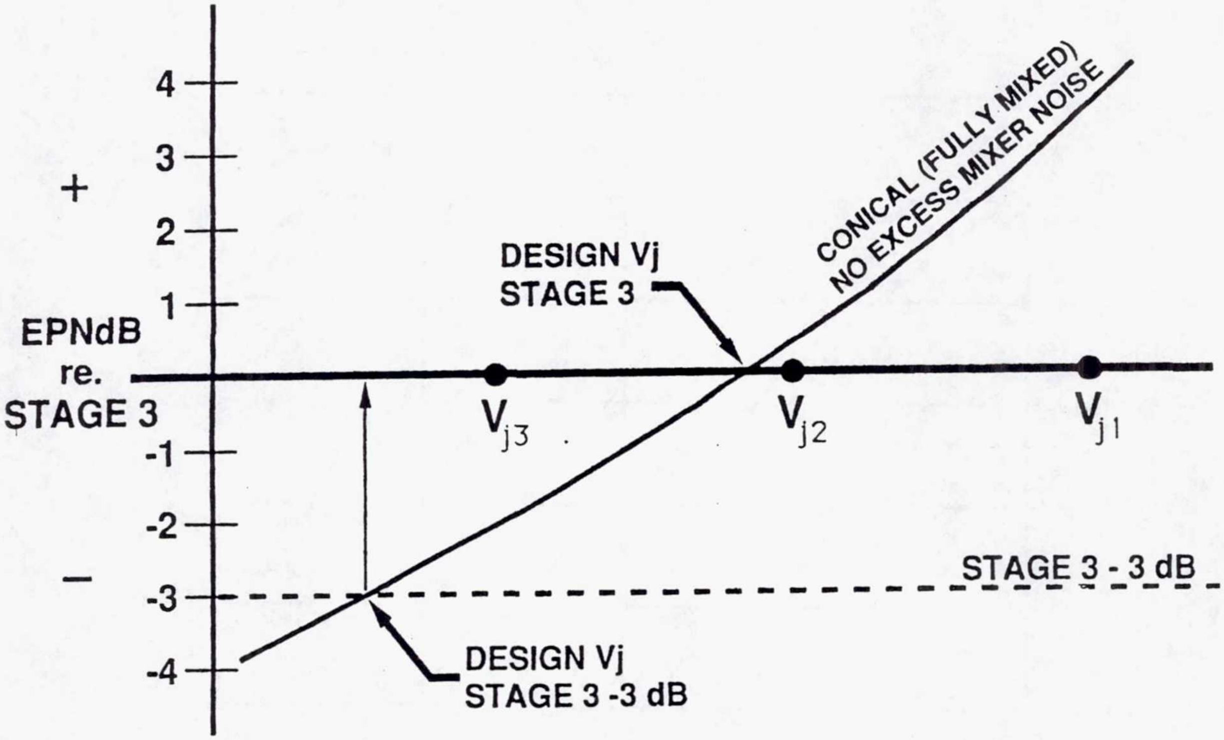

In order to achieve the sideline noise limit for each engine/nozzle concept, the aircraft is sized to meet the mission requirements at different engine thrust conditions (e.g. full power, 90% power, 80% power) supplied by the engine companies. The exhaust jet velocity required to meet the sideline Stage 3 and Stage 3 - 3dB limits can then be determined from the curve illustrated.

ENGINE OVERSIZING TO ACHIEVE MORE STRINGENT REQUIREMENT

FLADE D2 T.O.G.W. VS. Vj
M 2.4-1A 5,000 N.MI. RANGE
DAC PLANFORM

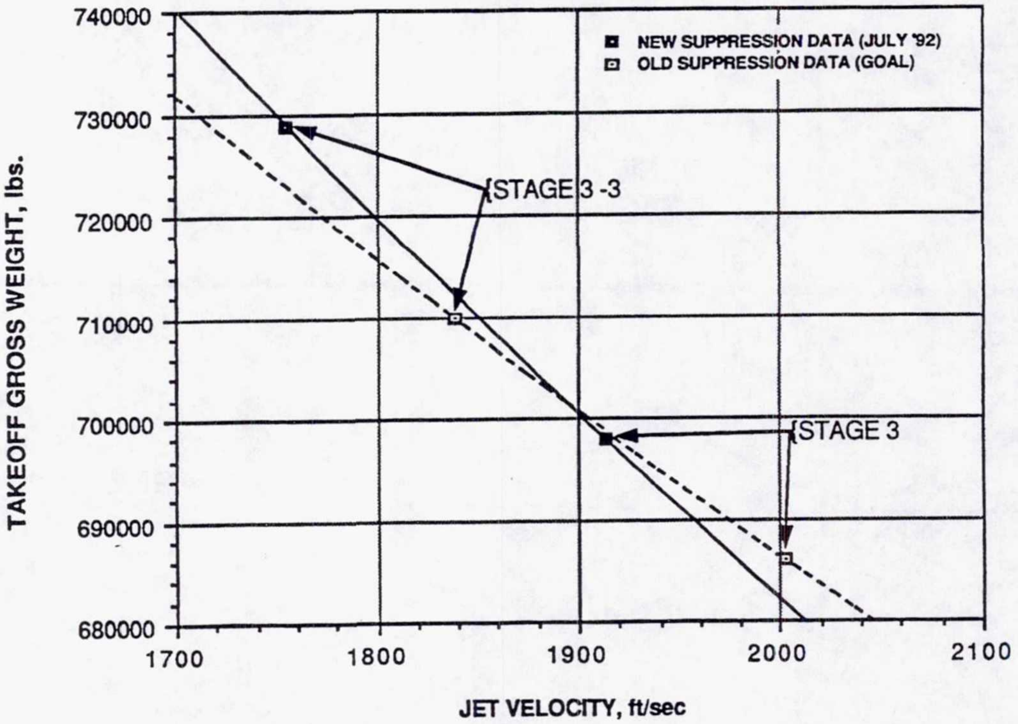

The current noise certification design goal is to achieve FAR Part 36 Stage 3 (ICAO Annex 16, Chapter 3) noise limits. If by the turn of the century the subsonic noise standard becomes more stringent, it may influence HSCT standards to comply with a similar rule. If we have to overcome this noise stringency (e.g. Stage 3-3dB) by oversizing the engine to achieve a lower exhaust jet velocity, the vehicle takeoff gross weight could be increased by approximately 27,000 lbs. depending on noise suppression data assumptions. However, if increased nozzle attenuation can be achieved, the aircraft size may grow at a slower rate (e.g. 12,000lbs.).

TYPICAL AIRCRAFT SIZING EXCHANGE RATES

(AT 5000 N. MLS)

NOISE:

- I EPNdB AT SIDELINE

= + 9,000 LB MTOW FOR OVERSIZING
= + 4,000 LB MTOW FOR INCREASING NOZZLE ATTENUATION

SUPERSONIC NOZZLE EFFICIENCY:

- 1% CFg = + 37,000 lb MTOW

= + 6% DOC PER SEAT MILE

As discussed on the previous figure, reducing sideline noise by engine oversizing could increase MTOW by approximately 9,000 lbs. for a reduction of 1dB at the sideline point. However, if the nozzle attenuation could be increased for a minimal thrust loss, the aircraft size may only increase by approximately 4,000 lbs. for a reduction of 1 dB at sideline. At supersonic cruise, the penalty of reducing the nozzle coefficient by 1% could increase the MTOW by approximately 37,000 lbs. which can be translated into an increase of approximately 6% DOC per seat mile. As the supersonic Nozzle coefficient appears to be a sensitive parameter impacting aircraft size and weight, it is important that noise suppression devices are made storable such that leakage and blockage do not effect the nozzle performance.

1999176570

ASSESSMENT OF INTEGRATED NOZZLE PERFORMANCE

H.H. Lambert and M. Mizukami
NASA Lewis Research Center
Cleveland, Ohio

533-07

409510

20P.

Presentation Outline

9'x15' Wind Tunnel PAI Test Results (PAIHSR1)

Mixer/ejector Inlet Distortion, an Experimental Study (MIDIS-E)

High-lift Engine Aero-acoustic Technology Test Plans (HEAT)

This presentation highlights the activities that researchers at the NASA Lewis Research Center (LeRC) have been and will be involved in to assess integrated nozzle performance. Three different test activities are discussed. First, the results of the Propulsion Airframe Integration for High Speed Research 1 (PAIHSR1) study are presented. The PAIHSR1 experiment was conducted in the LeRC 9'x15' wind tunnel from December 1991 to January 1992. Second, an overview of the proposed Mixer/ejector Inlet Distortion Study (MIDIS-E) is presented. The objective of MIDIS-E is to assess the effects of applying discrete disturbances to the ejector inlet flow on the acoustic and aero-performance of a mixer/ejector nozzle. Finally, an overview of the High-Lift Engine Aero-acoustic Technology (HEAT) test is presented. The HEAT test is a cooperative effort between the propulsion system and high-lift device research communities to assess wing/nozzle integration effects. The experiment is scheduled for FY94 in the NASA Ames Research Center (ARC) 40'x80' Low Speed Wind Tunnel (LWST).

PAIHSR1 Research Objectives

Primary Objective- Determine effects on the acoustic characteristics of a two-dimensional mixer/ejector nozzle due to the non-uniform flow from a wing entering the ejector inlet

Secondary Objective- Determine first-order effects on the aero-performance of a two-dimensional mixer/ejector nozzle due to the non-uniform flow a wing entering the ejector inlet

The PAIHSR1 experiment had two objectives. The primary objective was to determine integration effects on the acoustic performance of a two-dimensional mixer/ejector nozzle. The secondary objective was to determine integration effects on the aero-performance of the same two-dimensional mixer/ejector nozzle. Unfortunately, combustor failure precluded the acquisition of acoustic data. Warmed facility air (~200°F) was used for the primary flow to assess changes in mixing at the nozzle exit.

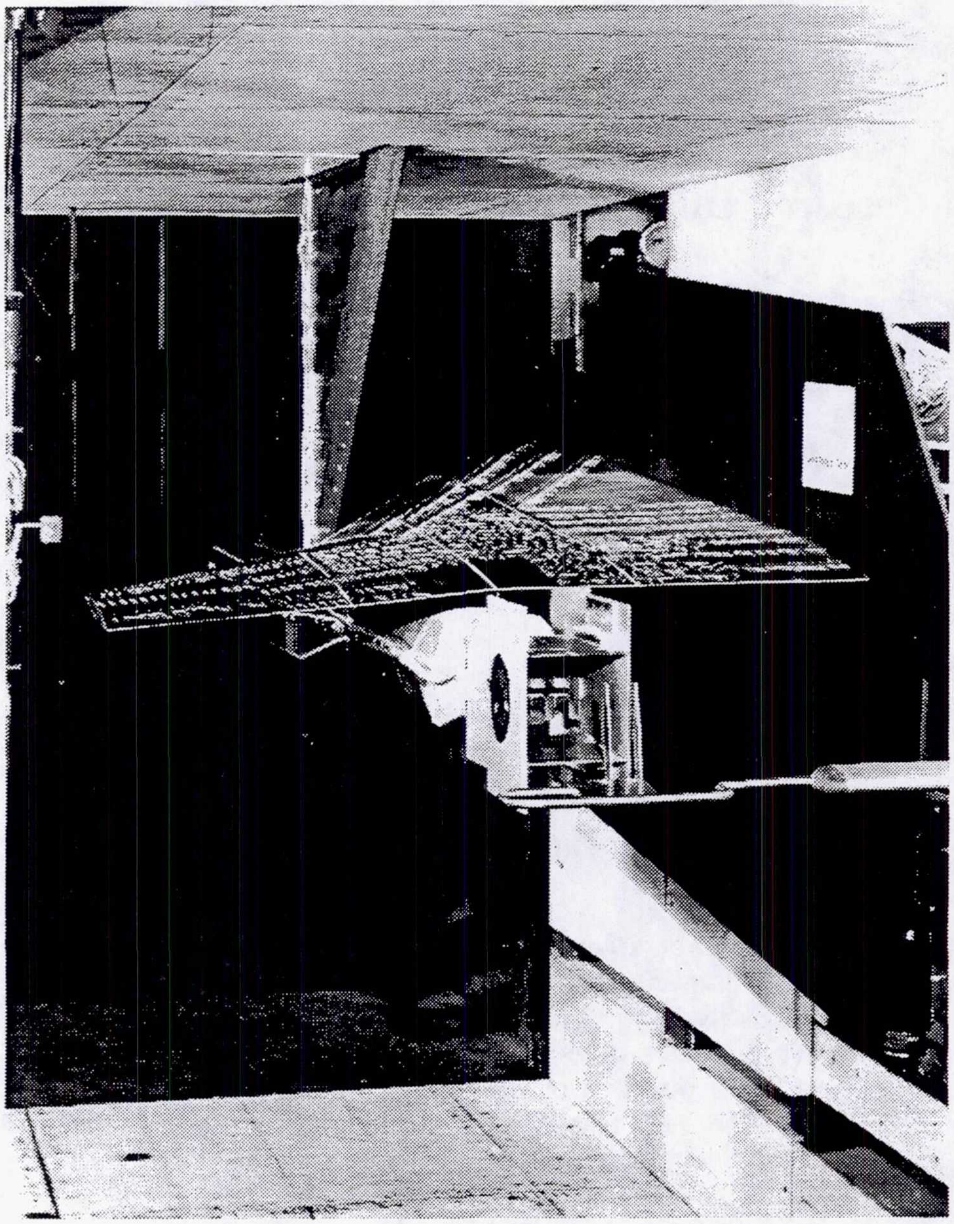

This figure is a photograph of the PAIHSR1 model hardware installation in the LeRC 9'x15' Wind Tunnel. The model hardware included a semi-span wing model, the Pratt & Whitney two-dimensional mixer/ejector nozzle with a vortical mixer, and the LeRC Jet Exit Rig (JER). The semi-span wing model had a generic supersonic planform and deflectable leading and trailing edge flaps. The section of the wing trailing edge directly above the JER, referred to as the interfairing, was not deflectable. Tufts, visible in the photograph, were applied to the wing for flow visualization study. One of the variable parameters in the experiment was ejector inlet orientation. The suppressor nozzle orientation shown is the horizontal orientation, with the ejector inlets oriented sideways with respect to the wing.

Test Parameters

Mach Number	**0.2**
Primary Nozzle Pressure Ratio	**1.4, 1.7, 2.5, 3.0, 3.5, 4.0/4.2**
Ejector Inlet Orientation	**Vertical, Horizontal**
Shroud Length	**Short, Long**
Flap deflection (LE/TE)	**0°/0°, 0°/20°, 20°/40°**
Wing Interfairing Length	**Short, Long**
Wing Position	

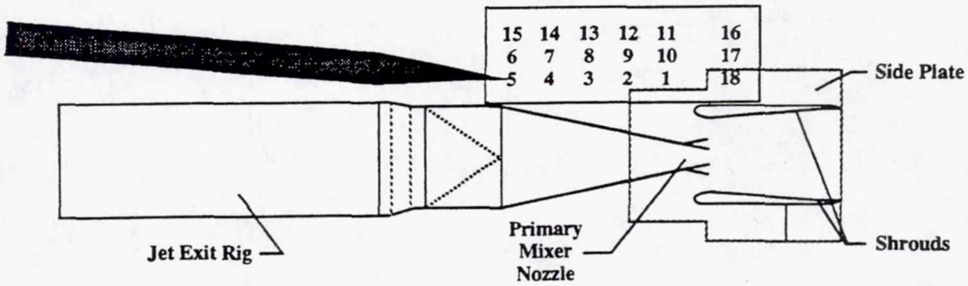

Six parameters were varied during the PAIHSR1 test: primary nozzle pressure ratio (NPR), ejector inlet orientation, shroud length, leading edge (LE) and trailing edge (TE) flap deflection, wing interfairing length, and wing position. Data was primarily recorded at the maximum tunnel Mach number of 0.2. The NPR was varied from 1.4 to ~4.0. Two ejector inlet orientations were examined: horizontal, as shown two pages previously, and vertical, with the ejector inlets oriented on the top and bottom with respect to the wing. Two shroud lengths were studied: long and short. were studied. Three sets of leading and trailing edge flap deflections were selected: 0° LE/0° TE, 0° LE/20° TE, and 20° LE/40° TE These sets of deflections were not selected to represent particular flight configurations but to create different flowfields in the proximity of the ejector inlets. Two interfairing lengths were studied: long and short. Finally, the wing was mounted to a positioning table that allowed the wing trailing edge location to vary axially and vertically with respect to the nozzle. Eighteen predefined positions were examined. A matrix showing the relative location of the different positions is shown.

Nozzle Instrumentation

Shroud Static Pressures

2 Rows of 20 static pressures

- **Primary mixer peak**
- **Primary mixer valley**

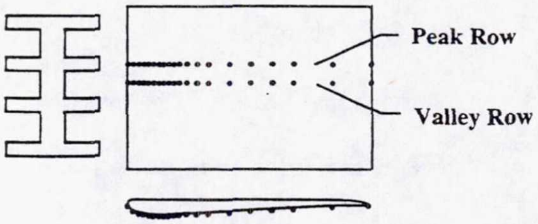

Nozzle Exhaust Flow Traverse

- **15 total pressure measurements**
- **15 total temperature measurements**

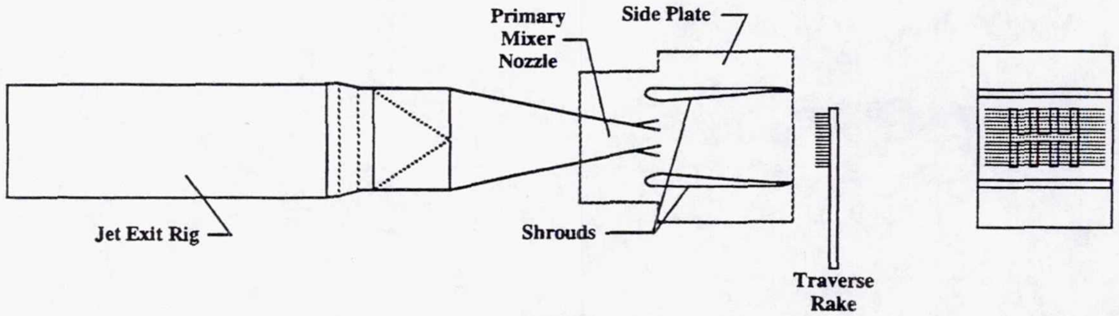

The data analyzed for this presentation are the shroud static pressures and the nozzle exhaust flow traverse total temperatures and total pressures. Two rows of 20 static pressures each are distributed axially along the nozzle's interior shroud walls. One row is located over the peak of a primary mixer lobe, the other over the valley of a primary mixer lobe. The shroud static pressure profiles are presented as a shroud static pressure ratio defined as Ps_{shroud}/Pt_0, where Pt_0 is the tunnel total pressure. A traverse rake was used to assess the nozzle exhaust flow total temperature and total pressure contours. The traverse rake included 15 total temperature and 15 total pressure measurements. The nozzle exit total temperature contours were examined to identify changes in the mixing characteristics of the nozzle due to integration effects. The total temperature measurements are presented as a non-dimensionalized contour value defined as $(T_T - T_{Tsecondary})/(T_{Tprimary} - T_{Tsecondary})$. The wing tuft flow visualization was recorded on video tape, and proved useful in understanding the nozzle data and installation effects.

Focus of Data Analysis

Vertical Ejector Inlet Orientation

- **Effect of varying wing position**
  - **Long shroud**
  - **Short shroud**
- **Effect of varying interfairing length**

Horizontal Ejector Inlet Orientation

- **Effect of varying wing position for fixed LE/TE flap deflections**
- **Effect of varying LE/TE flap deflections for fixed wing position**

The data for the PAIHSR1 experiment was divided into two sets for parametric analysis: data recorded with the vertical nozzle orientation and data recorded with the horizontal nozzle orientation. Data recorded with the vertical ejector inlet orientation was examined to asses the effect of varying wing interfairing length, wing position with the long shroud installed, and wing position with the short shroud installed. Data recorded with the horizontal ejector inlet orientation was examined to assess the effect of varying wing position for each set of leading edge and trailing edge flap deflections. The same data was also examined to assess the effect of varying leading edge and trailing edge flap deflections at fixed wing positions.

Experimental Results

Combuster failure precluded taking acoustic measurements - warmed facility air was used for the primary flow to assess mixing

Preliminary data was obtained which indicated no first-order PAI effects of the wing on the aero-performance of a two-dimensional mixer/ejector nozzle

- **Unrealistic flap deflections (20°LE/40°TE) were required to show any first order effects**
- **Varying wing position at extreme flap deflections resulted in noticeable changes**

The absence of measureable effects for most test configurations may have been a result of the hardware configuration and limited instrumentation

The PAIHSR1 experimental results indicate that for most of the configurations examined there are no first order effects of the wing on the aero-performance (shroud static pressure profiles and nozzle exhaust total temperature contours) of a two-dimensional mixer/ejector nozzle. Combustor failure precluded acquisition of acoustic data, however warmed facility air was used for the primary nozzle flow to assess nozzle mixing. Extreme flap deflections of 20° LE/40° TE were required to show any first order changes in the static pressure profiles or nozzle exhaust total temperature contours. At this extreme set of flap deflections, varying wing position resulted in changes in the static pressure profiles. It is appropriate to note that test limitations may have contributed to the absence of measurable PAI effects. In order to facilitate variation in wing position, the wing was placed closely above the JER, but the JER was not integrated onto the lower surface of the wing. Further, both the nozzle and external flowfield instrumentation were limited.

Experimental Results

Effect of Varying LE/TE Flap Deflections on the Inboard Shroud Static Pressures

Horizontal nozzle orientation
Short shroud
Long interfairing
NPR=3.5

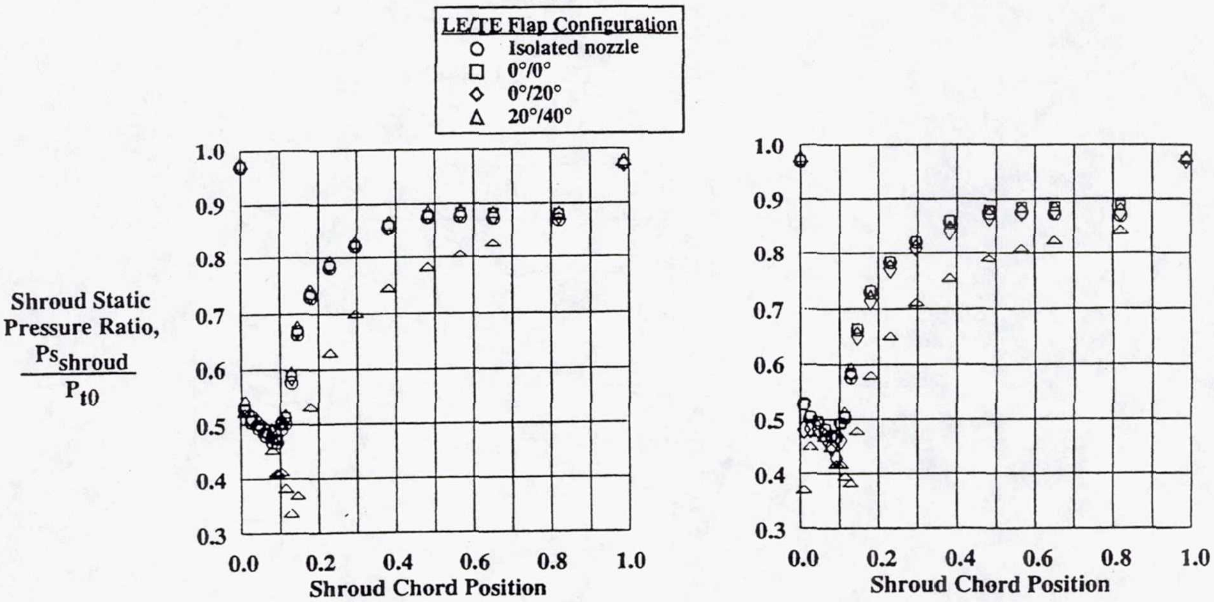

Wing Position 1

Wing Position 5

This figure demonstrates the integration effects observed on the shroud static pressure ratio profiles as a result of varying LE/TE flap deflections. Shroud static pressure ratios are presented as a function of shroud chord position for two different wing positions. Wing position 1 is low and aft with respect to the nozzle, while wing position 5 is low and forward. The data shown was recorded on the inboard shroud for the horizontal nozzle orientation at an NPR of 3.5. The long interfairing and short shroud were installed. Each plot shows the shroud static pressure ratios for the installed nozzle for each set of LE/TE flap deflections, as well as for the isolated nozzle. For both wing positions, the pressure ratio profiles obtained with 0° LE/0° TE and 0° LE/20° TE flap deflections are nearly identical to the profile for the isolated nozzle. The pressure ratio profiles obtained for 20° LE/40° TE flap deflections are significantly lower than the profiles for the other three cases. For all the wing positions examined, the profiles recorded at 20° LE/ 40° TE flap deflections were significantly lower than the profiles recorded for the isolated nozzle or the other flap configurations. The decrease in pressure along the shrouds may indicate an increase in the velocity of the entrained flow and, hence, increased pumping and thrust performance. The pressure decrease may also result from the entrainment of low pressure separated flow off the trailing edge flap. Flow visualization indicated regions of separated flow off the trailing edge flap for 40° deflection, although the flow in the immediate vicinity of the ejector inlets may have remained attached. Entraining separated flow may result in decreased pumping and thrust performance.

Experimental Results

Effect of Varying Wing Position on the Inboard Shroud Static Pressures at Extreme LE/TE Flap Deflections

Horizontal nozzle orientation
Short shroud
Long interfairing
NPR=3.5
20° LE /40° TE Flap Deflections

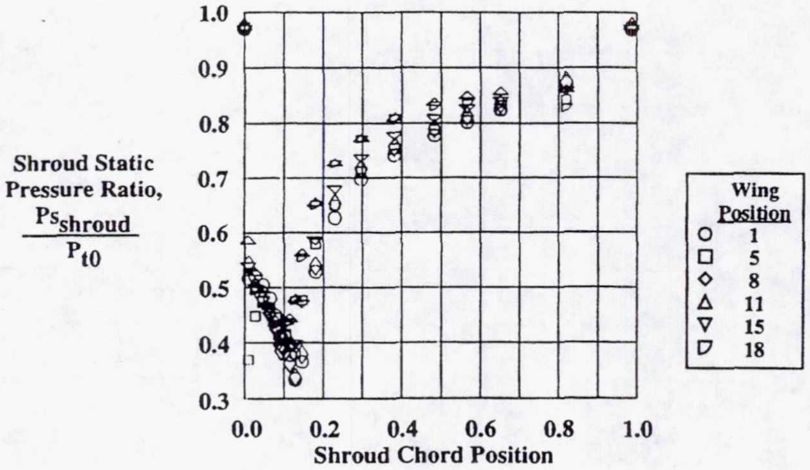

This figure demonstrates the effect of varying wing position on the shroud static pressure ratio profiles for extreme 20° LE/40° TE flap deflections. Shroud static pressure ratios are presented as a function of shroud chord position for six different wing positions. The data shown was recorded on the inboard shroud for the horizontal nozzle orientation at a NPR of 3.5. The long interfairing and short shroud were installed. As mentioned before, flow visualization indicated regions of separated flow off the trailing edge flap for 40° deflection, although the flow in the immediate vicinity of the ejector inlets may have remained attached. There is noticeable variation in the pressure ratio profiles for the different wing positions. The variation in the profiles is partly a function of the relative position of the deflected trailing edge flap to the ejector inlet. Varying wing position affected the acceleration of the entrained flow and the amount of separated flap flow in the proximity of the ejector inlets that may have been entrained.

Experimental Results

Effect of Varying LE/TE Flap Deflection on the Nozzle Exhaust Total Temperature Contours

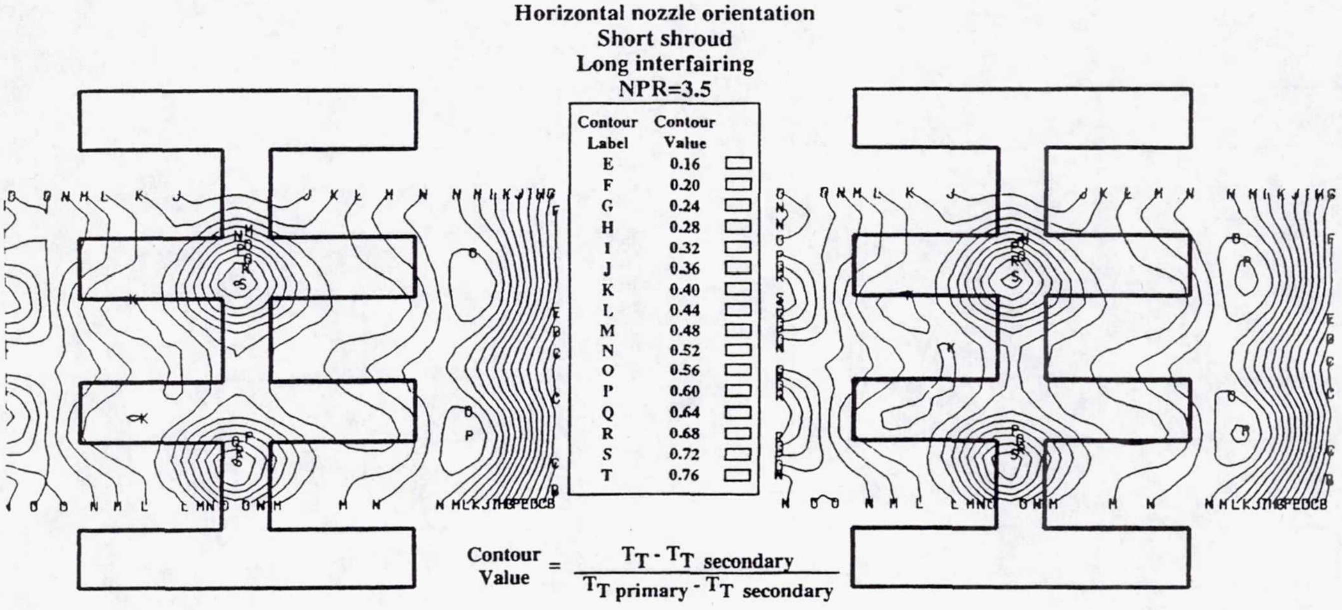

Horizontal nozzle orientation
Short shroud
Long interfairing
NPR=3.5

Contour Label	Contour Value	
E	0.16	☐
F	0.20	☐
G	0.24	☐
H	0.28	☐
I	0.32	☐
J	0.36	☐
K	0.40	☐
L	0.44	☐
M	0.48	☐
N	0.52	☐
O	0.56	☐
P	0.60	☐
Q	0.64	☐
R	0.68	☐
S	0.72	☐
T	0.76	☐

$$\text{Contour Value} = \frac{T_T - T_{T\ secondary}}{T_{T\ primary} - T_{T\ secondary}}$$

Isolated nozzle

Wing Position 5
0° LE/0° TE Flap Deflections

The next two figures demonstrate the effect of varying leading and trailing edge flap deflections on the nozzle exhaust total temperature contours. The nozzle exhaust total temperature contours shown were recorded for the horizontal nozzle orientation at a NPR 3.5. The long interfairing and short shroud were installed. This figure shows the total temperature contours for the isolated case and for 0° LE/0° TE flap deflections at wing position 5 (low and forward with respect to the nozzle). For the data shown on this figure, there is negligible difference in the location and intensity of the contour “hot spots”, implying little change in the mixing characteristics of the nozzle.

Experimental Results

Effect of Varying LE/TE Flap Deflection on the Nozzle Exhaust Total Temperature Contours

Horizontal nozzle orientation
Short shroud
Long interfairing
NPR=3.5

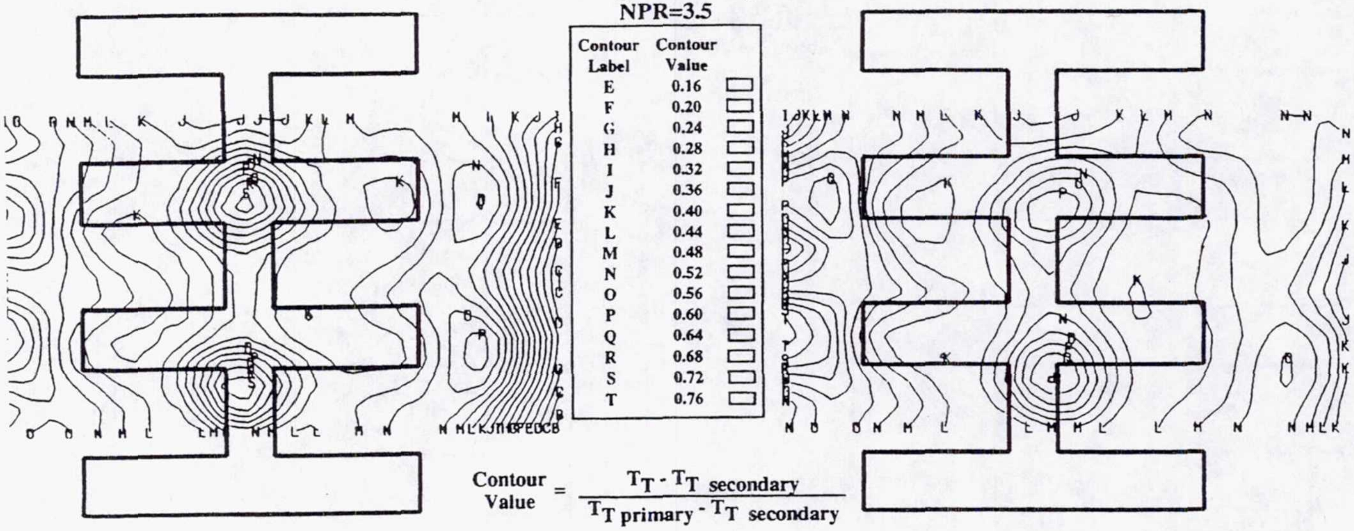

Contour Label	Contour Value	
E	0.16	☐
F	0.20	☐
G	0.24	☐
H	0.28	☐
I	0.32	☐
J	0.36	☐
K	0.40	☐
L	0.44	☐
M	0.48	☐
N	0.52	☐
O	0.56	☐
P	0.60	☐
Q	0.64	☐
R	0.68	☐
S	0.72	☐
T	0.76	☐

$$\text{Contour Value} = \frac{T_T - T_{T\ \text{secondary}}}{T_{T\ \text{primary}} - T_{T\ \text{secondary}}}$$

Wing Position 5
0° LE/20° TE Flap Deflections

Wing Position 5
20° LE/40° TE Flap Deflections

This figure shows the nozzle exhaust total temperature contours recorded at wing position 5 (low and forward with respect to the nozzle) for both 0° LE/20° TE and 20° LE/40° TE flap deflections. Comparison of the total temperature contours for 0° LE/20° TE flap configuration with the contours for the isolated nozzle and the 0° LE/0° TE flap configuration on the previous figure show negligible difference in hot spot location or intensity, again implying little change in the nozzle mixing characteristics. Comparison of the contours for the 20° LE/40° TE flap configuration with the other three cases, however, shows that the contour hot spots for the 20° LE/40° TE flap configuration have decreased in intensity from 0.72 to 0.60 , and have shifted slightly downward and to the right. The changes in the contours appear consistent will either entrainment of separated flap flow or increased secondary flow velocity.

PAISHR1 Comments

Isolated mixer/ejector nozzle testing may provide a viable method for designing the nozzle system, but higher-order PAI effects of an integrated nozzle, nacelle, and wing need to be understood

Wing influences on the acoustic characteristics of a two-dimensional mixer/ejector nozzle still need to be determined

Future test configurations of a mixer/ejector nozzle integrated with a wing should include a nacelle and pylon/diverter as well as increased internal and external flowfield measurements

In summary, the PAIHSR1 results indicate that isolated nozzle testing provides a viable method for the aero-performance design of a two-dimensional mixer/ejector nozzle system. Higher-order installation effects of an integrated mixer/ejector nozzle, nacelle, and wing on the nozzle flowfield and thrust performance need to be understood. Further, PAI effects on the acoustic performance of two-dimensional mixer/ejector nozzle still need to be determined. Based on the PAIHSR1 experiment, it is recommended that future PAI test configurations of a mixer/ejector nozzle and wing include a nacelle and pylon/diverter to more accurately model integration. Most importantly, future test configurations should include increased internal and external flowfield measurements.

OBJECTIVES

Gain a better understanding of the fluid dynamics of integrating an HSCT mixer-ejector nozzle with the airframe, and the impact on acoustics and aeroperformance.

What are the effects of flow distortion due to the wing, pylon, and flaps, that may be ingested by the ejector inlets?

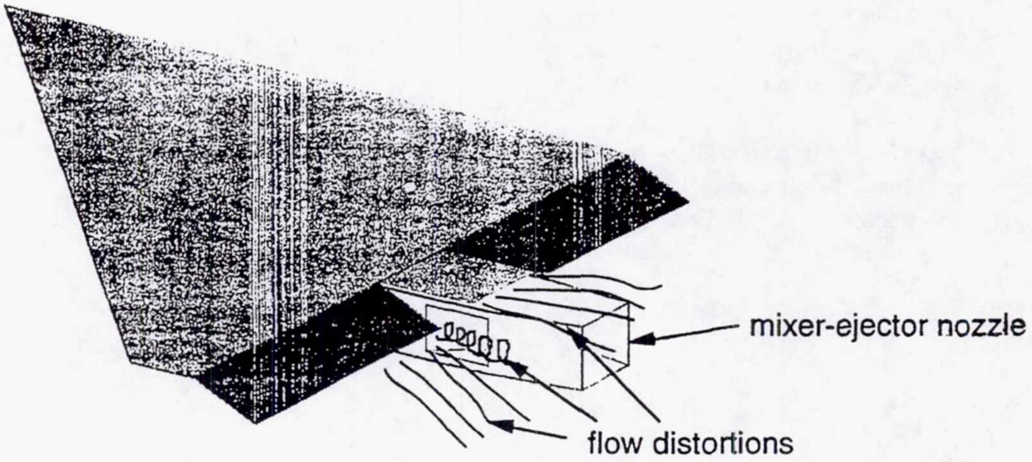

An experimenal study of mixer-ejector nozzle inlet distortion (MIDIS-E) is planned. This is a fundamental study of propulsion-airframe integration (PAI) for an HSCT mixer-ejector nozzle, in the NASA LeRC Nozzle Acoustic Test Rig (NATR). The objective of this study is to gain a better understanding of the fluid dynamics of integrating an HSCT mixer ejector nozzle with the wing, and its impact on acoustics. A more fundamental understanding of the flow physics may help designers to reduce the detrimental PAI effects, and take advantage of the constructive ones. Also, the results may be helpful in designing and interpreting data from future configuration oriented PAI tests, such as the HEAT test.

APPROACH

Discrete flow distortions, representative of flow features off the wing, pylon and flaps, will be applied upstream of ejector inlets.

Separating the overall flowfield into discrete components, and applying each one individually, is analogous to the technique used to study engine inlet distortions. A more fundamental understanding can be gained by studying the effect of each flow feature individually.

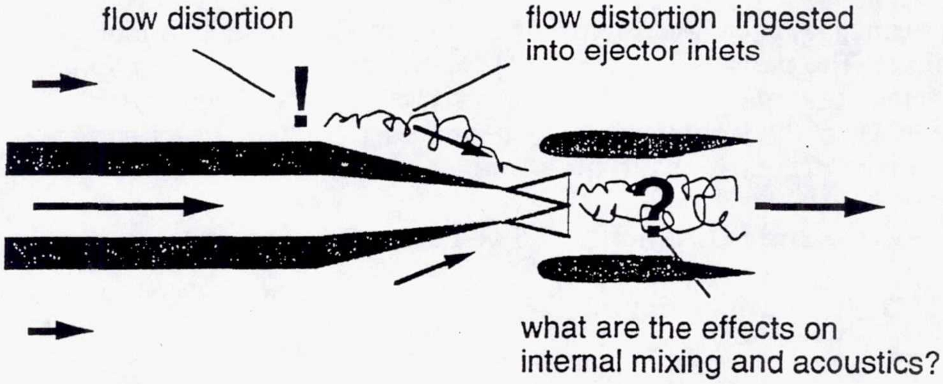

Discrete flow distortions will be applied upstream of the ejector inlets, that are representative of flow features expected near the ejector inlets of an installed nozzle, such as the flap nearfield wake, pylon wake, wing shear layer, etc. In contrast, a configuration-oriented test where a nozzle is installed on a model wing-flap-pylon can provide information on the effects of the overall distorted inflow on the acoustics, aeroperformance and mixing; however, it may not be clear as to which particular aspects of the distorted inflow are responsible for the observed effects. By isolating and studying the effect of each flow feature individually, a deeper and more fundamental understanding of the effects of particular flow distortions can be gained. This technique is similar to that used for engine inlet distortion studies; in this way, appropriate idealized flow distortions can be produced without having to construct a model of the entire aircraft forebody or wing.

APPROACH

Most of the time consuming flow surveys will be made with the nozzle running on warm air.

The applicability of the Munk and Prim approximate similarity principle will be verified. The principle asserts that properly chosen nondimensional performance parameters of the nozzle are similar, regardless of the temperatures of the incoming flows, as long as their Mach number and total pressure distributions are the same.

Existing hardware and instruments will be used to advantage

A parallel CFD study will be conducted

If the Munk & Prim approximate similarity principle can be verified for this type of flow, then scaling of cold flow nozzle data to the hot flow case can be done in a more rigorous way and with greater confidence. The principle has been investigated for turbofan forced mixers and STOVL-type ejectors, among other configurations, but apparently not yet explicitly for HSCT type mixer-ejector nozzles. The Pratt & Whitney 2-D vortical mixer nozzle with a short shroud will be used as the baseline configuration.

MEASUREMENTS

Detailed flowfield measurements

A. ejector inlet plane and upstream: flow angle surveys

B. ejector exit plane: total pressure, total temperature and static pressure surveys

C. mixing region: 2 component LDV surveys

D. surface static pressure taps

Acoustic measurements

Simple flow visualization

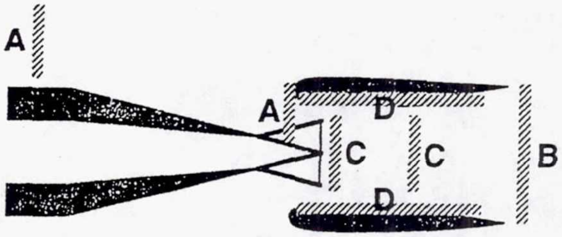

In order to gain greater insight into the nozzle fluid dynamics, detailed flow measurements will be made upstream of the ejector inlets, at the nozzle exit, and inside the mixing region. This information will also be useful for evaluating the Munk and Prim similarity principle.

FLOW DISTORTION DEVICES

Typical distortion generators, to model flow features found in wing - flap - pylon flowfields. Attempt to match the relevant flow parameters, e.g. vortex size and circulation, BL displacement and momentum thicknesses, etc.

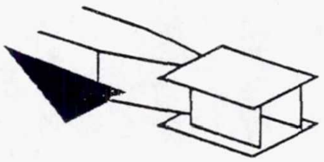

vortex generator for
flap tip vortex

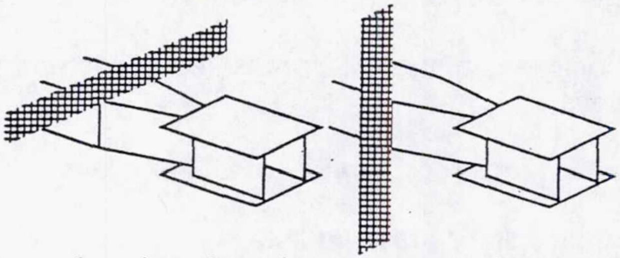

screens for wing shear layer, two nozzle orientations

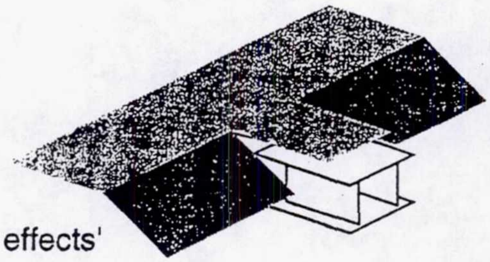

bent plate for 'flap effects'

Typical flow distortion devices are depicted.

HEAT Test Research Objectives

Identify suppressor-entrained flow effects on the efficiency of the high-lift device concepts under consideration for the HSR

Identify integration effects on the aero and acoustic performance of an HSR mixer/ejector suppressor nozzle

- **Quantify changes in the acoustic, force, and moment measurements**
- **Identify and *understand* the flow phenomena contributing to the changes**
- **Obtain an integrated design database for "optimizing" subsequent suppressor nozzle designs for integration; minimizing the impact of adverse flow dynamics, capitalizing on positive flow dynamics**

Cooperative effort between the High-Lift and Suppressor Nozzle Research communities to investigate wing/nozzle integration effects

ARC, LaRC, LeRC, and Industry collaboration

The HEAT test is scheduled for FY94 in the ARC 40'x80' LSWT, and represents a collaboration between NASA's Ames, Langley and Lewis Research Centers, as well as industry. From the High-lift perspective, the research objective is to identify the effects of secondary entrainment on the efficiency of the high-lift device concepts under consideration for the HSR program. From the propulsion system perspective, the HEAT test objective is to identify integration effects on the aero and acoustic performance of an HSR mixer/ejector suppressor nozzle. More specifically, there are three goals. The first is to quantify the changes in the nozzle acoustic, force and moment performance resulting from integration. The second is to identify and understand the flow phenomena contributing to the changes. The third is to obtain an integrated design database for use in subsequent suppressor nozzle designs. An understanding of integrated nozzle performance would allow designers to minimize the impact of adverse flowfield phenomena and capitalize on beneficial flowfield phenomena.

HEAT Test Hardware Description

- 13.5% semi-span model installation in the ARC 40'x80' Low Speed Wind Tunnel
  - Wing shape based on the Reference H geometry
- HSR suppressor nozzle
- Two nacelles, based on the Reference H geometry
  - Inboard powered nacelle with suppressor nozzle
  - Outboard flow-through nacelle
- Appropriate high-lift devices
- Take-off and climb-out configurations

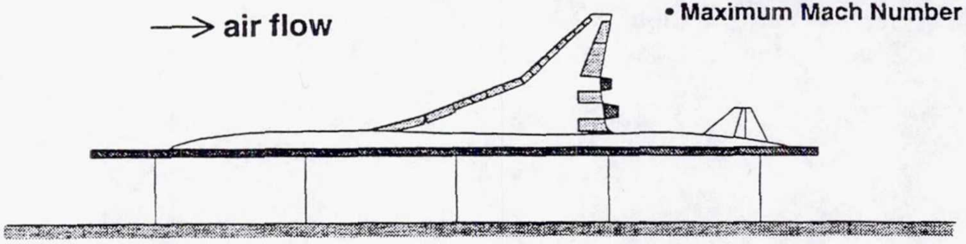

40x80 Flow Characteristics:

- **Turbulence intensity 0.5 %**
- **Maximum Mach Number 0.5**

A sketch of the proposed HEAT test model hardware installation is shown. The HEAT test model includes a semi-span wing installation, one HSR suppressor nozzle, two nacelles, and high-lift devices. The wing planform and nacelle shapes are based on the Boeing Reference H geometry definition. The suppressor nozzle will be mounted on the inboard nacelle, and powered with a propane burner. The outboard nacelle will be a flow-through nacelle. The 40'x80' LSWT has a maximum tunnel Mach number of 0.5, thus both take-off and climb-out configurations can be examined.

HEAT Test Status

Semi-span model design underway

Design of symmetry plane acoustic treatment underway
- **Initial test to verify symmetry plane acoustic treatment scheduled for November '92 in ARC 7'x10' wind tunnel**

Instrumentation definition
- **Near and farfield acoustic measurements**
- **Force and moment data for the integrated configuration as well as the isolated nozzle**
- **Flow visualization**

Additional instrumentation being considered
- **Assessment of wing flowfield via increased wing and nacelle static pressures and flow visualization**
- **Assessment of the ejector inlet flowfield using removeable inlet rakes**
- **Assessment of nozzle exhaust flow characteristics via total pressure/total temperature contours or laser technology measurements**
- ***Limited* assessment of the nozzle internal flow characteristics from shroud and wall static pressures**

The HEAT test planning is underway. The semi-span model design has been initiated. The design of the acoustic treatment for the symmetry plane has also been initiated. A preliminary test to verify the symmetry plane design is scheduled for November '92 in the ARC 7'x10' wind tunnel. The current instrumentation definition includes near and farfield acoustic measurements, force and moment data for integrated configuration as well as the isolated nozzle configuration, and flow visualization. Additional instrumentation is being considered to better assess the ejector inlet flowfield, the nozzle exhaust flow characteristics, the external flowfield, and to make a limited assessment of the nozzle internal flow characteristics.

1999176571

HIGH TEMPERATURE ACOUSTIC LINER TECHNOLOGY

Tony L. Parrott
NASA Langley Research Center
Hampton, Virginia

Michael G. Jones
Lockheed Engineering & Sciences Company
Hampton, Virginia

and

Joe W. Posey
NASA Langley Research Center
Hampton, Virginia

S34-07

409573
11p.

THE EJECTOR NOISE SUPPRESSION PROBLEM: Reduce radiated noise by 20 dB

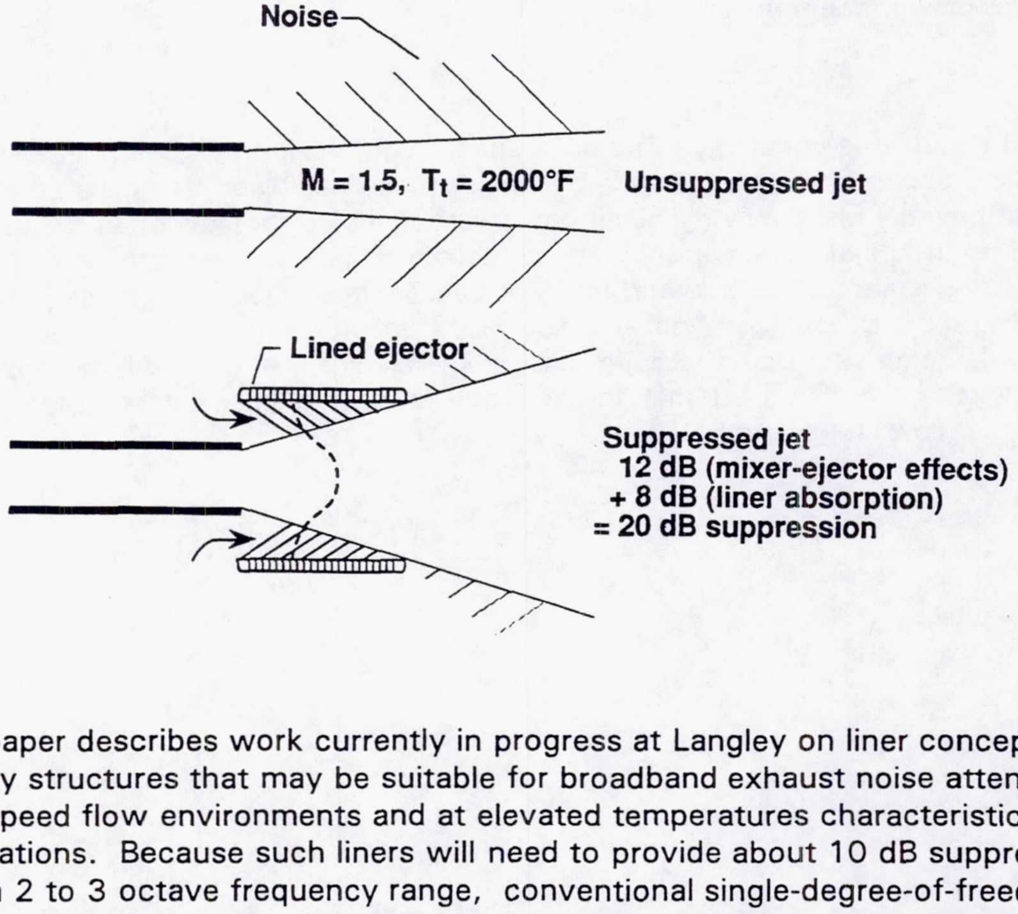

This paper describes work currently in progress at Langley on liner concepts that employ structures that may be suitable for broadband exhaust noise attenuation in high speed flow environments and at elevated temperatures characteristic of HSCT applications. Because such liners will need to provide about 10 dB suppression over a 2 to 3 octave frequency range, conventional single-degree-of-freedom resonant structures will not suffice. Bulk absorbers have the needed broadband absorption characteristic; however, at lower frequencies they tend to be inefficient.

HSCT LINER
CONCEPT DEVELOPMENT

- **OBJECTIVE:** Achieve 10 dB suppression over 3 octaves via absorptive liner

- **APPROACH:** Exploit CMC technology to achieve 'bulk-like' absorption characteristic

At Langley, we are investigating two concepts that exploit the characteristics of both resonant and bulk absorbers to provide the needed broadband exhaust noise suppression. For both concepts, the resistive component at the liner surface is supplied mainly by internal viscous dissipation. This possibility should allow more accurate impedance predictions at high temperature. If evolving ceramic matrix composite (CMC) materials technology permits the fabrication of such structures to withstand the harsh environment of HSCT exhaust nozzle systems, then reliable source noise/duct propagation analysis should enable one to accurately predict the noise reduction of lined jet mixer/ejector systems.

SINGLE LAYER RESONANT ABSORBER

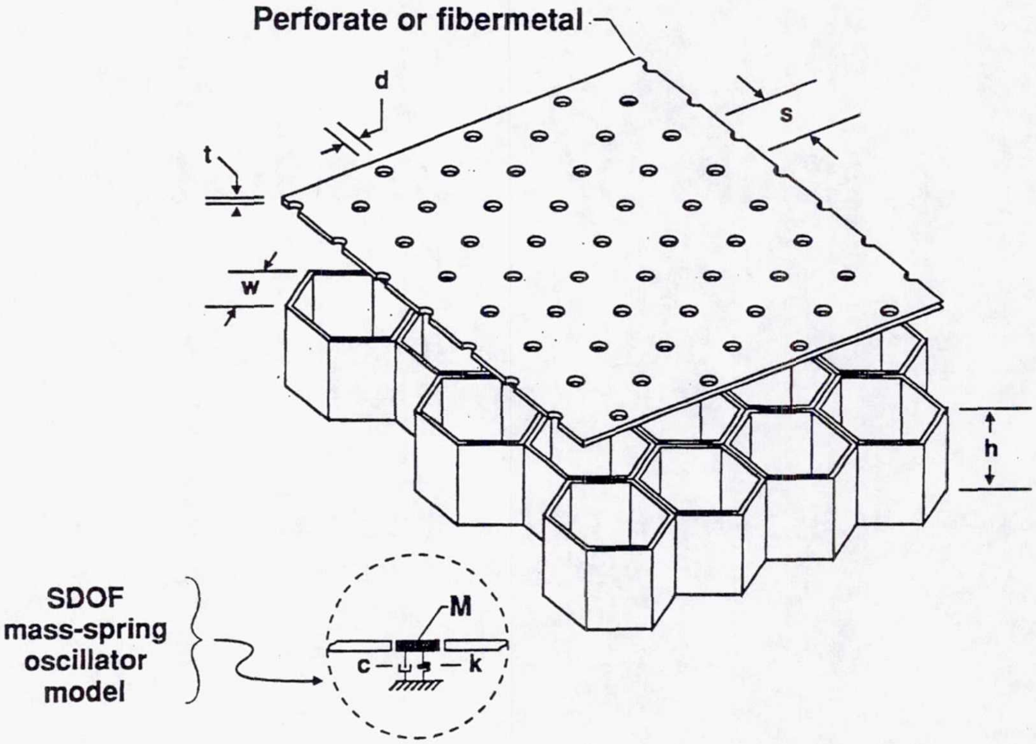

The conventional single layer resonant absorber is most simply implemented by attaching a perforate facesheet to airtight partitioned cavities as shown. The simplest model for the acoustics of such a system is an array of mass-spring oscillators as depicted in the sketch. The oscillator masses are defined by concentrated packets of kinetic energy in and around the perforate holes. The spring is provided by the trapped air in the honeycomb cavities and the damping (acoustic resistance) is dominated by fluid dynamic inertial losses (resulting in turbulent eddies) associated with the high sound pressure amplitudes that typically occur in aircraft applications (as opposed to viscous losses at low amplitudes).

Because of the inertial loss dominated resistance at high sound pressure levels, the resistance tends to be amplitude dependent. Grazing flow increases the resistance and tends to desensitize it to large sound pressure amplitudes. These nonlinear effects can be minimized by making the hole t/d large, or by using fibermetal facesheets that cause viscous losses to play a relatively greater role. Generally, it is necessary to characterize the resistive component with the aid of empirical procedures (ref 1). These procedures are unreliable outside the parameter range underlying the database for a particular structure of interest. Note that the mass-spring model for this liner predicts an absorption maximum at resonance. One effect of the non linear behavior mentioned above is to broaden the absorption spectrum.

ACOUSTIC POWER ABSORPTION
RESONANT ABSORBER

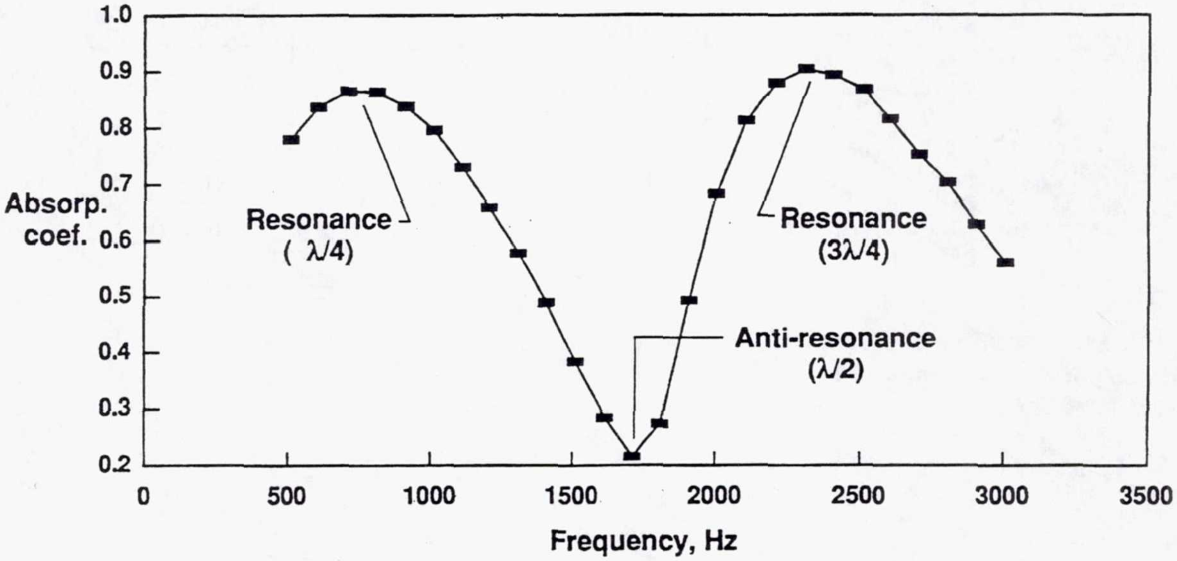

FM125/4 inch cavity depth
resistance = 0.24ρc

When wave motion in the partitioned cavities of the single layer resonant absorber is taken into account, higher harmonic resonances are predicted. An example of such an absorption spectrum measured at normal incidence is shown for a single layer absorber consisting of a fibermetal facesheet with a normalized flow resistance of 0.24 rho-c units (100 Rayls). Absorption maxima occur at the first and second resonances corresponding approximately to cavity lengths of 1/4 and 3/4 acoustic wavelengths. Note the absorption minimum at the anti-resonance. It is these absorption minima at the anti-resonances that restrict the bandwidth of resonant absorbers.

Because resonant behavior is set up by reflected waves in the cavities, the anti-resonance absorption minimum can be modified by coupling a second resonator in series (i.e. a double layer absorber) or by attenuating the propagating wave in the backing cavity. One way to attenuate the propagating wave is by stuffing the honeycomb cells with a fibrous material to a predetermined density that provides an appropriate propagation constant. Another more appealing way to accomplish the same thing is to reduce the diameter of the honeycomb cells to near capillary size, eliminate the facesheet and at the same time maintain a high frontal area porosity. This concept is depicted schematically in the next figure.

ACOUSTIC VISCO-THERMAL DISSIPATION IN TUBES (Approach to Broadband or 'Bulk-like' Absorbers)

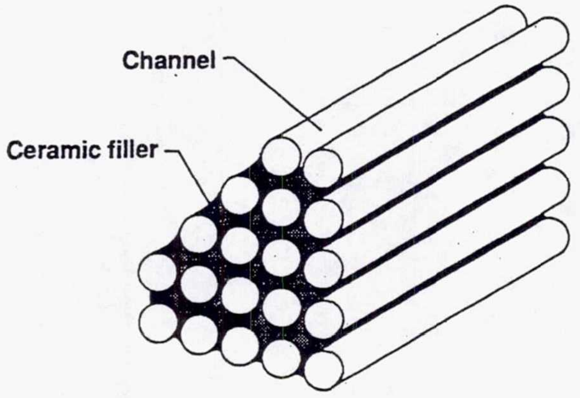

Surface averaged impedance of N capillary-like channels of depth L and diameter d_c:

$$S = \frac{ik}{N\Gamma}\left(\frac{d_s}{d_c}\right)^2 \mathrm{Coth}(\Gamma L)$$

Where $\Gamma = \alpha + i'\beta$ } Propagation constant in typical channel

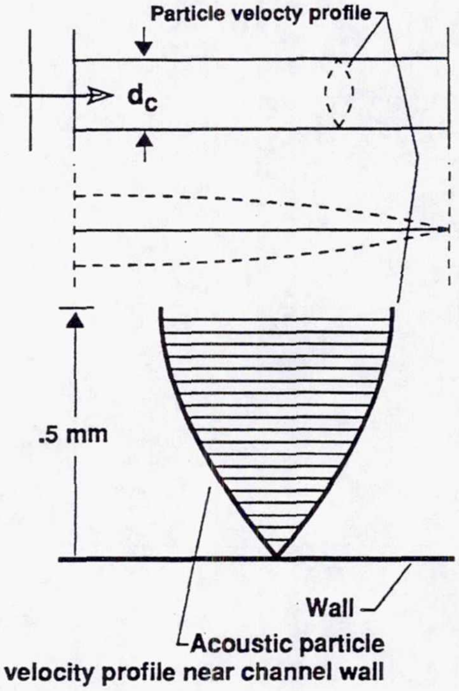

For a parallel array of capillary channels depicted, acoustic resistance is provided by viscous dissipation. The absorption spectra peaks can now be controlled by channel diameter, d_c, length, L, and frontal porosity. Instead of the dissipative process being concentrated near the face, it is now dispersed throughout the channel length. In addition to 'smoothing out' the resonant behavior of the absorption spectrum, the acoustic impedance is accurately predictable from first principles, i.e. the propagation constant in the channels depends on channel geometry and gas properties alone. Because the gas properties (sound speed, density, viscosity and thermal conductivity) are well known functions of temperature, acoustic absorption can be predicted at elevated temperatures. Furthermore, because the acoustic resistance arises from internal dissipation, grazing flow is expected to have minimal effect (ref 2).

Ceramic tubular structures (ceramic honeycomb) that can withstand temperatures up to 1800° F are available in the dimensions needed to provide a useful range of acoustic impedance for mixer/ejector models. While these structures are certainly not viable for direct HSCT exhaust nozzle applications (too heavy and mechanically fragile), they can serve as a development tool. In what follows, absorption spectra for two ceramic honeycomb geometries will be discussed.

IMPEDANCE MODEL FOR CERAMIC HONEYCOMB

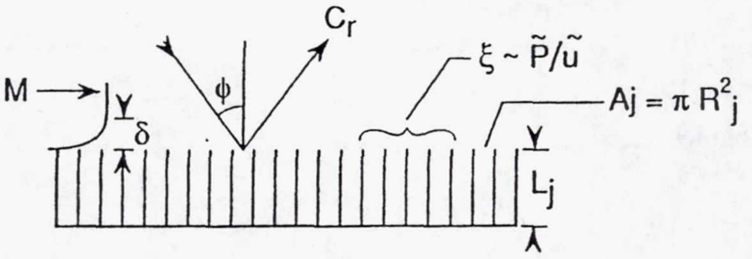

Surface admittance: $\beta = \frac{1}{\xi} = \frac{\rho c}{A} \sum_{j=1}^{N} \frac{A_j}{W_j \coth(\Gamma_j L_j)}$

Channel characteristic impedance: $W_j = \frac{ik\rho c}{\Gamma_j}$

Channel propagation constant

$$\Gamma_j = k \left\{ \frac{1}{\sqrt{2}} \left(\frac{\gamma - 1 + \sigma}{s\sigma} \right) + i \left[1 + \frac{1}{\sqrt{2}} \left(\frac{\gamma - 1 + \sigma}{s\sigma} \right) \right] \right\}$$

$$s = R_j \sqrt{\frac{\rho\omega}{\mu}}, \quad \sigma = \sqrt{Pr}$$

The effective surface admittance over an array of channels, occupying a frontal area A, is the sum of the individual channel admittances, taking into account the continuity of mass flow into the material. The accuracy of this model is critically dependent upon a knowledge the propagation constant inside a channel. Propagation in capillary tubes has been studied extensively and is summarized by Tijdeman (ref 3). A fairly accurate model for the wavelength range of interest here is shown at the bottom of the figure. In this formula, Pr is the Prandtl number and k is the acoustic free-space wavenumber. The so-called shear wavenumber, s, involves channel radius, gas density, viscosity and sound frequency. The key feature of note is that only the tube geometry and fundamental gas properties appear, i.e. no empirical constants are present.

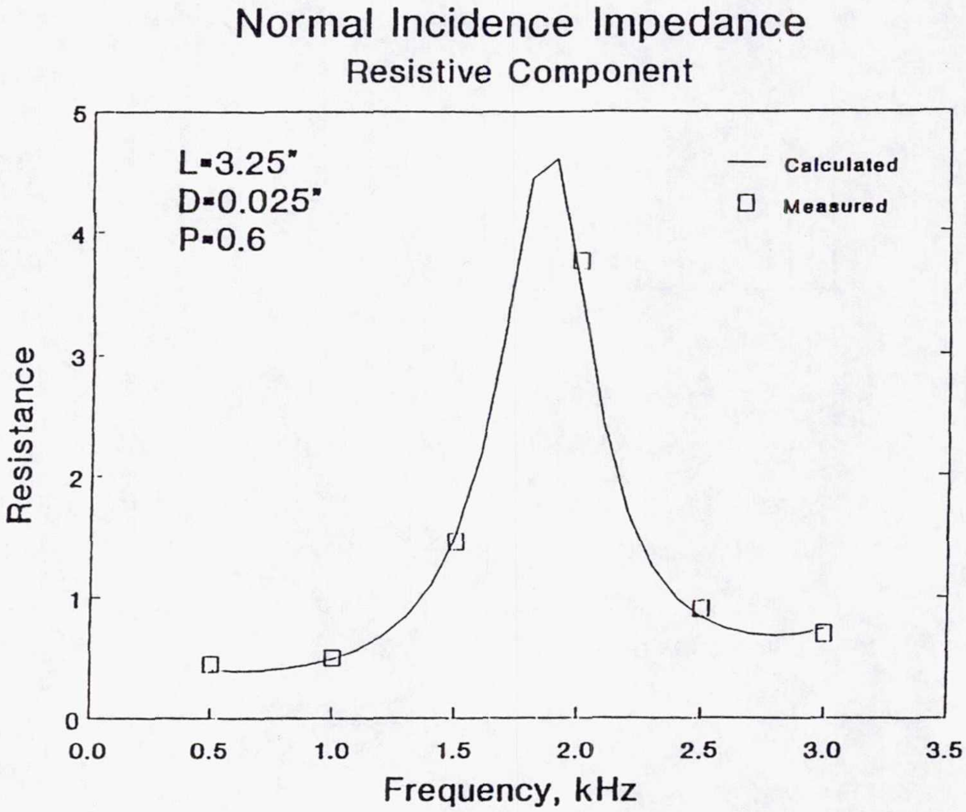

Calculated and measured resistance at the surface of a 3.25 inch length of ceramic honeycomb with channel diameters of 0.025 inches and a frontal porosity of 0.6 is shown in the figure. Note the resistance increase in the vicinity of the anti-resonance near 1.8 kHz which is well predicted by the theory.

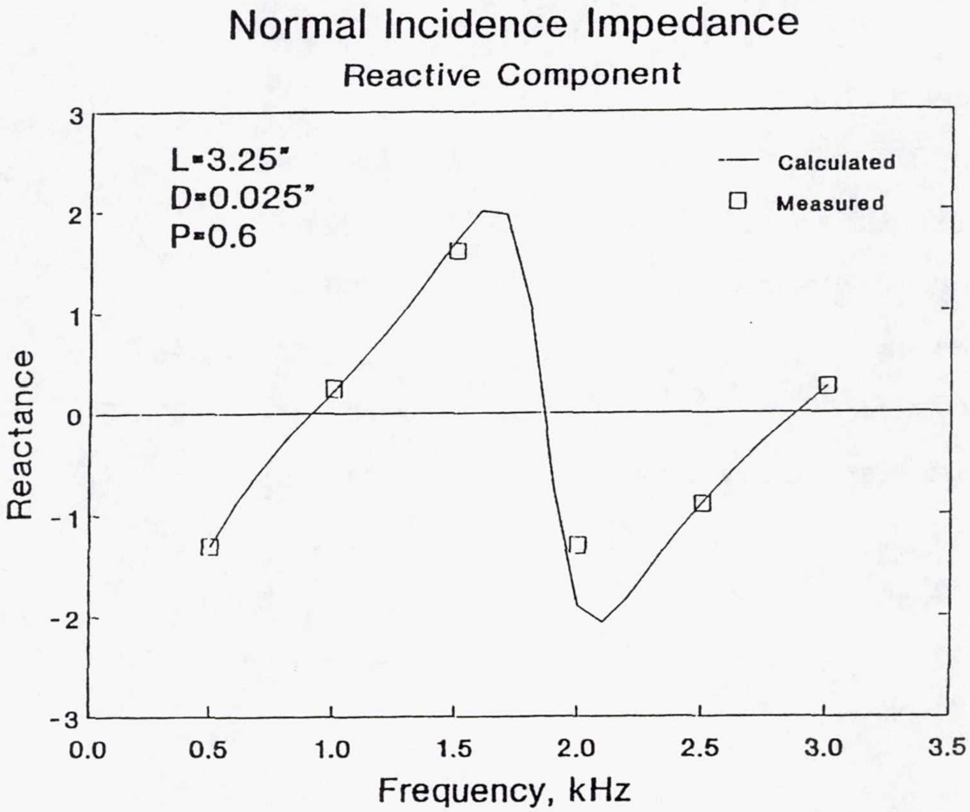

This figure shows a comparison of the calculated and measured reactive component for the surface impedance of the same material. The zero crossings with positive slope are resonances and the zero crossing with negative slope is the anti-resonance.

CERAMIC HONEYCOMB AS LABORATORY TEST LINER MATERIAL

Temperature Tolerant	1800°F
Thermal Shock Resistance	Excellent
Tangential Modulus of Rupture	1200 psi
Compressive Strength	4000 psi
Bulk Density	30 lbs/ft^3 (s.g.$\approx$0.5)
Pore Diameter	0.025 in.
Internal Surface Area/Volume	133 in.^{2}/in.^{3}
Cells/in.^{2}	1400
Face Porosity	73%
Cost	\$15-\$30/in.^{2}

Parameters of interest for ceramic honeycomb are listed. The bulk-like acoustic absorber properties arise from its high volume porosity of 73% and internal surface area per unit volume of 133 in^2/in^3. In addition to the possibility that such a structure may provide efficient acoustic absorption, it can also function at temperatures up to 1800° F and thus can serve as a laboratory test material for developing liner concepts for mixer/ejectors.

INSERTION LOSS MATH MODEL

Assumptions:

- **Acoustic waves experience one reflection at liner surface**
- **Acoustic attenuation due to liner absorption only**
- **Small boundary layer thickness to wavelength ratio,**
- **i.e. $\delta/\lambda < 1$**
- **No sound generation by liner roughness**

$\therefore$ **Insertion loss = 10 Log** $|C_r|^2$

where $C_r = \dfrac{\cos\phi\,(1 + M\sin\phi) - \beta}{\cos\phi\,(1 + M\sin\phi) + \beta}$

Given the effective surface admittance, ray acoustics can be employed to estimate liner insertion loss for a mixer/ejector configuration. An acoustic ray is assumed to experience one reflection before being convected out the ejector exit. The power lost to the absorber can be interpreted as an insertion loss in the reflected wave relative to that for a perfectly reflecting surface. The reflected wave amplitude, C_r, is given as a function of the incident angle, flow Mach number and surface admittance. We use the results of this calculation to provide a simple figure of merit to estimate relative performances of test liners in mixer/ejectors models.

ACOUSTIC ABSORPTION FOR CERAMIC HONEYCOMB

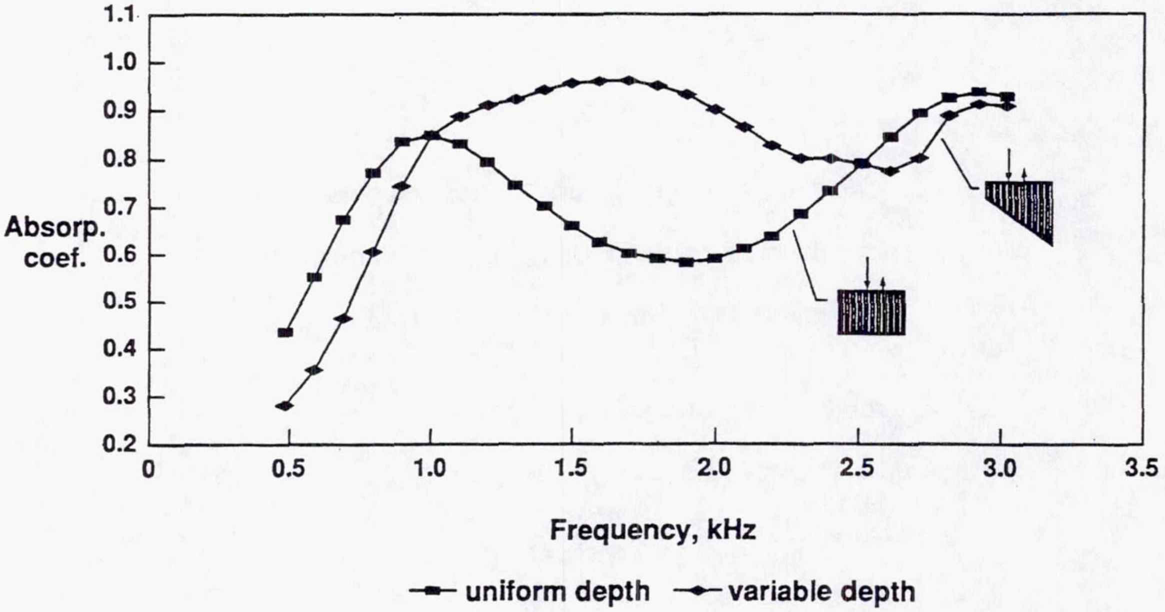

Absorption coefficient spectra for a uniform depth and a constant slope varying depth ceramic honeycomb structure is shown in this figure. Note that the resonant character of the channel length is still in evidence although significant absorption is occurring in the neighborhood of the anti-resonance at 1.8 kHz. For the constant slope variable depth specimen, a broad peak in absorption occurs across the entire span between the first two resonances. Thus the basically resonant system is behaving much like a bulk absorber. We would like to exploit this behavior to provide useful design concepts for HSCT liners.

POWER LEVEL OF REFLECTED WAVE RELATIVE TO INCIDENT WAVE FOR VARIABLE DEPTH LINER

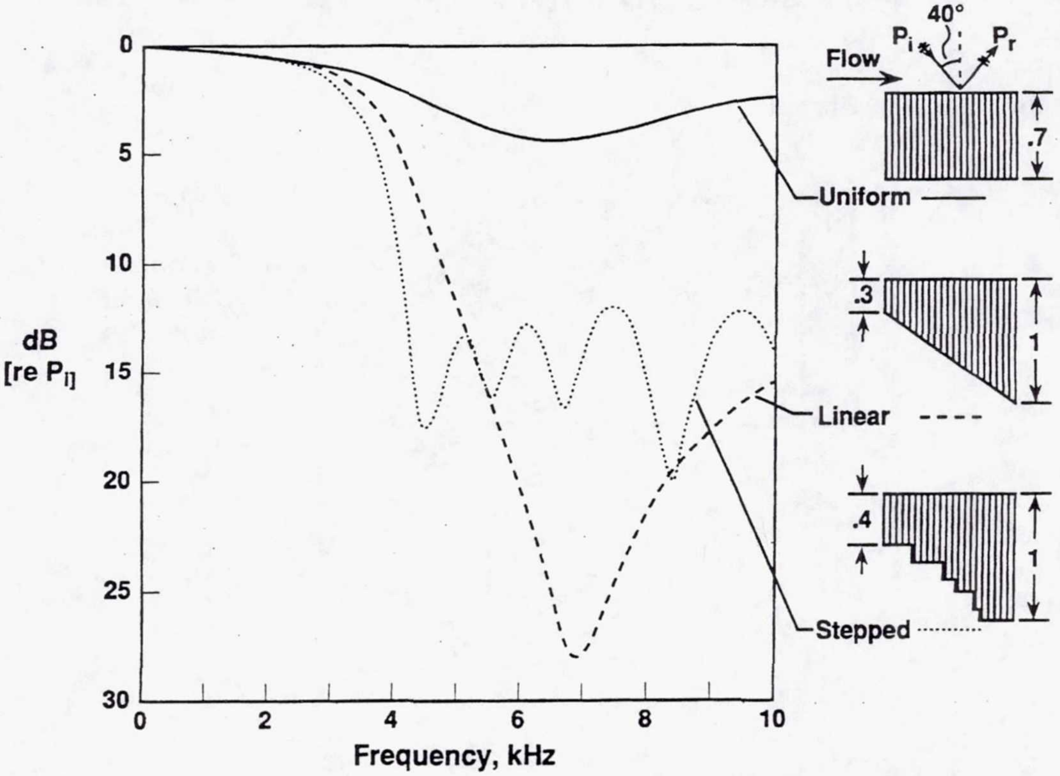

This figure shows effects of nonuniform liner depth on the reflected power relative to the incident power (insertion loss relative to hard wall) for a grazing flow of Mach number 0.5 and incidence angle of 40°. Note that the insertion losses for variable depth liners cannot be achieved by replacing them with their uniform average depth 'equivalents'. Also, changes in the variable depth profile (compare linear slope depth with stepped depth) causes significant changes in the absorption spectra. The solid line depicts the insertion loss of a liner with a uniform depth of 0.7 inches. The long- and short dashed lines show the insertion losses of a linear slope depth and stepped depth variation respectively. The stepped depth variation was an attempt to optimize the absorption bandwidth.

VARIABLE DEPTH SEPTUM, PARALLEL PLATE ACOUSTIC CHAMBER

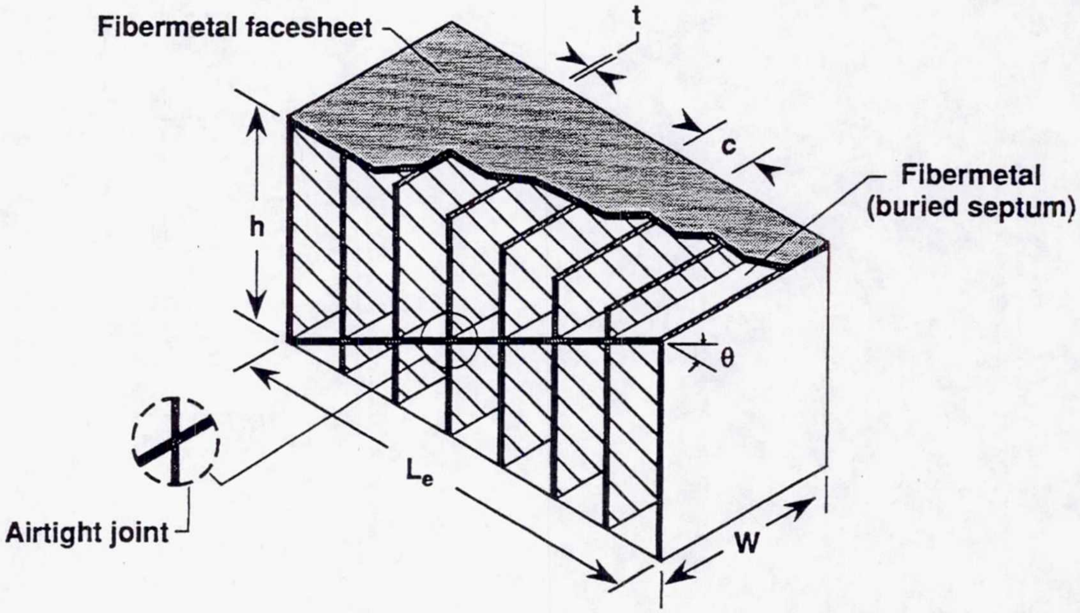

A second concept for achieving spatially variable impedance with the dominant dissipation component internal to the structure is illustrated in this figure. Here, a typical element consists of a series of channels covered with a porous face sheet and embedded with a variable depth, porous septum that supplies a resistive coupling between the upper and lower sections of each channel. The system is essentially an array of contiguous two-degree-of-freedom systems that provide a spatially varying impedance by changing the location of the coupling element (i.e. the porous buried septum). A key distinction between this concept and the capillary channel concept is that the small channel widths or diameters are no longer necessary, i.e. viscous dissipation which occurs along the channel walls is relatively insignificant. The parallel plate structure is intended to enhance heat transfer out of the structure for high temperature environments.

Power Level of Reflected Wave relative to Incident Wave for Variable Depth Septum

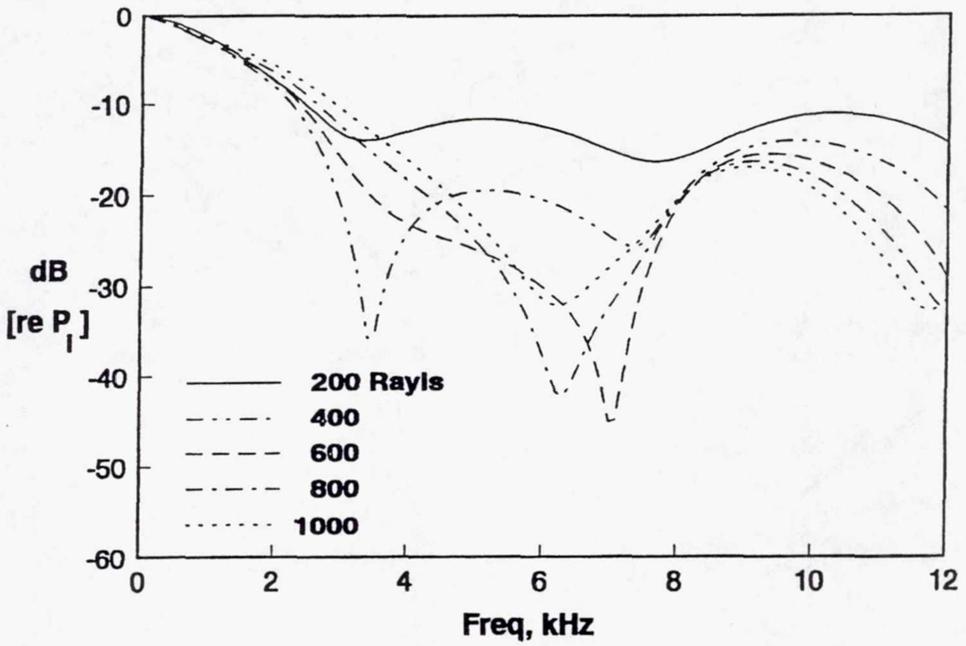

M = 0.5, T = 500 deg, Angle of Incidence = 40 deg

These curves show progressive changes of insertion loss spectra (i.e power loss in reflected wave relative to a hardwall reflector) for increasing values of the variable depth, buried septum flow resistance from 200 Rayls to 1000 Rayls. Note the progression from a double peak in the insertion loss for low resistance to a single peak at the higher resistance values. Clearly, insertion loss spectra can be tailored to some extent with an appropriate choice of septum flow resistance.

CALCULATIONS OF THE NOISE SUPPRESSION OF LINED EJECTORS

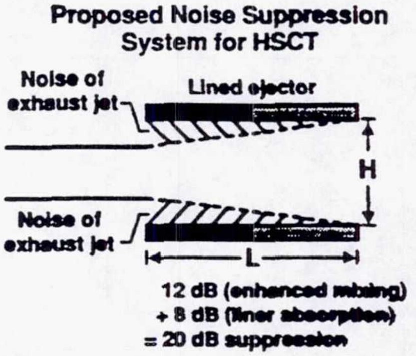

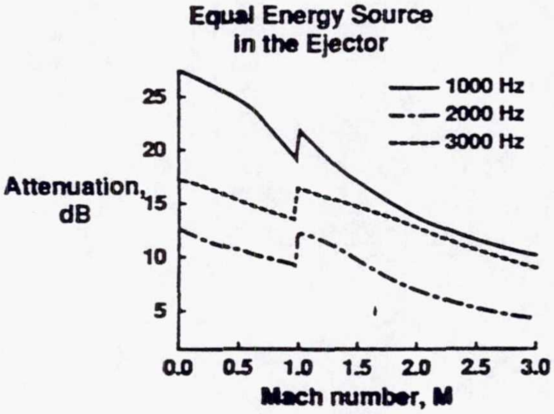

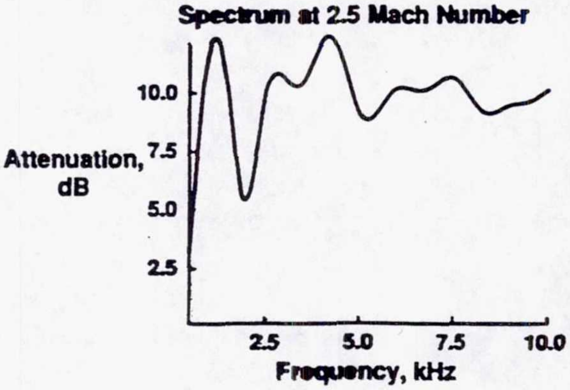

Ray acoustics provides an estimate of insertion losses for a jet mixer/ejector assuming all sound rays encounter a single reflection at the liner surface, i.e. that duct modes play no significant role. This figure shows the result of a modal analysis for a mixer/ejector like duct configuration with uniform flow and lined with a one inch thick layer ceramic honeycomb discussed above. The calculation was done for the first ten modes assuming no reflections at the duct exit. The duct length to height ratio was 2.6. A uniform flow and temperature profile was assumed. Dr. Willie Watson at Langley is further developing this approach to handle impedance discontinuities as well as continuously variable impedances. He also intends to include nonuniform flow and temperature profile effects.

The encouraging aspect of these results is the significant attenuations calculated for supersonic flows. Up to Mach numbers of 1.5, attenuations of at least 10 dB are calculated for a liner L/H of 2.6. Furthermore, the attenuation spectrum is broadband in character, even for a spatially uniform impedance. These results are encouraging.

SUMMARY

'Bulk-like' absorption characteristic potentially achievable by:

- **Variable depth, capillary channel structures**
- **Variable depth, porous septum structures**

Based on simple ray acoustic modeling, broadband absorption can apparently be achieved with variable depth, capillary tube structures. Such structures are available commercially. This material, although not viable for HSCT applications, can serve as a means to develop and validate acoustic liner concepts for high speed flow, elevated temperature jet-mixer/ejectors.

Broadband absorption spectra may also be achieved by spatially variable impedances implemented with built-up parallel plate structures with variable depth, porous, buried septa. Several such test structures are currently being fabricated for testing at Langley.

REFERENCES

1. Hubbard, Harvey H.: Aeroacoustics of Flight Vehicles: Theory and Practice. Volume 2, Chap. 14. NASA Reference Publication 1258, Vol. 2, WRDC TR 90-3052, August 1991

2. Parrott, T. L.; Watson, W. R.: and Jones, M. G.: Experimental Validation of a Two-Dimensional Shear-Flow Model for Determining Acoustic Impedance. NASA TP-2679, May 1987

3. Tijdeman, H.: On the Propagation of Sound Waves in Cylindrical Tubes. J. Sound Vib., vol. 39, no. 1, 1975, pp. 1-33.

1999176572

EXHAUST NOZZLE MATERIALS DEVELOPMENT FOR THE HIGH SPEED CIVIL TRANSPORT

J.E. Grady
NASA Lewis Research Center
Cleveland, Ohio

S35-07

409574
22P.

EPM Exhaust Nozzle Team Mission

"Develop and demonstrate by 1999 the materials and fabrication processes, and the design and life prediction methodology for an economically feasible, low noise HSCT exhaust nozzle"

Figure 1

The United States has embarked on a national effort to develop the technology necessary to produce a Mach 2.4 High Speed Civil Transport (HSCT) for entry into service by the year 2005. The viability of this aircraft is contingent upon its meeting both economic and environmental requirements. Two engine components have been identified as critical to the environmental acceptability of the HSCT. These include a combustor with significantly lower emissions than are feasible with current technology, and a lightweight exhaust nozzle that meets community noise standards.

The Enabling Propulsion Materials (EPM) program will develop the advanced structural materials, materials fabrication processes, structural analysis and life prediction tools for the HSCT combustor and low noise exhaust nozzle. This is being accomplished through the coordinated efforts of the NASA Lewis Research Center, General Electric Aircraft Engines and Pratt & Whitney. The mission of the EPM Exhaust Nozzle Team is to develop and demonstrate this technology by the year 1999 to enable its timely incorporation into HSCT propulsion systems.

NOZZLE MATERIALS DEVELOPMENT REQUIRES A MULTI-DISCIPLINARY TEAM

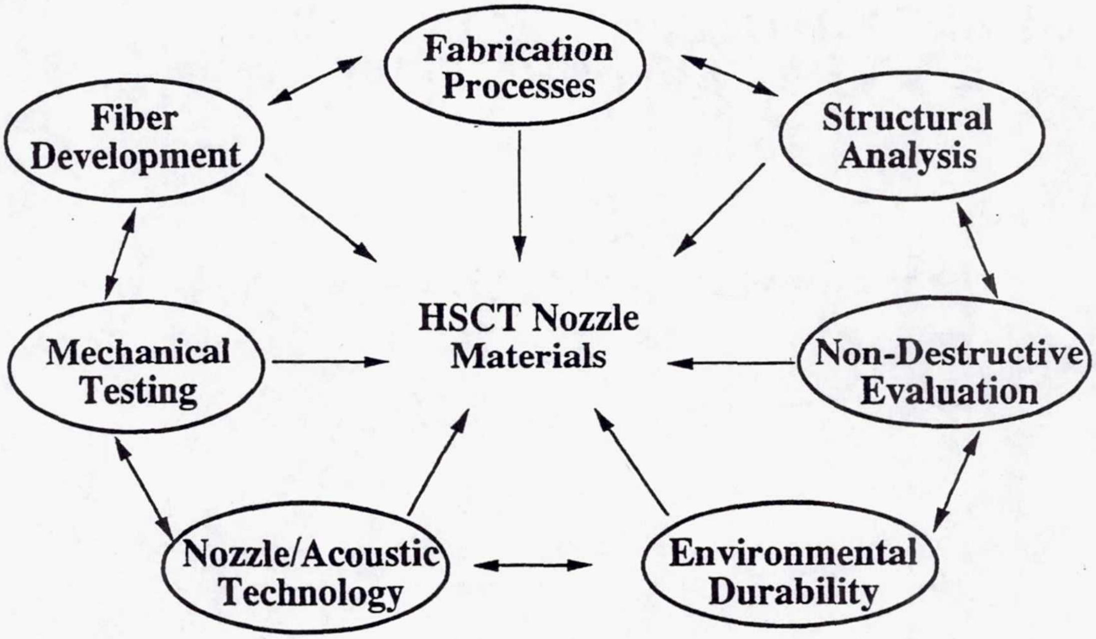

Figure 2

The successful and timely development of advanced materials technology for HSCT exhaust nozzle applications requires the integrated efforts of engineers in a variety of technical disciplines. These include material fabrication, fiber technology, mechanical testing, nozzle and acoustic technology, environmental durability, non-destructive evaluation and structural analysis. In addition, technical collaboration in each of these areas must be efficiently coordinated between NASA, GE, Pratt & Whitney and numerous subcontractors such that viable nozzle materials and designs are developed by 1999.

To accomplish this coordination between multiple organizations and technical disciplines, an Integrated Product Development management approach is used in the EPM program, in which technical and management decisions are made by multi-disciplinary teams that are composed of members from each of the three organizations.

HSCT MISSION CYCLE DEMANDS HIGH TEMPERATURE DURABILITY

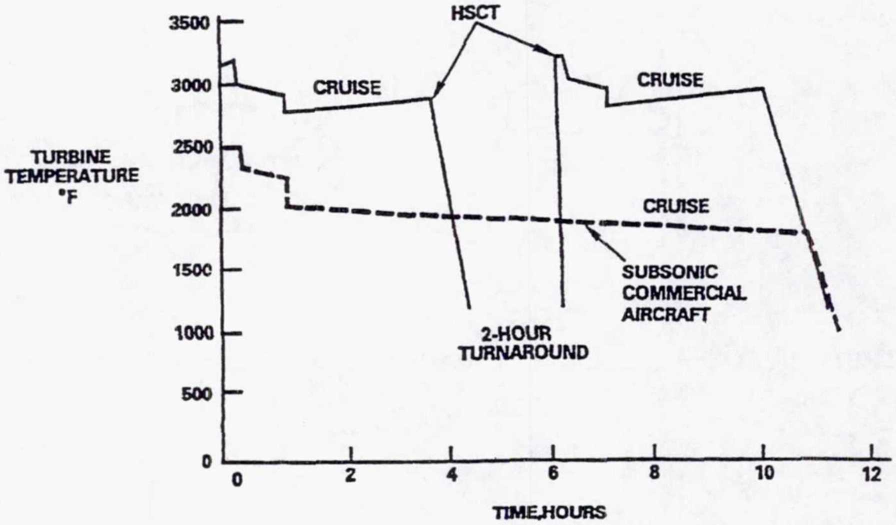

Figure 3

HSCT mission requirements are much more severe than those for current commercial engines. This is due primarily to the extended Mach 2.4 cruise, which results in cyclic thermal exposure of the engine materials for four-hour intervals at extreme temperatures, as shown in Figure 3. At cruise conditions, maximum material temperatures in critical nozzle components could range from 1800° to 2000°F. Thrust augmentation could increase temperatures to 2400°F in some components. The durability goal for nozzle materials is an 18,000 hour lifetime, with 3000 hours of that time spent in augmentation.

If the HSCT exhaust nozzle were made using current materials technology, cooling air would be required to reduce the material temperatures. Engine cycle studies have indicated that the use of fan cooling air in the nozzle would impose an acceptably high performance penalty. Therefore, advanced nozzle materials must be developed to operate at high temperatures with no fan cooling air.

TWO NOZZLE CONCEPTS ARE BEING CONSIDERED

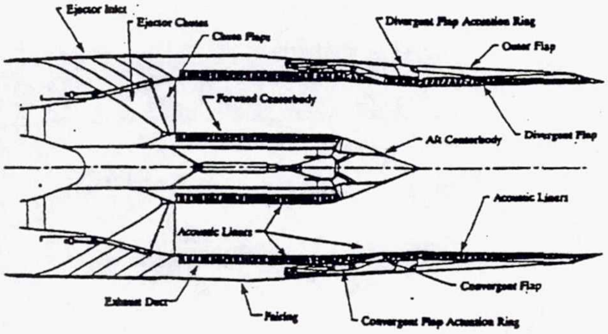

Axisymmetric No Plug Nozzle

2D Convergent/Divergent Nozzle

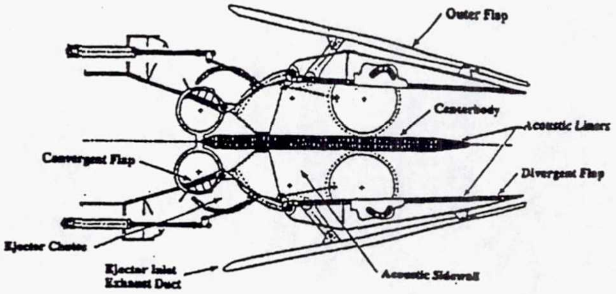

Figure 4

HSCT engines will also require various amounts of nozzle noise suppression in order to meet FAR 36 Stage III noise requirements. The amount of noise suppression required will depend on the exhaust velocity at takeoff, which varies with engine type. To meet the combined challenges of noise suppression and high temperature durability, two types of mixer-ejector nozzle designs are being evaluated, as shown in Figure 4. Depending on the engine exhaust velocity, nozzle flow entrainments of up to 120 percent of the engine core airflow may be required. The specific weight of the nozzle (nozzle weight/engine airflow) increases as the flow entrainment required for jet noise suppression is increased. Nozzle designs must therefore include acoustic/weight tradeoff considerations. In comparison to the 2D design, the axisymmetric nozzle has slightly better performance at the cost of increased design complexity and weight. To reduce weight, high specific strength composite materials will be used in critical nozzle subcomponents. The EPM goal is to develop high temperature, lightweight composite materials such that nozzle weight can be reduced by 30 percent relative to current materials technology, while achieving a life of 18,000 hours at temperatures up to 2400°F.

CRITICAL NOZZLE COMPONENTS HAVE BEEN IDENTIFIED

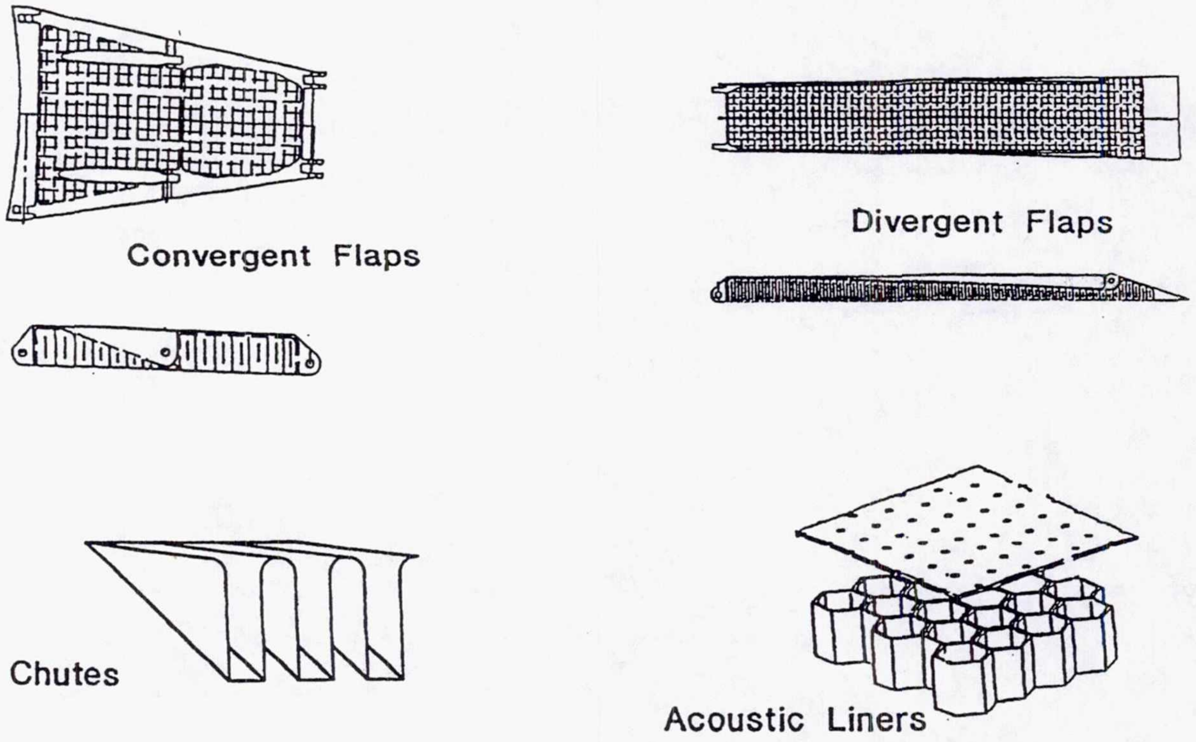

Figure 5

An evaluation of the individual nozzle subcomponents resulted in identification of the convergent and divergent flaps, ejector chutes and acoustic liners as critical subcomponents that would require advanced materials for HSCT applications. In addition to high temperature durability, the materials for these components must be damage tolerant to avoid catastrophic failure, and must have high cycle fatigue resistance to withstand acoustic and vibratory loads. The considerations involved in developing conceptual designs for these components, shown in Figure 5, include joining and attachment requirements, as well as ease of fabrication and machining. Geometric complexity is also an important factor when considering material fabrication and shaping requirements.

EPM MATERIALS DEVELOPMENT IS DIRECTED TOWARD COMPOSITE GOAL PROPERTIES

Physical Properties

Density	0.19 lb/in^3
Thermal expansion	6 - 8 in/in - °F
Elastic Modulus	30 - 40 Msi

Mechanical Properties

	Room Temperature	2200° - 2400°F
Tensile Strength	175 Ksi	100 Ksi
Yield Strength (0.2%)	170 Ksi	95 Ksi
Strain to Failure	1 - 2 %	2 - 10 %
Stress Rupture*	N/A	40 - 50 Ksi
Creep Elongation* (0.2%)	N/A	25 - 35 Ksi
Fracture Toughness	10 - 20 Ksi • in$^{1/2}$	10 - 20 Ksi • in$^{1/2}$
LCF (10,000 cycles)	50 Ksi	10 - 20 Ksi

*in 1000 hours

Figure 6

The current conceptual designs of critical nozzle subcomponents are based on projected properties of EPM materials in the year 1999. These "goal properties" were chosen with the assumption that significant improvements in the physical and mechanical properties of MMC/IMC materials would result from the material development efforts in the EPM program. Preliminary physical and mechanical goal properties for HSCT exhaust nozzle materials are shown in Figure 6.

ADVANCED HIGH TEMPERATURE COMPOSITES ARE NEEDED TO REACH MATERIAL GOAL PROPERTIES

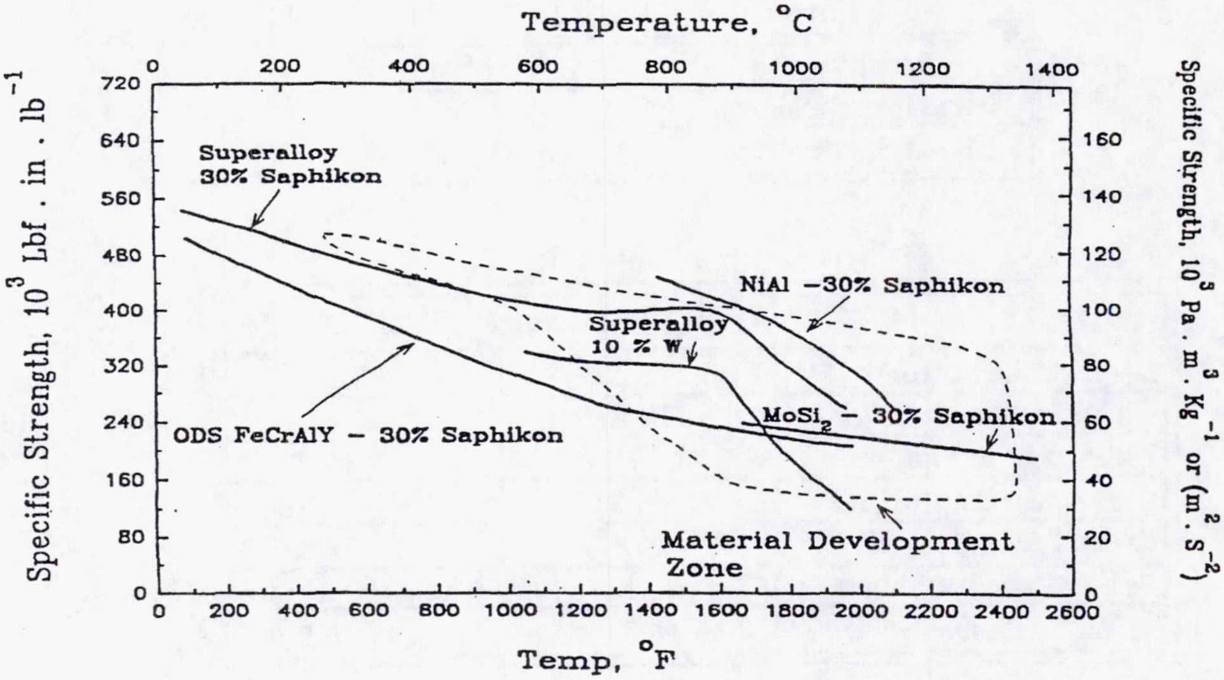

Figure 7

The initial selection of candidate exhaust nozzle structural materials is based primarily on the predicted specific strength and temperature capability of the materials. Specific strengths include tensile, creep, and rupture strength, while temperature capability includes oxidation resistance, microstructural and chemical stability, and durability. Advanced materials such as metal, intermetallic, and ceramic matrix composites (MMC, IMC, and CMC) offer the potential to replace current materials to produce a lighter exhaust nozzle that requires no fan cooling air. MMC/IMC composite systems identified as having the best potential for meeting HSCT exhaust material requirements include $MoSi_2$-, NiAl-, ODS-, MCrAl-, and superalloy-base composites. Commercially available ceramics are being considered for acoustic treatments. Figure 7 shows the material development zone of interest for HSCT nozzle applications, in which predicted specific strengths of candidate MMC and IMC systems are shown. A material development approach has been established that focuses on meeting material property requirements that are defined based on design needs. This development approach includes regular assessments of updated design requirements for material properties, along with consideration of new candidate materials. The materials development plan therefore includes three major efforts: Critical Screening/Process Evaluations, Materials Refinement, and Scale Up.

METAL MATRIX COMPOSITE DEVELOPMENT

- **Haynes alloy 230 (Ni-base alloy)**
  - ✓ **Good high temperature tensile Strength**
  - ✓ **High Ductility**
  - x **Poor Oxidation above 1000°C**
- **INCO MA 956 (Fe-base Alloy)**
  - ✓ **CTE slightly better than Ni-base alloy**
  - ✓ **Good tensile Strength to 1200°C**
  - x **Relatively Poor Ductility**
- **INCO MA3002 (Ni-base alloy)**
  - ✓ **Oxidation Resistance Comparable to MA 956**
  - ✓ **Good tensile Strength to 1200°C**
  - ✓ **Good Ductility**
  - x **CTE slightly worse than Fe-base alloy**

Figure 8

Superalloy and MCrAlY base matrices are considered good candidate materials for exhaust nozzle applications due to their high ductility and toughness at low temperatures, and proven oxidation resistance at temperatures as high as 2200°F. Composite metal matrix candidates include Fe and Ni base matrices such as MA 956 and Haynes 230, where elemental additions are designed to increase oxidation resistance or to provide high temperature strengthening. Candidate reinforcements can be separated into two categories: ceramic and refractory metal fibers. The first category includes alumina single crystal fiber and polycrystalline fiber tows. The alumina single crystal fiber is thermodynamically stable in the metal matrix alloys being considered, possesses relatively low density and is environmentally stable. Marginal strength at elevated temperature and fiber damage due to processing are major concerns, however. Protective coatings are being developed to minimize fiber damage during processing, and tailored fiber/matrix bonding approaches are being investigated. A comparatively small effort to develop composites using refractory metal reinforcements is also being considered. Concerns regarding refractory fibers include their relatively poor oxidation resistance and possible reaction with the MMC matrices.

INTERMETALLIC MATRIX COMPOSITE DEVELOPMENT

NiAl-Base Composite:

- **Stoichiometric NiAl:**
  - **✓ Excellent oxidation resistance (isothermal and Cyclic up to 2200°F**
  - **x Low Ductility at Room Temperature**
  - **x CTE Mismatch with Sapphire fibers**

MoSi2-Base Composite:

- **✓ Excellent High Temperature oxidation (Isothermal and Cyclic up to 2400°F**
- **✓ Elevated Tensile Strengths**
- **✓ Ductility above 1800°F**
- **✓ CTE close to Sapphire Fiber**
- **x Pesting**

Figure 9

Two material systems, NiAl-base alloys and $MoSi_2$-base alloys, are being considered as matrices for the development of intermetallic matrix composites. The stoichiometric NiAl compound has low density, excellent oxidation resistance, thermal stability to approximately 2000°-2200°F and reasonable strengths, but limited ductility at room temperature. Alloying additions are being investigated by several research groups within the EPM program to improve the ductility and strength of NiAl. Alumina single crystal fiber would be used as the reinforcement for this system. The effect of thermal expansion mismatch between the matrix and the fiber may require either the use of protective fiber coatings or the addition of a low thermal expansion phase to the matrix.

Molybdenum disilicide ($MoSi_2$) has excellent high temperature oxidation resistance, both isothermal and cyclic, to at least 2400°F, elevated temperature tensile strengths comparable to silicon carbide and silicon nitride, and ductility at temperatures above 1800°F. The evaluation of accelerated low temperature oxidation of $MoSi_2$, known as "pesting," is being addressed during the first critical screening phase of the program. The thermal expansion of $MoSi_2$ very closely matches that of sapphire, thereby minimizing thermal fatigue problems arising from fiber/matrix thermal expansion mismatch.

ACOUSTIC TESTING OF CANDIDATE LINER MATERIALS IS UNDERWAY

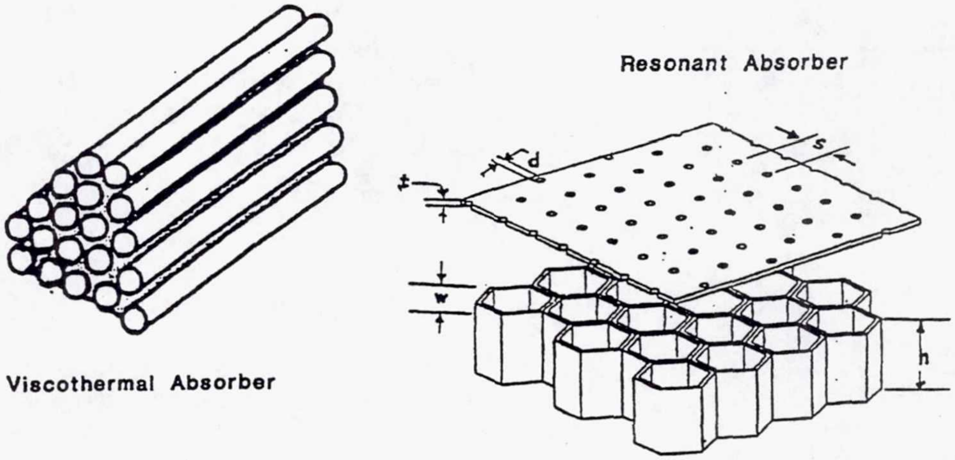
Viscothermal Absorber

Resonant Absorber

Figure 10

Acoustic liners are used to attenuate mixing noise generated by the entrainment of ambient air into the nozzle exhaust flow. Engine cycle analyses have shown that the temperatures of the acoustic liners could reach 2400°F during augmentation. A conceptual design of the HSCT exhaust nozzle assumes that the acoustic liner treatment is a ceramic matrix composite (CMC) tile of a lightweight bulk absorber material. The CMC tiles would be configured as an attenuator, analogous to current metal treatments, which consist of perforated plates with bulk absorbers or perforated plates with honeycomb attenuation structures, as shown in Figure 10. The materials under consideration for use in the nozzle acoustic liners include ceramic bulk absorbers, viscothermal absorbers, and CMC honeycomb resonant absorbers, which would present significant material fabrication challenges. An assessment of supplier fabrication capabilities is underway, and an industry consortium consisting of Boeing, 3M, McDonnell Douglas Technologies, Westinghouse and Dupont Lanxide has been formed to conduct acoustic trade studies and to perform the first in a series of laboratory acoustic tests on a variety of bulk absorber ceramics as part of the HSCT Ejector Liner Acoustic Technology Development Program.

FIBER DEVELOPMENT

SINGLE CRYSTAL OXIDE MONOFILAMENTS

- **Increase high temperature strength of Al_2O_3 fibers by process optimization**
- **Add small amount of dopant to alumina fibers to improve strength**
- **YAG and Al_2O_3/YAG fibers for better fiber toughness**

POLYCRYSTALLINE ALUMINA FIBER TOWS

- **Increase creep resistance of fiber by adding a small amount of other oxides**

Figure 11

Because the matrix materials for many intermetallic and superalloy-based composites do not have the required high temperature strength for HSCT nozzle applications, fibers are expected to carry practically all of the load at high temperatures. Single crystal and polycrystalline oxide fibers have been selected for NiAl-, superalloy-, and $MoSi_2$ - based composites, because of their chemical compatibility with the matrices and their environmental stability.

Initial development efforts have focused on alumina fibers. Single crystal (c-axis) alumina monofilaments with room temperature strengths greater than 400 ksi are currently commercially available from Saphikon, Inc. However, the strength of Saphikon fibers decreases to 100-150 ksi at 2000°F, which does not meet the requirements for HSCT nozzle materials. Therefore, development efforts have been initiated at Saphikon to increase the high temperature strength of Saphikon fibers. Several approaches are being pursued, including:

- Optimizing processing parameters for single crystal fiber growth
- Adding a small amount of dopant to the fibers.

Preliminary results from the process optimization studies are encouraging. Future efforts on single crystal oxide fiber development will include YAG and Al_2O_3 - YAG fibers.

FIBER COATING DEVELOPMENT

FUNCTION OF THE COATING	COMPOSITE SYSTEM		
	$NiAl/Al_2O_3$	Superalloy/ Al_2O_3	$MoSi_2/Al_2O_3$
Strengthen Fiber/Matrix Bond	X	X	
Reduce Residual Stress due to CTE Mismatch	X	X	
Increase Fracture Toughness at Room Temperature	X		X
Increase Fracture Toughness at Use Temperature			X
Prevent Fiber Strength Degradation During Processing	X	X	X

Figure 12

The fiber-matrix interface plays a key role in determining the mechanical properties of a composite material. The fiber/matrix interface can be modified via application of interfacial coatings to obtain the desired composite properties. Fiber coatings are needed for many different reasons, and are therefore system specific. The functions of fiber coatings in each of the composite material systems under consideration for HSCT nozzle applications are given below.

Al_2O_3/Superalloy
- Strengthen fiber-matrix bond
- Reduce the residual stresses due to CTE mismatch
- Prevent fiber strength degradation after processing

Al_2O_3/NiAl
- Strengthen fiber-matrix bond
- Reduce residual stresses due to CTE mismatch
- Increase room temperature fracture toughness
- Prevent fiber strength degradation after processing

$Al_2O_3/MoSi_2$
- Increase fracture toughness of composite
- Prevent fiber strength degradation after processing

Fiber coatings must be chemically compatible with both the matrix and the fiber; otherwise reaction barrier layers are required between the coating and the fiber or the matrix. The multiplicity of requirements for the fiber coatings, which are sometimes in contradiction to each other, make it difficult to select a coating composition for any given composite system. Multi-layer fiber coatings are sometimes used to accommodate conflicting coating requirements.

MATERIAL PROCESSING/FABRICATION APPROACHES ARE BEING EVALUATED

For MMC

- **Tape Casting**
- **Foil/Fiber/Foil Processing**
- **Transient Liquid Consolidation**
- **Low Pressure Plasma Spray**

For NiAl-base IMC

- **Tape Casting**
- **Melt Infiltration**
- **Fiber Coating by PVD**
- **Foil/Fiber/Foil Process**
- **Infiltration with Matrix Powder**
- **Directional Solidification**

For MoSi2-base IMC

- **Tape Casting**
- **Chemical Vapor Infiltration**
- **Reactive Infiltration**

Figure 13

The timely availability of advanced high temperature composites for use in HSCT engines depends upon our successful use of concurrent engineering concepts to develop acceptable fabrication processes for these materials. There are several potential methods of fabrication for each material under consideration in the EPM program. The applicability of any process depends on the particular material system that it is applied to, and the structural application. The processes under evaluation can be grouped into five general categories:

- Powder
- Foil
- Thermal Spray
- Casting
- Reaction

The specific processes that will be used to fabricate each of the composite material systems are shown in Figure 13.

EVALUATION CRITERIA GUIDE PROCESS DOWN-SELECTION

1 PROVEN FEASIBILITY
2 EXPERIENCE
3 REPRODUCIBILITY
4 PROPERTIES
5 FIBER ARCHITECTURES
6 ADAPTABILITY TO DESIGN REQUIREMENTS
7 COST
8 SUBCONTRACTOR BASE
9 SCALE-UP POTENTIAL

Figure 14

Critical assessments of the variety of fabrication processes investigated under the EPM program will be used to downselect those processes that are the most promising for the fabrication of nozzle materials. Initial process evaluations, based on characterization of the materials produced, will enable the early identification of material fabrication problems, and will provide insight into relationships among processing, structure, and material properties that will be used in down-selecting processes for further development. A critical test plan has been established to guide the evaluation of processes and to provide data for use in the down-select process. Nine separate criteria will be considered in the process down selection: proven feasibility, experience base, reproducibility, material properties, fiber architectures, adaptability to design requirements, cost, subcontractor base, and scale-up potential.

TAPE CASTING APPROACH WILL BE USED TO FABRICATE NOZZLE MATERIALS

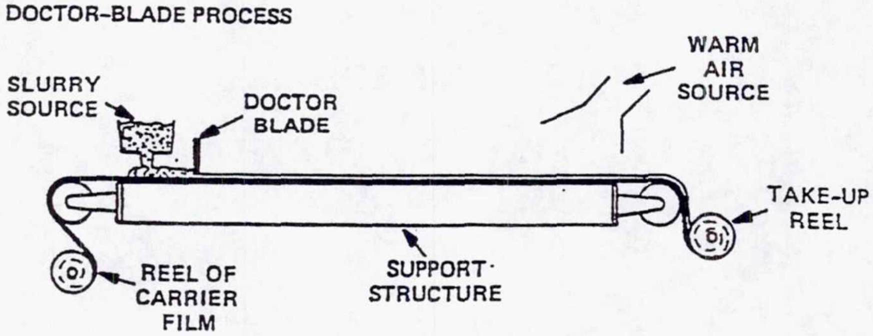

Figure 15

Tape casting is a primary candidate for fabrication of nozzle materials due to its simplicity, ease of operation, potential for scale-up and low cost. This process produces a flat monotape containing fugitive binders, and is well suited for fabrication of the large, flat sheets of material that will be required in much of the nozzle structure. Matrix material in the form of powder is combined with a binder and a solvent to obtain a slurry of the desired viscosity. As shown in Figure 15, this slurry is then spread as a film over a fiber mat which is fixed to a flat panel or cylindrical drum. After the solvent has evaporated, the material takes the form of a flexible monotape which binds the fiber at the desired spacing with the required volume fraction of matrix material. Monotapes produced in this manner are assembled into the desired architecture of fiber orientations and subsequently consolidated into a fully dense multi-ply panel. The primary technical issues involved in this fabrication process are determining the most suitable binder material and design of the consolidation process. One of the key aspects of consolidation is facilitating proper unzipping/decomposition and removal of the binder.

Consolidation Process Parameters Control The Extent Of Densification

8 - ply Al2O3/ MA 956 MMC VIA TAPECASTING

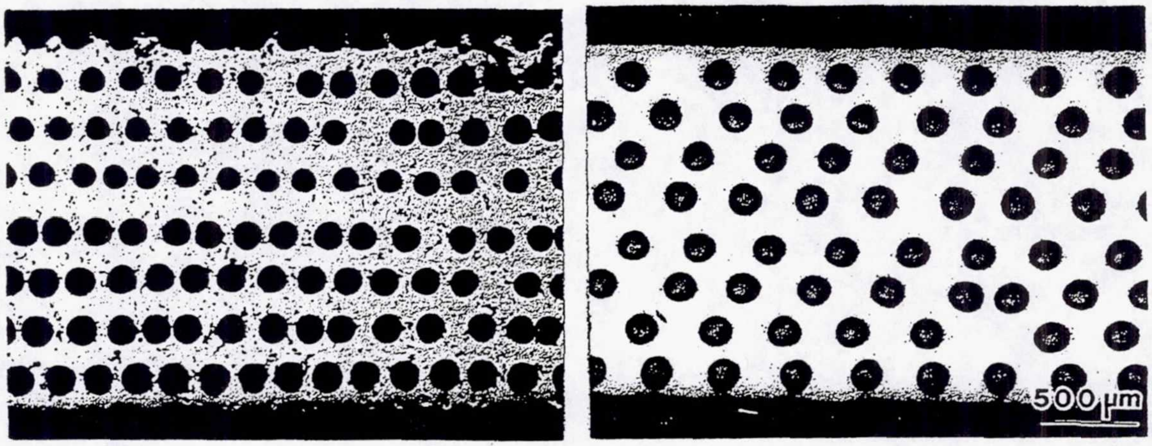

(a) Partial Consolidation **(b) Complete Consolidation**

Figure 16

After the consolidation step in the fabrication process, the composite materials must be characterized to evaluate the process used. Microstructural analysis is one of the critical assessments made in evaluating the materials fabricated. It provides important information on the matrix, the fiber, and the interface which is created between the two as a result of the fabrication process. It also reveals the spacing distribution of the fiber resulting from the process and whether a fully dense structure has been achieved. Figure 16 displays microstructures from two panels of one of the composite materials being developed under EPM. This material is an eight-ply, superalloy MMC of MA956 matrix reinforced with sapphire ceramic fiber. The composite panels were consolidated using different conditions from monotapes fabricated by tapecasting. The porosity evident in Figure 16(a) indicates that the consolidation process conditions were initially inadequate. A subsequent increase in the consolidation temperature produced full consolidation, as shown in Figure 16(b).

CRITICAL TESTS MEASURE PROGRESS IN MATERIALS DEVELOPMENT

	# of Tests	
Initial Screening Matrix	33	Several Composites
Preliminary Characterization Matrix	178	Best 4 Candidates
Detailed Characterization Matrix	602	Best Material and 1 Alternate

Figure 17

In order to generate the data required to support materials development, materials selection and component design for the exhaust nozzle, a wide variety of room and elevated temperature mechanical tests are planned. To ensure that all data are "correct" and consistent, standardized test procedures for MMC, IMC and CMC materials are being developed among NASA, GEAE and Pratt & Whitney. The nozzle testing flow-down plan is shown in Figure 17. Initially, a large number of candidate materials will be evaluated using a screening test matrix (33 tests per material) which will include tensile and thermal fatigue cycling, as well as environmental and physical property testing. The results of these tests will be used to provide feedback to the material development process. At the end of this phase, a preliminary characterization (178 tests per material) of the four leading candidate materials will be performed. A review of these results will lead to the selection of the final material for scale-up and detailed characterization, which will include 602 tests, and may also include limited testing on an alternate material. The detailed test matrix will involve a large number of cyclic and thermal mechanical fatigue tests, with emphasis on interactive effects and long-time durability.

CYCLIC OXIDATION IS A MAJOR DURABILITY CONCERN

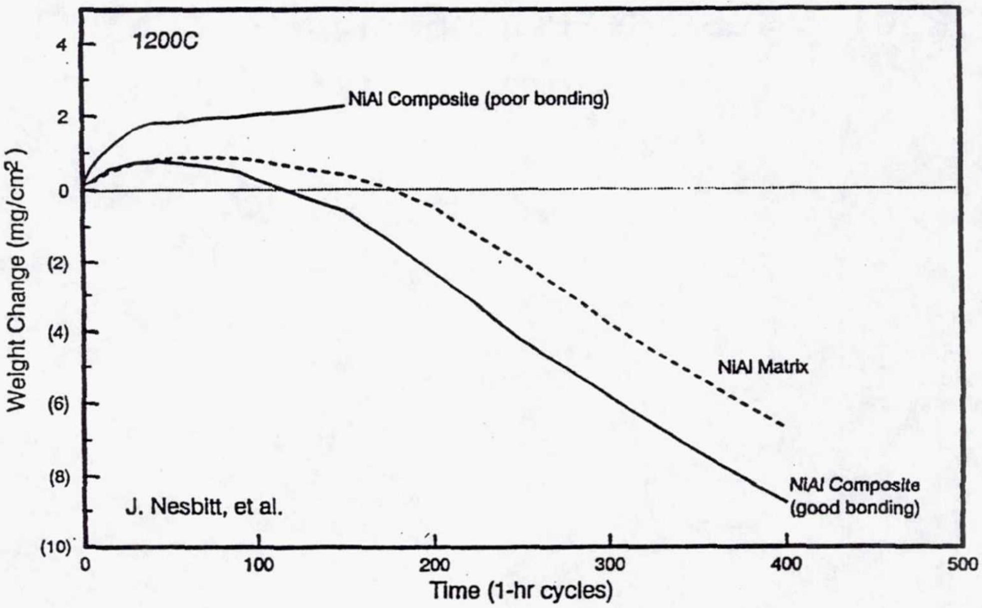

Figure 18

Nozzle materials must demonstrate 18,000 hour durability in oxidizing environments at temperatures up to 2400°F. Resistance to cyclic oxidation is a major concern because of the thermal cycling nature of engine applications. Oxidation resistance of the matrix and fiber alone do not guarantee oxidation resistance for the composite. The major issue in the oxidation of composites is the oxidation along the fiber/matrix interface. To produce oxidation resistant composites, strong bonding at the fiber/matrix interface is required so that the interface remains intact through thermal cycling and does not act as a fast diffusion path, allowing rapid oxidation.

The initial rate of weight gain in cyclic oxidation is similar to the isothermal rate, but it eventually goes through a maximum and then decreases. Weight loss in cyclic oxidation, which is the result of oxide spalling, represents a more rapid consumption of the alloy. The test data in Figure 18 show the effect of fiber/matrix bonding on the cyclic oxidation of a sapphire-reinforced NiAl composite. The composite with good bonding (5 percent fiber volume ratio) exhibited a weight change similar to monolithic NiAl. In this case, microstructural examination using a scanning electron microscope showed no oxidation along the fiber/matrix interface. However, the composite with poor bonding (30 percent fiber volume ratio) showed extensive oxide formation along the fiber/matrix interface after 150 cycles, resulting in a very high weight gain.

NON-DESTRUCTIVE TESTING PROVIDES QUALITY CONTROL

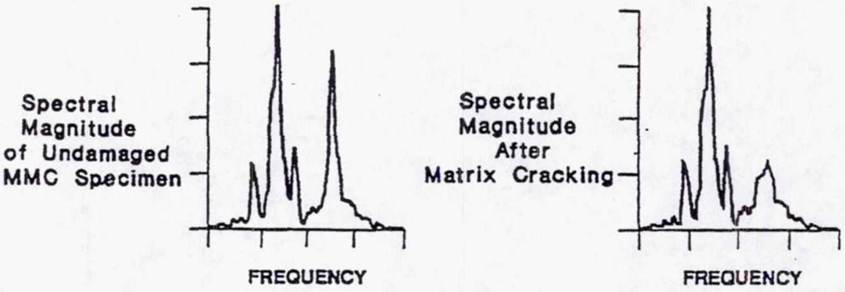

Figure 19

Non-Destructive Evaluation (NDE) methods have historically contributed to the development of state-of-the-art materials and structures, both as tools for the inspection and quality control of newly fabricated materials and for verifying the integrity of finished structural components. The non-destructive inspection of EPM developmental composite materials presents unique challenges because complex or experimental fabrication processes that may be used offer many opportunities for introducing a variety of defects into the materials. NDE techniques will be used to inspect EPM nozzle materials for potential defects such as matrix cracks, porosity, second phase content, fiber breakage, inhomogeneity and delamination. These defects would degrade the mechanical or thermal properties of a composite material, which in turn would reduce the lifetime of the structure. Specific NDE methods that will be applied to EPM nozzle materials include:

- Ultrasonic imaging, conventional and microfocus x-ray and thermography techniques will be used for screening panels, segments, sectors or liners for quality and homogeneity.

- Acoustic microscopy and acoustic emission methods will be used, along with those methods mentioned above, to characterize and monitor damage accumulation in support of analytical model development.

- Dynamic resonance, ultrasonic velocity and acousto-ultrasonics measurements will be used to verify material uniformity and will be correlated with micro- and macro- structural material characteristics to monitor damage accumulation, as shown in Figure 19.

Interdisciplinary Computational Analysis Methods Predict Design Feasibility

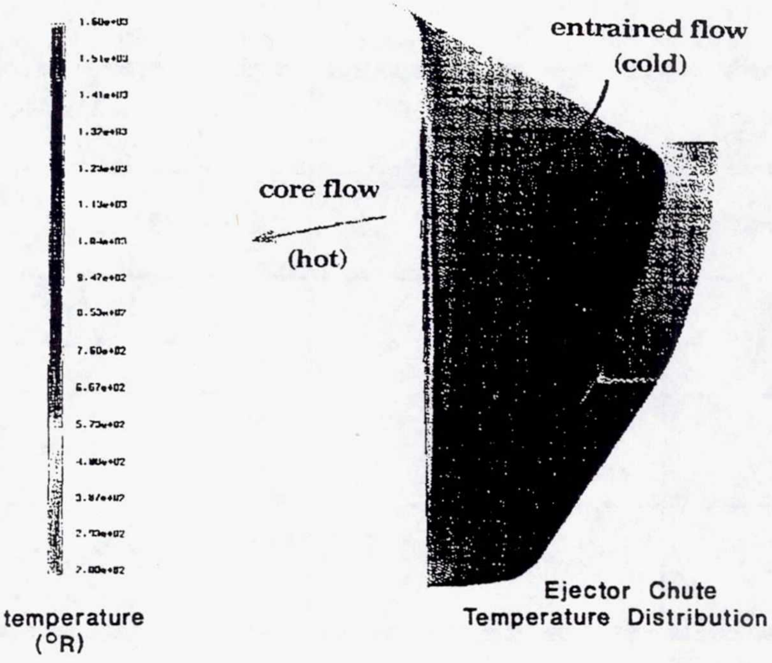

Figure 20

Computational structural analysis methods are being used to support the EPM materials development effort in two ways:

- Parametric studies are being conducted with several micromechanics-based computer codes to determine the mechanical properties of the fiber, matrix and interface that will be required to achieve the composite goal properties shown in Figure 6.

- The results of a series of computational fluid dynamics analyses are being used to calculate the aero/thermal loading on critical components (convergent and divergent flaps, chutes and acoustic liners) of candidate exhaust nozzle configurations. For example, the calculated temperature distribution on the cold side of an ejector chute structure from a 2DCD nozzle under takeoff conditions is shown in Figure 20. The temperature and pressure distributions calculated in this manner are used to define the loading for a thermal/structural finite element analysis, from which stresses in the critical components are calculated. By comparing these stresses with the strengths of candidate nozzle materials, a feasibility assessment of proposed material/design combinations can be made.

CRITICAL HSCT EXHAUST NOZZLE COMPONENTS NEED HIGH TEMPERATURE COMPOSITE MATERIALS

COMPONENT	1999 MATERIAL	TEMPERATURE RANGE (°F)
Convergent Flaps	IMC	1200 - 2300
Divergent Flaps	IMC	600 - 2400
Ejector Chutes	MMC	1600 - 2000
Acoustic Liners	Ceramic or CMC	1000 - 2400

Figure 21

The EPM Nozzle Integrated Product Development team has completed the initial identification of materials and structural approaches for advanced material technology (1999) exhaust nozzles. The convergent and divergent flaps, ejector chutes and acoustic liners require advanced materials for HSCT applications. Recommendations for the initial selection of materials for these critical nozzle components are shown in Figure 21. The divergent flaps will operate in the 600° - 2400°F temperature range; IMC materials are the primary candidates for these subcomponents, as well as for the convergent flaps. MMC materials are being considered for the ejector chutes, which will operate in temperatures up to 2000°F. Ceramic or CMC materials are designated for the acoustic liners, which will be exposed to 1000° - 2400°F temperatures during the engine cycle.

19991765 73

LeRC NATR FREE-JET DEVELOPMENT

M. Long-Davis and B.A. Cooper
NASA Lewis Research Center
Cleveland, Ohio

S36-09

AERODYNAMIC DESIGN OF THE NOZZLE ACOUSTIC TEST RIG

~409576

24 P.

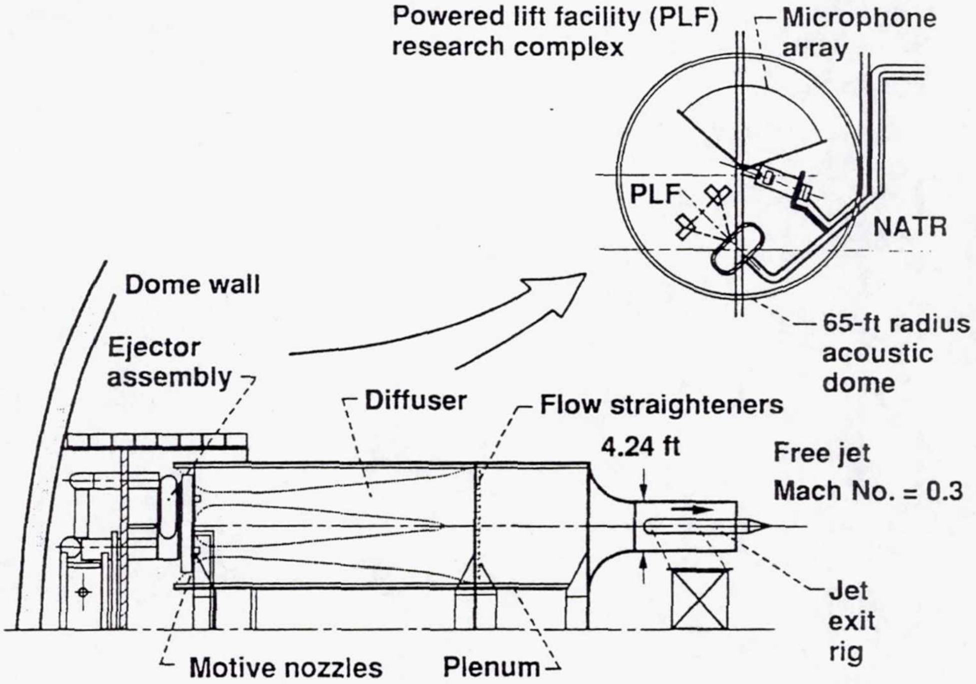

The Nozzle Acoustic Test Rig (NATR) was developed to provide additional test capabilities at Lewis needed to meet HSR program goals. The NATR is a large free-jet facility (free-jet diameter = 53 in.) with a design Mach number of 0.3. It is located inside a geodesic dome, adjacent to the existing Powered Lift Facility (PLF). The NATR allows nozzle concepts to be acoustically assessed for far-field (approximately 50 feet) noise characteristics under conditions simulating forward flight. An ejector concept was identified as a means of supplying the required airflow for this free-jet facility. The primary stream is supplied through a circular array of choked nozzles and the resulting low pressure in the constant, annular-area mixing section causes a "pumping" action that entrains the secondary stream. The mixed flow expands through an annular diffuser and into a plenum chamber. Once inside the plenum, the flow passes over a honeycomb/screen combination intended to remove large disturbances and provide uniform flow. The flow accelerates through an elliptical contraction section where it achieves a free-jet Mach number of up to 0.3.

OBJECTIVES OF 1/5-SCALE MODEL TEST PROGRAM

Determine ability of ejector system to overcome back pressure of configuration

Determine sensitivity of system to axial position, vertical alignment, and angular orientation of primary nozzle array

Determine velocity distortion levels at exit of the free-jet

Determine effect of blockage due to inlet tunnel enclosing primary nozzle array

Several issues regarding the performance/operation of the NATR ejector system were identified:

1. The ability of the ejector system to successfully overcome the back pressure produced by the configuration.
2. The sensitivity of the system to the axial position, vertical alignment, and angular orientation of the primary nozzle array.
3. The quality of the flow at the exit of the free-jet as determined by the velocity distortion levels measured.
4. The effect of blockage due to an inlet tunnel enclosing the immediate area around the primary nozzle array.

In order to address these issues, an experimental program was initiated, which involved building and testing a 1/5-scale model of the NATR.

1/5-SCALE MODEL OF THE NATR

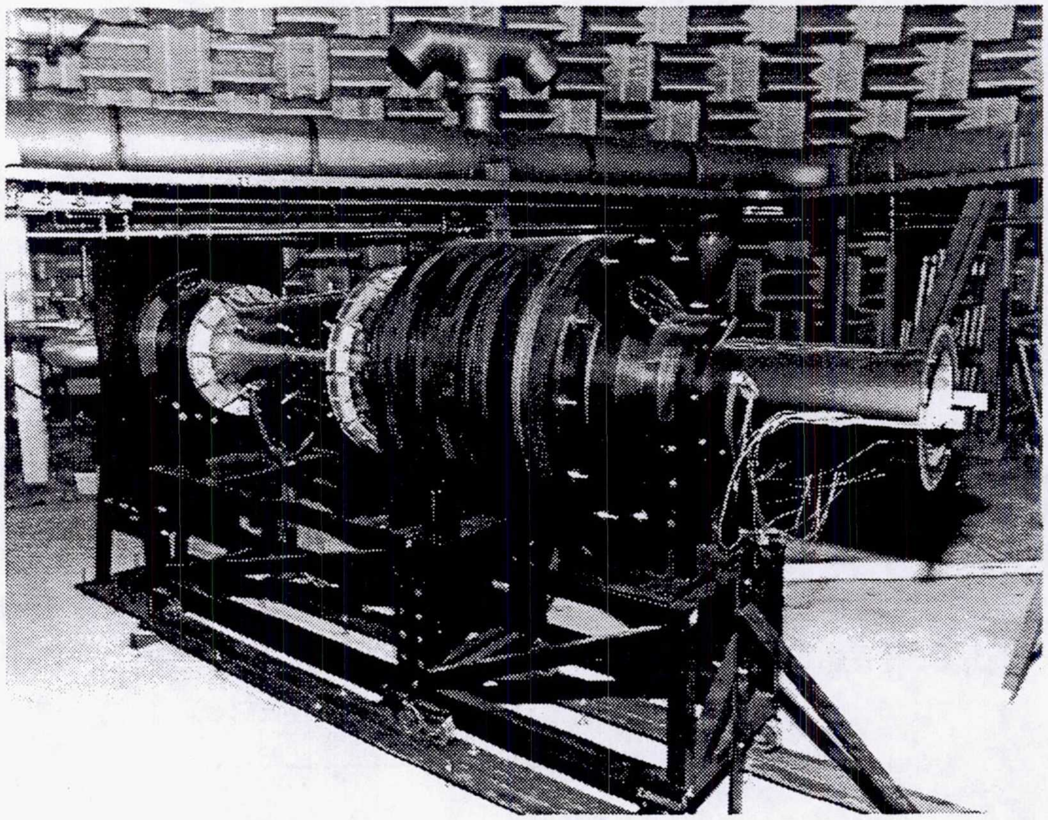

The 1/5-scale model of the NATR was designed by scaling (geometrically) the dimensions of the full-scale facility by 0.20. For ease of fabrication and cost considerations, the model was constructed from several different materials (i.e., wood, metal, plexiglass). In order to translate the model axially, it was mounted on v-groove rails. The large tolerances in the model supports and piping allowed the vertical and angular motion of the primary nozzle array. In order to investigate the effect of the honeycomb/screen position on the level of velocity distortion at the free-jet exit, the plenum was made of a series of 3-in. rings. One ring contained the honeycomb and another contained the screen. Their locations could be easily varied to determine if one configuration produced higher flow quality than another. Wall static pressures were measured longitudinally along the diffuser walls and the free-jet nozzle. A rake, extending completely across the diameter of the free-jet nozzle, measured total temperature and total pressure. A boundary layer rake was also located at the exit station of the free-jet nozzle in order to determine the boundary layer thickness.

1/5-SCALE MODEL PUMPING PERFORMANCE

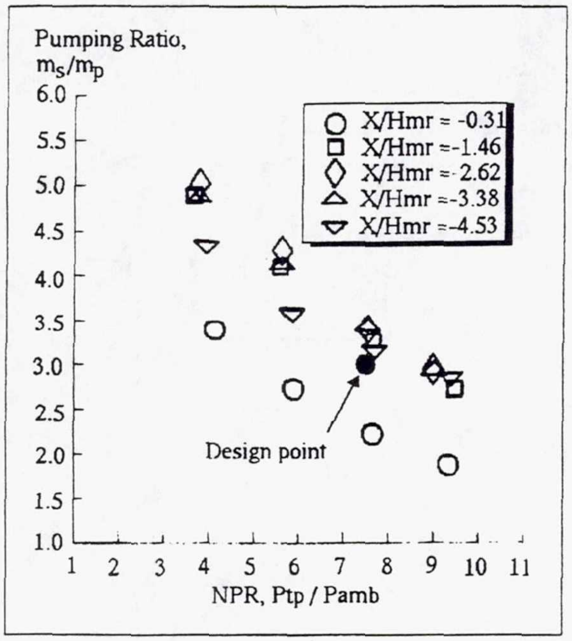

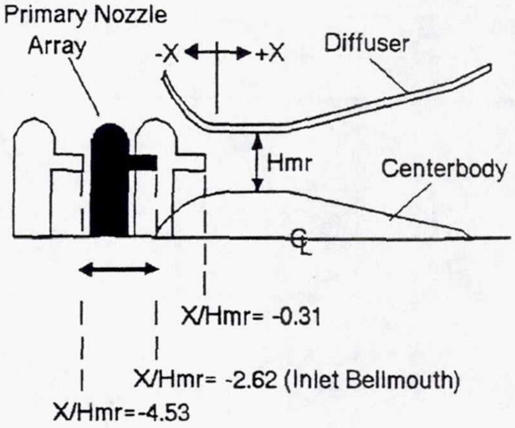

The figure above shows the pumping ratio, ms/mp, as a function of the primary nozzle pressure ratio for several primary nozzle axial positions. The axial position, X, is non-dimensionalized by the height of the mixing region annulus, H_{mr}. These performance results indicate the design pumping ratio of approximately 2.9 at primary nozzle pressure ratio of 7.5 was achieved for all the axial locations investigated, except $X/H_{mr} = -0.31$. The first objective of the 1/5-scale model program was accomplished-- the ejector system was able to overcome the back pressure produced by the system configuration and achieve the necessary levels of pumping. The results indicate that when the primary nozzle array was positioned with the primary nozzles flush with the entry plane of the inlet bellmouth (station $X/H_{mr} = -2.62$) the pumping performance was the highest. Slight changes in the axial position of the primary nozzles with respect to the inlet bellmouth did not affect the performance significantly. When the primary nozzles were placed extremely forward ($X/H_{mr} = 0.31$) or extremely aft ($X/H_{mr} = -4.53$) of the bellmouth, the pumping performance decreased. The inlet bellmouth station ($X/H_{mr} = -2.62$) was chosen as the optimum axial location for the primary nozzle array because of its convenient reference.

EFFECTS OF EJECTOR MISALIGNMENT

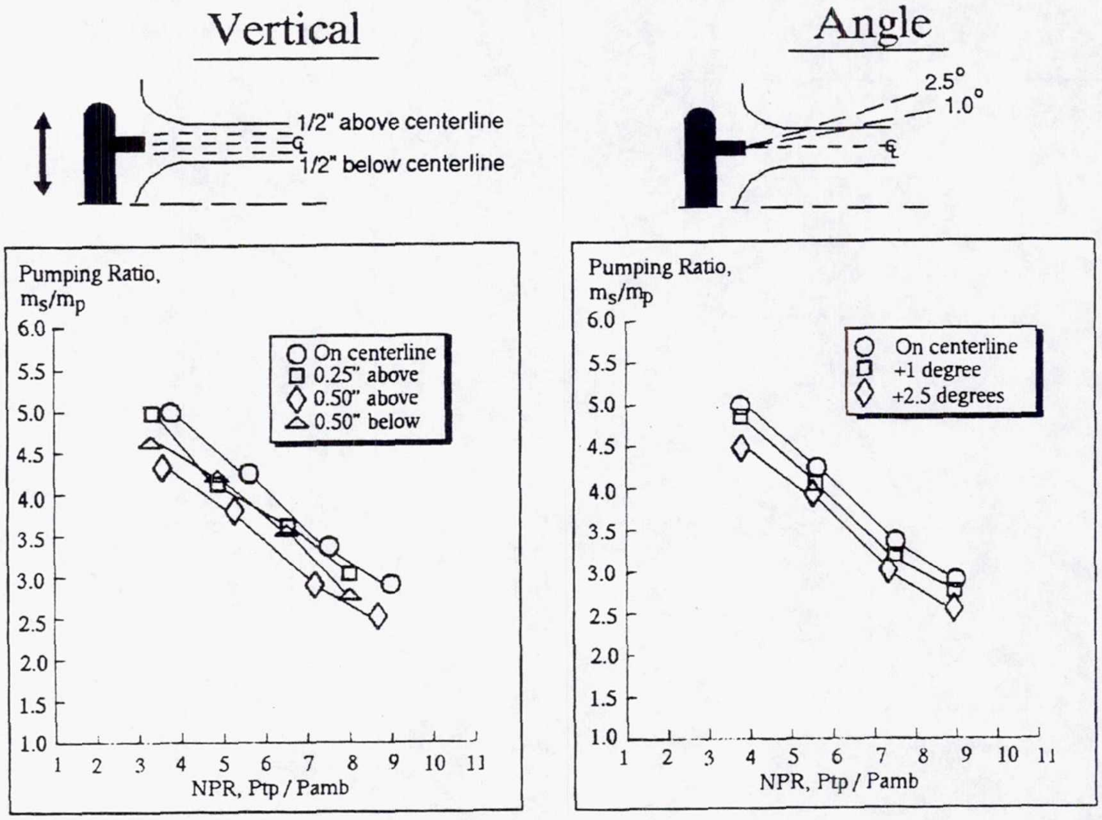

The results of shifting the centerline of the primary nozzle array up and down with respect to the annular mixing region centerline are shown in the figure. The data show that the ejector performance is very sensitive to vertical alignment of the primary nozzles. The array was shifted up and down 0.5 in. There was a decrease in the performance with any shift of the nozzle array. The greatest drop occurred with the nozzles positioned 0.5 in. above the centerline. Likewise, when the primary nozzle angle was changed, the pumping ratio suffered. The figure also presents the results of varying the nozzle angle. As evidenced, any angular misalignment of the primary nozzles caused a downward shift in the pumping performance curve. In general these results wee valuable when specifying the allowable tolerances of the full-scale NATR primary nozzle array installation.

FLOW QUALITY AT EXIT OF 1/5-SCALE MODEL FREE-JET NOZZLE

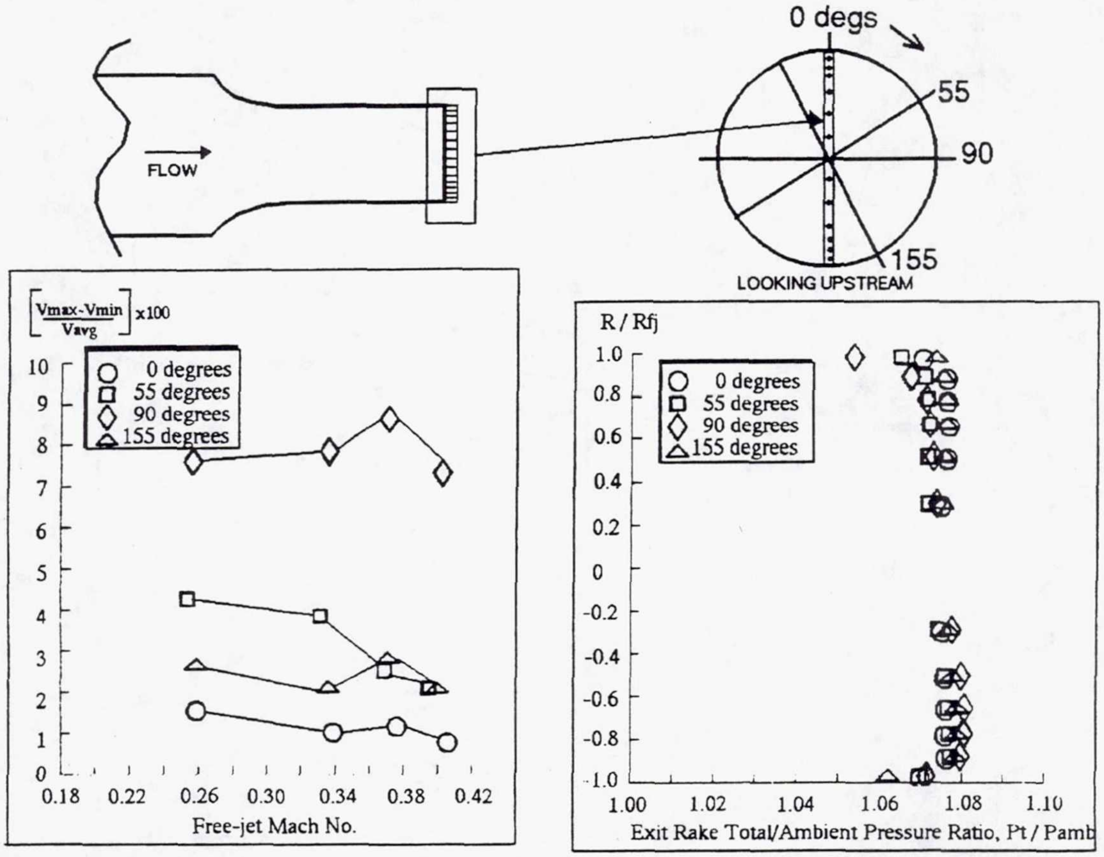

The second series of tests involved determining the flow quality at the exit of the free-jet exhaust. The figure shows the percent velocity distortion as a function of free-jet Mach number for each of the circumferential rake positions investigated. The results indicate that the velocity distortion levels were lower than 5% at three of the four circumferential positions. The distortion calculated at 90 degrees was approximately 3% higher than the others. The figure also shows the exit rake total pressure nondimensionalized by the ambient static pressure profiles for the 4 rake positions at a free-jet Mach number of approximately 0.34. It is clear that there is no single tube that appears to be causing the rake at 90 degrees to have an unusually high distortion level. As part of the flow visualization, smoke was used to study the inlet area of the ejector system. This investigation showed that the streamwise vortices, produced by the pumping action of the primary stream, had to turn sharply around the flanges of the primary nozzle array. The high distortion levels at the 90 degrees rake position are believed to have been caused by the interference of these flanges with the natural entrainment of the secondary stream.

EFFECT OF THE INLET TUNNEL

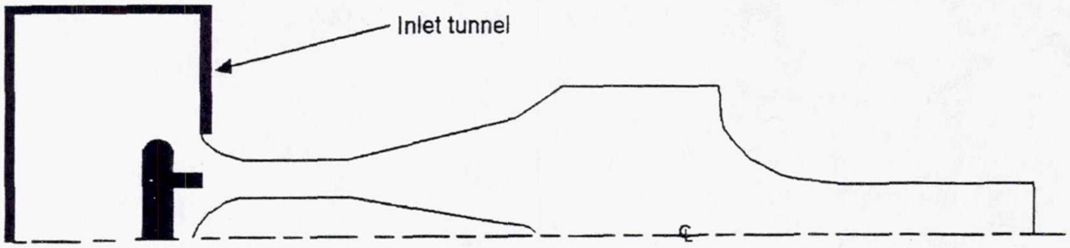

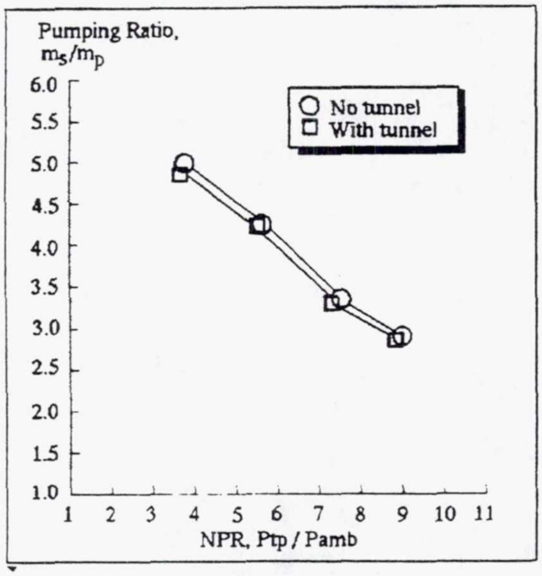

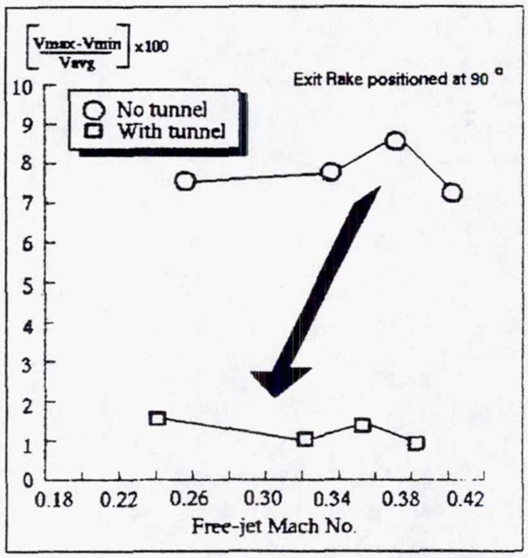

The figure above shows the results of adding the scaled inlet tunnel which enclosed the area around the primary nozzle array and inlet bellmouth. The effect of inlet blockage due to the tunnel was minimal on pumping performance. However, it is interesting to note that the inlet tunnel decreased the velocity distortion at the exit. The velocity distortion for the rake positioned at 90 degrees is plotted for both configurations (i.e., with and without the inlet tunnel added). As shown earlier, the distortion level without the tunnel is approximately 8%. With the tunnel installed, the distortion levels are lowered to approximately 1.5%. It is believed that the tunnel removed the interference effect of the flanges supporting the primary nozzle array and caused the secondary stream to be entrained more uniformly, from the frontal area only.

FULL-SCALE NATR FACILITY

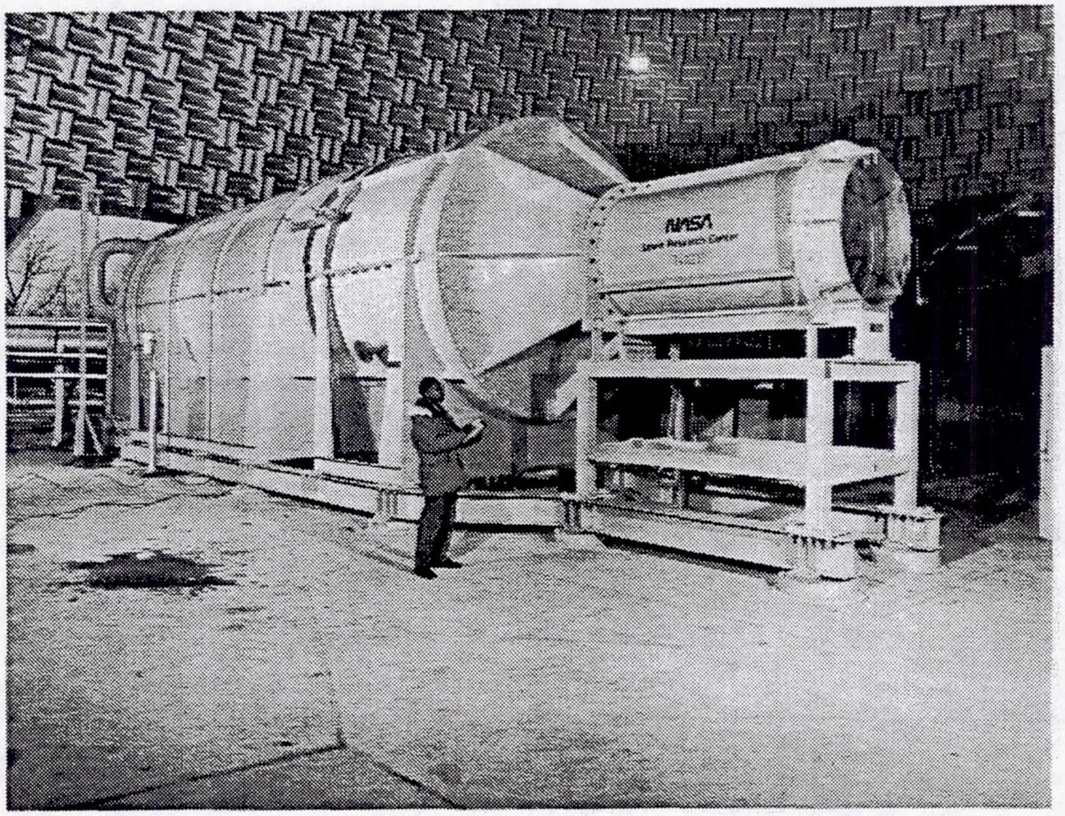

The full-scale facility is shown in the photograph above. It is located inside a geodesic dome, adjacent to the Powered Lift Facility. In the full-scale facility, (unlike in the scale model), the annular mixing region, the diffuser, the 6 radial splitters and the plenum surfaces were treated with an acoustic absorber material to attenuate the noise radiating axially and circumferentially from the ejector system of the NATR. This acoustic absorber consisted of a three layer sandwich of bulk absorber material, held in place by a wire screen and covered by a perforated plate. The primary nozzle array was mounted on rails in order to change its axial position and determine the effect of its position on pumping performance. The instrumentation of the full-scale facility included wall static pressure taps along the walls of the annular mixing region and the diffuser. There were three total pressure rakes and wall static pressure taps equally spaced around the circumference of the plenum. A row of longitudinal static pressure taps was placed along the wall of the free-jet nozzle. Four total pressure/total temperature rakes and three boundary layer rakes were located around the circumference of the free-jet nozzle exit.

FULL-SCALE AND 1/5-SCALE MODEL NATR PUMPING PERFORMANCE

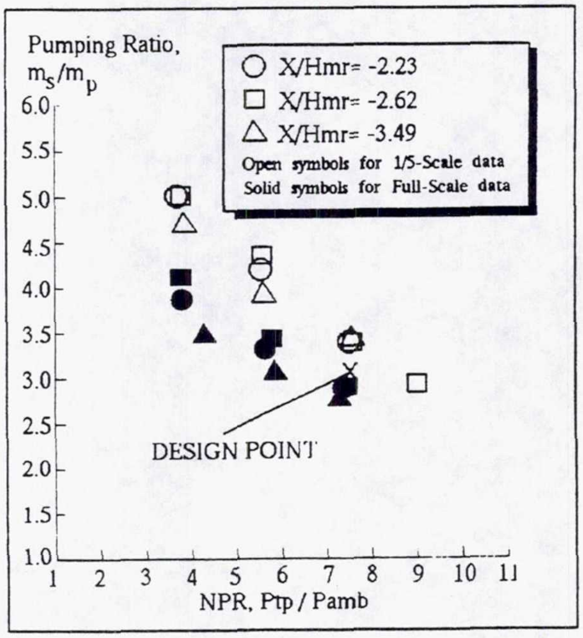

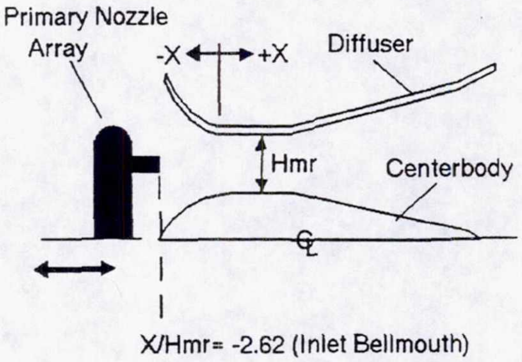

The figure above shows the pumping ratio versus the primary nozzle pressure ratio (NPR) for the 1/5-scale model and the full-scale NATR. The results show that the X/Hmr = -2.62 position (primary nozzles flush with the bellmouth) achieved the most favorable pumping ratio for both systems. The design point NPR of approximately 7.5 successfully produced the required pumping ratio of 2.9. The full-scale NATR, as expected, does not exhibit great sensitivity to the axial position of the primary nozzle array. The full-scale NATR pumping ratios are lower than those obtained for the 1/5-scale model. At the design NPR, the full-scale facility pumping ratio is 15% lower than the 1/5-scale model. Since, geometrically speaking, the scale model and the actual facility are the same, the cause of the different levels of pumping achieved may be attributed to the different fluid dynamics of the two systems. The net effects of the fluid dynamics of the flow (e.g., friction losses, boundary layer thickness, Reynolds number) are different for the full-scale facility because of the perforated plate in the mixing region. The perforated plate could produce a higher friction coefficient and a larger boundary layer thickness, and therefore a reduction in the secondary area available for flow entrainment.

FLOW QUALITY AT EXIT OF FULL-SCALE NATR FREE-JET NOZZLE

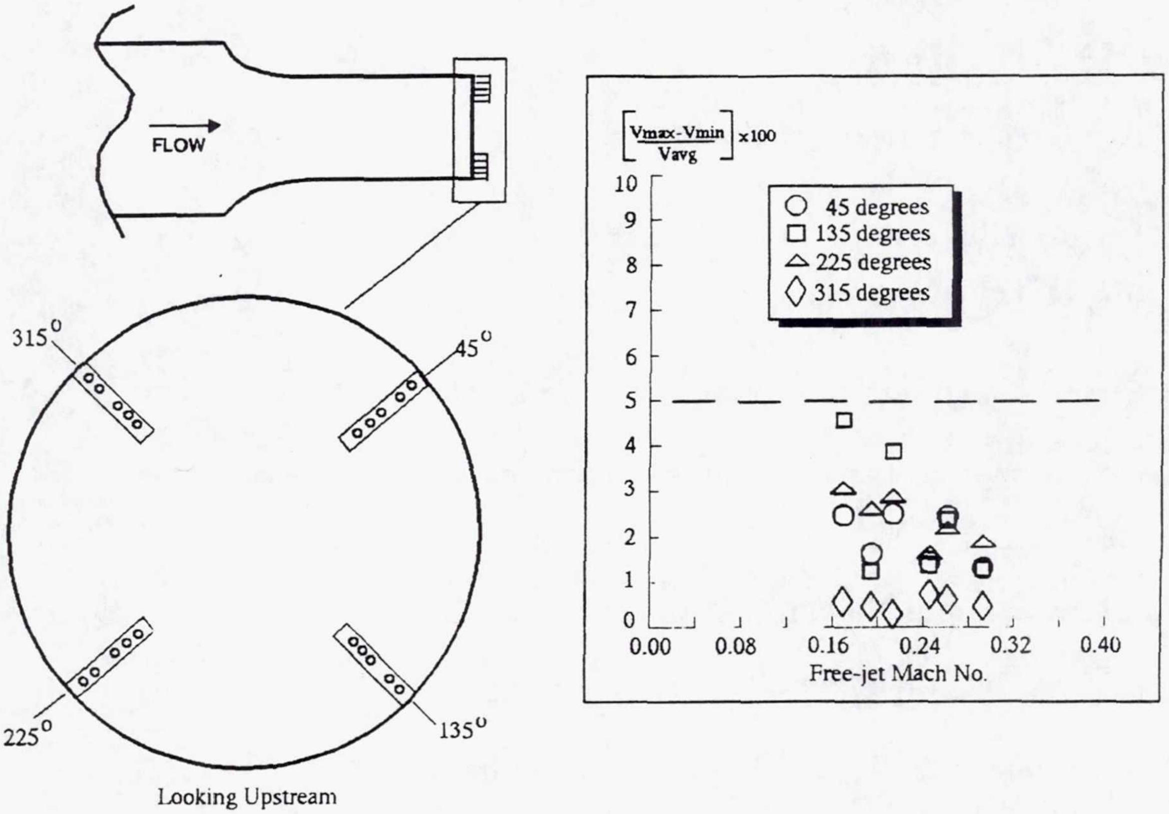

The figure above shows the velocity distortion levels measured by the four total pressure/temperature rakes at the exit of the full-scale free-jet nozzle. The plot shows all velocity distortion levels below 5% similar to 3 of the 4 scale model rake positions.

CONCLUSIONS

1/5-Scale Model

○ Achieved significant pumping performance

○ Flow quality at exit of free-jet nozzle determined to be acceptable

○ Effect of inlet tunnel on pumping performance was minimal

Full-scale NATR

● Achieved required pumping ratio to attain M=0.3

● Velocity distortion levels lower than 5%

● Full-scale and 1/5-scale results show similar trends

The 1/5-scale model of the NATR provided valuable information for the installation and operation of the full-scale facility. The experimental program verified that the ejector system achieved the necessary pumping ratios at the design primary nozzle pressure ratio. The scale model results indicated little sensitivity of the system to the axial position of the primary nozzles; however, the ejector system is extremely sensitive to vertical and angular misalignment of the primary nozzle array. The flow quality at the exit of the free-jet nozzle was determined to be acceptable. The calculated percent velocity distortion at the free-jet nozzle exit was lower than 5% at tall circumferential stations investigated except 90 degrees where the level was approximately 8%. The effect of the inlet tunnel on the ejector pumping performance was minimal; however, it did act to reduce the velocity distortion at the 90 degrees position to 1.5%. The results from the 1/5-scale model experimental program greatly aided in the design and installation of the full-scale facility. The full-scale facility achieved the required pumping ratio to attain a free-jet Mach number of 0.3. Similar to the 1/5-scale model resuts, the full-scale NATR showed little sensitivity to the axial position of the primary nozzle array. The velocity distortion levels were less than 5%.

OVERVIEW OF AEROACOUSTIC PROPULSION LABORATORY (APL) ACOUSTIC DESIGN ISSUES

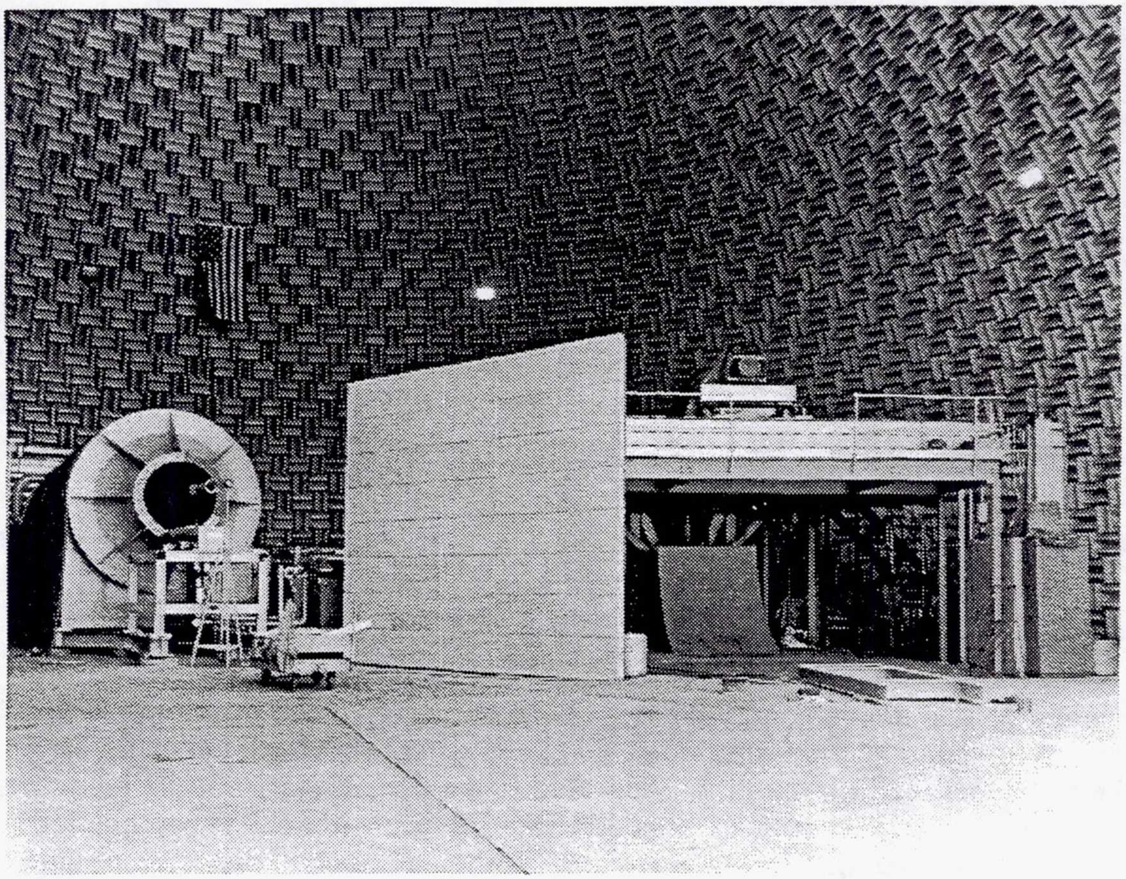

The Aeroacoustic Propulsion Laboratory (APL) Complex is a 130-ft diameter geodesic dome that provides a hemi-anechoic environment for aeroacoustic testing of aircraft propulsion systems while protecting Lewis Research Center's residential neighbors. The APL facility houses the new Nozzle Aeroacoustic Test Rig (NATR), an ejector-powered free jet for aeroacoustic testing of scale model supersonic aircraft exhaust nozzles, as well as the multi-axis force-measuring Powered Lift Facility (PLF) test stand for testing of Short Takeoff Vertical Landing (STOVL) vehicles.

FACILITY REQUIREMENTS AFFECTING APL AND NATR DESIGN PROCESSES

- REDUCE COMMUNITY NOISE LEVELS TO L_{DN} = 60 dBA
- PROVIDE ADDITIONAL CAPABILITY FOR AEROACOUSTIC NOZZLE TESTING (NATR)
- CO-LOCATE NATR AND PLF WITHIN ONE NOISE ABATEMENT STRUCTURE
- CONTAIN NATR AND PLF HARDWARE WITHIN CIRCULAR FOOTPRINT (GEODESIC DOME)
- PROVIDE HEMI-ANECHOIC INTERIOR ENVIRONMENT FOR ACOUSTIC TESTING

Originally conceived as a solution to a PLF community noise problem, APL was designed to reduce community noise levels to an acceptable level of L_{dn} = 60 dBA in residential areas (L_{dn} is a time-integrated noise metric that reflects a community's cumulative exposure to noise over a 24-hour period, with weighting applied for nighttime noise exposure). Midway through the APL design process, a need arose for an additional aeroacoustic nozzle test facility to supplement the capacity of the 9x15 Low Speed Wind Tunnel (LSWT). As a result of an extensive site selection study, the APL site was chosen for co-locating PLF with what is now NATR because of the availability of air services and existing control room as well as the expectation that NATR, as an outdoor free jet, would also require community noise control. The geodesic dome shape, which was proposed for its cost and structural advantages as well as for its all-weather and security features, gave rise to the requirement for a hemi-anechoic interior environment. These combined requirements: community noise reduction, NATR operations, PLF/NATR co-location, circular footprint, and hemi-anechoic interior; formed the basis of a tradeoff study to determine the size, orientation, and location of the dome structure as well as the geometry of the new NATR within that structure.

DESIGN CONSIDERATIONS INFLUENCING APL AND NATR GEOMETRY

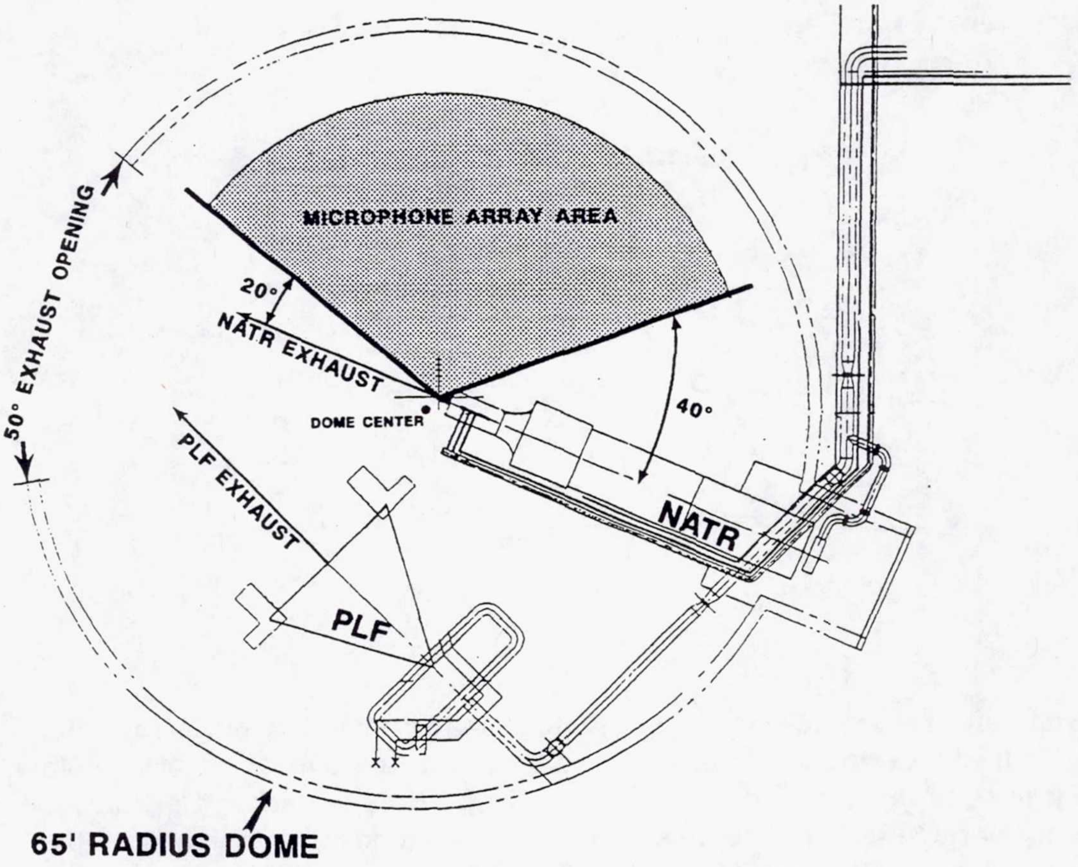

The geometry (size, location, orientation, and NATR geometry relative to the dome structure and PLF) were influenced by the following considerations: 1) overall dome size was minimized to control costs; 2) NATR and PLF were required to be able to run alternate day test schedules with minimal facility preparation; 3) NATR plume spread and temperature/velocity decay profiles dictated proximity of the rig to interior wall surfaces; 4) PLF aerodynamic concerns dictated proximity of PLF to interior walls; 5) the exhaust opening was tailored to be of the minimum size that would accommodate exhaust plumes of both rigs as well as operations vehicles, requiring the exhaust axis of NATR to be as coincident as possible with the PLF exhaust axis; 6) the planned 50' radial microphone array required a clear line of sight between the nozzle exit and the array area on one side of the jet axis; and 7) NATR was designed to accommodate 6-8" nozzles, which fixed the minimum free jet diameter, and, in turn, the minimum view angle to the upstream microphone array angles.

DESIGN OF DOME WALL PANELS FOR STC 55

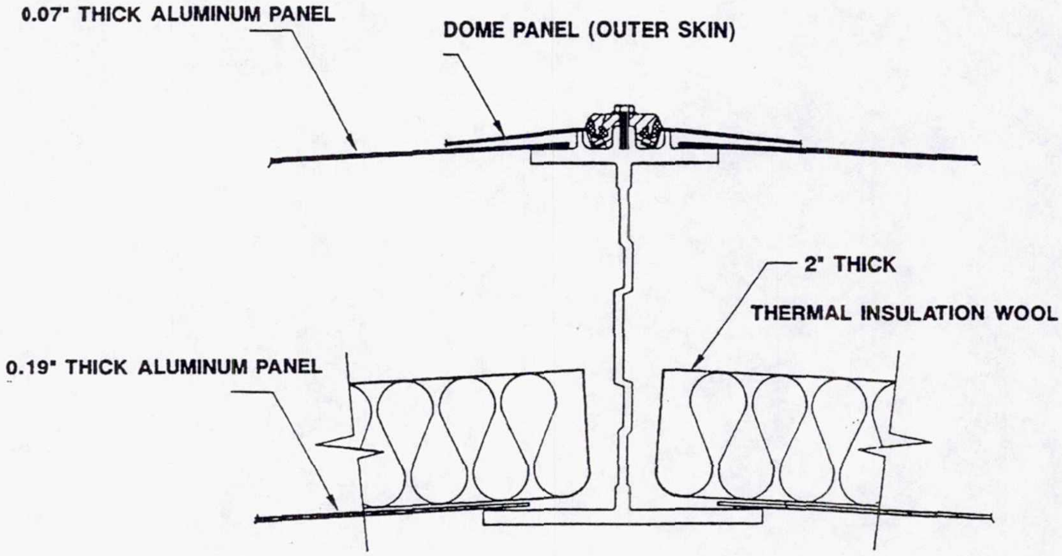

The dome wall panels were designed to provide a uniform level of noise reduction such that noise levels during APL test operations would be maintained at or below L_{dn} = 60 dBA in residential communities surrounding Lewis Research Center. A Sound Transmission Class (STC) requirement of 55 (a standard transmission loss vs. frequency contour named for its value at 500 Hz.) was identified to meet the noise reduction requirements at all 1/3 octave bands below 20 kHz. The custom-designed multi-layer "sandwich" panels, which were tested at Riverbank Acoustical Laboratories prior to dome construction, combine 2" of thermal insulating wool and a 6" airspace between two aluminum panels of differing thicknesses (.07" exterior; .19" interior). The custom-sized sandwich panels fit within the approximately 8" deep channels in the dome's structural beams and are enclosed on the interior side of a thin aluminum skin that covers the exterior surface of the dome.

DESIGN OF NOISE-ATTENUATING EJECTOR AIR INTAKE ENCLOSURE

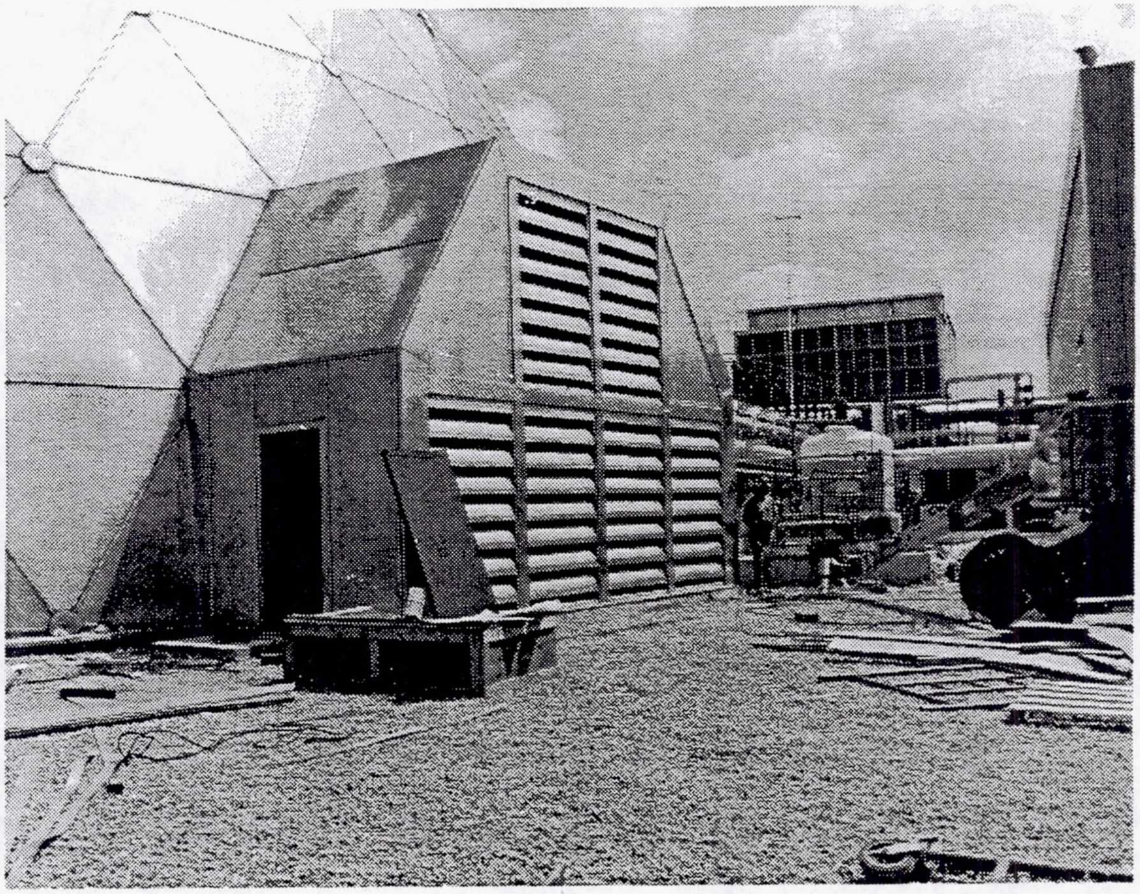

Secondary air for the ejector-powered free jet is entrained through a noise-attenuating low-pressure air intake enclosure. The enclosure is designed to provide required airflow area as well as reduction of the predicted forward quadrant noise generated by the annulus of ejector nozzles. Outdoor air entrained by the ejector flows into the bellmouth through a wall of double-stacked noise-attenuating louvers, each of which consists of a cascade of parallel airfoil-shaped splitter blades filled with sound absorbing material. The remaining walls are designed to match the construction of the dome, acoustically and visually. Noise reduction requirements for the air intake enclosure were specified such that the ejector noise would be reduced to the same level in the community as test nozzle noise after attenuation by dome wall panels.

PROCEDURE FOR EVALUATING DOME NOISE REDUCTION PERFORMANCE

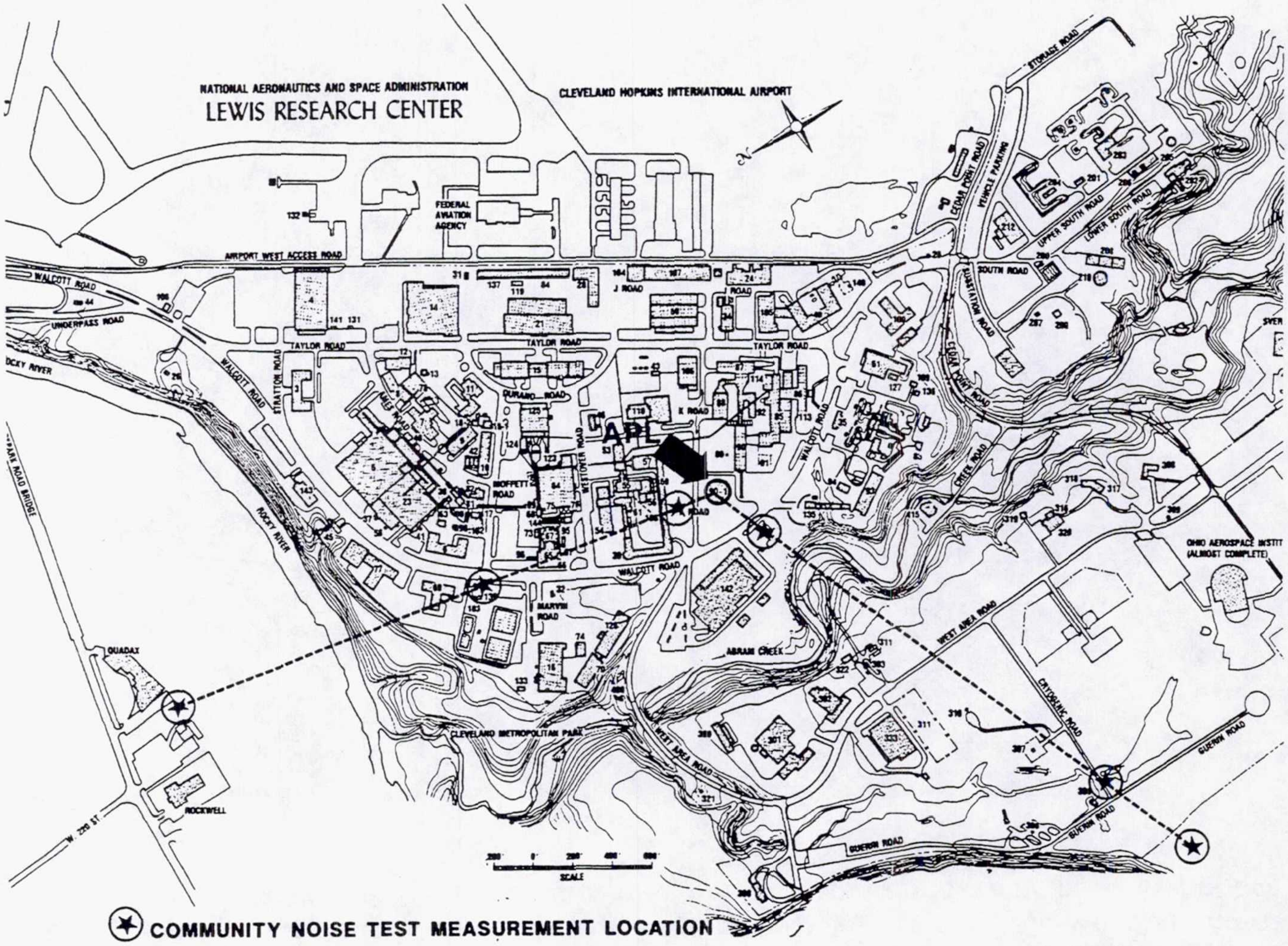

Preliminary results of initial noise reduction measurements conducted during NATR checkout tests in the Spring of 1992 indicate that the wall panels are performing as expected, and no noise complaints have been received since the completion of the dome construction. Detailed community noise tests are currently in progress, using a J85-21B (Lear Jet) engine as sound source. Noise levels will be measured along radial lines between the source and selected communities to identify locations, if any, where noise levels exceed acceptable L_{dn} limits or are grossly out of line with predicted community levels based on inverse square law (including atmospheric attenuation effects). If required, further noise abatement measures may be instituted.

HEMI-ANECHOIC INTERIOR ENVIRONMENT PROVIDED BY COMPREHENSIVE ABSORPTIVE TREATMENT

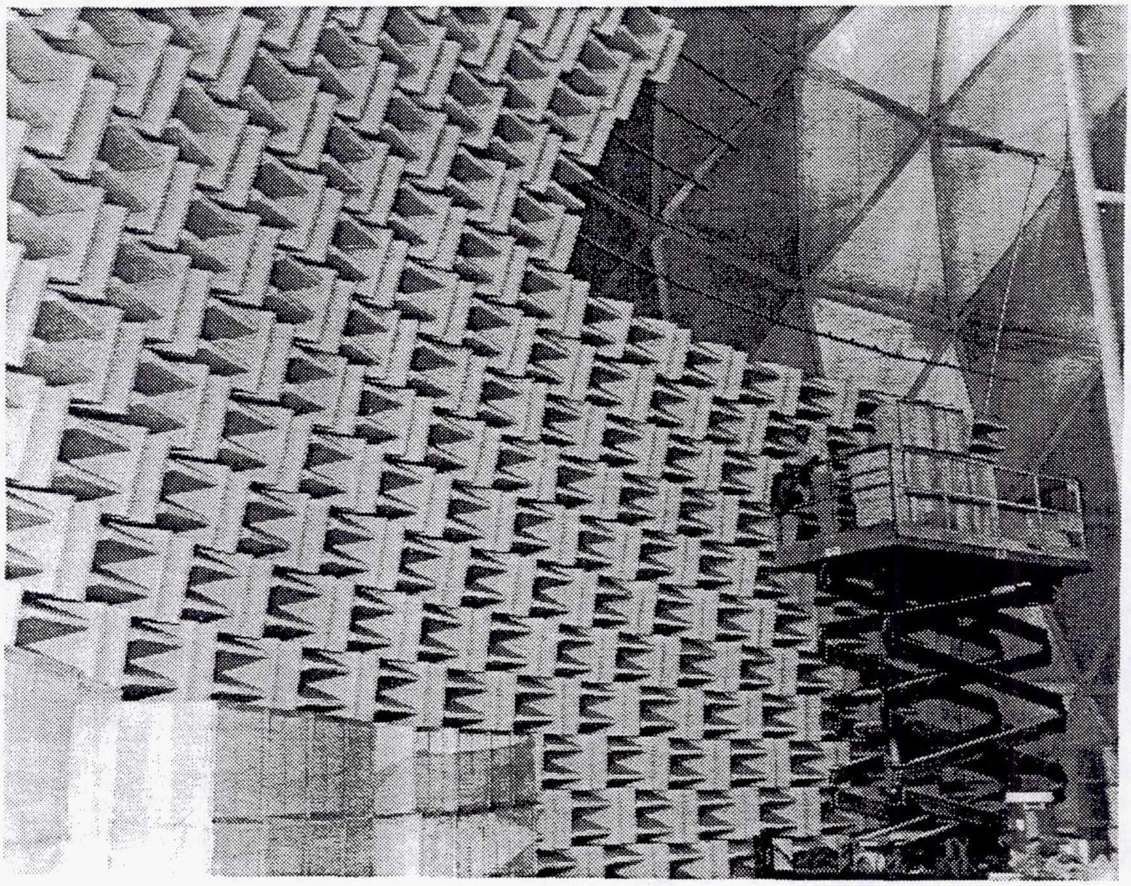

Fiberglass wedge treatment on the entire interior surface of the dome provides a hemi-anechoic interior environment for obtaining the accurate acoustic measurements required to meet research program goals. The 24" wedges are installed on a track system with a 2" airspace between the wedge base and the interior of the dome wall panel. The wedges are fully encased in fiberglass cloth and are held into the frames with 1/2" x 1" hardware cloth on all sloping edges of the wedge peaks. Results of impedance tube tests performed by the wedge manufacturer on the wedge material indicate an absorption coefficient of $\alpha = .99$ above 125 Hz. Potentially reflective surfaces on internal dome structures such as test hardware, facility plumbing, instrumentation stands, etc., have been covered or shielded with a variety of absorptive materials to ensure the highest quality acoustic environment.

PERFORMANCE MEASURES FOR INTERIOR ACOUSTIC TREATMENT

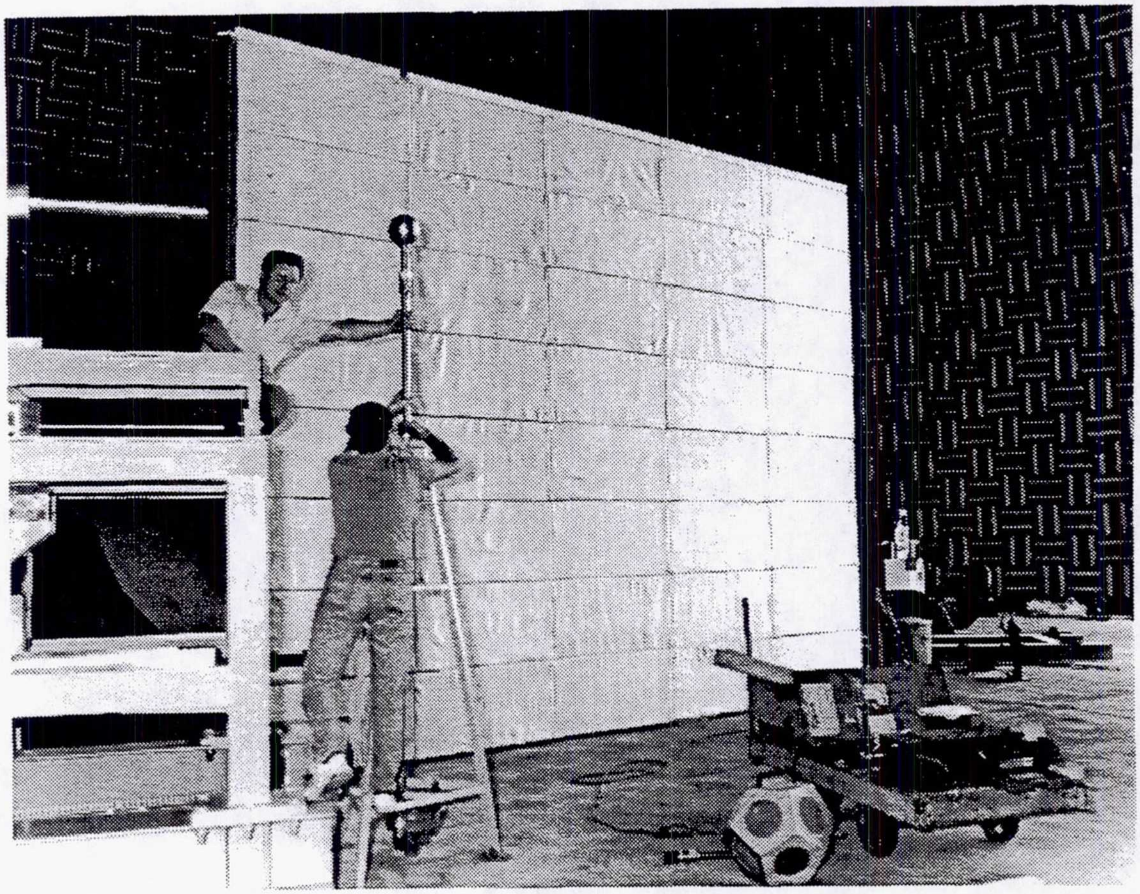

Extensive checkout tests were conducted during the summer of 1992 to evaluate the interior of the dome structure with respect to a number of accepted performance measures, among them the absorption coefficient of the wedge treatment and the observed behavior of sound with respect to the inverse square law of sound propagation. It is common for a facility of this type to have an inverse square law error with $\sigma = 1$ dB. Three calibration sound sources (high-frequency airball, dodecahedron speaker ball, and starter's pistol) were used to generate broadband and pure tone signals over the frequency range of interest as well as an impulsive signal for time delay analysis.

PROCEDURE FOR PERFORMING ACOUSTIC CALIBRATION OF INTERIOR TREATMENT

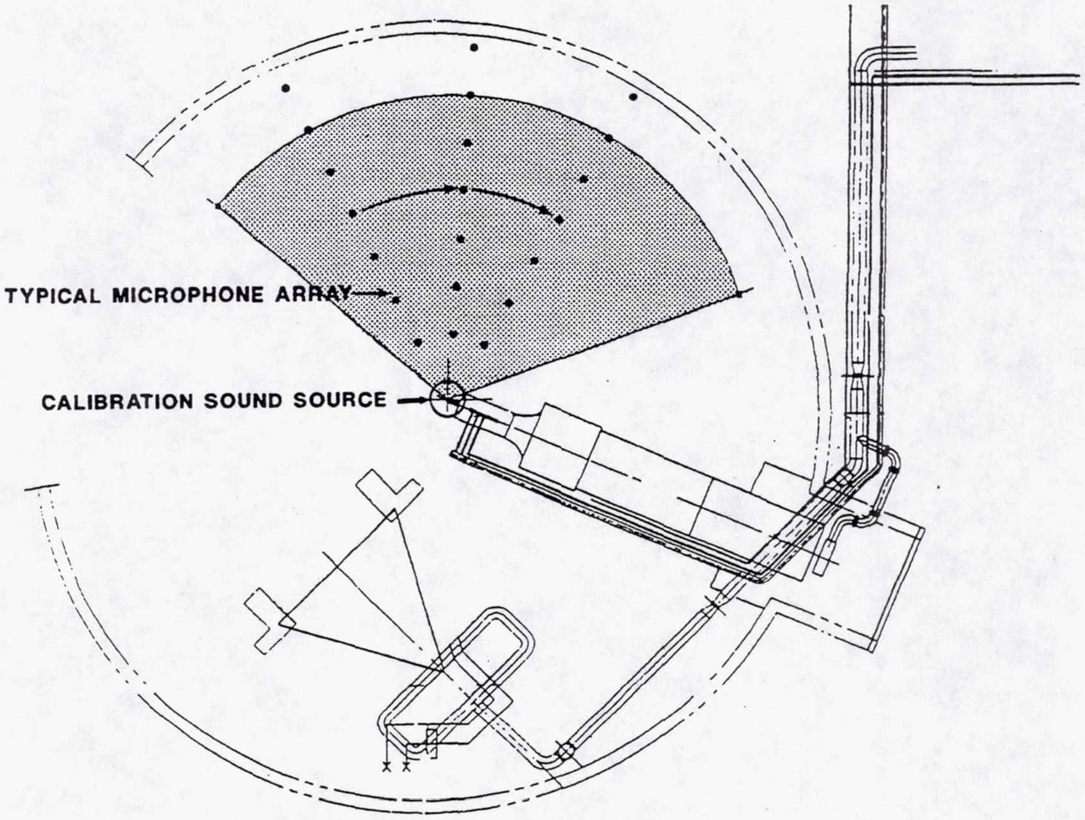

ANECHOIC CHECKOUT TEST

TYPICAL MICROPHONE ARRAYS

Radial arrays of pole and ground microphones at equivalent solid angles and distances were clocked through the microphone array region in 10° increments to measure direct and reflected sound in radial increments of 6'. Source directivity was also measured, and special tests were conducted to determine whether significant noise was being reflected from the fan opening at the top of the dome or from the wall of the 9x15 Low Speed Wind Tunnel, located about 250' from the center of the dome (through the exhaust opening). Analysis of this data using a variety of signal processing techniques will yield a frequency vs. spatial location map as well as a number of numerical indicators of the acoustic quality of the facility's intended microphone array region. Any sources of acoustically significant reflections will be identified and solutions implemented.

ACOUSTIC INSTRUMENTATION AND DATA ACQUISITION SYSTEMS FOR NATR

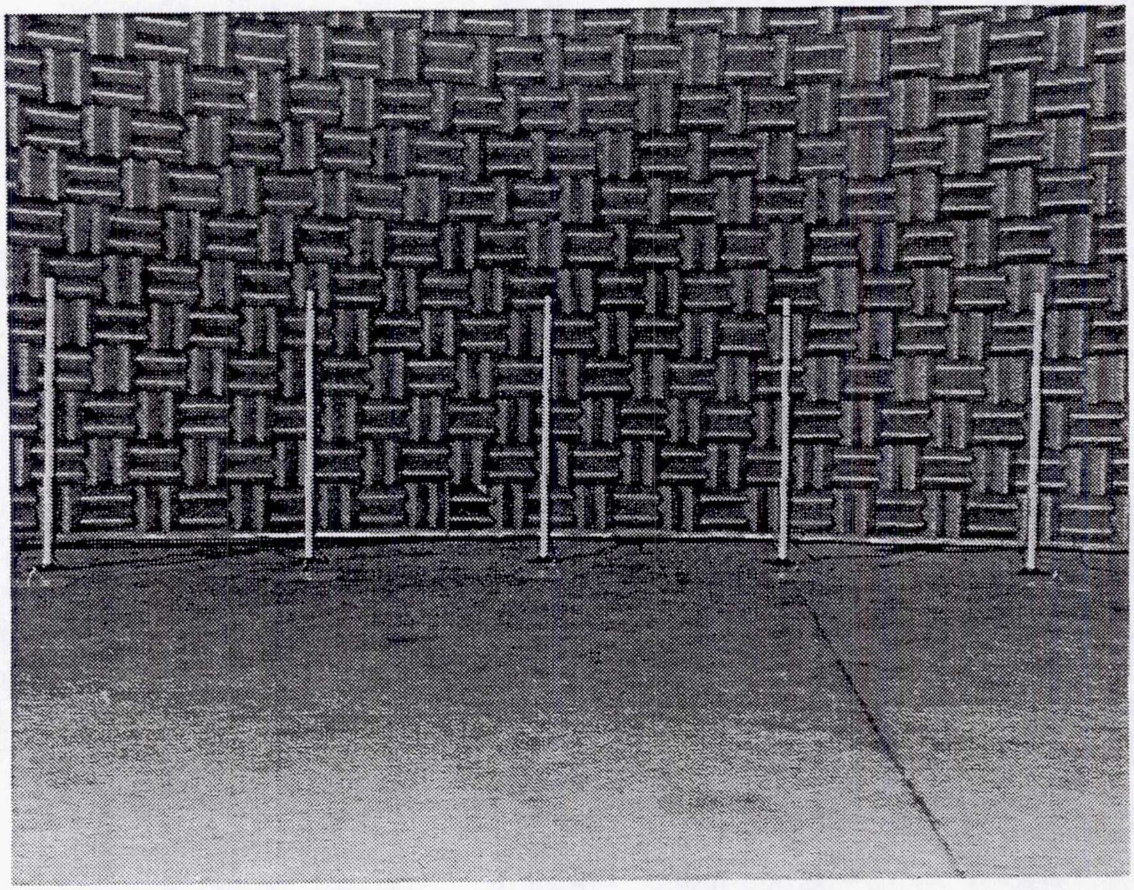

Typically, during HSR testing, acoustic measurements are taken with both ground and pole microphones at equivalent solid angles and radial distances. High frequency acoustic signals are measured with a farfield (50′) array of pole microphones at centerline height and a nearfield sideline centerline array. Ground microphones are used to acquire low-frequency signals that are free of ground reflections. A 32-channel computerized data acquisition and processing system provides narrow-band and 1/3 octave band spectral analysis with compensation for microphone frequency response/directivity and correction of acoustic data to standard day conditions. This allows for next day turnaround of processed data, providing timely support for test program decision-making.

FACILITY SELF-NOISE LEVELS ALLOW ACCURATE ACOUSTIC MEASUREMENTS

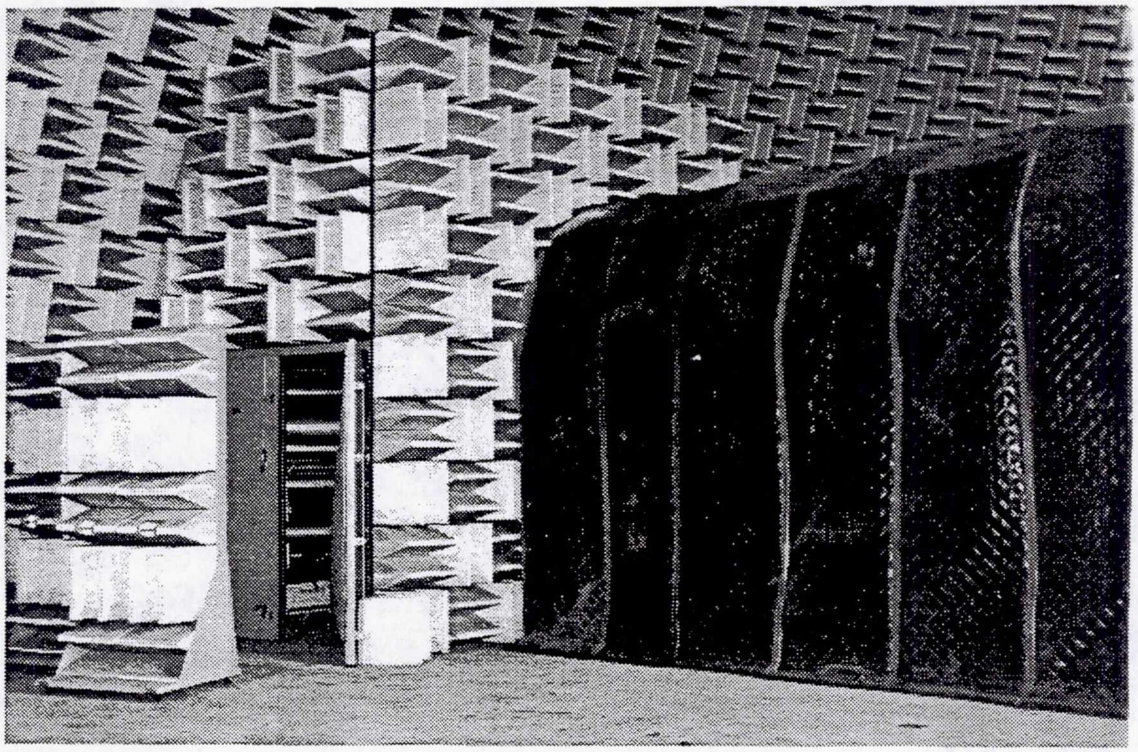

Facility self-noise levels have been maintained at acceptable levels by requiring safety and operational systems to meet strict noise criteria for generated and reflected sound, specifically 20 dB below predicted 1/3 octave band levels for a typical quiet suppressor nozzle. The NATR itself is by design a low-noise system whereby ejector noise is attenuated as it travels downstream through the NATR by absorptive treatment in the walls of the diffuser and plenum sections. The microphone arrays are shielded from radiated aft-quadrant self-noise generated by the annulus of ejector nozzles by a sealed noise-attenuation (STC 54) structure that surrounds the ejector portion of the NATR. Furthermore, new tabbed nozzles are currently being designed and fabricated for the ejector to reduce the off-design screech experienced with the current nozzles. A 40,000 cfm fan at the top of the dome provides the continuous but quiet exhaust that is mandated for safety reasons while the NATR facility is burning gaseous hydrogen fuel during HSR testing.

ACOUSTIC INTEGRITY MAINTAINED DURING FACILITY DESIGN/UPGRADES

- BIRD-RESISTANT HARDWARE CLOTH SCREEN PROTECTS WEDGES WITH MINIMUM ACOUSTIC INTERFERENCE
- ELECTRICAL CONDUIT AND JUNCTION BOXES ARE INSTALLED BEHIND WEDGES
- CUSTOM WEDGED DOORS PROVIDE ACCESS TO ELECTRICAL JUNCTION BOXES
- FACILITY LIGHTING AND VIDEO CAMERA HARDWARE SELECTED FOR LOW FRONTAL AREA
- ACOUSTICALLY UNOBTRUSIVE LIGHTING AND CAMERA INSTALLATIONS ARE RECESSED INTO WEDGES

Acoustic integrity of the facility has been maintained during the ongoing process of new equipment installations and facility modifications by considering each action with regard to its impact on the research quality of the acoustic environment. A good example of this is the recent installation of a bird-resistant hardware cloth screen over the entire interior wedged surface. Facility lighting and video cameras have been selected for low frontal area and are recessed into the wedged interior walls to be acoustically unobtrusive. Electrical conduit and junction boxes were installed behind the wedges, with specially custom-wedged doors for electrical system access. Further facility upgrades and modifications to accommodate new test programs on both PLF and NATR will be accomplished in a similarly acoustically responsible manner.

1999176574

DETERMINATION OF JET NOISE RADIATION PATTERNS AND SOURCE LOCATIONS USING 2-DIMENSIONAL INTENSITY MEASUREMENTS

S.M. Jaeger and C.S. Allen
Sterling Federal Systems
NASA Ames Research Center
Moffett Field, California

S37-71

409579

24P.

Outline

- **Jet Noise extrapolation to far field**
- **Two dimensional sound intensity**
- **Anechoic chamber cold jet test**
- **Results**
  - **Intensity levels**
  - **Vector maps**
  - **Source location centroids**
  - **Directivity**
- **Conclusions**

Jet Noise Extrapolation

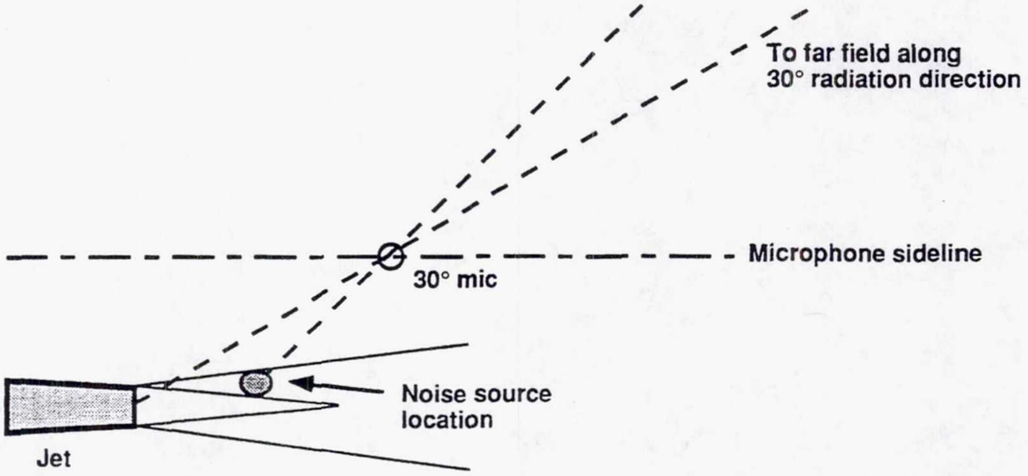

An inaccurate assumption for a noise source location will have an effect on the ability to extrapolate to the far field. In this figure, the sound pressure level seen at a near field microphone is extrapolated to the far field under the assumption that the source lies at the nozzle exit. This result will be in error since the actual source location is downstream. The jet plume will appear as a point source if measurements are made at a far field location. However, in a wind tunnel, it is not always possible to place microphones far enough away from the jet. Therefore it is advantageous to have a method for measuring the correct jet noise radiation pattern.

Extrapolation to Far Field

- Knowledge of sound pressure distribution at far field traverse location
- Knowledge of radiation angles at far field traverse location
- Extend sound along radiation vector to requested observer location assuming spherical spreading

The apparent noise sources and directivities for given frequencies are identified at a far field location along the jet axis. Therefore, the sound level at any observer position can be determined by applying radial spreading and atmospheric attenuation along the path from the noise source through the traverse position.

Sound Intensity Theory

- **Acoustic Intensity is a measure of the net flow of acoustic power per unit area**

P is the acoustic pressure at a point

v is the particle velocity at a point

$$I = \overline{P \cdot v}$$

The acoustic intensity is a vector quantity that describes the net flow of acoustic power that passes through a unit area. Sound intensity can also be defined as the time-averaged product of the acoustic pressure and the particle velocity at a given point.

Sound Intensity Theory (continued)

- Acoustic particle velocity is obtained with a finite difference approximation

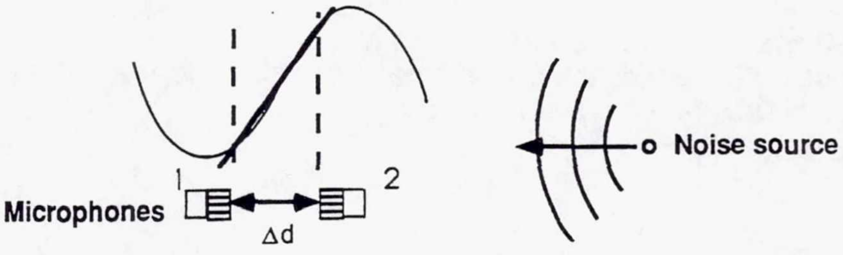

$$v_n = -\frac{1}{\rho}\int \frac{P_2 - P_1}{\Delta d}\,dt$$

- The units of sound intensity are dB (ref. 1 x 10^{-12} Watts/square meter)
- For a perfect point source in a free-field environment, the sound pressure level in dB (L_P) is equivalent to the sound intensity level in dB (L_I)

Two phase-matched pressure microphones separated by a known distance can measure sound intensity. The acoustic particle velocity is measured indirectly by applying a finite difference approximation to the pressures measured at each microphone.

Sound intensity is measured in decibels referenced to 1.0 picoWatts per square meter. The units of sound pressure level and sound intensity level are defined such that a perfect radial source in a free-field environment will have equivalent sound pressure and sound intensity levels.

Sound Intensity Theory (continued)

- Acoustic Intensity can be measured in the frequency domain using the cross-spectrum between the two microphones (G_{12})

  Where,

$$I(f) = \frac{\mathrm{Im}[G_{12}(f)]}{2\pi f \rho \Delta d}$$

- With four in-plane microphones the components of sound intensity in two directions can be measured

Each component of the sound intensity at a given frequency is obtained in the frequency domain from the cross-spectra between two microphones. Four in-plane microphones can measure the x- and y- components of the total sound intensity in the plane. The angle between the x- and y- components is taken to be the angle of incidence of the sound intensity at the probe center. A computer program controls the analyzer which measures the cross-spectrum for each microphone pair, adjusts the result for microphone phase differences and determines the sound intensity.

TWO-DIMENSIONAL SOUND INTENSITY PROBE

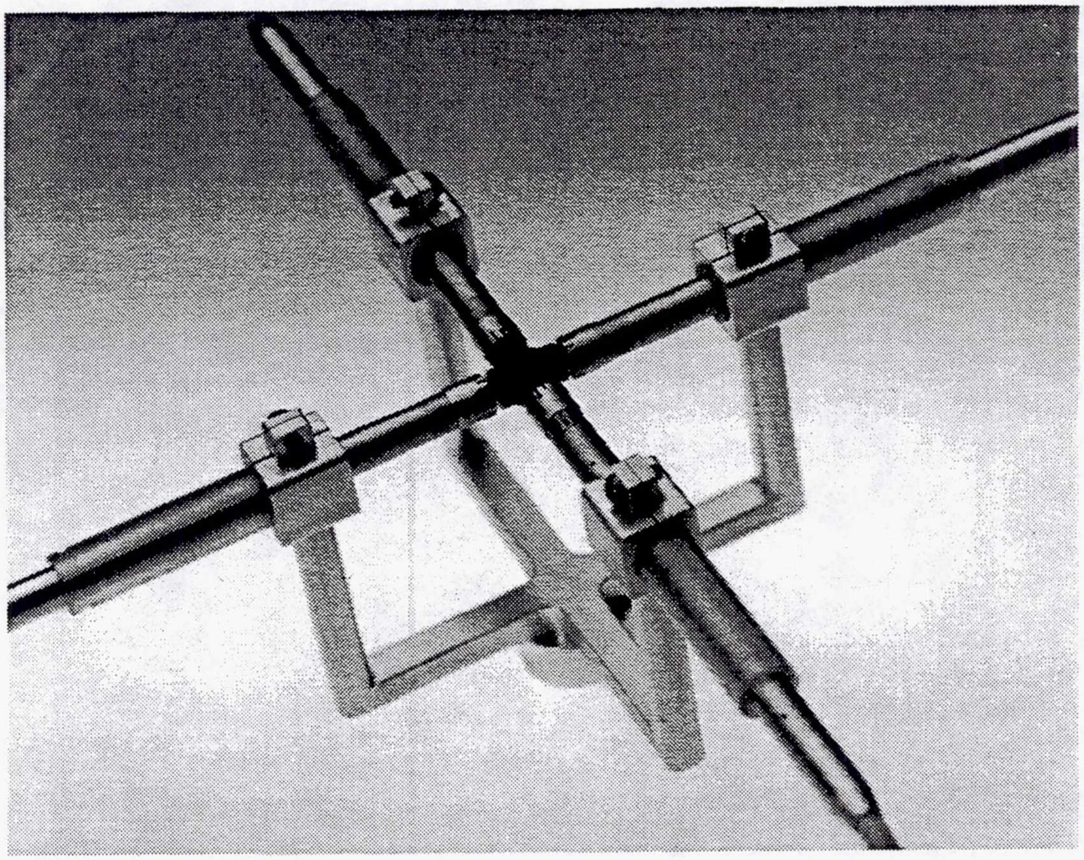

The probe holds four 1/4" microphones in a face to face arrangement. A 12 mm spacer separates each microphone pair. The separation distance between the microphones sets the frequency range at 150 Hz to 5000 Hz.

SOUND INTENSITY PROBE IN ANECHOIC CHAMBER

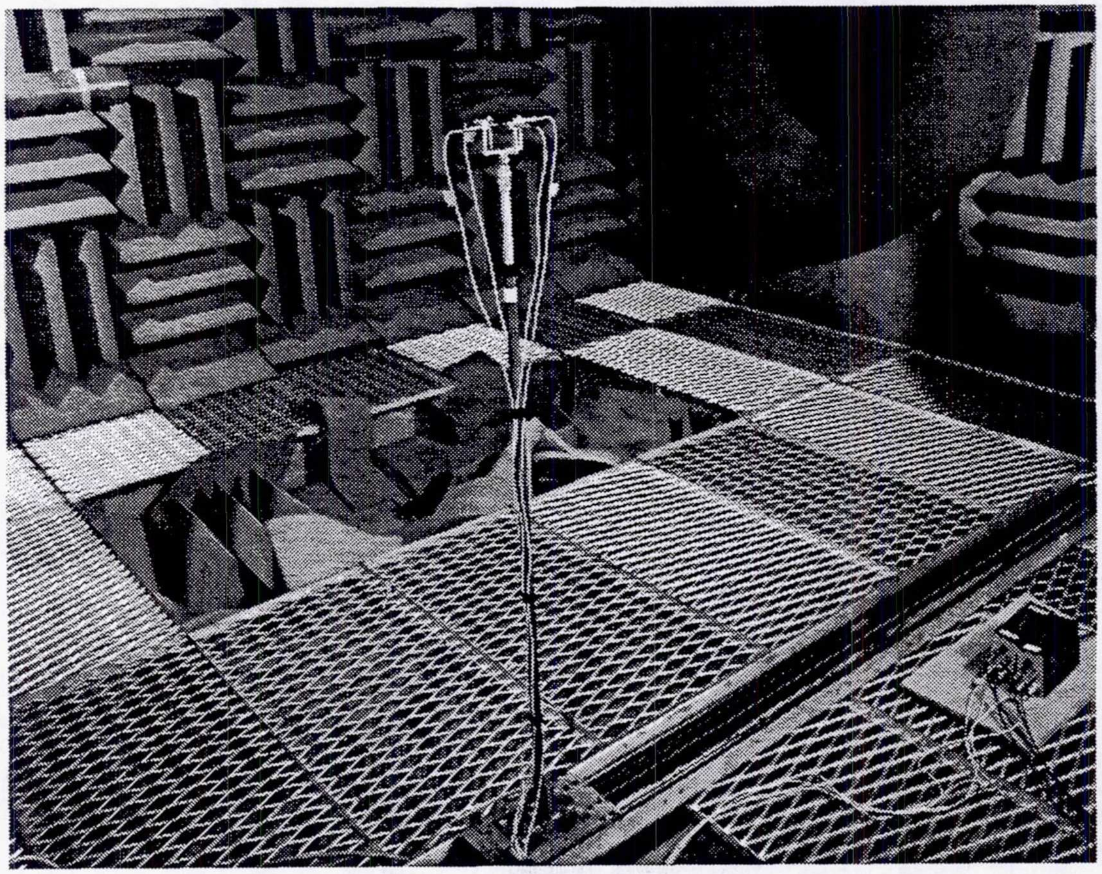

The 4" jet nozzle is in the left background of the photo. The probe was mounted at the level of the jet centerline on a traverse which could be operated during the test to move the probe parallel to the jet centerline.

NASA AMES ANECHOIC CHAMBER

Plan View of Anechoic Chamber

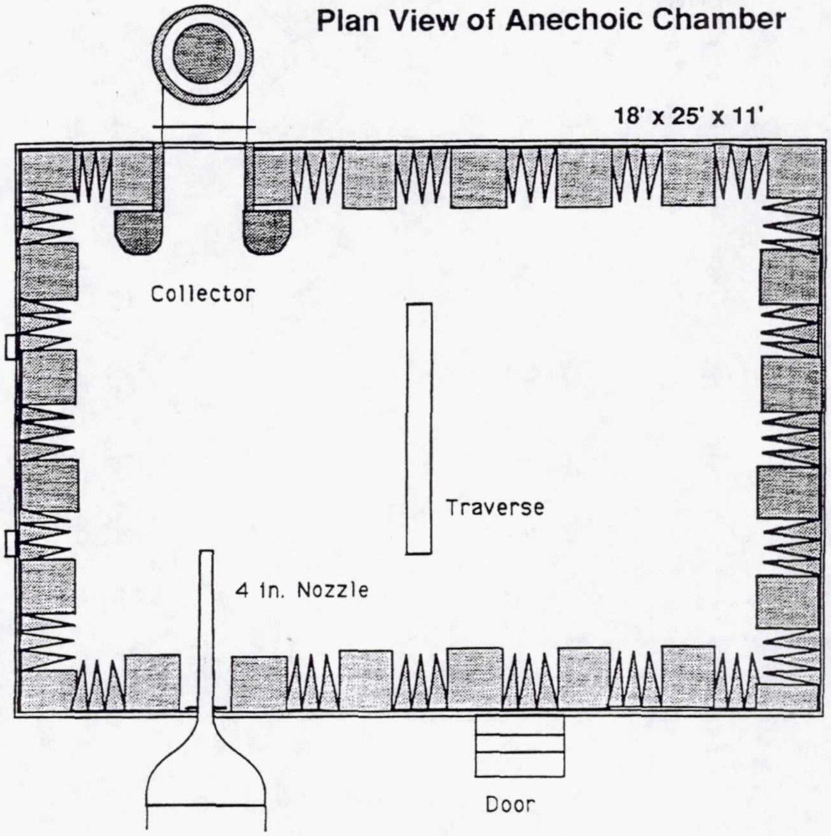

The chamber is anechoic for all frequencies above 150 Hz. A compressor, powered by two 400 HP electric motors forces air through the chamber jet's 4" nozzle. The jet is capable of reaching velocities up to Mach 0.8. The traverse motor control and data acquisition is in done in the acoustics lab next to the chamber.

Anechoic Chamber Jet and Traverse Positions

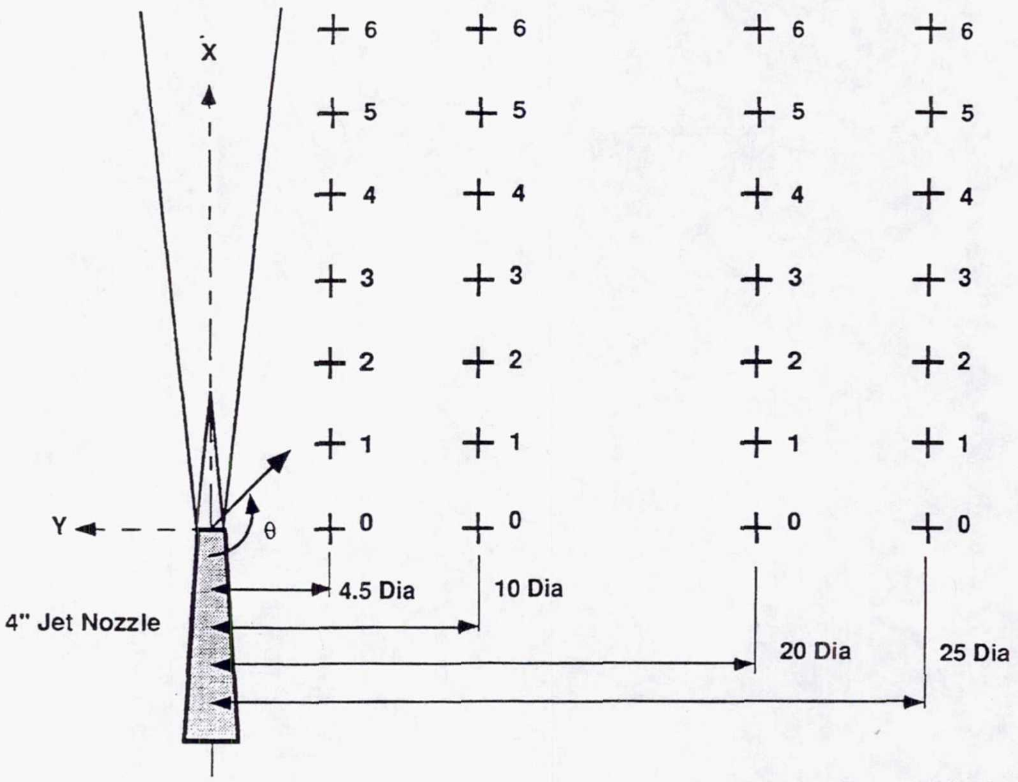

Scale: 3/4"=1'

The angle of intensity incidence was referenced to the jet exit plane and the jet centerline where 180● was downstream along the x-axis and 90● in the -y direction. The motorized traverse moved the intensity probe parallel to the jet axis. The traverse was placed at four parallel positions relative to the jet centerline: (y = -17 3/4", -39 1/4", -79" and -104").

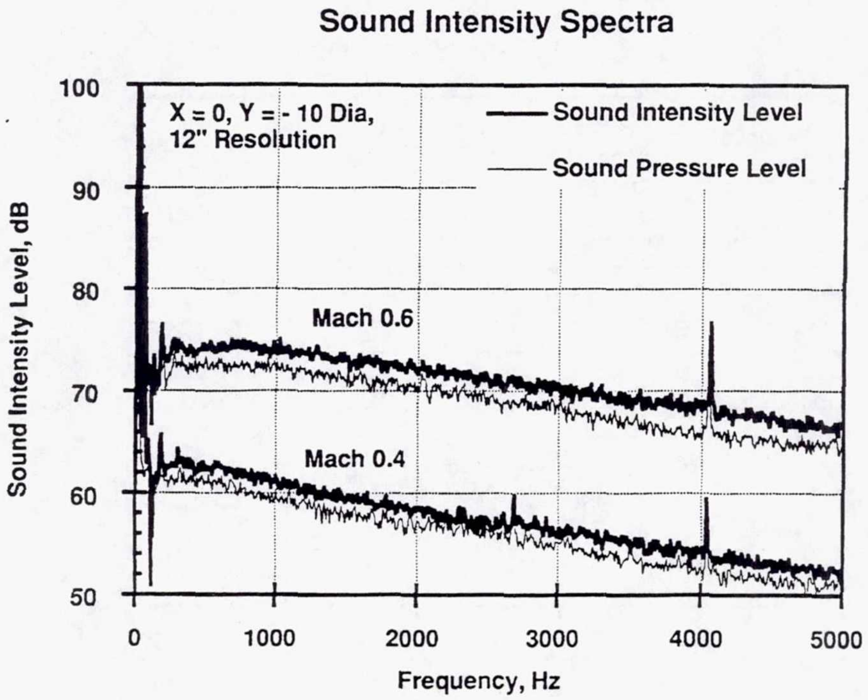

Sound Intensity Spectra

The figure shows typical sound intensity spectra for Mach 0.4 and Mach 0.6. This is the vectorally combined sound intensity of the x- and y- components. The results are typical for jet noise, where most of the noise is concentrated at low frequencies and then rolls off at higher frequencies. Note that below 200 Hz, the sound intensity becomes unreliable. The spikes are harmonics of the blower frequency. Also shown is the sound pressure level taken from one of the four microphones. The difference in levels between the sound intensity and the sound pressure is attributed to the distributed nature of the jet noise sources.

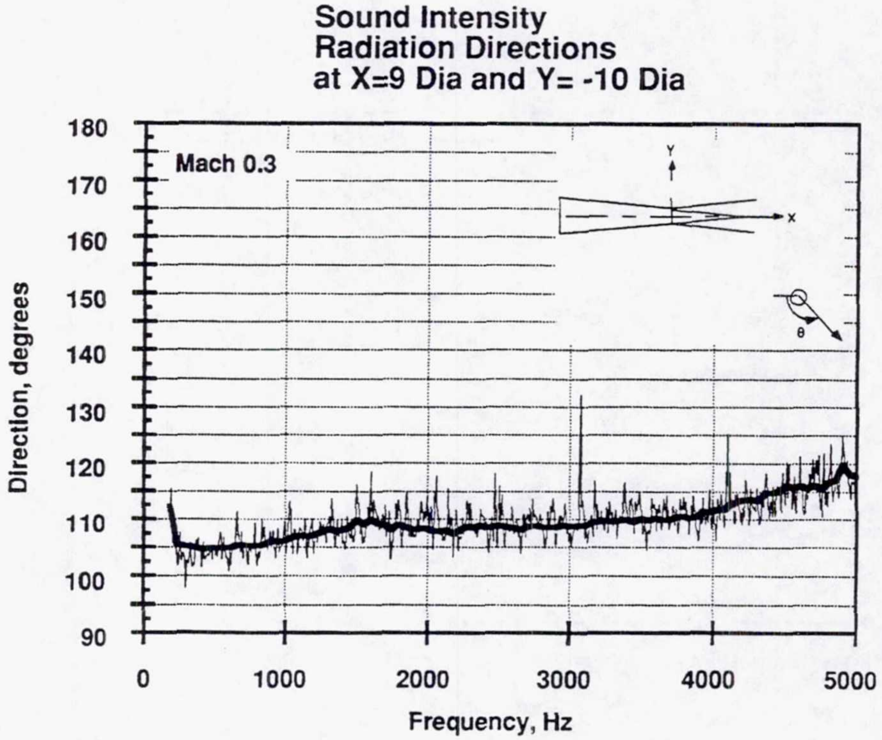

This figure shows sound intensity direction vs.. frequency for Mach 0.3. The traverse is at Y = -39 1/4" (10 jet diameters) from the jet centerline. The intensity probe is at X = 36" (9 jet diameters) from the nozzle exit. For this case with 150 time averages, the random error spread is about 5●. The results can be improved by using a curve fit as shown by the solid line. These results indicate that lower frequencies sources appear to emanate at smaller angles from the jet centerline, suggesting that they lie further downstream than higher frequencies sources. The peaks are harmonics of the blower frequency. They point toward the nozzle exit.

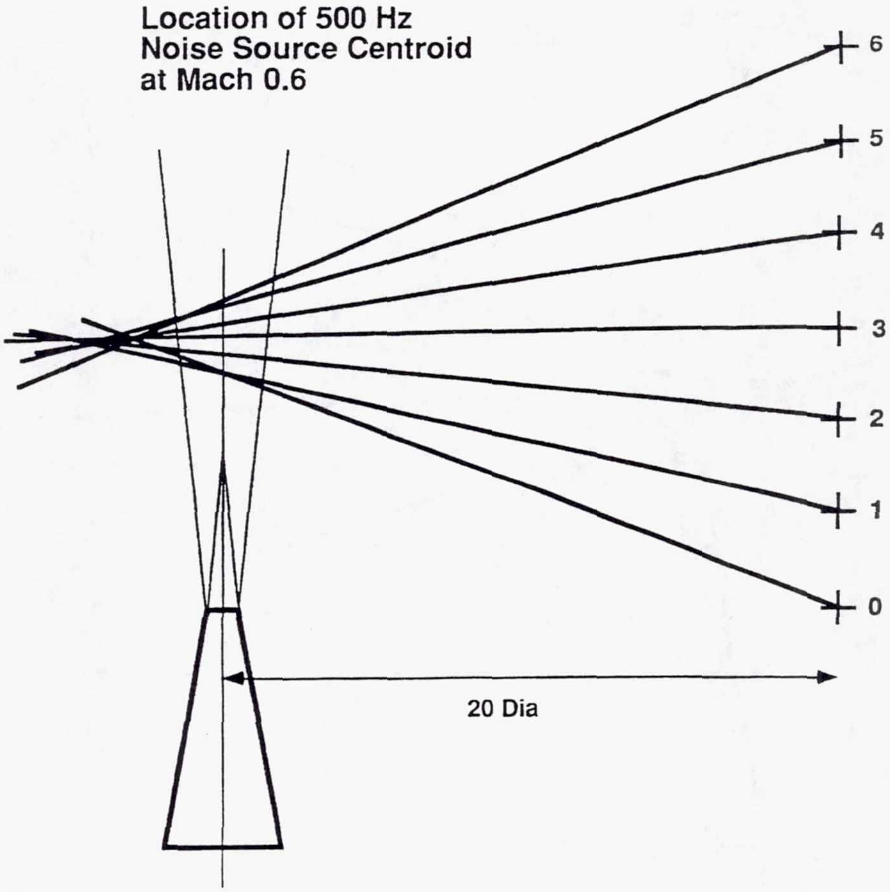

This figure shows the sound radiation pattern for 500 Hz at a Mach number of 0.6. These radiation directions are measured with the probe at 20 jet diameters from the jet centerline. The lines appear to coalesce on the opposite side of the jet plume. This is attributed to the fact that the noise source for this particular frequency is distributed over a finite region in the plume. The ability of the sound intensity probe to locate a noise source was tested by successfully locating a speaker mounted at various locations in the anechoic chamber.

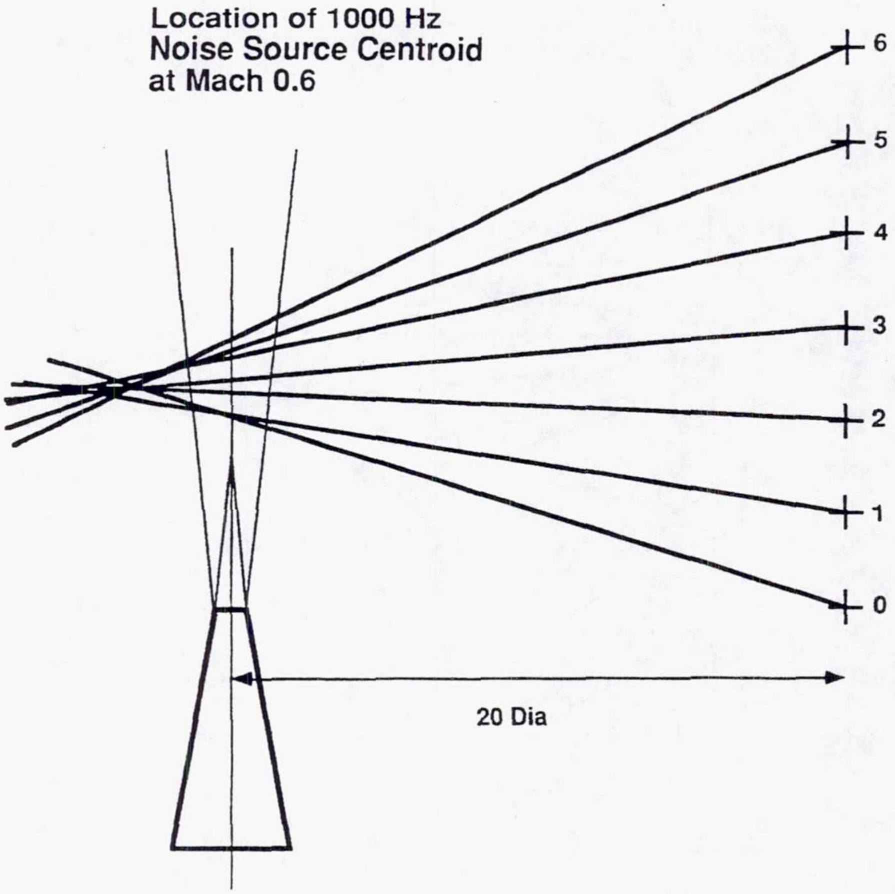

This figure shows the sound radiation pattern for 1000 Hz at a Mach number of 0.6. Note that the source centroid is closer to the jet nozzle exit than the 500 Hz noise source.

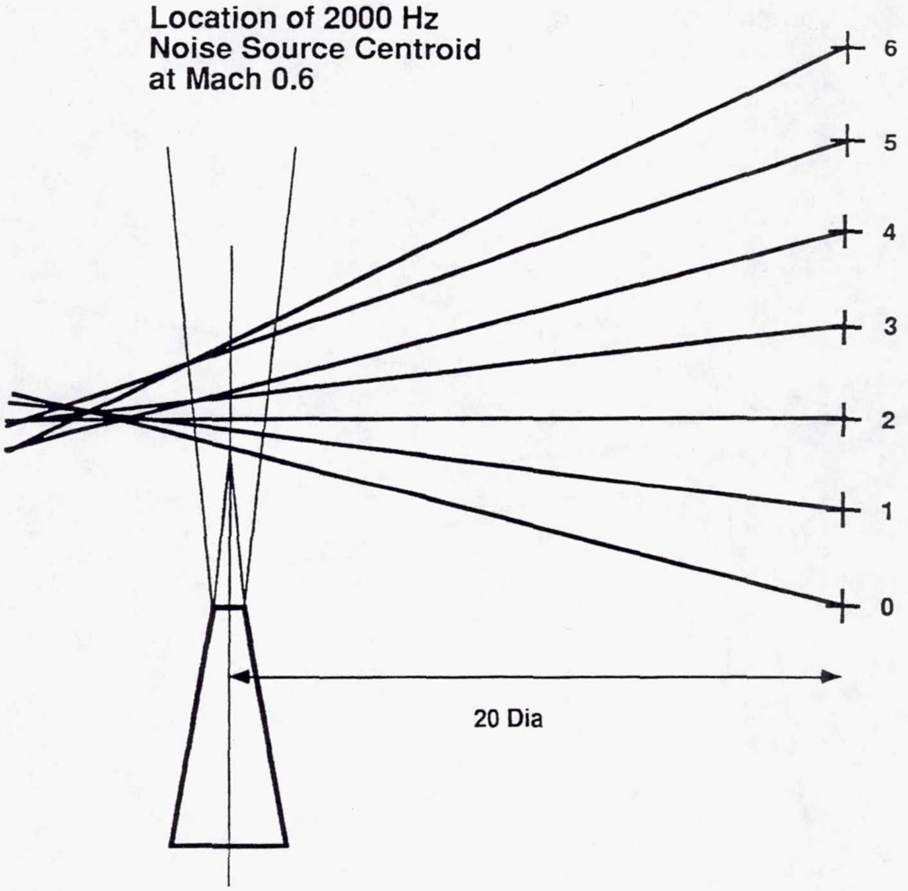

This figure shows the sound radiation pattern for 2000 Hz at a Mach number of 0.6.

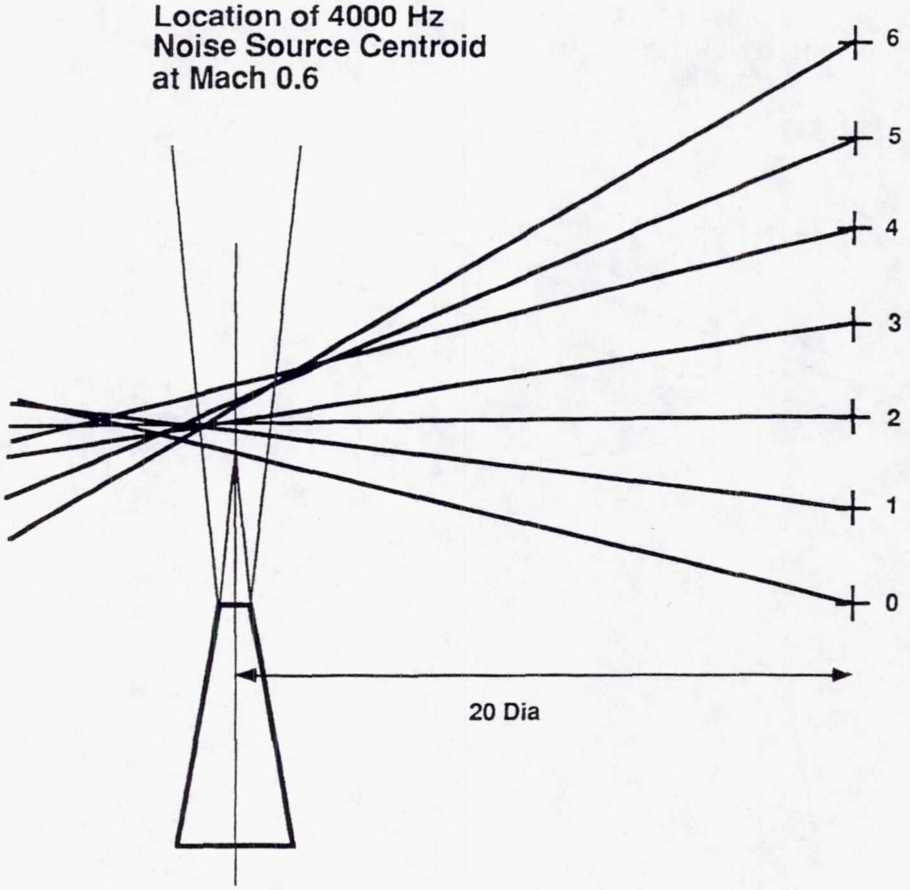

This figure shows the sound radiation pattern for 4000 Hz at a Mach number of 0.6.

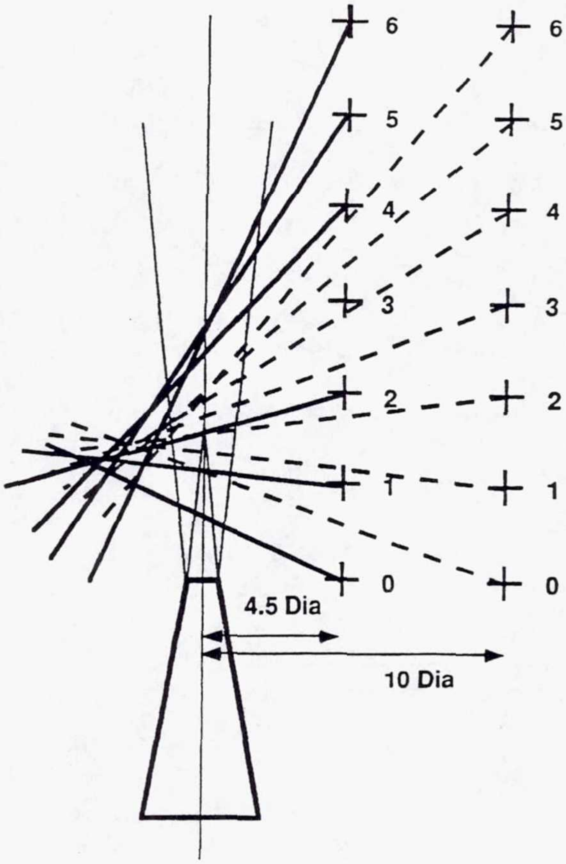

Location of 1000 Hz Noise Source Centroid at Mach 0.3 as Seen From Near Field

For each position along the traverse the radiation vector for 1000 Hz at Mach 0.3 is shown. The traverse was positioned at two near field location of y = -17 3/4" and -39 1/4". Note that the source position changes with traverse position. This indicates that near field effects distort the apparent location of the source centroid.

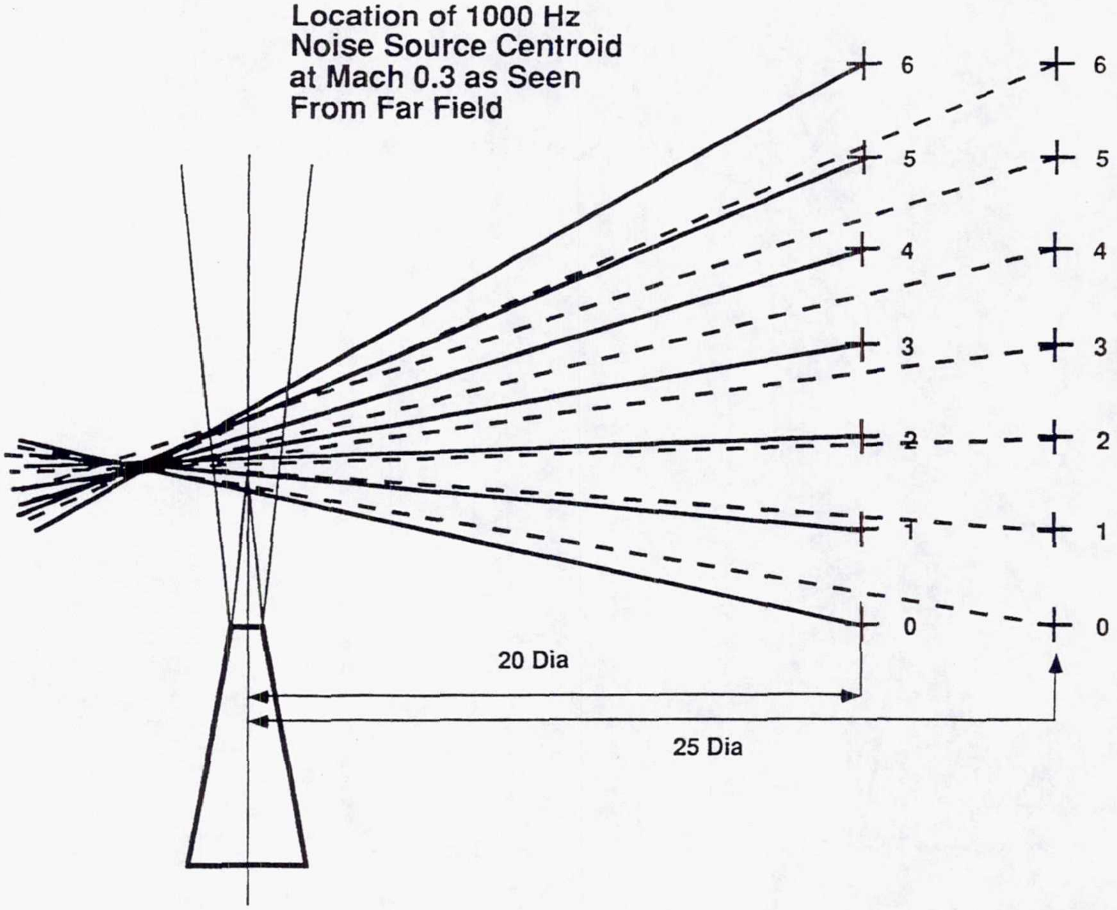

The radiation directions for 1000 Hz at Mach 0.3 are shown at two far field positions. The traverse locations are y = -79" and 104". Note that the Location of the jet source still appears to emanate from beyond the jet core. The source centroids appear at the same location for both traverse positions, indicating that near field effects are no longer an influence.

Peak Radiation Directions
for Mach 0.6

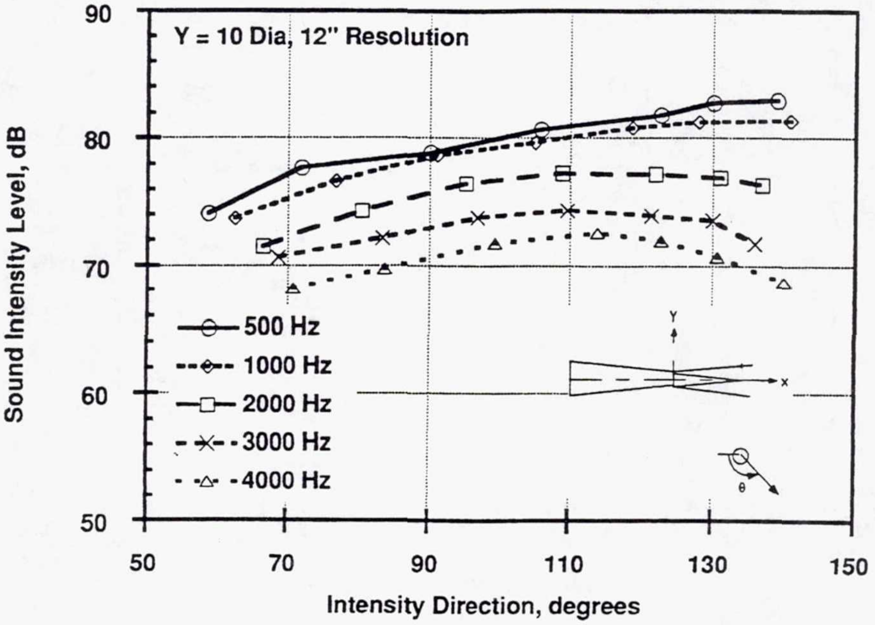

The figure shows sound intensity levels vs.. direction at each frequency for Mach 0.6. The traverse is about 10 nozzle diameters from the jet centerline. At 500 Hz the maximum level recorded of about 83 dB is found at almost 140° from the jet centerline while the maximum level for 4000 Hz is 72 dB at 113°.

Effect of Strouhal Number on
Noise Source Centroid Locations

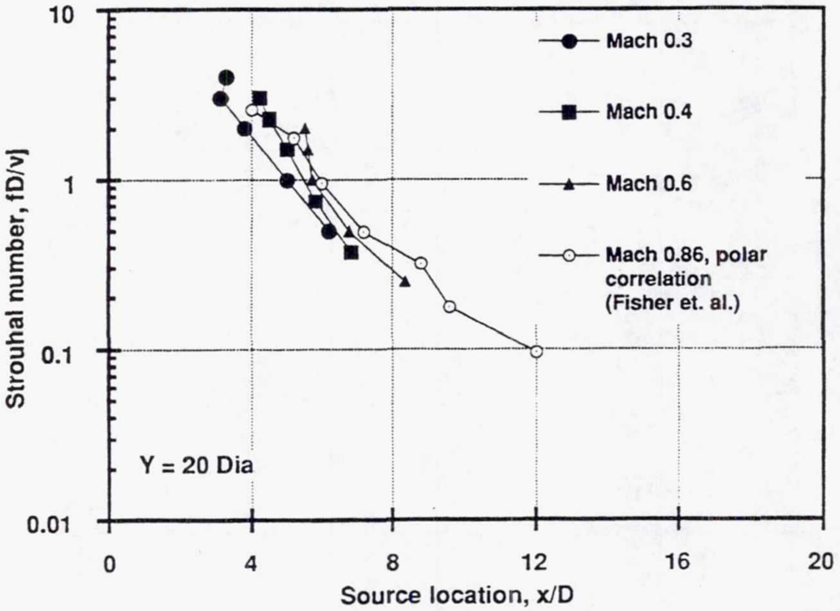

Strouhal number is plotted with each corresponding source location. The traverse is 20 jet diameters from the jet centerline. Note that each Mach number collapses at near the same source locations. For comparison, results obtained by Fisher et. al. for a 25 mm jet at Mach 0.86 are shown. The source locations for the 0.86 case were obtained using polar correlation.

Disadvantages of Sound Intensity

- **Broad frequency range requires multiple spacings (150 - 5000 Hz with 12 mm spacer)**
- **Intensity probe, at present, can only work with no flow over the probe**
- **Requires precise phase calibration**

The separation distance between the microphones of the sound intensity probe limits the frequency range. By using several different separation distances, the frequency range can be expanded. The application of a finite difference approximation requires that there is no ambient flow over the probe. Finally, sound intensity measurements require careful phase calibrations to obtain phase-matched microphones.

Advantages of Sound Intensity

- **Can find centroid of apparent noise sources**
- **Can find sound intensity specifically for each frequency**
- **Can build sound field map about sources**
- **Does not require an anechoic environment**

A sound intensity probe can readily locate noise source centroids. Also, using a cross-spectrum, sound intensity can be found directly in the frequency domain. A sound intensity map can be used to describe the radiation characteristics of sources. And because of the vector characteristics of sound intensity, an anechoic environment is not necessary for most sound intensity measurements.

Conclusions

- **Two Dimensional Intensity is useful for finding jet noise radiation patterns**
- **Knowledge of radiation patterns and far field intensity levels can be extrapolated to any observer location**
- **Increased time averages and increased resolution can improve radiation angle accuracy**

Measurements of sound intensity at different locations in the vicinity of a jet can identify the radiation characteristics of the jet noise sources. A measured sound intensity levels can then be extrapolated along a known radiation direction to a given far field location assuming spherical spreading and applying the appropriate atmospheric attenuation.

1999176575

DETERMINATION OF JET NOISE SOURCE LOCATIONS USING A DUAL SIDELINE CROSS-CORRELATION/SPECTRUM TECHNIQUE

C.S. Allen and S.M. Jaeger
Sterling Federal Systems
NASA Ames Research Center
Moffett Field, California

S38-71

409581

26P.

OUTLINE

- **Problem**
- **Experimental Set Up**
- **Technique**
- **Results**
- **Discussion**
- **Conclusions**

The above is a basic outline of the presentation.

PROBLEM

Extrapolation of Jet Noise to Far Field Requires

1. **Source Locations**
2. **Radiation Pattern**
3. **Sound Pressure Level (Lp) Distribution**

1 and 2 Are Not Obtainable from a Single Microphone Measurement

The goal of our efforts is to extrapolate nearfield jet noise measurements to the geometric far field where the jet noise sources appear to radiate from a single point. To accomplish this, information about the location of noise sources in the jet plume, the radiation patterns of the noise sources and the sound pressure level distribution of the radiated field must be obtained. Since source locations and radiation patterns can not be found with simple single microphone measurements, a more complicated method must be used.

Cross-correlation/Spectrum Technique

- Uses Correlation Coefficient and Coherence to
  - Determine Jet Radiation Field
  - Find Source Locations
- Information May Be Extrapolated To Far Field
- Can Theoretically Be Used In Wind

The dual sideline cross-correlation/spectrum technique uses the correlation coefficient and coherence functions to determine a jet plumes radiated acoustic field and source centroid locations. This information can then be extrapolated to the extreme far field with accurate results. The reason for investigating this technique is its applicability to measurements in flow.

SOUND INTENSITY

- Directly Measures
  - Radiation Angle
  - Lp
- Source Location Easy to Obtain
- Frequency Limited
- Wind Velocity Not Allowed

Another method of obtaining the necessary information is sound intensity. This method directly provides the radiation angle and sound pressure level that describes the entire acoustic field. Source centroid locations are also easily obtainable with this method. However, sound intensity is frequency limited with a given microphone spacing, but more importantly, is difficult to implement in a moving acoustic medium. Since one of the major goals of the High Speed Research Program (HSRP) is to determine the radiated acoustics of suppressor nozzle configurations with forward flight, another method must be developed for this case.

DEFINITIONS

Correlation Coefficient

$$\rho^2_{xy}(\tau)=\frac{R_{xy}(\tau)^2}{R_{xx}(0)R_{yy}(0)}$$

Coherence

$$\gamma^2_{xy}(f)=\frac{\left|G_{xy}(f)\right|^2}{G_{xx}(f)G_{yy}(f)}$$

The method investigated during this study is based on the correlation coefficient and coherence functions of two signals x and y. These functions are defined on the opposite page. The square of the correlation coefficient is defined as the square of the cross-correlation normalized by the product of the two autocorrelations evaluated at a time delay, *t*, of 0. The square of the coherence is defined as the square of the absolute value of the cross-spectrum normalized by the product of the two autospectrums. Note that these two functions contain the same information as they are related to each other by the Fourier Transform. Where the cross-correlation coefficient is a function of time delay, the coherence is a function of frequency, *f*.

Both of the coefficients are obtained by normalizing a function by the highest possible value, theoretically, of that function. This implies that a perfect correlation would have a correlation coefficient value of 1. A value of 1 also indicates a perfect coherence.

MICROPHONE LOCATIONS
Cross-correlation/Cross-spectrum Method

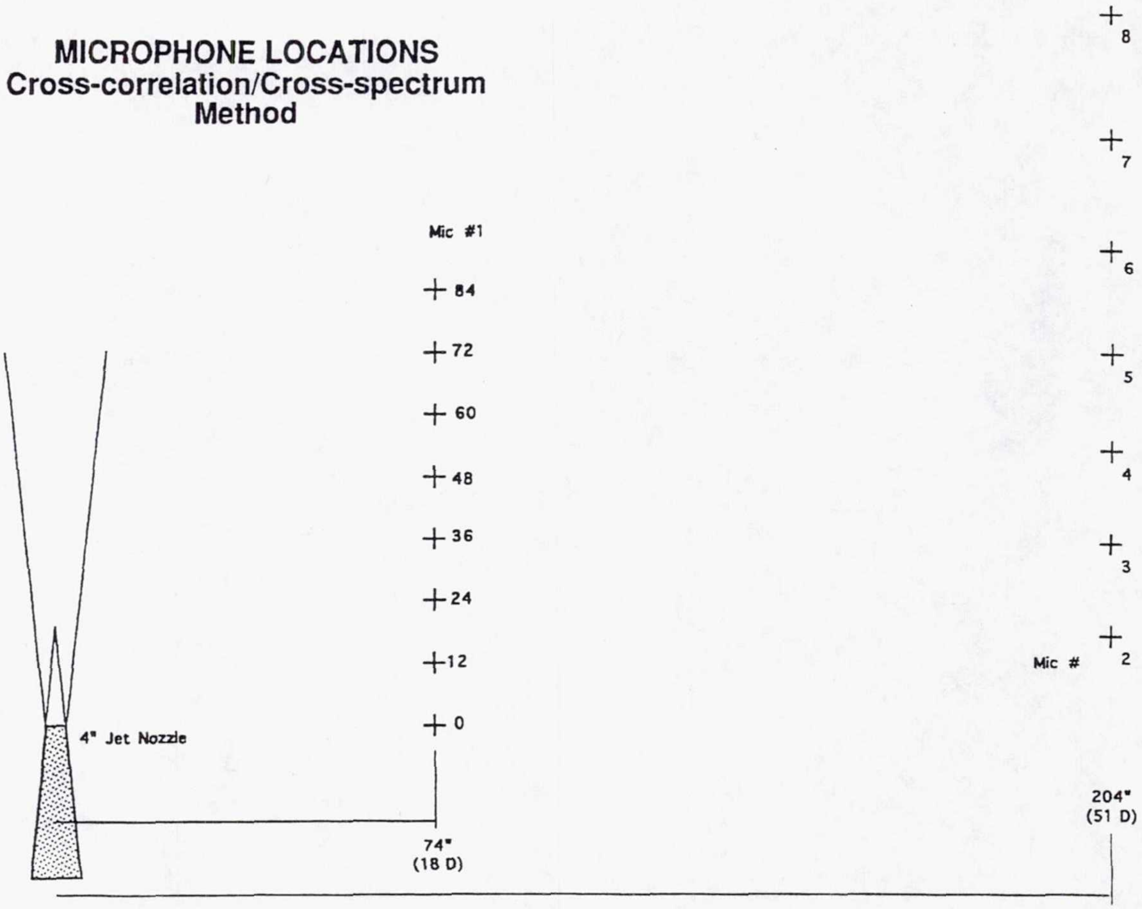

This diagram shows the microphone locations used in the anechoic chamber experiment. The 4 inch conical nozzle was used at Mach numbers up to 0.6 to simulate a jet nozzle. Microphone #1 was traversed to 8 positions along the close sideline which was located 74 in. from the axis of symmetry of the nozzle. The stations of Mic. #1 are given as the axial locations in inches downstream of the nozzle exit plane.

There were 7 stationary microphones located along the far sideline which was located 204 in. from the axis of symmetry of the nozzle. The stationary microphone positions are denoted by microphone numbers 2- 8. The stationary positions correspond to radiation angles every 5 degrees from 95 to 125 deg., centered at nozzle centroid where 0 deg. points directly upstream. All microphone locations lie in the same plane as the horizontal plane of symmetry of the jet.

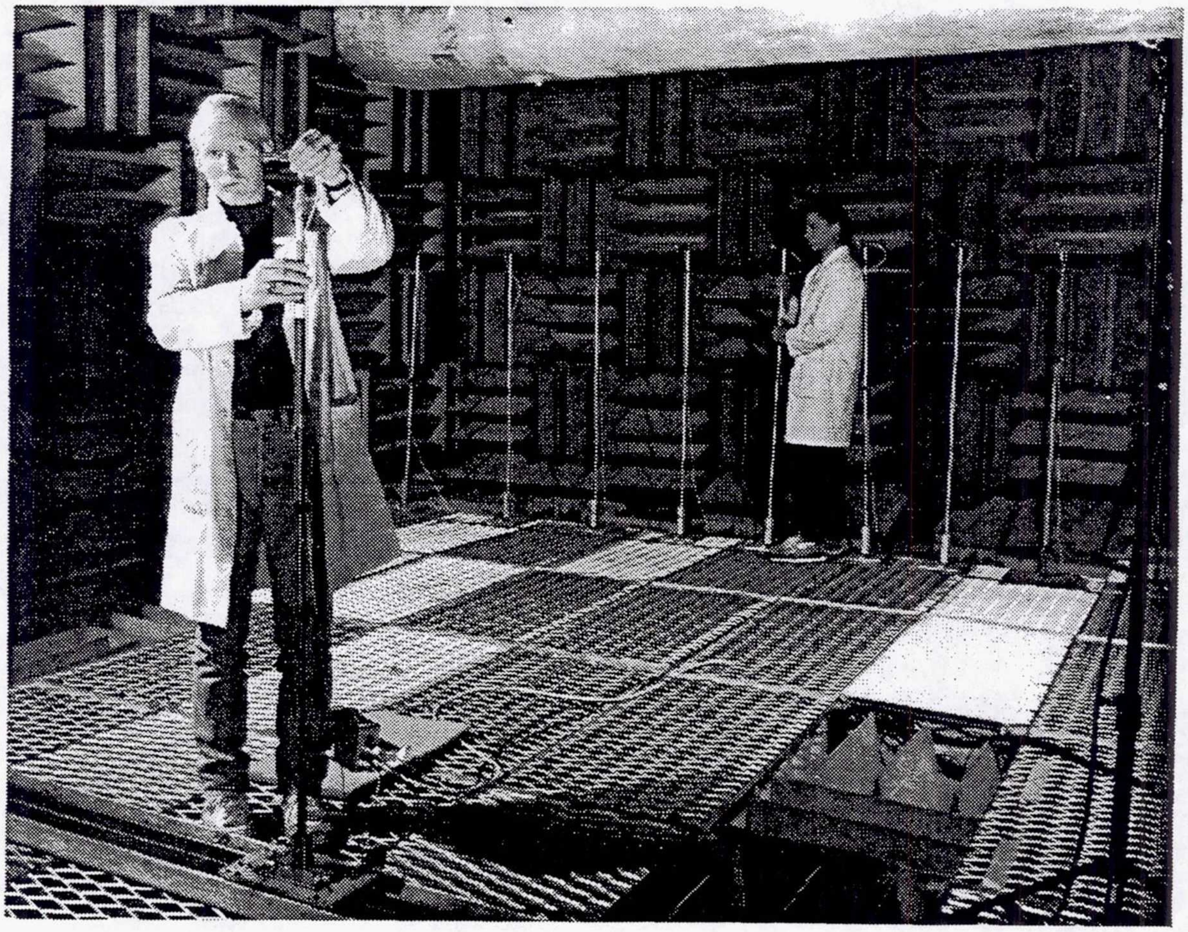

This photograph shows the experimental set up. The nozzle in the forefront is at the top of the picture, Mic. #1 mounted on the traverse is on the left and the far sideline microphones are in the background of the picture.

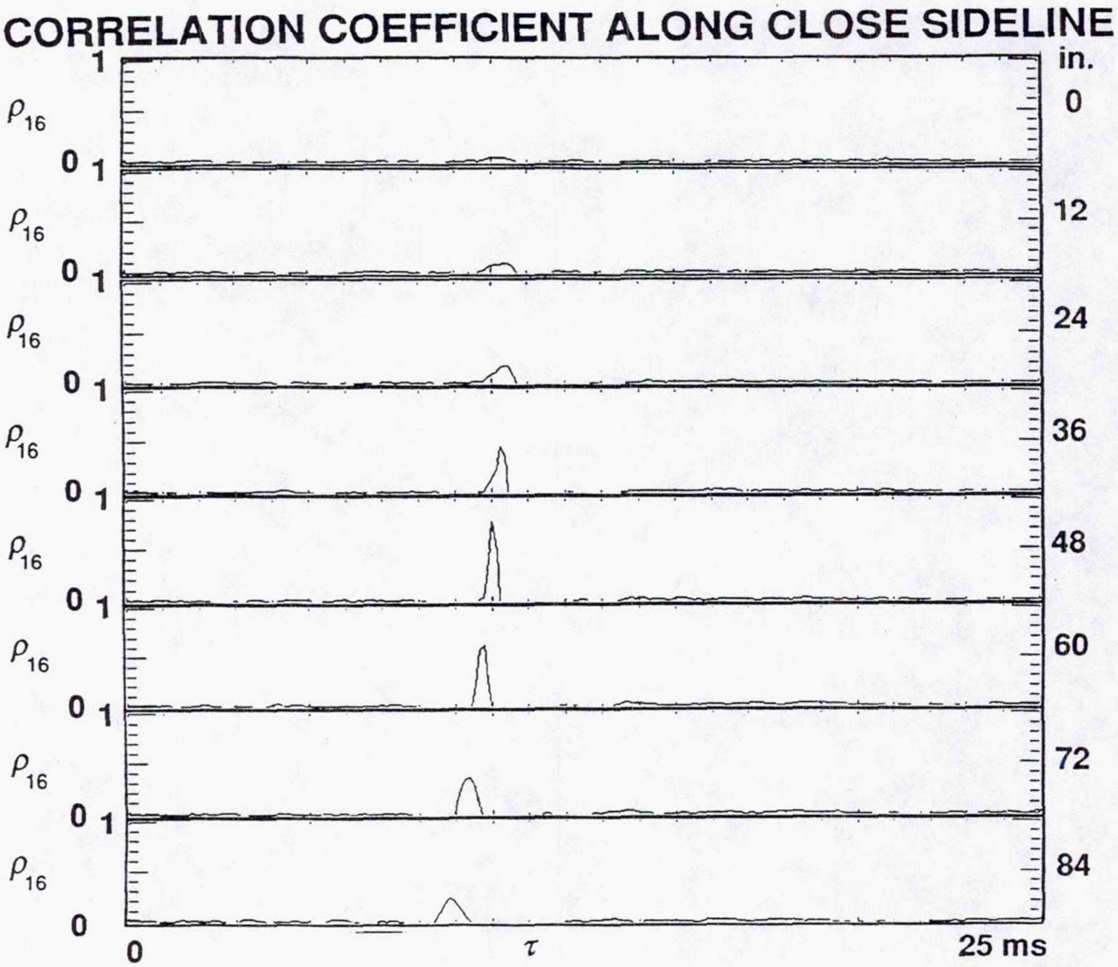

The data were reduced by comparing correlation coefficients of a far sideline microphone correlated to Mic. #1 at each of the positions along the close sideline. The resulting correlation coefficient plots for Mic. #6 are shown on the opposite page. Note that the value of the maximum correlation coefficient of each graph increases to a maximum and then decreases as the correlation procedure moves along the close sideline. This procedure was repeated for each far sideline microphone position.

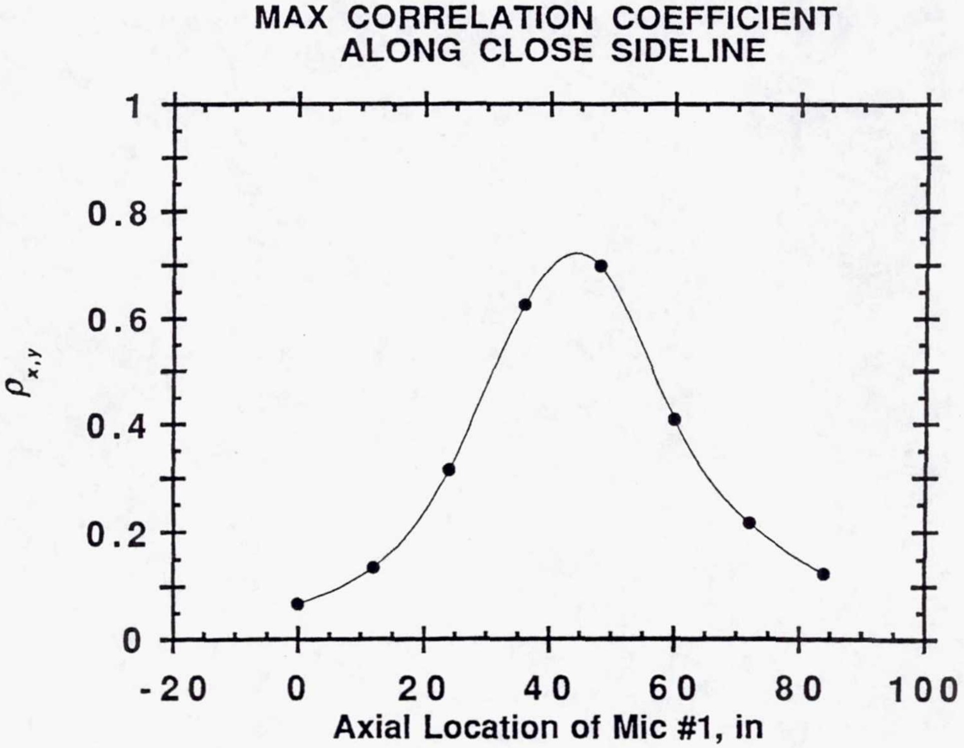

Plotting the maximum correlation coefficient of each cross-correlation of a far sideline microphone against the close sideline microphone location shows where most of the acoustic energy radiated from. A cubic spline curve fit is used to increase the accuracy of the maximum correlation coefficient location.

ONE RADIATION ANGLE
Cross-correlation/Cross-spectrum Method

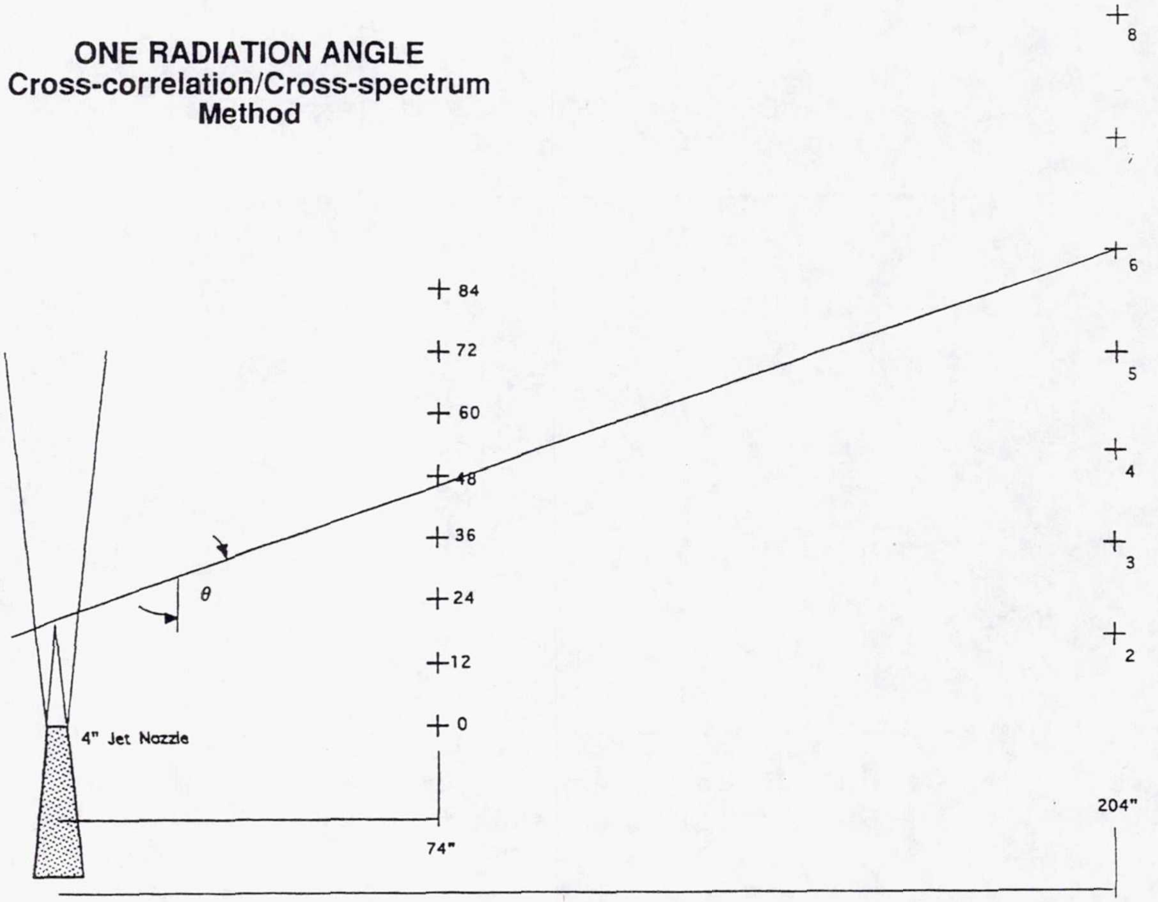

The radiation angle is drawn from the far sideline microphone position through the location of the maximum correlation coefficient given by the curve fit along the close sideline and extending through the jet plume. The intersection of the radiation line and the jet plume gives the approximate location of the centroid of sources radiating in the specified direction.

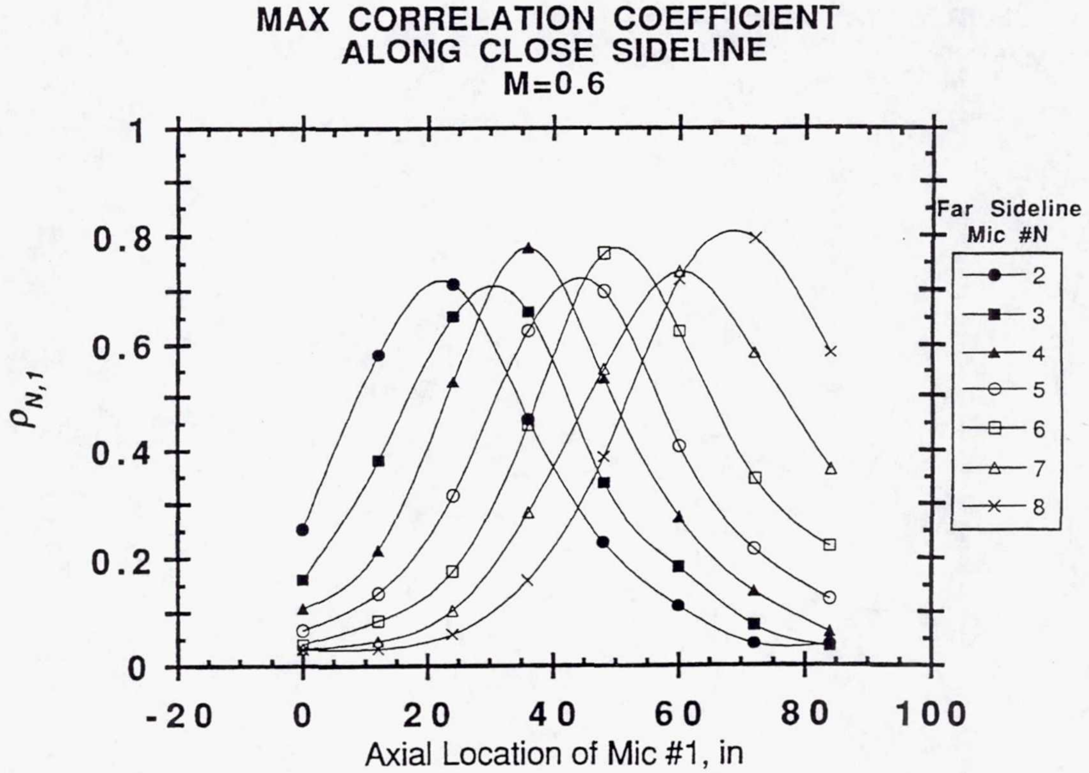

The maximum correlation coefficients for each far sideline microphone location are plotted against close sideline microphone location to determine the radiation angle for each far sideline microphone position.

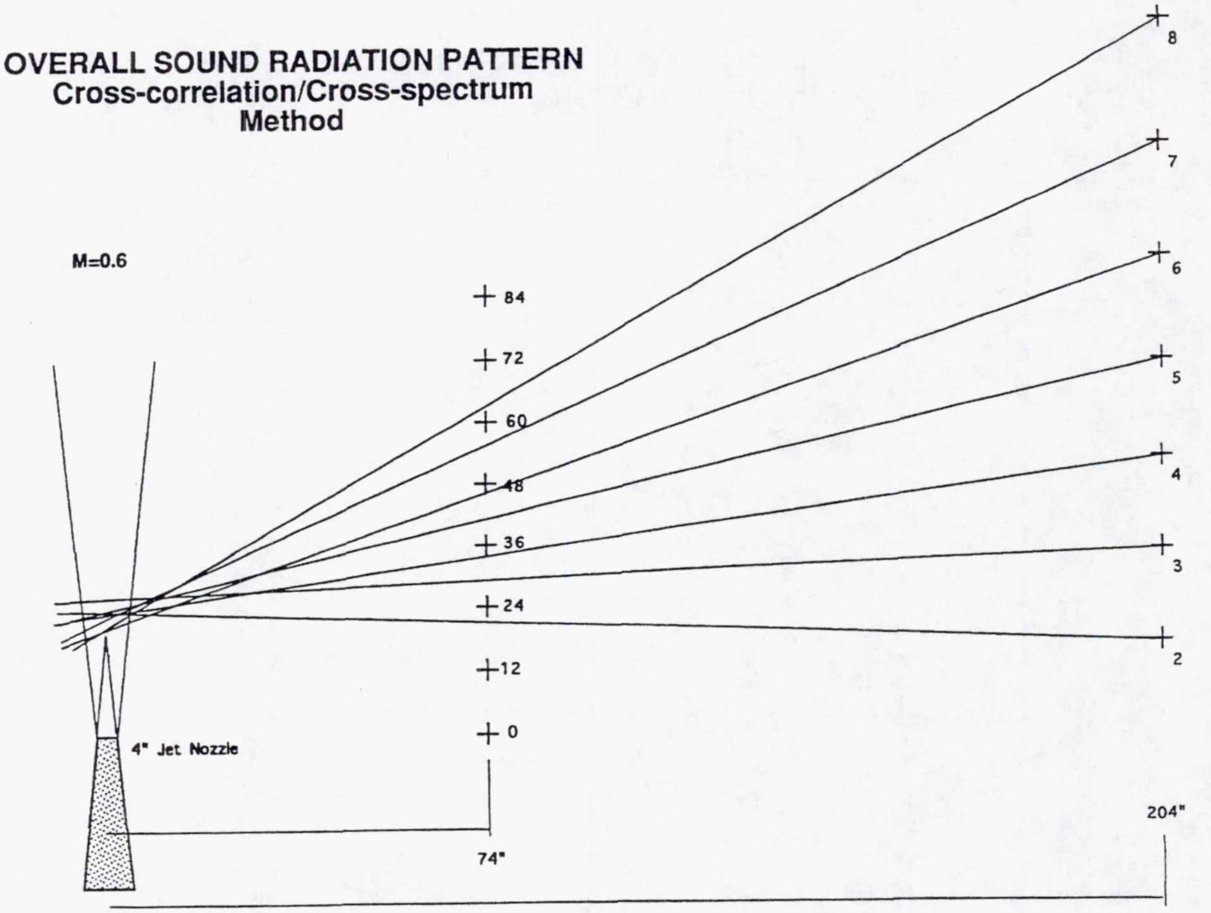

OVERALL SOUND RADIATION PATTERN
Cross-correlation/Cross-spectrum
Method

Drawing all of the radiation angles gives the radiation pattern of the jet plume for the given conditions. Note that since the correlation coefficient contains information over the entire frequency span, the resulting radiation pattern is valid for the overall noise only. To obtain frequency dependant radiation patterns, it is necessary to consider the coherence function of the different microphones.

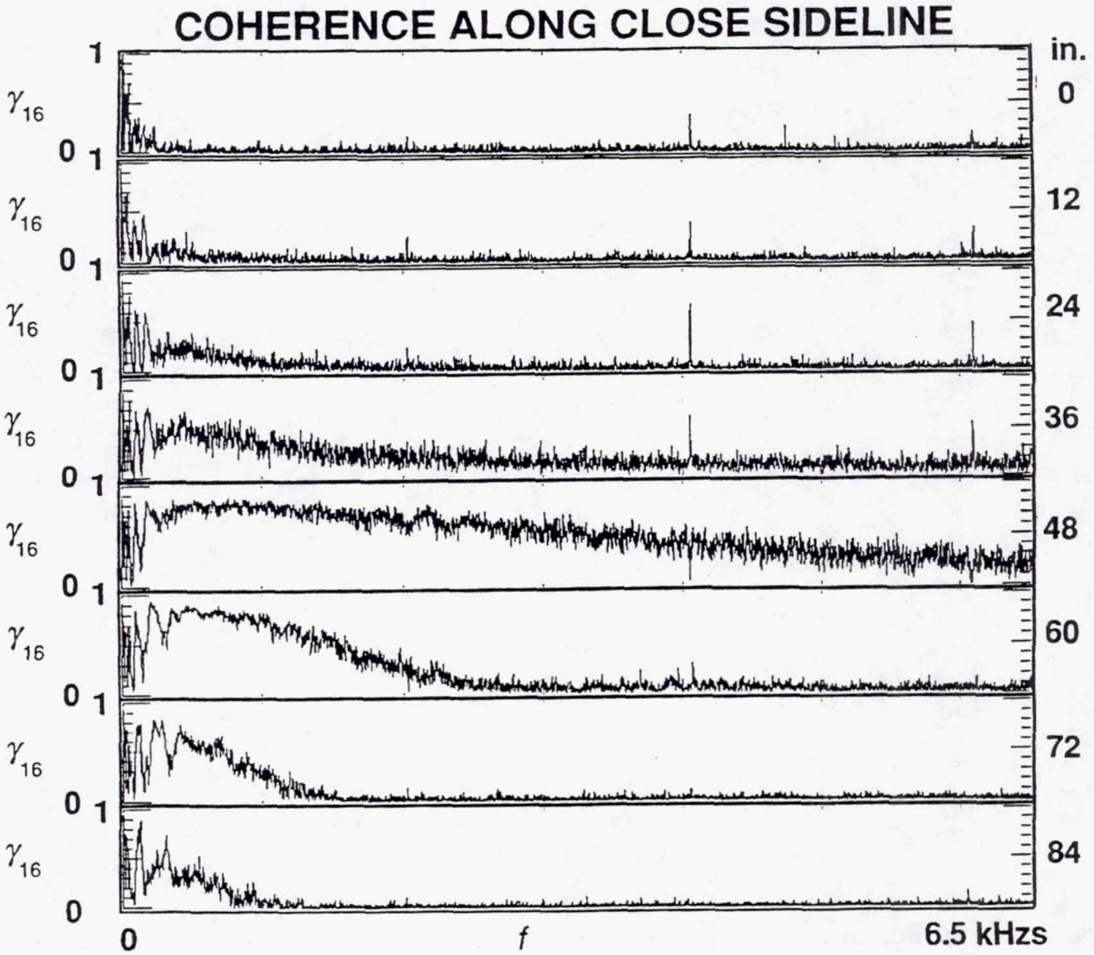

In the same manner as the correlation coefficients were obtained, the coherence is measured. These plots show the coherence of Mic. #6 with Mic. #1 at each of the close sideline locations. Again, this information is obtained for each far sideline microphone. To find the radiation angle as a function frequency, the coherence values of each graph at the desired frequency are plotted against the close sideline location.

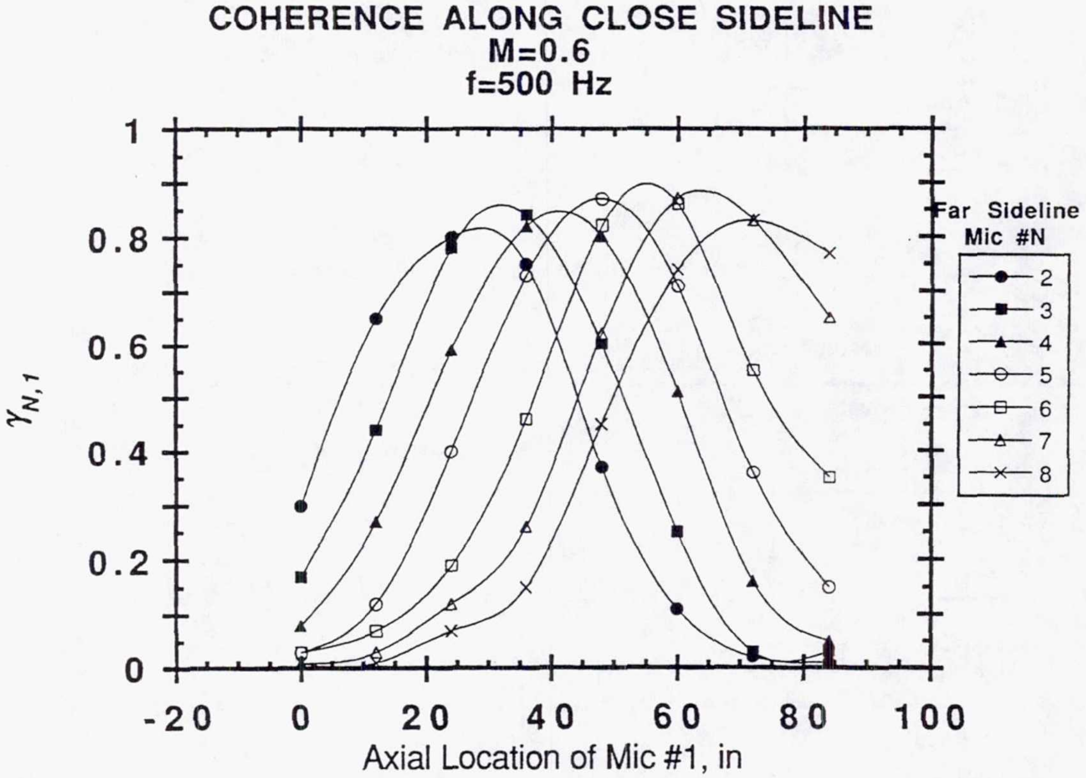

This plot shows how the maximum coherence value along the sideline is found. Again, the data were fit with a cubic spline to increase the accuracy of the determination. This plot is for a jet Mach number of 0.6 and a frequency of 500 Hz.

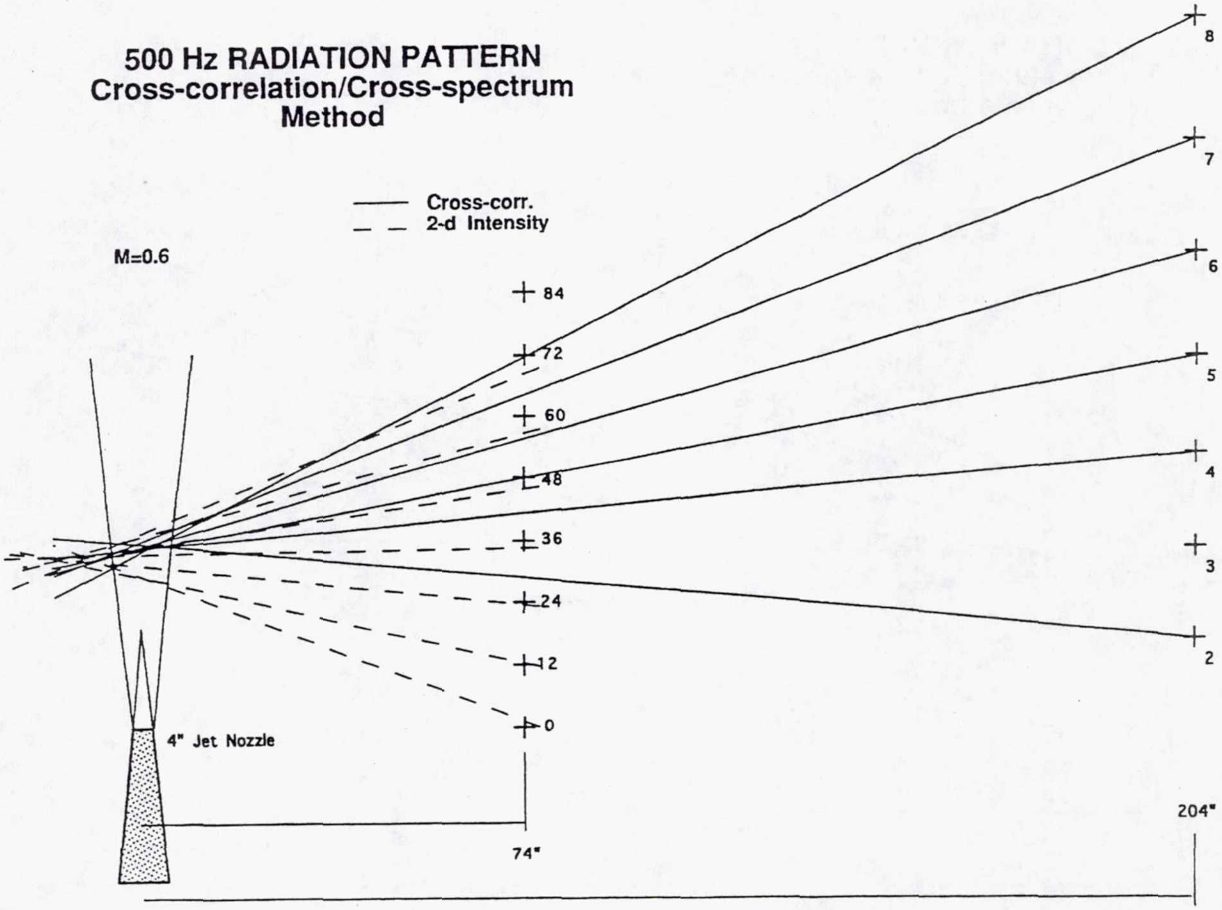

This figure shows the radiation pattern given by the method for a Mach number of 0.6 and a frequency of 500 Hz. Also shown in dashed lines is the radiation pattern found using the 2-d intensity technique for the same conditions and frequency. Note the good agreement between the two methods. The radiation angle for Mic. #3 was thrown out because it did not agree with the others.

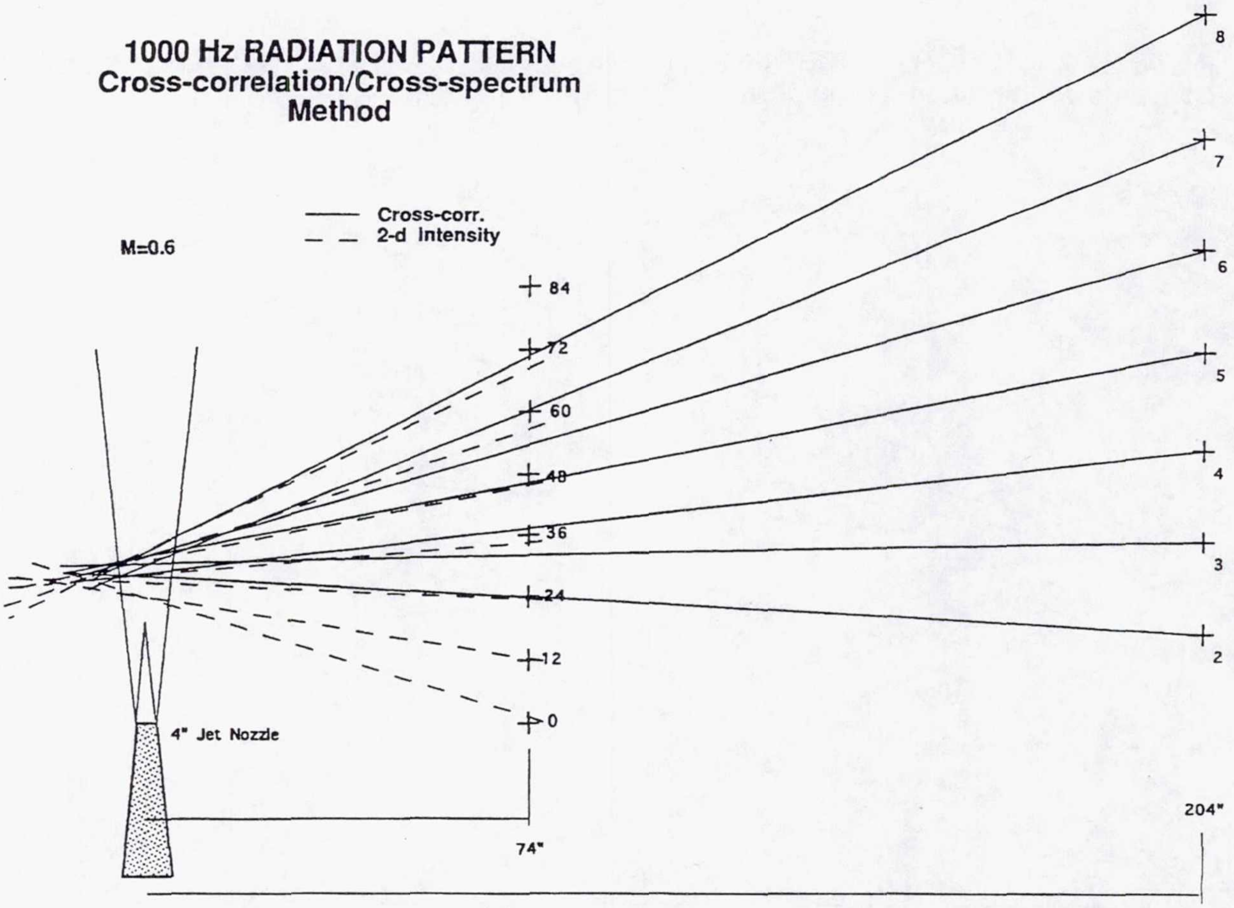

This figure shows the radiation pattern given by the method for a Mach number of 0.6 and a frequency of 1000 Hz. There is excellent agreement between the results using both the cross-correlation/spectrum technique and 2-d intensity techniques.

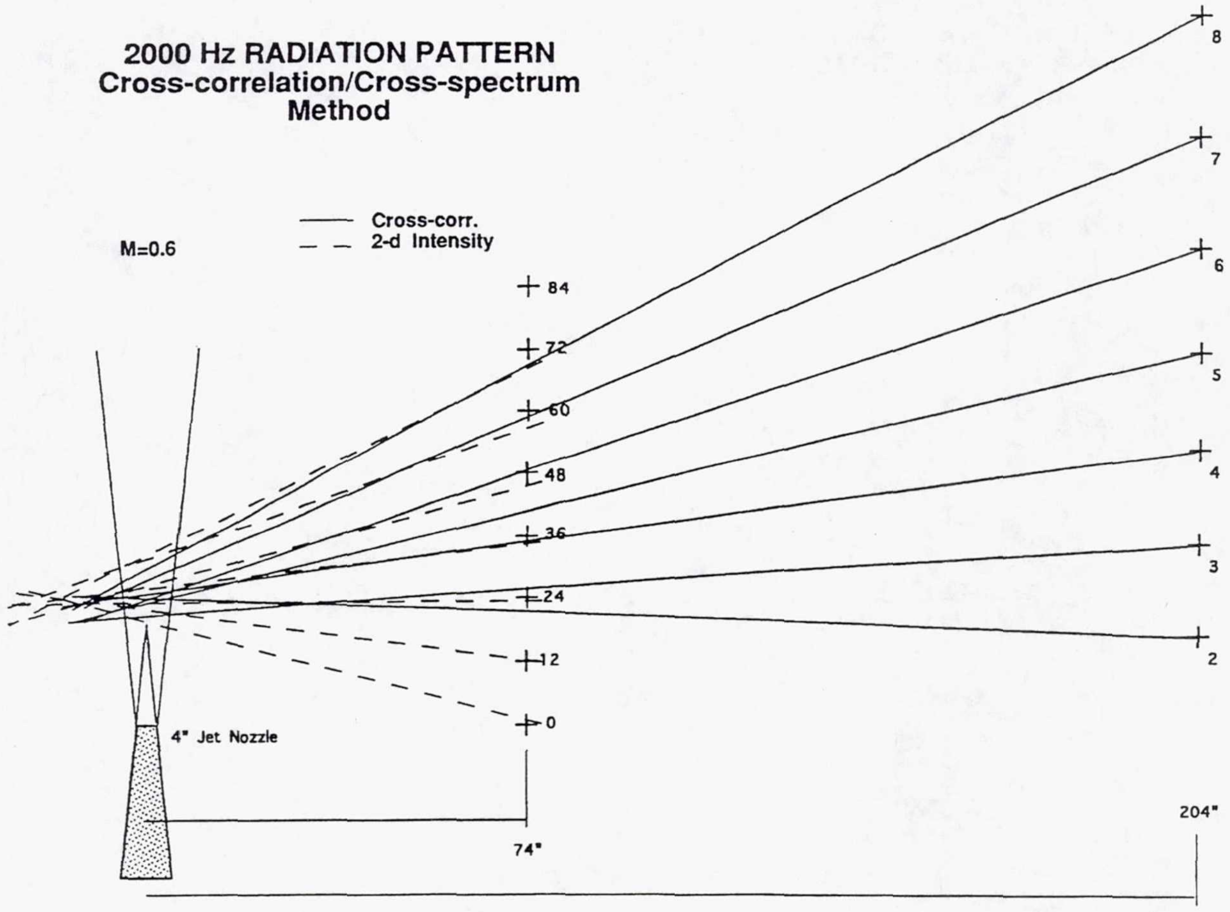

This figure shows the radiation pattern given by the method for a Mach number of 0.6 and a frequency of 2000 Hz. The agreement between the two methods is good but not quite as good as for the lower frequencies.

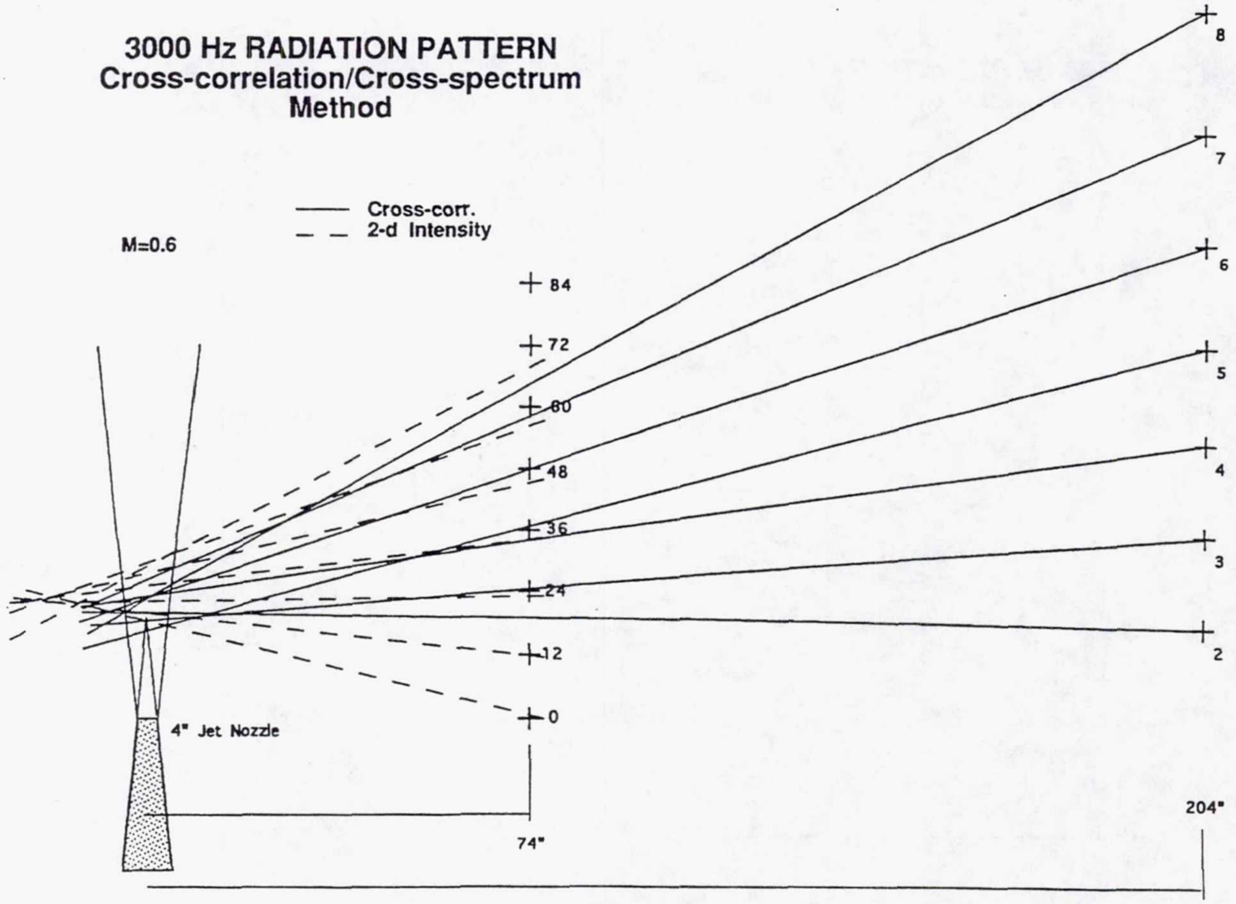

This figure shows the radiation pattern given by the method for a Mach number of 0.6 and a frequency of 3000 Hz. Again, the agreement is not as good as for the 500 and 1000 Hz cases but is still quite good.

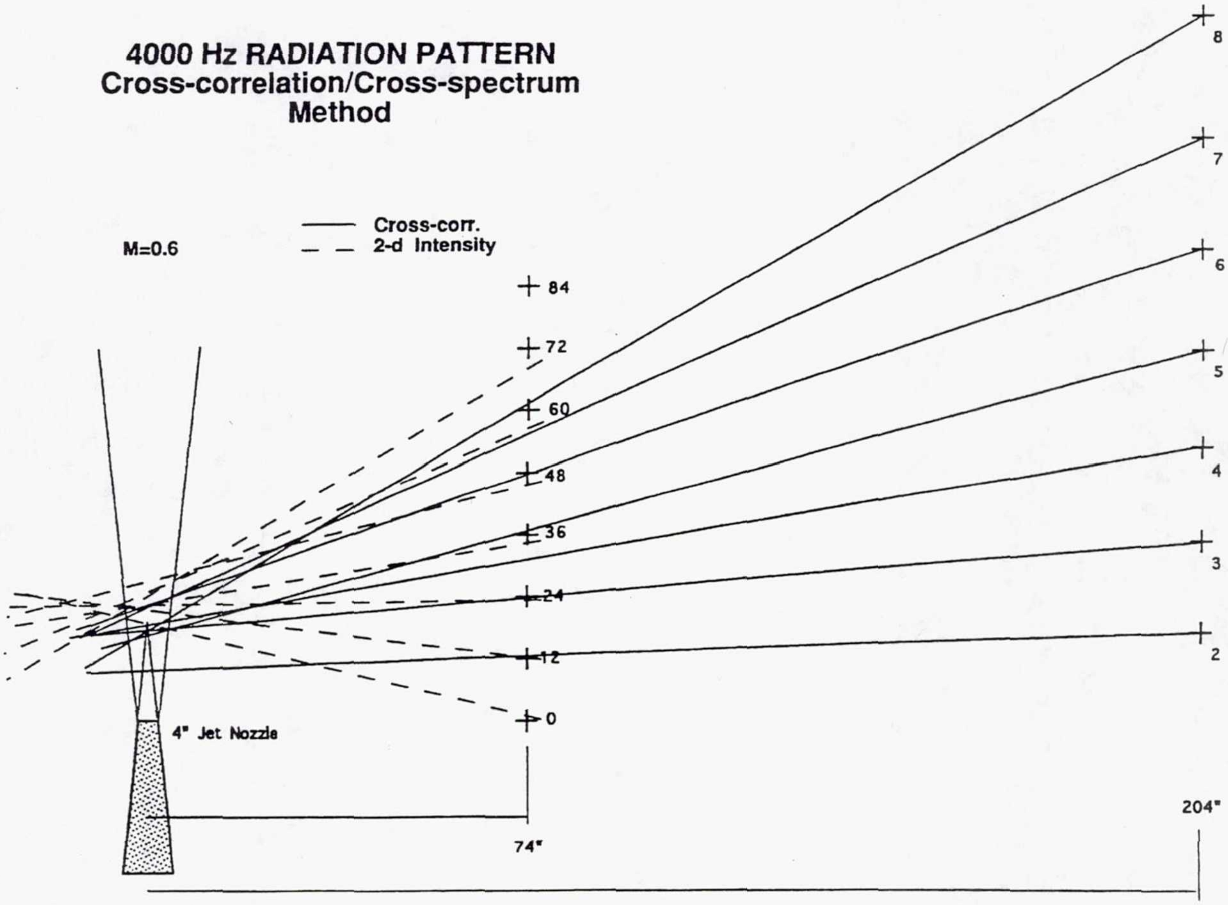

Finally, the radiation pattern given by the method for a Mach number of 0.6 and a frequency of 4000 Hz is shown. Except for a few radiation angles, the agreement between the two methods is very good and the location agreement on the source centroid location is excellent.

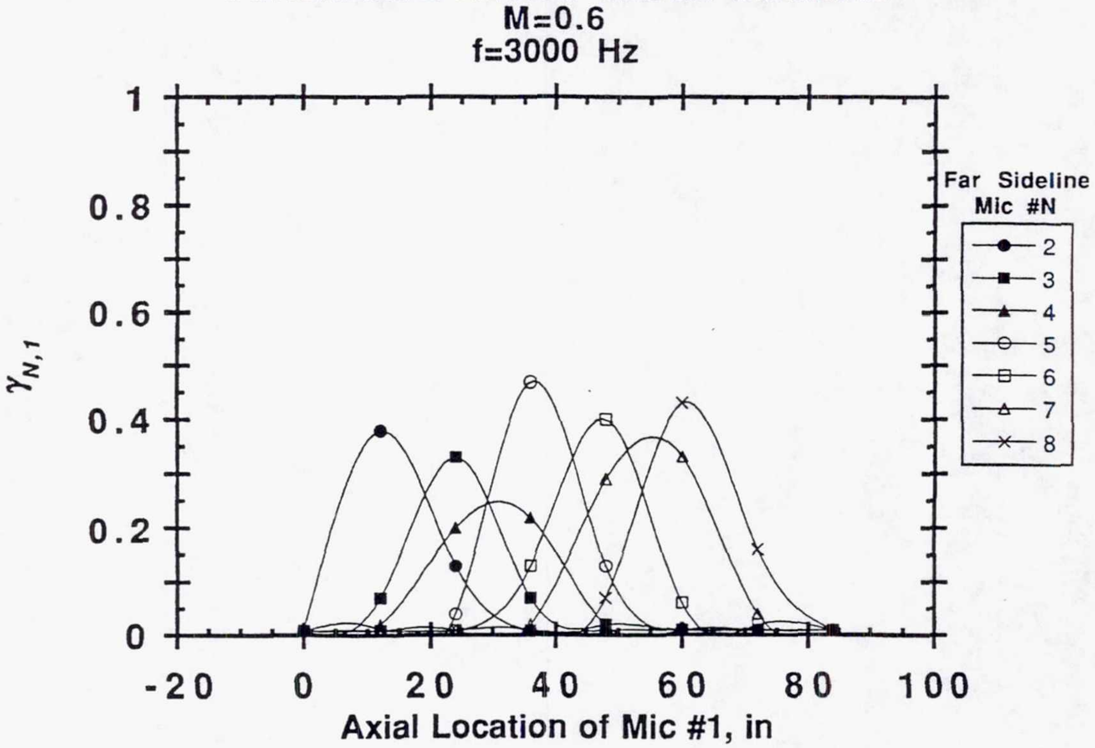

The inaccuracy of the higher frequency radiation angle results is due to the lower coherence values as shown in this plot. The lower coherence values decrease the number of points used in the curve fit thereby reducing the accuracy of the maximum coherence location prediction. This source of error can be overcome by increasing the spatial resolution along the close sideline so that more points may be used in the curve fit.

COMPARISON WITH PUBLISHED DATA

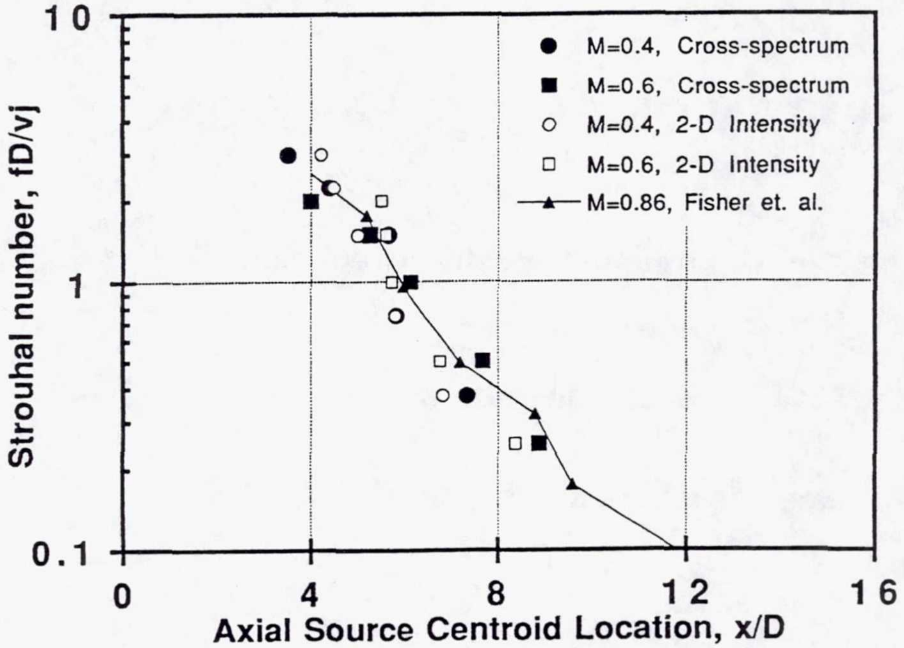

The variation of axial source location with Strouhal number is shown for the two different methods at two different Mach numbers. Also shown is the corresponding data gathered by Fisher et. al. using the polar correlation technique at a Mach number of 0.86. The agreement among the cross-correlation/spectrum technique, 2-d Intensity method and the polar correlation technique is excellent, validating the results of the former two methods.

EXTRAPOLATION TO FAR FIELD

- Cross-correlation/spectrum Technique Gives
  - Source Location
  - Radiation Pattern
- Need Levels Measured at Sideline

To extrapolate the results to far field, it is necessary to have a sound pressure level associated with each radiation angle. Combined with the source location,the extreme far field acoustics may then be determined.

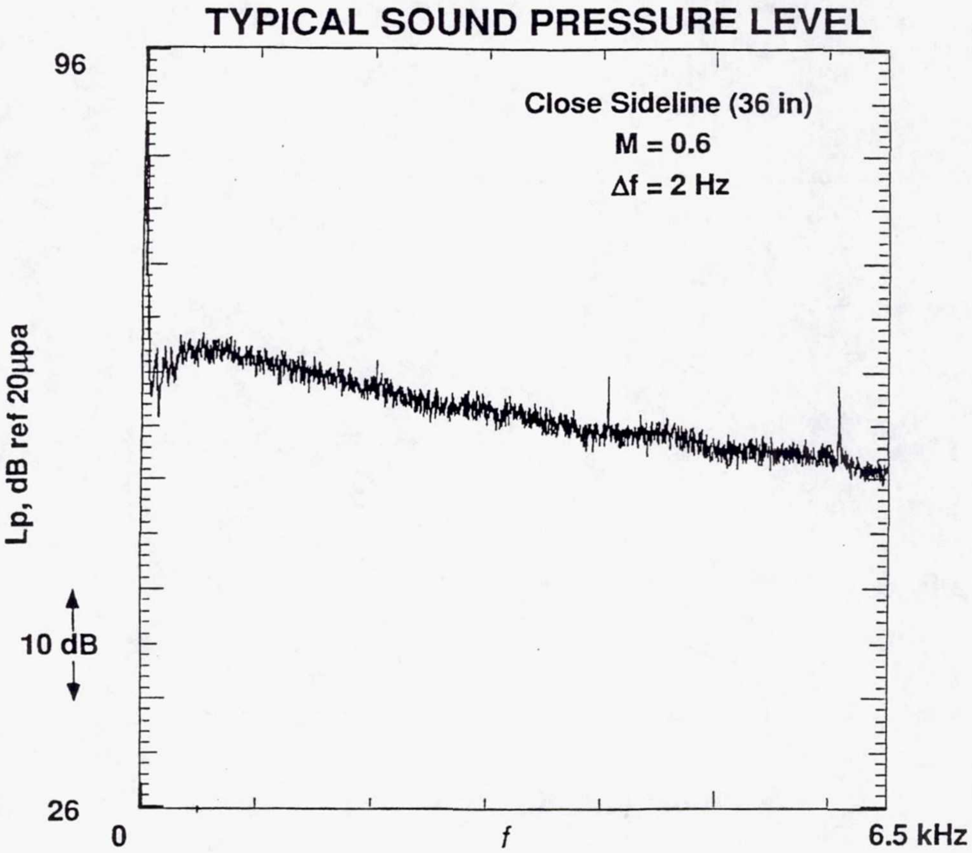

Opposite are typical sound pressure levels as a function of frequency for a microphone from each sideline.

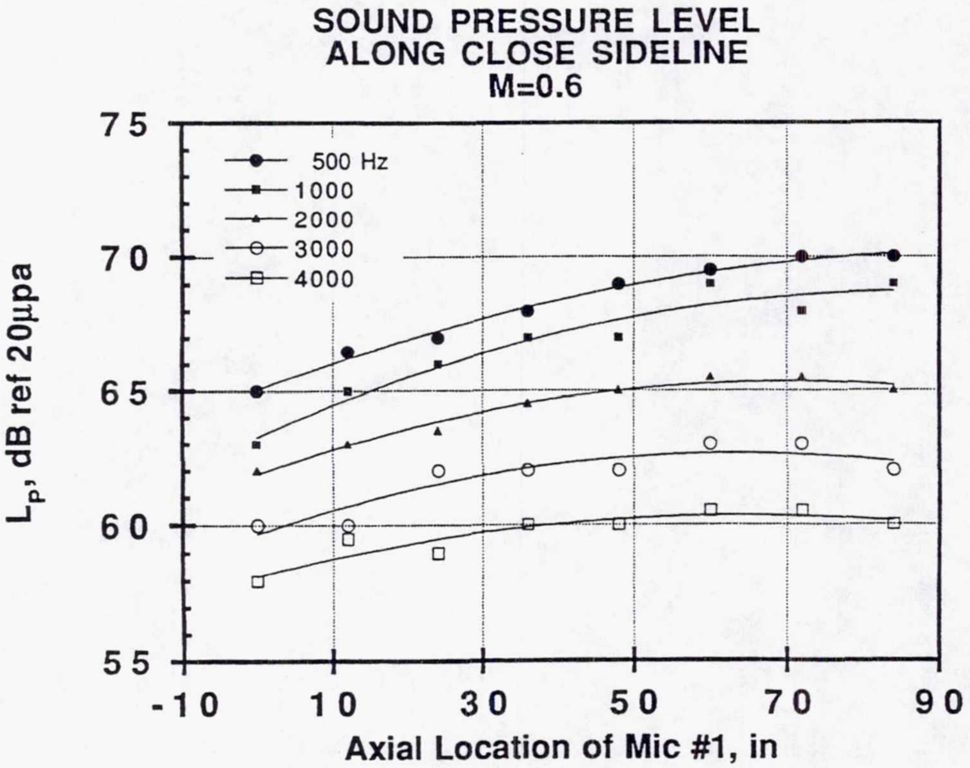

The sound pressure level variations along the close sideline are shown as a function of frequency. The data are fit with a polynomial curve to show the general trends. Note that as the frequency decreases, the location of the maximum sound pressure level moves downstream indicating a greater radiation angle or downstream shift of source centroid location.

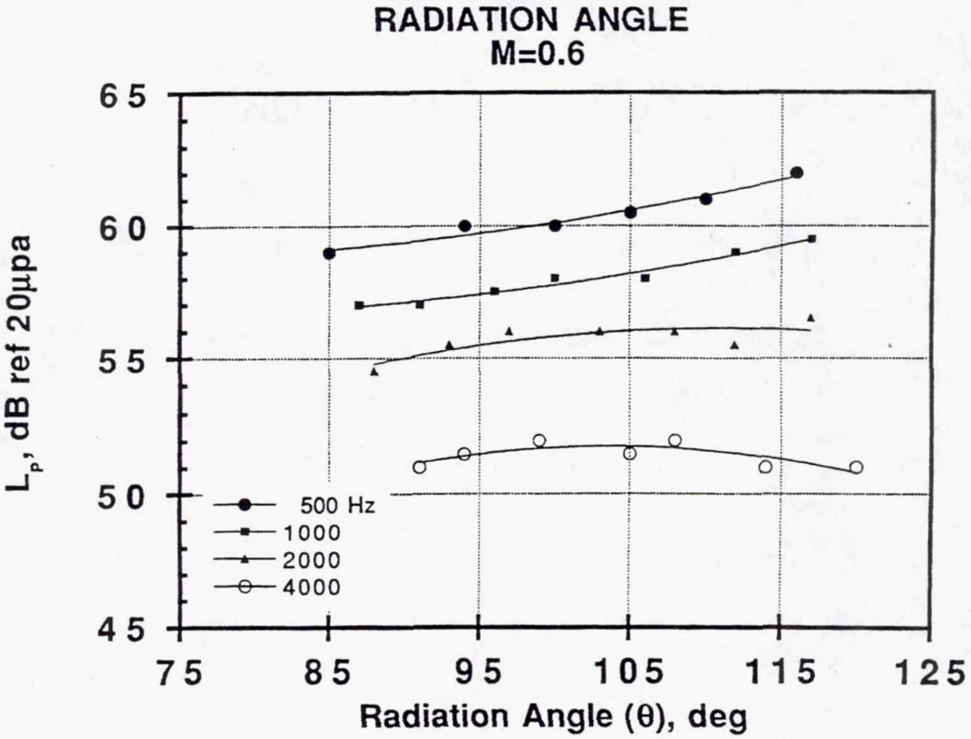

The sound pressure level variations with radiation angle are shown as a function of frequency. Again the data are fit with curves to show the general trends. Notice that as the frequency decreases, the angle of maximum sound pressure level increases showing that the lower frequencies tend to radiate most of their energy further downstream than the higher frequencies.

IMPROVEMENTS / FUTURE WORK

- **Increase Spatial Resolution**
- **Time Delay and Phase Requires**
  - **Phase Calibration**
  - **Measurement of Ambient Temp**
- **Test in Flow**

Currently, the method shows encouraging results. A way to improve the results is to increase the spatial resolution along the sideline being varied.

Another way to perhaps improve the accuracy of the method is to use the time delays given by the cross-correlation measurements and to use the phase information contained in the cross-spectrum measurements. To obtain useful results from this information, however, would require phase calibrations between the correlated microphones as well as the measurement of the ambient temperature.

The next step in the development of this method is to test it in a moving acoustic medium.

CONCLUSIONS

Cross-Corr/Spectrum	-vs-	2-D Intensity
Not Dependant on Nozzle		**Not Dependant on Nozzle**
Indirect Method		**Direct Method**
Not Frequency Limited		**Frequency Limited**
Many Mics. Required		**Few Mics. Required**
Time Averages Not Extensive		**Time Averages Extensive**
No Phase Calibration		**Phase Calibration**
Can Use in Wind		**Difficult to Use in Wind**

In conclusion, this page lists some of the advantages and disadvantages of both the cross-correlation/spectrum and 2-d intensity techniques. It may be beneficial to use both methods in conjunction with theoretical results so that each of their advantages may be used to help solve the very difficult problem of obtaining general jet noise source radiation fields.

REPORT DOCUMENTATION PAGE

Form Approved
OMB No. 0704-0188

1. AGENCY USE ONLY (*Leave blank*)	**2. REPORT DATE** September 1999	**3. REPORT TYPE AND DATES COVERED** Conference Publication

4. TITLE AND SUBTITLE

First NASA/Industry High Speed Research Program Nozzle Symposium

5. FUNDING NUMBERS

WU–537–05–23–00

6. AUTHOR(S)

Mary Jo Long-Davis

7. PERFORMING ORGANIZATION NAME(S) AND ADDRESS(ES)

National Aeronautics and Space Administration
John H. Glenn Research Center at Lewis Field
Cleveland, Ohio 44135–3191

8. PERFORMING ORGANIZATION REPORT NUMBER

E–11937

9. SPONSORING/MONITORING AGENCY NAME(S) AND ADDRESS(ES)

National Aeronautics and Space Administration
Washington, DC 20546–0001

10. SPONSORING/MONITORING AGENCY REPORT NUMBER

NASA CP—1999-209423

11. SUPPLEMENTARY NOTES

Project Manager, Mary Jo Long-Davis, High Speed Systems Office, NASA Glenn Research Center, organization code 2300, (216) 433–8708.

12a. DISTRIBUTION/AVAILABILITY STATEMENT

Unclassified - Unlimited
Subject Category: 07 Distribution: Nonstandard

This publication is available from the NASA Center for AeroSpace Information, (301) 621–0390.

12b. DISTRIBUTION CODE

13. ABSTRACT *(Maximum 200 words)*

The First High Speed Research (HSR) Nozzle Symposium was hosted by NASA Lewis Research Center on November 17-19, 1992 in Cleveland, Ohio, and was sponsored by the HSR Source Noise Working Group. The purpose of this symposium was to provide a national forum for the government, industry, and university participants in the program to present and discuss important low noise nozzle research results and technology issues related to the development of appropriate nozzles for a commercially viable, environmentally compatible, U.S. High-Speed Civil Transport. The HSR Phase I research program was initiated in FY90 and is approaching the first major milestone (end of FY92) relative to an initial FAR 36 Stage III nozzle noise assessment. Significant research results relative to that milestone were presented. The opening session provided a brief overview of the Program and status of the Phase II plan. The next five sessions were technically oriented and highlighted recent significant analytical and experimental accomplishments. The last Session included a panel discussion by the Session Chairs, summarizing the progress seen to date and discussing issues relative to further advances in technology necessary to achieve the Program Goals. Attendance at the Symposium was by invitation only and included only industry, academic, and government participants who are actively involved in the High-Speed Research Program. The technology presented in this meeting is considered commercially sensitive.

14. SUBJECT TERMS

Nozzle; HSR; Low noise

15. NUMBER OF PAGES

771

16. PRICE CODE

A99

17. SECURITY CLASSIFICATION OF REPORT	**18. SECURITY CLASSIFICATION OF THIS PAGE**	**19. SECURITY CLASSIFICATION OF ABSTRACT**	**20. LIMITATION OF ABSTRACT**
Unclassified	Unclassified	Unclassified	

NSN 7540-01-280-5500

Standard Form 298 (Rev. 2-89)
Prescribed by ANSI Std. Z39-18
298-102